Complexity

Advanced Control and Optimization for Complex Energy Systems

Lead Guest Editor: Chun Wei
Guest Editors: Xiaoqing Bai, Taesic Kim, and Jianwu Zeng

Advanced Control and Optimization for Complex Energy Systems

Complexity

Advanced Control and Optimization for Complex Energy Systems

Lead Guest Editor: Chun Wei
Guest Editors: Xiaoqing Bai, Taesic Kim, and Jianwu Zeng

Contents

Contents

Hindawi
Complexity
Volume 2020, Article ID 5908102, 3 pages
https://doi.org/10.1155/2020/5908102

Editorial

Advanced Control and Optimization for Complex Energy Systems

Chun Wei,[1] **Xiaoqing Bai**,[2] **and Taesic Kim**[3]

[1]*Zhejiang University of Technology, Hangzhou, China*
[2]*Guangxi University, Nanning, China*
[3]*Texas A&M University-Kingsville, Kingsville, USA*

Correspondence should be addressed to Chun Wei; cwei@huskers.unl.edu

Received 31 January 2020; Accepted 1 February 2020; Published 10 March 2020

The application of renewable energies such as wind and solar has become an inevitable choice for many countries in order to achieve sustainable and healthy economic development [1]. However, due to the intermittent characteristics of renewable energy, the issue with integrating a larger proportion of renewable energy into the grid becomes prominent. Currently, an energy system with weak coordination capability seriously affects the flexibility of power system operation [2]. As a result, this has led to the development of an effective way to integrate high-proportion renewable energy by developing multienergy systems including wind, solar, thermal, and energy storage to allow for the integration and coordination of different energy resources [3]. The major challenge of the multienergy system is its complexity with multispatial and multitemporal scales. Compared with the traditional power system, control and optimization of the complex energy system become more difficult in terms of modeling, operation, and planning [4, 5]. The main purpose of the complex energy system is to coordinate the operation with various distributed energy resources (DERs), energy storage systems, and power grids to ensure its reliability, while reducing the operating costs and achieving the optimal economic benefits. A total of 58 papers were received from different research fields. After the review process, 29 papers were accepted for publication (around 50% of acceptance ratio).

These papers can be organised in four groups. The focus of the first group of articles is control methods. The paper titled "Finite-Time Observer-Based Adaptive Control of Switched System with Unknown Backlash-Like Hysteresis" by G. Sun and Y. Xu investigates a finite-time observer problem for a class of uncertain switched nonlinear systems in strict-feedback form. The paper by G. Wang et al. entitled "A Decentralized Energy Flow Control Framework for Regional Energy Internet" proposed a decentralized energy flow control framework for regional energy internet. The paper "Finite Control Set Model Predictive Control for Complex Energy System with Large-scale Wind Power" by Y.-W. Shen et al. proposed a strategy to optimize a value function with errors of current magnitudes to predict switching status of the grid-side converter. The paper "Neural Network Identification and Sliding Mode Control for Hysteresis Nonlinear System with Backlash-Like Model" by R. Liu and X. Gao proposed a new neural network sliding mode control for a backlash-like hysteresis nonlinear system. The paper "Tracking Control for Hydrogen Fuel Cell Systems in Zero-Emission Ferry Ships" by M. Khooban et al. proposed a new modified backstepping controller to stabilize the microgrid voltage and currents. The paper "Steady-State Analysis and Output Voltage Minimization Based Control Strategy for Electric Springs in the Smart Grid with Multiple Renewable Energy Sources" by Y. Zou et al. presented a general steady-state analysis and minimal compensating voltage control scheme for the second generation of electric springs in the power system with substantial penetration of intermittent renewable energy sources. The paper "Boost Converters' Proximate Constrained Time-Optimal Sliding Mode Control Based on Hybrid Switching Model" by A. Taheri et al. proposed a proximate constrained time-optimal sliding mode controller based on the hybrid dynamical model of the converter and geometrical representation of its corresponding vector fields. The paper "Adaptive Fixed-Time Sliding Mode Control for Uncertain Twin-Rotor System with Experimental Validation" by L. Shen et al.

proposed an adaptive fixed-time control scheme for twin-rotor systems subject to the inertia uncertainties and external disturbances. The paper "Frequency Regulation and Coordinated Control for Complex Wind Power Systems" by C. Guo et al. presented a variable coefficient coordinated primary frequency regulation scheme for a synchronous generator and doubly fed induction generator. The paper "Homeomorphism Mapping Based Neural Networks for Finite Time Constraint Control of a Class of Nonaffine Pure-Feedback Nonlinear Systems" by J. Zhang et al. proposed a finite time adaptive law for training weights of neural networks. The paper "Variable Speed Pump Storage for the Mitigation of SSR in Power System with Wind Generation" by F. Ye et al. presented a new method of using a doubly fed induction machine based system of a variable speed pumped storage plant to mitigate SSR in the power system with high penetration of wind generation.

The second group of publications is about optimization methods. The paper "A Competitive Swarm Optimizer-Based Technoeconomic Optimization with Appliance Scheduling in Domestic PV-Battery Hybrid Systems" by B. Wang et al. investigated a technoeconomic optimization problem to minimize energy cost, maximize renewable energy penetration, and increase user satisfaction over a finite horizon. The paper "A Selection Hyper-Heuristic Algorithm for Multi-objective Dynamic Economic and Environmental Load Dispatch" by L. Yang et al. presented dynamic economic and environmental load dispatch models for a system consisting of thermal units, wind power generators, photovoltaic generators, and energy storage. The paper "An Optimal Allocation Strategy for Multienergy Networks Based on Double-Layer Nondominated Sorting Genetic Algorithms" by M. Mou et al. proposed an optimal allocation strategy to optimize the allocation of distributed generation and improve the system economy. The paper "Complementary Configuration and Optimal Energy Flow of CCHP-ORC Systems Using a Matrix Modeling Approach" by W. Huang et al. presented a matrix modeling approach to establish a mathematical model of the CCHP-ORC system. The paper "Joint Optimization of Energy Conservation and Migration Cost for Complex Systems in Edge Computing" by X. Xu et al. designed a balanced resource scheduling method for trade-offs between virtual machine migration cost and energy consumption of virtual machine migrations for edge server management. The paper "Convergence Time Calculation for Supertwisting Algorithm and Application for Nonaffine Nonlinear Systems" by J. Zhang et al. proposed an accurate convergence time of the supertwisting algorithm to build up a framework for non-affine nonlinear systems' finite-time control. The paper "Metaheuristic Optimization of Fractional Order Incremental Conductance (FO-INC) Maximum Power Point Tracking (MPPT)" by H. Ammar et al. proposed a method named FO-INC to control the output voltage of the PV arrays to obtain maximum power point tracking. The paper "A repeatable Optimization for Kinematic Energy System with Its Mobile Manipulator Application" by Y. Kong et al. proposed a special kind of repeatable optimization for kinematic energy minimization based on terminal-time Zhang neural network with finite-time convergence. The paper "A Survey on Optimal Control and Operation of Integrated Energy Systems" by C. Wei et al. reviewed the optimal control and operation behavior of the integrated energy system.

The third group of publications is about performance analysis. The paper "Available Transfer Capability Calculation Constrained with Small-Signal Stability Based on Adaptive Gradient Sampling" by P. Li et al. proposed a sequential quadratic programming method combined with gradient sampling in a dual formulation. The paper "Investigation of Var Compensation Schemes in Unbalanced Distribution Systems" by Y. Huang et al. demonstrated and analyzed the limitation of traditional Var compensation methods in voltage regulation with unbalanced PV power integration. The paper "Power Grid Fault Diagnosis Method Using Intuitionistic Fuzzy Petri Nets Based on Time Series Matching" by M. Tan et al. proposed a fault diagnosis method using intuitionistic fuzzy petri nets to improve the reliability of power grid fault diagnosis. The paper "Performance Analysis of Reheat Steam Temperature Control System of Thermal Power Unit Based on Constrained Predictive Control" by X. Li et al. analyzed the performance of the reheat temperature control system according to the data obtained based on the constrained predictive control algorithm. The paper "Performance Analysis for the Magnetically Coupled Resonant Wireless Energy Transmission System" by J. Liu et al. found the exact parameters of system optimization and verified them by simulation and experiments. The paper "Harmonic Modeling and Experimental Validation of the Converters of DFIG-Based Wind Generation System" by Y. Shen et al. studied the relation between the output current and the harmonic source at grid-side and rotor-side converters based on their control features in the DFIG system.

The last group of publications is related to planning, prediction, and multiagent system. The paper "Planning of Cascade Hydropower Stations with the Consideration of Long-Term Operations under Uncertainties" by C. Wang et al. developed an effective approach that deals with the long-term stochasticity due to the long-lasting effects of the location selections. The paper "Parallel LSTM-Based Regional Integrated Energy System Multienergy Source-Load Information Interactive Energy Prediction" by B. Wang et al. proposed an energy prediction strategy for multienergy information interaction in regional integrated energy systems from the perspective of horizontal interaction and vertical interaction. The paper "Sign-Consensus of Linear Multiagent Systems under a State Observer Protocol" by W. Diao et al. reconstructed the information of the agents' states and proposed a state observer-type sign-consensus protocol.

Conflicts of Interest

The Editors declare that they have no conflicts of interest regarding the publication of this Special Issue.

Acknowledgments

This work was supported by the National Natural Science Foundation of China under Grant nos. 51807179, 51777193,

and 51967001. We would like to thank Jianwu Zeng for his participation and support in managing this special issue.

Chun Wei
Xiaoqing Bai
Taesic Kim

References

[1] F. Cheng, L. Qu, W. Qiao, C. Wei, and L. Hao, "Fault diagnosis of wind turbine gearboxes based on DFIG stator current envelope analysis," *IEEE Transactions on Sustainable Energy*, vol. 10, no. 3, pp. 1044–1053, 2019.

[2] P. Singh and B. Khan, "Smart microgrid energy management using a novel artificial shark optimization," *Complexity*, vol. 2017, Article ID 2158926, 22 pages, 2017.

[3] C. Wei, M. Benosman, and T. Kim, "Online parameter identification for state of power prediction of lithium-ion batteries in electric vehicles using extremum seeking," *International Journal of Control, Automation and System*, vol. 17, no. 11, pp. 2906–2916, 2019.

[4] Q. Chen, H. Shi, and M. Sun, "Echo state network based backstepping adaptive iterative learning control for strict-feedback systems: an error-tracking approach," *IEEE Transactions on Cybernetics*, pp. 1–14, 2019.

[5] Q. Chen, S. Xie, M. Sun, and X. He, "Adaptive nonsingular fixed-time attitude stabilization of uncertain spacecraft," *IEEE Transactions on Aerospace and Electronic Systems*, vol. 54, no. 6, pp. 2937–2950, 2018.

Hindawi
Complexity
Volume 2020, Article ID 3912717, 10 pages
https://doi.org/10.1155/2020/3912717

Research Article

Available Transfer Capability Calculation Constrained with Small-Signal Stability Based on Adaptive Gradient Sampling

Peijie Li, Ling Zhu, Xiaoqing Bai, and Hua Wei

School of Electrical Engineering, Guangxi University, Nanning 530004, China

Correspondence should be addressed to Peijie Li; lipeijie@gxu.edu.cn

Received 18 June 2019; Revised 12 January 2020; Accepted 14 January 2020; Published 11 February 2020

Academic Editor: Oveis Abedinia

Due to the nonsmoothness of the small-signal stability constraint, calculating the available transfer capability (ATC) limited by small-signal stability rigorously through the nonlinear programming is quite difficult. To tackle this challenge, this paper proposes a sequential quadratic programming (SQP) method combined with gradient sampling (GS) in a dual formulation. The highlighted feature is the sample size of the gradient changes dynamically in every iteration, yielding an adaptive gradient sampling (AGS) process. Thus, the computing efficiency is greatly improved owing to the decrease and the parallelization of gradient evaluation, which dominates the computing time of the whole algorithm. Simulations on an IEEE 10-machine 39-bus system and an IEEE 54-machine 118-bus system prove the effectiveness and high efficiency of the proposed method.

1. Introduction

ATC is determined by a number of operating limits such as thermal limit, voltage limit, and transient stability limit [1, 2]. As the power system interconnects sustainably and the renewable energy sources penetrate increasingly, small-signal stability becomes a more significant limiting factor of determining power transfer capabilities, which may cause the occurrence of low-frequency oscillation before reaching the power transmission limit determined by traditional constraints. Therefore, the calculation of ATC considering small-signal stability is a problem to be solved urgently. Due to the nonsmoothness of small-signal stability constraint, the calculation of ATC with small-signal stability constraint (SSSC-ATC) has become a challenge. For there is no common solution to this kind of problem, a few people have made some exploration of it.

Chung et al. [3] propose a numerical-sensitivity-based rescheduling method to calculate the ATC subject to the small-signal stability constraint under a set of contingencies. The method is easy to handle; however, it cannot guarantee the convergency because it ignores the nonsmoothness of small-signal stability constraint calculation essentially.

Othman and Busan [4] introduce a straightforward approach based on a normalized participation factor to identify critical generators for rescheduling so that a secure power transfer during the outage of critical is calculated. Compared with [3], its major contribution is that it formulates a closed-form of eigenvalue sensitivity with respect to power generation in terms of participation factors. However, the formulation makes a significant approximation as the derivative for power generation with respect to rotor angle is formulated based on a simplified two-order machine model. Besides, it does not address the nonsmoothness of small-signal stability in ATC calculation.

Recently, Li et al. [5] propose an SQP method combined with GS to solve the optimal power flow problem with a nonsmooth small-signal stability constraint (SSSC-OPF). The GS procedure samples the gradients of the nonsmooth constraint within the neighborhood to yield a subgradient, thereby ensuring that good search directions are produced in nonsmooth regions. It can guarantee the SSSC-OPF is globally and efficiently convergent to stationary points.

Carrying on its idea, this paper makes a step forward in SSSC-ATC calculation field with general applicability and practical significance. The main contributions of our work includes three aspects. Firstly, an AGS process is proposed, in

which the sample size of the gradient changes dynamically during every iteration. Thus, the quantity of gradient evaluation is greatly decreased, which dominates the computing time of the whole algorithm, showing the superiority in sampling efficiency compared with SQP-GS [5]. Secondly, the use of a dual formulation of the QP subproblem clearly reflects the idea of gradient sampling when solving the nonsmooth constraints. Thirdly, as the sampling process is independent and random, a process of parallel sampling is applied to the simulation, greatly reducing the time-consumed by the algorithm which is shown in the test of IEEE 54-machine 118-bus system.

Section 2 describes a model of the ATC calculation with a small-signal stability constraint. The SQP-AGS algorithm applied to the proposed SSSC-ATC model is discussed in Section 3 in detail. Section 4 is case studies, and the conclusion is drawn in Section 5.

2. The Model of ATC Calculation with a Small-Signal Stability Constraint

Mathematically, ATC is defined as

$$\mathrm{ATC} = \mathrm{TTC} - \mathrm{TRM} - \mathrm{CBM} - \mathrm{ETC}, \tag{1}$$

where TTC is the total transfer capacity over the interconnected transmission network. TRM is the transmission reliability margin. CBM is the capacity benefit margin, and ETC is the existing transmission commitments. TRM and CBM are usually considered as constants or a percentage of TTC, and ETC can be easily obtained as the sum of the existing commitments. Thus, the calculation of TTC is the key to obtain ATC. An optimal power flow (OPF) model is formulated to the conventional ATC calculation [6]. Based on the model, the SSSC-ATC includes the following.

(1) The objective value:

$$\min f(\bullet) = -\sum_{i,j\in S_{\mathrm{link}}} P_{ij}, \tag{2}$$

where S_{link} is the set of tie lines between the source side and the receiving side. P_{ij} indicates the active power of the tie line (i, j), which is defined as $P_{ij} = V_i^2 Y_{ij}\cos\alpha_{ij} - V_i Y_{ij} V_j \cos\delta_{ij}$. V_i represents the voltage amplitude of the ith bus. Y_{ij} and α_{ij} are the admittance amplitude and the phase angle of line (i, j), respectively. $\delta_{ij} = \theta_i - \theta_j - \alpha_{ij}$, in which θ_i is the phase angle of the ith bus.

(2) For all buses in system denoted as collection S_{B}, the power flow equations for bus $i \in S_{\mathrm{B}}$ is

$$\begin{aligned} P_{\mathrm{G}i} - P_{\mathrm{L}i} - \sum_{j\in i} V_i Y_{ij} V_j \cos\delta_{ij} = 0, \\ Q_{\mathrm{G}i} - Q_{\mathrm{L}i} - \sum_{j\in i} V_i Y_{ij} V_j \sin\delta_{ij} = 0, \end{aligned} \tag{3}$$

where $P_{\mathrm{G}i}$ is the active power output of the ith generator, $Q_{\mathrm{G}i}$ is the reactive power output of the ith generator correspondingly, and $P_{\mathrm{L}i}$ and $Q_{\mathrm{L}i}$ are the active power load and the reactive power load of the ith bus, respectively.

(3) Technical constraints include

$$\begin{aligned} \underline{V}_i \le V_i \le \overline{V}_i, \quad & i \in S_{\mathrm{B}}, \\ \underline{P}_{\mathrm{G}i} \le P_{\mathrm{G}i} \le \overline{P}_{\mathrm{G}i}, \quad & i \in S_{\mathrm{G}}, \\ \underline{Q}_{\mathrm{G}i} \le Q_{\mathrm{G}i} \le \overline{Q}_{\mathrm{G}i}, \quad & i \in S_{\mathrm{G}}, \\ S_{ij}^2 \le \overline{S}_{ij}^2, \quad & (i, j) \in S_{\mathrm{line}}, \end{aligned} \tag{4}$$

where S_{G} is the collection of all the generator buses and S_{line} is the collection of all lines. S_{ij} represents the apparent power of line (i, j), and $\overline{(\cdot)}$ and $\underline{(\cdot)}$, respectively, denote the upper and lower limits.

(4) Initial equations which link the variables of the conventional ATC with the state and algebraic variables of the small-signal stability model:

$$\mathbf{S}_I(\mathbf{P}_{\mathrm{G}}, \mathbf{Q}_{\mathrm{G}}, \mathbf{V}, \boldsymbol{\theta}, \mathbf{x}) = 0, \tag{5}$$

where $\mathbf{x}$ is the state variable vector including the rotor angle vector $\boldsymbol{\delta}$, the d-axis and q-axis component vectors of the internal voltage are $\mathbf{E}'_d$ and $\mathbf{E}'_q$, the d-axis and q-axis component vectors of the internal current are $\mathbf{I}'_d$ and $\mathbf{I}'_q$, and the excitation output voltage vector is $\mathbf{E}_{fd}$.

(5) Small-signal stability constraint:

$$\eta(\mathbf{P}_{\mathrm{G}}, \mathbf{Q}_{\mathrm{G}}, \mathbf{V}, \boldsymbol{\theta}, \mathbf{x}) \le \overline{\eta}, \tag{6}$$

where η is the spectral abscissa of the system, which is the largest one of the real parts of the system's eigenvalues λ. $\overline{\eta}$ is an upper limit of spectral abscissa to represent a stability margin, which can be determined based on offline stability studies.

The spectral abscissa η in small-signal stability constraint is a nonsmooth function [7]. Thus, it failed to solve it by the interior point method (IPM), which is the workhorse in solving smooth constrained optimization problems. Fortunately, the spectral abscissa function has been proved to be locally Lipschitz and continuously differentiable on open dense subsets $\mathscr{D}$ of $\mathbb{R}^n$, which means that it is continuously almost everywhere and its gradient can be easily obtained where it is defined by calculating spectral abscissa derivative.

3. A Sequential Quadratic Programming Algorithm Combined with Gradient Sampling

There is no general method to solve the optimization problem with nonsmooth nonlinear constraints these years. Recently, a gradient sampling (GS) method is proposed for minimizing an objective function that is locally Lipschitz

continuous on an open dense subset of $\mathbb{R}^n$, which makes a step forward in nonsmooth optimization field [8]. Curtis and Overton [9] further generalized this idea to the optimization problems with nonsmooth nonlinear constraints or objective function by introducing the SQP algorithm framework.

3.1. The Gradient Sampling Theory with Unconstrained Minimization. The GS is basically a stabilized steepest descent algorithm. Considering an unconstrained optimization problem of the form

$$\min_{x\in\mathbb{R}^n} f(x), \tag{7}$$

defined in an open, dense subset $\mathscr{D} \in \mathbb{R}^n$, the objective function f is locally Lipschitz continuous which is nonsmooth and/or nonconvex.

As Figure 1 shows, the gradients of smooth points like x_1 and x_2 are easily obtained and unique. But it is unable to obtain the gradient at a nonsmooth point x_0. Moreover, the subgradient of nonsmooth point exists and is not unique. According to the definition,

$$\partial f := \{\mathbf{u} \mid f(x) \geq f(x_0) + \mathbf{u}^{\top}(x - x_0),\ \forall x \in \mathbb{R}^n \longrightarrow \mathbb{R}\}, \tag{8}$$

$\mathbf{u} \in \partial f$ denotes the subgradient at the nonsmooth point x_0. The set of subgradients $\mathbf{u}$ is called the subdifferential of f at x_0.

The GS technique approximates the subgradients of the objective function through the gradients sampled randomly near x_0 as

$$\partial f(x_0) \approx \left\{ \sum_{i\in P} y_{ki} \nabla f(x_{ki}) \,\middle|\, (\forall i:\ y_{ki} > 0) \wedge \sum_{i\in P} y_{ki} = 1 \right\}, \tag{9}$$

where P is the amount of the sampled gradients. Defining that $\mathbb{G}_k := \{\nabla f(x_{k0}), \nabla f(x_{k1}), \ldots, \nabla f(x_{kp})\}$ is a set of sampled gradients evaluating from a set of random and independent sampling points $\mathbf{X}_k := \{x_{k0}, x_{k1}, \ldots, x_{kp}\} \subset \mathbb{B}_\epsilon(x) \cap \mathscr{D}$ near x_0, where

$$\mathbb{B}_\epsilon(x_0) := \{x \mid \|x - x_0\| \leq \epsilon\}, \tag{10}$$

is the closed ball with a sample radius ϵ centered at x_0. The function f is locally Lipschitz and almost continuously differentiable.

The expression of $\partial f(x_0)$ is actually a convex hull of sampled gradients, which is the set of all convex combinations of the gradients. In the convex combination, each sampled gradient $\nabla f(x_{ki})$ in $\mathbb{G}_k$ is assigned a nonnegative weight or coefficient y_{ki} that all of them are summed to one. In such a way, the set of subgradients of x_0 is derived by changing y_{ki} into different values.

It is known that the conventional way to find the stationary point of a smooth function f is to find the point whose gradient values are zero, and the gradient value is generally taken as a key criterion to decide the descent direction of a smooth optimization problem. Corresponding to it, the Clarke stationarity is a criterion for determining the stationary point in a nonsmooth function, which points out that a point x_0 is Clarke stationary if

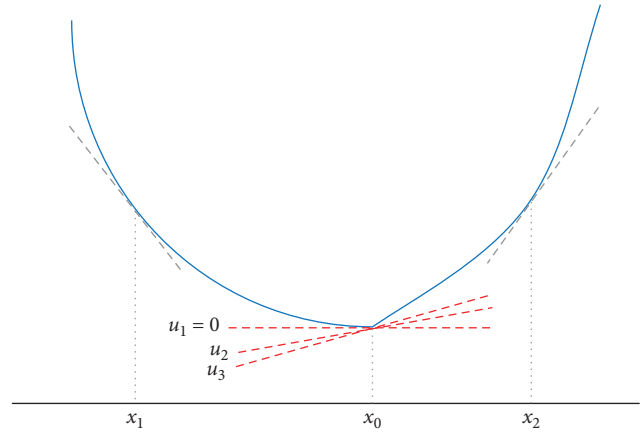

Figure 1: The subgradients of a nonsmooth point.

$$0 \in \partial f(x). \tag{11}$$

Figure 1 marks out a zero-valued subgradient $\mathbf{u}_1$ determining that x_0 is a Clarke stationary point. The Clarke stationarity is the key to the approach of finding a descent direction.

Hence, the descent direction of nonsmooth optimization can be determined as the subgradient which has the shortest distance to origin among all the subgradients. To find the subgradient $\mathbf{u}_k$ at the kth iteration, a following quadratic programming (QP) model is established:

$$\begin{aligned} \min_{y\in\mathbb{R}^{p+1}} \quad & \left\|\mathbb{G}_k \mathbf{y}_k\right\|_2^2, \\ \text{s.t.} \quad & \mathbf{e}^T \mathbf{y}_k = 1,\ \mathbf{y}_k \geq 0, \end{aligned} \tag{12}$$

where $\mathbf{y}_k$ is the coefficient vector at the kth iteration. The 2-norm in the objective function (12) represents the shortest distance from the set of subgradients to the origin. Solving this model, the coefficient vector $\mathbf{y}_k$ can be obtained. Then, the subgradient $\mathbf{u}_k$ can be calculated according to (9). The vector $\mathbf{d}_k = -\mathbf{u}_k / \|\mathbf{u}_k\|$ is defined as an approximate steepest descent direction. If $\|\mathbf{u}_k\| = 0$, the stationary point is found.

3.2. Sequential Quadratic Programming Algorithm Combined with Gradient Sampling for Nonsmoothly Constrained Optimization. Similar to the QP model used in the GS algorithm to calculate a search direction, a sequential quadratic programming algorithm (SQP) framework is built by centering on a QP subproblem to determine a search direction of nonsmooth constraint optimization problems. Generally, the limitation of the wide-used SQP algorithm lies in that it can only solve the smooth optimization problems but fail for nonsmooth optimization problems. However, combined with the GS algorithm, the SQP-GS algorithm can be used in in many nonsmooth problems even if the objective function is not locally Lipschitz continuous, which is basically in the following form:

$$\begin{aligned} \min_{\mathbf{x}} \quad & f(\mathbf{x}), \\ \text{s.t.} \quad & \mathbf{h}(\mathbf{x}) = 0, \\ & \mathbf{g}(\mathbf{x}) \le 0. \end{aligned} \tag{13}$$

The SQP-GS algorithm solves the model above in each iteration mainly by determining a search direction $\mathbf{d}_k$ centering on solving a regularized QP dual subproblem with the following form:

$$\min_{\mathbf{d}_k, \mathbf{y}_o, \mathbf{y}_h, \mathbf{y}_g} \quad \begin{bmatrix} -\mathbf{f}(\mathbf{x}_k) \\ -\mathbf{h}(\mathbf{x}_k) \\ \mathbf{h}(\mathbf{x}_k) \\ -\mathbf{g}(\mathbf{x}_k) \end{bmatrix}^{\top} \begin{bmatrix} \mathbf{y}_f \\ \mathbf{y}_h \\ \mathbf{y}_g \end{bmatrix} + \left[\mathbf{d}_k^{\top}, \mathbf{y}_f^{\top}, \mathbf{y}_h^{\top}, \mathbf{y}_g^{\top}\right] \mathbf{H}_k \begin{bmatrix} \mathbf{d}_k \\ \mathbf{y}_f \\ \mathbf{y}_h \\ \mathbf{y}_g \end{bmatrix}, \tag{14}$$

$$\text{s.t.} \quad \mathbf{H}_k \mathbf{d}_k + \nabla f\left(\mathbf{x}^f\right)^T \mathbf{y}_f + \begin{bmatrix} \nabla \mathbf{h}(\mathbf{x}^h) \\ -\nabla \mathbf{h}(\mathbf{x}^h) \\ \nabla \mathbf{g}(\mathbf{x}^g) \end{bmatrix}^{\top} \begin{bmatrix} \mathbf{y}_h \\ \mathbf{y}_g \end{bmatrix} = 0, \tag{15}$$

$$\forall \mathbf{x}^f \in \mathscr{B}_{\epsilon,k}^f, \forall \mathbf{x}^h \in \mathscr{B}_{\epsilon,k}^h, \forall \mathbf{x}^g \in \mathscr{B}_{\epsilon,k}^g,$$

$$\mathbf{e}^T \mathbf{y}_f = \rho, \tag{16}$$

$$\mathbf{e}^T \mathbf{y}_h = 1, \tag{17}$$

$$\mathbf{e}^T \mathbf{y}_g = 1, \tag{18}$$

$$\mathbf{y}_f \ge 0, \tag{19}$$

$$\mathbf{y}_h \ge 0, \tag{20}$$

$$\mathbf{y}_g \ge 0, \tag{21}$$

where ρ is a penalty parameter and $\mathbf{H}_k$ is the approximate Hessian of the Lagrangian optimization model. Incorporating the ideas from the GS algorithm, $\mathscr{B}_{\epsilon,k}^f$, $\mathscr{B}_{\epsilon,k}^h$, and $\mathscr{B}_{\epsilon,k}^g$ are sets of independent and identically distributed random points uniformly sampled from (10) with a sample size of p:

$$\mathscr{B}_{\epsilon,k}^f := \left\{\mathbf{x}_{k,0}^f, \mathbf{x}_{k,1}^f, \ldots, \mathbf{x}_{k,p}^f\right\}, \quad \text{where } \mathbf{x}_{k,0}^f := \mathbf{x}_k, \tag{22}$$

$$\mathscr{B}_{\epsilon,k}^{h^i} := \left\{\mathbf{x}_{k,0}^{h^i}, \mathbf{x}_{k,1}^{h^i}, \ldots, \mathbf{x}_{k,p}^{h^i}\right\}, \quad \text{where } \mathbf{x}_{k,0}^{h^i} := \mathbf{x}_k, \tag{23}$$

$$\mathscr{B}_{\epsilon,k}^{g^j} := \left\{\mathbf{x}_{k,0}^{g^j}, \mathbf{x}_{k,1}^{g^j}, \ldots, \mathbf{x}_{k,p}^{g^j}\right\}, \quad \text{where } \mathbf{x}_{k,0}^{g^j} := \mathbf{x}_k. \tag{24}$$

Consistent with the GS strategy, $\mathbf{y}_f = (y_{k,0}^f, y_{k,1}^f, \ldots, y_{k,p}^f)$, $\mathbf{y}_h = (y_{k,0}^{h^i}, y_{k,1}^{h^i}, \ldots, y_{k,p}^{h^i})$, and $\mathbf{y}_g = (y_{k,0}^{g^j}, y_{k,1}^{g^j}, \ldots, y_{k,p}^{g^j})$ are approximated minimum-norm elements of the subdifferential for objective function, equality and inequality constraints, respectively, which are obtained by solving the subproblem (14)–(21) at $\mathbf{x}_k$.

As a significant step to update $\mathbf{H}_k$ during each iteration, we introduce the limited-memory Broyden–Fletcher–Goldfrab–Shanno (L-BFGS) method which is an attempt to achieve fast convergence. We define

$$\begin{aligned} \mathscr{G}_k := & \sum_{n=1}^{p} y_{k,n}^f \nabla f\left(x_{k,n}^f\right) + \sum_{m=1}^{j} \sum_{n=1}^{p} y_{k,n}^{h^m} \nabla h\left(x_{k,n}^{h^m}\right) \\ & + \sum_{m=1}^{j} \sum_{n=1}^{p} y_{k,n}^{g^m} \nabla g\left(x_{k,n}^{g^m}\right), \end{aligned} \tag{25}$$

as the approximation of the minimum-norm element of the differential of (13) Lagrange function, relating to the choice of $\mathbf{H}_k$ made during each iteration. We initialize $\mathbf{H}_1 \longleftarrow \mathbf{I}$ at the 1th iteration and perform the update as

$$\mathbf{H}_l \longleftarrow \mathbf{H}_{l-1} - \frac{\mathbf{H}_{l-1} s_l s_l^{\top} \mathbf{H}_{l-1}^{\top}}{s_l^{\top} \mathbf{H}_{l-1} s_l} + \frac{y_l y_l^{\top}}{s_l^{\top} y_l}, \tag{26}$$

for $l = 2, \ldots, k$. Here, $s_l := x_l - x_{l-1}$ and $y_l := \mathscr{G}_l - \mathscr{G}_{l-1}$ are the displacements in $\mathbf{x}$ and in the approximations of the minimum-norm elements of the differential of (13) Lagrange function.

In order to reflect the iteration process, consider the penalty function with the penalty parameter ρ as the following form:

$$\phi_\rho(\mathbf{x}) := \rho f(\mathbf{x}) + \sigma(\mathbf{x}), \tag{27}$$

where $\sigma(\mathbf{x})$ is an infeasibility vector at the kth iteration defined as

$$\sigma_k(\mathbf{x}_k) := \begin{pmatrix} \left|\mathbf{h}(\mathbf{x}_k)\right| \\ \max\left(\mathbf{g}(\mathbf{x}_k), 0\right) \end{pmatrix}, \tag{28}$$

which is also an indicator in the step of parameter update.

Furthermore, let us define the local model

$$\begin{aligned} \mathbf{q}_\rho\left(\mathbf{d}_k; \mathbf{x}_k, \mathscr{B}_{\epsilon,k}, \mathbf{H}_k\right) := & \rho \max_{x \in \mathscr{B}_{\epsilon,k}^f} \left\{f(\mathbf{x}_k) + \nabla f(\mathbf{x})^{\top} \mathbf{d}_k\right\} \\ & + \sum_{i=1}^{m_h} \max_{x \in \mathscr{B}_{\epsilon,k}^{h^i}} \left|h^i(\mathbf{x}_k) + \nabla h^i(\mathbf{x})^{\top} \mathbf{d}_k\right| \\ & + \sum_{i=1}^{m_g} \max_{x \in \mathscr{B}_{\epsilon,k}^{g^j}} \left\{\max\left\{g^i(\mathbf{x}_k) + \nabla g^i(\mathbf{x})^{\top} \mathbf{d}_k, 0\right\}\right\} \\ & + \frac{1}{2} \mathbf{d}_k^{\top} \mathbf{H}_k \mathbf{d}_k. \end{aligned} \tag{29}$$

For a computed $\mathbf{d}_k$, the model reduction is defined to be $\triangle \mathbf{q}_\rho(\mathbf{d}_k; \mathbf{x}_k, \mathscr{B}_{\epsilon,k}, \mathbf{H}_k) := \mathbf{q}_\rho(0; \mathbf{x}_k, \mathscr{B}_{\epsilon,k}, \mathbf{H}_k) - \mathbf{q}_\rho(\mathbf{d}_k; \mathbf{x}_k, \mathscr{B}_{\epsilon,k}, \mathbf{H}_k)$, which values

$$\triangle \mathbf{q}_\rho\left(\mathbf{d}_k; \mathbf{x}_k, \mathscr{B}_{\epsilon,k}, \mathbf{H}_k\right) = \phi_\rho(\mathbf{x}) - \mathbf{q}_\rho\left(\mathbf{d}_k; \mathbf{x}_k, \mathscr{B}_{\epsilon,k}, \mathbf{H}_k\right). \tag{30}$$

The model reduction is nonnegative because $\mathbf{d}_k = 0$ yields an objective value, and $\triangle \mathbf{q}_\rho(\mathbf{d}_k; \mathbf{x}_k, \mathscr{B}_{\epsilon,k}, \mathbf{H}_k)$ can be zero only if $\mathbf{x}_k$ is ϵ-stationary. So a sufficiently small

reduction in $\triangle \mathbf{q}_\rho(\cdot; \mathbf{x}_k, \mathscr{B}_{\epsilon,k}, \mathbf{H}_k)$ indicates that a decrease in ϵ is appropriate.

However, GS produces the approximate ϵ-steepest descent directions by evaluating gradients of the objective function and constraint functions at p randomly generated points during each iteration, resulting in a high computational cost. As the QP subproblem data are computed afresh for every iteration, the computational effort required to solve each of these subproblems can be significant for the large-scale problem [10]. As a more time-saving way to reduce the computation, a generic adaptive gradient sampling (AGS) algorithm is introduced here in which GS is a special case.

The difference between GS and AGS is mainly in the process of sample points $x_{k,p} \in \mathscr{B}_{\epsilon,k}$. Initialize a sampling size value p at first, which is the total number of sample points in every iteration. For $\mathbf{X}_k \coloneqq \{\mathbf{x}_{k,1}, \ldots, \mathbf{x}_{k,p}\}$ (with $\mathbf{x}_{k,i} = \mathbf{x}_k$ for some i and $B_k \coloneqq \mathbb{B}_\epsilon(x_k) \cap \mathscr{D}$, AGS sets

$$\mathbf{X}_k \longleftarrow (\mathbf{X}_{k-1} \cap B_k) \cup \mathbf{x}_k \cup \overline{\mathbf{X}}_k, \tag{31}$$

where the sample set $\overline{\mathbf{X}}_k \coloneqq \{\overline{x}_{k,1}, \ldots, \overline{x}_{k,\overline{p}}\}$ is composed of $\overline{p}$ points generated uniformly in B_k. Denote the number of points selected by $(\mathbf{X}_{k-1} \cap B_k)$ is p_{re}. The actual sampling size of kth iteration changes to $\overline{p} = p - p_{re}$, equaling to the number of points in $\overline{\mathbf{X}}_k$.

It is apparent to see that AGS needs only to compute the unknown gradients at the updating sample points in $\mathbf{X}_k$ and change the sample size p adaptively, which cut down some of the workloads in computing the gradients and renewing the QP data at the kth iteration. The complete SQP-AGS algorithm is presented in Algorithm 1.

What is worth mentioning is that the sample size p can be chosen as zero when solving a smooth function for it is unnecessary to sample the function's gradients at nearby points, in which case the SQP-AGS algorithm reduces to the general SQP algorithm. Especially in a model with smooth and nonsmooth functions, the algorithm samples points of the nonsmooth part only, cutting down a lot of work in the process of sample points and evaluating gradients of the smooth part.

3.3. Solving SSSC-ATC by SQP-AGS. Combined the characteristic of the proposed SSSC-ATC model, we discuss the SQP-AGS in the specific solution process.

Firstly, the AGS technique is only applied to the small-signal stability constraint for it is the only the nonsmooth constraint in the proposed SSSC-ATC model. Therefore, the sample size of the SQP-AGS algorithm reduces to zero in solving the objective function and other smooth constraints.

Secondly, considering the different characteristics and capacity range of variables in the model, the sampling radiuses of variables are also specified. In detail, for active power $\mathbf{P}_G$ and reactive power $\mathbf{Q}_G$, the sample radiuses $\epsilon_{\mathbf{P}_G}$ and $\epsilon_{\mathbf{Q}_G}$ are stipulated as 20% of the capacity range. For voltage-type variables (per-unit value) like $\mathbf{V}$ and $\mathbf{E}$, the sample radiuses $\epsilon_{\mathbf{V}}$ and $\epsilon_{\mathbf{E}}$ are chosen as 0.03 p.u. For angle variables like θ, the sample radius ϵ_θ is chosen as 3°.

Thirdly, owing to the sample points are independent and randomly sampled, a multicore parallel computing technology is applied to solve the gradient calculation which occupies the majority of computing work of the whole process. The application of parallel computing technology will further improve the efficiency of SQP-AGS.

4. Case Studies

The proposed SQP-AGS method is applied to the IEEE 10-machine 39-bus system and the modified IEEE 54-machine 118-bus system to illustrate the effectiveness in solving SSSC-ATC. The full dynamic data of these two systems is extracted from [11, 12], respectively. For both systems, the generators are described by the two-axis model with an IEEE type-I exciter. The loads are modeled as constant power. All the simulations are performed on a workstation with the Intel(R) Xeon(R) E5-2667 v2 processor, which includes 16 cores with the base frequency of 3.30 GHz.

The SQP-AGS method is implemented in MATLAB by using the function *quadprog* as the QP solver for the subproblem. The eigenvalues and eigenvectors are computed by QR decomposition using the MATLAB function *eig*. A flat start is used for which all voltage angles are set to be zero, and all the voltage magnitudes are set to be 1.0 p.u., $P_G = (\overline{P}_G + \underline{P}_G)/2$ and $Q_G = (\overline{Q}_G + \underline{Q}_G)/2$. The parameters of SQP-AGS are chosen as $\rho = 2 \times 10^{-4}$ and $\mu_\rho = 0.05$. The selection of sample radius ϵ depends on the characteristics of the dependent variables as described in Subsection 3.3. Set $\mu_\epsilon = 1 \times 10^{-3}$, $\tau = 0.1$, $\mu_\tau = 0.8$, $\bar{\omega} = 1$, and $\gamma = 0.8$ from [9]. The tolerances ν_{in} and ν_s are set to be 5×10^{-3} and 2×10^{-3}, respectively.

4.1. Comparison of Results under Different Small-Signal Stability Constraints Run from IEEE 10-Machine 39-Bus System. The IEEE 10-machine 39-bus system is used for stability analysis with different small-signal stability constraints, which are three different spectral abscissa constrained values in the SSSC-ATC calculation model above. The specific regional division is shown in Figure 2. The generators G2, G3, and G10 which, respectively, correspond to bus 31, 32, and 39 are selected to locate at the receiving side, while the other generators are located at the source side.

For the voltage magnitude limits, we choose $\overline{V} = 1.1$ p.u. and $\underline{V} = 0.9$ p.u. for all buses. The results under different spectral abscissa constraints are listed in Table 1. In order to reflect the effect on the SQP-AGS algorithm applied on SSSC-ATC, we set the sample size as $p = 30$ and make a comparison of the following cases:

(1) Case 0: base case, which is a standard ATC calculation without any small-signal stability constraint

(2) Case 1: SSSC-ATC with an abscissa spectrum constraint of $\eta \leq -0.10$

(3) Case 2: SSSC-ATC with an abscissa spectrum constraint of $\eta \leq -0.192$

(i) Case 0: the classic IPM is used to solve the ATC problem without any small-signal stability

(1) **Initialization**: choose a sample radius $\epsilon > 0$, penalty parameter $\rho > 0$, constraint violation tolerance $\tau > 0$, sample size p, line search constant $\varpi \in (0, 1)$, backtracking constant $\gamma \in (0, 1)$, sample radius reduction factor $\mu_\epsilon \in (0, 1)$, penalty parameter reduction factor $\mu_\rho \in (0, 1)$, constraint violation tolerance reduction factor $\mu_\tau \in (0, 1)$, infeasibility tolerance $\nu_{\text{in}} > 0$, and stationarity tolerance parameter $\nu_s > 0$. Choose an initial iterate $\mathbf{x}_0 \in \mathcal{D}$ and set $k = 1$ and $k_{\max} = 200$.
(2) **Termination conditions check**: while $k < k_{\max}$, if $\|\mathbf{d}_k\| < \nu_s$ and $\max(\boldsymbol{\sigma}_k) < \nu_{\text{in}}$, output solution and stop.
(3) **Adaptive gradient sampling**: generate $\mathcal{B}^f_{\epsilon,k}$, $\mathcal{B}^h_{\epsilon,k}$, and $\mathcal{B}^g_{\epsilon,k}$ by (22)–(24) and (31).
(4) **Search direction calculation**: choose $\mathbf{H}_k \succ 0$, solve (14)–(21) to get $(\mathbf{d}_k, \mathbf{y}_o, \mathbf{y}_h, \mathbf{y}_g)$.
(5) **L-BFGS update**: update $\mathbf{H}_k$ by (26) for next iteration.
(6) **Parameter update**: if $\mathbf{d}_k > \nu_s\epsilon^2$, then go to step 9. Otherwise, if $\max(\boldsymbol{\sigma}_k) \le \tau$, set $\tau \longleftarrow \mu_\tau\tau$, but if $\max(\boldsymbol{\sigma}_k) > \tau$, set $\rho \longleftarrow \mu_\rho\rho$. Then, set $\epsilon \longleftarrow \mu_\epsilon\epsilon$, $\beta_k \longleftarrow 0$, and go to step 8.
(7) **Line search**: set β_k as the largest value in the sequence $\{1, \gamma, \gamma^2, \ldots\}$ such that $\mathbf{x}_{k+1} \longleftarrow \mathbf{x}_k + \beta_k\mathbf{d}_k$ satisfies:$\phi_\rho(\mathbf{x}_{k+1}) \le \phi_\rho(\mathbf{x}_k) - \varpi\beta_k\|\mathbf{d}_k\|$ and $\|\mathbf{x}_k + \beta_k\mathbf{d}_k - x_{k+1}\| \le \min\{\beta_k, \epsilon\}\|\mathbf{d}_k\|$
(8) **Iteration increment**: set $k \longleftarrow k + 1$ and go to step 3.
(9) **end do**

Algorithm 1: SQP-AGS algorithm.

constraint. The results are listed in the second column of Table 1, which shows the TTC is obtained as 1704.99 MW and the spectral abscissa is calculated to be 2.15, indicating the TTC is overoptimistic due to the fact that the system is not small-signal stable in this operation state. This further indicates that the influence of small-signal stability on ATC calculation needs to be considered. Extracting information from Table 1, it can be seen that the active generation of generators G2 and G3 which are located in the receiving side all reach the lower limit of the active power output in order to ensure the maximum of TTC.

(ii) Case 1: a spectral abscissa constraint $\eta \le -0.10$ is added to the ATC model as the small-signal stability constraint and SQP-AGS algorithm is run to solve it. The results are listed in the third column of Table 1, which shows the TTC is obtained as 498.62 MW, and the system is small-signal stable in this operation state. The result also shows that the generation in the receiving side is greatly increased compared with Case 0, especially as generator G3, possibly due to the larger time inertia coefficient of it, resulting in the reduction of TTC. It reflects that the small-signal stability does constrain the regional transmission directly.

(iii) Case 2: the spectral abscissa constraint is further reduced to $\eta \le -0.192$ in the SSSC-ATC model. The results run from the SQP-AGS algorithm shows that the calculation is still convergent and the TTC is reduced to 465.73 MW.

Comparing Case 0, Case 1, and Case 2 will find out a rule that TTC value reduces as the spectral abscissa decreases, which means the stricter restriction effect on ATC calculation when a spectral abscissa constraint gets smaller. The results under spectral abscissa constraints are more reasonable than the one without any small-signal stability constraint so that the ATC in this situation can be a guide to avoid the power oscillation caused by small-signal stability in the system.

4.2. Comparison of Different Methods in Calculating SSSC-ATC. Here, we compare the SQP-AGS's calculation effect on the same problem with a sensitivity method [3] and a participation factor method [4] for IEEE 39-bus system. The results run by the three methods are all restricted to a spectral abscissa constraint as $\eta \le -0.1$ and detailedly listed in Table 2.

The TTC calculated by SQP-AGS is 498.60 MW, while the TTC calculated by the sensitivity method and the participation factor method is 289.94 MW, and the one calculated by the participation factor method is 262.78 MW. All the three methods obtain a TTC value much smaller than which is calculated from the ATC model without small-signal stability constraint. In addition, compared with the result calculated by SQP-AGS, the other two methods' results are relatively conservative. In other words, it is to say that SQP-AGS can evaluate the SSSC-ATC problem in an optimization way. It further means this ATC result may bring more economic benefits that are more acceptable to the power industry in practice.

On the other hand, it is worth mentioning that when the spectral abscissa constraint decreases as $\eta \le -0.15$, the sensitivity method and the participation method both cannot converge to obtain a result, while the SQP-AGS can still effectively reduce the spectral abscissa of the system and achieve a good convergent result, as is shown in Table 1. This reveals the superiority of SQP-AGS in solving the SSSC-ATC problem compared with the other two mentioned methods.

4.3. Efficiency Tested in IEEE 54-Machine 118-Bus System. To test the efficiency of SQP-AGS, we make some comparisons on a modified version of the IEEE 54-machine 118-bus benchmark system which has 54 synchronous machines with IEEE type-1 exciters, 20 of which are synchronous compensators used only for reactive power support and 15 of which are motors. The specific regional division of IEEE 118-bus system is as follows:

(i) Receiving side: the region includes buses of 1, 4, 6, 8, 10, 12, 15, 18, 19, 24, 25, 26, 27, 31, 32, 34, 36, 40, 42,

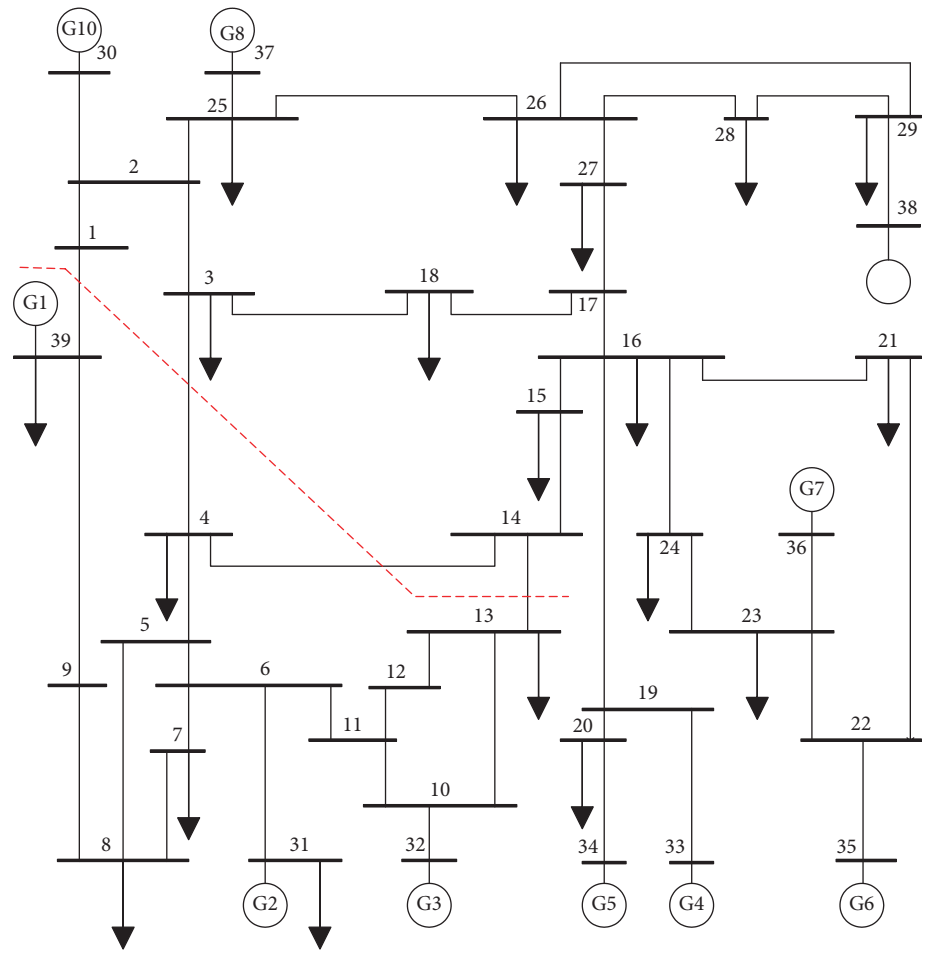

Figure 2: The regional division of the IEEE 39-bus system.

Table 1: Active output of generators and TTC in IEEE 39-bus system.

	Active output (MW)			Active output range (MW)
	Case 0	Case 1	Case 2	
G1	590.13	1102.59	1106.74	100 ~ 1380
G2	50.00	105.35	136.58	50 ~ 747.5
G3	50.00	677.18	676.12	50 ~ 920.0
G4	862.50	665.66	639.15	50 ~ 862.5
G5	747.50	529.28	564.18	50 ~ 747.5
G6	862.50	671.67	667.62	50 ~ 862.5
G7	862.50	581.69	603.44	50 ~ 862.5
G8	805.00	597.35	513.94	100 ~ 805.0
G9	1035.00	899.08	898.57	100 ~ 1035
G10	402.50	318.83	346.63	50 ~ 402.5
TTC (MW)	1704.99	498.62	465.73	—

46, 49, 54, 55, 56, 59, 61, 62, 65, 66, 69, 70, 72, 73, 113, and 116.

(ii) Source side: the region includes buses of 74, 76, 77, 80, 85, 87, 89, 90, 91, 92, 99, 100, 103, 104, 105, 107, 110, 111, and 112.

Lines 74–70, 75–70, 75–69, 77–69, and 81–68 are the tie lines between the two regions. For an ATC model without any small-signal stability constraint, the TTC is obtained as 1410.20 MW and the spectral abscissa is $\eta = 1.1$, which also means the calculated ATC is overoptimistic, and power oscillation will occur before the transmission between regions reaches this value. Applying SQP-AGS to solve an SSSC-ATC problem with a spectral abscissa constraint $\eta \leq -0.1$, the spectral abscissa is decreased meeting the constraint requirement after 17 iterations and the result is convergent, obtaining the TTC as 446.08 MW. The spectral abscissa changing with iterations is shown in Figure 3. It is easy to find that the descending trend of spectral abscissa is stable. Moreover, Figure 4 reflects the changes in the termination conditions with the iteration increases. As the trend shows, the infeasibility defined in (28) and the model reduction calculated by (30) both decrease to an acceptable tolerance.

In order to test the efficiency of SQP-AGS, the algorithm is going with a sample size of $p = 50$. Under the serial computing condition, we make a comparison between SQP-GS and SQP-AGS dealing with the same SSSC-ATC problem. The computing time of them is listed in second and third columns of Table 3.

It is clear to see that, for the 118-bus system, applying the serial SQP-GS method to solve an SSSC-ATC problem consumes 173.48s and 18 iterations while applying the serial

Table 2: Comparison of different methods for the 39-bus system.

	SQP-AGS (MW)	Sensitivity method (MW)	Participation factor method (MW)
G1	1102.59	1210.27	1357.84
G2	105.35	556.43	150.46
G3	677.18	407.27	704.98
G4	665.66	732.91	680.85
G5	529.28	599.08	673.28
G6	671.67	416.40	862.50
G7	581.69	764.68	50.00
G8	597.35	715.46	733.05
G9	899.08	790.18	627.21
G10	318.83	50.00	402.50
TTC (MW)	498.60	289.94	262.78

SQP-AGS needs only 66.29s and 17 iterations, cutting down a lot of time in solving the same model. Particularly, the time-consuming of gradient calculating accounts for the vast majority of the total time because of the repeating calculating processes of small-signal stability calculation and the sampling gradient calculation of nonsmooth constraint. Compared with SQP-GS, SQP-AGS spends much less time on gradient calculation due to the adaptive identification of sampling points which are within the sampling neighborhood of the current iteration point. In each iteration, SQP-AGS effectively utilizes the historical sampling data in the previous iteration and saves a lot of time for gradient calculation at current iteration, which greatly improves the efficiency of calculation. The intuitive sample point changes are shown in Figure 5.

Moreover, notice that the sample points for gradient calculation in each iteration are random and independent, we adopt the multicore parallel computing technology of MATLAB to carry out the gradient calculation when applying SQP-AGS. Parallel computing opens the parallel computing pool of specified number of workers through the *parpool* instruction in MATLAB and uses *parfor* statement to execute the operation process of the loop body. Testing it on the IEEE 118-bus system and comparing the efficiency with serial computing, we can obtain the result of calculation time, as shown in the fourth to the sixth columns of Table 3.

It shows that the time-consuming of SQP-AGS using parallel computing is much less than the one under the serial computing process, while the iterations of both of them are the same. The time-consuming is reduced with the number of increasing workers as well. On this basis, we calculate the speedup ratio and the efficiency of parallel computing with different numbers of workers running. The speedup ratio of parallel computing is defined as $S_n = T_1/T_n$, in which n is the number of parallel workers and T_1 is the computing time with only one worker. The efficiency of parallel computing is defined as $E_n = S_n/n$. Table 3 separately lists the speedup ratios of 2, 4, and 8 workers, respectively, which are $S_2 = 1.71$, $S_4 = 2.86$, and $S_8 = 4.05$. The efficiencies are $E_2 = 0.86$, $E_4 = 0.72$, and $E_8 = 0.51$, correspondingly. Due to the characteristic of sampled points, multicore parallel computing plays an important role in shortening the calculation time. Compared with the SQP-GS which is used in [5], the SQP-AGS with the multicore parallel computing

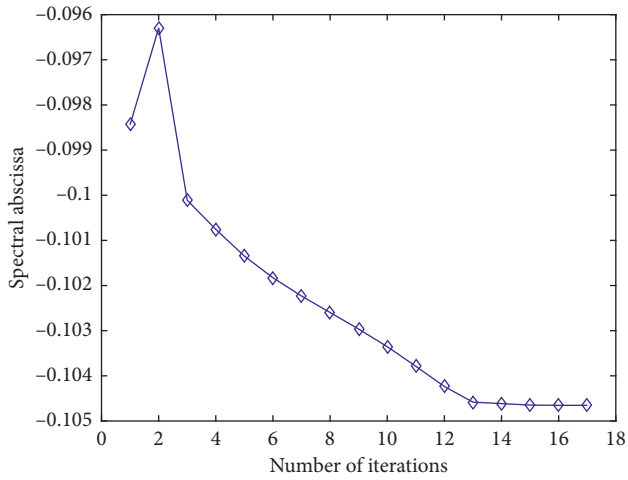

Figure 3: Spectral abscissa changes with iterations for the 118-bus system.

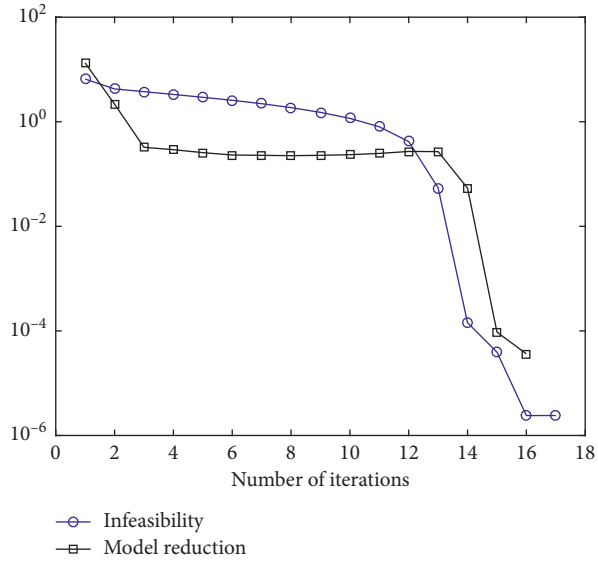

Figure 4: The termination conditions change with iterations for the 118-bus system.

Table 3: Efficiency comparison of the IEEE 118-bus system.

	Serial computing		Parallel computing for SQP-AGS		
	SQP-GS method	SQP-AGS method	Two cores	Four cores	Eight cores
Total time (s)	173.48	66.29	39.88	25.15	16.36
Gradient sampling time (s)	170.40	63.32	36.90	20.24	13.37
QP solver time (s)	2.78	2.67	2.68	2.62	2.69
Others' time (s)	0.30	0.30	0.30	0.29	0.30
Speedup ratio, S_n	—	—	1.71	2.86	4.05
Efficiency, E_n	—	—	0.86	0.72	0.51
Iteration	18	17	17	17	17

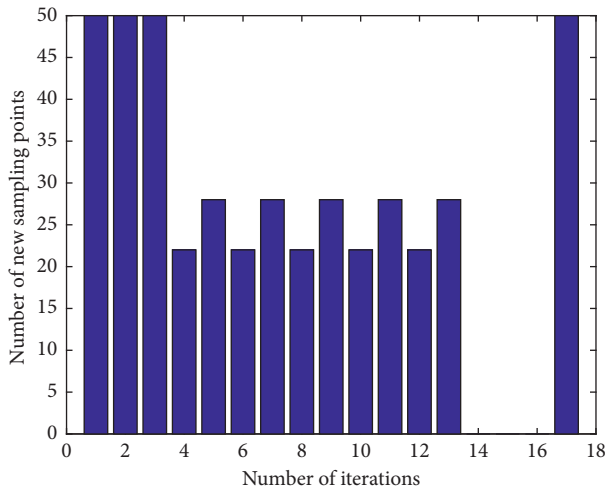

Figure 5: Number change of new sampling points.

technique greatly improves the computing efficiency of the SSSC-ATC problem of a large-scale power system, which has absolute advantages and more practical application prospects in practical engineering applications.

5. Conclusion

In this paper, we propose an SSSC-ATC calculating model with a spectral abscissa constraint which directly and fully considers the impact of small-signal stability on ATC calculation. An SQP-AGS method is adopted to solve the proposed SSSC-ATC problem, which is a nonsmooth optimization problem due to the property of the spectral abscissa function. The closed-form eigenvalue sensitivity is used to calculate the gradient of the spectral abscissa. In SQP-AGS, an AGS theory is adopted to evaluate the gradients around the current iteration points adaptively to make the search direction computation effective in the nonsmooth regions and practically improve the efficiency of calculation. The multicore computing technology further improves the effect on calculation efficiency. Simulation results on two test systems show that the proposed method solves the SSSC-ATC problem effectively without any convergence problem. Comparison of other two methods proves that the proposed method is more effective in calculating the SSSC-ATC problem.

Data Availability

The 10-machine 39-bus system and 54-machine 118-bus system data that support the findings of this study are available in the thesis [11] and at http://www.kios.ucy.ac.cy/testsystems/index.php/dynamicieee-test-systems/ieee-118-bus-modified-test-system [12].

Conflicts of Interest

The authors declare that they have no conflicts of interest.

Acknowledgments

This work was supported in part by the National Natural Science Foundation of China under Grant nos. 51967001 and 51667003, in part by Natural Science Foundation of Guangxi under Grant no. 2018GXNSFAA281194, and in part by Guangxi Key Laboratory of Power System Optimization and Energy Technology Research Grant.

References

[1] G. Hamoud, "Assessment of available transfer capability of transmission systems," *IEEE Transactions on Power Systems*, vol. 15, no. 1, pp. 27–32, 2000.

[2] L. H. Junji K and Y. Yue, "A study on the effect of generation shedding to total transfer capability by means of transient stability constrained optimal power flow," *IEEE Transactions on Power Systems*, pp. 347–355, 2009.

[3] C. Y. Chung, L. Wang, F. Howell, and P. Kundur, "Generation rescheduling methods to improve power transfer capability constrained by small-signal stability," *IEEE Transactions on Power Systems*, vol. 19, no. 1, pp. 524–530, 2004.

[4] M. M. Othman and S. Busan, "A novel approach of rescheduling the critical generators for a new available transfer capability determination," *IEEE Transactions on Power Systems*, vol. 31, no. 1, pp. 3–7, 2015.

[5] P. Li, J. Qi, J. Wang, H. Wei, X. Bai, and F. Qiu, "An sqp method combined with gradient sampling for small-signal stability constrained opf," *IEEE Transactions on Power Systems*, vol. 32, no. 3, pp. 2372–2381, 2017.

[6] W. L. Peng W and G. Zhizhong, *Determination of Optimal Total Transfer Capability Using a Probabilistic Approach*, pp. 862–868, 2006.

[7] A. S. Lewis and M. L. Overton, "Eigenvalue optimization," *Acta Numerica*, vol. 5, pp. 149–190, 1996.

[8] J. V. Burke, F. E. Curtis, A. S. Lewis, M. L. Overton, and L. E. A. Simes, "Gradient sampling methods for nonsmooth optimization," 2018.

[9] F. E. Curtis and M. L. Overton, "A sequential quadratic programming algorithm for nonconvex, nonsmooth constrained optimization," *SIAM Journal on Optimization*, vol. 22, no. 2, pp. 474–500, 2012.

[10] F. E. Curtis and X. Que, "An adaptive gradient sampling algorithm for non-smooth optimization," *Optimization Methods and Software*, vol. 28, no. 6, pp. 1302–1324, 2013.

[11] R. H. Yeu, *Small Signal Analysis of Power Systems: Eigenvalue Tracking Method and Eigenvalue Estimation Contingency Screening for DSA*, Ph.D. dissertation, University of Illinois at Urbana-Champaign, Champaign, IL, USA, 2010.

[12] IEEE 118-bus Modified Test System, KIOS Research Center for Intelligent Systems and Networks of the University of Cyprus, http://www.kios.ucy.ac.cy/testsystems/index.php/dynamic-ieee-test-systems/ieee-118-bus-modified-test-system.

Hindawi
Complexity
Volume 2020, Article ID 4939268, 18 pages
https://doi.org/10.1155/2020/4939268

Research Article

A Selection Hyper-Heuristic Algorithm for Multiobjective Dynamic Economic and Environmental Load Dispatch

Le Yang[1], **Dakuo He**[1,2] **and Bo Li**[1]

[1]*College of Information Science and Engineering, Northeastern University, Shenyang 110819, China*
[2]*State Key Laboratory of Integrated Automation for Process Industries, Northeastern University, Shenyang, China*

Correspondence should be addressed to Dakuo He; hedakuo@ise.neu.edu.cn

Received 26 July 2019; Revised 12 September 2019; Accepted 18 December 2019; Published 20 January 2020

Guest Editor: Xiaoqing Bai

Dynamic economic and environmental load dispatch (DEED) aims to determine the amount of electricity generated from power plants during the planning period to meet load demand while minimizing energy consumption costs and environmental pollution emission indicators subject to the operation requirements. This planning problem is usually expressed using a nonsmooth cost function, taking into account various equality and inequality constraints such as valve-point effects, operational limits, power balance, and ramp rate limits. This paper presents DEED models developed for a system consisting of thermal units, wind power generators, photovoltaic (PV) generators, and energy storage (ES). A selection hyper-heuristic algorithm is proposed to solve the problems. Three heuristic mutation operators formed a low-level operator pool to direct search the solution space of DEED. The high level of SHHA evaluates the performances of the low-level operators and dynamically adjusts the chosen probability of each operator. Simulation experiments were carried out on four systems of different types or sizes. The results verified the effectiveness of the proposed method.

1. Introduction

With the rapid growth of modern industry and global economy, people's demand for electricity in production and life is constantly increasing. Therefore, how to dispatch power production according to the forecasted load demand and improve the generation efficiency of generating units has always been an important research issue in power system operational planning. Traditional economic load dispatch aims to determine the operation status of each unit in a power plant within the planned time and minimize the energy consumption cost while meeting the demand for power load and the operational requirements of generating units. With the gradual attention of human beings to the ecological environment, the harmful substances such as sulfur oxides, nitrogen oxides, and carbon dioxide emitted from fossil fuels to the atmosphere in the combustion process have gradually attracted attention. While reducing energy consumption costs, further reducing environmental pollution emission indicators has become a new requirement for optimizing load dispatch.

For dispatching tasks, energy consumption cost and environmental pollution emissions are two key indicators and minor improvements can bring significant economic and environmental benefits [1]. The optimization of these two indicators is essentially contradictory. Economic and emission load dispatch (EED) is a multiobjective optimization problem that considers these two conflicting indicators at the same time [2]. In addition, because the mathematical expressions of the two indexes are nonconvex and nonsmooth objective functions, it is difficult to solve the optimization problem. The energy crisis caused by the long-term consumption of fossil energy and the global demand for clean energy promotes the development of renewable energy. Wind power, solar power, and plug-in electric vehicles have been widely developed in the last decade and might become the main alternatives in the power system in the near future [3, 4]. But at the same time, the introduction of these renewable energy sources will bring more complex planning and uncertainty to the power grid production [5].

Heuristic optimization algorithms are widely used to solve nonsmooth optimization problems with high

nonlinearity and discontinuity of input and output, such as the economic and environmental dispatch problem, due to their strong global search ability and low requirements for some mathematical properties of the objective function. An improved bacterial foraging algorithm with a parameter automation strategy and crossover operation is proposed to improve computational efficiency and solve the static/dynamic EED [6]. In [7], an improved particle swarm optimization algorithm is applied to EED including solar photovoltaic generation. In [8], a bilevel dynamic economic emission dispatch model is proposed considering wind power integration. Also, robust optimization and a nested solution method are proposed for EED considering wind power uncertainty. A dispatch model combining environmental awareness and risk perception is proposed in [9], and nondominated sorting genetic algorithm-II embedded constraints handling techniques are devised for the problem. In [10], an enhanced multiobjective bee colony optimization algorithm is proposed for solving short-term hydro-thermal-wind complementary scheduling considering the uncertainty of wind power. In [2], a dynamic economic emission dispatch (DEED) incorporating renewable energy and energy storage is formulated and an adaptive robust method is proposed to solve the problem.

There are many differences in EED models that have been solved in the existing research. Some scholars focus on the dynamic economic emission dispatch (DEED) problems which consider only thermal generation, single-objective DEED with renewable energy generation (REG), and the multiobjective static DEED with REG. This paper formulates a DEED model including thermal generation, wind energy generation, solar photovoltaic (PV) generation, and energy storage (ES). A selection hyper-heuristic algorithm is proposed to solve the Pareto optimal solution of the problem. Three operators formed a low-level operator pool to directly search the solution space. The high-level structure is responsible for managing low-level operators. The operators are evaluated and ranked by analyzing the results of the nondominated solutions. Then, the chosen probability of each low-level operator is determined by the selection mechanism, which is provided for the next call. The effectiveness of the optimization strategy is validated through a series of simulations. The results are compared with those of existing state-of-the-art optimization techniques.

The rest of this paper is organized as follows. Section 2 presents the DEED mathematical model. The application of the proposed hyper-heuristic method is described in Section 3. To illustrate its effectiveness, the proposed method was tested on a series of systems in Section 4. Conclusions and future research are discussed in Section 5.

2. Problem Formulation

In this section, we will discuss the mathematical model of the DEED problem, which is used to distribute the output power of all generators economically and environmentally during the dispatching period and satisfies a series of equality and inequality constraints.

2.1. Objective Function. Compared with the static EED, which is scheduled at a certain hour, DEED adopts dynamic scheduling for a load cycle of 24 hours. Consider a power system with N_G thermal power generators, N_W wind power generators, and N_{PV} PV generators over time intervals. The basic objective function of the DEED problem can be formulated as the following optimal function:

$$\begin{aligned}\min F &= \sum_{t=1}^{N_T}\left(\sum_{i=1}^{N_G} F_i\left(P_{i,t}\right) + \sum_{i=1}^{N_w} F_i\left(w_{i,t}\right) + \sum_{i=1}^{N_{PV}} F_i\left(\mathrm{PV}_{i,t}\right)\right),\\ \min E &= \alpha_i P_{i,t}^2 + \beta_i P_{i,t} + \gamma_i + \eta_i \exp\left(\delta_i P_{i,t}\right),\end{aligned} \tag{1}$$

where i and t are the number of generator and time interval, respectively. F denotes the total fuel costs over the dispatch period. $F_i(P_{i,t})$, $F_i(w_{i,t})$, and $F_i(\mathrm{PV}_{i,t})$ are cost functions of the thermal power generator, wind power generator, and solar power generator, respectively. N_T is the time horizon. $P_{i,t}$, $W_{i,t}$, and $\mathrm{PV}_{i,t}$ are the power output of thermal power generator, wind power generator, and PV generator, respectively. α_i, β_i, γ_i, η_i, and δ_i are environmental cost coefficients.

When the valve-point effect (VPE) is considered, the total fuel costs of thermal power generators can be written as follows:

$$F_i\left(P_{i,t}\right) = a_i P_{i,t}^2 + b_i P_{i,t} + c_i + \left|e_i \sin\left(f_i\left(P_i^{\min} - P_{i,t}\right)\right)\right|, \tag{2}$$

where $P_{i,\min}$ is the minimum power outputs of generator i. a_i, b_i, and c_i are the fuel cost coefficients of generator i. e_i and f_i are the coefficients of generator i reflecting the valve-point effects. Valve-point effect is the phenomenon of rapid increase consumption caused by valve drawing effects during start-up of thermal power generators.

The total economic costs of wind power generators can be written as follows:

$$\begin{aligned}F_i\left(w_{i,t}\right) &= c_{w,i}\left(w_{i,t}\right) + c_{p,w,i}\left(W_{it,\mathrm{av}} - w_{i,t}\right) + c_{r,w,i}\left(w_{i,t} - W_{it,\mathrm{av}}\right),\\ c_{wi}\left(w_{i,t}\right) &= d_i w_{i,t},\\ c_{p,wi} &= k_{p,i}\left(W_{ij,\mathrm{av}} - w_{i,t}\right) = k_{p,i}\int_{w_i}^{w_{ri}}\left(w - w_{i,t}\right) f_w(w)\mathrm{d}w,\\ c_{r,wi} &= k_{r,i}\left(w_{i,t} - W_{ij,\mathrm{av}}\right) = k_{r,i}\int_{0}^{w_i}\left(w_{i,t} - w\right) f_w(w)\mathrm{d}w,\end{aligned} \tag{3}$$

where $w_{i,t}$ and $W_{it,av}$ are the schedule and actual power of wind generator i at time interval t. $c_{w,i}$ denotes the cost function of generator i (payment to wind farm operators for actual use of wind power), which can be calculated by the cost coefficients and the wind probability density function. d_i is the direct cost coefficient of generator i. $c_{p,w,i}$ denotes the penalty cost function for not using all available power of generator i, which has a linear correlation with the difference between available power and actual power. $k_{p,i}$ is the underestimating penalty cost coefficient. $f_w(w)$ is the probability distribution function of wind power. $c_{r,w,i}$ denotes the reserve costs associated with wind power

uncertainty (penalties for estimating available wind power). w_{ri} is the rated power of generator i, and $k_{r,i}$ is the reserve cost coefficient.

The total economic costs of solar power generators can be written as follows:

$$\begin{aligned} F_i(w_{i,t}) &= c_{pvi}(\mathrm{pv}_{i,t}) + c_{p,pvi}(\mathrm{PV}_{it,\mathrm{av}} - \mathrm{pv}_{i,t}) \\ &\quad + c_{r,pvi}(\mathrm{pv}_{i,t} - \mathrm{PV}_{it,\mathrm{av}}), \\ c_{pvi}(\mathrm{pv}_{i,t}) &= h_i f_{\mathrm{pv}}(\mathrm{pv})\mathrm{pv}_{i,t}, \\ c_{p,pvi} &= k_{p,pvi}(\mathrm{PV}_{ij,\mathrm{av}} - \mathrm{pv}_{i,t}) \\ &= k_{p,pvi}\int_{\mathrm{pv}_i}^{\mathrm{pv}(k_{\max})}(\mathrm{pv} - \mathrm{pv}_{i,t}) f_{pv}(\mathrm{pv})\mathrm{d}pv, \\ c_{r,pvi} &= k_{r,pvi}(\mathrm{pv}_{i,t} - \mathrm{PV}_{ij,\mathrm{av}}) \\ &= e_{r,pvi}\int_0^{\mathrm{pv}_{ri}}(\mathrm{pv}_{i,t} - \mathrm{pv}) f_{pv}(\mathrm{pv})\mathrm{d}pv, \end{aligned} \tag{4}$$

where $\mathrm{pv}_{i,t}$ and $\mathrm{PV}_{it,\mathrm{av}}$ are the schedule and actual power of solar generator i at time interval t. c_{pvi} denotes the weighted cost of generator i based on solar irradiance, which can be calculated by the cost coefficients and the solar probability density function. $c_{p,pvi}$ and $c_{r,pvi}$ are the penalty cost function for not using all available power of generator and the reserve costs associated with power uncertainty, respectively. h_i is the operating cost coefficient of solar power operator. pv_{ri} is the rated power of generator i, and $\mathrm{pv}(k_{\max})$ is the upper limit of output of the corresponding operator. $k_{p,pvi}$ and $k_{r,pvi}$ are the underestimating penalty cost coefficient and the reserve cost coefficient, respectively. $f_{\mathrm{pv}}(\mathrm{pv})$ is the probability distribution function of solar power.

2.2. Constraints

(1) Real Power Balance Constrains

In order to ensure the safe and stable operation of generators, each generator needs to run in a specified power range:

$$\begin{aligned} \sum_{i=1}^{N_G} P_{i,t} + \sum_{i=1}^{N_w} w_{i,t} + \sum_{i=1}^{N_{\mathrm{PV}}} \mathrm{PV}_{i,t} + \sum_{i=1}^{N_{\mathrm{ES}}} \mathrm{ES}_{i,t} &= P_{D,t} + P_{L,t}, \quad t \in N_T, \\ P_{L,t} = \sum_{i=1}^{N_T}\sum_{j=1}^{N_T} P_{i,t}B_{ij}P_{j,t} + \sum_{i=1}^{N_T} B_{0i}P_{i,t} + B_{00}, &\quad t \in N_T, \end{aligned} \tag{5}$$

where $P_{i,\min}$ and $P_{i,\max}$ are the minimum and maximum power outputs of thermal generator i, respectively. $\mathrm{ES}_{ch,i}$ and $\mathrm{ES}_{\mathrm{dis},i}$ denote the charge and discharge power of the ith ES unit. $\mathrm{ES}_{i,\mathrm{cap}}$ is the power capacity of ith ES unit.

(2) Power Operating Constrains

In order to ensure the safe and stable operation of generators, each generator needs to run in a specified power range:

$$\begin{aligned} P_{i,\min} \le P_{i,t} \le P_{i,\max}, &\quad i \in N_G\, t \in N_T, \\ 0 \le w_{i,t} \le w_{ri}, &\quad i \in N_w\, t \in N_T, \\ 0 \le \mathrm{pv}_{i,t} \le \mathrm{pv}(k_{\max}), &\quad i \in N_{\mathrm{pv}}\, t \in N_T, \\ -\mathrm{ES}_{i,\mathrm{cap}} \le \mathrm{ES}_{ch,i} \le 0, &\quad i \in N_{\mathrm{ES}}, \\ 0 \le \mathrm{ES}_{\mathrm{dis},i} \le \mathrm{ES}_{i,\mathrm{cap}}, &\quad i \in N_{\mathrm{ES}}, \end{aligned} \tag{6}$$

where $P_{i,\min}$ and $P_{i,\max}$ are the minimum and maximum power outputs of thermal generator i, respectively. $\mathrm{ES}_{ch,i}$ and $\mathrm{ES}_{\mathrm{dis},i}$ denote the charge and discharge power of the ith ES unit. $\mathrm{ES}_{i,\mathrm{cap}}$ is the power capacity of the ith ES unit.

(3) Generator Ramp Rate Constrains

The power output of the generators should not fluctuate too much during the interval time interval. Ramp rate constraints are used to restrict the adjusting range of the generator power:

$$P_{i,t-1} - \mathrm{DR}_i \le P_{i,t} \le P_{i,t-1} + \mathrm{UR}_i, \quad i \in N_G, \tag{7}$$

where UR_i and DR_i are the ramp-up and ramp-down rate constraints of generator i, respectively.

(4) Spinning Reserve Requirements

Spinning reserve requirements (SRRs) refer to the readily available capacity, which can compensate for the generation gap caused by generator faults or power fluctuation in a short time. SRR constraints are frequently applied in the unit commitment problem and economic dispatch problem [11–13]. It can be employed to provide the operating reserves to balance the influence brought by the renewables uncertainty and forecast error [14].

$$\begin{aligned} &\sum_{i=1}^{N_G} P_{i,\max} - (P_{D,t} + P_{L,t}) \ge \mathrm{SR}_t, \quad t \in N_T, \\ &\sum_{i=1}^{N_G} (\min(P_{i,\max} - P_{i,t}, \mathrm{UR}_i)) \ge \mathrm{SR}_t, \quad t \in N_T, \\ &\sum_{i=1}^{N_G} \left(\min\left(P_{i,\max} - P_{i,t}, \frac{\mathrm{UR}_i}{6}\right)\right) \ge \mathrm{SR}'_t, \quad t \in N_T, \end{aligned} \tag{8}$$

where SR_t and SR'_t are the spinning reserves for the one-hour and 10-minute compensation time.

(5) Energy Storage SOC Constraints

The state of charge (SOC) denotes an ES's real-time power state, which is the variable that actually operates in the scheduling process. It is calculated according to the state at the previous time interval:

$$\mathrm{SOC}_{\min} \le \mathrm{SOC}_{i,t} \le \mathrm{SOC}_{\max}, \tag{9}$$

where $\mathrm{SOC}_{i,t}$ is the SOC of the ith ES at time interval t which lies between 0 and 1. $\mathrm{SOC}_{\min}$ and $\mathrm{SOC}_{\min}$ are the minimum and maximum limits of SOC, respectively.

3. Multiobjective Selection Hyper-Heuristic Algorithm

In this paper, a selection hyper-heuristic algorithm is used to solve the Pareto optimal solution of the DEED problem. The method consists of two levels, and the low-level structure contains an algorithm pool, which is composed of three heuristic operators to directly search the solution space. In the management of the high-level structure, the low-level operators are evaluated and ranked by calculating the results of nondominated solutions. Then, the chosen probability of each low-level operator is calculated through the selection mechanism, which is provided for the next call.

3.1. The Framework of Selection Hyper-Heuristic Algorithm. Hyper-heuristic algorithms are widely used in the field of automatic algorithm design [15]. Hyper-heuristics can be defined as "automated methods for selecting or generating heuristics to solve hard computing search problems." [16] This is different from most implementations of meta-heuristic methods that operate directly on solution spaces. It was originally used in 1997 to describe a protocol that combines several AI methods in the context of automatic theorem proving. The proposed multiobjective selection hyper-heuristic algorithm is shown in Figure 1. The low-level operator pool consists of three heuristic operators, and the high level of the proposed algorithm consists of an evaluation strategy and a selection mechanism.

The low-level operator pool plays an important role in searching the problem space effectively. A mutation operator pool composed of three different mutation operators is built in this section. These operators will be implemented under the guidance of an adaptive selection mechanism at different stages of the search. The operators are as follows:

$H1$: GA/derived from NSGA-II

$$c_k = p_k + \left(p_k^u - p_k^l\right)\delta_k. \tag{10}$$

$H2$: DE/rand/2

$$v_i^G = x_{r1}^G + F\left(x_{r2}^G - x_{r3}^G\right) + F\left(x_{r4}^G - x_{r5}^G\right). \tag{11}$$

$H3$: DE/current-to-best/1 derived from PSO

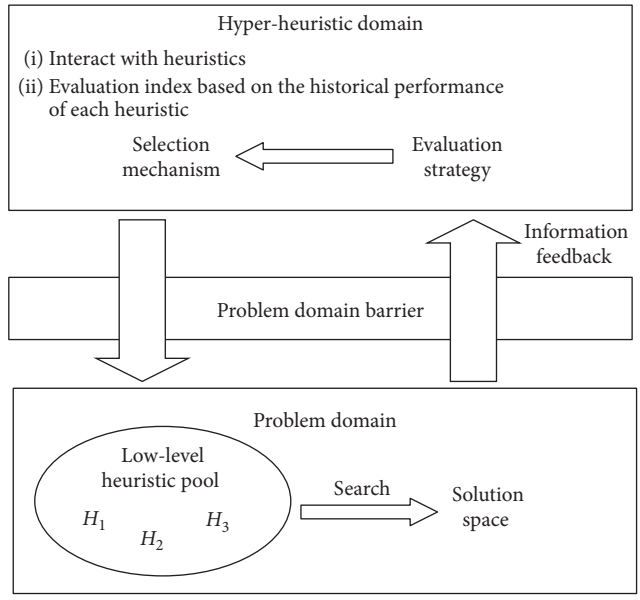

Figure 1: Framework of the proposed selection hyper-heuristic algorithm.

$$v_i^G = G_r x_{\text{best}}^G + (1 - G_r)x_i^G + F\left(x_{r1}^G - x_{r2}^G\right), \tag{12}$$

where c_k is the offspring and p_k is the parent with p_k^u being the upper bound on the parent component, p_k^u is the lower bound, and δ_k is small variation which is calculated from a polynomial distribution [17].

Instead of operating directly on a solution space, the high level of the hyper-heuristics evaluates and grades the historical performance of the low-level operators during a given stage. A selection mechanism is devised to manage the calls of the low-level operators at different stages in the searching process. The underlying assumption is that each low-level operator has different performance in different regions of search space or at different stages of the whole searching process [15]. In fact, due to the function landscapes of the problems and the characteristics of the operators, it is difficult for the operator to keep stable optimization capability in different regions of the whole search area. It is common that some operators perform well in the early stage of iteration, but lack optimization capability in the later stage. Here, we introduce a sliding time window (STW) to dynamically evaluate the historical performance of the low-level operators. The length of the STW is much smaller than the maximum number of iteration. The uniformity of the nondominated solution and the dominated relationship between parent and offspring individuals are used as the evaluation indexes.

The specific steps of the evaluation and selection mechanism are as follows:

Step 1 (evaluation): compute the spatial measure (uniformity) of nondominated solutions, sp.

Step 2: calculate the number of the parent dominated by the offspring $\mathrm{dom}_{o,p}$, and the number of the parent and the offspring does not dominate each other, dom.

Step 3: calculate FIR score:

$$\mathrm{FIR} = 1 * \mathrm{dom}_{o,p} + 0.5 * \mathrm{dom}. \tag{13}$$

Step 4: update the sliding window time, SWT(FIR, sp), and the historical information, history(FIR, sp).

Step 5 (selection): collect the number of call frequency of each operator, $Cn_{\mathrm{total}} = \mathrm{sum}(Cn)$.

Step 6: determine the chosen probability based on historical information:

$$Pn = \mathrm{FIR} + \frac{C_1 * Cn}{Cn_{\mathrm{total}}} + C_2 * sp + C_3 * \mathrm{history}(\mathrm{FIR}) + C_4 * \mathrm{history}(sp). \tag{14}$$

Step 7: select the low-level operator using the roulette method.

3.2. Elitist Nondominated Sorting Mechanism. In different periods of iteration, the crowding distance between individuals is used as an index to guide the selection of parent individuals. In the early stage of iteration, the combination of nondominated sorting and crowding distance is used to select individuals. Firstly, the nondominated sorting of solutions is performed to obtain different Pareto frontiers of solutions. Then, the individuals are sorted in descending order of crowding distance in each Pareto frontier. Finally, 75% of the larger crowding distance in each Pareto frontier is selected as the paternal individuals until the total number of parent individuals is satisfied. At the later stage of the iteration, the population converges gradually and the density of solutions in the population is high. This paper combines nondominated sorting, crowding distance, and hypercube grid to select parent individuals. Individuals will be screened in two ways. One is nondominated sorting. The other is a combination of nondominated sorting, crowding distance, and hypercube grid. A parameter λ is introduced to decide which way to choose. First, individuals are screened using the same steps as in the early stage. Then, the selected individuals are put into the grid, and the grid with larger individual density is screened. In each selected grid, some individuals are randomly selected for deletion to guarantee the uniform distribution of individuals. By introducing crowding distance and hypercube grid, not only the diversity of the population is guaranteed but also the individuals are evenly distributed in the solution space. This helps to improve the diversity of the algorithm and maintain its search capability (Algorithm 1).

3.3. Constraint Handling. DEED involves a number of equality and inequality constraints. We cannot guarantee every generated solution will satisfy all constraints, especially real power balance and ramp rate constraints. Penalty-based methods are the most commonly used methods to deal with these complex constraints, but it has some shortcomings in the calculation efficiency. Furthermore, how to determine the punishment degree is also a challenge. In this section, we devised a heuristic process to deal with the constraints. Compared with [18], our method can avoid the situation that the output power of the adjacent hour violates the power balance constraints, especially at the later stage of the adjustment process. Handling of the SRRs in this chapter is referenced from Ref. [19].

Step 1: randomly select an hour $t \in N_T$.

Step 2: calculate the corresponding feasible region of the adjustable output:

$$P_{i,t}^{\min} = \begin{cases} \max\left(P_{i,\min}, P_{i,t+1} - \mathrm{UR}_i\right), & t = 1, \\ \max\left(P_{i,\min}, P_{i,t-1} - \mathrm{DR}_i\right), & t = N_T, \\ \max\left(\max\left(P_{i,\min}, P_{i,t-1} - \mathrm{DR}_i\right), P_{i,t+1} - \mathrm{UR}_i\right), & 1 < t < N_T, \end{cases} \tag{15}$$

$$P_{i,t}^{\max} = \begin{cases} \min\left(P_{i,\max}, P_{i,t+1} + \mathrm{DR}_i\right), & t = 1, \\ \min\left(P_{i,\max}, P_{i,t-1} + \mathrm{UR}_i\right), & t = N_T, \\ \min\left(\min\left(P_{i,\max}, P_{i,t+1} + \mathrm{DR}_i\right), P_{i,t-1} + \mathrm{UR}_i\right), & 1 < t < N_T. \end{cases} \tag{16}$$

Step 3: adjust the output of each generator at the current hour to satisfy (15) and (16) using (17):

$$P_{i,t} = \begin{cases} P_{i,t}^{\min}, P_{i,t} < P_{i,t}^{\min}, \\ P_{i,t}, P_{i,t}^{\min} \le P_{i,t} \le P_{i,t}^{\max}, \\ P_{i,t}^{\max}, P_{i,t} > P_{i,t}^{\max}. \end{cases} \tag{17}$$

Step 4: tackle the SRR constraints: check if SRRs is satisfied and then go to Step 5; otherwise, calculate the violation of SRRs $\Delta_{\mathrm{SRRs},t}$ and set $t = t - 1$. Subtract $\Delta_{\mathrm{SRRs},t}$ from $P_{i,t}^{\max}$ which are equal to their upper limits. Then, generate a new feasible individual at hour $t - 1$. Calculate $\Delta_{\mathrm{SRRs},t-1}$ and repeat the adjust process until the SRR constraints are satisfied at an hour.

Step 5: tackle the demand-supply constraint by the following steps:

(1) Calculate the system transmission loss using (5).

(2) Calculate the difference between the power demand and the power grid output:

$$\mathrm{Dif} = P_{D,t} + P_{L,t} - \left(\sum_{i=1}^{N_G} P_{i,t} + \sum_{i=1}^{N_w} w_{i,t} + \sum_{i=1}^{N_{\mathrm{PV}}} \mathrm{PV}_{i,t} + \sum_{i=1}^{N_{\mathrm{ES}}} \mathrm{ES}_{i,t}\right). \tag{18}$$

Check if $\mathrm{Dif} \le \varepsilon_0$ and then go to Step 2 with the next randomly selected hour; otherwise, go to the next step. Here, ε_0 is a tolerance variable which decreases from early stages of the evolutionary process and is decreased gradually to a small value [20].

(3) Generate a random sequence $R = [r_1, r_2, \ldots, r_{N_G}]$. Select $P_{r,t}$ as the first slack generator and adjust its power as

Input: τ, λ, iterMax
Output: Screened individuals
(1) **initialize**: Set $\tau = 0.5$
(2) **if** iter $< \tau *$ iterMax **then**
(3) Screen using a combination of nondominated sorting and crowding distance
(4) **else**
(5) $\lambda = \tau + (1 - \tau) *$ (iter/iterMax)
(6) **if** rand $< \lambda$ **then**
(7) Screen using the nondominated sorting
(8) **else**
(9) Screen using a combination of nondominated sorting and crowding distance and hypercube grid
(10) **end if**
(11) **end if**

Algorithm 1: Elitist nondominated sorting strategy.

$$P_{r,t} = \begin{cases} P_{r,t} + \text{Dif} * \Delta, & \text{if Dif} > 0, \\ P_{r,t} - \text{Dif} * \Delta, & \text{if Dif} < 0. \end{cases} \quad (19)$$

(4) Adjust $P_{r,t}$ using (17) to satisfy the feasible region limit. Update Dif and select the next slack generator in turn according to R. Δ is a random value which lies between [0.2, 1].

Step 6: repeat the previous steps until a feasible solution is found.

3.4. Selection Hyper-Heuristic Algorithm for DEED. The detailed procedure of the proposed method for DEED is presented as follows:

Step 1: initialize the setting parameters of the algorithm, such as population size, the maximum number of iteration, number of objective, and parameters of low-level operators.

Step 2: generate the initial population, perform the nondominated sorting, and calculate the crowding distance.

Step 3: select individuals to build up the parent population using the tournament selection, and then generate the initial offspring population by calling the low-level operators.

Step 4: memorize the current iteration number and start the evolution process.

Step 5: combine the parent population and the offspring population, conduct the nondominated sorting strategy, and update the crowding distance.

Step 6: select the parent individuals using the proposed nondominated sorting strategy mentioned in the previous section, and then generate the offspring individuals.

Step 7: grade and rank the low-level operators using the evaluation method presented in the previous section.

Step 8: choose the low-level operator using the selection mechanism presented in the previous section.

Table 1: Related parameters for case study.

Population size	150
Maximum iteration	250
Parameters for ES	$\text{SOC}_{\min} = 0.2$, $\text{SOC}_{\max} = 1$, $E_{\max} = 300$ WM, $\Delta t = 0.92$
Parameters for high level	SWT = 15, $C_1 = C_2 = 0.4$, $C_3 = C_4 = 0.1$
Parameters for low level	$F_{\min} = 0.2$, $F_{\max} = 0.8$, $G_{r,\min} = 0.3$, $G_{r,\max} = 0.8$, $F = \text{rand}(F_{\min}, F_{\max})$
Operators	$G_r = G_{r,\min} + (G_{r,\max} - G_{r,\min}) * \exp(-2 * (\text{iterMax} - \text{iter}))/\text{iter}$

Step 9: memorize the optimal solution and check whether the current iteration is greater than the maximum iteration number. If not, continue the cycle; otherwise, output the global optima solution.

The flowchart of the proposed method is presented as follows.

4. Results and Discussion

For the experimental study, four test cases are studied to evaluate the performance of the proposed algorithm. The scheduling time N_T of all cases is selected as one day with 24 hours, and the valve-point effect and the ramp rate constraints are taken into account. Case 1 and Case 2 are classic DEEDs with 5 thermal units and 10 thermal units without considering wind and PV generation, respectively. We use these two cases to verify the effectiveness of our proposed method by comparing them with the existing algorithms. Case 3 comes from an IEEE 57 bus system; three PV and two wind generators are incorporated into this system. Case 4 considers the ES unit on the basis of Case 3. We use this case to study the impact of ES on the system operation and its role in peak shaving and valley filling in the power supply.

Wind power output depends on wind speed, type of wind turbine, and parameters of its power performance curve. Wind speed is a random variable that needs to be

Table 2: Optimal results for Case 1 (optimal cost).

H	P_1	P_2	P_3	P_4	P_5	P_L	E_c (\$)	E_m (lb)
1	20.24	98.62	30.00	125.04	139.91	3.82	1250.56	546.67
2	10.00	97.91	66.84	124.79	139.63	4.13	1425.15	534.83
3	10.00	98.41	106.83	124.89	139.76	4.78	1392.40	558.72
4	25.80	98.53	112.78	124.91	173.81	5.91	1732.18	682.12
5	19.31	98.51	112.68	124.84	209.36	6.63	1721.24	845.55
6	49.31	99.20	112.71	124.94	229.59	7.85	1785.23	977.50
7	68.80	98.43	112.66	124.89	229.52	8.31	1799.13	1002.70
8	74.99	98.51	112.67	147.37	229.53	9.05	1980.10	1053.38
9	62.16	98.45	112.65	197.37	229.53	10.12	2046.26	1152.18
10	63.96	98.57	112.71	209.81	229.51	10.56	1997.11	1194.64
11	74.51	98.50	112.67	209.81	235.47	11.04	2050.82	1251.31
12	74.98	98.52	112.67	180.08	285.45	11.77	2412.73	1570.83
13	73.53	98.54	112.67	130.08	300.00	10.77	2150.49	1624.19
14	64.27	98.51	112.67	124.90	300.00	10.37	2106.36	1599.32
15	34.27	98.52	112.68	124.89	292.92	9.34	2047.42	1486.71
16	10.00	96.91	112.65	124.90	242.92	7.28	1711.12	1046.39
17	10.00	92.79	107.59	124.88	229.52	6.71	1618.85	943.40
18	35.87	98.57	113.09	138.69	229.56	7.86	1854.71	987.96
19	34.05	98.48	112.50	188.67	229.52	9.14	1998.32	1098.70
20	64.05	98.54	112.67	209.74	229.51	10.56	1996.98	1194.40
21	39.29	98.59	112.68	209.79	229.53	9.90	1944.92	1166.62
22	10.00	96.86	112.61	209.82	183.54	7.91	1874.26	920.06
23	10.00	66.86	106.92	209.74	139.59	6.01	1651.80	693.75
24	10.02	36.86	71.38	209.82	139.76	4.80	1584.27	641.47
Total						194.61	44132	24773

predicted and has uncertainty. The previous study has proved that the wind speed at a given location closely follows a Weibull distribution over time [21]. The output power of wind turbines can be predicted by the PDF of wind speed and the wind speed-power curve. The detailed calculation steps and parameters can be found in [22]. The output power of the PV can be calculated by predicting solar radiation. However, the solar radiation reaching the Earth's surface depends upon the climatic conditions of a location [23]. The calculation steps of power of PV are detailed in [24]. The parameters used for solving DEED in this study are shown in Table 1. For each case, 20 independent trials were conducted to compare the solution quality and convergence characteristics. All experiments were executed in the MATLAB 2016a computational environment on a Pentium-core 3.2 GHz personal computer with 8 GB of RAM.

4.1. Case Study

4.1.1. Case 1: Classic 5-Generator System. This test system consists of five thermal generators with considering the transmission loss. The generating system data and B coefficients to compute transmission line losses are adapted from [25]. The best cost and emission solutions are given in Tables 2 and 3, respectively. The compromise solution considering economic and emission is presented in Table 4. H represents the dispatch hour, and P_i denotes the output power allocated to the ith thermal generator. P_L is the transmission line losses. E_c and E_m are the fuel cost and emission, respectively. The optimal cost and emission solutions are 44132 \$/day and 17852 lb/day, respectively. The minimum cost and emission of the best compromise solution are 47503 \$/day and 18066 lb/day, respectively. Table 5 gives the comparison among different methods, such as SA, MSL, EP, PS, PSO, MODE, and AGB-MOCDE. It is obvious that the proposed method can obtain solutions with lower total economic costs and emission than other reported methods.

4.1.2. Case 2: Classic 10-Generator System. This case consists of ten thermal generators with considering the transmission loss. The generating system data and B coefficients can be obtained in [26]. The best cost and emission solutions are given in Tables 6 and 7, respectively. The compromise solution considering economic and emission is presented in Table 8. The optimal cost and emission solutions are 2471526 \$/day and 291988 lb/day, respectively. The minimum cost and emission of the best compromise solution are 2514885 \$/day and 299585 lb/day, respectively. The simulation results of the proposed methods are compared in Table 5 with NSGA-II, EP, PSO, SQP, HMO-DE-PSO, RCGA, MADM, IBFA, and MODE. It is obvious that the proposed method can obtain solutions with lower total economic costs and emission than other reported methods.

To test the convergence characteristics of the proposed method, we conducted a comparison experiment in the same experiment situation for Case 2. Two typical methods, NSGA-II and MODE, are used to compare with SHHA. 20 independent trials were conducted to compare the convergence characteristics. Figure 1 shows the convergence

Table 3: Optimal results for Case 1 (optimal emission).

T_H	P_1	P_2	P_3	P_4	P_5	P_L	E_c ($)	E_m (lb)
1	54.70	58.19	116.56	110.45	73.53	3.45	1725.14	352.44
2	58.08	62.25	121.85	118.38	78.31	3.89	1780.62	385.95
3	63.38	69.20	129.91	129.92	87.22	4.64	1911.96	446.63
4	71.45	78.37	141.62	145.50	98.84	5.79	2133.65	544.63
5	75.00	83.35	147.28	153.69	105.10	6.43	2202.49	601.19
6	75.00	93.80	158.96	170.11	117.76	7.65	2243.16	715.00
7	75.00	97.29	163.13	175.88	122.81	8.12	2224.83	760.33
8	75.00	103.27	169.13	185.29	130.17	8.88	2220.35	835.62
9	75.00	111.46	175.00	197.50	140.94	9.91	2208.04	941.41
10	75.00	115.23	175.00	203.39	145.70	10.34	2255.86	985.83
11	75.00	119.96	175.00	209.65	151.21	10.83	2309.83	1039.14
12	75.00	125.00	175.00	217.44	159.02	11.47	2471.19	1109.73
13	75.00	115.47	175.00	203.26	145.60	10.34	2257.14	985.83
14	75.00	111.45	175.00	197.75	140.71	9.91	2204.96	941.40
15	75.00	103.10	169.04	185.62	130.10	8.88	2218.84	835.62
16	75.00	87.67	152.34	160.92	111.02	6.95	2237.17	649.10
17	75.00	83.06	147.41	154.03	104.91	6.43	2205.58	601.19
18	75.00	93.38	158.92	170.34	118.01	7.65	2244.08	714.99
19	75.00	103.32	169.05	185.41	130.09	8.88	2220.96	835.62
20	75.00	115.41	175.00	203.31	145.61	10.34	2256.62	985.83
21	75.00	108.69	174.99	193.68	137.25	9.62	2201.34	910.92
22	75.00	92.86	158.27	169.19	117.25	7.58	2244.93	707.67
23	70.84	77.94	141.08	144.61	98.25	5.73	2124.57	538.84
24	61.83	67.19	127.45	126.28	84.65	4.41	1849.31	427.50
Total						188.13	51953	17852

Table 4: Optimal compromise results for Case 1.

H	P_1	P_2	P_3	P_4	P_5	P_L	E_c ($)	E_m (lb)
1	60.68	65.18	112.89	124.70	50.07	3.51	1461.20	362.60
2	63.25	78.87	112.39	125.02	59.42	3.95	1538.25	396.97
3	72.17	81.73	117.52	124.93	83.33	4.67	1738.45	453.15
4	75.00	90.54	127.86	126.08	116.32	5.80	1838.91	557.48
5	74.99	97.06	132.76	126.87	132.76	6.43	1798.62	624.45
6	74.99	98.37	160.99	141.66	139.61	7.62	2000.13	730.30
7	75.00	98.21	160.02	169.65	131.22	8.11	2178.50	761.97
8	75.00	98.51	163.85	187.80	137.71	8.87	2144.33	837.33
9	75.00	100.43	174.97	209.76	139.77	9.91	2062.54	945.48
10	75.00	114.67	175.00	209.79	139.90	10.36	2172.01	986.93
11	75.00	125.00	175.00	210.00	145.86	10.86	2292.06	1040.11
12	75.00	125.00	175.00	214.67	161.79	11.46	2467.32	1109.97
13	75.00	114.34	174.98	209.80	140.24	10.36	2172.79	986.88
14	75.00	100.26	175.00	209.82	139.84	9.91	2061.54	945.54
15	75.00	98.40	165.56	184.52	139.39	8.86	2143.03	837.42
16	75.00	98.43	145.18	134.52	133.82	6.94	1926.89	665.95
17	74.81	97.49	134.45	125.36	132.33	6.43	1797.18	624.51
18	74.98	98.53	162.28	140.16	139.67	7.62	1988.62	731.37
19	75.00	98.48	166.20	185.63	137.55	8.86	2149.55	836.91
20	75.00	114.74	175.00	209.85	139.76	10.36	2171.44	986.96
21	74.39	98.34	174.96	202.34	139.58	9.61	2080.14	914.34
22	74.99	98.50	146.73	152.80	139.54	7.56	2039.88	719.77
23	74.91	98.19	114.13	125.80	119.74	5.77	1691.22	564.86
24	67.58	92.99	112.66	124.32	69.93	4.49	1588.60	444.58
Total						188.35	47503	18066

comparison when aiming to optimize the fuel cost. The figure indicates that the SHHA converges faster than other methods. In addition, the statistical results of the 20 trails are given in Table 9. It can be seen that the SHHA outperforms the other methods regardless of minimum cost, average cost, and maximum cost. The SHHA has a lower standard deviation which also shows a better robustness (Figures 2 and 3).

Table 5: Comparison of the results for Case 1 and Case 2.

Method	Minimum cost		Minimum emission		Compromise result		Computational time (min)
	E_c ($)	E_m ($)	E_c ($)	E_m ($)	E_c ($)	E_m (lb)	
Case 1							
SA [25]	47356	—	—	—	—	—	NA
MSL [27]	49216.81	—	—	—	—	—	NA
EP [28]	46777	—	—	17966	48628	21154	NA
PS [28]	46530	—	—	18192	47911	18927	4.91
PSO [29]	47852	22405	—	—	50893	20163	NA
MODE [30]	46934	18194	48841	18008	47714	18084	15
MOHDE-SAT [31]	46478	18208	50684	17884	48214	18011	14.55
AGB-MOCDE [25]	46230	18295	49866	17927	47589	18075	NA
This paper	44711	22000	51953	17852	47503	18066	9.33
Case 2							
NSGA-II [26]	—	—	—	—	2522600	309940	20.11
EP [32]	2585000	—	—	—	—	—	NA
PSO [14]	2572000	—	—	—	—	—	NA
SQP [14]	2519000	343400	2628000	308000	2535000	329300	
MOHDE-SAT [31]	2,508,195	334100	2606000	295900	2525000	303900	16.17
RCGA [26]	2516800	317400	2656300	304120	2525100	312460	18
MADM [33]	—	—	—	—	2590500	291960	15
IBFA [6]	2481733	327501	2614341	295833	2517116	299036	5.2
MODE [30]	2512327	301130	2543560	296387	2525841	298344	16.76
This paper	2471526	332300	2598103	291988	2517013	299005	10.85

NA denotes that the value was not available in the literature.

Table 6: Optimal results for Case 2 (optimal cost).

H	P_1	P_2	P_3	P_4	P_5	P_6	P_7	P_8	P_9	P_{10}	P_L	E_c ($)	E_m (lb)
1	150.00	135.00	75.14	120.50	172.79	122.55	129.58	120.00	20.01	10.00	19.57	60798.58	4485.67
2	150.00	135.00	73.00	117.92	222.60	122.44	129.57	120.00	22.03	40.00	22.57	64487.08	4918.49
3	150.00	135.00	153.00	120.66	222.64	159.94	129.83	120.00	52.03	43.42	28.52	71950.58	5760.26
4	150.00	135.00	209.67	170.66	243.00	160.00	129.77	120.00	80.00	43.42	35.52	80147.32	7479.89
5	150.00	135.00	286.36	220.46	222.60	159.98	129.59	120.00	52.05	43.41	39.46	84063.33	9712.09
6	150.00	135.00	340.00	270.46	243.00	160.00	130.00	120.00	80.00	47.64	48.10	93405.09	12978.59
7	150.00	176.95	340.00	300.00	243.00	160.00	130.00	120.00	80.00	55.00	52.95	99401.53	14135.31
8	177.00	229.55	340.00	300.00	243.00	160.00	130.00	120.00	80.00	54.86	58.41	106426.87	14930.24
9	257.00	309.55	340.00	300.00	243.00	160.00	130.00	120.00	80.00	55.00	70.55	122936.13	17298.48
10	284.06	389.55	340.00	300.00	243.00	160.00	130.00	120.00	80.00	55.00	79.60	135865.95	20609.76
11	303.25	462.82	340.00	300.00	243.00	160.00	130.00	120.00	80.00	55.00	88.07	148255.42	28462.03
12	344.53	470.00	340.00	300.00	243.00	160.00	130.00	120.00	80.00	55.00	92.53	155284.18	30916.87
13	331.62	396.80	340.00	300.00	243.00	160.00	130.00	120.00	80.00	55.00	84.42	143039.98	22128.58
14	251.62	316.80	340.00	300.00	243.00	160.00	130.00	120.00	80.00	53.16	70.58	123104.17	17386.73
15	178.45	236.80	340.00	291.24	243.00	160.00	130.00	120.00	80.00	55.00	58.49	107011.89	14778.29
16	150.00	156.80	294.04	241.24	222.60	160.00	129.61	120.00	80.00	43.42	43.71	89056.97	10573.98
17	150.00	135.00	297.38	191.48	240.65	159.98	129.59	120.00	52.07	43.41	39.56	84053.15	9763.75
18	150.00	156.80	340.00	241.48	243.00	160.00	130.00	120.00	80.00	54.98	48.26	94201.12	12445.67
19	222.06	236.80	308.04	291.48	243.00	160.00	129.99	120.00	80.00	43.42	58.79	108008.17	14093.97
20	302.06	316.80	340.00	300.00	243.00	160.00	130.00	120.00	80.00	55.00	74.87	129078.05	18306.48
21	226.63	371.79	308.69	300.00	243.00	160.00	130.00	120.00	80.00	55.00	71.11	124899.03	17709.46
22	150.00	291.79	229.80	250.00	222.72	160.00	129.59	120.00	80.00	43.42	49.32	98973.23	10940.48
23	150.00	211.79	163.00	200.02	172.74	122.45	129.59	120.00	51.54	43.41	32.54	78934.42	6807.68
24	150.00	135.00	84.04	180.84	222.61	122.46	129.60	120.00	21.54	43.42	25.51	68144.37	5678.15
Total											1293	2471526	332301

4.1.3. Case 3: IEEE 57 Bus System (Seven Thermal Units, Three Wind Generators, and Two PV). In this case, the proposed method is used to solve a DEED on an IEEE 57 bus system. Three PV and two wind generators are incorporated into this system. The data and information of this system can be obtained from [34]. The transmission loss coefficients were taken from [24]. The predictive wind power and PV power for the 24 hours of the next day are shown in Figure 4.

The optimal load allocation scheme considering the wind and solar power unit is given in Table 10. The cost and

Table 7: Optimal results for Case 2 (optimal emission).

H	P_1	P_2	P_3	P_4	P_5	P_6	P_7	P_8	P_9	P_{10}	P_L	E_c ($)	E_m (lb)
1	150.00	135.00	90.81	91.17	129.66	129.75	97.28	97.03	80.00	55.00	19.70	63031.92	3738.78
2	150.00	137.31	101.55	101.68	144.89	144.64	108.79	108.60	80.00	55.00	22.46	66989.68	4183.90
3	165.26	165.63	120.06	120.31	171.21	160.00	129.47	120.00	80.00	55.00	28.94	75201.36	5305.11
4	200.58	201.30	145.02	145.42	205.31	160.00	130.00	120.00	80.00	55.00	36.63	85948.84	6787.74
5	218.53	218.68	158.35	158.45	221.86	160.00	130.00	120.00	80.00	55.00	40.87	90504.17	7689.93
6	254.62	255.12	190.13	190.24	243.00	160.00	130.00	120.00	80.00	55.00	50.11	102891.69	9858.75
7	274.14	274.72	210.16	210.13	243.00	160.00	130.00	120.00	80.00	55.00	55.15	109619.52	11181.43
8	292.22	292.83	231.49	231.88	243.00	160.00	130.00	120.00	80.00	55.00	60.42	115611.53	12698.72
9	325.25	325.45	278.26	278.78	243.00	160.00	130.00	120.00	80.00	55.00	71.73	128950.53	16441.33
10	348.67	348.94	316.32	300.00	243.00	160.00	130.00	120.00	80.00	55.00	79.93	138563.29	19611.66
11	382.81	383.08	340.00	300.00	243.00	160.00	130.00	120.00	80.00	55.00	87.90	148746.87	23294.05
12	407.11	407.37	340.00	300.00	243.00	160.00	130.00	120.00	80.00	55.00	92.49	156050.30	26196.89
13	364.12	364.34	340.00	300.00	243.00	160.00	130.00	120.00	80.00	55.00	84.46	144035.67	21616.38
14	325.22	325.51	278.29	278.71	243.00	160.00	130.00	120.00	80.00	55.00	71.73	128951.79	16441.32
15	292.11	292.88	231.27	232.16	243.00	160.00	130.00	120.00	80.00	55.00	60.42	115603.52	12698.75
16	232.50	233.23	170.38	182.16	235.98	160.00	130.00	120.00	80.00	55.00	45.25	95810.32	8713.92
17	218.50	218.70	158.23	158.78	221.66	160.00	130.00	120.00	80.00	55.00	40.87	90506.53	7689.94
18	254.91	255.20	189.95	190.05	243.00	160.00	130.00	120.00	80.00	55.00	50.11	102913.73	9858.75
19	291.73	292.27	231.17	233.24	243.00	160.00	130.00	120.00	80.00	55.00	60.41	115546.07	12698.93
20	338.32	338.54	299.65	283.24	243.00	160.00	130.00	120.00	80.00	55.00	75.74	133883.72	17921.35
21	345.82	346.08	257.43	259.11	243.00	160.00	130.00	120.00	80.00	55.00	72.46	132421.73	16620.31
22	265.82	266.08	177.43	209.11	214.92	160.00	130.00	120.00	80.00	55.00	50.38	104485.09	9979.33
23	185.83	186.08	119.55	159.11	170.60	160.00	128.51	120.00	80.00	55.00	32.68	81076.04	6054.37
24	150.44	150.67	110.52	110.42	157.77	157.85	118.51	118.33	80.00	55.00	25.51	70760.05	4707.21
Total											1316	2598104	291989

Table 8: Optimal compromise results for Case 2.

H	P_1	P_2	P_3	P_4	P_5	P_6	P_7	P_8	P_9	P_{10}	P_L	E_c ($)	E_m (lb)
1	150.00	135.00	83.14	105.81	122.78	122.41	93.08	120.00	79.99	43.47	19.68	61883.02	3834.71
2	150.00	135.00	93.59	118.72	129.38	127.92	123.08	120.00	80.00	54.79	22.47	65850.56	4238.58
3	150.04	135.00	151.59	130.32	174.85	160.00	129.71	120.00	80.00	55.00	28.51	72937.12	5402.22
4	151.03	165.75	176.80	180.32	222.82	160.00	130.00	120.00	80.00	55.00	35.71	81513.33	7057.05
5	150.77	214.81	185.63	180.84	243.00	160.00	130.00	120.00	80.00	55.00	40.05	86940.85	7951.01
6	225.74	222.30	210.98	230.26	243.00	159.98	130.00	120.00	80.00	55.00	49.27	98933.28	10070.42
7	226.84	224.58	274.93	241.60	243.00	159.95	130.00	120.00	80.00	55.00	53.89	103218.06	11766.89
8	227.09	245.31	287.77	286.75	243.00	160.00	130.00	120.00	80.00	55.00	58.92	109001.40	13533.34
9	298.28	309.59	299.19	300.00	243.00	160.00	130.00	120.00	80.00	55.00	71.06	125030.20	16622.95
10	327.06	346.48	340.00	300.00	243.00	160.00	130.00	120.00	80.00	55.00	79.55	136668.76	19755.86
11	377.53	388.34	340.00	300.00	243.00	160.00	130.00	120.00	80.00	55.00	87.88	148487.46	23312.06
12	393.65	420.79	340.00	300.00	243.00	160.00	130.00	120.00	80.00	55.00	92.45	155752.75	26388.10
13	352.11	376.30	340.00	300.00	243.00	160.00	130.00	120.00	80.00	55.00	84.43	143741.53	21683.51
14	298.74	309.52	298.81	300.00	243.00	160.00	130.00	120.00	80.00	55.00	71.07	125046.92	16619.27
15	230.58	282.70	276.52	257.58	243.00	160.00	130.00	120.00	80.00	55.00	59.39	111102.30	13124.72
16	150.58	215.75	202.69	241.08	243.00	160.00	130.00	120.00	79.99	55.00	44.10	91219.05	9331.48
17	150.05	142.50	198.41	240.44	243.00	160.00	130.00	120.00	80.00	55.00	39.41	84745.32	8567.45
18	164.97	222.36	259.72	241.58	243.00	160.00	130.00	120.00	80.00	55.00	48.63	96388.38	10708.27
19	234.65	244.68	286.27	281.39	243.00	160.00	130.00	120.00	80.00	55.00	59.00	109550.71	13431.70
20	307.82	320.50	330.66	300.00	243.00	160.00	130.00	120.00	80.00	55.00	74.99	129799.15	18164.80
21	303.25	348.25	265.30	290.89	243.00	160.00	130.00	120.00	80.00	55.00	71.71	128557.39	16591.91
22	223.25	268.25	185.39	240.89	222.65	160.00	129.62	120.00	80.00	47.70	49.76	100925.52	10228.10
23	150.00	188.25	129.33	190.89	172.74	160.00	129.60	120.00	80.00	43.43	32.24	78684.55	6327.54
24	150.00	135.00	98.73	140.89	172.61	139.05	129.56	120.00	79.99	43.55	25.37	68907.17	4873.13
Total											1300	2514885	299585

emission are 111203.2 $/day and 115221.2 lb/day, respectively. MODE and NSGA-II were used for comparison. It can be seen that the proposed method has better performance both in cost and emission. Moreover, we studied the impact of the introduction of RES on the system. Figure 5 shows that both cost and emission have improved.

Table 9: Comparison with MODE and NSGA-II for Case 2.

Method	Minimum cost				Minimum emission			
	Minimum cost ($)	Mean cost ($)	Maximum cost ($)	Standard deviation	Minimum emission (lb)	Mean emission (lb)	Maximum emission (lb)	Standard deviation
NSGA-II	2520648	2521741	2522085	1307	298464	299157	300146	237
MODE	2512327	2515319	2519422	1876	296453	297150	298607	423
SHHA	2471526	2473890	2478533	757	291988	292013	292475	157

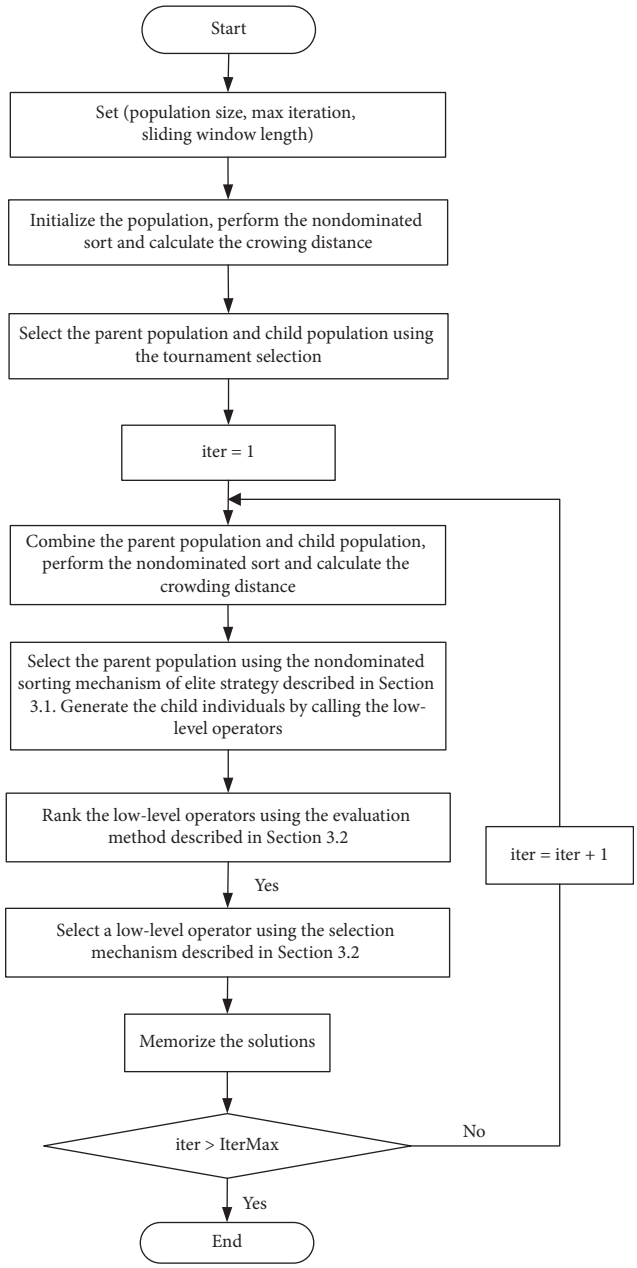

Figure 2: Flowchart of the proposed SHHA for DEED.

The cost and emission before introducing wind power and PV generators are 119305.6 $/day and 127416.7 lb/day, which means the introduction of RES will save about 8102.4 $ per day (approximately 2,957,376 $ per year) and reduce emissions 12195.5 lb per day (approximately 4,451,357 lb per year) (Table 11).

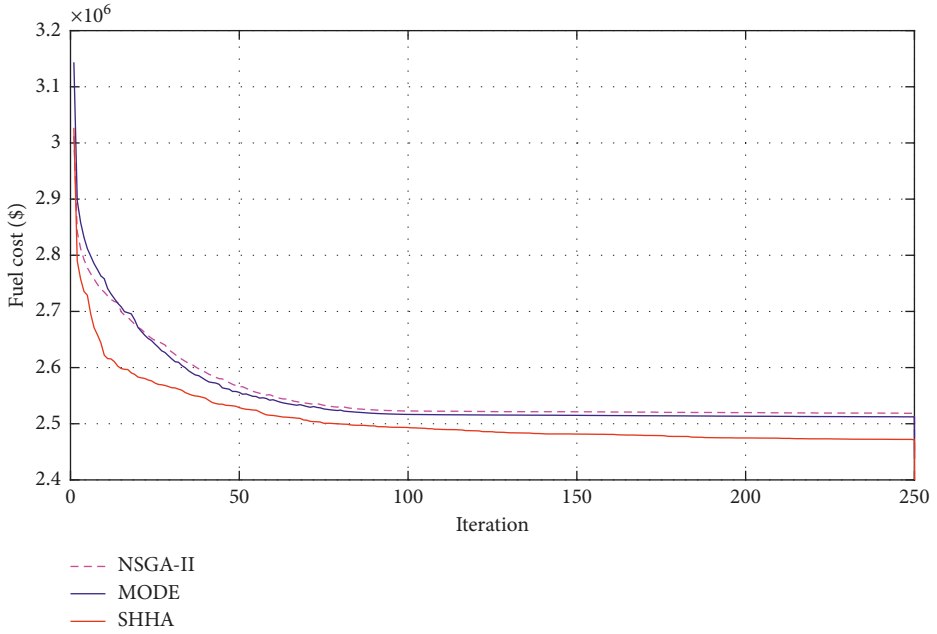

Figure 3: Convergence graphs of NSGA-II, MODE, and SHHA.

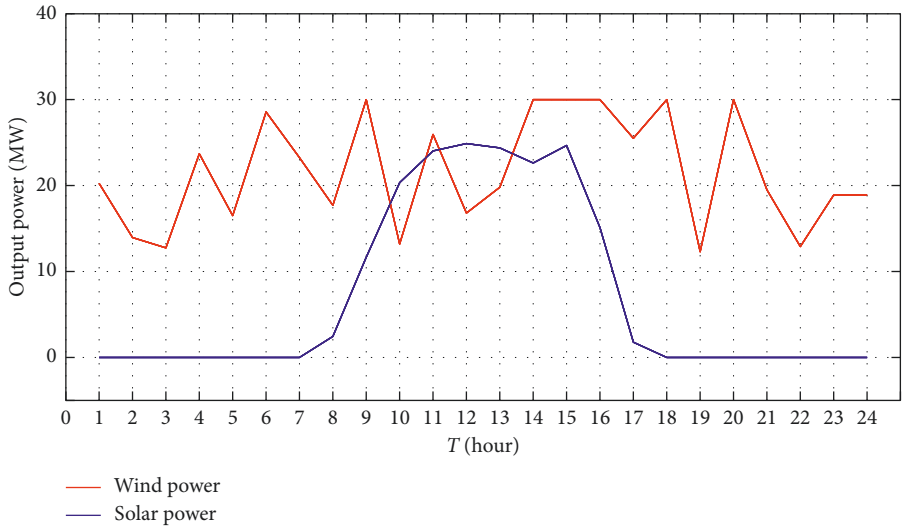

Figure 4: Predictive wind power and solar power for the 24 hours, next day t.

4.1.4. Case 4: Case 3 with Energy Storage. In this case, the ES unit is considered on the basis of Case 3. Relevant parameters of thermal units, wind power generators, PV generators, and transmission loss coefficient are consistent with Case 3. Parameters of ES can be found in Table 1. The initial value of SOC is set to 0.5, and the SOC at each hour can be accessed by

$$\begin{aligned} \mathrm{SOC}_i(t+1) &= \mathrm{SOC}_i(t) - \frac{\eta_c \mathrm{ES}_{i,t} \Delta t}{E \max}, \quad \mathrm{ES}_{i,t} < 0, \\ \mathrm{SOC}_i(t+1) &= \mathrm{SOC}_i(t) - \frac{\mathrm{ES}_{i,t}(\Delta t/\eta_d)}{E \max}, \quad \mathrm{ES}_{i,t} > 0, \end{aligned} \tag{20}$$

where η_c is the charge efficiency, η_d is the discharge efficiency, and $E_{\max}$ is the ES energy capacity. Table 12 lists the optimal compromise solution. The optimal compromise solution corresponding to the cost is 111317.6 $/day and the emission is 14565.4 lb/day. At the beginning of the day, the power load is in the low stage, at which time the power demand is less and the ES is in charge mode to store energy for future peak shaving. It is assumed that the initial SOC is 0.5 and the total charge power per hour should meet the upper limit. In the peak load stage, the ES is in the discharge mode to reduce the power generation of the grid. Finally, the ES state will be restored to 0.5 SOC at the end of the day. Figure 6 shows the effect of ES on load peak shaving and valley filling. Figure 6 reflects the impact of the introduction of ES on the Pareto optimal solution set. It can be seen that ES is beneficial to both cost and emission (Figure 7).

Table 10: Optimal compromise results for Case 3.

H	P_1	P_2	P_3	P_4	P_5	P_6	P_7	P_{w1}	P_{w2}	P_{w3}	P_{v1}	P_{v2}	P_L	E_c ($)	E_m (lb)
1	207.88	10.00	20.00	10.13	211.59	10.00	133.89	20.25	20.25	20.25	0.00	0.00	28.22	1722.8	1136.3
2	238.85	10.00	20.00	10.01	244.37	10.00	162.03	13.95	13.95	13.95	0.00	0.00	27.19	1970.3	1561.3
3	279.80	10.00	37.58	10.00	284.31	10.23	219.74	12.75	12.75	12.75	0.00	0.00	31.93	2516.1	2349.5
4	304.15	10.00	59.53	14.39	331.87	11.53	246.27	23.70	23.70	23.70	0.00	0.00	42.80	3050.7	3067.4
5	334.69	10.00	64.90	25.97	346.52	25.01	265.61	16.50	16.50	16.50	0.00	0.00	42.21	3552.5	3572.3
6	350.87	10.00	87.43	36.21	380.16	37.74	296.46	28.56	28.56	28.56	0.00	0.00	56.52	4252.1	4327.5
7	368.85	10.00	88.43	46.29	399.99	54.77	319.05	23.25	23.25	23.25	0.00	0.00	55.19	4762.5	4910.6
8	383.13	10.00	105.47	61.15	428.97	57.41	327.55	17.70	17.70	17.70	2.45	2.45	55.71	5272.2	5506.9
9	401.92	10.00	120.06	75.48	457.63	66.99	355.61	30.00	30.00	30.00	11.66	11.66	77.02	5941.2	6387.6
10	418.77	10.00	126.24	80.87	481.89	90.01	388.38	23.24	28.39	13.20	20.33	20.33	79.65	6862.5	7296.9
11	440.30	10.00	133.99	93.99	501.18	97.35	396.75	25.95	25.95	25.95	24.03	24.03	93.44	7088.3	7954.9
12	459.87	10.00	140.00	100.00	520.44	100.00	410.00	16.80	16.81	16.80	24.88	24.88	90.59	7436.2	8625.0
13	435.72	10.00	135.06	95.59	493.95	88.81	391.27	19.80	19.80	19.80	24.38	24.38	86.56	6950.3	7735.7
14	403.63	10.00	111.03	68.33	443.94	75.62	361.05	30.00	30.00	30.00	22.62	22.62	84.85	5859.9	6269.7
15	363.52	10.00	95.44	53.02	417.99	52.94	320.31	30.00	30.00	30.00	24.66	24.66	76.56	4922.9	5093.0
16	330.46	10.00	69.90	26.19	350.08	28.12	279.02	30.00	30.00	30.00	15.11	15.11	60.01	3679.4	3687.2
17	320.59	10.00	64.76	15.07	341.61	23.47	261.00	25.50	25.50	25.50	13.17	1.78	47.94	3469.3	3383.8
18	347.91	10.00	73.77	37.41	388.39	46.65	290.09	30.00	30.00	30.00	0.00	0.00	56.18	4240.5	4306.7
19	382.46	10.00	101.22	52.52	423.75	59.35	327.42	30.00	30.00	20.90	0.00	0.00	61.71	5521.6	5413.1
20	416.53	10.00	122.12	79.00	469.79	82.42	377.39	30.00	30.00	30.00	0.00	0.00	75.27	6355.6	6959.6
21	413.07	10.00	130.99	76.35	463.05	71.49	365.92	19.50	19.50	19.50	0.00	0.00	65.44	6196.3	6726.0
22	357.03	10.00	88.89	45.99	387.16	46.49	296.83	13.88	15.35	12.90	0.00	0.00	46.51	4537.3	4481.3
23	286.36	10.00	54.33	10.00	303.20	21.49	226.77	18.90	18.90	18.90	0.00	0.00	36.88	2862.5	2598.8
24	257.14	10.00	24.54	10.00	259.24	10.00	188.25	18.90	18.90	18.90	0.00	0.00	31.93	2180.4	1870.0
Total													1410	111203	115221

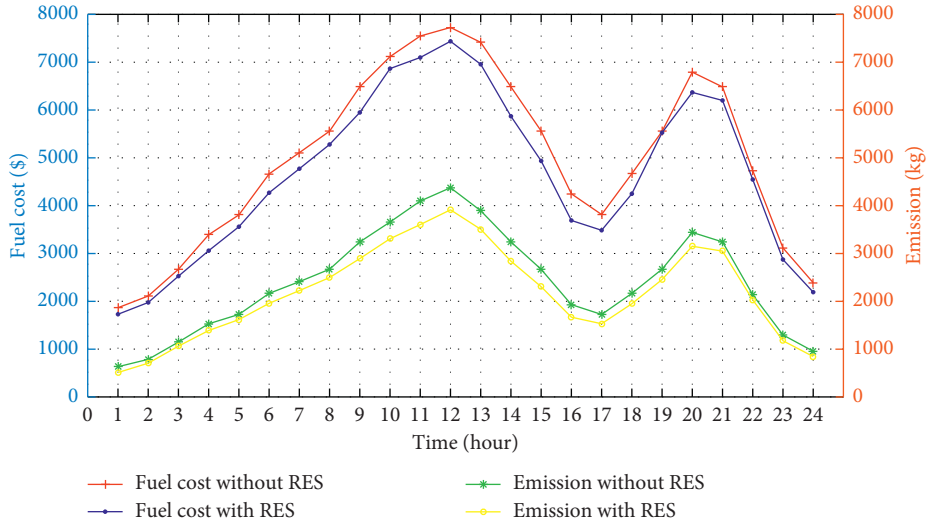

Figure 5: The impact of PV and wind power generation on cost and emission.

Table 11: Comparison with MODE and NSGA-II.

Method	Compromise result	
	E_c ($)	E_m (lb)
MODE	115067	118513
NSGA-II	113847	115854
With RES (this paper)	111203	115221

4.2. Effect of High-Level Strategy. In the hyper-heuristic method, the high-level strategy is used to evaluate each low-level operator and then determine the chosen probability of each operator for the following searching iterations. Figure 8 shows the change of the chosen probability of each low-level operator and it can be seen that the operators are adapting to the whole iteration. The operators show a significant difference in chosen probability at different iterations, which means that they have a different searching performance at different stages of the evolution process. Here, we only discuss the role of high-level strategy, without regard to the effect of the parameter setting of low-level operators.

Table 12: Optimal compromise results for Case 4.

H	P_1	P_2	P_3	P_4	P_5	P_6	P_7	P_{w1}	P_{w2}	P_{w3}	P_{v1}	P_{v2}	ES	P_L	E_c ($)	E_m (lb)
1	210.58	10.00	20.90	10.00	239.23	16.59	148.29	20.25	20.25	20.25	0.00	0.00	−51.84	28.48	1919.73	1346.75
2	227.56	10.00	23.66	10.08	285.41	12.60	169.08	13.95	13.95	13.95	0.00	0.00	−43.85	26.40	2132.58	1796.30
3	268.86	10.00	39.37	13.95	293.68	36.57	219.14	12.75	12.75	12.75	0.00	0.00	−30.80	31.02	2841.36	2372.17
4	329.83	10.00	62.87	15.25	323.36	13.60	246.87	23.70	23.70	23.70	0.00	0.00	−20.88	46.01	3156.58	3194.41
5	324.13	10.06	72.78	23.25	345.15	38.60	271.18	16.50	16.50	16.50	0.00	0.00	−12.65	42.00	3719.48	3557.49
6	361.42	10.18	82.90	41.83	366.08	40.23	300.99	28.56	28.56	28.56	0.00	0.00	−3.02	58.28	4307.78	4319.56
7	372.49	10.00	97.98	41.66	399.17	48.63	313.33	23.25	23.25	23.25	0.00	0.00	5.26	56.27	4710.99	4894.39
8	388.33	10.16	96.26	63.62	421.02	51.54	329.52	17.70	17.70	17.70	2.45	2.45	13.50	55.96	5154.90	5446.31
9	403.47	10.02	119.39	52.14	451.51	73.59	354.87	30.00	30.00	30.00	11.66	11.66	22.39	76.71	5728.31	6280.64
10	398.89	10.00	122.71	80.82	489.11	86.33	371.36	23.24	28.39	13.20	20.33	20.33	32.56	75.28	6678.22	6984.72
11	436.48	10.02	136.19	94.10	463.90	97.06	396.79	25.95	25.95	25.95	24.03	24.03	38.66	93.11	6962.08	7475.63
12	460.44	10.00	138.15	98.88	520.67	97.33	367.71	16.80	16.81	16.80	24.88	24.88	45.36	88.71	7194.52	8141.38
13	434.34	10.00	106.95	96.23	480.78	95.11	386.01	19.80	19.80	19.80	24.38	24.38	37.10	82.67	6709.36	7402.29
14	399.84	10.01	116.52	50.93	444.04	71.10	360.40	30.00	30.00	30.00	22.62	22.62	20.29	84.39	5647.54	6197.23
15	367.02	10.34	100.54	46.35	410.98	49.86	324.18	30.00	30.00	30.00	24.66	24.66	5.69	78.27	4865.17	5083.80
16	328.66	10.00	75.10	66.49	357.86	34.55	302.90	30.00	30.00	30.00	15.11	15.11	−80.00	61.78	4341.00	4030.14
17	306.08	10.01	78.12	23.07	405.77	30.02	262.76	25.50	25.50	25.50	13.17	1.78	−80.00	47.27	3898.79	3931.54
18	354.33	10.05	113.64	49.75	376.57	41.42	335.07	30.00	30.00	30.00	0.00	0.00	−80.00	62.82	4814.52	4788.80
19	339.83	10.00	99.48	54.99	421.26	60.38	324.08	30.00	30.00	20.90	0.00	0.00	40.76	55.69	5397.64	5008.34
20	400.81	10.01	130.39	45.46	464.70	60.33	362.39	30.00	30.00	30.00	0.00	0.00	80.00	72.08	5669.78	6485.53
21	405.26	10.00	93.05	81.18	462.29	41.22	351.87	19.50	19.50	19.50	0.00	0.00	80.00	59.37	5498.55	6290.76
22	353.10	10.21	85.54	46.98	387.28	47.03	299.69	13.88	15.35	12.90	0.00	0.00	2.38	46.34	4528.08	4466.87
23	285.78	10.32	54.28	10.36	301.81	22.10	269.04	18.90	18.90	18.90	0.00	0.00	−39.29	39.10	3023.24	2872.09
24	306.56	10.00	36.01	10.21	261.75	11.13	187.17	18.90	18.90	18.90	0.00	0.00	−58.54	37.00	2417.43	2198.29
Total														1405	111318	114565

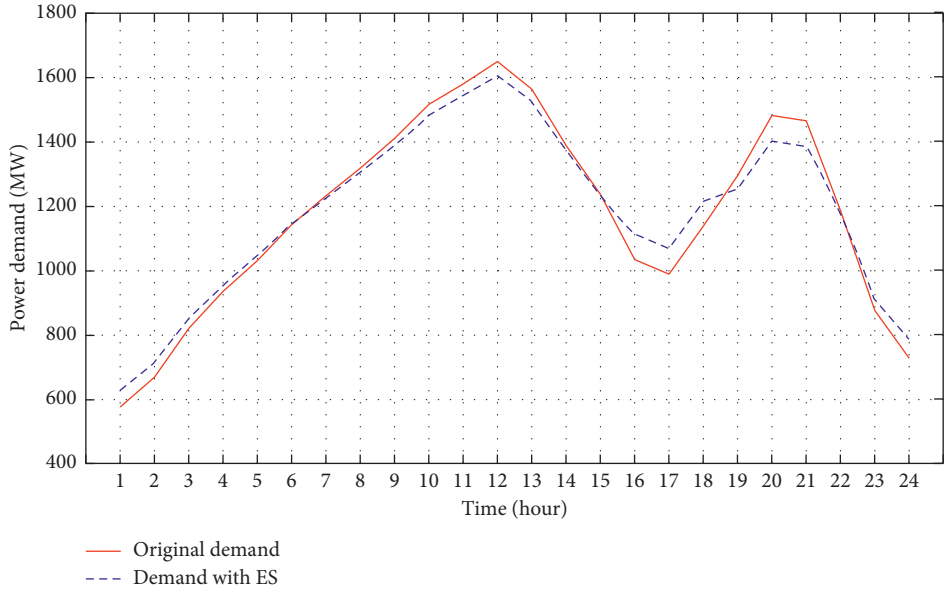

Figure 6: Effect of ES on load demand.

4.3. Effect of Elitist Nondominated Sorting Strategy. Population diversity is an important indicator to evaluate convergence and search performance of algorithms, especially in dealing with optimization problems with nonlinear and multipeak characteristics. To demonstrate the effectiveness of the proposed nondominated sorting strategy, we recorded the results of individual selection with and without the elite sorting strategy. Figure 9 shows the comparison results, where the red points represent the distribution of individuals screened by using the elite strategy. We can find from the figure that the population has better performance in individual distribution. The elite strategy effectively keeps the population diversity.

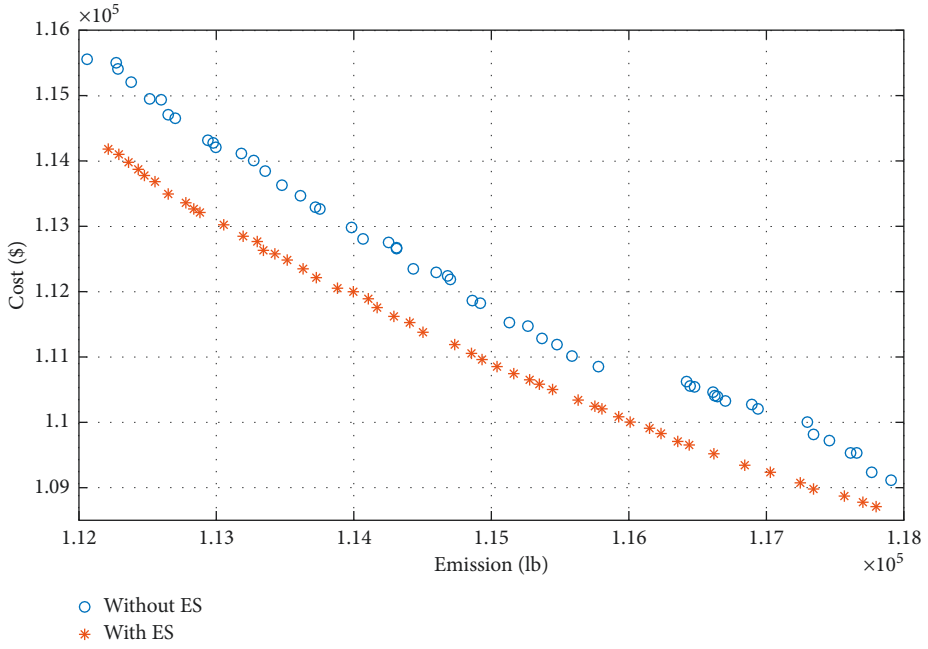

Figure 7: Effect of ES on load demand.

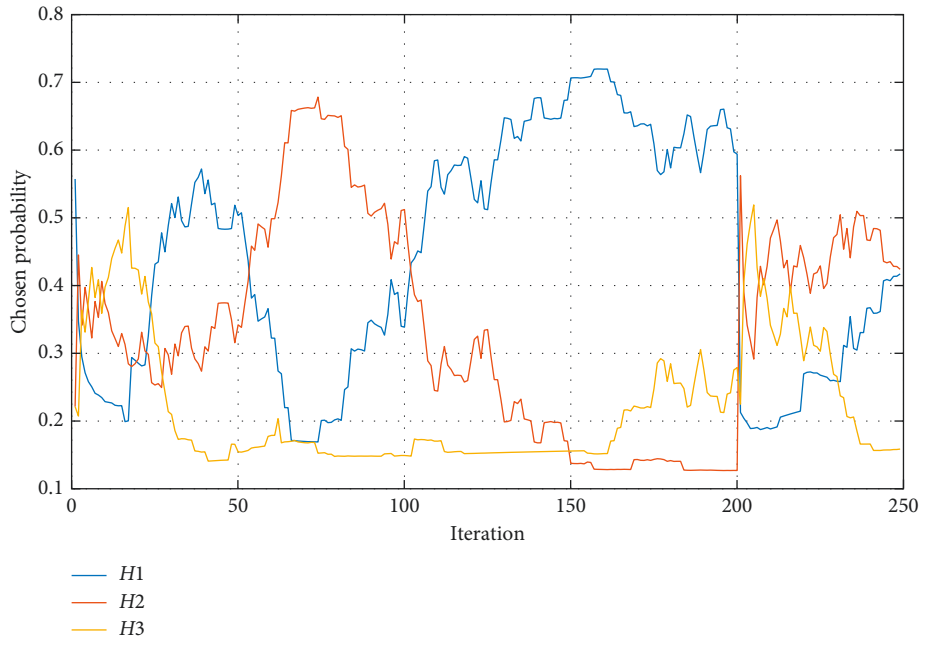

Figure 8: Chosen probability of low-level operators.

4.4. Effect of Constraint Handling. Constraint handling presented in Section 3 aims to transform the infeasible individuals into high-quality feasible individuals. To demonstrate its effectiveness, we record the average cost with and without the handling procedure in the same experiment situation. A constraint handling method in [35] is used for comparison, and we have further improved it on the basis of this method. The difference in power demand Dif is no longer added directly to the adjusted operator but multiplied with a random factor Δ. This will make the adjustment of power balance constraints more balanced without losing the characteristics of random allocation. Table 13 shows that each case with the proposed constraint handling can find a better solution. When a feasible solution P_t is obtained at the current hour, it may make it impossible for P_{t+1} to meet the power balance and ramp rate constraints at the next hour. Failure times refer to the number of times of the situation that the constraints cannot be met. Lower failure times mean an effective

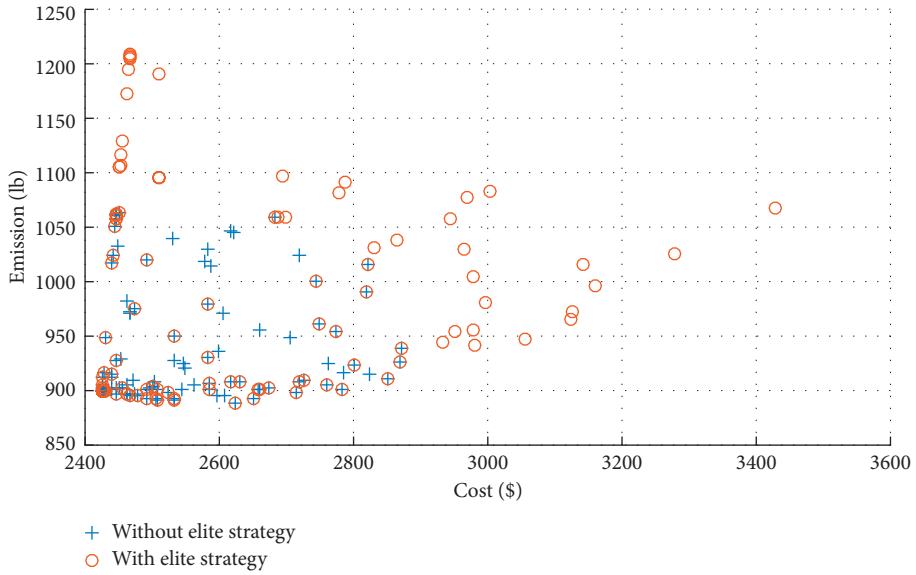

Figure 9: Impact of the elitist nondominated sorting strategy on individual screening.

Table 13: Comparison with and without the proposed constraint handling method.

System	Cost saving		Reduction percentage (%)
	E_c ($)/day	E_m (lb)/day	
Case 1	182	55	15
Case 2	412	177	19
Case 3	367	286	19
Case 4	201	137	12

constraint-handling strategy. We record the reduction percentage in the number of failures. It can be seen from Table 12 that the cost and emission are all improved and the number of failure times has been further reduced.

5. Conclusions

Building a low-carbon future has been an important and urgent task under Paris Global Agreement. Dynamic economic emission dispatch has long been a complex problem which aims to effectively save the fossil fuel cost, relief energy waste, and reduce environmental pollution. Moreover, as renewable energy is considered, the complexity of the DEED is further enhanced. In this paper, a mathematical model of the multiobjective dynamic economic and environmental load distribution problem including wind energy, solar power generation units, and ES is established. A multiobjective hyper-heuristic algorithm is proposed to solve the problem. Four test cases in 24-hour time period are tested to verify the effectiveness of the proposed algorithm.

The main contributions of this study can be summarized as follows: (1) we provide a new way of solving such coupled spatial-temporal scheduling problems in the power system. The hyper-heuristic algorithm is used to solve multiobjective DEED problems. Researchers can replace the low-level operators of our algorithm with their own methods to further improve the search capability. (2) For improving search capability and diversity distribution of Pareto front, an elitist nondominated sorting strategy is adopted to guide the screen of parent individuals. (3) An effective strategy is introduced to transform infeasible solutions towards feasible ones to enhance the quality of solutions and the convergence rate of the proposed algorithm.

In future work, we plan to further study the high level of the hyper-heuristics. The proposed algorithm is a selection hyper-heuristic algorithm, in which the low-level operators need to be pregiven. Further work will explore the generation hyper-heuristics to automatically designed operators. On the other hand, a renewable energy source such as electric vehicles will be integrated into the system dispatch to comprehensively study the power system.

Data Availability

The authors pledge to provide all the codes and the data underlying the findings of the study.

Conflicts of Interest

The authors declare that there are no conflicts of interest regarding the publication of this paper.

Acknowledgments

The authors would like to thank the National Natural Science Foundation of China (grant nos. 61773105, 61533007,

61873049, 61873053, 61703085, and 61374147) and the Fundamental Research Funds for the Central Universities (grant no. N182008004) for supporting this research work.

References

[1] Z. Yang, K. Li, Q. Niu, Y. Xue, and A. Foley, "A self-learning TLBO based dynamic economic/environmental dispatch considering multiple plug-in electric vehicle loads," *Journal of Modern Power Systems and Clean Energy*, vol. 2, no. 4, pp. 298–307, 2014.

[2] T. Cheng, M. Chen, and Y. Wang, "Adaptive robust method for dynamic economic emission dispatch incorporating renewable energy and energy storage," *Complexity*, vol. 2018, Article ID 2517987, 13 pages, 2018.

[3] C. Wei, L. Qu, and W. Qiao, "Evaluation of ANN estimation-based MPPT control for a DFIG wind turbine," in *Proceedings of the 2014 IEEE Symposium on Power Electronics and MDachines for Wind and Water Applications*, Milwaukee WI, USA, July 2014.

[4] X. Bai, W. Qiao, H. Wei, F. Huang, and Y. Chen, "Bidirectional coordinating dispatch of large-scale V2G in a future smart grid using complementarity optimization," *International Journal of Electrical Power & Energy Systems*, vol. 68, pp. 269–277, 2015.

[5] Y. Zhang, F. Yao, H. H.-C. Iu, T. Fernando, and K. P. Wong, "Sequential quadratic programming particle swarm optimization for wind power system operations considering emissions," *Journal of Modern Power Systems and Clean Energy*, vol. 1, no. 3, pp. 231–240, 2013.

[6] N. Pandit, A. Tripathi, S. Tapaswi, and M. Pandit, "An improved bacterial foraging algorithm for combined static/dynamic environmental economic dispatch," *Applied Soft Computing*, vol. 12, no. 11, pp. 3500–3513, 2012.

[7] N. A. Khan, A. B. Awan, A. Mahmood, S. Razzaq, A. Zafar, and G. A. S. Sidhu, "Combined emission economic dispatch of power system including solar photo voltaic generation," *Energy Conversion and Management*, vol. 92, pp. 82–91, 2015.

[8] Z. Hu, M. Zhang, X. Wang, C. Li, and M. Hu, "Bi-level robust dynamic economic emission dispatch considering wind power uncertainty," *Electric Power Systems Research*, vol. 135, pp. 35–47, 2016.

[9] J. Jin, D. Zhou, P. Zhou, S. Qian, and M. Zhang, "Dispatching strategies for coordinating environmental awareness and risk perception in wind power integrated system," *Energy*, vol. 106, pp. 453–463, 2016.

[10] J. Zhou, P. Lu, Y. Li, C. Wang, L. Yuan, and L. Mo, "Short-term hydro-thermal-wind complementary scheduling considering uncertainty of wind power using an enhanced multi-objective bee colony optimization algorithm," *Energy Conversion and Management*, vol. 123, pp. 116–129, 2016.

[11] F. Zaman, S. M. Elsayed, T. Ray, and R. A. Sarker, "Configuring two-algorithm-based evolutionary approach for solving dynamic economic dispatch problems," *Engineering Applications of Artificial Intelligence*, vol. 53, pp. 105–125, 2016.

[12] M. Nazari-Heris, B. Mohammadi-Ivatloo, and G. B. Gharehpetian, "A comprehensive review of heuristic optimization algorithms for optimal combined heat and power dispatch from economic and environmental perspectives," *Renewable and Sustainable Energy Reviews*, vol. 81, pp. 2128–2143, 2018.

[13] Z. Yang, K. Li, Q. Niu, and Y. Xue, "A comprehensive study of economic unit commitment of power systems integrating various renewable generations and plug-in electric vehicles," *Energy Conversion and Management*, vol. 132, pp. 460–481, 2017.

[14] G. Liu, Y. L. Zhu, and W. Jiang, "Wind-thermal dynamic economic emission dispatch with a hybrid multi-objective algorithm based on wind speed statistical analysis," *IET Generation, Transmission & Distribution*, vol. 12, no. 17, pp. 3972–3984, 2018.

[15] R. Bai, J. Blazewicz, E. K. Burke, G. Kendall, and B. McCollum, "A simulated annealing hyper-heuristic methodology for flexible decision support," *4OR*, vol. 10, no. 1, pp. 43–66, 2012.

[16] E. K. Burke, "A classification of hyper-heuristic approaches," in *Handbook of Metaheuristics*, M. Gendreau and J.-Y. Potvin, Eds., pp. 449–468, Springer, Boston, MA, USA, 2010.

[17] K. Deb, A. Pratap, S. Agarwal, and T. Meyarivan, "A fast and elitist multiobjective genetic algorithm: NSGA-II," *IEEE Transactions on Evolutionary Computation*, vol. 6, no. 2, pp. 182–197, 2002.

[18] Y. Zhang, D.-W. Gong, N. Geng, and X.-Y. Sun, "Hybrid bare-bones PSO for dynamic economic dispatch with valve-point effects," *Applied Soft Computing*, vol. 18, pp. 248–260, 2014.

[19] T. Niknam, R. Azizipanah-Abarghooee, M. Zare, and B. Bahmani-Firouzi, "Reserve constrained dynamic environmental/economic dispatch: a new multiobjective self-adaptive learning bat algorithm," *IEEE Systems Journal*, vol. 7, no. 4, pp. 763–776, 2013.

[20] W. Mingqiang, H. B. Gooi, S. Chen, and S. Lu, "A mixed integer quadratic programming for dynamic economic dispatch with valve point effect," in *Proceedings of the 2015 IEEE Power & Energy Society General Meeting*, Denver, CO, USA, July 2015.

[21] W. Center, *Wind and Solar Power Systems*, CRC Press, Boca Raton, FL, USA, 1999.

[22] J. Hetzer, D. C. Yu, and K. Bhattarai, "An economic dispatch model incorporating wind power," *IEEE Transactions on Energy Conversion*, vol. 23, no. 2, pp. 603–611, 2008.

[23] J. Zeng and W. Qiao, "Short-term solar power prediction using an RBF neural network," in *Proceedings of the 2011 IEEE Power and Energy Society General Meeting*, Detroit, MI, USA, July 2011.

[24] G. Mohy-ud-din, "Hybrid dynamic economic emission dispatch of thermal, wind, and photovoltaic power using the hybrid backtracking search algorithm with sequential quadratic programming," *Journal of Renewable and Sustainable Energy*, vol. 9, no. 1, Article ID 015502, 2017.

[25] C. K. Panigrahi, P. K. Chattopadhyay, R. N. Chakrabarti, and M. Basu, "Simulated annealing technique for dynamic economic dispatch," *Electric Power Components and Systems*, vol. 34, no. 5, pp. 577–586, 2006.

[26] M. Basu, "Dynamic economic emission dispatch using nondominated sorting genetic algorithm-II," *International Journal of Electrical Power & Energy Systems*, vol. 30, no. 2, pp. 140–149, 2008.

[27] S. Hemamalini and S. P. Simon, "Dynamic economic dispatch using Maclaurin series based Lagrangian method," *Energy Conversion and Management*, vol. 51, no. 11, pp. 2212–2219, 2010.

[28] J. S. Alsumait, M. Qasem, J. K. Sykulski, and A. K. Al-Othman, "An improved pattern search based algorithm to solve the dynamic economic dispatch problem with valve-point effect," *Energy Conversion and Management*, vol. 51, no. 10, pp. 2062–2067, 2010.

[29] M. Basu, "Dynamic economic emission dispatch using evolutionary programming and fuzzy satisfying method,"

International Journal of Emerging Electric Power Systems, vol. 8, no. 4, 2007.

[30] H. Zhang, "Adaptive grid based multi-objective Cauchy differential evolution for stochastic dynamic economic emission dispatch with wind power uncertainty," *PLoS One*, vol. 12, no. 9, Article ID e0185454, 2017.

[31] H. Zhang, D. Yue, X. Xie, S. Hu, and S. Weng, "Multi-elite guide hybrid differential evolution with simulated annealing technique for dynamic economic emission dispatch," *Applied Soft Computing*, vol. 34, pp. 312–323, 2015.

[32] P. Attaviriyanupap, H. Kita, E. Tanaka, and J. Hasegawa, "A hybrid EP and SQP for dynamic economic dispatch with nonsmooth fuel cost function," *IEEE Transactions on Power Systems*, vol. 17, no. 2, pp. 411–416, 2002.

[33] L. Xuebin, "Study of multi-objective optimization and multi-attribute decision-making for dynamic economic emission dispatch," *Electric Power Components and Systems*, vol. 37, no. 10, pp. 1133–1148, 2009.

[34] P. Karthikeyan, "Security constrained unit commitment problem with operational Power flow and environmental constraints," *WSEAS Transactions on Power Systems*, vol. 4, pp. 53–56, 2009.

[35] D. He, L. Yang, X. Tian, and Z. Wang, "An overlapped decomposition optimization method for dynamic economic dispatch," *IEEE Access*, vol. 6, pp. 45804–45820, 2018.

Hindawi
Complexity
Volume 2019, Article ID 9462158, 14 pages
https://doi.org/10.1155/2019/9462158

Review Article

A Survey on Optimal Control and Operation of Integrated Energy Systems

Chun Wei, Xiangzhi Xu, Youbing Zhang, and Xiangshan Li

College of Information Engineering, Zhejiang University of Technology, Hangzhou, Zhejiang 310023, China

Correspondence should be addressed to Youbing Zhang; zyoubing6858@sina.com

Received 18 July 2019; Accepted 19 August 2019; Published 25 December 2019

Guest Editor: Xiaoqing Bai

At present, the transformation of energy structure is at a critical stage, and emerging renewable energy technologies and multienergy equipment have been widely used. How to improve the energy efficiency of integrated energy system (IES) and promote large-scale absorption of renewable energy is of great significance to the application forms of energy in the future. The development of new internet technology and sensor technology provides strong technical support for the optimal operation and coordinated control of IES. In recent years, the IES is experiencing unprecedented changes, which has attracted great attention from academia and industry. In this paper, the optimal control and operation behavior of IES are reviewed. Firstly, the research status of IES in recent years is summarized. Then, the modeling methods of different equipment in IES are analyzed in detail. The optimal operation of user, regional, and cross-regional IES are taken as typical research objects and the research status of optimization problems and operation modes, energy management planning, and power market allocation are summarized and analyzed. Finally, the key scientific issues and related frontier technologies in the IES are concluded, and the future research directions are prospected.

1. Introduction

The environmental pollution in the process of energy conversion and transmission and the requirement of sustainable development of energy urge human beings to seek diverse supply and efficient use of green energy. It is difficult to maintain the long-term development of human society due to the exponential growth of energy consumption and the insufficient reserves of nonrenewable energy. The development of renewable energy, such as solar energy, wind energy, hydropower, geothermal energy, and biomass energy, makes it possible for sustainable use of energy [1].

Although the renewable energy-related technology has developed rapidly, the most important issue for power system is to ensure the reliable and secure operation. Due to the inherent intermittence and fluctuation of renewable energy, direct connection to power system will impact the voltage and frequency of the power grid [2]. Most of the renewable energy is connected to the power grid through power electronics devices. However, power electronics device itself is one of the main sources of harmonics in the power grid during the treatment of the power grid pollution. Although energy storage technology can directly solve the problem of renewable energy absorption, large-scale commercial application of energy storage in power grid cannot be carried out for the time being due to the high cost, low efficiency of energy storage technology, and special requirements for engineering application sites [3]. The renewable energy is also facing the problem of effective connection with external power grid, the economic problems in long-distance transmission such as high cost of infrastructure construction and wheeling cost of power flow, and the lack of market competition, which is not conducive to the development and promotion of renewable energy technology. In order to solve these problems, the concept of integrated energy system (IES) has been proposed. IES is a highly abstract classification of energy supply and energy demand, which integrates multifunctional collaborative technologies such as P2G (power to gas) and CCHP (combined cooling, heating and power supply) in the process of planning, construction, and operation of energy systems, thus achieving multienergy conversion, scheduling, and storage.

As an important component of the energy internet and the main carrier of social energy, IES integrates power, natural gas, hot and cold system, instead of a single energy system in traditional energy supply form, which is an effective way to solve the problem of low energy efficiency and the coupling of various types of energy [4]. As a multisupply system, IES can alleviate or eliminate the inefficiency of energy equipment

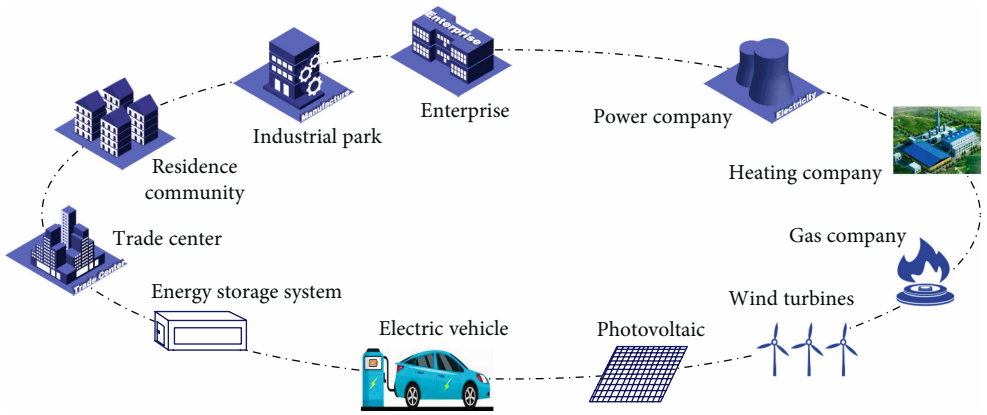

Figure 1: Open interconnection of multienergy systems.

through the coordination of subsystems [5]. It can also reduce the cost of system maintenance, realize the peak-valley interleaving of multienergy system, and fully absorb renewable energy through P2G technology [6]. IES can make full use of potential synergistic benefits, fully tap the potential of interconnected data and information networks, and achieve coordination, optimal scheduling, and synergistic utilization among different energy supply systems [7, 8].

The electricity, gas, heat, and other energy sources are complementary in IES to achieve time-sharing utilization of energy and improve the scope of renewable energy consumption, improve the utilization of social infrastructure and the flexibility of energy supply [9]. In the aspect of comprehensive use of energy, IES is regarded as one of the important development directions of the energy industry by all countries because of its advantages such as high energy efficiency and economy. IES can solve the shortcomings of traditional power system that cannot meet the energy demand under the new situation because of the one-way transmission of power load, and achieve the optimal allocation of resources through multienergy collaboration.

Many detailed researches on IES have been carried out in different countries, including modeling and planning for various scenarios, optimal operation, security assessment, and steady-state analysis of IES. This paper mainly reviews the related technologies of optimal operation and control of IES. Section 2 briefly introduces the main forms and development status of IES. Section 3 reviews the commonly used modeling methods of IES. Section 4 discusses the optimal operation and control methods of IES, Section 5 concludes the whole paper and summarizes the key scientific issues in IES research, and proposes future challenges and development trends of IES.

2. Brief Introduction of IES

2.1. Structure and Characteristic of IES. The inputs of IES are a variety of energy sources and the outputs are electricity, heat and cold energy, to meet the energy demand of different users. With the existence of electricity and gas distribution system, heating and water supply pipelines, and other related energy supply network, a coupling system is formed. The coupling between gas and electricity distribution system and the complementation of various energy sources result in the complexity of energy combination and the diversity of energy utilization. According to the size of geographical area and energy characteristics, IES can be divided into three types: park (building) level, city level, and cross-regional level [10]. Figure 1 illustrates the typical open interconnection of multienergy systems.

IES of building level mainly considers the coordination and complementation of multiple energies of buildings or users, and takes demand response, forecasting of demand load, electric vehicles, and cloud computing as the core technologies. There is a deep coupling relationship among energy networks [11]. IES of park level covers energy systems with various forms and characteristics [12], including underlying equipment, energy system units and systems with multienergy coupling, which has the characteristics of complementary utilization of energy, deep integration of physical information and coordinated interaction of source, network and storage. Regional IES mainly plays a connecting role of energy transmission, distribution, conversion and balance [13]. It takes hybrid energy storage system, energy conversion and active distribution network as the core technologies, and there is a strong coupling among energy systems. Cross-regional IES takes power electronics technology, information physics system, transmission, and energy router as its core technologies [14]. It mainly considers such factors as management, operation, scheduling (transmission) time between cross-regional energy systems.

Based on the energy management and control platform, IES in the park (building) level covers many controllable resources, such as cold, heat, electricity, gas, and water, so as to realize the complementation of multiple energies. Based on the interaction between multiple decision makers, regional IES and cross-regional IES study the operational efficiency and economic cost of distributed and centralized decision makers (joint dispatching center). At the same time, the optimal power flow problem in the process of multienergy flow transmission should be considered to ensure the safe and stable transmission of energy. Electric power system, natural gas system and thermal system are composed of different stakeholders. It is necessary to analyze the economic distribution

among different stakeholders, focusing on game theory and other related theories, so as to enhance the coupling relationship between multienergy flows.

2.2. Current Development Status of IES. Energy Internet is the product of the deep integration of traditional energy system and internet thinking. In the book "The Third Industrial Revolution", Jeremy Rifkin, a famous American scholar, first put forward the vision of energy internet, and believed that the third industrial revolution with energy internet as its core would subvert the use of traditional energy [15]. IES, as an important physical carrier of energy internet, focuses on collaborative optimization among different energy sources. Energy Internet emphasizes the deep integration of energy systems and the ICT (information and communication technology), which is marked by the technologies of internet, computer, automatic control, communication, data processing and network [16]. IES is not a new concept. In the field of energy integration, there are long-term cooperative optimal operation among energy sources, such as CHP system and CCHP system, which use heat energy in different levels to reduce energy waste; P2G technology uses wind power and solar energy to generate Hydrogen by electrolyzing water, which is then supplied to the existing gas pipeline network, or to produce methane by utilizing water and CO_2 in atmosphere to provide gas, so as to solve the problem of renewable energy absorption [17, 18].

IES has been extensively studied and developed based on the needs of energy strategies of various countries. In 2007, the U.S. incorporated IES into the energy sector, and promoted the construction of IES by means of additional funds, unified energy production, and distribution suppliers; in 2013, the National Renewable Energy Laboratory established the "Energy System Integration Research Group" [19], and IBM established "Smart City" and other projects. In 2014, the EU adopted the target of "40-27-27" in 2030. By 2030, greenhouse gas emissions will be reduced by 40% compared with 1990, 27% of energy consumption comes from renewable energy sources, and energy efficiency will be improved by 27% [20]. Since 2015, China has issued a number of IES-related policies and carried out a series of demonstration and practical projects, such as the demonstration project of Shanghai Disneyland Resort, which uses centralized energy control to make the primary energy utilization rate above 80%. The Chongming Island demonstration project in Shanghai builds a three-tier energy utilization framework for renewable energy, which realizes the joint optimization of wind farm running independently and megawatt container energy storage system in distribution network [21].

2.3. IES Related Technology. The development of IES needs the support of related technical fields such as renewable energy generation, energy storage, power electronics, new transmission, stability analysis and control of multienergy flow system, and artificial intelligence.

Renewable energy power generation has triggered the energy revolution, led to the large-scale development of emerging ecological industries, laid the foundation for the promotion and application of IES. The development of power storage, heat storage, cold storage, and hydrogen storage plays an important role in the absorption of renewable energy. The development of power electronics technology has improved the security and controllability of energy transmission and distribution, and promoted energy interconnection. Power flow calculation of multienergy flow system is the basis of the research of multienergy flow system and the premise of the related control technology research. Faced with the uncertainties, randomness and complexity of energy systems, the new generation of artificial intelligence technology needs to carry out a lot of research work in such areas as comprehensive perception, reliable transmission and intelligent processing of data information, machine learning algorithms, and artificial intelligence platform for power and energy applications.

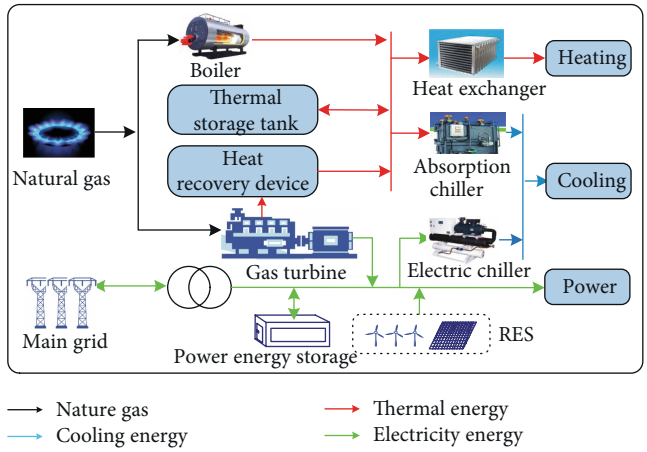

Figure 2: Basic structure of IES.

3. Modeling of IES

IES is composed of power system, natural gas system and thermodynamic system and the basic physical equipment of these systems is modeled in this section, which includes the equipment in the process of production, transmission, storage, and consumption of various energy sources such as electricity, heat, cold and gas. The basic physical structure of IES is shown in Figure 2.

3.1. Modeling of Independent Power Equipment. The traditional power equipment in IES mainly include PV, transmission and distribution network, energy storage battery, and electric vehicle, which are the core components of IES.

3.1.1. Model of PV Power Generation. PV power generation is the direct use of photovoltaic effect of semiconductor materials to convert solar energy into electricity. PV power generation system has short construction cycle, flexible installation, and wide application scenarios and will not cause disturbance to human living environment. The mathematical model of PV power generation is generally shown as follows [22]:

$$I = I_{sc} - I_{sc}D_1\left\{\exp\left(\frac{U}{D_2U_{se}}\right) - 1\right\}$$
$$\begin{cases} D_1 = \left(1 - \dfrac{I_m}{I_{sc}}\right)\exp\left(-\dfrac{U_m}{D_2U_{oc}}\right), \\ D_2 = \left(\dfrac{U_m}{U_{oc}} - 1\right)\left[\ln\left(1 - \dfrac{I_m}{I_{sc}}\right)\right]^{-1}, \end{cases} \quad (1)$$

where U and I are the voltage and current of a single PV module respectively; I_{sc}, U_{oc}, I_m, and U_m represent short-circuit current, open-circuit voltage, current and voltage at maximum power point, which are provided by PV cell manufacturers; D_1 and D_2 are intermediate variables. These parameters will vary with the environment and need to be determined according to the actual light intensity and temperature.

Then the output power of PV array in k period can be expressed as:

$$P_{PV}^k = U^k \times I^k \times C_a \times C_b \times \eta_{pv}, \quad (2)$$

where U_k and I_k are the voltage and current of a single PV module in k period, respectively; C_a is the number of PV modules in series; C_b is the number of PV modules in parallel; η_{pv} is the loss factor.

3.1.2. Model of Wind Power Generation. Wind power generation is the conversion of kinetic energy of wind into electricity through wind turbines. Wind energy is proportional to the cubic of wind speed and the mathematical model of wind power output is as follows [23]:

$$P_{wt} = \begin{cases} 0, & v_k < v^{ci} \text{ or } v_k \geq v^{co}, \\ P^r \dfrac{v_k^3 - \left(v^{ci}\right)^3}{v_R^3 - \left(v^{ci}\right)^3}, & v^{ci} \leq v_k \leq v^R, \\ P^r, & v^R \leq v_k \leq v^{co}, \end{cases} \quad (3)$$

where v_k is the actual wind speed in k period; v^{ci}, v^{co}, and v^R are cut-in, cut-out and rated wind speed, respectively; P^r is the rated power of wind turbine.

3.1.3. Model of Transmission and Distribution Network. The power model of transmission and distribution networks is usually expressed by [24]:

$$P_L = U_L I = P_{Lin}(1 - \eta_{line} - \eta_{sub}) = U_{Lin} I(1 - \eta_{line} - \eta_{sub}), \quad (4)$$

where P_L and P_{Lin} are the output and input power of the transmission and distribution network, respectively; U_{in} and U_{iL} are the input and output voltage of the transmission and distribution network; I is the operation current; η_{line} and η_{sub} are the tie-line loss of the transmission and distribution network and the substation loss, respectively.

3.1.4. Energy Storage Battery. The typical model of energy storage battery is expressed as [25]:

$$\begin{aligned} S_B(t) &= \left(1 - \delta_B\right) \cdot S_B(t-1) + P_B^{in} \cdot \Delta t \cdot \eta_B^{in}, \\ S_B(t) &= \left(1 - \delta_B\right) \cdot S_B(t-1) - \frac{P_B^{out} \cdot \Delta t}{\eta_B^{out}}, \end{aligned} \quad (5)$$

where $S_B(t)$ represents the remaining electricity of the energy storage system in t period; δ_B is the energy consumption rate in the energy storage process; P_B^{in} and P_B^{out} are the charging and discharging power, respectively.

3.1.5. Charging Pile. The typical model of charging pile is expressed as [26]:

$$P_{cp}^i = \sum_{n=1}^{n} S_{ta}(k) P_{cha}^n, \quad (6)$$

where P_{cp}^i is the total charging capacity of charging piles in area I; n represents the total number of charging piles in area I; $S_{ta}(k)$ is the charging state of k^{th} charging pile, whose value is 1 when charging and 0 when discharging; P_{cha}^n is the output power of n^{th} charging piles.

3.2. Modeling of Equipment with Electro-Thermal Coupling

3.2.1. Model of Gas Turbine. As the core equipment in electro-thermal coupling, Gas Turbine converts natural gas into electric energy and recovers waste heat for heating and refrigeration. The mathematical model of gas turbine is as follows [27]:

$$\begin{aligned} P_{gt}^t &= F_{gas}^t \gamma_{gt} \eta_{gt} \lambda_{gas}, \\ Q_{gt}^t &= F_{gas}^t \lambda_{gas}\left(1 - \eta_{gt} - \eta_{loss}\right)\eta_{rec}, \end{aligned} \quad (7)$$

where P_{gt}^t, Q_{gt}^t, and F_{gas}^t are the output power, recovery power of waste heat, and natural gas consumption of gas turbines in t period, respectively; γ_{gt} is the gas consumption rate of gas turbines; η_{gt}, η_{rec}, and η_{loss} are the efficiency of power generation, recovery efficiency of waste heat, and energy loss rate of gas turbines, respectively; λ_{gas} is the calorific value of natural gas.

3.2.2. Model of Heat Pump. Heat pump is mainly composed of heat exchan ger, compressor, throttling device, hot water storage tank and temperature acquisition device, which can convert low-grade heat energy into high-grade heat energy by using a small amount of electricity. The typical model of heat pump is as follows [28]:

$$Q_{HP}^t = C_{HP} \rho_{HP} \Delta T_{HP}, \quad (8)$$

where Q_{HP}^t is the heating power of heat pump in t period; C_{HP} is specific heat of heat pump fluids; ρ_{HP} is the density of hot water; ΔT_{HP} is the temperature difference of fluids before and after a cycle.

3.3. Modeling of Equipment with Electro-Gas Coupling. The main coupling parts between power system and natural gas system are gas turbine and P2G, which realizes a bidirectional coupling of electro-gas system.

P2G equipment is mainly composed of electrolytic water device, methanation reaction device, and pressure-adding device [29].

3.3.1. Model of Electrolytic Cell. At present, there are three main electrolytic technologies, which are alkaline electrolysis, proton exchange membrane (PEM) electrolysis, and solid oxide electrolysis. The alkaline electrolysis technology is mature, but its efficiency is low. High temperature electrolysis has strict environmental requirements, which needs to work in environment with high temperature and pressure, so the high cost is high. At present, the PEM technology has attracted wide attention because of its flexibility, better mechanical strength and chemical stability [30].

The PEM electrolysis model is:

$$\begin{cases} E_{\mathrm{eh}_2}^t = f\left(\eta_{\mathrm{eh}_2}\right)\pi_{\mathrm{eh}_2,\mathrm{rated}}, \\ f\left(\eta_{\mathrm{eh}_2}\right) = a_{\mathrm{eh}_2}\eta_{\mathrm{eh}_2}^2 + b_{\mathrm{eh}_2}\eta_{\mathrm{eh}_2} + c_{\mathrm{eh}_2}, \\ \eta_{\mathrm{eh}_2}^t = \dfrac{P_{\mathrm{eh}_2}^t}{P_{\mathrm{eh}_2}^{\mathrm{rated}}}, \end{cases} \tag{9}$$

where $E_{\mathrm{eh}_2}^t$ is the amount of hydrogen produced by the electrolyzer in t period $f\left(\eta_{\mathrm{eh}_2}\right)$ is the efficiency function of the electrolyzer; η_{eh_2} is the operational efficiency of the electrolyzer; $P_{\mathrm{eh}_2}^t$ is the input power of the electrolyzer in t period; $P_{\mathrm{eh}_2}^{\mathrm{rated}}$ is the rated input power of the electrolyzer; a_{eh_2}, b_{eh_2}, and c_{eh_2} are three coefficients of efficiency function of the electrolyzer.

3.3.2. Model of Methane Reactor. The hydrogen generated by P2G is sent to the methane reactor. The operating efficiency of the reactor is affected by the composition of syngas, the ratio of hydrogen, working temperature and pressure [31]. The methane reactor model is expressed as follows:

$$P_{M,g,t} = \frac{\eta_m E_{M,h_2,t}\lambda_{\mathrm{gas}} * 4}{\kappa}, \tag{10}$$

where $P_{M,g,t}$ is the natural gas power generated by methane reactor in t period; $E_{M,h_2,t}$ is quantity of hydrogen injected into methane reactor at t period; η_m is operational efficiency of methane reactor; λ_{gas} is calorific value of natural gas; κ is quality of gas corresponding to each m^3 of natural gas pipeline.

3.4. Modeling of Equipment with Other Coupling. Electric refrigerator is a typical electro-cooling coupling device; electric heating boiler is a typical electro-thermal coupling device; gas boiler is a typical gas-thermal coupling device; and adsorption refrigerator is a typical thermal-cold coupling device.

When the heating of gas turbine is insufficient, the gas boiler supplements the heating. The mathematical model of a gas boiler is expressed as [29]:

$$Q_{\mathrm{gb}}^t = F_{\mathrm{gb}}^t \eta_{\mathrm{gb}} \lambda_{\mathrm{gas}}, \tag{11}$$

where Q_{gb}^t and F_{gb}^t are the output heat power and consumption of natural gas of gas boiler in t period, respectively; η_{gb} is the operating efficiency of gas boiler.

The main coupler of the thermal-cooling system is the adsorption refrigerator, the main coupler of the electric-cooling system is the electric refrigerator, and the main coupler of the electric-heating system is the electric-heating boiler. The details of these modeling can be found in [27].

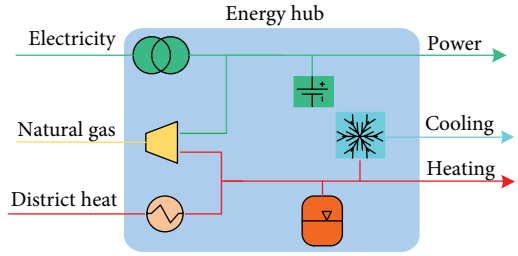

Figure 3: Basic model of energy hub.

3.5. Modeling Based on Energy Hub. Geidl and Andersson from Zurich Federal Institute of Technology firstly proposed the energy hub, which represents the interface between different energy infrastructures or loads [32]. It uses cogeneration technology, transformer, power electronic equipment, heat exchanger, and other equipment to convert and adjust the output of energy. In this model, the internal equipment is highly abstract, the static relationship of energy in the transmission and conversion process is considered, so it plays an important role in the planning and operation research of IES [33, 34]. Figure 3 shows a typical model of energy hub.

The energy hub represents the input and output of energy, which are connected by an energy coupling matrix as follows [35]:

$$\begin{bmatrix} P_{\mathrm{out}}^{\alpha} \\ P_{\mathrm{out}}^{\beta} \\ \vdots \\ P_{\mathrm{out}}^{\zeta} \end{bmatrix} = \begin{bmatrix} C_{\alpha\alpha} & C_{\beta\alpha} & \cdots & C_{\zeta\alpha} \\ C_{\alpha\beta} & C_{\beta\beta} & \cdots & C_{\zeta\beta} \\ \vdots & \vdots & \ddots & \vdots \\ C_{\alpha\zeta} & C_{\beta\zeta} & \cdots & C_{\zeta\zeta} \end{bmatrix} \begin{bmatrix} P_{\mathrm{in}}^{\alpha} \\ P_{\mathrm{in}}^{\beta} \\ \vdots \\ P_{\mathrm{in}}^{\zeta} \end{bmatrix}, \tag{12}$$

where P_{in} is the original energy input to the energy hub; P_{out} is the energy output after the energy hub; $C_{\xi\xi}$ is the coupling matrix between input and output energy of the system to characterize the coupling relationship between energy.

The advantages of energy hub are as follows: (1) It highly abstracts energy transmission, conversion, and scheduling processes, which are only related to energy input and output, and has good practicability and scalability. (2) It simplifies complex problems and provides a new way of thinking for the optimization of joint operation and scheduling of cross-regional and city-level IES, and for market trading mechanism, benefit distribution and other issues.

Disadvantages: (1) It cannot describe the dynamic behavior of the system well, and only considers the static analysis of energy. (2) When the coupling matrix is singular, the model cannot be solved. (3) With the development of various energy storage technologies, renewable energy technologies, demand response, and P2G technologies, the expansion of energy hub is required.

4. Optimal Operation of IES

At present, according to the size of geographical areas and energy characteristics, the research objects on optimal operation of IES are divided into three categories: park, region and

cross-region. Regional IES is mainly aimed at a certain region, which can be a part of a city or a region; cross-regional IES mainly refers to multiple cities or regions.

Park-level IES is mainly aimed at energy management of industrial parks and large buildings. The core research contents are energy equivalence and optimal allocation. The complementary forms and optimal coordination methods of IES are explored so as to realize flexible scheduling of the whole process of "source-network-load".

Optimization problems of regional and cross-regional IES mainly focus on energy interaction analysis with hybrid optimization of power flow as the core, exploring coordination and optimization among multiple IES. The optimization results provide theoretical guidance for large-scale optimization and transaction operation of IES.

The research related to optimal operation of IES in the park, region and cross-region will be reviewed in the following sections.

4.1. Optimization Objectives and Optimal Operating Constraints of IES

4.1.1. Optimization Objectives of IES. In park-level IES, there is only one IES that generates, transmits and distributes energy in a certain area. The optimal operation problem of IES is generally expressed as follows:

$$\begin{aligned} &\min\ f(P,E,x),\\ &s.t.\begin{cases} L_{\text{out}} = (C\ S)\begin{bmatrix} P \\ E \end{bmatrix},\\ P_{\min} \le P \le P_{\max},\\ E_{\min} \le E \le E_{\max},\\ 0 \le x \le 1, \end{cases} \end{aligned} \tag{13}$$

where $f(P,E,x)$ is the objective function related to energy input P, energy storage system E and energy allocation coefficient x; the constraint is the balance of energy input and output; $P_{\min}$ and $P_{\max}$ are lower and upper limits of energy input; $E_{\min}$ and $E_{\max}$ are lower and upper limits of energy storage system output; x is the energy allocation coefficient of IES, which generally refers to the proportion of a certain energy output to total energy output.

The optimization objectives of a single IES can be summarized as follows:

(1) Most of the optimization objectives of IES are to minimize the total operating cost of the system or maximize social welfare [36–39].

(2) There are also some studies whose optimization objectives are optimal carbon emissions or environmental benefits, to achieve the proportion of green energy in the operation of IES system [40–42]. There are still a few studies whose optimization objective is maximal absorption of renewable energy, to improve the proportion of energy supply from renewable energy in IES, so as to achieve better environmental benefits [43].

For regional and cross-regional IES, multiple IES are connected by power transmission network, natural gas transmission network, and thermal transmission network. The overall optimal dispatch of IES is mainly a problem of optimal hybrid power flow of multienergy.

Appropriate interconnection can reduce consumption and reserve capacity of generation, and make full use of power generation equipment, which is a method that can make the energy equipment the most effective in any region. There will be various forms of energy exchange between IES [44–47] and the concept of energy hub is constructed. Each energy hub is regarded as a generalized node in the network, and the energy flow on the transmission line is similar to the optimal power flow of the power system, which is called the optimal power flow of multienergy system [48]. Figure 4 shows a typical cross-regional IES schematic.

On the basis of the optimal hybrid power flow, the problem of IES at the regional and cross-regional levels is to calculate the optimal hybrid power flow of the system, thus revealing the operation mechanism of multiple IES, and providing theoretical guidance for the optimal operation and energy dispatch of IES at regional and cross-regional levels. Moreover, the optimal hybrid power flow calculation generally chooses the system operation economy as the optimization objective, and its constraints are energy flow equation constraints of IES, energy production and consumption constraints, conversion and energy storage equipment constraints, while considering the energy constraints of multienergy coupling equipment of IES [49–53].

The basic optimization model is shown as follows:

$$\begin{cases} \min\ f\left(P_i, F_j\right) \\ \text{s.t.}\ \ L_i = C_i P_i \\ \qquad G_\alpha\left(P_i\right) = 0, \\ \qquad F_j^{\min} \le F_j \le F_j^{\max} \\ \qquad P_i^{\min} \le P_i \le P_i^{\min} \end{cases} \tag{14}$$

where $f\left(p_i, F_j\right)$ the function related to energy input and power flow of energy network; the first and second constraints are energy flow equation constraints in energy networks and upper and lower limits in networks.

4.1.2. Optimal Operating Constraints of IES. In the research of optimizing constraints, besides the independent units of conventional power system, natural gas system and thermal system [54], the coupling system has also been discussed in previous studies [55]. The specific constraints are shown in Figure 5.

4.2. Optimal Operation of IES considering Electro-Thermal Coupling. As an important part of IES, electro-thermal coupling system connects power system and thermodynamic system through coupling elements such as CHP units and electric boilers to realize the conversion between electric energy and thermal energy. However, there are mutual restrictions between electric output and thermal output among electro-thermal units, which in some cases will affect the peak regulation of power system and absorption capacity of wind power, so some research introduces heat pumps and heat storage devices to increase the flexibility of the electro-thermal coupling system.

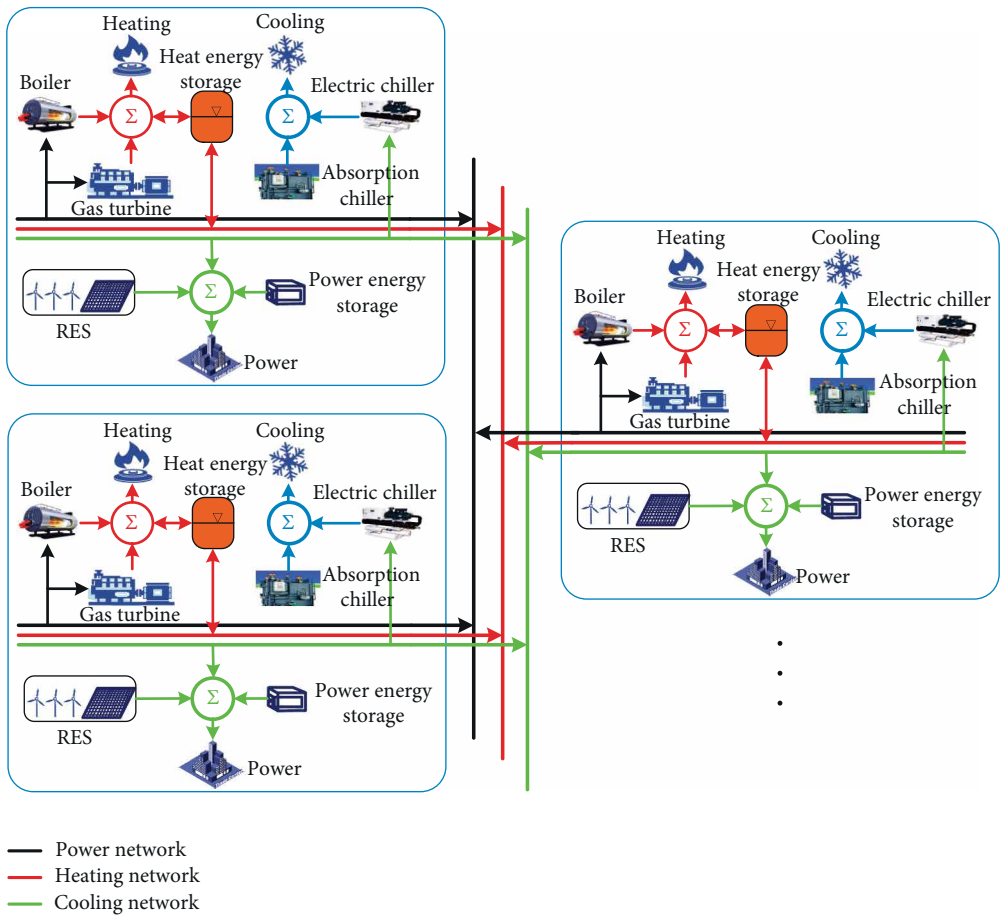

Figure 4: Schematic of cross-regional IES.

Park-level IES mainly considers the optimal dispatch of cogeneration units. Good et al. [56] chooses the optimal operation strategy for CHP system considering energy demand and integrated performance criterion under two operating modes of "electricity by heat" and "heat by electricity". The emergence of heat pumps and heat storage devices provides a powerful support for the flexibility of electro-thermal coupling systems. Fang et al. [57] presents a physics-based model which is applicable to both electricity generating ETTs (aggregated residential electro-thermal technology), the presented model determines the expected energy and discomfort costs for a variety of cases.

Research on CHP and CCHP has been mature. Power cycle that efficiently converts low-grade thermal energy into power combining organic Rankine cycle (ORC) has become a hot research topic. In [58], the ORC turbogenerator is used in cement industry to improve economy and energy efficiency by recycling heat.

The researches considering the characteristics of heat network and temperature variation of heat medium, and the connections of heat pump and heat storage into systems have also attracted extensive attention. Wang et al. [59] proposes an IES with solar energy heat pump, which shows that increasing solar energy heat pump can effectively reduce the cost of central heating supply of cogeneration unit. In addition, some scholars have refined the loss model in the process of heat energy transmission, and the thermal energy storage (TES) device is proposed in [60], which proves that TES device can provide flexibility for the electro-thermal coupling system. Sauter et al. [61] analyzes the impact of electro-thermal storage (ETS) system on the operation of community microgrid in northern China, and proved that ETS can significantly reduce the operating cost of the system and better absorb wind and solar energy. Pan et al. [62] develops an integrated quasi-dynamic model of integrated electricity and heating systems, a simulation method is proposed and quasi-dynamic interactions between electricity systems and heating systems are quantified with the highlights of transport delay, results show that both the transport delay and control strategies have significant influences on the quasi-dynamic interactions.

Some researches focus on demand response technology. The energy consumption behavior of users is influenced by demand response technology in [63], which shows that demand response can improve the regional wind power consumption. In [64], the Energy PLAN is used to model IES, and analyses the application of heat pump, heat storage equipment, and demand response technology in different scenarios. Results show that the total operating cost and carbon dioxide emissions of the system can be minimized, and the introduction of heat pump improves the operating efficiency of the system.

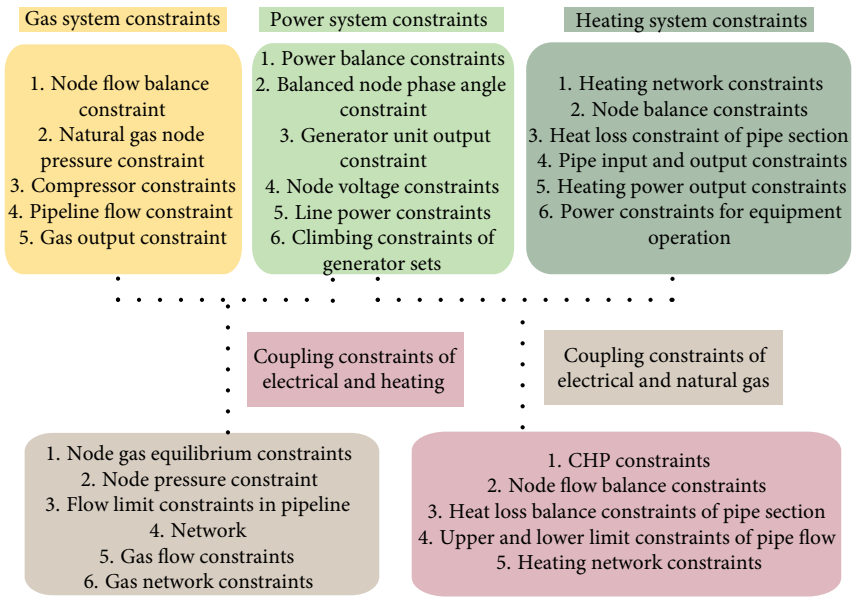

Figure 5: The specific constraints of IES.

Cooperative optimal operation of power system and thermal system can break the traditional mode of "electricity by heat" and improve the level of energy utilization. Relevant research has proved that large-scale thermal storage system can effectively improve the flexible dispatching ability of the system. However, new materials such as thermal storage or phase-change thermal storage need to be further studied [65]. At present, the related research of solar thermal power generation technology [66] has attracted wide attention. However, due to the high cost of power generation, related technologies need to be further studied.

4.3. Optimal Operation of IES considering Electro-Gas Coupling. The coupling relationship between power system and natural gas system is mainly caused by P2G equipment and gas turbine. For power system, P2G equipment is a load, and for natural gas system, it can be used as a gas source for transmission. The coupling between power system and natural gas system can make these two systems stand by each other and improve the flexibility of the system [67]. One-way transmission of energy between natural gas network and power grid is carried out by gas turbine. P2G device makes the power grid and natural gas network interconnected, and energy flow becomes bidirectional. As for the coupling relationship between power grid and natural gas system, the following literatures make positive exploration.

Clegg and Mancarella [68] evaluates multienergy systems considering the short-term flexibility provided by natural gas power generation. Chen et al. [69] considers the problem of optimal energy flow, gives the method of solving the optimal power flow, measuring the feasibility margin and the infeasibility of energy flow. It also proposes three models to solve the optimal energy flow, studies the identification method of solvability of optimal multienergy flow, and verifies the effectiveness of the proposed models through case studies.

Khani and EI-Taweel [70] considers the problems of reverse power flow of feeder, additional heating of transformer or incorrect operation of protective device caused by power generation of high-penetration renewable energy. This study reveals the application of bidirectional converter in integrated electric-gas system, and proposes a new real-time algorithm, which is verified effectively by simulation with real data. He and Shahidehpour [71] proposes a robust security-constrained unit commitment model to enhance the operating reliability of integrated electro-gas system against possible transmission lines outages. Zhang et al. [72] considers the N-1 accident of natural gas system and power system, a mixed integer linear programming (MILP) method is developed, and the experimental results show that the proposed method has good computational performance.

4.4. Optimal Operation of IES considering Electro-Gas-Thermal Coupling. IES with electricity, gas, and heat is composed of power system, thermal system, and natural gas system with various coupling units such as CHP, gas turbine and gas boiler. Energy hub is the key to the coupling of multienergy. The optimal operation and power flow with energy hubs as the core have attracted wide attention.

The coordinated optimization objectives of multienergy hubs are generally the optimal economy of own system, optimal overall economy or the least carbon emissions. Zhong et al. [73] establishes a multiobjective model for scheduling optimization of IES with the objective of minimizing the operating cost and pollutant emission. The improved bacterial population chemotaxis algorithm is used to optimize the comprehensive energy system scheduling model. The simulation verifies the effectiveness of the optimized scheduling model and the improved algorithm. Zhong and Yang [74] proposes a distributed auction mechanism with multienergy control. The energy hub uses dual consensus ADMM algorithm to distribute energy for users with the objective of maximizing social welfare. Finally, it organizes and builds load data, analyses and evaluates the performance of energy scheduling and verifies the compatibility of incentive mechanism.

Li et al. [67] uses cooperative game theory to optimize multiple IES systems by adjusting the existing IES control algorithm, and proves that the cooperative game has a balanced distribution point of economic benefit. Clegg and Mancarella [68] proposes an optimal operating framework for intelligent areas with multienergy devices and integrated energy networks. The framework is based on two-stage iterative modeling, involving linear approximation of MILP and nonlinear network equations. Practical cases in England prove that the proposed model can eliminate uncertainty to a certain level and has important reference value for evaluation of system flexibility.

4.5. Optimal Control and Operation of IES. Power flow calculation of multienergy flow in IES is to determine the power flow distribution of each subsystem, which is an important prerequisite for exploring coupling characteristics and optimizing scheduling.

Power flow calculation of multienergy flow in IES is expressed as followers:

$$\begin{cases} 0 = F\left(x_e, x_g, x_h, x_{eh}\right) \\ 0 = G\left(x_e, x_g, x_h, x_{eh}\right) \\ 0 = D\left(x_e, x_g, x_h, x_{eh}\right) \\ 0 = E_H\left(x_e, x_g, x_h, x_{eh}\right), \end{cases} \tag{15}$$

where x_e, x_g, x_h, and x_{eh} are variables of power system, natural gas system, thermal system, and energy hub; $F(\cdot)$ is the equation of power flow; $G(\cdot)$ is algebraic equation of natural gas system, including equations of gas pipeline and compressor; $D(\cdot)$ is the equation of thermal system, including equations of heat flow continuity, pressure loop, node flow and node mixed temperature; E_H is the input-output conversion equations of energy hub.

The gas distribution system mainly includes two parts: node and branch. Nodes are divided into pressure-known nodes and flow-known nodes [75], in which the pressure-known node is generally the gas source point with the pressure known and the flow to be calculated; the flow-known node is generally the load node with the pressure to be calculated. Because of the pressure drop at both ends of the pipeline, especially in the medium and high pressure gas transmission network with long distance and large capacity, it is necessary to configure a compressor to increase the pressure of the gas transmission pipeline [76].

The steady-state model of IES mainly includes AC power flow model of power system, natural gas pipeline model with compressor and steady-state model of thermodynamic system.

4.5.1. Energy Flow Analysis

Electric Power Network. Similar to the power flow model of traditional power system, the classical AC power flow model is generally used for IES. The power equation of the node is expressed as follows:

$$S_i = P_i + jQ_i = \dot{U}_i I_i^* = \dot{U}_i \sum_{j=1}^{n_e} Y_{ij}^* U_{ij}^*, \tag{16}$$

where P and Q are the active power and reactive power of the node, respectively; I_i is the current injected into node i; U_i and U_j are the voltage of node i and node j, respectively; n_e is the number of nodes; "$*$" is the conjugation of complex numbers; V is admittance matrix of the node and U is voltage vector of the node.

Thermal Network. Thermal network is composed of hydraulic model and thermal model. Generalized Kirchhoff's law should be satisfied at each node, i.e. injected flow should be equal to outgoing flow [77–80], that is

$$\begin{cases} A_h m = m_q \\ B_h h_f = 0 \\ h_f = Km|m|, \end{cases} \tag{17}$$

where A_h is the node-branch correlation matrix of heating network; m is flow of each pipeline; m_q is outgoing flow of each node, i.e., consumption flow of heat load node; B_h is the loop-branch correlation matrix of heating network; h_f is loss vector of pressure head; K is the resistance coefficient vector of pipeline.

The thermodynamic model is used to calculate the heating and regeneration temperature of heating network nodes. Heating equipment converts energy into heat energy through natural gas and other fuels, and transmits energy through heat network. For each heat load node, the thermal power and node temperature are expressed as follows:

$$\begin{aligned} &\Phi = C_{\text{shc}} m_q \left(T_{\text{strat}} - T_{\text{end}}\right), \\ &T_{\text{end}} = \left(T_{\text{start}} - T_g\right) \exp\left(-\frac{\lambda_{\text{pipe}} L}{C_{\text{shc}} m}\right) + T_g, \\ &\left(\sum m_{\text{out}}\right) T_{\text{out}} = \sum \left(m_{\text{in}} T_{\text{in}}\right), \end{aligned} \tag{18}$$

where Φ is the thermal power of the thermal network node; T_{start} and T_{end} are the temperature vectors at the beginning and end of the pipeline; L is the length of the pipeline; C_{shc} is the specific heat capacity of water; T_g is the environmental temperature; λ_{pipe} is the heat conductivity of the pipeline; m_{out} and m_{in} are the outflow and inflow of hot water, respectively; T_{out} and T_{in} are the temperature of outflow and inflow of hot water.

Natural Gas Network. The air flow through the pipeline depends on the pressure at both ends of the pipeline and is expressed as follows:

$$\begin{cases} f_r = \text{sgn}(\Delta p) \cdot K_r \cdot \sqrt{\text{sgn}(\Delta p) \cdot \left(p_n^2 - p_m^2\right)} \\ \Delta p = p_n - p_m \\ \text{sgn}(\Delta p) = \begin{cases} +1, & p_n > p_m, \\ -1, & p_n < p_m, \end{cases} \end{cases} \tag{19}$$

where f_r is the flow value of natural gas pipeline from node m to node n; Δp is the pressure difference between node n and m; $\text{sgn}(\Delta p)$ is the flow direction in pipeline; "1" means from node n to node m; "−1" means from node m to node n; K_r is the constant of pipeline, and generally calculated by

$$K_r = 7.57 \times 10^{-4} \frac{T_n}{p_n} \sqrt{\frac{D_r^5}{F L_r T_a Z_a G}}, \tag{20}$$

where T_n and p_n are the temperature and pressure under the standard condition; D_r and L_r are the diameter and length; F is the undirected friction coefficient; T_a is the average temperature of natural gas; Z_a is the average compressibility coefficient; G is the relative density. Both (19) and (20) do not consider the temperature change of natural gas during transmission.

4.5.2. Solution of Optimal Power Flow of Multienergy. At present, Newton-Raphson method is mainly used to solve the problem, which can be divided into unified solution method and decomposition solution method [81–83]. Based on the power flow calculation of power system, the unified solution method takes the variables of natural gas system and thermal system as extended variables, and solves the problem in a unified way. The iterative process of solving the unified power flow model by Newton-Raphson method is expressed as follows:

$$\begin{cases} \Delta x^{(k+1)} = \left(J^{(k)}\right)^{-1} \Delta F^{(k)} \\ x^{(k+1)} = x^{(k)} - \Delta x^{(k+1)}, \end{cases} \tag{21}$$

where ΔF is the deviation value of power flow equations; J is the Jacobian matrix; k is the number of iterations; $x^{(k)}$ and $\Delta x^{(k)}$ are the state variables of the system and its deviation value in k^{th} iteration, respectively; J is expressed as follows:

$$J = \begin{bmatrix} J_{\text{ee}} & J_{\text{eg}} & J_{\text{eh}} \\ J_{\text{ge}} & J_{\text{gg}} & J_{\text{gh}} \\ J_{\text{he}} & J_{\text{hg}} & J_{\text{hh}} \end{bmatrix}, \tag{22}$$

where the diagonal elements J_{ee}, J_{gg}, and J_{ehh} represent the relationship between the energy flow and the state variables of individual electrical, gas, and thermal systems, and nondiagonal elements represent the coupling relationship between different systems.

The decomposition method, also known as sequential solution method, solves the power flow equation separately from the natural gas system. In the current power flow program, the coupling nodes of natural gas system and thermal system are represented by PV nodes or PQ nodes. When solving natural gas system or thermodynamic system, the nodes coupled with other systems are equivalent to source nodes or load nodes.

To solve the hybrid power flow problem of multienergy flow in IES, the corresponding coupling model is first established, and different solving methods are adopted according to different application scenarios. In [15], a collaborative optimization method of adaptive robust day-ahead energy reserve for urban energy systems is proposed, which proves the economic benefits of the proposed adaptive robust framework. Cesena and Mancarella [4] introduces an optimal operation model of intelligent multienergy region constrained by internal energy network, and considers the relevant uncertainties. The results show that the physical constraints of the integrated network and the uncertainty of specific energy sources (such as PV) reduce the flexibility of the region. Nistor and Antunes [84] proposes an integrated energy management method using Markov process to reduce energy costs while maintaining consumer satisfaction. The results show that the proposed method can significantly reduce the system operation economy.

4.6. Research Status and Existing Problems. In view of the current research status of electro-gas coupling system, there are mainly the following difficulties.

Firstly, the transform of the original system on the basis of the existing equipment of power system or natural gas system, and the correctness and economy of selected scheme considering the coupling relationship need to be further analyzed. Because the existing system construction is difficult to come up with a set of extendable and applicable expansion scheme, it is easy to have problems such as large investment and small income. Secondly, the analysis and calculation of multienergy flow of electro-gas coupling system is still in the initial stage of research, lacking fast, accurate and practical methods.

Because the power system and natural gas system are dominated by different subjects, whether there are conflicts of interest and how to distribute interests need to be studied by game theory and other methods. It also has problems whether different subjects will implement scheme according to the scheduled. In addition, the price of hydrogen or methane generated by excess power or renewable energy in power system through P2G technology and whether hydrogen or methane is allowed directly into gas transmission and distribution pipelines by the main body of natural gas still need relevant research and investigation.

The reliability of natural gas supply and power system supply still needs further study. The reliability of single natural gas supply is mainly affected by pipeline capacity and gas storage capacity. The reliability of power system mainly consists of the reliability of power generation system, transmission system, distribution system, and main electrical connection of power plant/substation.

Generally, the operation of IES needs to consider the dynamic characteristics of the system, such as the delay of pipeline transmission, the nonlinearity of equipment conversion efficiency, and power flow constraints, which are nonlinear programming problems [4]. Traditional algorithms such as sequential quadratic programming (SQP) and primal dual interior point or intelligent algorithms, such as particle swarm optimization (PSO), genetic algorithm (GA), evolutionary algorithm (EO), and reinforcement learning (RL), are used to solve nonlinear programming problems [85, 86].

5. Conclusion

This paper first describes the basic structure and formal characteristics of integrated energy system, and introduces the related technologies. This paper systematically summarizes the theory of multienergy coupling, economic analysis, operation optimization and optimal control operation, and pays attention to the problems concerned by academia and industry at present. The methods of physical equipment modeling, energy hub modeling, multienergy flow calculation, economic analysis, coupling relationship, and multienergy flow optimal

solution are described, and analyzed from three levels of user level, regional level, and cross-regional level respectively.

Considering that the integrated energy system plays an important role in the energy revolution, further research is needed to achieve large-scale absorption of renewable energy and efficient utilization of energy. The hot research issues include:

(1) The general modeling theory of IES is the basis of analyzing and researching IES. Although the related physical models of IES system have been stated in the previous sections, due to the lack of in-depth research on control rules and optimization characteristics of new equipment in practical application scenarios, it is of great significance to explore the general modeling theory of integrated energy resources. How to embody the dynamic characteristics of multienergy system and how to build the wide adaptability of IES simulation platform still need to be further studied.

(2) Energy storage system can realize single/two-way conversion and storage of electric energy and other energy in IES. With the wide application of energy storage technology, the dynamic response characteristics of energy storage technology, such as heat storage, cold storage, electricity storage, and gas storage should also be considered during system operation. The impact of adding various types of energy storage systems on the planning and operation of IES needs to be further explored.

(3) Power flow calculation of multienergy flow is an important basic work for system planning, operation and control. How to sum up the general mathematical expressions about the power flow calculation of multienergy flow and achieve fast solution of model needs to be further studied. For the optimal power flow model of multienergy, the mixed integer nonlinear programming (MINLP) problem is solved by using related intelligent algorithms. The complexity of time and space in the optimization process still needs to be further studied.

(4) Considering many uncertainties in IES, the modeling of probabilistic power flow and fast solution methods need to be improved in related applications; due to the different dynamic response characteristics of energy flows, the delay of heat network and gas-heat transmission pipeline need to be studied; optimization problems with multiobjective, strong nonconvex and multiuncertainty coupling need to be efficiently solved. Moreover, there is large fluctuation of the output of wind turbine and solar energy, and the related uncertainty needs to be fully considered.

(5) At the same time, market mechanism and development mode are the direct driving force of IES development. It is necessary to establish a multilevel market mechanism and trading structure, including users, multitype energy producers, energy agents and energy service providers. Frameworks such as multienergy-coupled markets or decentralized trading need to be further studied. According to the actual situation, the way to adjust the interest relationship between integrated energy supply and integrated energy services, and to establish the trading structure and operation model of the future energy market remain to be further explored.

Conflicts of Interest

The authors declare that there is no conflict of interest regarding the publication of this paper.

Acknowledgments

This work is supported by the National Natural Science Foundation of China under Grant Nos. 51807179, 51777193, and 51967001.

References

[1] S. Mei, R. Li, X. Xue et al., "Paving the way to smart micro energy internet: concepts, design principles, and engineering practices," *CSEE Journal of Power & Energy Systems*, vol. 3, no. 4, pp. 440–449, 2016.

[2] C. Wei and Z. Zhang, "An adaptive network-based reinforcement learning method for MPPT control of PMSG wind energy conversion systems," *IEEE Transactions on Power Electronics*, vol. 31, no. 11, pp. 7837–7848, 2016.

[3] H. Qi, J. Zhang, J.-S. Lai, and W. Yu, "A high-efficiency grid-tie battery energy storage system," *IEEE Transactions on Power Electronics*, vol. 26, no. 3, pp. 886–896, 2011.

[4] E. Cesena and P. Mancarella, "Energy systems integration in smart districts: robust optimisation of multi-energy flows in integrated electricity, heat and gas networks," *Transactions on Smart Grid*, vol. 10, no. 1, pp. 1122–1131, 2018.

[5] Y. Li, T. Zhao, and W. Ping, "Optimal operation of multi-microgrids via *cooperative* energy and reserve scheduling," *IEEE Transactions on Industrial Informatics*, vol. 14, no. 8, pp. 3459–3468, 2018.

[6] S. Clegg and P. Mancarella, "Integrated modeling and assessment of the operational impact of power-to-gas(P2G)on electrical and gas transmission networks," *IEEE Transactions on Sustainable Energy*, vol. 6, no. 4, pp. 1234–1244, 2015.

[7] S. Bahrami and A. Sheikhi, "From demand response in smart grid toward integrated demand response in smart energy hub," *IEEE Transactions on Smart Grid*, vol. 7, pp. 650–658, 2015.

[8] F. Cheng, L. Qu, W. Qiao, C. Wei, and L. Hao, "Fault diagnosis of wind turbine gearboxes based on DFIG stator current envelope analysis," *Transactions on Sustainable Energy*, vol. 10, no. 3, pp. 1044–1053, 2019.

[9] C. Wei, M. Benosman, and T. Kim, "Online parameter identification for state of power prediction of lithium-ion batteries in electric vehicles using extremum seeking," *International Journal of Control, Automation and Systems*, 2019.

[10] D. Wang, L. Liu, H. Jia et al., "Review of key problems related to integrated energy distribution systems," *CSEE Journal of Power and Energy Systems*, vol. 4, no. 2, pp. 130–145, 2018.

[11] X. Jin, T. Jiang, Y. Mu et al., "Scheduling distributed energy resources and smart buildings of a microgrid via multi-time scale and model predictive control method," *IET Renewable Power Generation*, vol. 13, no. 6, pp. 816–833, 2019.

[12] X. P. Zhang, M. Shahidehpour, A. Alabdulwahab, and A. Abusorrah, "Optimal expansion planning of energy hub with multiple energy infrastructures," *Transactions on Smart Grid*, vol. 6, no. 5, pp. 2302–2311, 2015.

[13] S. Chen, Z. Wei, G. Sun, K. W. Cheung, D. Wang, and H. Zang, "Adaptive robust day-ahead dispatch for urban energy systems," *IEEE Transactions on Industrial Electronics*, vol. 66, no. 2, pp. 1379–1390, 2019.

[14] V. Vilma, S. S. Afzal, B. Zakeri, and A. Salo, "Market power with combined heat and power production in the nordic energy system," *IEEE Transactions on Power Systems*, vol. 33, no. 5, pp. 5263–5275, 2018.

[15] O. Heffernan, "The third industrial revolution: how lateral power is transforming energy, the economy, and the world," *Mature Climate Change*, vol. 2, no. 2, pp. 67–68, 2012.

[16] A. Q. Huang, M. L. Crow, G. T. Heydt, J. P. Zheng, and S. J. Dale, "The future renewable electric energy delivery and management (FREEDM) system: the energy internet," *Proceedings of the IEEE*, vol. 99, no. 1, pp. 133–148, 2011.

[17] C. P. M. Correa and S. M. Pedro, "Security-constrained optimal power and natural-gas flow," *IEEE Transactions on Power Systems*, vol. 29, no. 4, pp. 1780–1787, 2014.

[18] C. Stephen and M. Pierluigi, "Integrated modeling and assessment of the operational impact of power-to-gas(P2G) on electrical and gas transmission networks," *IEEE Transactions on Sustainable Energy*, vol. 6, no. 4, pp. 1234–1244, 2015.

[19] DOE opens new smart grid integration testing facility, http://spectrum.ieee.org/energywise/energy/the-smarter-grid/doe-launches-new-smart-grid-integration-testing-facility.

[20] European Union, "2030 climate and energy policy framework [EB/OL]. [2015-04-30]," http://ec.europa.eu/clima/policies/2030.

[21] R. Guo and H. Z. Yang, "Roadmap of renewable energy industry development in Chongming Ecoisland," *Journal of Tongji University (Natural Science)*, vol. 40, no. 8, pp. 1204–1209, 2012.

[22] B. Zhao, X. Zhang, J. Chen, C. S. Wang, and L. Guo, "Operation optimization of standalone microgrids considering lifetime characteristics of battery energy storage system," *IEEE Transactions on Sustainable Energy*, vol. 4, no. 4, pp. 934–943, 2013.

[23] N. Nguyen, A. Bera, and J. Mitra, "Energy storage to improve reliability of wind integrated systems under frequency security constraint," *IEEE Transactions on Industry Applications*, vol. 54, no. 5, pp. 4039–4047, 2018.

[24] A. Quelhas, E. Gil, J. D. Mccalley, and S. M. Ryan, "A multiperiod generalized network flow model of the U.S. integrated energy system: Part I—model description," *IEEE Transactions on Power Systems*, vol. 22, no. 2, pp. 829–836, 2007.

[25] G. Abolfazl, B. Mahdi, and R. Morteza, "Integrated energy scheduling under uncertainty in a micro energy grid," *IET Generation, Transmission & Distribution*, vol. 12, no. 12, pp. 2887–2896, 2018.

[26] H. Farzin and M. Moeini-Aghtaie, "Reliability studies of distribution systems integrated with electric vehicles under battery-exchange mode," *IEEE Transactions on Power Delivery*, vol. 31, no. 6, pp. 2473–2482, 2016.

[27] C. M. Correa-Posada and P. Sanchez-Martin, "Integrated power and natural gas model for energy adequacy in short-term operation," *IEEE Transactions on Power Systems*, vol. 30, no. 6, pp. 3347–3355, 2015.

[28] B. Hong, J. Chen, W. Zhang, Z. Shi, J. Li, and W. Miao, "Integrated energy system planning at modular regional-user level based on a two-layer bus structure," *CSEE Journal of Power and Energy Systems*, vol. 4, no. 2, pp. 188–196, 2018.

[29] L. Varga, M. Robinson, and P. Allen, "Multiutility service companies: a complex systems model of increasing resource efficiency," *Complexity*, vol. 21, no. S1, pp. 23–33, 2016.

[30] D. Peng, M. Fowler, A. Elkamel, A. Almansoori, and S. B. Walker, "Enabling utility-scale electrical energy storage by a power-to-gas energy hub and underground storage of hydrogen and natural gas," *Journal of Natural Gas Science and Engineering*, vol. 35, pp. 1180–1199, 2016.

[31] G. Diglio, D. P. Hanak, P. Bareschino et al., "Techno-economic analysis of sorption-enhanced steam methane reforming in a fixed bed reactor network integrated with fuel cell," *Journal of Power Sources*, vol. 364, pp. 41–51, 2017.

[32] M. Geidl, G. Koeppel, P. Favreperrod, B. Klockl, G. Andersson, and K. Frohlich, "Energy hubs for the future," *IEEE Power and Energy Magazine*, vol. 5, no. 1, pp. 24–30, 2007.

[33] L. Ma, N. Liu, J. Zhang, and L. Wang, "Real-time rolling horizon energy management for the energy-hub-coordinated prosumer community from a cooperative perspective," *IEEE Transactions on Power Systems*, vol. 34, no. 2, pp. 1227–1242, 2019.

[34] M. Moeiniaghtaie, H. Farzin, M. Fotuhifiruzabad, M., and R. Amrollahi, "Generalized analytical approach to assess reliability of renewable-based energy hubs," *IEEE Transactions on Power Systems*, vol. 32, no. 1, pp. 368–377, 2017.

[35] R. Dai, J. Zhang, and S. Zhang, "Standard setting with considerations of energy efficiency evolution and market competition," *Complexity*, vol. 2019, 21 pages, 2019.

[36] L. Han, T. Morstyn, and M. McCullon, "Incentivizing prosumer coalitions with energy management using cooperative game theory," *IEEE Transactions on Power Systems*, vol. 34, no. 1, pp. 303–313, 2019.

[37] A. Ali, N. Liu, and L. He, "Multi-party energy management and economics of integrated energy microgrid with PV/T and combined heat and power system," *IET Renewable Power Generation*, vol. 13, no. 3, p. 451, 2019.

[38] M. Deissenroth, M. Klein, K. Nienhaus, and M. Reeg, "Assessing the plurality of actors and policy interactions: agent-based modelling of renewable energy market integration," *Complexity*, vol. 2017, 24 pages, 2017.

[39] A. Ghasemi, M. Banejad, and M. Rahimiyan, "Integrated energy scheduling under uncertainty in a micro energy grid," *IET Generation Transmission & Distribution*, vol. 12, no. 12, pp. 2887–2896, 2018.

[40] A. Jahid, M. K. H. Monju, and M. Hossain, "Renewable energy assisted cost aware sustainable off-grid base stations with energy cooperation," *IEEE Access*, vol. 6, pp. 60900–60920, 2018.

[41] Y. Li, Y. Zou, Y. Tan et al., "Optimal stochastic operation of integrated low-carbon electric power, natural gas, and heat delivery system," *IEEE Transactions on Sustainable Energy*, vol. 9, no. 1, pp. 273–283, 2018.

[42] T. Jiang, H. Deng, L. Bai, R. Zhang, X. Li, and H. Chen, "Optimal energy flow and nodal energy pricing in carbon emission-embedded integrated energy systems," *CSEE Journal of Power and Energy Systems*, vol. 4, no. 2, pp. 179–187, 2018.

[43] B. Zeng, J. Zhang, and X. Yang, "Integrated planning for transition to low-carbon distribution system with renewable energy generation and demand response," *IEEE Transactions on Power Systems*, vol. 29, no. 3, pp. 1153–1165, 2014.

[44] N. Good and P. Mancarella, "Flexibility in multi-energy communities with electrical and thermal storage: a stochastic, robust approach for multi-service demand response," *IEEE Transactions on Smart Grid*, vol. 10, no. 1, pp. 503–513, 2019.

[45] S. Fan, Z. Li, and J. Wang, "Cooperative economic scheduling for multiple energy hubs: a bargaining game theoretic perspective," *IEEE Access*, vol. 6, pp. 27777–27789, 2018.

[46] L. Yang, J. Jian, and Y. Xu, "Multiple perspective-cuts outer approximation method for risk-averse operational planning of regional energy service providers," *IEEE Transactions on Industrial Informatics*, vol. 13, no. 5, pp. 2606–2619, 2017.

[47] H. Massrur, T. Niknam, and J. Aghaei, "Fast decomposed energy flow in large-scale integrated electricity-gas-heat energy systems," *IEEE Transactions on Sustainable Energy*, vol. 9, no. 4, pp. 1565–1577, 2018.

[48] Z. Pan, Q. Guo, and H. Sun, "Interactions of district electricity and heating systems considering time-scale characteristics based on quasi-steady multi-energy flow," *Applied Energy*, vol. 167, pp. 230–243, 2016.

[49] X. Liu and P. Mancarella, "Modelling assessment and Sankey diagrams of integrated electricity-heat-gas networks in multi-vector district energy systems," *Applied Energy*, vol. 167, pp. 336–352, 2016.

[50] M. Moeini-Aghtaie, A. Abbaspour, and M. Fotuhi-Firuzabad, "A decomposed solution to multiple-energy carriers optimal power flow," *IEEE Transactions on Power Systems*, vol. 29, no. 2, pp. 707–716, 2014.

[51] A. Zlotnik, L. Roald, and S. Backhaus, "Coordinated scheduling for interdependent electric power and natural gas infrastructures," *IEEE Transactions on Power Systems*, vol. 32, no. 1, pp. 600–610, 2017.

[52] M. Geidl and G. Andersson, "Optimal power flow of multiple energy carriers," *IEEE Transactions on Power Systems*, vol. 22, no. 1, pp. 145–155, 2007.

[53] X. Zhang and M. Shahidehpour, "Optimal expansion planning of energy hub with multiple energy infrastructures," *IEEE Transactions on Smart Grid*, vol. 6, pp. 2302–2311, 2015.

[54] S. Clegg and P. Mancarella, "Integrated electrical and gas network flexibility assessment in low-carbon multi-energy systems," *IEEE Transactions on Sustainable Energy*, vol. 7, no. 2, pp. 718–731, 2016.

[55] H. Yin and Z. Chen, "Decentralized real-time energy management for a reconfigurable multiple-source energy system," *IEEE Transactions on Industrial Informatics*, vol. 14, no. 9, pp. 4128–4137, 2018.

[56] N. Good, E. Karangelos, and A. Navarro-Espinosa, "Optimization under uncertainty of thermal storage-based flexible demand response with quantification of residential users' discomfort," *IEEE Transactions on Smart Grid*, vol. 6, no. 5, pp. 2333–2342, 2015.

[57] F. Fang, Q. H. Wang, and S. Yang, "A novel optimal operational strategy for the CCHP system based on two operating modes," *IEEE Transactions on Power Systems*, vol. 27, no. 2, pp. 1032–1041, 2012.

[58] P. Singh and B. Khan, "Smart microgrid energy management using a novel artificial shark optimization," *Complexity*, vol. 2017, 12 pages, 2017.

[59] J. Wang, H. Zhong, C. X. Tan Chen, R. Rajagopal, Q. Xia, and C. Kang, "Economic benefits of integrating solar-powered heat pumps into a CHP system," *IEEE Transactions on Sustainable Energy*, vol. 9, no. 4, pp. 1702–1712, 2018.

[60] Y. Dai, L. Chen, and Y, Min, "Integrated dispatch model for combined heat and power plant with phase-change thermal energy storage considering heat transfer process," *IEEE Transactions on Sustainable Energy*, vol. 9, no. 3, pp. 1234–1243, 2018.

[61] P. Sauter, B. Solanki, C. A. Canizares, K. Bhattacharya, and S. Hohmann, "Electric thermal storage system impact on northern communities' microgrids," *IEEE Transactions on Smart Grid*, vol. 10, no. 1, pp. 852–863, 2019.

[62] Z. Pan, J. Wu, H. Sun, Q. Guo, and M. Abeysekera, "Quasi-dynamic interactions and security control of integrated electricity and heating systems in normal operations," *CSEE Journal of Power and Energy Systems*, vol. 5, pp. 120–129, 2019.

[63] C. Shao, Y. Ding, J. Wang, and Y. Song, "Modeling and integration of flexible demand in heat and electricity integrated energy system," *IEEE Transactions on Sustainable Energy*, vol. 9, no. 1, pp. 361–370, 2018.

[64] M. Tahir and H. Chen, "Integrated energy system modeling of china for 2020 by incorporating demand response, heat pump and thermal storage," *IEEE Access*, vol. 7, pp. 400095–40108, 2019.

[65] F. Wei, Y. Li, and Q. Sui, "A novel thermal energy storage system in smart building based on phase change material," *IEEE Transactions on Smart Grid*, vol. 10, no. 3, pp. 2846–2857, 2019.

[66] S. Krishnan, D. Ezhilarasi, and G. Uma, "Pyroelectric-based solar and wind energy harvesting system," *IEEE Transactions on Sustainable Energy*, vol. 5, no. 1, pp. 73–81, 2014.

[67] T. Li, M. Eremia, and M. Shahidehpour, "Interdependency of natural gas network and power system security," *IEEE Transactions on Power Systems*, vol. 23, no. 4, pp. 1817–1824, 2008.

[68] S. Clegg and P. Mancarella, "Integrated electrical and gas network flexibility assessment in low-carbon multi-energy systems," *IEEE Transactions on Sustainable Energy*, vol. 7, no. 2, pp. 718–731, 2016.

[69] S. Chen, Z. Wei, and G. Sun, "Identifying optimal energy flow solvability in electricity-gas integrated energy systems," *IEEE Transactions on Sustainable Energy*, vol. 8, no. 2, pp. 846–854, 2017.

[70] H. Khani and N. EI-Taweel, "Real-time optimal management of reverse power flow in integrated power and gas distribution grids under large renewable power penetration," *IET Generation Transmission & Distribution*, vol. 12, no. 10, pp. 2325–2331, 2018.

[71] Y. He and M. Shahidehpour, "Robust constrained operation of integrated electricity-natural gas system considering distributed natural gas storage," *IEEE Transactions on Sustainable Energy*, vol. 9, no. 3, pp. 1061–1071, 2018.

[72] Y. Y. Zhang, Y. Hu, and J. Ma, "A mixed-integer linear programming approach to security-constrained co-optimization expansion planning of natural gas and electricity transmission systems," *IEEE Transactions on Power Systems*, vol. 33, no. 6, pp. 6368–6378, 2018.

[73] J. Zhong, L. Wang, and H. Z. Bo, "Research on optimisation of integrated energy system scheduling based on weak robust optimisation theory," *IET Generation, Transmission & Distribution*, vol. 13, no. 1, pp. 64–72, 2019.

[74] W. Zhong and C. Yang, "ADMM-based distributed auction mechanism for energy hub scheduling in smart buildings," *IEEE Access*, vol. 6, pp. 45635–45645, 2018.

[75] L. Han, T. Morstyn, and M. McCulloch, "Incentivizing prosumer coalitions with energy management using cooperative game theory," *IEEE Transactions on Power Systems*, vol. 34, no. 1, pp. 303–313, 2019.

[76] E. Cesena and P. Mancarella, "Energy systems integration in smart districts: robust optimisation of multi-energy flows in integrated electricity, heat and gas networks," *IEEE Transactions on Smart Grid*, vol. 10, no. 1, pp. 1122–1131, 2019.

[77] A. Martinez-Mares and C. Fuerte-Esquivel, "A unified gas and power flow analysis in natural gas and electricity coupled networks," *IEEE Transactions on Power Systems*, vol. 27, no. 4, pp. 2156–2166, 2012.

[78] C. Correa-Posada and P. Sanchez-Martin, "Integrated power and natural gas model for energy adequacy in short-term operation," *IEEE Transactions On Power Systems*, vol. 30, no. 6, pp. 3347–3355, 2015.

[79] W. Gu, Z. Wang, and Z. Wu, "An online optimal dispatch schedule for CCHP microgrids based on model predictive control," *IEEE Transactions on Smart Grid*, vol. 8, no. 5, pp. 2332–2342, 2017.

[80] A. Martinez and C. R. Fuerte-Esquivel, "A unified gas and power flow analysis in natural gas and electricity coupled networks," *IEEE Transactions on Power Systems*, vol. 27, no. 4, pp. 2156–2166, 2012.

[81] Q. Zeng, J. Fang, and J. Li, "Steady-state analysis of the integrated natural gas and electric power system with bi-directional energy conversion," *Applied Energy*, vol. 1784, pp. 1483–1492, 2016.

[82] Z. Pan, Q. Guo, and H. Sun, "Interactions of district electricity and heating systems considering time-scale characteristics based on quasi-steady multi-energy flow," *Applied Energy*, vol. 167, pp. 230–243, 2016.

[83] J. Li and J. Fang, "Optimal operation of the integrated electrical and heating systems to accommodate the intermittent renewable sources," *Applied Energy*, vol. 167, pp. 244–254, 2016.

[84] M. Nistor and C. Antunes, "Integrated management of energy resources in residential buildings—a Markovian approach," *IEEE Transactions on Smart Grid*, vol. 9, no. 1, pp. 240–251, 2018.

[85] B. Odetayo and M. Kazemi, "A chance constrained programming approach to the integrated planning of electric power generation, natural gas network and storage," *IEEE Transactions on Power System*, vol. 33, no. 6, pp. 6883–6893, 2018.

[86] A. Elgammal and M. El-Naggar, "Energy management in smart grids for the integration of hybrid wind–PV–FC–battery renewable energy resources using multiobjective particle swarm optimisation (MOPSO)," *The Journal of Engineering*, vol. 2018, no. 11, pp. 1806–1816, 2018.

Hindawi
Complexity
Volume 2019, Article ID 3765821, 11 pages
https://doi.org/10.1155/2019/3765821

Research Article

Variable Speed Pump Storage for the Mitigation of SSR in Power System with Wind Generation

Ye Fengchun,[1] Girmaw Teshager Bitew ,[2] Han Minxiao ,[2] Sun Yao,[2] and Zhang Hanhua[1]

[1]*Electric Power Research Institute, State Grid Ningxia Electric Power Co., Ltd., Yinchuan, China*
[2]*School of Electrical Engineering, State Key Laboratory of Alternate Electrical Power System with Renewable Energy Sources, North China Electric Power University, Beijing 102206, China*

Correspondence should be addressed to Han Minxiao; ncepu_vsc@163.com

Received 2 July 2019; Accepted 23 August 2019; Published 10 December 2019

Guest Editor: Xiaoqing Bai

Subsynchronous resonance (SSR) can bring significant negative effects on the grid system like stability, security, and even generator shaft damage. This work presents a new method of using a doubly-fed induction machine (DFIM) based system of variable speed pumped storage plant (VSPS) to mitigate SSR in the power system with high penetration of wind generation. The mitigation is reached based on the principle of balanced shaft mechanical input power and electromagnetic power. The fundamental concepts and phenomena of SSR with wind farm are discussed in brief in this work. For the sake of analysis and verification of performance of the proposed system, the network model including wind farm, VSPS, HVDC, and synchronous machine is built based on Ningxia grid for the SSR study using PSCAD platform. The result shows that VSPS brings significant effect to dampen the SSR in the power system with high penetration of wind generation.

1. Introduction

Subsynchronous resonance (SSR) in a power system is an electromechanical instability occurrence when the interaction exists between the torsional modes of generator shafts and effect of series-compensated transmission line running with less than the nominal grid frequency [1]. The studies have also confirmed that the wind farms constructed with doubly-fed induction generator (DFIG) and connected to series capacitor compensated transmission lines are quite vulnerable to subsynchronous interaction (SSI) and cause the escalation of SSR in the power system. SSR brings significant negative effects on the grid system like stability, security, and even generator shaft damage [2, 3]. So, the analysis and mitigation for SSR is imperative.

There are two categories in practice to mitigate SSR: one is primary machine parameters modification and the other one is the secondary control loop [4, 5]. The typical examples for the first one are pole-face amortisseur windings at the generator rotor, blocking filter, TCSC, NGH damper, phase shifters, static var compensator (SVC), etc. The most typical example of the second one is using generator excitation regulator. In addition, different supplementary damping measures of FACTS have been put forward in [6–8]. Besides, to mitigate SSR, a new method of using a doubly-fed induction machine (DFIM) based system of variable speed pumped storage plant (VSPS) is proposed based on the principle of balanced shaft mechanical input power and electromagnetic power. Electromagnetic power can be calculated by the power flow of DFIM terminal to the grid, and thus controlled by the converters connected to the DFIM. By regulating injecting or absorbing active power of DFIM according to the generator speed deviation, the balance of the shaft power will be maintained smooth; therefore, VSPS can provide damping for SSR and suppress transient torque amplification effect. Regulating the absorbing or generating reactive power by the converters of the VSPS also keeps the AC voltage oscillations damped quickly. To analyse SSR and validate the performance of the proposed system, the network model including wind farm, VSPS, HVDC, and synchronous machine is built based on Ningxia grid for the study of SSR using PSCAD platform.

2. Problem Description Associated with Wind Generation

The SSR of DFIG originates from the resonance of the inductance-capacitance (L-C) of the components, but is reinforced by the converter control of DFIG. The latter, by greatly enlarging the negative resistance at the slip frequency, serves as the primary reason for the self-excitation of SSR, even under the context of a very low series compensation. This has been explained by theoretical analysis and confirmed by field observations [6]. It would significantly increase the absolute value of the negative resistance and thus contribute a lot to an unstable oscillation [2]. Consequently, DFIG is made much more vulnerable to the subsynchronous control interaction (SSCI)-type SSR. SSCI is emerged that there is a growing risk of SSR caused by the interaction between DFIGs and series compensated transmission line due to the increasing applications of wind power energy and series compensation.

In the SSR event, the frequency at different locations is identical, meaning all wind turbine generators (WTGs) and the network are engaged in the same SSR mode. But its value is not fixed and keeps changing over time as well as the variation of the factors such as the network topology and number of online generators [6].

According to the study of [7], many SSR phenomena have been detected in Guyuan, Hebei in 2010. The current of both DFIG of the wind farm and transmission line oscillates with large magnitude at the subsynchronous frequency.

The proposed system in this paper is designed based on the IEEE second benchmark model of SSR so that the SSR can be well analysed. This wind generator model is shown in (Figure 1). An equivalent lumped machine is provided to represent a behaviour of a group of wind turbines. As many studies [11, 12] support this assumption, the aggregation of a wind farm provides a reasonable approximation for system interconnection studies. According to system studies [13–16], simulations of bulk system dynamics using a single machine equivalent is adequate for most planning studies.

Based on this lumped wind machine model, the system shown in (Figure 2) is considered for the case study for Ningxia grid that consists of large penetration of wind and PV generation with HVDC sending out. The synchronous machine mechanical system of the model consists of exciter, generator, low-pressure (LP) and high-pressure (HP) turbine sections. PSCAD model is built for Figure 2 for the case study and the detailed analysis is presented in the following section.

The effect of SSR is also distributed into the grid. The following Figures including Figures 3–5 show the effect of SSR on the voltage, power flow and speed responses of wind farm, and HVDC operations.

While the synchronous generator is connected to the infinite bus AC-source, the operation is responding very well. But, when the infinite bus AC-source is shunted by RL components, the SSR starts due to the dominant effect of the series capacitor which is interacted with the torsional shaft mode of operation of the generator.

The transition time is made at $t = 1.5$ seconds. The RL remains connected for 0.2 s. However, even if the RL is disconnected, the resonance and the disturbance continue as in Figure 4.

The effects of SSR in the power grid considered in Figure 5 are presented in the simulated waveforms shown in the following Figures.

It can be concluded that the SSR has significant effect on the quality of voltage and power flow of the grid. It is more pronounced on the proximity where SSR is emerged. It leads to system failure and is a threat of power security. Thus, it needs to be suppressed by the appropriate method or technique. Some methods used so far have been presented in the introduction section in this paper. Besides, a new method of using a doubly-fed induction machine (DFIM) based system of variable speed pumped storage plant (VSPS) to mitigate SSR is proposed in this paper and discussed in the following section.

3. VSPS for the Mitigation of the SSR

The VSPS plays important roles in the power grid for its energy management, stability control and renewable energy resources smoothening. If it deploys a DFIM topology, it is very suitable in independent and fast active and reactive power controls. Another advantage includes that the speed of the machine is no longer locked to system frequency. Thus, in the steady state, the controls select the optimum relationship between gate position and speed to get the desired power. Hence, the efficiency and the operation flexibility of the conventional pumped storage running at constant speed can be noticeably increased by using variable speed groups. The VSPS, in general, has an immense advantages and benefits for wind power fluctuation compensation and other renewable energy smoothening, stability control, frequency control, and AC voltage control among others. Thus, it is suitable and verified that this new method of using a doubly-fed induction machine (DFIM) based system of variable speed pumped storage (VSPS) is capable of mitigating the SSR based on the principle of power balance between the machine shaft power and electromagnetic power, which is regulated by the VSPS control strategy. The electromagnetic power can be calculated by the equivalent power flow of the VSPS in to the grid, and thus regulated by the converters connected to in the DFIM. The structure of the recommended system is illustrated with a single-line diagram shown in (Figure 6). The VSPS power is defined by (1) under $d-q$ frame.

$$P_s = \frac{3}{2}\left(v_{qs}i_{qs} + v_{ds}i_{ds}\right),$$
$$Q_s = \frac{3}{2}\left(v_{qs}i_{ds} - v_{ds}i_{qs}\right), \tag{1}$$

where P_s, Q_s, v_{dqs} and i_{dqs}, are, respectively, active power, reactive power, dq-axis voltages, and dq-axis currents of the stator terminal of the DFIM.

According to [12], the VSPS is very effective for regulating grid frequency and AC voltage, stability control and wind power compensation as it is proved and verified with the case study end experimental results. By regulating injecting or absorbing active power of DFIM, the balance of the power in the grid will be maintained. Regulating the absorbing or

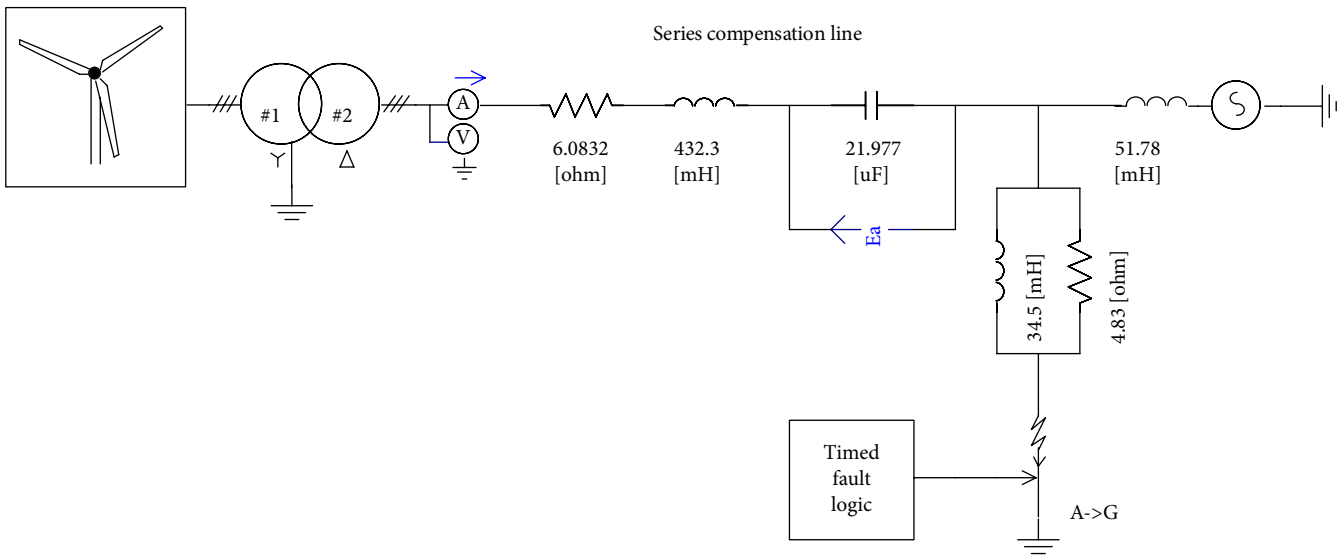

Figure 1: The PSCAD circuit diagram model of wind farm built based on IEEE second benchmark circuit model.

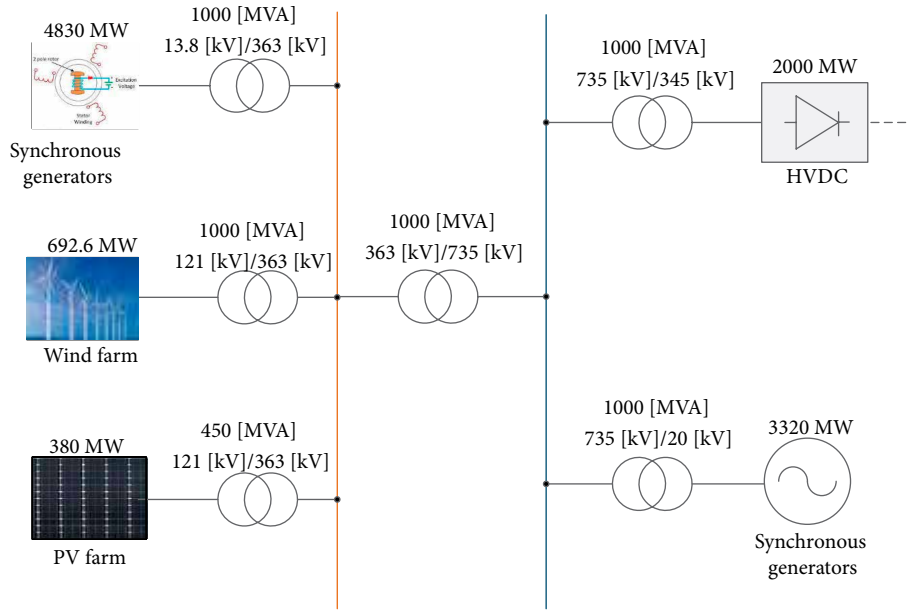

Figure 2: The structure of the power grid to study SSR, its effect, characteristics.

generating reactive power by the converters of the VSPS also keeps the AC voltage oscillations damped quickly. Therefore, this principle brings a balanced shaft mechanical input power and electromagnetic power, which is able to suppress the SSR very quickly. Hence, VSPS can provide damping for SSR and suppress transient torque amplification effect. To analyse SSR and validate the performance of the proposed system, IEEE second benchmark model of SSR is used.

Based on the basic theoretical description of the VSPS DFIM presented in (1), (2), and (3), flexible and fast control strategy is likely possible to design for mitigating the SSR in the power system. Since VSC allows the DFIM more versatile and flexible for controlling, the VSC system is a preferable option and used in this study. Basically, two main methods including voltage-mode control and current-mode control exist for controlling active and reactive power in the VSC system. In a voltage-mode control, there is no control loop closed on the VSC line current. As a result, the VSC is not protected against over-currents, whereas, in the current-mode control, the VSC line current is tightly regulated by a dedicated current-control scheme. In this study, thus, current-mode control strategy is employed for controlling the real and reactive power that each VSC system exchanges with the corresponding AC system. The VSC also allows to adopt the droop control mounted on the PQ-control. The control design is presented in the following section.

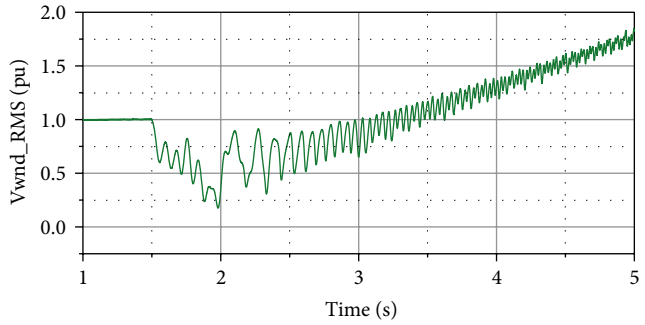

Figure 3: The wind farm machine terminal AC voltage characteristics.

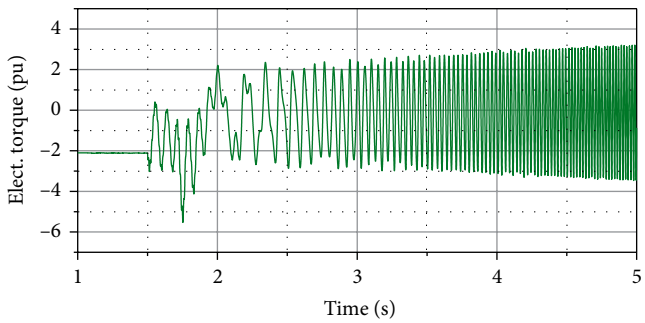

Figure 4: Electrical torque characteristics due to SSR in the wind farm.

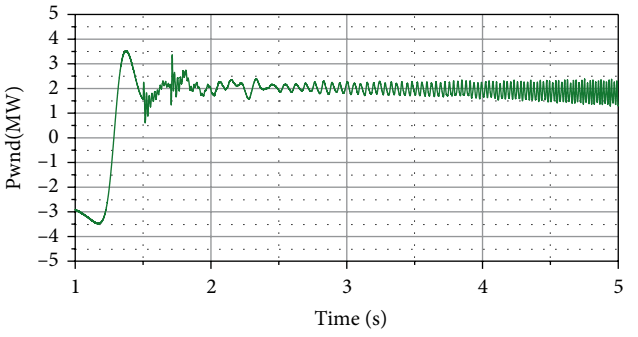

(a)

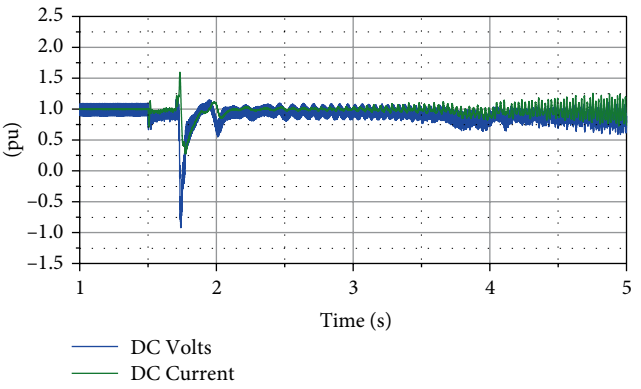

(b)

Figure 5: Effect of SSR in the grid. (a) Power flow in one of the wind farm turbines. (b) DC voltage and current responses in the HVDC.

4. Control Design of the VSPS

4.1. VSC Based DFIM Control. The hierarchical control structure (the current controllers in the inner loops and the active/reactive power control in the outer loops) of VSC based DFIM topology is implemented in this study for its effectiveness. To minimize the excursions of the grid frequency and AC voltage deviations caused by the contingencies, the outer loop control of the rotor side converter (RSC) is supported by the droop control. (Figure 7) illustrates the control structure proposed in this study. The droop control scheme is vested on the control strategy. Direct power control is an extension of direct torque control, which is a vector control family. In the implementation of direct power control, control of the instantaneous real and reactive power is independent, simple, and direct. In the application of VSPS, this type of control scheme attempts to assure having lower computational complexity and machine model dependency, direct controllability of active and reactive powers, very good transitory response, and lower overall implementation complexity than field-oriented control scheme. It is also characterized by its fast-dynamic response against parameter variations and it does not utilize a rotor current control loop. The estimation of active and reactive powers is carried out using current measurements, and directly controlled with hysteresis controllers and a switching table. However, the frequency and voltage control are considered as open loop control. Thus, they need feedback signals to track the frequency and voltage fluctuations very quickly for damping accordingly. The parameters determined and used in the VSPS plant are listed in Appendix.

4.2. Control of RSC. Starting with the dynamics model of the three-phase induction machine based on the synchronous reference frame, the electrical equations of the DFIM are expressed by.

$$\begin{aligned}
\frac{d\Psi_{ds}}{dt} &= V_{ds} - R_s i_{ds} + \omega_s \Psi_{qs},\\
\frac{d\Psi_{qs}}{dt} &= V_{qs} - R_s i_{qs} - \omega_s \Psi_{ds},\\
\frac{d\Psi_{dr}}{dt} &= V_{dr} - R_r i_{dr} + (\omega_s - \omega_r)\Psi_{qr},\\
\frac{d\Psi_{ds}}{dt} &= V_{qr} - R_s i_{qr} - (\omega_s - \omega_r)\Psi_{dr},
\end{aligned} \tag{2}$$

$$\begin{aligned}
\Psi_{ds} &= L_s i_{ds} + L_m i_{dr},\\
\Psi_{qs} &= L_s i_{qs} + L_m i_{qr},\\
\Psi_{dr} &= L_s i_{dr} + L_m i_{ds},\\
\Psi_{qr} &= L_s i_{qr} + L_m i_{qs},\\
L_r &= L_{lr} + L_m,\\
L_s &= L_{ls} + L_m,
\end{aligned} \tag{3}$$

where; Ψ_{dqr}: dq-axis rotor fluxes, Ψ_{dqs}: dq-axis stator fluxes, i_{dqr}: dq-axis rotor currents, i_{dqs}: dq-axis stator currents, V_{dqs}: dq-axis stator voltages, V_{dqr}: dq-axis rotor voltages, L_m: magnetizing reactance, L_{lr}: rotor leakage reactance, L_{ls}: stator leakage reactance, R_r: rotor resistance, R_s: stator resistance, ω_r: electrical angular speed, ω_s: synchronous angular speed.

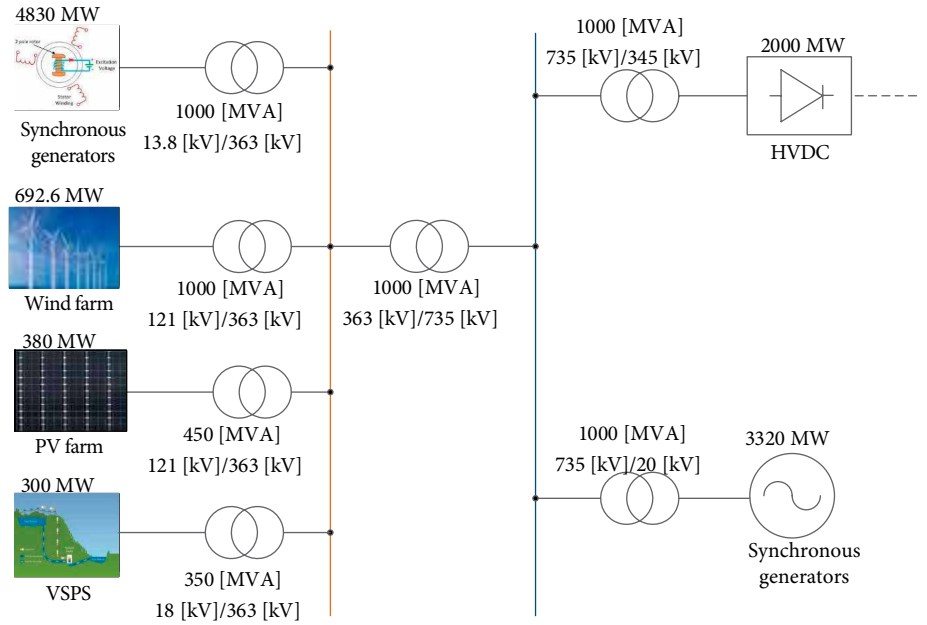

Figure 6: Structure of the proposed system to mitigate the effects of SSR in the power system.

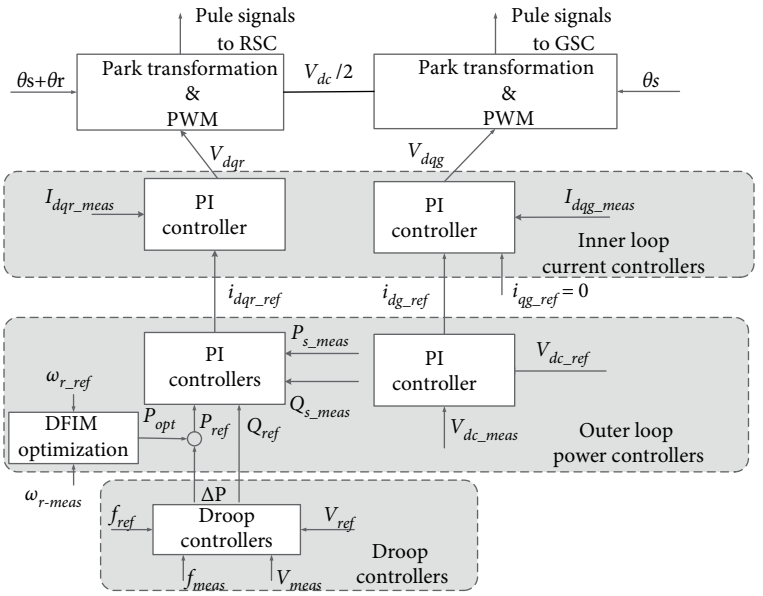

Figure 7: Overall structure of control strategy used in this paper implemented in the VSPS plant.

Based on [13], with the implementation of the vector control method, the stator flux is aligned with the d-axis. Taking the stator flux equations in (3), one can deduce that $\Psi_{qs} = 0$, and $\Psi_{ds} = \Psi_s$. Thus, from equations in (3), the following are obtained.

$$\begin{aligned} i_{ds} &= \frac{\Psi_s}{L_s} - \frac{L_m}{L_s} i_{dr}, \\ i_{qs} &= -\frac{L_m}{L_s} i_{qr}. \end{aligned} \tag{4}$$

Taking the assumption that the voltage drop across stator resistor is very small compared to the grid voltage, stator resistance can be neglected. Thus, $v_{ds} = 0$, and $v_{qs} = v_s$. Hence, substituting these and the values of $i_{qs} = 0$, and i_{ds} in (4) to (1), the following hold.

$$\begin{aligned} P_s &= \frac{3}{2} V_s \left(\frac{L_m}{L_s} \right) i_{qr}, \\ Q_s &= \frac{3}{2} V_s \left[\left(\frac{\Psi_s}{L_s} \right) - \left(\frac{L_m}{L_s} \right) i_{dr} \right]. \end{aligned} \tag{5}$$

Equation (5) explains that the active power and reactive power are independently controlled. This reveals that RSC offers a proper AC excitation for the windings of the rotor that provides the stator windings proper active power and used for controlling the turbine output power and the reactive power which is measured at the terminals of the stator of the machine

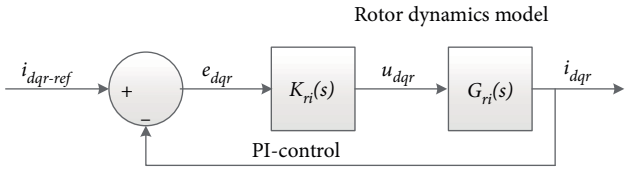

Figure 8: The PI current control (inner loop) structure of the RSC.

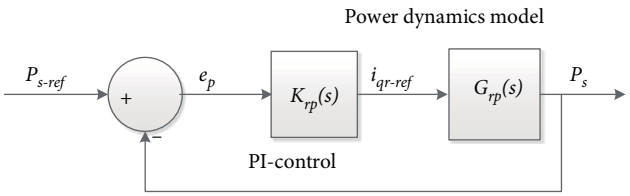

Figure 9: The PI active power control (outer loop) structure of the RSC.

[12]. The active power is regulated so as to follow a relationship of power and speed of the turbine of the DFIM.

The model used to control the currents is presented as under.

Taking the equation of (4) and differentiating the rotor flux leakage equation of the d-axis component with respect to time, the equation (6) holds.

$$\frac{d\Psi_{dr}}{dt} = L_r \frac{di_{dr}}{dt} + L_m \frac{di_{ds}}{dt}. \tag{6}$$

Substituting the derivative value of i_{qs} in (4) to (2), equation (7) is derived.

$$\frac{d\Psi_{dr}}{dt} = L_r \frac{di_{dr}}{dt} + L_m \frac{-L_m}{L_s} \frac{di_{ds}}{dt}. \tag{7}$$

Substituting the value of $d\Psi_{dr}/dt$ in (7) to the d-axis rotor equation of (2), equation (8) is derived.

$$V_{dr} = R_r i_{dr} + L_r^* \frac{di_{dr}}{dt} - (\omega_s - \omega_r)\left(L_r i_{qr} + L_m i_{qs}\right). \tag{8}$$

Following the same procedures to the q-axis, equation (9) holds.

$$V_{qr} = R_r i_{qr} + L_r^* \frac{di_{qr}}{dt} + (\omega_s - \omega_r)(L_r i_{dr} + L_m i_{ds}), \tag{9}$$

where $L_r^* = L_r - \left(L_m^2/L_s\right)$.

Equations of (8) and (9) are helpful to develop the inner current control loops. But, due to the presence of $L_r(\omega_s - \omega_r)$ terms in (8) and (9), the dynamics of i_{qr} and i_{dr} are coupled. To decouple the dynamics, one can determine m_{qr} and m_{dr}. Taking into account the theory of VSC, $mV_{dc}/2$ is the gain of the VSC. Thus, the computed signals V_{qr} and V_{dr} are divided by $V_{dc}/2$ to give, respectively, m_{qr} and m_{dr} signals. The modulated signals of m_{qr} and m_{dr} are defined by

$$\begin{aligned} m_{dr} &= \left(\frac{2}{V_{dc}}\right)\left[u_{dr} - (\omega_s - \omega_r)\left(L_r i_{qr} + L_m i_{qs}\right)\right], \\ m_{qr} &= \left(\frac{2}{V_{dc}}\right)\left[u_{qr} - (\omega_s - \omega_r)(L_r i_{dr} + L_m i_{ds})\right]. \end{aligned} \tag{10}$$

The two new control inputs are defined as

$$\begin{aligned} u_{dr} &= L_r^* \frac{di_{dr}}{dr} + R_r i_{dr}, \\ u_{qr} &= L_r^* \frac{di_{qr}}{dr} + R_r i_{qr}. \end{aligned} \tag{11}$$

Thus, the rotor electrical dynamics model is determined and representing two decoupled, first-order subsystems.

The plant transfer function is given by

$$G_{ri}(s) = \frac{I_{dqr}(s)}{U_{dqr}(s)} = \frac{1}{L_r^* s + R_r}. \tag{12}$$

These subsystems are the rotor-current control loops. Feedforward terms predicting V_{qr} and V_{dr} are provided on both inner loops. The loops can now control i_{qr} and i_{dr} with the PI compensators. The PI compensator with k_p^{ri} as proportional gain and k_i^{ri} as integral gain of the compensator is defined by

$$K_{ri}(s) = \frac{k_p^{ri} s + k_i^{ri}}{s}. \tag{13}$$

Based on these mathematical models of (12) and (13), the control structure is built and illustrated in Figure 8.

The outer loops are developed to generate the reference current $i_{dqr-ref}$ to the inner loops. From Figure 8, the closed loop transfer function of q-axis current can be defined by

$$i_{qr}(s) = \frac{K_{ri} G_{ri}}{1 + K_{ri} G_{ri}} i_{qr-ref}(s). \tag{14}$$

Based on (5) and substituting the value of $i_{qr}(s)$ in (14) to it (5), the active power is expressed by (15).

$$P_s = \frac{3}{2} \frac{L_m}{L_s} V_s \frac{K_{ri} G_{ri}}{1 + K_{ri} G_{ri}} i_{qr-ref}(s) = G_{rp}(s) i_{qr-ref}(s). \tag{15}$$

Therefore, the plant function of active power in (15) can be controlled by PI compensator. The control structure is shown in Figure 9.

Where the PI-control is denoted by.

$$K_{rp}(s) = \frac{k_p^{rp} s + k_i^{rp}}{s}, \tag{16}$$

with k_p^{rp} and k_i^{rp} are, respectively, proportional and integral gains of the controller. The refence value of P_{s-ref} is determined from the optimization of the hydraulic turbine.

Moreover, controlling of active power can ensure controlling of grid frequency. But, in the above model, frequency is controlled in a mode of open loop scheme. Thus, the frequency could not be fully regulated and leads to more excursions. Hence, the frequency needs to be designed in such a way that the frequency closed loop circuit is added to the above active power control loop as a concept of droop control. The droop control can compensate if some excursions of a grid frequency occur due to contingencies including SSR. The control structure is illustrated in (Figure 10). The droop constant K_f is computed by (17).

$$K_f = \frac{-\Delta f/f}{\Delta P/P}, \tag{17}$$

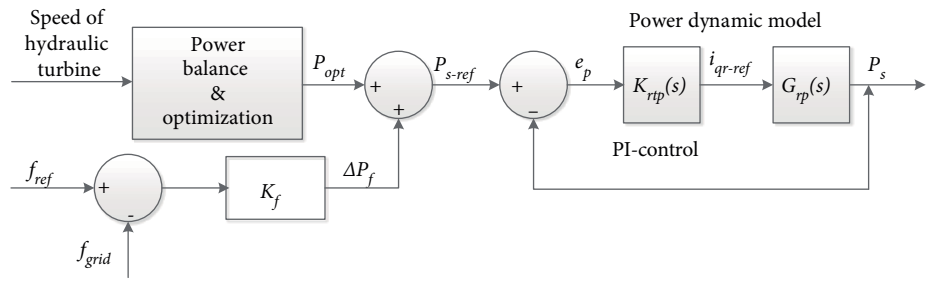

Figure 10: Droop-based direct power vector control structure for RSC of the VSPS (active power control loop).

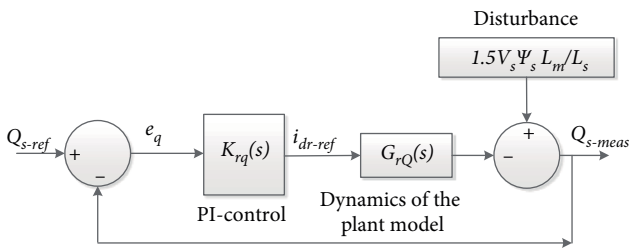

Figure 11: The PI reactive power control loop structure of the RSC.

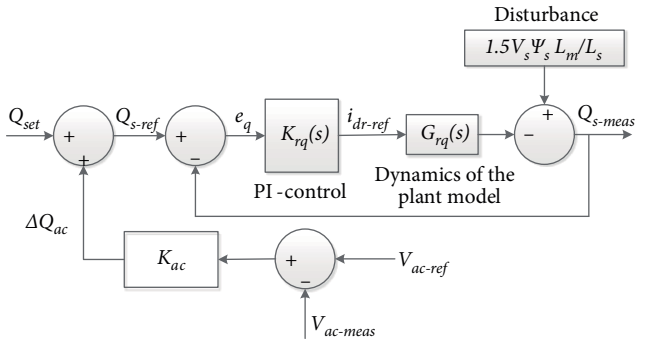

Figure 12: Droop-based direct power vector control structure for RSC of the VSPS (reactive power control loop).

where, Δf is allowable deviation of grid frequency, ΔP is and P is the maximum power carried by the converter.

The reactive power control design is presented as follow. From (5) and Figure 8, the equation (18) holds.

$$\begin{aligned} P_s &= -\frac{3}{2}\frac{L_m}{L_s}V_s\frac{K_{ri}G_{ri}}{1+K_{ri}G_{ri}}i_{dr-ref}(s)+\frac{3}{2}\frac{\Psi_s}{L_s} \\ V_s &= G_{rQ}(s)i_{qr-ref}(s)+\frac{3}{2}\frac{\Psi_s}{L_s}V_s. \end{aligned} \tag{18}$$

Thus, the dynamics of (18) can be controlled by applying PI control and the control structure is depicted in Figure 11.

In this model, the AC voltage is controlled through controlling reactive power but the reference of reactive is set to a fixed value. This leads to deviations and instability when contingencies occur. The reference value of the reactive value should be determined through the proportional value of change of AC voltage. This process is effective by providing the droop control loop to add with the above reactive power control loop. The control structure of this new idea is shown in the Figure 12.

The constant of the droop loop is determined based on the concept emerged from Figure 13.

From Figure 13, we can have (19).

$$\begin{aligned} V_{t-SG} &= e_{SG}+k_{SG}(R_{SG}+jX_{SG})i_{SG}, \\ V_{t-SG} &= e_{SG}+k_{SG}(R_{SG}+jX_{SG})i_{SG}. \end{aligned} \tag{19}$$

Equation (19) states that with the voltage control units connected in parallel, the load compensation is likely made.

4.3. Control of GSC. The objective of the active/reactive power controller of the VSC system is to regulate the active/reactive power exchange between the converter and the AC grid. Active

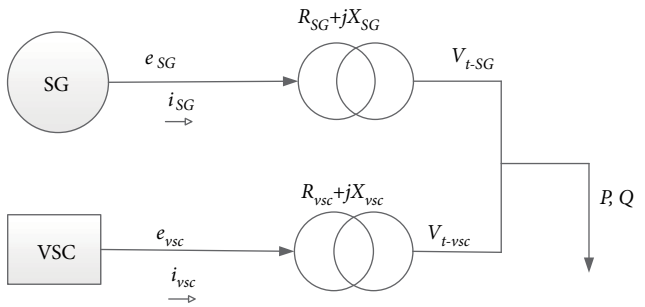

Figure 13: Block diagram of voltage-control units connected in parallel for briefing voltage droop control.

power is controlled by controlling the DC voltage that ensures the converter operation at unity power factor. The VSC based model also allows the GSC to absorb or generate reactive power. So, since there is no reactive power exchange initially, the reactive power control can be handled only by inner loop of current control. The control design is presented in the following.

Based on Figure 14, the voltage equations across the coupling inductor in dq-frame are determined. The same procedure as done in the RSC is followed for developing the inner loops (current controllers). The equations are expressed by

$$V_{dg} = Ri_{ds}+L\frac{di_{ds}}{dt}-\omega_s Li_{qs}+V_{ds}, \tag{20}$$

$$V_{qg} = Ri_{qs}+L\frac{di_{qs}}{dt}-\omega_s Li_{ds}+V_{qs}, \tag{21}$$

where R and L are resistance and inductance of the coupling inductor.

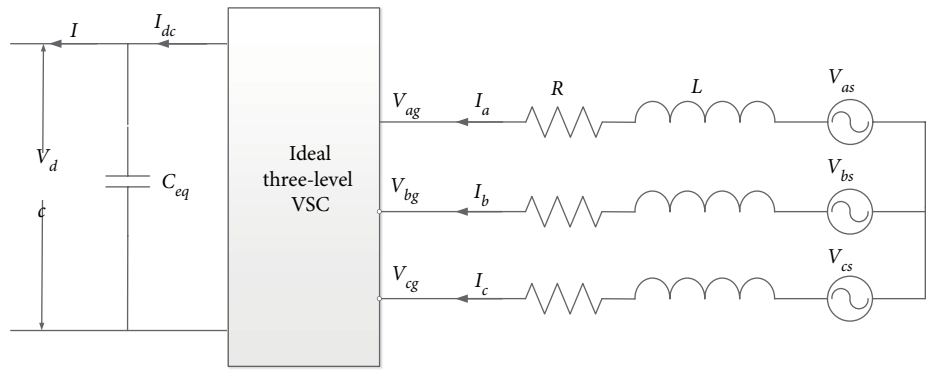

Figure 14: A simplified GSC equivalent circuit.

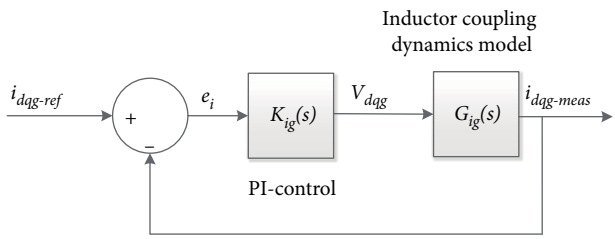

Figure 15: The control structure for the GSC current control (inner loops).

To decouple the dynamics of i_{dg} and i_{qg}, the modulated signals of m_{dg} and m_{qg} are determined as.

$$m_{dg} = \left(\frac{2}{V_{dc}}\right)\left[u_{dg} - \omega_s\left(Li_{qg} + L_m i_{qs}\right)\right], \tag{22}$$

$$m_{dg} = \left(\frac{2}{V_{dc}}\right)\left[u_{dg} - \omega_s\left(Li_{qg} + L_m i_{qs}\right)\right]. \tag{23}$$

Thus, the two new control inputs for the inner current loops are defined in (24) and (25) and supported by feed forward terms predicting V_{dg} and V_{qg}.

$$u_{dg} = L\frac{di_{dg}}{dt} + Ri_{dg}, \tag{24}$$

$$u_{qg} = L\frac{di_{qg}}{dt} + Ri_{qg}. \tag{25}$$

The compensator can be a simple proportional-integral (PI) compensator, $K_{gi}(s)$ to enable tracking of a respective reference signal. The compensator is defined by

$$K_{gi}(s) = \frac{k_p^{gi}s + k_i^{gi}}{s}. \tag{26}$$

Thus, based on the plant function, $G_{gi}(s) = 1/(Ls + R)$ and considering the compensator $K_{gi}(s)$ in (26), the closed-loop desired transfer function becomes

$$\frac{I_{dqg}(s)}{I_{dqg-ref}(s)} = G_{gi}(s) = \frac{1}{\tau_{gi}s + 1}, \tag{27}$$

if and only if $k_p^{gi} = L/\tau_{gi}$ and $k_i^{gi} = R/\tau_{gi}$.

Where k_p^{gi} and k_p^{gi} are proportional and integral gains. The gains are determined and then tuned based on the control stability theory until the better result is achieved. The control loop is illustrated in Figure 15.

The d-axis is, for control design purposes, supposed to be set in phase with the voltage across the resistor, and neglecting the harmonics and losses due to switching in the converter, the active power balance equation is given by:

$$\begin{aligned} V_{dc}I_{dc} &= 1.5v_{dg}i_{dg} = P_r, \\ \because v_{qg} &= 0, \end{aligned} \tag{28}$$

and on the output side, the dc current is

$$I_{dc} = C\frac{dv_{dc}}{dt} + i_L, \tag{29}$$

where V_{dc} and I_{dc} are dc output voltage and current respectively.

Thus, the d-component of the voltages in $d-q$ coordinates becomes v_{dg} and zero that of v_{qg}. So, the active and reactive power equations are deduced by (30) and (31) respectively.

$$P_g = 1.5v_{dg}i_{dg}, \tag{30}$$

$$Q_g = -1.5v_{dg}i_{qg}. \tag{31}$$

These equations prevail that active power is likely controlled by i_{dg} and reactive power by i_{qg}. Based on (32), the real power balance equation on the grid side can be given by:

$$P_g = 1.5v_{dg}i_{qg} = V_{dc}I_{dc}. \tag{32}$$

Equation (32) implies that the active power can be controlled by controlling the DC-bus voltage and in such a way that independently the DC voltage is controlled by controlling the d-axis current i_{dg}. In this controller, for the sake of mathematical formulation, it is supposed to be the DC side of the VSC is connected to an ideal DC voltage source that dictates the DC-bus voltage as shown in Figure 14. Thus, the DC-voltage V_{dc} of the grid port requires proper regulation.

The current controller as described earlier is ensured that the output current tracks the reference values generated by an additional external control loop, which performs the output active power regulation. This power regulation is confirmed by implementing the dc voltage control. The DC link dynamics of Figure 14 is given by

$$C\frac{dv_{dc}}{dt} = \frac{3}{2}\frac{V_{dg}}{V_{dc}}i_{dg} - i_L. \tag{33}$$

The minimum value of required DC side voltage [15] is given by the inverter output voltage as,

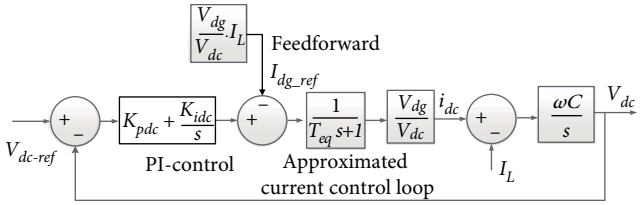

Figure 16: The control structure of the DC voltage control of the DC link in the VSCs.

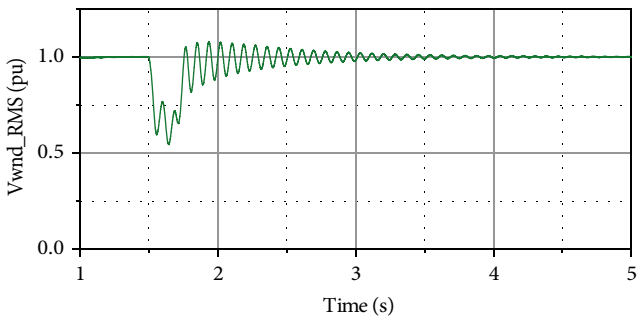

Figure 17: Voltage characteristics on the machine terminal voltage of the wind farm.

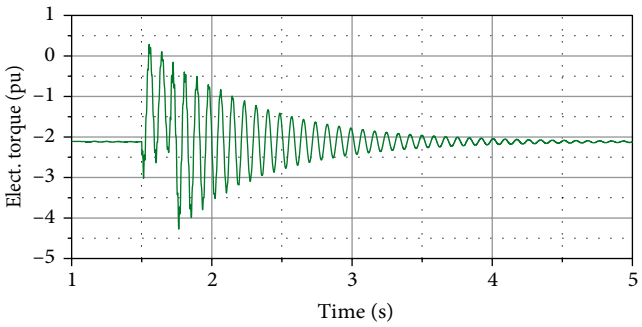

Figure 18: The electrical torque characteristics of the wind farm.

$$V_{dc} = 2\sqrt{\frac{2}{3}}\, V_{LL,rms} = 2V_{peak,ph}. \tag{34}$$

where $V_{peak,ph}$ is peak phase voltage at the ac side and $V_{LL,rms}$ is the line-line *rms* voltage.

Since the DC-link dynamics of (33) is a nonlinear equation, the PI control parameters are to be determined by linearizing the operating point of the system model. For linearization of the system model, the input value V_{dc-ref} is specified as a reference and it yields the transfer function as.

$$\frac{\Delta V_{dc}(s)}{\Delta i_{dg}(s)} = \frac{3}{2}\frac{V_{dg,0}}{V_{dc-\mathrm{ref}}}\frac{1}{sC}. \tag{35}$$

To analyse this control loop, the inner current control closed loop is approximately defined as first order system with time constant T_{eq} which is about to be $2T_a$ [14]. T_a is the time constant of the inner current loop plant function. Thus, the control structure of the DC voltage control is depicted in (Figure 16).

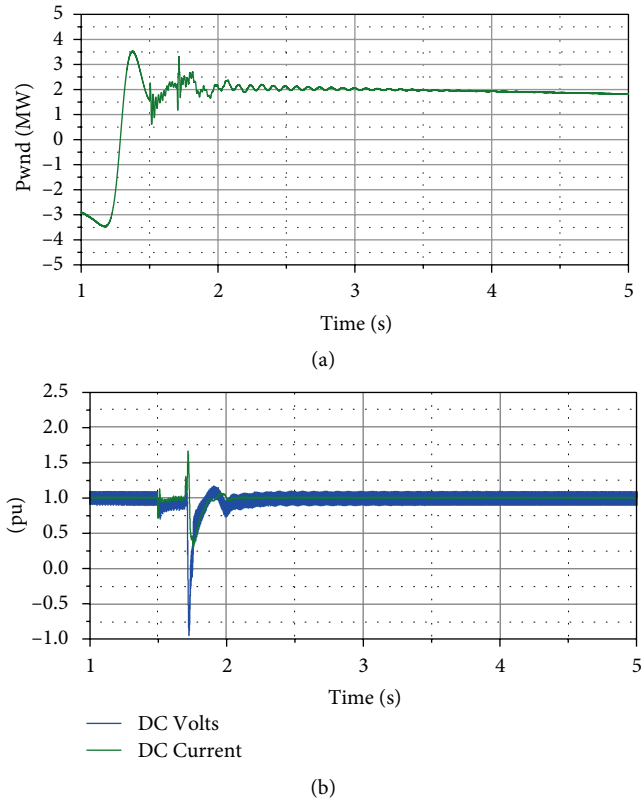

Figure 19: Evolution of the proposed network to demonstrate the SSR effect reduction on. (a) Power flow characteristics in the wind farm. (b) DC voltage and current response in the HVDC.

The capacitor current in dc link is controlled by the DC voltage controller to maintain the power balance between the grid and the converter. Thus, in balanced conditions, $i_c = 0$ and $I_{dc} = I_L$. Hence, the current reference value of I_{dg} should ensure exact compensation for load variation. The complete block diagram of dc-link voltage controller is represented as in Figure 10 as the system equations are analysed in per unit [14], where K_{pdc} and K_{idc} are PI controller parameters, and C is per unit capacitance of DC link.

The load variation can be greatly reduced if feed-forward method is used. Otherwise, to reduce the large error, the large gain of voltage controller which is important from stability viewpoint is not necessarily deployed.

5. Simulation Results and Discussion

Figures 17–19 show the responses of the proposed system and the analysis is compared with the simulated results presented in chapter two. The time duration for the case study is set as the same duration as the above discussion and description shown in Figures 3–5. This is for arguing and verifying the hypothesis of the proposed system.

Figures 17 and 18 show the response of machine terminal voltage and torque characteristics where the SSR model is in effect on the wind farm. Comparing with the responses shown in Figure 5, the oscillations in the torque characteristics are significantly reduced. This is because the control strategy designed on the VSPS is capable of balancing the mismatch

Table 1: The parameters of the VSPS.

Type of the parameter	Unit	Value
Turbine rating	MW	300
Rated hydraulic head	m	165
Piping area	m^2	11.15
Gate opening at no load	pu	0.06
Gate opening at full load	pu	0.94
Generator power capacity	MVA	333
Generator terminal voltage	kV	18
Base value of the power	MVA	333
Base value of the voltage	kV	220
Stator resistance	pu	0.0086
Stator leakage inductance	pu	0.152
Rotor resistance	pu	0.007
Rotor leakage inductance	pu	0.187
Magnetization inductance	pu	300
Inertia constant	Sec.	10.6
Friction coefficient	pu	0.02
Pairs of poles	No.	12
Converter rating	MVA	66
Converter DC-link voltage	kV	38
DC-link equivalent capacitance	mF	20
The coupling inductor resistance	pu	0.0025
The coupling inductor inductance	pu	0.25
The rotor side controller		
Current loop proportional gain	k_p^{ri}	1.25
Current loop integral gain	k_i^{ri}	15
Active power loop proportional gain	k_p^{rp}	1.5
Active power loop integral gain	k_i^{rp}	20
Reactive power loop proportional gain	k_p^{rq}	0.3
Reactive power loop integral gain	k_i^{rq}	5.5
Frequency droop constant	K_f	30
AC voltage droop constant	K_{AC}	60
The grid side controller		
Current loop proportional gain	k_p^{gi}	1.1
Current loop integral gain	k_i^{gi}	9
DC voltage loop proportional gain	K_{pdc}	0.001
DC voltage loop integral gain	K_{idc}	0.02
Grid connecting transformer		
Power capacity	MVA	350
Voltage transformation ratio	unitless	18/363
primary winding resistance	pu	0.0025
Secondary winding resistance	pu	0.0025
Primary winding inductance	pu	0.08
Secondary winding inductance	pu	0.08
Magnetization resistance	pu	500
Magnetization inductance	pu	500

power between the shaft power and electromagnetic power and in turn to reduce the torque oscillations and the regulated electromagnetic power to cancel the effect of shaft torque resonance interaction with series capacitor.

The voltage responses become improved from the oscillations due to SSR. It is the reason that the SSR is compensated by the VSPS reactive power control strategy. The VSPS is capable of generating and absorbing the reactive power and hence regulating the AC voltage oscillations based on the required and given reference voltage value using the AC droop controller.

Additionally, because of the SSR effects on the system frequency and power flow, the effects were elongated on the power flow in to HVDC system. However, due to the SSR reduction by the VSPS with its control strategy, the oscillation effects on the wind farm, HVDC and synchronous hydropower plant are being minimal. These results are shown in Figure 19.

6. Conclusion

This paper presents a study on the mitigation method of SSR in the power system using VSPS plant. This new method is deployed to mitigate the effects of SSR with the implementation of VSPS plant based on the principle of balanced shaft mechanical input power and electromagnetic power of the VSPS. The droop-based direct power control strategy on the bases of dq-coordinate technique is designed. For the sake of implementation, IEEE second benchmark model is used and its effect by simulation with the PSCAD platform discussed. A case of Ningxia power grid area is taken for the realization of the proposed system.

The results show that the proposed VSPS system along with its appropriate control strategy achieves well-regulated power flow and AC voltage so as to reduce the effects of SSR spreading in the power system. Hence, VSPS plant ensures to mitigate SSR which causes instability and security problem in the power grid.

Appendix

Table 1 includes the parameters of the VSPS in the proposed system studied in this paper.

Data Availability

The data used to support the findings of this study are included within the article.

Conflicts of Interest

The authors declare that they have no conflicts of interest.

Funding

This research is supported by the project assigned by State Grid Ningxia Electric Power Co., Ltd.

References

[1] R. Rajaraman and I. Dobson, "Justification of torque per unit velocity methods of analyzing subsynchronous resonance and a swing mode in power systems," *IEEE Transactions on Circuits and Systems I: Fundamental Theory and Applications*, vol. 45, no. 10, pp. 1109–1113, 1998.

[2] N. Johansson, L. Ängquist, and H. P. Nee, "A comparison of different frequency scanning methods for study of

subsynchronous resonance," *IEEE Transactions on Power Systems*, vol. 26, no. 1, pp. 356–363, 2011.

[3] M. Ghafouri, U. Karaagac, H. Karimi, S. Jensen, J. Mahseredjian, and S. O. Faried, "An LQR controller for damping of subsynchronous interaction in DFIG-based wind farms," *IEEE Transactions on Power Systems*, vol. 32, no. 6, pp. 4934–4942, 2017.

[4] C. Zhu, L. Fan, and M. Hu, "Control and analysis of DFIG-based wind turbines in a series compensated network for SSR damping," in *IEEE PES General Meeting, PES*, IEEEProvidence, RI, USA, 2010.

[5] U. Karaagac, S. O. Faried, J. Mahseredjian, and A. A. Edris, "Coordinated control of wind energy conversion systems for mitigating subsynchronous interaction in DFIG-based wind farms," *IEEE Transactions on Smart Grid*, vol. 5, no. 5, pp. 2440–2449, 2014.

[6] X. Xie, X. Zhang, H. Liu, H. Liu, Y. Li, and C. Zhang, "Characteristic analysis of subsynchronous resonance in practical wind farms connected to series-compensated transmissions," *IEEE Transactions on Energy Conversion*, vol. 32, no. 3, pp. 1117–1126, 2017.

[7] L. Yunhong, L. Hui, C. Xiaowei, H. Jing, and Y. Li, "Impact of PMSG on SSR of DFIGs connected to series-compensated lines based on the impedance characteristics," *The Journal of Engineering*, vol. 2017, no. 13, pp. 2184–2187, 2017.

[8] M. Pöller and S. Achilles, "Aggregated wind park models for analyzing power system dynamics," *Wind Engineering*, 2003.

[9] L. M. Fernández, F. Jurado, and J. R. Saenz, "Aggregated dynamic model for wind farms with doubly fed induction generator wind," *Renewable Energy*, vol. 33, no. 1, pp. 129–140, 2008.

[10] N. W. Miller, J. J. Sanchez-Gasca, W. W. Price, and R. W. Delmerico, "Dynamic modeling of GE 1.5 and 3.6 MW wind turbine-generators for stability simulations2003," in *IEEE Power Engineering Society General Meeting (IEEE Cat. No.03CH37491)*, IEEE, Toronto, Ont., Canada, 2004.

[11] R. Piwko, N. Miller, J. Sanchez-Gasca, X. Yuan, R. Dai, and J. Lyons, "Integrating large wind farms into weak power grids with long transmission lines," in *Conference Proceedings – IPEMC 2006: CES/IEEE 5th International Power Electronics and Motion Control Conference*, IEEE, Dalian, China, 2007.

[12] G. Bitew, M. Han, S. Mekonnen, and P. Simiyu, "A variable speed pumped storage system based on droop-fed vector control strategy for grid frequency and AC-bus voltage stability," *Electronics*, vol. 7, no. 7, p. 108, 2018.

[13] U. Nasir, I. Student, and Z. Iqbal, "Active and reactive power control of a variable speed pumped storage system," in *2015 IEEE 15th International Conference on Environment and Electrical Engineering (EEEIC)*, IEEE, pp. 6–11, Rome, Italy, 2015.

[14] T. Jacob, "Pumped storage in Switzerland: outlook beyond 2000," *International Journal on Hydropower and Dams*, 1997.

[15] C. Wei, M. Benosman, and T. Kim, "Online parameter identification for state of power prediction of lithium-ion batteries in electric vehicles using extremum seeking," *International Journal of Control, Automation and Systems*, pp. 1–11, 2019.

[16] F. Cheng, L. Qu, W. Qiao, C. Wei, and L. Hao, "Fault diagnosis of wind turbine gearboxes based on DFIG stator current envelope analysis," *IEEE Transactions on Sustainable Energy*, vol. 10, no. 3, pp. 1044–1053, 2019.

Hindawi
Complexity
Volume 2019, Article ID 6180135, 14 pages
https://doi.org/10.1155/2019/6180135

Research Article

Joint Optimization of Energy Conservation and Migration Cost for Complex Systems in Edge Computing

Xiaolong Xu,[1,2,3] **Yuan Xue**,[1] **Mengmeng Cui**,[1] **Yuan Yuan**,[4] **and Lianyong Qi**[5]

[1]*School of Computer and Software, Nanjing University of Information Science and Technology, Nanjing, China*
[2]*Jiangsu Engineering Center of Network Monitoring, Nanjing University of Information Science and Technology, Nanjing, China*
[3]*Jiangsu Collaborative Innovation Center of Atmospheric Environment and Equipment Technology (CICAEET), Nanjing University of Information Science & Technology, Nanjing, China*
[4]*Department of Computer Science and Engineering, Michigan State University, MI, USA*
[5]*School of Information Science and Engineering, Qufu Normal University, Qufu, China*

Correspondence should be addressed to Lianyong Qi; lianyongqi@gmail.com

Received 5 May 2019; Revised 25 July 2019; Accepted 19 August 2019; Published 4 December 2019

Guest Editor: Xiaoqing Bai

By means of the complex systems, multiple renewable energy sources are integrated to provide energy supply for users. Considering that there are massive services needed to process in complex systems, the mobile services are offloaded from mobile devices to edge servers for efficient implementation. In spite of the benefits of complex systems and edge servers, massive resource requirements for implementing the increasing resource requests decrease the execution efficiency and affect the whole resource usage of edge servers. Therefore, it remains an issue to achieve dynamic scheduling of the computing resources across edge servers. With the consideration of this issue, a Balanced Resource Scheduling Method, named BRSM, for trade-offs between virtual machine (VM) migration cost and energy consumption of VM migrations for edge server management, named BRSM, is designed in this paper. Technically, we analyze the load conditions of edge servers and formulate the energy consumption of VM migrations and VM migration cost as a multi-objective optimization problem. Then, we propose a dynamic resource scheduling method for WMAN to deal with the multi-objective optimization problem. In addition, nondominated sorting genetic algorithm III (NSGA-III) is adopted to generate optimal resource scheduling strategies. Finally, we conduct experiment simulations to testify the efficiency of the proposed method BRSM.

1. Introduction

In recent years, fossil fuels are adopted in most energy systems, which generate a lot of harmful substances and pollute the environment [1, 2]. In order to save fuel and reduce pollution to the environment, renewable energy gradually replaces the fossil energy. Nevertheless, renewable energy is intermittent and difficult to control. For example, provided that the wind stops, wind power generation is difficult to continue. With the intermittent nature of renewable energy, one type of renewable energy cannot meet the balance between supply and demand of current energy systems [3]. Therefore, it is of urgency to develop complex systems that integrate multiple renewable energy sources. Complex systems are systems of intelligent, adaptive subjects with a medium number of actions based on local information, which are defined by attributes like feedback and adaptation. Considering the intermittent nature of renewable energy, a large number of mobile devices are used in complex systems. The mobile devices are arranged to collect real-time environmental parameters to provide reliable references for strategy formulation.

Although the environmental information is valuable, in view of the huge volume of data in complex systems, the resource consumption of mobile devices rises sharply [4]. Constrained by numerous factors such as limited battery life and limited capacity, mobile devices gradually fail to meet the requirements of mobile services and application execution is of less efficiency in local mobile devices. Therefore, it is suitable to offload the computing applications or services to the cloud platform, considering that the resources in the cloud are accessed conveniently [5]. In the cloud platform, physical resources are provided in the form of multiple virtual machines (VMs) and each mobile device corresponds to a cloud clone which is deployed on a VM. Users are able to access the configurable computing resources shared pool in the cloud and use the required cloud clone to perform the offloaded mobile services [6].

Nevertheless, the transmission delay is unneglectable in terms of the long distance between mobile devices and the

remote cloud. Besides, transmitting mobile services to the cloud consumes massive energy in complex systems, violating the concept of green cloud computing [7]. Edge server, which is co-located with access point (AP), is proposed to be a substitute for the cloud. Mobile users access computing resources of edge servers through APs. Compared to the cloud, edge servers are in close proximity with mobile devices, reducing the data transmission delay [8]. Furthermore, the virtualization technology is used in edge computing as well. By means of the virtualization technology, hardware resources in edge servers are decoupled from software and the same type of VM can run in different physical devices [9]. Consequently, mobile software is enabled to execute on multiple hardware, increasing the utilization of hardware resources as well as achieving the energy conservation.

Despite the advantages, the adoption of edge servers in complex systems has several shortcomings. In fact, compared to remote cloud clusters, the computing resources of edge servers are limited. In densely populated areas, as the number of mobile devices increases dramatically, there is a high possibility that a mass of users intends to offload the computation-intensive services or applications to edge servers nearby. Hence, the edge servers need to response the resource requirements from a large number of mobile devices. As edge servers cannot provision sufficient computing resources for abundant services simultaneously, the computing resources of edge servers run out, resulting in the rejection of new service requests [10, 11]. The applications whose requests are rejected are queued in the edge server until the previous application is completed and the needed resources are available again. Especially, provided that the waiting applications are latency-sensitive, unexpected consequences take place and the quality of experience (QoE) for users greatly drops off. Thus, it is necessary to offload the queued service quests to the edge servers with unoccupied computing resources through VM migration.

Apart from the waiting time, energy consumption is a key criterion for resource management in complex systems. With the explosive growth of consumed energy for information and communication technology (ICT), numerous greenhouse gases are emitted into the atmosphere [12]. Thus, energy conservation plays a significant role in the implementation of future wireless communication. Considering that edge computing is of great use in wireless communication, the energy consumption of edge computing is a research hotspot for better communication modes [13]. In complex systems, the energy consumption of computation offloading includes two parts. The first part is the energy used for information transmission across edge servers. With the virtualization technology, the transmission is in the form of VM migrations. That is to say, the first part of energy consumption is the energy consumption of VM migrations. Moreover, the other part is the energy consumption of infrastructures, including the energy caused by data processing in edge servers and the energy caused by sending and receiving data in APs. As the configuration of each edge server is the same and, the energy consumption of data processing is the same for a service. With the consideration of time consumption and energy consumption, it is of utmost significance to develop a strategy to achieve the joint optimization of migration cost and energy consumption.

Table 1: Key terms and descriptions.

Terms	Descriptions
N	The number of edge servers
C	The set of edge servers, $C = \{c_1, c_2, \ldots, c_N\}$
c_n	The n-th edge server in C
φ_n	The capacity of the n-th edge server c_n
Q	The number of APs
W	The set of APs, $W = \{w_1, w_2, \ldots, w_Q\}$
w_q	The q-th AP in W
Z	The number of mobile services
S	The set of mobile services, $S = \{s_1, s_2, \ldots, s_Z\}$
s_z	The n-th mobile service in S
os_z	The occupied start time of s_z
od_z	The duration time of s_z
nv_z	The amount of VMs of s_z
pv_z	The packaged VM to perform s_z

The main contributions of this paper are summarized as follows:

(i) We present the basic concepts and definitions to analyze the VM migration cost and the energy consumption of VM migrations in complex systems.

(ii) We design a Balanced Resource Scheduling Method for trade-offs between VM migration cost and energy consumption of VM migrations for edge server management, named BRSM, to dynamically provision resource management in complex systems by live VM migration technique.

(iii) We adopt nondominated sorting genetic algorithm III (NSGA-III) [14] to bring about the multi-objective optimization. Multi-criteria decision-making (MCDM) and simple additive weighting (SAW) are employed to select the optimal VM migration strategy.

(iv) We conduct simulations to verify the efficiency of our proposed method BRSM.

The remainder of this paper is organized as follows. Section 2 introduces the basic concepts and the completed modeling as well as formulation. Section 3 elaborates the proposed dynamic resource management method. Section 4 shows the comparison analysis of the simulation experiments. Section 5 reviews the related work. Finally, Section 6 outlines the conclusions and future work.

2. System Model and Problem Formulation

In this section, basic concepts and definitions for complex systems in edge computing are introduced. Besides, VM migration cost and energy consumption of VM migrations are also analyzed. Key terms and the descriptions are listed in Table 1.

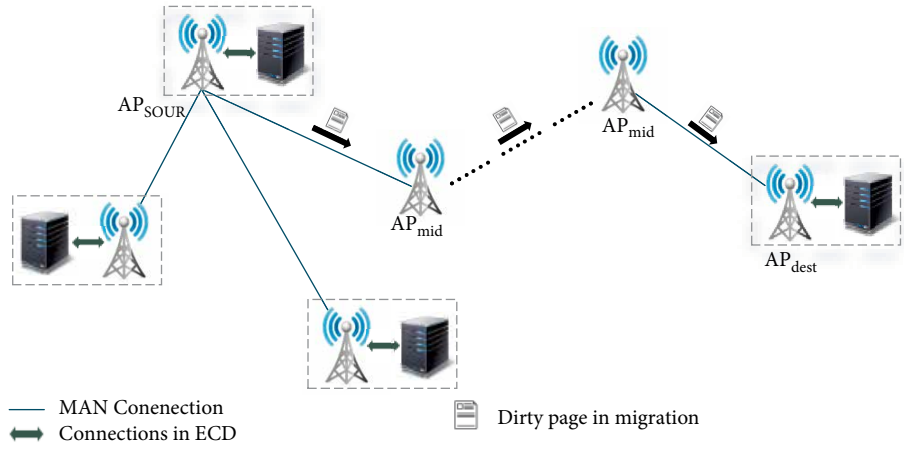

Figure 1: An instance of VM migration in ECD-based complex systems.

2.1. Basic Concepts and Definitions. In complex systems, the experience of mobile users are promoted continuously and edge servers provide computing services which are in close proximity to mobile terminals, increasing the QoE for mobile users. There is an AP which is located with an edge server, forming an edge computing device (ECD). Mobile users are able to access the resources in the edge server through the co-located AP. Assume that there are N edge servers in complex systems, which are denoted as $C = \{c_1, c_2, \ldots, c_N\}$.

Due to the loss of generality, there is a physical machine (PM) in each edge server to provide mobile services. As the virtualized technique plays a critical role in the resource management for infrastructure, it is appropriate to adopt the virtualized technique in complex systems. The physical resources in an edge server are provided in the form of virtual machines (VMs). By means of the virtualized technique, the physical resources in the edge server are abstracted as several resource units, which are known as VM instances, to accommodate mobile services. Aiming to measure the capacity of each edge server, let φ_n be the number of VM instances in the n-th ($n = \{1, 2, \ldots, N\}$) edge server c_n. Considering that there are separate access points, we assume that there are Q access points, denoted as $W = \{w_1, w_2, \ldots, w_Q\}$, and the q-th ($q = \{1, 2, \ldots, Q\}$) access point is denoted as w_q.

The mobile service set offloaded to VMs is denoted as $S = \{s_1, s_2, \ldots, s_Z\}$ and Z represents the number of mobile services. For resource provisioning, the mobile service s_z ($z = \{1, 2, \ldots, Z\}$) in S requires multiple VMs which are in the requirements of desired execution time.

Definition 1 (VM occupation requirement of s_z). A 3-tuple, which is denoted as $r_z = (nv_z, os_z, od_z)$, is used to define the VM occupation requirement of s_z, nv_z, os_z and od_z are the number of VMs of s_z, the occupied start time, the duration time respectively.

To avoid the unnecessary transmission delay, the VMs which host the same mobile service are deployed in the same edge server, decreasing the communication cost.

Definition 2 (packaged VM for s_z). Let pv_z represent the packaged VM for the mobile service s_z. The packaged VM pv_z contains all VMs to host the mobile service s_z, whose number is nv_z.

Figure 1 presents an instance of mobile service offloading in the form of VM migration. The AP which is deployed next to the source edge server is named as $\mathrm{AP}_{\mathrm{sour}}$ and the AP deployed next to the destination edge server is named as $\mathrm{AP}_{\mathrm{dest}}$. There are several APs between the $\mathrm{AP}_{\mathrm{sour}}$ and $\mathrm{AP}_{\mathrm{dest}}$, each of which is named as $\mathrm{AP}_{\mathrm{mid}}$. In a VM migration strategy, the VM image and the dirty pages caused by migrations are transmitted from the $\mathrm{AP}_{\mathrm{sour}}$ to the $\mathrm{AP}_{\mathrm{dest}}$ across $\mathrm{AP}_{\mathrm{mid}}$s.

2.2. Migration Cost Analysis of VM Migrations. Considering that VM migration takes a lot of time and it is not always possible to be done, it is necessary to calculate the cost caused by the VM migrations during the whole execution period $[T_s, T_e]$. The migration cost, which also represents VM downtime, consists of the access time of the log file and the switch time of the VMs [18]. Suppose the transmission times of the memory image is $H_z(t)$ during the migration process of pv_z from c_n to $c_{n'}$.

At the time instant t, $F_z^n(t)$ is a binary variable to judge whether pv_z is deployed on c_n, which is defined by

$$F_z^n(t) = \begin{cases} 1, & \text{if } pv_z \text{ is deployed on } c_n, \\ 0, & \text{otherwise.} \end{cases} \tag{1}$$

$P_z^{n,n'}(t)$ is a binary variable to judge whether pv_z is migrated from c_n to $c_{n'}$, which is defined by

$$P_z^{n,n'}(t) = \begin{cases} 1, & \text{if } pv_z \text{ is migrated from } c_n \text{ to } c_{n'}, \\ 0, & \text{otherwise.} \end{cases} \tag{2}$$

When the dirty page transfers at $h_z(t)$ time, let $AT_z^{h_z}(t)$ be the access time of all log files which contains $T_{edge}^{h_z}(t)$ and $T_{mid}^{h_z}(t)$ [18]. When pv_z needs to be migrated between the edge server and the AP which is located next to the edge server, the time consumption is defined as

$$T_{edge}^{h_z}(t) = \sum_{z=1}^{Z} \sum_{n'=1}^{N} F_z^n(t) \cdot P_z^{n,n'}(t) \cdot \frac{S_z^{h_z}(t)}{\phi}, \tag{3}$$

where $S_z^{h_z}(t)$ is the size of dirty page produced by the migration of pv_z at $h_z(t)$ time, and ϕ is the bandwidth between the edge server and its corresponding AP.

Suppose $I_{n,n'}$ is the total number of APs between c_n and $c_{n'}$, including a AP_{sour}, a AP_{dest} and several AP_{mid}s. The AP_{sour} is located next to c_n and the AP_{dest} is located next to $c_{n'}$. Thus, the time consumption caused by the migration of pv_z from AP_{sour} to AP_{dest} is calculated by

$$T_{mid}^{h_z}(t) = \sum_{z=1}^{Z}\sum_{n'=1}^{N} F_z^n(t)\cdot P_z^{n,n'}(t)\cdot \frac{S_z^{h_z}(t)}{\lambda}\cdot\left(I_{n,n'}-1\right), \quad (4)$$

where λ is the bandwidth between APs.

The process of VM migration is divided to into multiple rounds. In the first round, the VM image would be sent to the destination PM while after that the dirty page produced in the previous round is sent to the destination PM in each subsequent round. Therefore, the size of dirty page is calculated by

$$S_z^{h_z}(t) = \begin{cases} M_z(t), & \text{if } h = 0, \\ R_z(t)\cdot\left(2T_{edge}^{h_z-1}(t) + T_{mid}^{h_z-1}(t)\right), & \text{otherwise}, \end{cases} \quad (5)$$

where $M_z(t)$ refers to the size of the image memory of pv_z and $R_z(t)$ is the producing rate of the dirty page.

The switch time of pv_z in the migration operation is calculated by

$$OT_z(t) = \sum_{z=1}^{Z}\sum_{n'=1}^{N} F_z^n(t)\cdot P_z^{n,n'}(t)\cdot 2\zeta_z(t), \quad (6)$$

where $\zeta_z(t)$ represents the switch time of the packaged VM pv_z.

Definition 3 (migration cost of a packaged VM inc_n). The migration cost represents the time consumption of a VM migration. When pv_z is migrated from c_n to $c_{n'}$, the migration cost is calculated by

$$d_n(t) = 2T_{edge}^{h_z}(t) + T_{mid}^{h_z}(t) + OT_z(t). \quad (7)$$

The average migration cost is calculated by

$$d(t) = \frac{1}{Z}\sum_{n=1}^{N}\left(2T_{edge}^{h_z}(t) + T_{mid}^{h_z}(t) + OT_z(t)\right). \quad (8)$$

During the whole execution period $[T_s, T_e]$, the migration cost is calculated by

$$D = \frac{1}{T_e - T_s}\int_{T_s}^{T_e} d(t)dt. \quad (9)$$

2.3. Energy Consumption Analysis of VM Migrations. Apart from the VM migration cost, we consider the energy consumption in complex systems during the whole execution period $[T_s, T_e]$. Generally, we calculate the energy consumption of edge servers and APs. With the adoption of virtualized technique, the energy consumption of edge servers mainly includes the energy consumption of VMs in edge servers. Considering that each edge server configuration is the same, the energy consumption of data processing is the same for a service whatever the offloading strategy is. Therefore, the energy consumption of data processing is not calculated in this paper.

Input: A, t, c_n
Output: $is_{t,n}$
$is_{t,n} = \varphi_n$
for $m = 1$ to M **do**
  if $ac_m == c_n$ **then**
    if $t >= as_m$ **then**
      $ft_z = as_m + ad_m$
      if $t < ft_z$ **then**
        $is_{t,n} = is_{t,n} - 1$
      end if
    end if
  end if
end for
Return $is_{t,n}$

Algorithm 1: Edge server idle space acquisition

At the time instant t, the energy consumption of running VMs in edge servers is calculated by

$$E_{active}(t) = \sum_{n=1}^{N}\sum_{z=1}^{Z} F_z^n(t)\cdot nv_z\cdot od_z\cdot\alpha_z, \quad (10)$$

where α_z is the energy consumption rate of each running VM.

The edge server keeps running until all VMs in this edge server have finished the hosted tasks. Therefore, the running time of the n-th edge server c_n is calculated by

$$t_n(t) = \max_{z=1}^{Z}\left\{F_z^n(t)\cdot od_z\right\}. \quad (11)$$

The energy consumption of idle VMs in edge servers is calculated by

$$\begin{aligned} E_{idle}(t) = {} & \sum_{n=1}^{N}\sum_{z=1}^{Z} F_z^n(t)\cdot nv_z\cdot\left(t_n(t) - od_z\right)\cdot\beta_z \\ & + \left(\varphi_n - F_z^n(t)\cdot nv_z\right)\cdot t_n(t)\cdot\beta_z, \end{aligned} \quad (12)$$

where β_z is the energy consumption rate of VMs in idle mode.

The basic energy consumption of edge servers is calculated by

$$E_{base}(t) = \sum_{n=1}^{N}\gamma_n\cdot t_n(t), \quad (13)$$

where γ_n is the basic energy consumption rate of c_n.

During the VM migrations, APs frequently receive and send data, contributing to the energy consumption in complex systems. The energy consumption rate of w_q is calculated by

$$\rho_q(t) = b_q + tm_q\cdot tc_q\cdot\sum_{p\in W}\frac{td_q}{lr_{pq}}, \quad (14)$$

where b_q, tm_q, tc_q, td_q, lr_q respectively represents the baseline power of w_q, the signal transmission power factor of w_q, the signal transceiver power factor of w_q, the traffic demand of w_q and the link rate between w_q and w_p.

Based on the energy consumption rate of APs, the energy consumption of APs is calculated by

$$E_{AP}(t) = \sum_{q=1}^{Q} \rho_q(t). \tag{15}$$

Besides, the energy consumption of the switch operation of VMs is calculated by

$$E_{switch}(t) = \sum_{z=1}^{Z} \sum_{n=1}^{N} \sum_{n'=1}^{N} 2\xi_z(t) \cdot F_z^n(t) \cdot P_z^{n,n'}(t) \cdot \alpha_z. \tag{16}$$

Definition 4 (energy consumption of VM migrations). The energy consumption of VM represents the consumed amount of energy after a VM migration. The total energy consumption is calculated by

$$E_{all}(t) = E_{active}(t) + E_{idle}(t) + E_{base}(t) + E_{AP}(t) + E_{switch}(t). \tag{17}$$

During the whole execution period $[T_s, T_e]$, the energy consumption is calculated by

$$E = \frac{1}{T_e - T_s} \int_{T_s}^{T_e} E_{all}(t)dt. \tag{18}$$

2.4. Problem Definition. From the foregoing, the migration cost of VMs and the energy consumption of VM migrations are analyzed and quantified. In this paper, we aim to achieve the goal of minimizing the migration cost presented in (9) and reducing the energy consumption presented in (18) while meeting the capacity constraints of ECDs. The problem is formulated by

$$\min\ D,\ \min\ E. \tag{19}$$

$$s.t.\ \sum_{z=1}^{Z} pv_z \cdot nv_z \cdot F_z^n(t) \le \varphi_n. \tag{20}$$

3. BRSM: A Balanced Resource Scheduling Method

In this section, the occupation conditions of edge servers are detected and updated during the dynamic resource scheduling process. Then NSGA-III is adopted to generate resource scheduling strategies to select. Finally, SAW and MCDM are employed to evaluate the resource scheduling strategies and select the appropriate resource scheduling strategy.

3.1. Edge Server Status Detecting and Updating. As the formulation of the resource scheduling strategies largely depends on the load of edge servers, it is necessary to detect the resource usage of each edge server. In this section, the analysis of the allocation record is utilized to preserve the resource usage of edge servers. Assume that there are M allocation records during the execution period, which are denoted as $A = \{a_1, a_2, \ldots, a_M\}$.

Input: t, s_m, dc, dv
Output: A
1: $x = -1$, $ft = 0$
2: for $m = 1$ to $|A|$ **do**
// Migrating a VM to a destination VM
3: **if** $ae_m == s_z$ **then**
4: **if** $t >= as_m$ && $t < as_m + ad_m$ **then**
5: $x = m$, $ft = as_m + ad_m$
6: $ad_m = t - as_m$
7: Update a_m according with ad_m
8: **end if**
9: **end if**
10: end for
11: $M = |A| + 1$
12: $ae_M = ae_x$, $ac_M = dc$, $av_M = dv$, $as_M = t$, $ad_M = ft - t$
13: Generate the record a_M
14: Add a_M to A
15: Return A

Algorithm 2: Allocation record updating.

Definition 5 (allocation record a_m). The m-th ($m = \{1, 2, \ldots, M\}$) allocation record, which is denoted as $a_m = (ae_m, ac_m, av_m, as_m, ad_m)$, preserves the distribution for the packaged VM. In the m-th allocation record, ae_m, ac_m, av_m, as_m and ad_m represent the allocated mobile service, the occupied edge server, the employed VM, the requested start time and the duration time respectively.

According to the number of VM instances for a mobile service, the same number of allocation records are generated. By means of the allocation records, the idle space of each edge server is presented dynamically, considering that the allocation record combines the elapsed time of an edge server.

Algorithm 1 specifies the key idea for edge server idle space acquisition. Through identifying the occupied VM instances, the key idea is to acquire the number of idle VM instances. We input the allocation record collection A, the scheduling instant t and the edge server c_n. The output is the spare space $is_{t,n}$ for the edge server c_n at t.

On the other hand, since the mobile services are offloaded almost continuously, the load distribution of the edge servers changes dynamically. Therefore, migrating the VMs from the overload edge servers to the underload edge servers is urgent.

Due to the real holding time of VMs, when a VM is migrated from one edge server to another, the original allocation record needs to be updated and revised. Moreover, the migration leads to a generation of new allocation records for the referred VM instance. In this new allocation record, the migration time is the start occupation time while the duration time is determined by the rest hosting time of the mobile service.

In Algorithm 2, the allocation record updating is specified. We input the scheduling instant t, the processed objective edge server s_m, the destination edge server dc and the destination VM dv. The output is the updated allocation record

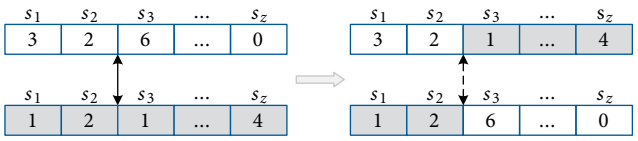

Figure 2: An instance of crossover operation.

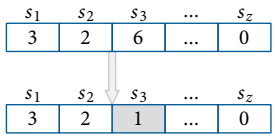

Figure 3: An instance of mutation operation.

collection A. At the migration instant t, the allocation record is updated for the objective mobile service s_z (Lines 1–10). Besides, a new allocation record with the VM instance d_v is produced at the destination edge server d_c and the new allocation record is added to the allocation record collection A (Lines 11–16).

3.2. Resource Scheduling Method Using NSGA-III. As the VM instances are migrated from the overload edge server to the underload edge server, the resource scheduling problem is defined as a multi-objective optimization problem to minimize the VM migration cost and the energy consumption of VM migrations. Compared with traditional genetic algorithms, NSGA-III reduces the complexity of the noninferior sorting genetic algorithm and expands the sampling space, thus greatly improving the convergence speed [14]. Considering that NSGA-III solves multi-objective optimization problem efficiently, NSGA-III is employed to solve the optimization problem.

3.2.1. Encoding. In this subsection, each packaged VM has a scheduling strategy and we encode for the VM scheduling strategies. In the genetic algorithm (GA), a gene represents a migration strategy of a packaged VM and a chromosome, which is composed of a set of genes, represents a hybrid migration strategy of VMs in the same schedule. The destination edge server of VM migrations is encoded, depending on the edge server set $C = \{c_1, c_2, \ldots, c_N\}$.

3.2.2. Fitness Functions and Constraints. A chromosome represents the offloading strategies of all packaged VMs which are in the same schedule. In the population, each chromosome confirms a solution in the aspect of the resource allocation optimization problem. Therefore, fitness functions emerge as standards to measure the superiority of possible solutions. In this paper, the fitness functions include two categories: the VM migration cost and the energy consumption of VM migrations, presented respectively in (9) and (18). As shown in (19) and (20), the design intent of the method is to select an appropriate resource allocation strategy for trade-offs between the two fitness functions as well as satisfying the potential constraints. With efficiency and effectiveness, NSGA-III is adopted to solve the optimization problem while satisfying the constraints simultaneously.

3.2.3. Initialization. In the initialization, the parameters of GA are firstly determined, including the population size H, the maximum times of iteration I, the probability of crossover P_c and the probability of mutation P_m.

In GA, each chromosome represents the computation offloading strategies of the services or VMs in the same schedule. Besides, the offloading strategy of the z-th mobile service in the h-th chromosome is denoted as $c_{h,z}$ and the h-th chromosome is represented as $C_{h,i} = (c_{h,1}, c_{h,2}, \ldots, c_{h,Z})(h = 1, 2, \ldots, H)$.

3.2.4. Crossover and Mutation. The crossover operation, which combines two chromosomes, is the single-point crossover in this paper. Figure 2 shows the crossover operation for two chromosomes in one schedule. In this instance, we select a crossover point and swap the genes which are around the selected crossover point. In particular, the crossover operation starts at s_3 and the swap creates two new chromosomes.

Aiming to enhance the fitness values, the mutation operation is taken to modify genes to create new chromosomes. Each gene has the same probability of being modified. Figure 3 illustrates an instance of the mutation operation. In this instance, the code of s_3 is mutated from 6 to 1.

3.2.5. Selection Operation for the Next Generation. For better solutions, the individuals are selected to generate the next population in this subsection. After the operation of crossover and mutation, the size of population is $2H$. The migration cost and the energy consumption of each scheduling strategy are calculated respectively to judge whether the scheduling strategy is optimal. According to fitness values, the scheduling strategies, which are also known as solutions, are sorted by the usual domination principle. Therefore, the nondominated fronts are successfully generated.

As the preparation is completed, the selection operation of chromosomes is conducted. Each time one solution is selected from the highest nondominated front until there are H selected solutions. We define that the last added solution is in the u-th nondominated front. Provided that all of the solutions in the u-th nondominated front are selected, the selection operation finfishes and the H selected solutions form the next generation. This kind of selection is called primary selection.

Whereas in reality, all solutions in the u-th nondominated front are not be selected. As the solutions in the u-th nondominated front are not all included, further selection needs to be conducted. Consider the number of selected solutions in the u-th nondominated front is w. We need a series of operations to ensure that the selected w solutions are better. This kind of selection is called further selection.

First, we normalize the $2Z$ fitness values of individuals in the population. We search the minimum values of the VM migration cost and the energy consumption, which are denoted as D_m and E_m. Thus, the fitness values for the solutions are updated as

$$D' = D - D_m, \tag{21}$$

$$E' = E - E_m. \tag{22}$$

Input: P_t, R
Output: P_{t+1}
1: Q_t =Crossover and mutation (P_t)
2: $R_t = P_t \cup Q_t$
3: for the solutions in R_t **do**
4: Calculate B by formula (8)
5: Calculate D by formula (16)
6: end for
7: for the $2H$ solutions in R_t **do**
8: Non-dominant sorting the solutions
9: end for
10: Do primary selection
11: if partial solutions in the u-th front are included **do**
12: Do further selection
13: Normalize solutions by formulas (19)–(24)
14: Generate the reference points
15: Associate solutions with the closest reference points
16: Do the selection of w solutions
17: end if
18: return P_{t+1}

Algorithm 3: Selecting using NSGA-III.

Based on the fitness values, the extreme values of the VM migration cost and the energy consumption of VM migrations, which are denoted as EV_D and EV_E, are calculated by

$$EV_D = \max \frac{D'}{W_D}, \tag{23}$$

$$EV_E = \max \frac{E'}{W_E}, \tag{24}$$

where W_B and W_D is the weight vector of the two fitness functions respectively.

We use each fitness function as a measure of an axis. In the hyperplane, the intercept of each axis is calculated respectively. The $2Z$ fitness values of individuals in the population are normalized as

$$D'' = \frac{D'}{EV_D}, \tag{25}$$

$$E'' = \frac{E'}{EV_E}. \tag{26}$$

After the normalization process, the two fitness values are put in the domain [0, 1). Then the distributed reference points are connected with selected solutions, which improves the diversity of solutions. With the normalization, the intercept of each axis is 1 and each axis is divided into k parts. Besides, the number of the reference points is denoted as χ. To ensure that every solution is associated with a reference point, χ is approximately equal to the number of solutions H, which is calculated by

$$\chi = \binom{2Z + k - 1}{k}. \tag{27}$$

According to the number of reference points that each solution associates with, the solutions in the u-th nondominated front are sorted and one of the solutions is randomly selected. This process repeats until w solutions are selected.

Algorithm 3 represents the selection operation for the next generation. In this algorithm, we input the t-th generation population P_t and a set of reference point R while the output is the $(t + 1)$-th generation population P_{t+1}. In each iteration, the fitness values of every solution are calculated (Lines 1–4). With the operation of crossover and mutation, there are $2H$ solutions to be chosen (Lines 5–6). Then the $2H$ solutions are sorted according to the nondominated principle (Lines 7–9). Finally, by means of the reference points, H solutions are selected as the next generation (Lines 10–17). The process of Algorithm3 would repeat until the maximum iteration.

3.3. Scheduling Strategy Based on SAW and MCDM. In a population, there are H chromosomes which are also called solutions. Each chromosome represents a feasible hybrid scheduling strategy. For the chromosomes, our designed method is to achieve the trade-offs between reducing the VM migration cost as well as optimizing the energy consumption of VM migrations. For the generated solutions, SAW and MCDM are employed to select the relatively optimal solutions.

As the criterions are divided into positive criterions and negative criterions, the migration cost is a negative criterion, which means that the lower the migration cost is, the better the solution is. Similarly, the energy consumption is also a negative criterion.

The migration cost is normalized as

$$V(D) = \begin{cases} \dfrac{D^{\max} - D}{D^{\max} - D^{\min}}, & D^{\max} - D^{\min} \neq 0, \\ 1, & D^{\max} - D^{\min} = 0, \end{cases} \tag{28}$$

where $D^{\max}$ and $D^{\min}$ represent the maximum and minimum of the migration cost in the population respectively. Moreover, the energy consumption is normalized as

$$V(E) = \begin{cases} \dfrac{E^{\max} - E}{E^{\max} - E^{\min}}, & E^{\max} - E^{\min} \neq 0, \\ 1, & E^{\max} - E^{\min} = 0, \end{cases} \tag{29}$$

where $E^{\max}$ and $E^{\min}$ represent the maximum and minimum of the energy consumption in the population respectively.

There is no feasible way how to minimize both latency and energy at the same time, it is rather a trade-off between these two objectives. Consequently, each of the two objectives is given a weight. Through different values of the two weights, the impact of each objective on the offloading strategy changes accordingly and the trade-off can be realized. Let μ_1, μ_2 be the weight of the migration cost and the energy consumption respectively. For the comprehensive utility values evaluation of the solutions, the optimization of the VM migration cost

and energy consumption of VM migrations are both taken into consideration. Since the two objectives have the same degree of influence on the selection of the offloading strategy, the weights of the fitness function are set equal in this paper. Therefore, the utility value of the h-th solution is calculated by

$$V(C_h) = \mu_1 V(D) + \mu_2 V(E) \quad (\mu_1 = \mu_2 = 0.5). \tag{30}$$

Based on the utility value of the h-th solution, the optimal solution, which is denoted as $V(C)$, is calculated by

$$V(C) = \max_{h=1}^{H} V(C_h) \quad (1 \le h \le H). \tag{31}$$

At this point, the optimal solutions with maximum utility value have been selected from the population.

3.4. Method Overview. In this paper, we aim to minimize the migration cost and the energy consumption of each service offloading strategy. The resource scheduling problem is quantified as a multi-objective optimization problem. NSGA-III is utilized to generate the resource scheduling strategies. First, we specify the real-time conditions of edge servers and build the resource allocation record collection. Then the randomly generated resource scheduling strategies are encoded. Besides, the fitness functions and potential constraints are proposed to judge each solution. In order to generate new solutions, the operation of crossover and mutation are taken, leading to a total of $2H$ solutions. For the next generation, the usual domination principle and the reference points are used to select the relatively appropriate H solutions. Finally, in spite of SAW and MCDM, the optimal solutions are selected from the population.

Algorithm 4 shows the overview of the proposed method BRSM. The input includes the initialized population X, the allocation record set A and the maximum iteration times I. The output is the new allocation record set A. In this algorithm, we first update the running mobile service collection S and obtain the spare space of edge servers (Lines 3–6). Then we formulate the initial resource scheduling strategies randomly and conduct crossover and mutation operation to generate $2H$ solutions (Line 9). Aiming to select the appropriate H solutions, we calculate the fitness functions for each solution and do the selection operation according to Algorithm 3 (Lines 10–13). This process would repeat until the number of iterations reached I. Based on the utility value of each solution, the alternative solutions are sorted and we select the optimal solution which has the highest utility value (Lines 16–20). The flow chart of selecting the optimal strategy is shown in Figure 4. Finally, the resource allocation records are updated and output (Line 21).

4. Experimental Results and Analysis

In this section, simulations and experiments are conducted to evaluate the performance of the proposed method BRSM. First, the parameter settings are introduced. Then, the performance evaluation on BRSM is presented.

Input: X, A, I, S
Output: A
1: $t = T_s$
2: While $t < T_e$ **do**
3: Update the running mobile service collection S
4: **for** $n = 1$ to N **do**
5: Obtain $is_{t,n}$ by Algorithm 1
6: **end for**
7: i = 1
8: **While** i≤I **do**
9: Conduct crossover and mutation
10: **for** the solutions in X **do**
11: Calculate fitness values
12: **end for**
13: Conduct selection by Algorithm 3
14: i = i+1
15: **end while**
16: **for** $h = 1$ to H **do**
17: Calculate utility values by formulas (26)–(28)
18: **end for**
19: Sort the solutions according to the utility values
20: Select the optimal strategy by formula (29)
21: Update A by Algorithm 2
22: end while
23: return A

Algorithm 4: Balanced resource scheduling method ***BRSM.***

4.1. Simulation Setup. In the experiment, we select LENOVO TS250 as the edge server, which consists Intel Xeon-E3-1225V6, Quad-Processor clocked at 3.4 GHz and 4 GB of RAM. To conduct the experiment evaluation, 5 datasets of different scales are generated, whose number of mobile services are 1000, 2000, 3000, 4000, 5000 respectively. Additionally, the concrete parameter settings in the experiment are presented in Table 2 [18]. Specifically, datasets can be downloaded at https://pan.baidu.com/s/1coXNu8B5_YdXAWTBJSn6uQ.

The VM migration cost and the energy consumption of VM migrations are the two criteria to judge whether the method BRSM is efficient. Aiming to represent the superiority of BRSM intuitively, we adopt comparative methods to conduct the experiment evaluation. The comparative methods are specifically described as follows.

(i) *First Fit (FF).* In the order of starting addresses of edge servers, the resources in each edge server are checked and the mobile services are respectively assigned to the first edge server encountered with enough resources.

(ii) *Best Fit (BF).* The mobile services are offloaded to the edge server with enough resources respectively while the destination edge server has the least resources among all edge servers.

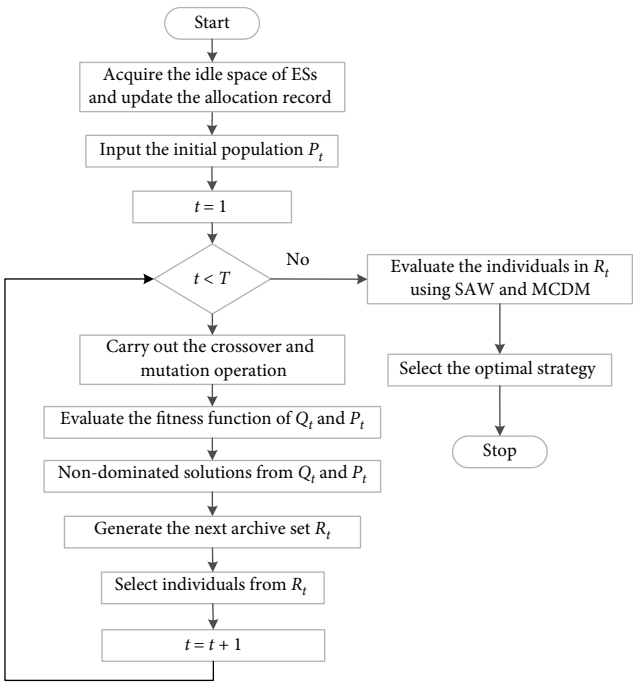

Figure 4: The flow chart of selecting the optimal strategy.

Table 2: Parameter settings.

Parameter description	Value
The number of VMs in each edge server	11
The number of running VMs in each edge server	[1, 7]
The transmission rate between Aps	540 Mb/s
The transmission rate between AP and edge server	1200 Mb/s
The duration time of VM	[1, 3]
The transmission data of VM (G)	[0.5, 0.8]

(iii) *First Fit Decreasing (FFD).* The mobile services are sorted in descending order according to the amount of required resources. Then the first mobile service is offloaded to the first edge server encountered with enough resources. This procedure continues until all mobile services are offloaded to edge servers.

(iv) *Best Fit Decreasing (BFD).* The mobile services are sorted in descending order according to the amount of required resources. Then the first mobile service is offloaded to the edge server which has the least resources among all edge servers but enough for the mobile service. This procedure is repeated until all mobile services are offloaded to edge servers.

4.2. Performance Evaluation of BRSM. In this section, we evaluate the number of employed edge servers, the resource utilization of edge servers, the VM migration cost and the energy consumption of VM migrations. The corresponding evaluation results are shown as follows.

4.2.1. Evaluation on the Utility Value of the Solutions. In the five sub-figures in Figure 5, the comparison of the utility value of solutions at different mobile service scales is presented. As can be seen from the figures, regardless of the number of mobile services, there are always 3 solutions generated by BRSM. Among the generated solutions, the most balanced service offloading strategy is acquired, depending on the utility value in (30). The service offloading strategy with maximum utility value is selected as the most optimal offloading strategy. For instance, in Figure 4(a), the final service offloading strategy is solution 2 as it has the highest utility value.

4.2.2. Evaluation on the Amount of Employed Edge Servers. In the edge server-based WMAN, the number of employed edge servers is a key factor to measure the resource utilization of edge servers. Therefore, it is necessary to evaluate the number of employed edge servers. Given the 5 different scale datasets employed in FF, BF, FFD, BFD, and BRSM, the number of employed edge servers differs from each other after VM migrations, which is illustrated in Figure 6. In Figure 6, it is obvious that FF and BF utilize the same number of edge servers. FFD as well as BFD also utilizes the same number of edge servers. However, BRSM employs fewer edge servers than the other four methods.

4.2.3. Evaluation on Resource Utilization. Resource utilization of edge servers is of great significance, which is calculated by virtue of the number of running VMs in each edge server. High resource utilization represents the rational utilization of resources.

In Figure 7, the comparison of average resource utilization by FF, BF, FFD, BFD, and BRSM is presented. FF and BF have the same resource utilization, while FFD and BFD likewise achieve the same utilization. Distinctly, compared with FF, BF, FFD and BFD, BRSM has the highest resource utilization value, proving the superiority of the proposed method BRSM in the respect of resource utilization.

In the process of dynamic VM migrations, the resource utilization of edge servers, which changes with time instants, is taken into consideration. To monitor resource usage in real time, we track the resource utilization of edge servers when there are 5000 mobile services during the execution period. Figure 8 illustrates the comparison of real-time resource utilization by FF, BF, FFD, BFD, and BRSM. According to the analysis, the resource utilization of edge servers exceeds 80% during the execution period. Besides, BRSM achieves better resource utilization than FF, BF, FFD, and BFD in almost every instant, guaranteeing the good performance of BRSM.

4.2.4. Evaluation on Migration Cost. The migration cost represents the time consumption of VM migrations across edge servers. However, the migration cost is divided into two parts, which are the cost between AP and edge server as well as the cost between APs.

Moreover, the transmission time of dirty pages caused by last round of data transmission is considered. Figure 9 shows the comparison of migration cost by FF, BF, FFD, BFD, and BRSM, using 5 different scales datasets. It is intuitive that FF and BF own the same migration cost while FFD and BFD also own the same migration cost. Nevertheless, our proposed

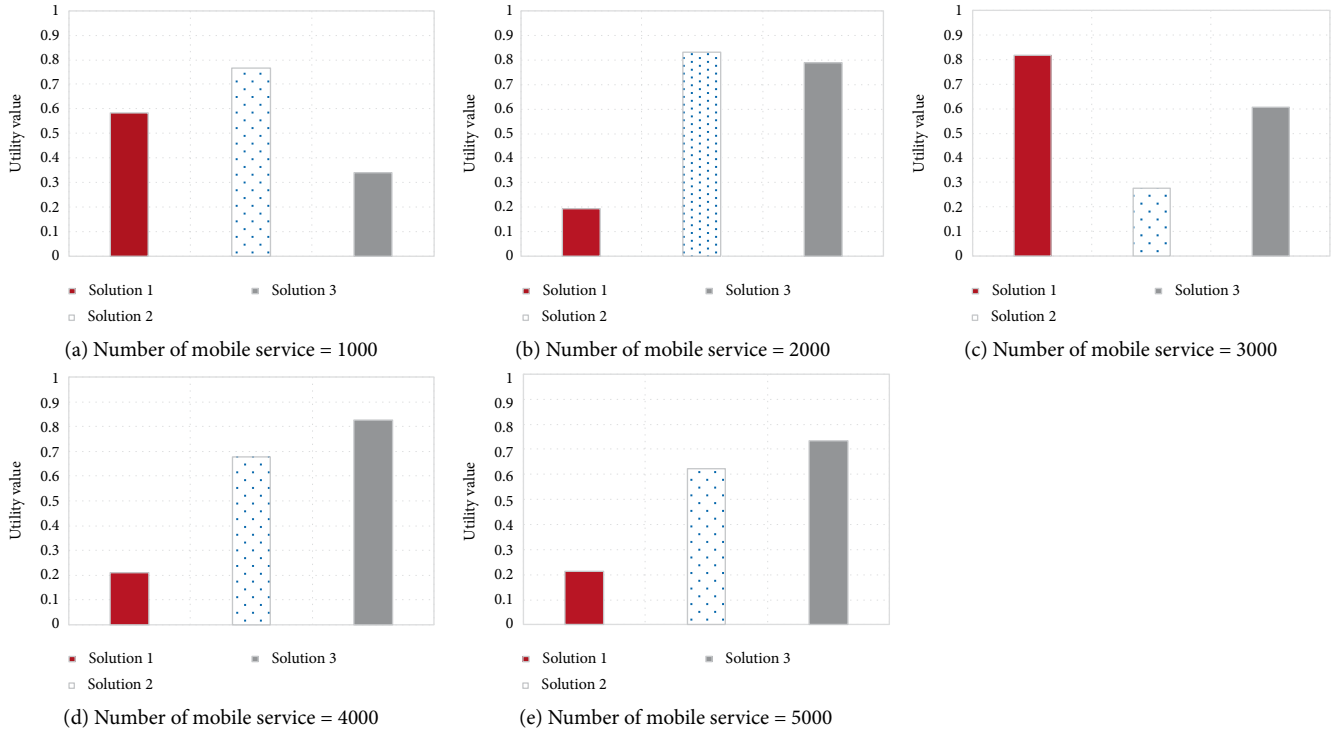

(a) Number of mobile service = 1000

(b) Number of mobile service = 2000

(c) Number of mobile service = 3000

(d) Number of mobile service = 4000

(e) Number of mobile service = 5000

Figure 5: Comparison of the utility value of solutions at different mobile service scales.

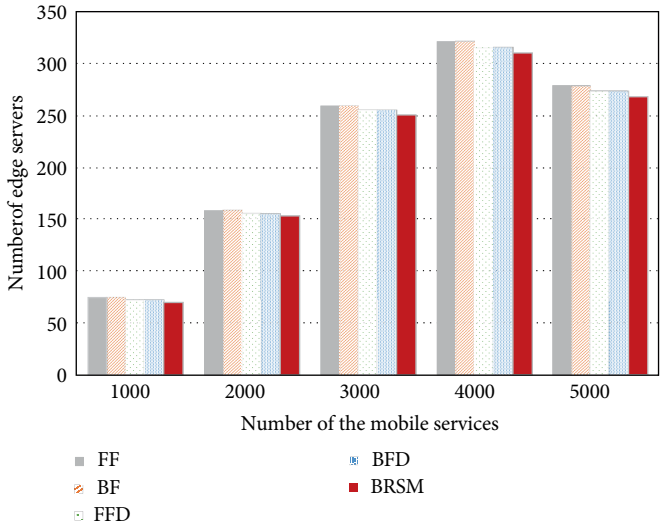

Figure 6: Comparison of the number of employed edge servers by FF, BF, FFD, BFD and BRSM.

method BRSM has the least migration cost when compared with the other 4 methods.

4.2.5. Evaluation on Energy Consumption. As mentioned in section 2, the energy consumption of VM migrations is an important criterion to judge whether the offloading situation of the offloading strategy is suitable. The lower the energy consumption is, the more efficient the offloading strategy becomes. Thus, the energy consumption of FF, BF, FFD, BFD, and BRSM are compared in Figure 10. Under the different scales of mobile services, the energy consumption of VM migrations are different. It is obvious that FF and BF has the same energy consumption during the VM migrations, and FFD, as well as BFD, also has the same energy consumption. Moreover, the energy consumption of BRSM is lower than the energy consumption of FF, BF, FFD, and BFD, which draws the conclusion that BRSM achieves better energy conservation than the 4 comparative methods.

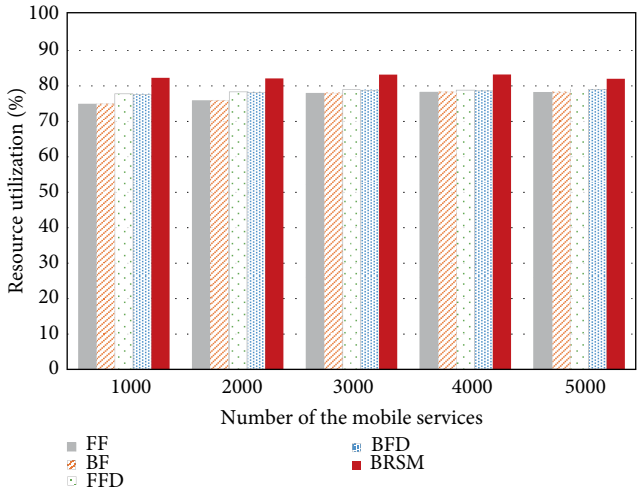

Figure 7: Comparison of the average resource utilization of edge servers by FF, BF, FFD, BFD and BRSM.

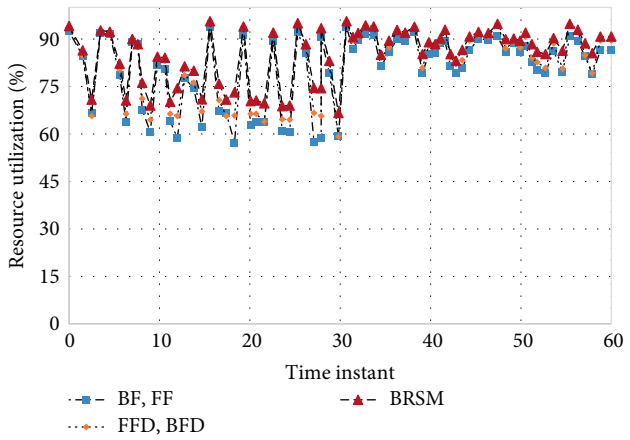

Figure 8: Comparison of real-time resource utilization of 5000 mobile services by FF, BF, FFD, BFD and BRSM.

5. Related Work

With the adoption of fossil fuels, various problems such as air pollution and rapid resource consumption have aroused, jeopardizing the sustainable development of environment [1, 15]. To improve the environment, renewable energy is used as a substitute for fossil fuels [15, 16]. However, the supply of renewable energy depends on many uncontrollable natural factors, which is intermittent. Consequently, complex systems are utilized to integrate kinds of renewable energy to achieve continuous supply of stable energy [17, 18]. With the large-scale data in complex systems, cloud computing emerges as an applied paradigm [19, 20]. The mobile devices transmit the data to the cloud platform while the long distance between mobile devices and the cloud leads to unneglectable transmission delay. Thus, the data are transmitted to the edge servers which are close to mobile devices, reducing the transmission time consumption [21–23]. Edge computing has been studied thoroughly in many aspects, including virtual resource allocation strategy formulation [24], energy consumption of mobile stations [25], QoE and operation cost of users movement [26], security problems of data transmission [27], load balance of the network [28].

Zhou et al. [24] formulated a heterogeneous networks framework to support computing and content caching. Sheu et al. [25] proposed an advanced power saving mechanism named A-PSM, which uses the average packet inter-arrival time to adjust the sleep window to get command of power usage. Guan et al. [26] divided a metropolitan area into different clusters to minimize the sum of handovers between MEC regions, increasing the QoE and reducing the operation cost in WMAN. Baskaran et al. [27] presented an enhanced scheme compared with Privacy Key Management Protocol Version 2 (e-PKMv2). By feat of a new technique named Blind Key Distribution (BKD), the security and reliability problems could be improved. Jakimoski et al. [28] designed a vertical handover decision algorithm to optimize the load of WMAN, relying on the velocity of the mobile devices and load of the whole network.

Generally, the applications would be more computation-intensive as various requirements would be added to them for resource response [5, 29]. Therefore, the transmission delay during the process of connecting the mobile users and servers is costly in complex systems [5, 30, 31]. Offloading tasks to edge servers is a suitable way to reduce the delay of applications. Edge servers are reliable server clusters and the physical resources of edge servers are provided in the form of different kinds of VMs. Thus, users could resort VMs to deal with computing tasks through establishing wireless communication with nearby edge servers.

Cui et al. [32] devised a software-defined cooperative offloading model based on the regularities of distribution of users and used an online task scheduling algorithm to reasonably distribute energy among devices. Similarly, Chen et al. [33] studied the edge server deploy problem as well, aiming to minimize the access delay of users and decrease the total cost which is represented by the number of edge servers. To achieve the goals, heuristic and clustering algorithms were designed for reducing delay while an integer linear programming is formulated to lessen the used edge servers. Panigrahi et al. [34] proposed an energy efficient offloading approach to increase the resource utilization of edge servers for better energy usage. Analogously, Gai et al. [35] designed a dynamic energy-aware edge server-based mobile cloud computing model for energy saving according to dynamic edge servers (DCL)-based model.

When the scale of mobile users expands rapidly, they access the edge servers frequently and the resources run out rapidly. Consequently, the new requests from mobile devices could be rejected and a large number of users are queued. As the access delay caused by waiting is nonnegligible, negative effects would be brought about and the QoE for users would drop dramatically [36, 37]. Different aspects of researches on edge servers are conducted to reduce the transmission delay [36–38].

Jia et al. [36] devised an algorithm to optimize the edge server placement problem in WMAN. The algorithm could assign mobile users to edge servers which have been placed to balance the workload. On the other hand, a novel model is

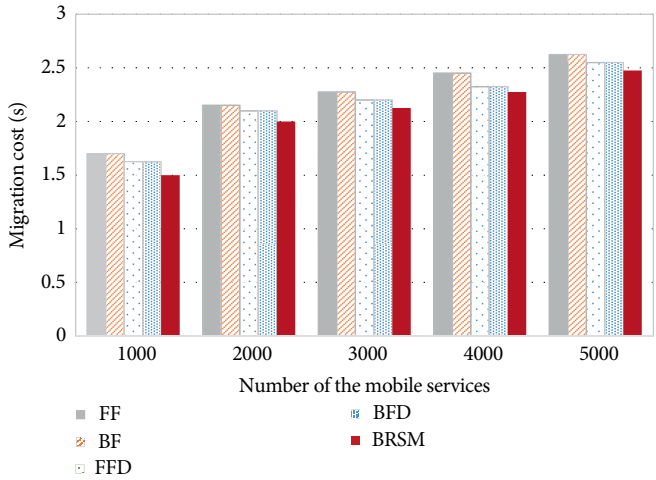

Figure 9: Comparison of migration cost by FF, BF, FFD, BFD and BRSM.

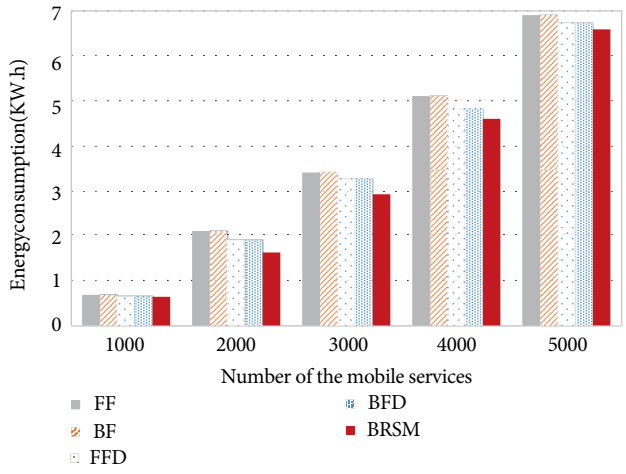

Figure 10: Comparison of energy consumption by FF, BF, FFD, BFD and BRSM.

introduced to calculate the response delay of offloading tasks and utilized two algorithms to solve the optimization problem which could minimize the maximum response time [39]. Ma et al. [40] presented a new heuristic algorithm (NHA) and particle swarm optimization (PSO) algorithm for reducing delay which are more effective than existing methods. Rodrigues et.al. [41] designed a scheme to minimize service delay with two edge server servers, focusing on communication and computation elements and using VM migration to control processing delay and transmission delay.

6. Conclusion and Future Work

The ability to provide multifarious cloud services is significant for the modern WMAN system. In this paper, a balanced resource scheduling method, named BRSM, is developed for trade-offs between VM migration cost and energy consumption for edge server management. In terms of the real-time load conditions of edge servers and the number of the offloading requests, the proposed method allows the system to formulate appropriate service offloading strategies to relieve the load on the overload edge servers and realize efficient application execution. With the increasing service requests sent from mobile users, the cloud services are guaranteed not to be greatly influenced through offloading the services in the overload edge servers to other edge servers which have idle computing resources and storage. First, the offloading problem is defined as a multi-objective optimization problem to reduce the VM migration cost and achieve energy conservation during the offloading process. Then, NSGA-III is adopted to deal with the multi-objective optimization problem. Finally, relative experiments are conducted to evaluate the performance of the proposed method BRSM.

In future work, the proposed method BRSM would be extended to the real-world scenario of WMAN. Besides, execution time limits are specified for computing tasks to identify a computation offloading scheme to reduce the migration cost as well as the energy consumption.

Data Availability

The edge service data used to support the findings of this study are included within the article.

Conflicts of Interest

The authors declare that they have no conflicts of interest.

Acknowledgments

This research is supported by the National Natural Science Foundation of China under grant nos. 61702277 and 61872219. This work is also supported by the Priority Academic Program Development of Jiangsu Higher Education Institutions (PAPD) fund, Jiangsu Collaborative Innovation Center on Atmospheric Environment and Equipment Technology (CICAEET), and

College Students' Enterprise and Entrepreneurship Education Program of NUIST, CSEEEP.

References

[1] B. V. Mathiesen, H. Lund, D. Connolly et al., "Smart energy systems for coherent 100% renewable energy and transport solutions," *Applied Energy*, vol. 145, pp. 139–154, 2015.

[2] C. Wei, M. Benosman, and T. Kim, "Online parameter identification for state of power prediction of lithium-ion batteries in electric vehicles using extremum seeking," *International Journal of Control, Automation and Systems*, 2019.

[3] D. Flórez-Orrego, I. B. Henriques, T.-V. Nguyen et al., "The contributions of prof. Jan Szargut to the exergy and environmental assessment of complex energy systems," *Energy*, vol. 161, pp. 482–492, 2018.

[4] A. Alrawais, A. Alhothaily, J. Yu, C. Hu, and X. Cheng, "SecureGuard: a certificate validation system in public key infrastructure," *IEEE Transactions on Vehicular Technology*, vol. 67, no. 6, pp. 5399–5408, 2018.

[5] V. Meena, M. HariPrasath, V. Kalpana, K. ArunKumar, and J. SenthilKumar, "Optimal resource reservation for offloaded tasks in mobile cloud computing," in *2017 2nd International Conference on Communication and Electronics Systems*, IEEE, Coimabatore, India, 2017.

[6] X. Chen, "Decentralized computation offloading game for mobile cloud computing," *IEEE Transactions on Parallel and Distributed Systems*, vol. 26, no. 4, pp. 974–983, 2015.

[7] K. Gai, M. Qiu, H. Zhao, L. Tao, and Z. Zong, "Dynamic energy-aware cloudlet-based mobile cloud computing model for green computing," *Journal of Network and Computer Applications*, vol. 59, pp. 46–54, 2016.

[8] Z. Xu, W. Liang, W. Xu, M. Jia, and S. Guo, "Capacitated cloudlet placements in wireless metropolitan area networks," in *2015 IEEE 40th Conference on Local Computer Networks*, IEEE, Clearwater Beach, FL, USA, 2015.

[9] R. Morabito, "Virtualization on internet of things edge devices with container technologies: a performance evaluation," *IEEE Access*, vol. 5, pp. 8835–8850, 2017.

[10] Y. Liu, M. J. Lee, and Y. Zheng, "Adaptive multi-resource allocation for edge server-based mobile cloud computing system," *IEEE Transactions on Mobile Computing*, vol. 15, no. 10, pp. 2398–2410, 2016.

[11] M. Chen, Y. Hao, Y. Li, C. F. Lai, and D. Wu, "On the computation offloading at ad hoc edge server: architecture and service modes," *IEEE Communications Magazine*, vol. 53, no. 6, pp. 18–24, 2015.

[12] K. Zhang, Y. Mao, S. Leng et al., "Energy-efficient offloading for mobile edge computing in 5G heterogeneous networks," *IEEE access*, vol. 4, pp. 5896–5907, 2016.

[13] W. Shi, J. Cao, Q. Zhang, Y. Li, and L. Xu, "Edge computing: vision and challenges," *IEEE Internet of Things Journal*, vol. 3, no. 5, pp. 637–646, 2016.

[14] K. Deb and H. Jain, "An evolutionary many-objective optimization algorithm using reference-point-based nondominated sorting approach, part I: solving problems with box constraints," *IEEE Transactions on Evolutionary Computation*, vol. 18, no. 4, pp. 577–601, 2013.

[15] A. H. Fathima and K. Palanisamy, "Optimization in microgrids with hybrid energy systems–a review," *Renewable and Sustainable Energy Reviews*, vol. 45, pp. 431–446, 2015.

[16] L. Qi, Q. He, F. Chen et al., " Finding all you need: web APIs recommendation in web of things through keywords search," *IEEE Transactions on Computational Social Systems*, pp. 1–10, 2019.

[17] D. Alahakoon and X. Yu, "Smart electricity meter data intelligence for future energy systems: a survey," *IEEE Transactions on Industrial Informatics*, vol. 12, no. 1, pp. 425–436, 2016.

[18] L. Qi, Y. Chen, Y. Yuan, F. Shucun, Z. Xuyun, and X. Xiaolong, "A QoS-aware virtual machine scheduling method for energy conservation in cloud-based cyber-physical systems," *World Wide Web*, 2019.

[19] A. Botta, W. De Donato, V. Persico, and A. Pescapé, "Integration of cloud computing and internet of things: a survey," *Future Generation Computer Systems*, vol. 56, pp. 684–700, 2016.

[20] G. Wenwen, Q. Lianyong, and X. Yanwei, "Privacy-aware multidimensional mobile service quality prediction and recommendation in distributed fog environment," *Wireless Communications and Mobile Computing*, vol. 2018, 8 pages, 2018.

[21] P. Mach and Z. Becvar, "Mobile edge computing: a survey on architecture and computation offloading," *IEEE Communications Surveys & Tutorials*, vol. 19, no. 3, pp. 1628–1656, 2017.

[22] Z. Yang, Y. Huang, L. Xing et al., "Efficient secure data provenance scheme in multimedia outsourcing and sharing," *Computers, Materials & Continua*, vol. 56, no. 1, pp. 1–17, 2018.

[23] Y. Zhang, Y. Zhou, F. Wang, Z. Sun, and Q. He, "Service recommendation based on quotient space granularity analysis and covering algorithm on Spark," *Knowledge-Based Systems*, vol. 147, pp. 25–35, 2018.

[24] Y. Zhou, F. R. Yu, J. Chen, and Y. Kuo, "Resource allocation for information-centric virtualized heterogeneous networks with in-network caching and mobile edge computing," *IEEE Transactions on Vehicular Technology*, vol. 66, no. 12, pp. 11339–11351, 2017.

[25] S. T. Sheu, L. W. Chen, and J. Chen, "Advanced power saving mechanism in IEEE 802.16 m wireless metropolitan area networks," in *2012 IEEE 75th Vehicular Technology Conference*, IEEE, Yokohama, Japan, 2012.

[26] X. Guan, X. Wan, J. Wang, X. Ma, and G. Bai, "Mobility aware partition of MEC regions in wireless metropolitan area networks," in *IEEE INFOCOM 2018-IEEE Conference on Computer Communications Workshops*, IEEE, USA, 2018.

[27] S. B. M. Baskaran and G. Raja, "Blind key distribution mechanism to secure wireless metropolitan area network," *CSI transactions on ICT*, vol. 4, no. 2-4, pp. 157–163, 2016.

[28] K. Jakimoski and T. Janevski, "Vertical handover improvements from WLAN to WMAN or WWAN technologies," in *2013 11th International Conference on Telecommunication in Modern Satellite, Cable and Broadcasting Services*, IEEE Serbia, 2013.

[29] Y. Yuan and W. Banzhaf, "Arja: automated repair of java programs via multi-objective genetic programming," *IEEE Transactions on Software Engineering*, 2018.

[30] J. Zhang, N. Xie, X. Zhang, K. Yue, W. Li, and D. Kumar, "Machine learning based resource allocation of cloud computing in auction," *Computers, Materials & Continua*, vol. 56, no. 1, pp. 123–135, 2018.

[31] Y. Zhang, K. Wang, Q. He et al., "Covering-based web service quality prediction via neighborhood-aware matrix factorization," *IEEE Transactions on Services Computing*, 2019.

[32] Y. Cui, J. Song, K. Ren et al., "Software defined cooperative offloading for mobile edge servers," *IEEE/ACM Transactions on Networking*, vol. 25, no. 3, pp. 1746–1760, 2017.

[33] L. Chen, J. Wu, G. Zhou, and L. Ma, "QUICK: QoS-guaranteed efficient edge server placement in wireless metropolitan area networks," *The Journal of Supercomputing*, vol. 74, no. 8, pp. 4037–4059, 2018.

[34] C. R. Panigrahi, B. Pati, and M. Tiwary, "EEOA: Improving energy efficiency of mobile edge servers using efficient offloading approach," in *2015 IEEE International Conference Advanced Networks and Telecommuncations Systems*, IEEE Kolkata, 2015.

[35] K. Gai, M. Qiu, H. Zhao, L. Tao, and Z. Zong, "Dynamic energy-aware edge server-based mobile cloud computing model for green computing," *Journal of Network and Computer Applications*, vol. 59, pp. 46–54, 2016.

[36] M. Jia, J. Cao, and W. Liang, "Optimal edge server placement and user to edge server allocation in wireless metropolitan area networks," *IEEE Transactions on Cloud Computing*, vol. 5, no. 4, pp. 725–737, 2017.

[37] Y. Yuan, Y. S. Ong, and A. Gupta, "Objective reduction in many-objective optimization: evolutionary multiobjective approaches and comprehensive analysis," *IEEE Transactions on Evolutionary Computation*, vol. 22, no. 2, pp. 189–210, 2018.

[38] C. Wu, E. Zapevalova, Y. Chen, and F. Li, "Time optimization of multiple knowledge transfers in the big data environment," *Computers, Materials & Continua*, vol. 54, no. 3, pp. 269–285, 2018.

[39] M. Jia, W. Liang, Z. Xu, M. Huang, and Y. Ma, "QoS-aware edge server load balancing in wireless metropolitan area networks," *IEEE Transactions on Cloud Computing*, p. 1, 2018.

[40] L. Ma, J. Wu, L. Chen, and Z. Liu, "Fast algorithms for capacitated edge server placements," in *2017 IEEE 21st International Conference on Computer Supported Cooperative Work in Design*, IEEE, New Zealand, 2017.

[41] T. G. Rodrigues, K. Suto, H. Nishiyama, and N. Kato, "A PSO model with VM migration and transmission power control for low service delay in the multiple edge servers ECC scenario," in *2017 IEEE International Conference on Communications*, IEEE, Paris, France, 2017.

Hindawi
Complexity
Volume 2019, Article ID 1534598, 23 pages
https://doi.org/10.1155/2019/1534598

Research Article

Planning of Cascade Hydropower Stations with the Consideration of Long-Term Operations under Uncertainties

Changjun Wang [1] **and Shutong Chen** [1,2]

[1]*Glorious Sun School of Business and Management, Donghua University, Shanghai 200051, China*
[2]*Department of Industrial and Systems Engineering, Virginia Tech, Blacksburg, VA 24061, USA*

Correspondence should be addressed to Changjun Wang; cjwang@dhu.edu.cn

Received 8 July 2019; Revised 21 September 2019; Accepted 8 October 2019; Published 28 November 2019

Guest Editor: Chun Wei

In the location-related planning of a hydropower system, the consideration of future operations under uncertainties can make the decisions sustainable and robust. Then, it is of great importance to develop an effective approach that deals with the long-term stochasticity due to the long-lasting effects of the location selections. Thus, we propose a multistage stochastic programming model to optimize the planning decisions of cascade hydropower stations and the long-term stochastic operations in an integrated way. The first stage (i.e., the planning stage) in the model deals with the location and capacity decisions of the hydropower stations, while the subsequent stages implement the scheduling decisions under each stagewise stochastic scenario. To address the curse of dimensionality caused by the long-term stochastic operations, we further propose a novel dimensionality reduction approach based on dual equilibrium to transform the multistage model into a tractable two-stage stochastic program. The applicability of our approach is validated by a case study based on a basin of Yangtze River, China, and corresponding sensitivity analysis.

1. Introduction

Given a basin, the hydropower stations to-be-built usually could be multiple. Even only a hydropower station in the current timetable, it is still necessary to consider the impacts of other possible hydropower stations in the future because of their interdependence. Moreover, such a plan that involves major capital investments must be made for a longstanding future. Hence, subsequent operations of all the stations, which influence the effect of the planning decisions, should be considered. Such an integrated way can help to get the global optimum in disasters mitigation, irrigation water supply, and clean power production [1, 2]. However, in the long-term operations, natural or social uncertainties, such as water inflows and demands, are inevitable and influence the performance of the hydropower system significantly [3]. Thus, the problem faced by the decision-maker is long-term stochastic optimization. The "long-term" we mentioned here is far beyond the long-term scale considered in previous works, such as 3–5 years in Gjelsvik et al. [4] or 12-period used in Cheng et al. [5], Wang et al. [6], and Xu and Mei [7], because of the long-lasting effects of the location decisions. Hence, the challenge is how to handle such overlong stochastic nature.

In previous works, the decisions on locations and operations of a hydropower system have been extensively, but separately, studied. Specifically, when a decision-maker plans a hydropower station, advanced technologies, such as geographical information system (GIS), are often utilized to obtain geological, climatic, and topographical information in most recent studies. Based on this information, different mathematical methods are further utilized for spotting site by synthesizing natural, engineering, and social criteria. For example, Larentis et al. [8] propose a GIS-based DEM (digital elevation model) composed of the preidentification of promising

sites and the multicriteria feasibility assessment of the final set, in which energy, technical, and environmental factors are considered together. Another GIS-based DEM is proposed by Kusre et al. [9] which use a hydrologic model to assess water resource utilization under different site candidates. Similar works can be referred to Serpoush et al. [10], Zaidi and Khan [11], etc. Besides the above assessment models, the optimization technique becomes another alternative in recent years. For example, Hosnar and Kovač-Kralj [12] identify the optimal installation locations by maximizing an ecoprofit objective at technological, economic, environmental, and social constraints. To identify the appropriate hydropower dam location, Loannidou and O'Hanley [13] develop a mixed-integer linear programming model to optimize the hydropower potential with the consideration of river connectivity. In these studies, the future power generation and hydrologic dynamics are described by the empirical formulas in the cumulative form. Thus, time-varying operations under uncertainties are ignored in the setting of location-related planning.

The optimization of the multistage operational activities, such as water storage, supply, and power generation, is an important issue which has drawn lots of studies. Most of them focus on a given hydropower system involving a single hydropower plant (e.g., Vieira et al. [14]) or multistations. For the multistation operations in the deterministic setting, two main stream of approaches have been applied. At first, to pursue the optimality, mathematical programming methods, especially dynamic programming (DP), are often used but also suffer from the computational challenge due to the number of stages and stations. Thus, Cheng et al. [15] reduce the scale of the problem by limiting their work in the "short-term" horizon. Li et al. [16] consider a decomposition-coordination mechanism to reduce dimensionality. Li et al. [17] and Cheng et al. [5] propose to parallelize the DP algorithm to reduce the computation time. The former uses the distributed memory architecture and the message passing interface protocol, while the latter considers the Fork/Join parallel framework in a multicore environment. Feng et al. [18] and Feng et al. [19] focus on the simplification of state set to accelerate the implementation of DP. Cheng et al. [20] and Feng et al. [21] adopt progressive optimality algorithm to modify the conventional DP by dividing the multistage problem into a sequence of subproblems and thus reduce the computational burden. Second, in order to address the computational complexity, numerous heuristic algorithms have been considered by sacrificing some optimality in recent years. Typical methods used in this stream include particle swarm optimization [22, 23, 24], electromagnetism-like mechanism [25, 26], genetic algorithm [27], water cycle algorithm [7], and artificial intelligence algorithms [28]. However, all these studies focus on the deterministic setting.

Uncertainties extensively exist in hydropower systems. For example, water inflows usually vary and cannot be accurately predicted since long-term meteorological forecasts are unreliable [29, 30]. Thus, the optimization of hydropower operations under uncertainties is basically a risk-based decision-making problem [31]. The stagewise stochastic process can be represented as a scenario tree; hence, the multistage stochastic programming (MSSP) model, which optimizes the expected value based on the scenario set, has been popularly used. For example, Fleten and Kristoffersen [32] develop an MSSP model to make the decisions on power generation, in which uncertain water inflows and electricity market prices are considered, with the optimization of the expected benefit. Chazarra et al. [33] propose an MSSP model for a hydropower system, taking uncertain water inflows and electricity market prices into account, to simultaneously maximize the expected profit in both energy and regulation reserve markets. To deal with uncertain streamflow, a multiobjective MSSP model is presented by Xu et al. [34] to optimize scheduling strategies. The first objective is to maximize direct revenue from energy production, and the second one is to minimize the expected energy shortfall percentage. Séguin et al. [35] address the stochastic hydropower unit commitment and loading problem under the uncertain inflows. However, all these works only consider the short-term horizon. Thus, off-the-shelf solvers can be applied to solve these models directly.

With the increase of the number of decision stages, the size of the MSSP grows dramatically which often requires decomposition methods [36]. A state-of-the-art one is the stochastic dual DP algorithm which is a sampling-based variant of nested Benders decomposition. Hjelmeland et al. [37] use it to handle a medium-term scheduling issue for a single producer under uncertain inflows and prices within one to three-year horizon. Most related works consider the medium-term setting as Gjelsvik et al. [4]; Helseth et al. [38]; Hjelmeland et al. [39]; and Poorsepahy-Samian et al. [40]. However, as indicated by Hjelmeland et al. [39], although decomposition methods can help to alleviate the solving complexity, the computation would significantly become slow with the increase of system size and decision stages. It shows the difficulty of multistage stochastic optimization with high dimensions of uncertainty.

In summary, a considerable amount of research has been conducted for the hydropower system design and operation. However, to the best of our knowledge, the location decisions in existing studies have not taken multistage operations into account. In terms of operations, numerous studies focus on developing efficient exact or heuristic algorithms for the deterministic setting, whereas many endeavors utilize the MSSP to address the stochastic operations. However, the high dimensionality characteristic has become the main bottleneck limiting the application of optimization approaches [41]. Even in the deterministic setting, the computation of the hydropower

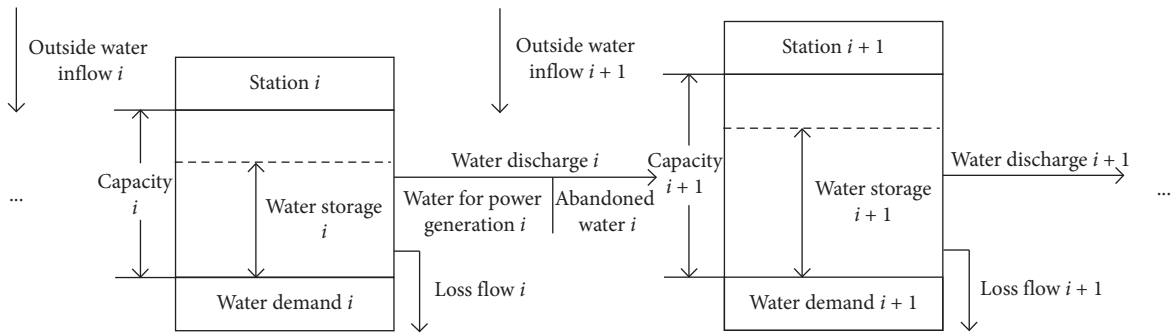

Figure 1: Illustration of operational activities.

system operation problem is highly complex when the number of operational stages is big [19]. With the consideration of randomness, the optimization of the MSSP should be implemented on all the stagewise stochastic realizations, which further increase the solving burden. Hence, most existing works only focus on short- or medium-term stochasticity. However, the location selection is the planning decision that involves major capital investments and has an overlong effect. Thus, such a decision should be made from the long-lasting perspective, in which uncertainties would occur inevitably. Hence, the long-term stochasticity should be considered in the hydropower design, which is a difficult task.

We contribute to the existing literature by planning a cascade hydropower system with the consideration of long-term stochastic operations. Most mainstream algorithms, including DP for the deterministic setting and the decomposition methods for the stochastic setting, suffer from the number of stages. Few papers have looked specifically into long-term stochastic models. Considering that the purpose of our work is the location decisions rather than providing accurate schedules, in order to address the dimensionality issue, an intuitive idea is to keep the influence of stochastic operations while reducing the number of stages. Thus, applying the method of dual equilibrium (DE) [42, 43], we propose a novel dimensionality reduction approach which aggregates the long-term operational impacts on the present and thus simplifies the MSSP model to a two-stage one. Our method can handle the stochastic problem regardless of the number of stages and provide an alternative approach for the overlong setting.

The remainder of the study is presented as follows. In Section 2, the MSSP model is developed. The dimensionality reduction approach based on DE is presented in Section 3. Specifically, Section 3.1 focuses on the reduction of the scenario tree while Section 3.2 implements the transformation of the MSSP model accordingly. In Section 4, the application in one section of Yangtze River, China, is displayed and analyzed. The last section presents conclusions and remarks about some directions for future research.

2. Problem Definition and Mathematical Formulation

2.1. Problem Statement. Consider a basin, where a government prepares a construction plan of cascade hydropower stations to control flood or drought, satisfy irrigation, and pursue profits from power generation. Thus, the location and capacity decision-making problem of cascade hydropower stations is studied here, in which the long-term stochastic operations should be taken into account. The integrated MSSP model is formulated to optimize the total performance which involves the construction costs in the planning stage, as well as operational costs, penalty costs, and profits of power generation in the subsequent multiple stages.

Six decisions of the model can be divided into two groups. The first group should be made in the planning stage, including (1) the final selection of hydropower stations from the candidates; (2) the capacity of each selected hydropower station. The decisions in the second group are in each operational stage. They are (3) water storage of each selected hydropower station in each stage; (4) loss flow of each selected hydropower station in each stage; (5) water discharge to downstream from each hydropower station in each stage; and (6) water discharge of power generation in each selected hydropower station each stage. During these operational stages, we consider uncertain water inflows (including precipitation and inflows from tributaries) and water demands (from residents, agriculture, and industry). The number of stages, defined as T, could be extremely large.

As shown in Figure 1, given the locations of cascade hydropower stations, three scheduling activities: water discharge of power generation, abandoned water spill (go downstream directly without passing generator units) and loss flow should be periodically made. The water storage of each hydropower station is determined by its scheduling activities and random water inflows. Notice that the loss flow mentioned is discharged to local areas, rather than downstream. When the loss flow is larger than the actual demand, it would incur corresponding penalties. Moreover, the physical limits on the levels of water discharge, loss flow, and power generation of each hydropower station should be satisfied in each operational stage.

Table 1: Model variables.

Types of variables	Symbol	Description
Sets	R	Set of hydropower station candidates
	S	Set of scenarios of the operational stages
Deterministic variables	T	The planning horizon is composed of T operational stages
	$R_{\min}$	The minimum required number of hydropower stations in the plan
	e	Unit construction fee (RMB/m^3)
	f	Unit profit of power generation (RMB/KWh)
	Δt	Time interval of each operational stage (h, which is the abbreviation of hour)
	c_i	Penalty coefficient per unit in hydropower station candidate i (RMB/m^3)
	K_i	Coefficient of output of candidate i (kg/(m^2·s^2))
	$N_{i\min}$	The minimum output of candidate i (kW)
	$N_{i\max}$	The maximum output of candidate i (kW)
	H_i	Water head of candidate i (m)
	$V_{i\min}$	The minimum required water storage of candidate i when it is selected (m^3)
	$Q_{i\max}$	The maximum discharge limit of local area around candidate i (m^3/h)
	$QF_{i\max}$	The upper limit water discharge of candidate i (m^3/h)
	$QF_{i\min}$	The lower limit water discharge of candidate i (m^3/h)
	$r_i(t)$	Unit operational cost of candidate i at stage t (RMB/(m^3·h))
Stochastic variables	p^s	The probability of stagewise scenario s
	$\varepsilon_i^s(t)$	Outside water inflows in candidate i at stage t under scenario s (m^3/h)
	$Q_{i\min}^s(t)$	Water demands in candidate i at stage t under scenario s (m^3/h)
	$Q_{i\min}^{'s}(t)$	Acceptance level of water discharge in local area surrounding candidate i at stage t under scenario s (m^3/h)

Table 2: Decision variables.

Types of variables	Symbol	Description
The planning stage	x_i	1 if hydropower station i is chosen, 0 otherwise
	Cap_i	The maximum capacity of hydropower station candidate i
The operational stages	$y_i^s(t)$	Water storage of candidate i at stage t under scenario s (m^3)
	$QL_i^s(t)$	Loss flow of candidate i at stage t under scenario s (m^3/h)
	$Q_i^s(t)$	Water discharge to downstream in candidate i at stage t under scenario s (m^3/h)
	$QE_i^s(t)$	Water discharge of power generation in candidate i at stage t under scenario s (m^3/h)
	$QA_i^s(t)$	Water spill in candidate i at stage t under scenario s (m^3/h)

2.2. Model Formulation. Sets, exogenous deterministic and stochastic variables are given in Table 1. Table 2 displays the decision variables in all stages.

The MSSP model which integrates the planning decisions and stochastic operational impacts is proposed as follows:

$$\min \quad \sum_{i\in R} e\cdot \mathrm{Cap}_i + \sum_{t=1}^{T}\left(\Delta t\cdot \sum_{i\in R} r_i(t)\cdot \mathrm{Cap}_i\right) + \sum_{t=1}^{T}\sum_{s\in S}\left[p^s\cdot \sum_{i\in R}\left[\Delta t\cdot\left(c_i\cdot x_i\cdot\left(QL_i^s(t)-Q_{i\min}^{'s}(t)\right)-f\cdot K_i\cdot QE_i^s(t)\cdot H_i\right)\right]\right], \tag{1a}$$

s.t.

$$R_{\min}\le \sum_{i\in R} x_i\le R, \tag{1b}$$

$$\mathrm{Cap}_i\le MM\cdot x_i,\quad i\in R, \tag{1c}$$

$$QE_i^s(t)\le MM\cdot x_i,\quad t=1,2,\ldots,T;\ i\in R;\ s\in S, \tag{1d}$$

$$x_i\cdot N_{i\min}\le K_i\cdot QE_i^s(t)\cdot H_i\le N_{i\max},\quad t=1,2,\ldots,T;\ i\in R;\ s\in S, \tag{1e}$$

$$V_{i\min}\cdot x_i\le y_i^s(t)\le \mathrm{Cap}_i,\quad t=1,2,\ldots,T;\ i\in R;\ s\in S, \tag{1f}$$

$$y_i^s(t)-y_i^s(t-1)=\Delta t\cdot\left[Q_{i-1}^s(t)+\varepsilon_i^s(t)-Q_i^s(t)-QL_i^s(t)\right],\quad t=1,2,\ldots,T;\ i\in R;\ s\in S, \tag{1g}$$

$$Q_i^s(t)=QE_i^s(t)+QA_i^s(t),\quad t=1,2,\ldots,T;\ i\in R;\ s\in S, \tag{1h}$$

$$QF_{i\min}\le QE_i^s(t)+QA_i^s(t)\le QF_{i\max},\quad t=1,2,\ldots,T;\ i\in R;\ s\in S, \tag{1i}$$

$$Q_{i\min}^s(t)\le QL_i^s(t)\le x_i\cdot Q_{i\max}+(1-x_i)\cdot Q_{i\min}^s(t),\quad t=1,2,\ldots,T;\ i\in R;\ s\in S, \tag{1j}$$

$$\mathrm{Cap}_i,\ y_i^s(t),QL_i^s(t),QE_i^s(t),Q_i^s(t),QA_i^s(t)\ge 0,\ x_i\in\{0,1\},\quad t=1,2,\ldots,T;\ i\in R;\ s\in S. \tag{1k}$$

The objective function (1a) is composed of the construction costs of all selected hydropower stations and the expected value of the operational costs, the environmental penalty costs, and the benefits of power generation under all the stagewise scenarios.

Constraint (1b) limits the number of hydropower stations to be chosen. Thus, Constraints (1c) and (1d) ensure that the corresponding maximum capacity and water discharge of unselected hydropower stations are zero in which MM is a number big enough. Constraint (1e) gives the power generation limits. Constraint (1f) ensures that the water storage of the selected hydropower station is between the minimum required water storage and maximum capacity. Constraint (1g) gives water balance equations. Constraint (1h) shows the relationship between water discharge to downstream and water discharge of power generation, as well as water spill in each hydropower station candidate. Constraint (1i) presents the upper and lower limits of water discharge between two adjacent selected hydropower stations. Constraint (1j) guarantees that if the candidate is chosen, its loss flow should meet the local demand and cannot exceed the maximum discharge limit. And if a candidate is not selected, its loss flow is equal to the water demands. Constraint (1k) specifies the domains of the decision variables.

3. Model Transformation

Even the deterministic version of the proposed MSSP model is NP-hard. Besides, the dimension of stochastic scenarios in the MSSP model increases with the number of stages exponentially. It would further increase the solving difficulty. DE is a useful approach to handle the dimension problem of the large-scale setting [44]. It was first proposed in [42] to simplify the multistage deterministic convex optimization problem and then was applied to a multistage stochastic production-inventory programming model in [43]. The essence of DE is going to add up all the influence after a time point in the future by a so-called discount factor to compress stages. Hence, it coincides with our idea of aggregating the operational impacts on the planning decisions.

Next, we proposed a DE-based dimensionality reduction approach to address the above MSSP model. Specifically, because the size of the scenario tree is one of the main causes resulting in the computational difficulty, we first show how to compress the stages of the scenario tree at first (see Section 3.1). Along with the simplification of the scenario tree, we further show how to aggregate the operational decision variables and the deterministic parameters. With the compression of all these variables, the proposed MSSP

model would be integrated into a two-stage one which is tractable (see Section 3.2).

3.1. Scenarios Generation and Simplification. Because the acceptance level of water discharge includes the quantity of water demands, we assume these two factors have a deterministic linear relationship. Thus, we focus on random water inflows and water demands here. Before we give the dimensionality reduction approach, we first show the generation and simplification procedures of stochastic scenarios by taking uncertain water inflows as an example. Uncertain water demands can be handled similarly.

We match each operational stage with a season. At seasonal stage $t = 1, 2, \ldots, T$, assume that $\xi = 1$, 2, and 3 correspond to three levels of random inflows: high, medium, and low, with the corresponding probability of p_{1H}, p_{1M}, and p_{1L}, respectively. The quantities of water inflows in hydropower station candidate i at stage t with level ξ can be represented as $\varepsilon_i^{\xi}(t)$, $i \in R$. There are multiple stages considered in this study. Hence, each stagewise scenario of inflows, defined as s_1 ($\in S_1$), can be represented as a branch from $t = 0 \sim T$ of the scenario tree, in which $t = 0$ represents the planning stage. The corresponding probability $p(s_1)$ is the product of occurrence probabilities of all the nodes on this branch. Figure 2 gives the scenario tree faced by hydropower station candidate 1.

As can be seen, the number of inflow scenarios of one candidate is up to 3^T in T seasonal stages. For example, if we consider a 10 year horizon, the scenario size of inflows of one candidate would be $3^{40}(\approx 1.049 \times 10^{19})$. Obviously, a simplification way is required. Here, we can remain the scenarios in early stages, while inflows in subsequent stages are replaced by corresponding constant estimated values. We do this for two reasons. The first is that the stochastic scenarios in subsequent stages are harder to give than these of early stages due to forecasting difficulty. Second, random inflows have intrinsic periodicity which means inflows in subsequent stages can be offset. Hence, an approximated way is to use the corresponding estimated values to replace the seasonal inflows in subsequent stages.

Thus, the scenario tree in Figure 2 is simplified to that in Figure 3 in which the uncertainties of $t = 1 \sim 4$ remain. Denote the stagewise scenario in Figure 3 as $\hat{s}_1$ and the corresponding scenario set as $\hat{S}_1$. After simplification, the number of the decision variables is still large because of the big T. Hence, the dimensionality reduction approach is proposed to address this issue.

3.1.1. Step 1 of Dimensionality Reduction—Stages Reduction by Aggregating the Random Factors of the Same Season. The dimensionality reduction approach includes two steps. We focus on the first one in this section.

Due to the seasonal periodicity of inflows, we propose to aggregate the inflows of the same season together (see Figure 4). Specifically, take the inflows of candidate 1 in the first stage ($t = 1$), i.e., $\varepsilon_1^{\xi}(1)$, as an example. Without loss of generality, assume that T is the multiple of four. The subsequent water inflows with the same season, i.e., stage $4\tau + 1$ ($\tau = 1, 2, \ldots, (T/4)-1$), have the same value, denoted as $\bar{\varepsilon}_1(1)$. Similarly, $\bar{\varepsilon}_1(2)$, $\bar{\varepsilon}_1(3)$, and $\bar{\varepsilon}_1(4)$ represent other three seasonal values of water inflows at candidate 1. Referring to the concept of present value, we use factor δ ($0 < \delta < 1$) to discount the impacts of subsequent stages. Thus, the corresponding aggregated water inflows of candidate 1 in the first stage ($t = 1$) under the case of ξ, denoted as $\varepsilon_1^{*\xi}(1)$, are the discounted value which can be expressed as

$$\begin{aligned}\varepsilon_1^{*\xi}(1) &= \varepsilon_1^{\xi}(1) + \delta^4 \cdot \bar{\varepsilon}_1(1) + \cdots + \delta^{4\tau} \cdot \bar{\varepsilon}_1(1) + \cdots + \delta^{T-4} \cdot \bar{\varepsilon}_1(1) \\ &= \varepsilon_1^{\xi}(1) + \bar{\varepsilon}_1(1) \cdot \frac{1-\delta^T}{1-\delta^4}, \quad \tau = 1, 2, \ldots, \frac{T}{4} - 1.\end{aligned} \tag{2}$$

Then, $\varepsilon_1^{*\xi}(2)$, $\varepsilon_1^{*\xi}(3)$, and $\varepsilon_1^{*\xi}(4)$ can be obtained similarly. Thus, the scenario tree in Figure 3 is compressed into Figure 5, in which the value associated with each node is a discounted value now. However, the number of branches ($\hat{s}_1$) and their corresponding occurrence probabilities ($p(\hat{s}_1)$) remain unchanged.

3.1.2. Step 2 of Dimensionality Reduction—Stages Reduction Across Seasons. It is worth recalling that this study focuses on the planning problem with the consideration of future operational activities under uncertainties. Thus, the second step of the dimensionality reduction approach is to implement the further aggregation of the impacts of operational stages together. In other words, the random variables ($t = 2, 3, 4$) on a branch in Figure 5 will be integrated into the first operational stage ($t = 1$). For the example that the inflows of candidate 1 under stagewise scenario $\hat{s}_1$ which is composed of four high-level stages (i.e., $\xi = 1$), its present value can be given as

$$\varepsilon_1^{**\hat{s}_1} = \varepsilon_1^{*1}(1) + \delta \cdot \varepsilon_1^{*1}(2) + \delta^2 \cdot \varepsilon_1^{*1}(3) + \delta^3 \cdot \varepsilon_1^{*1}(4). \tag{3}$$

Although the impacts of scenario $\hat{s}_1$ is aggregated now, such process would not change the number of scenario $\hat{s}_1$ and its probability $p(\hat{s}_1)$.

The stochastic scenario of random water demands could be handled similarly, and the corresponding final scenario set is denoted as $\hat{S}_2$ which is composed by scenario $\hat{s}_2$ with the probability $p(\hat{s}_2)$. Hence, the set of total scenarios S used in the proposed MSSP model is simplified to $\hat{S}$, which is the Cartesian product of $\hat{S}_1$ and $\hat{S}_2$:

$$\hat{S} = \hat{S}_1 \times \hat{S}_2 = \left\{(\hat{s}_1, \hat{s}_2) \,\middle|\, \hat{s}_1 \in \hat{S}_1, \hat{s}_2 \in \hat{S}_2\right\}. \tag{4}$$

The corresponding probability of new scenario $\hat{s}$ ($\in \hat{S}$), which is the union of $\hat{s}_1$ and $\hat{s}_2$, can be calculated as

$$p(\hat{s}) = p(\hat{s}_1) \times p(\hat{s}_2). \tag{5}$$

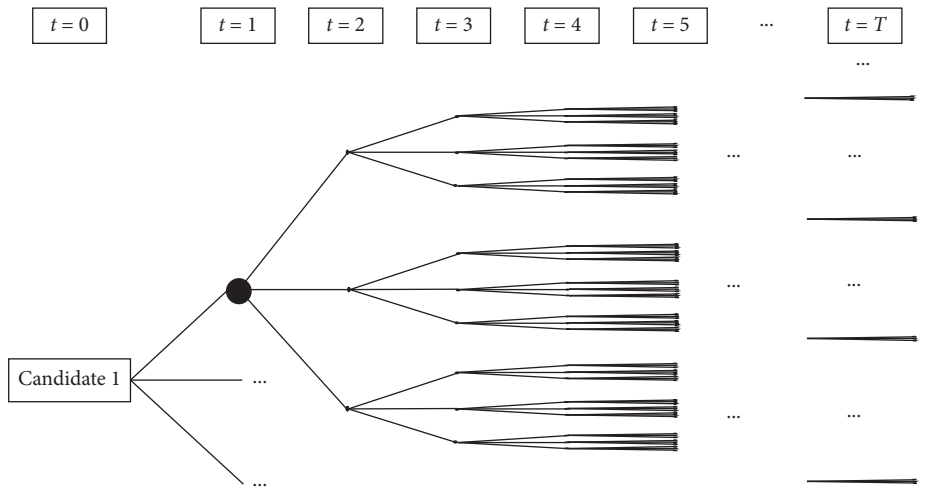

Figure 2: Original multistage scenario tree (random inflows of candidate 1).

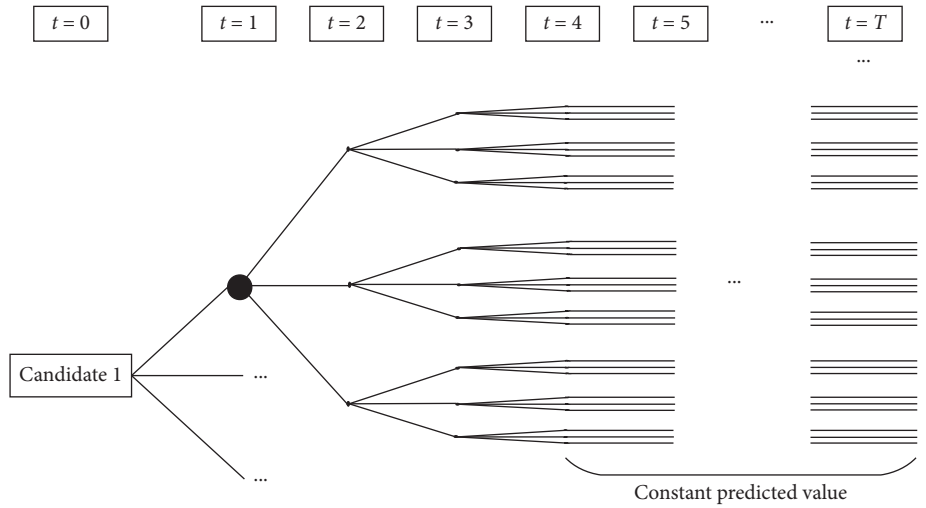

Figure 3: Simplified multistage scenario tree (random inflows of candidate 1).

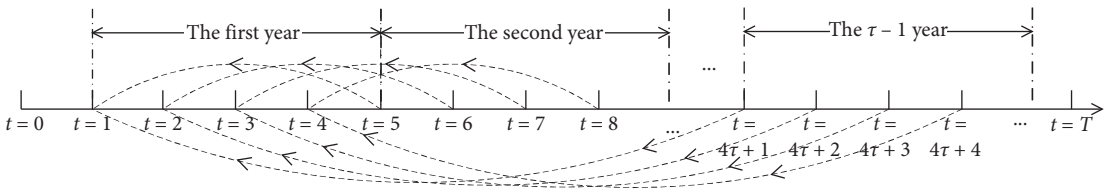

Figure 4: Illustration of stage reduction by aggregating the random factors of the same season.

Till now, the stagewise scenario tree is compressed into a one-stage scenario set $\widehat{S}$.

3.2. Transformation of the MSSP Model. The above work simplifies the scenario tree by discounting the random variables. Accordingly, with the compression of the scenario tree, the deterministic parameters and the decision variables should also be aggregated, and thus, the MSSP model would be simplified. The transformation process also includes two steps.

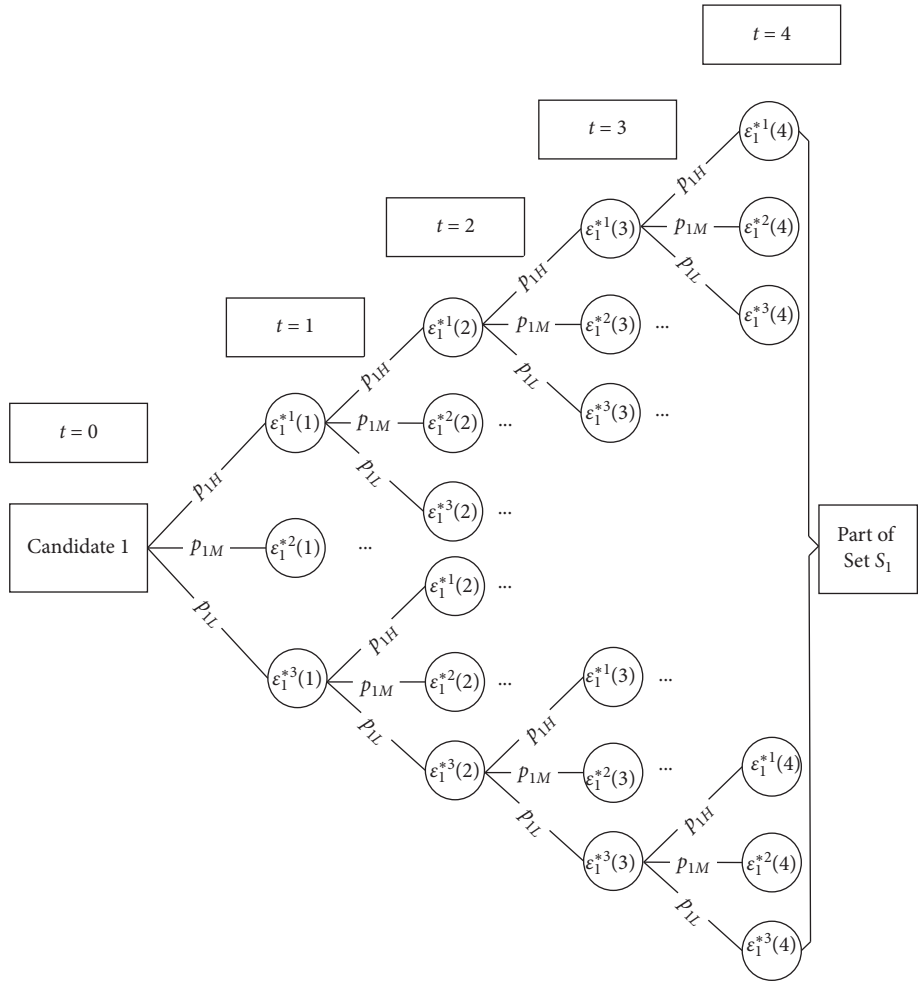

Figure 5: Scenario tree (random inflows of candidate 1).

3.2.1. Step 1 of Dimensionality Reduction. At first, we decompose the operational stages of MSSP model into multiple submodels according to each stagewise scenario s ($\in S$). Then, such submodel is not only multistage but also deterministic because it is given based on the independent scenario. For the submodel, we show how to simplify the variables and the model along with the reduction of the stages.

To facilitate the implementation of DE, we first reformulate the submodel as the following equivalent:

$$\min \quad \sum_{j=1}^{4} \sum_{\tau=0}^{(T/4)-1} \left\{ \sum_{i \in R} \Delta t \cdot \left[c_i \cdot x_i \cdot \left(QL_i(4\tau + j) - Q'_{i\min}(4\tau + j) \right) - f \cdot K_i \cdot QE_i(4\tau + j) \cdot H_i \right] \right\}, \tag{6a}$$

s.t.

$$QE_i(4\tau + j) \le MM \cdot x_i, \quad i \in R; \tau = 0, \ldots, \frac{T}{4} - 1; j = 1, 2, 3, 4, \tag{6b}$$

$$x_i \cdot N_{i\min} \le K_i \cdot QE_i(4\tau + j) \cdot H_i \le N_{i\max}, \quad i \in R; \tau = 0, \ldots, \frac{T}{4} - 1; j = 1, 2, 3, 4, \tag{6c}$$

$$V_{i\min} \cdot x_i \le y_i(4\tau + j) \le \mathrm{Cap}_i, \quad i \in R; \tau = 0, \ldots, \frac{T}{4} - 1; j = 1, 2, 3, 4, \tag{6d}$$

$$y_i(4\tau+j)-y_i(4\tau+j-1)=\Delta t\cdot\left[Q_{i-1}(4\tau+j)+\varepsilon_i(4\tau+j)-Q_i(4\tau+j)-QL_i(4\tau+j)\right],\quad i\in R;\tau=0,\ldots,\frac{T}{4}-1;j=1,2,3,4, \tag{6e}$$

$$Q_i(4\tau+j)=QE_i(4\tau+j)+QA_i(4\tau+j),\quad i\in R;\tau=0,\ldots,\frac{T}{4}-1;j=1,2,3,4, \tag{6f}$$

$$QF_{i\min}\le QE_i(4\tau+j)+QA_i(4\tau+j)\le QF_{i\max},\quad i\in R;\tau=0,\ldots,\frac{T}{4}-1;j=1,2,3,4, \tag{6g}$$

$$Q_{i\min}(4\tau+j)\le QL_i(4\tau+j)\le x_i\cdot Q_{i\max}+\left(1-x_i\right)\cdot Q_{i\min}(4\tau+j),\quad i\in R;\tau=0,\ldots,\frac{T}{4}-1;j=1,2,3,4. \tag{6h}$$

Step 1. Here, we focus on the objective. Specifically, similar to formula (2), the objective values at stage $4\tau+j$ ($\tau=0,\ 1,\ \ldots,\ (T/4)-1,\ j=1,\ 2,\ 3,\ 4$) also should be compressed into the corresponding stage j. Thus, with the introduction of the discount factor δ, (6a) can be reformulated as (7):

$$\min\sum_{j=1}^{4}\sum_{\tau=0}^{(T/4)-1}\left\{\delta^{4\tau}\cdot\sum_{i\in R}\Delta t\cdot\left[c_i\cdot x_i\cdot\left(QL_i(4\tau+j)-Q'_{i\min}(4\tau+j)\right)-f\cdot K_i\cdot QE_i(4\tau+j)\cdot H_i\right]\right\}. \tag{7}$$

Step 2. Along with simplification of the scenario tree, the decision variables and the deterministic parameters should also be aggregated. Because they exist in both the objective and the constraints, to facilitate our transformation, we integrate the constraints into the objective. Specifically, we use dual multipliers $\beta_{k,4\tau+j}$ ($k=1,\ldots,7$) to relax the k-th one of Constraints (6b)~(6h) of stage $4\tau+j$ ($\tau=0,1,\ldots,(T/4)-1$, $j=1,\ 2,\ 3,\ 4$). Then, the optimization problem ((6b)~(6h), (7)) can be transformed into the unconstrainted problem (8):

$$\begin{aligned}\min\sum_{j=1}^{4}\sum_{\tau=0}^{(T/4)-1}\Bigg\{&\delta^{4\tau}\cdot\sum_{i\in R}\Delta t\cdot\left[c_i\cdot x_i\cdot\left(QL_i(4\tau+j)-Q'_{i\min}(4\tau+j)\right)-f\cdot K_i\cdot QE_i(4\tau+j)\cdot H_i\right]\\&+\beta^{+}_{1,4\tau+j}\cdot\left(QE_i(4\tau+j)-MM\cdot x_i\right)+\beta^{+}_{2,4\tau+j}\cdot\left(K_i\cdot QE_i(4\tau+j)\cdot H_i-N_{i\max}\right)+\beta^{-}_{2,4\tau+j}\\&\cdot\left(K_i\cdot QE_i(4\tau+j)\cdot H_i-x_i\cdot N_{i\min}\right)+\beta^{+}_{3,4\tau+j}\cdot\left(y_i(4\tau+j)-Cap_i\right)+\beta^{-}_{3,4\tau+j}(j)\cdot\left(y_i(4\tau+j)-V_{i\min}\cdot x_i\right)\\&+\beta_{4,4\tau+j}\cdot\left(y_i(4\tau+j)-y_i(4\tau+j-1)-\Delta t\cdot\left(Q_{i-1}(4\tau+j)+\varepsilon_i(4\tau+j)-Q_i(4\tau+j)-QL_i(4\tau+j)\right)\right)\\&+\beta_{5,4\tau+j}\cdot\left(Q_i(4\tau+j)-QE_i(4\tau+j)-QA_i(4\tau+j)\right)+\beta^{+}_{6,4\tau+j}\cdot\left(QE_i(4\tau+j)+QA_i(4\tau+j)-QF_{i\max}\right)\\&+\beta^{-}_{6,4\tau+j}\cdot\left(QE_i(4\tau+j)+QA_i(4\tau+j)-QF_{i\min}\right)+\beta^{+}_{7,4\tau+j}\cdot\left(QL_i(4\tau+j)-x_i\cdot Q_{i\max}-\left(1-x_i\right)\cdot Q_{i\min}(4\tau+j)\right)\\&+\beta^{-}_{7,4\tau+j}\cdot\left(QL_i(4\tau+j)-Q_{i\min}(4\tau+j)\right)\Bigg\}.\end{aligned} \tag{8}$$

The DE approach assumes the dual multipliers have the linear relationship with the discount factor δ [42]. Thus, let the dual multipliers here take the form $\beta_{k,4\tau+j}=\delta^{4\tau}\cdot\beta_k(j)$. Then, problem (8) can further be reformulated as

$$\min \sum_{j=1}^{4} \sum_{\tau=0}^{(T/4)-1} \delta^{4\tau} \cdot \left\{ \sum_{i \in R} \Delta t \cdot \left[c_i \cdot x_i \cdot \left(QL_i(4\tau + j) - Q_{i\min}'(4\tau + j) \right) - f \cdot K_i \cdot QE_i(4\tau + j) \cdot H_i \right] + \beta_1^+(j) \cdot \left(QE_i(4\tau + j) - MM \cdot x_i \right) \right.$$
$$+ \beta_2^+(j) \cdot \left(K_i \cdot QE_i(4\tau + j) \cdot H_i - N_{i\max} \right) + \beta_2^-(j) \cdot \left(K_i \cdot QE_i(4\tau + j) \cdot H_i - x_i \cdot N_{i\min} \right) + \beta_3^+(j) \cdot \left(y_i(4\tau + j) - Cap_i \right)$$
$$+ \beta_3^-(j) \cdot \left(y_i(4\tau + j) - V_{i\min} \cdot x_i \right) + \beta_4(j) \cdot \left(y_i(4\tau + j) - y_i(4\tau + j - 1) - \Delta t \cdot \left(Q_{i-1}(4\tau + j) + \varepsilon_i(4\tau + j) \right. \right.$$
$$\left. \left. - Q_i(4\tau + j) - QL_i(4\tau + j) \right) \right) + \beta_5(j) \cdot \left(Q_i(4\tau + j) - QE_i(4\tau + j) - QA_i(4\tau + j) \right) + \beta_6^+(j) \cdot \left(QE_i(4\tau + j) \right.$$
$$\left. + QA_i(4\tau + j) - QF_{i\max} \right) + \beta_6^-(j) \cdot \left(QE_i(4\tau + j) + QA_i(4\tau + j) - QF_{i\min} \right)$$
$$\left. + \beta_7^+(j) \cdot \left(QL_i(4\tau + j) - x_i \cdot Q_{i\max} - (1 - x_i) \cdot Q_{i\min}(4\tau + j) \right) + \beta_7^-(j) \cdot \left(QL_i(4\tau + j) - Q_{i\min}(4\tau + j) \right) \right\}. \tag{9}$$

Step 3. Thus, similar to the discounting way of the random variables in Section 3.1.1, we can integrate the decision variables and the parameters under the same season together by δ. To make the above model concise, the so-called 'integrated' primal variables are introduced to replace the corresponding discounted values. For example,

$$QL_i^*(j) = \sum_{\tau=0}^{(T/4)-1} \delta^{4\tau} \cdot QL_i(4\tau + j), \quad j = 1, 2, 3, 4; i \in R, \tag{10a}$$

$$Q_{i\max}^* = \sum_{\tau=0}^{(T/4)-1} \delta^{4\tau} \cdot Q_{i\max}, \quad i \in R. \tag{10b}$$

Other integrated primal variables can be given similarly, and all of them take an asterisk at their top right corner. Thus, with the introduction of the 'integrated' primal variables, the symbol $\sum_{\tau=0}^{(T/4)-1}(\cdot)$ in Objective (9) could be removed, and then, the operational stages 5~T in the submodel could be compressed into the stages 1~4, respectively. Thus, we have

$$\min \sum_{j=1}^{4} \left\{ \sum_{i \in R} \Delta t \cdot \left[c_i \cdot x_i \cdot \left(QL_i^*(j) - Q_{i\min}^{'*}(j) \right) - f \cdot K_i \cdot QE_i^*(j) \cdot H_i \right] \right.$$
$$+ \beta_1^+(j) \cdot \left(QE_i^*(j) - MM \cdot x_i \right) + \beta_2^+(j) \cdot \left(K_i \cdot QE_i^*(j) \cdot H_i - N_{i\max}^* \right) + \beta_2^-(j) \cdot \left(K_i \cdot QE_i^*(j) \cdot H_i - x_i \cdot N_{i\min}^* \right)$$
$$+ \beta_3^+(j) \cdot \left(y_i^*(j) - Cap_i^* \right) + \beta_3^-(j) \cdot \left(y_i^*(j) - V_{i\min}^* \cdot x_i \right)$$
$$+ \beta_4(j) \cdot \left(y_i^*(j) - y_i^*(j-1) - \Delta t \cdot \left(Q_{i-1}^*(j) + \varepsilon_i^*(j) - Q_i^*(j) - QL_i^*(j) \right) \right) + \beta_5(j) \cdot \left(Q_i^*(j) - QE_i^*(j) - QA_i^*(j) \right) \tag{11}$$
$$+ \beta_6^+(j) \cdot \left(QE_i^*(j) + QA_i^*(j) - QF_{i\max}^* \right) + \beta_6^-(j) \cdot \left(QE_i^*(j) + QA_i^*(j) - QF_{i\min}^* \right)$$
$$\left. + \beta_7^+(j) \cdot \left(QL_i^*(j) - x_i \cdot Q_{i\max}^* - (1 - x_i) \cdot Q_{i\min}^*(j) \right) + \beta_7^-(j) \cdot \left(QL_i^*(j) - Q_{i\min}^*(j) \right) \right\}.$$

Step 4. Notice that the above transformation is for the submodel which is under a specific scenario. Specifically, Step 2 relaxes the constraints to get a unconstrainted model, and then, Step 3 aggregates the multistage for this model. Here, we need to extract the relaxed constraints back at first and then combine the model with each scenario $\hat{s}$ ($\in \hat{S}$) (see Figure 5) and the planning stage. Thus, we can get the following intermediate model:

$$\min \quad \sum_{i\in R} e\cdot \mathrm{Cap}_i + \sum_{j=1}^{4}\left(\Delta t\cdot \sum_{i\in R} r_i^*(j)\cdot \mathrm{Cap}_i\right) + \sum_{\widehat{s}\in\widehat{S}} p^{\widehat{s}}\cdot \sum_{j=1}^{4}\sum_{i\in R}\Delta t\cdot\left[c_i\cdot x_i\cdot\left(QL_i^{*\widehat{s}}(j) - Q'^{*\widehat{s}}_{i\min}(j)\right) - f\cdot K_i\cdot QE_i^{*\widehat{s}}(j)\cdot H_i\right], \tag{12a}$$

s.t.

$$R_{\min} \le \sum_{i\in R} x_i \le R, \tag{12b}$$

$$\mathrm{Cap}_i \le MM\cdot x_i, \quad i\in R, \tag{12c}$$

$$QE_i^{*\widehat{s}}(j) \le MM\cdot x_i, \quad i\in R;\widehat{s}\in\widehat{S};\ j=1,2,3,4, \tag{12d}$$

$$x_i\cdot N^*_{i\min} \le K_i\cdot QE_i^{*\widehat{s}}(j)\cdot H_i \le N^*_{i\max}, \quad i\in R;\widehat{s}\in\widehat{S};\ j=1,2,3,4, \tag{12e}$$

$$V^*_{i\min}\cdot x_i \le y_i^{*\widehat{s}}(j) \le \mathrm{Cap}_i^*, \quad i\in R;\widehat{s}\in\widehat{S};\ j=1,2,3,4, \tag{12f}$$

$$y_i^{*\widehat{s}}(j) - y_i^{*\widehat{s}}(j-1) = \Delta t\cdot\left[Q_{i-1}^{*\widehat{s}}(j) + \varepsilon_i^{*\widehat{s}}(j) - Q_i^{*\widehat{s}}(j) - QL_i^{*\widehat{s}}(j)\right], \quad i\in R,\widehat{s}\in\widehat{S};\ j=1,2,3,4, \tag{12g}$$

$$Q_i^{*\widehat{s}}(j) = QE_i^{*\widehat{s}}(j) + QA_i^{*\widehat{s}}(j), \quad i\in R;\widehat{s}\in\widehat{S};\ j=1,2,3,4, \tag{12h}$$

$$QF^*_{i\min} \le QE_i^{*\widehat{s}}(j) + QA_i^{*\widehat{s}}(j) \le QF^*_{i\max}, i\in R;\widehat{s}\in\widehat{S};\ j=1,2,3,4, \tag{12i}$$

$$Q^{*\widehat{s}}_{i\min}(j) \le QL_i^{*\widehat{s}}(j) \le x_i\cdot Q^*_{i\max} + (1-x_i)\cdot Q^{*\widehat{s}}_{i\min}(j), \quad i\in R;\widehat{s}\in\widehat{S};\ j=1,2,3,4, \tag{12j}$$

$$x_i\in\{0,1\}, \mathrm{Cap}_i\ge 0, \quad i\in R, \tag{12k}$$

in which the primal variables Cap_i^* can be given as follows:

$$\mathrm{Cap}_i^* = \sum_{\tau=0}^{(T/4)-1}\delta^{4\tau}\cdot\mathrm{Cap}_i = \mathrm{Cap}_i\cdot\left(\delta^0+\delta^4+\delta^8+\cdots+\delta^{T-8}+\delta^{T-4}\right) = \mathrm{Cap}_i\cdot\frac{1-\delta^T}{1-\delta^4} \approx \mathrm{Cap}_i\cdot\frac{1}{1-\delta^4}; \quad i\in R, \tag{12l}$$

in which δ^T can be approximated as zero when the number of stages T is large enough. Similarly, the parameters $r_i^*(j)$ could be given as

$$r_i^*(j) = \sum_{\tau=0}^{(T/4)-1}\delta^{4\tau}\cdot r_i(4\tau+j), \quad j=1,2,3,4; i\in R. \tag{12m}$$

We can assume the unit operational cost of candidate i at each stage t is the same, i.e., r_i. Then, (12m) can be further represented as

$$r_i^*(j) = r_i\cdot\frac{1-\delta^T}{1-\delta^4} \approx r_i\cdot\frac{1}{1-\delta^4}, \quad i\in R. \tag{12n}$$

Moreover, it is easy to know that Cap_i^*, $y_i^{*\widehat{s}}(j)$, $QL_i^{*\widehat{s}}(j)$, $QE_i^{*\widehat{s}}(j)$, $Q_i^{*\widehat{s}}(j)$, an d$QA_i^{*\widehat{s}}(j)$ are all nonnegative.

Till now, along with the stage reduction as shown in Section 3.1.1, the T-stage operations of the MSSP model is integrated into a four-stage model. The corresponding scenario tree of this intermediate model is shown in Figure 5.

3.2.2. Step 2 of Dimensionality Reduction. Further model transformation is required due to the stage reduction in Section 3.1.2. Notice that j (=1, 2, 3, 4) in the intermediate model (12) refers to the first four operational stages. Here, we use symbol t to replace the corresponding j and then integrate stage $t=2, 3, 4$ into the first stage ($t=1$) as illustrated in Section 3.1.2. The way how to transform is similar to that in Section 3.2.1.

We still focus on the operational stage under a specific stagewise scenario. Thus, the corresponding submodel can be described as follows:

$$\min \quad \sum_{t=1}^{4}\sum_{i\in R}\left\{\Delta t\cdot\left[c_i\cdot x_i\cdot\left(QL_i^*(t)-Q_{i\min}^{'*}(t)\right)-f\cdot K_i\cdot QE_i^*(t)\cdot H_i\right]\right\}, \tag{13a}$$

s.t.

$$QE_i^*(t)\le MM\cdot x_i,\quad i\in R;t=1,2,3,4, \tag{13b}$$

$$x_i\cdot N_{i\min}^*\le K_i\cdot QE_i^*(t)\cdot H_i\le N_{i\max}^*,\quad i\in R;t=1,2,3,4, \tag{13c}$$

$$V_{i\min}^*\cdot x_i\le y_i^*(t)\le\frac{1}{1-\delta^4}\cdot \mathrm{Cap}_i,\quad i\in R;t=1,2,3,4, \tag{13d}$$

$$y_i^*(t)-y_i^*(t-1)=\Delta t\cdot\left[Q_{i-1}^*(t)+\varepsilon_i^*(t)-Q_i^*(t)-QL_i^*(t)\right],\quad i\in R,t=1,2,3,4, \tag{13e}$$

$$Q_i^*(t)=QE_i^*(t)+QA_i^*(t),\quad i\in R;t=1,2,3,4, \tag{13f}$$

$$QF_{i\min}^*\le QE_i^*(t)+QA_i^*(t)\le QF_{i\max}^*,\quad i\in R;t=1,2,3,4, \tag{13g}$$

$$Q_{i\min}^*(t)\le QL_i^*(t)\le x_i\cdot Q_{i\max}^*+(1-x_i)\cdot Q_{i\min}^*(t),\quad i\in R;t=1,2,3,4, \tag{13h}$$

Step 5. The discount factor δ is still used to aggregate the value of the objective function at stage t (=2, 3, 4). Then, the objective function (13a) is transformed as

$$\min\sum_{t=1}^{4}\left\{\delta^{t-1}\cdot\sum_{i\in R}\Delta t\cdot\left[c_i\cdot x_i\cdot\left(QL_i(t)-Q_{i\min}'(t)\right)-f\cdot K_i\cdot QE_i(t)\cdot H_i\right]\right\}. \tag{14}$$

Step 6. Similar to Step 2, use dual multipliers $\beta_{7+k,t}$ ($k=1,\ldots,7$), to relax the k-th one of Constraints (13b)~(13h) of stage t. Thus, the operational optimization problem under stage $t=1$~4 ((13b)~(13h), (14)) can be transformed to an unconstrainted one:

$$\begin{aligned}\min\sum_{t=1}^{4}\Bigg\{&\delta^{t-1}\cdot\sum_{i\in R}\Delta t\cdot\left[c_i\cdot x_i\cdot\left(QL_i^*(t)-Q_{i\min}^{'*}(t)\right)-f\cdot K_i\cdot QE_i^*(t)\cdot H_i\right]\\&+\beta_{8,t}^{+}\cdot\left(QE_i^*(t)-MM\cdot x_i\right)\\&+\beta_{9,t}^{+}\cdot\left(K_i\cdot QE_i^*(t)\cdot H_i-N_{i\max}^*\right)+\beta_{9,t}^{-}\cdot\left(K_i\cdot QE_i^*(t)\cdot H_i-x_i\cdot N_{i\min}^*\right)\\&+\beta_{10,t}^{+}\cdot\left(y_i^*(t)-\frac{1}{1-\delta^4}\cdot Cap_i\right)+\beta_{10,t}^{-}\cdot\left(y_i^*(t)-V_{i\min}^*\cdot x_i\right)\\&+\beta_{11,t}\cdot\left(y_i^*(t)-y_i^*(t-1)-\Delta t\cdot\left(Q_{i-1}^*(t)+\varepsilon_i^*(t)-Q_i^*(t)-QL_i^*(t)\right)\right)\\&+\beta_{12,t}\cdot\left(Q_i^*(t)-QE_i^*(t)-QA_i^*(t)\right)\\&+\beta_{13,t}^{+}\cdot\left(QE_i^*(t)+QA_i^*(t)-QF_{i\max}^*\right)\\&+\beta_{13,t}^{-}\cdot\left(QE_i^*(t)+QA_i^*(t)-QF_{i\min}^*\right)\\&+\beta_{14,t}^{+}\cdot\left(QL_i^*(t)-x_i\cdot Q_{i\max}^*-(1-x_i)\cdot Q_{i\min}^*(t)\right)+\beta_{14,t}^{-}\cdot\left(QL_i^*(t)-Q_{i\min}^*(t)\right)\Bigg\},\end{aligned} \tag{15}$$

in which the dual multipliers follow the form $\beta_{7+k,t} = \delta^{t-1} \cdot \beta_{7+k}$. Hence, problem (15) can further be expressed as

$$\begin{aligned}
\min \sum_{t=1}^{4} \delta^{t-1} \cdot \Bigg\{ & \sum_{i \in R} \Delta t \cdot \left[c_i \cdot x_i \cdot \left(QL_i^*(t) - Q_{i\min}^{'*}(t) \right) - f \cdot K_i \cdot QE_i^*(t) \cdot H_i \right] \\
& + \beta_8^+ \cdot \left(QE_i^*(t) - MM \cdot x_i \right) \\
& + \beta_9^+ \cdot \left(K_i \cdot QE_i^*(t) \cdot H_i - N_{i\max}^* \right) + \beta_9^- \cdot \left(K_i \cdot QE_i^*(t) \cdot H_i - x_i \cdot N_{i\min}^* \right) \\
& + \beta_{10}^+ \cdot \left(y_i^*(t) - \frac{1}{1-\delta^4} \cdot \mathrm{Cap}_i \right) + \beta_{10}^- \cdot \left(y_i^*(t) - V_{i\min}^* \cdot x_i \right) \\
& + \beta_{11} \cdot \left(y_i^*(t) - y_i^*(t-1) - \Delta t \cdot \left(Q_{i-1}^*(t) + \varepsilon_i^*(t) - Q_i^*(t) - QL_i^*(t) \right) \right) \\
& + \beta_{12} \cdot \left(Q_i^*(t) - QE_i^*(t) - QA_i^*(t) \right) + \beta_{13}^+ \cdot \left(QE_i^*(t) + QA_i^*(t) - QF_{i\max}^* \right) \\
& + \beta_{13}^- \cdot \left(QE_i^*(t) + QA_i^*(t) - QF_{i\min}^* \right) \\
& + \beta_{14}^+ \cdot \left(QL_i^*(t) - x_i \cdot Q_{i\max}^* - (1 - x_i) \cdot Q_{i\min}^*(t) \right) + \beta_{14}^- \cdot \left(QL_i^*(t) - Q_{i\min}^*(t) \right) \Bigg\}.
\end{aligned} \tag{16}$$

Step 7. Similar to Step 3, the "integrated" primal variables are introduced to replace the corresponding discounted values, respectively. Taking $QL_i(t)$ and $Q_{i\max}$ as examples, we have:

$$QL_i^{**} = \sum_{t=1}^{4} \delta^{t-1} \cdot QL_i^*(t), \quad i \in R, \tag{17a}$$

$$Q_{i\max}^{**} = \sum_{t=1}^{4} \delta^{t-1} \cdot Q_{i\max}^*, \quad i \in R. \tag{17b}$$

Here, all the primal variables have double asterisks in their top right corner. Thus,

$$\begin{aligned}
\min \sum_{i \in R} \Bigg\{ & \Delta t \cdot \left[c_i \cdot x_i \cdot \left(QL_i^{**} - Q_{i\min}^{'**} \right) - f \cdot K_i \cdot QE_i^{**} \cdot H_i \right] + \beta_8^+ \cdot \left(QE_i^{**} - MM \cdot x_i \right) \\
& + \beta_9^+ \cdot \left(K_i \cdot QE_i^{**} \cdot H_i - N_{i\max}^{**} \right) + \beta_9^- \cdot \left(K_i \cdot QE_i^{**} \cdot H_i - x_i \cdot N_{i\min}^{**} \right) \\
& + \beta_{10}^+ \cdot \left(y_i^{**} - \frac{1}{1-\delta^4} \cdot \mathrm{Cap}_i^* \right) + \beta_{10}^- \cdot \left(y_i^{**} - V_{i\min}^{**} \cdot x_i \right) + \beta_{11} \cdot \left(y_i^{**} - y_i^{**}(0) - \Delta t \cdot \left(Q_{i-1}^{**} + \varepsilon_i^{**} - Q_i^{**} - QL_i^{**} \right) \right) \\
& + \beta_{12} \cdot \left(Q_i^{**} - QE_i^{**} - QA_i^{**} \right) + \beta_{13}^+ \cdot \left(QE_i^{**} + QA_i^{**} - QF_{i\max}^{**} \right) + \beta_{13}^- \cdot \left(QE_i^{**} + QA_i^{**} - QF_{i\min}^{**} \right) \\
& + \beta_{14}^+ \cdot \left(QL_i^{**} - x_i \cdot Q_{i\max}^{**} - (1 - x_i) \cdot Q_{i\min}^{**} \right) + \beta_{14}^- \cdot \left(QL_i^{**} - Q_{i\min}^{**} \right) \Bigg\},
\end{aligned} \tag{18}$$

in which

$$\mathrm{Cap}_i^* = \sum_{t=1}^{4} \delta^{t-1} \cdot \mathrm{Cap}_i = \frac{1-\delta^4}{1-\delta} \cdot \mathrm{Cap}_i, \quad i \in R, \tag{19}$$

and for each i ($\in R$), y_i^{**} is a discounted value that can be expressed as

$$y_i^{**} = \sum_{t=1}^{4} \delta^{t-1} \cdot y_i^*(t) = \sum_{t=1}^{4} \delta^{t-1} \cdot \sum_{\tau=0}^{(T/4)-1} \delta^{4\tau} \cdot y_i(4\tau + t). \tag{20}$$

From (20), we have

$$\delta \cdot y_i^{**} = \sum_{t=1}^{4} \delta^t \cdot \sum_{\tau=0}^{(T/4)-1} \delta^{4\tau} \cdot y_i(4\tau + t). \tag{21}$$

Refer to (20), the discounted value $y_i^{**}(0)$ can be denoted as

$$y_i^{**}(0) = \sum_{t=1}^{4} \delta^{t-1} \cdot y_i^{*}(t-1) = \sum_{t=1}^{4} \delta^{t-1} \cdot \sum_{\tau=0}^{(T/4)-1} \delta^{4\tau} \cdot y_i(4\tau + t - 1). \tag{22}$$

From (21) and (22), we have

$$y_i^{**}(0) = \delta \cdot y_i^{**} + \delta^0 \cdot y_i(0) - \delta^T \cdot y_i(T). \tag{23}$$

Using (23) to replace $y_i^{**}(0)$ in (18), we have the discounted objective as follows:

$$\begin{aligned}
\min \sum_{i \in R} \Big\{ & \Delta t \cdot \left[c_i \cdot x_i \cdot \left(QL_i^{**} - Q_{i\min}^{'**} \right) - f \cdot K_i \cdot QE_i^{**} \cdot H_i \right] \\
& + \beta_8^{+} \cdot \left(QE_i^{**} - MM \cdot x_i \right) \\
& + \beta_9^{+} \cdot \left(K_i \cdot QE_i^{**} \cdot H_i - N_{i\max}^{**} \right) + \beta_9^{-} \cdot \left(K_i \cdot QE_i^{**} \cdot H_i - x_i \cdot N_{i\min}^{**} \right) \\
& + \beta_{10}^{+} \cdot \left(y_i^{**} - \frac{1}{1-\delta^4} \cdot \frac{1-\delta^4}{1-\delta} \cdot \mathrm{Cap}_i \right) + \beta_{10}^{-} \cdot \left(y_i^{**} - V_{i\min}^{**} \cdot x_i \right) \\
& + \beta_{11} \cdot \left(y_i^{**} - \delta \cdot y_i^{**} - y_i(0) + \delta^T \cdot y_i(T) - \Delta t \cdot \left(Q_{i-1}^{**} + \varepsilon_i^{**} - Q_i^{**} - QL_i^{**} \right) \right) \\
& + \beta_{12} \cdot \left(Q_i^{**} - QE_i^{**} - QA_i^{**} \right) \\
& + \beta_{13}^{+} \cdot \left(QE_i^{**} + QA_i^{**} - QF_{i\max}^{**} \right) + \beta_{13}^{-} \cdot \left(QE_i^{**} + QA_i^{**} - QF_{i\min}^{**} \right) \\
& + \beta_{14}^{+} \cdot \left(QL_i^{**} - x_i \cdot Q_{i\max}^{**} - (1 - x_i) \cdot Q_{i\min}^{**} \right) + \beta_{14}^{-} \cdot \left(QL_i^{**} - Q_{i\min}^{**} \right) \Big\}.
\end{aligned} \tag{24}$$

Similarly, δ^T in (24) can be approximated as zero due to the large T. Then, by extracting the relaxed constraints from the above objective function, we have

$$\min \quad \sum_{i \in R} \Delta t \cdot \left[c_i \cdot x_i \cdot \left(QL_i^{**} - Q_{i\min}^{'**} \right) - f \cdot K_i \cdot QE_i^{**} \cdot H_i \right], \tag{25a}$$

s.t.

$$QE_i^{**} \le MM \cdot x_i, \quad i \in R, \tag{25b}$$

$$x_i \cdot N_{i\min}^{**} \le K_i \cdot QE_i^{**} \cdot H_i \le N_{i\max}^{**}, \quad i \in R, \tag{25c}$$

$$V_{i\min}^{**} \cdot x_i \le y_i^{**} \le \frac{1}{1-\delta} \cdot \mathrm{Cap}_i, \quad i \in R, \tag{25d}$$

$$(1-\delta) y_i^{**} - y_i(0) = \Delta t \cdot \left(Q_{i-1}^{**} + \varepsilon_i^{**} - Q_i^{**} - QL_i^{**} \right), \quad i \in R, \tag{25e}$$

$$Q_i^{**} = QE_i^{**} + QA_i^{**}, \quad i \in R \tag{25f}$$

$$QF_{i\min}^{**} \le QE_i^{**} + QA_i^{**} \le QF_{i\max}^{**}, \quad i \in R, \tag{25g}$$

$$Q_{i\min}^{**} \le QL_i^{**} \le x_i \cdot Q_{i\max}^{**} + (1 - x_i) \cdot Q_{i\min}^{**}, \quad i \in R. \tag{25h}$$

Step 8. Combine the above model with each scenario $\hat{s}$ ($\in \widehat{S}$), which is given in Section 3.1.2 and then integrate with the planning stage of the original MSSP model. Thus, the final DE model, which is a two-stage stochastic program, is developed as (26a)~(26k).

$$\begin{aligned}
\min & \sum_{i \in R} e \cdot \mathrm{Cap}_i + \Delta t \cdot \sum_{i \in R} \left(r_i^{**} \cdot \mathrm{Cap}_i \right) \\
& + \sum_{\hat{s} \in \widehat{S}} \left\{ p^{\hat{s}} \cdot \sum_{i \in R} \Delta t \cdot \left[c_i \cdot x_i \cdot \left(QL_i^{\hat{s}} - Q_{i\min}^{'**\hat{s}} \right) - f \cdot K_i \cdot QE_i^{\hat{s}} \cdot H_i \right] \right\},
\end{aligned} \tag{26a}$$

s.t.

$$R_{\min} \le \sum_{i \in R} x_i \le R, \tag{26b}$$

$$\mathrm{Cap}_i \le MM \cdot x_i, \quad i \in R, \tag{26c}$$

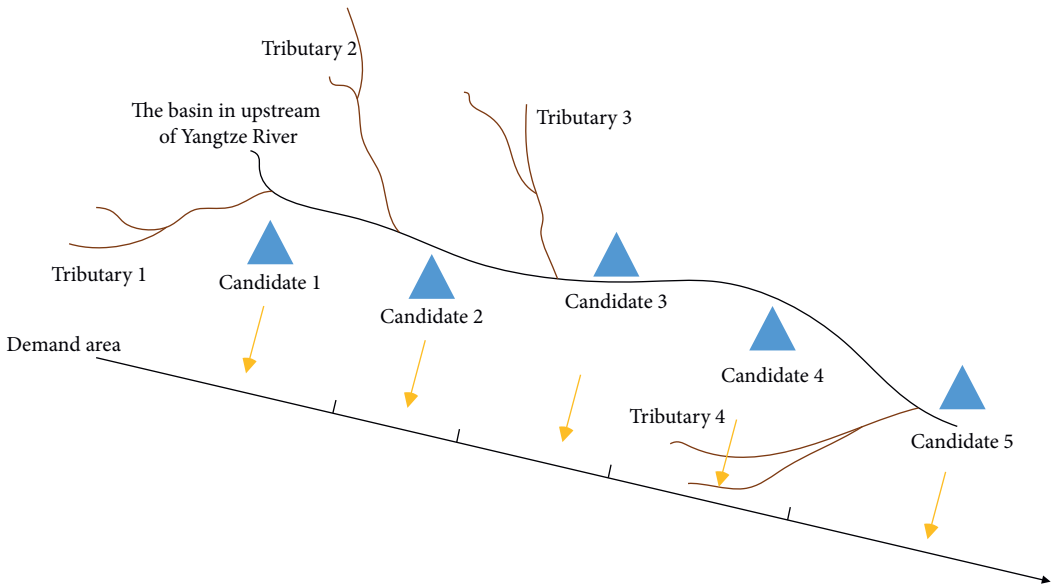

Figure 6: Illustration of hydropower station candidate in upstream of Yangtze river.

Table 3: Related parameters of hydropower station candidates.

Candidate i	K_i (kg/(m^2·s^2))	$N_{i\min}$ (KW)	$N_{i\max}$ (KW)	H_i (m)	c_i (RMB/m^3)	r_i (RMB/(m^3·year))	$Q_{i\max}$ (m$^3\times10^8$/h)
1	8.4	2546250	5092500	105	0.1	0.06	0.4676
2	8.4	1506750	3013500	93	0.125	0.072	0.8550
3	8.4	1500000	3000000	90	0.15	0.05	0.5177
4	8.4	3742500	7485000	110	0.175	0.08	0.4662
5	8.4	2625000	5250000	112	0.2	0.1	0.3301

Table 4: Minimum storage and limitation of water flows of hydropower station candidates.

Candidate i	$V_{i\min}$ (m$^3\times10^8$)	$QF_{i\min}$ (m$^3\times10^8$/h)	$QF_{i\max}$ (m$^3\times10^8$/h)
1	0.0311	0.0648	1.5732
2	0.0213	0.0468	1.7928
3	0.0131	0.0432	0.4248
4	0.0420	0.1620	3.5568
5	0.0115	0.0396	0.6912

Table 5: Random water inflows in each seasonal stage of each hydropower station candidate.

Candidate i	Inflows level	Water inflows (m$^3\times10^7$/h)			
		Spring	Summer	Autumn	Winter
1	H	1.2846	5.7276	2.2020	0.2031
	L	0.9867	4.3995	1.6914	0.1560
2	H	0.5932	1.6312	0.6677	0.0985
	L	0.4589	1.2617	0.5165	0.0762
3	H	0.5653	1.2849	0.6739	0.0969
	L	0.4441	1.0093	0.5294	0.0762
4	H	0.3645	0.5958	0.3356	0.0930
	L	0.2575	0.4209	0.2371	0.0657
5	H	0.6900	1.1642	0.5710	0.1515
	L	0.6482	1.0936	0.5363	0.1423
Probability	H	0.4	0.7	0.55	0.25
	L	0.6	0.3	0.45	0.75

Table 6: Predicted water inflows in each seasonal stage.

	Candidate i	Stage (t = 1, 2, 3, 4)			
		Spring	Summer	Autumn	Winter
Water inflows $\bar{\varepsilon}_i(t)$ (m$^3\times10^7$/h)	1	1.1059	5.3292	1.9722	0.1678
	2	0.5126	1.5203	0.5997	0.0817
	3	0.4926	1.2202	0.6089	0.0813
	4	0.3003	0.5433	0.2912	0.0725
	5	0.6649	1.1431	0.5554	0.1446

$$QE_i^{\hat{s}} \le MM \cdot x_i, \quad \hat{s} \in \hat{S}; i \in R, \tag{26d}$$

$$x_i \cdot N_{i\min}^{**} \le K_i \cdot QE_i^{\hat{s}} \cdot H_i \le N_{i\max}^{**}, \quad \hat{s} \in \hat{S}; i \in R, \tag{26e}$$

$$V_{i\min}^{**} \cdot x_i \le y_i^{\hat{s}} \le \frac{1}{1-\delta} \cdot \mathrm{Cap}_i, \quad \hat{s} \in \hat{S}; i \in R, \tag{26f}$$

$$(1-\delta) y_i^{\hat{s}} - y_i' = \Delta t \cdot \left[Q_{i-1}^{\hat{s}} + \varepsilon_i^{**\hat{s}} - Q_i^{\hat{s}} - QL_i^{\hat{s}} \right], \hat{s} \in \hat{S}; \ i \in R \tag{26g}$$

$$Q_i^{\hat{s}} = QE_i^{\hat{s}} + QA_i^{\hat{s}}, \quad \hat{s} \in \hat{S}; i \in R, \tag{26h}$$

$$QF_{i\min}^{**} \le QE_i^{\hat{s}} + QA_i^{\hat{s}} \le QF_{i\max}^{**}, \quad \hat{s} \in \hat{S}; i \in R, \tag{26i}$$

Table 7: Predicted water demands in each seasonal stage.

	Candidate i	Stage ($t = 1, 2, 3, 4$)			
		Spring	Summer	Autumn	Winter
Water demands $\overline{Q}_{i\min}(t)$ ($m^3 \times 10^6$/h)	1	0.1871	0.2299	0.2196	0.1218
	2	0.3420	0.4204	0.4016	0.2228
	3	0.2071	0.2546	0.2432	0.1349
	4	0.1865	0.2292	0.2189	0.1215
	5	0.1321	0.1623	0.1551	0.0860

Table 8: Estimation gaps of the DE model.

Discount factor δ	Planning stages		
	$T = 4$	$T = 8$	$T = 12$
0.99	25.53%	22.51%	19.94%
0.95	17.89%	6.71%	−2.99%
0.90	8.72%	−9.76%	−24.32%
0.85	−0.51%	−23.20%	−39.73%
0.80	−9.16%	−34.34%	−50.97%
0.75	−17.29%	−43.92%	−59.59%
0.70	−24.72%	−51.99%	−66.37%
0.65	−31.44%	−58.62%	−71.61%
0.60	−37.53%	−64.02%	−75.64%

Table 9: Average computational time (ms) of both models.

Model	$T = 4$	$T = 8$	$T = 12$
DE model	1224.00	1206.44	1170.22
MSSP model	300.22	3095.56	159373.22

Table 10: Probabilistic distributions of water inflows and demands in each seasonal stage.

Stage	Water inflows (p_{1H}, p_{1M}, p_{1L})	Water demands (p_{2H}, p_{2L})
Spring	(0.2, 0.4, 0.4)	(0.5, 0.5)
Summer	(0.5, 0.4, 0.1)	(0.65, 0.35)
Autumn	(0.3, 0.5, 0.2)	(0.6, 0.4)
Winter	(0.1, 0.3, 0.6)	(0.3, 0.7)

$$Q_{i\min}^{**\widehat{s}} \le QL_i^{\widehat{s}} \le x_i \cdot Q_{i\max}^{**} + (1 - x_i) \cdot Q_{i\min}^{**\widehat{s}}, \quad \widehat{s} \in \widehat{S}; i \in R, \tag{26j}$$

$$\mathrm{Cap}_i, y_i^{\widehat{s}}, QL_i^{\widehat{s}}, QE_i^{\widehat{s}}, Q_i^{\widehat{s}}, QA_i^{\widehat{s}} \ge 0, \quad x_i \in \{0, 1\}, i \in R; \widehat{s} \in \widehat{S}, \tag{26k}$$

in which the discounted value of water inflows and demands $\varepsilon_i^{**\widehat{s}}$ and $Q_{i\min}^{**\widehat{s}}$ ($i \in R$) can be obtained similar to the way used in formula (3). Besides, r_i^{**} in (26a) is an integrated variable:

$$r_i^{**} = \sum_{t=1}^{4} \delta^{t-1} \cdot r_i^*(t), \quad i \in R. \tag{26l}$$

Moreover, for simplicity, the double asterisks of the decision variables are omitted.

After transformation, the planning decisions x_i and Cap_i remain unchanged, while the operational stages are aggregated. Therefore, the proposed approach not only keeps the future impacts but also reduces the solving complexity.

4. Experimental Study

To validate the applicability of our proposed approach, we give the data of a case in Section 4.1 at first. Then, based on this case, we compare our approach with the MSSP model in the small-scale setting in Section 4.2. Furthermore, we apply our approach to an overlong-term case in Section 4.3 and finally implement sensitivity analysis in Section 4.4.

4.1. Description of the Case. Yangtze River flows through 11 provinces in China with a drainage area of 1.8 million square kilometers. The whole river can be divided into the upstream, midstream, and downstream, among which the basin with a length of 1030 km in upstream is studied here. According to Wang et al. [45], five hydropower station candidates could be considered in this basin. Its schematization is shown in Figure 6 which also involves the main tributaries.

Among the five hydropower station candidates, at least two of them should be chosen in the plan. Unit construction fee (e) and unit profit of power generation (f) in Table 1 are set to be 5.09 (RMB/m^3) and 0.25 (RMB/KWh), respectively [46]. Related parameters regarding five candidates are displayed in Table 3. Once the hydropower station candidate is chosen, the planned lowest water storage and upper and lower limit of water discharge are shown in Table 4. The initial water flows from upstream to each hydropower station candidate is set to be 0.2141, 0.0988, 0.0942, 0.0429, and 0.1080 ($m^3 \times 10^8$/h), respectively. And the initial water storage of each chosen hydropower station is assumed as the twice of the lowest water storage.

4.2. Comparison with the MSSP Model by Small-Scale Cases. The developed DE model is an approximate version of the MSSP model (1). In this section, we aim to evaluate the performance of our approach by comparing the planning decisions as well as the operational performance with these of the MSSP model. Due to the curse of dimensionality faced by the MSSP model, we consider small-scale cases based on Section 4.1.

4.2.1. Parameters in Small-Scale Experiments. To limit the dimensionality here, we set the planning horizon as 1, 2, and 3 years, respectively. According to the seasonal features of which, one year is divided into four stages: spring (March to May), summer (June to August), autumn (September to November), and winter (December to February). Then, each stage has 2160 (h) (i.e., Δt). Thus, the number of operational stages T is 4, 8, and 12, respectively. Besides, we merely consider the uncertainty caused by water inflows. Two kinds of stochastic outside water inflows (H, L), as well as the

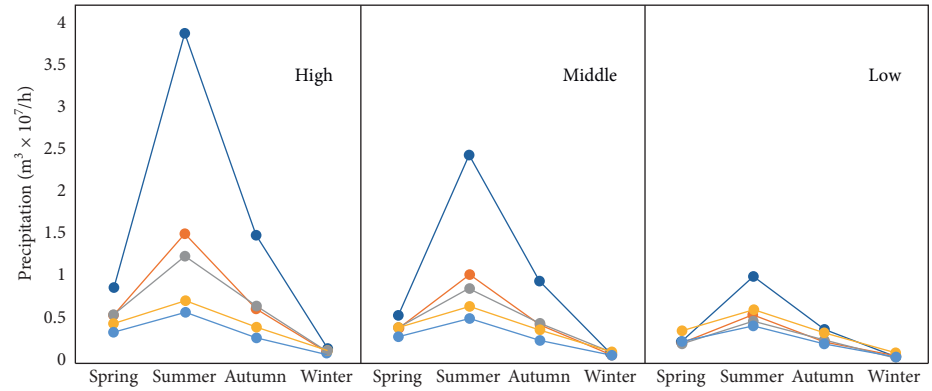

	Spring	Summer	Autumn	Winter	Spring	Summer	Autumn	Winter	Spring	Summer	Autumn	Winter
1	0.8675	3.8679	1.487	0.1372	0.5451	2.4303	0.9343	0.0862	0.2226	0.9927	0.3816	0.0352
2	0.5468	1.5035	0.6155	0.0908	0.3702	1.0181	0.4168	0.0615	0.1937	0.5327	0.2181	0.0322
3	0.5412	1.2302	0.6452	0.0928	0.3724	0.8464	0.4439	0.0639	0.2035	0.4625	0.2426	0.0349
4	0.4292	0.7015	0.3951	0.1095	0.3968	0.6487	0.3654	0.1013	0.3645	0.5958	0.3356	0.093
5	0.3378	0.57	0.2795	0.0742	0.2912	0.4913	0.2409	0.0639	0.2445	0.4126	0.2023	0.0537

Stage

Figure 7: High, middle, low-level precipitation in each seasonal stage of each hydropower station candidate.

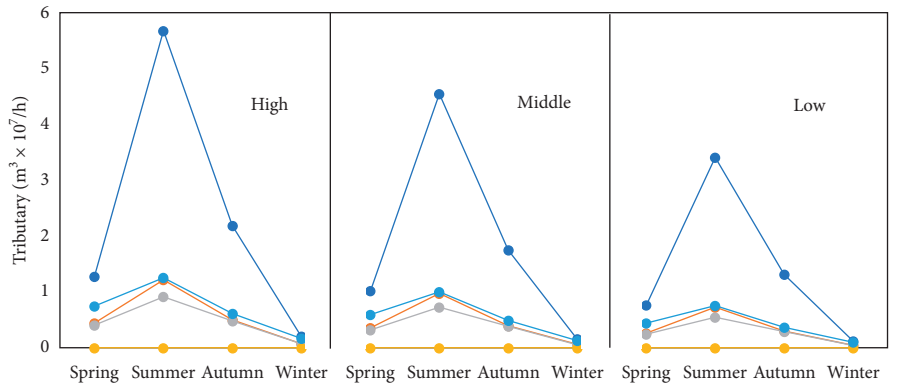

	Spring	Summer	Autumn	Winter	Spring	Summer	Autumn	Winter	Spring	Summer	Autumn	Winter
1	1.2735	5.6781	2.183	0.2014	1.0188	4.5425	1.7464	0.1611	0.7641	3.4068	1.3098	0.1208
2	0.4419	1.2151	0.4974	0.0734	0.3535	0.9721	0.3979	0.0587	0.2651	0.7291	0.2984	0.044
3	0.401	0.9113	0.478	0.0688	0.3208	0.7291	0.3824	0.055	0.2406	0.5468	0.2868	0.0413
4	0	0	0	0	0	0	0	0	0	0	0	0
5	0.7425	1.2527	0.6144	0.163	0.594	1.0022	0.4915	0.1304	0.4455	0.7516	0.3686	0.0978

Stage

Figure 8: High, middle, low-level tributary in each seasonal stage of each hydropower station candidate.

corresponding probabilities (p_{1H}, p_{1L}), in each seasonal stage are given in Table 5. The constant water inflows and water demands used in the simplification are displayed in Tables 6 and 7, respectively. The acceptance level of the water spill is assumed as twice of the demands.

Because the random inflows fluctuate with seasons, we assume the water inflows of each candidate take the same uncertain level in each season. Thus, for the MSSP model, 16(=2^4), 256(=2^8), and 4096(=2^{12}) stagewise scenarios are constructed, respectively. Furthermore, according to the generation and simplification process of the scenario set displayed in Section 3.1, 16 scenarios are generated for the two-stage DE model. Assume that spring is the first operational season. The discount factor δ used in the DE model is set to be 0.99, 0.95, . . ., 0.60, respectively.

4.2.2. Computational Results. We optimally solve the DE model and the MSSP model by IBM ILOG CPLEX 12.6.3 on a PC with 8 GB memory and a CPU at 2.5 GHz.

It is found that the DE model can generate the same planning results with the MSSP model for all these small-scale cases. Besides, in terms of the operations, the DE model considers the multistage operational impacts by the aggregated way. Hence, it is interesting to observe how accurate the DE model is in the estimation of the future operational performance of the cascade hydropower system. We use DE_2nd and MSSP_2nd to denote the operational performance generated by the DE model and the MSSP model, respectively. Table 8 displays the estimation gap (=(DE_2nd-MSSP_2nd)/MSSP_2nd) under different discount factors.

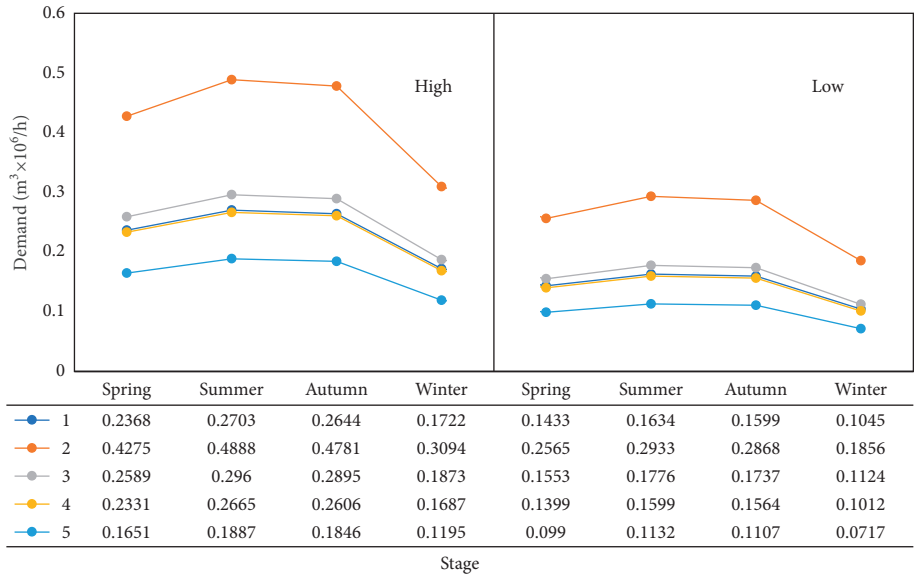

Figure 9: High, low-level water demand in each seasonal stage of each hydropower station candidate.

Table 11: Predicted water inflows and demands in each seasonal stage.

	Candidate i	Stage ($t = 1, 2, 3, 4$)			
		Spring	Summer	Autumn	Winter
Water inflows $\bar{\varepsilon}_i(t)$ ($m^3 \times 10^7$/h)	1	1.4484	8.0021	2.7796	0.2017
	2	0.6708	2.2816	0.8445	0.0982
	3	0.6433	1.8019	0.8559	0.0975
	4	0.3904	0.6698	0.3683	0.0971
	5	0.8462	1.6252	0.7486	0.1729
Water demands $\overline{Q}_{i\min}(t)$ ($m^3 \times 10^6$/h)	1	0.1871	0.2299	0.2196	0.1218
	2	0.3420	0.4204	0.4016	0.2228
	3	0.2071	0.2546	0.2432	0.1349
	4	0.1865	0.2292	0.2189	0.1215
	5	0.1321	0.1623	0.1551	0.0860

Table 12: Planning decisions and the cost/benefit.

Candidate i	Cap_i ($m^3 \times 10^8$)	Operational cost (RMB $\times 10^8$)	Penalty cost (RMB $\times 10^8$)	Benefit (RMB $\times 10^8$)
1	0.214	0.063	347.191	550.002
4	0.043	0.017	0	808.401
5	0.108	0.053	0	567.013

Table 13: Operational decisions under scenario 16.

Candidate i	1	2	3	4	5
QL_i^{16} ($m^3 \times 10^8$/h)	2.154	0.066	0.040	0.036	0.026
QE_i^{16} (m^3/h)	115476	0	0	162013	111607
QA_i^{16} ($m^3 \times 10^8$/h)	4.690	6.714	8.496	9.246	11.014
y_i^{16} ($m^3 \times 10^8$)	4.282	0	0	0.858	2.161
Q_i^{16} ($m^3 \times 10^8$/h)	4.691	6.714	8.496	9.248	11.015

Table 14: Operational decisions under scenario 1281.

Candidate i	1	2	3	4	5
QL_i^{1281} ($m^3 \times 10^8$/h)	0.874	0.073	0.044	0.040	0.028
QE_i^{1281} (m^3/h)	115476	0	0	162013	111607
QA_i^{1281} ($m^3 \times 10^8$/h)	5.171	6.936	8.496	9.219	10.847
y_i^{1281} ($m^3 \times 10^8$)	4.282	0	0	0.858	0.230
Q_i^{1281} ($m^3 \times 10^8$/h)	5.172	6.936	8.496	9.221	10.848

Table 15: Corresponding cost terms and benefit.

Operational stages	Candidate i	Total performance (RMB $\times 10^8$)	Operational cost (RMB $\times 10^8$)	Penalty cost (RMB $\times 10^8$)	Power generation (RMB $\times 10^8$)
$T=40$	1	471.396	0.063	77.453	550.002
	4	808.165	0.017	0	808.401
	5	566.410	0.053	0	567.013
	Total	1845.971	0.134	77.453	1925.416
$T=80$	1	236.358	0.063	312.491	550.002
	4	808.165	0.017	0	808.401
	5	566.410	0.053	0	567.013
	Total	1610.933	0.134	312.491	1925.416
$T=120$	1	205.604	0.063	343.245	550.002
	4	808.165	0.017	0	808.401
	5	566.410	0.053	0	567.013
	Total	1580.179	0.134	343.245	1925.416
$T=160$	1	201.653	0.063	347.196	550.002
	4	808.165	0.017	0	808.401
	5	566.410	0.053	0	567.013
	Total	1576.228	0.134	347.196	1925.416
$T=200$	1	201.150	0.063	347.699	550.002
	4	808.165	0.017	0	808.401
	5	566.410	0.053	0	567.013
	Total	1575.725	0.134	347.699	1925.416

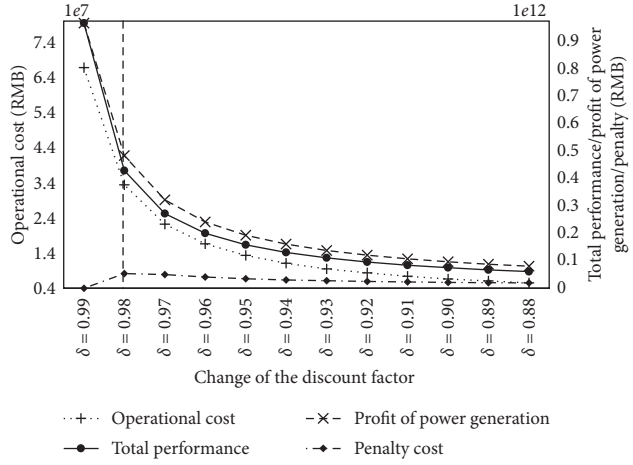

Figure 10: Cost and profit of power generation under the different discount factors.

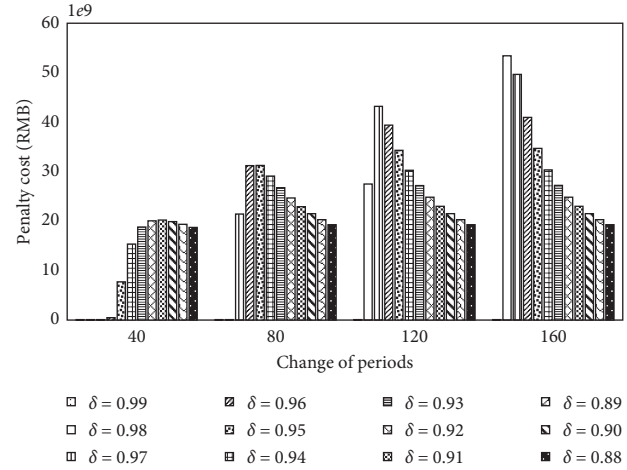

Figure 11: Penalty cost under the different discount factors and planning horizons.

It is found that the operational performance generated by the DE model significantly varies with the discount factors. Specifically, when δ is large, more future impacts would be taken into account which results in the overestimation. Hence, the estimation gap is positive. With the decrease of δ, less future performance would be discounted. Thus, the estimation gap tends to be negative gradually. It also means that the DE model can generate accurate estimation of the future operational performance by choosing the appropriate discount factor.

Moreover, the computational time of the DP model outperforms that of the MSSP model greatly especially when the horizon is large, as shown in Table 9.

In summary, the DP model can yield the same location decisions with the MSSP model and the accurate estimation of the future operational performance by choosing a suitable discount factor, while less calculational time is required.

4.3. Real Case Study. Section 4.2 validates the effectiveness of our proposed DE model in the small-scale setting. In this section, we further apply our approach to a large-scale case to illustrate its applicability.

4.3.1. Parameters in the Large-Scale Case. Based on the case given in Section 4.1, we consider the 40-year planning horizon (i.e., $T=160$). Three kinds of stochastic water inflows (H, M, and L) and two kinds of stochastic water demands (H, L) are taken into account in each seasonal stage. The corresponding probabilities of two random variables are (p_{1H}, p_{1M}, p_{1L}) and (p_{2H}, p_{2L}) as shown in Table 10. Refer to

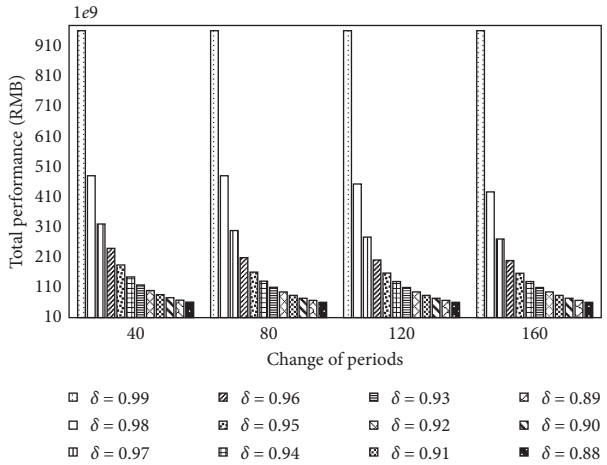

Figure 12: Total performance under the different discount factors and planning horizons.

Wang et al. [47] and Yang and Zhang [48]. Uncertain water inflows which mainly include precipitation and water from main tributaries (drainage areas larger than ten thousand square kilometers) are given in Figures 7 (precipitation) and 8 (tributary), respectively. Random demands are given in Figure 9. Besides, the predicted water inflows and demands used in the DE model are shown in Table 11, and the random acceptance level of water spill is also assumed as twice of the corresponding demands.

Thus, the number of stagewise scenarios in the MSSP model is up to $6^{160}(\approx 3.193 \times 10^{124})$, which is impossible to handle exactly. By the DE model, the number of scenarios is reduced to 1296. The discount factor δ is set to be 0.95 here.

4.3.2. Computational Results of the DE Model. The optimal solution of the DE model can be obtained by within 2047 (ms) by IBM ILOG CPLEX 12.6.3, in which Candidates 1, 4, and 5 are selected. Table 12 shows the capacity decisions and the operational performance, including the operational cost, the penalty cost, and the profit of power generation, of each selected candidate. The total performance value including the planning stage and the operational stages is 1.576×10^{11} (RMB).

We further observe two extreme scenarios. One is scenario 16 (high-level inflows and low-level demands in all four seasons), and another scenario is 1281 (low-level inflows and high-level demands in all four seasons). The corresponding scenario-dependent operational results of five hydropower station candidates under two scenarios are shown in Tables 13 and 14, respectively.

As shown in Tables 13 and 14, the daily scheduling strategies would be adjusted according to different scenarios. First, in terms of loss flow (QL), when scenario 16 happens, the value is relatively high in hydropower station 1 to prevent the flood (see Table 13). While if scenario 1281 occurs, the loss flow merely satisfies demand (see Table 14). Then, regarding water storage (y), the value is high in hydropower station 5 under scenario 16 due to the high-level inflows and the low-level demands. However, scenario 1281, which represents the low-level inflows and the high-level demands, requires hydropower stations to utilize their storage efficiently and then results in low water storage. Furthermore, in the computational results, the scheduling strategies would ensure that the values of water discharge (Q) are between the upper and lower limits in both scenarios, making it capable of preventing flood and drainage. Notice that the water discharges of power generation under two scenarios are the same and the upper limit of output has been reached under both scenarios. Thus, the scheduling strategies can always pursue maximum benefits of power generation under different scenarios. In such a way, the proposed DE model can optimize the global performance in the uncertain setting.

4.4. Sensitivity Analysis. In this section, we carry out the sensitivity analysis to reveal how critical parameters influence the strategic decisions and the performance of the cascade hydropower stations. Because one of the merits is to handle overlong stochasticity by the idea of aggregation, two natural concerns are how long and how much are discounted. Here, we focus on the planning horizon (T) and the discount factor (δ).

4.4.1. Sensitivity Analysis of the Planning Horizon. The planning horizon (T) is one of the main factors causing the curse of dimensionality [19, 41]. The DE model aggregates the multiple operational stages, but T would influence the results of the model transformation. Hence, we focus on the length of the planning horizon here. Considering the long-lasting effects of the location decisions, we set the length of the planning horizon as 10, 20, 30, 40, and 50 years, respectively. That is, we consider $T = 40$, 80, 120, 160, and 200. Other parameters are the same as those in Section 4.3.

After calculation, it is found that the decisions of location and capacity under different T, which are the planning results we care about in our study, are the same as these of $T = 160$ (see Table 12). It means these planning horizons would not alter the strategic decisions of the DE model.

Furthermore, the cost terms and the profit of power generation are displayed in Table 15. It is found that the operational cost and the profit of power generation remain unchanged while the penalty approaches to be stable with the increase of T. Specifically, the operational cost is the capacity-related cost within the planning horizon. In the DE model, the impacts of the capacity-related cost are aggregated by δ^T, respectively. When T is extremely large, δ^T can be approximated as zero, see (12l) and (12n). Hence, the operational cost keeps unchanged. Besides, to calculate the benefit of the power generation, it is found that the maximum output is reached in our cases. Thus, after aggregation by δ^T, the benefit of the power generation also remains constant. Moreover, the penalty of hydropower station 4 and 5 are zero because the loss flows are smaller than the corresponding penalty thresholds. However, T would influence y_i^{**} (see (20)) at first and then the loss flow by constraints (25e). Hence, the penalty of hydropower station 1 would increase gradually until coming to be stable.

Based on the above three terms, with the increase of T, the total performance also shows a trend of increasing first and then approaches to be stable. This result coincides with the essence of the DE model. Specifically, the farther the future is, the fewer the impacts would be taken into account. Thus, the results would close to be stable finally. It is also in accord with the decision-making in the real-world, i.e., the coming future would be put more emphasis than the superfar future. Hence, when T is large enough, the calculational results of the DE model would tend to be stable. It means that the DE model could describe the steady results of long-term stochastic operations. Thus, for the decision-makers (DMs), it is not necessary to increase the planning horizon infinitely.

4.4.2. Sensitivity Analysis of the Discount Factor. Discount factor (δ) is an exogenous variable introduced by the DE model to help to reduce dimensionality. In Section 4.2, we have shown that the DE model can generate accurate operational performance estimation by selecting appropriate δ. In this section, we further explore the impacts of the discount factor in the large-scale setting. We vary it as 0.99, 0.98, ..., 0.88. Other parameters are the same as those of Section 4.3.

The calculational results show the discount factors in the value range above will not influence the final strategic decisions. Besides, the operational cost, the penalty cost, the profit of power generation, and the total performance under different discount factors are shown in Figure 10. Firstly, it is shown that, with the decrease of the discount factor, both the operational cost and the profit decline with a decreasing speed since they are discounted more. Moreover, in terms of the penalty cost, it remains zero when δ is large (0.99). This is because the discounted penalty threshold also decreases but is still larger than the loss flow. Then, the penalty cost increases significantly with the decline of δ to 0.98. The reason is that the discounted penalty threshold begins to be smaller than the loss flow, leading to the larger penalty. Finally, with its continuous decrease (less than 0.98), δ dominates the penalty term which makes the aggregated penalty smaller.

These results indicate different discount factors will not influence the location decisions but result in the variation of the operational performance. Hence, the DMs should carefully choose the discount factor if they want to get an accurate estimation of the operational performance.

4.4.3. Mutual Effects of Two Factors. We further investigate the mutual impacts of two factors on decisions and objective terms. We set T as 40, 80, 120, 160, and 200 and δ as 0.99, 0.98, ..., 0.88 and then calculate the model under each combination of two kinds of parameters.

From the calculational results, we find that the locations and capacities of hydropower stations remain unchanged under the different combinations of planning horizon and discount factor. Given a δ, the operational cost and the profit of power generation will not be influenced by the change of T, which is similar to Table 15. Hence, we focus on the penalty and the total operational performance.

Figure 11 shows the varying pattern of the penalty with the decrease of δ under each T. Specifically, the penalty increases first and then decreases. The reason is the same as that in Figure 10. However, with the increase of T, the peak point would appear earlier. It is because bigger T can bring significant discounting effects due to δ^T.

Furthermore, we show the change of the total performance in Figure 12. The variations under different T are very similar. Specifically, with the decline of δ, the total performance gradually decreases and finally tends to be stable. Besides, as δ becomes smaller, the total performance would reach its steady state within a shorter planning horizon, specifically, around 120 periods when $\delta = 0.96$ and around merely 40 periods when $\delta = 0.90$. Thus, we conclude that when the low δ is considered, the DMs could only consider a relatively shorter planning horizon since the impacts in the long-term future would be significantly discounted.

5. Conclusions and Future Research Directions

The integrated planning of cascade hydropower stations, which takes the operational strategies under future uncertainty into account, can bring global benefit. An MSSP model is developed to deal with the location and capacity decisions of cascade hydropower stations with the consideration of the expected long-term performance. To address the computational issue caused by the overlong stochasticity, a dimensionality reduction approach based on DE is designed to transform the MSSP model into a two-stage stochastic programming model, in which future impacts remain by aggregating the operational stages together. Thus, the optimization of the large-scale hydropower stations could be addressed regardless of the number of operational stages.

Experiments based on Yangtze River in China are implemented. First, by the comparison with the MSSP model under the small-sized cases, it is found that our approach can obtain the same planning results and accurate estimation for future operational performance with a short computational time. Then, a large-scale case is studied to show how the approach is applied to solve a practical problem. Moreover, to evaluate the influence of critical parameters in the proposed DE model, sensitivity analysis is conducted based on the planning horizon and the discount factor. The results reveal that our model is robust to different parameter settings to obtain stable location-related planning results, while the estimation of the future performance would be influenced by the planning horizon and the discount factor. The corresponding observations and implications are also obtained from the results.

In the future, we can extend our study in the following aspects. First, the discount factor plays an important role in our study. Specifically, it not only discounts the future impacts to get the so-called net present value but also has the internal relationship between the dual multipliers. Thus, it influences the accuracy of the future estimation of the DE model. In this paper, we follow the way of Grinold [42] and King and Wallace [43] to give the discount factor directly. But, how to select the appropriate discount factor to get

better performance estimation should be considered in the future study. It is a hard issue but deserves further effort. Second, the minimum installed power and the nonlinearity, like the stage-storage curve, are ignored in this paper. The consideration of these requirements and constraints could help to improve the applicability of our approach to practical problems, which leaves certain spaces for future study. Finally, in this paper, the impacts of time-varying stochastic operations are considered in the form of expected value. Another popular way is to formulate the objective of Value-at-Risk or Conditional Value-at-Risk to incorporate the DMs' risk attitudes. Then, is it possible to utilize the characteristics of Value-at-Risk or Conditional Value-at-Risk to facilitate our scenario tree reduction? It is another interesting research direction.

Data Availability

All data included in this paper are available upon request by contact with the corresponding author.

Conflicts of Interest

The authors declare that there are no conflicts of interest regarding the publication of this paper.

Acknowledgments

The authors wish to express their gratitude to the five anonymous referees for their constructive criticism, which led to substantial improvements of the paper. This research was partly supported by the National Natural Science Foundation of China (Grant no. 71971053, 71832001, 71572033) and the MOE (Ministry of Education in China) Project of Humanities and Social Sciences (Grant no. 18YJA630129).

References

[1] A. Afshar, F. Sharifi, and M. R. Jalali, "Non-dominated archiving multi-colony ant algorithm for multi-objective optimization: application to multi-purpose reservoir operation," *Engineering Optimization*, vol. 41, no. 4, pp. 313–325, 2009.

[2] P. Fraenkel, O. Paish, V. Bokalders, A. Harvey, and A. E. Brown, *Micro-Hydro Power: A Guide for Development Workers*, IT Publications Ltd., London, UK, 1999.

[3] G. Eiger and U. Shamir, "Optimal operation of reservoirs by stochastic programming," *Engineering Optimization*, vol. 17, no. 4, pp. 293–312, 1991.

[4] A. Gjelsvik, B. Mo, and A. Haugstad, "Long- and medium-term operations planning and stochastic modelling in hydro-dominated power systems based on stochastic dual dynamic programming," in *Handbook of Power Systems I; Energy Systems; Section 2*, Springer, Berlin, Germany, 2010.

[5] C. Cheng, S. Wang, K.-W. Chau, and X. Wu, "Parallel discrete differential dynamic programming for multireservoir operation," *Environmental Modelling & Software*, vol. 57, pp. 152–164, 2014.

[6] C. Wang, J. Zhou, P. Lu, and L. Yuan, "Long-term scheduling of large cascade hydropower stations in Jinsha river, China," *Energy Conversion and Management*, vol. 90, no. 15, pp. 476–487, 2015.

[7] Y. Xu and Y. Mei, "A modified water cycle algorithm for long-term multi-reservoir optimization," *Applied Soft Computing*, vol. 71, pp. 317–332, 2018.

[8] D. G. Larentis, W. Collischonn, F. Olivera, and C. E. M. Tucci, "GIS-based procedures for hydropower potential spotting," *Energy*, vol. 35, no. 10, pp. 4237–4243, 2010.

[9] B. C. Kusre, D. C. Baruah, P. K. Bordoloi, and S. C. Patra, "Assessment of hydropower potential using GIS and hydrological modeling technique in Kopili river basin in Assam (India)," *Applied Energy*, vol. 87, no. 1, pp. 298–309, 2010.

[10] B. Serpoush, M. Khanian, and A. Shamsai, "Hydropower plant site spotting using geographic information system and a MATLAB based algorithm," *Journal of Cleaner Production*, vol. 152, pp. 7–16, 2017.

[11] A. Z. Zaidi and M. Khan, "Identifying high potential locations for run-of-the-river hydroelectric power plants using GIS and digital elevation models," *Renewable and Sustainable Energy Reviews*, vol. 89, pp. 106–116, 2018.

[12] J. Hosnar and A. Kovač-Kralj, "Mathematical modelling and MINLP programming of a hydro system for power generation," *Journal of Cleaner Production*, vol. 65, no. 4, pp. 194–201, 2014.

[13] C. Loannidou and J. R. O'Hanley, "Eco-friendly location of small hydropower," *European Journal of Operational Research*, vol. 264, pp. 907–918, 2018.

[14] D. A. G. Vieira, L. S. M. Guedes, A. C. Lisboa, and R. R. Saldanha, "Formulations for hydroelectric energy production with optimality conditions," *Energy Conversion and Management*, vol. 89, pp. 781–788, 2015.

[15] C. T. Cheng, J. J. Shen, and X. Y. Wu, "Short-term scheduling for large-scale cascaded hydropower systems with multi-vibration zones of high head," *Journal of Water Resource Planning and Management*, vol. 138, no. 3, pp. 257–267, 2012.

[16] C. Li, J. Zhou, S. Ouyang, X. Ding, and L. Chen, "Improved decomposition-coordination and discrete differential dynamic programming for optimization of large-scale hydropower system," *Energy Conversion and Management*, vol. 84, pp. 363–373, 2014.

[17] X. Li, J. Wei, T. Li, G. Wang, and W. W.-G. Yeh, "A parallel dynamic programming algorithm for multi-reservoir system optimization," *Advances in Water Resources*, vol. 67, no. 4, pp. 1–15, 2014b.

[18] Z.-K. Feng, W.-J. Niu, C.-T. Cheng, and S.-L. Liao, "Hydropower system operation optimization by discrete differential dynamic programming based on orthogonal experiment design," *Energy*, vol. 126, pp. 720–732, 2017.

[19] Z.-K. Feng, W.-J. Niu, C.-T. Cheng, and X.-Y. Wu, "Optimization of hydropower system operation by uniform dynamic programming for dimensionality reduction," *Energy*, vol. 134, pp. 718–730, 2017.

[20] C. Cheng, J. Shen, X. Wu, and K.-W. Chau, "Short-term hydroscheduling with discrepant objectives using multi-step progressive optimality algorithm," *JAWRA Journal of the American Water Resources Association*, vol. 48, no. 3, pp. 464–479, 2012.

[21] Z.-K. Feng, W.-J. Niu, and C.-T. Cheng, "Optimizing electrical power production of hydropower system by uniform progressive optimality algorithm based on two-stage search mechanism and uniform design," *Journal of Cleaner Production*, vol. 190, pp. 432–442, 2018.

[22] W.-J. Niu, Z.-K. Feng, C.-T. Cheng, and X.-Y. Wu, "A parallel multi-objective particle swarm optimization for cascade hydropower reservoir operation in southwest China," *Applied Soft Computing*, vol. 70, pp. 562–575, 2018.

[23] G. Zhang, Y. Wu, F. Zhang, and X. Liu, "Application of adaptive quantum particle swarm optimization algorithm for optimal dispatching of cascaded hydropower stations," in *Intelligent Computing Theories and Applications, Lecture Notes in Computer Science*, Springer, Berlin, Germany, 2012.

[24] J. Zhang, Q. Tang, Y. Chen, and S. Lin, "A hybrid particle swarm optimization with small population size to solve the optimal short-term hydro-thermal unit commitment problem," *Energy*, vol. 109, pp. 765–780, 2016.

[25] S. Ouyang, J. Zhou, C. Li, X. Liao, and H. Wang, "Optimal design for flood limit water level of cascade reservoirs," *Water Resources Management*, vol. 29, no. 2, pp. 445–457, 2015.

[26] C.-T. Tseng, Y.-L. Lee, and C.-C. Chou, "An ambient intelligence system for water release scheduling in cascade hydropower systems," *Journal of Ambient Intelligence and Humanized Computing*, vol. 6, no. 1, pp. 47–55, 2015.

[27] Z. K. Feng, W. J. Niu, J. Z. Zhou, C. T. Cheng, H. Qin, and Z. Q. Jiang, "Parallel multi-objective genetic algorithm for short-term economic environmental hydrothermal scheduling," *Energies*, vol. 10, no. 2, pp. 1–22, 2017.

[28] W. J. Niu, Z. K. Feng, B. F. Feng, Y. W. Min, C. T. Cheng, and J. Z. Zhou, "Comparison of multiple linear regression, artificial neural network, extreme learning machine, and support vector machine in deriving operation rule of hydropower reservoir," *Water*, vol. 11, pp. 1–17, 2019.

[29] Q. Mao, S. F. Mueller, and H.-M. H. Juang, "Quantitative precipitation forecasting for the Tennessee and cumberland river watersheds using the NCEP regional spectral model," *Weather and Forecasting*, vol. 15, no. 1, pp. 29–45, 2000.

[30] C. E. M. Tucci, R. T. Clarke, W. Collischonn, P. L. D. S. Dias, and G. S. D. Oliveira, "Long-term flow forecasts based on climate and hydrologic modeling: Uruguay river basin," *Water Resources Research*, vol. 39, no. 7, p. 1181, 2003.

[31] B. Xu, P.-A. Zhong, R. C. Zambon, Y. Zhao, and W. W.-G. Yeh, "Scenario tree reduction in stochastic programming with recourse for hydropower operations," *Water Resources Research*, vol. 51, no. 8, pp. 6359–6380, 2015.

[32] S.-E. Fleten and T. K. Kristoffersen, "Short-term hydropower production planning by stochastic programming," *Computers & Operations Research*, vol. 35, no. 8, pp. 2656–2671, 2008.

[33] M. Chazarra, J. García-González, J. I. Pérez-Díaz, and M. Arteseros, "Stochastic optimization model for the weekly scheduling of a hydropower system in day-ahead and secondary regulation reserve markets," *Electric Power Systems Research*, vol. 130, pp. 67–77, 2016.

[34] B. Xu, P.-A. Zhong, Y. Wu, F. Fu, Y. Chen, and Y. Zhao, "A multiobjective stochastic programming model for hydropower hedging operations under inexact information," *Water Resources Management*, vol. 31, no. 14, pp. 4649–4667, 2017.

[35] S. Séguin, S.-E. Fleten, P. Côté, A. Pichler, and C. Audet, "Stochastic short-term hydropower planning with inflow scenario trees," *European Journal of Operational Research*, vol. 259, no. 3, pp. 1156–1168, 2017.

[36] J. R. Birge and F. Loveaux, *Introduction to Stochastic Programming*, Springer-Verlag, Berlin, Germany, 2nd edition, 2011.

[37] M. N. Hjelmeland, J. Zou, A. Helseth, and S. Ahmed, "Nonconvex medium-term hydropower scheduling by stochastic dual dynamic integer programming," *IEEE Transactions on Sustainable Energy*, vol. 10, no. 1, pp. 481–490, 2018.

[38] A. Helseth, M. Fodstad, and B. Mo, "Optimal medium-term hydropower scheduling considering energy and reserve capacity markets," *IEEE Transactions on Sustainable Energy*, vol. 7, no. 3, pp. 934–942, 2016.

[39] M. N. Hjelmeland, A. Helseth, and M. Korpås, "Medium-term hydropower scheduling with variable head under inflow, energy and reserve capacity price uncertainty," *Energies*, vol. 12, pp. 1–15, 2019.

[40] H. Poorsepahy-Samian, V. Espanmanesh, and B. Zahraie, "Improved inflow modeling in stochastic dual dynamic programming," *Journal of Water Resources Planning and Management*, vol. 142, no. 12, Article ID 04016065, 2016.

[41] Z.-K. Feng, W.-J. Niu, and C.-T. Cheng, "China's large-scale hydropower system: operation characteristics, modeling challenge and dimensionality reduction possibilities," *Renewable Energy*, vol. 136, pp. 805–818, 2019.

[42] R. C. Grinold, "Model building techniques for the correction of end effects in multistage convex programs," *Operations Research*, vol. 31, no. 3, pp. 407–431, 1983.

[43] A. J. King and S. W. Wallace, *Modeling with Stochastic Programming*, Springer International Publishing, New York, USA, 2012.

[44] A. K. Konicz, D. Pisinger, K. M. Rasmussen, and M. Steffensen, "A combined stochastic programming and optimal control approach to personal finance and pensions," *OR Spectrum*, vol. 37, no. 3, pp. 583–616, 2015.

[45] M. L. Wang, X. Y. Wan, P. A. Zhong, Y. Zhang, and C. Liu, "Characteristics of precipitation in upper reaches of the Yangtze river and its temporal and spatial evolution," *South-to-North Water Transfers and Water Science & Technology*, vol. 14, no. 4, pp. 65–71, 2016.

[46] M. Zhang, C. J. Li, Y. C. Zhang, and X. H. Yuan, "Application of minimum risk control model to hydropower generation scheduling," *Journal of Huazhong University of Science and Technology (Natural Science Edition)*, vol. 36, no. 9, pp. 25–28, 2008.

[47] Y. Wang, K. L. Xin, P. Zhao, and J. R. Zhou, "Prediction of seasonal water consumption by Winters method," *Water and Wastewater Engineering*, vol. 37, no. s1, pp. 183–186, 2011.

[48] Y. D. Yang and Y. Z. Zhang, "On water use situation in the Yangtze river basin," *Yangtze River*, vol. 37, no. 8, pp. 10-11, 2006.

Hindawi
Complexity
Volume 2019, Article ID 7687891, 13 pages
https://doi.org/10.1155/2019/7687891

Research Article

Metaheuristic Optimization of Fractional Order Incremental Conductance (FO-INC) Maximum Power Point Tracking (MPPT)

Hossam Hassan Ammar,[1,2] Ahmad Taher Azar,[3,4] Raafat Shalaby,[1,5] and M. I. Mahmoud[5]

[1]*School of Engineering and Applied Science, Nile University, Giza, Egypt*
[2]*Smart Engineering Systems Research Center (SESC), Nile University, 12588 Shaikh Zayed City, Giza, Egypt*
[3]*Robotics and Internet-of-Things Lab (RIOTU), Prince Sultan University, Riyadh 12435, Saudi Arabia*
[4]*Faculty of Computers and Artificial Intelligence, Benha University, Banha, Egypt*
[5]*Faculty of Electronic Engineering, Menofia University, Menofia, Egypt*

Correspondence should be addressed to Ahmad Taher Azar; ahmad_t_azar@ieee.org

Received 25 July 2019; Revised 7 October 2019; Accepted 18 October 2019; Published 28 November 2019

Guest Editor: Jianwu Zeng

This paper seeks to improve the photovoltaic (PV) system efficiency using metaheuristic, optimized fractional order incremental conductance (FO-INC) control. The proposed FO-INC controls the output voltage of the PV arrays to obtain maximum power point tracking (MPPT). Due to its simplicity and efficiency, the incremental conductance MPPT (INC-MPPT) is one of the most popular algorithms used in the PV scheme. However, owing to the nonlinearity and fractional order (FO) nature of both PV and DC-DC converters, the conventional INC algorithm provides a trade-off between monitoring velocity and tracking precision. Fractional calculus is used to provide an enhanced dynamical model of the PV system to describe nonlinear characteristics. Moreover, three metaheuristic optimization techniques are applied; Particle Swarm Optimization (PSO), Ant Colony Optimization (ACO), and AntLion Optimizer (ALO) are used for tuning the FO parameters of the proposed INC-MPPT. A MATLAB-Simulink-based model of the PV and optimization have been developed and simulated for different INC-MPPT techniques. Different techniques aim to control the boost DC-DC converter towards the MPP. The proposed optimization algorithms are, also, developed and implemented in MATLAB to tune the target parameters. Four performance indices are also introduced in this research to show the reliability of the comparative analysis of the proposed FO-INC with metaheuristic optimization and the conventional INC-MPPT algorithms when applied to a dynamical PV system under rapidly changing weather conditions. The simulation results show the effective performance of the proposed metaheuristic optimized FO-INC as a MPPT control for different climatic conditions with disturbance rejection and robustness analysis.

1. Introduction

Green energy sources are the primary research goal nowadays as they are viable, ecological, and cost-effective energy sources. Solar, wind, tidal, and biomass energy have penetrated the electric power production market in recent years due to the diverse methods and their renewable nature. The benefits of developing renewable power include reducing fossil fuel usage, mitigating the greenhouse impact, and reducing air pollution [1]. In addition, control approaches and optimization have shown that the performance of photovoltaic devices depends upon climate conditions (sunlight and temperature) and load impedance [2]. However, its low energy conversion effectiveness (especially in low radiation and temperatures) is the primary disadvantage of PV systems. The MPPT needs to be operated for ideal efficiency and operation as mentioned [3]. One of the pioneering challenges of the PV devices is their nonlinear current-voltage I-V relationship dynamic which generates a distinctive MPP in the power-voltage P-V relationship as noted [4]. Because of the P-V relationship with climate and load circumstances, the MPPT method becomes complex. MPPT methods do not only enhance the power performance of PV and energy

delivered to the load, but they also increase the operating life of the PV system [5]. Previous studies have suggested several MPPT methods; most MPPT techniques demonstrate higher efficiency under stable weather [6]. MPPT algorithms are usually used as electronic power conversion devices and the control signal is a duty cycle for peak load energy [7]. A wide variety of methods for solving the MPPT issue have been implemented, such as the perturb and observe (P&O) method, incremental conductance (INC) algorithm, and artificial intelligence includes fuzzy logic, neural networks, and metaheuristic techniques. The P&O and INC are the most common algorithms used for PV-MPPT systems [8]. The P&O technique is frugal and very easy to execute; its operation is based on the iterative measurement of the voltage and current of the PV system to obtain the duty cycle and consequently the MPP. Its main disadvantage, however, is that it provides an oscillatory power around the MPP and is also unable to manipulate PV power variations due to climatic effects or inherent disturbances of the MPPT. The INC approach is based on the behavior of PV, given that a MPP is reached by zero in a pitch of the PV curve, positive to the left and negative to the right of the PV curve. On the basis of this, the technique calculates the DC-DC converter duty cycle by relating iterative conductivity to the incremental conductivity. The primary drawback in the INC technique is that the system's reaction to the MPP may be slow under some conditions. However, the INC technique exhibits less oscillatory behavior around the MPP compared to the P&O method [9]. Fractional calculus introduces the nonintegral order/fractional of derivatives and integrals. Many of the real systems show a nonlinear and fractional order dynamical behavior, such as heat conduction in solids, electrical behavior in R-L transportation lines, mass diffusion, and electromagnetic waves [10]. The nonlinear characteristics of the current-voltage of a PV cell occur because the PV cells are manufactured from semiconducting materials (crystalline silicon, c-Si). The power of PV cell depends on the inherent voltage drop across the p-n junction (energy band) which produces a photoelectric current (current source). The light and ambient temperature interaction also shows anomalous diffusion which can be described as fractional order diffusion [11]. Therefore, Grunwald–Letnikov fractional approximation [12] is introduced to control the fractional order differentiation for current and voltage nonlinear dynamical behavior. To improve dynamic performance, FO-INC based on the nonlinear and fractional order changes of the PV voltage and current has been proposed to track the maximum output power [13]. It is very important to select the proper converter [14] to enhance the MPPT performance. The MPPT techniques have been compared using MATLAB and Simulink tools created by MathWorks, considering all the design and implementation specs [15]. Therefore, metaheuristic optimization techniques' robustness and ability to find the optimal solution in different nonlinear systems have demonstrated itself in numerous past research studies. Metaheuristic abilities are powerful techniques of resolving optimization problems for nonlinear and fractional order systems [15]. In power systems, different optimization techniques have been utilized. Considering the different constraints in PV systems and difference in the nature of DC-DC converter system, the ACO algorithm has been used [16]. It has been proved to be very robust, consistent, and performs better than conventional optimization techniques (e.g., PSO and GA) [16]. The experiments show computational effectiveness and time decrease in monitoring for a small PV Systems. The AntLion optimizer (ALO) is a recent metaheuristic algorithm that replicates the hunting scheme of antlions in catching ants [17]. ALO also gives a good performance results in PV-MPPT systems [18].This research aims to extract maximum power from PV systems by using FO-INC and metaheuristic optimization technique. This enhanced system efficiency in different climatic conditions using fixed and variable-step FO-INC with PSO, ACO, and ALO optimization techniques. This paper is organized as follows: Section 2 addresses the modeling of the complete PV system, and Section 3 describes the MPPT algorithm design and operation. Section 4 gives the operation of metaheuristic optimization algorithms. Sections 5 and 6 illustrate the experimental results and conclusions to show the efficiency of the proposed technique.

2. Photovoltaic (PV) System Modeling and Simulation

The proposed PV system is constituted by a PV module, the Buck–Boost converter as a DC-DC converter between the PV panel and the DC load, and the MPPT controller to achieve maximum power point of the PV panels. The model of the solar panels used in the proposed system will be illustrated, and the PV system is introduced [19]. The inputs to MPPT are the PV voltage and current which are used to calculate and deliver the control signal (duty cycle) to the Buck–Boost converter, as shown in Figure 1. The main function of the MPPT algorithm is to automatically track the voltage/current change of the PV panel and feed the Buck–Boost converter with the appropriate duty cycle to get the MPP under specific climatic conditions.

2.1. Modeling of PV Panel. The nonlinear equations of the PV system which describe the relationships between the different PV model parameters are developed and solved via MATLAB and Simulink tools where the PV cell electric circuit model is shown in Figure 2. The PV output current I_{PV} can be obtained using equation (1) where N_p and N_s are the number of parallel and series cells, respectively:

$$I_{PV} = N_p \times (I_G - I_D - I_{sh}). \tag{1}$$

The nonlinear equation of I-V characteristics of one-diode PV model was expressed by Milici et al. [9] as follows:

$$I_{PV} = N_p \times I_G - N_s \times I_o \left[e^{\left((q/\eta k T_k) \times \left((V_{PV}/N_s) + (I_{PV}/N_p) R_s\right) - 1\right)} \right] - \frac{N_p}{R_{sh}} \times \left(\frac{V_{PV}}{N_s} + \frac{I_{PV} R_s}{N_p} \right), \tag{2}$$

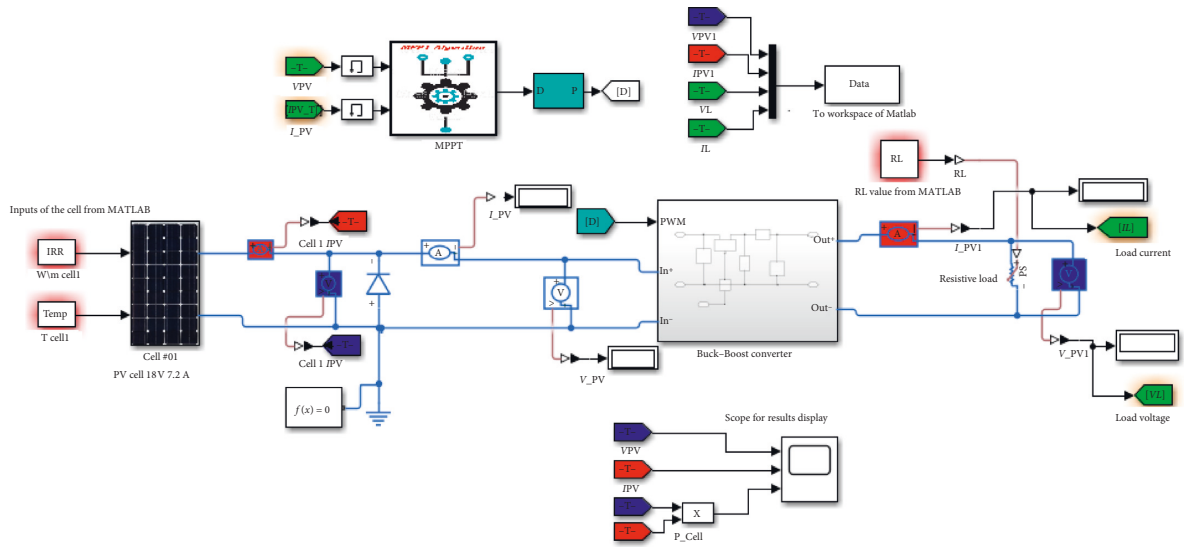

Figure 1: Complete PV system model using MATLAB and Simscape.

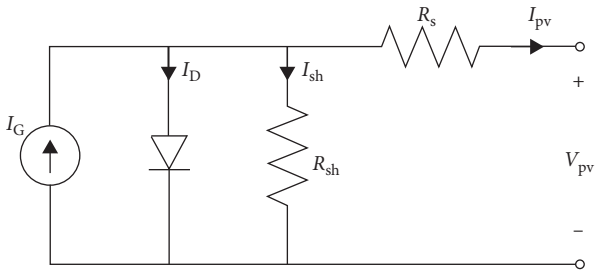

Figure 2: PV cell equivalent electric circuit model.

where V_{PV} and I_{PV} are the PV terminal voltage and current, respectively, R_s and R_{sh} are the series and shunt resistance, respectively, η is the ideality factor, the Boltzmann's constant is k, q is the electron charge, T_k is the temperature degree in Kelvin, I_G is photo-generated current, and the diode saturation current is I_o. The PV panel parameters are shown in Table 1.

The I-V and P-V nonlinear characteristic curves of the PV array simulated using MATLAB at different climatic conditions (temperature and irradiance) are shown in Figure 3.

2.2. DC-DC Converter. Simulink and Simscape tools have been selected as platforms for modeling, implementation, and testing the Buck–Boost converter. The state space modeling is primarily represented by equation (3), where A, B, C, and D are the system matrices, x is the state variable vector, x' is the state variable derivative vector with respect to time, u is the input, and y is the output [14]:

$$x' = Ax + Bu,$$
$$y = Cx + Du. \quad (3)$$

Figure 4 shows the Buck–Boost model using Simscape which is simulated at different duty cycles and fixed load

Table 1: PV panel parameters.

Parameter value	Value
Max power P_{max}	735.72 W
Open circuit voltage V_{oc}	65.9 V
Short circuit current I_{sh}	15.21 A
Temperature coefficient of V_{OC}	$-1.23 \times 10e^{-1}$ V/C
Temperature coefficient of I_{sh}	$3.18 \times 10e^{-3}$ A/C

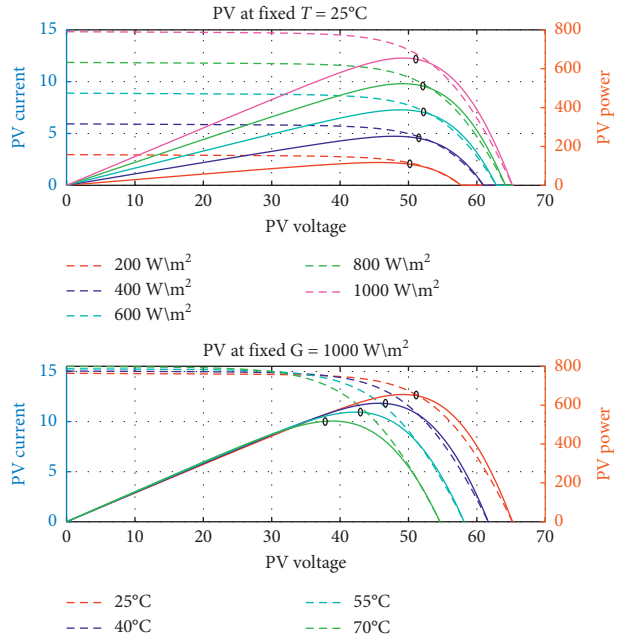

Figure 3: P-V and I-V characteristic curves at different climatic conditions.

according to the state space model represented in equation (4), where $x_1 = I_L$, $x_2 = V_{C_{out}}$, and d = duty cycle. The simulation results at different duty cycles are shown in Figure 5:

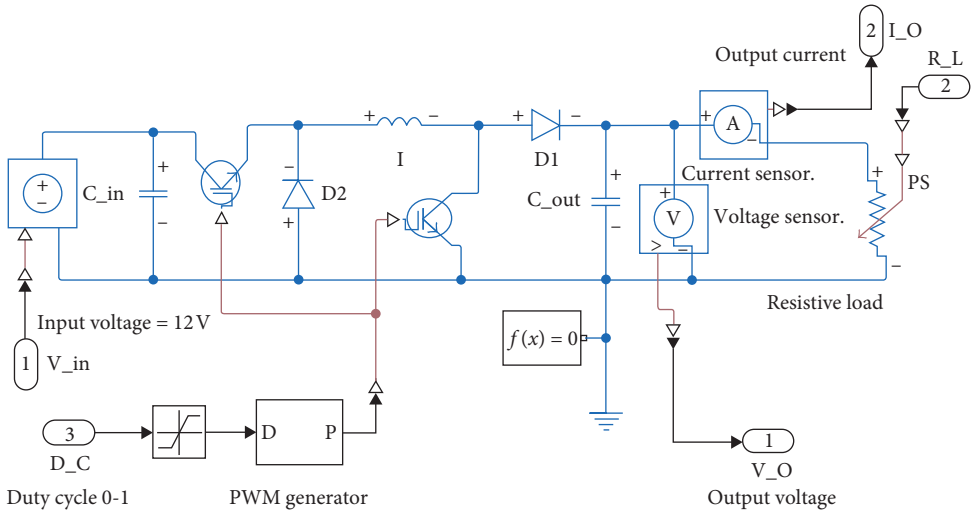

Figure 4: Buck–Boost Simscape model.

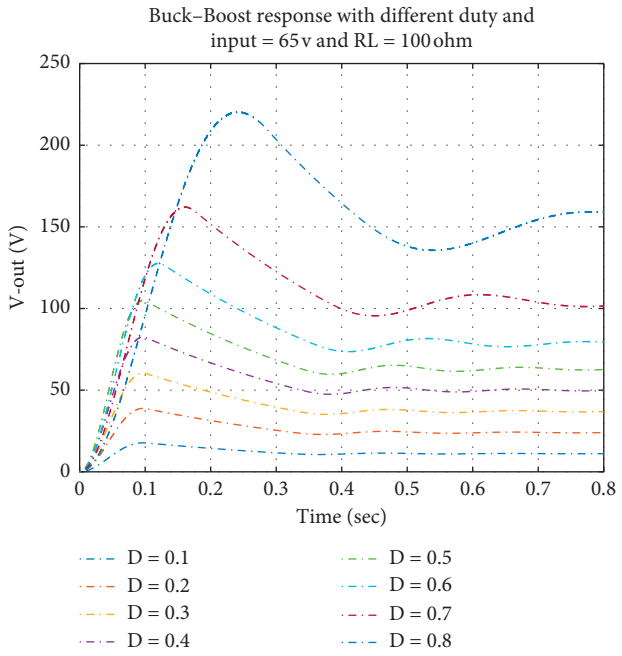

Figure 5: Buck–Boost output voltage at different duty cycles.

$$\begin{bmatrix} x_1' \\ x_2' \end{bmatrix} = \begin{bmatrix} 0 & \frac{1-d}{L} \\ \frac{-(1-d)}{C} & \frac{-1}{RC} \end{bmatrix} \begin{bmatrix} x_1 \\ x_2 \end{bmatrix} + \begin{bmatrix} \frac{d}{L} \\ 0 \end{bmatrix} u_1, \quad (4)$$

$$\begin{bmatrix} y_1 \\ y_2 \end{bmatrix} = \begin{bmatrix} 1 & 0 \\ 0 & 1 \end{bmatrix} \begin{bmatrix} I_L \\ V_{C_{\text{out}}} \end{bmatrix} + \begin{bmatrix} 0 \\ 0 \end{bmatrix} u_1.$$

The proposed Buck–Boost has been designed and simulated using the parameters illustrated in Table 2.

Table 2: Buck–Boost design parameters.

Parameter value	Value
Load resistance	4.5 Ω
Filter inductance	1 mH
Output filter capacitance	4700 μF
Input filter capacitance	47 μF
Switching frequency	25000 Hz

3. Design and Implementation of MPPT

The primary feature of the PV system is the total energy monitoring in which the power of the PV modules can be extracted in a certain climatic situation. As shown in the literature, the most commonly used MPPT algorithm is INC. The INC algorithm is based on the reality that the PV output energy derivative for the output voltage at the MPP is zero ($dP/dV = 0$), positive on the left side of MPP ($dP/dV > 0$) and negative on the right side of MPP ($dP/dV < 0$) [5].

3.1. Fixed-step INC Method. The INC algorithm is used to detect the condition of MPP via the conductance (dI/dV) behavior of the PV system. The INC-MPPT can be executed through the following sequence [20]:

(1) The voltage and current of the PV module are sensed by the MPPT controller

(2) If ($dI/dV < -I/V$) is satisfied, the duty cycle of the converter needs to be decreased and vice versa

(3) No change in the duty cycle occurs if $I + V(dI/dv) = 0$ is satisfied

The duty cycle (PV reference voltage (V_{ref})) increasing or decreasing occurs with fixed step.

3.2. Variable-Step INC Method. The INC variable step size algorithm proposed by Motahhir et al. [5] can improve the MPPT controller's tracking effectiveness. The algorithm

sequences are mostly comparable to the standard increments; the only distinction is the calculation of the step size. Step $= N * \text{abs}(\text{d}P/\text{d}V)$ is used in the variable step size algorithm to change the duty cycle step size, where N is the scaling factor.

3.3. Fractional Order INC Method (FO-INC). Many computational requests for fractional order derivatives according to the definition have been suggested by Riemann–Liouville and Grunwald–Letnikov, [9]. The general form of fractional order differentiator can be expressed by Kamal and Ibrahim [21]; supposed that $f_m(t) = t^m$ and $m = 1, 2, 3, \ldots$, is demonstrated at

$$D_\alpha^t t^m \approx \frac{\Gamma(m+1)}{\Gamma((m+1)-\alpha)} t^{(m-\alpha)}, \tag{5}$$

where $\Gamma(\cdot)$ represents Eular's gamma function and α is the order number of derivative, when its value is $0 < \alpha < 1$, representing physical phenomenon of fractional order [9]. The FO-INC MPPT main criteria can be expressed by equations (7) and (8):

$$\frac{\text{d}^\alpha I(V)}{\text{d}V^\alpha} = \lim_{\Delta V \longrightarrow 0} \frac{I(V) - \alpha(V - \Delta V)}{\Delta V_\alpha}, \tag{6}$$

$$\frac{\text{d}^\alpha I}{\text{d}V^\alpha} \approx \frac{I - \alpha I_0}{(V - V_0)^\alpha}, \tag{7}$$

$$\frac{\text{d}^\alpha}{\text{d}V^\alpha}\left(\frac{-I_0}{V_0}\right) = \left(\frac{-1}{V}\right)\left(\frac{\Gamma(2)}{\Gamma(2-\alpha)}\right)(I_0)^{1-\alpha} - I_0\frac{\Gamma(0)}{\Gamma(-\alpha)}V_0^{1-\alpha}. \tag{8}$$

The control procedure of the FO-INC algorithm can be expressed by the flowchart depicted in Figure 6. The procedure starts with measuring the PV's voltage and current to determine the MPPT action according to the following conditions:

Condition 1. If $(\Delta V^\alpha \neq 0 \& (\text{d}^\alpha I/\text{d}V^\alpha) = (\text{d}^\alpha/\text{d}V^\alpha)(-I_0/V_0))$ or $(\Delta V^\alpha = 0 \& \Delta I = 0)$, keep the current duty cycle, fix the duty cycle

Condition 2. If $(\Delta V^\alpha \neq 0 \& (\text{d}^\alpha I/\text{d}V^\alpha) > (\text{d}^\alpha/\text{d}V^\alpha)(-I_0/V_0))$ or $(\Delta V^\alpha = 0 \& \Delta I > 0)$, decrease the duty cycle of the Buck–Boost converter (increase V_{ref} as in equation (9))

Condition 3. If $(\Delta V^\alpha \neq 0 \& (\text{d}^\alpha I/\text{d}V^\alpha) < (\text{d}^\alpha/\text{d}V^\alpha)(-I_0/V_0))$ or $(\Delta V^\alpha = 0 \& \Delta I < 0)$, increase the duty cycle of the Buck–Boost converter (decrease V_{ref} as in equation (9))

Condition 4. Calculate $P_o = V_o \times I_o$ and $P = V \times I$. If $P > P_o \longrightarrow$ terminate, otherwise update the voltage $V_o = V$, current $I_o = I$, and power $P_o = P$

The duty cycle of the Buck–Boost converter can be calculated based on the output of the FO-INC controller V_{ref} as in

$$V_L = \frac{D}{1-D} \times V_{PV} \text{ then,}$$
$$D = \frac{V_L}{(V_0 \pm \Delta V^\alpha) + V_L}, \tag{9}$$

where V_L is the resistive load voltage, $V_{PV} = V_{\text{ref}}$, and D is the duty cycle.

Both fixed- and variable-step FO-INC MPPT have been implemented to improve the performance of the MPP tracking of the nonlinear PV system with Buck–Boost converter and resistive load. In case of fixed step, the effective parameter of MPPT performance is alpha α. For variable step both alpha (α) and step size S are affecting the MPPT performance as shown in Figure 6.

4. Metaheuristic Optimization Algorithms

Genetic algorithms, Particle Swarm Optimization, and Ant Colony Optimization are among the most frequent algorithms in this field. However, these algorithms can solve many real and difficult problems. As one of the recent algorithms, the AntLion Optimizer Optimizer will be introduced along with its basic working principle, updated criteria, and pseudo algorithms. According to Pradhan et al. [20], the searching techniques of different optimizers are as follows:

(1) Initialize solution randomly
(2) Specify the search direction
(3) Specify the update criteria
(4) Specify the stopping criteria

4.1. Particle Swarm Optimization (PSO). The inspiration of the particle swarm algorithm is to simulate the navigation and foraging of swarm of birds or school of fishes. PSO was developed by James Kennedy and Russel Eberhart in 1995 while studying the social behaviors of animals working in swarms [22]. The PSO is seeking high-quality optimization by refining, iteratively, a candidate solution. The pseudo code of the PSO algorithm is illustrated in detail with the steps in Algorithm 1.In Algorithm 1, N is the number of particles, C_1 and C_2 are the acceleration coefficients, and $W_{\min}$ and $W_{\max}$ are the ranges of weight of particles. PSO uses fewer resources than the other optimization techniques. Usually, it does not require the problem to be differentiable as the gradient of the problem is not taken into consideration. As a result, there might be chances that PSO does not converge to optimal solution.

4.2. Ant Colony Optimization (ACO). Ant Colony Optimization (ACO) introduces an artificial algorithm motivating actual ant colonies that solve discrete optimization problem. It was first presented by Marco Dorigo in 1992 as a major aspect of his Ph.D thesis and called it the ant system [12]. While further improvements were carried out to ant colony by Gambardella Dorigo in 1997 [23]. Pseudo code for ant colony optimization is implemented with the steps as Algorithm 2.

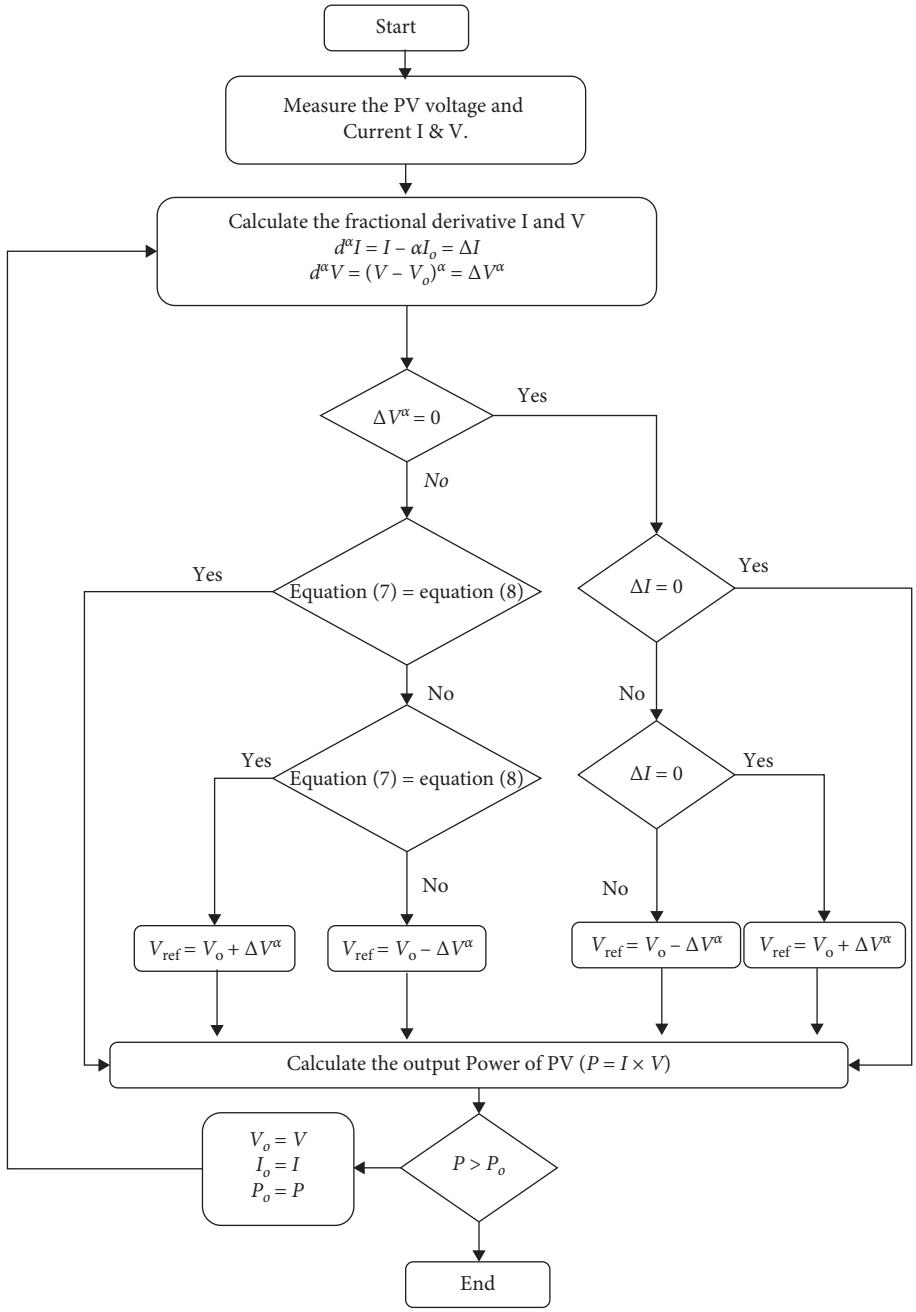

Figure 6: Fractional order INC MPPT flowchart.

In Algorithm 2, $\tau_{ij}(t)$ represents the intensity of trail on connection (i, j) at time t, L(ant) is the cost function result at each ant, and λ is pheromone decay coefficient between time (t and $t+1$) (i.e., $0 < \lambda < 1$). Evaporation occurs in real trails, but it is too slow to play an important role. For continuous improvements it allows the search routine to forget errors and poor quality solution in favor of better ones.

4.3. AntLion Optimizer Optimization (ALO). The primary motive of ALO is the running behavior of larvae of antlions. ALO is suggested based on the Emary and Zawbaa [24] mathematical model. The ALO algorithm simulates the interaction between the traps. The ants must move across the search area in order to model such interactions, and the antlions are permitted to chase and fit the traps. Given that ants move randomly to find food in actual life, a random walk algorithm is selected as shown in Heidari et al. [25] to model the ants' motion.

In Algorithm 3, I is a ratio, c^t is the minimum of all variables at tth iteration, and d^t indicates the vector including the maximum of all variables at tth iteration. $I = 10^{w}(T/t)$, where t is the current iteration, T is the

Result: MPPT parameter to achieve MPP
Initialize the PSO parameters (N, C_1, C_2, $W_{\min}$, $W_{\max}$, $V_{\max}$)
while the termination criteria not achieved (MPP) **do**
For (each Particle i)
Simulate and calculate the MPP and the cost function. **if** CostFunction (i) < Objective (MPP)
then
The Best Cost (i) = Cost Function (i)
The Best Solution (i) = The particle (i)
else
The Best Cost (i) = The Best Cost ($i-1$)
The Best Solution (i) = The Best Solution ($i-1$)
end
(a) Update the velocity (V): $V_i^{t+1} = V_i^t + C_1 r_1 (P_i - X_i^t) + C_2 r_2 (P_g - X_i^t)$
where V_i^t is inertia, $C_1 r_1 (P_i - X_i^t)$ is cognitive component and $C_2 r_2 (P_g - X_i^t)$ is social component
(b) Update the position of particles: $X_i^{t+1} = X_i^{t+1} + V_i^t$
end

Algorithm 1: PSO-MPPT.

Result: MPPT parameter to achieve MPP
Initialize the ACO parameters
while the termination criteria not achieved (MPP) **do**
For (each ant i)
Simulate and calculate the MPP and the cost Function.
if CostFunction (i) < Objective (MPP) **then**
The Best Cost (i) = Cost Function (i)
The Best Solution (i) = The particle (i)
else
The Best Cost (i) = The Best Cost ($i-1$)
The Best Solution (i) = The Best Solution ($i-1$)
end
(a) Update pheromone for each ant: $\tau_{ij}(t+1)$, $\Delta\tau_{ij}(t) = \sum_{\text{ant}=1}^{\text{ants}} \Delta\tau_{ij}^{\text{ant}}(t)$
(i) Calculate the solution $\Delta\tau_{ij}^{\text{ant}}(t) = \begin{cases} (1/L_{\text{best}}) \longrightarrow \text{if ant}(t) \text{ travels on edge}(i, j) \\ 0 \longrightarrow \text{otherwise} \end{cases}$
(b) Apply evaporation and globally update the ants position, according to the optimum solutions calculated earlier
end

Algorithm 2: ACO-MPPT.

maximum number of iterations, and w is a constant defined based on the current iteration. $X(t)$ is ant' movement, cumsum calculates the cumulative sum, n is the maximum number of iteration, t shows the step of random walk, and $r(t)$ is a stochastic function. Also, a_i is the minimum of random walk and b_i is the maximum of random walk in ith variable. R_{A}^t is the random walk around the antlion selected by the roulette wheel at tth iteration and R_{E}^t is the random walk around the elite at tth iteration. The pseudo code of ALO for MPPT developed as mentioned in Algorithm 3.

5. Modeling and Simulation Results

The proposed system has been modeled and simulated using MATLAB and Simscape software environments in order to study the system behavior and MPPT performance with different metaheuristic optimization algorithms. The block diagram describing the total PV system with MPPT and optimizer is shown in Figure 7, where the MPPT algorithm is changed between conventional INC methods and FO-INC (fixed and variable step). The MPPT is optimized by one of the metaheuristic techniques (PSO, ACO, and ALO).

The operation sequence of PV with MPPT and optimization process is a closed loop as shown in Figure 8, and it starts with measuring the irradiance (G) and temperature (T) applied to the PV system to get the reference maximum power point from PV characteristics curves (P_{MPP}). A closed loop of PV with MPPT and Buck–Boost converter is running in Simscape environment for two seconds to measure the PV output power. The mean squared-error (MSE) between the MPP (P_{MPP}) and output power of the PV system (P_{PV}) is the cost function of the metaheuristic optimizer calculated

Result: MPPT parameter to achieve MPP
Initialize the first population of ants and antlions randomly
while the termination criteria not achieved (MPP) **do**
For (each antlion (i))
Select an antlion using Roulette wheel algorithm [16].
Simulate and calculate the MPP and the cost Function. **if** CostFunction (i) < Objective (MPP)
then
The Best Cost (i) = Cost Function (i)
The elite (i) = The The Best Solution (i)
else
The Best Cost (i) = The Best Cost ($i-1$)
The elite (i) = The Best Solution ($i-1$)
end
(a) Update c and d using equations: $C^t = (C^t/I)$ and $d^t = (d^t/I)$
(b) Create a random walk and normalize it using: $X(t) = [0, \ldots, \text{cumsum}(2r(t_n) - 1)]$, where $n = 1, 2, 3, \ldots, n$ and $X_i^t = ((X_i^t - a_i) \times (d_i - c_i^t)/(d_i^t - a_i)) + c_i$
(c) Update the position of antlions using $\text{ant}_i^t = (R_A^t + R_E^t)/2$
(d) Calculate the fitness of all ants according to the optimum solutions calculated earlier
end

Algorithm 3: ALO-MPPT.

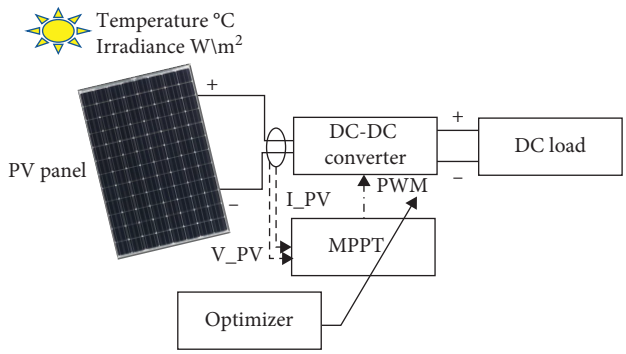

Figure 7: The proposed PV system with metaheuristic optimization.

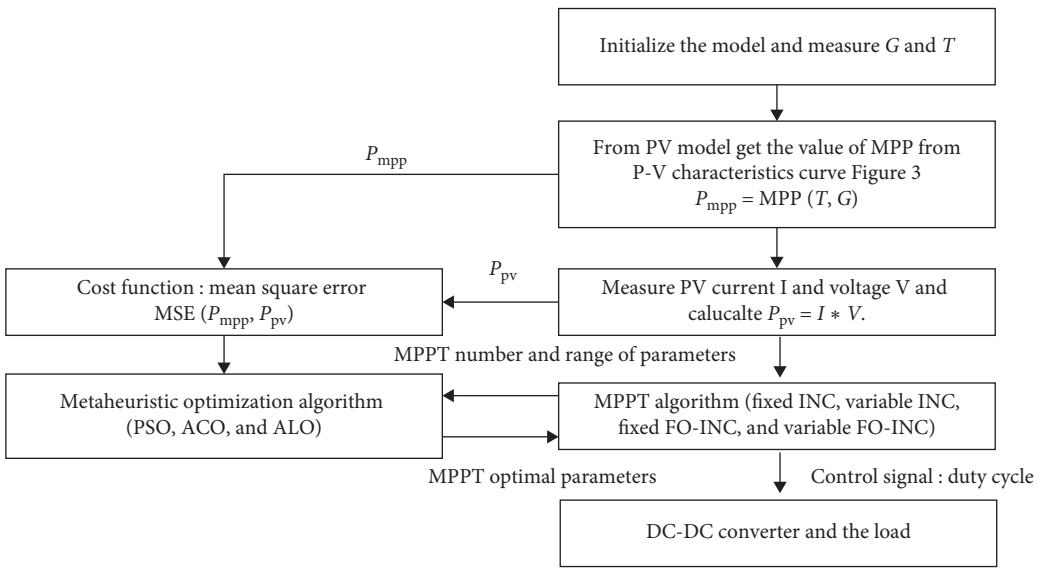

Figure 8: The proposed system implementation flowchart.

Table 3: Comparative results between MPPT algorithms at 800 W/m^2.

MPPT	Climatic condition							
	800 W/m^2 and 25°C				800 W/m^2 and 35°C			
	Max power (Watt)	MPP steps	Oscillation avg. (Watt)	No. of iterations	Max power (Watt)	MPP steps	Oscillation avg. (Watt)	No. of iterations
Fixed-step INC	321.84	137	5.87	—	319.73	131	4.92	—
Variable-step INC	324.63	125	4.89	—	319.90	127	4.17	—
FO-INC fixed step + PSO	420.28	121	4.28	100	400.01	127	4.34	100
FO-INC fixed step + ACO	470.62	115	4.067	100	462.24	121	3.089	100
FO-INC fixed step + ALO	487.22	118	3.067	100	474.24	125	3.089	100
FO-INC variable step + PSO	490.28	128	3.28	100	480.01	132	3.34	100
FO-INC variable step + ACO	510.62	115	3.067	100	490.24	121	3.089	100
FO-INC variable step + ALO	515.52	120	3.269	100	510.26	127	3.802	100

Table 4: Comparative results between MPPT algorithms at 1000 W/m^2

MPPT	Climatic condition							
	1000 W/m^2 and 25°C				1000 W/m^2 and 35°C			
	Max power (Watt)	MPP steps	Oscillation avg. (Watt)	No. of iterations	Max power (Watt)	MPP steps	Oscillation avg. (Watt)	No. of iterations
Fixed-step INC	428.84	145	4.87	—	419.73	153	5.92	—
Variable-step INC	420.73	155	5.87	—	419.90	139	5.17	—
FO-INC fixed step + PSO	436.88	120	4.88	100	410.51	121	4.84	100
FO-INC fixed step + ACO	650.82	101	2.067	100	632.24	112	2.089	100
FO-INC fixed step + ALO	667.32	118	3.87	100	664.24	120	3.889	100
FO-INC variable step + PSO	590.28	86	2.28	100	580.23	92	2.34	100
FO-INC variable step + ACO	720.62	65	2.067	100	705.24	71	2.079	100
FO-INC variable step + ALO	725.32	80	2.369	100	710.63	96	2.802	100

in MATLAB environment to get the optimal MPPT parameters. The optimal parameters are applied to the chosen MPPT technique in Simscape. Performance index is calculated in MATLAB through a dynamical data exchange between MATLAB and Simscape.

The proposed MPPT contribution is generated by measuring the output energy of the PV system under different solar irradiances. Simulation was conducted when solar radiation and cell temperature change with a transient method of approximately 2 sec with 0.01 sec sampling. The characteristics of the PV array will be altered when the natural radiation and cell temperature alter, which causes the I-V curves of the PV array to change. In addition, the particular irradiance ranges from 400 to 1000 W/m^2 and the cell temperature ranges from 20°C to 40°C which makes it more realistic as shown in Tables 3 and 4.

Figure 9 shows the I-V and P-V curves of fixed-step INC under different temperature and radiation with small step which in return gives it better results and less oscillation; however, it takes more time to get maximum power. The variable-step INC curves, shown in Figure 10, give better results than the fixed INC. However, in variable-step INC, improper selection of the initial step size may require large number of steps to reach the MPP. Also, improper selection of the scaling factor may lead to oscillations.

The objective of PSO, ACO, and ALO is to select the best value of α for the fixed-step FO-INC and the best values of α and S for variable step to get the maximum PV power. Fixed-step FO-INC MPPT results optimized by PSO, ACO, and ALO are shown in Figure 11. Fixed-step FO-INC-PSO gives better results than conventional INC methods, less number of MPPT steps to maximum power value, and less oscillation, yet PSO optimization needs more iterations to get the

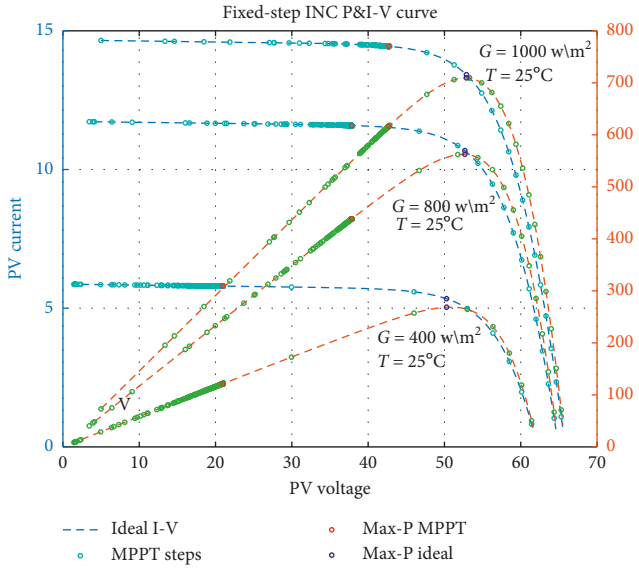

Figure 9: Fixed-step INC I-V and P-V curves.

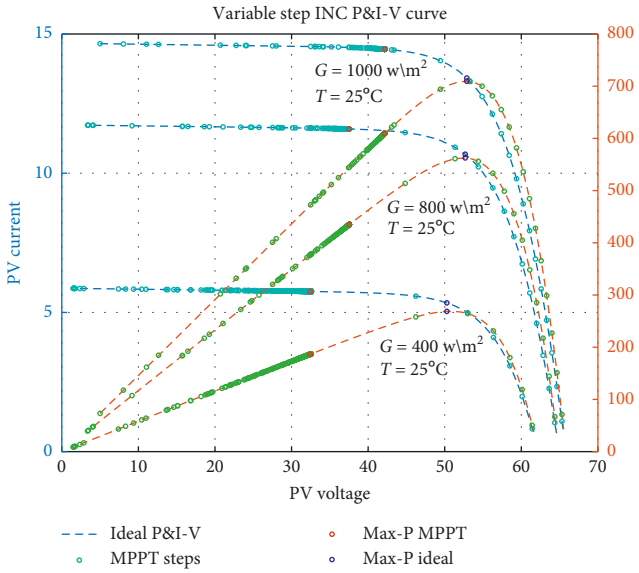

Figure 10: Variable-step INC I-V and P-V curves.

optimal MPPT parameter. Fixed-step FO-INC-ACO gives less number of MPPT steps than PSO and ALO, however, not the optimum parameter that can be obtained by ALO with fewer number of MPPT steps. The output power and voltage of the PV system generated using the optimization of fixed-step FO-INC-ACO gives less oscillation yet not as much maximum power as given by ALO as shown in Figure 12. Variable-step FO-INC gives better results than conventional INC and fixed-step FO-INC methods, less number of MPPT steps to maximum power value, and less oscillation. PSO needs more number of iterations than ACO and ALO to get the optimal MPPT parameters. ALO gives the optimum parameters for the maximum power with larger number of MPPT steps and vice-versa with ACO as shown in Figures 13 and 14.

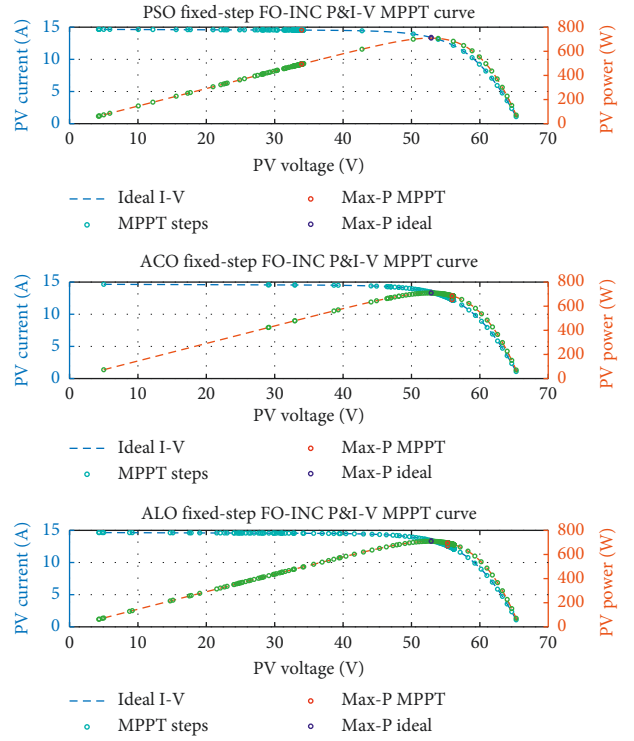

Figure 11: Optimization of fixed-step FO-INC I-V and P-V curves.

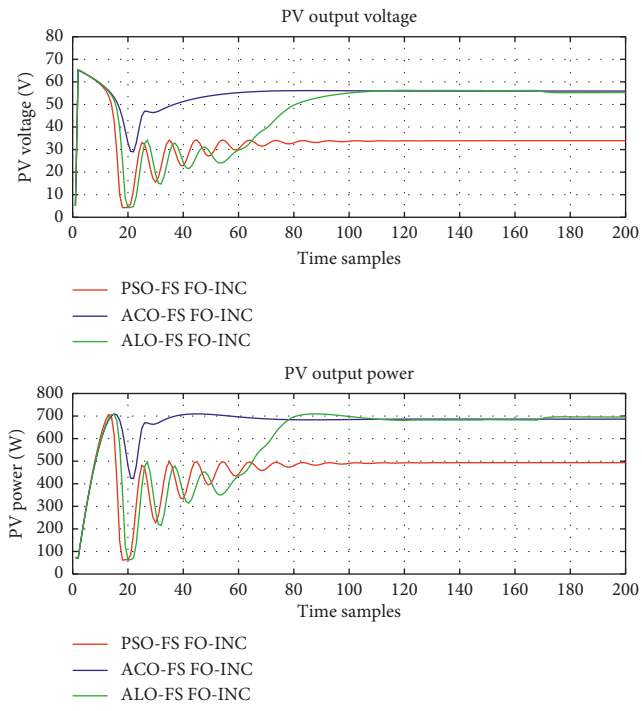

Figure 12: Optimization of fixed FO-INC output response.

The MPPT performance η can be monitored as in equation (10) for all the abovementioned MPPT techniques. Irradiance, temperature, power, and maximum power time waveform of the system using the proposed MPPT methods have been used

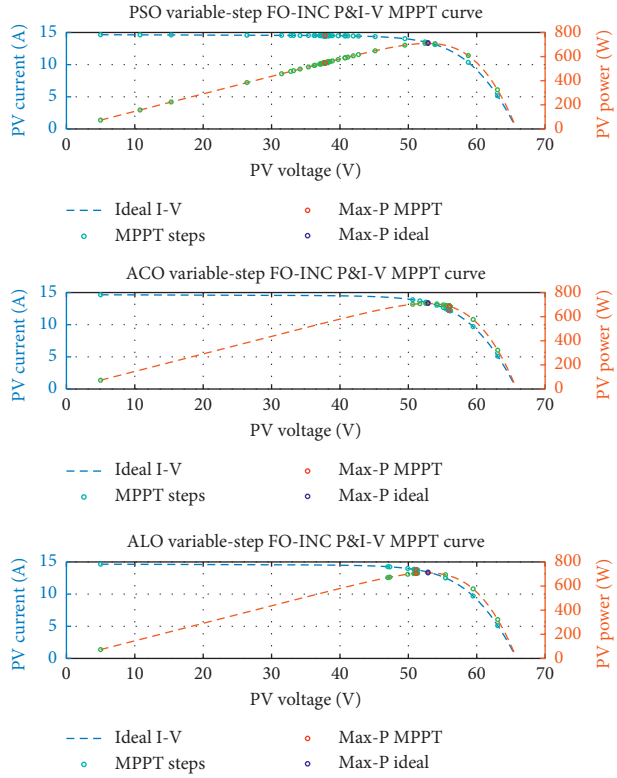

Figure 13: Optimization of variable-step FO-INC I-V and P-V curves.

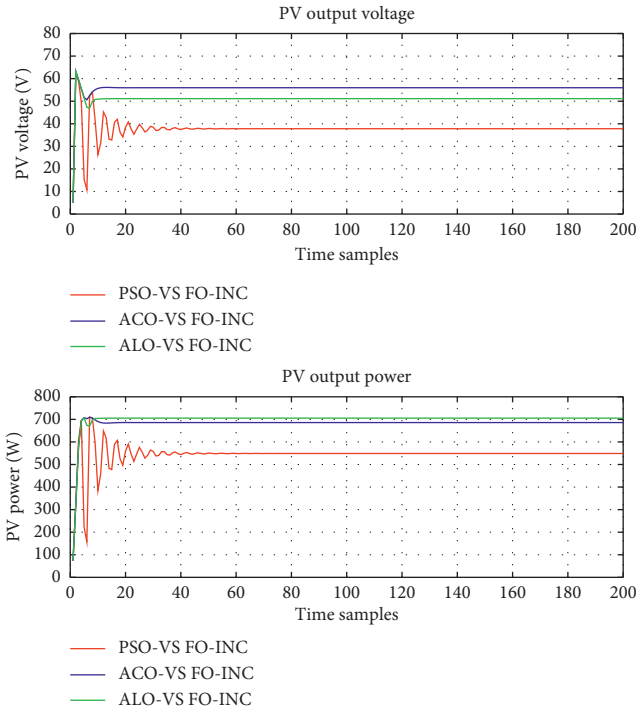

Figure 14: Optimization of variable FO-INC output response.

to get η. The irradiance and temperature variation mean that output power follows the highest maximum power profile very closely, and the higher performance is obtained in case of variable-step FO-INC with ALO (98.1) as noted from Table 5:

Table 5: MPPT algorithms efficiency.

MPPT method	Efficiency (η)
Fixed-step INC	75.9
Variable-step INC	82.1
Fixed-step FO-INC + PSO	90.2
Fixed-step FO-INC + ACO	92.3
Fixed-step FO-INC + ALO	93.2
Variable-step FO-INC + PSO	94.7
Variable-step FO-INC + ACO	97.5
Variable-step FO-INC + ALO	98.1

$$\eta = \frac{\int P_{\mathrm{PV}}(t)\,\mathrm{d}t}{P_{\mathrm{MPP}}}. \tag{10}$$

6. Conclusion and Future Work

The output power of the PV system will be changed by irradiance and temperature according to the simulation results of the system with different climatic conditions as illustrated in Tables 3 and 4. The proposed incremental fractional order FO-INC demonstrates better results than traditional INC under environmental changing processes and improves the efficiency of MPPT as FO-INC is able to provide a dynamical mathematical model for describing the nonlinear and fractional properties. The incremental change in the fractional order as a dynamic variable is used to adjust the MPPT service cycle. Using metaheuristic optimization enhances the performance of FO-INC and

provides another dynamical variable to the MPPT control. Compared to ACO and ALO, the PSO uses less number of variables and shorter calculation time for the same number of iterations. However, sometimes it cannot achieve the optimal solution. The ALO uses larger number of variables and takes the longest calculation time, yet it gives more optimal solution compared to ACO and PSO. This work could be extended by changing the resistance using another dynamical load, e.g., DC motor, or by applying different optimization techniques on the FO-INC.

Data Availability

No data were used to support this study.

Conflicts of Interest

The authors declare that they have no conflicts of interest.

Acknowledgments

The authors would like to thank Prince Sultan University, Riyadh, Saudi Arabia for supporting and funding this work. Special acknowledgment to Robotics and Internet-of-Things Lab (RIOTU) at Prince Sultan University, Riyadh, SA.

References

[1] M. A. Jusoh, M. F. Naim Tajuddin, S. M. Ayob, and M. A. Roslan, "Maximum power point tracking charge controller for standalone PV system," *TELKOMNIKA (Telecommunication Computing Electronics and Control)*, vol. 16, no. 4, pp. 1413–1426, 2018.

[2] P. G. Bueno, F. J. Ruiz-Rodriguez, and J. C. Hernández, "Stability assessment for transmission systems with large utility-scale photovoltaic units," *IET Renewable Power Generation*, vol. 10, no. 5, pp. 584–597, 2016.

[3] B.-R. Peng, K.-C. Ho, and Y.-H. Liu, "A novel and fast mppt method suitable for both fast changing and partially shaded conditions," *IEEE Transactions on Industrial Electronics*, vol. 65, no. 4, pp. 3240–3251, 2018.

[4] H. Bahri and A. Harrag, "Variable step size P&O MPPT controller to improve static and dynamic PV system performances," *Journal of Advanced Engineering and Computation*, vol. 2, no. 2, pp. 86–93, 2018.

[5] S. Motahhir, A. El Ghzizal, S. Sebti, and A. Derouich, "Modeling of photovoltaic system with modified incremental conductance algorithm for fast changes of irradiance," *International Journal of Photoenergy*, vol. 2018, Article ID 3286479, 13 pages, 2018.

[6] M. Seyedmahmoudian, T. Kok Soon, E. Jamei et al., "Maximum power point tracking for photovoltaic systems under partial shading conditions using bat algorithm," *Sustainability*, vol. 10, no. 5, p. 1347, 2018.

[7] L. Li, H. Wang, X. Chen et al., "High efficiency solar power generation with improved discontinuous pulse width modulation (dpwm) overmodulation algorithms," *Energies*, vol. 12, no. 9, p. 1765, 2019.

[8] J. Li and H. Wang, "A novel stand-alone PV generation system based on variable step size INC MPPT and SVPWM control," in *Proceedings of the 2009 IEEE 6th International Power Electronics and Motion Control Conference*, pp. 2155–2160, IEEE, Wuhan, China, May 2009.

[9] C. Milici, G. Drăgănescu, and J. T. Machado, *Introduction to Fractional Differential Equations*, vol. 25, Springer, Basel, Switzerland, 2019.

[10] K.-N. Yu, C.-K. Liao, and H.-T. Yau, "A new fractional-order based intelligent maximum power point tracking control algorithm for photovoltaic power systems," *International Journal of Photoenergy*, vol. 2015, Article ID 493452, 8 pages, 2015.

[11] M. A. Ebrahim and R. Mohamed, "Comparative study and simulation of different maximum power point tracking (MPPT) techniques using fractional control & grey wolf optimizer for grid connected pv system with battery," in *Electric Power Conversion*, IntechOpen, London, UK, 2019.

[12] M. Dorigo and T. Stützle, "Ant colony optimization: overview and recent advances," in *Handbook of Metaheuristics*, pp. 311–351, Springer, 2019.

[13] J. Kumar, K. V. Azar Ahmad Taher, and R. K. P. Singh, "Design of fractional order fuzzy sliding mode controller for nonlinear complex systems," in *Mathematical Techniques of Fractional Order Systems*, pp. 249–282, Elsevier, 2018a.

[14] Y. Sun and Y. Yihan, "Non-inverting buck-boost converter control," US Patent App. 15/729,366, 2018.

[15] A. Mohapatra, *Optimized parameter estimation, array configuration and MPPT control of standalone photovoltaic system*, Ph.D. thesis, National Institute of Technology, Rourkela, India, 2018.

[16] K. Sundareswaran, V. Vigneshkumar, P. Sankar, S. P. Simon, P. S. R. Nayak, and S. Palani, "Development of an improved P&O algorithm assisted through a colony of foraging ants for mppt in PV system," *IEEE Transactions on Industrial Informatics*, vol. 12, no. 1, pp. 187–200, 2015.

[17] S. Duman, N. Yorukeren, and I. H. Altas, "A novel MPPT algorithm based on optimized artificial neural network by using FPSOGSA for standalone photovoltaic energy systems," *Neural Computing and Applications*, vol. 29, no. 1, pp. 257–278, 2018.

[18] R. Sahu and B. Shaw, "Design of solar system by implementing alo optimized pid based mppt controller," *Trends in Renewable Energy*, vol. 4, no. 3, pp. 44–55, 2018.

[19] B. Oubbati, M. Boutoubat, M. Belkheiri, and A. Rabhi, "Extremum seeking and P&O control strategies for achieving the maximum power for a PV array," in *International Conference in Artificial Intelligence in Renewable Energetic Systems*, pp. 233–241, Springer, Cham, Switzerland, 2018.

[20] R. Pradhan, S. Pradhan, and B. B. Pati, "Design and performance evaluation of fractional order PID controller for heat flow system using particle swarm optimization," in *Computational Intelligence in Data Mining*, pp. 261–271, Springer, Cham, Switzerland, 2019.

[21] N. A. Kamal and A. M. Ibrahim, "Conventional, intelligent, and fractional-order control method for maximum power point tracking of a photovoltaic system: a review," in *Fractional Order Systems*, pp. 603–671, Elsevier, Amsterdam, Netherlands, 2018.

[22] Y. Michimura, K. Komori, A. Nishizawa et al., "Particle swarm optimization of the sensitivity of a cryogenic gravitational wave detector," *Physical Review D*, vol. 97, no. 12, p. 122003, 2018.

[23] P. M. Kumar, U. Devi G, G. Manogaran, R. Sundarasekar, N. Chilamkurti, and R. Varatharajan, "Ant colony optimization algorithm with internet of vehicles for intelligent traffic control system," *Computer Networks*, vol. 144, pp. 154–162, 2018b.

[24] E. Emary and H. M. Zawbaa, "Feature selection via lèvy antlion optimization," *Pattern Analysis and Applications*, vol. 22, no. 3, pp. 857–876, 2018.

[25] A. A. Heidari, H. Faris, S. Mirjalili, I. Aljarah, and M. Mafarja, "Ant lion optimizer: theory, literature review, and application in multi-layer perceptron neural networks," in *Nature-Inspired Optimizers*, pp. 23–46, Springer, Cham, Switzerland, 2020.

Hindawi
Complexity
Volume 2019, Article ID 7414318, 13 pages
https://doi.org/10.1155/2019/7414318

Research Article

Parallel LSTM-Based Regional Integrated Energy System Multienergy Source-Load Information Interactive Energy Prediction

Bo Wang,[1] **Liming Zhang**,[1] **Hengrui Ma**,[2] **Hongxia Wang**,[1] **and Shaohua Wan**[3]

[1]*School of Electrical Engineering, Wuhan University, Wuhan 430070, China*
[2]*Tus-Institute for Renewable Energy, Qinghai University, Xining, China*
[3]*School of Information and Safety Engineering, Zhongnan University of Economics and Law, Wuhan 430073, China*

Correspondence should be addressed to Shaohua Wan; shaohua.wan@ieee.org

Received 16 July 2019; Accepted 17 October 2019; Published 22 November 2019

Guest Editor: Xiaoqing Bai

The multienergy interaction characteristic of regional integrated energy systems can greatly improve the efficiency of energy utilization. This paper proposes an energy prediction strategy for multienergy information interaction in regional integrated energy systems from the perspective of horizontal interaction and vertical interaction. Firstly, the multienergy information coupling correlation of the regional integrated energy system is analyzed, and the horizontal interaction and vertical interaction mode are proposed. Then, based on the long short-term memory depth neural network time series prediction, parallel long short-term memory multitask learning model is established to achieve horizontal interaction among multienergy systems and based on user-driven behavioral data to achieve vertical interaction between source and load. Finally, uncertain resources composed of wind power, photovoltaic, and various loads on both sides of source and load integrated energy prediction are achieved. The simulation results of the measured data show that the interactive parallel prediction method proposed in this article can effectively improve the prediction effect of each subtask.

1. Introduction

With the depletion of fossil energy, the contradiction between energy demand growth and energy shortage in the process of social and economic development, energy utilization, and environmental protection is becoming more and more serious. Under such background, the consumption system of traditional energy production with fossil energy as the core has been difficult to sustain, so building a multienergy complementary and optimized energy supply and demand system and guiding the overall transformation of the energy industry have become the top priority of China's energy sector development [1]. On the basis of energy system source-network-load-storage vertical optimization, the multienergy supply systems are coordinated and optimized in a horizontal direction by the multienergy coupling relationships to realize integrated energy system for energy cascade utilization and multienergy coordinated scheduling, which will play a key role in the abovementioned energy revolution [2]. On the one hand, it will improve energy efficiency through comprehensive development and utilization of energy, and on the other hand, it will increase the potential energy penetration rate by converting electricity into heat, cold, natural gas, electric vehicle energy storage, etc.

The extension of IES in end users is called regional integrated energy system (RIES). In the RIES with intermittent renewable energy such as wind power/photovoltaic, due to the coupling and interconnection of various energy subsystems such as power system, thermal system, natural gas system, and transportation system, the energy consumption data are scattered and multidimensional of the versatile load such as electric load, heat load, and gas load on the user side. Such huge amount of data information is of great value in situational awareness, especially in new energy generation and load forecasting [3]. Zhang et al. [4] used

data analysis and prediction algorithms to verify the correlation between energy consumption behavior and distributed PV output and input the prediction results into the predicted energy management system to optimize load-side energy consumption and balance the system's energy supply and load demand. Deng et al. [5] proposed the energy 5.0 concept based on cyber-physical-social systems (CPSS) and analyzed the social behavior characteristics of load-side energy consumption in smart home energy systems, by collecting a variety of operational information in the actual system by using the "data driven + physical model" approach to form a new energy forecasting agent to achieve optimal operational control [6–8]. In addition, in the energy prediction of RIES, deep learning prediction technology has attracted the attention of many scholars at home and abroad. Wang et al. [9] have made extensive analysis and discussion on renewable energy forecasting methods based on deep learning, discussed the current problems facing this direction, and prospected the future development direction. Wang et al. [10] proposed a wind speed prediction model based on deep confidence network and achieved good prediction results. Chen et al. [11] proposed a new two-layer nonlinear combination short-term wind speed prediction method (EEL-ELM). In the first layer, the extreme learning machine (ELM), Elman neural network (ENN), and long short-term memory (LSTM) neural network are used to predict wind speed, and three prediction results are obtained. Then, the nonlinear aggregation mechanism of extreme learning machine (ELM) is used to alleviate the inherent weakness of single method and linear combination. Liu et al. [12] combined variational mode decomposition (VMD), singular spectrum analysis (SSA), long short-term memory (LSTM) network, and extreme learning machine (LEM) and proposed a new multistep wind speed prediction model. The simulation results show that the method is more effective and robust in extracting trend information. On the basis of multiple long short-term memory (LSTM) learning, the literature [13] combines the extreme value optimization algorithm and the support vector machine model to integrate the LSTM layer prediction results and predicts the wind speed in a short time. In literature [14], the LSTM deep neural network algorithm is used, and the user's energy data of various types of equipment are used to predict the residential load on the load side in a short term, which proves the data value of the load energy information in the forecasting field. Multitask learning has been studied for about 20 years [15–17]. At present, multitask learning methods can be roughly summarized into two categories. One is to share the same parameters between different tasks, and the other is to mine the shared data features hidden between different tasks [18]. Argyriou et al. [19] detailed the four multitasking learning methods of feature selection, kernel selection, adaptive pooling, and graphical model structure. Jebara [20] proposed a typical multitask model for mining common features between multitasks. A framework for multitask feature learning is given in this paper, which becomes the basis for many multitask learning references [21, 22]. Inspired by the above literature, this paper argues that it is necessary to explore the value of multienergy coupling information and load-side user behavior characteristics for energy system operation and use the information correlation characteristics between multiple energy sources to expand the concept of multienergy interaction to the forecasting stage. The "information interaction" strategy is proposed and explored the data information implied in each link of RIES by combining deep learning technology, and the energy utilization efficiency is maximized through multienergy interaction. Based on the existing research, this paper comprehensively considers the horizontal and vertical information interaction characteristics between multiple energy loads in RIES and proposes a parallel energy LSTM based on multienergy-load information interactive short-term energy prediction strategy. Firstly, the RIES multi-energy-charge coupling correlation is analyzed, and the horizontal and vertical "information interaction" modes of multienergy load are proposed. Then, from the perspective of information interaction, based on the LSTM deep neural network time series prediction, the parallel LSTM multitask learning model is established to realize the horizontal interaction between multienergy systems. At the same time, based on the user's energy behavior data driving, the vertical interaction between the source and the load is realized, and the uncertain sources are used for integrated energy prediction of the wind power, photovoltaic, and various loads on both sides of the source and the load. Finally, based on the measured data of a region's RIES, the prediction model is trained and verified. The simulation results show that the proposed information interactive parallel prediction method can effectively improve the prediction effect of each subtask.

2. Regional Integrated Energy System

2.1. Basic Structure of Regional Integrated Energy System. The regional integrated energy system takes the electricity as the core, is based on smart grid, and is led by clean energy. It uses advanced information communication and energy conversion technologies to organically connect the links of producing, transporting, storing, and consuming in the multienergy systems such as electricity, gas, and heat so as to achieve optimal allocation of energy, multienergy coupling, and complement [23]. RIES structurally includes regional energy production input network, multienergy coupling network, and regional internal load-side energy output network. It can fully absorb all kinds of renewable energy such as wind power and photovoltaic and access various types of loads such as electricity, gas, heat, and cold to achieve efficient energy allocation. At the same time, its top layer has an integrated information communication support system to achieve the interactive fusion of energy flow and information flow. The basic architecture of the RIES described in this paper is shown in Figure 1.

2.2. Characteristics of Regional Integrated Energy System "Information Interconnection". Under the support of the energy Internet and multienergy key technologies characterized by "open" and "interconnected," the coupling interaction of multienergy-network-load-storage in RIES is

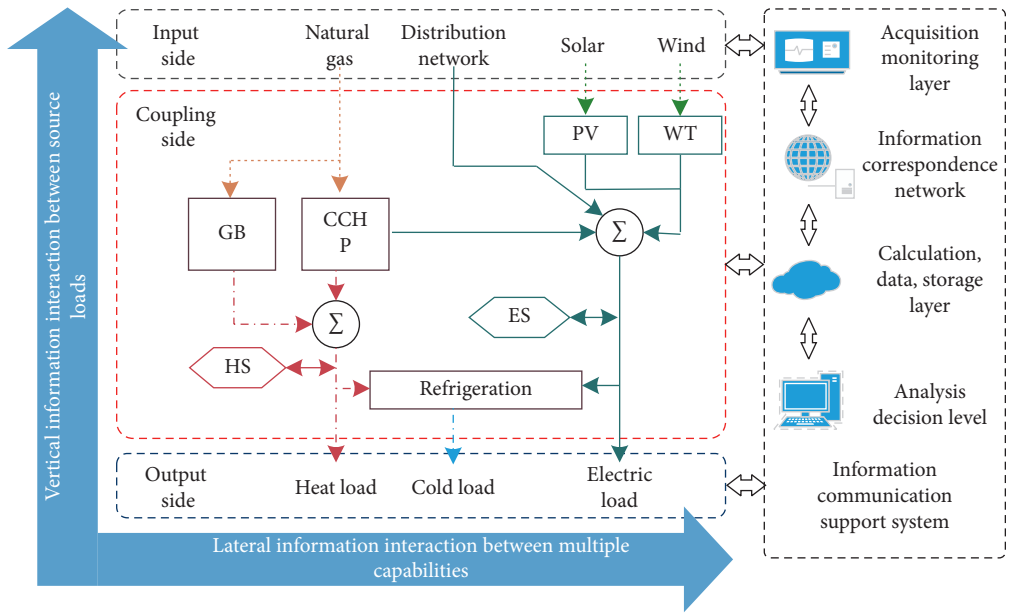

Figure 1: Basic framework of RIES.

more tight [24]. (1) From the perspective of horizontal interconnection, RIES will integrate the energy subsystems such as cold/heat/electric/gas/traffic to construct a multienergy flow system. The energy is converted and flowed between the systems through the coupling components, and the various energy forms complement each other. The energy resources have to be optimally configured in a wide area, that is, to achieve the "horizontal information interconnection" of the energy Internet. (2) From the perspective of vertical interconnection, based on the traditional energy supply network, RIES will realize the real-time sharing of information resources in the source-network-load-storage through Internet technology. This resource sharing mechanism has two-way conduction characteristics. The user has information bidirectional conduction capability between the information control system, the energy supply module, and the multienergy intelligent delivery module. The interactive sharing of energy information can also be realized between users, that is, to realize the "vertical information interconnection" of the energy Internet.

3. RIES Multienergy Coupling Correlation Analysis

3.1. RIES Horizontal Multienergy Information Coupling. The horizontal multienergy information coupling correlation of RIES is represented by the correlation between different energy flow subsystems such as electricity, gas, and heat.

From the perspective of coupling, the composition of the RIES can be divided into a coupling unit and a noncoupling unit. As shown in Figure 2, the coupling unit connects different energy flow subsystems and consumes one or more energy sources to generate other energy sources. Typical coupling forms are as follows: cold and heat electricity

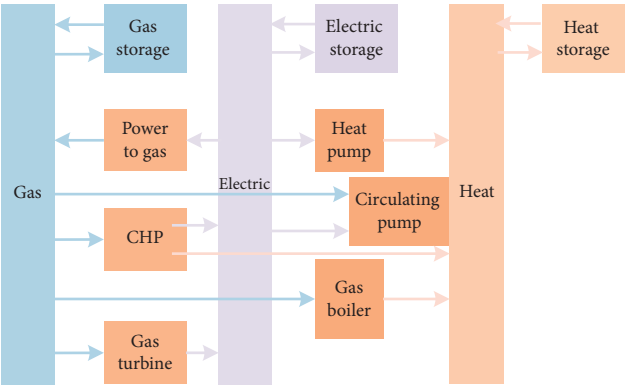

Figure 2: Transverse multicoupling schematic diagram.

supply units consume coal or natural gas to generate electricity, heat, and cold. The heat pump consumes electrical energy to generate thermal energy, the electrical hydrogen consumes electrical energy to generate hydrogen, and the coupling unit causes the energy flow subsystems to interact. The uncoupled unit includes the network and equipment inside each energy flow subsystem and other uncoupled boundary conditions such as source and load. The uncoupled unit also affects other systems through the coupling unit [25]. Therefore, different energy flow subsystems have strong coupling between them, and there is a large amount of horizontal multienergy coupling information existing in the multienergy system data, resulting in great correlation between various units within the system.

3.2. RIES Vertical Source-Load Information Coupling. The vertical source-load information coupling correlation of RIES is represented by the correlation between the multienergy supply of the source and the user's energy behavior of

the load. Different energy behaviors correspond to different load characteristics [26]. For example, the lighting behavior in RIES is a typical user energy behavior. Through advanced measurement devices, the user's lighting behavior can be reflected as a lighting load curve.

From the perspective of user energy behavior, there are multiple coupling relationships between multiple energy loads in RIES. Taking the user's lighting behavior as an example, if the cloud suddenly covers a certain area and reduces the ambient light intensity, it will affect the user's lighting behavior: people will increase the lighting equipment usage to meet the lighting demand, and the lighting load will increase. At the same time, such cloud movements will also have an impact on photovoltaic power generation: cloud clusters will block the photovoltaic panels, which will affect the irradiance reduction on the photovoltaic panels and affect the photovoltaic power generation. In order to prove the characteristics of this behavioral feature, this paper takes the data of three days from January 24 to 26, 2016, of RIES in a certain area of Tianjin for quantitative analysis. The photovoltaic power output curve and the user lighting load curve are shown in Figure 3.

The upper part of Figure 3 is the curve trend of the photovoltaic power output, and the lower part is the curve trend of the user's lighting load. (1) Both the user's lighting load and the photovoltaic power output have a day and night cycle. The distribution of them is mainly concentrated in the daytime. The peak of the user's lighting load is generally distributed between 18 : 00 and 20 : 00, and the peak output of the photovoltaic power supply is generally distributed between 12 : 00 and 14 : 00 at noon. (2) Taking the three-day short-term data for comparison analysis, the overall output of photovoltaic power generation on the third day was significantly larger than the previous two days. Accordingly, the lighting load on the third day between 10 : 00 and 16 : 00 is reduced compared to the previous two days and it is reduced to the low of the day. It shows that when the output of photovoltaic power generation increases, it also affects the user's energy consumption behavior when the ambient light intensity is large, which means that the user's demand for lighting energy is reduced. (3) Take the ultra-short-term data analysis from 12 : 00 to 16 : 00 on the first day, and the photovoltaic power output reaches the peak of one day at 13 : 00, and the lighting load is also reduced to low of the daytime at this moment. During the period from 13 : 00 to 14 : 00, a sudden downward climb occurs, and the lighting load increases at the corresponding time. This "mutation" phenomenon should be caused by the cloudy weather affected by the cloud. From the above analysis, it can be found that there is a strong information coupling correlation between the "source" photovoltaic power output and the "charge end" user's lighting load.

3.3. RIES Multienergy Information Interaction Mode. RIES has both horizontal multienergy information coupling correlation characteristics and vertical source-load information coupling correlation characteristics. From the perspective of information interaction energy management,

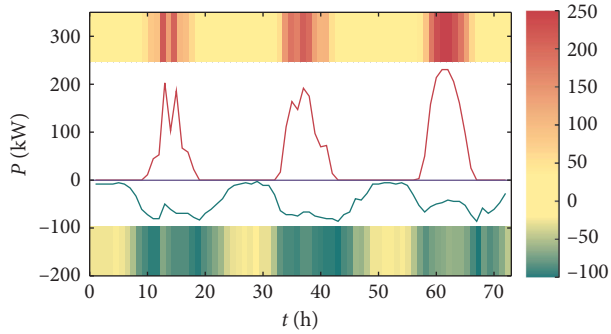

Figure 3: The relationship between the photovoltaic power curve and the lighting load curve of the user.

there are also two horizontal and vertical information interaction modes.

The horizontal information interaction mode is based on multienergy conversion information sharing. On the basis of obtaining the measurement data of the multienergy flow subsystem, the nonlinear artificial intelligence deep learning technology is used to process the multienergy data in parallel, and it effectively utilizes the complex shared information of energy conversion, identifies the abstract features of the training data, and improves the precision of subtask prediction of the energy management.

The vertical information interaction mode is based on user behavior information sharing. On the basis of obtaining multicategory data on both sides of the source and the load, the deep learning method is used to dig the user-side behavior characteristics, and the associated user behavior information data are taken as input to guide the source-side energy management prediction and improve the prediction accuracy of the energy supply end.

4. Multitask Learning Mechanism for Deep Learning Energy Prediction

4.1. LSTM Recurrent Neural Network

4.1.1. Principle of LSTM Cyclic Neural Network. The training objects of the source-charged uncertain resources have obvious timing characteristics, and the sequence data have strong correlation before and after. From the perspective of learning and training, recurrent neural network (RNN) can process sequences with temporal correlation of arbitrary length by using neurons with self-feedback, which has obvious advantages in processing sequence data [27]. The structure of the RNN is shown in Figure 4(a). The LSTM network is a variant of RNN that overcomes the traditional RNN gradient demise problem [28]. The hidden layer is no longer a simple neural unit, but an LSTM unit with a unique memory mode. Each LSTM unit contains a state cell that describes the current state of the LSTM unit [29]. c represents the current state quantity of the LSTM unit, and h represents the current output of the LSTM unit.

LSTM reads and modifies state units by controlling the forget gates, input gates, and output gates [30], which are

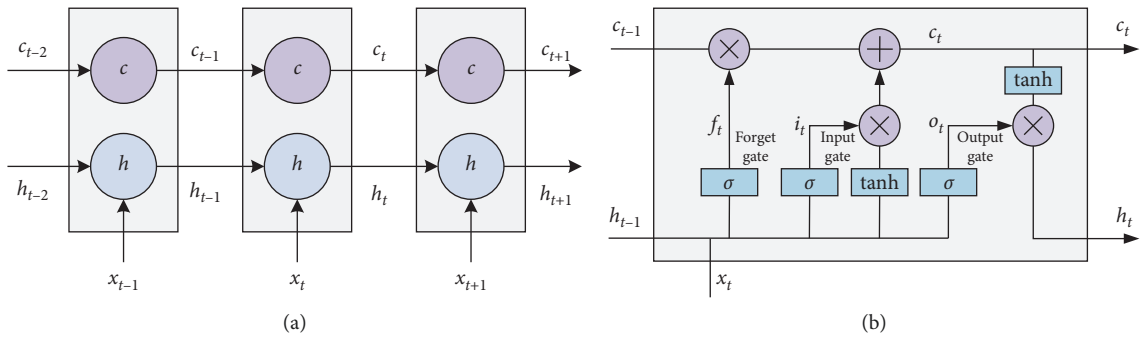

Figure 4: Schematic diagram of RNN and LSTM. (a) The structure of the RNN. (b) The structure of the LSTM cell.

typically formed by sigmoid or tanh functions and Hadamard product operation. As shown in Figure 4(b), the forget gate determines c_{t-1} of the previous moment and how many components of the cell state c_t remain at the current time, and the input gate determines how many components of the network input are saved to the cell state c_t at the current time x_t and how many components of the output gate control cell state c_t are output to the current value h_t of the LSTM.

The calculation formula between the variables of the LSTM unit is as follows:

$$\begin{aligned} f_t &= \sigma\left(W_{fx}x_i + W_{fh}h_{t-1} + b_f\right), \\ i_t &= \sigma\left(W_{ix}x_i + W_{ih}h_{t-1} + b_i\right), \\ g_t &= \phi\left(W_{gx}x_t + W_{gh}h_{t-1} + b_g\right), \\ c_t &= f_t \odot c_{t-1} + i_t \odot g_t, \\ o_t &= \sigma\left(W_{ox}x_t + W_{oh}h_{t-1} + b_o\right), \\ h_t &= o_t \odot \phi\left(c_t\right). \end{aligned} \tag{1}$$

In the formula, $W_{fx}, W_{fh}, W_{ix}, W_{ih}, W_{gx}, W_{gh}, W_{ox}$, and W_{oh} are the weight matrices corresponding to the input of the network activation function; b_f, b_i, b_g, and b_o are the offset vectors; $\odot$ represents the multiplication of the Hadamard product matrix; σ represents the sigmoid activation function, and ϕ represents the tanh activation function.

4.1.2. LSTM Deep Learning Training Algorithm. The training of LSTM network adopts BP-based backpropagation through time (BPTT) [31]. The algorithm steps are as follows: (1) Calculate the output value of each neuron forward. For the LSTM unit, the values of the six vectors, such as f_t, i_t, g_t, c_t, o_t, and h_t, are calculated. (2) Calculate the error term of each neuron in reverse. Similar to traditional RNN, the backpropagation of the LSTM error term consists of two levels: one is at the spatial level, and the error term is propagated to the upper layer of the network; the other is at the time level, which propagates back in time. For example, from the current time of t, the error at each moment is calculated. (3) Calculate the gradient of each weight according to the corresponding error term, and update the network weight parameter. (4) Jump to the first step and continue to perform the first 3 steps until the network error is less than the given value.

4.2. LSTM Network Multitask Learning Mechanism. Multitask learning (MTL), as an inductive migration mechanism, avoids the underfitting of model training by using the correlation between multiple tasks, digging the hidden common features, and improving the generalization learning ability of the model [32]. RIES source wind and light prediction and load-end electricity, gas, heat, and cold load prediction can be regarded as different tasks in multitask learning [33]. Multiple tasks share some common data or model structures, that is, there is a certain correlation between the multienergy prediction tasks. The multitask learning prediction model based on the LSTM network proposed in this paper shares the hidden layer nodes among all prediction tasks through the hard parameter sharing method and trains the training data corresponding to the multienergy prediction tasks at the same time, considering the correlation information between tasks to improve the learning ability of all predictive tasks [34]. A comparison of single-task and multitask learning based on the LSTM network is shown in Figure 5. The multisource historical data in the figure is a collection of five types of historical data including wind power, photovoltaic, electric load, heat load, and cold load.

5. Parallel LSTM-Based RIES Information Interactive Energy Prediction Method

5.1. RIES Multienergy Prediction Model Design. RIES has uncertainties at both the source and the load end, so accurate prediction of uncertain resources is the basis for implementing RIES energy optimization management and scheduling [35]. The source mainly includes wind power prediction and photovoltaic power prediction, and the load mainly includes electric load prediction, thermal load prediction, and cold load prediction.

As described in the second section of this paper, there are intricate mutual coupling relationships between multiple energy loads of RIES, and the prediction tasks of uncertain resources on both sides of the source and load have strong correlation. It can effectively improve the overall prediction accuracy of the RIES uncertain resources by learning this coupling relationship through joint prediction training [36]. From the perspective of RIES multienergy-load information interaction, this paper proposes the concept of "parallel

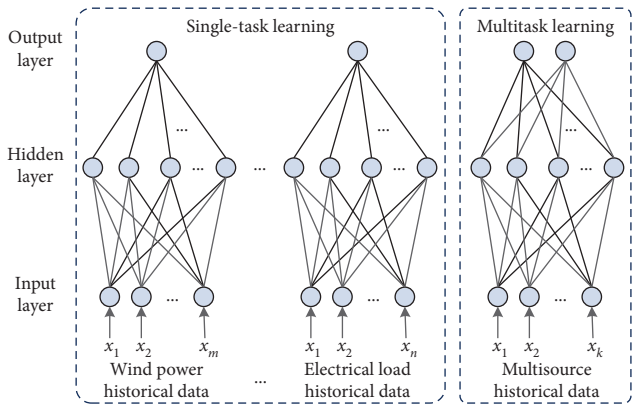

Figure 5: Comparison of single-task and multitasking learning based on the LSTM network.

prediction" and utilizes the strong nonlinear learning ability and historical memory advantages of LSTM deep learning network to conduct integrated prediction of uncertain resources at both source and load. As shown in Figure 6, the horizontal information interaction based on multienergy conversion information sharing mainly utilizes the multitask learning parameter sharing mechanism of the parallel LSTM prediction network; the vertical information interaction based on the user behavior information sharing mainly uses the user behavior data to guide source-load multitask prediction as an additional unified input information. Parametric sharing is weight sharing, which takes advantage of the correlation between subtasks. Input sharing refers to data sharing. Different subtasks share historical power data such as wind power, photovoltaic power, power load, thermal load, and cooling load.

5.2. Data Preprocessing. The training samples select the wind power generation time series on the source side, the photovoltaic power generation time series, the charge side on the load side, the heat load, the cold load time series, and the illumination load series data. Considering the input and output range of the nonlinear activation function in the model, in order to avoid neuron saturation, the data are normalized and mapped between $[-1, 1]$, as shown in the following equation:

$$x' = \frac{x - (x_{\max} + x_{\min})/2}{(x_{\max} - x_{\min})/2}. \quad (2)$$

In the equation, x is the actual input or output data and $x_{\max}$ and $x_{\min}$ are the maximum and minimum values of the variable, respectively.

5.3. Task Construction. The essence of using the multitask learning method for multienergy-load integration prediction lies in the close correlation of each prediction subtask [37]. The traditional single-task prediction method uses a single dimension of historical observations to predict its future output, and the model output is a single attribute. The multitask learning integration prediction uses the multidimensional data on both sides of the source and the load as a common input to effectively utilize the sample. On the other hand, through the shared hidden layer node division method, the five attributes of wind, photovoltaic power generation, electricity, heat, and cold load are simultaneously predicted to play the role of inductive bias and improve prediction accuracy.

5.4. Model Training. The LSTM-based source-charge integrated prediction model mainly needs to determine the following parameters: input layer dimension, input layer time step, hidden layer number, each hidden layer dimension, and output layer dimension [38].

The time step of the input layer is generally the length of the variable time series used for the source-load integration prediction. According to the periodic characteristics of the prediction object sequence, the input layer time step is set to 24, that is, the historical data whose resolution ratio is 1 h during the first seven days before the input is used for forecasting and it takes up one input node per day. The input layer dimension is the number of nodes. The input layer node of this paper contains six objects: wind power generation time series, photovoltaic power generation time series, charge side load, heat load, cold load time series, and lighting load series, which constitutes totally 42 nodes, so the input layer dimension is set to 42. Since this paper simultaneously predicts six attributes of wind power, photovoltaic, electricity, heat, and cold load, the output layer has 5 nodes, that is, the output layer dimension is set to 5. In this paper, based on experience and multiple trial and comparison, the number of hidden layers is set to 2, and the dimension of the hidden layer is set to 30. The selection of the activation function is as shown in Figure 4(a), the batch_size is set to 42, the numbers of iterations of an epoch is set to 8784, the learning rate is set to 0.80, and the learning delay rate is set to 0.05. The network training function uses the BPTT algorithm mentioned above.

5.5. Evaluation Indicators. Multienergy-load integration forecasting simultaneously trains multiple forecasting tasks. To comprehensively measure the forecasting effect, it is necessary to evaluate the integrated forecasting accuracy as a whole [39]. In this paper, the average accuracy evaluation index based on weight coefficient is proposed. For the importance degree of different energy on the two sides of the RIES, the corresponding weight coefficient is given to different energy output types. For an RIES, the uncertainties of the source-side wind, light, and other uncertain resources are large and have a great influence on the stable operation of the system and the energy dispatch management. Therefore, the source-side wind forecasting is set to a higher weight; in addition, as the power grid plays a leading role in the integrated energy system by virtue of its perfect architecture and central hub advantages, correspondingly, the power load forecast is set to a higher weight.

This paper proposes three calculation indicators, namely, mean absolute percentage error (MAPE), mean accuracy

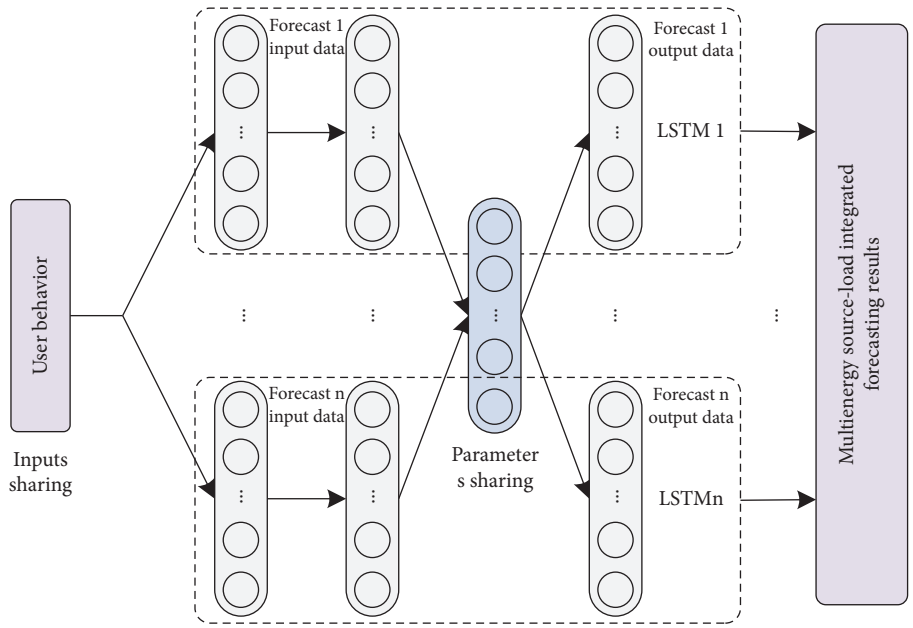

Figure 6: Interactive energy prediction model of RIES information based on parallel LSTM.

(MA), and weighted mean accuracy (WMA), as shown in the following equation:

$$\begin{aligned} \mathrm{MAPE} &= \frac{1}{n}\sum_{i=1}^{n}\left|\frac{P(i)-\widehat{P}(i)}{P(i)}\right| \times 100\%, \\ \mathrm{MA} &= 1 - \mathrm{MAPE}, \\ \mathrm{WMA} &= \lambda_1 \mathrm{MA}_1 + \lambda_2 \mathrm{MA}_2 + \cdots + \lambda_k \mathrm{MA}_k. \end{aligned} \tag{3}$$

In the equation, $P(i)$ and $\widehat{P}(i)$, respectively, represent the actual energy value and the predicted energy value at the first moment; n is the sample data amount; MA_k represents the prediction accuracy of the k prediction task; and λ_k represents the weight coefficient of the k prediction task. In this paper, the weight ratios of the energy predictions on both sides of the source and the load are set as shown in Table 1.

6. Simulation Analysis

6.1. Data Description. The experimental data in this paper are derived from the measured data provided by RIES in a certain area of Tianjin. The RIES consists of a power system, a thermal system, and a natural gas system. The source side includes energy supply equipment, such as wind turbines and photovoltaic power generation equipment. Coupling links include energy conversion equipment, such as cold and thermal power supply equipment, electric boilers, and gas boilers. Energy demand mainly includes power load, heat load, and cooling load. The load side and the energy storage side contain devices such as electrical energy storage and thermal energy storage to improve the flexibility of the system. In addition, in order to prove the validity of the source-load vertical information interaction, the historical data of the lighting load reflecting the typical electricity usage behavior of the user are also sampled. All historical energy data sampling interval is 1 h, data from July 2015 to June 2016 are used as training set data, and data from July 2016 are used as test set data, with 1 h as time step; based on the historical data of the first 7 days, the energy supply and energy demand on both sides of the source and the load in the next day are predicted. The total 57168 samples were divided into two parts (92% as the train set and 8% as the test set). The forecasting models were trained by the train dataset and validated on the test dataset. The statistical information of the above dataset is shown in Table 2.

6.2. Analysis of Examples. This section analyzes the effect of RIES multienergy information interactive energy prediction. The selected sunny day and rainy day of the test set were analyzed separately. The energy prediction results of wind power output, photovoltaic output, electric load, heat load, and cold load on both sides of the source and the load in the two scenarios are shown in Figures 7 and 8, respectively.

The prediction results of Figures 7 and 8 show that the proposed source-load parallel LSTM learning model can obtain ideal results in wind energy, photovoltaic, electric load, thermal load, and cold load energy prediction in sunny day scenario and rainy day scenario, which confirms the effectiveness of the model proposed in this paper. The prediction effect of each subtask in the parallel prediction results shows a large difference. Compared with the wind and light prediction on the source side, the predicted curves of the charge, heat, and cold load on the charge side are closer to the actual sequence curve, which is due to the intermittent and random nature of source-side wind power and photovoltaics.

Comparing Figures 7(c)–7(e), it can be found that the electric load is more volatile than the thermal load and the cold load, which is because the thermal inertia and cold

Table 1: Weight settings of source-load double-sided energy prediction tasks.

Prediction task	Wind power	PV power	Electric load	Heat load	Cold load
Weight coefficient	0.25	0.25	0.2	0.15	0.15

Table 2: The description of simulation dataset.

Data type	Max (kW)	Median (kW)	Min (kW)	Mean (kW)	Std (kW)	Train set size	Test set size
Wind power	317.561	233.774	36.612	216.102	78.964	8784	744
Photovoltaic power	235.000	0.000	0.000	42.507	70.557	8784	744
Electric load	696.585	584.923	209.872	523.803	139.174	8784	744
Heat load	148.473	92.719	60.532	100.076	27.240	8784	744
Cold load	436.964	223.213	39.046	221.949	135.304	8784	744
Lighting load	03.333	50.000	2.778	44.792	27.734	8784	744
Multisource fusion	—	—	—	—	—	52704	4464

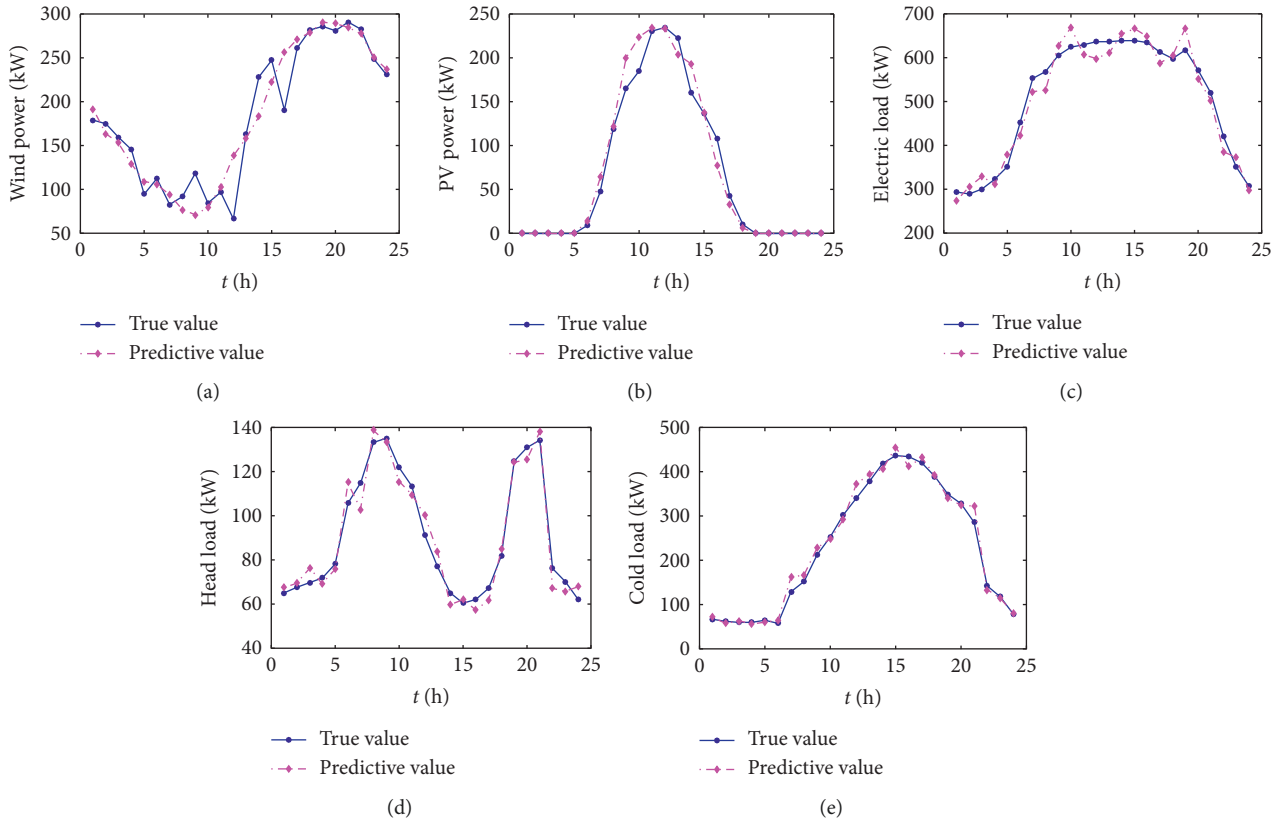

Figure 7: The results of source-load bilateral energy prediction within a sunny day. (a) Prediction of wind power. (b) Prediction of PV power. (c) Prediction of electric load. (d) Prediction of heat load. (e) Prediction of cold load.

inertia of the thermal system are stronger [39], and the volatility is also even smaller. Thermal inertia means that the dynamic change of the thermal system is a slow process from a time scale. Compared with the power system, the heat energy transmission exhibits a delay effect, and the upper and lower fluctuations of the heat load exhibit an inertial effect, and the cold inertia is similar. Because of the existence of thermal inertia and cold inertia, the thermal load in the thermal system is less random in the short-term predicted time scale, showing a characteristic of smooth variation, so its prediction uncertainty is also small, and the thermal load and the cold load are relative to the electricity. The prediction error of the load is also relatively small. Comparing Figures 7 and 8, it can be found that the uncertainty of actual photovoltaic power and actual wind power in rainy day scenes is larger than that of sunny days. The forecast curve of photovoltaic and wind power in sunny scenes is closer to the true value; the electric load and heat load in rainy scenes

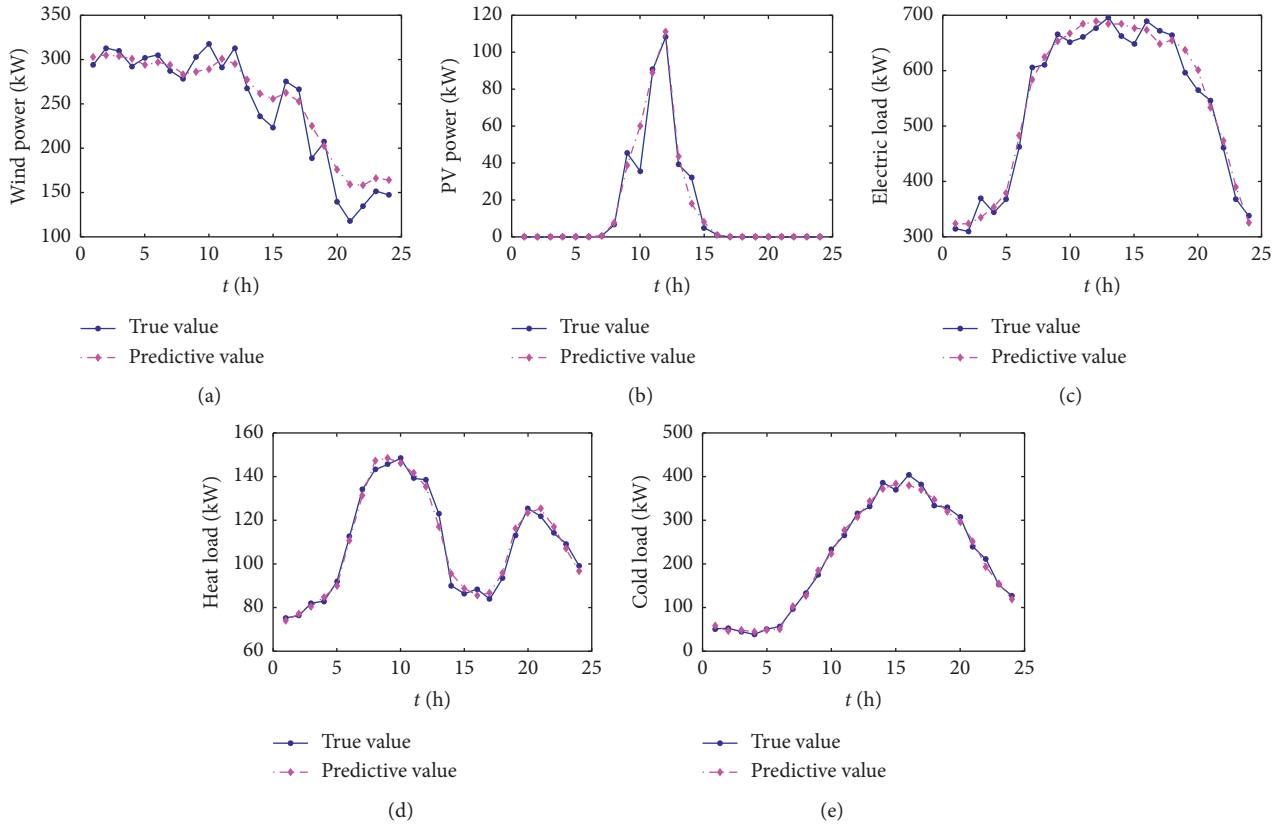

Figure 8: The results of source-load bilateral energy prediction within a rainy day. (a) Prediction of wind power. (b) Prediction of PV power. (c) Prediction of electric load. (d) Prediction of heat load. (e) Prediction of cold load.

should increase as a whole. This is due to the cold weather in the rainy scenes, which affects the user's energy use behavior and increases the user's demand for electricity and heat, thus increasing the electrical load and heat load.

6.2.1. Comparative Analysis of Multienergy Load Information Interaction. In order to verify the effect of interactive learning of horizontal and vertical multienergy information, the parallel LSTM predictions considering user energy behavior and parallel LSTM prediction without considering user energy behavior and the results of single LSTM prediction without considering user energy behavior are proposed to conduct a comparative analysis. In order to ensure the fairness of the experimental test, this paper uses the same dataset for training and testing.

The comparison experiment setup is shown in Table 3. In the parallel LSTM learning without considering the user's energy behavior, the input sample is based on the original prediction model A, and the lighting load data reflecting the user behavior in the input sample are not considered. The prediction is based only on the historical data of the predicted object; the model C does not consider the single LSTM prediction of the user's energy behavior, and the input and output of each subprediction model only consider the input and output of a single energy, and there is also no parameter sharing between the LSTM unit of the different submodels. Model B uses parallel LSTM learning. There is parameter sharing among each subtask, which belongs to a multitask learning. Model C uses a single LSTM learning, and each subtask does not affect each other. It belongs to a single-task learning.

The prediction accuracy of the multienergy charge information interaction comparison experiment is shown in Table 4 and Figure 9. Through the analysis of Table 4 and Figure 9, it shows that the average prediction accuracy of the weights of the models A, B, and C are 0.9009, 0.8917, and 0.8728, respectively. The prediction result of the model A is the best, the model B is the second, and the model C is the third. That is, considering the interaction of vertical and horizontal information, the energy predictions on both sides of the source and the load show better prediction accuracy.

Comparing the prediction results of Model B and Model C, for the five subprediction tasks, when the different quality energies are predicted together in parallel, a higher precision than the single prediction is obtained. It can be seen that parallel LSTM learning considering horizontal multienergy information interaction utilizes the coupled data between different systems to fully exploit the interactive information between different quality energy sources of the integrated energy system, so that the prediction performance of a certain energy can be improved. In addition, considering the multienergy horizontal information interaction, the predicted accuracy of the load-side electrical load, heat load, and

Table 3: Contrast experiment setting of multisource source information interaction.

Model	Vertical interaction	Horizontal interaction
Model A	User energy behavior is considered	Parallel LSTM learning
Model B	User energy behavior is not considered	Parallel LSTM learning
Model C	User energy behavior is not considered	Single-LSTM learning

Table 4: Three kinds of model prediction results of information interaction comparison experiment.

Precision	Wind power	PV power	Electric load	Heat load	Cold load	Mean precision
Model A	0.8602	0.8735	0.9236	0.9445	0.9407	0.9009
Model B	0.8542	0.8576	0.9113	0.9401	0.9368	0.8917
Model C	0.8414	0.8453	0.8836	0.9169	0.9124	0.8728

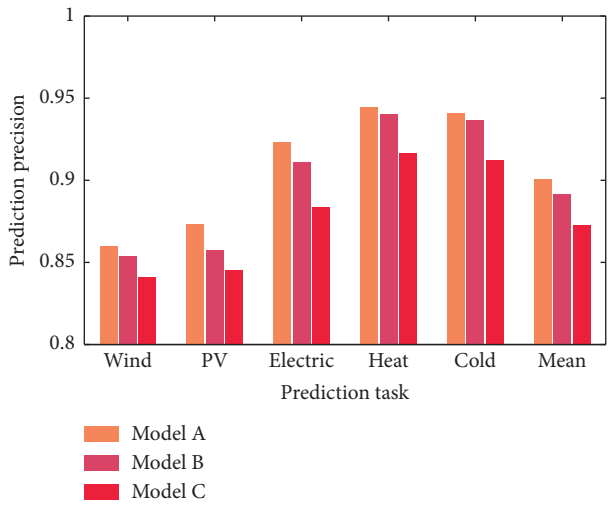

Figure 9: Comparison of prediction effects of three models.

cold load are increased by 3.13%, 2.53%, and 2.67%, respectively, while the predicted accuracy of the source-side wind power and photovoltaic is increased by 1.52% and 1.46% and the energy prediction accuracy of the charge side is relatively high. It can be seen that the source-side uncertainty resources are also affected by other energy interactions in the system, but the impact is small, while the charge side demand is largely affected by other energy interactions in the system. And the information interaction is more intimate between each other.

Comparing the prediction results of Model A and Model B, when the user's energy behavior information interacts between the source and the load in vertical direction, the average weight accuracy of the overall prediction is increased by 1.03%. Comparing the performance improvement effects of the five subprediction tasks, it can be found that the percentage improvement of PV prediction accuracy is 1.85%, and the improvement effect is relatively best, followed by the electrical load, while the prediction accuracy of wind power, heat load, and cooling load is not obvious. It can be seen that considering the source-load vertical information interaction can improve the energy prediction accuracy on both sides of the source and the load, but the specific user energy behavior has different differences in the energy prediction of different types of users, and the user lighting behavior is obviously related to photovoltaic power generation and user electricity. The interaction between loads is more tight, and its effect on PV prediction and electric load forecasting is more obvious.

6.2.2. Comparison of Deep Neural Network Algorithms with Other Algorithms. In order to verify the prediction effect of the LSTM deep neural network algorithm, the LSTM model and the autoregressive integrated moving average model (ARIMA) algorithm and the classic BP neural network (BPNN) algorithm in this paper are proposed. The simulation results of them were compared and analyzed. In order to ensure the fairness of the experimental test, this paper uses the same dataset for training and testing, and both use a single-task prediction strategy. The prediction results of the three algorithms are shown in Table 5 and Figure 10.

Observing the prediction results, the prediction effect of ARIMA algorithm is the most general, and the prediction accuracy of BPNN algorithm is much higher than that of ARIMA algorithm. The prediction accuracy of each task of LSTM deep learning prediction algorithm proposed in this paper is the highest. The ARIMA algorithm can not effectively use the historical information in the long-term sequence because it only uses a part of the historical information to train, which leads to the large prediction error. The LSTM algorithm can fully utilize its strong nonlinear learning ability and long-term and short-term memory advantages to exploit the information value of long-term historical data, so the grasp of the energy prediction law is more precise.

In addition, comparing the energy prediction results of the LSTM algorithm and the BPNN algorithm one by one, the LSTM algorithm predicts that the accuracy of the thermal load and the cold load prediction is more obvious. It can be seen that due to the greater inertia of the thermal system, the time scale of the change law is longer, which makes the prediction accuracy of the long-term and short-term deep learning on the heat load and the cold load significantly higher than the electric load.

In order to evaluate the computational efficiency of algorithms, four forecasting scenarios are performed ten times so that the forecasting results can reliably be summarized as in Table 6. Parallel LSTM and Single LSTM have longer training time, but the prediction time is kept within

Table 5: Comparison of prediction results of three algorithms.

Precision	Wind power	PV power	Electric load	Heat load	Cold load	Mean precision
LSTM	0.8414	0.8453	0.8836	0.9169	0.9124	0.8728
BPNN	0.8216	0.8314	0.8695	0.8912	0.8889	0.8542
ARMIA	0.7733	0.7824	0.8282	0.8454	0.8408	0.8075

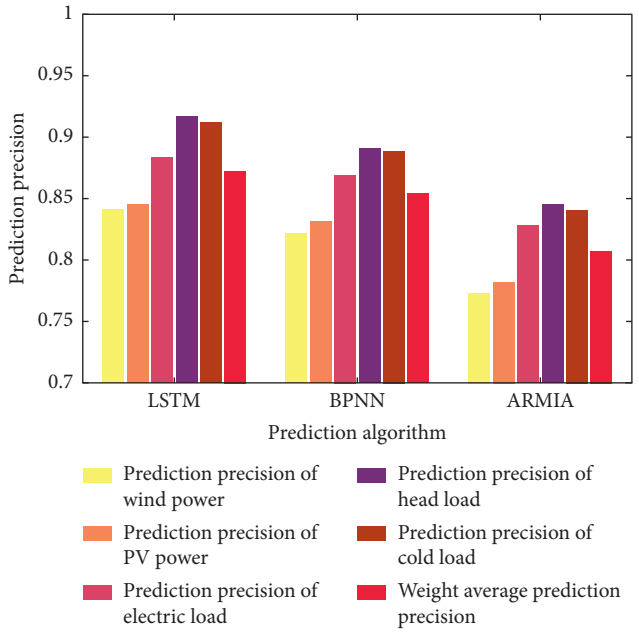

Figure 10: Comparison of prediction effects of three algorithms.

Table 6: Comparison of computational efficiency of four algorithms.

Algorithm	Training time average (sec)	Prediction time average (sec)
Parallel LSTM	4363.74	10.02
Single LSTM	12183.37	36.62
BPNN	10949.11	22.53
ARMIA	546.96	2.15

one minute and can meet the requirements of short-term forecasting. Further analysis shows that the parallel training time and prediction time of parallel LSTM is greatly improved compared to single LSTM due to the combination of five subtasks into one multitask learning. In summary, although the LSTM algorithm is time consuming in training time, for short-term prediction, the training process does not require online completion, and the prediction time of the LSTM algorithm, especially parallel LSTM, can fully meet the requirements of short-term prediction. Considering the prediction accuracy, the sacrifice of the LSTM algorithm in computing time is worthwhile.

7. Conclusion

In this paper, the horizontal and vertical information interaction characteristics between multiple energy loads in RIES are considered. Using LSTM network deep learning algorithm, a parallel LSTM-based multienergy-load information interactive short-term energy prediction method is proposed. Through the simulation of the test data, the following conclusions are drawn:

(1) The "information interaction" strategy proposed in this paper can effectively improve the prediction performance of source-load energy prediction in regional integrated energy systems

(2) Parallel prediction considering horizontal interaction mainly affects the prediction effect on the load side, while the information sharing of user illumination behavior considering vertical interaction mainly affects the improvement of PV prediction effect

(3) Compared with the conventional prediction algorithm, the LSTM deep learning algorithm can learn the deep hidden information of historical data, improve the prediction accuracy while meeting calculation time, and prove the effectiveness of the algorithm in the prediction of time series feature sequence

However, the performance of the proposed parallel LSTM algorithm may be further enhanced by some evolutionary algorithms or multiobjective optimization algorithms, such as differential evolution algorithm [40], multiobjective extremal optimization [41], and evolutionary multiobjective optimization algorithms [42–47]. Of course, some significant topics are worth researching on the optimization of the proposed parallel LSTM by multiobjective optimization.

Data Availability

The data used to support the findings of this study are available from the corresponding author upon request.

Conflicts of Interest

The authors declare no potential conflicts of interest.

Acknowledgments

This work was fully supported by the National Key Research and Development Program of China (no. 2018YFB0904200).

References

[1] A. Q. Huang, M. L. Crow, G. T. Heydt, J. P. Zheng, and S. J. Dale, "The future renewable electric energy delivery and management (FREEDM) system: the energy internet," *Proceedings of the IEEE*, vol. 99, no. 1, pp. 133–148, 2011.

[2] I. Colak, S. Sagiroglu, G. Fulli, M. Yesilbudak, and C. Covrig, "A survey on the critical issues in smart grid technologies,"

Renewable and Sustainable Energy Reviews, vol. 54, pp. 396–405, 2016.

[3] C. Tu, X. He, Z. Shuai, and F. Jiang, "Big data issues in smart grid-a review," *Renewable and Sustainable Energy Reviews*, vol. 79, pp. 1099–1107, 2017.

[4] Y. Zhang, R. Yang, K. Zhang, H. Jiang, and J. J. Zhang, "Consumption behavior analytics-aided energy forecasting and dispatch," *IEEE Intelligent Systems*, vol. 32, no. 4, pp. 59–63, 2017.

[5] J. Deng, F. Wang, Y. Chen, and X. Zhao, "From industry 4.0 to energy 5.0: the concept, connotation and system framework of intelligent energy systems," *Journal of Automation*, vol. 41, no. 12, pp. 2003–2016, 2015.

[6] Q. Sun, L. Shi, Y. Ni, D. Si, and J. Zhu, "An enhanced cascading failure model integrating data mining technique," *Protection and Control of Modern Power Systems*, vol. 2, 2017.

[7] D. Zheng, A. T. Eseye, J. Zhang, and H. Li, "Short-term wind power forecasting using a double-stage hierarchical ANFIS approach for energy management in microgrids," *Protection and Control of Modern Power Systems*, vol. 2, pp. 1–10, 2017.

[8] Z. Li, L. Ye, Y. Zhao, X. Song, J. Teng, and J. Jin, "Short-term wind power prediction based on extreme learning machine with error correction," *Protection and Control of Modern Power Systems*, vol. 1, no. 1, pp. 1–8, 2016.

[9] H. Z. Wang, Z. X. Lei, X. Zhang, B. Zhou, and J. C. Peng, "A review of deep learning for renewable energy forecasting," *Energy Conversion and Management*, vol. 198, pp. 1–16, 2019.

[10] H. Z. Wang, G. B. Wang, G. Q. Li, J. C. Peng, and Y. T. Liu, "Deep belief network based deterministic and probabilistic wind speed forecasting approach," *Applied Energy*, vol. 182, pp. 80–93, 2016.

[11] M.-R. Chen, G.-Q. Zeng, K.-D. Lu, and J. Weng, "A two-layer nonlinear combination method for short-term wind speed prediction based on ELM, ENN, and LSTM," *IEEE Internet of Things Journal*, vol. 6, no. 4, pp. 6997–7010, 2019.

[12] H. Liu, X. Mi, and Y. Li, "Smart multi-step deep learning model for wind speed forecasting based on variational mode decomposition, singular spectrum analysis, LSTM network and ELM," *Energy Conversion and Management*, vol. 159, pp. 54–64, 2018.

[13] J. Chen, G.-Q. Zeng, W. Zhou, W. Du, and K.-D. Lu, "Wind speed forecasting using nonlinear-learning ensemble of deep learning time series prediction and extremal optimization," *Energy Conversion and Management*, vol. 165, pp. 681–695, 2018.

[14] W. Kong, Z. Y. Dong, Y. Jia, D. J. Hill, Y. Xu, and Y. Zhang, "Short-term residential load forecasting based on LSTM recurrent neural network," *IEEE Transactions on Smart Grid*, vol. 10, no. 1, 2017.

[15] H. Gao, W. Huang, X. Yang, Y. Duan, and Y. Yin, "Toward service selection for workflow reconfiguration: an interface-based computing solution," *Future Generation Computer Systems*, vol. 87, pp. 298–311, 2018.

[16] L. Qi, Q. He, F. Chen et al., "Finding all you need: web APIs recommendation in web of things through keywords search," *IEEE Transactions on Computational Social Systems*, vol. 6, no. 5, 2019.

[17] L. Qi, R. Wang, C. Hu, S. Li, Q. He, and X. Xu, "Time-aware distributed service recommendation with privacy-preservation," *Information Sciences*, vol. 480, pp. 354–364, 2019.

[18] Y. Zhang and Q. Yang, "An overview of multi-task learning," *National Science Review*, vol. 5, no. 1, pp. 34–47, 2018.

[19] A. Argyriou, M. T. Evgeniou, and M. Pontil, "Convex multi-task feature learning," *Machine Learning*, vol. 73, no. 3, pp. 243–272, 2008.

[20] T. Jebara, "Multitask sparsity via maximum entropy discrimination," *Journal of Machine Learning Research*, vol. 12, no. 1, pp. 75–110, 2011.

[21] L. Qi, Y. Chen, Y. Yuan, S. Fu, X. Zhang, and X. Xu, "A QoS-aware virtual machine scheduling method for energy conservation in cloud-based cyber-physical systems," *World Wide Web*, vol. 5, pp. 1–23, 2019.

[22] R. Zhang, P. Xie, C. Wang, G. Liu, and S. Wan, "Classifying transportation mode and speed from trajectory data via deep multi-scale learning," *Computer Networks*, vol. 162, p. 106861, 2019.

[23] W. Wang, D. Wang, H. Jia et al., "Review of steady-state analysis of typical regional integrated energy system under the background of energy internet," *Proceedings of the CSEE,12*, pp. 3292–3306, 2016.

[24] S. Ding, S. Qu, Y. Xi, and S. Wan, "Stimulus-driven and concept-driven analysis for image caption generation," *Neurocomputing*, 2019.

[25] P. Vrba, V. Marik, P. Siano et al., "A review of agent and service-oriented concepts applied to intelligent energy systems," *IEEE Transactions on Industrial Informatics*, vol. 10, no. 3, pp. 1890–1903, 2014.

[26] W. Jia, C. Kang, and Q. Chen, "Analysis on demand-side interactive response capability for power system dispatch in a smart grid framework," *Electric Power Systems Research*, vol. 90, pp. 11–17, 2012.

[27] Z. C. Lipton, J. Berkowitz, and C. Elkan, "A critical review of recurrent neural networks for sequence learning," *CoRR*, 2015, https://arxiv.org/pdf/1506.00019.pdf.

[28] T. N. Sainath, O. Vinyals, A. Senior, and H. Sak, "Convolutional, long short-term memory, fully connected deep neural networks," in *Proceedings of the 2015 IEEE International Conference on Acoustics, Speech and Signal Processing (ICASSP)*, pp. 4580–4584, IEEE, Brisbane, Australia, April 2015.

[29] Y. Guo, Z. Cheng, L. Nie, Y. Wang, J. Ma, and M. Kankanhalli, "Attentive long short-term preference modeling for personalized product search," *ACM Transactions on Information Systems (TOIS)*, vol. 37, no. 2, p. 19, 2019.

[30] A. Graves, "Long short-term memory," *Neural Computation*, vol. 9, pp. 1735–1780, 1997.

[31] F. A. Gers, J. Schmidhuber, and F. Cummins, "Learning to forget: continual prediction with LSTM," *Neural Computation*, vol. 12, no. 10, pp. 2451–2471, 2000.

[32] M. L. Seltzer and J. Droppo, "Multi-task learning in deep neural networks for improved phoneme recognition," in *Proceedings of the 2013 IEEE International Conference on Acoustics, Speech and Signal Processing*, pp. 6965–6969, IEEE, Vancouver, Canada, May 2013.

[33] S. Wan, Y. Zhao, T. Wang, Z. Gu, Q. H. Abbasi, and K.-K. R. Choo, "Multi-dimensional data indexing and range query processing via Voronoi diagram for internet of things," *Future Generation Computer Systems*, vol. 91, pp. 382–391, 2019.

[34] Z. Gao, D. Y. Wang, S. H. Wan, H. Zhang, and Y. L. Wang, "Cognitive-inspired class-statistic matching with triple-constrain for camera free 3D object retrieval," *Future Generation Computer Systems*, vol. 94, pp. 641–653, 2019.

[35] C. A. Kang, A. R. Brandt, and L. J. Durlofsky, "Optimal operation of an integrated energy system including fossil fuel

power generation, CO2 capture and wind," *Energy*, vol. 36, no. 12, pp. 6806–6820, 2011.

[36] Q. Zhang, S. Wan, B. Wang, D. W. Gao, and H. Ma, "Anomaly detection based on random matrix theory for industrial power systems," *Journal of Systems Architecture*, vol. 95, pp. 67–74, 2019.

[37] Z. Gao, H. Z. Xuan, H. Zhang, S. Wan, and K. K. R. Choo, "Adaptive fusion and category-level dictionary learning model for multi-view human action recognition," *IEEE Internet of Things Journal*, p. 1, 2019.

[38] W. Wu, K. Chen, Y. Qiao, and Z. Lu, "Probabilistic short-term wind power forecasting based on deep neural networks," in *Proceedings of the 2016 International Conference on Probabilistic Methods Applied to Power Systems (PMAPS)*, pp. 1–8, Beijing, China, October 2016.

[39] K. M. Powell, A. Sriprasad, W. J. Cole, and T. F. Edgar, "Heating, cooling, and electrical load forecasting for a large-scale district energy system," *Energy*, vol. 74, pp. 877–885, 2014.

[40] A. Peimankar, S. J. Weddell, T. Jalal, and A. C. Lapthorn, "Multi-objective ensemble forecasting with an application to power transformers," *Applied Soft Computing*, vol. 68, pp. 233–248, 2018.

[41] G.-Q. Zeng, J. Chen, L.-M. Li et al., "An improved multi-objective population-based extremal optimization algorithm with polynomial mutation," *Information Sciences*, vol. 330, pp. 49–73, 2016.

[42] Y.-L. Hu and L. Chen, "A nonlinear hybrid wind speed forecasting model using LSTM network, hysteretic ELM and Differential Evolution algorithm," *Energy Conversion and Management*, vol. 173, pp. 123–142, 2018.

[43] G.-Q. Zeng, J. Chen, Y.-X. Dai, L.-M. Li, C.-W. Zheng, and M.-R. Chen, "An improved Design of fractional order PID controller for automatic regulator voltage system based on multi-objective extremal optimization," *Neurocomputing*, vol. 160, pp. 173–184, 2015.

[44] X. Xu, R. Gu, F. Dai, L. Qi, and S. Wan, "Multi-objective computation offloading for internet of vehicles in cloud-edge computing," *Wireless Networks*, pp. 1–19, 2019.

[45] S. Wan, X. Li, Y. Xue, W. Lin, and X. Xu, "Efficient computation offloading for internet of vehicles in edge computing-assisted 5G networks," *The Journal of Supercomputing*, pp. 1–30, 2019.

[46] B. Wang, S. Wan, X. Zhang, and K.-K. R. Choo, "A novel index for assessing the robustness of integrated electrical network and a natural gas network," *IEEE Access*, vol. 6, pp. 40400–40410, 2018.

[47] Y. Yin, F. Yu, Y. Xu, L. Yu, and J. Mu, "Network location-aware service recommendation with random walk in cyber-physical systems," *Sensors*, vol. 17, no. 9, p. 2059, 2017.

Hindawi
Complexity
Volume 2019, Article ID 5358316, 9 pages
https://doi.org/10.1155/2019/5358316

Research Article

Tracking Control for Hydrogen Fuel Cell Systems in Zero-Emission Ferry Ships

Mohammad Hassan Khooban,[1] **Navid Vafamand**,[2] **and Jalil Boudjadar**[1]

[1]*Department of Engineering, Aarhus University, Åbogade 34, 8200 Aarhus N, Denmark*
[2]*Department of Power and Control, Shiraz University, Shiraz 71946-84471, Iran*

Correspondence should be addressed to Mohammad Hassan Khooban; mhkhoban@gmail.com

Received 11 June 2019; Revised 10 August 2019; Accepted 23 September 2019; Published 15 November 2019

Guest Editor: Taesic Kim

For more than a century, conventional marine vessels spatter the atmosphere with CO_2 emissions and detrimental particles when operated by diesel motors/generators. Fuel cells have recently emerged as one of the most promising emission-free technologies for the electrification of ship propulsion systems. In fuel cell-based ship electrification, the entire marine power system is viewed as a direct current (DC) microgrid (MG) with constant power loads (CPLs). A challenge of such settings is how to stabilize the voltages and currents of the ship's grid. In this paper, we propose a new modified backstepping controller to stabilize the MG voltage and currents. Finally, to study the performance and efficiency of our proposal, we run an experiment simulation using dSPACE real-time emulator.

1. Introduction

Nowadays, air emissions (e.g., carbon dioxide (CO_2) and sulfur dioxide gases) are changing habitats all over the world. Big parts of these air emissions originate from burning distinct forms of fuel in cars, vessels, and aircraft. According to the International Maritime Organization (IMO), the massive marine transport system streaming through oceans and seas accounts for 2% of the global world CO_2 emission. Nevertheless, vessels play a significant role in the international trading system, providing occupations and transportation as well as supporting offshore businesses like fishing [1–4].

Even though marine vessel emissions have not been considered in the Kyoto accord, stringent rules have been established by first world countries. For instance, the European Union (EU) has applied stringent rules to control and monitor the sulfur dioxide emission in exclusively sensitive sea zones, containing the Baltic Sea Zones and the Western European seas. In the mentioned zones, the fuel utilized in marine vessel systems should not contain sulfur over 0.1%. But, in most ship fuels, this value is more than 1%. Thus, the importance of developing substitutive renewable energy supplies has become a significant problem for the marine vessel propulsion [5, 6].

One of the most promising renewable energy source technologies, which can be utilized in marine power systems, is fuel cell (FC) systems [7]. FCs, dissimilar to energy storage devices, utilize an outside supply of the hydrogen and oxygen to generate power and work as long as the hydrogen gas and oxygen source are sustained [8, 9]. The main advantages of FCs, which cause them as the best possible alternative marine power source, are their great power production density, efficiency, reliability, and durability [1]. In general, a hydrogen fuel cell converts oxygen and hydrogen (or air) into the direct current power. In practice, fuel cells in most immobile and mobile vehicle applications are paired with other power electronic devices (such as DC/DC boost converters) to improve the performance and reliability of the whole system and also accurately regulate the output voltage of the FC [10]. There have been very few successful implementations of FCs for vehicles [7] and marine applications [9, 11, 12] in the past few years. Most of the existing results for the FCs use linearized representation and controllers [13]. To improve the performance, nonlinear control methods such as model predictive [14], intelligent-based PID [15], and sliding mode control [10, 16] are presented. However, in a marine power system with FC, power electronic devices and loads can be considered as a kind of mobile DC microgrid with constant

power loads (CPLs). In other words, FC in the special DC maritime MG is considered as a distributed generation, and ship motors and loads can be considered as CPLs, whenever a load is regulated to keep constant output power. Now, by considering this particular case study, a robust and high-performance controller is required to stabilize the voltage and current of the marine power grid, which is not investigated in the abovementioned approaches.

Up to now, many different approaches are suggested to reduce the detrimental effects of CPLs in DC maritime MGs [17–25]. Passive damping and active damping are two elementary methods to solve this issue [17]. In passive damping resistors, by increasing damping resistors to the filters, the destructive effect of CPLs can be mitigated. In spite of the fact that this technique has some advantages (e.g., it is simple and effective), it generates a huge dissipation [10]. On the other hand, active damping applies a modified control loop, which operates a virtual resistor [18]. In general, in active damping methods, the power is actively injected into the grid to diminish the effects of CPLs [19]. Furthermore, the methods based on small-signal models for the active damping can only guarantee system stability close to the operating point. In [17, 26], the model predictive controller is proposed for controlling the switching function of a converter that it sources a constant power load. Nevertheless, according to its computational burden, the proposed control method is not useful for real-time high-order industrial applications [27]. In [28], by controlling the duty ratio, a new modified nonlinear controller based on the sliding mode technique is suggested to stabilize a buck converter that it sources a constant power load. The proposed method in [14] can easily stabilize the whole system under any operating range changes. Nonetheless, this approach needs to measure the current of the capacitor, which is very expensive and causes ripple filtering degradation and the output impedance increase [29]. However, in those approaches, it is assumed that the DC source is ideal and the source current is independent of its voltage. This assumption is not applicable to the marine systems fed by FCs.

To sum up, this work studies an adaptive tracking control for hydrogen fuel cell systems in maritime applications. The marine power system with fuel cell and power electronic devices can be regarded as a special mobile stand-alone DC microgrid with constant power loads. Therefore, we first investigate a dynamic model of a special DC MG with CPLs for the marine power system by considering fuel cell and ship motors. Next, we extract the mathematical model of the whole system to apply the proposed control technique. Then, we develop a backstepping nonlinear control approach to stabilize the voltage and current of the ship's grid. From the control engineering viewpoint, the main difficulty in utilizing a backstepping controller for the fuel cell-based marine power systems is that the overall structure of the fuel cell does not belong to the strict-feedback form and the virtual control inputs are not affine. Therefore, in this paper, we propose a novel control method to achieve the tracking issue of the DC MG voltage and currents. The proposed control is inspired by conventional backstepping controller methods. Finally, we apply the dSPACE real-time emulator system to investigate the performance and effectiveness of our approach for marine applications.

2. Stand-Alone DC Marine Microgrid Dynamics

In general, a marine power system with a fuel cell (as a main source of the ship power), power electronic devices (as interfaces for renewable energy systems), and loads (like ship motors and navigation systems) can be considered as a special mobile islanded DC microgrid with constant power loads. Figure 1 presents the general concept of maritime DC MG with CPLs.

In the maritime systems, for the case of a ship constant speed, the ship engine should generate a constant torque. Therefore, it should receive constant power. However, in practice, any voltage fluctuations may change the power of the ship engine. Here, in this paper, the concept of the CPL is utilized in which the ship engine consuming power is tightly regulated by a DC/DC converter, and the DC bus voltage variation will not affect the ship speed. Besides the ship engine, which is assumed to act as a CPL behavior, resistive loads of the ship are also connected by the DC bus. Consequently, the fuel cell generator must feed a CPL and resistive loads. It is proved that the nonlinear CPLs degrade the stability of the DC MG, and if the voltage and/or the current of the DC bus vary from the equilibrium operating point of the system, then the overall DC MG will be unstable, which leads to a sudden drop in the DC bus voltage and spoils the CPL behavior. On the other hand, the fuel cell is a slow-response generator and any small perturbation on the DC MG makes it unstable. This fact shows the necessity of the active control of the DC bus voltage and the fuel cell power, as well, to assure the closed-loop stability and performance. To theoretically assure the stability, it is necessary to derive the state-space representation of the maritime DC MG.

Now, we work on extracting the mathematical model of the islanded marine DC MG with CPLs extracted. Totally, in the special case study of this paper, the fuel cell is used as a main power source of the ship to reduce the cost of fossil fuels and air emissions. Moreover, the power electronic devices (e.g., DC/DC boost converter) are utilized to connect the fuel cell, ship engine, and load to the DC bus link. Figure 2 shows the circuit diagram of the stand-alone DC marine MG with the fuel cell and a CPL. In this work, the ship engine is considered as a constant power load to tightly regulate the speed of the marine vessel system via a DC/DC converter. The mathematical model of the case study based on Figure 2 can be written as follows [10, 30]:

$$\frac{dV_{CPL}}{dt} = \frac{1}{C_b}\left(i_{hfc}\left(1-u_1\right) - \frac{P_{CPL}}{V_{CPL}} - \frac{V_{CPL}}{R}\right), \tag{1}$$

$$\begin{aligned}\frac{di_{hfc}}{dt} = &-\frac{nR_{ohm}}{L}i_{hfc} - \frac{n}{L}V_{at} - \frac{V_{CPL}}{L}\left(1-u_1\right)\\ &+ \frac{nR_gT_{st}}{2LF_{ar}}\left(\ln\left(P_{H_2}\right) + \frac{1}{2}\ln\left(P_{O_2}\right)\right)\\ &+ \frac{n}{2LF_{ar}}\left(\Delta G_1 + \Delta s_1\left(T_{st} - T_{hfc}\right)\right),\end{aligned} \tag{2}$$

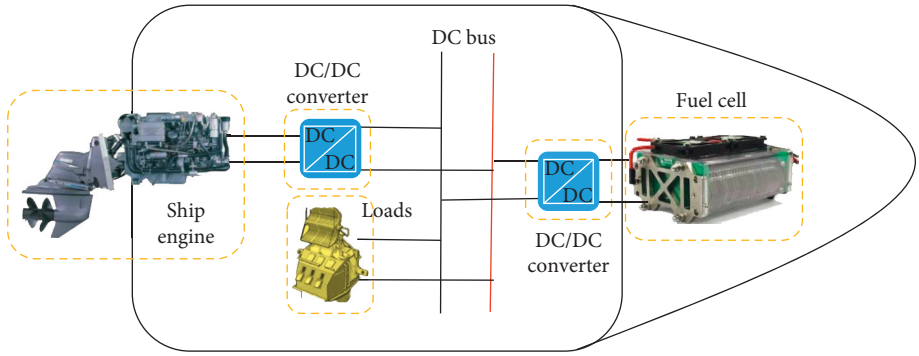

Figure 1: The overall scheme of the stand-alone DC zero-emission ferry ships.

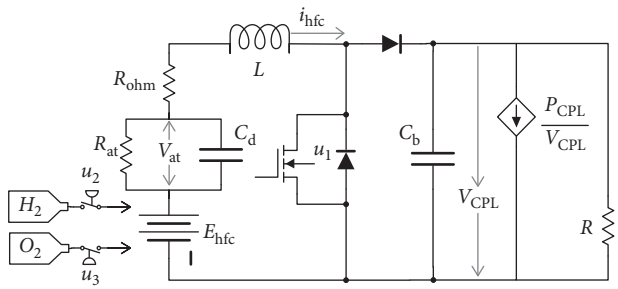

Figure 2: Circuit diagram of the marine DC MG with a fuel cell and a CPL.

$$\frac{dV_{at}}{dt} = \frac{i_{hfc}}{C_d} - \frac{V_{at}}{R_{at}C_d}, \tag{3}$$

$$\frac{dP_{H_2}}{dt} = -\frac{P_{H_2}}{\tau_{H_2}} + \frac{q^{in}_{H_2} - 2k_\gamma i_{hfc}}{\tau_{H_2}k_{H_2}}, \tag{4}$$

$$\frac{dP_{O_2}}{dt} = -\frac{P_{O_2}}{\tau_{O_2}} + \frac{q^{in}_{O_2} - 2k_\gamma i_{hfc}}{\tau_{O_2}k_{O_2}}, \tag{5}$$

$$\frac{dq^{in}_{H_2}}{dt} = \frac{u_2 - q^{in}_{H_2}}{\tau_{qH_2}}, \tag{6}$$

$$\frac{dq^{in}_{O_2}}{dt} = \frac{u_3 - q^{in}_{O_2}}{\tau_{qO_2}}. \tag{7}$$

As shown in Figure 2, a proton exchange membrane fuel cell has been applied in this study to transform the chemical energy liberated during the electrochemical reaction of hydrogen and oxygen to electrical energy [31].

The detailed definition and value of the system parameters can be found in [10]. Also, the nominal values of the parameters of the system are provided in Table 1. The control inputs u_1, u_2, and u_3 are related to the DC/DC converter connected to the fuel cell and the injecting hydrogen and oxygen flows of the fuel cell. These control inputs will be designed by applying the backstepping control as explained in Section 3.

Table 1: The parameters of the DC marine microgrid.

Parameter and definition	Nominal value
F_{ar} (Faraday constant)	96485.309 C/mol
T_{st} (fuel cell operating temperature)	353 K
T_{hfc} (fuel cell reference temperature)	298.15 K
R_g (universal gas constant)	8.3143 J/(mol.K)
ΔG (Gibbs free energy)	237160.89 J/mol
ΔS (standard molar entropy)	164.025 J/(mol.K)
τ_{H_2} (hydrogen actuator flow rate valve time constant)	3.37 sec
τ_{O_2} (oxygen actuator flow rate valve time constant)	6.47 sec
K_γ (consumed hydrogen flow rate)	9.07×10^{-8} mol/C
K_{H_2} (hydrogen molar constant)	4.22×10^{-5} Kmol.atm/sec
K_{O_2} (oxygen molar constant)	2.11×10^{-5} Kmol.atm/sec
n (number of fuel cells)	5
C_d (double-layered capacitor)	35×10^{-6} F
R_{ohm} (variable internal resistor of the fuel cell)	1.5 Ω
L_{DC} (DC/DC converter inductor)	4×10^{-3} H
C_{DC} (DC/DC converter inductor)	5×10^{-4} F
P_{CPL} (CPL power)	400 W
R (ship resistive load)	80 Ω

3. Modified Backstepping Controller

In this section, we present the procedure of designing the backstepping controller. Since the two desired references are introduced, the backstepping design procedure is split into two parts. The primary control objective is to manipulate the DC/DC boost converter that stabilizes the voltage of the DC bus V_{CPL} toward its desired value V_{ref}. The control signal is then used to generate pulse-width modulation (PWM) gate signals for the converter [32]. Moreover, the secondary goal is to manipulate the fuel cell generator to provide the power to the loads. Assuming that the DC/DC converter is ideal and does not consume power, therefore, the generated power should be equal to the demand power. Here, since only CPLs are considered, the total power demand will be the net sum of the instantaneous CPL power. Without loss of generality, consider one CPL with the power level P_{CPL} and the one resistive load R. Thus, the current should track the reference [32] $I_{ref} = P_{totall}/V_{thfc}$, where $P_{totall} = P_{cpl} + (V^2_{CPL}/R)$ and V_{thfc} is the voltage of the fuel cell and input of the DC/DC converter, computed as follows [10]:

$$
\begin{aligned}
V_{\text{thfc}} &= nV_{\text{hfc}},\\
V_{\text{hfc}} &= E_{\text{hfc}} - i_{\text{hfc}}R_{\text{ohm}} - V_{\text{at}},\\
E_{\text{hfc}} &= \frac{1}{2F_{\text{ar}}}\Big(\Delta G_1 + \Delta s_1\left(T_{\text{st}} - T_{\text{hfc}}\right)\\
&\quad + R_{\text{g}}T_{\text{st}}\Big(\ln\left(P_{\text{H}_2}\right) + \frac{1}{2}\ln\left(P_{\text{O}_2}\right)\Big)\Big).
\end{aligned}
\tag{8}
$$

For the dynamic (1), the goal of V_{CPL} is tracking V_{ref}. Defining the error $e_1 = V_{\text{CPL}} - V_{\text{ref}}$ and variable change $v_1 = 1 - u_1$ results in

$$
\dot{e}_1 = \dot{V}_{\text{CPL}} - \dot{V}_{\text{ref}} = -\frac{P_{\text{CPL}}}{C_{\text{b}}V_{\text{CPL}}} - \frac{V_{\text{CPL}}}{C_{\text{b}}R} - \dot{V}_{\text{ref}} + \frac{i_{\text{hfc}}}{C_{\text{b}}}v_1. \tag{9}
$$

Let us choose the control input v_1 as

$$
v_1 = \frac{C_{\text{b}}}{i_{\text{hfc}}}\left(-\gamma_1 e_1 + \frac{P_{\text{CPL}}}{V_{\text{CPL}}C_{\text{b}}} + \frac{V_{\text{CPL}}}{C_{\text{b}}R} + \dot{V}_{\text{ref}}\right), \tag{10}
$$

the dynamic (9) will be then

$$
\dot{e}_1 = -\gamma_1 e. \tag{11}
$$

In the next part, the goal is to design the control inputs u_2 and u_3 such that i_{hfc} tracks the $i_{\text{ref}}(t)$. Let $v_3 = \ln(P_{\text{H}_2}) + (1/2)\ln(P_{\text{O}_2})$ to be the virtual control input in (2), $e_2 = i_{\text{hfc}} - i_{\text{ref}}$ and $e_3 = v_3 - v_{3\text{d}}$. Therefore,

$$
\dot{e}_2 = \frac{\text{d}i_{\text{hfc}}}{\text{d}t} - \dot{i}_{\text{ref}} = \frac{nR_{\text{g}}T_{\text{st}}}{2LF_{\text{ar}}}e_3 + \Gamma_1 + \frac{nR_{\text{g}}T_{\text{st}}}{2LF_{\text{ar}}}v_{3\text{d}} - \dot{i}_{\text{ref}}. \tag{12}
$$

Selecting $v_{3\text{d}} = ((2LF_{\text{ar}})/(nR_{\text{g}}T_{\text{st}}))(-\gamma_2 e_2 - \Gamma_1 + \dot{i}_{\text{ref}})$ provides

$$
\dot{e}_2 = \frac{nR_{\text{g}}T_{\text{st}}}{2LF_{\text{ar}}}e_3 - \gamma_2 e_2. \tag{13}
$$

Taking time derivative of the Lyapunov candidate $V_2 = (1/2)e_2^2$ along with the (13) results in

$$
\dot{V}_2 = e_2\dot{e}_2 = -\gamma_2 e_2^2 + \frac{nR_{\text{g}}T_{\text{st}}}{2LF_{\text{ar}}}e_2e_3. \tag{14}
$$

In the next stage, the dynamic of the error e_3 is computed as

$$
\begin{aligned}
\dot{e}_3 = \dot{v}_3 - \dot{v}_{3\text{d}} &= \frac{1}{P_{\text{H}_2}}\frac{\text{d}P_{\text{H}_2}}{\text{d}t} + \frac{1}{2P_{\text{O}_2}}\frac{\text{d}P_{\text{O}_2}}{\text{d}t} - \dot{v}_{3\text{d}}\\
&= -\frac{1}{\tau_{\text{H}_2}} + \frac{q_{\text{H}_2}^{\text{in}} - 2k_\gamma i_{\text{hfc}}}{\tau_{\text{H}_2}k_{\text{H}_2}P_{\text{H}_2}} - \frac{1}{2\tau_{\text{O}_2}} + \frac{q_{\text{O}_2}^{\text{in}} - 2k_\gamma i_{\text{hfc}}}{2\tau_{\text{O}_2}k_{\text{O}_2}P_{\text{O}_2}} - \dot{v}_{3\text{d}}\\
&= \Gamma_2 + \frac{q_{\text{H}_2}^{\text{in}}}{\tau_{\text{H}_2}k_{\text{H}_2}P_{\text{H}_2}} + \frac{q_{\text{O}_2}^{\text{in}}}{2\tau_{\text{O}_2}k_{\text{O}_2}P_{\text{O}_2}},
\end{aligned}
\tag{15}
$$

where $\Gamma_2 = -(1/\tau_{\text{H}_2}) - (1/(2\tau_{\text{O}_2})) - ((2k_\gamma i_{\text{hfc}})/(\tau_{\text{H}_2}k_{\text{H}_2}P_{\text{H}_2})) - ((k_\gamma i_{\text{hfc}})/(\tau_{\text{O}_2}k_{\text{O}_2})) - \dot{v}_{3\text{d}}$. Now, we define $e_4 = q_{\text{H}_2}^{\text{in}} - x_{4\text{d}}$ and $e_5 = q_{\text{O}_2}^{\text{in}} - x_{5\text{d}}$. Therefore,

$$
\dot{e}_3 = \frac{e_4}{\tau_{\text{H}_2}k_{\text{H}_2}P_{\text{H}_2}} + \frac{e_5}{2\tau_{\text{O}_2}k_{\text{O}_2}P_{\text{O}_2}} + \Gamma_2 + \frac{x_{4\text{d}}}{\tau_{\text{H}_2}k_{\text{H}_2}P_{\text{H}_2}} + \frac{x_{5\text{d}}}{2\tau_{\text{O}_2}k_{\text{O}_2}P_{\text{O}_2}}. \tag{16}
$$

Let us write

$$
\begin{aligned}
x_{4\text{d}} &= \tau_{\text{H}_2}k_{\text{H}_2}P_{\text{H}_2}\left(-\frac{\gamma_3}{2}e_3 - \frac{\Gamma_2}{2} - \frac{nR_{\text{g}}T_{\text{st}}}{4LF_{\text{ar}}}e_2\right),\\
x_{5\text{d}} &= 2\tau_{\text{O}_2}k_{\text{O}_2}P_{\text{O}_2}\left(-\frac{\gamma_3}{2}e_3 - \frac{\Gamma_2}{2} - \frac{nR_{\text{g}}T_{\text{st}}}{4LF_{\text{ar}}}e_2\right),
\end{aligned}
\tag{17}
$$

Therefore, (16) will be rewritten as follows:

$$
\dot{e}_3 = \frac{e_4}{\tau_{\text{H}_2}k_{\text{H}_2}P_{\text{H}_2}} + \frac{e_5}{2\tau_{\text{O}_2}k_{\text{O}_2}P_{\text{O}_2}} - \gamma_3 e_3 - \frac{nR_{\text{g}}T_{\text{st}}}{2LF_{\text{ar}}}e_2. \tag{18}
$$

Taking time derivative of $V_3 = V_2 + (1/2)e_3^2$ results in

$$
\begin{aligned}
\dot{V}_3 = \dot{V}_2 + e_3\dot{e}_3 &= -\gamma_2 e_2^2 + \frac{nR_{\text{g}}T_{\text{st}}}{2LF_{\text{ar}}}e_2e_3\\
&\quad + e_3\left(\frac{e_4}{\tau_{\text{H}_2}k_{\text{H}_2}P_{\text{H}_2}} + \frac{e_5}{2\tau_{\text{O}_2}k_{\text{O}_2}P_{\text{O}_2}} - \gamma_3 e_3 - \frac{nR_{\text{g}}T_{\text{st}}}{2LF_{\text{ar}}}e_2\right)\\
&= -\gamma_2 e_2^2 - \gamma_3 e_3^2 + \frac{e_3e_4}{\tau_{\text{H}_2}k_{\text{H}_2}P_{\text{H}_2}} + \frac{e_3e_5}{2\tau_{\text{O}_2}k_{\text{O}_2}P_{\text{O}_2}}.
\end{aligned}
\tag{19}
$$

In the final stage, we compute the dynamics e_4 and e_5 as follows:

$$
\dot{e}_4 = \dot{q}_{\text{H}_2}^{\text{in}} - \dot{x}_{4\text{d}} = \frac{u_2 - q_{\text{H}_2}^{\text{in}}}{\tau_{\text{qH}_2}} - \dot{x}_{4\text{d}}, \tag{20}
$$

$$
\dot{e}_5 = \dot{q}_{\text{O}_2}^{\text{in}} - \dot{x}_{5\text{d}} = \frac{u_3 - q_{\text{O}_2}^{\text{in}}}{\tau_{\text{qO}_2}} - \dot{x}_{5\text{d}}. \tag{21}
$$

Let the control inputs be

$$
u_2 = \tau_{\text{qH}_2}\left(-\gamma_4 e_4 - \frac{e_3}{\tau_{\text{H}_2}k_{\text{H}_2}P_{\text{H}_2}} + \frac{q_{\text{H}_2}^{\text{in}}}{\tau_{\text{qH}_2}} + \dot{x}_{4\text{d}}\right), \tag{22}
$$

$$
u_3 = \tau_{\text{qO}_2}\left(-\gamma_5 e_5 - \frac{e_3}{2\tau_{\text{O}_2}k_{\text{O}_2}P_{\text{O}_2}} + \frac{q_{\text{O}_2}^{\text{in}}}{\tau_{\text{qO}_2}} + \dot{x}_{5\text{d}}\right). \tag{23}
$$

Therefore, the dynamics (20) and (21) are simplified as follows:

$$
\begin{aligned}
\dot{e}_4 &= -\frac{e_3}{\tau_{\text{H}_2}k_{\text{H}_2}P_{\text{H}_2}} - \gamma_4 e_4,\\
\dot{e}_5 &= -\frac{e_3}{2\tau_{\text{O}_2}k_{\text{O}_2}P_{\text{O}_2}} - \gamma_5 e_5.
\end{aligned}
\tag{24}
$$

Taking time derivative of $V_4 = V_3 + (1/2)e_4^2 + (1/2)e_5^2$ results in

$$\dot{V}_4 = \dot{V}_3 + e_4\dot{e}_4 + e_5\dot{e}_5 - \gamma_2 e_2^2 - \gamma_3 e_3^2 + \frac{e_3 e_4}{\tau_{H_2} k_{H_2} P_{H_2}} + \frac{e_3 e_5}{2\tau_{O_2} k_{O_2} P_{O_2}} + e_4\left(-\frac{e_3}{\tau_{H_2} k_{H_2} P_{H_2}} - \gamma_4 e_4\right) + e_5\left(-\frac{e_3}{2\tau_{O_2} k_{O_2} P_{O_2}} - \gamma_5 e_5\right) = -\gamma_2 e_2^2 - \gamma_3 e_3^2 - \gamma_4 e_4^2 - \gamma_5 e_5^2. \quad (25)$$

Finally, by considering the Lyapunov candidate $V = V_4 + V_1$, we obtain

$$\dot{V} = -\gamma_1 e_1^2 - \gamma_2 e_2^2 - \gamma_3 e_3^2 - \gamma_4 e_4^2 - \gamma_5 e_5^2. \quad (26)$$

Since the time derivative of the Lyapunov function is negative definite, the error is asymptotically stable and the states V_{CPL} and i_{hfc} track the desired references. The proof is complete.

Remark 1 (difficulties of the design of the proposed controller). This work proposes a novel backstepping control law which is proposed for the marine power systems (1)–(7). These dynamics are not in the form of the conventional strict-feedback forms as the virtual inputs P_{H_2} and P_{O_2} are not affine in (2) and the overall dynamics comprise three control inputs. So, the conventional backstepping design procedure [32] is not applicable. However, in this paper, such difficulties are handled by (i) defining the tracking error e_3 as a nonlinear function of the virtual inputs, (ii) splitting the overall design procedure into two parts, and (iii) introducing an additional time-varying reference for the current of the fuel cell based on the properties of the nonlinear DC MG. These are the main distinctive features of the proposed approach over the existing backstepping techniques. The overall schematic of the proposed backstepping controllers to the regulate DC MG is given in Figure 3. Also, the detailed algorithm of deriving the control inputs u_1, u_2, and u_3 is given in Algorithm 1.

4. Model-in-the-Loop Results

In this section, to show the applicability and low computational time of the proposed nonlinear controller, we carry out a model-in-the-loop (MiL) real-time simulation [33]. For the MiL simulation as depicted in Figure 4, dSPACE 1202 board has been selected as the rapid prototyping solution. The solver is the Euler method, and the sampling frequency is 10 kHz. The MiL application of the suggested technique was done on a real-time simulator (RTS) wherein both the controller and grid system are embedded in a single RTS. The load-side converter tightly regulates the voltage of the ship engine. Therefore, the consuming power of the ship engine is constant and the overall converter and load act as a CPL. This control action is dependent on the proposed control actions u_1, u_2, and u_3. However, the load-side converter regulation action and the proposed control laws are designed by the dSPACE simulator.

First control input (u_1)
(1) Get V_{ref}.
(2) Compute $\dot{V}_{ref}$ and $e_1 = V_{CPL} - V_{ref}$.
(3) Compute ν_1 by (10).
(4) Apply the control input $u_1 = 1 - \nu_1$.
Second and third control inputs (u_2 and u_3)
(5) Get i_{ref}.
(6) Compute $\dot{I}_{ref}$ and $e_2 = i_{hfc} - i_{ref}$.
(7) Compute $\nu_{3d} = ((2LF_{ar})/(nR_gT_{st}))(-\gamma_2 e_2 - \Gamma_1 + \dot{i}_{ref})$.
(8) Compute $\dot{\nu}_{3d}$ and $e_3 = \nu_3 - \nu_{3d}$.
(9) Compute x_{4d} and x_{5d} by (17).
(10) Compute $\dot{x}_{4d}$, $\dot{x}_{5d}$, $e_4 = x_4 - x_{3d}$ and $e_5 = x_5 - x_{5d}$.
(11) Apply the control inputs (22) and (23).

Algorithm 1: The algorithm of computing control inputs.

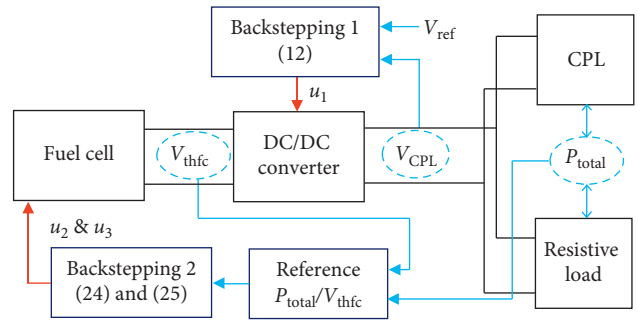

Figure 3: The overall schematic of the proposed control approach.

The MiL simulation is carried out for the system parameters given in Table 1 and the CPL voltage reference $V_{ref} = 400$ V. Note that, in practice, the parameters R_{at}, C_d, and R_{ohm} are uncertain parameters, but in the controller law, their nominal values given in Table 1 are considered.

Moreover, the control design parameters of the proposed backstepping controller are set as $\gamma_i = 1$ for $i = 1, 2, \ldots, 5$.

Furthermore, to show the performance improvement of the proposed approach, the sliding mode controller designed for the same case study in [10] is considered. In [10], in addition to the fuel cell, a supercapacitor is also connected to the DC bus through a buck/boost converter. Furthermore, only resistive loads are considered. However, to apply the sliding mode approach of [10] to the considered case study, the PWM input signal of the buck/boost converter is assumed to be zero and the dynamic of the DC bus voltage is updated to involve the CPL behavior. The parameters of the sliding mode controller and the way of its implementation are presented in [10].

Figures 5(a)–5(c) show the current, voltage, and generated power of the fuel cell, respectively, for both proposed approach and sliding mode controller [10].

As one can see in Figures 5(a)–5(c), the proposed approach leads to a more smooth current and voltage for the fuel cell and less power fluctuation than in [10]. The main source of these fluctuations is uncertainties in the fuel cell

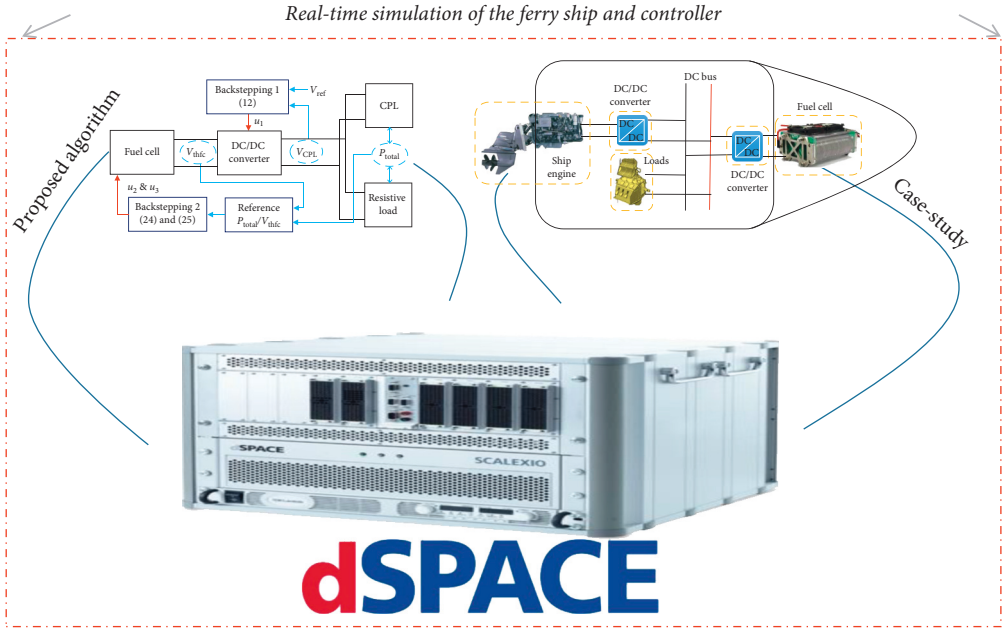

(a)

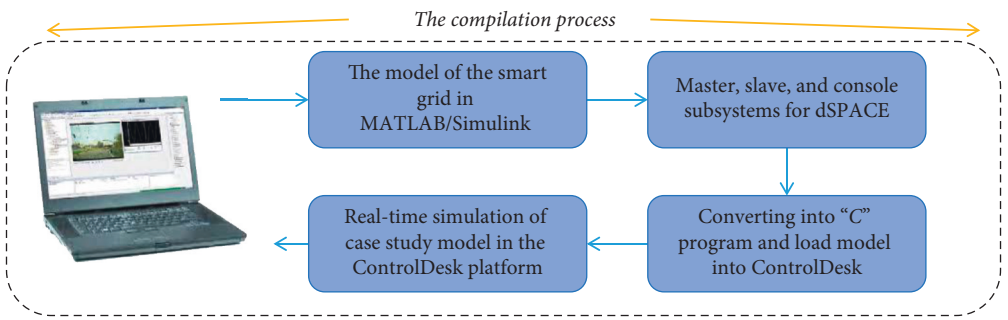

(b)

Figure 4: MiL real-time setup and configuration of the marine DC MG benchmark.

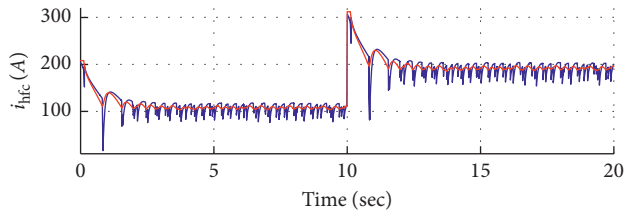

(a)

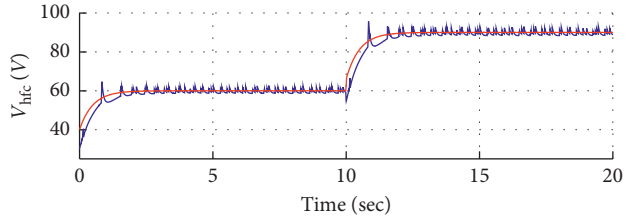

(b)

Figure 5: Continued.

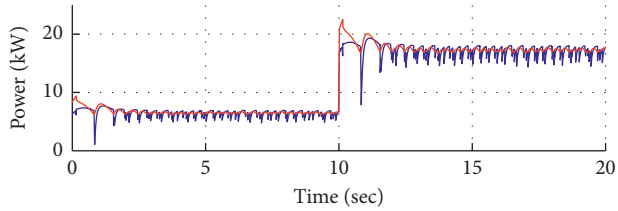

(c)

Figure 5: The (a) current, (b) voltage, and (c) generated power of the fuel cell (the proposed approach by the red line and the sliding mode approach by the blue line).

parameters. Since both the proposed sliding mode approaches use the nominal values and the considered fuel cell dynamics are severely nonlinear, power and voltage fluctuations are inevitable.

Figure 6 illustrates the voltage of the DC bus for both approaches. Figure 6 reveals reliable marine DC MG. The reason is that the voltage of the DC bus (i.e., the CPL voltage) is regulated to its desired reference better and more accurate than that of [10]. For instance, the DC bus voltage based on the proposed controller converges to its reference almost at $t = 2$ sec and the fluctuation amplitude is less than 2V. However, the sliding mode approach [10] leads to about 6V fluctuations in the DC bus voltage.

However, from Figure 7, one concludes that there are still some oscillations in the DC but voltage, especially, when the power level of the CPL changes promptly at $t = 10$ sec. The reason is that the fuel cell generator is a slow-response unit and it takes time to precisely regulate its power. Since there are no other fast-response units such as a battery or a supercapacitor, the injecting power to the CPL and resistive load is not constant and equal to the demand power. So, the resistive load receives nonconstant power and its voltage is changed by time.

The power received to the resistive load is illustrated in Figure 7. As can be seen in Figures 5(c) and 7, the proposed approach provides a smoother power than the sliding mode approach [10]. Furthermore, the approach of [10] injects more extra power to the resistive load. The ideal value for the resistive load power is 2kW, for which the DC but voltage will kept at 400V. The higher injected power not only reduces the performance of the system but also results in more hydrogen and oxygen consumption. Therefore, the compressed tanks for the hydrogen and oxygen will be emptied faster than the proposed approach. However, note that the power surplus (undersupply) and the voltage oscillation can be compensated by connecting a battery or a supercapacitor to the DC bus. However, in this paper, such compensation is not considered and only the attempt was made to propose a novel nonlinear control approach to enhance the transient and steady-state regulation of the hydrogen fuel cell.

Moreover, to show the steady-state performance of the proposed approach and the sliding mode control [10], Table 2 is provided. As can be seen in Table 2, the steady-state error of the proposed approach is more than 60 % which is improved over the sliding mode approach [10].

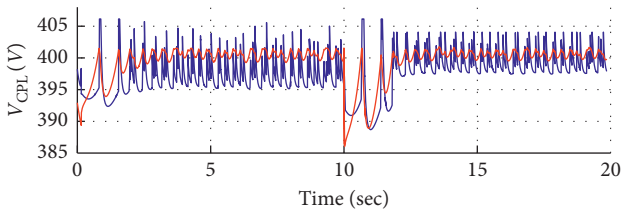

Figure 6: The voltage of the DC bus (the proposed approach by the red line and the sliding mode approach by the blue line).

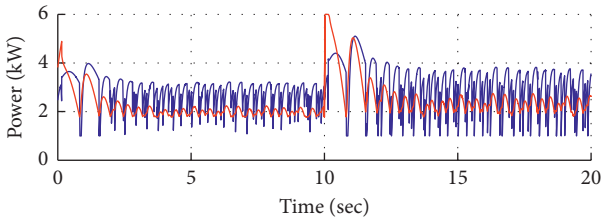

Figure 7: The injected power to the resistive load (the proposed approach by the red line and the sliding mode approach by the blue line).

Table 2: Steady-state error of different approaches.

	Proposed approach	Sliding mode approach [10]	Performance improvement (%)
V_{CPL}	1.572	4.103	61.68
i_{hfc}	3.637	47.323	92.31
V_{hfc}	0	3.191	100
Power	498.344	1578.723	68.43 %

5. Conclusion

The goal of this research was to stabilize a special DC marine MG that has uncertain time-varying loads and drive the DC voltage of the bus to track the desired voltage. To this aim, an additional reference for the current of the hydrogen fuel cell is defined and the controller design procedure is carried out by considering two backstepping controllers operating in parallel. To implement the controllers, first, some nonlinear error dynamics are defined to facilitate stabilizing the non-strict-feedback model of the system. Then, the virtual control signals are obtained step by step, by constructing suitable control Lyapunov functions (CLF) and providing the stability conditions, until the desired control signal is obtained. To illustrate

the effectiveness of the proposed controller, it is compared with the state-of-the-art method sliding mode controller. The real-time simulation results demonstrated the ability of the proposed controller in tracking the desired voltage of the bus for sudden and continuous changes of the load power.

Data Availability

The data used to support the findings of this study are available from the corresponding author upon request.

Conflicts of Interest

The authors declare that there are no conflicts of interest regarding the publication of this paper.

Acknowledgments

This work was supported by the Energy Technology Development and Demonstration Program (EUDP) under Grant (64018-0721), "HFC: Hydrogen Fuel Cell and Battery Hybrid Technology for Marine Applications".

References

[1] J. Han, J.-F. Charpentier, and T. Tang, "An energy management system of a fuel cell/battery hybrid boat," *Energies*, vol. 7, no. 5, pp. 2799–2820, 2014.

[2] M.-H. Khooban, T. Dragicevic, F. Blaabjerg, and M. Delimar, "Shipboard microgrids: a novel approach to load frequency control," *IEEE Transactions on Sustainable Energy*, vol. 9, no. 2, pp. 843–852, 2018.

[3] M. H. Khooban and M. Gheisarnejad, "Islanded microgrid frequency regulations concerning the integration of tidal power units: real-time implementation," *IEEE Transactions on Circuits and Systems II: Express Briefs*, pp. 1–11, 2019.

[4] M. Gheisarnejad, M.-H. Khooban, and T. Dragicevic, "The future 5G network based secondary load frequency control in maritime microgrids," *IEEE Journal of Emerging and Selected Topics in Power Electronics*, p. 1, 2019.

[5] A. Miola, B. Ciuffo, E. Giovine, and M. Marra, "Regulating air emissions from ships: the state of the art on methodologies, technologies and policy options," Reference reports, Publications Office of the European Union, Brussels, Belgium, 2010.

[6] L. K. C. Tse, S. Wilkins, N. McGlashan, B. Urban, and R. Martinez-Botas, "Solid oxide fuel cell/gas turbine trigeneration system for marine applications," *Journal of Power Sources*, vol. 196, no. 6, pp. 3149–3162, 2011.

[7] J. T. Pukrushpan, H. Peng, and A. G. Stefanopoulou, "Control-oriented modeling and analysis for automotive fuel cell systems," *Journal of Dynamic Systems, Measurement, and Control*, vol. 126, no. 1, p. 14, 2004.

[8] M. Gheisarnejad, J. Boudjadar, and M.-H. Khooban, "A new adaptive type-II fuzzy-based deep reinforcement learning control: fuel cell air-feed sensors control," *IEEE Sensors Journal*, vol. 19, no. 20, pp. 9081–9089, 2019.

[9] S. Bahrebar, F. Blaabjerg, H. Wang et al., "A novel type-2 fuzzy logic for improved risk analysis of proton exchange membrane fuel cells in marine power systems application," *Energies*, vol. 11, p. 721, 2018.

[10] R. Ashok and Y. Shtessel, "Control of fuel cell-based electric power system using adaptive sliding mode control and observation techniques," *Journal of the Franklin Institute*, vol. 352, no. 11, pp. 4911–4934, 2015.

[11] F. Li, Y. Yuan, X. Yan, R. Malekian, and Z. Li, "A study on a numerical simulation of the leakage and diffusion of hydrogen in a fuel cell ship," *Renewable and Sustainable Energy Reviews*, vol. 97, pp. 177–185, 2018.

[12] L. van Biert, M. Godjevac, K. Visser, and P. V. Aravind, "A review of fuel cell systems for maritime applications," *Journal of Power Sources*, vol. 327, pp. 345–364, 2016.

[13] P. Thounthong, S. Rael, and B. Davat, "Control strategy of fuel cell and supercapacitors association for a distributed generation system," *IEEE Transactions on Industrial Electronics*, vol. 54, no. 6, pp. 3225–3233, 2007.

[14] S. Vazquez, J. Rodriguez, M. Rivera, L. G. Franquelo, and M. Norambuena, "Model predictive control for power converters and drives: advances and trends," *IEEE Transactions on Industrial Electronics*, vol. 64, no. 2, pp. 935–947, 2017.

[15] C. Damour, M. Benne, C. Lebreton, J. Deseure, and B. Grondin-Perez, "Real-time implementation of a neural model-based self-tuning PID strategy for oxygen stoichiometry control in PEM fuel cell," *International Journal of Hydrogen Energy*, vol. 39, no. 24, pp. 12819–12825, 2014.

[16] S. M. Rakhtala, A. R. Noei, R. Ghaderi, and E. Usai, "Design of finite-time high-order sliding mode state observer: a practical insight to PEM fuel cell system," *Journal of Process Control*, vol. 24, no. 1, pp. 203–224, 2014.

[17] N. Vafamand, M. H. Khooban, T. Dragicevic, and F. Blaabjerg, "Networked fuzzy predictive control of power buffers for dynamic stabilization of DC microgrids," *IEEE Transactions on Industrial Electronics*, vol. 66, no. 2, pp. 1356–1362, 2019.

[18] L. Ding, Q.-L. Han, L. Y. Wang, and E. Sindi, "Distributed cooperative optimal control of DC microgrids with communication delays," *IEEE Transactions on Industrial Informatics*, vol. 14, no. 9, pp. 3924–3935, 2018.

[19] M. A. Kardan, M. H. Asemani, A. Khayatian et al., "Improved stabilization of nonlinear DC microgrids: cubature Kalman filter approach," *IEEE Transactions on Industry Applications*, vol. 54, no. 5, pp. 5104–5112, 2018.

[20] N. Vafamand, M. H. Khooban, T. Dragicevic, F. Blaabjerg, and J. Boudjadar, "Robust non-fragile fuzzy control of uncertain DC microgrids feeding constant power loads," *IEEE Transactions on Power Electronics*, vol. 34, 2019.

[21] E. Hossain, "Addressing instability issues in microgrids caused by constant power loads using energy storage systems," Theses and Dissertations, University of Wisconsin-Milwaukee, Milwaukee, WI, USA, 2016.

[22] N. Vafamand, A. Khayatian, and M. H. Khooban, "Stabilisation and transient performance improvement of DC MGs with CPLs: non-linear reset control approach," *IET Generation, Transmission & Distribution*, vol. 13, no. 14, pp. 3169–3176, 2019.

[23] J. Wu and Y. Lu, "Adaptive backstepping sliding mode control for boost converter with constant power load," *IEEE Access*, vol. 7, pp. 50797–50807, 2019.

[24] N. Vafamand, S. Yousefizadeh, M. H. Khooban, J. D. Bendtsen, and T. Dragicevic, "Adaptive TS fuzzy-based MPC for DC microgrids with dynamic CPLs: nonlinear power observer approach," *IEEE Systems Journal*, vol. 13, pp. 1–8, 2018.

[25] H. Farsizadeh, M. Gheisarnejad, M. Mosayebi, M. Rafiei, and M. H. Khooban, "An intelligent and fast controller for DC/DC converter feeding CPL in a DC microgrid," *IEEE Transactions On Circuits And Systems II: Express Briefs*, p. 1, 2019.

[26] T. Dragicevic, "Dynamic stabilization of DC microgrids with predictive control of point of load converters," *IEEE Transactions on Power Electronics*, vol. 33, p. 1, 2018.
[27] R. Cheng, J. F. Forbes, and W. S. Yip, "Price-driven coordination method for solving plant-wide MPC problems," *Journal of Process Control*, vol. 17, no. 5, pp. 429–438, 2007.
[28] Y. Zhao, W. Qiao, and D. Ha, "A sliding-mode duty-ratio controller for DC/DC buck converters with constant power loads," *IEEE Transactions on Industry Applications*, vol. 50, no. 2, pp. 1448–1458, 2014.
[29] A. M. Rahimi and A. Emadi, "Active damping in DC/DC power electronic converters: a novel method to overcome the problems of constant power loads," *IEEE Transactions on Industrial Electronics*, vol. 56, no. 5, pp. 1428–1439, 2009.
[30] J. T. Pukrushpan, A. G. Stefanopoulou, and H. Peng, *Control of Fuel Cell Power Systems*, Springer London, London, UK, 2004.
[31] W. K. Na and B. Gou, "Feedback-linearization-based nonlinear control for PEM fuel cells," *IEEE Transactions on Energy Conversion*, vol. 23, no. 1, pp. 179–190, 2008.
[32] S. Yousefizadeh, J. D. Bendtsen, N. Vafamand, M. H. Khooban, T. Dragicevic, and F. Blaabjerg, "Tracking control for a DC microgrid feeding uncertain loads in more electric aircraft: adaptive backstepping approach," *IEEE Transactions on Industrial Electronics*, vol. 66, no. 7, pp. 5644–5652, 2018.
[33] M. Gheisarnejad, P. Karimaghaee, J. Boudjadar, and M.-H. Khooban, "Real-time cellular wireless sensor testbed for frequency regulation in smart grids," *IEEE Sensors Journal*, pp. 1–11, 2019.

Hindawi
Complexity
Volume 2019, Article ID 6090427, 13 pages
https://doi.org/10.1155/2019/6090427

Research Article

Performance Analysis for the Magnetically Coupled Resonant Wireless Energy Transmission System

Jinguo Liu,[1] **Xuebin Zhang**,[2] **Jiahui Yu**,[3] **Zhenyao Xu**,[1] **and Zhaojie Ju**[1,3]

[1]*State Key Laboratory of Robotics, Shenyang Institute of Automation, Chinese Academy of Sciences, Shenyang 110016, China*
[2]*Beijing Institute of Structure and Environment Engineering, Beijing 100076, China*
[3]*School of Computing, University of Portsmouth, Portsmouth PO1 3HE, UK*

Correspondence should be addressed to Zhaojie Ju; zhaojie.ju@port.ac.uk

Received 19 July 2019; Accepted 10 October 2019; Published 11 November 2019

Guest Editor: Jianwu Zeng

As a new wireless energy transmission technology, magnetically coupled resonant wireless energy transmission system (MCRETS) is not easily affected by obstacles in the transmission process, and the transmission distance is relatively far. However, how to balance the relationship between transmission efficiency and power to achieve optimal performance is still a huge challenge. In addition, few studies have theoretically investigated the factors affecting the wireless energy transmission system to obtain an optimal solution. Here, through unprecedented theoretical analysis, we find the exact parameters of system optimization and verify them by simulation and experiments. First, the optimal topology of MCRETS is obtained through theoretical analysis and comparison of topologies. Second, to improve the transmission performance of MCRETS, its impact factors, including transmission distance, resonant frequency, relay coil, and relative position of launch and receiving coils, are analyzed in detail to get accurate parameters. Furthermore, based on the analysis, we propose an unprecedented concept for balancing optimal efficiency and power, which is named the power product. Finally, the effectiveness of the proposed method is verified through analysis and experimental results. These findings shed light on the relationship between efficiency and power and provide a comprehensive theoretical basis for subsequent research.

1. Introduction

With the increase in the number of traditional receiving terminals of cable power supply, the drawbacks, such as socket exposure, plugs prone to sparks, and other issues, become increasingly evident. To solve these problems, wireless power transfer (WPT) is utilized and it achieves wireless transmission through mutual coupling among physical fields. This technology has improved both equipment safety and functionality and has currently gained attention in the field of electrical research [1], especially in the current hotspots of electric vehicles [2] and wireless sensor networks [3]. At present, noncontact WPT can be divided into three forms, namely, electromagnetic induction, microwave, and magnetic resonant coupling. Electromagnetic induction and microwave development are relatively mature and are mainly used in maglev trains [4] and bodies of microcamera power supplies [5]. In a magnetically coupled resonant wireless energy transmission system (MCRETS), the magnetic fields serve as transmission media and create energy for wireless transmission through their resonance [6–8]. This technology has high transmission efficiency, can transmit a large amount of power, and is not susceptible to certain metals found in transmission channels [9]. Compared with electromagnetic induction and microwave transmission techniques, MCRETS is essentially different in the following ways: first, magnetic resonant coupling has greater transmission distance limit that is far beyond the limit of electromagnetic induction [10], and moreover, its transmission distance can be further increased even without regard to the impact of other factors, such as the loss of energy in the air, the influence of magnetic material, and other devices emitting electromagnetic interference in the transmission space; second, compared with the microwave WPT, transmission power of magnetic resonant coupling is greater. Overall, MCRETS is new and more widely used [11],

given that it meets the requirements for electromagnetic compatibility and has a high application value and broad applications in medical implantation machinery [12], robots [13], wireless sensors [5], and consumer appliances [14].

Researchers have made numerous breakthroughs in the study on MCRETS [15]. For example, Soljacic used the principle of magnetic resonant coupling to light a 60 W bulb from a distance of 2.16 m. The transmission efficiency of the bulb reached 40%. The energy transfer mechanism between the two resonators was analyzed by using the coupling mode theory. In [16], the coupling mode theory was also utilized in analyzing the energy transfer among three resonant coils and the influence of relay coil. In [17], a physical model of the equivalent circuit of transmitting and receiving coils was established, a four-coil wireless energy transmission model for medical implants was optimized, and the main factors that influenced the efficiency of the system were theoretically analyzed. In [18], a two-layer nested optimization method based on the differential evolution algorithm was proposed, and the maximum transmission efficiency of the transmission system was theoretically studied and verified through the finite element method. Another study introduced the working principle of MCRETS, and the impact factors of the transmission performance (e.g., transmission distance) of the system were theoretically analyzed [19]. In [20], physical analysis of the wireless energy transmission system with a magnetic field repeater was performed, and the influence of the magnetic relay on transmission performance of the system was theoretically analyzed. In [21], the physical structure and working principle of the low-power wireless energy transmission system applied to medical devices were theoretically analyzed. Besides, research on high-power applications has made some progress. In [22], researchers studied the optimization of the coil; in [23], the magnetic coupling has been improved, through using the method of adding ferrite core materials. However, most of the designs in previous studies have modeled single transmissions, maximum power transmission, or transmission at highest efficiency. No design based on dual transmission indices, such as those that modeled simultaneous transmission or maximum transmission efficiency, is available. In addition, few papers have theoretically analyzed the influence of multiple factors on transmission performance because the bulk of the few existing studies contends with single impact factors. Moreover, considerably few experiments have performed to verify theories on optimization of transmission, such as those that posit low transmission efficiency occurs when wireless energy transmission system meets the maximum transmission power.

To address the above issues, a complete modeling and analysis of the wireless energy transmission system based on the transmission efficiency and power is conducted in this study. The basic structure, working principles of the wireless energy transmission system, and topology are analyzed and compared. The four impact factors of transmission performance (i.e., transmission distance, system resonance frequency, relay structure, and relative position of transmitting and receiving coils) are theoretically analyzed to derive the degree of influence of each factor. Although the size and shape of the coil have an impact on the transmission performance, the nature of such effects is the coil's own parameter settings, such as resistance, which have little effect on practical applications. Therefore, the research factors in this paper set the transmission distance, the resonant frequency, and the relative position of the transmitting and receiving coils. The main reason is that the influence of these factors is more common in practical applications. The validity of the theoretical analysis is experimentally verified. This study also creatively presents the power product parameters, which are theoretically analyzed to obtain a conductive transmission state and optimize the transmission power and transmission efficiency. This analysis can provide theories and solutions for the design and optimization of MCRETSs. The main contributions of this paper are summarized as follows:

(1) We present the complete modeling and analysis of the wireless energy transmission system based on the transmission efficiency and transmission power of two transmission indicators, analysis of its basic structure and working principle, and analysis and comparison for the optimal topology.

(2) The influencing factors of this paper are different from the traditional methods and previous studies. Firstly, we get the exact effect of the four influencing factors from the theoretical deduction and then verify the correctness of the theoretical deduction through experiments. In addition, we get the theoretical value of the turning point, which has a certain significance for optimizing practical problems.

(3) Comparing the factors that affect this system performance listed before, considering the problem that power and efficiency optimization cannot be both concerned in practical applications, this paper presents a novel method of optimal selection, named as power product and elaborates its derivation principle and experimental process in detail.

(4) The theoretical analysis is verified through an experiment, and power product parameters are proposed to reach an optimal transmission power and efficiency of the system, with theoretical analysis.

The remainder of this paper is as follows: Section 2 reviews the related work of the wireless energy system. In Section 3, we introduce the process of the proposed method. The validation of the proposed method using finite element simulation is presented in Section 4. In Section 5, we report various experimental results as well as the comparison with the state-of-the-art methods. Finally, Section 6 concludes this paper with the summary and discussion.

2. Structure and Working Principle of the Wireless Energy Transmission System

In a vibrating system, strong coupling states often exist among several parts with the same intrinsic frequency [24]. The magnetically coupled resonance is a strong coupling

method of adjacent magnetic fields, wherein loss of energy in the transmission is minimized even with high transmission efficiency. It is not easily affected by metal barriers and other disruptive materials found in the transmission channel, and it can generate nondirectional transmission.

The core structure of MCRETS comprises two or more designed resonant coils: a matching module for supplying high-frequency energy that is equal to the intrinsic frequency of the resonant coil and supporting modules that receive high-frequency energy and change in the form of energy required. Figure 1 shows a typical midrange block diagram of MCRETS, which mainly includes a frequency AC power supply, a rectifier filter module, a RF amplifier, an impedance matching and regulation control circuit, transmitting and receiving coils, a rectifier, and a load. After the RF amplifier receives transmission, the receiver coil resonates a current, and the wireless energy transmission system achieves the maximum efficiency.

MCRETS has an external capacitor resonant compensation for each loop. External capacitors can be divided into series and parallel compensations by the capacitive access circuit. The compensation structure is discussed separately for the primary and secondary circuits. Resonant compensation structures can be divided into series-series (SS), series-parallel (SP), parallel-series (PS), and parallel-parallel (PP) [25]. The four circuit compensation structures are shown in Figure 2.

In Figure 2, the subscript P denotes the primary circuit, U is the primary-induced voltage source, IP is the loop current, LP and RP are the equivalent circuit parameters of the coil, and CP is the tuning capacitance in the primary circuit. Subscript S represents the secondary circuit, RL is the load, IS is the loop current, LS and RS are coil equivalent circuit parameters in the secondary circuit, CS is the tuning capacitor in the secondary circuit, and M is the mutual inductance between the two circuits.

If the frequency of the transmission system is f, the equations of the primary and secondary circuits are as follows:

$$\begin{cases} \omega = 2\pi f, \\ Z_{\mathrm{P}}\dot{I}_{\mathrm{P}} - j\omega M\dot{I}_{\mathrm{S}} = U, \\ -j\omega M\dot{I}_{\mathrm{P}} + Z_{\mathrm{S}}\dot{I}_{\mathrm{S}} = 0, \end{cases} \tag{1}$$

where ZP and ZS are the impedances of the primary and secondary circuits. The currents of the primary and secondary circuits, IP and IS, can be obtained from (1):

$$\begin{cases} \dot{I}_{\mathrm{P}} = \dfrac{U}{Z_{\mathrm{P}} + (\omega M)^2/Z_{\mathrm{S}}}, \\ \dot{I}_{\mathrm{S}} = \dfrac{j\omega MU/Z_{\mathrm{P}}}{Z_{\mathrm{S}} + (\omega M)^2/Z_{\mathrm{P}}}, \end{cases} \tag{2}$$

where $Z_{\mathrm{PS}} + (\omega M)^2/Z_{\mathrm{S}}$ is the response impedance of the secondary circuit to the primary circuit and $Z_{\mathrm{SP}} + (\omega M)^2/Z_{\mathrm{P}}$ is the response impedance of the primary circuit to the secondary circuit. When $\omega_0 = 1/\sqrt{L_{\mathrm{S}}C_{\mathrm{S}}}$, the resonant frequency of each coil in a transmission system is consistent with the resonant frequency of the excitation source, and the system transmission efficiency is the highest. Moreover, the currents in the two loops are affected by the opposing loops in (2).

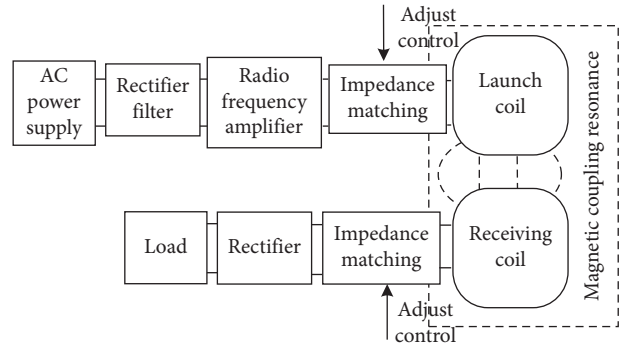

Figure 1: Block diagram of a medium-distance MCRETS.

When the resonant compensation circuit is a series structure, impedance ZPS is purely resistant to the resonant frequency, whereas the two coexist in a parallel structure. When the system has a SS compensation structure, the external resonant capacitor is unaffected by the impedance of the secondary loop, the transmission distance, or load characteristics, and the resonant frequency does not affect the choice of the resonant capacitor, so the system design optimization is more convenient. Thus, the topology of the external resonant capacitance has a SS structure.

3. Theoretical Analysis of the Transmission Performance of MCRETS

In traditional methods, most of the previous studies are directly through simulation to get the optimal parameters of each influencing factor, so only the optimal parameters range can be obtained. This paper is different from traditional methods. Firstly, starting with the theoretical model, the exact value of the optimal parameters is deduced by formula, and then the deduced results are verified by simulation and experiment. In this way, we can find the essence of each factor and provide a theoretical basis for future research.

In this chapter, we theoretically analyze the influence factors of transmission performance (transmission distance, system resonance frequency, relay structure, relative position of transmitting, and receiving coils) and get the influence of each factor.

3.1. Influence of Transmission Distance on the Transmission Performance of MCRETS. The results and discussion may be presented separately, or in one combined section, and may optionally be divided into headed subsections. The transmission efficiency of MCRETS is defined as the ratio of the power at the load side to the power transmitted by the transmitter. The transmission performance of MCRETS is susceptible to the four factors, namely, transmission distance, resonant frequency, relay coil, and relative position of

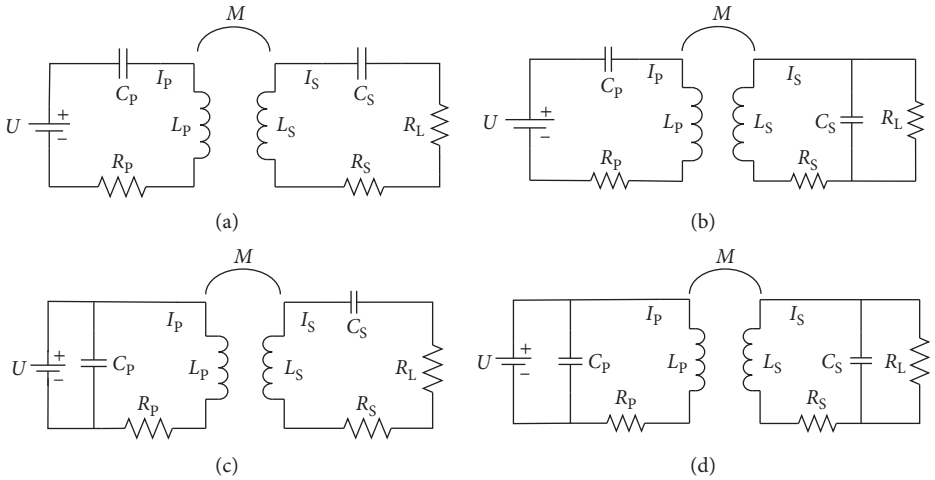

Figure 2: Four basic resonant compensation structure circuits: (a) SS mode; (b) SP mode; (c) PS mode; (d) PP mode.

transmitting and receiving coils. According to the mechanism of magnetic coupling of resonant wireless energy transmission, resonant frequency is proportional to and can directly affect the transmission distance. In principle, the energy efficiency of short-range applications can be quite high, but it will drop rapidly as the transmission distance increases [26, 27]. In this study, the impact factor of transmission distance is theoretically analyzed. The diagram of the reception and equivalent circuits of MCRETS is shown in Figure 3.

The equivalent impedance of the transmitting and receiving circuits is

$$\begin{cases} Z_P = \dfrac{R_P + 1}{j\omega C_P + j\omega L_P}, \\ Z_S = \dfrac{R_S + 1}{j\omega C_S + j\omega L_S}, \end{cases} \tag{3}$$

when the resonant frequency of the system $\omega = 1/\sqrt{C_P L_P} = 1/\sqrt{C_S L_S}$, the equivalent impedance of the series resonant of the transmitting circuit is approximately 0, and the equivalent impedance of the parallel resonator is infinite. In the coil-resonant coupling circuits shown in Figure 3, the SS topology can be easily analyzed by systematically integrating it into a resonant system that only contains transmitting and receiving coils. The following formula can be obtained from Figure 3:

$$\begin{cases} Z_P \dot{I}_P - j\omega M \dot{I}_S = \dot{U}_i, \\ -j\omega M \dot{I}_P + Z_S \dot{I}_S = 0. \end{cases} \tag{4}$$

Then,

$$\begin{cases} Z_P = \dfrac{R_P + 1}{j\omega C_P + j\omega L_P}, \\ Z_S = \dfrac{R_S + 1}{j\omega C_S + j\omega L_S}. \end{cases} \tag{5}$$

ZP and ZS are incorporated into (5), as follows:

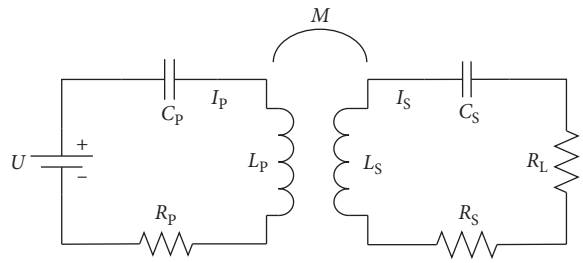

Figure 3: Equivalent circuit diagram of the transmitting and receiving circuits.

$$\begin{cases} \left(\dfrac{R_P + 1}{j\omega C_P + j\omega L_P}\right)\dot{I}_P - j\omega M \dot{I}_S = \dot{U}_i, \\ -j\omega M \dot{I}_P + \left(\dfrac{R_S + 1}{j\omega C_S + j\omega L_S}\right)\dot{I}_S = 0. \end{cases} \tag{6}$$

When $\omega_0 = 1/\sqrt{C_S L_S} = 1/\sqrt{C_P L_P}$, the system reaches a resonant state. The mutual inductance expression between the two coaxially parallel hollow coils is

$$M = \frac{\pi \mu_0 r^4 n^2}{2\left(\sqrt{2r^2 + D^2}\right)^3}. \tag{7}$$

Coil resistance can be equivalent to $R_P = R_S \approx R_0 = \sqrt{\omega\mu_0/2\sigma} nr/a$, where σ is the conductivity, D is the transmission distance, μ_0 is the vacuum permeability, r is the radius of the transmitter and receiver, and a and n indicate the radius of the wire of the receiving and transmitting coils and the number of turns of the two coils, respectively.

Equation (6) is solved as follows:

$$\begin{cases} I_P = \dfrac{(R_0 + R_L)U_i}{R_0(R_0 + R_L) + (\omega M)^2}, \\ I_S = \dfrac{j\omega M U_i}{R_0(R_0 + R_L) + (\omega M)^2}. \end{cases} \tag{8}$$

The output power and transmission efficiency of the load can be expressed as follows:

$$\begin{cases} P_0 = I_S^2 R_L = \dfrac{(\omega M)^2 U_i R_L}{\left[R_0 (R_0 + R_L) + (\omega M)^2\right]^2}, \\ \eta = \dfrac{P_0}{P_i} = \dfrac{I_d^2 R_L}{I_P U_i} = \dfrac{(\omega M)^2}{(\omega M)^2 + R_0 (R_0 + R_L)}. \end{cases} \tag{9}$$

When resonant frequency ω, load resistance R_L, transmitting and receiving coil parameters, and coil mutual inductance M can affect the transmission efficiency and output power of MCRETS, the magnitude of the mutual inductance is related to the transmitting distance. Thus, the transmission distance is related to the mutual inductance between the transmitting and receiving coils, the transmission efficiency of the wireless energy transmission system, and the output power.

From (9), the output power is derived from mutual inductance M; that is, when $dP_0/dM = 0$, the extreme point is obtained as

$$\begin{cases} M = \dfrac{\sqrt{(R + R_0)(R_0 + R_L)}}{\omega}, \\ M = \dfrac{\pi \mu_0 r^4 n^2}{2\left(\sqrt{2r^2 + D^2}\right)^3}. \end{cases} \tag{10}$$

The extreme distance can be derived from (10), as follows:

$$D_0^2 = \sqrt[3]{\frac{(\omega^2 T^2)}{[(R + R_0)(R_0 + R_L)]}} - 2r^2. \tag{11}$$

Then, $T = \pi \mu_0 r^4 n^2 / 2$.

Furthermore, when $D < D_0$, $P_0 < P$ max; when $D < D_0$, $P_0 < P$ max; and when $D = D_0$, $P_0 = P$ max, in which the power is the largest. Thus, when the transmission distance changes, the output power of the load initially increases and then decreases with the increase in the transmission distance.

Similarly, the relationship between mutual inductance and transmission efficiency can be obtained from mutual inductance M:

$$\frac{d\eta}{dM} = \frac{2\omega^2 M (R + R_0)(R_0 + R_L)}{\left[(R + R_0)(R_0 + R_L) + (\omega M)^2\right]^2}, \tag{12}$$

where $d\eta/dM > 0$ is established; that is, transmission efficiency is proportional to the size of mutual inductance because the mutual inductance and transmission distance are inversely proportional. Consequently, transmission efficiency decreases with the increase in transmission distance.

3.2. Influence of Resonant Frequency on the Transmission Performance of MCRETS. The resonant frequency of MCRETS is the driving signal frequency. When the driving signal frequency and the natural frequency of the transmitting and receiving coils are consistent, the system can reach a resonant state. When the output power in (9) is derived from the resonant frequency, that is, $dP_0/d\omega = 0$, the extreme frequency can be derived as follows:

$$\omega_0 = \frac{\sqrt{(R + R_0)(R_0 + R_L)}}{M}. \tag{13}$$

Based on the above analysis, when $\omega < \omega_0$, $dP_0/d\omega > 0$; when $\omega > \omega_0$, $dP_0/d\omega < 0$; and when $\omega = \omega_0$, $dP_0/d\omega = 0$. Thus, the output power of the system initially increases and then decreases with the increase of the resonant frequency. When $\omega = \omega_0$, the output power is the largest.

The resonant frequency is derived from the transmission efficiency, that is, $d\eta/d\omega = 0$:

$$\frac{d\eta}{d\omega} = \frac{2\omega M^2 (R + R_0)(R_0 + R_L)}{\left[(R + R_0)(R_0 + R_L) + (\omega M)^2\right]^2}. \tag{14}$$

In (14), $d\eta/d\omega > 0$ is established; thus, the transmission efficiency increases with the resonant frequency. However, in an actual setup, the skin effect will increase the transmission efficiency of the system and increases in the resonant frequency tend to be stable.

3.3. Wireless Energy Transmission System with a Relay Structure. The four-coil structure of MCRETS can achieve energy in a medium-distance transmission. When the distance of wireless energy transmission exceeds the critical coupling distance and into the under-coupled area, the transmission performance of the system will decline. However, adding a relay coil between the transmitting and receiving coils will improve the transmission performance of the system. The diagram of a five-coil wireless energy transmission system is shown in Figure 4, in which the relay and resonant coils can be consistent.

In this structure, the relay coil is equivalent to the circuit, and the resonant capacitor is serially connected with the circuit. The equivalent circuit of the five-coil wireless energy transmission system is shown in Figure 5. To simplify the model, the mutual inductance between nonadjacent coils can be ignored.

The relay and transmitting coils are near with each other; thus, they can be regarded as a transmitting source with a relay coil. The relay coil itself has a high-quality factor, which can increase the resonant current and enhance the magnetic field effect. This condition allows the relay and receiving coils in the long-distance coupling resonance to increase the transmission distance and enhance the transmission effect.

3.4. Influence of Relative Position of Transmitting and Receiving Coils on the Transmission Performance of MCRETS. Nondirectional propagation is a distinguishable feature of magnetically coupled resonance that sets it apart from the electromagnetic induction. In the electromagnetic induction coupling, a slight rotation and translation of the coil significantly induces energy loss in the receiving coil. However, when transmission is performed through MCRETS, the

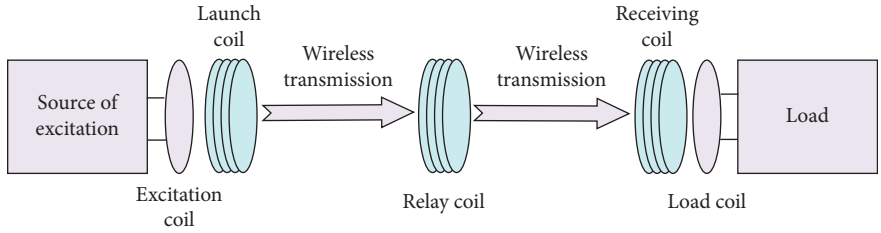

Figure 4: Schematic of the five-coil wireless energy transmission system.

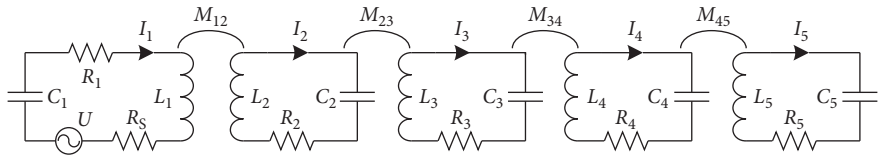

Figure 5: Equivalent circuit model for a five-coil wireless energy transfer system.

transmission and rotation of the coil within a certain transmission range will have a relatively small transmission loss. When the relative position of the transceiver coil goes beyond the range of the changing position, the rotation of the receiving coil has a considerable effect on the output power.

4. Finite Element Method Verification

In this paper, the launch coil and receiving coil are simulated by ANSYS 10.0 software. Because of the different analysis objects and different analysis methods, the nodal method of SOLID97 unit type is adopted in the analysis of the ray coil, which has the characteristics of simplicity, rapidity, and effectiveness. The simulation calculation of adding iron core between the launch coil and the receiving coil by using the edge method of the SOLID117 unit type can be simpler and more accurate.

Taking SOLID97 as an example, we set the degrees of freedom as AX, AY, and AZ. Then, the three-dimensional model of the cylindrical coil and the air can be built. Because the magnetic induction intensity produced by the coil model is relatively symmetrical, in order to save calculation time, the copper wire is chosen as the current-carrying winding coil, whose resistivity is $2.135 \times 10^{-8}\Omega \cdot m$ and relative permeability is 1. The coil model is shown in Figure 6. The coil diameter is 100 mm, the height is 100 mm, the wire diameter is 3 mm, the number of turns is 5, and the current per turn is 50 A.

For the following simulation, the following assumptions and conventions are made: approximate material isotropy; the influence of temperature change is not considered for the time being; the air region is considered as infinite; when iron core is added to the simulation, the B-H curve of iron core is approximately considered linear; when iron core is added to the simulation, the effect of eddy current demagnetization is not considered for the time being.

For the ANSYS analysis model, network partitioning is particularly important. The accuracy and speed of solution are greatly affected by the density of network partitioning.

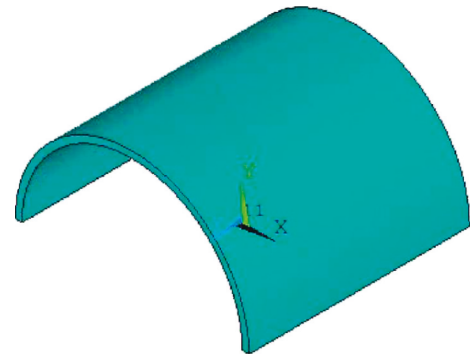

Figure 6: Cylindrical coil model.

In this paper, the coil and air dimensions of the model are quite different, so it cannot be divided in one time. The size of coil/iron core and air setting unit need to be separately divided freely. Considering the requirement of solving accuracy and solving time, the coil region needs to be partitioned in detail, while the air region follows the partitioning rule from inner to outer meshes to dense to sparse meshes. Figure 7 is a partition diagram with coils. Figure 8 is a general partition diagram of air and coils. The denser the black grid is, the finer the coil area is. The densest part in the middle is the coil.

The coil in simulation is a planar spiral coil. In order to effectively limit the number of subdivision units in FEM simulation, it is necessary to simplify the coil shape in modeling. Simplifying the coil shape will not affect the magnetic field distribution in the transmission channel too much. In the simulation software, the model is shown in Figure 9. The cross section is simplified, including the square cross section instead of the circular cross section of the conductor, whose side length is 5 mm, the turn number is 8 turns, the maximum external diameter is 38 cm, and the turn distance is 3 mm.

During the simulation, Maxwell and Simplorer are used to simulate the magnetic field distribution. The result of magnetic field distribution is shown in Figure 10. The distribution of magnetic field intensity when the magnetic field

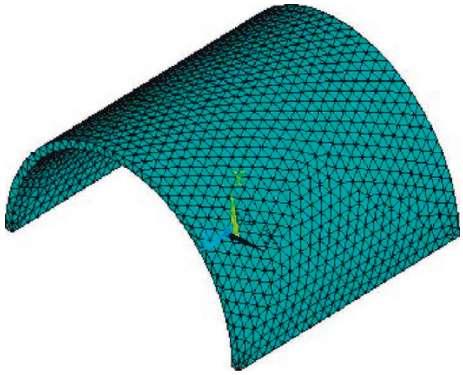

Figure 7: Grid of coils.

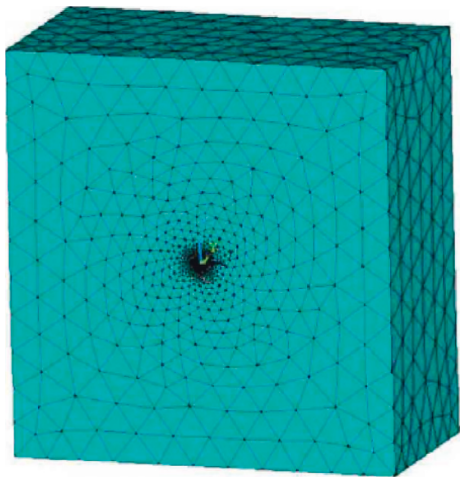

Figure 8: Overall grid with air.

intensity of the transmitting coil is maximum is shown in Figure 11. From the magnetic field intensity around the coil, it can be seen that the current is generated in the resonant coil at the receiving end.

Because of the similarity of the design simulation experiment process, this paper takes the above process as an example. By resetting the parameters of the simulation process, including transmission distance, system resonance frequency, relay structure, and relative position of transmitting and receiving coils, we can get multiple sets of simulation data through repeated simulation. In the next chapter, these simulated data will be used to compare and discuss with experimental data.

5. Experimental Verification of the Transmission Performance of MCRETS

The corresponding experimental physical device is built based on the working principle of MCRETS. The theoretical analysis results of the transmission performance of the wireless energy transmission system can be verified experimentally through this device, which is shown in Figure 12. The parameters of the relevant experimental equipment are shown in Table 1. The device comprises five parts, namely, transmitting device, transmitting coil, receiving coil, receiving device, and load. The transmitting device emits energy. The receiving coil receives energy and then powers the load. During the experiment, the input and output voltages, input and output currents, input and output powers, and other related data are displayed by the transmitter and receiver. Photographs of the receiving coil and the launch coil are presented in Figure 13, and the experimental setup is shown in Figure 14.

5.1. Influence of Transmission Distance on the Transmission Performance of MCRETS. The results of the transmission distance are experimentally verified. In the experiment, the position of the transmitting coil is kept constant, the receiving coil is moved to the right, and the transmission distance of the system is gradually increased. The relevant experimental data are collected by the transmitting and receiving devices. Data can be obtained from the theoretical analysis and experiment. The graph of the relationship between transmission distance and transmission power is shown in Figure 15(a) and that between transmission distance and transmission efficiency is shown in Figure 15(b).

From Figure 7, the output power of wireless energy transmission system initially increases and then decreases with the increase in transmission distance, whereas the transmission efficiency of the wireless energy transmission system decreases with the increase in transmission distance. These changes are consistent with the above theoretical analysis.

5.2. Influence of Resonant Frequency on the Transmission Performance of MCRETS. The resonant compensation capacitor of the wireless energy transmission system can be matched. The change in the resonant frequency of the system can be achieved by a change in the resonant compensation capacitor. In the experiment, the transmission distance is fixed at 2.5, 3.0, and 3.5 cm. Experimental data are collected from the changes in the resonant frequency of the system and then graphed with simulated data to show the relationships between the resonant frequency and output power and between the resonant frequency and transmission efficiency. The graph of the relationship between the output power and the resonant frequency is shown in Figure 16(a) and that between the resonant frequency and transmission efficiency is shown in Figure 16(b).

From Figure 16, with transmission distance kept constant, the output power of the system initially increases and then decreases with the increase in the resonant frequency of the system, whereas transmission and resonant frequencies of the system have a direct relationship. However, the existence of the skin effect in the actual system will increase its transmission efficiency, and any increase in resonant frequency tends to be stable. Experimental and theoretical analyses of the transmission efficiency value gap show a gradual increase. Therefore, when the resonant frequency of the wireless energy transmission system is low, a large output power should be kept close to the transmission, whereas if the resonant frequency in the wireless energy transmission

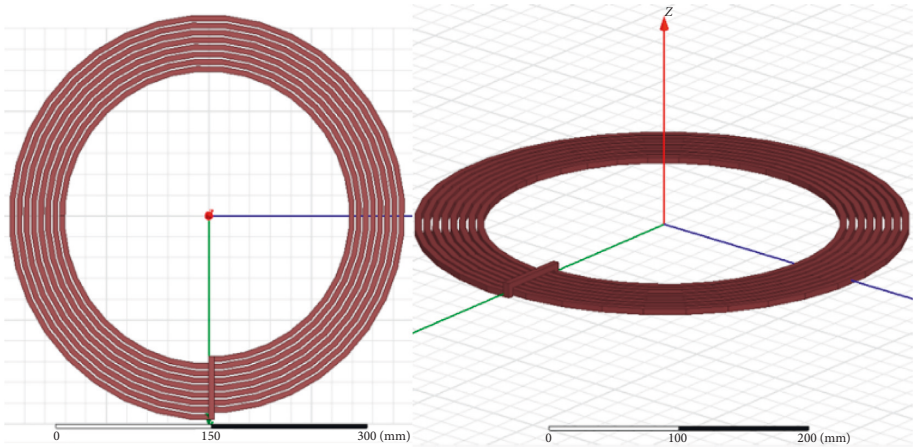

Figure 9: Coil 3D model drawn in Maxwell.

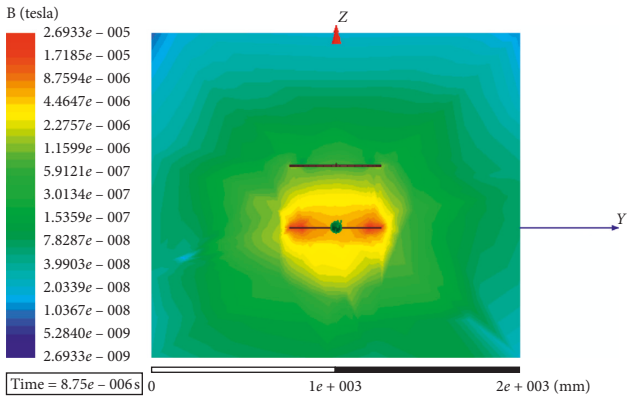

Figure 10: The maximum value of the magnetic field of the transmitting coil in transient field simulation.

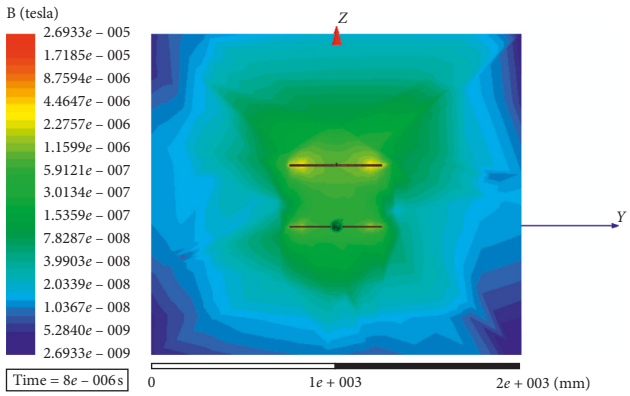

Figure 11: Transient field simulation receiver coil maximum magnetic field.

system is high, a large output power should be kept far from the transmission.

5.3. Influence of Relay Coils on the Transmission Performance of MCRETS. The experimental data of the relay and non-relay coils are collected by the experimental devices. The

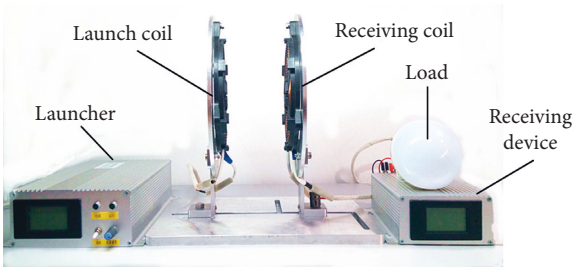

Figure 12: Physical diagram of MCRETS.

Table 1: Experimental equipment-related parameter.

Parameter item	Value
Device input voltage	220 V AC/50 Hz
Maximum device input	1600 W, 220 V AC/8 A
Maximum output power of the device	400 W, 24 V DC/5 A
Transmitting and receiving coil radius	3 mm
Transceiver turns	20
Coil winding radius	100 mm
The minimum distance between transmitting and receiving coils	10 mm

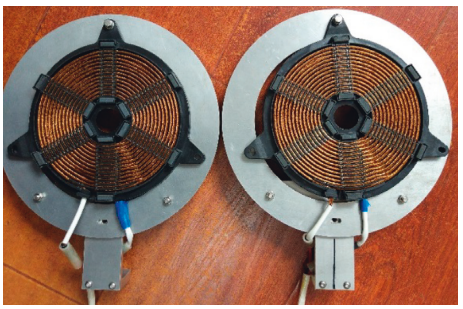

Figure 13: Receiving coil and launch coil of the practical MCRETS system.

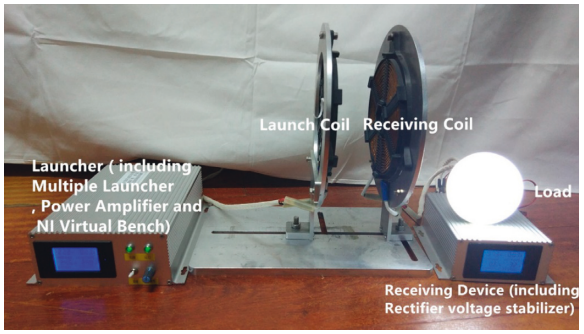

Figure 14: Experimental setup of the proposed MCRETS system.

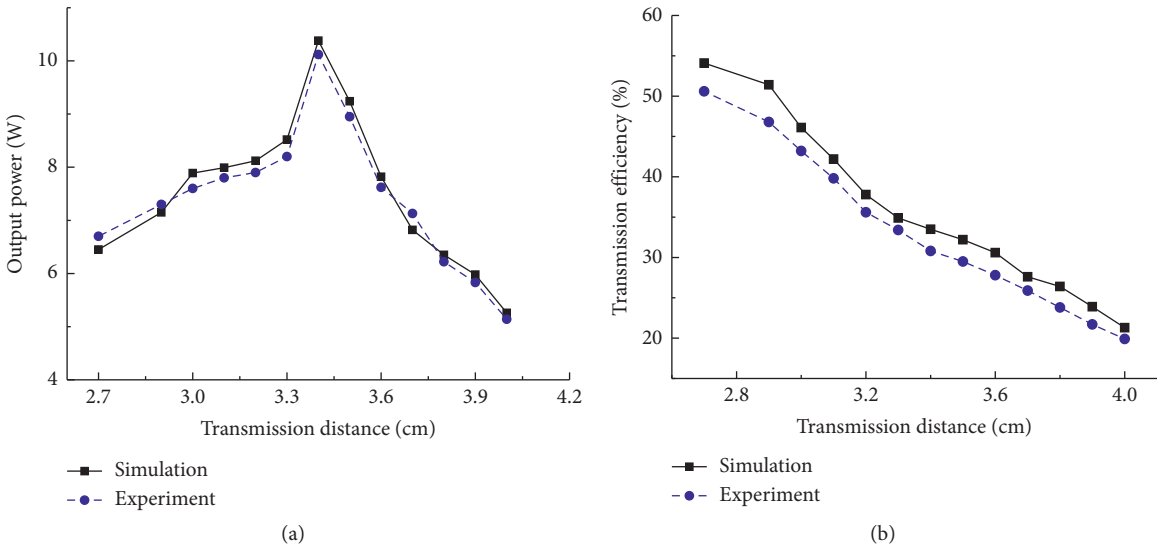

Figure 15: Transmission distance-output power and transmission distance-transmission efficiency curves.

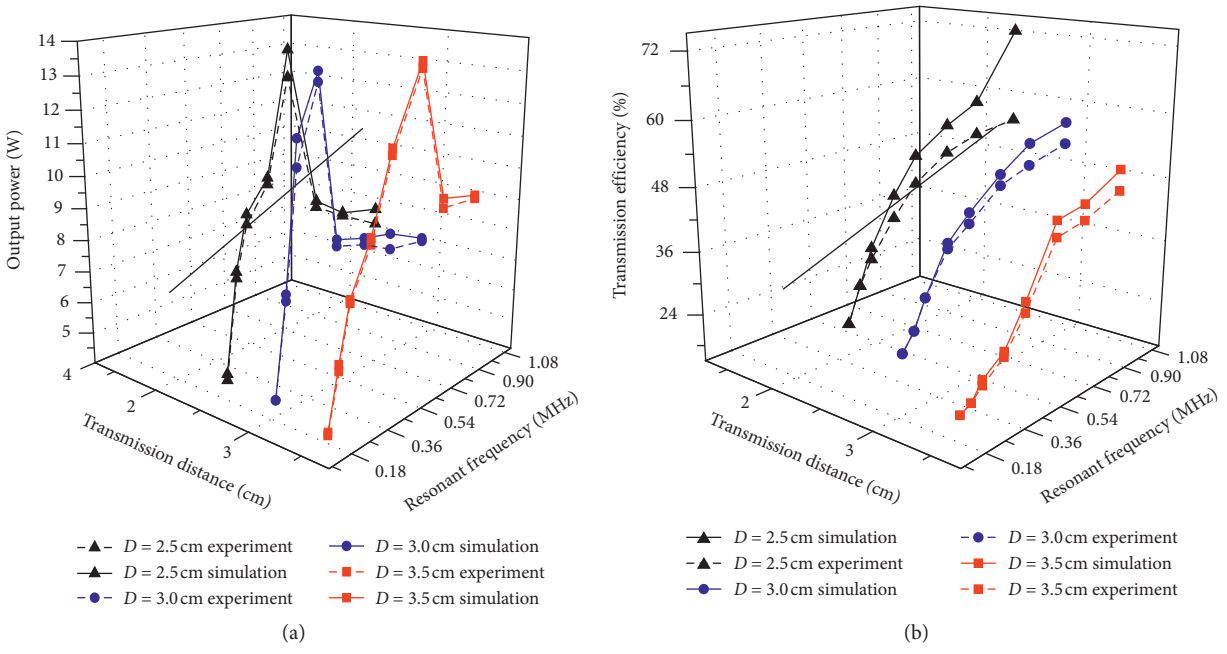

Figure 16: (a) Resonant frequency-output power efficiency relationships; (b) resonant frequency-transmission efficiency relationships.

relevant experimental data, which are fluctuations in the receiving terminal voltage as transmission distance changes, are collected, and the curves of the voltage and transmission distance of the relay and the nonrelay are drawn. The comparison chart is shown in Figure 17.

The variation curve in Figure 17 reveals that the voltage value of the receiver terminal is inversely proportional to the transmission distance. The curve for the transmission distance of the relay coil is slower than the curve for the transmission distance of the nonrelay coil. The magnitude of the attenuation of the magnetic field or the relay coil increases the range of the magnetic field. At the same time, the relay coil effectively increases the transmission distance of the system and enhances the transmission effect. The experimental results are consistent with the theoretical analysis results.

5.4. Influence of the Relative Position of Receiving and Transmitting Coils on the Transmission Performance of MCRETS. Findings from the theoretical analysis in this study are verified through an experiment. Before the start of the experiment, the angle between the receiving coils is set at −40° and the receiving coil is then rotated slowly in the direction vertical to the coil diameter until it rotates to an angle of 35°. The value of the output power during rotation is recorded. The output power varies with the rotation angle of the receiving coil. The experimental data are graphed in Figure 18. However, the theoretical derivation of the relative position of the launch and receiving coils has not yet been accurate. We only conducted preliminary verification through experiments and obtained preliminary conclusions after verification. In the future research, we will further derive the theoretical basis.

5.5. Transmission Characteristics of SS Topological System in Maximum Power Product. The above theoretical analysis and experiments reveal that when the system output power is at maximum, the transmission efficiency is often extremely low. A wireless energy transmission system is a relatively easily affected system, and its transmission performance is easily affected by many factors. At present, many scholars are analyzing the power and efficiency of the wireless energy transmission system, but this cannot guarantee the optimal transmission performance of the system. This paper combines the power and efficiency problems of wireless energy system transmission, that is, taking into account the power and efficiency of transmission and optimizing the system transmission performance. This kind of research is still rare.

The literature [28] compared and analyzed the two models of the four-coil end-opening coil and the short-circuited string-capacitor four-coil based on the spiral coil through the electromagnetic simulation. But this is only from the point of view of electromagnetic simulation, lack of specific reasoning calculation process cannot optimize the output power and transmission efficiency of the system, and it is even more impossible to optimize the system

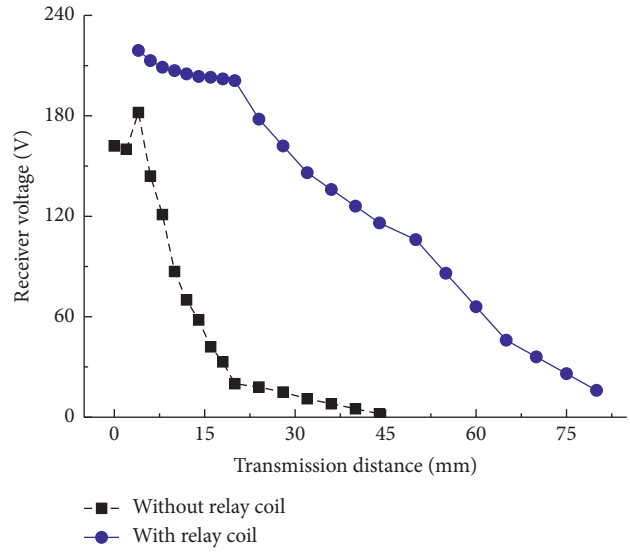

Figure 17: Receipt of voltage change of the experimental device, with distance changing with or without relay coil.

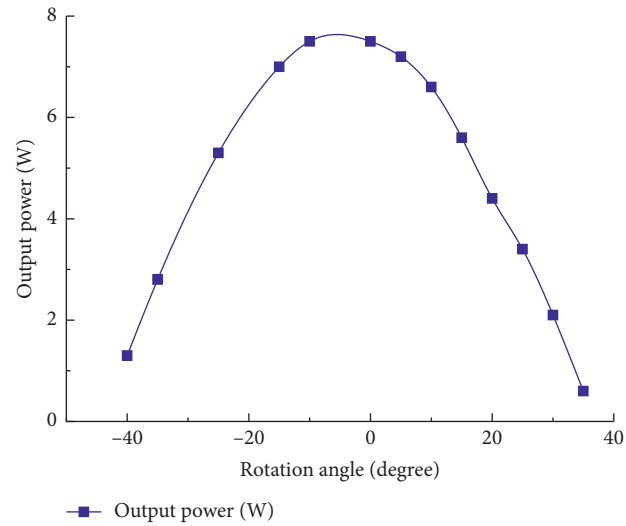

Figure 18: Output voltage-direction curve.

transmission performance. In this literature [29], two basic structures are analyzed and the equations of the transfer efficiency are deduced. Two important factors, namely, the transfer quality factor and the load matching factor, are explored. However, there is no research on how to balance the transmission efficiency and power in order to optimize the transmission performance of the wireless energy transmission system.

For the above problem, this study proposes the power product. The optimal parameters for the wireless energy transmission system are analyzed to allow higher transmission efficiency in the system even when the output power is high. The power product is the product of the output power and the transmission efficiency, and it can be expressed by Ψ (its unit is the product of two variable units: *W*), as shown in the following:

$$\Psi = P_0 \cdot \eta = \frac{(\omega M)^4 U_i^2 R_L}{\left[(\omega M)^2 + (R + R_0)(R_0 + R_L)\right]^3}. \quad (15)$$

For simplicity, the wireless energy transmission system is assumed to be in the ideal state and that the remaining items are constant; thus, the amount of change is only one-unit resonance frequency. It is necessary to set a series of parameters according to the idealized situation. According to the parameters set, the related formulas can be analyzed more effectively and conveniently. The analysis is simpler and clearer. System parameters are listed in Table 2. From equation (15), the curve of the power product Ψ and resonant frequency ω can be obtained, as shown in Figure 19. In order to find a relatively optimal value, it can meet the transmission power and transmission efficiency in a certain situation to achieve a relatively optimal value.

In Figure 11, when at the peak where $d\Psi/d\omega = 0$, the extreme point can be derived as follows:

$$\omega_0 = \frac{\sqrt{2(R + R_0)(R_0 + R_L)}}{M}. \quad (16)$$

The solvable output power $P_{0-\Psi}$ and transmission efficiency η_Ψ of the system are follows:

$$P_{0-\Psi} = \frac{2U_i^2}{9R_W}, \qquad \eta_\Psi = \frac{2}{3}. \quad (17)$$

From the above analysis, it shows that when $\omega = \sqrt{(R + R_0)(R_0 + R_W)}/M$, the output power reaches the optimal value, and we can get the corresponding output power P_{0-P} and the transmission efficiency at the maximum output power η_P:

$$P_{0-P} = \frac{U_i^2}{4R_W}, \qquad \eta_P = \frac{1}{2}. \quad (18)$$

α and β are the change ranges of the output power and transmission efficiency, respectively. when $\alpha = -11.1\%$ and $\beta = 33.3\%$, the output power of the system is reduced by 11.1%, and the transmission efficiency is increased by 33.3%.

Similarly, if other conditions are not changed, only the change in transmission distance is controlled. When the transmission distance satisfies $D^2 = \sqrt[3]{\omega^2 T^2/2(R + R_0)(R_0 + R_W)} - 2r^2$, the system's power product reaches its maximum. At this time, the output power is $P_{0-\psi} = 2U_i^2/9R_W$, and the transmission efficiency is $\eta_\psi = 2/3$. Under the maximum power index, when the transmission distance satisfies $D^2 = \sqrt[3]{\omega^2 T^2/2(R + R_0)(R_0 + R_W)} - 2r^2$, the output power takes the maximum value $P_{0-P} = U_i^2/4R_W$, and the transmission efficiency is then $\eta_P = 0.5$.

In summary, the use of power product parameters for optimization ensures that the output and transmission powers will be relatively high, which optimizes the transmission performance.

Table 2: System parameters.

DC input voltage	LS (Ld)	R_0
15 V	14.25 μH	0.27 Ω
F	RW	R
500 kHz	5 Ω	2.5 Ω

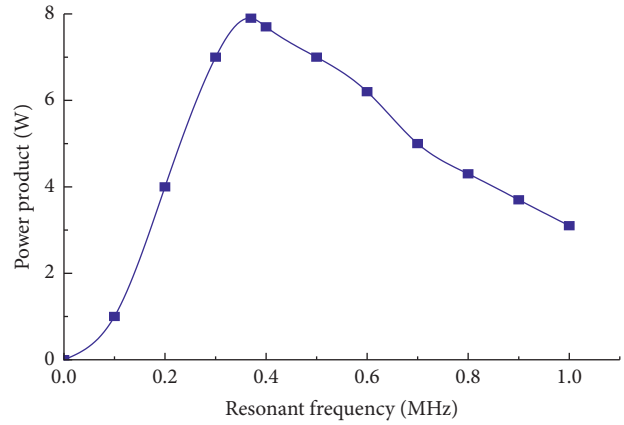

Figure 19: Relationship between the power product and resonant frequency.

6. Conclusions

This study introduced the MCRETS model, obtaining an optimal topology through modeling and analysis of its four topological structures. Theoretical analysis and experimental verification of the factors, which affect the transmission performance of the MCRETS (i.e., transmission distance, resonant frequency, relay coil, and relative position of transmitting and receiving coils) were conducted and discussed. The theoretical analysis and experimental results show that these factors greatly influence the transmission performance of the wireless energy transmission system, such that the factors can further improve the transmission performance once optimized. Based on the above analysis, this study proposed the parameters of the power product to ensure a relatively high transmission power with the maximized performance. This concept is of great significance in practical application. For example, the problem of choosing the highest power or higher charging efficiency has always existed. With the concept of power product, the maximum efficiency product can be preferentially selected, which is more conducive to the optimization of charging performance.

However, the research on the transmission structure of MCRETS is limited because it is based on a two-coil structure. Further research will study the effect of single or multiple power supply charging using a one-to-one structure or a network of structures. Based on the analysis, further research on the design for a more efficient, more powerful, and more stable MCRETS is also desirable.

Data Availability

The data used to support the findings of this study are available from the corresponding author upon request.

Conflicts of Interest

The authors declare that they have no conflicts of interest.

Acknowledgments

The authors would like to acknowledge the support from the National Key R&D Program of China (grant no. 2018YFB1304600), CAS Interdisciplinary Innovation Team (grant no. JCTD-2018-11), DREAM project of EU FP7-ICT (grant no. 611391), and National Natural Science Foundation of China (grant nos. 51575412, 51575338, and 5157540).

References

[1] S. Y. R. Hui, W. Zhong, and C. K. Lee, "A critical review of recent progress in mid-range wireless power transfer," *IEEE Transactions on Power Electronics*, vol. 29, no. 9, pp. 4500–4511, 2014.

[2] J. G. Kim, G. Wei, M. H. Kim, J. Y. Jong, and C. Zhu, "A comprehensive study on composite resonant circuit-based wireless power transfer systems," *IEEE Transactions on Industrial Electronics*, vol. 65, no. 6, pp. 4670–4680, 2017.

[3] A. Ibrahim, M. Meng, and M. Kiani, "A comprehensive comparative study on inductive and ultrasonic wireless power transmission to biomedical implants," *IEEE Sensors Journal*, vol. 18, no. 9, pp. 3813–3826, 2018.

[4] M. Soljacic, *Wireless Energy Transfer Can Potentially Recharge Laptops, Cell Phones without Cords*, Institute of Technology, San Francisco, MA, USA, 2006.

[5] K. M. Silay, C. Dehollain, and M. Declercq, "Inductive power link for a wireless cortical implant with biocompatible packaging," in *Proceedings of the Sensors*, pp. 94–98, Kona, HI, USA, November 2010.

[6] B. Zhu, J. Li, W. Hu, and X. Gao, "Review of magnetic coupling resonance wireless energy transmission," *International Journal of u- and e-Service, Science and Technology*, vol. 8, no. 3, pp. 257–272, 2015.

[7] T. Deyle and M. Reynolds, "Surface based wireless power transmission and bidirectional communication for autonomous robot swarms," in *Proceedings of the IEEE International Conference on Robotics and Automation*, pp. 1036–1041, Pasadena, CA, USA, June 2008.

[8] F. Zhang, S. Hackworth, X. Liu et al., "Wireless power delivery for wearable sensors and implants in body sensor networks," in *Proceedings of the Engineering in medicine and biology society*, pp. 692–695, Buenos Aires, Argentina, August 2010.

[9] Y. Jang and M. M. Jovanovic, "A contactless electrical energy transmission system for portable-telephone battery chargers," *IEEE Transactions on Industrial Electronics*, vol. 50, no. 3, pp. 257–272, 2003.

[10] R. Johari, J. V. Krogmeier, and D. J. Love, "Analysis and practical considerations in implementing multiple transmitters for wireless power transfer via coupled magnetic resonance," *IEEE Transactions on Industrial Electronics*, vol. 61, no. 4, pp. 1774–1783, 2014.

[11] M. Pinuela, D. C. Yates, S. Lucyszyn, and P. D. Mitcheson, "Maximizing DC-to-load efficiency for inductive power transfer," *IEEE Transactions on Power Electronics*, vol. 28, no. 5, pp. 2437–2447, 2013.

[12] M. Kiant, U. M. Jow, and M. Ghovanloo, "Design and optimization of a 3-coil inductive link for efficient wireless power transmission," *IEEE Transactions on Biomedical Circuits and Systems*, vol. 5, no. 6, pp. 579–591, 2011.

[13] T. Sun, X. Xie, G. Li et al., "A two-hop wireless power transfer system with an efficiency-enhanced power receiver for motion-free capsule endoscopy inspection," *IEEE Transactions on Biomedical Engineering*, vol. 59, no. 11, pp. 3247–3254, 2012.

[14] C. Jiang, K. T. Chau, C. Liu, and C. H. T. Lee, "An overview of resonant circuits for wireless power transfer," *Energies*, vol. 10, no. 7, p. 894, 2017.

[15] A. Kurs, A. Karalis, R. Moffatt, J. D. Joannopoulos, P. Fisher, and M. Soljacic, "Wireless power transfer via strongly coupled magnetic resonances," *Science*, vol. 317, no. 5843, pp. 83–86, 2007.

[16] K. Jinwook, S. Hyeon-Chang, K. Kwan-Ho et al., "Efficiency analysis of magnetic resonance wireless power transfer with intermediate resonant coil," *IEEE Antennas and Wireless Propagation Letters*, vol. 10, pp. 389–392, 2011.

[17] A. K. Ramrakhyani, S. Mirabbasi, and M. Chiao, "Design and optimization of resonance-based efficient wireless power delivery systems for biomedical implants," *IEEE Transactions on Biomedical Circuits and Systems*, vol. 5, no. 1, pp. 48–63, 2011.

[18] X. Zhang, S. L. Ho, and W. N. Fu, "Analysis and optimization of magnetically coupled resonators for wireless power transfer," *IEEE Transactions on Magnetics*, vol. 48, no. 11, pp. 4511–4514, 2012.

[19] M. Sawan, Y. Yamu Hu, and J. Coulombe, "Wireless smart implants dedicated to multichannel monitoring and microstimulation," *IEEE Circuits and Systems Magazine*, vol. 5, no. 1, pp. 21–39, 2005.

[20] D. Ahn and S. Hong, "A study on magnetic field repeater in wireless power transfer," *IEEE Transactions on Industrial Electronics*, vol. 60, no. 1, pp. 360–371, 2013.

[21] F. Zhang, S. Hackworth, X. Liu et al., "Wireless energ y transfer platform for medical sensors and implantable devices," in *Proceedings of the 2009 Annual International Conference of the IEEE Engineering in Medicine and Biology Society*, pp. 1045–1048, Minneapolis, MN, USA, September 2009.

[22] D. Ahn, S. M. Kim, S. W. Kim, J. I. Moon, and I. K. Cho, "Wireless power transfer receiver with adjustable coil output voltage for multiple receivers application," *IEEE Transactions on Industrial Electronics*, vol. 66, no. 5, pp. 4003–4012, 2018.

[23] D. H. Kim and D. Ahn, "Maximum efficiency point tracking for multiple-transmitters wireless power transfer," *IEEE Transactions on Power Electronics*, 2019.

[24] K. M. Silay, C. Dehollain, and M. Declercq, "Inductive power link for a wireless cortical implant with two-body packaging," *IEEE Sensors Journal*, vol. 11, no. 11, pp. 2825–2833, 2011.

[25] M. K. Watfa, H. AlHassanieh, and S. Selman, "Multi-hop wireless energy transfer in WSNs," *IEEE Communications Letters*, vol. 15, no. 12, pp. 1275–1277, 2011.

[26] E. Waffenschmidt and T. Staring, "Limitation of inductive power transfer for consumer applications," in *Proceedings of the 2009 13th European Conference on Power Electronics and Applications*, pp. 1–10, IEEE, Barcelona, Spain, September 2009.

[27] J. O. Mur-Miranda, G. Fanti, Y. Feng et al., "Wireless power transfer using weakly coupled magnetostatic resonators," in *Proceedings of the IEEE ECCE*, pp. 4179–4186, Atlanta, GA, USA, September 2010.

[28] H. H. T. AmanoN Kikuma et al., "A consideration of open and short-·end type helical antennas for magnetic-coupled resonant wireless power transfer," in *Proceedings of the 2012 6th European Conference on Antennas and Propagation (EUCAP)*, pp. 3009–3013, Prague, Czech Republic, March 2012.

[29] Y. Zhang, Z. Zhao, and K. Chen, "Frequency decrease analysis of resonant wireless power transfer," *IEEE Transactions on Power Electronics*, vol. 29, no. 3, pp. 1058–1063, 2014.

Hindawi
Complexity
Volume 2019, Article ID 3010465, 6 pages
https://doi.org/10.1155/2019/3010465

Research Article

Sign-Consensus of Linear Multiagent Systems under a State Observer Protocol

Wei-Lu Diao and Cui-Qin Ma

School of Mathematical Sciences, Qufu Normal University, Qufu 273165, Shandong, China

Correspondence should be addressed to Cui-Qin Ma; cuiqinma@amss.ac.cn

Received 26 July 2019; Accepted 18 September 2019; Published 3 November 2019

Guest Editor: Chun Wei

The sign-consensus problem for linear time-invariant systems under signed digraph is considered. The information of the agents' states is reconstructed, and then, a state observer-type sign-consensus protocol is proposed, whose performance is analyzed using matrix analysis and ordinary differential equation theory. Sufficient conditions for ensuring sign-consensus are given. It is proven that if the adjacency matrix of the signed digraph has strong Perron–Frobenius property or is eventually positive, sign-consensus can be achieved under the proposed protocol. In particular, conventional consensus is a special case of sign-consensus under mild conditions.

1. Introduction

Consensus, as the key to coordination of multiagent systems (MASs), has been investigated extensively in recent years [1–9]. Most existing studies on consensus of MASs usually assume cooperative interactions among the agents, while in many cases, the agents can not only cooperate but also compete with each other, resulting in the coexistence of cooperation and competition in MASs, e.g., the two-party political system and the business alliance of competitors. To describe this scenario, the concept of bipartite consensus is proposed in [10], which means that all agents converge to the same value as required by conventional consensus but with different signs in bipartite consensus. Altafini [10] proves that, under the assumption of signed digraph being strongly connected, single-integrator MASs reach bipartite consensus if and only if the signed digraph is structurally balanced. Following this line, the strongly connected requirement on signed digraph in [10] is relaxed in [11], bipartite consensus under switched signed digraph is investigated in [12], and bipartite consensus for general linear MASs has also been studied in [13]. In [14–18], measurement noise is further considered. As pointed out in [15], the signed digraph being structurally balanced is one of the necessary and sufficient communication conditions to guarantee bipartite consensus regardless of measurement noise. This means that structural balance plays a crucial role in bipartite consensus. Structural balance is fragile and can be easily broken by changing the sign of some edge weight or by adding or deleting an edge in a signed digraph, meaning that structural unbalance can be more often seen in practice.

In fact, studies on structurally unbalanced signed digraph have already been reported in [14, 15, 19–24], etc. In [14, 15], agents converge to zero in mean square under arbitrary initial conditions. In [19], the agents' states are proved to lie in between the polarized values, which are called the interval bipartite consensus. Another topic closely related to structural unbalance is the unanimity of opinion [21]; that is, all agents achieve an agreement or disagreement on a certain subject but with different extents. This concept is further extended in [23] to sign-consensus, meaning that agents reach values with the same sign but different modulus. The concept of sign-consensus is rooted in reality. For example, in a social network, people rarely have the same comment on a topic, but may have the same tendency. In the pioneering work [23], it is shown that, for the linear time-invariant (LTI) MASs, if the graph adjacency matrix is eventually positive, sign-consensus is achieved under a state feedback sign-consensus protocol and a fully distributed sign-consensus protocol, respectively. The fixed signed

digraph in [23] is extended in [24] to being switched over time. Sign-consensus protocols are proposed for three types of time-varying graphs, respectively. It is shown that sign-consensus can be reached if the graph adjacency matrix is frequently eventually positive. We notice that both works [23, 24] propose state feedback-type sign-consensus protocols. However, in reality, due to constraints on measurement, it is usually hard to directly measure agents' states, but only the state estimates are available. Hence, it would be more convenient to synthesize consensus protocols based on the agents' state estimates.

With these observations, in this work, we investigate sign-consensus for LTI MASs under signed digraphs. The agents' states are reconstructed, and state observer-type protocols based on them are given. By using tools from matrix analysis and ordinary differential equation theory, the closed-loop system is analyzed. It is shown that if the graph adjacency matrix has strong Perron–Frobenius property or is eventually positive, sign-consensus for LTI MASs can be achieved. Our main contributions are as follows. First, the agent dynamics are extended to be LTI system, not limited to integrators [21, 22]. Second, state observer-type consensus protocols based on state estimates between neighboring agents are proposed, which are more practical than most existing protocols based on the agents' states [23, 24].

1.1. Organization. The state observer-type consensus protocol is proposed in Section 2. The main results with respect to sign-consensus are given in Section 3. A simulation example is given to verify the proposed theoretical results in Section 4. The paper is concluded in Section 5.

1.2. Notations and Preliminaries. For a matrix or vector A, if all its elements are positive, A is said to be positive, denoted as $A > 0$. For $A \in \mathbb{R}^{n\times n}$, $\lambda_i(A)\,(i = 1, \ldots, n)$ is the eigenvalue of A, $\mathrm{Re}(\lambda_i(A))$ is the real part of $\lambda_i(A)$, and $\rho(A)$ is the spectral radius, which is the smallest positive real number satisfying $\rho(A) \geq |\lambda_i(A)|, \forall i = 1, \ldots, n$. $A \in \mathbb{R}^{n\times n}$ has the strong Perron–Frobenius property if $\rho(A)$ is a simple positive eigenvalue of A, and its corresponding right eigenvector $v_r > 0$. $A \in \mathbb{R}^{n\times n}$ is eventually positive if $\exists l_0 \in \mathbb{N}$ satisfying $A^l > 0$, $\forall l \geq l_0$. For a given vector $v = (v_1, \ldots, v_n)^T \in \mathbb{R}^n$, $\mathrm{sign}(v) = (\mathrm{sign}(v_1), \ldots, \mathrm{sign}(v_n))^T$, where $\mathrm{sign}(\,)$ is the sign function. $1_n = (1, \ldots, 1)^T \in \mathbb{R}^n$, $\otimes$ is the Kronecker product.

$\mathcal{G} = (\mathcal{V}, \varepsilon, \mathcal{F})$ is a signed digraph with $\mathcal{V} = \{1, \ldots, N\}$, $\varepsilon \subset \mathcal{V} \times \mathcal{V}$, and the adjacency matrix $\mathcal{F} = (f_{ij}) \in \mathbb{R}^{N\times N}$. $\mathcal{N}_i = \{(j, i) \in \mathcal{E}\}$. Generally, $\mathcal{F} = (f_{ij}) \in \mathbb{R}^{N\times N}$ is defined by $f_{ii} = 0$, $f_{ij} \neq 0 \Longleftrightarrow (j, i) \in \varepsilon$; otherwise, $f_{ij} = 0$. Denote $D_{\mathcal{F}} = \rho(\mathcal{F})I_N - \mathcal{F}$ with $\rho(\mathcal{F})$ being the spectral radius of $\mathcal{F}$.

Lemma 1 (see [23]). *Assume $\mathcal{G} = (\mathcal{V}, \varepsilon, \mathcal{F})$ is a signed digraph. If $\mathcal{F}$ is eventually positive, then $\mathcal{G}$ is structurally unbalanced.*

Lemma 2 (see [25]). *For $A \in \mathbb{R}^{n\times n}$, A has the strong Perron–Frobenius property $\Longleftrightarrow$ A is eventually positive.*

2. Problem Formulation

Consider an MAS with N agents with each agent being described by

$$\begin{aligned} \dot{x}_i &= Ax_i + Bu_i, \\ y_i &= Cx_i, \quad \forall i = 1, \ldots, N, \end{aligned} \tag{1}$$

where $x_i \in \mathbb{R}^n$, $u_i \in \mathbb{R}^m$, and $y_i \in \mathbb{R}^q$ are the state, input, and output, respectively. It is assumed that (A, B, C) is controllable and observable.

The communication topology among agents is represented by a signed digraph $\mathcal{G} = (\mathcal{V}, \varepsilon, \mathcal{F})$, where $\mathcal{V} = \{1, \ldots, N\}$ and $\mathcal{F} = (f_{ij})_{N\times N}$. This paper is to synthesize a state observer-type control for each agent such that agents in (1) reach sign-consensus. Firstly, we give the definition of sign-consensus for the system in (1).

Definition 1 (see [24]). The system in (1) is said to achieve sign-consensus if there exists a consensus protocol $\{u_i, i = 1, \ldots, N\}$ such that for any given initial states $x_i(0)\,(i = 1, \ldots, N)$,

$$\lim_{t\longrightarrow\infty}\left(\mathrm{sign}\left(x_i(t)\right) - \mathrm{sign}\left(x_j(t)\right)\right) = 0, \quad i, j \in \{1, \ldots, N\}. \tag{2}$$

From Definition 1, given any initial value, the states of agents in (1) converge to values with the same sign but different modulus.

Let $\overline{x}_i$ and $\overline{y}_i$ be the estimates of agent i's state and output, respectively. Denote $\widehat{y}_i = y_i - \overline{y}_i = Cx_i - C\overline{x}_i$ as agent i's output estimate error. In practice, it is usually hard to measure the agent's state. Hence, it would be more convenient to design consensus protocols based on the estimates of the agents' states. The useful information for agent i is synthesized by other agents' state estimates as

$$\overline{\delta}_i = -\sigma_i\overline{x}_i + \sum_{j\in N_i} f_{ij}\overline{x}_j, \quad i = 1, \ldots, N, \tag{3}$$

where $\sigma_i > 0$ denotes the degradation rate of the system. A state observer-type consensus protocol is given as follows:

$$\begin{aligned} u_i &= aH\overline{\delta}_i = aH\left(-\sigma_i\overline{x}_i + \sum_{j\in N_i} f_{ij}\overline{x}_j\right), \\ \dot{\overline{x}}_i &= A\overline{x}_i + Bu_i - aG\widehat{y}_i, \quad i = 1, \ldots, N, \end{aligned} \tag{4}$$

where

(i) $a \in \mathbb{R}$ satisfies $a \geq 1/(2\min_{i\in\Delta}\mathrm{Re}(\lambda_i(D_{\mathcal{F}})))$ with $\Delta = \{i \mid \mathrm{Re}(\lambda_i(D_{\mathcal{F}})) > 0, i = 1, \ldots, N\}$;

(ii) H is designed as $H = R^{-1}B^TP$, where P is the positive definite solution of the algebraic Riccati equation

$$A^TP + PA + Q - PBR^{-1}B^TP = 0, \tag{5}$$

where Q and R are positive definite matrices;

(iii) Since (A, C) is observable, G can be chosen such that $A + aGC$ is Hurwitz.

Next, we will demonstrate that the system in (1) achieves sign-consensus under the protocol in (4).

3. Main Results

Theorem 1. *Suppose that $\mathcal{F}$ has the strong Perron–Frobenius property. Then, the system in (1) can reach sign-consensus under the protocol in (4) with $\sigma_i = \rho(\mathcal{F})$ $(\forall i = 1, \ldots, N)$. Moreover, the state estimate error will converge to 0, i.e., $\lim_{t\longrightarrow\infty}(x_i - \overline{x}_i) = 0$ and $\forall i = 1, \ldots, N$.*

Proof. Define $X = [x_1^T, \ldots, x_N^T]^T$ and $\overline{X} = [\overline{x}_1^T, \ldots, \overline{x}_N^T]^T$. Applying the protocol in (4) to the system in (1), we obtain

$$\dot{X} = (I_N \otimes A)X - (aD_{\mathcal{F}} \otimes BH)\overline{X}. \tag{6}$$

By direct calculation, we obtain

$$\dot{\overline{X}} = (I_N \otimes A - aD_{\mathcal{F}} \otimes BH)\overline{X} - (aI_N \otimes GC)\widehat{X}, \tag{7}$$

where $\widehat{X} = X - \overline{X}$. Clearly,

$$\dot{\widehat{X}} = [I_N \otimes (A + aGC)]\widehat{X}. \tag{8}$$

Since G is chosen such that $A + aGC$ is Hurwitz, $I_N \otimes (A + aGC)$ is Hurwitz. Immediately, one has

$$\begin{aligned} &\lim_{t\longrightarrow\infty} \widehat{X} = 0, \\ &\text{i.e., } \lim_{t\longrightarrow\infty} (x_i - \overline{x}_i) = 0, \quad i = 1, \ldots, N. \end{aligned} \tag{9}$$

By assumption, $\mathcal{F}$ has the strong Perron–Frobenius property. This implies that $\rho(\mathcal{F})$ is a simple positive eigenvalue of $\mathcal{F}$, and its corresponding right eigenvector $v_r > 0$. Noting that $D_{\mathcal{F}} = \rho(\mathcal{F})I_N - \mathcal{F}$. Hence, $\lambda_i(D_{\mathcal{F}}) = \rho(\mathcal{F}) - \lambda_i(\mathcal{F})$, $i = 1, \ldots, N$. Clearly, 0 is a simple eigenvalue of $D_{\mathcal{F}}$ with corresponding right eigenvector v_r. For simplicity, we assume $\lambda_1(D_{\mathcal{F}}) = 0$. Then, $\mathrm{Re}(\lambda_i(D_{\mathcal{F}})) > 0$, $i = 2, \ldots, N$. There must exist a nonsingular matrix $\mathcal{S} = [v_r | S_2] \in \mathbb{R}^{N\times N}$ with $S_2 \in \mathbb{R}^{N\times(N-1)}$ such that

$$\mathcal{S}^{-1} D_{\mathcal{F}} \mathcal{S} = J = \begin{bmatrix} 0 & 0 \\ 0 & J_{N-1} \end{bmatrix}, \tag{10}$$

where $J_{N-1} \in \mathbb{R}^{(N-1)\times(N-1)}$ is a Jordan block with $\lambda_i(D_{\mathcal{F}})(i = 2, \ldots, N)$ on its diagonal. Let $W(t) = (\mathcal{S}^{-1} \otimes I_n) X \triangleq [W_1^T(t), \ldots, W_N^T(t)]^T = [W_1^T(t) \mid \Omega^T(t)]^T$ and $\widehat{W}(t) = (\mathcal{S}^{-1} \otimes I_n)\widehat{X} \triangleq [\widehat{W}_1^T(t)[\widehat{\Omega}^T](t)]^T$. Then, by (6)–(8), we have

$$\dot{W}(t) = (I_N \otimes A - aJ \otimes BH)W(t) + (aJ \otimes BH)\widehat{W}(t), \tag{11}$$

or equivalently,

$$\begin{aligned} \dot{W}_1(t) &= AW_1(t), \\ \dot{\Omega}(t) &= (I_{N-1} \otimes A - aJ_{N-1} \otimes BH)\Omega(t) + (aJ_{N-1} \otimes BH)\widehat{\Omega}(t). \end{aligned} \tag{12}$$

Obviously, $I_{N-1} \otimes A - aJ_{N-1} \otimes BH$ is an upper triangle block matrix with diagonal blocks $A - a\lambda_i(D_{\mathcal{F}})BH$, $i = 2, \ldots, N$. Notice that $a \geq 1/(2\min_{i\in\Delta}\mathrm{Re}(\lambda_i(D_{\mathcal{F}})))$ and $H = R^{-1}B^TP$, where P is positive definite solution of (5). Then, by adopting the similar arguments as in [26], we obtain that $A - a\lambda_i(D_{\mathcal{F}})BH\,(i = 2, \ldots, N)$ is Hurwitz. By (9), we know that $\lim_{t\longrightarrow\infty}\widehat{W}(t) = \lim_{t\longrightarrow\infty}(\mathcal{S}^{-1} \otimes I_n)\widehat{X} = 0$, and hence, $\lim_{t\longrightarrow\infty}\widehat{\Omega}(t) = 0$. According to (12) and the ordinary differential equation theory, we obtain

$$\begin{aligned} &\lim_{t\longrightarrow\infty} W_1(t) = \lim_{t\longrightarrow\infty} e^{At} W_1(0), \\ &\lim_{t\longrightarrow\infty} \Omega(t) = 0. \end{aligned} \tag{13}$$

Since $X = (\mathcal{S} \otimes I_n)W(t) = (v_r \otimes I_n)W_1(t) + (S_2 \otimes I_n)\Omega(t)$,

$$\lim_{t\longrightarrow\infty} X(t) = (v_r \otimes I_n) \lim_{t\longrightarrow\infty} e^{At} W_1(0), \tag{14}$$

or equivalently,

$$\lim_{t\longrightarrow\infty} x_i(t) = v_{r_i} \lim_{t\longrightarrow\infty} e^{At} W_1(0), \tag{15}$$

where v_{r_i} is the ith component of v_r. Note that $v_{r_i} > 0$, $\forall i = 1, \ldots, N$. Thus, by Definition 1, the system in (1) can achieve sign-consensus under the protocol in (4). □

Remark 1. In Theorem 1, sign-consensus is achieved based on a state observer-type protocol. This is different from protocols in [23, 24] where state feedback protocols are proposed. Communication topology $\mathcal{G} = (\mathcal{V}, \varepsilon, \mathcal{F})$ is directed, and it is assumed that $\mathcal{F}$ has the strong Perron–Frobenius property. Such an assumption together with Lemma 1 implies that $\mathcal{G}$ is structurally unbalanced.

Theorem 2. *For the system in (1), suppose that $\mathcal{F}$ is eventually positive. Then, the system in (1) can achieve sign-consensus under the protocol in (4) with $\sigma_i = \rho(\mathcal{F})$ $(\forall i = 1, \ldots, N)$.*

Proof. By assumption, $\mathcal{F}$ is eventually positive. This together with Lemma 2 gives that $\mathcal{F}$ has the strong Perron–Frobenius property. Applying the same procedure as in Theorem 1, one sees that the system in (1) can achieve sign-consensus under the protocol in (4).

From (14), we know that v_r is vital to the collective behavior of MASs. In particular, if $v_r = 1_n$, then conventional consensus is achieved. □

Corollary 1. *For the system in (1), suppose that $\mathcal{F}$ has the strong Perron–Frobenius property. Then, the system in (1) can achieve conventional consensus under the protocol in (4) with $v_r = 1_n$ and $\sigma_i = \rho(\mathcal{F})$ $(\forall i = 1, \ldots, N)$.*

Remark 2. In Corollary 1, if the requirement on $\mathcal{F}$ is changed to being eventually positive, Corollary 1 still holds.

4. Simulation

Example 1. Consider the system in (1) with 6 agents, where

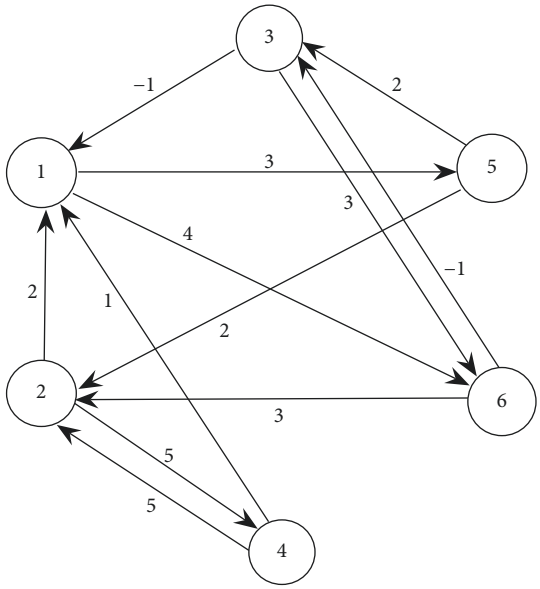

Figure 1: Communication topology among 6 agents.

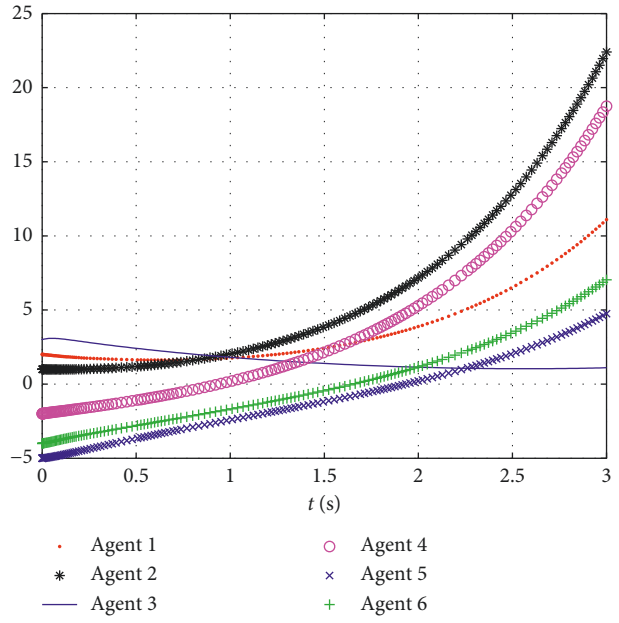

Figure 2: State trajectories of x_{i1} for 6 agents.

$$A = \begin{bmatrix} 1 & 1 \\ 0 & 0 \end{bmatrix},$$
$$B = \begin{bmatrix} 0 \\ 1 \end{bmatrix}, \tag{16}$$
$$C = \begin{bmatrix} 2 & 1 \\ 0 & 1 \end{bmatrix}.$$

Obviously, (A, B, C) is controllable and observable. Assume that interactions among the 6 agents are represented by $\mathcal{G} = (\mathcal{V}, \varepsilon, \mathcal{F})$, where $\mathcal{V} = \{1, \ldots, 6\}$ and $\mathcal{F} = (f_{ij}) \in \mathbb{R}^{6\times 6}$ with $f_{12} = f_{25} = f_{35} = 2$, $f_{13} = f_{36} = -1$, $f_{14} = 1$, $f_{24} = f_{42} = 5$, $f_{26} = f_{51} = f_{63} = 3$, and $f_{61} = 4$. From Figure 1, $\mathcal{G}$ is structurally unbalanced. By direct calculation, one has $\mathcal{F}^l > 0$, $\forall l \geq 7$. This implies that $\mathcal{F}$ is eventually positive. Therefore, by Lemma 2, one sees that $\mathcal{F}$ has strong Perron–Frobenius property, and hence, communication conditions in Theorem 1 and Theorem 2 are satisfied.

Note that $\lambda_1(D_{\mathcal{F}}) = 0$, $\lambda_2(D_{\mathcal{F}}) = 10.4347$, $\lambda_3(D_{\mathcal{F}}) = 6.7544 - 1.4418j$ ($j^2 = -1$), $\lambda_4(D_{\mathcal{F}}) = 6.7544 + 1.4418j$, $\lambda_5(D_{\mathcal{F}}) = 5.5158 - 2.1144j$, and $\lambda_6(D_{\mathcal{F}}) = 5.5158 + 2.1144j$. Therefore, $a \geq 1/(2\min_{2\leq i\leq 6}\mathrm{Re}(\lambda_i(D_{\mathcal{F}}))) = 0.0906$, and hence, we assume $a = 1$. Let $G = \begin{bmatrix} -1 & 0 \\ 0 & -1 \end{bmatrix}$. By calculation, one obtains that $A + aGC$ is Hurwitz. Choose $Q = CC^T$ and

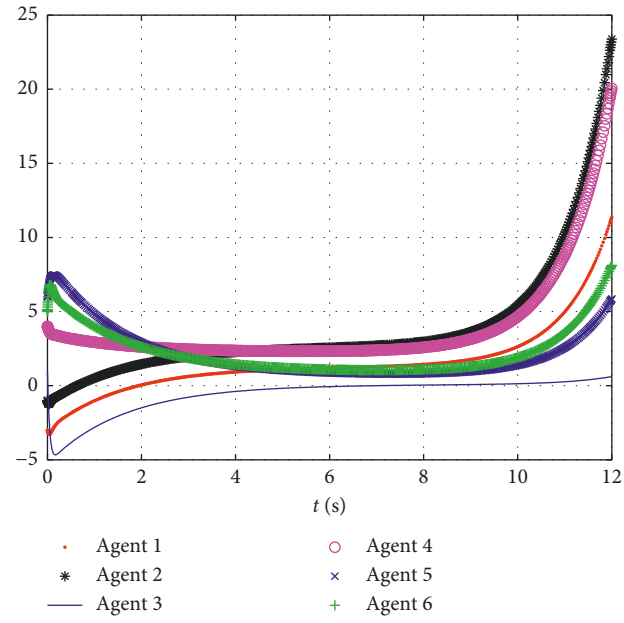

Figure 3: State trajectories of x_{i2} for 6 agents.

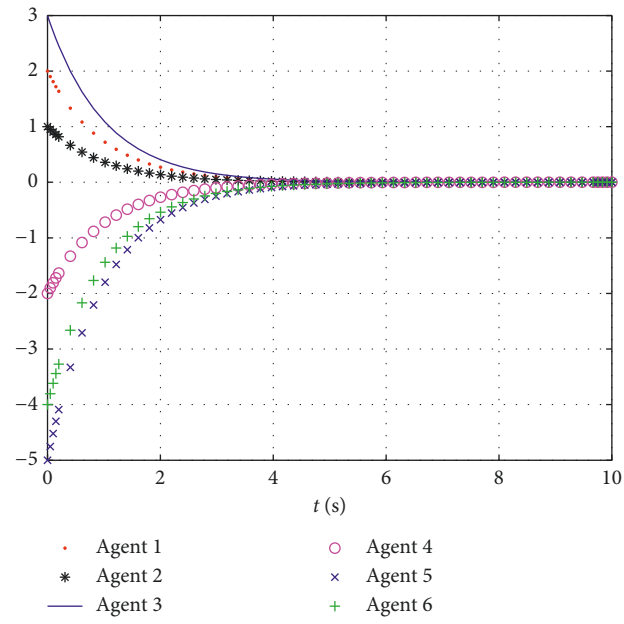

Figure 4: State estimate error trajectories of x_{i1}.

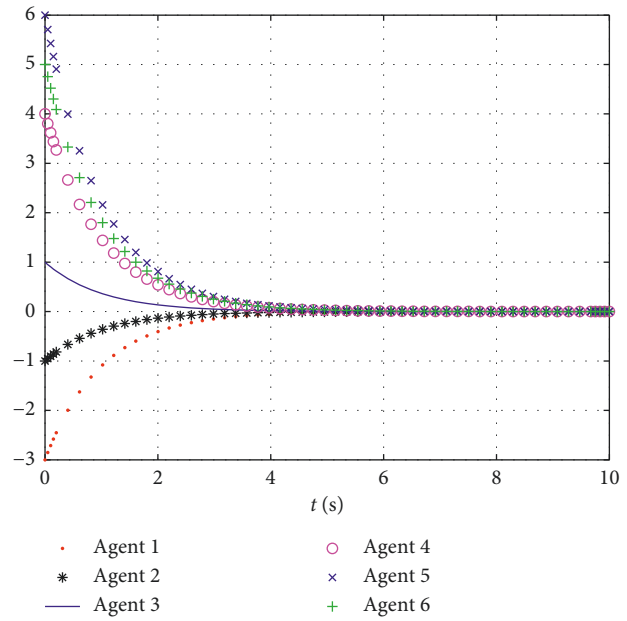

FIGURE 5: State estimate error trajectories of x_{i2}.

$R = 1$. Then, one can get $P = \begin{bmatrix} 12.3485 & 5.4495 \\ 5.4495 & 3.4495 \end{bmatrix}$ which is the positive definite solution of (5), and $H = R^{-1}B^T P = [5.4495\ 3.4495] \in \mathbb{R}^{1\times 2}$. Applying the protocol in (4) to the system in (1), we obtain that sign-consensus is achieved. The simulation results are given in Figures 2 and 3, where x_{i1} and x_{i2} are the first and second components of agent i, respectively. Moreover, from Figures 4 and 5, we see that state estimate error converges to zero. Thus, the simulation example verifies the validity of Theorem 1 and Theorem 2.

5. Conclusions

The sign-consensus of MASs is investigated where each agent is described by an LTI system. A state observer-type protocol is designed, which is more practical than the usual state feedback protocols. It is shown that if the adjacency matrix has strong Perron–Frobenius property or is eventually positive, then sign-consensus can be achieved based on the proposed protocols.

Data Availability

The MATLAB code used in the example can be obtained from the corresponding author.

Conflicts of Interest

The authors declare that they have no conflicts of interest.

Acknowledgments

This work was supported by the National Natural Science Foundation of China (grant no. 61973183), Natural Science Foundation of Shandong Province (grant no. ZR2019MF041), and the Youth Creative Team Sci-Tech Program of Shandong Universities (grant no. 2019KJI007).

References

[1] R. Olfati-Saber and R. M. Murray, "Consensus problems in networks of agents with switching topology and time-delays," *IEEE Transactions on Automatic Control*, vol. 49, no. 9, pp. 1520–1533, 2004.

[2] W. Ren and R. W. Beard, "Consensus seeking in multiagent systems under dynamically changing interaction topologies," *IEEE Transactions on Automatic Control*, vol. 50, no. 5, pp. 655–661, 2005.

[3] C. Q. Ma, T. Li, and J. F. Zhang, "Necessary and sufficient conditions for consensusability of linear multi-agent systems," *IEEE Transactions on Automatic Control*, vol. 55, no. 5, pp. 1263–1268, 2010.

[4] Z. K. Li, Z. S. Duan, G. R. Chen, and L. Huang, "Consensus of multiagent systems and synchronization of complex networks: a unified viewpoint," *IEEE Transactions on Circuits and Systems*, vol. 57, no. 1, pp. 213–224, 2010.

[5] C. Q. Ma, T. Li, and J. F. Zhang, "Consensus control for leader-following multi-agent systems with measurement noises," *Journal of Systems Science and Complexity*, vol. 23, no. 1, pp. 35–49, 2010.

[6] B. C. Wang and J. F. Zhang, "Distributed control of multi-agent systems with random parameters and a major agent," *Automatica*, vol. 48, no. 9, pp. 2093–2106, 2012.

[7] Y. Sun, Z. Wu, and F. Meng, "Common weak linear copositive Lyapunov functions for positive switched linear systems," *Complexity*, vol. 2018, Article ID 1365960, 7 pages, 2018.

[8] C. Wei, M. Benosman, and T. Kim, "Online parameter identification for state of power prediction of Lithium-ion batteries in electric vehicles using extremum seeking," *International Journal of Control, Automation and Systems*, vol. 17, pp. 1–11, 2019.

[9] M. Xing, H. Shen, and Z. Wang, "H_∞ synchronization of semi-markovian jump neural networks with randomly occurring time-varying delays," *Complexity*, vol. 2018, Article ID 8094292, 16 pages, 2018.

[10] C. Altafini, "Consensus problems on networks with antagonistic interactions," *IEEE Transactions on Automatic Control*, vol. 58, no. 4, pp. 935–946, 2013.

[11] J. P. Hu and W. X. Zheng, "Emergent collective behaviors on coopetition networks," *Physics Letters A*, vol. 378, no. 26-27, pp. 1787–1796, 2014.

[12] A. V. Proskurnikov, A. S. Matveev, and M. Cao, "Opinion dynamics in social networks with hostile camps: consensus vs. polarization," *IEEE Transactions on Automatic Control*, vol. 61, no. 6, pp. 1524–1536, 2016.

[13] H. Zhang and J. Chen, "Bipartite consensus of multi-agent systems over signed graphs: state feedback and output feedback control approaches," *International Journal of Robust and Nonlinear Control*, vol. 27, no. 1, pp. 3–14, 2017.

[14] C. Q. Ma and Z. Y. Qin, "Bipartite consensus on networks of agents with antagonistic interactions and measurement noises," *IET Control Theory and Applications*, vol. 10, no. 17, pp. 2306–2313, 2016.

[15] C. Q. Ma, Z. Y. Qin, and Y. B. Zhao, "Bipartite consensus of integrator multi-agent systems with measurement noise," *IET Control Theory and Applications*, vol. 11, no. 18, pp. 3313–3320, 2017.

[16] C. Q. Ma, W. W. Zhao, and Y. B. Zhao, "Bipartite linear χ-consensus of double-integrator multi-agent systems with

measurement noise," *Asian Journal of Control*, vol. 20, no. 1, pp. 577–584, 2018.

[17] C. Q. Ma, W. W. Zhao, and Y. B. Zhao, "Bipartite consensus of discrete-time double-integrator multi-agent systems with measurement noise," *Journal of Systems Science and Complexity*, vol. 31, no. 6, pp. 1525–1540, 2018.

[18] C. Q. Ma and L. H. Xie, "Necessary and sufficient conditions for leader-following bipartite consensus with measurement noise," *IEEE Transactions on Systems, Man, and Cybernetics: Systems*, pp. 1–6, 2018.

[19] D. Meng, M. Du, and Y. Jia, "Interval bipartite consensus of networked agents associated with signed digraphs," *IEEE Transactions on Automatic Control*, vol. 61, no. 12, pp. 3755–3770, 2016.

[20] J. P. Hu and W. X. Zheng, "Bipartite consensus for multi-agent systems on directed signed networks," in *Proceedings of the 52nd IEEE Conference on Decision and Control (CDC)*, pp. 3451–3456, Florence, Italy, December 2013.

[21] C. Altafini and G. Lini, "Predictable dynamics of opinion forming for networks with antagonistic interactions," *IEEE Transactions on Automatic Control*, vol. 60, no. 2, pp. 342–357, 2015.

[22] W. Xia, M. Cao, and K. H. Johansson, "Structural balance and opinion separation in trust-mistrust social networks," *IEEE Transactions on Control of Network Systems*, vol. 3, no. 1, pp. 46–56, 2016.

[23] Y. Jiang, H. Zhang, and J. Chen, "Sign-consensus of linear multi-agent systems over signed directed graphs," *IEEE Transactions on Industrial Electronics*, vol. 64, no. 6, pp. 5075–5083, 2017.

[24] Y. Jiang, H. Zhang, and J. Chen, "Sign-consensus over cooperative-antagonistic networks with switching topologies," *International Journal of Robust and Nonlinear Control*, vol. 28, no. 18, pp. 6146–6162, 2018.

[25] D. Noutsos, "On Perron-Frobenius property of matrices having some negative entries," *Linear Algebra and Its Applications*, vol. 412, no. 2-3, pp. 132–153, 2006.

[26] H. W. Zhang, F. L. Lewis, and A. Das, "Optimal design for synchronization of cooperative systems: state feedback, observer and output feedback," *IEEE Transactions on Automatic Control*, vol. 56, no. 8, pp. 1948–1952, 2011.

Hindawi
Complexity
Volume 2019, Article ID 7968914, 13 pages
https://doi.org/10.1155/2019/7968914

Research Article

Harmonic Modeling and Experimental Validation of the Converters of DFIG-Based Wind Generation System

Yang-Wu Shen,[1] **Ding Wang**,[1] **Xiang-Tian Deng**,[2] **Qing Li**,[3] **and Jian Zuo**[1]

[1]*State Grid Hunan Electric Power Corporation Limited Research Institute, Changsha, China*
[2]*School of Automation, Wuhan University of Technology, Wuhan, China*
[3]*China Electric Power Research Institute, Beijing, China*

Correspondence should be addressed to Xiang-Tian Deng; dengxt@whut.edu.cn

Received 2 July 2019; Revised 29 August 2019; Accepted 14 September 2019; Published 3 November 2019

Guest Editor: Taesic Kim

The double-fed induction wind generator- (DFIG-) based wind generation system contains power electronic converters and filter capacitor and inductor, which will bring about high-frequency harmonics under the influence of controllers. Aiming at this problem, this paper studies the relation between the output current and the harmonic source at grid-side and rotor-side converters based on their control features in the DFIG system. Furthermore, the harmonic equivalent models of these two converters are built, and the influence of different factors on harmonic features is explored from four perspectives, i.e., modulation method, altering controller parameters, altering output power, and the unbalance of three-phase voltage. Finally, the effectiveness of the proposed model is verified through the 2 MW DFIG real-time hardware-in-the-loop test platform by StarSim software and real test data, respectively.

1. Introduction

New energy power generation technologies have become hot spots as the energy and environmental issues obtained prominent attention. Wind energy has been widely applied in power systems because of its clean, harmless, and abundant nature in natural resources. The double-fed wind power generation system has become the mainstream in wind power generation systems because of its small capacity in the field converter, low cost, and variable-speed constant-frequency operation features [1–6]. However, the double-fed wind power generation system contains a power electronic converter, in which the interactions among converters and passive components of the filter can lead to harmonic resonances, thus causing serious harmonic pollution and reducing the power quality [7–10].

With regard to the harmonic problem in the double-fed wind power generation system, relevant researches and analyses have been carried out [11–14]. In the literature [11], the source of stator harmonic current of the double-fed wind turbine is analyzed. It is pointed out that the harmonic modulation of the converter, the cogging harmonic of the motor itself, and the grid background harmonic affect the stator output harmonics of the double-fed wind turbine. In [12], the harmonic characteristics of the double-fed wind turbine converter are analyzed, and the effect of the converter harmonic on the system overall output harmonic is analyzed by establishing the equivalent circuit of the asynchronous motor. Based on the mathematically electromagnetic relationship of the asynchronous motor, literature [13] proposes a harmonic equivalent circuit of the double-fed asynchronous motor and studies the influence of harmonics generated by the wind turbine on the power grid. According to the characteristics of the asynchronous motor, literature [14] analyzes the interaction between the grid-side converter harmonic and the rotor-side converter harmonic in the double-fed wind power generation system.

From the above literature studies, the grid-side or rotor-side converters in the double-fed wind power generation system are viewed as a simple harmonic voltage source when modeling and analyzing the converter output harmonic characteristics, while the influence of converter control

factors on system harmonic output characteristics is not considered.

Literature studies [15, 16] point out that the harmonics generated by PWM (pulse-width modulation) are mainly distributed near the double switching frequency. Reference [17] studies the harmonic resonance characteristics of the photovoltaic power generation system by establishing the Norton equivalent model of the photovoltaic converter. Considering the control characteristics of different types of converters [18], Wang et al. establish the converter equivalent model of voltage source control and current source control, respectively.

However, there is little literature on the harmonic characteristics of the double-fed wind power generation system at present. The main contributions of this paper can be summarized as follows:

(1) Based on the existing harmonic model, the influence of component parameters and control parameters on the harmonic output of the RSC and GSC is studied, and the harmonic output characteristics of the RSC and GSC are summarized. Furthermore, a novel method for suppressing the output harmonic amplitude of the DFIG by adjusting PI control parameters is proposed, and the effectiveness of the proposed method has been verified by the simulation case.

(2) The harmonic model of the typical DFIG is established, and the parameters of the harmonic model of the DFIG are corrected by the measured data. With the correction of harmonic model parameters, the harmonic characteristics of the corrected harmonic model of the DFIG are consistent with the harmonic characteristics of the actual DFIG.

The rest of this paper is organized as follows: Section 2 presents the harmonic source analysis of the double-fed wind power generation system. Section 3 presents the characteristics analyses of the converter harmonic model. Case studies are presented in Section 4 to validate the proposed harmonic model of the DFIG. Conclusion is presented in Section 5.

2. Harmonic Source Analysis of Double-Fed Wind Power Generation System

The structure of the double-fed wind power generation system is shown in Figure 1. Two back-to-back PW-modulated converters are used for AC excitation through a DC link. Effective control of converters enables variable-speed constant-frequency operation and maximum wind energy tracking within a certain range [10, 19, 20].

The harmonic sources of the double-fed wind power generation system mainly include the harmonics caused by the asynchronous motor itself and the harmonics caused by the converter modulation [14]. In addition, the output harmonic of the double-fed wind power system may exceed the standard when there are background harmonics in the grid and irrational converter control parameters. The cogging harmonics caused by the asynchronous motor itself due to the uneven air gap can be suppressed or eliminated by rational motor structure designing. Thus, this paper mainly considers the PW modulation harmonics of the converter and the background harmonics of the power grid. The harmonic output characteristics of the double-fed wind power generation system are studied by establishing the harmonic equivalent model.

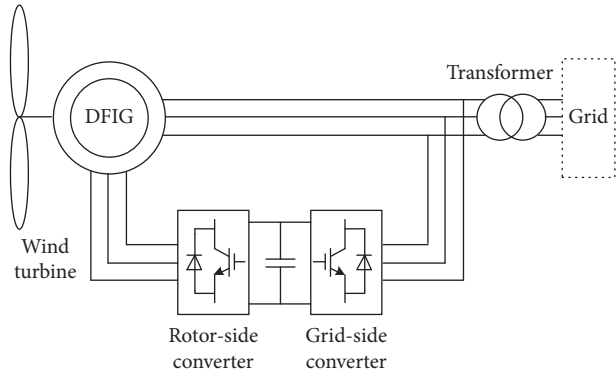

Figure 1: Double-fed wind power generation system.

3. Harmonic Modeling of Double-Fed Wind Power Converter

Because of the fact that the dynamics of DC-side voltage is slower than the harmonic dynamics, the voltage across the capacitor between the grid-side converter and the rotor-side converter of the double-fed wind power system remains constant. Therefore, the two converters can be discussed separately in harmonic modeling. In this section, the harmonic equivalent models of the grid-side and rotor-side converters are established to study their harmonic output characteristics and influencing factors. Note that there are subsynchronous and low-frequency oscillations which lie below the fundamental frequency in wind power generation systems, and this paper mainly discusses the harmonics above the fundamental frequency [9].

The harmonic amplitude is proportional to the switching frequency, dead time, and DC-side voltage and inversely proportional to the harmonic order. The amplitude is negligible, so the voltage generated by the dead zone effect is mainly low, such as 3, 5, 7, and 9. For a converter with a high switching frequency, the dead time is long in one switching cycle, and the low-order harmonic generated by the dead zone is more obvious, while the large-capacity converter with a lower switching frequency is generated by the dead zone effect. In this paper, the switching delay of the converter is not taken into consideration for the harmonic model of converters.

3.1. Harmonic Modeling of Grid-Side Converter. For a three-phase balancing system, the system can be equivalent to a single-phase system. The command signal of the inner current loop in the grid-side converter is given by the outer voltage loop. Consider the response of the voltage loop is much slower than the response of the current loop. Thus, by ignoring the voltage loop, the control block diagram of the

grid-side converter is obtained and shown in Figure 2. The converter-side current feedback control which is more stable than the grid-side current feedback current control is adopted, as shown in Figure 2 [21].

In Figure 2, K_{pwm} is the linear gain of the pulse-width modulation (PWM) converter bridge, $i_{1\text{ref}}$ is the reference of the current loop, u_{gh} is the harmonic voltage generated by PWM, G_{ig} is the transfer function of the current regulator which adopts the proportional resonance controller, and u_{PCC} is the voltage at the grid-connected point. The harmonic model shown in Figure 2 considers two kinds of harmonic sources: (1) the harmonic voltage u_{gh} generated by the PWM and (2) the grid background harmonic voltage u_{PCC} at the grid-connected point.

In the steady-state operation, the current reference $i_{1\text{ref}}$ remains constant [22]. Thus, according to the Mason formula, the complex frequency-domain expression among i_2, u_{gh}, and u_{PCC} can be obtained as follows.

$$i_2 = N_g(s)u_{gh} - Y_{\text{eqg}}(s)u_{\text{PCC}}, \tag{1}$$

where s is the complex frequency-domain variable and $N_g(s)$ and $Y_{\text{eqg}}(s)$ are expressed as

$$\begin{cases} N_g(s) = \dfrac{Z_C}{Z_1Z_2 + Z_1Z_C + Z_2Z_C + G_{ig}K_{\text{pwm}}(Z_2 + Z_C)}, \\ Y_{\text{eqg}}(s) = \dfrac{Z_1 + Z_C + G_{ig}K_{\text{pwm}}}{Z_1Z_2 + Z_1Z_C + Z_2Z_C + G_{ig}K_{\text{pwm}}(Z_2 + Z_C)}, \end{cases} \tag{2}$$

where K_{pwm} is usually taken as 1; $Z_1 = sL_1 + R_1$, $Z_2 = sL_2 + R_2$, and $Z_C = 1/sC$, in which L_1, R_1, L_2, and R_2 are the LCL filter inductance and equivalent resistance and C is the filter capacitor; and G_{ig} is expressed as

$$G_{ig} = k_{pg} + \frac{sk_{ig}}{s^2 + \omega_g^2}, \tag{3}$$

where k_{pg} and k_{ig} are the proportional and integral coefficients of the current controller and ω_g is the fundamental frequency.

According to Figure 1 and (1), the Norton equivalent circuit of the grid-side converter can be obtained, which is shown in Figure 3. In Figure 3, $N_g(s)u_{gh}$ is the PW-modulated harmonic and u_{PCC} is the grid background harmonic.

3.2. Harmonic Modeling of Rotor-Side Converter. The rotor-side converter adopts the motor stator flux-oriented feedforward decoupling control. The outer control loop is the speed control or active power control, and the output of the outer loop controller is the reference of the inner current loop. Similarly, the response of the inner loop is much faster than that of the outer loop. Therefore, the outer control loop is neglected, and the balanced three-phase system is equivalent to a single-phase system. The current control block diagram of the rotor-side converter is shown in Figure 4.

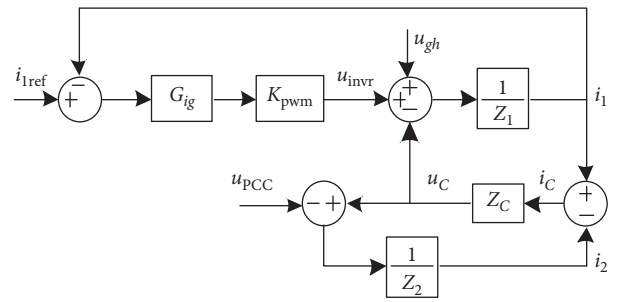

Figure 2: Current control block diagram of the grid-side converter.

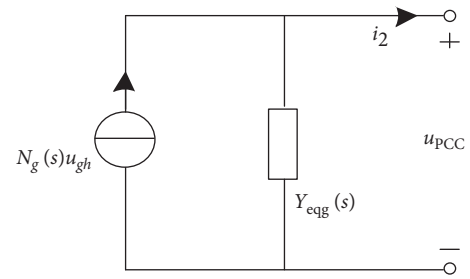

Figure 3: Norton equivalent circuit of the grid-side converter.

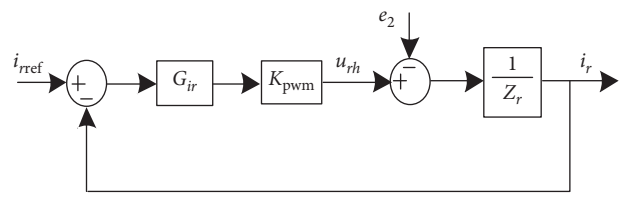

Figure 4: Current control block diagram of the rotor-side converter.

In Figure 4, $i_{r\text{ref}}$ is the current reference, u_{rh} is the harmonic voltage generated by PWM, and G_{ir} is the transfer function of the current controller and the proportional resonance controller is used; e_2 is the rotor-side phase electromotive force of the asynchronous machine. In Figure 4, the output current is

$$i_r = N_r(s')u_{rh} - Y_{\text{eqr}}(s')e_2, \tag{4}$$

where s' is the rotor-side complex frequency-domain variable. Note that $s' = s_{\text{slip}}$, where s_{slip} is the slip. The detailed expressions of s_{slip}, $N_r(s')$, and $Y_{\text{eqr}}(s')$ are shown as follows:

$$\begin{cases} s_{\text{slip}} = \dfrac{s - j\omega_m}{s}, \\ N_r(s') = \dfrac{1}{Z_r + G_{ir}K_{\text{pwm}}}, \\ Y_{\text{eqr}}(s') = \dfrac{1}{Z_r + G_{ir}K_{\text{pwm}}}, \end{cases} \tag{5}$$

where ω_m is the rotor speed of the asynchronous motor; $Z_r = s'L_r + R_r$, in which L_r and R_r are the rotor leakage inductance and resistance; and G_{ir} is expressed as

$$G_{ir} = k_{pr} + \frac{s' k_{ir}}{s'^2 + \left(\omega_g - \omega_m\right)^2}, \tag{6}$$

where k_{pr} and k_{ir} are the proportional and integral coefficients of the current controller, respectively.

According to Figure 4 and (4) and combining with the asynchronous motor equivalent circuit [11, 12], the Norton equivalent model of the rotor-side converter can be obtained, which is shown in Figure 5(a). Note that the rotor-side variables are converted to the stator side by the generator conversion. With the circuit conversion, Figure 5(a) can be equivalent to Figure 5(b). From Figure 5(b), we have

$$i_s = N_s(s) u_{rh} - Y_{\text{eqs}}(s) u_{\text{PCC}}, \tag{7}$$

where i_s is the stator-side output current of the asynchronous motor and $N_s(s)$ and $Y_{\text{eqs}}(s)$ are expressed as

$$\begin{cases} N_s(s) = \dfrac{Z_m N_r(s')}{Z_m + Z_s + s_{\text{slip}} Y_{\text{eqr}}(s') Z_m Z_s}, \\ Y_{\text{eqs}}(s) = \dfrac{1 + s_{\text{slip}} Y_{\text{eqr}}(s') Z_m}{Z_m + Z_s + s_{\text{slip}} Y_{\text{eqr}}(s') Z_m Z_s}, \end{cases} \tag{8}$$

where $Z_m = sL_m$ and $Z_s = sL_s + R_s$, in which L_m is the excitation inductance of the asynchronous motor and L_s and R_s are the stator leakage inductance and resistance.

4. Characteristics Analyses of Converter Harmonic Model

Based on the harmonic models of grid-side and rotor-side converters established in Section 3, the effects of component parameters and control parameters on harmonic characteristics are studied. The detailed parameters of the DFIG used in the simulation are shown in Table 1.

4.1. Characteristic Analysis of Harmonic Model of Grid-Side Converter. According to the Norton equivalent model shown in Figure 3 and (1) and (2), the Bode diagram of $N_g(s)$ and $Y_{\text{eqg}}(s)$ is shown in Figure 6. It can be seen from the figure that there are resonance peaks (magnitude greater than 0 dB) at a frequency of about 1450 Hz in $N_g(s)$ and $Y_{\text{eqg}}(s)$. It indicates that the converter output current will undergo harmonic amplification when the frequency of u_{gh} and u_{PCC} is close to the resonant frequency, thus affecting the power quality. Besides, it should be noted that the magnitude-frequency curves of $N_g(s)$ and $Y_{\text{eqg}}(s)$ are obviously declining when the frequency is higher than 2000 Hz, indicating that the converter has a strong suppression to high-frequency harmonics.

Ignoring the equivalent resistance of the filter inductor as it is usually small, and taking $K_{\text{pwm}} = 1$, the denominator of $N_g(s)$ and $Y_{\text{eqg}}(s)$ shown in (2) can be expanded to

$$\text{den}_g = \frac{1}{sC}\left[s^3 C L_1 L_2 + s\left(L_1 + L_2\right) + s^2 k_{pg} C L_2 + k_{pg} + \frac{s^2 k_{ig} C L_2}{s^2 + \omega_g^2} + \frac{s k_{ig}}{s^2 + \omega_g^2}\right]. \tag{9}$$

It can be seen from (9) that the cubic term and the primary term of s in the brackets form a pair of resonant poles whose resonant frequency is

$$\omega_{rg} = \pm\sqrt{\frac{L_1 + L_2}{C L_1 L_2}}. \tag{10}$$

The resonant frequency ω_{rg} calculated by (10) is coincident with the resonant frequency of the LCL filter. Therefore, it can be inferred that the resonant peak in Figure 6 is determined by the filter inductance. This means that choosing the right filter parameters can suppress as many harmonics as possible in the high frequency. Since the PWM harmonics are mainly concentrated near the double switching frequency [15, 16], the harmonic frequency is higher and can be suppressed. The range of grid background harmonic frequency is wide, and there are many lower harmonics such as the 5th, 7th, and 11th. Therefore, it is necessary to further study the harmonic output characteristics of the converter affected by the grid background harmonics.

In the vicinity of the resonant frequency ω_{rg}, an approximate expression is obtained as $s_2 \gg \omega g_2$ and the capacitance of the filter capacitor is small.

$$\text{den}_g \approx s^2 L_1 L_2 + \frac{L_1 + L_2}{C} + s k_{pg} L_2. \tag{11}$$

It is not difficult to see from (11) that the product of k_{pg} and L_2 provides damping for the resonance. The larger the product, the stronger the damping effect.

Since the current control parameter k_{pg} is relatively easier to change than L_2 in practice, only the influence of k_{pg} is studied in Figure 7.

It can be seen from Figure 7 that when the parameter of the current loop controller k_{pg} is relatively small, the magnitude-frequency curve of $Y_{\text{eqg}}(s)$ has a resonance peak. As k_{pg} increases, the resonance peak gradually decreases to disappear. In addition, Figure 7 also shows that the controller parameter k_{pi} has less effect on the magnitude-frequency curve of $Y_{\text{eqg}}(s)$ since the integral term of G_{ig} is almost zero at high frequencies.

In summary, the existence of LCL filter resonance may cause harmonic amplification in the output of the grid-side converter of the wind power generation system, and the resonance can be suppressed by adjusting the parameter of the current controller k_{pg}. It should be noted that k_{pg} also affects the dynamic response and stability of the converter control system, and this is beyond the scope of this paper. Therefore, the parameter k_{pg} should be increased as much as possible to suppress the harmonic output of the converter under the premise of meeting the dynamic performance and stability requirements of the system.

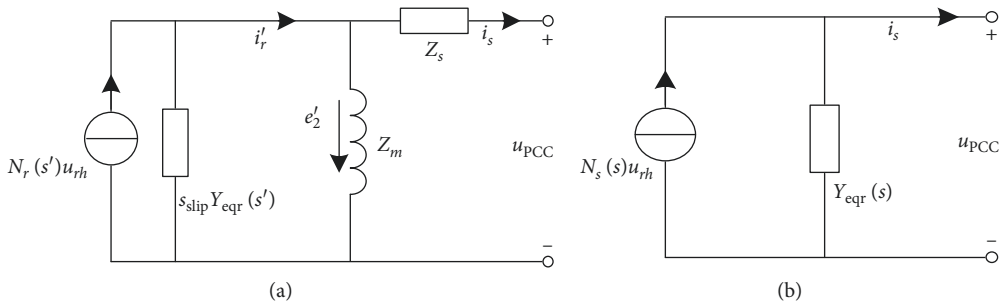

Figure 5: Norton equivalent circuit of the rotor-side converter: (a) detailed circuit of the rotor-side converter and asynchronous machine; (b) equivalent model.

Table 1: Detailed parameters of the DFIG simulation platform.

Parameters	Values
LCL filter (L_1)	2 mH
LCL filter (L_2)	1 mH
LCL filter (C)	18 μF
Asynchronous motor (L_r)	0.404 mH
Asynchronous motor (R_r)	0.0079 Ω
Asynchronous motor (L_s)	0.08 mH
Asynchronous motor (R_s)	0.0025 Ω
Asynchronous motor (L_m)	4.4 mH
s_{slip}	−0.2

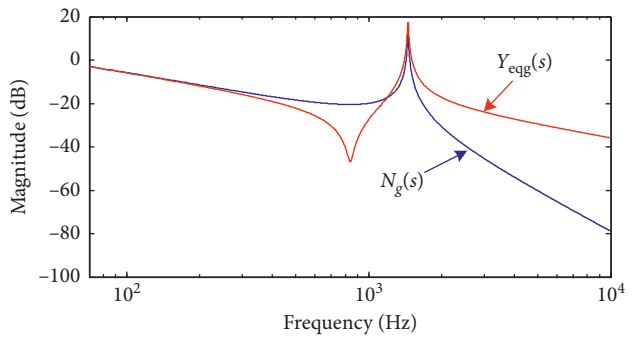

Figure 6: Magnitude-frequency curves of $N_g(s)$ and $Y_{eqg}(s)$.

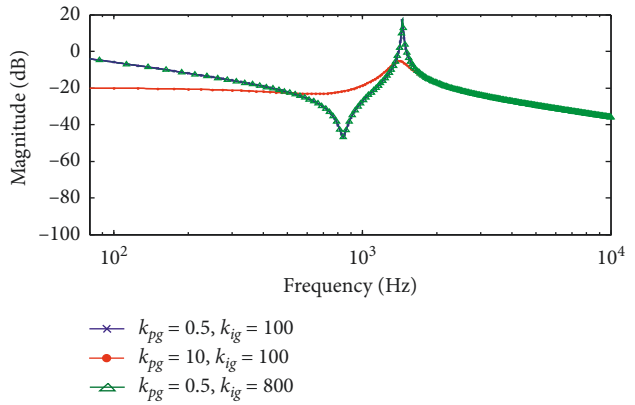

Figure 7: Magnitude-frequency curves of $Y_{eqg}(s)$ with different k_{pg}.

4.2. Characteristic Analysis of Harmonic Model of Rotor-Side Converter. According to (4)–(8) and Figure 5, the magnitude-frequency curves of $N_s(s)$ and $Y_{eqs}(s)$ are obtained and shown in Figure 8. It can be seen from the curves in Figure 8 that, at higher frequencies, the rotor-side converter has an effect of suppressing the higher-frequency PWM harmonics and the grid background harmonics. Since there is no capacitor in the rotor-side converter and asynchronous motor, the magnitude-frequency curves of $N_s(s)$ and $Y_{eqs}(s)$ do not show obvious resonance peaks. However, it should also be noted that, at lower frequencies (about 300 Hz in Figure 8), there are peak slopes (magnitude exceeds 0 dB). Thus, further characteristic study of $Y_{eqs}(s)$ is needed for the lower secondary grid background harmonics.

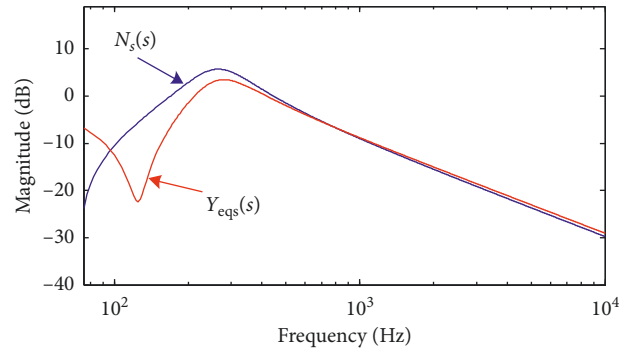

Figure 8: Magnitude-frequency curves of $N_s(s)$ and $Y_{eqs}(s)$.

As to the rotor-side converter, the denominator of $N_r(s')$ and $Y_{ekr}(s')$ in (5) can be expanded (R_r is ignored and $K_{pwm} = 1$ is considered for the same reason) to

$$\begin{aligned} \text{den}_r &= s'L_r + k_{pr} + \frac{s'k_{ir}}{s'^2 + (\omega_g - \omega_m)^2} \\ &= (s - j\omega_m)L_r + k_{pr} + \frac{(s - j\omega_m)k_{ir}}{(s - j\omega_m)^2 + (\omega_g - \omega_m)^2}. \end{aligned} \tag{12}$$

It can be seen from (12) that when the frequency is 3 times higher than the fundamental frequency of the rotor, that is, $s - j\omega_m > 3(\omega_g - \omega_m)$ (it is considered that the smaller term can be ignored when the difference between two terms is more than 10 times in engineering application), the denominator den_r can be approximated to

$$\text{den}_r \approx (s - j\omega_m)L_r + k_{pr} + \frac{k_{ir}}{s - j\omega_m}. \tag{13}$$

With (13), it can be found that the first and third terms form a pair of resonant poles whose resonant frequency is

$$\omega_{rr} = \omega_m \pm \sqrt{\frac{k_{ir}}{L_r}}. \tag{14}$$

Although there is no resonance in the rotor-side converter caused by the capacitor and inductor of the LCL filter, (14) shows that there will be resonance caused by the interaction between the controller integral term and the rotor leakage inductance. Besides, it can be seen from (8) that this resonance will be finally reflected to the stator side by $N_s(s)$ and $Y_{eqs}(s)$.

From (13) and (14), the resonant frequency is related to the rotor speed ω_m, the rotor leakage inductance L_r, and the controller parameter k_{ir}. The rotor leakage inductance L_r is related to the motor parameters and is fixed after the motor is manufactured. The rotor speed varies according to the actual wind speed, and the range of variation is limited. Only the controller parameter k_{ir} is easy to change. Similar to the grid-side converter, the controller parameter k_{pr} has an effect of damping.

Figure 9 shows the magnitude-frequency curves of $Y_{eqs}(s)$ with different k_{ir}, k_{pr}, and ω_m. It can be seen from Figure 9 that, on increasing k_{ir}, the peak slope of $Y_{eqs}(s)$ shifts to a lower frequency and the magnitude decreases. On the contrary, the magnitude-frequency curve of $Y_{eqs}(s)$ declines to a large extent as k_{pr} is increased. The slip s_{slip} changes from −0.2 (corresponding to $\omega_m = 1.2\,\omega_g$) to −0.1 (corresponding to $\omega_m = 1.1\,\omega_g$), and the peak slope of $Y_{eqs}(s)$ shifts to a lower frequency. Considering that the actual range of slip variation is small, the parameters k_{pr} and k_{ir} are the main factors affecting the harmonic output characteristics of the rotor-side converter.

4.3. Harmonic Model of Double-Fed Wind Power Generation System considering Grid Impedance. According to the equivalent harmonic models of grid-side and rotor-side converters shown in Figures 3 and 5, the overall equivalent harmonic model of the double-fed wind system is shown in Figure 10. In Figure 10, Z_g is the grid equivalent impedance and u_g is the grid voltage. According to Figure 10, the current i_g can be obtained as

$$i_g = N_{gg}(s)u_{gh} + N_{sg}(s)u_{rh} - Y_{gg}(s)u_g, \tag{15}$$

where $N_{gg}(s)$, $N_{sg}(s)$, and $Y_{gg}(s)$ are shown as follows:

$$\begin{cases} N_{gg}(s) = \dfrac{N_g(s)}{1 + Z_g\left(Y_{eqg}(s) + Y_{eqs}(s)\right)}, \\ N_{sg}(s) = \dfrac{N_s(s)}{1 + Z_g\left(Y_{eqg}(s) + Y_{eqs}(s)\right)}, \\ Y_{gg}(s) = \dfrac{Y_{eqg}(s) + Y_{eqs}(s)}{1 + Z_g\left(Y_{eqg}(s) + Y_{eqs}(s)\right)}. \end{cases} \tag{16}$$

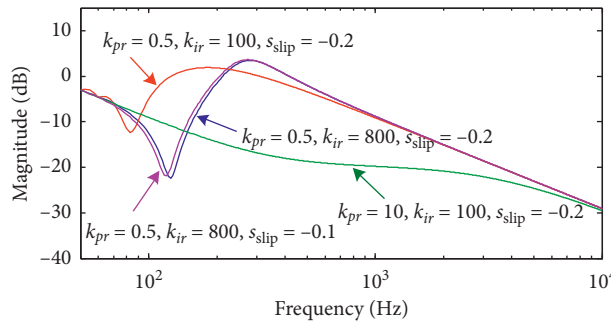

Figure 9: Magnitude-frequency curves of $Y_{eqs}(s)$.

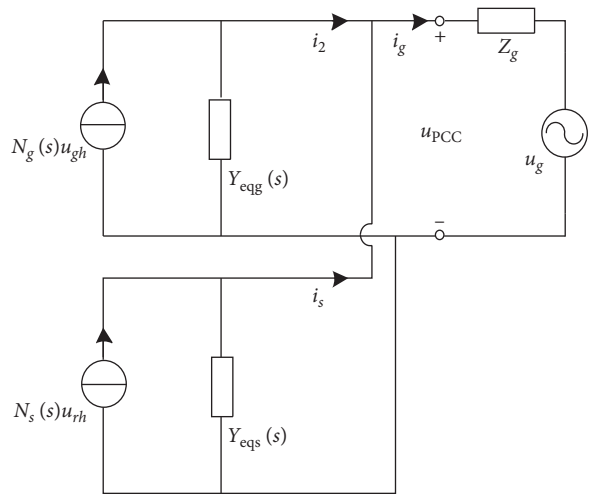

Figure 10: Norton equivalent circuit of the double-fed wind generator.

Considering the influence of grid background harmonics, the magnitude-frequency curve of $Y_{gg}(s)$ according to (15) and (16) is shown in Figure 11. It can be seen from Figure 11 that when there exists significant resonance in both $Y_{eqg}(s)$ and $Y_{eqg}(s)$, there appears similar resonant frequency in $Y_{gg}(s)$. The resonant peak of $Y_{gg}(s)$ is suppressed as the parameters k_{pg}, k_{pr}, and k_{ir} are appropriately increased, which shows similar features to $Y_{eqg}(s)$ and $Y_{eqg}(s)$ in Figures 7 and 9. Therefore, in the presence of the grid impedance, the grid background harmonics still can be suppressed by appropriately adjusting the controller parameters.

5. Case Study

5.1. Simulation Verification. In order to verify the above characteristics analyses, a real-time hardware-in-the-loop (HIL) system from ModelingTech is built, as shown in Figure 12. Each electromagnetic transient model of the DFIG and control algorithm is constructed by StarSim software and implemented on NI FPGA board 7868R (real-time simulator). The control algorithm is implemented on the PXIe-8821 controller (rapid control prototype (RCP)).

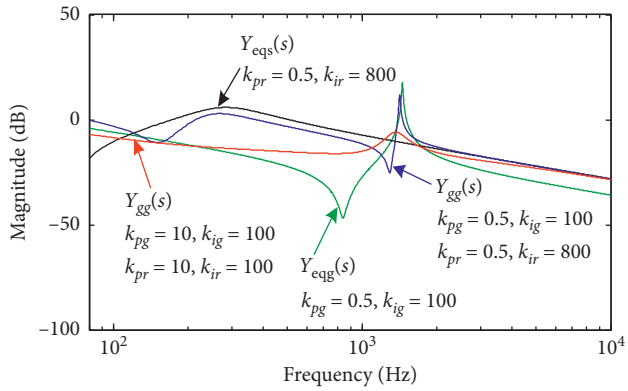

FIGURE 11: Magnitude-frequency curves of $Y_{eqs}(s)$, $Y_{eqg}(s)$, and $Y_{gg}(s)$.

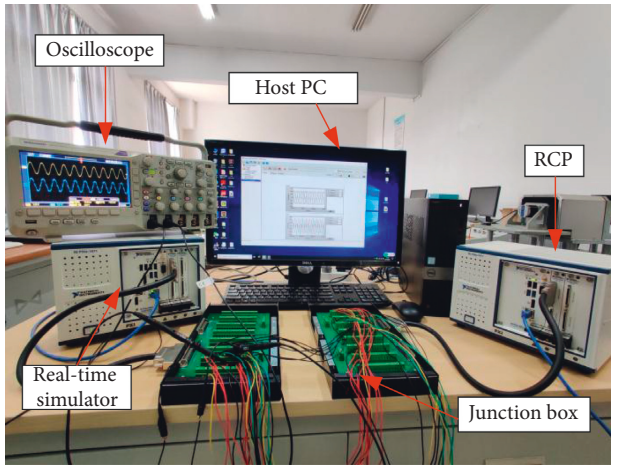

FIGURE 12: HIL simulation platform.

The LCL filter parameters of the grid-side converter are $L_1 = 2$ mH, $L_2 = 1$ mH, and $C = 18\,\mu$F. The asynchronous motor parameters are $L_r = 0.404$ mH, $R_r = 0.0079\,\Omega$, $Ls = 0.08$ mH, $R_s = 0.0025\,\Omega$, $L_m = 4.4$ mH, and $s_{slip} = -0.2$. The grid equivalent inductance is $L_1 = 0.1$ mH. The 5th, 7th, 11th, 13th, 17th, 19th, 23rd, 25th, 29th, 31st, 35th, and 37th harmonic sources with a magnitude of 0.02 pu are in series on the grid.

Figure 13 shows the grid-side converter output current i_{ga}, the asynchronous motor stator-side current i_{sa}, and the grid current i_a for different control parameter cases. Figure 13 shows the magnitude of harmonic current measured under different cases. The parameters in different cases are set as follows: (1) case 1: $k_{pg} = 0.5$, $k_{ig} = 100$, $k_{pr} = 0.5$, and $k_{ir} = 800$; (2) case 2: $k_{pg} = 10$, $k_{ig} = 100$, $k_{pr} = 0.5$, and $k_{ir} = 800$; (3) case 3: $k_{pg} = 0.5$, $k_{ig} = 100$, $k_{pr} = 10$, and $k_{ir} = 100$; and (4) case 4: $k_{pg} = 10$, $k_{ig} = 100$, $k_{pr} = 10$, and $k_{ir} = 100$.

Figures 13(a) and 14 show that there are both high-frequency harmonic amplification (about 29th resonance frequency amplification due to LCL filter resonance) and low-frequency harmonic amplification (about 5th and 7th harmonic amplification caused by improper control parameters of the rotor-side converter) due to the presence of harmonic voltages in the grid. Figures 13(b), 13(d), and 14 show that, by appropriately increasing k_{pg}, it is possible to suppress the high-frequency harmonic (nearby 29th harmonic current) caused by the resonance of the LCL filter.

Figures 13(c), 13(d), and 14 show that a proper increase in k_{pr} and a decrease in k_{ir} can suppress the low-frequency harmonic (near 5th and 7th harmonic current) caused by inappropriate rotor-side converter control parameters. The simulation results are consistent with the theoretical analyses.

5.2. Experiment Test. To further verify the theory, a test platform containing the actual wind power converter is built in the laboratory, as shown in Figure 15. In the test platform, the AC servo motor is used to emulate the wind turbine and an actual wind power converter is adopted. The rated voltages of the DFIG and the grid are 690 V and 380 V, respectively, which are connected by a transformer.

The rated power of the converter is 2.0 MW. LC filters are utilized for the grid-side converter, with the inductance of filtering being 0.43 mH. Three-phase capacitors are connected in a triangle shape, and the capacitance is 120 μF. LC filters and the grid-side line resistances together with the transformer equivalent impedance are combined into an LCL filter. L filters are used on the rotor side, with the inductance being 0.15 mH. The switch frequency of the converter on the grid side is 3000 Hz and that on the rotor side is 2000 Hz, and the modulation method is SVPWM. The DC-side voltage is 1050 V, and the AC-side grid frequency is 50 Hz. The detailed parameters of the test platform are shown in Table 2.

The acquisition device is installed at PCC to obtain samples of voltage and current signals synchronously, with the sampling rate being 6000 Hz. In this part, the accuracy of the proposed harmonic modeling of the DFIG is verified from four perspectives, i.e., modulation method, altering controller parameters, altering output power, and the unbalance of three-phase voltage.

5.2.1. Modulation Method. Figure 16 shows the waveforms of the voltage and current at PCC, as well as their harmonic spectrums. The switch frequency of the grid-side converter and rotor-side converter is 3000 Hz and 2000 Hz, respectively, and there are obvious harmonics with high frequency close to switch frequency. The high-frequency harmonic components of the voltage and current are distributed at 1920, 1980, 2020, and 2080 Hz for the grid-side converter and 2800 and 2900 Hz for the rotor-side converter.

5.2.2. Altering Control Parameters. In order to study the influence of different controller parameters on the current harmonic components at PCC, different PI controller's parameters of the inner current loop are set for the DFIG's grid-side converter. Specifically, at first, k_p is set to be 0.23 and 0.71, respectively, when k_i remains as 30. Secondly, k_p is set to be 21 and 45, respectively, when ki remains as 0.45. Figure 17 shows the output current harmonic spectrums of the DFIG converter under different PI control parameters.

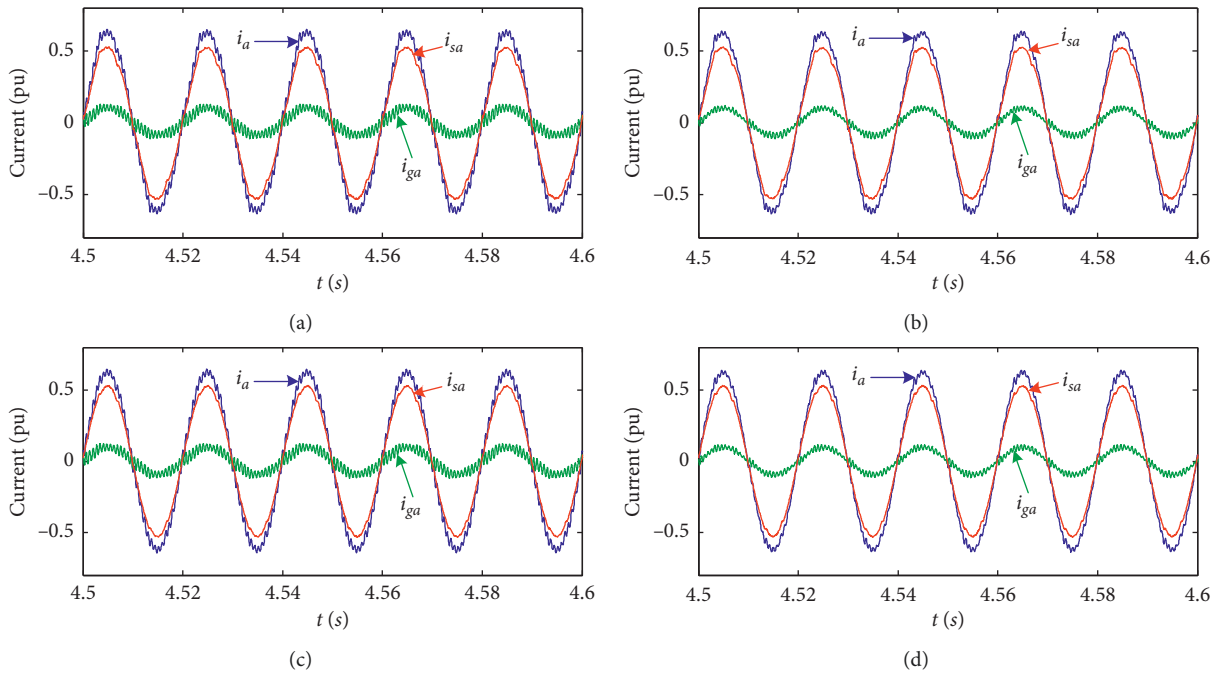

Figure 13: Currents i_{ga}, i_{sa}, and i_a: (a) case 1; (b) case 2; (c) case 3; (d) case 4.

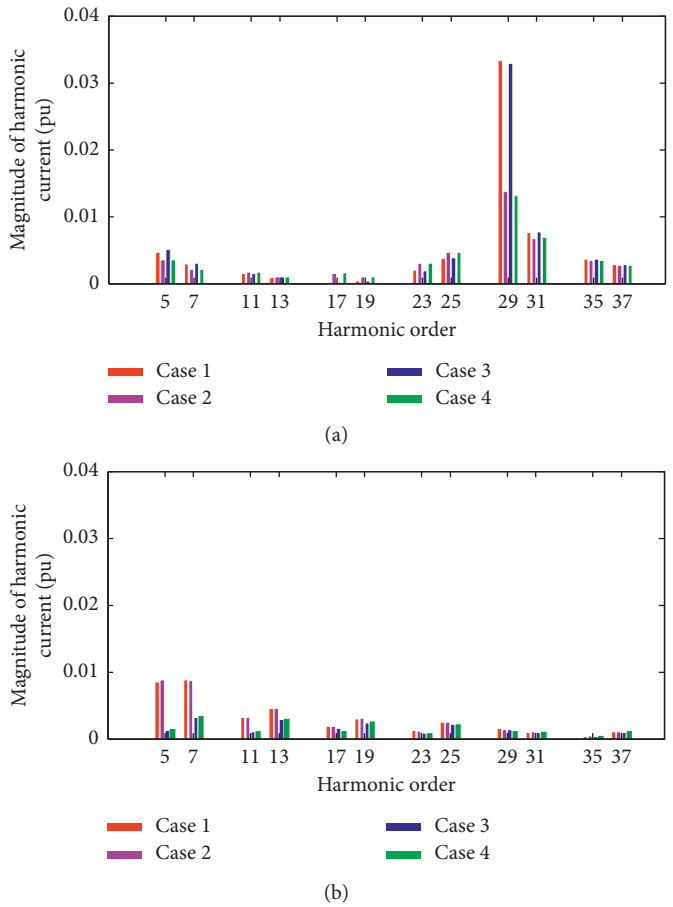

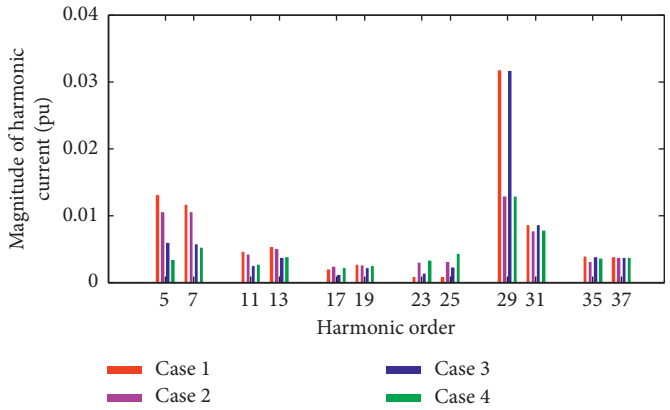

(c)

FIGURE 14: Harmonic current graphs of (a) i_{ga}, (b) i_{sa}, and (c) i_a.

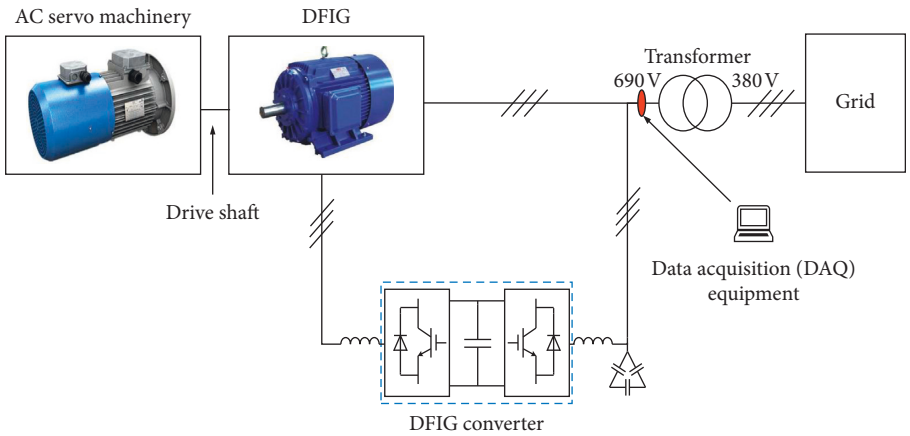

(a)

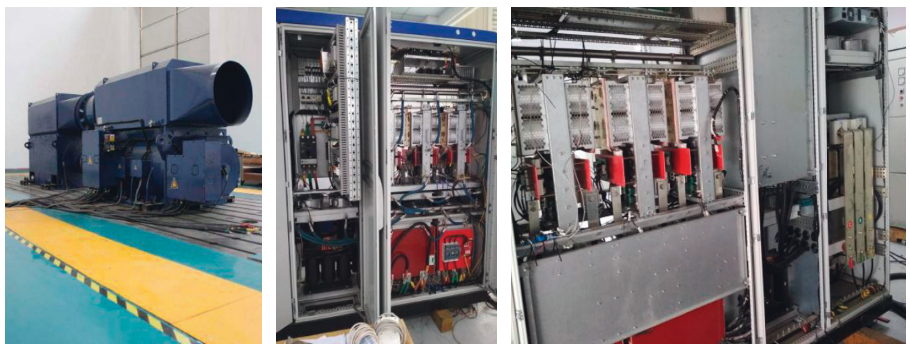

(b)

FIGURE 15: (a) Schematic diagram and (b) physical photograph of the experimental system.

When k_p of the current inner loop PI controller of the grid-side converter increases, the lower harmonic current of the DFIG below 1500 Hz is reduced, indicating that the parameter k_p has some damping effect. Meanwhile, when k_i of the current inner loop PI controller of the grid-side converter changes, the harmonic current of the DFIG does not change significantly, indicating that the parameter k_i change has little effect on the harmonic output of the wind turbine, which is consistent with the theoretical analysis.

5.2.3. Altering Output Power. Figure 18 shows the current harmonic diagrams under different active power conditions, i.e., when the output active power is 300 kW and

Table 2: Detailed parameters of the DFIG test platform.

Parameters	Values
Rated power (S_n)	2 MW
Rated grid frequency	50 Hz
Rated grid voltage (U_g)	380 V
Rated DFIG voltage (U_d)	690 V
Rated DC-link voltage (U_{dc})	1050 V
Grid-side inductance (L_g)	0.43 mH
Grid-side capacitance (C_g)	120 μF
Rotor-side inductance (L_r)	0.15 mH
Modulation method	SVPWM
Switch frequency of the rotor-side converter	2 kHz
Switch frequency of the grid-side converter	3 kHz

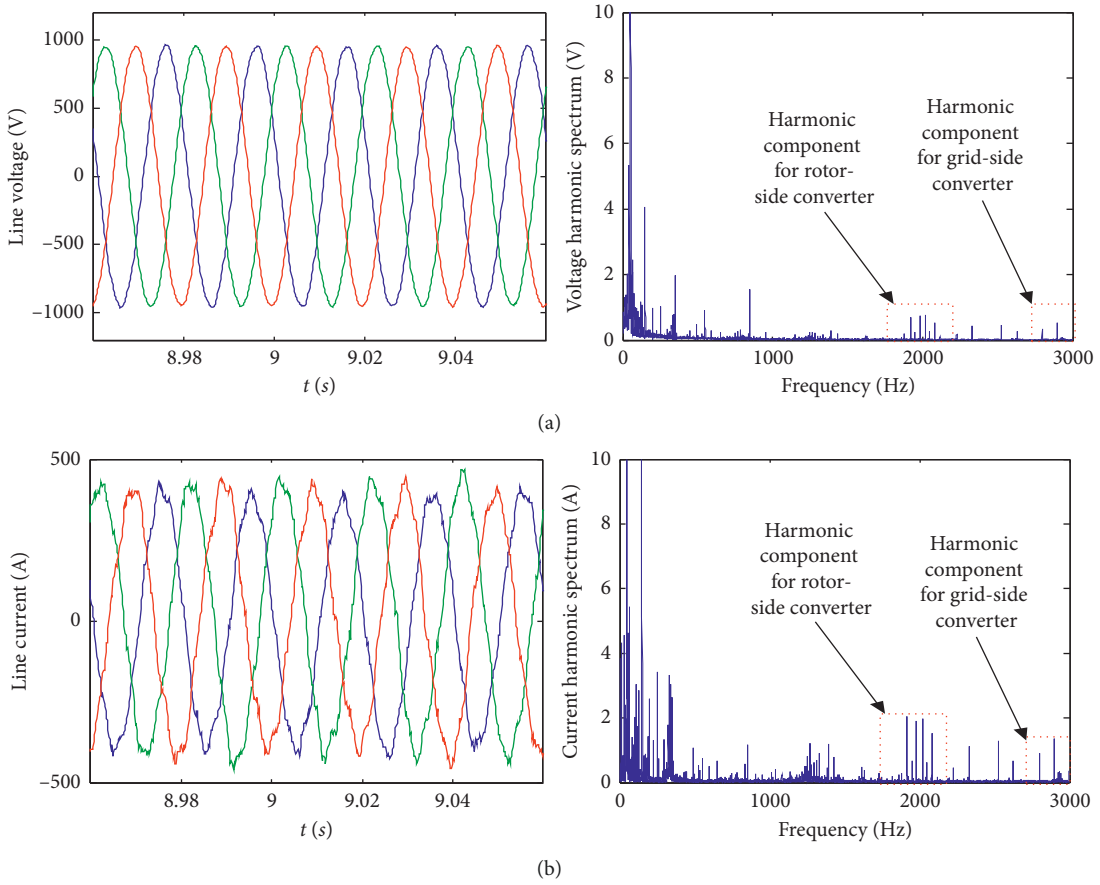

Figure 16: (a) Voltage waveform and harmonic spectrum and (b) current waveform and harmonic spectrum of the DFIG at PCC.

2000 kW, respectively. As shown in Figure 18, when the output active power of the wind turbine increases, the output power of the DFIG converter increases as well, and the harmonic current whose frequency is close to switch frequency also increases.

5.2.4. Three-Phase Voltage Unbalance. In order to verify the effect of three-phase voltage unbalance on the harmonic characteristics of the DFIG, the grid voltage irregularities were set to be 20% and 50%, respectively. Figure 19 shows that the larger the unbalance of the three-phase voltage, the larger the amplitude of the 3rd harmonic current i_s, which is consistent with the theoretical analysis.

5.2.5. Correction of the Harmonic Model Based on Measured Data. The harmonic model is corrected based on the harmonic test data of the test platform for the DFIG. Table 3 shows the precorrected and corrected parameters of the DFIG converter model. The simulated results shown in Figure 20 illustrate the harmonic current of the DFIG converter before and after correction under the rated operation condition. As can be seen from Figure 20, when the

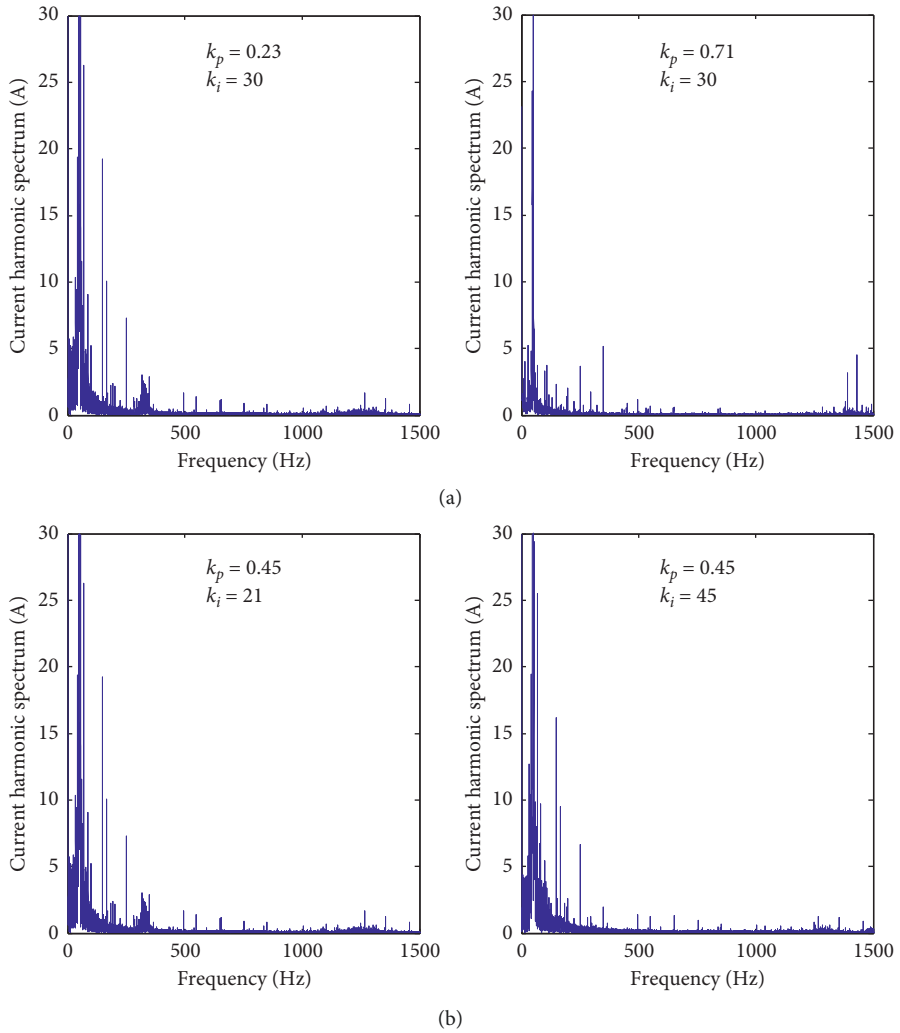

Figure 17: (a) Voltage waveform and harmonic spectrum and (b) current waveform and harmonic spectrum of the DFIG at PCC.

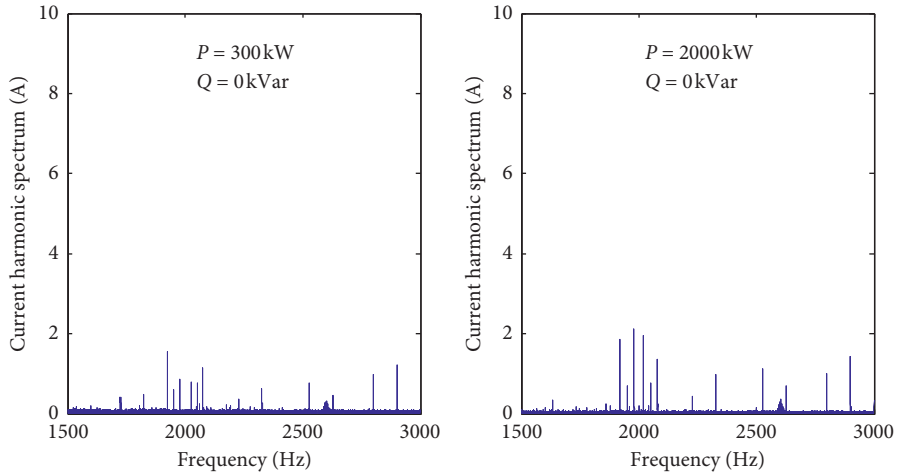

Figure 18: Current waveforms and harmonic spectrum of the DFIG under different active power conditions.

parameters of the simulation model are the same as those in the real test platform, the simulation results of harmonic current are much greater than what have been measured in practice. When correcting the simulation model using the data in Table 3, the value of harmonic current whose frequency is close to the switch frequency (which is 2000 and

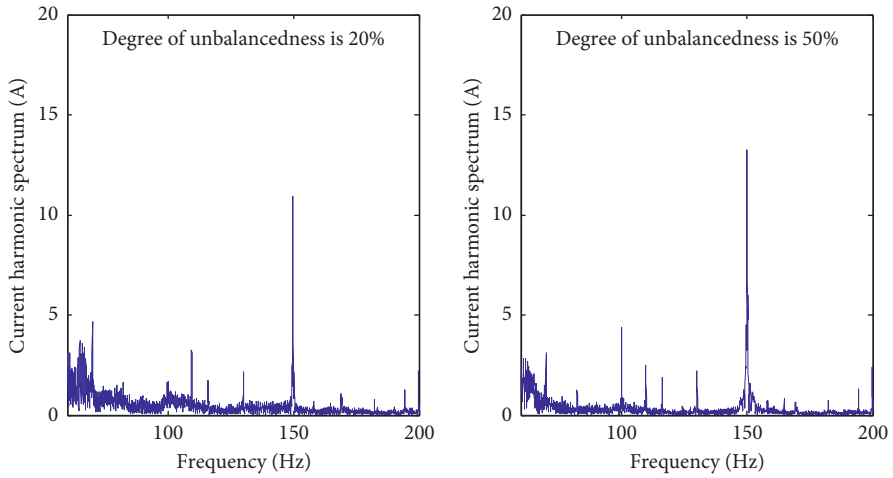

Figure 19: Current waveforms and harmonic spectrum of the DFIG under three-phase voltage unbalance.

Table 3: Model parameter correction.

Parameter type		Precorrected parameter	Corrected parameter
Filter parameter	L_1	0.43 mH	0.5 mH
	C	120 μF	120 μF
Grid equivalent inductance	L_g	—	0.18 mH
Current loop's PI control parameter of the grid-side converter	k_{pg}	1	5.0
	k_{ig}	13	100
Current loop's PI control parameter of the rotor-side converter	k_{pr}	0.5	1.5
	k_{ir}	2.5	100

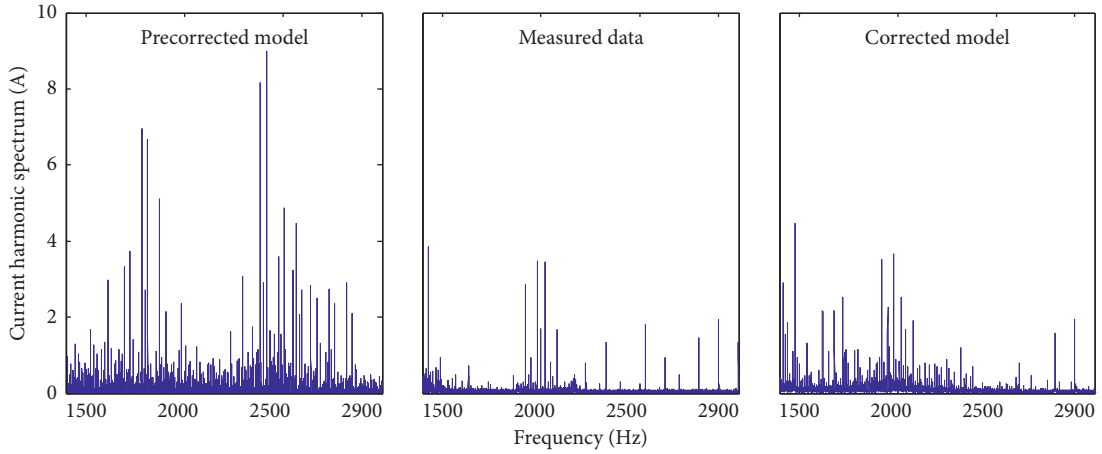

Figure 20: Comparison before and after harmonic model correction of the DFIG.

3000 Hz) in simulation is close to the data in the real test. Therefore, the modified model can be used to emulate the harmonic characteristics of the actual wind turbine.

6. Conclusion

In this paper, the harmonic equivalent models of the grid-side converter and rotor-side converter of the double-fed wind power generation system are established, and the harmonic output characteristics of both converters are studied based on the established models. The researches show that the resonance of the LC or LCL filter in the grid-side converter may lead to harmonic amplification in the neighboring resonace frequency, and the harmonic amplification can be suppressed by reasonably adjusting the current controller parameter k_{pg}. The integral term of the current controller in the rotor-side converter resonates with the rotor leakage inductance, which may cause the lower-frequency harmonic amplification in stator-side output current of the asynchronous motor, and the harmonic can be suppressed by appropriately increasing k_{pr} and reducing k_{ir} of the rotor-side current controller. The real-time HIL test results verify the correctness of the theoretical analyses. Furthermore, the effectiveness of the proposed model is

verified based on the actual DFIG test data, which can also provide guidance for the correction of the theoretical model.

Data Availability

The data used to support the findings of this study are included within the article.

Conflicts of Interest

The authors declare that there are no conflicts of interest regarding the publication of this paper.

Acknowledgments

This research was supported by State Grid Corporation Science and Technology Project under Grant NYB17201700081 and Hubei Natural Science Foundation under Grant 2018CFB205.

References

[1] Y.-W. Shen, D.-P. Ke, Y.-Z. Sun, D. S. Kirschenau, W. Qiao, and X.-T. Deng, "Advanced auxiliary control of an energy storage device for transient voltage support of a doubly fed induction generator," *IEEE Transactions on Sustainable Energy*, vol. 7, no. 1, pp. 63–76, 2016.

[2] R. Tao, F. Li, W. Chen, Y. Fan, C. Liang, and Y. Li, "Research on the protection coordination of permanent magnet synchronous generator based wind farms with low voltage ride through capability," *Protection and Control of Modern Power Systems*, vol. 2, no. 1, pp. 311–319, 2017.

[3] Y.-W. Shen, D.-P. Ke, W. W. Qiao, Y.-Z. Sunau, D. S. Kirschenau, and C. Weiau, "Transient reconfiguration and coordinated control for power converters to enhance the LVRT of a DFIG wind turbine with an energy storage device," *IEEE Transactions on Energy Conversion*, vol. 30, no. 4, pp. 1679–1690, 2015.

[4] S. Liao, J. Xu, Y. Sun, Y. Bao, and B. Tang, "Control of energy-intensive load for power smoothing in wind power plants," *IEEE Transactions on Power Systems*, vol. 33, no. 6, pp. 6142–6154, 2018.

[5] T. S. L. V. Ayyarao, "Modified vector controlled DFIG wind energy system based on barrier function adaptive sliding mode control," *Protection and Control of Modern Power Systems*, vol. 4, no. 1, pp. 34–41, 2019.

[6] W. Wu, Y. Liu, Y. He, H. S. H. Chung, M. Liserre, and F. Blaabjerg, "Damping methods of resonances caused by LCL-filter-based current-controlled grid-tied power inverters: an overview," *IEEE Transactions on Industrial Electronics*, vol. 64, no. 9, pp. 7402–7413, 2007.

[7] C. Wei, M. Benosman, and T. Kim, "Online parameter identification for state of power prediction of lithium-ion batteries in electric vehicles using extremum seeking," *International Journal of Control, Automation and Systems*, pp. 1–11, 2019.

[8] Y.-W. Shen, J.-R. Yuan, F.-F. Shen, J.-Z. Xu, C.-K. Li, and D. Wang, "Finite control set model predictive control for complex energy system with large-scale wind power," *Complexity*, vol. 2019, Article ID 4358958, 13 pages, 2019.

[9] O. Noureldeen and I. Hamdan, "A novel controllable crowbar based on fault type protection technique for DFIG wind energy conversion system using adaptive neuro-fuzzy inference system," *Protection and Control of Modern Power Systems*, vol. 3, no. 1, pp. 328–339, 2018.

[10] S. Boubzizi, H. Abid, A. El hajjaji, and M. Chaabane, "Comparative study of three types of controllers for DFIG in wind energy conversion system," *Protection and Control of Modern Power Systems*, vol. 3, no. 1, pp. 214–225, 2018.

[11] Z. Wang, Y. Z. Sun, G. J. Li et al., "Stator current harmonics analysis of double-fed induction generator," *Electric Power Automation Equipment*, vol. 30, no. 6, pp. 1–5, 2010.

[12] L. K. Wan, W. L. Yang, A. W. Yan et al., "Harmonic analysis of converter based on double-fed induction generator," *Electric Machines & Control Application*, vol. 38, no. 8, pp. 31–35, 2011.

[13] C. J. Zhang and Q. Q. Jia, "Probabilistic harmonic load flow calculation containing double fed induction generator," *Power Electronics*, vol. 45, no. 11, pp. 108–111, 2011.

[14] M. Nayeripour and M. Mahdi Mansouri, "An advanced analytical calculation and modeling of the electrical and mechanical harmonics behavior of doubly fed induction generator in wind turbine," *Renewable Energy*, vol. 81, pp. 275–285, 2015.

[15] N. Xie, A. Luo, F. J. Ma et al., "Harmonic interaction between large-scale photovoltaic power stations and grid," *Proceedings of the CSEE*, vol. 34, pp. 9–16, 2013.

[16] C. Zhang, X. Wang, L. Li et al., "Study on modulation function and harmonics of SVPWM," *Journal of Guizhou University (Natural Sciences)*, vol. 29, no. 6, pp. 63–67, 2012.

[17] J. L. Agorreta, M. Borrega, J. López, and L. Marroyo, "Modeling and control of N -paralleled grid-connected inverters with LCL filter coupled due to grid impedance in PV plants," *IEEE Transactions on Power Electronics*, vol. 26, no. 3, pp. 770–785, 2011.

[18] X. Wang, F. Blaabjerg, M. Liserre, Z. Chen, J. He, and Y. Li, "An active damper for stabilizing power-electronics-based AC systems," *IEEE Transactions on Power Electronics*, vol. 29, no. 7, pp. 3318–3329, 2014.

[19] D. Yang, X. Ruan, and H. Wu, "Impedance shaping of the grid-connected inverter with LCL filter to improve its adaptability to the weak grid condition," *IEEE Transactions on Power Electronics*, vol. 29, no. 11, pp. 5795–5805, 2014.

[20] Y.-W. Shen, L.-Q. Liang, M. J. Cui, F. Shen, B. Zhang, and T. Cui, "Advanced control of DFIG to enhance the transient voltage support capability," *Journal of Energy Engineering*, vol. 144, no. 2, Article ID 04018009, 2018.

[21] J. Rodriguez and P. Cortes, "Predictive control of power converters and electrical drives," *IEEE Transactions on Industrial Electronics*, vol. 63, no. 7, pp. 4472–4474, 2016.

[22] S. Rivera, S. Kouro, B. Wu et al., ""Multilevel direct power control—a generalized approach for grid-tied multilevel converter applications," *IEEE Trans. Power Electronics*, vol. 29, no. 10, pp. 5592–5604, 2014.

Hindawi
Complexity
Volume 2019, Article ID 6582405, 11 pages
https://doi.org/10.1155/2019/6582405

Research Article

Adaptive Fixed-Time Sliding Mode Control for Uncertain Twin-Rotor System with Experimental Validation

Linwu Shen,[1,2] **Qiang Chen**,[1] **Meiling Tao**,[1] **and Xiongxiong He**[1]

[1]*Data-Driven Intelligent Systems Laboratory, College of Information Engineering, Zhejiang University of Technology, Hangzhou 310023, China*
[2]*Department of Electrical and Electronic Technology, Zhejiang Institute of Mechanical and Electrical Engineering, Hangzhou 310053, China*

Correspondence should be addressed to Qiang Chen; sdnjchq@zjut.edu.cn

Received 26 July 2019; Accepted 9 September 2019; Published 29 October 2019

Guest Editor: Xiaoqing Bai

This paper proposes an adaptive fixed-time control scheme for twin-rotor systems subject to the inertia uncertainties and external disturbances. First of all, a fixed-time sliding mode surface is constructed and the corresponding controller is developed such that the fixed-time uniform ultimate boundedness of the sliding variable and tracking error could be guaranteed simultaneously, and the setting time is independent of the initial values. The adaptive update laws are developed to estimate the upper bounds of the lumped uncertainties and external disturbances such that no prior knowledge on the system uncertainties and disturbances is required. Finally, a twin-rotor platform is constructed to verify the effectiveness of proposed scheme. Comparative results show better position tracking performance of the proposed control scheme.

1. Introduction

As a novel application of the small unmanned aerial vehicle, multirotor is a trending topic due to its wide advantages in practical systems [1–7]. So far, many research studies have been carried out on the control of multirotor systems such as robust adaptive control [8–12], backstepping control [13], and sliding mode control [14, 15]. However, only the asymptotic stability is achieved in the aforementioned control methods.

Compared with the asymptotic stability of the system, the finite-time control is proposed to realize the better control performance, and it has been extensively employed in the multirotor attitude control [16–24]. In [21], a finite-time control was developed based on the first-order command filter and the prescribed performance boundary to realize the finite-time attitude stabilization of rigid spacecraft. In [22], a continuous multivariable attitude control law was constructed in a supertwisting-like algorithm, which drove the attitude tracking errors of quadrotor to origin in finite time. In [23], a model-free terminal sliding mode controller was constructed to control both the attitude and position of a quadrotor in the presence of inertia uncertainties and external disturbances. In [24], a finite-time integral sliding mode control scheme was developed for the quadrotor attitude tracking control with uncertainties and external disturbances.

Based on the aforementioned literatures, the finite-time convergence of the system states is dependent on the initial values. However, when the initial system states are unknown, it is a challenge to require the exact estimation for the upper bound of the setting time [25–27]. In [28], a fixed-time convergence of the system was initially proposed, and the setting time was bounded by a designed constant with the unknown initial states, and the fixed-time technology was applied in some practical systems [29]. In [30], a nonsingular fixed-time sliding mode control law was presented to realize the fixed-time convergence of the rigid spacecraft, and the setting time is irrelevant of the system initial states. In [31], an inverse trigonometric function is used to construct a double power reaching law in a fixed-time fault-tolerant controller, which could speed up the state

stabilization and reduce the chattering phenomenon simultaneously.

Motivated by the aforementioned discussions, an adaptive fixed-time control law is proposed for twin-rotor systems subject to the inertia uncertainties and external disturbances. The two main contributions are summarized as follows:

(1) A fixed-time sliding mode controller is constructed to achieve the fixed-time uniform ultimate boundedness of the sliding variable and tracking error, and the setting time is independent of the initial values

(2) A twin-rotor platform is constructed to verify the effectiveness of the proposed control scheme, and the comparative results show better position tracking performance of the proposed scheme

The framework of this paper is shown as follows. Section 2 describes the mathematical model and problem formulation. Section 3 introduces an adaptive fixed-time control scheme. The fixed-time convergence of the system states is analyzed in Section 4. Experiment results are shown in Section 5.

2. Mathematical Model and Problem Formulation

2.1. Dynamic Model. To describe system dynamics of twin-rotor rigid body, a twin-rotor equalizing bar with a single degree of freedom is considered. As shown in Figure 1, the twin-rotor equalizing bar consists of mechanical and electrical parts. The mechanical part includes a base plate, a bracket, an equalizing bar, and two bearings, and the bearings' axis is the mass center of the equalizing bar rotating around the bracket. The electrical part, including a controller unit (CU), an electron speed regulator (ESR), and two brushless direct current (BLDC) motors, is used to control the attitude and angular velocity. The blades of the two BLDC motors have contrast rotational directions in order to eliminate contrast axis torque effect of the BLDC motors.

Since the twin-rotor equalizing bar is a single degree of freedom (i.e., only the pitch axis is used), the system model is given by

$$\begin{cases} \dot{x}_1 = x_2, \\ \dot{x}_2 = bu + f(x_1, x_2) + d(t, x_1, x_2), \\ y = x_1, \end{cases} \tag{1}$$

where x_1 and x_2 are the outputs of the Gyro attitude angle and angular velocity, respectively, $u \in R$ is the control input, $b > 0$ is a known positive constant, $f(x_1, x_2)$ are the unknown smooth nonlinear uncertainties, and $d(t, x_1, x_2)$ represents the unknown external disturbances, satisfying the following assumptions.

Assumption 1. The unknown smooth nonlinear uncertainties $f(x_1, x_2)$ are assumed to be bounded. Therefore, for all $u \in R$, there exists a constant $F > 0$ such that $|f(x_1, x_2)| \le F$.

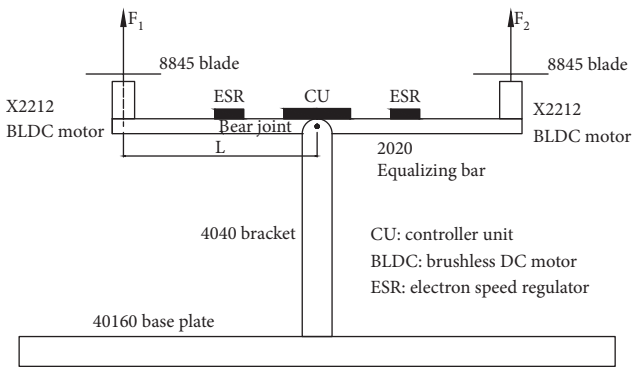

Figure 1: The twin-rotor equalizing bar.

Assumption 2. The lumped external disturbances $d(t, x_1, x_2)$ are assumed to be bounded. Therefore, for all $u \in R$ and $t \ge 0$, there exists a constant $D > 0$ such that $|d(t, x_1, x_2)| \le D$.

2.2. Preliminaries. Before the controller design, a few useful lemmas are given as follows.

Lemma 1 (see [32]). *If $\alpha > 1$, the following inequality holds:*

$$\sum_{i=1}^{N} |y_i|^{\alpha+1} \ge N^{(1-\alpha)/2} \left(\sum_{i=1}^{N} |y_i|^2 \right)^{(1+\alpha)/2}, \tag{2}$$

and if $\beta < 1$, the following inequality holds:

$$\sum_{i=1}^{N} |y_i|^{\beta+1} \ge \left(\sum_{i=1}^{N} |y_i|^2 \right)^{(1+\beta)/2}, \tag{3}$$

where N is a positive integer and $y_i > 0$.

Lemma 2 (see [33]). *For a scalar system,*

$$\dot{y} = -k_1 y^{a_1} - k_2 y^{a_2}, \quad y(0) = y_0, \tag{4}$$

where $k_1 > 0$, $k_2 > 0$, $a_1 > 1$, and $0 < a_2 < 1$.

The convergence time T of (4) is a fixed time and expressed as follows:

$$T < T_{\max} = \frac{1}{k_1 (a_1 - 1)} + \frac{1}{k_2 (1 - a_2)}. \tag{5}$$

Furthermore, if $\delta = (a_1 - 1)/(1 - a_2) \le 1$, a higher precise upper-bound estimation of the convergence time is obtained as follows:

$$T < T'_{\max} = \frac{1}{(1 - a_2)} \left(\frac{1}{k_1 k_2} \tan^{-1} \sqrt{\frac{k_1}{k_2}} + \frac{1}{k_1 \delta} \right). \tag{6}$$

3. Adaptive Fixed-Time Controller Design

In this section, we construct a fixed-time sliding mode surface with the convergence time independent of the system

initial states and design an adaptive fixed-time controller to ensure the shorter reaching time and sliding time than the general fast terminal sliding mode control and linear sliding mode control with the same parameters.

3.1. Fixed-Time Sliding Mode Surface. The fixed-time sliding mode surface of the system (1) is formulated by

$$s = \dot{e} + k_1 \mathrm{sig}^{a_1} e + k_2 \mathrm{sig}^{a_2} e, \tag{7}$$

where $e = x_1 - x_d$, $\dot{e} = x_2 - \dot{x}_d$, $k_1 > 0$, $k_2 > 0$, $a_1 > 1$, $0 < a_2 < 1$, and x_d and $\dot{x}_d$ are the setting inputs of the sliding mode controller.

The time derivative of (7) is expressed as

$$\dot{s} = \ddot{e} + k_1 a_1 |e|^{a_1 - 1} \dot{e} + k_2 a_2 |e|^{a_2 - 1} \dot{e}. \tag{8}$$

In (8), owing to $a_2 - 1 < 0$, $|e|^{a_2 - 1} \longrightarrow \infty$, $\dot{s} \longrightarrow \infty$; when $\dot{e} = 0$ or $\ddot{e} \neq 0$, there exists a singularity problem. To solve the singularity and carry out in practical application, the following function is found to take place of the term $\mathrm{sig}^{a_2} e$.

$$\phi(e) = \begin{cases} |e|^{a_2} \mathrm{sgn}(e), & s = 0 \text{ or } s \neq 0, |e| > \mu, \\ l_1 e + l_2 |e|^2 \mathrm{sgn}(e), & s \neq 0, |e| \leq \mu, \end{cases} \tag{9}$$

where μ is a small positive bounded constant, $l_1 = (2 - a_2)\mu^{a_2 - 1}$, and $l_2 = (a_2 - 1)\mu^{a_2 - 1}$.

Deriving (9) leads to

$$\dot{\phi}(e) = \begin{cases} a_2 |e|^{a_2 - 1} \dot{e}, & s = 0 \text{ or } s \neq 0, |e| > \mu, \\ l_1 \dot{e} + 2 l_2 |e| \dot{e}, & s \neq 0, |e| \leq \mu. \end{cases} \tag{10}$$

Based on the former analysis, (7) and (8) are rewritten as

$$s = \dot{e} + k_1 \mathrm{sig}^{a_1} e + k_2 \phi(e), \tag{11}$$

$$\dot{s} = \ddot{e} + k_1 a_1 |e|^{a_1 - 1} \dot{e} + k_2 \dot{\phi}(e). \tag{12}$$

3.2. Controller Design. For the system (1), the sliding mode controller u is designed as

$$\begin{aligned} u = -\frac{1}{b} \big(& k_1 a_1 |e|^{a_1 - 1} \dot{e} + k_2 \dot{\phi}(e) - \ddot{x}_d \\ & + \alpha \, \mathrm{sig}^{\gamma_1} s + \beta \, \mathrm{sig}^{\gamma_2} s + \widehat{F} \, \mathrm{sgn}(s) + \widehat{D} \, \mathrm{sgn}(s) \big), \end{aligned} \tag{13}$$

where $\alpha > 0$, $\beta > 0$, $\gamma_1 > 1$, $0 < \gamma_2 < 1$, α, β, γ_1, and γ_2 are the designed parameters and $\ddot{x}_d$ is the desirable angular acceleration.

The adaptive update laws are given by

$$\dot{\widehat{F}} = \frac{1}{\theta_0 c_1} \left(|s| - p_1 \widehat{F} \right), \tag{14}$$

$$\dot{\widehat{D}} = \frac{1}{\theta_0 c_2} \left(|s| - p_2 \widehat{D} \right), \tag{15}$$

where p_1, p_2, c_1, c_2, and θ_0 satisfy $p_1 > 0$, $p_2 > 0$, $c_1 > 0$, $c_2 > 0$, and $\theta_0 > 0$.

4. Stability Analysis

Lemma 3. *Considering the fixed-time sliding mode surface (7), once the sliding mode manifold $s = 0$ is achieved, the attitude error e and angular velocity error $\dot{e}$ could be guaranteed in fixed time, and the setting time T_s satisfies the following inequality:*

$$T_s < \frac{1}{2^{(a_1+1)/2}} \frac{2}{k_1 (a_1 - 1)} + \frac{1}{2^{(a_2+1)/2}} \frac{2}{k_2 (1 - a_2)}. \tag{16}$$

Proof. Construct the following Lyapunov candidate function:

$$V_0 = \frac{1}{2} e^2. \tag{17}$$

Once the sliding mode manifold $s = 0$ is achieved, from (7), the time derivative of (17) is

$$\begin{aligned} \dot{V}_0 &= e\dot{e} \\ &= e\left(-k_1 \mathrm{sig}^{a_1} e - k_2 \mathrm{sig}^{a_2} e\right) \\ &= -2^{(a_1+1)/2} k_1 \left| \frac{1}{2} e^2 \right|^{(a_1+1)/2} - 2^{(a_2+1)/2} k_2 \left| \frac{1}{2} e^2 \right|^{(a_2+1)/2} \\ &= -2^{(a_1+1)/2} k_1 |V_0|^{(a_1+1)/2} - 2^{(a_2+1)/2} k_2 |V_0|^{(a_2+1)/2}, \end{aligned} \tag{18}$$

where k_1, $k_2 > 0$, $a_1 > 1$, and $0 < a_2 < 1$.

From (18), it is concluded according to Lemma 2 that once the sliding mode manifold $s = 0$ is achieved, the convergence of the attitude error e and angular velocity error $\dot{e}$ could be guaranteed in fixed time, and the setting time T_s satisfies the following inequality:

$$T_s < \frac{1}{2^{(a_1+1)/2}} \frac{2}{k_1 (a_1 - 1)} + \frac{1}{2^{(a_2+1)/2}} \frac{2}{k_2 (1 - a_2)}. \tag{19}$$

This completes the proof. □

Theorem 1. *Considering the system (1) with the sliding mode surface (11), the control law (13), and the adaptive update laws (14) and (15), all signals of the closed-loop system are uniformly ultimately bounded within a fixed time.*

Proof. Construct the following Lyapunov candidate function:

$$V = \frac{1}{2} s^2 + \frac{1}{2} c_{r1} \widetilde{F}^2 + \frac{1}{2} c_{r2} \widetilde{D}^2, \tag{20}$$

where $c_{r1} > 0$, $c_{r2} > 0$, $\widetilde{F} = F - \widehat{F}$, and $\widetilde{F} = F - \widehat{F}$.

By using (1) and (12), the derivative of (20) is obtained as

$$\begin{aligned}\dot{V} &= s\dot{s} + c_{r1}\tilde{F}\dot{\tilde{F}} + c_{r2}\tilde{D}\dot{\tilde{D}}\\ &= s\left(f + d + bu - \ddot{x}_{\mathrm{d}} + k_1 a_1 |e|^{a_1 - 1}\dot{e} + k_2\dot{\phi}(e)\right)\\ &\quad + c_{r1}\tilde{F}\dot{\tilde{F}} + c_{r2}\tilde{D}\dot{\tilde{D}}\\ &\le s\left(F\cdot \mathrm{sgn}(s) + D\cdot \mathrm{sgn}(s)\right.\\ &\quad \left. + bu - \ddot{x}_{\mathrm{d}} + k_1 a_1 |e|^{a_1 - 1}\dot{e} + k_2\dot{\phi}(e)\right)\\ &\quad + c_{r1}\tilde{F}\dot{\tilde{F}} + c_{r2}\tilde{D}\dot{\tilde{D}}.\end{aligned} \tag{21}$$

Substituting (13) into (21) yields

$$\begin{aligned}\dot{V} &\le s - \alpha\,\mathrm{sig}^{\gamma_1}(s) - \beta\,\mathrm{sig}^{\gamma_2}(s) - \hat{F}\cdot \mathrm{sgn}(s) - \hat{D}\cdot \mathrm{sgn}(s)\\ &\quad + F\cdot \mathrm{sgn}(s) + D\cdot \mathrm{sgn}(s)) + c_{r1}\tilde{F}\dot{\tilde{F}} + c_{r2}\tilde{D}\dot{\tilde{D}}\\ &= -\alpha|s|^{\gamma_1 + 1} - \beta|s|^{\gamma_2 + 1} + \tilde{F}|s| + \tilde{D}|s| + c_{r1}\tilde{F}\dot{\tilde{F}} + c_{r2}\tilde{D}\dot{\tilde{D}}\\ &= -2^{(\gamma_1+1)/2}\alpha\left(\frac{1}{2}s^2\right)^{(\gamma_1+1)/2} - 2^{(\gamma_2+1)/2}\beta\left(\frac{1}{2}s^2\right)^{(\gamma_2+1)/2}\\ &\quad - \left(\frac{1}{2}c_{r1}\tilde{F}^2\right)^{(\gamma_1+1)/2} - \left(\frac{1}{2}c_{r1}\tilde{F}^2\right)^{(\gamma_2+1)/2}\\ &\quad - \left(\frac{1}{2}c_{r2}\tilde{D}^2\right)^{(\gamma_1+1)/2} - \left(\frac{1}{2}c_{r2}\tilde{D}^2\right)^{(\gamma_2+1)/2} + \left(\frac{1}{2}c_{r1}\tilde{F}^2\right)^{(\gamma_1+1)/2}\\ &\quad + \left(\frac{1}{2}c_{r1}\tilde{F}^2\right)^{(\gamma_2+1)/2} + \left(\frac{1}{2}c_{r2}\tilde{D}^2\right)^{(\gamma_1+1)/2}\\ &\quad + \left(\frac{1}{2}c_{r2}\tilde{D}^2\right)^{(\gamma_2+1)/2} + \tilde{F}|s| + \tilde{D}|s| - c_{r1}\tilde{F}\dot{\hat{F}} - c_{r2}\tilde{D}\dot{\hat{D}}.\end{aligned} \tag{22}$$

Substituting (14) and (15) into (22) yields

$$\begin{aligned}\dot{V} &\le -\eta_1\left(\left(\frac{1}{2}s^2\right)^{(\gamma_1+1)/2} + \left(\frac{1}{2}c_{r1}\tilde{F}^2\right)^{(\gamma_1+1)/2}\right.\\ &\quad \left. + \left(\frac{1}{2}c_{r2}\tilde{D}^2\right)^{(\gamma_1+1)/2}\right) - \eta_2\left(\left(\frac{1}{2}s^2\right)^{(\gamma_2+1)/2}\right.\\ &\quad \left. + \left(\frac{1}{2}c_{r1}\tilde{F}^2\right)^{(\gamma_2+1)/2} + \left(\frac{1}{2}c_{r2}\tilde{D}^2\right)^{(\gamma_2+1)/2}\right)\\ &\quad + \left(\frac{1}{2}c_{r1}\tilde{F}^2\right)^{(\gamma_1+1)/2} + \left(\frac{1}{2}c_{r1}\tilde{F}^2\right)^{(\gamma_2+1)/2} + \left(\frac{1}{2}c_{r2}\tilde{D}^2\right)^{(\gamma_1+1)/2}\\ &\quad + \left(\frac{1}{2}c_{r2}\tilde{D}^2\right)^{(\gamma_2+1)/2} + p_1\tilde{F}\hat{F} + p_2\tilde{D}\hat{D},\end{aligned} \tag{23}$$

where $\eta_1 = \min\{2^{(\gamma_1+1)/2}\alpha, 1\}$, $\eta_2 = \min\{2^{(\gamma_2+1)/2}\beta, 1\}$, $c_{r1} = \theta_0 c_1$, and $c_{r2} = \theta_0 c_2$.

According to Lemma 1, (23) can be rewritten as

$$\begin{aligned}\dot{V} &\le -\left(3^{(1-\gamma_1)/2}\eta_1 V^{(\gamma_1+1)/2} + \eta_2 V^{(\gamma_2+1)/2}\right)\\ &\quad + \left(\frac{1}{2}c_{r1}\tilde{F}^2\right)^{(\gamma_1+1)/2} + \left(\frac{1}{2}c_{r1}\tilde{F}^2\right)^{(\gamma_2+1)/2}\\ &\quad + \left(\frac{1}{2}c_{r2}\tilde{D}^2\right)^{(\gamma_1+1)/2} + \left(\frac{1}{2}c_{r2}\tilde{D}^2\right)^{(\gamma_2+1)/2} + p_1\tilde{F}\hat{F} + p_2\tilde{D}\hat{D}.\end{aligned} \tag{24}$$

Due to Young's inequalities, the following formulations hold:

$$\begin{aligned}p_1\tilde{F}\hat{F} &= p_1\tilde{F}(F - \tilde{F})\\ &= p_1\left(\tilde{F}F - \tilde{F}^2\right)\\ &\le p_1\left(\frac{\tilde{F}^2}{2\theta_1} + \frac{\theta_1 F^2}{2} - \tilde{F}^2\right)\\ &= \frac{p_1(1 - 2\theta_1)\tilde{F}^2}{2\theta_1} + \frac{p_1\theta_1 F^2}{2},\end{aligned} \tag{25}$$

$$\begin{aligned}p_2\tilde{D}\hat{D} &= p_2\tilde{D}(D - \tilde{D})\\ &= p_2\left(\tilde{D}D - \tilde{D}^2\right)\\ &\le p_2\left(\frac{\tilde{D}^2}{2\theta_2} + \frac{\theta_2 D^2}{2} - \tilde{D}^2\right)\\ &= \frac{p_2(1 - 2\theta_2)\tilde{D}^2}{2\theta_2} + \frac{p_2\theta_2 D^2}{2},\end{aligned} \tag{26}$$

where $\theta_1 > (1/2)$ and $\theta_2 > (1/2)$.

Combining (25) and (26) into (24), (24) is transformed into

$$\begin{aligned}\dot{V} &\le -\left(3^{(1-\gamma_1)/2}\eta_1 V^{(\gamma_1+1)/2} + \eta_2 V^{(\gamma_2+1)/2}\right)\\ &\quad + \frac{p_1\theta_1 F^2}{2} + \frac{p_2\theta_2 D^2}{2} + \left(\frac{1}{2}c_{r1}\tilde{F}^2\right)^{(\gamma_1+1)/2}\\ &\quad + \left(\frac{1}{2}c_{r1}\tilde{F}^2\right)^{(\gamma_2+1)/2} + \left(\frac{1}{2}c_{r2}\tilde{D}^2\right)^{(\gamma_2+1)/2}\\ &\quad + \left(\frac{1}{2}c_{r2}\tilde{D}^2\right)^{(\gamma_2+1)/2} - c_1\tilde{F}^2 - c_2\tilde{D}^2\\ &\le -\left(3^{1-\gamma_1/2}\eta_1 V^{(\gamma_1+1)/2} + \eta_2 V^{(\gamma_2+1)/2}\right)\\ &\quad + \frac{p_1\theta_1 F^2}{2} + \frac{p_2\theta_2 D^2}{2} + \left(\frac{1}{2}c_{r1}\tilde{F}^2\right)^{(\gamma_1+1)/2}\\ &\quad + \left(\frac{1}{2}c_{r1}\tilde{F}^2\right)^{(\gamma_2+1)/2} + \left(\frac{1}{2}c_{r2}\tilde{D}^2\right)^{(\gamma_1+1)/2}\\ &\quad + \left(\frac{1}{2}c_{r2}\tilde{D}^2\right)^{(\gamma_2+1)/2} - \left(\frac{1}{2}\theta_0\right)^{(\gamma_2+1)/2}c_1\tilde{F}^2 - \left(\frac{1}{2}\theta_0\right)^{(\gamma_2+1)/2}\\ &\quad \cdot c_2\tilde{D}^2 - \left(1 - \left(\frac{1}{2}\theta_0\right)^{(\gamma_2+1)/2}\right)c_1\tilde{F}^2 - \left(1 - \left(\frac{1}{2}\theta_0\right)^{(\gamma_2+1)/2}\right)c_2\tilde{D}^2,\end{aligned} \tag{27}$$

where $c_1 = ((2\theta_1 - 1)p_1)/2\theta_1$, $c_2 = ((2\theta_2 - 1)p_2)/2\theta_2$, and θ_0 satisfying $((1/2)\theta_0)^{(\gamma_2+1)/2} + (1/2)\theta_0 - 1 = 0$.

Because $c_{r1} = c_1\theta_0$ and $c_{r2} = c_2\theta_0$, (27) is rewritten as

$$\begin{aligned}\dot{V} \le & -\left(3^{(1-\gamma_1)/2}\eta_1 V^{(\gamma_1+1)/2} + \eta_2 V^{(\gamma_2+1)/2}\right) \\ & + \frac{p_1\theta_1 F^2}{2} + \frac{p_2\theta_2 D^2}{2} + \left(\frac{1}{2}c_1\theta_0\widetilde{F}^2\right)^{(\gamma_1+1)/2} \\ & + \left(\frac{1}{2}c_1\theta_0\widetilde{F}^2\right)^{(\gamma_2+1)/2} + \left(\frac{1}{2}c_2\theta_0\widetilde{D}^2\right)^{(\gamma_1+1)/2} \\ & + \left(\frac{1}{2}c_2\theta_0\widetilde{D}^2\right)^{(\gamma_2+1)/2} - \left(\frac{1}{2}\theta_0\right)^{(\gamma_2+1)/2} \\ & \cdot c_1\widetilde{F}^2 - \left(\frac{1}{2}\theta_0\right)^{(\gamma_2+1)/2} c_2\widetilde{D}^2 \\ & - \frac{1}{2}\theta_0 c_1\widetilde{F}^2 - \frac{1}{2}\theta_0 c_2\widetilde{D}^2.\end{aligned} \tag{28}$$

□

Case 1. When $c_1\widetilde{F}^2 \ge 1$, we have $(c_1\widetilde{F}^2)^{(\gamma_2+1)/2} - c_1\widetilde{F}^2 \le 0$.

Case 2. When $0 < c_1\widetilde{F}^2 < 1$, $c_1\widetilde{F}^2 = (2/(\gamma_2+1))^{2/(\gamma_2-1)}$, and $v_0 = (2/(\gamma_2+1))^{(\gamma_2+1)/(\gamma_2-1)} - (2/(\gamma_2+1))^{2/(\gamma_2-1)}$, the term of $(c_1\widetilde{F}^2)^{(\gamma_2+1)/2} - c_1\widetilde{F}^2$ satisfies the following inequality:

$$0 < \left(c_1\widetilde{F}^2\right)^{(\gamma_2+1)/2} - c_1\widetilde{F}^2 < v_0. \tag{29}$$

Combining Cases 1 and 2, we can obtain $(c_1\widetilde{F}^2)^{(\gamma_2+1)/2} - c_1\widetilde{F}^2 < v_0$. Similarly, $(c_2\widetilde{D}^2)^{(\gamma_2+1)/2} - c_2\widetilde{D}^2 < v_0$. (28) is rewritten as

$$\begin{aligned}\dot{V} \le & -\left(3^{(1-\gamma_1)/2}\eta_1 V^{(\gamma_1+1)/2} + \eta_2 V^{(\gamma_2+1)/2}\right) \\ & + \left(\frac{1}{2}\theta_0 c_1\widetilde{F}^2\right)^{(\gamma_1+1)/2} + \left(\frac{1}{2}\theta_0 c_2\widetilde{D}^2\right)^{(\gamma_1+1)/2} \\ & - \frac{1}{2}\theta_0 c_1\widetilde{F}^2 - \frac{1}{2}\theta_0 c_2\widetilde{D}^2 + v_1,\end{aligned} \tag{30}$$

where

$$v_1 = 2\left(\frac{1}{2}\theta_0\right)^{(\gamma_2+1)/2} v_0 + \frac{p_1\theta_1 F^2}{2} + \frac{p_2\theta_2 D^2}{2}. \tag{31}$$

Case 3. When $\xi \le \min\{\sqrt{2}/\sqrt{\theta_0 c_1}, \sqrt{2}/\sqrt{\theta_0 c_2}\}$, ξ is the value interval of $\widetilde{F}$ and $\widetilde{D}$; then, $((1/2)\theta_0 c_1\widetilde{F}^2)^{(\gamma_1+1)/2} \le (1/2)\theta_0 c_1\widetilde{F}^2$ and $((1/2)\theta_0 c_2\widetilde{D}^2)^{(\gamma_1+1)/2} \le (1/2)\theta_0 c_2\widetilde{D}^2$, i.e.,

$$\left(\frac{1}{2}\theta_0 c_1\widetilde{F}^2\right)^{(\gamma_1+1)/2} - \frac{1}{2}\theta_0 c_1\widetilde{F}^2 \le 0, \tag{32}$$

$$\left(\frac{1}{2}\theta_0 c_2\widetilde{D}^2\right)^{(\gamma_1+1)/2} - \frac{1}{2}\theta_0 c_2\widetilde{D}^2 \le 0. \tag{33}$$

From (32) and (33), (30) is expressed as

$$\dot{V} \le -\left(3^{(1-\gamma_1)/2}\eta_1 V^{(\gamma_1+1)/2} + \eta_2 V^{(\gamma_2+1)/2}\right) + v_1. \tag{34}$$

Case 4. When $\xi > \min\{\sqrt{2}/\sqrt{\theta_0 c_1}, \sqrt{2}/\sqrt{\theta_0 c_2}\}$, then

$$\begin{aligned}& \left(\frac{1}{2}\theta_0 c_1\widetilde{F}^2\right)^{(\gamma_1+1)/2} + \left(\frac{1}{2}\theta_0 c_2\widetilde{D}^2\right)^{(\gamma_1+1)/2} \\ & - \frac{1}{2}\theta_0 c_1\widetilde{F}^2 - \frac{1}{2}\theta_0 c_2\widetilde{D}^2 \\ & \le 2\left(\frac{1}{2}\theta_0 c_{\max}\xi^2\right)^{(\gamma_1+1)/2} - 2\left(\frac{1}{2}\theta_0 c_{\max}\xi^2\right),\end{aligned} \tag{35}$$

where $c_{\max} = \{c_1, c_2\}$.

(34) is rewritten as

$$\begin{aligned}\dot{V} \le & -\left(3^{(1-\gamma_1)/2}\eta_1 V^{(\gamma_1+1)/2} + \eta_2 V^{(\gamma_2+1)/2}\right) \\ & + v_1 + 2\left(\frac{1}{2}\theta_0 c_{\max}\xi^2\right)^{(\gamma_1+1)/2} - 2\left(\frac{1}{2}\theta_0 c_{\max}\xi^2\right).\end{aligned} \tag{36}$$

Based on the mentioned analysis, the time derivative of V is given by

$$\dot{V} \le -\left(3^{(1-\gamma_1)/2}\eta_1 V^{(\gamma_1+1)/2} + \eta_2 V^{(\gamma_2+1)/2}\right) + v, \tag{37}$$

where

$$v = \begin{cases} v_1, & \xi \le \min\left\{\dfrac{\sqrt{2}}{\sqrt{\theta_0 c_1}}, \dfrac{\sqrt{2}}{\sqrt{\theta_0 c_2}}\right\}, \\ v_1 + 2\left(\dfrac{1}{2}\theta_0 c_{\max}\xi^2\right)^{(\gamma_1+1)/2} - 2\left(\dfrac{1}{2}\theta_0 c_{\max}\xi^2\right), & \xi > \min\left\{\dfrac{1}{\sqrt{\theta_0 c_1}}, \dfrac{1}{\sqrt{\theta_0 c_2}}\right\}. \end{cases} \tag{38}$$

The sliding variable s converges to the region given by (39) in the fixed time:

$$\Delta s = \min\left\{2^{1/2}\left(\frac{v}{3^{(1-\gamma_1)/2}\eta_1}\right)^{1/(\gamma_1+1)}, 2^{1/2}\left(\frac{v}{\eta_2}\right)^{1/(\gamma_2+1)}\right\}. \tag{39}$$

Moreover, the sliding variable s in (7) is rewritten as follows:

$$\dot{e} + k_1 \mathrm{sig}^{a_1} e + k_2 \mathrm{sig}^{a_2} e = \varepsilon, \tag{40}$$

where $|\varepsilon| \le \Delta s$.

According to Lemma 3, the attitude error convergence is fixed time, and the attitude error converges to the following region in the fixed time:

$$|e| \le \min\left\{\left(\frac{\varepsilon}{k_1}\right)^{1/a_1}, \left(\frac{\varepsilon}{k_2}\right)^{1/a_2}\right\}. \tag{41}$$

Based on (40), the convergence region of angular velocity error is given by

$$|\dot{e}| \le |\varepsilon| + k_1|e|^{a_1} + k_2|e|^{a_2} \le 3\Delta s. \tag{42}$$

According to Lemma 2, the setting time upper boundary of the sliding variable s in the reaching phase is given by

$$T_r < \frac{2}{3^{(1-\gamma_1)/2}\eta_1(\gamma_1 - 1)} + \frac{2}{\eta_2(1-\gamma_2)}. \tag{43}$$

The setting time upper bound of the attitude and angular velocity errors in the sliding phase is given by

$$T_s < \frac{1}{2^{(a_1+1)/2}} \frac{2}{k_1(a_1-1)} + \frac{1}{2^{(a_2+1)/2}} \frac{2}{k_2(1-a_2)}. \tag{44}$$

Then, the system setting time T is depicted as

$$T < T_r + T_s = \frac{2}{3^{(1-\gamma_1)/2}\eta_1(\gamma_1-1)} + \frac{2}{\eta_2(1-\gamma_2)} + \frac{1}{2^{(a_1+1)/2}} \frac{2}{k_1(a_1-1)} + \frac{1}{2^{(a_2+1)/2}} \frac{2}{k_2(1-a_2)}. \tag{45}$$

In terms of former analysis, the sliding variable s, attitude error e, and angular velocity $\dot{e}$ are uniformly ultimately bounded in a fixed time. This completes the proof.

Remark 1. From (43) and (44), it is seen that the setting time is upper bounded and independent of initial conditions, such as the initial attitude, but depends on the designed parameters, such as k_1, k_2, a_1, a_2, γ_1, γ_2, η_1, and η_2.

Remark 2. From (43) and (44), large $k_1, k_2, a_1, \gamma_1, \eta_1$, and η_2 and less a_2 and γ_2 will reduce the setting time. However, too large parameter values of $k_1, k_2, a_1, \gamma_1, \eta_1$, and η_2 may lead to a high controller gain. Consequently, the parameter values should be chosen appropriately with a trade-off between the settling time and controller gain.

5. Experiment Results

5.1. Description of the Twin-Rotor Equalizing Bar System. To verify the applicability of the proposed control scheme, a twin-rotor equalizing bar platform is built based on $STM32F103C8T6$ and employed as the test rig, as shown in Figure 2, which includes two BLDC motors ($X2212$) , two ESRs ($SKYWALKER40A$), a DC adapter, a Gyro module ($WT931$), a CU ($STM32F103C8T6$) performing controller, a host Lenovo $W520$ workstation operating for display and data analysis, and two universal serial bus (USB) communication circuits receiving and sending the data between the host and the CU. The proposed control scheme is implemented via a C program in the Keil IDE uVision V5.21 Evaluation in the CU.

In the experiments, the data transmission baud rate between the twin-rotor and the host PC is 921600 bps, and 38 variables from the twin-rotor to the host PC with 8 bytes per variable are transferred within 6 ms of the sampling period. It spends about 3.6 ms to complete a cycle data transmission. Furthermore, the direct memory access (DMA) in CU is adopted to realize data sending and receiving without affecting other software operation. Consequently, the data transmission is reliable and timely. The Gyro module $W931T$ with an attitude dynamic precision 0.1° and an angular velocity range ±1000°/s meets the requirements of the practical application.

This test rig is employed to implement the transient performance control for given attitude references. Only the pitch axis is used in the experiments, and a sampling rate of 6 ms is selected, which is significantly faster than the later considered closed-loop demand frequencies.

The procedure of conducting an experiment is depicted in the following steps:

(1) Adjust a location screw to set the proper initial attitude

(2) Turn on the CU power and the ESR DC adapter power in sequence

(3) Compile the control schemes and download the compiling code to the CU via the $STlinkV2$ debugger

(4) Send a standby message 0x00 0x01 to the CU via the USB1 interface

(5) Send a run operation code 0x00 0x02 to perform the control schemes

(6) The test data will be on display in the host and saved as a text file

(7) After finishing the experiment, transmit a terminal message 0x00 0x00, close all of powers, and restore to the initial states

5.2. Design of Comparative Controllers. Comparative the control scheme experiments are conducted in the CU. To validate the effectiveness of the control scheme transient performance and the fixed-time property, three different control schemes are arranged, including ($M1$) adaptive

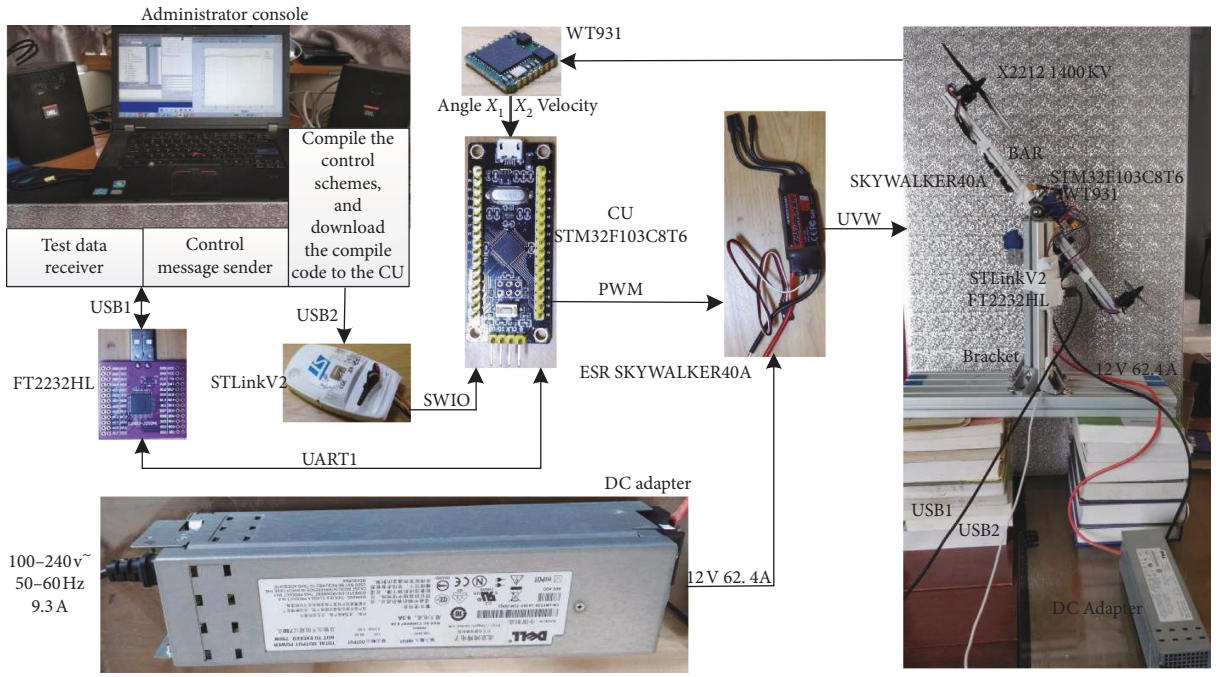

Figure 2: Diagram of the twin-rotor equalizing bar platform.

Table 1: M1 parameters.

Parameter	Value
k_1	3.0
k_2	3.0
a_1	23.0/17.0
a_2	17.0/23.0
μ	0.1
α	0.02307
β	0.1725
γ_1	21.0/17.0
γ_2	11.0/17.0
θ_0	0.692
θ_1	0.6
θ_2	0.6
p_1	0.45
p_2	0.45
$\widehat{F}_0$	10.0
$\widehat{D}_0$	10.0

Table 2: M2 parameters.

Parameter	Value
k_1	3.0
k_2	3.0
a_2	17.0/23.0
μ	0.1
α	0.02307
β	0.1725
γ_2	11.0/17.0
θ_0	0.692
θ_1	0.6
θ_2	0.6
p_1	0.45
p_2	0.45
$\widehat{F}_0$	10.0
$\widehat{D}_0$	10.0

fixed-time sliding mode control, ($M2$) adaptive finite-time sliding mode control [34], and ($M3$) adaptive linear sliding mode control [35]. Adaptive items are adopted to approximate model uncertainties and external disturbances, and a switching scheme is taken to solve the singularity problem of sliding manifold and control laws. For fair comparison, the corresponding parameters in three different control schemes are defined as the same.

5.2.1. Adaptive Fixed-Time Sliding Mode Control. In M1, the sliding variable is designed as (11), the control law is addressed by (13), and the adaptive update laws are depicted in (14) and (15), respectively, and the parameters are listed in Table 1, where $\widehat{F}_0$, $\widehat{D}_0$ are the initial values of $\widehat{F}$, $\widehat{D}$.

5.2.2. Adaptive Finite-Time Sliding Mode Control. In M2, the fast terminal sliding variable is selected as

$$s = \dot{e} + k_1 e + k_2 \phi(e), \tag{46}$$

where $k_1 > 0$, $k_2 > 0$, and $\phi(e)$ is the same as (9).

The control law is

$$u = -\frac{1}{b}\Big(k_1 \dot{e} + k_2 \dot{\phi}(e) - \ddot{x}_d + \alpha s + \beta \operatorname{sig}^{\gamma_2} s + \widehat{F} \operatorname{sgn}(s) + \widehat{D} \operatorname{sgn}(s)\Big), \tag{47}$$

where $\alpha > 0$, $\beta > 0$, $0 < \gamma_2 < 1$, and $\dot{\phi}(e)$ is expressed in (10).

The adaptive update laws are defined as

Table 3: M3 parameters.

Parameter	Value
k_1	3.0
α	0.02307
θ_1	0.6
θ_2	0.6
p_1	0.45
p_2	0.45
$\hat{F}_0$	10.0
$\hat{D}_0$	10.0

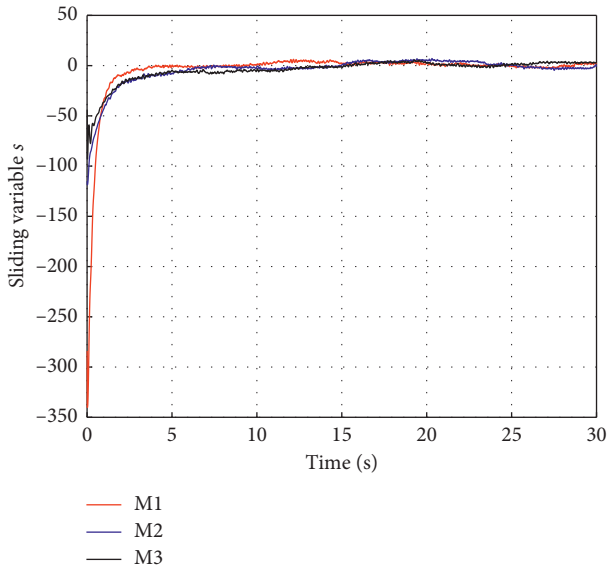

Figure 3: Time response of the sliding variable s under the initial value (i).

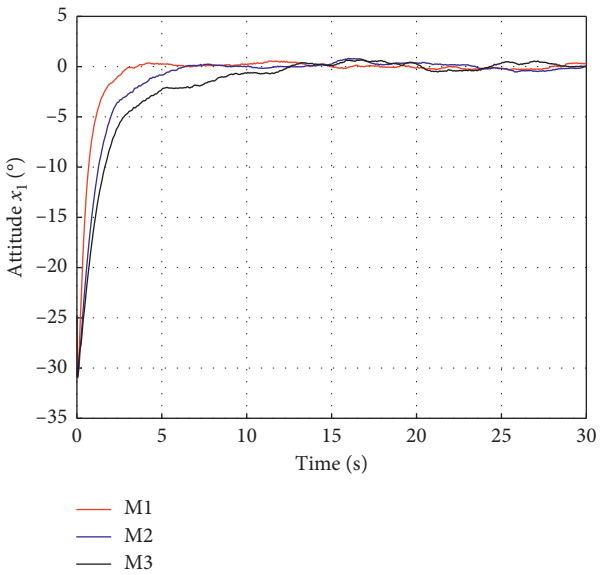

Figure 4: Time response of the attitude x_1 under the initial value (i).

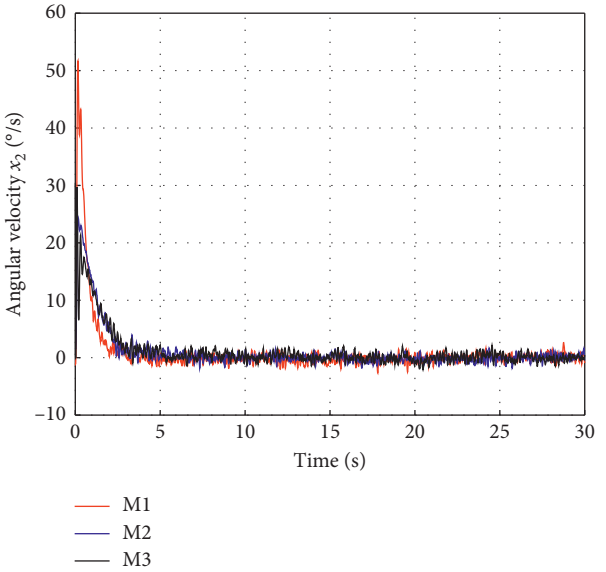

Figure 5: Time response of the angular velocity x_2 under the initial value (i).

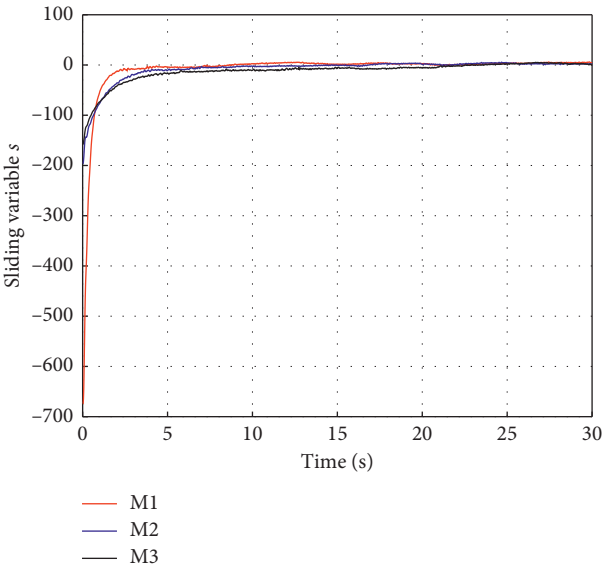

Figure 6: Time response of the sliding variable s under the initial value (ii).

$$\dot{\hat{F}} = \frac{1}{\theta_0 c_1}\left(|s| - p_1 \hat{F}\right), \tag{48}$$

$$\dot{\hat{D}} = \frac{1}{\theta_0 c_2}\left(|s| - p_2 \hat{D}\right), \tag{49}$$

where $p_1 > 0$, $p_2 > 0$, $\theta_1 > (1/2)$, $\theta_2 > (1/2)$, $c_1 = ((2\theta_1 - 1)p_1)/2\theta_1$, $c_2 = ((2\theta_2 - 1)p_2)/2\theta_2$, and θ_0 satisfying $((1/2)\theta_0)^{(\gamma_2+1)/2} + (1/2)\theta_0 - 1 = 0$. The parameters are listed in Table 2.

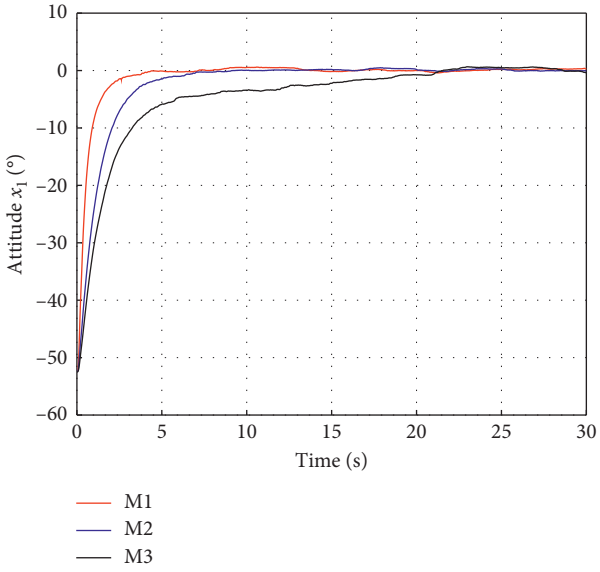

Figure 7: Time response of the attitude x_1 under the initial value (ii).

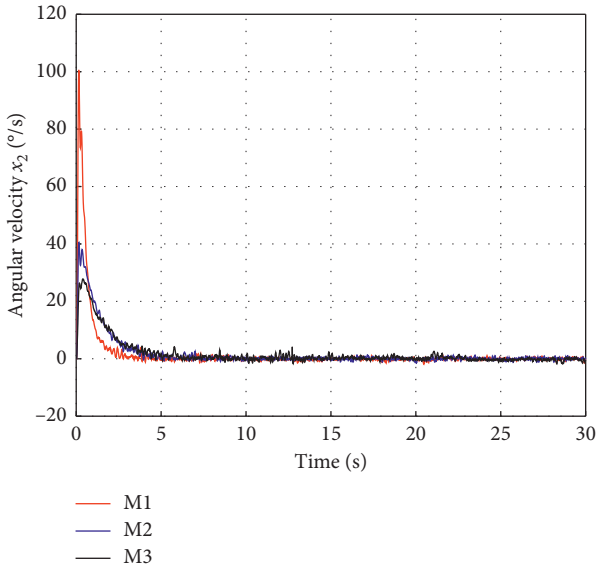

Figure 8: Time response of the angular velocity x_2 under the initial value (ii).

5.2.3. Adaptive Linear Sliding Mode Control. The sliding variable of M3 is given as

$$s = \dot{e} + k_1 e. \tag{50}$$

The control law is expressed as

$$u = -\frac{1}{b}\left(k_1\dot{e} - \ddot{x}_d + \alpha s + \hat{F}\,\mathrm{sgn}(s) + \hat{D}\,\mathrm{sgn}(s)\right). \tag{51}$$

The adaptive update laws are acquired by

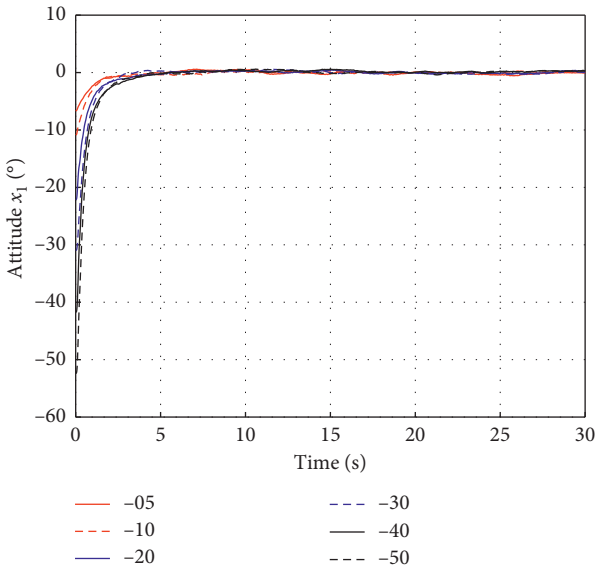

Figure 9: Time response of attitude in M1 under different initial values.

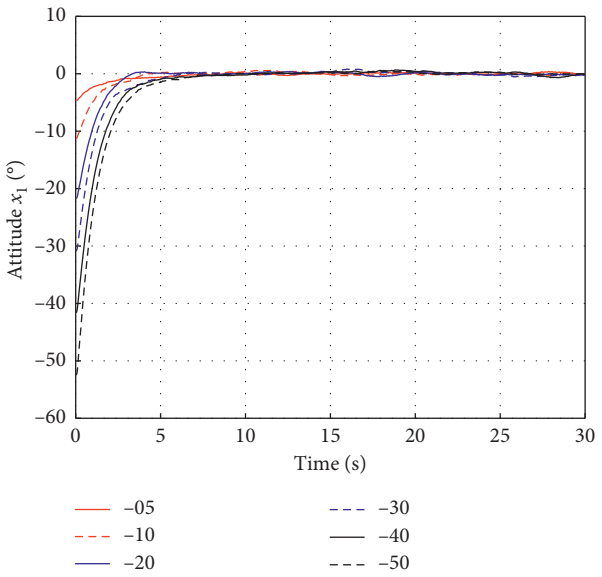

Figure 10: Time response of attitude in M2 under different initial values.

$$\dot{\hat{F}} = \frac{1}{c_1}\left(|s| - p_1\hat{F}\right), \tag{52}$$

$$\dot{\hat{D}} = \frac{1}{c_2}\left(|s| - p_2\hat{D}\right), \tag{53}$$

where $p_1 > 0$, $p_2 > 0$, $\theta_1 > (1/2)$, $\theta_2 > (1/2)$, $c_1 = ((2\theta_1 - 1)p_1)/2\theta_1$, and $c_2 = ((2\theta_2 - 1)p_2)/2\theta_2$, and the design parameters are listed in Table 3.

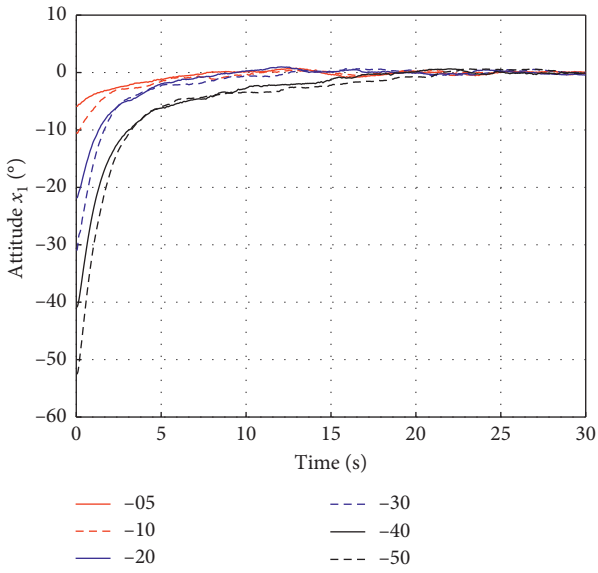

Figure 11: Time response of attitude in M3 under different initial values.

5.3. Comparative Results. For the system given by (1), the compared experiments are based on the different initial values of attitude $x_1(0)$, i.e.,

(i) $x_1(0) = -30^\circ$

(ii) $x_1(0) = -50^\circ$

The experiment results are shown in Figures 3–5. Figures 3–5 depict the time response of the sliding variable, attitude, and angular velocity for M1–M3 control schemes under the initial value (i), respectively. Compared with M2 and M3, the proposed M1 could achieve less reaching time and faster convergence speed as shown in Figures 3–5.

The time response of the sliding variable, attitude, and angular velocity for M1–M3 control schemes under the initial value (ii) is shown in Figures 6–8, respectively. From Figures 6–8, the convergence time of M1 is irrelevant to the initial states, but the convergence time of M2 and M3 is related to the initial states of the twin-rotor system.

To further illustrate the transient performance, based on six different initial attitude values, the time response of system states in the experiments is shown in Figures 9–11. The attitude convergence time of M1 in Figure 9 is almost unchanged, the attitude convergence time of M2 in Figure 10 is about 6.5 s to 9.4 s, and the attitude of M3 is asymptotic convergence in Figure 11.

From Figures 3–11, it is shown that less reaching time and faster convergence speed could be guaranteed with the proposed M1.

6. Conclusion

This paper proposed an adaptive fixed-time control scheme for the uncertain twin-rotor systems. A fixed-time sliding mode controller is designed, and the sliding variable and tracking error are both guaranteed to be uniformly ultimately bounded within the fixed time, which is independent of the initial values. With the proposed control scheme, the prior knowledge on the system uncertainties and disturbances is not needed, and the upper bounds of the lumped uncertainties could be estimated by developing the adaptive update laws. The effectiveness of the proposed control scheme is verified on a twin-rotor platform, and comparative experimental results illustrate the superior performance of the presented scheme.

Data Availability

The data used to support the findings of the study are available from the corresponding author upon request.

Conflicts of Interest

The authors declare that there are no conflicts of interest regarding the publication of this paper.

Acknowledgments

This study was supported by the National Natural Science Foundation of China (Project nos. 61873239, 61473262, and 61973274) and Zhejiang Provincial Natural Science Foundation (no. LY17F030018).

References

[1] A. Tayebi and S. McGilvray, "Attitude stabilization of a VTOL quadrotor aircraft," *IEEE Transactions on Control Systems Technology*, vol. 14, no. 3, pp. 562–571, 2006.

[2] Q. Chen, L. Shi, J. Na, X. Ren, and Y. Nan, "Adaptive echo state network control for a class of pure-feedback systems with input and output constraints," *Neurocomputing*, vol. 275, no. 1, pp. 1370–1382, 2018.

[3] M. Fanni and A. Khalifa, "A new 6-DOF quadrotor manipulation system: design, kinematics, dynamics, and control," *IEEE/ASME Transactions on Mechatronics*, vol. 22, no. 3, pp. 1315–1326, 2017.

[4] F. Cheng, L. Qu, W. Qiao, C. Wei, and L. Hao, "Fault diagnosis of wind turbine gearboxes based on dfig stator current envelope analysis," *IEEE Transactions on Sustainable Energy*, vol. 10, no. 3, pp. 1044–1053, 2019.

[5] C. Wei, M. Benosman, and T. Kim, "Online parameter identification for state of power prediction of lithium- ion batteries in electric vehicles using extremum seeking," *International Journal of Control, Automation and System*, pp. 1–11, 2019.

[6] B. Xiao and S. Yin, "A new disturbance attenuation control scheme for quadrotor unmanned aerial vehicles," *IEEE Transactions on Industrial Informatics*, vol. 13, no. 6, pp. 2922–2932, 2017.

[7] J. Na, Y. Li, Y. Huang, G. Gao, and Q. Chen, "Output feedback control of uncertain hydraulic servo systems," *IEEE Transactions on Industrial Electronics*, vol. 67, no. 1, pp. 490–500, 2019.

[8] B. Zhao, B. Xian, Y. Zhang, and X. Zhang, "Nonlinear robust sliding mode control of a quadrotor unmanned aerial vehicle based on immersion and invariance method," *International Journal of Robust and Nonlinear Control*, vol. 25, no. 18, pp. 3714–3731, 2015.

[9] B. Zhao, B. Xian, Y. Zhang, and X. Zhang, "Nonlinear robust adaptive tracking control of a quadrotor UAV via immersion

and invariance methodology," *IEEE Transactions on Industrial Electronics*, vol. 62, no. 5, pp. 2891–2902, 2015.

[10] R. Sun, J. Na, and B. Zhu, "Robust approximation-free prescribed performance control for nonlinear systems and its application," *International Journal of Systems Science*, vol. 49, no. 3, pp. 511–522, 2018.

[11] M. Sun, T. Wu, L. Chen, and G. Zhang, "Neural AILC for error tracking against arbitrary initial shifts," *IEEE Transactions on Neural Networks and Learning Systems*, vol. 29, no. 7, pp. 2705–2716, 2018.

[12] J. Na, A. S. Chen, G. Herrmann, R. Burke, and C. Brace, "Vehicle engine torque estimation via unknown input observer and adaptive parameter estimation," *IEEE Transactions on Vehicular Technology*, vol. 67, no. 1, pp. 409–422, 2018.

[13] Q. Chen, H. Shi, and M. Sun, "Echo state network-based backstepping adaptive iterative learning control for strict-feedback systems: an error-tracking approach," *IEEE Transactions on Cybernetics*, pp. 1–14, 2019.

[14] S. Ding, K. Mei, and S. Li, "A new second-order sliding mode and its application to nonlinear constrained systems," *IEEE Transactions on Automatic Control*, vol. 64, no. 6, pp. 2545–2552, 2019.

[15] Q. Chen, L. Tao, Y. Nan, and X. Ren, "Adaptive nonlinear sliding mode control of mechanical servo system with lugre friction compensation," *Journal of Dynamic Systems, Measurement and Control*, vol. 138, no. 2, Article ID 021003–1–9, 2016.

[16] Q. Chen, X. Ren, and J. Na, "Robust finite-time chaos synchronization of uncertain permanent magnet synchronous motors," *ISA Transactions*, vol. 58, no. 9, pp. 262–269, 2015.

[17] Q. Chen, X. Ren, J. Na, and D. Zheng, "Adaptive robust finite-time neural control of uncertain PMSM servo system with nonlinear dead zone," *Neural Computing and Applications*, vol. 28, no. 12, pp. 3725–3736, 2017.

[18] J. Yu, P. Shi, and L. Zhao, "Finite-time command filtered backstepping control for a class of nonlinear systems," *Automatica*, vol. 92, pp. 173–180, 2018.

[19] L. Fang, L. Ma, S. Ding, and D. Zhao, "Finite-time stabilization for a class of high-order stochastic nonlinear systems with an output constraint," *Applied Mathematics and Computation*, vol. 358, pp. 63–79, 2019.

[20] H. Gui, L. Jin, and S. Xu, "Simple finite-time attitude stabilization laws for rigid spacecraft with bounded inputs," *Aerospace Science and Technology*, vol. 42, pp. 176–186, 2015.

[21] Z. Chen, Q. Chen, X. He, and M. Sun, "Adaptive finite-time command filtered fault-tolerant control for uncertain Spacecraft with Prescribed Performance," *Complexity*, vol. 2018, Article ID 4912483, 12 pages, 2018.

[22] B. Tian, L. Liu, H. Lu, Z. Zuo, Q. Zong, and Y. Zhang, "Multivariable finite time attitude control for quadrotor UAV: theory and experimentation," *IEEE Transactions on Industrial Electronics*, vol. 65, no. 3, pp. 2567–2577, 2018.

[23] H. Wang, X. Ye, Y. Tian, G. Zheng, and N. Christov, "Model-free-based terminal SMC of quadrotor attitude and position," *IEEE Transactions on Aerospace and Electronic Systems*, vol. 52, no. 5, pp. 2519–2528, 2016.

[24] B. Mu, K. Zhang, and Y. Shi, "Integral sliding mode flight controller design for a quadrotor and the application in a heterogeneous multi-agent system," *IEEE Transactions on Industrial Electronics*, vol. 64, no. 12, pp. 9389–9398, 2017.

[25] S. Wang, H. Yu, J. Yu, J. Na, and X. Ren, "Neural-network-based adaptive funnel control for servo mechanisms with unknown dead-zone," *IEEE Transactions on Cybernetics*, pp. 1–12, 2018.

[26] J. Na, S. Wang, Y.-J. Liu, Y. Huang, and X. Ren, "Finite-time convergence adaptive neural network control for nonlinear servo systems," *IEEE Transactions on Cybernetics*, pp. 1–12, 2019.

[27] J. Na, Y. Huang, X. Wu, G. Gao, G. Herrmann, and J. Z. Jiang, "Active adaptive estimation and control for vehicle suspensions with prescribed performance," *IEEE Transactions on Control Systems Technology*, vol. 26, no. 6, pp. 2063–2077, 2018.

[28] A. Polyakov, "Nonlinear feedback design for fixed-time stabilization of linear control systems," *IEEE Transactions on Automatic Control*, vol. 57, no. 8, pp. 2106–2110, 2012.

[29] Q. Chen, M. Gao, L. Tao, and Y. Nan, "Adaptive fixed time parameter estimation and synchronization control for multiple robotic manipulators," *International Journal of Control, Automation and Systems*, vol. 17, no. 9, pp. 2375–2387, 2019.

[30] Q. Chen, S. Xie, M. Sun, and X. He, "Adaptive nonsingular fixed-time attitude stabilization of uncertain spacecraft," *IEEE Transactions on Aerospace and Electronic Systems*, vol. 54, no. 6, pp. 2937–2950, 2018.

[31] M. Tao, Q. Chen, X. He, and M. Sun, "Adaptive fixed-time fault-tolerant control for rigid spacecraft using a double power reaching law," *International Journal of Robust and Nonlinear Control*, vol. 29, no. 12, pp. 4022–4040, 2019.

[32] M. Sun, "Two-phase attractors for finite-duration consensus of multiagent systems," *IEEE Transactions on Systems, Man, and Cybernetics: Systems*, pp. 1–9, 2018.

[33] Z. Zuo, "Non-singular fixed-time terminal sliding mode control of non-linear systems," *IET Control Theory & Applications*, vol. 9, no. 4, pp. 545–552, 2015.

[34] L. Yang and J. Yang, "Nonsingular fast terminal sliding-mode control for nonlinear dynamical systems," *International Journal of Robust and Nonlinear Control*, vol. 21, no. 16, pp. 1865–1879, 2011.

[35] S. Yu, X. Yu, B. Shirinzadeh, and Z. Man, "Continuous finite-time control for robotic manipulators with terminal sliding mode," *Automatica*, vol. 41, no. 11, pp. 1957–1964, 2005.

Hindawi
Complexity
Volume 2019, Article ID 3760401, 14 pages
https://doi.org/10.1155/2019/3760401

Research Article

Finite-Time Observer-Based Adaptive Control of Switched System with Unknown Backlash-Like Hysteresis

Guofa Sun and Yaming Xu

School of Information and Control Engineering, Qingdao University of Technology, Qingdao 266520, China

Correspondence should be addressed to Yaming Xu; xuyaming2000@163.com

Received 24 July 2019; Revised 6 September 2019; Accepted 26 September 2019; Published 29 October 2019

Guest Editor: Chun Wei

This work investigates a finite-time observer problem for a class of uncertain switched nonlinear systems in strict-feedback form, preceded by unknown hysteresis. By using a finite-time performance function, a finite-time switched state observer (FTSO) is derived using radial basis function neural networks (RBFNNs) to estimate the unmeasured states. An adaptive feedback neural network tracking control is derived based on the backstepping technique, which guarantees that all the signals of the closed-loop system are bounded, the output tracking error converges to zero, and the observer error converges to a prescribed arbitrarily small region within a finite-time interval. In addition, two simulation studies and an experiment test are provided to verify the feasibility and effectiveness of the theoretical finding in this study.

1. Introduction

In the past decades, great attentions and developments have been gained in finite-time adaptive control design, which developed a great number of typical design approaches in the literature (see, e.g., [1–15]). A variety of different types of complex nonlinear systems have been explored by using neural networks or the fuzzy logic system-based adaptive backstepping technique. For instance, in [1–3], by utilizing the finite-time stability theory, barrier Lyapunov functions, and the adaptive backstepping method, various finite-time adaptive control strategies were proposed with unknown dead-zone, unknown hysteresis, and unknown time-delayed in the nonlinear system, respectively. Considering the full-state constraints in the nonlinear systems, an adaptive fuzzy controller was constructed to address the finite-time tracking control problem for a class of strict-feedback nonlinear systems in [4]. Besides, Wang et al. [5] developed a novel adaptive neural finite-time control strategy which considered quantized problems for single-input and single-output quantized nonlinear systems. Meanwhile, growth condition assumption was removed under the presented control approach. That assumption was also eliminated in [6]. Li et al. [6] presented a finite-time fuzzy adaptive output feedback control for the first time for nonstrict-feedback nonlinear systems, while it overcame the problem of explosion of complexity by using the dynamic surface control technique. Moreover, Yu et al. [7] investigated an adaptive finite-time quantized tracking problem with input and output quantization and asymmetric actuator saturation, and they designed an observer-based adaptive finite-time quantized tracking controller at the same time. In [8], Liu et al. studied a finite-time adaptive fuzzy tracking control problem and proposed a finite-time adaptive state feedback fuzzy tracking controller with a new concept named finite-time performance function. Although a novel assessment standard of the finite-time semiglobal practical stability (SGPS) was found in [1–8], the main innovations of those literatures are designed controllers for nonswitched systems. Sui et al. [9] solved a finite-time switching control issue for nonstrict-feedback nonlinear switched systems, and they also constructed a novel finite-time SGPS for switched systems. Meanwhile, by utilizing a comparison theorem and a mean value theorem of integrals, a significant finite-time stability criterion for stochastic nonlinear systems was first set up in [10]. Chen et al. [11] studied an adaptive finite-time

synchronization controller given for multiple robotic manipulators. It was worth noting that there existed some controllers to solve finite-time control problems in [12–15].

As a class of nonlinear inputs, hysteresis widely exists in the industrial system. Besides, the nonlinear characteristics of backlash-like hysteresis could seriously affect tracking performance, and it may cause a severe effect on the whole system. To capture hysteresis dynamics and achieve precise control, many scholars have made efforts to eliminate its effect. The hysteresis models can be roughly divided into two classes in [16, 17]: the operator-based hysteresis model [17–19] and the differential equation-based hysteresis model, such as Bouc–Wen model [20, 21] and backlash-like model [22–26]. For instance, in [18], Mayergoyz described a new approach to the scalar Preisach model of hysteresis which emphasized its phenomenological nature and mathematical generality. Zhang et al. [19] designed a hysteresis compensator to compensate the hysteresis nonlinearity described by a generalized PI hysteresis model, and the Krasnoselskii–Pokrovskii model was applied in [17]. The modeling accuracy can be guaranteed by increasing the number of superposed elementary operators for the operator-based hysteresis model, but also cause the computational burden during implementation. We continue to investigate the backlash-like hysteresis model in this paper since it has fewer parameters and has analytical solution. In [22], Ma et al. dealt with adaptive control for a class of switched nonlinear systems preceded by unknown backlash-like hysteresis, where the hysteresis was modeled by a differential equation. Similarly, Li et al. [23] investigated an adaptive neural output feedback control for a class of nonlinear systems with unknown backlash-like hysteresis of the actuator. Zhang and Lin [24] proposed a robust adaptive DSC control for a class of uncertain perturbed strict-feedback nonlinear systems preceded by unknown backlash-like hysteresis. On one hand, it is an active issue to study the systems with hysteresis nonlinearities which exist widely in the practical systems, such as manipulator system [22, 27], four-motor servomechanism [28, 29], and electrical circuit [30]. On the other hand, to date, there are no systematic methods to achieve a satisfactory result on finite-time switched state estimate of switched nonlinear systems with backlash-like hysteresis, which motivates our research interest. Hence, considering the inevitability of the backlash-like hysteresis constraint in many practical applications, it is worth further studying how to design a finite-time switched state observer (FTSO) for switched strict-feedback nonlinear systems with unknown backlash-like hysteresis.

During the development of control and applications, there exists a design algorithm which links observer design and hysteresis compensation. In [31], a novel hysteresis compensation method based on extended high-gain observer was presented without any specific hysteresis models. Besides, there exist several seminal observers designed with a system of hysteresis results [30, 32–34]. Huo et al. proposed an MIMO switched fuzzy observer to estimate the system states with hysteresis nonlinearities, which was less conservative than using a common observer for all subsystems. As stated in [33], they addressed the consensus tracking problem of a class of nonlinear multiagent system with hysteresis. And then, they developed a distributed adaptive neural output feedback control scheme proposed by constructing a state observer and using the backstepping technique. In order to improve the functional approximation capability and disturbance compensation ability for a system with unknown backlash-like hysteresis, Wang et al. [34] considered the coupler design between the radial basis function neural network and observer. Wei et al. [30] presented an extremum seeking algorithm to accurately estimate the state-of-power by an electrical circuit incorporating hysteresis effect. However, those contributions in [30–34] do not include finite-time convergence of observers, which further improves the tracking effect of the control strategy.

This study considers the finite-time adaptive switched observer problem for a kind of nonlinear systems with unknown hysteresis from a new perspective. Based on RBFNN approximation and finite-time performance function, the FTSO is proposed, which guarantees that observer error converge to a small neighborhood of the origin point in finite-time. Meanwhile, an adaptive tracking neural network controller is designed by the backstepping technique, which guarantees that all the signals of the switched closed-loop system are bounded and the observation error is converged to a small neighborhood of the origin point in a finite time. Compared with the existing results, the prominent contributions of this work are as follows:

(1) This paper proposes design process of a novel finite-time switched state observer which is designed to improve control performances for the switched system with unknown backlash-like hysteresis. In contrast with [1–15] which studies finite-time adaptive tracking controller, the smaller tracking error will be achieved with an FTSO for the same controller. In addition, with the presented control approach, all known state assumptions are removed by using the FTSO.

(2) To the best of our knowledge, it is the first time that the finite-time convergence problem of observer error is taken into consideration in a class of uncertain switched nonlinear systems with unknown backlash-like hysteresis, by using a finite-time performance function to obtain a better tracking performance. For switched systems with unknown backlash-like hysteresis, a control strategy with the FTSO can be applied more effectively and exactly.

This paper is organized as follows. Sections 2 presents the problem and the preliminaries. In Section 3, an adaptive finite-time switched state observer is designed. Section 4 draws control design and stability analysis. Simulation studies are conducted in Section 5 to illustrate the effectiveness of the proposed scheme. Finally, the paper is ended by concluding remarks in Section 6.

2. Problem Formulation and Preliminaries

This section begins by presenting the control problem for a class of uncertain switched nonlinear systems with unknown

backlash-like hysteresis. Then, it reviews some preliminaries about RBFNNs to facilitate the proposed observer and controller design procedure. Finally, a finite-time performance function is given to ensure observer error finite-time convergence.

2.1. Proposed System Descriptions. Consider a class of switched strict-feedback nonlinear systems with unknown hysteresis in the form of

$$\begin{cases} \dot{x}_i = g_{i,\sigma(t)} x_{i+1} + f_{i,\sigma(t)}(\overline{x}_i) + d_{i,\sigma(t)}(t), \\ \dot{x}_n = g_{n,\sigma(t)} u(v) + f_{n,\sigma(t)}(\overline{x}_n) + d_{n,\sigma(t)}(t), \\ y = x_1, \end{cases} \tag{1}$$

where $\overline{x}_i = [x_1, x_2, \cdots, x_i]^T \in R^i$, $i = 1, 2, \cdots, n-1$, denotes the vectors of system states, $y \in R$ is the output of the switched nonlinear system, $f_i(\cdot)$ are smooth unknown nonlinear functions, and g_i are known constants and $g_i \neq 0$. $\sigma(t) : [0, \infty) \longrightarrow M = \{1, \ldots, m\}$ expressing the switching signal, which is a piecewise right continuous function. In addition, $\sigma(t) = j$ denotes the j^{th} subsystem. $d_i(t)$ stands for the bounded external disturbance. $u(v) \in R$ is the output signal of backlash-like hysteresis described as

$$\dot{u} = \alpha|\dot{v}|(cv - u) + b\dot{v}, \tag{2}$$

where v indicates the input of the unknown backlash-like hysteresis. α, c, and b are unknown constants with $c > b$.

It follows from the analysis in [22, 23, 35] that the solution of system (2) is expressed as

$$u(t) = cv(t) + l(v), \tag{3}$$

where $l(v)$ is bounded and satisfies

$$l(v) = (u_0 - cv_0)e^{-\alpha(v - v_0)\operatorname{sgn}\dot{v}} + e^{-\alpha v \operatorname{sgn}\dot{v}} \int_{v_0}^{v} (b - c)e^{\alpha\xi \operatorname{sgn}\dot{v}} d\xi, \tag{4}$$

where u_0 and v_0 are the initial values of u and v, respectively.

Figure 1 shows that a typical backlash-like hysteresis is generated. By (3), rewrite (1) as

$$\begin{cases} \dot{x}_i = g_{i,j} x_{i+1} + f_{i,j}(\overline{x}_i) + d_{i,j}(t), \\ \dot{x}_n = b_{0,j} v(t) + F_{n,j}(\overline{x}_n) + d_{n,j}(t), \\ y = x_1, \end{cases} \tag{5}$$

with $F_n(\overline{x}_{n,j}) = f_{n,j}(\overline{x}_n) + g_{n,j} l(v)$ and $b_{0,j} = g_{n,j} c$.

This paper aims to derive an FTSO-based adaptive neural control signal v for nonlinear system (1) with unknown backlash-like hysteresis (2), so that the following objectives can be achieved:

(1) Observer errors converge to an arbitrarily small specified neighborhood at a finite-time

(2) All the variables of the closed-loop system are bounded, and the tracking errors could converge to an arbitrarily small specified neighborhood

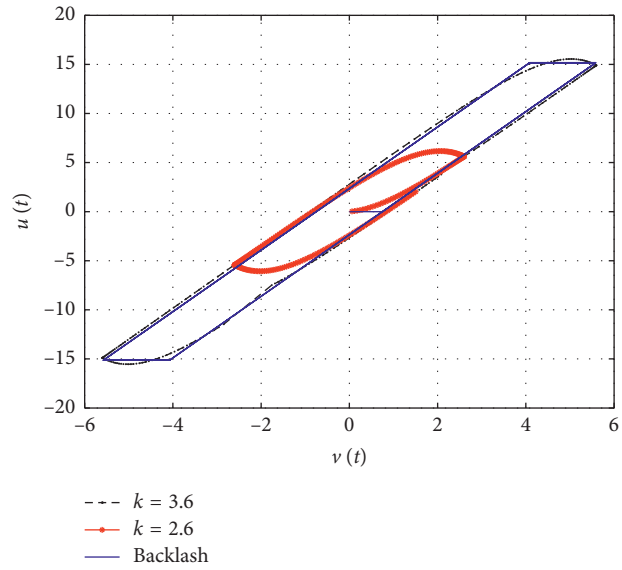

Figure 1: Hysteresis curves given by (2) with $\alpha = 1, c = 3.1635$, and $b = 0.345$ for $v(t) = k\sin(2.3t)$ with $k = 2.6$ (red solid line) and $k = 3.6$ (dashed line) to approximate backlash (blue solid line).

Lemma 1 (see [36, 37]). *For a nonlinear switching system of $t \in [0, T_f]$, $N_\sigma(t, T_f)$ denotes the number of times and $\sigma(t)$ switches within a time interval $[0, T_f]$. If*

$$N_\sigma(t, T_f) \leq N_0 + \frac{T_f - t}{\tau_a}, \tag{6}$$

where τ_a and N_0 are positive constants, then τ_a is average dwell time. In order to facilitate calculation, the buffeting bound N_0 is generally taken.

Lemma 2 (see [36, 37]). *A Lyapunov function candidate is defined as*

$$V_P = x^T P_{\sigma(t)} x, \quad \forall x \in R^n, \tag{7}$$

where $P_{\sigma(t)}$ is switched in accordance with the piecewise constant switching signal $\sigma(t)$. Then, the following properties are obtained:

(1) Each $V_{P\sigma(t)} = x^T P_{\sigma(t)} x$ in (7) is continuous. There exist constant scalars $\chi_2 \geq \chi_2 \geq 0$ such that

$$\chi_1(||x||) \leq V_{Pj}(x) \leq \chi_2(||x||), \quad \forall x \in R^n, \forall j \in M. \tag{8}$$

(2) There exist constant scalars $\zeta \geq 1$ such that

$$V_{Pi}(x) \leq \zeta V_{Pj}(x), \quad \forall x \in R^n, \forall i, j \in M. \tag{9}$$

2.2. Radial Basis Function Neural Networks. The RBFNN has the ability to approximate the unknown smooth function $F(X) : R^q \longrightarrow R$, and the form of $F(X)$ is as follows:

$$F(X) = \theta^T \phi(X) + \eta(X), \tag{10}$$

where $X = [X_1, \cdots, X_q]^T \in R^q$ and $\theta \in R^q$ are the weight vectors of the neural network, $\phi(X) = [\phi_1(X), \cdots, \phi_q(X)]^T \in R^q$ are the basis function vector of the neural network, and $\eta(X)$ is approximation error of neural network function, and $\eta(X)$ satisfies that $|\eta(X)| < \eta^*$, where η^* is the upper bound of the estimated error.

In the following, ϕ is used to represent $\phi(X)$ and η is used to represent $\eta(X)$, where the estimated error of the observer and the controller are expressed as η_o and η_C, respectively.

The RBFNN is an approximator for nonlinear smooth function $f_i(\overline{x}_i)$ which is approximated as

$$\begin{aligned} \widehat{f}_i\left(\widehat{\overline{x}}_i \,\middle|\, \widehat{\theta}_i\right) &= \theta_i^T \phi_i\left(\widehat{\overline{x}}_i\right), \\ \widehat{\overline{x}}_i &= [y, x2, \cdots, x_n]^T, \end{aligned} \tag{11}$$

where $\widehat{\overline{x}}_i$ is the estimation of $\overline{x}_i$.

The ideal parameter vectors θ_i^* are defined as

$$\theta_i^* = \arg\min_{\theta_i \in \Omega_i} \left[\sup_{\widehat{\overline{x}} \in U_i} \left| \widehat{f}_i\left(\widehat{\overline{x}}_i \,\middle|\, \widehat{\theta}_i\right) - f_i(\overline{x}_i) \right| \right], \tag{12}$$

where U_i and Ω_i are compact regions for $\widehat{x}_i$ and θ_i, respectively. Define the minimum approximation error η_i as

$$\eta_i = \widehat{f}_i\left(\widehat{\overline{x}}_i \,\middle|\, \theta_i^*\right) - f_i(\overline{x}_i). \tag{13}$$

Lemma 3 (see [38]). *The following inequality holds*

$$\phi^T(X)\phi(X) \le \frac{1}{\phi^T(\overline{x}_i)\phi(\overline{x}_i)}, \tag{14}$$

for any inter $i \le n$, where $\phi(\overline{x}_i) = [\pi_1(\overline{x}_i), \pi_2(\overline{x}_i), \cdots, \pi_N(\overline{x}_i)]^T / \sum_{k=1}^{N} \pi_k(\overline{x}_i)$ and $\pi_k(\overline{x}_i) = exp[-(\overline{x}_i - l_i)^T(\overline{x}_i - l_i)/2\gamma_i^2]$.

2.3. Finite-Time Performance Function

Definition 1. Different from a classical prescribed performance function in [39], a smooth function $\xi(t)$ is called finite-time performance function (FTPF) for all $\xi(0) = \xi_0$. There exists a settling time $0 < T_0 < \infty$, such that $\xi(t) < \xi(T_0) = \xi_{T_0}$, which is an arbitrarily small positive number. $\forall t \ge T_0 = \xi(t)$, in this work, is defined by

$$\xi(t) = \begin{cases} (\xi(0) - \tau\lambda t)^{1/\tau} + \xi_{T_0}, & 0 \le t \le T_0, \\ \xi_{T_0}, & t > T_0, \end{cases} \tag{15}$$

where $\lambda, \tau, \xi(0)$, and ξ_{T_0} are chosen as positive constants, and let $\tau = (q/p) \in (0, 1]$, where p and q are chosen positive constants. Moreover, it has $T_0 = \xi(0)/\tau\lambda$.

3. Finite-Time Switched State Observer Design

In this section, an FTSO is derived, involving the use of FTPF. Stability of the developed observer, estimating the states of switched nonlinear system (1) with unknown hysteresis (2), is proved by Lyapunov function.

For the switched nonlinear system (5), an FTSO is designed as follows:

$$\begin{cases} \varepsilon_1 = \widehat{x}_1 - x_1, \\ \dot{\widehat{x}}_1 = \alpha_1 + \widehat{f}_1\left(\widehat{\overline{x}}_1 \,\middle|\, \widehat{\theta}_1\right), \\ \alpha_1 = g_{1,j}\widehat{x}_2 - k_{1,j}\varepsilon_1, \\ \cdots \\ \varepsilon_i = \widehat{x}_i - \dfrac{\alpha_{i-1}}{g_{i-1,j}}, \\ \dot{\widehat{x}}_i = \alpha_i + \widehat{f}_i\left(\widehat{\overline{x}}_i \,\middle|\, \widehat{\theta}_i\right), \\ \alpha_i = g_{i,j}\widehat{x}_{i+1} - k_{i,j}\varepsilon_i, \quad i = 2, \cdots, n-1, \\ \cdots \\ \varepsilon_n = \widehat{x}_n - \dfrac{\alpha_{n-1}}{g_{n-1,j}}, \\ \dot{\widehat{x}}_n = \alpha_n + \widehat{F}_n\left(\widehat{\overline{x}}_i \,\middle|\, \widehat{\theta}_n\right) + b_{0,j}\nu, \\ \alpha_n = -k_{n,j}\varepsilon_n, \end{cases} \tag{16}$$

where $\widehat{x} = [\widehat{x}_1, \ldots, \widehat{x}_n]^T$ is the estimation of real system states. $g_{i,j} = [g_{1,j}, \ldots, g_{n,j}]^T$ and $k_{i,j} = [k_{1,j}, \ldots, k_{n,j}]^T$, $i = 1, \ldots, n$, are parameters to be designed. Furthermore, combining (16), the transfer error of the observer ε_i are further expressed as

$$\begin{cases} \varepsilon_1 = \widehat{x}_1 - x_1, \\ \varepsilon_i = \dfrac{\alpha_{i-1}k_{i-1,j}}{g_{i-1,j}}\varepsilon_{i-1}, \\ \varepsilon_n = \dfrac{\alpha_{n-1}k_{n-1,j}}{g_{n-1,j}}\varepsilon_{n-1}. \end{cases} \tag{17}$$

Further, define the observer error $\overline{e}_o$ as

$$\begin{cases} e_{o1} = \widehat{x}_1 - x_1, \\ e_{oi} = \widehat{x}_i - x_i, \\ e_{on} = \widehat{x}_n - x_n. \end{cases} \tag{18}$$

From (16) and (18), the differential with respect to t of $\overline{e}_o$ becomes

$$\begin{cases} \dot{e}_{o1} = g_{1,j}e_{o2} + \widetilde{\theta}_1^T\phi_1\left(\widehat{\overline{x}}_1\right) + \eta_1 - k_{1,j}\varepsilon_1, \\ \dot{e}_{oi} = g_{i,j}e_{o(i+1)} + \widetilde{\theta}_i^T\phi_i\left(\widehat{\overline{x}}_i\right) + \eta_i - k_{i,j}\varepsilon_i, \\ \dot{e}_{on} = \widetilde{\theta}_n^T\phi_n\left(\widehat{\overline{x}}_n\right) + \eta_n - k_{n,j}\varepsilon_n, \end{cases} \tag{19}$$

where $\widetilde{\theta}_i = \theta_i - \theta_i^*$ $(i = 1, \ldots, n)$ is the adaptive parameter error.

Define the error transform function $h(z_i)$ as

$$e_{oi} = \xi h(z_i), \tag{20}$$

where $h(z_i) = (2/\pi)\arctan(z_i)$. $h(z_i)$ is a smooth and strictly increasing function and $h(z_i) \in (-1, 1)$. It also satisfies $\lim_{z_i \longrightarrow +\infty} h(z_i) = 1$ and $\lim_{z_i \longrightarrow -\infty} h(z_i) = -1$. Define a new function as

$$L(z_i) = \frac{1}{2}\left(\frac{d(h(z_i))}{dz_i}z_i + h(z_i)\right), \tag{21}$$

which satisfies $L(z_a) > L(z_b)$, when $z_a > z_b$. Combining (20) and (21),

$$\frac{1}{2}(z_i + h(z_i)) > L(z_i) > \frac{1}{2}(h(z_i)). \tag{22}$$

Differentiating (20) with respect to t yields

$$\dot{e}_{oi} = \dot{\xi}h(z_i) + \xi\frac{\partial h(z_i)}{\partial z_i}\dot{z}_i. \tag{23}$$

Then, the dynamic system errors are expressed as

$$\begin{cases} \dot{z}_i = M(\xi, z_i)\left(g_{i,j}\xi h(z_{i+1}) - \prod_{i=1}^{n-1} k_{i,j}\xi h(z_1) - \dot{\xi}h(z_i)\right) \\ \quad + M(\xi, z_i)\left(\widetilde{\theta}_i^T\phi_i\left(\widehat{\overline{x}}_i\right) + \eta_i\right), \\ \dot{z}_n = M(\xi, z_i)\left(-\prod_{i=1}^{n} k_{i,j}\xi h(z_1) - \dot{\xi}h(z_n)\right) \\ \quad + M(\xi, z_n)\left(\widetilde{\theta}_n^T\phi_n\left(\widehat{\overline{x}}_n\right) + \eta_n\right), \end{cases} \tag{24}$$

where $M(\xi, z_i) = 1/\xi(\partial h(z_i)/\partial z_i)$.

Step 1. Construct a Lyapunov function candidate as

$$V_i = \frac{1}{M}z_i h(z_i) + \frac{1}{M}z_i^2, \quad i = 1, \ldots, n-1. \tag{25}$$

Differentiating (25),

$$\begin{aligned} \dot{V}_i &= -\left(\frac{1}{M}\right)^2\dot{M}z_i h(z_i) + \frac{1}{M}\left(\dot{z}_i h(z_i) + z_i\dot{z}_i\dot{h}(z_i)\right) \\ &\quad - \left(\frac{\dot{M}}{M^2}\right)z_i^2 + \frac{1}{M}z_i\dot{z}_i \\ &= -\left(\frac{\dot{M}}{M^2}\right)z_i h(z_i) - \left(\frac{\dot{M}}{M^2}\right)z_i^2 \\ &\quad + \left[g_{i,j}\xi h(z_{i+1}) - \prod_{i=1}^{i} k_i\xi h(z_1) - \dot{\xi}h(z_i)\right] \\ &\quad \cdot \left(h(z_i) + z_i\dot{h}(z_i)\right) \\ &\quad + \left(\widetilde{\theta}_i^T\phi_i\left(\widehat{\overline{x}}_i\right) + \eta_i\right)\left(h(z_i) + z_i\dot{h}(z_i)\right) \\ &\quad + z_i\left[g_{i,j}\xi h(z_{i+1}) - \prod_{i=1}^{i} k_{i,j}\xi h(z_1) - \dot{\xi}h(z_i)\right] \\ &\quad + z_i\left(\widetilde{\theta}_i^T\phi_i\left(\widehat{\overline{x}}_i\right) + \eta_i\right). \end{aligned} \tag{26}$$

Computing $(g_{i,j}\xi h(z_{i+1}) - \prod_{i=1}^{i} k_{i,j}\xi h(z_1) - \dot{\xi}h(z_i))(h(z_i) + z_i\dot{h}(z_i))$ gives

$$\begin{aligned} &\left(g_{i,j}\xi h(z_{i+1}) - \prod_{i=1}^{i} k_{i,j}\xi h(z_1) - \dot{\xi}h(z_i)\right)\left(h(z_i) + z_i\dot{h}(z_i)\right) \\ &= 2\left[g_{i,j}\xi h(z_{i+1}) - \prod_{i=1}^{i}\xi h(z_1) - \dot{\xi}h(z_i)\right]L(z_i) \\ &\le g_{i,j}\xi h(z_{i+1})(z_i + h(z_i)) \\ &\quad - \left(\prod_{i=1}^{i} k_{i,j}\xi h(z_1) + \dot{\xi}h(z_i)\right)h(z_i). \end{aligned} \tag{27}$$

Then, $(\widetilde{\theta}_1^T\phi_1(\widehat{\overline{x}}_1) + \eta_1)(h(z_1) + z_1\dot{h}(z_1))$ is rewritten as

$$\begin{aligned} &\left(\widetilde{\theta}_i^T\phi_i\left(\widehat{\overline{x}}_i\right) + \eta_i\right)\left(h(z_i) + z_i\dot{h}(z_i)\right) \\ &\le \left(\widetilde{\theta}_i^T\phi_i\left(\widehat{\overline{x}}_i\right) + \eta_i\right)(h(z_i) + z_i). \end{aligned} \tag{28}$$

Computing $z_i[g_{i,j}\xi h(z_{i+1}) - \prod_{i=1}^{i} k_{i,j}\xi h(z_1) - \dot{\xi}h(z_i)]$ gives

$$\begin{aligned} &z_i\left[g_{i,j}\xi h(z_{i+1}) - \prod_{i=1}^{i} k_{i,j}\xi h(z_1) - \dot{\xi}h(z_i)\right] \\ &\le -\left(\prod_{i=1}^{i} k_{i,j}\xi\right)z_i h(z_1) - \dot{\xi}z_i h(z_i) + g_{i,j}\xi z_i h(z_{i+1}). \end{aligned} \tag{29}$$

Combining (27)–(29) into (26),

$$\begin{aligned}\dot{V}_i \le & -\left(\frac{\dot{M}}{M^2}\right)z_i h(z_i) - \left(\frac{\dot{M}}{M^2}\right)z_i^2 \\ & + g_{i,j}\xi h(z_{i+1})(z_i + h(z_i)) \\ & - \left(\prod_{i=1}^{i} k_{i,j}\xi h(z_1) + \dot{\xi}h(z_i)\right)h(z_i) \\ & - \left(\prod_{i=1}^{i} k_{i,j}\xi\right)z_i h(z_1) - \dot{\xi}z_i h(z_i) + g_{i,j}\xi z_i h(z_{i+1}) \\ & + \left(\tilde{\theta}_i^T \phi_i(\hat{\bar{x}}_i) + \eta_i\right)(h(z_i) + 2z_i).\end{aligned} \tag{30}$$

In the light of Young's inequality and the characteristic of $h(.)$, we have

$$\begin{aligned} 2h(z_{i+1})(z_i + h(z_i)) &\le 2h^2(z_{i+1}) + z_i^2 + h^2(z_i), \\ 2z_i h(z_{i+1}) &\le h^2(z_{i+1}) + z_i^2, \\ h^2(z_i) &\le z_i^2, \\ \left(\tilde{\theta}_i^T \phi_i(\hat{\bar{x}}_i) + \eta_i\right)(h(z_i) + 2z_i) &\le \left\|\tilde{\theta}_i\right\|^2 + \eta_i^2 + 3z_i^2. \end{aligned} \tag{31}$$

By substituting (31) into (30), it follows

$$\begin{aligned}\dot{V}_i \le & -\left(\frac{\dot{M}}{M^2} + \dot{\xi}\right)z_i h(z_i) - \left(\frac{\dot{M}}{M^2} + \dot{\xi} - \frac{3g_{i,j}\xi}{2} - 3\right)z_i^2 \\ & + \frac{3g_{i,j}\xi}{2}z_{i+1}^2 - \prod_{i=1}^{i} k_{i,j}\xi h(z_1)h(z_i) \\ & - \left(\prod_{i=1}^{i} k_{i,j}\xi\right)z_i h(z_1) + \left\|\tilde{\theta}_i\right\|^2 + \eta_i^2.\end{aligned} \tag{32}$$

Step 2. Consider the Lyapunov function candidate as

$$V_n = \frac{1}{M}z_n h(z_n) + \frac{1}{M}z_n^2. \tag{33}$$

Similar to Step 1,

$$\begin{aligned}\dot{V}_n \le & -\left(\frac{\dot{M}}{M^2}\right)z_n h(z_n) - \left(\frac{\dot{M}}{M^2}\right)z_n^2 \\ & - \left(\prod_{i=1}^{n} k_{i,j}\xi h(z_1) + \dot{\xi}h(z_n)\right)h(z_n) \\ & - \left(\prod_{i=1}^{n} k_{i,j}\xi\right)z_n h(z_1) - \dot{\xi}z_n h(z_n) \\ & + \left(\tilde{\theta}_n^T \phi_n(\hat{\bar{x}}_n) + \eta_n\right)(h(z_n) + 2z_n) \\ \le & -\left(\frac{\dot{M}}{M^2} + \dot{\xi}\right)z_n h(z_n) - \left(\frac{\dot{M}}{M^2} + \dot{\xi} - 3\right)z_n^2 \\ & - \prod_{i=1}^{n} k_{i,j}\xi h(z_1)h(z_n) - \left(\prod_{i=1}^{n} k_{i,j}\xi\right)z_n h(z_1) \\ & + \left\|\tilde{\theta}_n\right\|^2 + \eta_n^2.\end{aligned} \tag{34}$$

We augment the Lyapunov candidate V_o as

$$V_o = \sum_{i=1}^{n} V_i. \tag{35}$$

Synthesizing (32), (34), and (35),

$$\begin{aligned}\dot{V}_o \le & -\sum_{i=1}^{n}\left(\frac{\dot{M}}{M^2} + \dot{\xi}\right)z_i h(z_i) \\ & - \left(\frac{\dot{M}}{M^2} + \dot{\xi} - \frac{3g_{1,j}\xi}{2} - 3\right)z_1^2 \\ & - \sum_{i=2}^{n-1}\left(\frac{\dot{M}}{M^2} + \dot{\xi} - \frac{3g_{i,j}\xi}{2} - \frac{3g_{i-1,j}\xi}{2} - 3\right)z_i^2 \\ & - \left(\frac{\dot{M}}{M^2} + \dot{\xi} - \frac{3g_{n-1,j}\xi}{2} - 3\right)z_n^2 \\ & - \sum_{i=1}^{n}\left(\left(\prod_{i=1}^{n} k_{i,j}\xi\right)(h(z_1)h(z_i) + z_i h(z_1))\right) \\ & + \sum_{i=1}^{n}\left(\left\|\tilde{\theta}_n\right\|^2 + \eta_n^2\right).\end{aligned} \tag{36}$$

Stability analysis is described in the following two parts.

Case 1. z_1 and z_i have the same sign (such as both z_1 and z_i are positive or negative).

Computing $-(h(z_1)h(z_i)+z_ih(z_1))$ gives

$$-\left(h(z_1)h(z_i)+z_ih(z_1)\right)\le 0. \tag{37}$$

Substituting (37) into (36), one obtains

$$\begin{aligned}\dot V_o \le & -\sum_{i=1}^{n}\left(\frac{\dot M}{M^2}+\dot{\bar\xi}\right)z_ih(z_i)-\left(\frac{\dot M}{M^2}+\dot{\bar\xi}-\frac{3g_{1,j}\xi}{2}-3\right)z_1^2\\ & -\sum_{i=2}^{n-1}\left(\frac{\dot M}{M^2}+\dot{\bar\xi}-\frac{3g_{i,j}\xi}{2}-\frac{3g_{i-1,j}\xi}{2}-3\right)z_i^2\\ & -\left(\frac{\dot M}{M^2}+\dot{\bar\xi}-\frac{3g_{n-1,j}\xi}{2}-3\right)z_n^2\\ & -\sum_{i=1}^{n}\left(\left\|\tilde\theta_n\right\|^2+\eta_n^2\right).\end{aligned} \tag{38}$$

Case 2. z_1 and z_i have opposite signs.

$$\begin{aligned}&\text{Computing } -(h(z_1)h(z_i)+z_ih(z_1)) \text{ gives}\\ &-\left(h(z_1)h(z_i)+z_ih(z_1)\right)\\ &\le\frac{1}{2}\left(\left(-h(z_1)\right)^2+h^2(z_i)+z_i^2+\left(-h(z_1)\right)^2\right)\\ &\le z_1^2+z_i^2.\end{aligned} \tag{39}$$

Theorem 1. *Consider system (5) with unknown backlash-like hysteresis under Definition 1 and error transform function (20), applying the proposed FTSO mechanism in (16), observer errors (18) converge to a small neighborhood of the origin point in a settling time* T_0.

Proof. Substituting (39) into (36), one obtains

$$\begin{aligned}\dot V_o \le & -\sum_{i=1}^{n}\left(\frac{\dot M}{M^2}+\dot{\bar\xi}\right)z_ih(z_i)\\ & -\left(\frac{\dot M}{M^2}+\dot{\bar\xi}-\frac{3g_{1,j}\xi}{2}-3-2\sum_{i=1}^{n}\left(\prod_{i=1}^{n}k_{i,j}\xi\right)\right)z_1^2\\ & -\sum_{i=2}^{n-1}\left(\frac{\dot M}{M^2}+\dot{\bar\xi}-\frac{3g_{i,j}\xi}{2}-\frac{3g_{i-1,j}\xi}{2}-3-\sum_{i=1}^{n}\left(\prod_{i=1}^{n}k_{i,j}\xi\right)\right)z_i^2\\ & -\left(\frac{\dot M}{M^2}+\dot{\bar\xi}-\frac{3g_{n-1,j}\xi}{2}-3-\sum_{i=1}^{n}\left(\prod_{i=1}^{n}k_{i,j}\xi\right)\right)z_n^2\\ & +\sum_{i=1}^{n}\left(\left\|\tilde\theta_n\right\|^2+\eta_n^2\right).\end{aligned} \tag{40}$$

For simplification of the expression, reconfigure the parameters $\lambda_1=(\dot M/M^2)+\dot{\bar\xi}-(3g_{1,j}\xi/2)-3-2\sum_{i=1}^{n}\prod_{i=1}^{n}k_{i,j}\xi>0$, $\lambda_i=\sum_{i=2}^{n-1}((\dot M/M^2)+\dot{\bar\xi}-(3g_{i,j}\xi/2)-(3g_{i-1,j}\xi/2)-3-\sum_{i=1}^{n}\prod_{i=1}^{n}k_{i,j}\xi)>0, i=2,\ldots,n$, and $\lambda_n=(\dot M/M^2)+\dot{\bar\xi}-(3g_{n-1,j}\xi/2)-3-\sum_{i=1}^{n}(\prod_{i=1}^{n}k_{i,j}\xi)>0$. Futhermore, denote $\lambda=\min(\dot M/M^2)+\dot{\bar\xi},\lambda_1,\ldots,\lambda_n$ and $D_o=\sum_{i=1}^{n}(\|\tilde\theta_n\|^2+\eta_n^2)$. The Laypunov function V_o consequently takes the form

$$\dot V_o\le\lambda V_o+D. \tag{41}$$

Integrating (41) from 0 to t produces

$$0\le V_o(t)\le\frac{D}{\lambda}+V_o(0)e^{-\lambda t}. \tag{42}$$

Therefore, the observer errors converge to a small neighborhood of the origin point in a finite-time interval $[0,T_0]$, and all of the closed-loop systems signals are bounded.

This completes the proof of Theorem 1.

4. Adaptive Controller Design and Stability Analysis

In this section, an adaptive control scheme is developed for nonlinear system with unknown backlash-like hysteresis by using the above FTSO and the backstepping technique. To facilitate the design procedure, the following errors are defined as

$$\begin{cases}e_{c1}=\hat x_1-x_d,\\ e_{ci}=\hat x_i-\gamma_{i-1},\quad i=2,\cdots,n,\end{cases} \tag{43}$$

where γ_{i-1} are virtual intermediate control signals which will be defined later.

The feedback control laws (44), (45), and adaptive laws (46) are chosen as

$$\gamma_1=-\frac{e_{c1}\hat\theta_1}{4\phi_1^T(\hat{\bar x}_1)\phi_1(\hat{\bar x}_1)}-h_{1,j}e_{c1}, \tag{44}$$

$$\gamma_i=-\frac{e_{ci}\hat\theta_i}{4\phi_i^T(\hat{\bar x}_i)\phi_i(\hat{\bar x}_i)}-h_{i,j}e_{ci}+\frac{\dot\gamma_{i-1}}{g_{i,j}},\quad i=2,\ldots,n, \tag{45}$$

$$\dot{\hat\theta}_i=\frac{d_ig_{i,j}e_{ci}^2}{4\phi_n^T(\hat{\bar x}_i)\phi_i(\hat{\bar x}_i)}-p_i\hat\theta_i,\quad i=1,\ldots,n, \tag{46}$$

where $v=\gamma_n$. $h_{1,j}>1$, $d_1>0$, $p_1>0$, $h_{i,j}>1$, $d_i>0$, and $p_i>0$ are the design parameters.

Step 1. Consider a Lyapunov candidate function in the form of

$$V_{c1}=\frac{1}{2}e_{c1}^2+\frac{1}{2d_1}\tilde\theta_1^2, \tag{47}$$

where $\tilde\theta_1=\hat\theta_1-\theta_1^*$, with $\hat\theta_1$ being the estimation of $\theta_1^*=\|\hat\theta_1\|^2$.

$$\dot V_{c1}=e_1\dot e_1+\frac{1}{d_1}\tilde\theta_1^T\dot{\hat\theta}_1. \tag{48}$$

From (16) and (43), one obtains

$$\begin{aligned}\dot e_{c1}&=g_{1,j}\hat x_2-k_{1,j}\varepsilon_1+\hat f_1\left(\hat{\bar x}_1\middle|\hat\theta_1\right)-\dot x_d\\ &=g_{1,j}\hat x_2-k_{1,j}\varepsilon_1+\hat\theta_1^T\phi_1(\hat{\bar x}_1)\\ &\quad+\eta_1-\dot x_d\\ &=g_{1,j}(e_{c2}+\gamma_1)-k_{1,j}\varepsilon_1+\hat\theta_1^T\phi_1(\hat{\bar x}_1)\\ &\quad+\eta_1-\dot x_d.\end{aligned} \tag{49}$$

From (48) and (49), it is obtained that $\dot{V}_{c1}$ is

$$\begin{aligned}\dot{V}_{c1} &= e_{c1}\left(g_{1,j}\left(e_{c2}+\gamma_1\right)+\widehat{\theta}_1^T\phi_1\left(\widehat{\bar{x}}_1\right)\right)\\ &\quad+e_{c1}\left(-k_{1,j}\varepsilon_1+\eta_1-\dot{x}_d\right)+\frac{1}{d_1}\widetilde{\theta}_1^T\dot{\widehat{\theta}}_1.\end{aligned}\tag{50}$$

Based on Young's inequality and Lemma 3, the following inequalities are obtained

$$\begin{aligned}e_{c1}\widehat{\theta}_1^T\phi_1\left(\widehat{\bar{x}}_1\right) &\le \frac{g_{1,j}e_{c1}^2\left\|\theta_1\right\|^2\phi_1^T\left(\widehat{\bar{x}}_1\right)\phi_1\left(\widehat{\bar{x}}_1\right)}{4}+\frac{1}{g_{1,j}}\\ &\le \frac{g_{1,j}e_{c1}^2\theta_1^*}{4\phi_1^T\left(\widehat{\bar{x}}_1\right)\phi_1\left(\widehat{\bar{x}}_1\right)}+\frac{1}{g_{1,j}}.\end{aligned}\tag{51}$$

Substituting (44), (46), and (51) into (50) gives

$$\begin{aligned}\dot{V}_{c1} &= e_{c1}\left(g_{1,j}\left(e_{c2}+\gamma_1\right)+\frac{g_{1,j}e_{c1}\left(\widehat{\theta}_1-\widetilde{\theta}_1\right)}{4\phi_1^T\left(\widehat{\bar{x}}_1\right)\phi_1\left(\widehat{\bar{x}}_1\right)}\right)\\ &\quad+e_{c1}\left(-k_{1,j}\varepsilon_1+\eta_1-\dot{x}_d\right)+\frac{1}{d_1}\widetilde{\theta}_1^T\dot{\widehat{\theta}}_1+\frac{e_{c1}(0)}{g_{1,j}}\\ &\quad+e_{c1}\left(g_{1,j}\left(e_{c2}-h_{1,j}e_{c1}\right)\right)\\ &\quad+e_{c1}\left(-k_{1,j}\varepsilon_1+\eta_1-\dot{x}_d\right)+\frac{p_1}{d_1}\widetilde{\theta}_1\widehat{\theta}_1+\frac{e_{c1}(0)}{g_{1,j}}.\end{aligned}\tag{52}$$

Via Young's inequality, we have

$$-\frac{p_1}{d_1}\widetilde{\theta}_1\widehat{\theta}_1\le-\frac{p_1}{2d_1}\widetilde{\theta}_1^2+\frac{p_1}{2d_1}\theta_1^{*2},\tag{53}$$

$$e_{c1}\left(-k_{1,j}\varepsilon_1+\eta_1-\dot{x}_d\right)\le\frac{1}{2}e_{c1}^2+\frac{1}{2}\varsigma^2,\tag{54}$$

where $\varsigma=-k_{1,j}\varepsilon_1+\eta_1-\dot{x}_d$. ε_1, η_1, and $\dot{x}_d$ are bounded.

Thus, (52) is modified as

$$\dot{V}_{c1}=-\left(h_{1,j}g_{1,j}-\frac{1}{2}\right)e_{c1}^2-\frac{p_1}{2d_1}\widetilde{\theta}_1^2+g_{1,j}e_{c1}e_{c2}+E_1,\tag{55}$$

where $E_1=(p_1/2d_1)\theta_1^{*2}+(1/2)\varsigma^2+e_{c1}(0)/g_{1,j}$.

Step i $(i=2,\cdots,n-1)$. Similar to Step 1, consider a Lyapunov candidate function in the form of

$$V_{ci}=\frac{1}{2}e_{ci}^2+\frac{1}{2d_i}\widetilde{\theta}_i^2,\tag{56}$$

where $\widetilde{\theta}_i=\widehat{\theta}_i-\theta_i^*$.

$$\dot{V}_{ci}=e_i\dot{e}_i+\frac{1}{d_i}\widetilde{\theta}_i^T\dot{\widehat{\theta}}_i.\tag{57}$$

From (43) and (45), one obtains

$$\dot{e}_{ci}=g_{i,j}\left(e_{ci+1}+\gamma_i\right)-\prod_{i=1}^{i}k_{i,j}\varepsilon_1+\widehat{\theta}_i^T\phi_n\left(\widehat{\bar{x}}_i\right)+\eta_i-\dot{\gamma}_{i-1}.\tag{58}$$

From (57) and (58), $\dot{V}_{ci}$ is given by

$$\begin{aligned}\dot{V}_{ci} &= e_{ci}\left(g_{i,j}\left(e_{ci+1}+\gamma_i\right)+\widehat{\theta}_i^T\phi_i\left(\widehat{\bar{x}}_i\right)\right)\\ &\quad+e_{ci}\left(-\prod_{i=1}^{i}k_{i,j}\varepsilon_1+\eta_i-\dot{\gamma}_{i-1}\right)+\frac{1}{d_i}\widetilde{\theta}_i^T\dot{\widehat{\theta}}_i.\end{aligned}\tag{59}$$

Based on Young's inequality and Lemma 3, the following inequalities are obtained:

$$\begin{aligned}e_{ci}\widehat{\theta}_i^T\phi_i\left(\widehat{\bar{x}}_i\right) &\le \frac{g_{i,j}e_{ci}^2\left\|\theta_i\right\|^2\phi_i^T\left(\widehat{\bar{x}}_i\right)\phi_i\left(\widehat{\bar{x}}_i\right)}{4}+\frac{1}{g_{i,j}}\\ &\le \frac{g_{i,j}e_{ci}^2\theta_i^*}{4\phi_i^T\left(\widehat{\bar{x}}_i\right)\phi_i\left(\widehat{\bar{x}}_i\right)}+\frac{1}{g_{i,j}}.\end{aligned}\tag{60}$$

Thus,

$$\begin{aligned}\dot{V}_{ci} &= e_{ci}\left(g_{i,j}\left(e_{ci+1}-h_{i,j}e_{ci}\right)\right)\\ &\quad+e_{ci}\left(-\prod_{i=1}^{i}k_{i,j}\varepsilon_1+\eta_i\right)-\frac{p_i}{d_i}\widetilde{\theta}_i\widehat{\theta}_i+\frac{e_{ci}(0)}{g_{i,j}}.\end{aligned}\tag{61}$$

From Young's inequality,

$$-\frac{p_i}{d_i}\widetilde{\theta}_i\widehat{\theta}_i\le-\frac{p_i}{2d_i}\widetilde{\theta}_i^2+\frac{p_i}{2d_i}\theta_i^{*2},\tag{62}$$

$$e_{ci}\left(-\prod_{i=1}^{n-1}k_{i,j}\varepsilon_1+\eta_i\right)\le\frac{1}{2}e_{ci}^2+\frac{1}{2}\varsigma_i^2,\tag{63}$$

where $\varsigma_i=-\prod_{i=1}^{i}k_{i,j}\varepsilon_1+\eta_i$ and η_i are bounded.

Substituting (62) and (63) into (61) gives

$$\dot{V}_{ci}=-\left(h_{i,j}g_{i,j}-\frac{1}{2}\right)e_{ci}^2-\frac{p_i}{2d_i}\widetilde{\theta}_i^2+g_{i,j}e_{ci}e_{ci+1}+E_i,\tag{64}$$

where $E_i=(p_i/2d_i)\theta_i^{*2}+(1/2)\varsigma_i^2+(e_{ci}(0)/g_{i,j})$.

Step n. Similar to Step i, consider a Lyapunov candidate function in the form of

$$V_{cn}=\frac{1}{2}e_{cn}^2+\frac{1}{2d_n}\widetilde{\theta}_n^2,\tag{65}$$

where $\widetilde{\theta}_n=\widehat{\theta}_n-\theta_n^*$.

Similar to Step i, one obtains

$$\dot{e}_{cn}=-\prod_{i=1}^{n}k_{i,j}\varepsilon_1+\widehat{\theta}_n^T\phi_n\left(\widehat{\bar{x}}_n\right)+\eta_n-\dot{\gamma}_{n-1}+b_{0,j}\nu.\tag{66}$$

Moreover, the time-derivative of V_{cn} is given by

$$\begin{aligned}\dot{V}_{cn} &= e_{cn}\left(b_{0,j}\upsilon+\widehat{\theta}_n^T\phi_n\left(\widehat{\bar{x}}_n\right)\right)\\ &\quad+e_{cn}\left(-\prod_{i=1}^{n}k_{i,j}\varepsilon_1+\eta_n-\dot{\gamma}_{n-1}\right)+\frac{1}{d_n}\widetilde{\theta}_n^T\dot{\widehat{\theta}}_n.\end{aligned}\tag{67}$$

Based on Young's inequality and Lemma 3, the following inequalities are obtained:

$$e_{cn}\widehat{\theta}_n^T\phi_n(\widehat{\bar{x}}_n) \le \frac{b_{0,j}e_{cn}^2\|\theta_n\|^2\phi_n^T(\widehat{\bar{x}}_n)\phi_n(\widehat{\bar{x}}_n)}{4} + \frac{1}{b_{0,j}} \le \frac{b_{0,j}e_{cn}^2\theta_n^*}{4\phi_n^T(\widehat{\bar{x}}_n)\phi_n(\widehat{\bar{x}}_n)} + \frac{1}{b_{0,j}}. \tag{68}$$

Substituting (45), (67), and (68) gives

$$\dot{V}_{cn} = e_{cn}\left(b_{0,j}\left(-h_{n,j}e_{cn}\right)\right) + e_{cn}\left(-\prod_{i=1}^{n}k_{n,j}\varepsilon_1 + \eta_n\right) - \frac{p_n}{d_n}\widetilde{\theta}_n\widehat{\theta}_n + \frac{e_{cn}(0)}{b_{0,j}}. \tag{69}$$

By using Young's inequality,

$$-\frac{p_n}{d_n}\widetilde{\theta}_n\widehat{\theta}_n \le -\frac{p_n}{2d_n}\widetilde{\theta}_n^2 + \frac{p_n}{2d_n}\theta_n^{*2}, \tag{70}$$

$$e_{cn}\left(-\prod_{i=1}^{n}k_{i,j}\varepsilon_1 + \eta_n\right) \le \frac{1}{2}e_{cn}^2 + \frac{1}{2}\varsigma_n^2, \tag{71}$$

where $\varsigma_n = -\prod_{i=1}^{n}k_{i,j}\varepsilon_1 + \eta_n$ and η_n are bounded.

Thus, (69) is modified to be

$$\dot{V}_{cn} = -\left(h_{n,j}b_{0,j} - \frac{1}{2}\right)e_{cn}^2 - \frac{p_n}{2d_n}\widetilde{\theta}_n^2 + E_n, \tag{72}$$

where $E_n = (p_n/2d_n)\theta_n^{*2} + (1/2)\varsigma_n^2 + (e_{cn}(0)/b_{0,j})$.

A Lyapunov function V_c is chosen as

$$V_c = \sum_{i=1}^{n}V_{ci} = \sum_{i=1}^{n}\frac{1}{2}e_{ci}^2 + \sum_{i=1}^{n}\frac{1}{2d_i}\widetilde{\theta}_i^2. \tag{73}$$

The differentiation of equation (73) is

$$\dot{V}_c = \sum_{i=1}^{n}\dot{V}_{ci} \le -\sum_{i=1}^{n-1}\left(h_{i,j}g_{i,j} - \frac{1}{2}\right)e_{ci}^2 - \sum_{i=1}^{n}\frac{p_i}{2d_i}\widetilde{\theta}_i^2 + \sum_{i=1}^{n-1}g_{i,j}e_{ci}e_{ci+1} + \sum_{i=1}^{n}E_i - \left(h_{n,j}b_{0,j} - \frac{1}{2}\right)e_{cn}^2. \tag{74}$$

Based on Young's inequality, it is obtained that

$$g_{i,j}e_{ci}e_{ci+1} \le g_{i,j}\left(\frac{h_{i,j}}{2}e_{ci}^2 + \frac{1}{2h_i}e_{ci+1}^2\right) \le g_{i,j}\left(\frac{h_{i,j}}{2}e_{ci}^2 + \frac{1}{2}e_{ci+1}^2\right), \tag{75}$$

with $h_{i,j} > 1$.

Thus, equation (74) is modified as

$$\dot{V}_c \le -\sum_{i=1}^{n-1}\left(h_{i,j}g_{i,j} - \frac{1}{2}\right)e_{ci}^2 - \sum_{i=1}^{n}\frac{p_i}{2d_i}\widetilde{\theta}_i^2 + \sum_{i=1}^{n-1}g_{i,j}\left(\frac{h_{i,j}}{2}e_{ci}^2 + \frac{1}{2}e_{ci+1}^2\right) + \sum_{i=1}^{n}E_i - \left(h_{n,j}b_{0,j} - \frac{1}{2}\right)e_{cn}^2 \le -\frac{1}{2}\sum_{i=1}^{n-1}\left(h_{n,j}g_{i,j} - 2\right)e_{ci}^2 - \frac{1}{2}\left(2h_{n,j}b_{0,j} - 2\right)e_{cn}^2 - \sum_{i=1}^{n}\frac{p_i}{2d_i}\widetilde{\theta}_i^2 + \sum_{i=1}^{n}E_i. \tag{76}$$

Furthermore, denote $\mu = \min\{h_{1,j}g_{1,j} - 2, \cdots, h_{n-1,j}g_{n-1,j} - 2, 2h_{n,j}b_{0,j} - 2, p_1, p_2, \cdots, p_n\}$ and $E_c = \sum_{i=1}^{n}E_i$. The Laypunov function V_c consequently takes the form of

$$\dot{V}_c \le -\mu V_c + E_c. \tag{77}$$

Theorem 2. *For switched strict-feedback nonlinear systems with unknown hysteresis (1), FTSO (16), feedback control laws (44) and (45), and adaptive laws (46), if the average dwell time of the switching signal $\sigma(t)$ satisfies the condition $\tau_a > (\ln\zeta/\mu)$ ($\zeta = \max\{\lambda_{\max}(P_k)/\lambda_{\min}(P_l)\}, k, l \in M$), the control scheme based on FTSO ensures that all variables of the closed-loop system are bounded. By properly selecting the parameters, the controller and observer error converge to origin, such that $\lim_{T\longrightarrow\infty}z_1^2 \le 0$ and $\lim_{T\longrightarrow\infty}e_1^2 \le 0$.*

Proof. There is a piecewise differentiable function $W(t) = e^{\mu t}V_j(\varepsilon(t))$ in any interval $[t_{i-1}, t_i]$. Then, its time differentiation on $[t_{i-1}, t_i]$ is

$$\dot{W}(t) = \mu e^{\mu t}V_j(\varepsilon(t)) + e^{\mu t}\dot{V}_j(\varepsilon(t)). \tag{78}$$

From (76) and (78),

$$\dot{W}(t) \le E_c e^{\mu t}. \tag{79}$$

Then, noting that at the switching point $V(t_i) \le \zeta V(t_i^*)$ from Lemma 2, where $t_i^* = \lim_{t\longrightarrow t_i}t$, it follows that

$$W(t_i) = e^{\mu t_i}V_{\sigma(t_i)}(\varepsilon(t_i)) \le \zeta e^{\mu t_i}V_{\sigma(t_{i-1})} + (\varepsilon(t_i)) = \zeta W(t_i^*) \le \zeta\left(W(t_{i-1}) + \int_{t_{i-1}}^{t_i}E_c e^{\mu t}\mathrm{d}t\right). \tag{80}$$

Let $T_f > t_0 = 0$ and $i \in [1, N(0, T_f)]$, then equation (80) is further expressed as

$$
\begin{aligned}
W\left(T_f^*\right) &\le W\left(t_{N\left(0,T_f\right)}\right) + \int_{tN\left(0,T_f\right)}^{T_f} E_c e^{\mu t}\,\mathrm{d}t \\
&\le \zeta\left[W\left(t_{N\left(0,T_f\right)^{-1}}\right) + \int_{tN\left(0,T_f\right)-1}^{tN\left(0,T_f\right)} E_c e^{\mu t}\,\mathrm{d}t\right] \\
&\quad + \int_{tN\left(0,T_f\right)}^{T_f} E_c e^{\mu t}\,\mathrm{d}t \\
&\le \zeta^2\left[W\left(t_{N\left(0,T_f\right)^{-2}}\right) + \int_{tN\left(0,T_f\right)-2}^{tN\left(0,T_f\right)-1} E_c e^{\mu t}\,\mathrm{d}t\right] \\
&\quad + \zeta\int_{tN\left(0,T_f\right)-1}^{tN\left(0,T_f\right)} E_c e^{\mu t}\,\mathrm{d}t \\
&\quad + \int_{tN\left(0,T_f\right)}^{T_f} E_c e^{\mu t}\,\mathrm{d}t \\
&\le \cdots \\
&\le \zeta^{N\left(0,T_f\right)} W(0) \\
&\quad + \zeta^{N\left(0,T_f\right)} \sum_{i=1}^{N\left(0,T_f\right)+1} \zeta^{1-i}\int_{t_{i-1}}^{t_i} E_c e^{\mu t}\,\mathrm{d}t.
\end{aligned}
\tag{81}
$$

Since $\tau_a > (\ln\zeta/\mu)$ and Lemma 1, for any $T_f > 0$,

$$
N\left(0,T_f\right) \le N_0 + \frac{\mu T_f}{\ln\zeta}. \tag{82}
$$

Substituting (82) from (81),

$$
\begin{aligned}
W\left(T_f^*\right) &\le \zeta^{N\left(0,T_f\right)} W(0) + \zeta^{N\left(0,T_f\right)}\int_0^{T_f} E_c e^{\mu t}\,\mathrm{d}t \\
&\le \zeta^{N_0} e^{-\mu T_f} W(0) \\
&\quad + \zeta^{N_0} e^{-\mu T_f}\frac{E_c}{\mu}\left(e^{\mu T_f} - 1\right).
\end{aligned}
\tag{83}
$$

By Lemma 2 and (83), one has

$$
\begin{aligned}
\chi_1\left(\|\varepsilon(T)\|\right) &\le V_{\sigma(T^*)}\left(\varepsilon\left(T^*\right)\right) \\
&= \zeta^{N_0} e^{-\mu T} W(0) + \zeta^{N_0}\frac{E_c}{\mu}\frac{\left(1 - e^{-\mu T}\right)}{e^{\mu t}} \\
&\le e^{N_0\ln\zeta} e^{-2\mu T}\chi_2\left(\|\varepsilon(0)\|\right) \\
&\quad + \zeta^{N_0} e^{-\mu T}\frac{E_c}{\mu}\left(1 - e^{-\mu T}\right).
\end{aligned}
\tag{84}
$$

Therefore, from (84), it follows that

$$
\lim_{T\longrightarrow\infty} z_1^2 \le e^{N_0\ln\zeta} e^{-2\mu T}\chi_2\left(\|\varepsilon(0)\|\right) + \zeta^{N_0} e^{-\mu T}\frac{\kappa}{\mu}\left(1 - e^{-\mu T}\right) = 0. \tag{85}
$$

Similarly, one obtains

$$
\lim_{T\longrightarrow\infty} e_1^2 \le 0. \tag{86}
$$

That is, using (85) and (86), observation errors and tracking errors converge to zero.

5. Simulation Results

In this section, three examples are considered to test the proposed control method. Consider the following second-order nonlinear system:

$$
\begin{cases}
\dot{x}_1 = g_{1,\sigma(t)} x_2 + f_{1,\sigma(t)}\left(\overline{x}_1\right) + d_{1,\sigma(t)}(t), \\
\dot{x}_2 = g_{2,\sigma(t)} u + f_{2,\sigma(t)}\left(\overline{x}_2\right) + d_{2,\sigma(t)}(t),
\end{cases}
\tag{87}
$$

where $g_{1,1} = 1$, $g_{1,2} = 1$, $f_{1,1}(\overline{x}_1) = (x_1 - x_1^3)/(1 + x_1^4)$, $f_{1,1}(\overline{x}_1) = (x_1 - x_1^2)/(1 + x_1^5)$, $g_{2,1} = 1$, $g_{2,2} = 1$, $f_{2,1}(\overline{x}_2) = -\exp(-x_1^2)\sin(5x_2)$, $f_{2,1}(\overline{x}_2) = -\sin(5x_2)$, $u(t) = v(t) + l(v)$, $l(v) = (u_0 - v_0)\exp(-5(v - v_0)\mathrm{sgn}\dot{v}) + \exp(-5v\mathrm{sgn}\dot{v})\int_{v_0}^{v}(0.345 - 1)\exp(5\xi\mathrm{sgn}\dot{v})d\xi$, $d_{1,1}(t) = 0.2\sin t$, $d_{1,2}(t) = 0.3\sin t$, $d_{2,1}(t) = 0.2\cos t$, and $d_{2,2}(t) = 0.3\cos t$.

The selection guidelines of the design parameters in the proposed control design method are summarized in the following:

Step 1. During selection of design parameters of observer (16), the parameter $k_{i,j} > 0$ are selected before $k_{i+1,j} > 0$. Then, the values are usually chosen to ensure $k_{i,j} < k_{i+1,j}$.

Step 2. Determine the parameters of finite-time performance function (15) in FTSO (16). In this step, one needs to choose finite-time $T_0 = 0.3$, the initial values $\xi(0) = 0.99$, and the final value $\xi_{T0} = 0.01$. Then, $\tau = 0.5$ and $\lambda = 6.66$ are chosen. Moreover, it is obtained that $T_0 = \xi(0)/\tau\lambda$.

Step 3. Select controller parameters of $h_{i,j} > 1$, $d_i > 0$, and $p_i > 0$ to ensure $\mu > 0$, which is defined in (76).

Step 4. Initial values of the system states and observer are set according to the proof of Theorem 1. The appropriate initial conditions are given in order to make the contrast effect of control and observation more clear. In this simulation, $x(0) = [0\,0]^T$ and $\widehat{x}(0) = [0\,0]^T$.

For better illustration, we consider such two cases: (1) the proposed adaptive controller scheme with FTSO and (2) the proposed adaptive controller scheme with the observer in [12]. The reference signals x_d are selected for $x_d = 2$ and $x_d = 1.5\sin 2t$. The basis function vector $\phi(x)$ is chosen as the form of the Gaussian function:

$$
\Phi_i(\overline{x}) = \exp\left[-\frac{\left(\overline{x} - \mu_i\right)^T\left(\overline{x} - \mu_i\right)}{2\gamma_i^2}\right], \tag{88}
$$

with five nodes, the width $\gamma_1 = 0.5$ and $\gamma_2 = 0.8$, and the centers $\mu_i\,(i = 1, 2)$ are equally distributed between $[2, 2]$.

The chosen control parameters are $d_1 = 1$, $d_2 = 1$, $p_1 = 2$, $p_2 = 2$, $h_{1,1} = 30$, $h_{1,2} = 30$, $h_{2,1} = 3$, and $h_{2,2} = 9$ and $x(0) = [0\,0]^T$, $\widehat{x}(0) = [0\,0]^T$, and $\widehat{\theta}(0) = [0\,0]^T$. The FTSO parameters are selected as $k_{1,1} = 5.1$, $k_{1,2} = 5.2$, $k_{2,1} = 9$, and

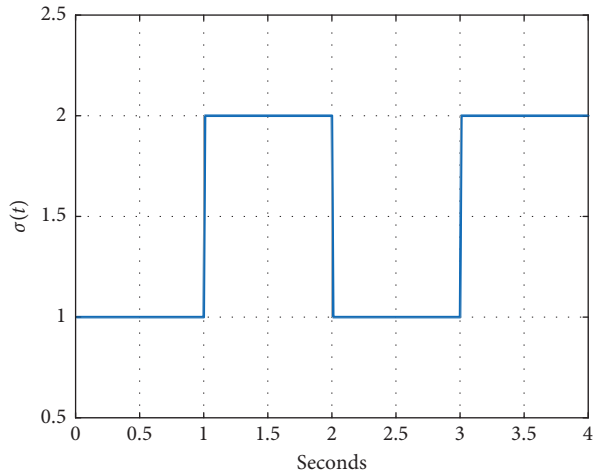

FIGURE 2: Switching signal $\sigma(t)$ in simulation.

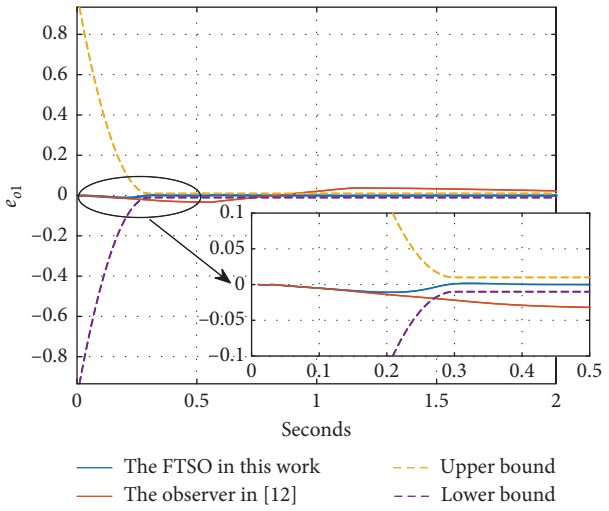

FIGURE 3: The observer compared results of e_{o1}.

$k_{2,2} = 9.5$, and the other observer parameters are $k_{1,1} = 10$, $k_{1,2} = 11$, $k_{2,1} = 21$, and $k_{2,2} = 20$.

Example 1. $x_d = 2$.

Switching signal $\sigma(t)$ is shown in Figure 2, and the observer errors e_{o1} with the FTSO and the observer in [12] are shown in Figure 3. The tracking performance of the switched system are shown in Figure 4, while the tracking errors e_{c1} and the control input v of two schemes are shown in Figures 5 and 6, respectively.

Example 2. $x_d = 1.5 \sin 2t$.

The tracking responses and errors with the FTSO and the contrastive observer are depicted in Figure 7. Furthermore, in order to further analyze the performance of the tracking effect with the same controller in Figure 7, the performance evaluation, including average tracking error and average fluctuation of tracking error, is summarized in Table 1.

Figures 8 and 9 show the observer error e_{o1} compared and the control input v for two cases, respectively.

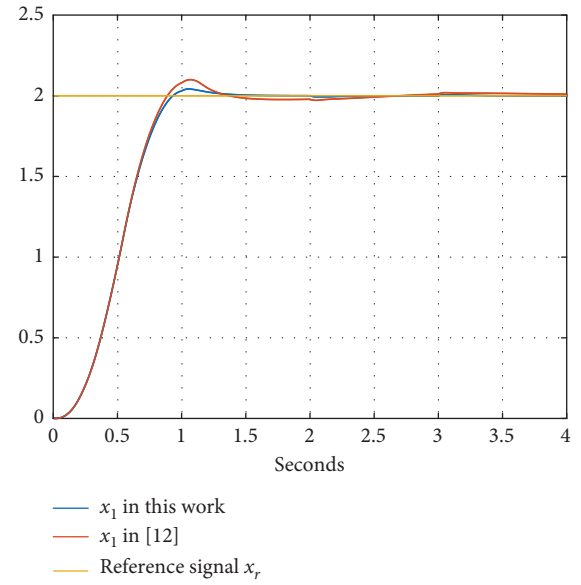

FIGURE 4: The observer compared results of x_1.

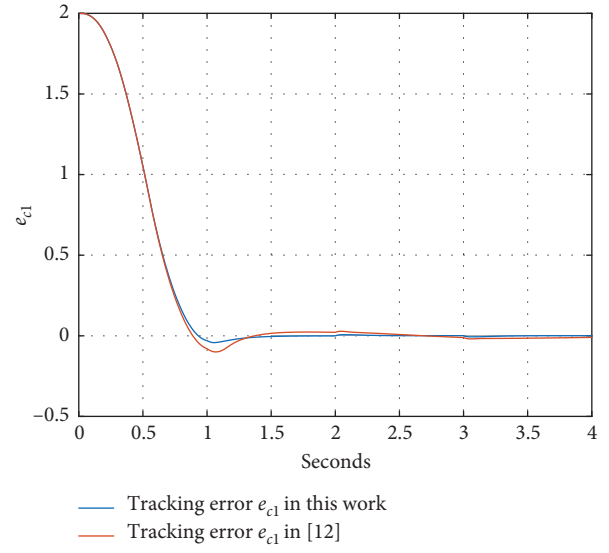

FIGURE 5: The observer compared results of e_{c1}.

Example 3. In order to provide the convictive proof of the proposed control approach, a test is proceeded on a servo test rig (as shown in Figure 10), which is given as follows:

$$\begin{cases} J_m \ddot{x}_1 = -b_m \dot{x}_1 - \tau_s + \tau_m, \\ J_l \ddot{x}_2 = -b_l \dot{x}_2 + \tau_s - \tau_d, \end{cases} \tag{89}$$

where x_1 and x_2 denote the displacement of motor subsystem and the load subsystem, respectively. τ_s is the transmitted torque. τ_m is the driving torque of the system, and τ_d is the disturbance torque at the driven gear. $J_m = 0.01$, $J_l = 0.05$, $b_m = 0.1$, and $b_l = 0.12$.

The reference signal $y_d = 0.8 \sin(t)$(rad), where parameters are selected as $h_1 = 4$, $h_2 = 6$, $k_1 = 200$, and $k_2 = 200$. The initial state of the switched system and observer are $x_1(0) = 0$, $x_2(0) = 0$, $\hat{x}_1(0) = 0$, and $\hat{x}_2(0) = 0$.

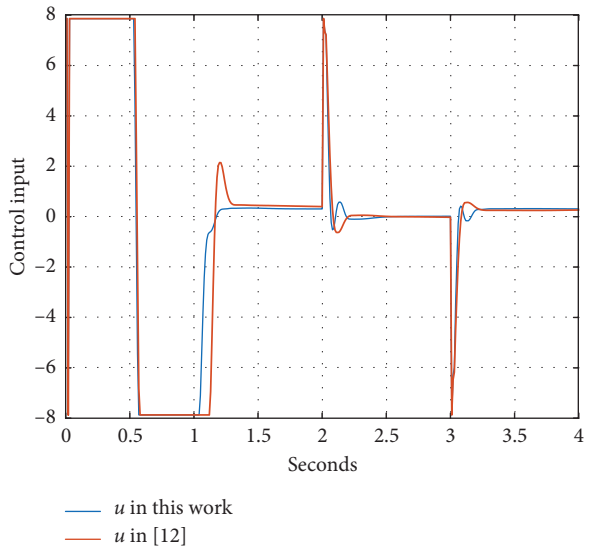

Figure 6: Control input v.

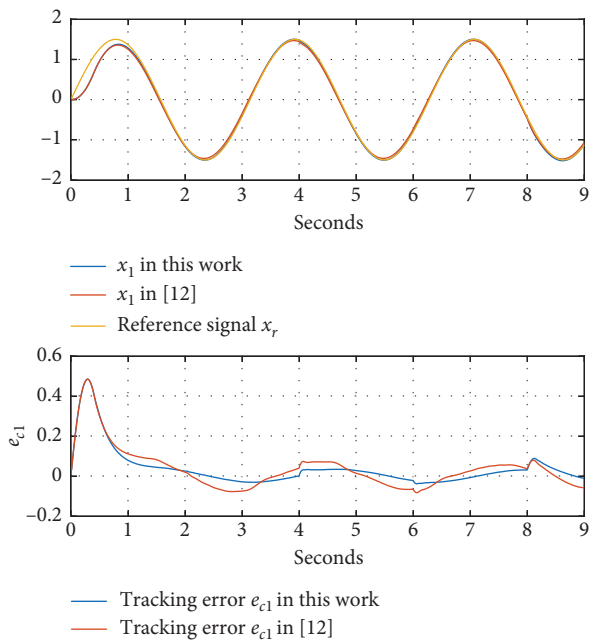

Figure 7: The output tracking responses of x_1 and the tracking error e_{c1}.

Table 1: Position tracking performance evaluation.

Method	Average tracking error	Fluctuation of tracking error
With the FTSO	0.0362	0.5220
With the observer in [12]	0.0571	1.6707

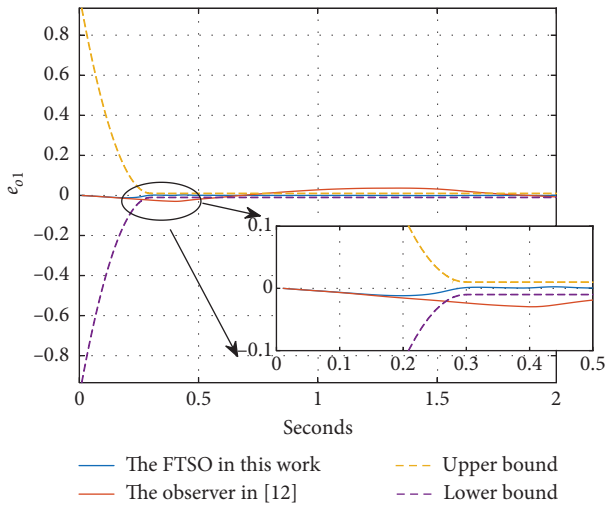

Figure 8: The observer compared results of e_{o1}.

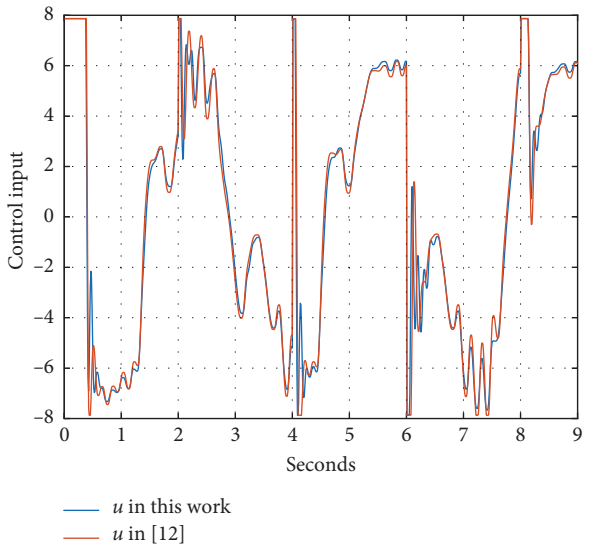

Figure 9: Control input v.

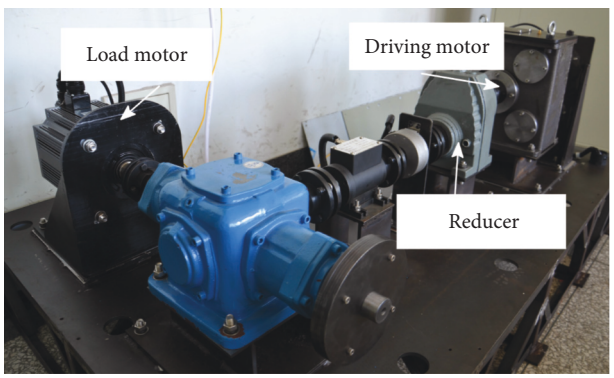

Figure 10: Motor driving test rig.

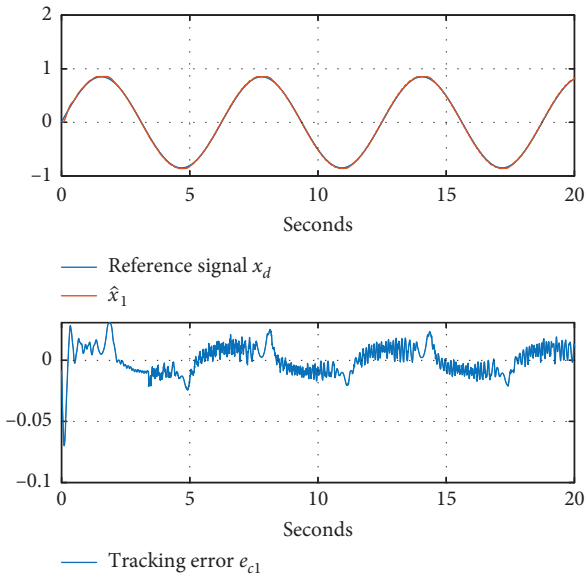

Figure 11: Tracking effect and tracking error.

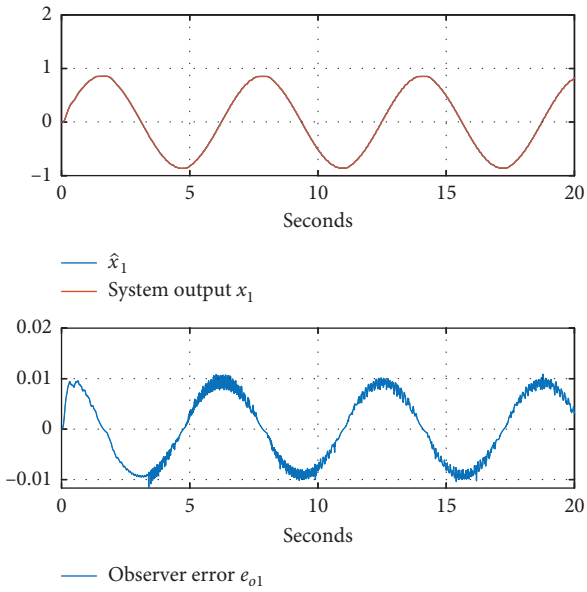

Figure 12: Observer effect and error.

The trajectory shown in Figure 11 is the estimation of output $\hat{x}_1$ and reference signal x_d and the tracking error. Figure 12 shows the trajectories of system output x_1 and $\hat{x}_1$ and the error between system output and estimation of output.

6. Conclusion

In this paper, the adaptive switched control with a finite-time switched state observer has been investigated for a class of uncertain nonlinear systems with unknown backlash-like hysteresis in a strict-feedback form. A finite-time switched state observer has been adopted to estimate the unmeasurable states and obtain a better tracking performance, with the help of finite-time performance function and neural network technologies. By transforming the tracking error into a virtual variable and based on the backstepping technique, an adaptive control method has been proposed. It has been proved that the observer error is bounded and finite time is convergent with the proposed control scheme. Moreover, the signals of the resulting system are bounded and the output tracking error is convergent to a small compact set of the origin.

Data Availability

The data used to support the findings of this study are available from the corresponding author upon request.

Conflicts of Interest

The authors declare that they have no conflicts of interest.

Acknowledgments

This work was supported by the National Natural Science Foundation of China under Grant nos. 61703224, 61620304, and 21606141.

References

[1] Q. Chen, X. Ren, J. Na, and D. Zheng, "Adaptive robust finite-time neural control of uncertain PMSM servo system with nonlinear dead zone," *Neural Computing and Applications*, vol. 28, no. 12, pp. 3725–3736, 2017.

[2] W. Lv and F. Wang, "Finite-time adaptive fuzzy tracking control for a class of nonlinear systems with unknown hysteresis," *International Journal of Fuzzy Systems*, vol. 20, no. 3, pp. 782–790, 2018.

[3] S. Li, X. Peng, Y. Tang, and Y. Shi, "Finite-time synchronization of time-delayed neural networks with unknown parameters via adaptive control," *Neurocomputing*, vol. 308, no. 25, pp. 65–74, 2018.

[4] J. Xia, J. Zhang, W. Sun, B. Zhang, and Z. Wang, "Finite-time adaptive fuzzy control for nonlinear systems with full state constraints," *IEEE Transactions on Systems, Man, and Cybernetics: Systems*, vol. 49, no. 7, pp. 1541–1548, 2019.

[5] F. Wang, B. Chen, C. Lin, J. Zhang, and X. Meng, "Adaptive neural network finite-time output feedback control of quantized nonlinear systems," *IEEE Transactions on Cybernetics*, vol. 48, no. 6, pp. 1839–1848, 2018.

[6] Y. Li, K. Li, and S. Tong, "Finite-time adaptive fuzzy output feedback dynamic surface control for MIMO nonstrict feedback systems," *IEEE Transactions on Fuzzy Systems*, vol. 27, no. 1, pp. 96–110, 2019.

[7] Z. Yu, Y. Yang, S. Li, and J. Sun, "Observer-based adaptive finite-time quantized tracking control of nonstrict-feedback nonlinear systems with asymmetric actuator saturation," *IEEE Transactions on Systems, Man, and Cybernetics: Systems*, pp. 1–12, 2018.

[8] Y. Liu, X. Liu, Y. Jing, and Z. Zhang, "A novel finite-time adaptive fuzzy tracking control scheme for nonstrict feedback systems," *IEEE Transactions on Fuzzy Systems*, vol. 27, no. 4, pp. 646–658, 2019.

[9] S. Sui, C. L. P. Chen, and S. Tong, "Neural network filtering control design for nontriangular structure switched nonlinear

systems in finite time," *IEEE Transactions on Neural Networks and Learning Systems*, vol. 30, no. 7, pp. 2153–2162, 2019.

[10] F. Wang, B. Chen, Y. Sun, and C. Lin, "Finite time control of switched stochastic nonlinear systems," *Fuzzy Sets and Systems*, vol. 365, no. 15, pp. 140–152, 2019.

[11] Q. Chen, M. Gao, L. Tao, and Y. Nan, "Adaptive fixed time parameter estimation and synchronization control for multiple robotic manipulators," *International Journal of Control, Automation and Systems*, vol. 17, no. 9, pp. 2375–2387, 2019.

[12] M.-M. Jiang and X.-J. Xie, "Adaptive finite-time stabilisation of high-order uncertain nonlinear systems," *International Journal of Control*, vol. 91, no. 10, pp. 2159–2169, 2018.

[13] Q. Chen, X. Ren, and J. Na, "Robust finite-time chaos synchronization of uncertain permanent magnet synchronous motors," *ISA Transactions*, vol. 58, pp. 262–269, 2015.

[14] Q. Chen, S. Xie, M. Sun, and X. He, "Adaptive nonsingular fixed-time attitude stabilization of uncertain spacecraft," *IEEE Transactions on Aerospace and Electronic Systems*, vol. 54, no. 6, pp. 2937–2950, 2018.

[15] M. Tao, Q. Chen, X. He, and M. Sun, "Adaptive fixed-time fault-tolerant control for rigid spacecraft using a double power reaching law," *International Journal of Robust and Nonlinear Control*, vol. 29, no. 12, pp. 4022–4040, 2019.

[16] V. Hassani, T. Tjahjowidodo, and T. N. Do, "A survey on hysteresis modeling, identification and control," *Mechanical Systems and Signal Processing*, vol. 49, no. 1-2, pp. 209–233, 2014.

[17] Z. Li, J. Shan, and U. Gabbert, "Inverse compensation of hysteresis using Krasnoselskii-Pokrovskii model," *IEEE/ASME Transactions on Mechatronics*, vol. 23, no. 2, pp. 966–971, 2018.

[18] I. Mayergoyz, "Mathematical models of hysteresis," *IEEE Transactions on Magnetics*, vol. 22, no. 5, pp. 603–608, 1986.

[19] X. Zhang, Z. Li, C.-Y. Su, and Y. Lin, "Robust adaptive output-feedback control for a class of nonlinear systems with hysteresis compensation controller," *International Journal of Adaptive Control and Signal Processing*, vol. 31, no. 11, pp. 1636–1654, 2017.

[20] W. Lv, F. Wang, and Y. Li, "Finite-time adaptive fuzzy output-feedback control of MIMO nonlinear systems with hysteresis," *Neurocomputing*, vol. 296, pp. 74–81, 2018.

[21] Y. Jian, D. Huang, J. Liu, and D. Min, "High-precision tracking of piezoelectric actuator using iterative learning control and direct inverse compensation of hysteresis," *IEEE Transactions on Industrial Electronics*, vol. 66, no. 1, pp. 368–377, 2019.

[22] L. Ma, X. Huo, X. Zhao, B. Niu, and G. Zong, "Adaptive neural control for switched nonlinear systems with unknown backlash-like hysteresis and output dead-zone," *Neurocomputing*, vol. 357, no. 10, pp. 203–214, 2019.

[23] C. Li and X. Yang, "Adaptive neural output feedback control for a class of switched non-linear systems with unknown backlash-like hysteresis of the actuator," *Transactions of the Institute of Measurement and Control*, vol. 41, no. 4, pp. 900–910, 2019.

[24] X.-Y. Zhang and Y. Lin, "A robust adaptive dynamic surface control for nonlinear systems with hysteresis input," *Acta Automatica Sinica*, vol. 36, no. 9, pp. 1264–1271, 2010.

[25] S. Sui, S. Tong, C. L. P. Chen, and K. Sun, "Fuzzy adaptive optimal control for nonlinear switched systems with actuator hysteresis," *International Journal of Adaptive Control and Signal Processing*, vol. 33, no. 4, pp. 609–625, 2019.

[26] Y. Wang, H. Lei, J. Ye, X. Bu, and Y. Xue, "Guaranteeing prescribed performance control for gyrostabilized platform with unknown control direction preceded by hysteresis," *International Journal of Aerospace Engineering*, vol. 2019, pp. 1–12, 2019.

[27] J. Na, Q. Chen, X. Ren, and Y. Guo, "Adaptive prescribed performance motion control of servo mechanisms with friction compensation," *IEEE Transactions on Industrial Electronics*, vol. 61, no. 1, pp. 486–494, 2014.

[28] M. Wang, X. Ren, Q. Chen, S. Wang, and X. Gao, "Modified dynamic surface approach with bias torque for multi-motor servomechanism," *Control Engineering Practice*, vol. 50, pp. 57–68, 2016.

[29] M. Wang, X. Ren, and Q. Chen, "Robust tracking and distributed synchronization control of a multi-motor servomechanism with H-infinity performance," *ISA Transactions*, vol. 72, no. 1, pp. 147–160, 2018.

[30] C. Wei, M. Benosman, and T. Kim, "Online parameter identification for state of power prediction of lithium-ion batteries in electric vehicles using extremum seeking," *International Journal of Control, Automation and Systems*, pp. 1–11, 2019.

[31] D. Chowdhury, Y. Al-Nadawi, and X. Tan, "Hysteresis compensation using extended high-gain observer and dynamic inversion," *ASME Proceedings & Mechatronics*, no. DSCC2018-9082, 9 pages, 2018.

[32] X. Huo, L. Ma, X. Zhao, B. Niu, and G. Zong, "Observer-based adaptive fuzzy tracking control of MIMO switched nonlinear systems preceded by unknown backlash-like hysteresis," *Information Sciences*, vol. 490, pp. 369–386, 2019.

[33] J. Wang, K. Chen, Q. Liu, and Q. Ma, "Observer-based adaptive consensus tracking control for nonlinear multi-agent systems with actuator hysteresis," *Nonlinear Dynamics*, vol. 95, no. 3, pp. 2181–2195, 2019.

[34] X. Wang, X. Yin, and F. Shen, "Disturbance observer based adaptive neural prescribed performance control for a class of uncertain nonlinear systems with unknown backlash-like hysteresis," *Neurocomputing*, vol. 299, pp. 10–19, 2018.

[35] Y. Feng, C. A. Rabbath, T. Chai, and C. Su, "Robust adaptive control of systems with hysteretic nonlinearities: a Duhem hysteresis modelling approach," in *Proceedings of the 2009 IEEE Conference on Africon*, Nairobi, Kenya, September 2010.

[36] G. Zhai, B. Hu, K. Yasuda, and A. Michel, "Piecewise Lyapunov functions for switched systems with average dwell time," *Asian Journal of Control*, vol. 2, no. 3, pp. 192–197, 2000.

[37] G. Lai, Z. Liu, Y. Zhang, C. L. P. Chen, and S. Xie, "Adaptive inversion-based fuzzy compensation control of uncertain pure-feedback systems with asymmetric actuator backlash," *IEEE Transactions on Fuzzy Systems*, vol. 25, no. 1, pp. 141–155, 2017.

[38] S. Tong, Y. Li, and S. Sui, "Adaptive fuzzy tracking control design for SISO uncertain nonstrict feedback nonlinear systems," *IEEE Transactions on Fuzzy Systems*, vol. 24, no. 6, pp. 1441–1454, 2016.

[39] Q. Chen, L. Shi, J. Na, X. Ren, and Y. Nan, "Adaptive echo state network control for a class of pure-feedback systems with input and output constraints," *Neurocomputing*, vol. 275, no. 1, pp. 1370–1382, 2018.

Hindawi
Complexity
Volume 2019, Article ID 5367403, 11 pages
https://doi.org/10.1155/2019/5367403

Research Article

An Optimal Allocation Strategy for Multienergy Networks Based on Double-Layer Nondominated Sorting Genetic Algorithms

Min Mou, Da Lin, Yuhao Zhou, Wenguang Zheng, Jiongming Ruan, and Dongdong Ke

Huadian Electric Power Research Institute Co., Ltd., Hangzhou, Zhejiang 310013, China

Correspondence should be addressed to Min Mou; min-mou@chder.com

Received 26 July 2019; Accepted 4 September 2019; Published 29 October 2019

Guest Editor: Xiaoqing Bai

Aiming at the problems of complex structures, variable loads, and fluctuation of power outputs of multienergy networks, this paper proposes an optimal allocation strategy of multienergy networks based on the double-layer nondominated sorting genetic algorithm, which can optimize the allocation of distributed generation (DG) and then improve the system economy. In this strategy, the multiobjective nondominated sorting genetic algorithm is adopted in both layers, and the second-layer optimization is based on the optimization result of the first layer. The first layer is based on the structure and load of the multienergy network. With the purpose of minimizing the active power loss and the node voltage offset, an optimization model of the multienergy network is established, which uses the multiobjective nondominated sorting genetic algorithm to solve the installation location and the capacity of DGs in multienergy networks. In the second layer, according to the optimization results of the first layer and the characteristics of different DGs (wind power generator, photovoltaic panel, microturbine, and storage battery), the optimization model of the multienergy network is established to improve the economy, reliability, and environmental benefits of multienergy networks. It uses the multiobjective nondominated sorting genetic algorithm to solve the allocation capacity of different DGs so as to solve the optimal allocation problem of node capacity in multienergy networks. The double-layer optimization strategy proposed in this paper greatly promotes the development of multienergy networks and provides effective guidance for the optimal allocation and reliable operation of multienergy networks.

1. Introduction

Energy is the driving force and foundation for social and economic development. As traditional fossil energy sources are increasingly exhausted, improving energy efficiency, developing new energy sources, and strengthening multienergy complementarity have become inevitable choices to solve the contradiction between energy demand growth and energy shortage in the process of social and economic development. The multienergy network is a hybrid energy supply system that integrates multiple DGs, energy storage units, loads, and monitoring and protection devices. It can be flexibly connected to the grid or operated on isolated islands, which can effectively improve the flexibility, economy, and cleanliness of power system operation, and meet the requirements of users for power supply reliability, safety, and power quality. Since wind resources and solar resources are clean energy, the power generation of the micro gas turbine (MT) is stable and controllable, and the battery can suppress system power fluctuations. The node diagram of a typical multienergy network is shown in Figure 1. Therefore, the multienergy network studied in this paper includes a wind turbine generator (WTG), a photovoltaic (PV) panel, an MT, and a storage battery (SB).

However, the installation location and capacity of DG and the allocation capacity of various DGs in multienergy networks will have a great impact on the operating technical indicators and economic indicators of the system. Therefore, it is of great importance and necessity to study the optimal allocation of DG in multienergy networks. At present, a lot of researches have been carried out

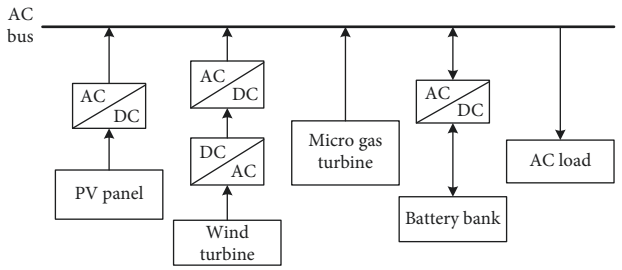

Figure 1: Multienergy network node architecture.

on the optimal allocation of DGs for multienergy networks at home and abroad. For example, literature study [1] adopts a modified particle swarm optimization algorithm to optimize the cost, reliability, and pollutant emissions of hybrid power generation systems. Literature study [2] uses the harmony search algorithm to model and analyze the cost of hybrid systems which include a PV panel, a wind generator (WG), and diesel and then compares them with conventional PV panel/WG/diesel/battery systems. And literature study [3] applies a novel improved fruit fly optimization algorithm-based multiobjective optimization method to optimize the annual total cost and the pollutant emission of the stand-alone hybrid photovoltaic panel-wind generator-diesel-battery system. In addition, literature studies [4–7] have introduced multiobjective optimization algorithms for multiple distributed energy systems. With economic and environmental benefits as optimization objectives, different optimization algorithms are used to optimize the DG allocation capacity of multienergy networks. Besides, literature studies [8–10] introduce a specific allocation method of DG, which is aimed at low system loss or high voltage stability and solves the allocation capacity of DG. However, all of the above studies use the single-level multiobjective optimization function to solve the optimal allocation capacity of DG in multienergy networks when the location of DG is determined, while the installation location of DG needs to be determined by other algorithms.

In this paper, firstly, the first-layer optimization objective function of the minimum active power loss and node voltage offset in the multienergy network system is constructed. The multiobjective optimization strategy based on the nondominated sorting genetic algorithm is used to solve the DG location and sizing. Secondly, in view of the power characteristics of various DGs and the optimization results of the first-layer algorithm, the second-layer algorithm takes into account the economic cost, power supply reliability, and environmental benefits and combines the multiobjective nondominated sorting genetic algorithm to optimize the allocation of various DG capacities. Finally, the proposed algorithm is applied to a multienergy network in a certain area. The results show that the operation performance, economy, reliability, and environmental protection of the multienergy network optimized by the double-layer nondominated sorting genetic algorithm are greatly improved.

2. Multiobjective Nondominated Sorting Genetic Algorithms

2.1. Mathematical Description of the Multiobjective Optimization Algorithm. Taking minimizing multiobjective function with constraints as an example, multiobjective optimization problems can be described as follows:

$$\begin{cases} \min f(X) = [f_1(X), f_2(X), \ldots, f_n(X)], \\ g_i(X) \le 0, \quad i = 1, 2, 3, \ldots, \\ h_j(X) = 0, \quad j = 1, 2, 3, \ldots, \end{cases} \tag{1}$$

where $f(X)$ is a vector space with n objective functions, $g_i(X)$ is the ith inequality constraint function, $h_j(X)$ is the jth equation constraint, and $X = (x_1, x_2, \ldots, x_m)$ is a vector space with m decision variables.

2.2. Decision-Making in Multiobjective Optimization. The multiobjective nondominated sorting genetic algorithm is used to obtain a series of discrete solutions [11–13]. How to choose an optimal solution among these discrete points is the key of the multiobjective optimization. In this paper, an optimal scheme selection method based on the geometric distance method is proposed. The central idea is that the geometric distance between the optimal solution and the positive ideal solution is the shortest, while the geometric distance between the optimal solution and the negative ideal solution is the longest. The optimal solution comes from the optimized Pareto frontier. The positive ideal solution refers to the solution that can satisfy the optimality of each objective function. And the negative ideal solution refers to the solution that does not satisfy any objective functions.

The geometric distance d_i^+ of any solution i on the Pareto frontier to the positive ideal solution is calculated as follows:

$$d_i^+ = \sqrt{\sum_{j=1}^{m} \left(S_{ij} - S_j^{p-\text{ideal}}\right)^2}, \tag{2}$$

where m is the number of objective functions, j is the dimension in which it is located, and $S_{ij} - S_j^{p-\text{ideal}}$ is the linear distance of the jth dimension from the solution i to the positive ideal solution.

The geometric distance d_i^- of any solution on the Pareto frontier to the negative ideal solution is calculated as follows:

$$d_i^- = \sqrt{\sum_{j=1}^{m} \left(S_{ij} - S_j^{n-\text{ideal}}\right)^2}, \tag{3}$$

where $S_{ij} - S_j^{n-\text{ideal}}$ refers to the linear distance of the jth dimension between the solution i and the negative ideal solution.

The coefficient ω_i is defined as follows:

$$\omega_i = \frac{d_i^+}{d_i^+ + d_i^-}. \tag{4}$$

The ω_i corresponding to any solutions in the Pareto frontier can be calculated by (1) to (3), and then the solution corresponding to the smallest ω_i is selected, which is the final optimal solution.

3. First layer: Location and Capacity Optimization of DG

3.1. Decision Variables of the First Layer. The rational planning of the DG in the multienergy network can effectively improve the operating performance of the system, so the decision variables of the first layer are the installation location and capacity of the DG.

This paper uses a set of two-dimensional vectors to represent the decision variables of the first layer, namely, the optimal position and optimal capacity of DG, as shown in Table 1.

3.2. Objective Function of the First-Layer Optimization Algorithm. Reasonable DG installation location and capacity configuration can improve power quality and optimize power flow while taking into account economic benefits. Moreover, some studies have testified that unreasonable locations or sizes of DG may result in greater system losses than the ones in the existing network [14]. The multiobjective optimization function should include economic indicators and technical indicators. The economic index of this layer mainly refers to the minimum active power loss of the multienergy network, and the technical index mainly refers to the minimum voltage offset of load nodes. The objective function is as follows (the function that has to be minimized consists of two objectives: one is economical and the other is technical):

$$\begin{cases} \min P_{\text{loss}} = \sum_{k=1}^{N_1} G_{k(i,j)}\left(U_i^2 + U_j^2 - 2U_iU_j\cos\delta_{ij}\right), \\ \min \Delta U = \sum_{i=1}^{N_d}\left(\dfrac{U_i - U_i^{\text{spec}}}{\Delta U_i^{\max}}\right)^2, \end{cases} \tag{5}$$

where P_{loss} is the active power loss of the multienergy network; ΔU is the offset of the load node voltage in the multienergy network; N_1 represents the number of branches of the multienergy network; N_d represents the number of nodes; $G_{k(i,j)}$ represents the conductance of the branch k (i and j are the node numbers at both ends of the branch k); U_i and U_j represent the voltage amplitudes of the nodes i and j, respectively; δ_{ij} refers to the phase angle difference of the nodes i and j; U_i^{spec} is the desired voltage value of the node i; and $\Delta U_i^{\max}$ is the maximum allowable voltage deviation of the node i, i.e., $\Delta U_i^{\max} = U_i^{\max} - U_i^{\min}$.

3.3. Constraints of the First-Layer Optimization Algorithm. In multienergy networks, constraints are divided into equality constraints and inequality constraints.

Equality constraints are mainly network power flow balancing. Equality constraints of the node i are as follows:

Table 1: Decision variables.

Unit 1		Unit 2		...	Unit n	
Position	Capacity	Position	Capacity	...	Position	Capacity

$$\begin{cases} P_{Gi} + P_{DGi} - P_{Li} - U_i\sum_{j=1}^{N_d} U_j\left(G_{ij}\cos\delta_{ij} + B_{ij}\sin\delta_{ij}\right) = 0, \\ Q_{Gi} - Q_{Li} - U_i\sum_{j=1}^{N_d} U_j\left(G_{ij}\sin\delta_{ij} + B_{ij}\cos\delta_{ij}\right) = 0, \end{cases} \tag{6}$$

where P_{Gi}, P_{DGi}, and P_{Li} refer to the active power of the generator, DG, and load of the node i, respectively; G_{ij} and B_{ij} represent the conductance and admittance between nodes i and j, respectively; and Q_{Gi} and Q_{Li} represent the reactive power of the generator and load of the node i, respectively.

Inequality constraints mainly include the following aspects:

(1) Node voltage constraints:

$$V_{i\min} \le V_i \le V_{i\max}, \quad i = 1, 2, \ldots, N_d, \tag{7}$$

where $V_{i\min}$ and $V_{i\max}$ are the upper and lower limits of the voltage of the node i, respectively.

(2) DG active power upper-limit constraints:

$$0 \le P_{DGi} \le P_{DG\max}, \quad i = 1, 2, \ldots, N_{DG}, \tag{8}$$

where $P_{DG\max}$ is the upper limit of the DG active power and N_{DG} is the number of DGs.

(3) Branch transmission power constraints:

$$|P_k| \le P_{k\max}, \quad k = 1, 2, \ldots, N_1, \tag{9}$$

where $P_{k\max}$ is the upper limit of the transmission power of the branch k.

4. Second Layer: Optimal Capacity Allocation for Various Types of DGs

4.1. DG Modeling. Multienergy networks generally include a WTG, a PV panel, an MT, and an SB [15]. This section establishes power models for various distributed power sources at first.

4.1.1. WTGs. Because of the volatility of wind resources, the power output from the WTG is also unstable. According to the working principle of the WTG, when the wind speed is less than the cut-in wind speed, the WTG does not generate electricity; when the wind speed is greater than the cut-in wind speed and less than the rated wind speed, the WTG generates electricity, and the output electric power varies with the wind speed; when the wind speed is greater than the rated wind speed and less than the cut-out wind speed, the WTG outputs rated power; when the wind speed is greater

than the cut-out wind speed, the WTG stops working and does not generate electricity [16].

The output $P_{\text{wind}}(t)$ of the WTG at time t is as follows [17]:

$$P_{\text{wind}}(t) = \begin{cases} 0, & v(t) \le v_{\text{in}} \text{ or } v(t) \ge v_{\text{out}}, \\ \dfrac{v(t)^3 - v_{\text{in}}^3}{v_{\text{r}}^3 - v(t)^3} * P_{\text{r}}, & v_{\text{in}} \le v(t) \le v_{\text{r}}, \\ P_{\text{r}}, & v_{\text{r}} \le v(t) \le v_{\text{out}}, \end{cases} \tag{10}$$

where $v(t)$ represents the wind speed at time t; v_{in}, v_{r}, and v_{out} represent the cut-in wind speed, the rated wind speed, and the cut-out wind speed, respectively; and P_{r} refers to the rated power of the WTG.

4.1.2. PV Panels. The output voltage and current of the PV panel vary with the change of the illumination intensity and the junction temperature of the battery. They have strong nonlinear characteristics, and there is one maximum power output point under certain working conditions. In order to make full use of solar energy for PV cells, it is necessary to make the working point of PV cells fall at the maximum power point when the illumination intensity and temperature change. Under the maximum power mode, the expressions of power $P_{\text{PV}}(t)$, voltage $V_{\text{PV}}(t)$, and current $I_{\text{PV}}(t)$, that is, the optimum working point t of the PV cell, are as follows [18]:

$$\begin{aligned} P_{\text{PV}}(t) &= V_{\text{PV}}(t) * I_{\text{PV}}(t), \\ V_{\text{PV}}(t) &= V_{\text{mp}} * \left[1 + 0.0539 * \log\left(\frac{H_{\text{T}}(t)}{1000}\right)\right] + \beta * \Delta T(t), \\ I_{\text{PV}}(t) &= I_{\text{SC}} * \left\{1 - a * \left[\exp\left(\frac{V_{\text{PV}}(t) - \Delta V(t)}{b * V_{\text{OC}}}\right) - 1\right]\right\} + \Delta I(t), \\ a &= \left(1 - \frac{I_{\text{mp}}}{I_{\text{SC}}}\right) * \exp\left[\frac{-V_{\text{mp}}}{b * V_{\text{OC}}}\right], \\ b &= \frac{\left(V_{\text{mp}}/V_{\text{OC}}\right) - 1}{\ln\left(1 - \left(I_{\text{mp}}/I_{\text{SC}}\right)\right)}, \\ \Delta T(t) &= T_{\text{A}}(t) + 0.02 * H_{\text{T}}(t) - 25, \\ \Delta V(t) &= V_{\text{PV}}(t) - V_{\text{mp}}, \\ \Delta I(t) &= \alpha * \left(\frac{H_{\text{T}}(t)}{1000}\right) * \Delta T(t) + \left(\frac{H_{\text{T}}(t)}{1000} - 1\right) * I_{\text{SC}}, \end{aligned} \tag{11}$$

where V_{mp} and I_{mp} represent the maximum power point voltage and current of the PV cell, respectively; V_{OC} represents the open circuit voltage; I_{SC} represents the short circuit current; $H_{\text{T}}(t)$ represents the illumination radiance at time t; α represents the current temperature coefficient of the PV cell module; β represents the voltage temperature coefficient of the PV cell module; and $T_{\text{A}}(t)$ represents the ambient temperature at time t.

4.1.3. MTs. MTs are widely used in distributed systems because of their high reliability, long service life, low environmental pollution, and flexible control. Their working principle is that natural gas and high-pressure gas are mixed and burned in the combustion chamber to produce high-quality gas that drives compressors and generators to generate heat and electricity. Suppose that a certain type of MT is operating under full operating conditions and that the electric load is supplied while satisfying the user's cooling and heating load demands. The output power of the MT at time t is as follows [19]:

$$P_{\text{MT}}(t) = \rho * V_{\text{in}}(t) * \text{LH} + C_{\text{P}} * \rho * V_{\text{in}}(t) * \left(T_2(t) - T_1(t)\right), \tag{12}$$

where $P_{\text{MT}}(t)$ represents the power output of the MT at time t, $V_{\text{in}}(t)$ represents the fuel intake amount at time t, ρ is the gas density, LH is the low heating value, C_{P} represents the specific heat capacity, and $T_1(t)$ and $T_2(t)$ indicate the intake air temperature and exhaust gas temperature of the fuel at time t, respectively.

4.1.4. SBs. The SB can suppress the fluctuation of distributed power supply, has the performance of peak shaving and valley filling, and maintains power stability. The output power of the SB is closely related to the operation status of the system [20].

Assuming that lead-acid batteries are used, the state of time t is related to the state of time $t-1$ and the supply and demand of electricity from time $t-1$ to time t. When the total output power of the DG is greater than the load power consumption, the battery pack is in a charging state; otherwise, the battery pack is in a discharging state. The charge of the battery pack at time t can be expressed as follows [19]:

$$P_{\text{SB}}(t) = \begin{cases} P_{\text{SB}}(t-1) + \left(P_{\text{total}}(t) - \dfrac{P_{\text{load}}(t)}{\eta_{\text{inv}}}\right) * \eta_{\text{charge}}; & \text{charge}, \\ P_{\text{SB}}(t-1) - \dfrac{\left(\left(P_{\text{load}}(t)/\eta_{\text{inv}}\right) - P_{\text{total}}(t)\right)}{\eta_{\text{discharge}}}; & \text{discharge}, \end{cases} \tag{13}$$

where $P_{\text{total}}(t) = P_{\text{wind}}(t) + P_{\text{PV}}(t) + P_{\text{MT}}(t)$, $P_{\text{SB}}(t)$ represents the amount of electricity stored in the SB at time t, $P_{\text{total}}(t)$ is the amount of electricity supplied by the DG in the multienergy network at time t, $P_{\text{load}}(t)$ is the load of the system at time t, η_{inv} represents the conversion efficiency of the inverter, η_{charge} is the charging efficiency of the SB, and $\eta_{\text{discharge}}$ is the discharging efficiency of the SB.

4.2. Decision Variables of the Second Layer. The multiobjective optimization algorithm of the first-layer multienergy network has obtained the distributed power supply installation location and total capacity. But the construction

cost, operation cost, output stability, and environmental impact of different types of distributed power supplies are different, so it is necessary to carry out the second-layer multiobjective optimization to obtain the optimal capacity allocation of various distributed power sources.

The main decision variables at the second layer of the network are as follows:

$$X = \{N_{\text{wind}}, N_{\text{PV}}, N_{\text{MT}}, N_{\text{SB}}\}, \tag{14}$$

where $N_{\text{wind}}, N_{\text{PV}}, N_{\text{MT}}$, and N_{SB} represent the number of WTGs, PV cells, MTs, and SBs, respectively.

4.3. Objective Function of the Second-Layer Optimization Algorithm. The objectives of the second-layer optimization algorithm are mainly to consider economy, power supply reliability, and environmental protection. The objective functions are as follows.

4.3.1. Economy. The economy of the multienergy network is mainly reflected by the construction cost and operation cost of the DG system [21]. The objective functions of the economy are as follows:

$$\begin{aligned}
\min C_{\text{total}} &= \min\left(C_{\text{Cpt}} + C_{\text{Mtn}}\right),\\
C_{\text{Cpt}} &= C_{\text{Cpt}}^{\text{wind}} + C_{\text{Cpt}}^{\text{PV}} + C_{\text{Cpt}}^{\text{MT}} + C_{\text{Cpt}}^{\text{SB}},\\
C_{\text{Cpt}}^{\text{wind}} &= N_{\text{wind}} * e_{\text{wind}} * P_{\text{wind}} * \frac{r * (1+r)^{m_{\text{wind}}}}{(1+r)^{m_{\text{wind}}} - 1},\\
C_{\text{Cpt}}^{\text{PV}} &= N_{\text{PV}} * e_{\text{PV}} * P_{\text{PV}} * \frac{r * (1+r)^{m_{\text{PV}}}}{(1+r)^{m_{\text{PV}}} - 1},\\
C_{\text{Cpt}}^{\text{MT}} &= N_{\text{MT}} * e_{\text{MT}} * P_{\text{MT}} * \frac{r * (1+r)^{m_{\text{MT}}}}{(1+r)^{m_{\text{MT}}} - 1},\\
C_{\text{Cpt}}^{\text{SB}} &= * e_{\text{SB}} * P_{\text{SB}} * \frac{r * (1+r)^{m_{\text{SB}}}}{(1+r)^{m_{\text{SB}}} - 1},\\
C_{\text{Mtn}} &= N_{\text{wind}} * \mu(P_{\text{wind}}) + N_{\text{PV}} * \mu(P_{\text{PV}})\\
&\quad + N_{\text{MT}} * \mu(P_{\text{MT}}) + N_{\text{SB}} * \mu(P_{\text{SB}}),
\end{aligned} \tag{15}$$

where C_{total} is the total cost of power generation; C_{Cpt} and C_{Mtn} represent the cost of construction and operation and maintenance of DG in the multienergy network, respectively; $P_{\text{wind}}, P_{\text{PV}}, P_{\text{MT}}$, and P_{SB} represent the output power of each WTG, PV cell, MT, and SB, respectively; $e_{\text{wind}}, e_{\text{PV}}, e_{\text{MT}}$, and e_{SB} represent the unit cost of the WTG, PV cell, MT, and SB, respectively; $\mu(P_{\text{wind}}), \mu(P_{\text{PV}})$, $\mu(P_{\text{MT}})$, and $\mu(P_{\text{SB}})$ represent the operation and maintenance costs of each WTG, PV cell, MT, and SB, respectively; $m_{\text{wind}}, m_{\text{PV}}, m_{\text{MT}}$, and m_{SB} represent the depreciation life of the WTG, PV cell, MT, and SB, respectively; and r is the discount rate of the equipment, generally 8%.

4.3.2. Power Supply Reliability. Multienergy networks contain fluctuating DGs, and the load of multienergy networks also changes with time [22]. Therefore, it is necessary to evaluate the power supply reliability of the system; that is, the rate of load shortage is required. The smaller the rate of power shortage, the higher the reliability of power supply, and vice versa [23]. This paper takes one day ($T = 24$ h) as the period for evaluating the power supply reliability of the system and divides this period into 24 sections. Assuming that the wind speed, light, temperature, and load are constant in each section (1 h), the load shortage rate in one evaluation period of the system is as follows:

$$\begin{aligned}
\min \text{LSRP} &= \sum_{t=1}^{T}\left[\frac{P_{\text{load}}(t) - P_{\text{DG}}(t) * \eta_{\text{inv}}}{P_{\text{load}}(t)} * U(t)\right],\\
P_{\text{DG}}(t) &= N_{\text{wind}} * P_{\text{wind}}(t) + N_{\text{PV}} * P_{\text{PV}}(t) + N_{\text{MT}}\\
&\quad * P_{\text{MT}}(t) + N_{\text{SB}} * \left[P_{\text{SB}}(t) - P_{\text{SB}\min}\right],\\
U(t) &= \begin{cases} 1, & P_{\text{DG}}(t) < P_{\text{load}}(t),\\ 0, & P_{\text{DG}}(t) \geq P_{\text{load}}(t), \end{cases}
\end{aligned} \tag{16}$$

where LSRP represents the one-day load shortage rate of the system; $P_{\text{load}}(t)$ represents the load at time t; $P_{\text{wind}}(t), P_{\text{PV}}(t), P_{\text{MT}}(t)$, and $P_{\text{SB}}(t)$ refer to the output power of the WTG, PV cell, MT, and SB at time t, respectively; $P_{\text{SB}\min}$ represents the minimum residual power allowed by the SB; and η_{inv} represents the efficiency of the inverter.

4.3.3. Environmental Protection. Environmental protection is mainly reflected by the emission of pollutants (NO_x, CO, CO_2, and SO_2) from DGs. WTG power generation and PV power generation belong to clean energy generation, and they do not emit pollutants. Although the output power of the MT can be flexibly controlled, it will emit pollutants. The higher the emission of pollutants, the worse the environmental protection [24]. The environmental cost of power generation EM_{plt} in the evaluation cycle is as follows:

$$\min \text{EM}_{\text{plt}} = \sum_{t=1}^{T}\sum_{i=1}^{n} N_{\text{MT}} * P_{\text{MT}}(t) * (\alpha_i * Q_i), \tag{17}$$

where α_i refers to the i^{th} emission of pollutants of unit power of the MT, Q_i is the treatment fee of i^{th} pollutants of unit power of emission, $P_{\text{MT}}(t)$ denotes the output power of the MT at time t, and N_{MT} is the input quantity of the MT in the system.

4.4. Constraints of the Second-Layer Optimization Algorithm

4.4.1. Power Balance Constraint. In this paper, the DG capacity of the multienergy network solved by the first-layer optimization algorithm is the sum of all kinds of DGs in the second layer so as to ensure the minimum active power loss and voltage offset of the multienergy network. The power constraints are as follows:

$$\left|\frac{\left[P_{\text{DG}}(t) - P_{\text{DG}}^{*}(t)\right]}{P_{\text{DG}}^{*}(t)}\right| \leq \delta(t), \tag{18}$$

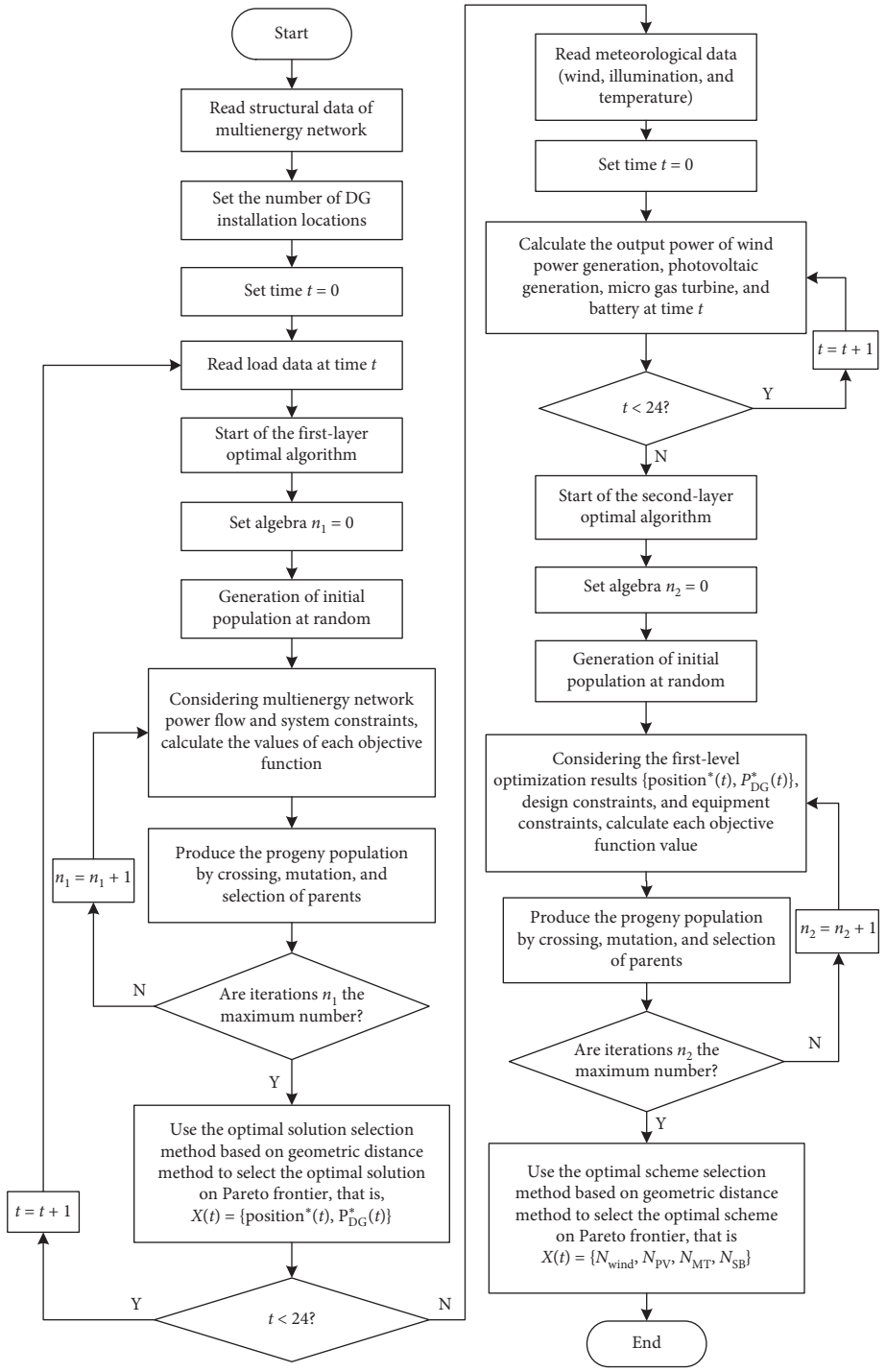

Figure 2: Flow chart of the algorithm.

where $P_{DG}(t) = N_{wind} * P_{wind}(t) + N_{PV} * P_{PV}(t) + N_{MT} * P_{MT}(t) + N_{SB} * P_{SB}(t)$, $P^*_{DG}(t)$ denotes the installed capacity of DGs obtained from the first-layer optimization algorithm at time t, and $\delta(t)$ denotes the maximum unbalanced rate of power that the system can withstand at time t.

4.4.2. Bounds of Design Variables. The bounds of design variables are as follows:

$$\begin{cases} 0 \le N_{wind} \le N^{max}_{wind}, \\ 0 \le N_{PV} \le N^{max}_{PV}, \\ N^{min}_{MT} \le N_{MT} \le N^{max}_{MT}, \\ 0 \le N_{SB} \le N^{max}_{SB}, \end{cases} \tag{19}$$

where N^{max}_{wind}, N^{max}_{PV}, N^{max}_{MT}, and N^{max}_{SB}, respectively, represent the maximum number of WTGs, PV cells, MTs, and SBs that meets the system load demand and N^{min}_{MT} is the minimum

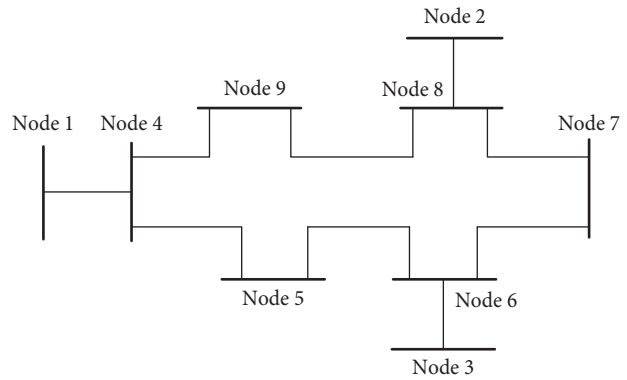

Figure 3: Multienergy network architecture.

number of MTs that meets the condition of "fixing electricity by heat."

4.4.3. Battery Constrains. The battery constraints are as follows:

$$P_{\mathrm{SB\,min}} \le P_{\mathrm{SB}}(t) \le P_{\mathrm{SB\,max}}, \tag{20}$$

where $P_{\mathrm{SB\,max}}$ represents the maximum storage capacity allowed by the SB.

5. Algorithmic Flow

The flow chart of the optimal allocation strategy for the multienergy network based on the double-layer nondominated sorting genetic algorithm proposed in this paper is shown in Figure 2.

6. Case Study

In this paper, a 9-node multienergy network system is taken as an example to verify the optimization effect of the double-layer nondominated sorting genetic algorithm. The topological structure of this multienergy network system is shown in Figure 3. Among them, node 1 is a balanced node, node 3 is a PV node, and the rest nodes are all PQ nodes. The grid parameters (unit values) are shown in Table 2. The evaluation period T of this example is chosen as one day (24 h), and the load data (per unit) and meteorological data in the evaluation period are shown in Figures 4–7 separately. The parameters of lines, WTG, PV panel, MT, and SB and pollutant treatment fee are shown in Tables 2–8, respectively [25].

The optimal allocation strategy proposed in this paper is used to optimize the 9-node multienergy network. The population size of the double-layer optimization algorithm is 200, the number of iterations is 100, and there are two locations in the network where DG can be installed. The first-layer multiobjective optimization algorithm optimizes the location capacity of 24-hour DG in real time based on the 24-hour real-time load data of the network. The second-layer multiobjective optimization algorithm solves the capacity optimization of various DGs with the constraints of the first-layer optimization results, equipment characteristics, and design.

Table 2: Line parameters.

Initial points of the line	End of the line	Resistance	Inductance	Capacitance
1	4	0.000	0.025	0.000
4	5	0.007	0.040	0.017
5	6	0.016	0.073	0.039
3	6	0.000	0.025	0.000
6	7	0.005	0.043	0.023
7	8	0.004	0.031	0.016
8	2	0.000	0.027	0.000
8	9	0.014	0.070	0.033
9	4	0.004	0.037	0.019

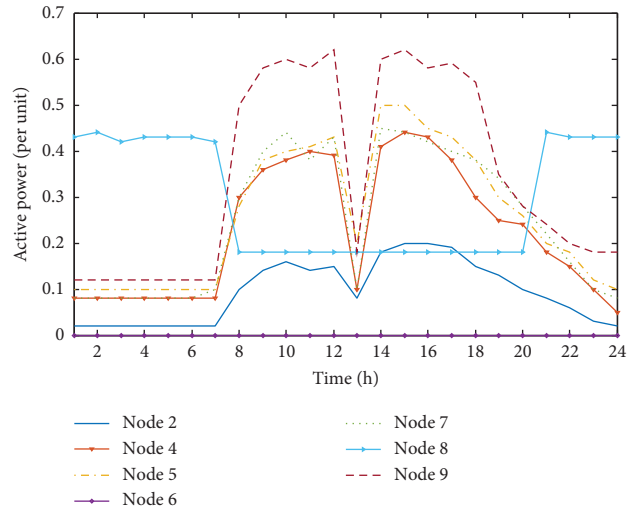

Figure 4: Active power data of the load at each node.

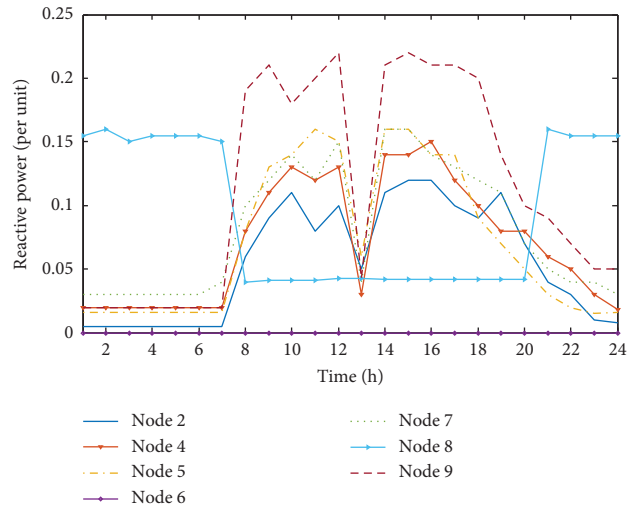

Figure 5: Reactive power data of the load at each node.

The results of the first-layer optimization algorithm are shown in Tables 9 and 10, and the Pareto solution of 100 generations of evolution at a certain time (such as at 13:00) is shown in Figure 8.

The above operation results show that, after adopting the optimal allocation strategy of the multienergy network based

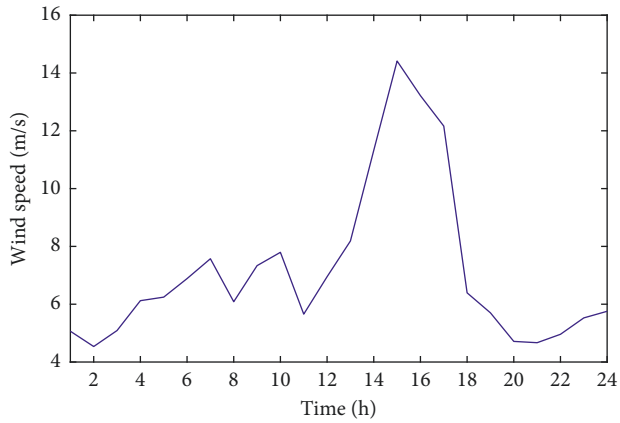

Figure 6: Wind resource data.

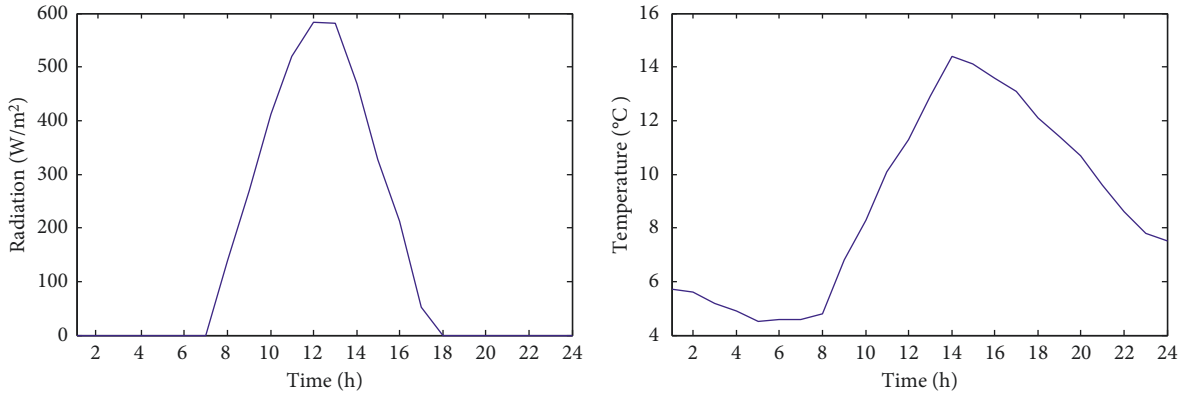

(a) (b)

Figure 7: Solar resource data. (a) Radiation. (b) Temperature.

Table 3: Wind turbine generator parameters.

P_r (kW)	V_{in} (m/s)	V_r (m/s)	V_{out} (m/s)	N_{wind}^{max}
500	3	12	25	8

Table 4: PV panel parameters.

P_r (kW)	V_{OC} (V)	I_{sc} (A)	V_{mp} (V)	I_{mp} (A)	Series number	Parallel number	N_{PV}^{max}
100	64.6	6.14	54.7	5.76	5	64	30

Table 5: MT parameters.

P_r (kW)	C_p (kJ/kg·K)	LH (MJ/m³)	ρ (kg/m³)	T_1 (°C)	T_2 (°C)	N_{MT}^{max}	N_{MT}^{min}
300	2.16	32.6	0.75	25	280	20	1

Table 6: Battery parameters.

P_r (kW)	$P_{SB\,ini}$ (kW)	$P_{SB\,min}$ (kW)	$P_{SB\,max}$ (kW)	η_{charge}	$\eta_{discharge}$	η_{inv}	N_{SB}^{max}
24	9.6	4.8	24	0.85	0.98	0.87	40

Table 7: Cost values.

Type	Life span (years)	Unit cost ($/kW)	Maintenance cost ($/kW)
WTG	20	523	38
PV panel	20	508	29
MT	20	1160	92
SB	10	156	22

Table 8: Pollutant emission of the MT.

Type	NO_x	CO_2	CO	SO_2
Value (g/kWh)	0.6188	184.0829	0.1702	0.000928
Maintenance ($/kg)	0.250	0.00125	0.020	0.125

Table 9: The first-layer decision variables.

Time	First location	First sizing	Second location	Second sizing
1:00	8	0.7587	9	0.2803
2:00	8	0.2184	9	0.8181
3:00	8	0.4325	9	0.5976
4:00	8	0.7628	9	0.2839
5:00	8	0.7074	9	0.3300
6:00	8	0.7541	9	0.2678
7:00	8	0.2695	9	0.7638
8:00	8	0.7190	9	0.7229
9:00	8	0.8485	9	0.7799
10:00	8	0.8922	9	0.7764
11:00	8	0.8608	9	0.8028
12:00	8	0.8887	9	0.8094
13:00	8	0.3797	9	0.4001
14:00	8	0.7833	9	0.9528
15:00	8	0.8063	9	0.9492
16:00	8	0.9274	9	0.7632
17:00	8	0.8883	9	0.7713
18:00	8	0.7370	9	0.8519
19:00	8	0.5159	9	0.7931
20:00	8	0.4600	9	0.7055
21:00	8	0.8561	9	0.3772
22:00	8	0.7965	9	0.3319
23:00	8	0.6882	9	0.3499
24:00	8	0.5463	9	0.4537

Table 10: Comparison of the optimization index.

	System loss ($\times 10^{-3}$)	Voltage deviation
Before optimization	8.435	0.416
After optimization	0.413~5.603	0.015~0.351
Final optimal solution	3.815	0.215

on the double-layer nondominated sorting genetic algorithm, the active power loss of the multienergy network is reduced by 54.77% and the system voltage deviation is reduced by 48.32%. This proves that this strategy can effectively improve the operating conditions of the system, guarantee the stability and economic benefits, and improve the power quality.

The results of the second-layer optimization algorithm are shown in Table 11, and the Pareto solution of the 100-generation evolution is shown in Figure 9. Comparing the optimization solution of this paper with the nonoptimization solution, the results are shown in Table 12. Nonoptimization solution only consists of a single type of DG such as WTG, PV, MT, and SB, and its capacity is capped.

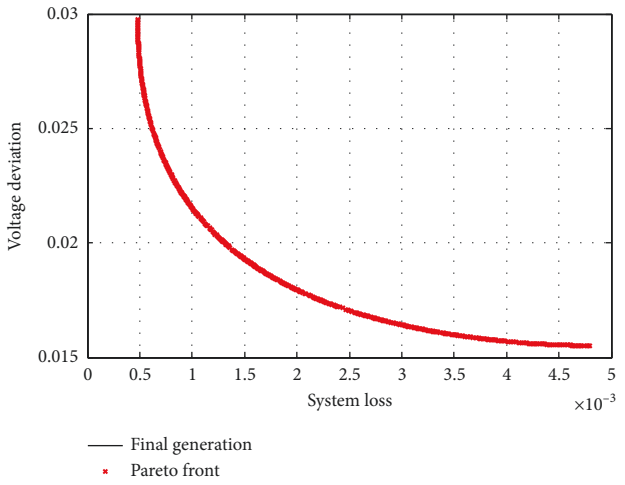

Figure 8: The Pareto front result at 13:00.

Table 11: The second-layer decision variables.

DG location	N_{wind}	N_{PV}	N_{MT}	N_{SB}
First	2	7	17	7
Second	1	8	13	23

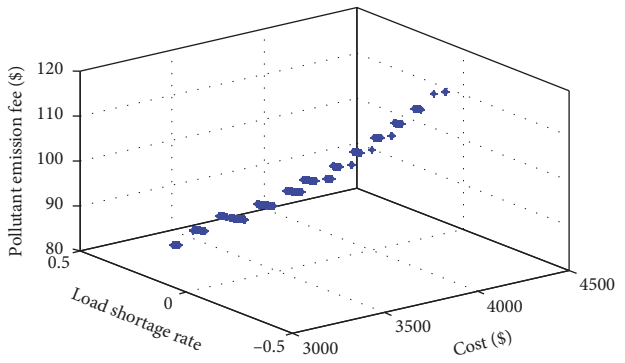

Figure 9: The second Pareto front result.

Table 12: Comparison of the optimization index.

	N_{wind}	N_{PV}	N_{MT}	N_{SB}	C_{total} ($)	LSRP	EM_{plt} ($)
Without optimization	16	0	0	0	949.63	6.64	0.0
	0	60	0	0	561.77	10.24	0.0
	0	0	40	0	2656.32	3.49	111.84
	0	0	0	80	127.96	19.57	0.0
	16	60	40	80	4295.67	0.0	111.84
With optimization	3	15	30	30	3448.83	0.26	81.08

When there are no optimization and only a single type of DG, although the costs of construction, operation, and maintenance are relatively low, the power shortage rate and the cost of pollutant treatment are relatively high. When there are no optimization and all kinds of DGs, although the load power shortage rate is 0, the cost of construction, operation, maintenance, and pollutant treatment is relatively high. Considering the economy, reliability, and environmental protection of the system at the same time, it is necessary to optimize DG allocation of the multienergy network by using the double-layer nondominated sorting genetic algorithm. After optimization, the relative environmental cost and load power shortage rate of the multienergy network are maintained at a relatively low level, which improves the economic effect, environmental protection benefits, and power supply reliability.

7. Conclusion

Aiming at the complex and changeable multienergy network, this paper proposes a multienergy network optimal allocation strategy based on the double-layer nondominated sorting genetic algorithm. Firstly, according to the network load and grid structure, the first-layer optimization algorithm calculates the optimal location and capacity of DG in the multienergy network with the purpose of reducing the network loss and the system voltage offset. Subsequently, the second-layer optimization algorithm takes the first-layer calculation results as constraints and calculates the optimal allocation of different types of DGs, whose purpose is to improve economy, power supply reliability, and environmental protection. The double-layer optimization algorithm uses the optimal scheme selection method based on the geometric distance method to solve the decision variables. Finally, the case study in this paper shows that the double-layer optimal allocation strategy can effectively reduce network loss, improve system voltage, reduce system cost, improve system power supply reliability, increase system environmental benefits, and provide guidance for the design and optimal operation of multienergy networks.

Data Availability

The data used to support the findings of this study are included within the article.

Conflicts of Interest

Min Mou, Da Lin, Yuhao Zhou, Wenguang Zheng, Jiongming Ruan, and Dongdong Ke are employees of Huadian Electric Power Research Institute Co., Ltd., Hangzhou, Zhejiang 310013, China.

Acknowledgments

This work was supported by the National Key R&D Program of China under No. 2018YFB0905101.

References

[1] L. Wang and C. Singh, "Multicriteria design of hybrid power generation systems based on a modified particle swarm optimization algorithm," *IEEE Transaction on Energy Conversion*, vol. 24, no. 1, pp. 163–172, 2009.

[2] A. Maleki and F. Pourfayaz, "Sizing of stand-alone photovoltaic/wind/diesel system with battery and fuel cell storage devices by harmony search algorithm," *Journal of Energy Storage*, vol. 2, pp. 30–42, 2015.

[3] J. Zhao and X. Yuan, "Multi-objective optimization of stand-alone hybrid PV-wind-diesel-battery system using improved fruit fly optimization algorithm," *Soft Computing*, vol. 20, no. 7, pp. 2841–2853, 2016.

[4] Y.-Y. Hong and R.-C. Lian, "Optimal sizing of hybrid wind/PV/diesel generation in a stand-alone power system using Markov-based genetic algorithm," *IEEE Transactions on Power Delivery*, vol. 27, no. 2, pp. 640–647, 2012.

[5] M. A. Abido, "Environmental/economic power dispatch using multiobjective evolutionary algorithms," *IEEE Transactions on Power Systems*, vol. 18, no. 4, pp. 1529–1537, 2003.

[6] Q. Lin, J. Chen, Z. Zhan et al., "A hybrid evolutionary immune algorithm for multiobjective optimization problems," *IEEE Transaction on Evolutionary Computation*, vol. 20, no. 5, pp. 711–728, 2016.

[7] W. Kellogg, M. H. Nehrir, G. Venkataramanan, and V. Gerez, "Optimal unit sizing for a hybrid wind/photovoltaic generating system," *Electric Power Systems Research*, vol. 39, no. 1, pp. 35–38, 1996.

[8] M. Gandomkar, M. Vakilian, and M. Ehsan, "A genetic-based Tabu search algorithm for optimal DG allocation in distribution networks," *Electric Power Components and Systems*, vol. 33, no. 12, pp. 1351–1362, 2005.

[9] C. L. T. Borges and D. M. Falcão, "Optimal distributed generation allocation for reliability, losses, and voltage improvement," *International Journal of Electrical Power & Energy Systems*, vol. 28, no. 6, pp. 413–420, 2006.

[10] A. Kazemi and M. Sadeghi, "Distributed generation allocation for loss reduction and voltage improvement," in *Proceedings of the 2009 Asia-Pacific Power and Energy Engineering Conference*, pp. 518–524, IEEE, Wuhan, China, March 2009.

[11] H. Li and Q. Zhang, "Multiobjective optimization problems with complicated Pareto sets, MOEA/D and NSGA-II," *IEEE Transactions on Evolutionary Computation*, vol. 13, no. 2, pp. 284–302, 2009.

[12] K. Deb, *Multi-Objective Optimization Using Evolutionary Algorithms*, Wiley, New York, NY, USA, 2001.

[13] D. Liu, K. C. Tan, C. K. Goh, and W. K. Ho, "A multiobjective memetic algorithm based on particle swarm optimization," *IEEE Transactions on Systems, Man, and Cybernetics, Part B (Cybernetics)*, vol. 37, no. 1, pp. 42–50, 2007.

[14] T. Griffin, K. Tomsovic, D. Secrest, and A. Law, "Placement of dispersed generations systems for reduced losses," in *Proceedings of the 33rd Annual Hawaii International Conference on System Sciences*, Maui, HI, USA, January 2000.

[15] X. Q. Kong, R. Z. Wang, and X. H. Huang, "Energy optimization model for a CCHP system with available gas turbines," *Applied Thermal Engineering*, vol. 25, no. 2-3, pp. 377–391, 2005.

[16] F. Cheng, L. Qu, W. Qiao, C. Wei, and L. Hao, "Fault diagnosis of wind turbine gearboxes based on DFIG stator current envelope analysis," *IEEE Transactions on Sustainable Energy*, vol. 10, no. 3, pp. 1044–1053, 2019.

[17] Y. Z. Sun, J. Wu, G. J. Li, and J. He, "Dynamic economic dispatch considering wind power penetration based on wind speed forecasting and stochastic programming," *Proceedings of the CSEE*, vol. 29, no. 4, pp. 41–47, 2009.

[18] B. S. Borowy and Z. M. Salameh, "Methodology for optimally sizing the combination of a battery bank and PV array in a wind/PV hybrid system," *IEEE Transactions on Energy Conversion*, vol. 11, no. 2, pp. 367–375, 1996.

[19] R. Wang, *Research on Multi-Objective Optimization Design and Coordinated Control of Distributed Generation and Microgrid*, Shandong University, Jinan, China, 2013.

[20] C. Wei, M. Benosman, and T. Kim, "Online parameter identification for state of power prediction of lithium-ion batteries in electric vehicles using extremum seeking," *International Journal of Control, Automation and Systems*, 2019.

[21] W. El-Khattam, K. Bhattacharya, Y. Hegazy, and M. M. A. Salama, "Optimal investment planning for distributed generation in a competitive electricity market," *IEEE Transaction on Power System*, vol. 19, no. 3, pp. 1674–1684, 2004.

[22] D. Singh, D. Singh, and K. S. Verma, "Multiobjective optimization for DG planning with load models," *IEEE Transaction on Power System*, vol. 24, no. 1, pp. 427–436, 2009.

[23] A. A. Chowdhury, S. K. Agarwal, and D. O. Koval, "Reliability modeling of distributed generation in conventional distribution systems planning and analysis," *IEEE Transaction on Industry Application*, vol. 39, no. 5, pp. 1493–1498, 2003.

[24] M. Abido, "Environment/economic power dispatch using multiobjective evolutionary algorithm," *IEEE Transaction on Power System*, vol. 18, no. 4, pp. 1529–1537, 2003.

[25] W. D. Kellogg, M. H. Nehrir, G. Venkataramanan, and V. Gerez, "Generation unit sizing and cost analysis for stand-alone wind, photovoltaic, and hybrid wind/PV systems," *IEEE Transactions on Energy Conversion*, vol. 13, no. 1, pp. 70–75, 1998.

Hindawi
Complexity
Volume 2019, Article ID 7824743, 13 pages
https://doi.org/10.1155/2019/7824743

Research Article

Investigation of Var Compensation Schemes in Unbalanced Distribution Systems

Yinuo Huang[1], **Licheng Wang**[2] **and Kai Wang**[1]

[1]*College of Electrical Engineering, Qingdao University, Qingdao 266071, China*
[2]*College of Information Engineering, Zhejiang University of Technology, Hangzhou 310023, China*

Correspondence should be addressed to Licheng Wang; wanglicheng@zju.edu.cn

Received 26 July 2019; Accepted 23 September 2019; Published 28 October 2019

Guest Editor: Xiaoqing Bai

Distributed rooftop photovoltaic (PV) generators prospered distributed generation (DG) in recent years. Certain randomness of rooftop PV connection may lead to significant PV power imbalance across three phases, especially in low-voltage distribution systems. Due to interphase line coupling, traditional Var compensation methods which typically have competent voltage regulation performance may become less effective in such PV imbalance scenarios. In this paper, the limitation of traditional Var compensation methods in voltage regulation with unbalanced PV power integration is demonstrated and comprehensively analyzed. After describing the voltage regulation challenge, based on the voltage sensitivity analysis, it is revealed that PV power unbalanced level together with equivalent mutual impedance among phase conductors has a significant impact on the effectiveness of traditional Var compensation methods on voltage regulation. On this basis, to improve the performance of voltage regulation methods, some suggestions are proposed for both current system operation and future distribution system planning. Numerical studies demonstrate the effectiveness of the proposed suggestions. Future rooftop PV integration in LV systems can benefit from this research.

1. Introduction

In recent years, various distributed generation and storage systems including photovoltaic, wind power, electric vehicles, etc., have been developed vigorously [1–6]. As one of the most attractive options of distributed generation (DG) [7–10], more and more single-phase rooftop photovoltaic (PV) generators are integrated into low-voltage distribution systems. These small-size PV systems installed on rooftops of customers' houses as distributed generators can support household appliances and feed excessive PV power back to the grid. However, as PV penetration increases, consequent reverse power flow might induce significant voltage rise at the end of distribution feeders [11, 12].

To avoid the potential overvoltage problem, the maximum PV penetration of a distribution system should be carefully assessed. In early research, single-phase equivalent systems are used to estimate possible voltage problems with high PV penetration levels [13, 14]. While in [15], a stochastic method is designed to imitate the random connection of single-phase PV generators and to estimate the corresponding three-phase voltage problem in low-voltage systems.

In order to accommodate more rooftop PV generators, Var compensation devices are required to actively participate in voltage regulation [16–19]. Optimal voltage/Var control methods of inverters have been discussed by many previous publications [20–25]. However, distribution network optimization requires full or partial observability of the entire network through communication systems and information exchange systems, which are not available for most low-voltage distribution systems nowadays. Furthermore, since optimal methods take time, its respond speed might not be fast enough to follow the variation in sunlight intensity. To simplify the optimal control methods and shorten computing time, some multilevel dispatch is proposed. In [26], zonal voltage control combining day-ahead dispatch and real-time control for distribution networks with high proportion of PV power is researched. In [27], a bilevel voltage/Var optimization to coordinate smart

inverters with voltage control devices is carried out. However, a PV system may lose 70% of its generation in a short period due to fast-moving cloud coverage [28], which makes centralized optimal control methods difficult to keep up with fast fluctuating PV power. Therefore, optimal methods to coordinate all distributed PV inverters in distribution network are still in the academic discussion stage.

On the other hand, Var compensation methods that only rely on local measurements (e.g., PV generation and local line-to-ground voltage) also have already been widely implemented in centralized PV plants for the point of common coupling (PCC) voltage regulation [29–31]. The main advantage of these methods is their rapid response speed, which makes them suitable to counter fast voltage fluctuations caused by PV power variations and with more attractive options for distributed rooftop PV generators. In this field, previous research mainly focuses on the design of Q(P) and Q(V) curves in order to improve their voltage regulation performance [32, 33].

However, since single-phase rooftop PV generators are integrated into low-voltage distribution systems randomly, PV power penetration across three phases tends to be unbalanced. In such situations, widely implemented locally dependent Var compensation methods that can successfully control the PCC voltage of large-scale PV plants may become less effective in voltage regulation with distributed rooftop PV generators. In this paper, the limitation of locally dependent Var compensation methods in voltage regulation with unbalanced PV power integration is comprehensively analyzed.

The remainder of this paper is organized as follows: Section 2 introduces background of proposed problem. In Section 3, the limitation of locally dependent Var compensation methods in voltage regulation with unbalanced PV power integration is revealed. Section 4 analyzed this voltage regulation problem. Some suggestions are proposed for both current system operation and future distribution system planning in Section 5. Numerical studies are presented in Section 6. Finally, Section 7 concludes the paper.

2. Background Introduction

2.1. Rooftop PV Generators and Reverse Power Flow. Rooftop PV generators are becoming more and more popular in recent days, not only due to its clean and renewable characteristics, but these PV systems can sell excessive power back to the utility after providing power supply for customers' household appliances.

PV panels generate active power only in the daytime, with a peak value during noon as shown in Figure 1(a). While, for typical residential load profiles such as in Figure 1(b), peak load usually occurs in the morning and evening, with valley load during noon and night. The valley load during noon can be less than 30% of its peak value. Therefore, PV power would exceed load demand during noon, and reverse power flow would be caused (by negative load) in distribution feeders as shown in Figure 1(c).

2.2. PV System Var Generation Control. Schematic diagram of a PV system with corresponding control loops is displayed in Figure 2 [34]. The main control task for a PV system is to regulate its DC-link voltage following a maximum power-point tracking (MPPT) scheme which is designed to maximize the electricity power harvested from PV panels. At the same time, PV inverters may also be required to generate a certain amount of reactive power for system voltage regulation. Specifically, the control tasks as discussed above can be realized following the three coordinated parts.

2.2.1. Phase-Locked loop (PLL). A PLL component is adopted to synchronize PWM and control schemes to the PCC voltage. In this way, the AC signals are converted into dq-frame correspondence signals, and the controllers can deal with their DC equivalent values instead of the original sinusoidal signals.

2.2.2. DC-Link Voltage-Control Loop. The error between the square of the DC voltage v_{dc}^2 and its corresponding reference value v_{dcref}^2 is dealt with by using a feed-forward compensator, which neutralizes the instability and nonlinearity of PV panels and improves the stability of the PV system. v_{dcref} is usually obtained from MPPT schemes, with a certain variation range in order to ensure safe operation of inverters. The output of the compensation is enhanced by the feed-forward signal, and the current command i_{dcref} is generated.

2.2.3. Current-Control Loop. The current commands are transmitted to a current-control scheme, which is established in a dq-frame drive i_{d} to track i_{dcref} and dq-frame drive i_{q} to track i_{qcref}. It is worth noting that the active power output P_{PV} is controlled by i_{d}, while i_{q} is responsible for adjusting the reactive power generation of a PV inverter. Its value of Var generation can be determined by specific Var compensation strategies, which will be introduced in the next section. In addition, the current-control scheme also protects the PV inverter from overload and external faults, as long as the value of i_{dcref} is properly limited by saturation blocks.

2.3. Locally Dependent Var Compensation Methods. Reverse power flow caused by a large amount of PV power integration will significantly increase system voltage at the end of distribution feeders, which might induce overvoltage issues. In order to mitigate the voltage rise, PV inverters are required to provide Var compensation.

Due to the effectiveness and easy implementation, Var compensation methods that only rely on local measurements have already been widely applied on voltage regulation for large-scale PV plants so far. Two typical locally dependent Var compensation methods are shown in Figure 3. On the one hand, in Figure 3(a), PV inverters are required to operate with a constant power factor (e.g., 0.9 leading). Namely, the reactive power generation of a PV inverter

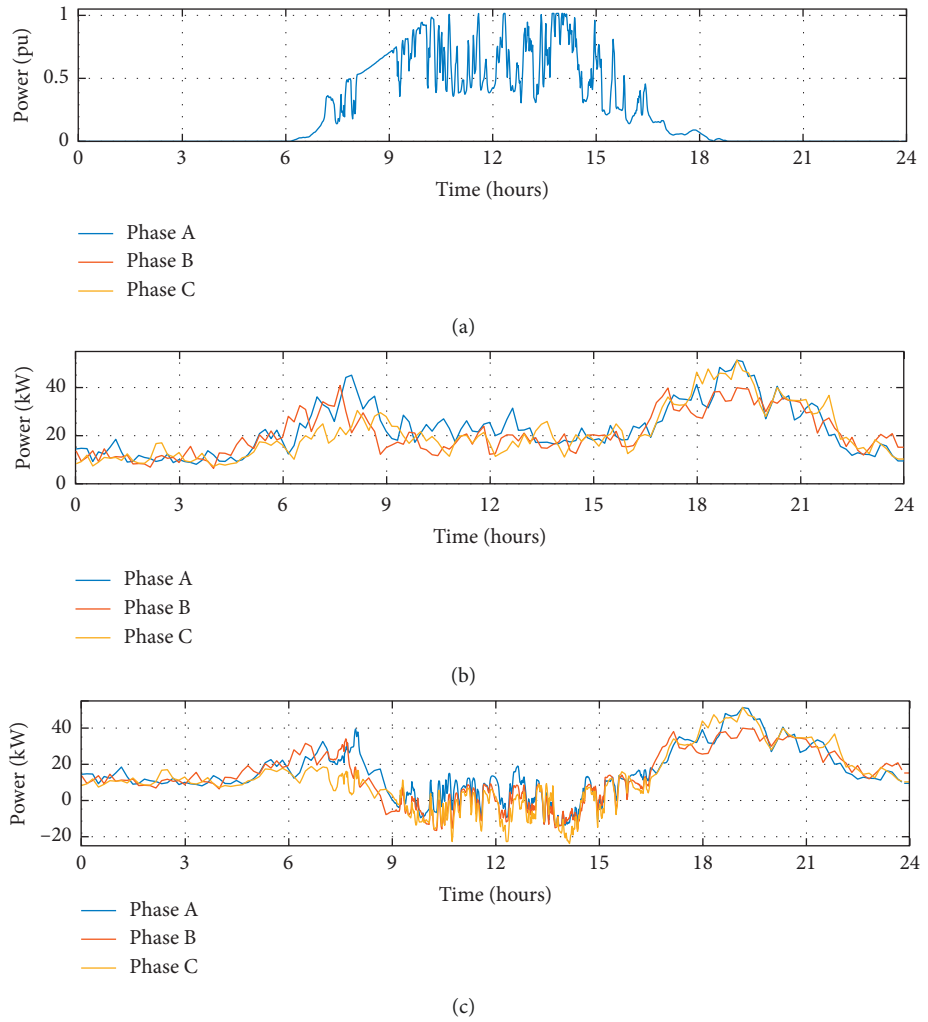

Figure 1: PV power and load demand in one day: (a) normalized PV power profile; (b) load profile without PV power integration; (c) load profile with PV power integration.

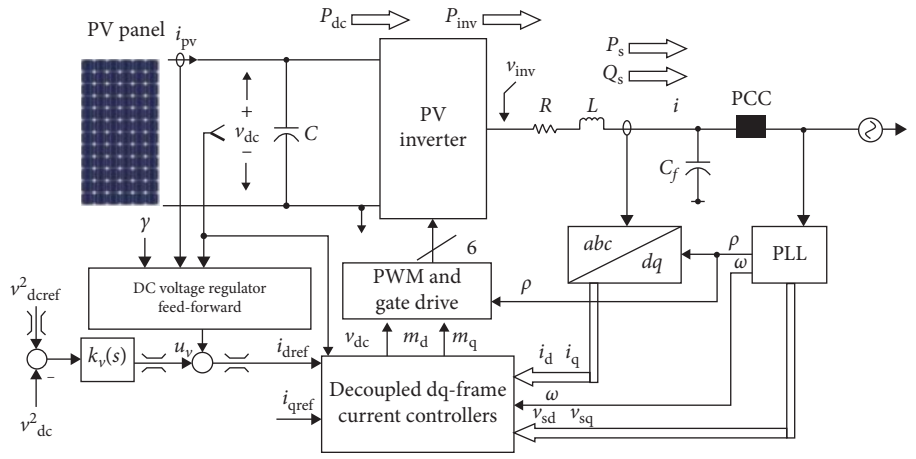

Figure 2: PV system schematic diagram.

should always be in proportion to its active power output. In application, local PV active power generation $P_{PV}(t)$ at time instant t is measured in real time, and the reactive power generation $Q_{PV}(t)$ can be obtained according to $P_{PV}(t)$ and the constant power factor PF. On the other hand, Figure 3(b) is a power factor droop curve, through which the power factor of a PV inverter varies according to its local voltage. Specifically, if the local voltage is too high, PV inverters will

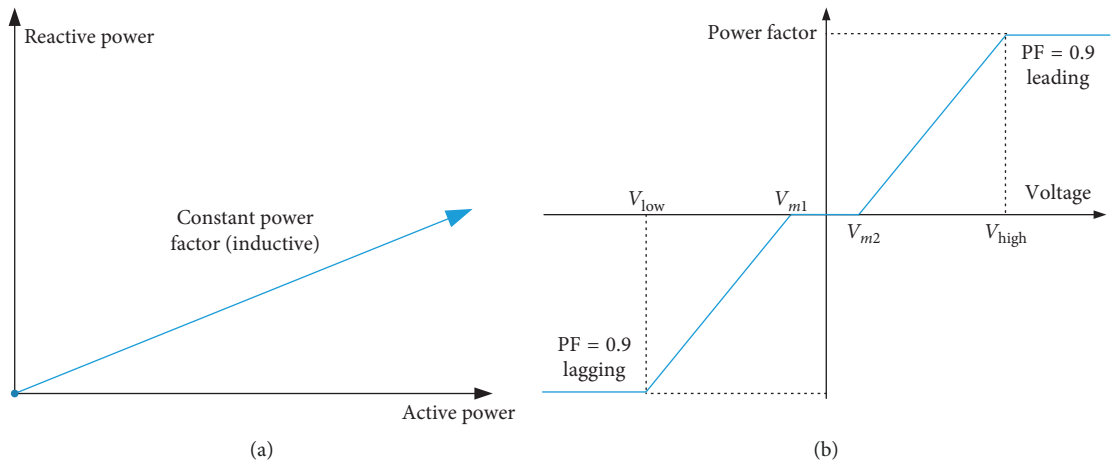

Figure 3: Traditional Var compensation methods: (a) constant power factor curve; (b) power factor droop curve [31].

operate with a leading power factor to absorb reactive power from the grid. Conversely, PV inverters will operate with a lagging power factor to inject reactive power into the grid. In real life application, both local voltage $V(t)$ and PV generation $P_{PV}(t)$ will be measured in real time. No matter which method is used, the power factor of grid-connected PV inverters is generally restricted within the range from 0.9 lagging to 0.9 leading by the utility [35].

3. Problem Description

3.1. Voltage Regulation in Traditional Distribution Systems. Residential customers are almost directly connected to 415 V low-voltage systems which are fed by 11 kV/415 V distribution transformers. Since the 11 kV/415 V transformer cannot participate in system voltage regulation due to its fixed tap position, voltage fluctuations in the 11 kV side have a significant impact on 415 V systems. A month-long voltage profile recorded from the secondary side of an 11 kV/415 V distribution transformer is displayed in Figure 4, which mainly fluctuates within the range between 1.0 pu and 1.05 pu. Therefore, 415 V systems were designed for safe operation with its all possible load levels as long as the secondary side voltage of the 11 kV/415 V transformer fluctuates within the normal range.

3.2. Voltage Regulation Problem. In traditional distribution systems, residential loads are approximately balanced across three phases. However, rooftop PV generators are usually installed randomly. Therefore, PV power integration tends to be unbalanced especially in low-voltage systems with limited customers. A possible scenario (PV penetration is 25%, 30%, and 45% in Phases A to C, respectively) is assumed in Case 1. Detailed load and PV capacity are shown in Table 1. In such a situation, two locally dependent Var compensation methods shown in Figure 3 are implemented on PV inverters, respectively, in order to test their voltage regulation performance with unbalanced PV power integration. As shown in Table 2, in a low load but high PV generation scenario, voltage at Phase B is much higher than that of the other two phases and neither the constant power factor method nor the power factor droop curve method can eliminate this overvoltage problem (>1.06 [16]) on Phase B.

Nevertheless, there exists an interesting phenomenon that with the PV penetration of all three phases increased to 50% as in Case 2, the overvoltage problem on Phase B could be successfully eliminated by either of those two locally dependent Var compensation methods. Detailed case data and voltage regulation performance are, respectively, listed in Tables 1 and 2.

Generally, since a large amount of PV power integration might cause overvoltage problem, the maximum allowable PV penetration level should be estimated by utilities. However, based on voltage regulation performance in Case 1 and Case 2, if a higher but balanced PV penetration is regarded as the most severe case, the potential overvoltage issue might be under estimated. An overvoltage problem might occur before the estimated PV integration level with a lower but unbalanced PV penetration.

Besides, it is worth mentioning that the phase with highest PV penetration does not necessarily have the highest voltage. As in Table 1, phase C has the highest PV penetration in Case 1 (45%), but its voltage might be the lowest among three phases (shown in Table 2). In some researches, the utility is suggested to connect new installed PV generators to the phase with lowest voltage if all PV inverters operate with a unit power factor. However, with locally dependent Var compensation methods applied on PV inverters, this connection dispatch might lead to even unbalanced PV power integration across three phases and worse overvoltage issues.

4. Problem Analysis

The limitation of locally dependent Var compensation methods in voltage regulation with unbalanced PV power integration is revealed above. In this section, the reason for this voltage regulation problem is analyzed.

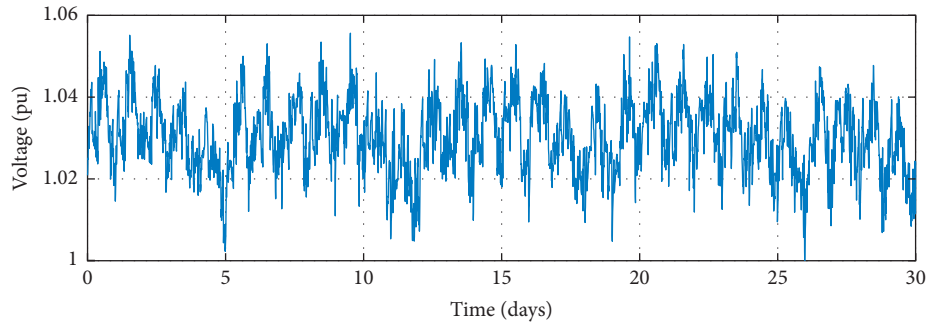

Figure 4: Recorded one-month voltage profile at the secondary side of an 11 kV/415 V transformer.

Table 1: Load and PV installation capacity.

	Phase A	Phase B	Phase C
Peak load	58 kW, 11.6kVar	60 kW, 12kVar	62 kW, 12.4kVar
PV capacity (Case 1)	14.5 kW (25%)	18 kW (30%)	28 kW (45%)
PV capacity (Case 2)	29 kW (50%)	30 kW (50%)	31 kW (50%)

Table 2: Voltage regulation performance with different cases.

Voltage regulation method	Phase A	Phase B	Phase C
Case 1: unbalanced PV integration (25%, 30%, and 45%)			
Constant power factor (0.9)	1.038	1.069	1.036
Power factor droop curve	1.041	1.065	1.043
Case 2: balanced PV integration (50%)			
Constant power factor (0.9)	1.053 pu	1.054 pu	1.046 pu
Power factor droop curve	1.054 pu	1.054 pu	1.050 pu

4.1. Power Flow Equations. For distribution systems with 3-phase 4-wire overhead lines, the voltage drop along a feeder can be expressed as [36]

$$\begin{bmatrix} \mathbf{V}_{1ag} \\ \mathbf{V}_{1bg} \\ \mathbf{V}_{1cg} \\ \mathbf{V}_{1ng} \end{bmatrix} = \begin{bmatrix} \mathbf{V}_{2ag} \\ \mathbf{V}_{2bg} \\ \mathbf{V}_{2cg} \\ \mathbf{V}_{2ng} \end{bmatrix} + \begin{bmatrix} \mathbf{Z}^0_{aa} & \mathbf{Z}^0_{ab} & \mathbf{Z}^0_{ac} & \mathbf{Z}^0_{an} \\ \mathbf{Z}^0_{ba} & \mathbf{Z}^0_{bb} & \mathbf{Z}^0_{bc} & \mathbf{Z}^0_{bn} \\ \mathbf{Z}^0_{ca} & \mathbf{Z}^0_{cb} & \mathbf{Z}^0_{cc} & \mathbf{Z}^0_{cn} \\ \mathbf{Z}^0_{na} & \mathbf{Z}^0_{nb} & \mathbf{Z}^0_{nc} & \mathbf{Z}^0_{nn} \end{bmatrix} \cdot \begin{bmatrix} \mathbf{I}_a \\ \mathbf{I}_b \\ \mathbf{I}_c \\ \mathbf{I}_n \end{bmatrix}, \tag{1}$$

where $\mathbf{V}_{1ig}$ $(i \in a, b, c, n)$ represents the phase or neutral-to-ground voltage at Bus 1; $\mathbf{V}_{2ig}$ $(i \in a, b, c, n)$ represents the phase or neutral-to-ground voltage at Bus 2; $\mathbf{Z}^0_{ij}$ $(i, j \in a, b, c, n)$ represents the primitive self or mutual impedance of conductors; and $\mathbf{I}_i$ $(i \in a, b, c, n)$ represents the conductor current. Since neutral points are grounded at each bus ($\mathbf{V}_{1ng} = \mathbf{V}_{2ng} = 0$), equation (1) can be simplified by Kron reduction as

$$\begin{bmatrix} \mathbf{V}_{1ag} \\ \mathbf{V}_{1bg} \\ \mathbf{V}_{1cg} \end{bmatrix} = \begin{bmatrix} \mathbf{V}_{2ag} \\ \mathbf{V}_{2bg} \\ \mathbf{V}_{2cg} \end{bmatrix} + \begin{bmatrix} \mathbf{Z}_{aa} & \mathbf{Z}_{ab} & \mathbf{Z}_{ac} \\ \mathbf{Z}_{ba} & \mathbf{Z}_{bb} & \mathbf{Z}_{bc} \\ \mathbf{Z}_{ca} & \mathbf{Z}_{cb} & \mathbf{Z}_{cc} \end{bmatrix} \cdot \begin{bmatrix} \mathbf{I}_a \\ \mathbf{I}_b \\ \mathbf{I}_c \end{bmatrix}, \tag{2}$$

where equivalent self and mutual impedance $\mathbf{Z}_{ij}$ $(i, j \in a, b, c)$ can be obtained from the primitive impedance $\mathbf{Z}^0_{ij}$ in the 4×4 impedance matrix of (1) as

$$\mathbf{Z}_{ij} = \mathbf{Z}^0_{ij} - \frac{\mathbf{Z}^0_{in}\mathbf{Z}^0_{jn}}{\mathbf{Z}^0_{nn}}, \quad (i, j \in a, b, c). \tag{3}$$

Due to the existence of equivalent mutual impedance ($\mathbf{Z}_{ab}$, $\mathbf{Z}_{bc}$, and $\mathbf{Z}_{ca}$), active and reactive power flow in one phase will cause voltage variations not only on its own phase conductor but also on conductors of the other two phases.

4.2. Voltage Sensitivity Analysis. To investigate the voltage regulation performance with unbalanced PV power integration, the three-phase voltage sensitivity with respect to single-phase active power injection is demonstrated in this section. Without loss of generality, a certain amount of active power is assumed to be injected into Phase C, which results in line current $\mathbf{I}_c$. At the same time, both Phases A and B remain as open circuit. Therefore, with $\mathbf{I}_a$ and $\mathbf{I}_b$ set to be zero in (2), the downstream three-phase voltage at Bus 2 can be expressed as

$$\begin{bmatrix} \mathbf{V}_{2ag} \\ \mathbf{V}_{2bg} \\ \mathbf{V}_{2cg} \end{bmatrix} = \begin{bmatrix} \mathbf{V}_{1ag} - \mathbf{Z}_{ac}\mathbf{I}_c \\ \mathbf{V}_{1bg} - \mathbf{Z}_{bc}\mathbf{I}_c \\ \mathbf{V}_{1cg} - \mathbf{Z}_{cc}\mathbf{I}_c \end{bmatrix}. \tag{4}$$

The voltage-current relationship given in (4) can be displayed by using a vector diagram shown in Figure 5(a). In this vector diagram, there are something worth pointing out: (1) balanced three-phase voltage source at Bus 1 ($\mathbf{V}_{1ag}$, $\mathbf{V}_{1bg}$, and $\mathbf{V}_{1cg}$) is assumed; (2) $\mathbf{I}_c$ with a negative value represents reverse power flow; (3) since only active power is injected into Phase C of Bus 2, $\mathbf{V}_{2cg}$ and $\mathbf{I}_c$ have a 180-degree phase angle difference ($\mathbf{V}_{2cg}$ and $\mathbf{I}_c$ will have a 0-degree phase angle difference if only active power is absorbed from the grid); (4) $\mathbf{I}_c R_{ic}$ $(i \in a, b, c)$ has the same phase angle with $\mathbf{I}_c$, while $\mathbf{I}_c jX_{ic}$ $(i \in a, b, c)$ has a 90-degree phase angle difference with $\mathbf{I}_c$.

As shown in Figure 5(a), there are different voltage responses on different phases to the same reverse-active

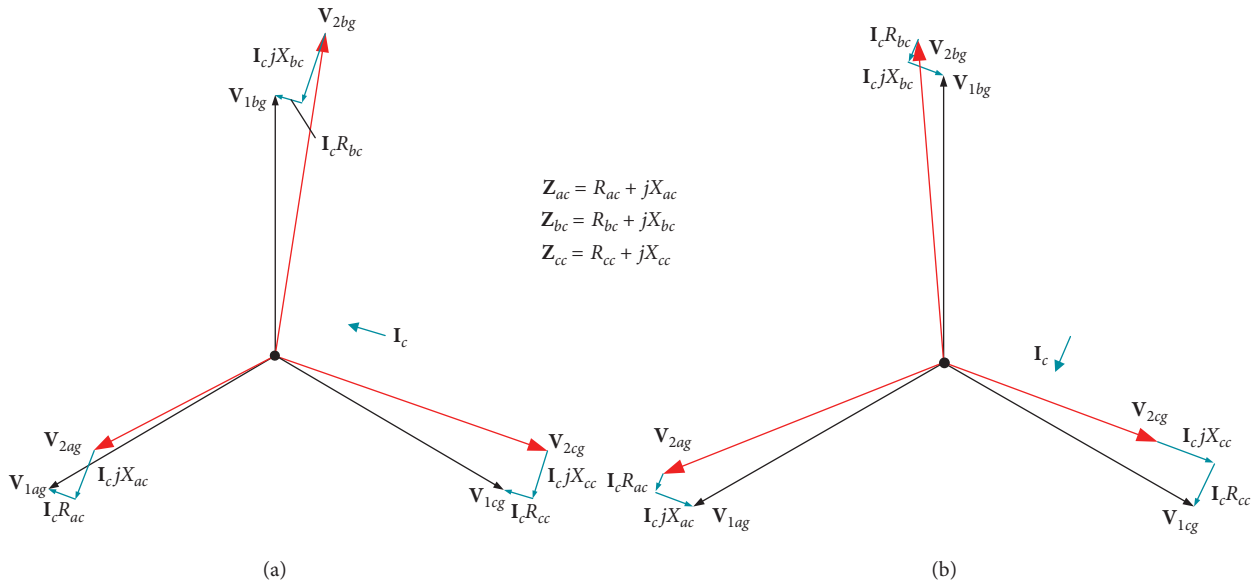

Figure 5: Three-phase voltage sensitivity with respect to single-phase power flow: (a) only active power injection at Phase C; (b) only reactive power absorption from Phase C.

power flow in Phase C. With active power injected into Phase C, voltage magnitude at both Phases B and C is increased. However, a voltage drop can be observed at Phase A. In this situation, with locally dependent Var compensation methods, PV inverters installed on Phase C will absorb to compensate local voltage rise.

To figure out the impact of reactive power absorption on phase voltage, similar analysis is given. In Figure 5(b), the three-phase voltage variations induced only by single-phase reactive power absorption from Phase C is displayed. In this case, $\mathbf{V}_{2cg}$ and $\mathbf{I}_c$ have a 90-degree phase angle difference due to pure reactive power absorption. As shown in this figure, reactive power absorption from Phase C can substantially reduce the voltage of its own phase. However, it will lift the voltage of both Phase A and Phase B. To summarize, active power injected into Phase C would lift the voltage of Phase B and reactive power absorption by PV inverts on Phase C would induce a further voltage rise on Phase B.

Three-phase voltage variations caused by single-phase active power injection or reactive power absorption are summarized as in Table 3. Now let us revisit the voltage regulation problem proposed in Section 3. In Case 1 of Table 1, much more PV inverters are installed on Phase C compared with that on Phase B. PV inverters operating with leading power factors on Phase C contribute a significant voltage rise at Phase B, which will make the voltage regulation ability of limited PV inverters on Phase B saturated. Although active power injection into Phase A can mitigate such a voltage rise at Phase B, as shown in Table 3, this effect can be feeble due to less PV power integration in Phase A in this case. As a result, overvoltage issue occurs on Phase B when PV inverters generate reactive power only relying on local measurements. While, for Case 2 of Table 1, each phase has higher but the same PV penetration (50%). Consequently, the interaction among phases can be compensated by each other. Hence, voltage rise caused by PV power injection can be sufficiently mitigated by locally dependent Var compensation methods.

Table 3: Summary of three-phase voltage sensitivity.

Three-phase voltage variation			
P injection at phase A	$V_a \uparrow$	$V_b \downarrow$	$V_c \uparrow$
P injection at phase B	$V_a \uparrow$	$V_b \uparrow$	$V_c \downarrow$
P injection at phase C	$V_a \downarrow$	$V_b \uparrow$	$V_c \uparrow$
Q absorption at phase A	$V_a \downarrow$	$V_b \uparrow$	$V_c \uparrow$
Q absorption at phase B	$V_a \uparrow$	$V_b \downarrow$	$V_c \uparrow$
Q absorption at phase C	$V_a \uparrow$	$V_b \uparrow$	$V_c \downarrow$

To summarize, due to equivalent mutual impedance among phase conductors, active and reactive power flows in one phase can have significant impact on voltage rise or drop in other two phases. Furthermore, unbalanced PV power integration also makes locally dependent Var compensation methods less effective, which significantly challenges the effectiveness of voltage regulation methods. In order to improve the effectiveness, some suggestions are proposed.

5. Suggestions

5.1. Definition of PV Power Imbalance Index. Most previous researches highlight that high PV penetration may cause voltage regulation issues in distribution systems. However, based on Section 4, besides the PV penetration level, the distribution of PV generators across three phases is also an important factor that influences potential overvoltage problems. Therefore, an imbalance index of PV power integration is designed to describe the distribution of PV generators across three phases in this section.

Since the end of a distribution feeder is most vulnerable to severe overvoltage problems caused by excessive PV power injection, all PV power installation capacities at different buses are first converted to the end of a feeder as

$$P'_{\text{ph}} = \sum_{j=1}^{n} \frac{P^j_{\text{ph}} \cdot l_j}{l_n}, \quad \text{ph} \in a, b, c, \tag{5}$$

where P'_{ph} represents the equivalent PV installation capacity of Phase ph after conversion; P^j_{ph} represents the actual PV installation capacity of Phase ph Bus j; l_j and l_n represent the distance from slack bus to Bus j and Bus n, respectively. Assume Bus n is the farthest bus of the system and all line segments have the same impedance matrix. Since

$$\mathbf{I}'_{\text{ph}} = \left(\frac{P'_{\text{ph}}}{\mathbf{V}_{\text{ph}}}\right)^*, \quad \text{ph} \in a, b, c, \tag{6}$$

where $\mathbf{I}'_{\text{ph}}$ represents the equivalent PV current caused by equivalent PV power P'_{ph} on phase ph and $\mathbf{V}_{\text{ph}}$ represents the voltage at phase ph. Assume $\mathbf{V}_a$, $\mathbf{V}_b$, and $\mathbf{V}_c$ are $1\angle 0^\circ$ pu, $1\angle -120^\circ$ pu, and $1\angle 120^\circ$ pu, respectively. By applying the symmetrical component theory, the imbalance index of PV power integration can be defined as the imbalance of equivalent PV current:

$$\text{imbalance index} = \left|\frac{\mathbf{I}_2}{\mathbf{I}_1}\right|, \tag{7}$$

where

$$\begin{bmatrix} \mathbf{I}_0 \\ \mathbf{I}_1 \\ \mathbf{I}_2 \end{bmatrix} = \begin{bmatrix} 1 & 1 & 1 \\ 1 & a^2 & a \\ 1 & a & a^2 \end{bmatrix}^{-1} \begin{bmatrix} \mathbf{I}'_{\text{a}} \\ \mathbf{I}'_{\text{b}} \\ \mathbf{I}'_{\text{c}} \end{bmatrix} \approx \begin{bmatrix} 1 & 1 & 1 \\ 1 & a^2 & a \\ 1 & a & a^2 \end{bmatrix}^{-1} \begin{bmatrix} P'_a \\ P'_b \cdot a^2 \\ P'_c \cdot a \end{bmatrix}, \quad a = e^{j(2\pi/3)}. \tag{8}$$

With such a definition, this imbalance index will be zero if PV power integration is totally balanced across three phases. On the contrary, if all PV generators are connected to one phase, the imbalance index will be one. In other cases, the possible range of the defined PV power imbalance index is (0, 1). The PV penetration level together with the PV power imbalance index can approximately reflect the integration of single-phase rooftop PV generators in low-voltage distribution systems. It is worth mentioning that the value of PV power imbalance index does not absolutely indicate the effectiveness of the reactive power compensation method in voltage regulation. The performance of voltage regulation is also affected by other factors such as mutual impedance.

5.2. Comparison of Locally Dependent Methods. Although the limitation in voltage regulation is inevitable to all locally dependent Var compensation methods, different methods have different voltage regulation performance. For example, when PV penetration is unbalanced, the power factor droop curve scheme results in lower overvoltage in comparison to that of the constant power factor scheme as in Case 1 of Table 2. Actually, when photovoltaic imbalance occurs, the power factor droop curve scheme does have a better performance in the voltage regulation than the constant power factor method.

According to the three-phase voltage sensitivity summarized in Table 3, properly reducing the reactive power absorption from Phase A and Phase C is an alternative option to mitigate the overvoltage in Phase B when the reactive power generation in Phase B becomes saturated due to the power factor constraint. Compared with the constant power factor (0.9 leading) scheme, the power factor droop curve scheme allows PV inverters to operate with a power factor higher than 0.9 before the voltage violates its limit. As a result, less reactive power will be absorbed from Phases A and C, which will lead to a lower voltage at Phase B according to Table 3. Therefore, the power factor droop curve scheme has better voltage regulation performance compared with that of the constant power factor scheme when PV penetration is unbalanced.

In order to further mitigate the overvoltage issue of Phase B, the dead band (distance between V_{m1} and V_{m2}) of a power factor droop curve can be widened as shown in Figure 6. The corresponding voltage regulation performance is compared in Table 4 with different parameters of power factor droop curves and the same unbalanced PV power integration (Case 1 of Table 1).

As the dead band of a power factor droop curve becomes wider, less reactive power will be absorbed with the same local voltage before voltage violation. Therefore, the reactive power absorption from Phases A and C can be further reduced, which will lead to a voltage rise at both Phases A and C as in Table 4. At the same time, overvoltage at Phase B can be mitigated. To avoid the oscillation with a steep power factor droop curve, a first-order inertia element $K/(1 + \tau s)$ can be added in the voltage/Var controller [36].

5.3. Suggestions for Future Distribution System Planning. As revealed in Section 4, unbalanced PV power integration together with the equivalent mutual impedance among phase conductors make locally dependent Var compensation methods less effective in overvoltage mitigation. Therefore, if the mutual impedance can be properly reduced, those locally dependent methods may successfully regulate system voltage with unbalanced PV power integration.

According to (3), equivalent mutual impedance $\mathbf{Z}_{ij}$ is dependent on primitive self-impedance of neutral $\mathbf{Z}^0_{nn}$ and primitive mutual impedance $\mathbf{Z}^0_{ij}(i, j \in a, b, c, n; i \neq j)$, which can be expressed as in (9) and (10), respectively [37]. In these two equations, r_n represents the resistance of neutral conductor; f represents the system frequency; ρ represents the earth resistivity; GMR_i represents the geometric mean radius of conductor i; D_{ij} represents the distance between conductor i and conductor j. A proper design of the line configuration on a utility pole can reduce the equivalent mutual impedance $\mathbf{Z}_{ij}$. For example, if the distance between two phase conductor scans be properly increased and a neutral conductor with larger GMR value is selected in the future distribution system planning, smaller $\mathbf{Z}^0_{ij}(i, j \in a, b, c; i \neq j)$ and $\mathbf{Z}^0_{nn}$ can be obtained. Consequently, the equivalent mutual impedance $\mathbf{Z}_{ij}$ can be correspondingly reduced according to (3). Therefore, such distribution systems can be more bearable to unbalanced PV

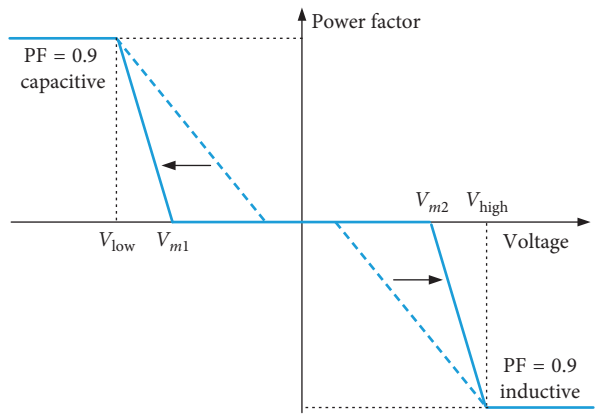

Figure 6: Power factor droop curve with wider dead band.

Table 4: Voltage regulation performance with different power factor droop curves.

Parameters of power factor droop curve	Phase A	Phase B	Phase C
$V_{low} = 0.94,\ V_{m1} = 0.99,\ V_{m2} = 1.01,\ V_{high} = 1.06$	1.041 pu	1.065 pu	1.043 pu
$V_{low} = 0.94,\ V_{m1} = 0.95,\ V_{m2} = 1.05,\ V_{high} = 1.06$	1.050 pu	1.059 pu	1.053 pu

power integration with locally dependent Var compensation methods:

$$\mathbf{Z}^0_{nn} = r_n + 0.0015836 \cdot f + j0.00202237 \cdot f \cdot \frac{\left(ln\left(1/\mathrm{GMR}_n\right) + 7.6786 + (1/2)ln(\rho/f)\right)\Omega}{\text{mile}}, \quad (9)$$

$$\mathbf{Z}^0_{ij} = 0.0015836 \cdot f + j0.00202237 \cdot f \cdot \left(ln\frac{1}{D_{ij}} + 7.6786 + \frac{1}{2}ln\frac{\rho}{f}\right)\Omega/\text{mile}. \quad (10)$$

6. Case Studies

A 415 V low-voltage distribution system with 64 customers shown in Figure 7 and the recorded three-phase load data shown in Figure 1(b) are used in all simulations in this section. Each bus in Figure 6 represents a utility pole which services 2 to 7 residential customers. The number in triangles represents the amount of individual houses connected to the corresponding utility pole. Voltage profiles of Bus 9 are demonstrated as results of following time-series simulations since Bus 9 is most vulnerable to voltage regulation problems.

6.1. Before PV Power Integration. 415 V distribution systems were designed to operate with all possible load levels and upstream (11 kV side) voltage fluctuations. Assuming that the secondary side voltage of an 11 kV/415 V transformer varies between 1.0 pu and 1.05 pu, the corresponding three-phase voltage profiles of Bus 9 in one day with highest and lowest upstream voltages are shown in Figures 8(a) and 8(b), respectively. As shown in this figure, the 415 V system can operate within its allowable voltage range before the PV power integration. In order to focus on overvoltage issues, the voltage at the secondary side of the 415 V transformer is assumed to be 1.05 pu for all following simulations.

6.2. PV Power Integration with Different Imbalance Indices. As analyzed in this paper, besides PV power penetration, PV power imbalance index also has a significant impact on distribution system voltage regulation. If PV installation capacity has an approximately balanced distribution across three phases (24 kW, 25 kW, and 26 kW in Phase s A to C, with a total capacity of 75 kW), the imbalance index of PV power is 0.023 according to the definition in Section 5.1. In this situation, locally dependent Var compensation methods are very effective in mitigating voltage rise induced by PV power injection. For simplification, all houses are assumed to have the same PV installation capacity for the same phase, and all rooftop PV generators have the same normalized PV power profile as shown in Figure 1(a).

Figures 9(a) and 9(b) demonstrate the corresponding voltage profiles when the constant power factor (0.9 leading) scheme and the power factor droop curve scheme (V_{low}, V_{m1}, V_{m2}, and V_{high} are 0.94 pu, 0.99 pu, 1.01 pu, and 1.06 pu, respectively) are applied on all PV inverters, respectively. As in this figure, no overvoltage issue occurs with either locally dependent Var compensation method.

However, since rooftop PV generators are randomly distributed across three phases, it is inevitable to face unbalanced PV power integration in distribution systems. With the same total installation capacity (75 kW), if PV installation capacity in each phase is 17 kW, 24 kW, and 34 kW, respectively, the limitation of locally dependent Var compensation methods arises. In this situation, the PV power imbalance index is 0.2.

Corresponding time-series simulation results with the constant power factor scheme and the power factor droop

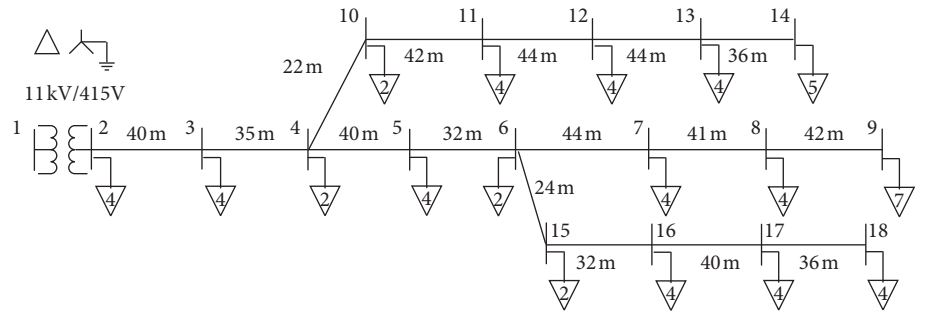

Figure 7: A typical 415 V low-voltage distribution system with 64 customers.

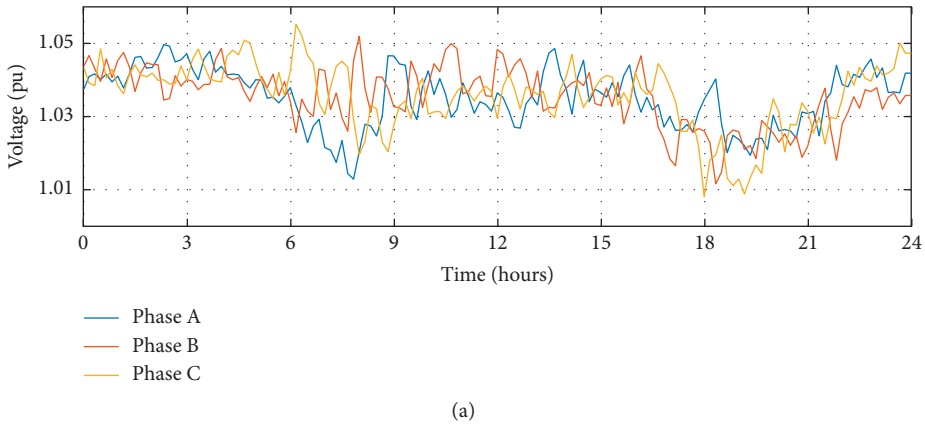

(a)

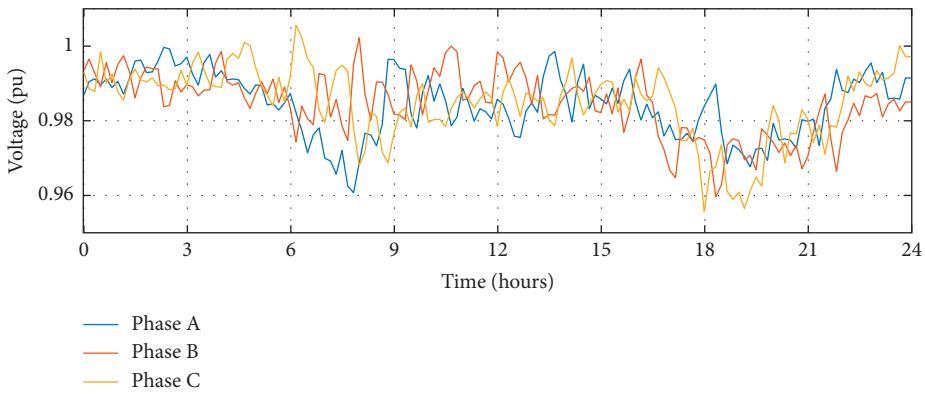

(b)

Figure 8: Three-phase voltage at Bus 9 before PV power integration with different upstream voltages: (a) highest upstream voltage (1.05 pu); (b) lowest upstream voltage (1.0 pu).

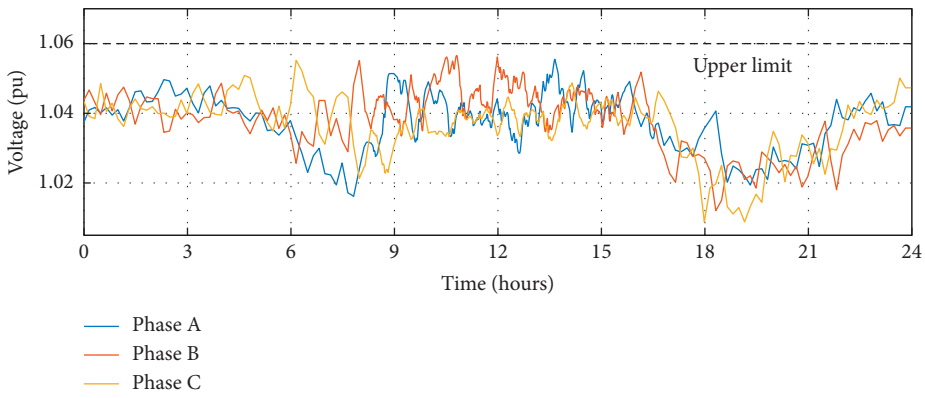

(a)

Figure 9: Continued.

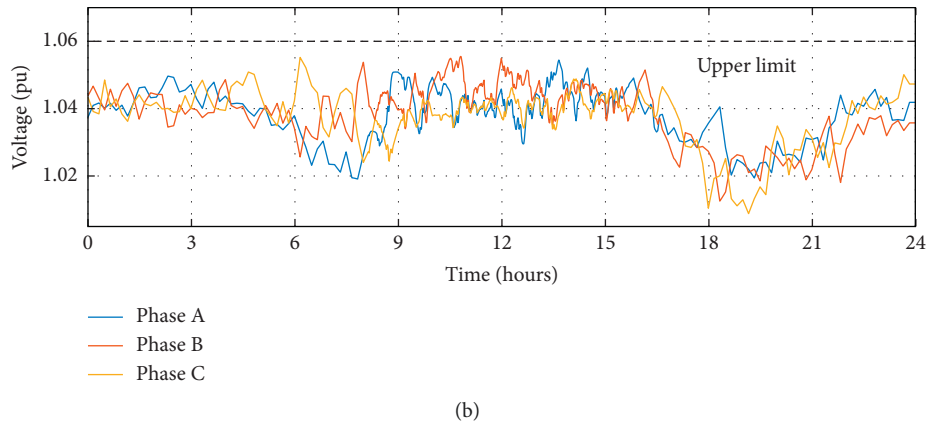

(b)

Figure 9: Voltage regulation performance with approximately balanced PV power integration: (a) constant power factor; (b) power factor droop curve.

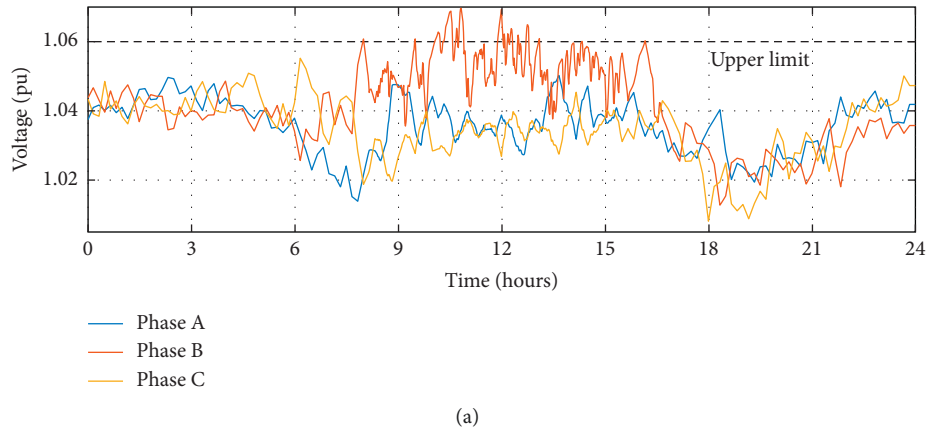

(a)

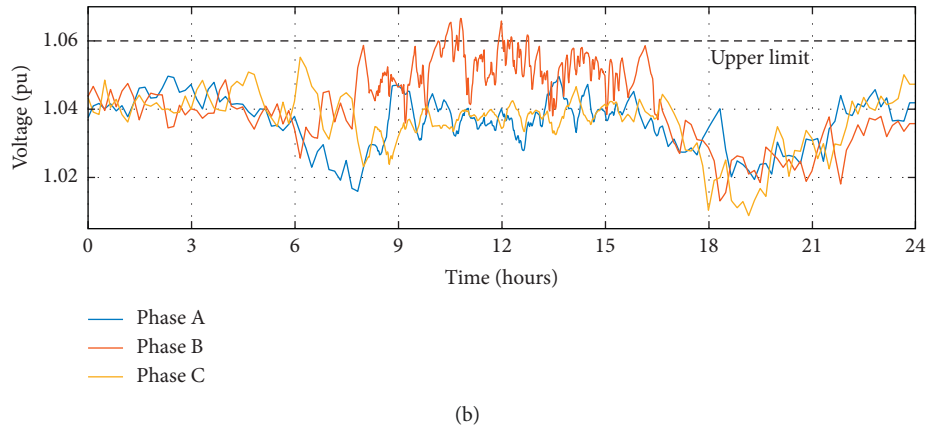

(b)

Figure 10: Three-phase voltage profiles with different locally dependent Var compensation methods: (a) constant power factor; (b) power factor droop curve.

curve scheme are shown in Figures 10(a) and 10(b), respectively. Both locally dependent Var compensation methods will make the voltage at Phase B much higher than other two phases, and overvoltage issue can be observed during noon when PV generation is high and load demand level is low. These results are consistent to the analysis in Sections 3 and 4.

6.3. Power Factor Droop Curve with a Wide Dead Band. Overvoltage problem can be mitigated in a certain extent if locally dependent Var compensation follows a power factor droop curve with a wide dead band. Figures 11(a) and 11(b) demonstrates the voltage regulation performance of power factor droop curves with different parameters. Time-series simulation results verify that power factor droop curve with

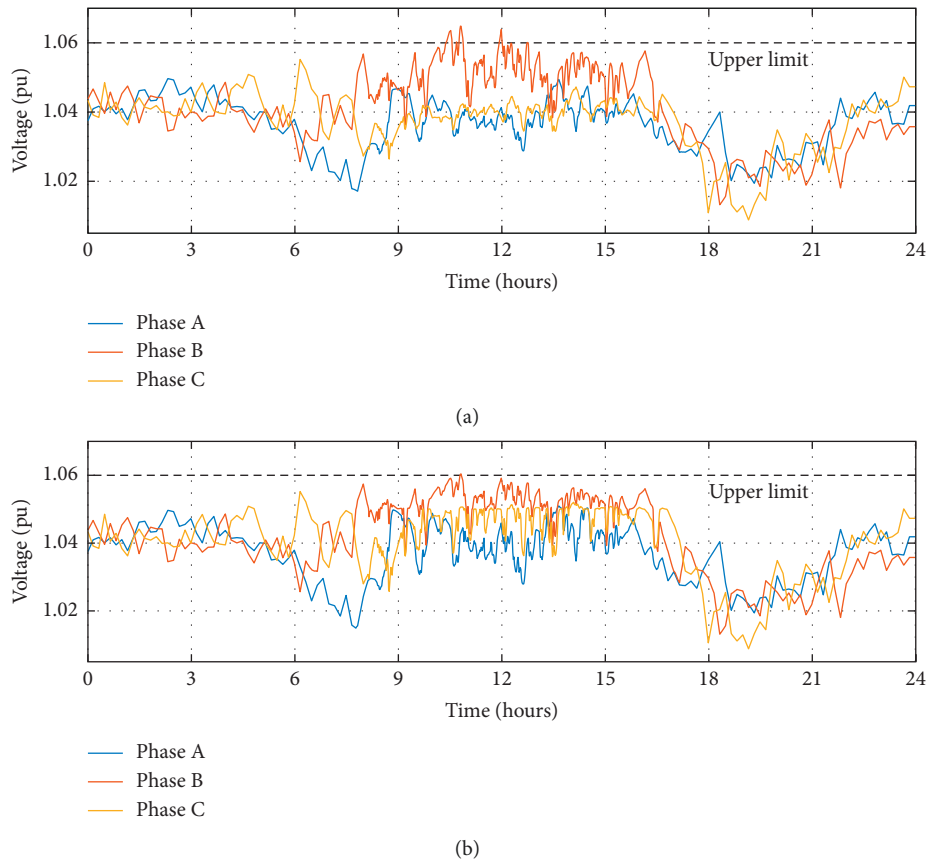

FIGURE 11: Voltage regulation performance of power factor droop curves with different parameters: (a) V_{low}, V_{m1}, V_{m2}, and V_{high} are 0.94 pu, 0.97 pu, 1.03 pu, and 1.06 pu, respectively; (b) V_{low}, V_{m1}, V_{m2}, and V_{high} are 0.94 pu, 0.95 pu, 1.05 pu, and 1.06 pu, respectively.

a wider dead band can have a better voltage regulation performance in the situation with unbalanced PV power integration across three phases.

7. Conclusion

With random connection of rooftop PV generators, PV penetration tends to be unbalanced across three phases especially in low-voltage distribution systems. In such situations, locally dependent Var compensation methods may become less effective in overvoltage mitigation.

The voltage regulation problem is analyzed in this paper. The analysis result indicates that the equivalent mutual impedance among phase conductors together with unbalanced PV power integration make locally dependent Var compensation methods less effective.

On this basis, some suggestions are proposed for utilities in both current system operation and future planning. Specifically, (1) utilities are suggested to use both PV penetration and the PV imbalance index to describe the integration of rooftop PV generators; (2) the power factor droop curve with a wider dead band is suggested to be applied on rooftop PV generators due to its better voltage regulation performance with unbalanced PV integration; (3) for future distribution system planning, utilities are suggested to design future distribution feeders with less equivalent mutual impedance among phase conductors in order to accommodate more randomly connected rooftop PV generators.

Data Availability

The data used to support the findings of this study are available from the corresponding author upon request.

Conflicts of Interest

The authors declare that they have no conflicts of interest.

References

[1] C. Wei, M. Benosman, and T. Kim, "Online parameter identification for state of power prediction of lithium-ion batteries in electric vehicles using extremum seeking," *International Journal of Control, Automation and System*, pp. 1–11, 2019.

[2] F. Cheng, L. Qu, W. Qiao, C. Wei, and L. Hao, "Fault diagnosis of wind turbine gearboxes based on DFIG stator current envelope analysis," *IEEE Transactions on Sustainable Energy*, vol. 10, no. 3, pp. 1044–1053, 2019.

[3] C. Guo and D. Wang, "Frequency regulation and coordinated control for complex wind power systems," *Complexity*, vol. 2019, Article ID 8525397, 12 pages, 2019.

[4] K. Wang, L. W. Li, W. Xue et al., "Electrodeposition synthesis of PANI/MnO_2/graphene composite materials and its

electrochemical performance," *International Journal of Electrochemical Science*, vol. 12, no. 9, pp. 8306–8314, 2017.

[5] Y. W. Shen, J. R. Yuan, F. F. Shen, J.-Z. Xu, C.-K. Li, and D. Wang, "Finite control set model predictive control for complex energy system with large-scale wind power," *Complexity*, vol. 2019, Article ID 4358958, 13 pages, 2019.

[6] Y. T. Zhou, Y. N. Huang, J. B. Pang, and K. Wang, "Remaining useful life prediction for supercapacitor based on long short-term memory neural network," *Journal of Power Sources*, vol. 440, Article ID 227149, 2019.

[7] Y. Li, B. Feng, G. Li, J. Qi, D. Zhao, and Y. Mu, "Optimal distributed generation planning in active distribution networks considering integration of energy storage," *Applied Energy*, vol. 210, pp. 1073–1081, 2018.

[8] A. Hoke, J. Giraldez, B. Palmintier et al., "Setting the smart solar standard: collaborations between Hawaiian electric and the national renewable energy laboratory," *IEEE Power and Energy Magazine*, vol. 16, no. 6, pp. 18–29, 2018.

[9] M. Zeraati, M. E. H. Golshan, and J. M. Guerrero, "A consensus-based cooperative control of PEV battery and PV active power curtailment for voltage regulation in distribution network," *IEEE Transactions on Smart Grid*, vol. 10, no. 1, pp. 670–680, 2019.

[10] F. Bernadette, F. Andreas, A. Hans, and L. Georg, "Economic assessment and business models of rooftop photovoltaic systems in multi apartment buildings: case studies for Austria and Germany," *Journal of Renewable Energy*, vol. 2018, Article ID 9514260, 16 pages, 2018.

[11] J. D. Watson, D. Santos-Martin, S. Lemon, A. R. Wood, A. J. V. Miller, and N. R. Watson, "Impact of solar photovoltaics on the low-voltage distribution network in New Zealand," *IET Generation, Transmission & Distribution*, vol. 10, no. 1, pp. 1–9, 2016.

[12] H. Y. Hadi, S. Farhad, and M. I. Syed, "Impact of distributed rooftop photovoltaic systems on short circuit faults in the supplying low voltage networks," *Electric Power Components and Systems*, vol. 45, no. 20, pp. 2257–2274, 2017.

[13] R. A. Shayani and M. A. G. de Oliveira, "Photovoltaic generation penetration limits in radial distribution systems," *IEEE Transactions on Power Systems*, vol. 26, no. 3, pp. 1625–1631, 2011.

[14] A. Parchure, S. J. Tyler, M. A. Peskin, K. Rahimi, R. P. Broadwater, and M. Dilek, "Investigating PV generation induced voltage volatility for customers sharing a distribution service transformer," *IEEE Transactions on Industry Applications*, vol. 53, no. 1, pp. 71–79, 2017.

[15] D. Schwanz, F. Moller, S. K. Ronnberg, J. Meyer, and M. H. J. Bollen, "Stochastic assessment of voltage unbalance due to single-phase-connected solar power," *IEEE Transactions on Power Delivery*, vol. 32, no. 2, pp. 852–861, 2017.

[16] SAI Global, *AS/NZS 4777.2: Grid Connection of Energy Systems via Inverters*, SAI Global, Sydney, Australia, 2015.

[17] S. Pawan and K. Baseem, "Smart microgrid energy management using a novel artificial shark optimization," *Complexity*, vol. 2017, Article ID 2158926, 22 pages, 2017.

[18] G. T. Xia, C. Li, K. Wang, and L.-W. Li, "Structural design and electrochemical performance of PANI/CNTs and MnO_2/CNTs super capacitor," *Science of Advanced Materials*, vol. 11, pp. 1079–1086, 2019.

[19] K. Wang, L. W. Li, Y. Lan, P. Dong, and G. Xia, "Application research of Chaotic carrier frequency modulation technology in two-stage matrix converter," *Mathematical Problems in Engineering*, vol. 2019, Article ID 2614327, 8 pages, 2019.

[20] X. J. Su, M. A. S. Masoum, and P. J. Wolfs, "Optimal PV inverter reactive power control and real power curtailment to improve performance of unbalanced four-wire LV distribution networks," *IEEE Transactions on Sustainable Energy*, vol. 5, no. 3, pp. 967–977, 2014.

[21] A. Krishnan, L. P. M. I. Sampath, Y. S. Eddy, and H. B. Gooi, "Optimal scheduling of a microgrid including pump scheduling and network constraints," *Complexity*, vol. 2018, Article ID 9842025, 20 pages, 2018.

[22] B. Zhang, A. Y. S. Lam, A. D. Dominguez-Garcia, and D. Tse, "An optimal and distributed method for voltage regulation in power distribution systems," *IEEE Transactions on Power Systems*, vol. 30, no. 4, pp. 1714–1726, 2015.

[23] Z. Wang, H. Chen, J. Wang, and M. Begovic, "Inverter-less hybrid voltage/var control for distribution circuits with photovoltaic generators," *IEEE Transactions on Smart Grid*, vol. 5, no. 6, pp. 2718–2728, 2014.

[24] S. Ibrahim, A. Cramer, X. Liu, and Y. Liao, "PV inverter reactive power control for chance-constrained distribution system performance optimisation," *IET Generation, Transmission & Distribution*, vol. 12, no. 5, pp. 1089–1098, 2018.

[25] J. Soares, F. Lezama, and T. Pinto, "Complex optimization and simulation in power systems," *Complexity*, vol. 2018, Article ID 6562876, 3 pages, 2018.

[26] C. L. Xiao, B. Zhao, M. Ding, Z. Li, and X. Ge, "Zonal voltage control combined day-ahead scheduling and real-time control for distribution network with high proportion of PVs," *Energies*, vol. 10, no. 10, Article ID 1464, 2017.

[27] R. R. Jha, A. Dubey, C. C. Liu, and K. P. Schneider, "Bi-level Volt-VAR optimization to coordinate smart inverters with voltage control devices," *IEEE Transactions on Power Systems*, vol. 34, no. 3, pp. 1801–1813, 2019.

[28] L. Wang, F. Bai, R. Yan, and T. K. Saha, "Real-time coordinated voltage control of PV inverters and energy storage for weak networks with high PV penetration," *IEEE Transactions on Power Systems*, vol. 33, no. 3, pp. 3383–3395, 2018.

[29] M. I. Hossain, T. K. Saha, and R. Yan, "Investigation of the interaction between step voltage regulators and large-scale photovoltaic systems regarding voltage regulation and unbalance," *IET Renewable Power Generation*, vol. 10, no. 3, pp. 299–309, 2016.

[30] E. Bullich-Massagué, O. Gomis-Bellmunt, L. Serrano-Salamanca, R. Ferrer-San-José, C. Pacheco-Navas, and M. Aragüés-Peñalba, "Power plant control in large-scale photovoltaic plants: design, implementation and validation in a 9.4 MW photovoltaic plant," *IET Renewable Power Generation*, vol. 10, no. 1, pp. 50–62, 2016.

[31] L. Wang, R. Yan, and T. K. Saha, "Voltage management for large scale PV integration into weak distribution systems," *IEEE Transactions on Smart Grid*, vol. 9, no. 5, pp. 4128–4139, 2018.

[32] A. Samadi, R. Eriksson, and L. Soder, "Coordinated active power-dependent voltage regulation in distribution grids with PV systems," *IEEE Transactions on Smart Grid*, vol. 29, no. 3, pp. 1454–1464, 2014.

[33] A. O'Connell and A. Keane, "Volt-var curves for photovoltaic inverters in distribution systems," *IET Generation, Transmission & Distribution*, vol. 11, no. 3, pp. 730–739, 2017.

[34] P. P. Dash and A. Yazdani, "A mathematical model and performance evaluation for a single-stage grid-connected photovoltaic (PV) system," *International Journal of Emerging Electric Power Systems*, vol. 9, no. 6, 2008.

[35] Forum Netztechnik/Netzbetriebim VDE (FNN), *Power Generation Systems Connected to the Low/Voltage Distribution*

Network, VDE-AR-N 4105:2011-08, Forum Netztechnik/ Netzbetriebim VDE (FNN), Berlin, Germany, 2011.

[36] P. Jahangiri and D. C. Aliprantis, "Distributed volt/var control by PV inverters," *IEEE Transactions on Power Systems*, vol. 28, no. 3, pp. 3429–3439, 2013.

[37] W. H. Kersting, *Distribution System Modeling and Analysis*, CRC Press, Boca Raton, FL, USA, 2002.

Hindawi
Complexity
Volume 2019, Article ID 3928268, 10 pages
https://doi.org/10.1155/2019/3928268

Research Article

A Decentralized Energy Flow Control Framework for Regional Energy Internet

Guofeng Wang, Kangli Zhao, Yu Yang, Junjie Lu, and Youbing Zhang

College of Information Engineering, Zhejiang University of Technology, Hangzhou 310023, China

Correspondence should be addressed to Youbing Zhang; zyoubing6858@sina.com

Received 26 July 2019; Accepted 17 September 2019; Published 28 October 2019

Guest Editor: Xiaoqing Bai

As a new form of smart grid, the energy transmission mode of the Energy Internet (EI) has changed from one direction to the interconnected form. Centralized scheduling of traditional power grids has the problems of low communication efficiency and low system resilience, which do not contribute to long-term development in the future. Owing to the fact that it is difficult to achieve an optimal operation for centralized control, we propose a decentralized energy flow control framework for regional Energy Internet. Through optimal scheduling of regional EI, large-scale utilization and sharing of distributed renewable energy can be realized, while taking into consideration the uncertainty of both demand side and supply side. Combing the multiagent system with noncooperative game theory, a novel electricity price mechanism is adopted to maximize the profit of the regional EI. We prove that Nash equilibrium of theoretical noncooperative game can realize consensus in the multiagent system. The numerical results of real-world traces show that the regional EI can better absorb the renewable energy under the optimized control strategy, which proves the feasibility and economy of the proposed decentralized energy flow control framework.

1. Introduction

The third industrial revolution is emerging, represented by new energy technologies and Internet technologies. Construction of Energy Internet (EI) can promote industrial technology upgrading and structural adjustment in modern energy industry [1, 2]. The concept of Energy Internet combines advanced power electronics technology, the Internet of Things (IoT) technology, and intelligent control technology. In EI, a large number of energy nodes, distributed energy harvesting devices, distributed energy storage devices, and various types of loads are interconnected to achieve energy multidirectional flowing and peer-to-peer energy sharing and trading.

As a subnetwork of Energy Internet, energy local network (ELN) has a variety of energy absorption methods. The ELN is a multienergy operation system, where different energy networks have strong coupling. The complementarity of energy can greatly improve the energy efficiency of the system to achieve cascade utilization of diverse energy sources [3–5]. On the contrary, the relationship between the demand side and the ELN is more flexible, which brings significant uncertainty to the operation and management in practice [6, 7]. The energy flow model of the heating network is established in [8], which explored the optimization of integrated energy system operation with a heat network. The northern part of Haidian District in Beijing was selected as a practical case in [9]. An optimal joint-dispatch scheme of energy and reserve is proposed in [10] for combined cooling, heating, and power (CCHP)-based MGs to effectively provide more reserve capability for the power system.

Due to the diversification of load patterns and stochastic nature of renewable energy sources in EI, the traditional centralized optimization scheduling method is difficult to apply in practice in actual operation. How to cope with the problem has become urgent to be solved in the management and optimization operation of EI [11, 12]. A hierarchical control architecture suitable for the energy management system of ELN is proposed, and a demonstration case of ELN energy management system a in [13]. The generalized "source-network-load-storage" of

the coordinated and optimized operation mode and public energy policy suggestion of ELN is proposed in [14]. The framework of hierarchical integration is designed to solve the problem of energy and information management for network connection in large-scale renewable energy source (RES) in [15]. However, the above research focuses on the architecture of operation, which neglects the impact of individuality and the flexibility of conversion in the regional EI. The overall description of the multi-ELN systems structure and the extraction of typical characteristics are missing, so the feasibility has been limited in practice.

Motivated by the above facts, we analyze the operation pattern of energy flow in a typical architecture of the ELN framework in order to obtain the optimal operation of multienergy. A strategy of optimal operation in EI is proposed based on the multiagent system (MAS) combined with noncooperative game theory to realize the decentralized control of the ELN system. The real-time electricity price is obtained by iterative optimization, which maximizes the overall profit of the EI system. For each ELN, a quadratic programming problem is developed with the aim to increase the individual economic benefit. Through energy trading and conversion between ELNs, the balance of supply side and demand side of the overall EI system is enhanced. As a result, the resilience and economy of the EI system are significantly enhanced.

The remainder of the paper is organized as the following. In Section 2, the typical architecture of ELN is demonstrated and the basic models in ELN are provided. An optimal energy flow control framework based on the multiagent system and the novel electricity price in the ELN is proposed in Section 3. Simulation results and conclusions are provided in Sections 4 and 5, respectively.

2. Multi-ELN System Configuration

2.1. The Architecture of ELN. ELN is a collection of a complete future-oriented energy system constructed from the aspects of energy production, transmission, distribution, transformation, and consumption. It is a power-centric interactive and shared platform for all kinds of energy which enables smart mutual supply of different types of loads. Figure 1 shows a typical architecture for ELN constructed in this paper. The system of ELN includes primary energy, energy conversion devices, energy storage devices, and intelligent load. Primary energy can meet the side of the electrical/thermal/cooling load requirements through the energy conversion device. Through the correlation and complementarity of multiple energy systems in discrete-time scales, multienergy cascade utilization can be realized, which enables load peak transferring. Carbon emission can be significantly reduced by increasing the utilization rate of RES.

The EI consists of ELNs, which are highly coupled products of multiple type energy and information networks. With huge number of diverse energy equipment in EI, centralized control cannot deal with the rapidly increasing data complexity, and it is difficult to make full use of the energy in EI. As a result, the stability and economy of the power system will be impacted. Based on the aforementioned, we propose a decentralized energy flow control framework of multiagent EI to effectively improve computing and execution of system operating.

A discrete-time model is considered in this paper. Assume that the optimal range (e.g., 24 h) is divided into T discrete periods with an interval of Δt, which is denoted by t.

2.2. Basic Model in ELN. As the basic scheduling unit in EI, the energy storage system (ESS) can compensate for the power difference caused by the volatility of the RESs and the load. The model of the ESS can be described as follows:

$$I_i = \left[S_i^0, S_i^{\mathrm{E}}, Q_i^{\max}, P_i^{\mathrm{c}}, P_i^{\mathrm{d}}\right], \tag{1}$$

where S_i^0 represents the initial state of charge in the energy storage system; S_i^{E} represents the expected capacity of the energy storage system; $Q_i^{\max}$ represents the rated capacity of ESS; and P_i^{c} and P_i^{d} represent the charging/discharging power of i ESS, respectively.

We assumed that all energy storage systems have the same lithium-ion battery pack and the charging/discharging power over a single period of time is considered constant [16]. Therefore, the model and constraints of the energy storage system battery are established as follows:

$$\begin{cases} S_i^{t+1} = M_i S_i^t + B_i P_i^t, \\ Y_i^t = C_i S_i^t + D_i P_i^t, \end{cases} \tag{2}$$

where S_i^{t+1} and S_i^t represent the state of SOC at period $t+1$ and t, respectively; Y_i^t represents the output of PEV i at period t; M_i, B_i, C_i, and D_i represent the system matrix, input matrix, output matrix, and feed-forward matrix, respectively; and P_i^t represents the power of SOC at period t, which can be denoted as

$$\begin{gathered} P_i^t = \left[P_{\mathrm{ch},i}^t, P_{\mathrm{dch},i}^t\right]^{\mathrm{T}}, \\ \left(M_i, B_i, C_i, D_i\right) = \left(1, \frac{\Delta t}{Q_i^{\max}}\left[\eta_{\mathrm{ch}} - \frac{1}{\eta_{\mathrm{dch}}}\right], 0, [1 - 1]\right), \end{gathered} \tag{3}$$

where $P_{\mathrm{ch},i}^t$ and $P_{\mathrm{dch},i}^t$ represent the charging/discharging power of the energy storage system at period t, respectively, and η_{ch} and η_{dch} represent the charging/discharging efficiency, respectively.

Since the SOC at period t are bounded by the rated capacity of ESS, we have

$$Q_i^{\min} \le S_i^t \le Q_i^{\max}, \tag{4}$$

where $Q_i^{\min}$ and $Q_i^{\max}$ denote the minimum and maximum capacity of ESS, respectively.

2.3. Gas Turbine Model. Gas turbine is a vital device for EI with high efficiency, which can fully utilize natural gas energy and contribute to reducing environmental pollution. The output of the gas turbine is expressed as follows:

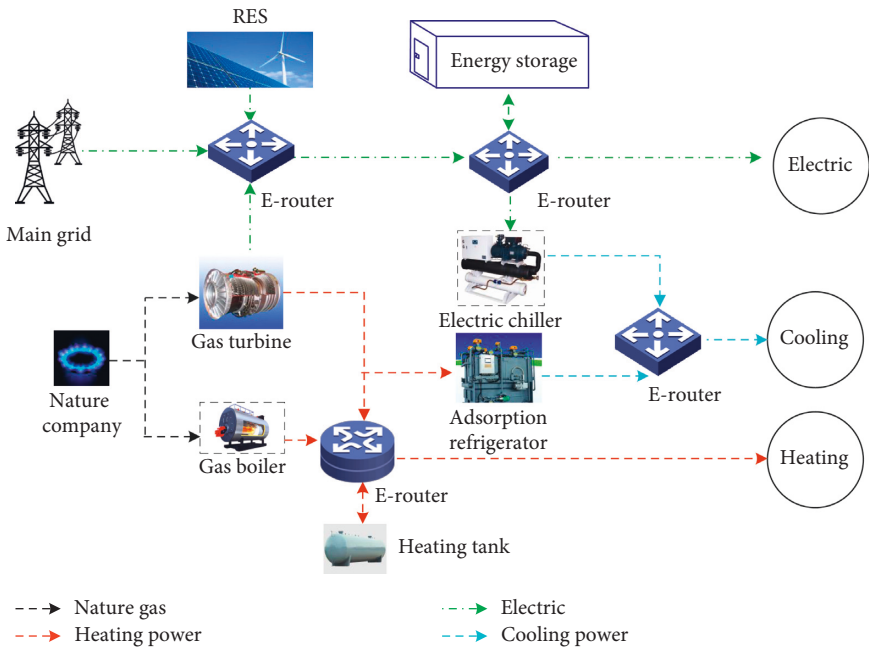

Figure 1: The typical architecture of ELN framework.

$$P^t_{\mathrm{GT},i} = \eta_c \lambda_{\mathrm{gas}} \gamma_{\mathrm{gt}},$$

$$Q^t_{\mathrm{r},i} = \frac{P^t_{\mathrm{GT},i}\eta_r}{\eta_c}, \tag{5}$$

$$0 \le P^t_{\mathrm{GT},i} \le P^{\max}_{\mathrm{GT},i},$$

where $P^t_{\mathrm{GT},i}$ represents power generation of the gas turbine in i ELN at t period; $P^{\max}_{\mathrm{GT},i}$ represents maximum power generation of gas turbines; $Q^t_{\mathrm{r},i}$ represents waste heat recovery power of the gas turbine in i ELN at t period; η_c and η_r represent power generation efficiency and waste heat recovery efficiency for gas turbines, respectively; γ_{gt} represents the gas consumption rate; and λ_{gas} represents the calorific value of natural gas.

The active power output of the gas turbine is bounded by the ramping constraints, denoted as

$$\begin{cases} P^{t+1}_{\mathrm{GT},i} - P^t_{\mathrm{GT},i} \le P^{\mathrm{Up}}_{\mathrm{GT},i}, \\ P^t_{\mathrm{GT},i} - P^{t+1}_{\mathrm{GT},i} \le P^{\mathrm{Down}}_{\mathrm{GT},i}, \end{cases} \tag{6}$$

where $P^{\mathrm{Up}}_{\mathrm{GT},i}$ and $P^{\mathrm{Down}}_{\mathrm{GT},i}$ represent the ramp-up power and ramp-down power constraints, respectively.

2.4. Cold/Heat Load Model. The gas turbine waste heat is mainly recycled by heat exchangers and adsorption refrigerators for refrigeration. Specific physical modeling is shown as follows:

(1) Heat exchanger:

$$P^t_{\mathrm{HX},i} = Q^t_{\mathrm{HX},i}\eta_{\mathrm{HX}}, \tag{7}$$

where $P^t_{\mathrm{HX},i}$ represents the output heat power of the heat exchanger; $Q^t_{\mathrm{HX},i}$ represents the heat absorbed by the heat exchanger from the gas turbine; and η_{HX} represents heat exchange efficiency of the heat exchanger.

(2) Adsorption refrigerator:

$$P^t_{\mathrm{AR},i} = Q^t_{\mathrm{AR},i}\eta_{AR}, \tag{8}$$

where $P^t_{\mathrm{AR},i}$ represents the output cooling power of the adsorption refrigerator; $Q^t_{\mathrm{AR},i}$ represents the heat absorbed by an adsorption refrigerator from a gas turbine; and η_{AR} represents the refrigeration efficiency of the adsorption refrigeration machine. The total absorption heat power of heat exchange gas and adsorption refrigerators should meet the following requirements:

$$Q^t_{\mathrm{AR},i} + Q^t_{\mathrm{HX},i} \le Q^t_{r,i}. \tag{9}$$

(3) Gas boiler:

When the thermal power of the system is insufficient, it is supplemented by the heat generated by the gas-fired boiler. The output thermal power of the gas-fired boiler is expressed as follows:

$$F_{\mathrm{GB},i} = \frac{\sum_{t=1}^{T} P^t_{\mathrm{GB},i}}{\eta_{GB}\lambda_{\mathrm{gas}}},$$

$$0 \le P^t_{\mathrm{GB},i} \le P^{\max}_{\mathrm{GB},i}, \tag{10}$$

where $P^t_{\mathrm{GB},i}$ represents the thermal power of gas fired boilers; $F_{\mathrm{GB},i}$ is the amount of natural gas consumed by gas fired boilers at $[t, T]$ period; $P^{\max}_{\mathrm{GB},i}$ represents the maximum output heat power of gas fired boilers; and η_{GB} represents the operating efficiency of gas fired boilers.

2.5. Uncertainty Analysis. The scenario in power grid is a kind of operation state of the power system [17]. The scene reduction is to eliminate the unrepresentative or error scenes and retain the typical scenes, without affecting the accuracy of the evaluation. We use the reduction method of typical scenes to characterize the uncertainty of load and output of renewable generation [18]. Multiple scenes are simulated by Monte Carlo method, based on the prediction of wind speed and solar radiation angle. Random scenes are generated by the method of distributed sampling which simulates fluctuations in predicted values under actual conditions.

The random distribution error is obtained by the forecasting error and its probability distribution which is determined based on historical data. The random variable of RES is converted to output power based on the output characteristic curve. In this paper, the predicted value of RES output at period T in the future is expressed as time series based on the method of backward reduction. The scenario of output is assumed as $\omega_i = (\lambda_i^0, \lambda_i^1, \ldots, \lambda_i^t, \lambda_i^T)$, where λ_i^t represents the value of scene i at period t; the corresponding probability of occurrence of scene ω_i is P_i; and the minimum probability distance between the scene set reduction and the final reserved scene subset is expressed as follows:

$$\mathrm{Min} \sum_{i \in \alpha} p_i \times \min_{j \notin \alpha} d\left(\omega_i, \omega_j\right), \tag{11}$$

where α represents the scene collection which is eventually deleted; the total number of scenes is set as 3000. The reserved set $S = \{\omega_0, \omega_1, \omega_i, \omega_s\}$ is initialized. We add another scene with the smallest distance of probability in the actual reduction set. The probability of the scene ω_l closest to the reduced set is changed to $p(\omega_l') = p(\omega_l) + p(\theta_k)$, until the number of scenes contained in the reduction set meets the requirements.

RES system operates in the Maximum Power Point Tracking (MPPT) mode which can adapt to environmental changes in real time to achieve maximum output [19]. Based on the short-time prediction results, the active power of RES output and basic load is shown as

$$\begin{aligned} P_{\mathrm{PV},i} &= \left[P_{\mathrm{PV},i}^1, P_{\mathrm{PV},i}^2, \ldots, P_{\mathrm{PV},i}^{\mathrm{T}}\right], \quad i \in [1, 2, \ldots, n], \\ P_{\mathrm{WT},i} &= \left[P_{\mathrm{WT},i}^1, P_{\mathrm{WT},i}^2, \ldots, P_{\mathrm{WT},i}^{\mathrm{T}}\right], \quad i \in [1, 2, \ldots, n], \\ P_{\mathrm{Load},i} &= \left[P_{\mathrm{Load},i}^1, P_{\mathrm{Load},i}^2, \ldots, P_{\mathrm{Load},i}^{\mathrm{T}}\right], \quad i \in [1, 2, \ldots, n]. \end{aligned} \tag{12}$$

The total power of RES output in this paper is

$$P_{\mathrm{RES},i} = P_{\mathrm{PV},i} + P_{\mathrm{WT},i}. \tag{13}$$

According to the components of the power supply side and the demand side in the ELN, the power balance model can be obtained:

$$\begin{aligned} P_{\mathrm{RES},i}^t + P_{\mathrm{GT},i}^t - P_{\mathrm{Load},i}^t - P_{\mathrm{dch},i}^t - P_{\mathrm{EC},i}^t &= u_{\mathrm{grid},i}^t + P_{\mathrm{ch},i}^t, \\ u_{\mathrm{grid},i}^t &\le u_{\mathrm{grid},i}^{\max}, \end{aligned} \tag{14}$$

where $u_{\mathrm{grid},i}^t$ represents the interaction power between i ELN and the EI system; $P_{\mathrm{EC},i}^t$ represents the electric refrigerator power which provides cold load for the system; and $u_{\mathrm{grid},i}^{\max}$ represents the power constraint of timeline.

3. A Decentralized Energy Flow Control Framework

3.1. The Construction of MAS in EI. Multiagent is a network structure composed of agents with the characteristics of autonomy, decentralized control, and bidirectional communication with other agents [20, 21]. Autonomous and intelligent systems have been widely used in energy systems. The centralized control cannot handle a variety of global information. Each agent in the multiagent system (MAS) could collect its own environmental information to solve the optimization problems and reach global consensus eventually in the autonomous region EI [22]. Considering the different characteristics and functions of nodes, the types of agents can be classified into the following:

(1) Intelligent measurement agent (IMA): it monitors and reports the operation status, power output status, and load demand status of internal equipment in the ELN system, which is responsible for the monitoring for the balance of the supply side and the demand side.

(2) Scheduling management agent (SMA): according to the information uploaded by the IMA and electricity price agent (EPA), the internal equipment output optimization is executed. When there is a shortage or excess load, the information is reported to the EPA for further addressing.

(3) Electricity price agent (EPA): it receives information of each ELN by the IMA and SMA. According to the real-time supply-demand balance of the system, the global optimal equilibrium solution is calculated. As the most essential agent, the strategy of maximizing EI benefits is the consensus reached by all EPAs in decentralized decision-making [23].

3.2. The Mechanism of Electricity Price. Different from the previous method of static electricity price that determines its own electricity price by the power grid [24], we adopt a new mechanism of electricity price. The electricity price in the EI is obtained based on the competition between ELN and the consensus reached by the MAS.

Since multiple energy sources can be converted into electricity, we use electricity as the core of trading in the energy flow control mechanism. In the electricity market of EI, the agent of electricity price takes part in the bidding to maximize the benefit of ELN.

The key problem is to obtain the optimal electricity price which maximizes the profit of ELN:

$$P = \sum_{t=1}^{\tau}\left[\left(\widehat{r}_{\mathrm{b}} - r_{\mathrm{b}}\right)^2 + \left(\widehat{r}_{\mathrm{s}} - r_{\mathrm{s}}\right)^2\right] + \lambda_n \times \sum_{t=1}^{\tau}\left[\left(r_{\mathrm{b}} - a_1^t\right)^2 + \left(r_{\mathrm{b}} - a_2^t\right)^2\right], \tag{15}$$

$$a_1^t = \begin{cases} \dfrac{m_1^t}{c_1^t}, & c_1^t \neq 0, \\ \lambda_{\mathrm{b}}, & c_1^t = 0, \end{cases} \qquad a_2^t = \begin{cases} \dfrac{m_2^t}{c_2^t}, & c_2^t \neq 0, \\ \lambda_{\mathrm{s}}, & c_2^t = 0, \end{cases} \tag{16}$$

where P represents the optimization goal of the electricity price agent in the rolling time periods; λ_n represents a flexible constraint coefficient of electricity price variables; r_{b} and r_{s} represent the internal purchasing price and internal selling price of electricity during the day, respectively; λ_{b} and λ_{s} represent the initial values of the internal purchasing price and internal selling price of electricity during the day, respectively; $\widehat{r}_{\mathrm{b}}$ and $\widehat{r}_{\mathrm{s}}$ represent the day-ahead internal purchase price and internal sale price; and a_1^t and a_2^t represent the reference price of power balance, which correspond to the electricity price in power selling and purchasing when the net load is zero, respectively. In addition, the expressions of the four variables c_1^t, c_2^t, m_1^t, and m_2^t are as follows:

$$\begin{cases} c_1^t = \displaystyle\sum_{i\in \mathrm{B}}\left(u_{\mathrm{grid},i}^t + \frac{P_{\mathrm{Load},i}^{\mathrm{E},t}\lambda_{\mathrm{b}}}{r_{\mathrm{b}}}\right), \\ c_2^t = \displaystyle\sum_{i\in \mathrm{S}}\left(u_{\mathrm{grid},i}^t + \frac{P_{\mathrm{Load},i}^{\mathrm{E},t}\lambda_{\mathrm{s}}}{r_{\mathrm{s}}}\right), \\ m_1^t = \displaystyle\sum_{i\in \mathrm{B}}\left(P_{\mathrm{Load},i}^{\mathrm{E},t}\lambda_{\mathrm{b}}\right), \\ m_2^t = \displaystyle\sum_{i\in \mathrm{S}}\left(P_{\mathrm{Load},i}^{\mathrm{E},t}\lambda_{\mathrm{s}}\right), \end{cases} \tag{17}$$

where $P_{\mathrm{Load},i}^{\mathrm{E},t}$ represents the basic load in i ELN and $u_{\mathrm{grid},i}^t$ represents the interactive power between the i ELN and EI.

3.3. Components of Game Theoretic Model. The mixed integer model is established by the problem of optimization in optimization periods; the following are the detailed components of the game model.

3.3.1. Players. The players are all the agents of electricity price in the set N^+ which includes RES and the battery energy storage system (BESS).

3.3.2. Game Rules

(i) Action: for any $i \in N^+$ in the k period, $A_i^k = \{P \mid \text{Constraints}\,(14) - (17)\}$ is the collection of all players' action.

(ii) Information: it includes RESs and various demand load and strategies adopted by other players.

(iii) Strategies: each participant's revenue is maximized by an optimized strategy, which can be expressed as a feasible strategy set ρ_i, shown as follows:

$$\rho_i = \{J \mid \text{Constraints}\,(1) - (3), (14) - (17)\}. \tag{18}$$

3.3.3. Payoffs. It is used to measure the benefit of the players in the game; the payoff of each player is maximized, expressed as U_i:

$$U_i = \left\{J + P \times U_{\mathrm{grid}} \mid \text{Constraints}\,(1) - (3), (13) - (17)\right\}. \tag{19}$$

Based on the above set of strategy, $A_i = \{A_1, A_2, \ldots, A_N\}$ if and only if the following conditions are satisfied:

$$U_i(A^*) \geq U_i(A), \quad \forall P \in A_i, \forall i \in N^+, \tag{20}$$

where A^* represents the set after updating the policy set, and the policy vector A^* is called Nash equilibrium, where no regional ELN can improve the respective benefits by unilaterally changing the strategy [25].

The strategy P_i is the interaction price of i ELN; the energy price strategy of the i ELN is A_i; $P_{\max}$ is the maximum value of the exchangeable electricity price; and A_i is a compact convex subset, while the participants sell power during the game. The electrical strategy P exists; therefore, the set A_i is not empty.

Prove that $U_i(A)$ is a concave function; then, S has a pure strategy Nash equilibrium point. For the second derivation, the second derivative is as follows:

$$\frac{\partial^2 U}{\partial a_i^2} = 2 - 4\lambda_n \times \left[\frac{2P_{\mathrm{Load},i_1}\lambda_{\mathrm{b}}r_{\mathrm{b}}^3}{\left(u_{\mathrm{grid},i_1}r_{\mathrm{b}} + P_{\mathrm{Load},i_1}\lambda_{\mathrm{b}}r_{\mathrm{b}}\right)^4} + \frac{2P_{\mathrm{Load},i_2}\lambda_{\mathrm{b}}r_{\mathrm{b}}^3}{\left(u_{\mathrm{grid},i_2}r_{\mathrm{b}} + P_{\mathrm{Load},i_2}\lambda_{\mathrm{b}}r_{\mathrm{b}}\right)^4}\right]. \tag{21}$$

Since $r_{\mathrm{b}}, \lambda_{\mathrm{b}}, P_{\mathrm{Load},i_1}$ $(i = 1, 2, 3, \ldots, N)$ is nonnegative, that is, $(\partial^2 U/\partial a_i^2) < 0$, U_i is strictly concave [26]. In summary, the automated demand response game is a typical strictly concave N-person game [27, 28]; therefore, the existence and uniqueness of the NE is proved.

3.4. Daily Cost Model of ELNs. In the game model, each agent can know others strategies in each round of decision-making [29]. Based on the short-term load forecasting data, the decision variables are optimized and updated. The optimization goal of this paper is to minimize the total operating cost of a single ELN. The optimization problem of a single

(1) Initialization: P_{PV}, P_{WT}, P_{Load}, and each EPA.
(2) Transmit initial strategy according to players' requirements to its neighbors.
(3) A new iteration starts when the strategy information is updated.
(4) **Real-time optimization**
(5) **for** $i = 1$ **do**
(6) **for** $k = 1 : 48$ **do**
(7) Input predicted value of P_{PV}, P_{WT}, and P_{Load}.
(8) Update P and J_i based on (15) and (22).
(9) **while** there is no further improvement **do**
(10) $k = k + 1$.
(11) **end while**
(12) **end for**
(13) **if** the optimized scheduling is different from the previous scheduling strategy **then**
(14) Send the new strategy to the MAS.
(15) **else**
(16) Denied, retain the previous control strategy.
(17) **end if**
(18) **end for**

Algorithm 1: Decentralized energy flow control strategy.

ELN in the rolling time domain can be expressed as a quadratic programming problem:

$$\begin{aligned} J_i = & \sum_{i=1}^{M}\sum_{i=1}^{\tau}\left(\widehat{u}_{\text{grid},i}^{t} - u_{\text{grid},i}^{t}\right)^2 \\ & + A \times \sum_{i=1}^{\tau}\left(\widehat{Q}_{\text{s},i}^{t} - Q_{\text{s},i}^{t}\right)^2 + B \times \sum_{i=1}^{\tau}\left(\widehat{P}_{\text{GT},i}^{t} - P_{\text{GT},i}^{t}\right)^2 \\ & + C \times \sum_{i=1}^{\tau}\left(\widehat{Q}_{\text{HX},i}^{t} - Q_{\text{HX},i}^{t}\right)^2 + D \times \sum_{i=1}^{\tau}\left(\widehat{Q}_{\text{AR},i}^{t} - Q_{\text{AR},i}^{t}\right)^2 \\ \text{s.t.} \quad & (2) - (10), (13) - (17), \end{aligned} \tag{22}$$

where J_i represents the time domain length in optimized scrolling; $\widehat{u}_{\text{grid},i}^{t}$ and $u_{\text{grid},i}^{t}$ represent the day-ahead and the real-time energy interaction power, respectively; $\widehat{Q}_{\text{s},i}^{t}$ and $Q_{\text{s},i}^{t}$ represent the day-ahead and real-time remaining capacity of ESS, respectively. $\widehat{P}_{\text{GT},i}^{t}$ and $P_{\text{GT},i}^{t}$ represent the day-ahead and real-time power generation of the gas turbine, respectively; $\widehat{Q}_{\text{HX},i}^{t}$ and $Q_{\text{HX},i}^{t}$ represent the day-ahead and real-time waste heat of the gas turbine for heating, respectively; $\widehat{Q}_{\text{AR},i}^{t}$ and $Q_{\text{AR},i}^{t}$ represent the day-ahead and real-time waste heat of the gas turbine for refrigeration, respectively; and A, B, C, and D represent the flexible constraint coefficient corresponding to the four components, respectively.

3.5. Solution Process. According to the aforementioned models, the proposed decentralized energy flow control strategy will be used to determine the regional ELN scheduling plan, which is shown in Algorithm 1.

4. Case Studies

To verify the validity of the proposed energy flow control strategy, four typical ELNs with different structures are chosen for case analysis [30]. The power supply side of each ELN consists of PV, WT, gas turbine, ESS, and the main grid; and the demand side is equipped with basic loads and electric refrigerators. Among them, energy interaction between the ELN is completed by a single bus, and the energy net payload is interacted with the external power grid through a single bus after the interaction. The parameters of rated power of PV output, WT output, BESS capacity, and gas turbine capacity of each ELN system are shown in Table 1. The ELN bus power transmission capacity is set to 4000 kW, and the maximum charging and discharging power of ESS is set to 2000 kW. In addition, the parameters associated with the energy conversion equipment are provided in Table 2.

The output power of RESs is given in Figure 2, which shows the output power of PV and WT of four ELNs in a typical day, respectively. Output power of cooling/heating load is shown in Figure 3.

In order to precisely quantify the optimization effect of the proposed energy flow control strategy, in this section, we simulate the following three models simultaneously in the EI. The three cases are demonstrated as follows:

Case I. No optimization mode is implemented. The power generation equipment is running at full capacity in an ELN, with no power interactions with other ELNs.

Case II. Each ELN performs power interactions without further optimization.

Case III. The proposed energy flow control strategy based on noncooperative game with MAS.

Analyze and compare the energy net load characteristics and economy of the three operating modes. The load curve of the three cases is depicted in Figure 4.

As shown in Figure 4, compared with Case I and Case II, Case III is decreased by 82.44% and 29.22% in terms of peak-to-valley difference, respectively. The volatility is reduced by 80.05% and 27.08%, respectively. The proposed energy flow control strategy can effectively reduce the power difference

Table 1: The basic parameters of ELN.

Types	PV (kW)	WT (kW)	BESS (kWh)	Gas turbine (kW)
ELN 1	3000	2500	13000	2000
ELN 2	3300	3550	13000	2000
ELN 3	4000	3900	13000	1000
ELN 4	3500	3750	13000	1000

Table 2: The parameters of energy conversion equipment.

Types	Heat exchanger (kW)	Absorption chiller (kW)	Gas boiler (kW)	Electric refrigerator (kW)
ELN 1	2000	2000	1500	1000
ELN 2	2000	0	1500	0
ELN 3	0	2000	0	1000
ELN 4	0	0	0	0

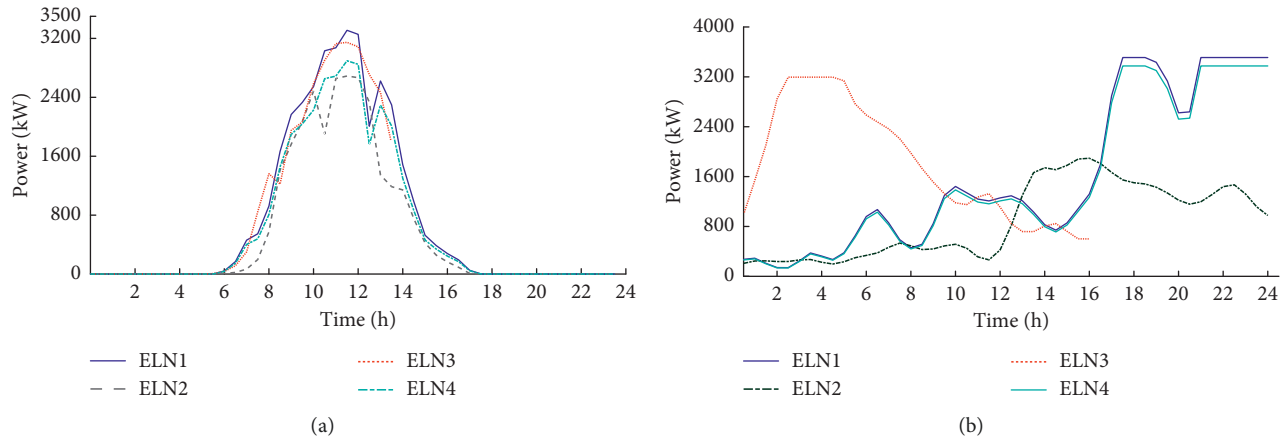

Figure 2: Active power of PV and WT output in a typical day.

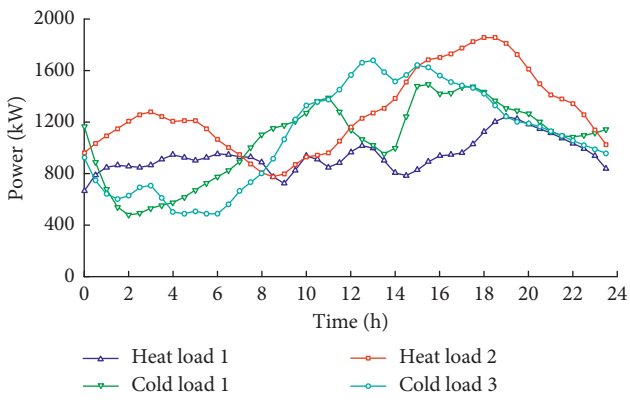

Figure 3: The cooling and heating loads of ELNs.

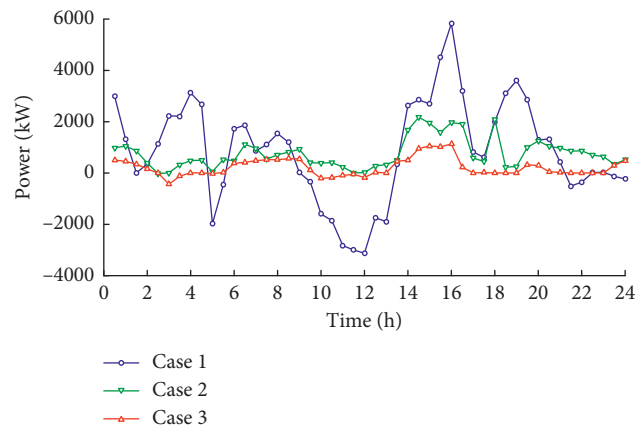

Figure 4: The net load of the Energy Internet under three cases.

existing in the EI and improve the stability and resilience of the system. In addition, compared with Case I, the energy utilize efficiency in the other two cases has significantly improved.

It can be observed from Figure 5, when the output power of RESs is insufficient, the ESS and gas turbine is operated. Each ELN actively conducts power interactions to stabilize system load fluctuations, where the ESS and gas turbine play a vital role in outputting power. When the gas turbine output is in deficit, the waste heat utilization is also insufficient. At this time, the heat load is mainly provided by the gas boiler, while the cooling load is mainly provided by the electric refrigerator. When the gas turbine output is surplus, the heat load is mainly provided by the gas turbine and the remaining heat is fully utilized. In addition, refrigeration can meet the demand

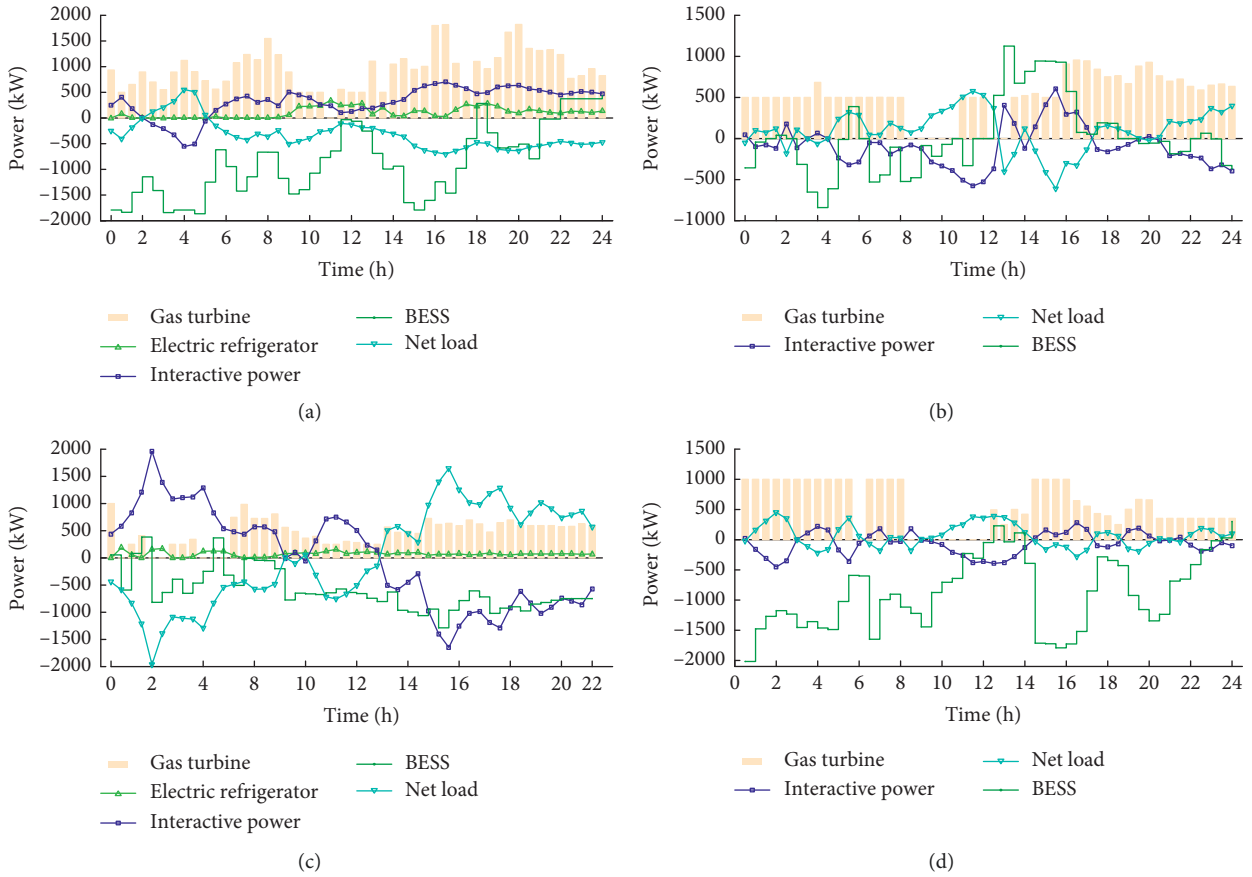

Figure 5: Optimal scheduling results of four ELNs.

for cold load. As a result, the overall operating efficiency and fuel utilization of the EI system are significantly improved.

The detailed comparison of time-of-use pricing and real-time pricing obtained by the proposed game theoretic model as mentioned above is illustrated in Figure 6. Time-of-use electricity prices cannot demonstrate the internal energy difference, which has a negative effect on energy interaction. According to the internal energy consumption of each ELN, the ultimate interaction price is determined through mutual game process. After multiple iterations, the electricity price tends to be stable. All participants choose not to change their strategies and maximize their respective interests. Each participant in the EI network price gets the optimal strategy through the game, repeating this convergence process, and finally realizes the consensus that no ELN can obtain more profit.

Table 3 presents the detailed results of various costs in three cases.

(1) Comparing Case II and Case III with Case I, the RES utilization rate has been significantly improved, when the abandoned RES power loss is close to 0. The photoelectric subsidy has increased by 4.85% and 4.82%, respectively. In addition, Case 3 has a slight increase in charging/discharging loss, power loss, and operation and maintenance costs compared with Case II, indicating that the optimization process has little influence on the economy with less transaction cost.

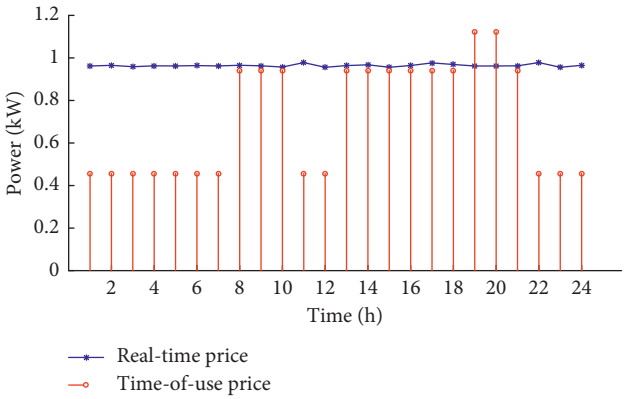

Figure 6: Comparison of two types of electricity price.

(2) Compared with Case I and Case II, Case III has increased the total revenue by 290.06% and 123.31%, respectively, indicating that the game-theoretical decentralized optimization process can significantly improve the economics of EI. It is obvious that the overall benefit is significantly increased by fully utilizing the output of RES with real-time electricity price mechanism.

(3) Compared with Case I, natural gas costs of Case II and Case III have increased by 11.01% and 4.52%,

Table 3: Economic statistics of three cases.

Types	Case I	Case II	Case III
Loss cost of RES abandoning (yuan)	2240.5	0	17.5
Transaction cost of power grid (yuan)	25991.7	17172.2	4804. 4
Charging and discharging loss (yuan)	0	1129.6	1173.2
Photoelectric subsidy (yuan)	77532.6	81296.6	81267.2
Operational and maintenance cost	6268.2	6587.6	6662.9
Gas cost (yuan)	66357.5	73663.3	69358.9
Multienergy supply income (yuan)	31453.4	31453.4	31453.4
Power loss (yuan)	0	2233.2	2319.5
Generation cost of gas turbine (yuan/kWh)	0.3243	0.3889	0.3733
Total revenue (yuan)	8128	14197.3	31703.8

respectively. The average power generation cost of gas turbines has increased by 19.92% and 15.11%, respectively, indicating that Cases II and Case III can transform heating and cooling power in more effective ways. Comparing Case III with Case II, it can be observed that the increase in natural gas costs is less which indicates that multienergy can actively participate in system optimization to reduce gas turbine output. The utilization of RES has also greatly improved the economic and environmental performance of the EI system.

5. Conclusion

In this paper, a decentralized energy flow control framework of optimal operation considering the uncertainty of the supply side and demand side has been proposed for the Energy Internet. A typical architecture of ELN is established with system models which can better reflect the characteristics and requirements of EI. In addition, a novel electricity price mechanism for energy interaction is proposed to respond to the supply-demand difference. The theoretical noncooperative game is proposed with the objective to minimize the daily operational cost of the EI system. Through iterative calculation, the game reaches the Nash equilibrium, which is the consensus reached by the MAS. The case study based on real-world data proves the feasibility and effectiveness of the proposed framework. The proposed decentralized framework combining with optimized operational strategy can contribute to reducing the system load volatility and decreasing the operating economic cost as well as improving the reliability and resilience of the EI system.

Data Availability

The data used to support the findings of this study are included within the article.

Conflicts of Interest

The authors declare no conflicts of interest.

Acknowledgments

This work was supported by the National Natural Science Foundation of China under grant 51777193.

References

[1] D. Cheng, "Controllability of switched bilinear systems," *IEEE Transactions on Automatic Control*, vol. 50, no. 4, pp. 511–515, 2005.

[2] A. Q. Huang, M. L. Crow, G. T. Heydt, J. P. Zheng, and S. J. Dale, "The future renewable electric energy delivery and management (FREEDM) system: the energy internet," *Proceedings of the IEEE*, vol. 99, no. 1, pp. 133–148, 2011.

[3] L. Ju, Z. Tan, H. Li, Q. Tan, X. Yu, and X. Song, "Multi-objective operation optimization and evaluation model for CCHP and renewable energy based hybrid energy system driven by distributed energy resources in China," *Energy*, vol. 111, pp. 322–340, 2016.

[4] S. Rech and A. Lazzaretto, "Smart rules and thermal, electric and hydro storages for the optimum operation of a renewable energy system," *Energy*, vol. 147, pp. 742–756, 2018.

[5] Q. Sun, R. Han, H. Zhang, J. Zhou, and J. M. Guerrero, "A multiagent-based consensus algorithm for distributed coordinated control of distributed generators in the energy internet," *IEEE Transactions on Smart Grid*, vol. 6, no. 6, pp. 3006–3019, 2015.

[6] N. Ahmed, M. Levorato, and G. P. Li, "Residential consumer-centric demand side management," *IEEE Transactions on Smart Grid*, vol. 9, no. 5, pp. 4513–4524, 2018.

[7] J. Wang, N. E. Redondo, and F. D. Galiana, "Demand-side reserve offers in joint energy/reserve electricity markets," *IEEE Transactions on Power Systems*, vol. 18, no. 4, pp. 1300–1306, 2003.

[8] G. U. Wei, L. U. Shuai, J. Wang, X. Yin, C. Zhang, and Z. Wang, "Modeling of the heating network for multi-district integrated energy system and its operation optimization," *Proceedings of the CSEE*, vol. 37, no. 5, pp. 1305–1316, 2017.

[9] C. Lin, L. Chen, S. Zhu, T. Hao, and X. Shen, "Study of micro energy internet based on multi-energy interconnected strategy," *Power System Technology*, vol. 40, no. 1, 2016.

[10] J. Wang, H. Zhong, Q. Xia, C. Kang, and E. Du, "Optimal joint-dispatch of energy and reserve for CCHP-based microgrids," *IET Generation, Transmission & Distribution*, vol. 11, no. 3, pp. 785–794, 2017.

[11] H. Ren, W. Zhou, K. i. Nakagami, W. Gao, and Q. Wu, "Multi-objective optimization for the operation of distributed energy systems considering economic and environmental aspects," *Applied Energy*, vol. 87, no. 12, pp. 3642–3651, 2010.

[12] Z. Huang, H. Yu, X. Chu, and Z. Peng, "A novel optimization model based on game tree for multi-energy conversion systems," *Energy*, vol. 150, no. 12, pp. 109–121, 2018.

[13] R. Lu, S. H. Hong, and X. Zhang, "A dynamic pricing demand response algorithm for smart grid: reinforcement learning approach," *Applied Energy*, vol. 220, pp. 220–230, 2018.

[14] M. Zeng, Y. Yang, D. Liu et al., ""Generation-grid-load-storage" coordinative optimal operation mode of energy internet and key technologies," *Power System Technology*, vol. 40, pp. 114–124, 2016.

[15] K. Wang, Y. Wang, Y. Sun, S. Guo, and J. Wu, "Green industrial internet of things architecture: an energy-efficient perspective," *IEEE Communications Magazine*, vol. 54, no. 12, pp. 48–54, 2016.

[16] C. Wei, M. Benosman, and T. Kim, "Online parameter identification for state of power prediction of lithium-ion batteries in electric vehicles using extremum seeking," *International Journal of Control, Automation and System*, pp. 1–11, 2019.

[17] P. Meibom, R. Barth, B. Hasche, H. Brand, C. Weber, and M. O'Malley, "Stochastic optimization model to study the operational impacts of high wind penetrations in Ireland," *IEEE Transactions on Power Systems*, vol. 26, no. 3, pp. 1367–1379, 2011.

[18] K. Mason, J. Duggan, and E. Howley, "Forecasting energy demand, wind generation and carbon dioxide emissions in Ireland using evolutionary neural networks," *Energy*, vol. 155, pp. 705–720, 2018.

[19] A. Lashab, D. Sera, J. M. Guerrero, L. Mathe, and A. Bouzid, "Discrete model predictive control-based maximum power point tracking for PV systems: overview and evaluation," *IEEE Transactions on Power Electronics*, vol. 33, no. 8, pp. 7272–7287, 2018.

[20] S. D. J. Mcarthur, E. M. Davidson, V. M. Catterson et al., "Multi-agent systems for power engineering applications—part II: technologies, standards, and tools for building multi-agent systems," *IEEE Transactions on Power Systems*, vol. 22, no. 4, pp. 1753–1759, 2007.

[21] R. Rahmani, I. Moser, and M. Seyedmahmoudian, "Multi-agent based operational cost and inconvenience optimization of PV-based microgrid," *Solar Energy*, vol. 150, pp. 177–191, 2017.

[22] F. Grabowski, "Nonextensive model of self-organizing systems," *Complexity*, vol. 18, no. 5, pp. 28–36, 2013.

[23] R. Hao, Q. Ai, Y. Zhu, and Y. Gao, "Cooperative optimal control of energy internet based on multi-agent consistency," *Automation of Electric Power Systems*, vol. 41, no. 15, pp. 10–17, 2017.

[24] M. Davison, C. L. Anderson, B. Marcus, and K. Anderson, "Development of a hybrid model for electrical power spot prices," *IEEE Power Engineering Review*, vol. 22, no. 3, p. 58, 2002.

[25] X. Yang, G. Wang, H. He, J. Lu, and Y. Zhang, "Automated demand response framework in elns: decentralized scheduling and smart contract," *IEEE Transactions on Systems, Man, and Cybernetics: Systems*, pp. 1–15, 2019.

[26] A. Ben-Tal and A. Nemirovski, "Robust convex optimization," *Mathematics of Operations Research*, vol. 23, no. 4, pp. 769–805, 1998.

[27] J. B. Rosen, "Existence and uniqueness of equilibrium points for concave *n*-person games," *Econometrica*, vol. 33, no. 3, pp. 520–534, 1965.

[28] M. N. Szilagyi and I. Somogyi, "Agent-based simulation of an *n*-person game with parabolic payoff functions," *Complexity*, vol. 15, no. 3, pp. 50–60, 2009.

[29] W. Saad, Z. Han, H. V. Poor, and T. Basar, "Game-theoretic methods for the smart grid: an overview of microgrid systems, demand-side management, and smart grid communications," *IEEE Signal Processing Magazine*, vol. 29, no. 5, pp. 86–105, 2012.

[30] G. Wang, W. Cai, Y. Zhang, K. Zhao, and X. Xu, "Lyapunov optimization based online energy flow control for multi-energy community microgrids," in *Proceedings of the 2019 IEEE PES GTD Grand International Conference and Exposition Asia (GTD Asia)*, Bangkok, Thailand, March 2019.

Hindawi
Complexity
Volume 2019, Article ID 5834741, 14 pages
https://doi.org/10.1155/2019/5834741

Research Article

Boost Converters' Proximate Constrained Time-Optimal Sliding Mode Control Based on Hybrid Switching Model

Asghar Taheri,[1,2] **Amir Ghasemian**,[2] **and Hai-Peng Ren**[1]

[1]*Xi'an Technological University, Xian 710021, China*
[2]*University of Zanjan, Zanjan 4537138791, Iran*

Correspondence should be addressed to Hai-Peng Ren; renhaipeng@xaut.edu.cn

Received 21 June 2019; Revised 19 August 2019; Accepted 28 August 2019; Published 27 October 2019

Guest Editor: Chun Wei

It is well known in the literature studies that the theoretical time-optimal control of boost converters can be achieved using switching surfaces based on the converter's natural state trajectories. However, this method has two important drawbacks: First, the transient current peak of the time-optimal controller is far beyond the current limitations of related circuit elements in many practical cases. Second, switching based on the converter's natural trajectories has high computational complexity and high dependence on circuit parameters. In this paper, based on the hybrid dynamical model of the converter and geometrical representation of its corresponding vector fields, a proximate constrained time-optimal sliding mode controller is proposed. The proposed method has a fast response that is near that of a time-optimal controller, with less computational complexity and sensitivity to parameter changes. The proposed method and its relevant theoretical framework are validated on an experimental setup with a boost converter prototype and an eZdsp TMS320F2812 processor board.

1. Introduction

Because of high demand for renewable-energy (RE) sources, power electronic systems as links between sources, storages, and loads play an increasingly important role in modern power systems [1]. In many RE applications, such as fuel cell and photovoltaic energy systems, the required load voltage is higher than the source voltage. In these cases, boost converters as a small-sized, low-cost, and power-efficient DC-DC converter are of special importance [2]. In addition, many of these RE applications need higher performance power converters with new control strategies. Therefore, any improvement of boost converters' performance such as faster transient response or better response to source voltage and load variations would be beneficial and welcomed in the field of RE systems.

The common approaches to control the boost converter and other DC-DC power converters are based on linearized averaged models and standard frequency-domain design methods [3]. Nonlinear state space-averaged models are also used in many works to achieve better response [3]. An important assumption in the state space-averaging model is that the switching signal varies slowly compared with the changes in state variables [3]. This assumption causes the slow time response of the control method based on the model. Hybrid dynamical system modeling of converters, which directly takes into account the switching nature of the DC-DC converters, promises better transient response and large signal stability [4–9]. A useful outcome of considering the switching nature of DC-DC converters is the time-optimal control (TOC) of the converters [10–12]. Although there has been a vast body of work on TOC of boost converters [10, 13, 14], most of the focus has been on optimization of specific controllers or optimization based on approximate ideal waveforms of the converter [15–17]. Theoretical TOC of buck and boost converters has been done in recent studies [11, 12] using optimal control theory methods like Pontryagin's maximum principle. These researches show that the TOC of buck and boost converters is the minimum switching control based on the bang-bang property [11]. The ideal time-optimal (TO) controller can be implemented using the sliding mode controller (SMC)

framework with switching surfaces based on natural state trajectories. This TO controller has high computational complexity and high sensitivity to circuit parameters [12]. Some linear approximations for this optimal switching surface in the buck converter are proposed to relieve the computational complexity and circuit parameter dependence [7, 13, 16].

Up to date, SMC has been extensively studied [18–22]. Valuable studies are performed on novel sliding surfaces for some applications [23–25]. However, challenges of SMC may not be the same in different application areas. For example, DC-DC converters are switching systems in nature. These systems are designed to achieve desired dynamics by rapidly switching between two or more subsystems. In this case, the control variable is a discrete signal that determines the ON/OFF state of the switches. Hence, the chattering issue in this application is different from the traditional one [23]. The key point to be addressed is finding the time-optimal sliding surface with a stable margin as to relieve the sensitivity to parameter changes [21, 22].

Besides computational complexity and circuit parameter dependence, the traditional time-optimal control of the boost converter has two other important drawbacks. First, high transient current peak may exceed the current limit of the inductor element or the power source. Second, there are higher voltage and current fluctuations around the operating point.

In this paper, the boost converter is modeled as a switched affine (SA) system, and its behavior is studied using the phase portrait. We propose a proximate constrained time-optimal (PCTO) SMC to overcome the shortcomings of the traditional TOC using a piecewise linear switching surface. The proposed method satisfies the reaching and existence conditions of the sliding mode controller, which is visualized by the phase portrait and geometric analysis. The proposed method keeps the inductor current within the determined limits during the transient stage and, at the same time, on the switching surface in the other regions of the state space; the switching surface keeps the state vector on a linear approximation of the ideal switching surface to achieve fast and precise response. The speed response of the proposed method remains close to that of the TOC, while it needs less computational complexity and can be simply implemented using the digital signal processor (DSP). In addition, the performance of the proposed method has less sensitivity to circuit parameter changes.

An experimental prototype based on an eZdsp TMS320F2812 processor board with a sensor and signal conditioning circuit and a boost converter is built to verify our theoretical analysis and effectiveness of the proposed method.

2. Boost Converter as a Hybrid Dynamical System

2.1. Switched Affine Model. Figure 1 shows a standard boost converter circuit considering the equivalent series resistances (ESRs) of the inductor and capacitor given by r_L and r_C, respectively. When the switch S is closed, the current of the inductor increases and energy gets stored in the inductor, and when it is open, the inductor current transfers the stored energy through the diode to the load side. A filter capacitor, C, regulates the output voltage to achieve a smooth voltage at the load side.

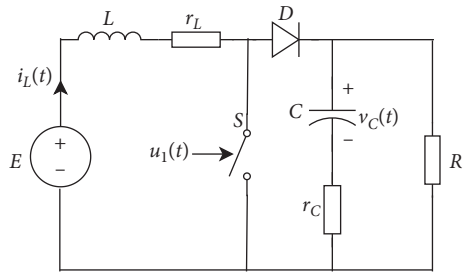

Figure 1: Standard boost converter circuit considering ESRs.

The boost converter shown in Figure 1 has a linear dynamical model for each of the possible configurations of its power electronic switches. This converter has three operation states. In subsystem 1, the switch is ON and the diode is OFF. The dynamics of the system in this state is modeled by

$$x'(t) = f_1(x) = A_1 x + b_1, \tag{1}$$

where

$$A_1 = \begin{bmatrix} \dfrac{-r_L}{L} & 0 \\ 0 & \dfrac{-1}{(R + r_C)C} \end{bmatrix},$$

$$b_1 = \begin{bmatrix} \dfrac{1}{L} \\ 0 \end{bmatrix} E, \tag{2}$$

$$x = \begin{bmatrix} i_L \\ v_C \end{bmatrix}.$$

In subsystem 2, the switch is OFF and the diode is ON. The boost converter is modeled as

$$x'(t) = f_2(x) = A_2 x + b_2, \tag{3}$$

where

$$A_2 = \begin{bmatrix} \dfrac{-1}{L}\left(r_L + \dfrac{r_C R}{(R + r_C)}\right) & \dfrac{-R}{(R + r_C)L} \\ \dfrac{R}{(R + r_C)C} & \dfrac{-1}{(R + r_C)C} \end{bmatrix},$$

$$b_2 = \begin{bmatrix} \dfrac{1}{L} \\ 0 \end{bmatrix} E. \tag{4}$$

Subsystem 3 corresponds to the case when both switches are OFF for which the state space model is as follows:

$$x'(t) = f_3(x) = A_3 x + b_3, \tag{5}$$

where

$$A_3 = \begin{bmatrix} 0 & 0 \\ 0 & \dfrac{-1}{(R + r_C)C} \end{bmatrix}, \qquad b_3 = \begin{bmatrix} 0 \\ 0 \end{bmatrix} E. \tag{6}$$

This model represents a hybrid dynamical system, and its discrete variable can be determined by the switch status and the switching condition of the diode, or simply by its operating state. Although the operating state is both state and input dependent, in many cases, the controller is designed so that mode 3 of operation does not occur corresponding to the continuous conduct mode (CCM) of the converter. In this case, the boost converter model can be simplified to an SA system with two input-dependent operating states:

$$x'(t) = A_q x + b_q, \quad q = 1, 2. \tag{7}$$

This SA system model is used in the following sections to study the boost converter's behavior.

2.2. Time Response. Time response for a nonhomogeneous linear system like

$$\begin{cases} x'(t) = Ax + g(t), \\ x(0) = x_0 \end{cases} \tag{8}$$

can be described by

$$x(t) = e^{tA} x_0 + e^{tA} \int_0^t e^{-\tau A} g(\tau) d\tau, \tag{9}$$

where e^{tA} represents the matrix exponential. Each subsystem of the boost converter is a linear nonhomogeneous system similar to (8) with a constant g. Therefore, the time response for the state q of the converter is given by

$$x(t) = e^{tA_q} x_0 + e^{tA_q} \int_0^t e^{-\tau A_q} b_q d\tau. \tag{10}$$

Since A^{-1} and A commute, using matrix exponential properties, we have

$$x(t) = e^{tA_q} x_0 + e^{tA_q} A_q^{-1} b_q - A_q^{-1} b_q. \tag{11}$$

Finally, in each subsystem, the boost converter's time response is represented as follows:

$$x(t) = e^{tA_q}(x_0 - x_e) + x_e, \quad x_e = A_q^{-1} b_q. \tag{12}$$

For $t = 0$, the matrix exponential equals the identity matrix, so the initial condition is satisfied. If the eigenvalues of A_q have negative real parts, the matrix exponential will converge to the zero matrix as t goes to infinity. In that case, the equilibrium of the boost converter is

$$x_e = A_q^{-1} b_q. \tag{13}$$

The state matrix A_1 has two real eigenvalues, implying that the equilibrium point is a simple node. The eigenvalues of A_2 are two complex numbers with negative real parts; hence, the equilibrium point is a spiral asymptotically stable point. The above equations are used for the phase portrait of the boost converter in its different operating modes in the following sections.

2.3. Phase Portrait Representation. Phase portrait representations for a boost converter with the second circuit parameter set given in Table 1 are depicted in Figure 2. In this section, circuit 1 is used for better representation of the boost converter's state trajectories in its different operating subsystems. In the remaining parts of this paper, specifications of circuit 2 in Table 1 are used in all simulation and experimental tests.

As can be seen in Figure 2, in subsystem 1, each of the state trajectories converges to a point on the i_L axis. Subsystem 2 has a spiral stable point in the middle of the continuous state space. The control input of a boost converter is a discrete switching signal which turns the switch ON or OFF. Fast switching between two phase portraits with varying average dwell time results in custom state trajectories in the continuous state space. Figure 2(c) shows a sample state trajectory for the fixed PWM input with 35% of duty cycle. To better illustrate the switching effect, the carrier frequency is kept low in this PWM signal.

Figure 2(c) also depicts the possible equilibrium points of the converter state vector. To have closed-loop stability in a boost converter control system, the desired state values cannot be arbitrary points on the continuous state space. To hold the state trajectory in a neighborhood around a desired point, there should be a suitable switching sequence which moves the states in a limit cycle around the desired point. These possible equilibrium points form a conic section in the continuous state space and can be calculated by simulating the PWM signals with different duty cycles. The result of this simulation is shown in Figure 2(c).

3. Time-Optimal Control

In [15], it is shown using Pontryagin's maximum principle that time-optimal control of a boost converter is a bang-bang control, and it is proved that this time-optimal control is also minimum switching control [7]. In a physical sense, when the load resistance steps up, the controller should turn the switch ON to store sufficient energy in the inductor. The controller will turn the switch OFF when the state variables reach a special trajectory of the switch OFF mode. This trajectory will reach the desired state variable point. Then, the controller will keep the state variables near the desired point. This time-optimal control can be implemented as a sliding mode controller whose switching surface is defined

Table 1: Specifications of used boost converters.

Description	Circuit 1	Circuit 2	Parameter
Nominal input	20 V	5 V	V_S
Desired output	30 V	15 V	V_O
Load resistance	10 Ω	112 Ω	R
Inductance	700 μH	128 μH	L
Inductor DCR	0.4 Ω	0.2 Ω	r_L
Capacitance	15 μF	470 μF	C
Capacitor ESR	0.2 Ω	0.5 Ω	r_C

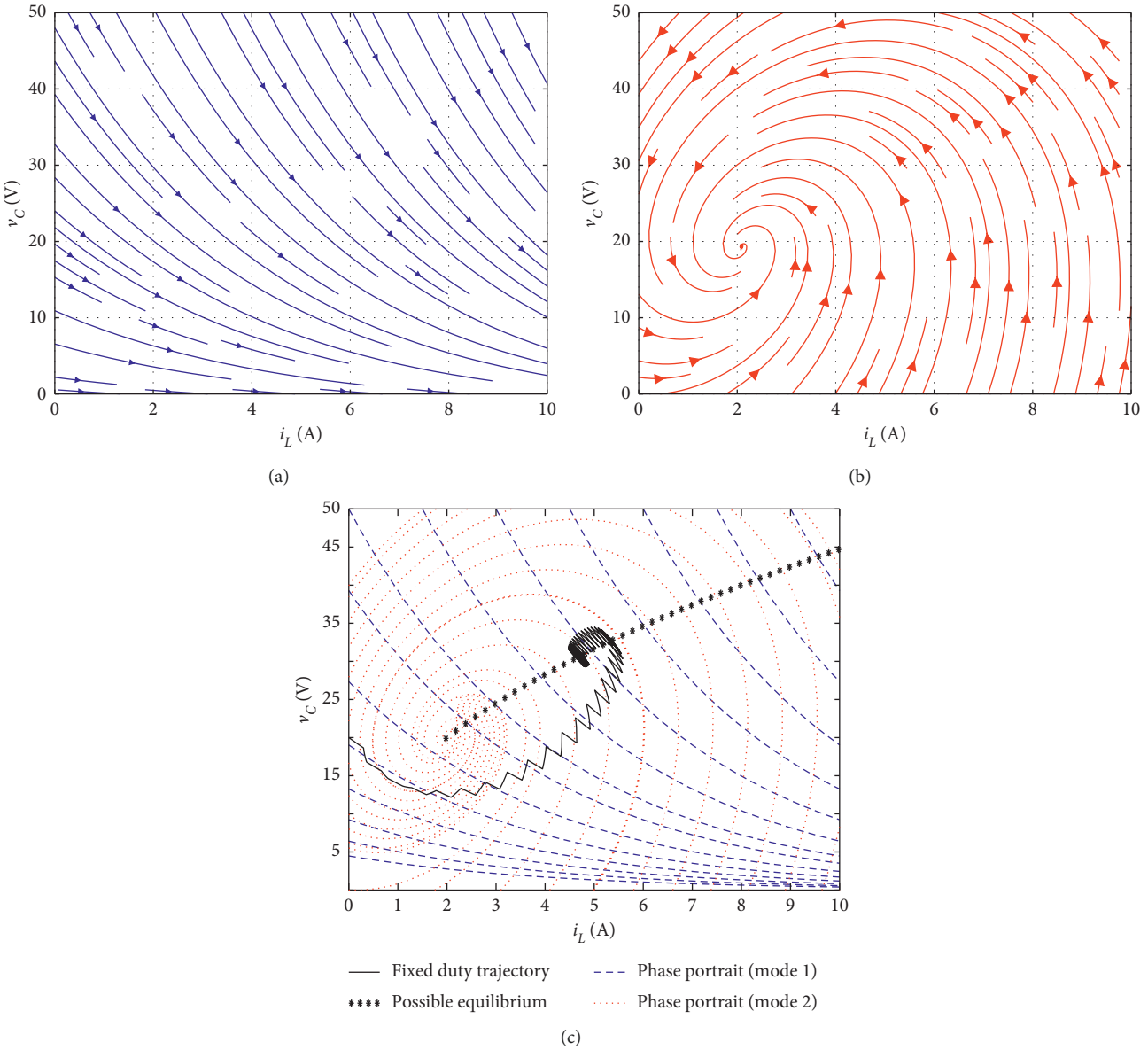

Figure 2: Phase portrait representation of system behavior. (a) Phase portrait of mode 1. (b) Phase portrait of mode 2. (c) Fixed duty cycle trajectory.

by combining two natural state trajectories of subsystem 1 and subsystem 2 of the boost converter [6].

Figure 3 shows an ideal state trajectory for time-optimal control of a boost converter with specifications of circuits given in Table 1. Voltage and current waveforms of the ideal time-optimal controller are depicted in Figure 3. Despite the fast response time, this time-optimal controller has the following four major drawbacks:

(1) High computational complexity

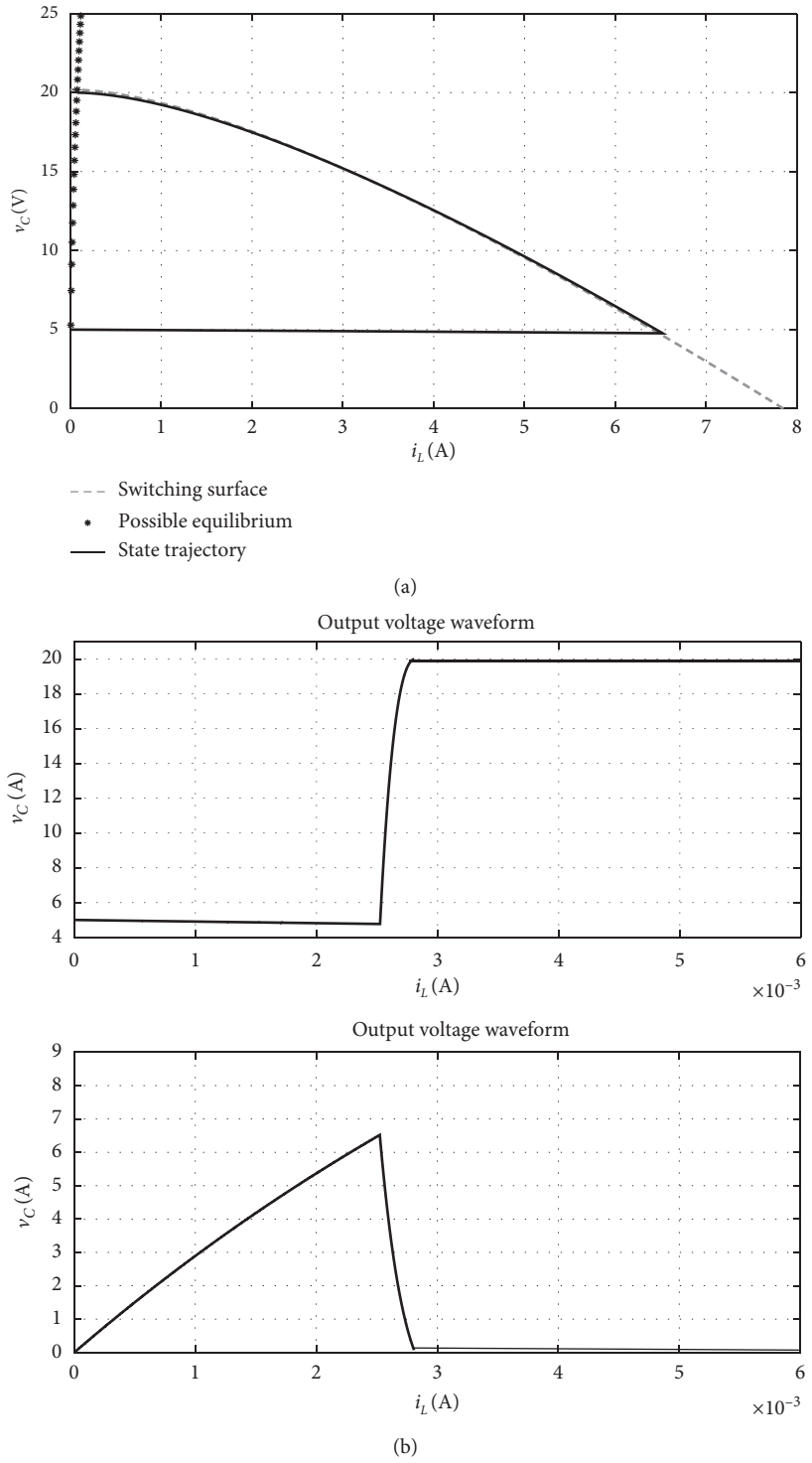

Figure 3: Ideal TOC: (a) state trajectory; (b) waveforms.

(2) Circuit parameter dependence

(3) Big transient current overshoot

(4) High steady-state voltage ripples

Although the simulated waveforms show good steady-state operation, in experimental tests, high current and voltage fluctuations will occur because of the aligned direction of the switching surface and trajectories.

Linear approximations of the optimal state trajectories can be used to overcome the first issue highlighted above and to some extent the second issue. In this paper, a conventional sliding mode controller is tuned to reduce the current overshoot within the determined limits. Then, to improve the response time, we investigate piecewise linear switching surfaces to maintain the inductor current within its allowed maximum designed value.

4. Tuned SMC

4.1. Sliding Mode Control Principle. In this section, a conventional SMC is tuned to keep the boost converter's response time low while maintaining the current limit. In the SMC, the system state trajectory first moves toward a surface in the state space, namely, the sliding surface. Second, the system state slides near the surface and converges to a desired equilibrium point (8) [14]. The first and second parts of the SMC state trajectory are called the reaching mode and sliding mode, respectively (8). The design procedure of an SMC has two major steps. In the first step, a switching surface is defined which has the desired convergence properties and provides the required asymptotic behavior. In the second step, a switching law is designed so that the reaching condition is guaranteed.

4.2. Sliding Surface Definition. The sliding surface of a conventional SMC for the boost converter can be defined as

$$S = k\left(i_L - i_{\text{ref}}\right) + \left(v_C - v_{\text{ref}}\right) = \begin{bmatrix} k \\ 1 \end{bmatrix}^T \left(x - x_r\right), \tag{14}$$

where $x_r = [i_{\text{ref}}, v_{\text{ref}}]^T$ and v_{ref} and i_{ref} are the desired output voltage and inductor current, respectively. The desired output voltage is determined by the specification of applications; the desired inductor current is determined by both the desired output voltage and the switching law.

The corresponding switching law for the defined sliding is

$$q = \begin{cases} 1, & S \le 0, \\ 2, & S > 0, \end{cases} \tag{15}$$

where q is the index for subsystems defined in Section 2.

4.3. Existence Condition. The existence condition for the sliding surface guarantees that there exists a region near the sliding surface, in which the switching law can steer each initial state inside it to hit the sliding surface. This condition is formulated as

$$\exists \varepsilon > 0 \text{ satisfying} \begin{cases} S' > 0, & \text{for } -\varepsilon < S < 0, \\ S' < 0, & \text{for } 0 < S < \varepsilon. \end{cases} \tag{16}$$

This condition guarantees that, in some regions around the surface, the switching law steers state variables toward them. According to (1), (3), (15), and (16), the time derivative S' is

$$S' = \sum \frac{dS}{dx_i}\frac{dx_i}{dt} = \nabla S \cdot x' = \begin{cases} S_1' = \begin{bmatrix} k \\ 1 \end{bmatrix}^T f_1(x), & S < 0, \\ S_2' = \begin{bmatrix} k \\ 1 \end{bmatrix}^T f_2(x), & S > 0. \end{cases} \tag{17}$$

Since state transition functions of both modes are continuous, S_1' and S_2' are continuous. Hence, for the existence condition, it is sufficient that

$$S_1'\big|_{S=0} > 0 \wedge S_2'\big|_{S=0} < 0, \tag{18}$$

where $\wedge$ represents intersection and

$$\begin{cases} S_1' = \begin{bmatrix} k \\ 1 \end{bmatrix}^T f_1(x) = \begin{bmatrix} k \\ 1 \end{bmatrix}^T . \left(A_1 x + b_1\right), \\ S_2' = \begin{bmatrix} k \\ 1 \end{bmatrix}^T f_2(x) = \begin{bmatrix} k \\ 1 \end{bmatrix}^T . \left(A_2 x + b_2\right). \end{cases} \tag{19}$$

Condition $S = 0$ in (18) makes i_L and v_C dependent so that the inequalities are functions of i_L and k. For an ideal boost converter without parasitic elements, the existence of inequalities (17) can be solved to derive limitations for the parameter k factor. However, when parasitic elements exist, these inequalities are expanded as follows.

Inequality 1

$$S_1' = P_1 k i_L + P_2 k + P_3 > 0, \tag{20}$$

where

$$\begin{aligned} P_1 &= \frac{P_3}{v_{\text{ref}}} - \frac{r_L}{L}, \\ P_2 &= \frac{v_s}{L} - \frac{P_3 i_{\text{ref}}}{v_{\text{ref}}}, \\ P_3 &= \frac{v_{\text{ref}}}{C\left(R + r_C\right)}. \end{aligned} \tag{21}$$

Inequality 2

$$S_2' = Q_1 k^2 i_L + Q_2 k^2 + Q_3 k i_L + Q_4 k + Q_5 i_L + Q_6 < 0, \tag{22}$$

where

$$\begin{aligned} Q_1 &= \frac{R}{L\left(R + r_C\right)}, \\ Q_2 &= -Q_1 * i_r, \\ Q_3 &= \frac{-r_L}{L} - r_C Q_1 + \frac{Q_5}{R}, \\ Q_4 &= \frac{E}{L} - Q_1 * v_r + Q_6 * \frac{i_r}{v_r}, \\ Q_5 &= Q_1 * \frac{L}{C}, \\ Q_6 &= -Q_5 * \frac{v_r}{R}. \end{aligned} \tag{23}$$

It can be shown analytically that inequality 1 holds for positive values of i_L and k. But S_2' in inequality 2 has a third-order two-variable function, and it is better to solve it numerically. Figure 4 depicts a contour plot for S_1' and S_2'

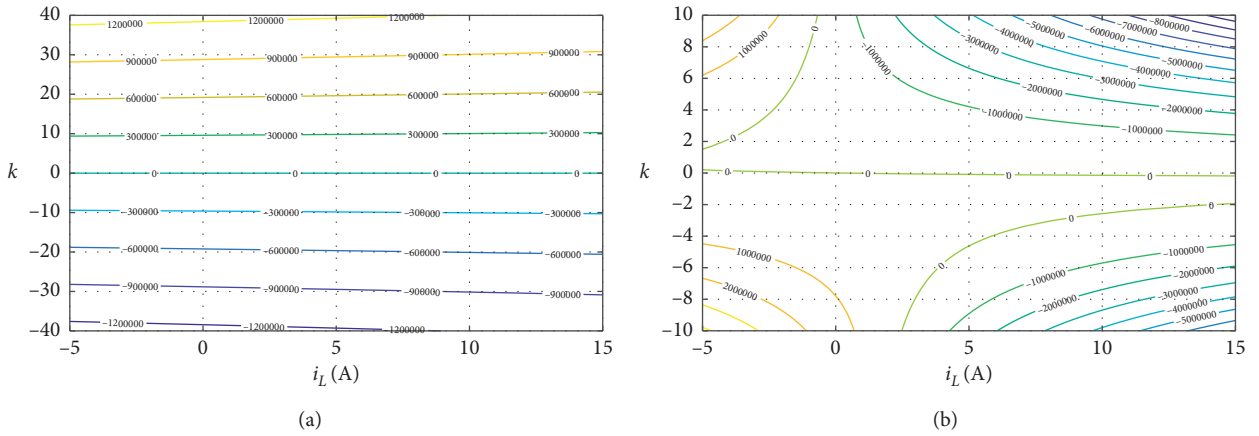

Figure 4: Contour plot for existence condition inequalities. (a) Contour plot for inequality 1. (b) Contour plot for inequality 2.

with respect to k and i_L for a sample boost converter with circuit 1 parameters given in Table 1.

According to (18), S_1' should be greater than zero. Figure 4 shows that there are no limitations when i_L and k are positive. According to (18), S_2' should be smaller than zero. For every positive value of k, there is a minimum value of i_L for S_2' to be positive. The zero level of the contour determines this limit.

4.4. Reaching Condition. The existence condition guarantees sliding and remaining on the surface when the state is near the defined sliding surface, but the reaching condition guarantees that when the initial state is far from the sliding surface, it will reach the surface in finite time. The reaching condition of states to the surface is simply proved according to the time response of the converter in (11). From this equation, it can be concluded that as long as the eigenvalues of state matrices have negative real parts, the trajectory will converge to x_e for different subsystems:

$$\lim_{t\longrightarrow\infty} x(t) = x_{e_q} = \begin{cases} -A_1^{-1}b_1, & q = 1, \\ -A_2^{-1}b_2, & q = 2. \end{cases} \tag{24}$$

According to the switching rule in (15), the switch will be ON when $S < 0$ and OFF when $S > 0$; then, all trajectories will reach the sliding surface if the following conditions are met:

$$\begin{cases} \text{if } (x_{e_1}) > 0, \\ \text{if } (x_{e_2}) < 0. \end{cases} \tag{25}$$

This reaching condition can be properly interpreted in the phase portrait.

It can be proved that if the equilibrium point of one subsystem is located in the opposite region where the other subsystem works, then the reaching condition is satisfied. Figure 5 depicts a representation of this condition.

4.5. Sliding Dynamics. The equivalent dynamics of the system on the sliding surface will steer the state toward the desired state. Suppose that the system state is on the surface

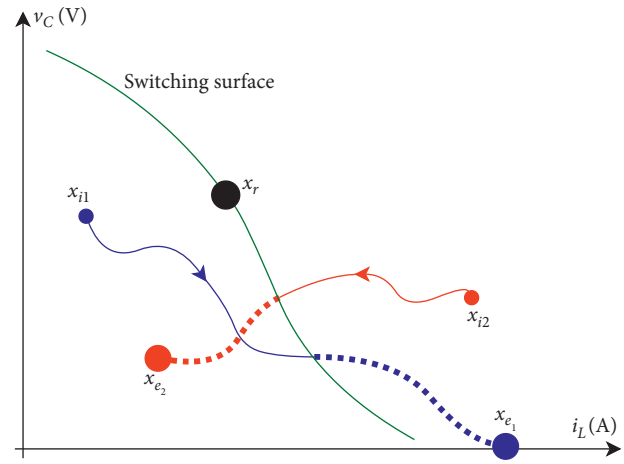

Figure 5: Reaching condition of the SMC.

and slides on it, then the equivalent time derivative of S should be zero. From (19), we have

$$\begin{cases} S = \begin{bmatrix} k \\ 1 \end{bmatrix}^T (x - x_r) = m^T (x - x_r) = 0, \\ S_{e_q}' = [S_1', S_2'] \cdot r = m^T [f_1(x), f_2(x)] \cdot r = 0, \end{cases} \tag{26}$$

where m is the slope and r is a vector which plays a role similar to the duty cycle in PWM switching. A candidate solution to r will be defined as

$$r = \begin{bmatrix} -f_2 \\ f_1^T \end{bmatrix} m. \tag{27}$$

Sliding dynamics of the system is the dynamics of the state variable on the sliding surface. A measure of the state variable position on the sliding surface is defined by

$$D = \begin{bmatrix} -1 \\ k \end{bmatrix}^T (x - x_r) = n^T (x - x_r), \tag{28}$$

where n is a vector perpendicular to m and parallel to the surface. Therefore, the sliding dynamics will be the time derivative of this defined position:

$$D' = n^T [f_1(x), f_2(x)] r = n^T [f_1(x), f_2(x)] \begin{bmatrix} -f_2^T \\ f_1^T \end{bmatrix} m,$$
$$D' = \|m\|^2 \times \det[f_1(x), f_2(x)]. \tag{29}$$

But the above determinant is positive below the conic section of possible equilibrium points and negative above it. Since R is positive above x_r and above the conic section for positive k values, we have

$$D \times D' < 0, \quad \text{for all } x \text{ on } S = 0. \tag{30}$$

Therefore, the system state converges to x_r for any initial state.

4.6. Simulation of Tuned SMC. The performance of the tuned conventional SMC is simulated using the MATLAB software. Figure 6 shows the state trajectory and waveforms for the sample boost converter. This SMC reduces the transient current overshoot and can be simply implemented. However, voltage and current waveforms show that the time response is slow compared with the time-optimal control. Another drawback of this controller is the output voltage dependent on circuit parameters.

5. Proximate Constrained Time-Optimal SMC

5.1. Principle of Operation. Although the tuned conventional SMC takes care of the inductor current limit and has an acceptable response speed, the conventional controller may not be the fastest controller with this determined constraint. To achieve the fastest possible response, it is necessary to hold the converter's current in its maximum allowed value during the transient. This idea leads to a constrained TOC. But TOC has a high computational complexity again. In this section, a modified piecewise linear switching surface will be defined. This modified surface keeps the inductor current high enough in the transient state, and then the system state converges to its desired value in a suitable manner near the time-optimal trajectory. This method keeps the response speed as fast as possible and the steady-state voltage oscillations as low as possible.

5.2. Piecewise Sliding Surface. The new piecewise switching surface of the proposed SMC is defined as

$$S = \begin{cases} k(i_L - i_{\text{ref}}) + (v_C - v_{\text{ref}}), & i_L < i_{\max}, \\ (i_L - i_{\max}), & i_L \geq i_{\max}, \end{cases} \tag{31}$$

where $i_{\max}$ represents the maximum allowed inductor current. In (31), k is a positive factor but has small values to keep the time response fast.

5.3. Existence Condition. The existence condition for the first part of the new sliding surface is similar to that of the conventional SMC, but for the second part corresponding to a constant-current region, it is investigated as follows. The derivative of the surface function for the constant-current region is

$$S'_{CC1}\big|_{S=0} > 0 \wedge S'_{CC2}\big|_{S=0} < 0, \tag{32}$$

where

$$S'_{CC} = \begin{cases} S'_{CC1} = \begin{bmatrix} 1 \\ 0 \end{bmatrix}^T f_1(x), & S < 0, \\ S'_{CC2} = \begin{bmatrix} 1 \\ 0 \end{bmatrix}^T f_2(x), & S > 0. \end{cases} \tag{33}$$

Condition $S = 0$ in (32) makes i_L and v_C dependent so that the inequalities are functions of i_L and k. Therefore, the inequalities can be expanded as follows.

Inequality 3

$$S'_{CC1} = \frac{-r_L i_L}{L} + \frac{v_s}{L} > 0, \quad i_L = \underset{\rightarrow}{i}_{\max} i_{\max} < \frac{v_s}{r_L}. \tag{34}$$

Since $r_L \ll 1$, this inequality is true in most practical cases. The second inequality can be derived as follows.

Inequality 4

$$S'_2 = \frac{-i_L}{L}\left(r_L + \frac{R r_C}{R + r_C}\right) + \frac{-R v_C}{L(R + r_C)} + \frac{v_s}{L} < 0, \tag{35}$$

$$v_C > v_s\left(\frac{R + r_C}{R}\right) - i_{\max}\left(\frac{r_L(R + r_C)}{R} + r_C\right). \tag{36}$$

Assume that $r_o \gg r_C$, then (36) becomes

$$v_C > v_s - i_{\max}(r_L + r_C) r_L, \quad r_C \ll \underset{\longrightarrow}{1} \; v_C > v_s. \tag{37}$$

This inequality guarantees that if the initial voltage is greater than the source voltage, the output current can slide on the constant-current switching surface, and it will not exceed it. But when the initial voltage is much lower than the source voltage, the converter may exceed the maximum current limits. It can be seen in the phase portrait of the vector fields that this is a natural property of the boost converter and does not belong to the proposed controller. To overcome this overcurrent problem for small initial voltages, it is suitable to start the converter with a startup higher resistance load and then switch to the full load.

5.4. Reaching Condition. Reaching condition can be proved similarly to the conventional SMC case. Since the equilibrium point of subsystem 1 is in the opposite side of the switching surface, any trajectory starting from the subsystem 1 side will hit the sliding surface. This is true for trajectories starting from the subsystem 2 side, similarly.

5.5. Sliding Dynamics. Sliding dynamics for the first part of the surface is exactly the same as that of the conventional SMC. For the constant-current part, the following definitions lead to a similar proof:

$$m = [1, 0]^T,$$
$$n = [0, 1]^T, \tag{38}$$
$$D = n^T(x - x_s),$$

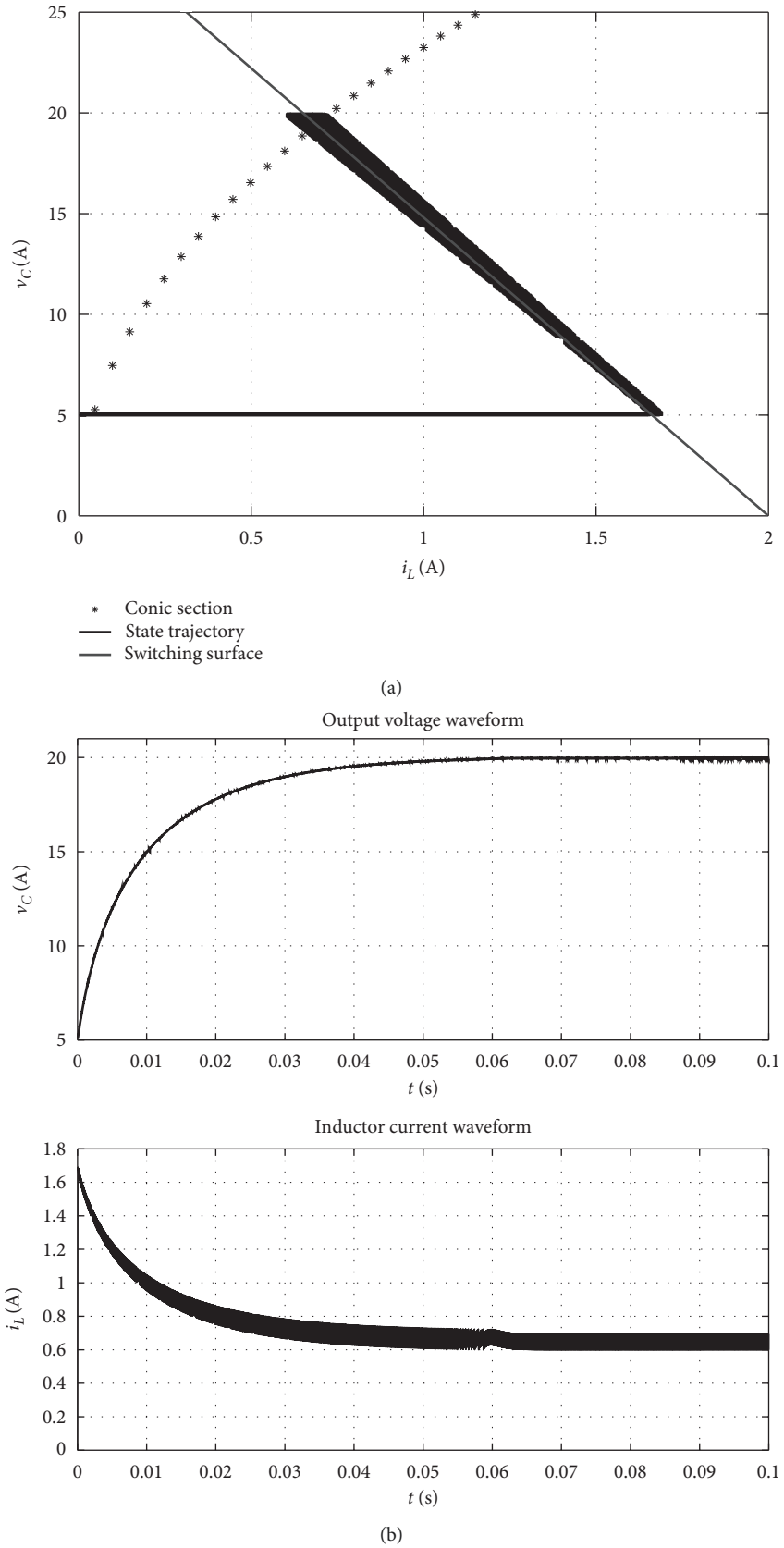

Figure 6: (a) State trajectory and (b) waveforms of the tuned SMC.

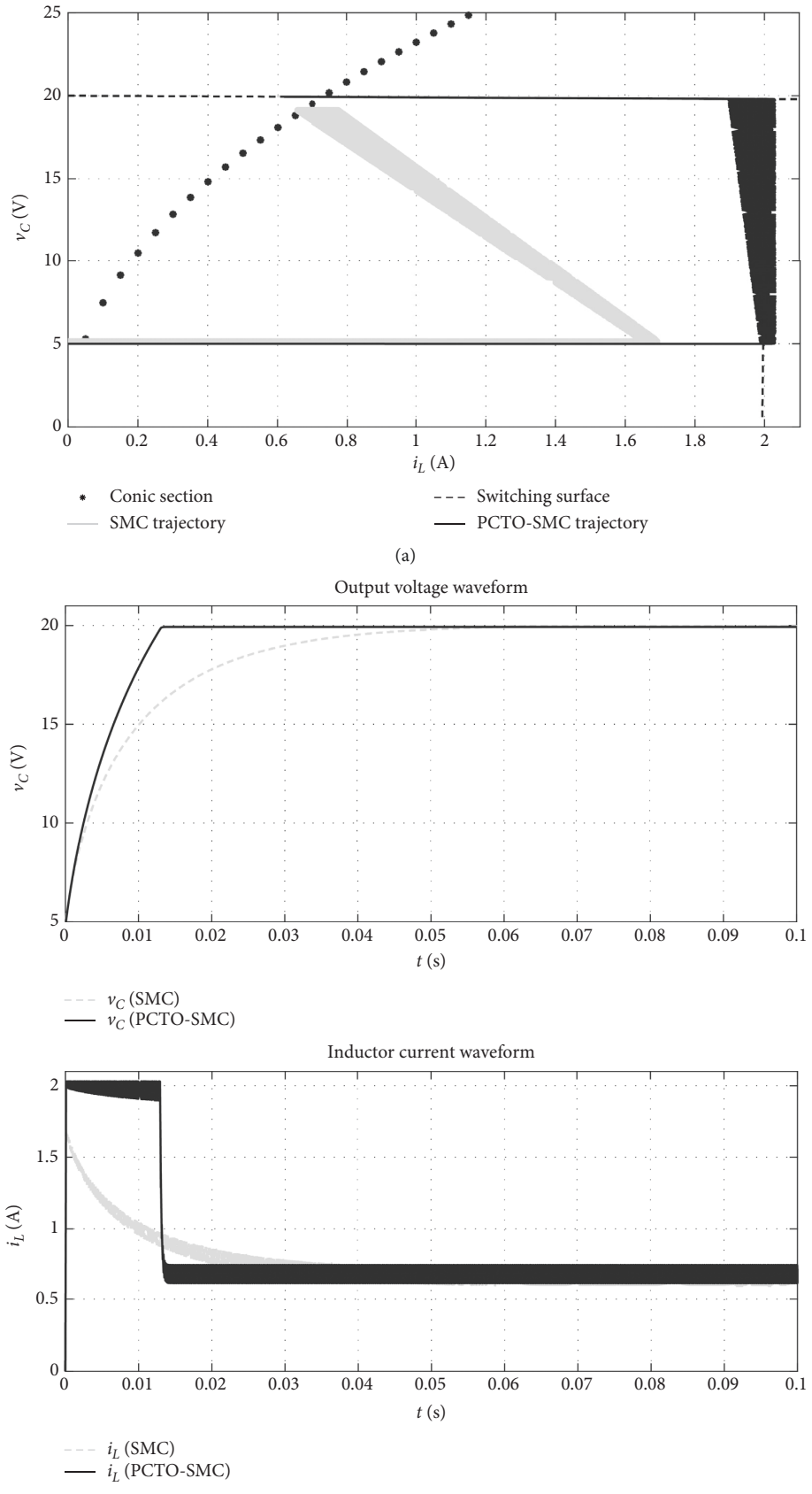

Figure 7: (a) State trajectory and (b) waveforms of the PCTO-SMC.

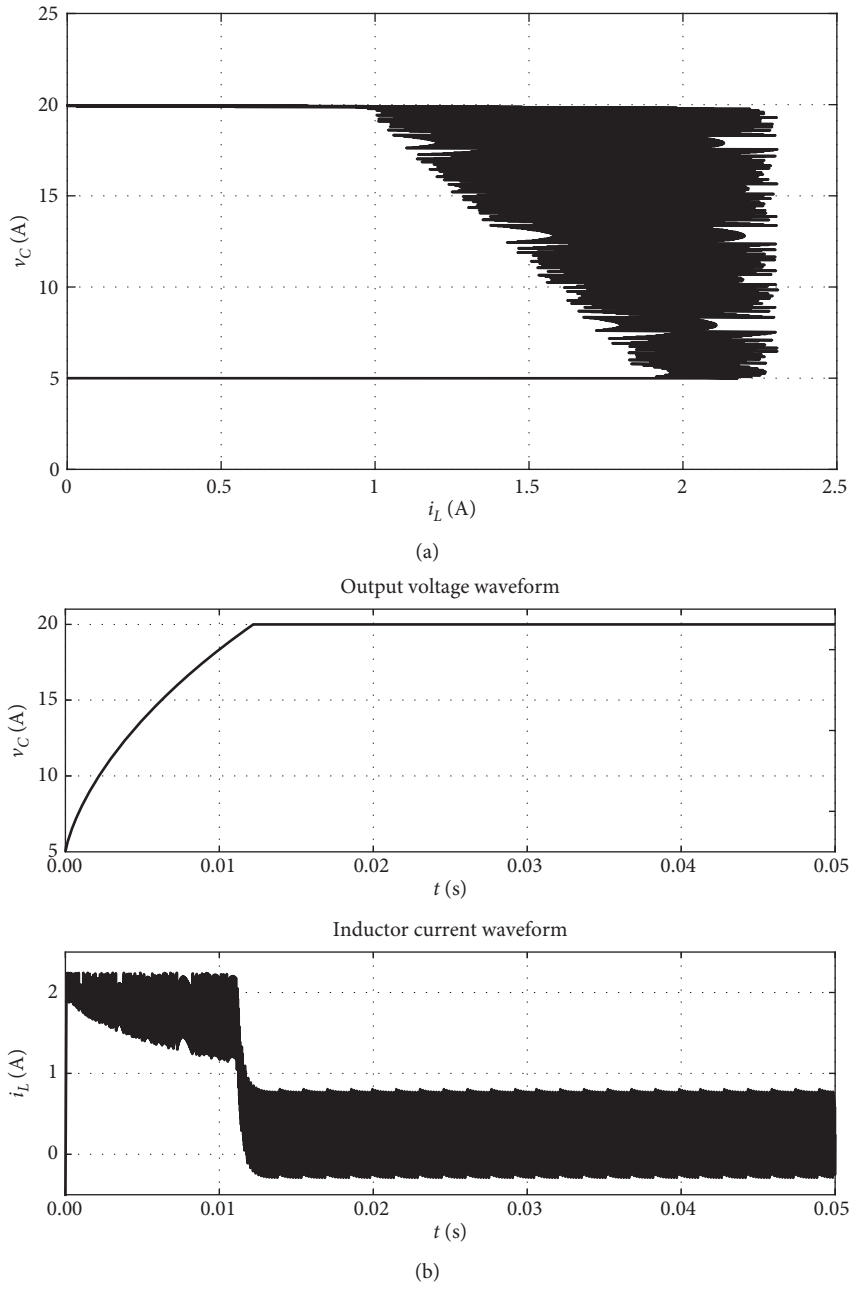

Figure 8: (a) State trajectory and (b) waveform simulations of the PCTO-SMC ($T_s = 10\,\mu$s).

where x_s is the intersection of the constant-current line with the conic section. Using these definitions, it can be shown that if the system state reaches the constant-current surface, it will slide up to the corner of the two switching surfaces and then toward the desired state.

5.6. Simulation of the Proposed Controller. Simulation results of the proposed PCTO-SMC for circuit 2 parameters given in Table 1 are shown in Figure 7. These simulation results show that the proposed controller has a faster time response and a voltage rise time of about 17 ms which is a better result as compared to the conventional SMC with about 40 ms rise time.

5.7. Controller Parameters. The switching surface of (31) can be simply implemented by DSP-based controllers. The controller parameters include i_{ref}, v_{ref}, $i_{\max}$, and k. The k parameter determines the slope of the near-optimal part of the switching surface. In practice, since $r_l, r_c \ll 1$, the existence condition, (20) and (22), can be simplified as $k > k_{\min}$ where $k_{\min} = L \cdot v_{\text{ref}}/(R \cdot C \cdot v_s)$ is the slope of the time-optimal switching surface and has a small positive value. For example,

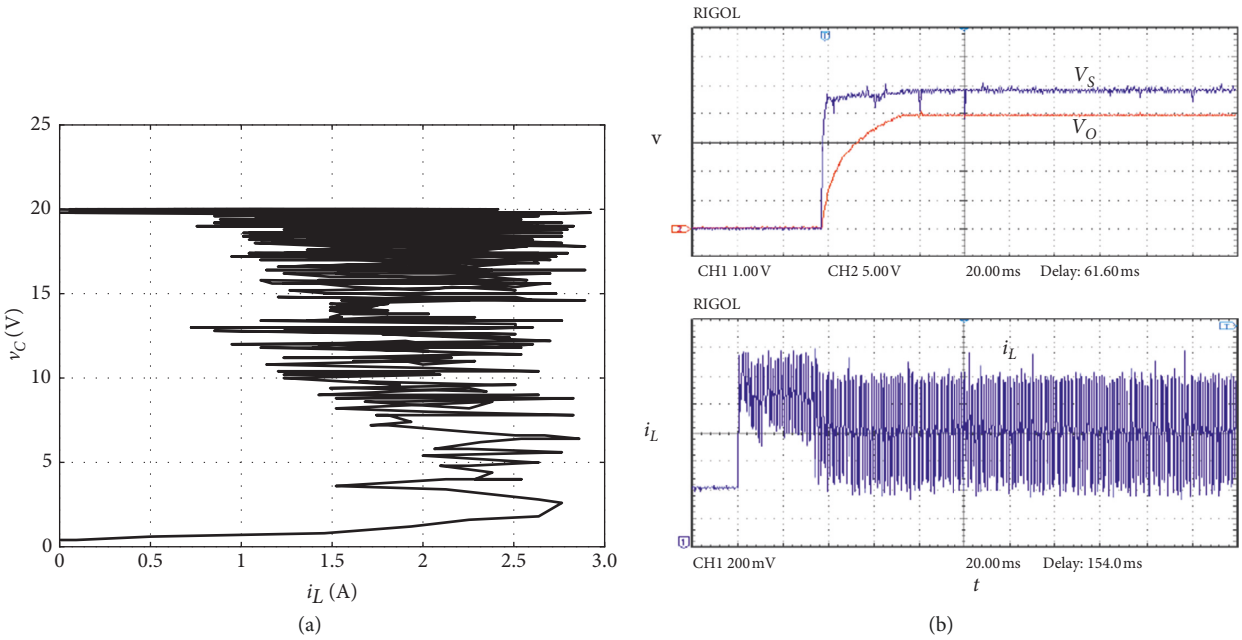

Figure 9: Experiment: (a) state trajectory; (b) waveforms.

for circuit 2 parameters given in Table 1, $k_{\min} = 0.007$. Hence, as long as k is near $k_{\min}$, the controller's response speed remains close to that of the time-optimal controller. On the contrary, when k is very close to $k_{\min}$, the controller has a marginal behavior in sliding existence and stability.

The v_{ref} parameter is the desired output voltage which is an input to the controller in DC-DC converters. The i_{ref} parameter is dependent on v_{ref} and can be approximated by $v_{\text{ref}} \approx v^2/(R \cdot v_s)$. However, in practice, because of low values of k, selecting $i_{\text{ref}} = 0$ in (31) gives rise to less than 0.1% error in the output voltage. Hence, the switching surface can be simplified by removing i_{ref} in (31).

6. Experimental Validation

6.1. State Trajectory and Startup. Simulation results in the previous sections show faster time response for the proximate constrained time-optimal SMC. But the other capabilities of this controller, which are proved in previous sections, are better illustrated in experimental results. The proposed controller's performance is validated in the laboratory using a prototype boost converter with the parameters of circuit 2 in Table 1. An eZdsp F2812 board is used to implement the controller.

Because of switching frequency limitations, the sample time of the eZdsp board is set to 10 μs. This sample time causes higher current fluctuations in the state trajectory and current waveforms. Therefore, for comparison with the experimental waveforms, simulation results with the practical sampling frequency will be compared here. Figure 8 shows the state trajectory and waveforms of the PCTO-SMC with 10 μs sample time and 5 V source voltage and 20 V desired output voltage starting from an initial voltage of 5 V. It is shown in these simulations that, with larger sample time, the converter's current ripple will be higher. The corresponding experimental results for voltage and current waveforms are shown in Figure 9. The state trajectory is exported to the personal computer using the Oscilloscope software tool and then plotted in Figure 9. It is depicted in this figure that the experimental validation has similar results to the previous simulations. The reminder of this section shows the experimental results related to changes in load, source voltage, and output voltage reference.

6.2. Response to Load, Source Voltage, and Reference Voltage Changes. Several experimental tests were carried out to investigate the controller's response to the load resistance, source voltage, and reference output changes. Possible changes of load between $R = 112\,\Omega$ and $R = 56\,\Omega$ and between $R = 112\,\Omega$ and $R = 232\,\Omega$ have been tested. Figure 10 shows some of these results. Output voltage varies about 1% of its nominal voltage in response to load changes. Note that sensitivity to the load changes can be further reduced by tuning the switching surface slope k. Reducing the k parameter leads to smaller output voltage variations but more current fluctuations. Current fluctuations can be reduced again by increasing the switching speed (corresponding to shortening the sampling time). This is not possible in the present experimental setup.

Source voltage changes between 1.5 V, 3.3 V, 5 V, and 10 V have been tested. Figure 10(c) shows output voltage response when the source voltage changes from 10 V to 5 V. The results show less than 0.5% of nominal value changes in the output voltage. Several experimental tests for step changes in the reference voltage were also performed. Figure 10(d) shows output voltage and inductor current response to reference voltage changes between 10 V and 20 V. Experimental results show about 20 ms rise time and 40 ms fall time in the output voltage waveform.

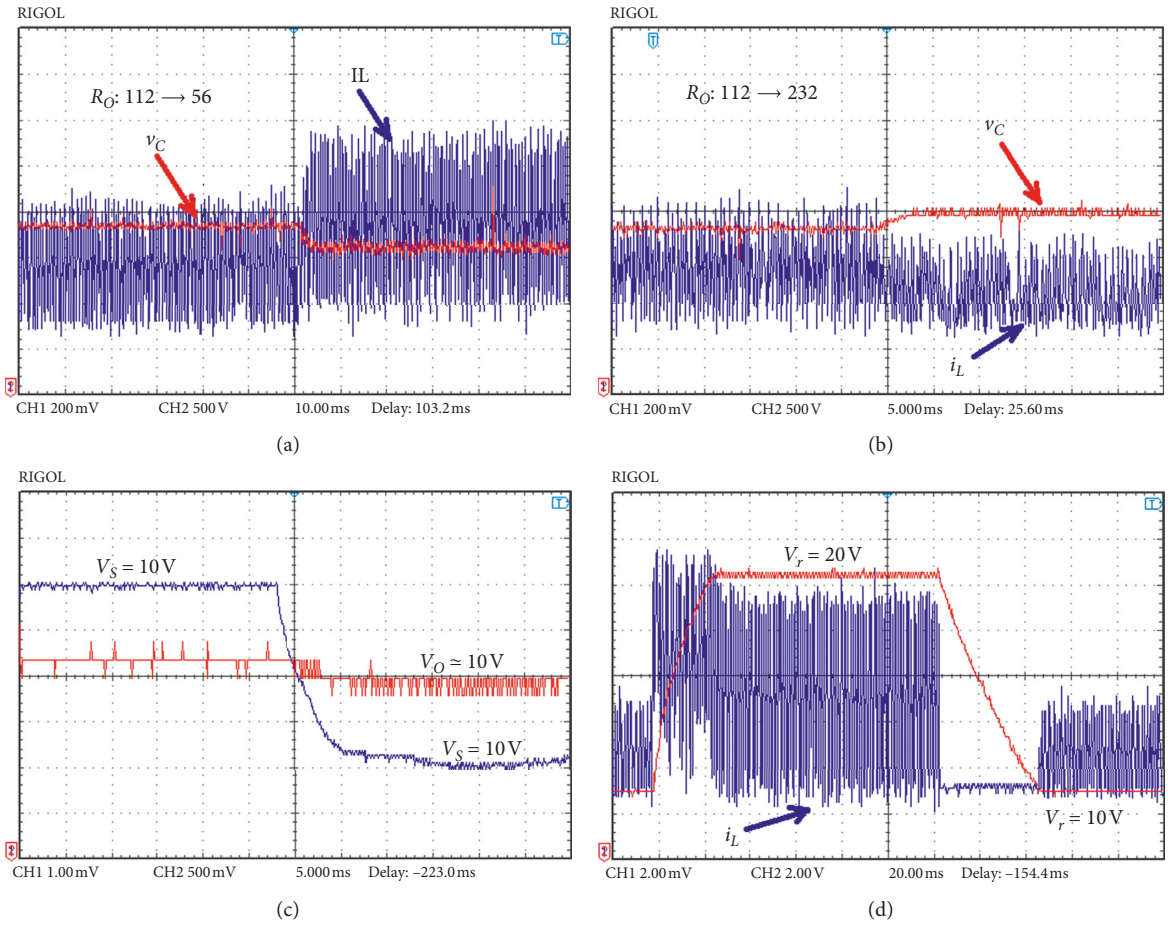

FIGURE 10: Experimental results of voltage and current response to load, source voltage, and reference voltage changes. (a) Response 1 to R_O change. (b) Response to V_S change. (c) Response 2 to R_O change. (d) Response to V_r change.

7. Conclusion

A hybrid switching system model of the boost converter and phase portrait geometric representation of the corresponding vector fields lead to better description of its behavior. Then, a new proximate constrained time-optimal sliding mode controller is proposed which directly controls the converter switch. This controller has faster response time compared to conventional SMC. The proposed method has a current limitation capability by designing a piecewise sliding surface to maintain the inductor current constraint. Experiment results show good response to changes in load resistance, source voltage, and output voltage reference. Limited current and low output variation in load and source variations are beneficial in many RE applications. Compared to the time-optimal control, the proposed controllers achieve much lower current peak and steady-state voltage fluctuations and also lower computational complexity.

Data Availability

The MATLAB file data used to support the findings of this study are available from the corresponding author upon request.

Conflicts of Interest

The authors declare that they have no conflicts of interest.

Acknowledgments

This paper was supported in part by the Shaanxi Provincial Special Support Program for Science and Technology Innovation Leader and in part by the Shaanxi Industrial Key Project (2018GY-165).

References

[1] J. M. Carrasco, L. G. Franquelo, J. T. Bialasiewicz et al., "Power-Electronic systems for the grid integration of renewable energy sources: a survey," *IEEE Transactions on Industrial Electronics*, vol. 53, no. 4, pp. 1002–1016, 2006.

[2] İ. Yazici and E. K. Yaylaci, "Fast and robust voltage control of DC–DC boost converter by using fast terminal sliding mode controller," *IET Power Electronics*, vol. 9, no. 1, pp. 120–125, 2016.

[3] R. D. Middlebrook and S. Cuk, "A general unified approach to modelling switching-converter power stages," in *Proceedings of the Power Electronics Specialists Conference*, Cleveland, OH, USA, 1976.

[4] T. A. F. Theunisse, J. Chai, R. G. Sanfelice, and W. P. M. H. Heemels, "Robust global stabilization of the DC-DC boost converter via hybrid control," *IEEE Transactions on Circuits and Systems I: Regular Papers*, vol. 62, no. 4, pp. 1052–1061, 2015.

[5] H. Molla-Ahmadian, F. Tahami, A. Karimpour, and N. Pariz, "Hybrid control of DC–DC series resonant converters: the direct piecewise affine approach Approach," *IEEE Transactions on Power Electronics*, vol. 30, no. 3, pp. 1714–1723, 2015.

[6] S. A. Evangelou and M. A. Rehman-Shaikh, "Hybrid electric vehicle fuel minimization by DC-DC converter dual-phase-shift control," *Control Engineering Practice*, vol. 64, pp. 44–60, 2017.

[7] H.-P. Ren, X. Guo, Y.-C. Zi, and J. Li, "Double loop control of boost converter based current switching controller and voltage compensator," in *Proceedings of 7th International Conference on Electronics, Computers and Artificial Intelligence (ECAI)*, pp. E11–E16, Bucharest, Romania, June, 2015.

[8] H.-P. Ren, M.-M. Zheng, and J. Li, "A simplified mixed logical dynamic model and model predictive control of boost converter with current reference compensator," in *Proceedings of the 2015 IEEE 24th International Symposium on Industrial Electronics (ISIE)*, pp. 61–65, Armação dos Búzios, Brazil, June, 2015.

[9] J. Li, T. Zheng, and H.-P. Ren, "Method of increasing the output voltage precision for switching control of power converter," Patent in China, No. 201210093047, 2014.

[10] C. Olalla, I. Queinnec, R. Leyva, and A. El Aroudi, "Robust optimal control of bilinear DC-DC converters," *Control Engineering Practice*, vol. 19, no. 7, pp. 688–699, 2011.

[11] J. Nazarzadeh and M. J. Jafarian, "Applying bilinear time-optimal control system in boost converters," *IET Power Electronics*, vol. 7, no. 4, pp. 850–860, 2014.

[12] M. Jafarian and J. Nazarzadeh, "Time-optimal sliding-mode control for multi-quadrant buck converters," *IET Power Electronics*, vol. 4, no. 1, pp. 143–150, 2014.

[13] E. Meyer, Z. Zhang, and Y.-F. Liu, "Digital charge balance controller to improve the loading/unloading transient response," *IEEE Transactions On Power Electronics*, vol. 27, no. 3, pp. 1314–1326, 2012.

[14] C. Olalla, I. Queinnec, R. Leyva, and A. El Aroudi, "Optimal state-feedback control of bilinear DC–DC converters with guaranteed regions of stability," *IEEE Transactions On Industrial Electronics*, vol. 59, no. 10, pp. 3868–3880, 2012.

[15] W. Feng, F. C. Lee, and P. Mattavelli, "Optimal trajectory control of LLC resonant converters for LED PWM dimming," *IEEE Transactions On Power Electronics*, vol. 29, no. 2, pp. 979–987, 2014.

[16] S. Kapat and P. T. Krein, "Improved time optimal control of a buck converter based on capacitor current," *IEEE Transactions On Power Electronics*, vol. 27, no. 3, pp. 1444–1454, 2012.

[17] L. Corradini, A. Babazadeh, A. Bjeleti´, and D. Maksimović, "Current-limited time-optimal response in digitally controlled DC–DC converters," *IEEE Transactions On Power Electronics*, vol. 25, no. 11, pp. 2869–2880, 2012.

[18] V. Utkin, "Variable structure systems with sliding modes," *IEEE Transaction on Automatic Control*, vol. 22, no. 2, pp. 212–222, 1977.

[19] R. A. DeCarlo, S. H. Zak, and G. P. Mathews, "Variable structure control of nonlinear multivariable systems: a tutorial," *Proceedings of the IEEE*, vol. 76, no. 3, pp. 212–232, 1988.

[20] Y. Shtessel, C. Edwards, L. Fridman, and A. Levant, *Sliding Mode Control and Observation*, Springer, Berlin, Germany, 2014.

[21] S.-N. Mirebrahimi, F. Merrikh-Bayat, and A. Taheri, "Voltage-mode robust controller design for DC–DC boost converter at the presence of wide load and input voltage variations based on finite-state-machine model," *IET Power Electronics*, vol. 11, no. 5, pp. 866–875, 2018.

[22] A. Ghasemian and A. Taheri, "Constrained near-time-optimal sliding-mode control of boost converters based on switched affine model analysis," *IEEE Transactions on Industrial Electronics*, vol. 65, no. 1, pp. 887–897, 2018.

[23] Q. Chen, S. Xie, M. Sun, and X. He, "Adaptive nonsingular fixed-time attitude stabilization of uncertain spacecraft," *IEEE Transactions on Aerospace and Electronic Systems*, vol. 54, no. 6, pp. 2937–2950, 2018.

[24] M. Tao, Q. Chen, X. He, and M. Sun, "Adaptive nonsingular fixed-time attitude stabilization of uncertain spacecraft," *International Journal of Robust and Nonlinear Control.*vol. 29, no. 12, pp. 4022–4040, 2019.

[25] L. Tao, Q. Chen, and Y. Nan, "Disturbance-observer based adaptive control for second-order nonlinear systems using chattering-free reaching law," *International Journal of Control, Automation and Systems*, vol. 17, no. 2, pp. 356–369, 2019.

Hindawi
Complexity
Volume 2019, Article ID 6235190, 15 pages
https://doi.org/10.1155/2019/6235190

Research Article

Convergence Time Calculation for Supertwisting Algorithm and Application for Nonaffine Nonlinear Systems

Jianhua Zhang[1,2] **Quanmin Zhu**[3] **and Yang Li**[1,2]

[1]*Hebei University of Science and Technology, Shijiazhuang, Hebei 050018, China*
[2]*Hebei Provincial Research Center for Technologies in Process Engineering Automation, Shijiazhuang, Hebei 050018, China*
[3]*Department of Engineering Design and Mathematics, University of the West of England, Coldharbour Lane, Bristol BS16 1QY, UK*

Correspondence should be addressed to Jianhua Zhang; jianhuazhang@aliyun.com

Received 25 July 2019; Revised 1 September 2019; Accepted 7 September 2019; Published 20 October 2019

Guest Editor: Chun Wei

In this study, an accurate convergence time of the supertwisting algorithm (STA) is proposed to build up a framework for nonaffine nonlinear systems' finite-time control. The convergence time of the STA is provided by calculating the solution of a differential equation instead of constructing Lyapunov function. Therefore, precise convergence time is presented instead of estimation of the upper bound of the algorithm's reaching time. Regardless of affine or nonaffine nonlinear systems, supertwisting control (STC) provides a general solution based on virtual control law skill ensuring the output of the systems converges to the origin point at exact time. Benchmark tests are simulated to demonstrate the effectiveness and efficiency of the algorithm.

1. Introduction

Sliding mode control (SMC) has become one of the most efficient techniques to control uncertain complex systems and engineering [1–3]. Theoretically, such controllers are able to compensate and match disturbances by confining the systems' trajectories in a properly chosen hypersurface (the so-called sliding manifold) [4–6] and, under the chosen surface, make the origin of the state space an asymptotically stable equilibrium point for the closed-loop systems [7–9]. Both the convergence to the sliding manifold and convergence to the origin are guaranteed in a finite time interval if the control action is large enough to counteract the effect of the uncertain terms and hypersurface is defined suitably [10–12].

STA is a well-known second-order sliding mode (SOSM) algorithm introduced in [13], and it is a possible solution for chattering reduction and widely used for control, observation, and robust exact differentiation. The reaching time estimation and the finite-time control method design are essentially complex problems with the sliding mode control systems' study [14–16]. Finite-time convergence and robustness of the STA have been proved with some methods, such as geometrical methods [17], homogeneity properties of the algorithm [18], and Lyapunov methods [19]. The Lyapunov stability theorem and Lyapunov function provide a means of determining stability without explicit knowledge on system solutions [20–22]. Traditionally, quadratic Lyapunov functions are constructed to analyze and control design of nonlinear dynamic systems [23–25]. It should be noted that there also exist some other formats of Lyapunov functions, such as integral Lyapunov function, barrier Lyapunov function, and vector Lyapunov function. Such attempts have enhanced Lyapunov function applications in control system design. A strict Lyapunov function is provided to ascertain finite-time convergence, and it would provide an estimate of the convergence time, as well as the robustness of the finite-time or ultimate boundedness for the STA [19, 26]. By a detailed analysis of the Lyapunov function in finite time, robust convergence for the STA is proved, and it is not possible to provide necessary and sufficient conditions to estimate the convergence time from it.

However, the form of the estimate of the convergence time contained arbitrary positive matrixes which are related by the algebraic Lyapunov equation (ALE), making it difficult to operate with it for applications or further developments [24, 27, 28]. For nonlinear systems, numerical

techniques (open solutions) have played a significant role in the controller design process [29–31]. As general solutions to the complicated nonlinear dynamic problem, the U model uses linear approaches to design nonlinear control [32, 33]. Specifically, it can be concluded that the applicable systems fall into classes of an increasing order of complexity: strict feedback, pure feedback, affine form, and nonaffine systems [34]. Nonaffine systems are difficult to control because of the complexity of the systems.

Motivated by the above observations, this paper presents accurate convergence time of the STA without and with perturbation and designs the nonaffine STA finite-time control. The main contributions are listed as follows:

(1) Accurate convergence time is proposed for the STA based on the analytical solution of the differential equation. The main advantages are that the output of the systems converges to the origin point at exact time and the exact time is determined by the designer before the controller is implemented.

(2) To overcome the main obstacle, the trajectory of the STA is analyzed by the analytical solution of the differential equation and LaSalle's invariance principle instead of Lyapunov stability theory used commonly in the traditional sliding mode control.

(3) Technically, for nonaffine nonlinear systems, sliding mode control based on the STA and backstepping achieves finite-time stabilization. The closed-loop control systems will achieve stability in finite time without violation of the constraint.

The rest of this study is organized as follows: In Section 2, the problem formulation and preliminaries are presented, which also contains some definitions and lemmas about the STA. They are presented to establish a basis for designing and analyzing the STA. In Section 3, accurate convergence time for finite-time convergence of the STA is developed by the parametric equation in different initial conditions. In Section 4, accurate convergence time is developed by the parametric equation in different initial conditions with perturbation. In Section 5, STA control is designed for nonaffine nonlinear systems based on the backstepping skill. The closed-loop systems' trajectory is analyzed, and the output can be obtained effectively by the finite-time algorithm. In Section 6, three simulated case studies are conducted to initially demonstrate the efficiency and effectiveness of the procedure. In Section 7, the conclusions are given to summarize the study.

2. System Description and Preliminaries

The STA can be written as

$$\begin{aligned} \dot{x}_1 &= -k_1 |x_1|^{1/2} \operatorname{sign}(x_1) + x_2, \\ \dot{x}_2 &= -k_2 \operatorname{sign}(x_1), \end{aligned} \tag{1}$$

where x_1 and x_2 are the scalar state variables: $x_1(0) = a$ and $x_2(0) = b$, and k_1 and k_2 are gains to be designed.

If $k_1 > 0$ and $k_2 > 0$, the states x_1 and x_2 of the system reach the origin in finite time T; therefore, the system undergoes finite-time convergence [19], using $\{x_1, x_2 \mid t, k_1, k_2, a, b\}$ to indicate STA (1).

Lemma 1 (see [35]). *For differential equation,*

$$y y'_x - y = Ax + B, \quad A \neq 0. \tag{2}$$

The solution is in the parametric form:

$$\begin{aligned} x &= C \exp\left(- \int \frac{\tau d\tau}{\tau^2 - \tau - A} \right) - \frac{B}{A}, \\ y &= C\tau \exp\left(- \int \frac{\tau d\tau}{\tau^2 - \tau - A} \right). \end{aligned} \tag{3}$$

More details about the solution of the parametric equation (3) are presented in Appendix A.

3. Finite-Time Convergence of STA

As mentioned, when $k_1 > 0$ and $k_2 > 0$, the accurate convergence time is considered. To show the trajectory of the STA, the analytic method is used to describe the system.

If the initial condition $x_1(0) = a$, then x_1 will reach the origin point in finite time at $x_1(t_{a0}) = 0$, where t_{a0} indicates the time of state when x_1 reaches the origin, and let $T_{a0} = \{t \mid 0 < t < t_{a0}\}$; if the initial condition $x_1(0) = 0$, then x_1 will reach the origin point in finite time at $x_1(t_{00}) = 0$, where t_{00} indicates the time of state when x_1 reaches the origin, and let $T_{00} = \{t \mid 0 < t < t_{00}\}$.

The main contribution are the following three facts:

Fact 1. For the STS (1), when $k_1 > 0, k_2 > 0$, and $A \geq -(1/4)$ hold, the initial conditions are $x_1(0) = a$ and $x_2(0) = b$; if $a \neq 0$ holds, the system state x_1 arrives at the zero point in finite time.

As shown in Figure 1, $x_1(0) = a, x_2(0) = b$, and $x_1(t_{a0}) = 0$ hold.

Fact 2. This is the most important fact; for the STS (1), when $k_1 > 0, k_2 > 0$, and $A \geq -(1/4)$ hold, the initial conditions are $x_1(0) = a$ and $x_2(0) = b$; if $a = 0$ holds, the system states x_1 and x_2 arrive at the zero point simultaneously.

As shown in Figure 2, the initial conditions $x_1(0) = 0$ and $x_2(0) = b$ hold, in period T_{00}; then at time t_{00}, $x_1(t_{00}) = 0$ and $x_2(t_{00}) = 0$ hold.

Fact 3. For the STS (1), when $k_1 > 0, k_2 > 0$, and $A \geq -1/4$ hold, the initial conditions are $x_1(0) = a$ and $x_2(0) = b$, and the system states x_1 and x_2 arrive at the zero point simultaneously.

As shown in Figure 3, the initial conditions $x_1(0) = a$ and $x_2(0) = b$ hold, and then system states change as in Figure 1 in period T_{a0}, where state x_1 converges to zero at time t_{a0}; after that, as in Figure 2, states x_1 and x_2 converge to zero in period T_{00} at time $t_{a0} + t_{00}$, where $x_1(t_{a0} + t_{00}) = 0$ and $x_2(t_{a0} + t_{00}) = 0$ hold.

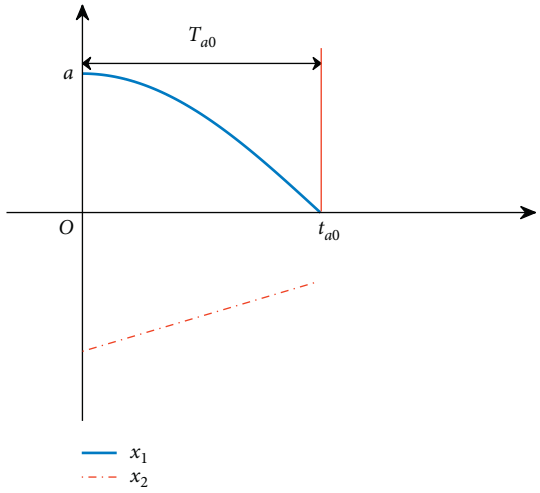

Figure 1: Trajectory of the STS with $a \neq 0$.

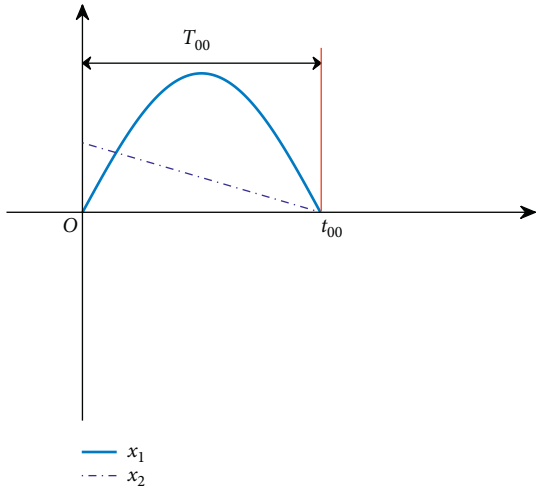

Figure 2: Trajectory of the STS with $a = 0$.

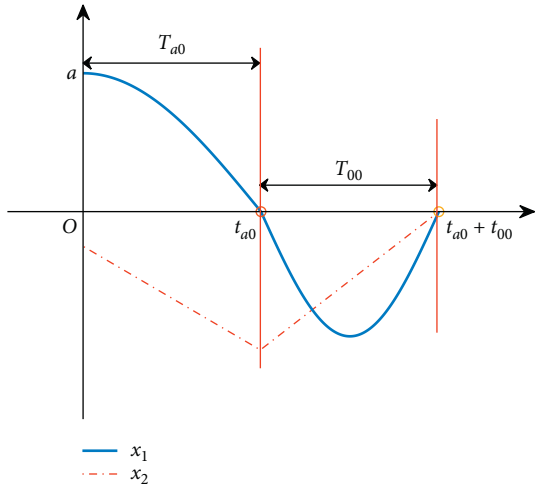

Figure 3: Trajectory of STS in the convergence procedure.

To prove the facts above, in $t \in T_{a0}$, let

$$y = -\frac{2}{k_1}|x_1|^{1/2}. \tag{4}$$

Its derivative on the trajectories of (B.2) and (B.6) can be obtained as follows:

$$y\dot{y} - y = At + B, \tag{5}$$

where

$$\begin{aligned} A &= -\frac{2k_2}{k_1^2}, \\ B &= \frac{2b}{k_1^2}\text{sign}\,(2\text{sign}\ (a) + \text{sign}\,(b)). \end{aligned} \tag{6}$$

The details about the parameters of equation (6) are presented in Appendix B.

Then, based on the parametric solution in Appendix A and general form of (5), define the solution in different situations by the parameter A and define the trajectory in different parameters and different initial conditions.

Case I. For the supertwisting system, when $(A = (-1/4))$ and $a \neq 0$, the trajectory is

$$\begin{cases} t\,(s) = Cs\exp\,(s) - \dfrac{B}{A}, \\ \\ y\,(s) = \dfrac{C}{2}\,(s+1)\exp\,(s), \end{cases} \tag{7}$$

where the parameter C is determined by initial conditions $s = s_0$, $t = 0$, and $y = a_1 = -(2/k_1)|a|^{1/2}$ as follows:

$$\begin{cases} 0 = Cs_0\exp\,(s_0) - \dfrac{B}{A}, \\ \\ a_1 = \dfrac{C}{2}\,(s_0+1)\exp\,(s_0). \end{cases} \tag{8}$$

Therefore, the initial parameter can be obtained as

$$s_0 = \frac{B}{2a_1A - B}, \tag{9}$$

and then the parameter C is obtained as

$$C = \frac{B}{As_0\exp\,(s_0)}. \tag{10}$$

Then, the whole trajectory can be obtained for the parametric equation, when $s_1 = -1$, $s_2 = -\infty$, and $y = 0$:

$$\begin{aligned} t\,(s_1) &= -C\exp\,(-1) - \frac{B}{A}, \\ t\,(s_2) &= -\frac{B}{A}. \end{aligned} \tag{11}$$

The state x_1 will arrive at the origin point at t_{a0} where the following conditions are met:

(a1) When $s_2 < s_1 < s_0$, $t_{a0} = t\,(s_1)$.

(a2) When $s_2 < s_0 < s_1$, if $(\partial t/\partial s) > 0$, $t_{a0} = t\,(s_1)$.

(a3) When $s_2 < s_0 < s_1$, if $(\partial t/\partial s) < 0$, $t_{a0} = t(s_2)$.

Therefore, for the STS at time t_{a0},

$$\begin{cases} x_1(t_{a0}) = 0, \\ x_2(t_{a0}) = -k_2 \text{sign}(a) t_{a0} + b. \end{cases} \tag{12}$$

Remark 1. If $t_{a0} = b/(k_2 \text{sign}(a))$ holds, $x_2(t_{a0}) = 0$ in (12), and the system converges to the origin point at time t_{a0}; if not, the system changes into another STA with initial conditions $a = 0$ and $b \neq 0$ because of the time invariance of the STA.

Case II. For the supertwisting system, when $A = -(1/4)$ and $a = 0$,

$$\begin{cases} t(s) = Cs \exp(s) - \dfrac{B}{A}, \\ \\ y(s) = \dfrac{C}{2}(s+1)\exp(s). \end{cases} \tag{13}$$

For the initial conditions, (13) becomes

$$\begin{cases} 0 = Cs_0 \exp(s_0) - \dfrac{B}{A}, \\ \\ 0 = \dfrac{C}{2}(s_0 + 1)\exp(s_0). \end{cases} \tag{14}$$

Therefore, the initial parameter can be obtained as

$$s_0 = -1, \tag{15}$$

and then the parameter C can be obtained as

$$C = -\frac{B}{A \exp(-1)}. \tag{16}$$

Then, for the parametric equation, when $s_1 = -\infty$ and $y = 0$,

$$t_{00} = -\frac{B}{A}. \tag{17}$$

According to system (7) and convergence time (17), the states of the system reach the origin point at the same time:

$$\begin{cases} x_1(t_{00}) = 0, \\ x_2(t_{00}) = 0. \end{cases} \tag{18}$$

Therefore, the system reaches finite-time stability.

Remark 2. If the initial condition $a = 0$, based on the convergence time t_{00}, both the states reach the origin point at the same time.

The supertwisting system is the time invariance system, and states reach finite-time stability when $k_1, k_2 > 0$; therefore, if the initial condition $a \neq 0$, based on the convergence time t_{a0}, by calculating both the states at t_{a0}, a new supertwisting system with the initial condition $a = 0$ can be obtained. Combining process initial conditions $a = 0$ and $a \neq 0$, the supertwisting system convergence time can be obtained.

Theorem 1. *The supertwisting system (1) reaches finite-time stability, if gains $k_1 > 0$ and $k_2 > 0$ satisfy $k_1^2 = 8k_2$ and system's initial condition $x_1(0) = a$ and $x_2(0) = b$; the finite time T satisfies $T = t_{a0} + t_{00}$, where t_{a0} is the time when state x_1 reaches the origin point in first time $x_2 = b_1 \neq 0$, and then time $t_{00} = -(B_1/A)$ is elapsed, when both states reach the origin point at the same time; therefore, the STS reaches the origin point at time T where the following conditions are met:*

(b1) When $s_2 < s_1 < s_0$, $t_{a0} = -C \exp(-1) - (B/A)$.

(b2) When $s_2 < s_0 < s_1$, if $C < 0$, $t_{a0} = -C \exp(-1) - (B/A)$.

(b3) When $s_2 < s_0 < s_1$, if $C > 0$, $t_{a0} = -(B/A)$.

Here,

$$\begin{aligned} A &= -\frac{2k_2}{k_1^2}, \\ B &= \frac{2b}{k_1^2}\text{sign}(2\text{sign}(a) + \text{sign}(b)), \\ B_1 &= \frac{2b_1}{k_1^2}\text{sign}(b_1), \\ b_1 &= -k_2 \text{sign}(a) t_{a0} + b, \\ s_0 &= \frac{-B}{(4/k_1)|a|^{1/2}A + B}, \\ s_1 &= -1, \\ s_2 &= -\infty, \\ C &= \frac{B}{As_0 \exp(s_0)}. \end{aligned} \tag{19}$$

Proof of Theorem 1. Based on the supertwisting system and gains k_1 and k_2, if $A = -(1/4)$, the parametric solution can be obtained in the form of (7); based on the initial condition, parameters s_0 and C can be obtained by (9) and (10), and then t_{a0} can be obtained in following different situations: (b1)–(b3).

When $t = t_{a0}$, the states of the system change as in (12), and then the system will elapse the period t_{00}, given by (17), which the parameter B satisfies:

$$B = \frac{2b_1}{k_1^2}\text{sign}(b_1), \tag{20}$$

where

$$b_1 = -k_2 \text{sign}(a) t_{a0} + b. \tag{21}$$

Then, at $t_{00} = -(B/A)$, the states of the supertwisting system reach the origin point:

$$\begin{cases} x_1(t_{00}) = 0, \\ x_2(t_{00}) = 0. \end{cases} \tag{22}$$

This completes the proof of Theorem 1. □

Case III. For the supertwisting system, when $A > -(1/4)$ and $a \neq 0$, the trajectory is

$$\begin{cases} t(s) = Cs(1+ps)^q - \dfrac{B}{A}, \\ \\ y(s) = C\left(1 + \dfrac{1}{2}s + \dfrac{p}{2}s\right)(1+ps)^q, \end{cases} \tag{23}$$

where $p = \sqrt{4A+1}$ $(0 < p < 1)$ and $q = (1/2p) - (1/2)$ $(q > 0)$.

$$\begin{cases} 0 = Cs_0(1+ps_0)^q - \dfrac{B}{A}, \\ \\ a_1 = C\left(1 + \dfrac{1}{2}s_0 + \dfrac{p}{2}s_0\right)(1+ps_0)^q. \end{cases} \tag{24}$$

Therefore,

$$s_0 = \frac{1}{(a_1 A/B) - (1/2) - (p/2)}, \tag{25}$$

$$C = \frac{B}{As_0(1+ps_0)^q}. \tag{26}$$

Then, the whole trajectory can be obtained for the parametric equation, when $s_1 = -(2/1+p), s_2 = -(1/p)$, $y = 0$, and $s_2 < s_1$:

$$t(s_1) = C\frac{((p/2) - (1/2))^q}{(-(p/2) - (1/2))^{q+1}} - \frac{B}{A}, \tag{27}$$

$$t(s_2) = -\frac{B}{A}. \tag{28}$$

The state x_1 will reach the origin point at t_{a0}, where the following conditions are met:

(c1) When $s_2 < s_1 < s_0$, $t_{a0} = t_1$.

(c2) When $s_0 < s_2 < s_1$, $t_{a0} = t_1$.

(c3) When $s_2 < s_0 < s_1$, if $\partial t/\partial s|_{s=s_0} > 0$, $t_{a0} = t(s_1)$.

(c4) When $s_2 < s_0 < s_1$, if $\partial t/\partial s|_{s=s_0} > 0$, $t_{a0} = t(s_2)$.

Then, the states of the supertwisting system at time t_{a0} become

$$\begin{cases} x_1(t_{a0}) = 0, \\ x_2(t_{a0}) = -k_2 \operatorname{sign}(a) t_{a0} + b. \end{cases} \tag{29}$$

Case IV. For the supertwisting system, when $A > -(1/4)$ and $a = 0$, the trajectory is

$$\begin{cases} t(s) = Cs(1+ps)^q - \dfrac{B}{A}, \\ \\ y(s) = C\left(1 + \dfrac{1}{2}s + \dfrac{p}{2}s\right)(1+ps)^q. \end{cases} \tag{30}$$

For the initial conditions $t = 0$ and $y = 0$,

$$\begin{cases} 0 = Cs_0(1+ps_0)^q - \dfrac{B}{A}, \\ \\ 0 = C\left(1 + \dfrac{1}{2}s_0 + \dfrac{p}{2}s_0\right)(1+ps_0)^q. \end{cases} \tag{31}$$

Therefore,

$$s_0 = -\frac{2}{1+p}, \tag{32}$$

$$C = \frac{B}{As_0(1+ps_0)^q}, \tag{33}$$

for the parametric equation

$$s_2 = -\frac{1}{p}. \tag{34}$$

Therefore, the convergence time is

$$t_{00} = -\frac{B}{A}, \tag{35}$$

$$\begin{cases} x_1(t_{00}) = 0, \\ x_2(t_{00}) = 0. \end{cases} \tag{36}$$

Therefore, the system reaches finite-time stability.

Theorem 2. *The supertwisting system (1), if gains $k_1 > 0$ and $k_2 > 0$ satisfy $k_1^2 > 8k_2$ and system initial conditions $x_1(0) = a$ and $x_2(0) = b$, reaches finite-time stability; the finite time T satisfies $T = t_{a0} + t_{00}$, where t_{a0} is the time when state x_1 reaches the origin point in first time $x_2 = b_1 \neq 0$, and then time $t_{00} = -(B_1/A)$ is elapsed, when both states reach the origin point at the same time.*

(d1) When $s_2 < s_1 < s_0$, $t_{a0} = t(s_1)$.

(d2) When $s_0 < s_2 < s_1$, $t_{a0} = t(s_1)$.

(d3) When $s_2 < s_0 < s_1$, if $\partial t/\partial s|_{s=s_0} > 0$, $t_{a0} = t(s_1)$.

(d4) When $s_2 < s_0 < s_1$, if $\partial t/\partial s|_{s=s_0} < 0$, $t_{a0} = t(s_2)$.

Here,

$$\begin{aligned} A &= -\frac{2k_2}{k_1^2}, \\ B &= \frac{2b}{k_1^2}\operatorname{sign}(2\operatorname{sign}(a) + \operatorname{sign}(b)), \\ B_1 &= \frac{2b_1}{k_1^2}\operatorname{sign}(b_1), \\ b_1 &= -k_2 \operatorname{sign}(a) t_{a0} + b. \end{aligned} \tag{37}$$

Proof of Theorem 2. Based on the supertwisting system and gains k_1 and k_2, if $A > -(1/4)$, the parametric solution can be obtained in the form of (23); based on the initial condition, parameters s_0 and C can be obtained by (25) and (26), and then t_{a0} can be obtained in following different situations: (d1)–(d4).

When $t = t_{a0}$, the states of the system change as in (29), and then the system will elapse period t_{00}, given by (35), which the parameter B satisfies:

$$B = \frac{2b_1}{k_1^2}\operatorname{sign}(b_1), \tag{38}$$

where

$$b_1 = -k_2\operatorname{sign}(a)t_{a0} + b. \tag{39}$$

Then, $t_{00} = -(B/A)$, and the states of the supertwisting system reach the origin point at time T:

$$\begin{cases} x_1(T) = 0, \\ x_2(T) = 0. \end{cases} \tag{40}$$

This completes the proof of Theorem 2. □

Remark 3. From Theorem 1 and Theorem 2, the convergence time is $T = t_{a0} + t_{00}$ and then k_1 and k_2 exist in both t_{a0} and t_{00} in the form of B/A; therefore, the gain parameter k_1 is not influenced by the convergence time.

4. Finite-Time Convergence of STA with Perturbation

The STA with perturbation can be written as

$$\begin{aligned} \dot{z}_1 &= -h_1|z_1|^{1/2}\operatorname{sign}(z_1) + z_2 + \rho_1(t), \\ \dot{z}_2 &= -h_2\operatorname{sign}(z_1) + \rho_2(t), \end{aligned} \tag{41}$$

where z_1 and z_2 are the scalar state variables, with initial conditions $z_1(0) = a$ and $z_2(0) = b$; $h_1, h_2 > 0$ are gains to be designed; and ρ_1 and ρ_2 are the perturbation terms. It is well known that the STA is robustly stable to perturbations globally bounded, and the equilibrium point is $(0 \;\; -\rho_1)$; therefore, suppose the perturbation terms of the system.

Assume that $|\rho_1| \le d_1$, $|\rho_2| \le d_2$, $|\dot{\rho}_1| \le d_3$, and $|\dot{\rho}_2| \le d_4$.

Let

$$\begin{aligned} x_1 &= z_1, \\ x_2 &= z_2 + \rho_1, \end{aligned} \tag{42}$$

then system (41) can be changed as

$$\begin{aligned} \dot{x}_1 &= -h_1|x_1|^{1/2}\operatorname{sign}(x_1) + x_2, \\ \dot{x}_2 &= -h_2\operatorname{sign}(x_1) + \rho_2 + \dot{\rho}_1. \end{aligned} \tag{43}$$

Next, let

$$\begin{aligned} k_1 &= h_1, \\ k_2 &= h_2 - (\rho_2 + \dot{\rho}_1)\operatorname{sign}(x_1), \end{aligned} \tag{44}$$

then the system can be written as

$$\begin{aligned} \dot{x}_1 &= -k_1|x_1|^{1/2}\operatorname{sign}(x_1) + x_2, \\ \dot{x}_2 &= -k_2\operatorname{sign}(x_1). \end{aligned} \tag{45}$$

The initial conditions are $x_1(0) = a$ and $\underline{b} < x_2(0) < \overline{b}$ and parameters are $k_1 = h_1$ and $\underline{k}_2 < k_2 < \overline{k}_2$, where $\underline{b} = b_z - d_1$, $\overline{b} = b_z + d_1$, $\underline{k}_2 = h_2 - d_2 - d_3$, *and* $\overline{k}_2 = h_2 + d_2 + d_3$.

Under the conditions on STA without perturbation in Theorem 2, the robust finite time is presented for STA with perturbation. Assume $A = -(2k_2/k_1^2) > -(1/4)$, then $h_1^2 > 8(h_2 - d_2 - d_3) > 0$. The finite time is presented by $T_P = t_{Pa0} + t_{P00}$, where t_{Pa0} and t_{P00} can be obtained by Theorem 2 in different initial conditions and gains.

In Theorem 2, t_{Pa0} is dependent on k_1, k_2, a, and b and is then calculated in different situations to get the maximum. To compare the influence of perturbation, three STAs are built:

$$\begin{cases} \text{STA 1: } \{x_1, x_2 | t, k_1, k_2, a, b\}, \\ \text{STA 2: } \{\overline{x}_1, \overline{x}_2 | t, k_1, \overline{k}_2, a, \overline{b}\}, \\ \text{STA 3: } \{\underline{x}_1, \underline{x}_2 | t, k_1, \underline{k}_2, a, \underline{b}\}. \end{cases} \tag{46}$$

Without loss of generality, assume that $a > 0$, in time phasing $t \in [0, t_{Pa0}]$.

For the perturbation of the STS at different gains k_2 and different initial conditions b, assume states x_2, $\underline{x}_2$, and $\overline{x}_2$ as $x_2 = b - k_2 t$, $\underline{x}_2 = \underline{b} - \overline{k}_2 t$, and $\overline{x}_2 = \overline{b} - \underline{k}_2 t$; therefore, $\underline{x}_2 \le x_2 \le \overline{x}_2$ and $\underline{x}_1 \le x_1 \le \overline{x}_1$ in $t \in [0, t_{Pa0}]$.

The convergence time satisfies $t_{a0}(k_1, \overline{k}_2, a, \underline{b}) \le t_{Pa0} \le t_{a0}(k_1, \underline{k}_2, a, \overline{b})$.

Assume that $a = 0$ and $b > 0$; to compare the influence of perturbation, three STAs are built:

$$\begin{cases} \text{STA 1: } \{x_1, x_2 | t, k_1, k_2, a, b\}, \\ \text{STA 2: } \{\overline{x}_1, \overline{x}_2 | t, k_1, \overline{k}_2, a, b\}, \\ \text{STA 3: } \{\underline{x}_1, \underline{x}_2 | t, k_1, \underline{k}_2, a, b\}. \end{cases} \tag{47}$$

Choose a sliding mode surface as $s = c_1 x_1 + c_2 x_2$, $\overline{s} = c_1 \overline{x}_1 + c_2 \overline{x}_2$, and $\underline{s} = c_1 \underline{x}_1 + c_2 \underline{x}_2$, where $c_1 > 0$ and $c_2 > 0$; therefore,

$$\begin{aligned} \dot{s} &= c_1 \dot{x}_1 + c_2 \dot{x}_2 \\ &= -c_1 k_1 |x_1|^{1/2}\operatorname{sign}(x_1) + c_1 x_2 - c_2 k_2 \operatorname{sign}(x_1) \\ &= -c_1 k_1 |x_1|^{1/2} + c_1 b - c_1 k_2 t - c_2 k_2, \end{aligned} \tag{48}$$

because of

$$\begin{aligned} -c_1 k_1 |x_1|^{1/2} + c_1 b - c_1 \overline{k}_2 t - c_2 \overline{k}_2 \le \dot{s} \le -c_1 k_1 |x_1|^{1/2} + c_1 b \\ - c_1 \underline{k}_2 t - c_2 \underline{k}_2. \end{aligned} \tag{49}$$

Therefore,

$$\dot{\bar{s}} \le \dot{s} \le \dot{\underline{s}}. \tag{50}$$

Because trajectories $\bar{x}_1, \bar{x}_2, \underline{x}_1, \underline{x}_2, \bar{s}$, and $\underline{s}$ converge to origin in finite time, the trajectory s reaches origin in finite time. Parameters c_1 and c_2 are arbitrary positive constants; therefore, $s = 0$ could be equivalent to $x_1 = 0$ and $x_2 = 0$. The convergence time satisfies

$$t_{a0}\left(k_1, \bar{k}_2, a, b\right) \le t_{P00} \le t_{a0}\left(k_1, \underline{k}_2, a, b\right). \tag{51}$$

Theorem 3. *For the supertwisting algorithm with perturbation (41), if $h_1, h_2 > 0$ and $h_1^2 > 8(h_2 - d_2 - d_3) > 0$ hold, the system converges to the origin point in finite time, and the maximum convergence time is $T_P = t_{Pa0} + t_{P00}$, where $t_{Pa0} = t_{a0}(k_1, \underline{k}_2, a, \bar{b})$ and $t_{P00} = \max\left\{|\bar{b}|, |\underline{b} - \bar{k}_2 t_{Pa0}|\right\}/\underline{k}_2$.*

Proof of Theorem 3. For STA with perturbation, when the initial condition $a \neq 0$, in the first stage, the state x_1 would arrive at the origin point in finite time $t_{Pa0} = t_{a0}(k_1, \underline{k}_2, a, \bar{b})$, and then when the system is in the second stage, both states x_1 and x_2 arrive at the origin point in finite time:

$$t_{P00} = \frac{\max\left\{|\bar{b}|, \left|\underline{b} - \bar{k}_2 t_{Pa0}\right|\right\}}{\underline{k}_2}. \tag{52}$$

Then, the maximum finite time is presented as $T_P = t_{Pa0} + t_{P00}$. □

5. STC for Nonaffine Systems

To illustrate the STA, nonlinear system STC is proposed for the nonaffine system:

$$\dot{y} = f(y, u). \tag{53}$$

Using the coordinate transform,

$$x_1 = y - y_d. \tag{54}$$

The virtual control law is

$$\alpha = -k_1 \left|x_1\right|^{1/2} \operatorname{sign}(z_1) + u - f(y, u) + \dot{y}_d. \tag{55}$$

Then,

$$\dot{x}_1 = -k_1 \left|x_1\right|^{1/2} \operatorname{sign}(x_1) + x_2, \tag{56}$$

where

$$x_2 = u - \alpha. \tag{57}$$

Choose the ideal control law

$$v = -k_2 \operatorname{sign}(x_1) + \dot{\alpha}, \tag{58}$$

then

$$\dot{x}_2 = -k_2 \operatorname{sign}(x_1). \tag{59}$$

Therefore, the system satisfies Theorem 1 and Theorem 2 by choosing the gain parameters k_1 and k_2.

To overcome the nonaffinity, the virtual control and backstepping skill are used. They are extremely important to ensure the successful design of the proposed STC.

6. Simulation

Several simulated examples were selected to conduct bench tests of the STA and STC. Example 1–Example 6 were testing simple STA, and the purpose of testing these examples was to investigate whether the convergence time is solved from the parametric equation. Examples 7–10 were designed for the test of STC for nonaffine nonlinear systems and demonstrated the superiority of STC and convergence time of the STA.

Example 1. Consider the STS given by (1), with $k_1 = 1$, $k_2 = 1/8$, $a = 2$, and $b = -1$ in Case I; based on (9) and (10), we can get $s_0 = -0.5858$ and $C = -24.5332$, respectively, and then we can get $t_{a0} = 1.0253$; therefore, the state x_1 reaches the zero point at time 1.0253.

Example 2. Consider the STS given by (1), with $k_1 = 1$, $k_2 = 1/8$, $a = 0$, and $b = -1.1282$ in Case II; based on (16) and (17), we can get $s_0 = -1$ and $C = -(B/A \exp(-1))$, respectively, and then we can get $t_{00} = 9.0256$; therefore, the states x_1 and x_2 reach the zero point at time 9.0256.

Example 3. Consider the STS given by (1), with $k_1 = 3$, $k_2 = 1$, $a = 3$, and $b = -3$ in Case III; based on (25) and (26), we can get $s_0 = -0.9510$ and $C = -4.6188$, respectively, and then we can get $t_{a0} = 0.4641$; therefore, the state x_1 reaches the zero point at time 0.4641.

Example 4. Consider the STS given by (1), with $k_1 = 3$, $k_2 = 1$, $a = 0$, and $b = -3.4641$ in Case IV; based on (32) and (33), we can get $s_0 = -(2/1 + p)$ and $C = (B/As_0(1 + ps_0)^q)$, respectively, and then we can get $t_{00} = 3.4641$; therefore, the states x_1 and x_2 reach the origin point at time 3.4641.

Example 5. Consider the supertwisting system given by

$$\begin{aligned} \dot{x}_1 &= -\left|x_1\right|^{1/2} \operatorname{sign}(x_1) + x_2, \\ \dot{x}_2 &= -\frac{1}{8} \operatorname{sign}(x_1), \end{aligned} \tag{60}$$

with $k_1 = 1, k_2 = 1/8$, and $A = -(1/4)$ and initial conditions $x_1(0) = 2$ and $x_2(0) = -1$.

Based on Theorem 1, the system (60) reaches finite-time stability and calculates the time from parametric equation (7) step by step. Firstly, the initial parameter $s_0 = -0.5858$ is calculated from (9) and $C = -24.5332$ from (10) because $s_2 < s_1 < s_0$ holds; therefore, $t_{a0} = t(s_1)$ and $t(s_1)$ can be obtained from (11) as $t_{a0} = 1.0253$ and $x_2(t_{a0}) = -1.1282$ in Figure 4. Secondly, $t_{00} = 9.0256$ is calculated from (17) in Figure 5. Finally, the reaching time $t = t_{a0} + t_{00} = 10.0509$ in Figure 6.

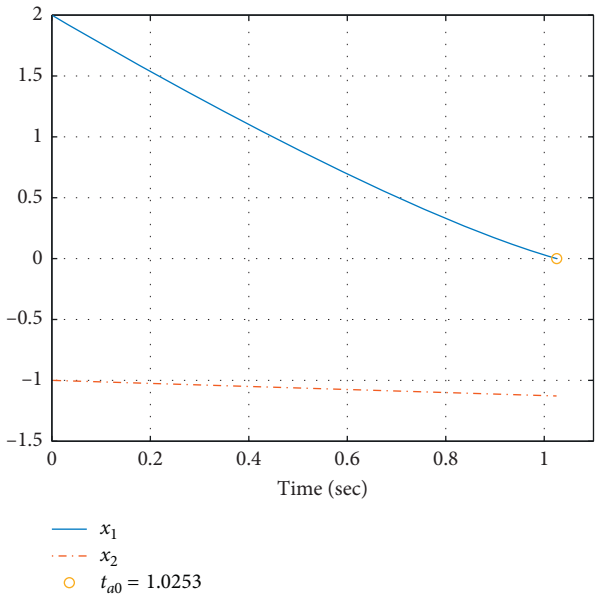

Figure 4: Finite-time convergence to the origin point with the nonzero initial condition of the state ($A = (-1/4)$).

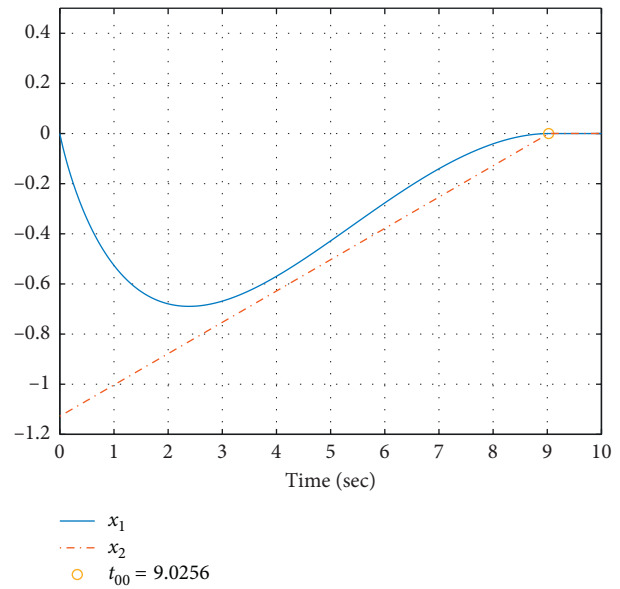

Figure 5: Finite-time convergence with the zero initial condition of the state ($A = (-1/4)$).

Example 6. Consider the supertwisting system given by

$$\begin{aligned} \dot{x}_1 &= -3\left|x_1\right|^{1/2}\operatorname{sign}(x_1) + x_2, \\ \dot{x}_2 &= -\operatorname{sign}(x_1), \end{aligned} \tag{61}$$

with $k_1 = 3, k_2 = 1$, and $A = -(2/9)$ and initial conditions $x_1(0) = 3$ and $x_2(0) = -3$.

Firstly, the initial parameter $s_0 = -0.9510$ is calculated from (25) and $C = -4.6188$ from (26) because $s_1 = -1.5$, $s_2 = -3$, and $s_2 < s_1 < s_0$ hold; therefore, $t_{a0} = t(s_1)$ and $t(s_1)$ can be obtained from (27) as $t_{a0} = 0.4641$ and $x_2(t_{a0}) = -3.4641$ in Figure 7. Secondly, $t_{00} = 3.4641$ is calculated from (35) in Figure 8. Finally, the reaching time $t = t_{a0} + t_{00} = 3.9282$ in Figure 9.

Example 7. Consider the STA with perturbation as given by (45), as $k_1 = 4, 0.5 \le k_2 \le 1.5, a = 3$, and $-5 \le b \le -1$:

$$\text{STA 1:} \begin{cases} \dot{x}_1 = -4\left|x_1\right|^{1/2}\operatorname{sign}(x_1) + x_2, \\ \dot{x}_2 = -\operatorname{sign}(x_1) + 0.3\cos(t) + 0.2\cos(0.1t), \\ x_1(0) = 3, \\ x_2(0) = -3, \end{cases}$$

$$\text{STA 2:} \begin{cases} \dot{\overline{x}}_1 = -4\left|\overline{x}_1\right|^{1/2}\operatorname{sign}(\overline{x}_1) + \overline{x}_2, \\ \dot{\overline{x}}_2 = -0.5\operatorname{sign}(\overline{x}_1), \\ \overline{x}_1(0) = 3, \\ \overline{x}_2(0) = -1, \end{cases}$$

$$\text{STA 3:} \begin{cases} \dot{\underline{x}}_1 = -4\left|x_1\right|^{1/2}\operatorname{sign}(\underline{x}_1) + \underline{x}_2, \\ \dot{\underline{x}}_2 = -1.5\operatorname{sign}(\underline{x}_1), \\ \underline{x}_1(0) = 3, \\ \underline{x}_2(0) = -5. \end{cases} \tag{62}$$

In Figure 10, states of three STAs are presented to indicate stability in finite time, and convergence time is $t_{a0} = 0.4099$, $\overline{t}_{a0} = 0.5816$, and $\underline{t}_{a0} = 0.3135$, respectively. The trajectory indicates states x_1, $\overline{x}_1$, and $\underline{x}_1$ with the same initial condition reach zero at different time because of different x_2, $\overline{x}_2$, and $\underline{x}_2$. The trajectories x_1 and x_2 are in between $\underline{x}_1$ and $\overline{x}_1$ and between $\underline{x}_2$ and $\overline{x}_2$, respectively. State $\overline{x}_1$ is the last state that reaches zero; therefore, the maximum convergence time $\overline{t}_{a0} = 0.5816$. In addition, the maximum of the state $|x_2|$ is $|\underline{x}_2(\overline{t}_{a0})| = 5.8723$ and absolutely necessary to estimate finite time t_{00} in the next step.

Example 8. Consider the STA with perturbation as given by (45), as $k_1 = 4, 0.5 \le k_2 \le 1.5, a = 0$, and $b = -5.8723$:

$$\text{STA 1:} \begin{cases} \dot{x}_1 = -4\left|x_1\right|^{1/2}\operatorname{sign}(x_1) + x_2, \\ \dot{x}_2 = -\operatorname{sign}(x_1) + 0.3\cos(t) + 0.2\cos(0.1t), \\ x_1(0) = 0, \\ x_2(0) = -5.8723, \end{cases}$$

$$\text{STA 2:} \begin{cases} \dot{\overline{x}}_1 = -4\left|\overline{x}_1\right|^{1/2}\operatorname{sign}(\overline{x}_1) + \overline{x}_2, \\ \dot{\overline{x}}_2 = -0.5\operatorname{sign}(\overline{x}_1), \\ \overline{x}_1(0) = 0, \\ \overline{x}_2(0) = -5.8723, \end{cases}$$

$$\text{STA 3:} \begin{cases} \dot{\underline{x}}_1 = -4\left|x_1\right|^{1/2}\operatorname{sign}(\underline{x}_1) + \underline{x}_2, \\ \dot{\underline{x}}_2 = -1.5\operatorname{sign}(\underline{x}_1), \\ \underline{x}_1(0) = 0, \\ \underline{x}_2(0) = -5.8723. \end{cases} \tag{63}$$

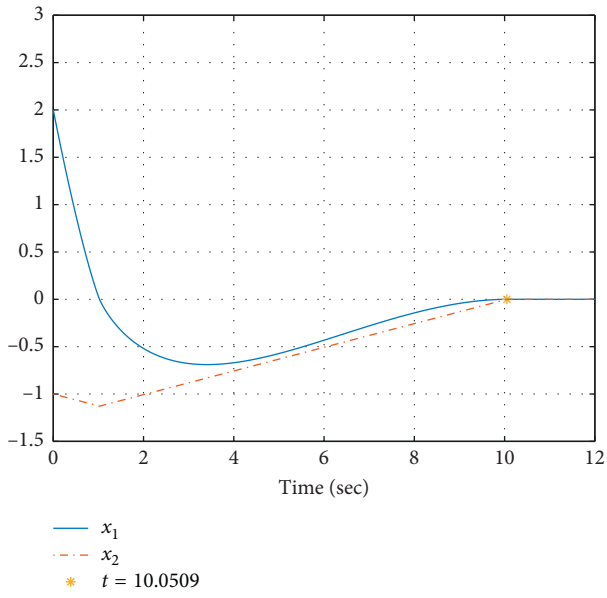

Figure 6: Finite-time convergence ($A = -(1/4)$).

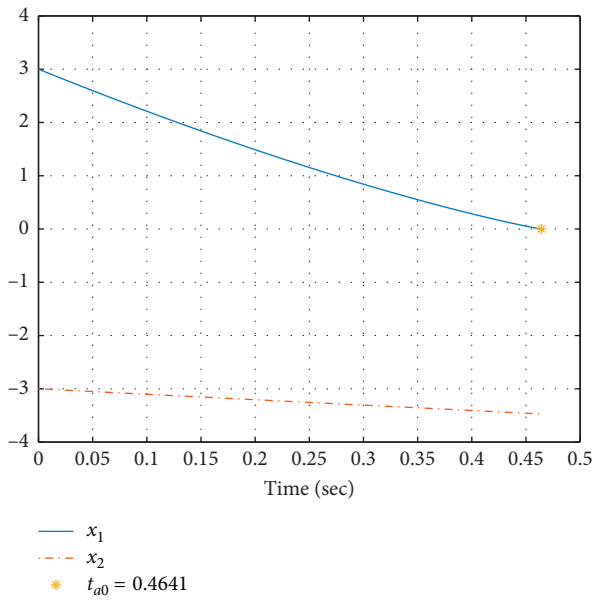

Figure 7: Finite-time convergence to the origin point with the nonzero initial condition of the state ($A = (-2/9)$).

In Figure 11, states of three STAs are presented to indicate stability in finite time, and convergence time is $t_{00} = 5.6589$, $\overline{t}_{00} = 11.7447$, and $\underline{t}_{00} = 3.9149$, respectively. The trajectories x_1, x_2, and s are in between $\underline{x}_1$ and $\overline{x}_1$, $\underline{x}_2$ and $\overline{x}_2$, and $\underline{s}$ and $\overline{s}$, respectively. State $\overline{x}_1$ is the last state that reaches zero; therefore, the maximum convergence time $\overline{t}_{00} = 11.7447$. In addition, states of the sliding mode surface indicate the state s is in between $\underline{s}$ and $\overline{s}$, providing evidence that $\overline{t}_{00}$ is the maximum convergence time.

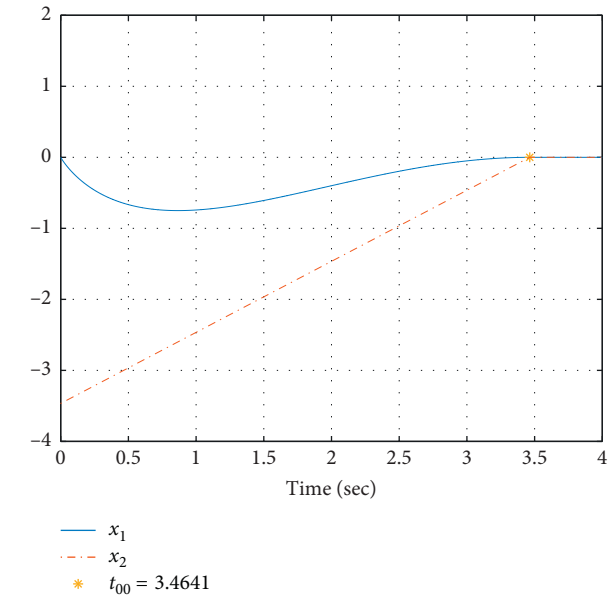

Figure 8: Finite-time convergence with the zero initial condition of the state ($A = (-2/9)$).

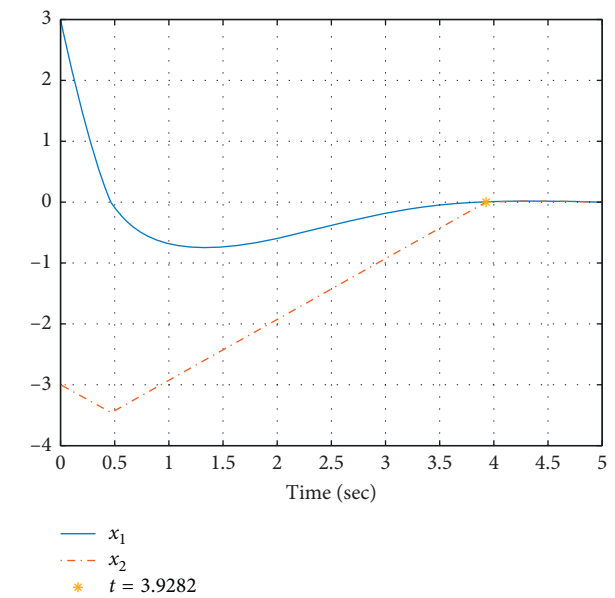

Figure 9: Finite-time convergence ($A = -(2/9)$).

Example 9. Consider the supertwisting system with perturbation given by

$$\begin{aligned} \dot{z}_1 &= -h_1 |z_1|^{1/2} \operatorname{sign}(z_1) + z_2 + \rho_1(t), \\ \dot{z}_2 &= -h_2 \operatorname{sign}(z_1) + \rho_2(t), \end{aligned} \tag{64}$$

where z_1 and z_2 are the scalar state variables, with initial conditions $z_1(0) = 3$ and $z_2(0) = -3$; $h_1 = 4$ and $h_2 = 1$ are gains; and $\rho_1(t) = 2\sin(0.1t)$ and $\rho_2(t) = 0.3\cos(t)$ are perturbation terms. Therefore, the system (64) changes as

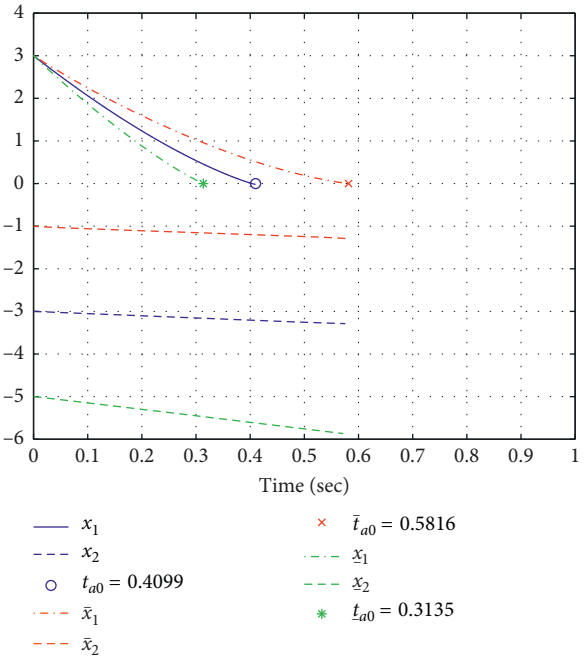

Figure 10: Finite-time convergence of the output with perturbation.

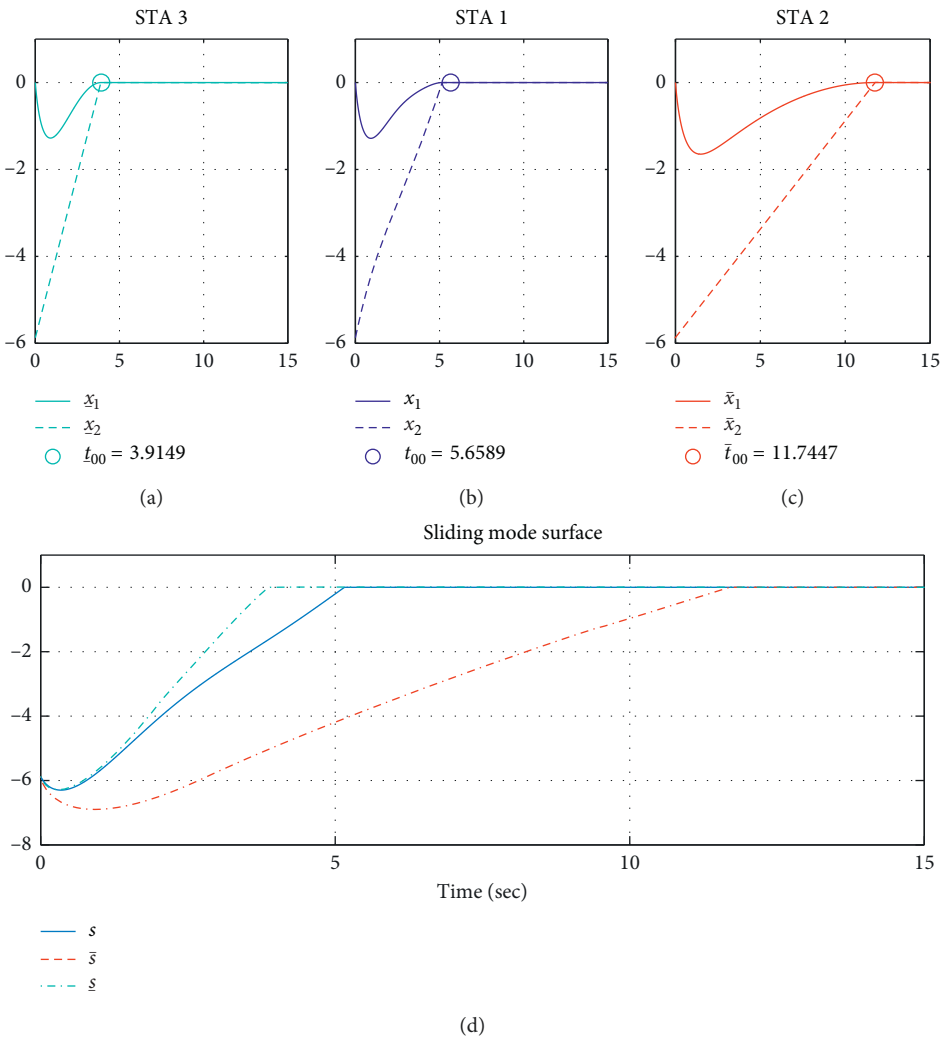

Figure 11: Finite-time convergence of the output and sliding mode surface.

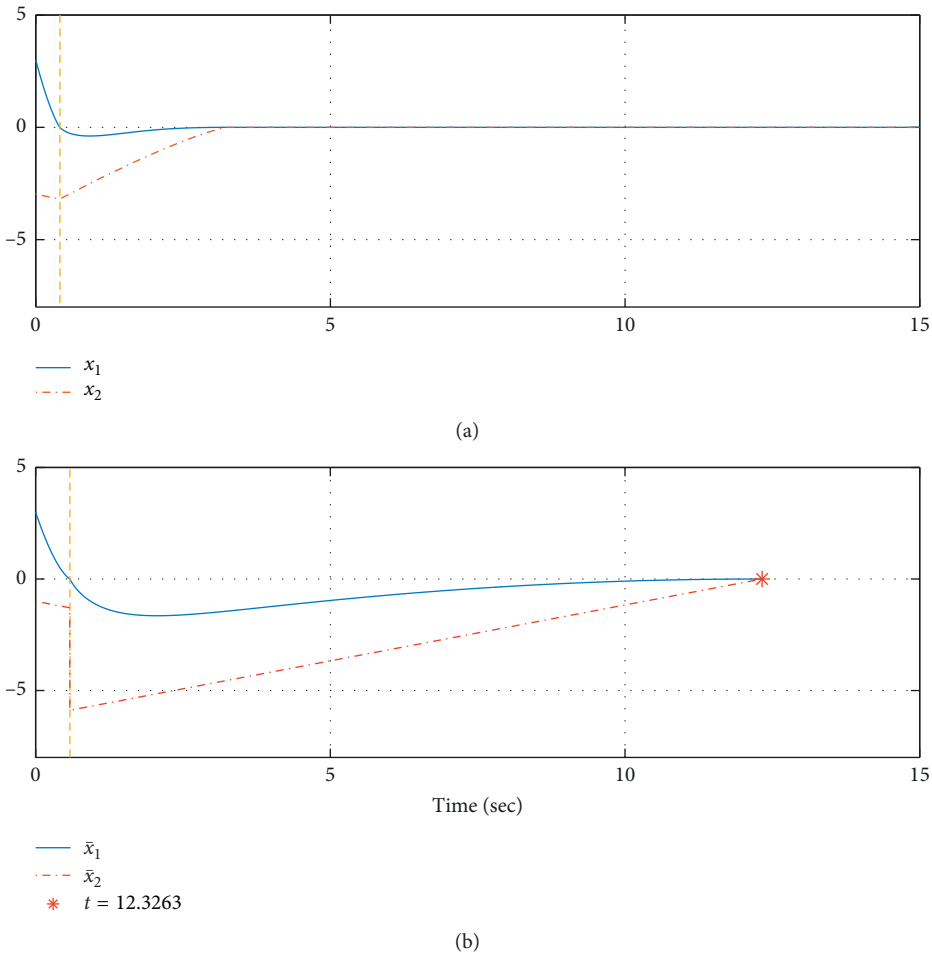

Figure 12: Finite-time convergence of the output and maximum stage.

$$\begin{aligned}\dot{x}_1 &= -h_1\left|x_1\right|^{1/2}\operatorname{sign}\left(x_1\right) + x_2,\\ \dot{x}_2 &= -h_2\operatorname{sign}\left(x_1\right) + \rho_2 + \dot{\rho}_1,\end{aligned} \tag{65}$$

where $x_1 = z_1$ and $x_2 = z_2 + \rho_1$; therefore, parameters are $k_1 = 4$ and $0.5 \le k_2 \le 1.5$, and initial conditions are $a = 3$ and $-5 \le b \le -1$; based on Theorem 3, the convergence time can be obtained.

The whole convergence process can be split into three stages. Firstly, the state x_1 from initial condition $x_1(0)$ reaches zero in finite time t_{pa0}, and at this time, $x_2(t_{pa0}) \neq 0$. Secondly, both states x_1 and x_2 reach zero at the same time and elapse time t_{p00} in this stage. Finally, after last two stages, the states x_1 and x_2 would stay at zero.

From Figure 12, it can be seen that, in the first stage, state x_1 from the initial condition reaches zero in finite time as in Figure 10 for Example 7, and the maximum convergence time $t_{a0} = 0.5816$ is calculated, and in this stage, the maximum of state $|x_2|$ is $|x_2(t_{a0})| = 5.8723$. Therefore, in the next stage, the initial condition is $x_2(0) = -5.8723$, such as in Figure 11 for Example 8, and then the maximum convergence time $t_{00} = 11.7447$ is calculated. Finally, the total finite convergence time $t = 12.3263$; therefore, the system converges to zero after 12.3263.

Example 10. Consider a nonaffine nonlinear system

$$\dot{y} = y + y^3 + 2u + \sin(u), \tag{66}$$

where y and u are the output and input, respectively, and the reference output is taken as y_d. The control objective is to design the STC for the system such that the output follows the given reference signal y_d in finite time.

Choose states $x_1 = y - y_d$ and $x_2 = u - \alpha$ with virtual control where

$$\begin{aligned}\alpha &= -3\left|x_1\right|^{1/2}\operatorname{sign}\left(x_1\right) + y_d - y - y^3 - u - \sin(u),\\ v &= -\operatorname{sign}\left(x_1\right) + \dot{\alpha}.\end{aligned} \tag{67}$$

The states satisfy the STA condition $A = -(2/9)$ and initial conditions $x_1(0) = 3$ and $x_2(0) = -3$. Therefore, the states x_1 and x_2 satisfy the condition in Figure 9 and output and reference output in Figure 10.

It can be observed that, for the nonaffine system, the closed-loop system has been controlled in finite time effectively in Figures 13–15, and time can be calculated and designed by control gain and initial condition.

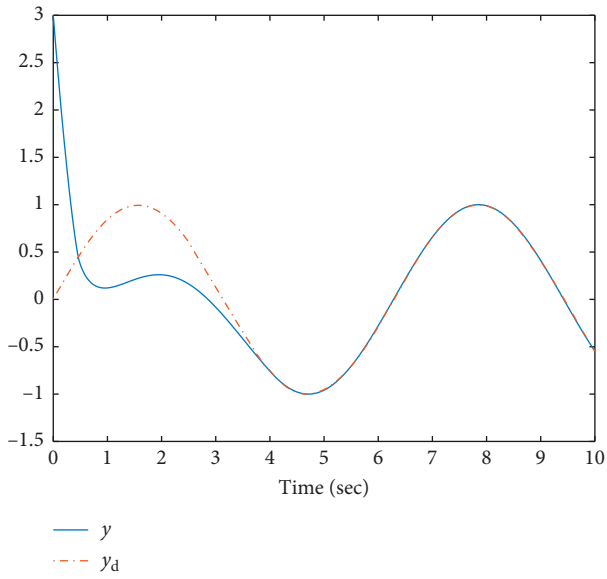

Figure 13: Finite-time convergence of the output and reference signal in control.

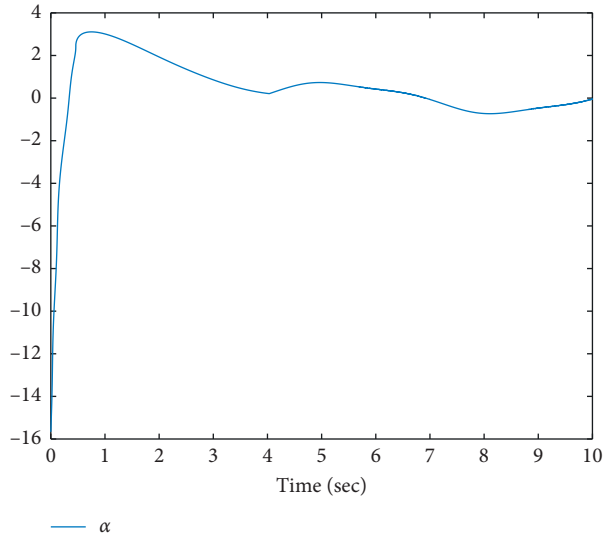

Figure 14: State of virtual control.

7. Conclusion

A method to calculate the accurate convergence time of the STA has been provided, and an STC method for nonaffine nonlinear systems based on the STA is given. The trajectory of the STA is solved in the form of the parametric equation, and reaching time is calculated accurately. The result indicated the gain parameter k_1 is not influenced by the convergence time. For the application of the STA, STC is designed to solve the nonaffine systems' control problem by backstepping skill.

Furthermore, after a certain prefixed gain and initial conditions, the reaching time of the STA is also useful to design STC. In the future, there still exist some problems to face with, such as $A < -(1/4)$ in the STA and higher order twisting algorithm.

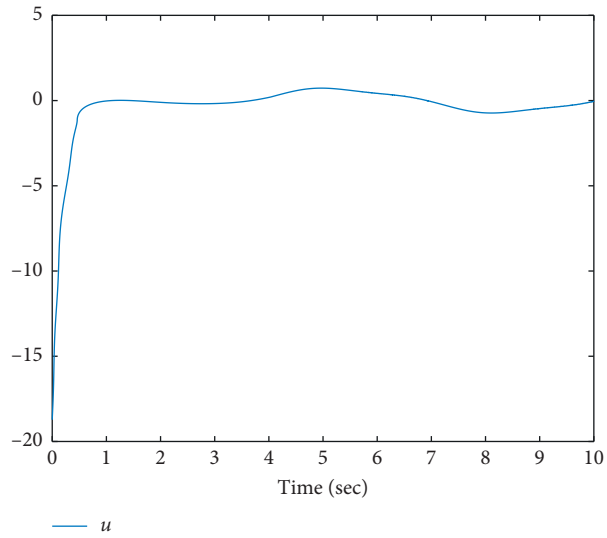

Figure 15: State of the controller.

Appendix

A. Parameter Solution

Base on Lemma 1, the following solution can be obtained:

$$\begin{cases} t = Cf(\tau) - \dfrac{B}{A}, \\ \\ y = C\tau f(\tau), \end{cases} \tag{A.1}$$

where $f(\tau) = \exp(-\int \tau\, d\tau/(\tau^2 - \tau - A))$; calculating the integral $\int \tau\, d\tau/(\tau^2 - \tau - A)$, we get

$$\int \frac{\tau}{\tau^2 - \tau - A} d\tau = \frac{1}{2}\ln\left|\tau^2 - \tau - A\right| + \frac{1}{2}\int \frac{1}{\tau^2 - \tau - A} d\tau, \tag{A.2}$$

and then calculating the integral $\int 1/(\tau^2 - \tau - A)d\tau$, we get

$$\int \frac{1}{\tau^2-\tau-A}dx=\begin{cases}-\dfrac{1}{\tau-(1/2)}+C_3, & \left(A=-\dfrac{1}{4}\right),\\[2ex] \dfrac{1}{\sqrt{4A+1}}\ln\left|\dfrac{2\tau-1-\sqrt{4A+1}}{2\tau-1+\sqrt{4A+1}}\right|+C_3, & \left(A>-\dfrac{1}{4}\right),\\[2ex] \dfrac{2}{\sqrt{-4A-1}}\arctan\left(\dfrac{2\tau-1}{\sqrt{-4A-1}}\right)+C_3, & \left(A<-\dfrac{1}{4}\right).\end{cases} \tag{A.3}$$

Therefore, the solution of the parametric equation is discussed in different cases.

Case I. $A=-(1/4)$; based on equations (A.2) and (A.3), the solution can be obtained as

$$\begin{cases} t=C\dfrac{\exp(1/2\tau-1)}{2\tau-1}-\dfrac{B}{A},\\[2ex] y=C\tau\dfrac{\exp(1/2\tau-1)}{2\tau-1}.\end{cases} \tag{A.4}$$

To get finite time clearly using $s=1/(2\tau-1)$, equation (A.4) is changed as

$$\begin{cases} t=Cs\exp(s)-\dfrac{B}{A},\\[2ex] y=\dfrac{C}{2}(s+1)\exp(s),\end{cases} \tag{A.5}$$

where s is a new parameter variable.

ase II. $A>-(1/4)$; based on equations (A.2) and (A.3), the solution can be obtained as

$$\begin{cases} t=C\dfrac{|2\tau-1+\sqrt{4A+1}|^{(1/2\sqrt{4A+1})-(1/2)}}{|2\tau-1-\sqrt{4A+1}|^{(1/2\sqrt{4A+1})-(1/2)}}-\dfrac{B}{A},\\[2ex] y=C\dfrac{\tau|2\tau-1+\sqrt{4A+1}|^{(1/2\sqrt{4A+1})-(1/2)}}{|2\tau-1-\sqrt{4A+1}|^{(1/2\sqrt{4A+1})-(1/2)}}.\end{cases} \tag{A.6}$$

To get finite time clearly using $s=1/(\tau-(1/2)-(p/2))$, equation (A.6) is changed as

$$\begin{cases} t=Cs(1+ps)^q-\dfrac{B}{A},\\[2ex] y=C\left(1+\dfrac{1}{2}s+\dfrac{p}{2}s\right)(1+ps)^q,\end{cases} \tag{A.7}$$

where $p=\sqrt{4A+1}$ and $q=(1/2p)-(1/2)$ because of $A=-2k_2/k_1^2$ and $A>-(1/4)$; therefore, $0<p<1$ and $q>0$.

Case III. $A<-(1/4)$; based on equations (A.2) and (A.3), the solution can be obtained as

$$\begin{cases} t=\dfrac{C}{\sqrt{\tau^2-\tau-A}\,\exp((1/\sqrt{-4A-1})\arctan(2\tau-1/\sqrt{-4A-1}))}\\[2ex] \quad -\dfrac{B}{A},\\[2ex] y=\dfrac{C\tau}{\sqrt{\tau^2-\tau-A}\,\exp((1/\sqrt{-4A-1})\arctan(2\tau-1/\sqrt{-4A-1}))}.\end{cases} \tag{A.8}$$

B. Parameter Equation

To indicate (5) holds, three different situations are considered based on the sign of the initial condition a.

Firstly, assume that $a>0$, then $x_1(t)>0$, for $t\in T_{a0}$. Let us discuss the trajectory when $t\in T_{a0}$, $x_1(0)=a, x_2(0)=b$, and $x_1(t_{a0})=0$, then based on the STA in $t\in T_{a0}$

$$x_2=-k_2t+b. \tag{B.1}$$

Substituting (B.1) into (1) leads to

$$\dot{x}_1=-k_1x_1^{1/2}-k_2t+b. \tag{B.2}$$

Let

$$y=-\frac{2}{k_1}x_1^{1/2}, \tag{B.3}$$

then its derivative on the trajectory of (B.2) can be obtained as follows:

$$y\dot{y}-y=-\frac{2k_2}{k_1^2}t+\frac{2b}{k_1^2}. \tag{B.4}$$

Secondly, if the initial condition $a<0$, then

$$x_2=k_2t+b. \tag{B.5}$$

Substituting (B.5) into (1) leads to

$$\dot{x}_1=k_1\sqrt{(-x_1)}+k_2t+b. \tag{B.6}$$

Let

$$y=-\frac{2}{k_1}(-x_1)^{1/2}, \tag{B.7}$$

then its derivative on the trajectory of (B.6) can be obtained as follows:

$$y\dot{y} - y = -\frac{2k_2}{k_1^2}t - \frac{2b}{k_1^2}. \tag{B.8}$$

Finally, if $a = 0$ because $x_2(0) = b \neq 0$, $x_1(t) \neq 0$, and $\text{sign}(x_1) = \text{sign}(b)$ when $t \in T_{a0}$, then based on the STA in $t \in T_{a0}$

$$x_2 = -k_2 \text{sign}(b)t + b. \tag{B.9}$$

Substituting (B.9) into (1) leads to

$$\dot{x}_1 = -k_1 \text{sign}(b)\left|x_1\right|^{1/2} - k_2 \text{sign}(b)t + b. \tag{B.10}$$

Let

$$y = -\frac{2}{k_1}\left|x_1\right|^{1/2}, \tag{B.11}$$

then its derivative on the trajectory of (B.10) can be obtained as follows:

$$y\dot{y} - y = -\frac{2k_2}{k_1^2}t + \frac{2|b|}{k_1^2}. \tag{B.12}$$

Based on (B.4), (B.8), and (B.12), the general form of (5) holds.

Data Availability

The data in this paper are simulated with MATLAB. No other data are present.

Conflicts of Interest

The authors declare that they have no conflicts of interest.

References

[1] V. Utkin, "Discussion aspects of high-order sliding mode control," *IEEE Transactions on Automatic Control*, vol. 61, no. 3, pp. 829–833, 2016.

[2] A. Levant, "Chattering analysis," *IEEE Transactions on Automatic Control*, vol. 55, no. 6, pp. 1380–1389, 2010.

[3] R. Liu and X. Gao, "Neural network identification and sliding mode control for hysteresis nonlinear system with backlash-like model," *Complexity*, vol. 2019, Article ID 4949265, 10 pages, 2019.

[4] M. P. Aghababa, "Control of non-integer-order dynamical systems using sliding mode scheme," *Complexity*, vol. 21, no. 6, pp. 224–233, 2016.

[5] S. Mobayen, "Fast terminal sliding mode controller design for nonlinear second-order systems with time-varying uncertainties," *Complexity*, vol. 21, no. 2, pp. 239–244, 2015.

[6] Q. Chen, H. Shi, and M. Sun, "Echo state network-based backstepping adaptive iterative learning control for strict-feedback systems: an error-tracking approach," *IEEE Transactions on Cybernetics*, pp. 1–14, 2019.

[7] Q. Chen, T. Liang, Y. Nan, and X. Ren, "Adaptive nonlinear sliding mode control of mechanical servo system with LuGre friction compensation," *Journal of Dynamic Systems Measurement & Control*, vol. 138, no. 2, Article ID 021003, 2015.

[8] Q. Chen, S. Xie, M. Sun, and X. He, "Adaptive nonsingular fixed-time attitude stabilization of uncertain spacecraft," *IEEE Transactions on Aerospace & Electronic Systems*, vol. 54, no. 5, pp. 2937–2350, 2018.

[9] X. Luo, S. Ge, J. Wang, and G. Xinping, "Time delay estimation-based adaptive sliding-mode control for non-holonomic mobile robots," *International Journal of Applied Mathematics in Control Engineering*, vol. 1, no. 1, pp. 1–8, 2018.

[10] Q. Chen, X. Ren, N. Jing, and D. Zheng, "Adaptive robust finite-time neural control of uncertain PMSM servo system with nonlinear dead zone," *Neural Computing & Applications*, vol. 28, no. 2, pp. 3725–3736, 2017.

[11] Q. Chen, L. Shi, N. Jing, X. Ren, and Y. Nan, "Adaptive echo state network control for a class of pure-feedback systems with input and output constraints," *Neurocomputing*, vol. 275, pp. 1370–1382, 2018.

[12] M. Tan, J. Li, X. Chen, and X. Cheng, "Power grid fault diagnosis method using intuitionistic fuzzy petri nets based on time series matching," *Complexity*, vol. 2019, Article ID 7890652, 14 pages, 2019.

[13] A. Levant, "Sliding order and sliding accuracy in sliding mode control," *International Journal of Control*, vol. 58, no. 6, pp. 1247–1263, 1993.

[14] A. Polyakov and A. Poznyak, "Reaching time estimation for "super-twisting" second order sliding mode controller via Lyapunov function designing," *IEEE Transactions on Automatic Control*, vol. 54, no. 8, pp. 1951–1955, 2009.

[15] V. I. Utkin and A. S. Poznyak, "Adaptive sliding mode control with application to super-twist algorithm: equivalent control method," *Automatica*, vol. 49, no. 1, pp. 39–47, 2013.

[16] Y. Dvir and A. Levant, "Accelerated twisting algorithm," *IEEE Transactions on Automatic Control*, vol. 60, no. 10, pp. 2803–2807, 2015.

[17] A. Levant, "Principles of 2-sliding mode design," *Automatica*, vol. 43, no. 4, pp. 576–586, 2007.

[18] A. Levant, "Homogeneity approach to high-order sliding mode design," *Automatica*, vol. 41, no. 5, pp. 823–830, 2005.

[19] J. A. Moreno and M. Osorio, "Strict Lyapunov functions for the super-twisting algorithm," *IEEE Transactions on Automatic Control*, vol. 57, no. 4, pp. 1035–1040, 2012.

[20] R. Seeber, M. Horn, and L. Fridman, "A novel method to estimate the reaching time of the super-twisting algorithm," *IEEE Transactions on Automatic Control*, vol. 63, no. 12, pp. 4301–4308, 2018.

[21] F. Cheng, L. Qu, W. Qiao, C. Wei, and L. Hao, "Fault diagnosis of wind turbine gearboxes based on DFIG stator current envelope analysis," *IEEE Transactions on Sustainable Energy*, vol. 10, no. 3, pp. 1044–1053, 2019.

[22] W. Chun, M. Benosman, and T. Kim, "Online parameter identification for state of power prediction of lithium-ion batteries in electric vehicles using extremum seeking," *International Journal of Control, Automation and System*, pp. 11–11, 2019.

[23] M. Tao, Q. Chen, X. He, and M. Sun, "Adaptive fixed-time fault-tolerant control for rigid spacecraft using a double power reaching law," *International Journal of Robust and Nonlinear Control*, vol. 29, no. 12, pp. 4022–4040, 2019.

[24] L. Tao, Q. Chen, and Y. Nan, "Disturbance-observer based adaptive control for second-order nonlinear systems using chattering-free reaching law," *International Journal of Control, Automation and Systems*, vol. 17, no. 2, pp. 356–369, 2019.

[25] G. Xu, Q. Liu, and L. Sun, "Terminal sliding mode control without singular for a class of uncertain system," *Complexity*, vol. 21, no. S1, pp. 566–572, 2016.

[26] R. Seeber and M. Horn, "Stability proof for a well-established super-twisting parameter setting," *Automatica*, vol. 84, pp. 241–243, 2017.

[27] M. Tao, Q. Chen, X. He, and M. Sun, "Adaptive fixed-time fault-tolerant control for rigid spacecraft using a double power reaching law," *International Journal of Robust and Nonlinear Control*, vol. 29, no. 12, pp. 4022–4040, 2019.

[28] Q. Zhu and L. Z. Guo, "A pole placement controller for non-linear dynamic plants," *Proceedings of the Institution of Mechanical Engineers, Part I: Journal of Systems and Control Engineering*, vol. 213, no. 6, pp. 467–476, 2002.

[29] C. Hua, Y. Li, H. Wang, and X. Guan, "Decentralised fault-tolerant finite-time control for a class of interconnected non-linear systems," *IET Control Theory & Applications*, vol. 9, no. 16, pp. 2331–2339, 2015.

[30] C. Hua, L. Zhang, and X. Guan, "Decentralized output feedback adaptive NN tracking control for time-delay stochastic nonlinear systems with prescribed performance," *IEEE Transactions on Neural Networks and Learning Systems*, vol. 26, no. 11, pp. 2749–2759, 2015.

[31] J. Zhang, Q. Zhu, X. Wu, and Y. Li, "A generalized indirect adaptive neural networks backstepping control procedure for a class of non-affine nonlinear systems with pure-feedback prototype," *Neurocomputing*, vol. 121, pp. 131–139, 2013.

[32] Q. M. Zhu, D. Y. Zhao, and J. Zhang, "A general U-block model-based design procedure for nonlinear polynomial control systems," *International Journal of Systems Science*, vol. 47, no. 14, pp. 3465–3475, 2016.

[33] X. Wu, J. Zhang, and Q. Zhu, "A generalized procedure in designing recurrent neural network identification and control of time-varying-delayed nonlinear dynamic systems," *Neurocomputing*, vol. 73, no. 7–9, pp. 1376–1383, 2010.

[34] J. Zhang, Q. Zhu, L. Yang, and X. Wu, "Homeomorphism mapping based neural networks for finite time constraint control of a class of nonaffine pure-feedback nonlinear systems," *Complexity*, vol. 2019, Article ID 9053858, 11 pages, 2019.

[35] A. D. Polyanin and V. F. Zaitsev, *Handbook of Exact Solutions for Ordinary Differential Equations*, Chapman & Hall/CRC, Boca Raton, FL, USA, 2003.

Hindawi
Complexity
Volume 2019, Article ID 7604320, 6 pages
https://doi.org/10.1155/2019/7604320

Research Article

Adaptive Optimizing Control for Nonlinear Synchronous Generator System with Uncertain Disturbance

Guiyang Deng,[1] **Lianglun Cheng**,[1] **and Baojian Yang**[2]

[1]*School of Automation, Guangdong University of Technology, Guangzhou, Guangdong 510006, China*
[2]*Faculty of Intelligent Manufacturing, Wuyi University, Jiangmen, Guangdong 529020, China*

Correspondence should be addressed to Baojian Yang; kurt.yang@163.com

Received 19 June 2019; Revised 28 July 2019; Accepted 20 August 2019; Published 16 October 2019

In this paper, an adaptive optimizing control is proposed for nonlinear synchronous generator system with uncertain disturbance. Considering the issue of uncertain item, a low-order Extended State Observer (ESO) is constructed to track each order states. Then, combining Backstepping technology and proposed ESO, a dynamic compensation control is designed to compensate the uncertainty disturbance in each state quantity. The proposed method demonstrated that stability of the system can be ensured, and tracking burden of ESO can be reduced. Finally, simulation results can show a good tracking performance and anti-interference ability by the proposed control method.

1. Introduction

At present, the energy development in the world is mostly hydraulic power generation, thermal power generation, wind power generation and so on. In modern power industry, synchronous generator is the most commonly used alternator, which is widely used in thermal power generation, diesel engine power generation, nuclear power generation, and so on [1–3]. During the operation of synchronous generators, there are many system uncertainties and serious external disturbances. It would lead to great energy loss and bring great negative impact on energy conversion efficiency. Therefore, how to effectively compensate for uncertain nonlinearity and improve energy conversion efficiency is an open issue. To achieve high-performance power system control, it is necessary to overcome the negative effects of uncertainties and nonlinear factors in the system. For the complex synchronous generator model, it is feasible to analyze the stability of synchronous generator directly by using Lyapunov function, but the calculation process is complex and the amount of calculation is large [4–6]. There are many uncertain disturbances in the actual application scenario of synchronous generator, which makes the design of control method greatly difficult.

Since there are many uncertainties and unknown disturbances during the operation of the synchronous generator, it is very difficult to construct the Lyapunov function directly. At present, some scholars use Backstepping technology to construct Lyapunov functions effectively. They have completed the design of the whole system control law [7–9]. Although Backstepping technology effectively reduces the difficulty of constructing Lyapunov functions, it is still difficult to construct systems with multiple uncertainties. In this regard, some scholars use adaptive control based on the Backstepping technology to compensate for uncertainty interference [10–15]. However, this method increases the number of adaptive parameters, so that the amount of calculation increases.

On the other hand, for systems with uncertainties, Extended State Observer (ESO) is used to achieve effective dynamic tracking [16–20]. The ESO is used to expand the uncertain disturbances in the system into a new state. By adopting ESO, the uncertain disturbances can be tracked efficiently. Moreover, the control accuracy of the system can be improved by using the tracking values of uncertain disturbances. However, the ESO designed for the whole system model will accumulate disturbances as the dimension of the system model increases. This will result in the performance of the observer greatly reduced. Furthermore, in practical application scenarios, synchronous generators are structure complex system. And uncertain disturbances are uncertain. In

order to broaden the application scenario of ESO, it is necessary to optimize the construction method of ESO.

To sum up, this paper designs a controller based on Backstepping technology and low-order ESO to enhance the anti-interference ability of the system and improve the efficiency of energy conversion. The specific mathematical model of this paper is described in Section 2. The proposed control method is described in detail in Section 3. The corresponding simulation is shown in Section 4.

2. Mathematical Model of Synchronous Generator

In this paper, a mathematical model of synchronous generator based on rotor $d-q$ axis is considered. And $L = L_q = L_d$ is one of the assumptions.

$$\begin{cases} \dot{\theta} = \omega, \\ \dot{\omega} = \frac{1}{J}\left(\frac{3p\phi_f}{2} i_q - B\omega\right) - d, \\ \dot{i}_d = \frac{1}{L} u_d + p\omega i_q - \frac{R}{L} i_d, \\ \dot{i}_q = \frac{1}{L} u_q - \frac{p\phi_f}{L}\omega - \frac{R}{L} i_q - p\omega i_d + f, \end{cases} \tag{1}$$

where θ is the rotor angle, B is the viscous friction coefficient, p is the pole logarithm, and J is the moment of inertia of the rotor. R and L are the stator resistance and phase inductance, respectively. ω the mechanical angular velocity. i_d and i_q are current of $d-q$ axis. ϕ_f is the permanent magnet flux. u_d and u_q are voltage of $d-q$ axis. d represents the unknown load torque disturbances. f is the externally uncertain bounded disturbances term.

In the magnetic field control of a synchronous generator, the direct current i_d is generally set to zero. Therefore, the model (1) of the synchronous generator can be simplified as follows:

$$\begin{cases} \dot{\theta} = \omega, \\ \dot{\omega} = -c_1\omega + c_2 i_q - d, \\ \dot{i}_q = -c_3\omega - c_4 i_q + b u_q + f, \end{cases} \tag{2}$$

where $c_1 = B/J$, $c_2 = k_T/J$, $c_3 = p\phi_f/L$, $c_4 = R/L$, $b = 1/L$, and $k_T = 3p\phi_f/2$.

In order to facilitate the design of the controller, $x_1 = \theta$, $x_2 = \omega$, and $x_3 = i_q$ are the system status. Thus, the model (2) can be described as follows:

$$\begin{cases} \dot{x}_1 = x_2, \\ \dot{x}_2 = -c_1 x_2 + c_2 x_3 - d, \\ \dot{x}_3 = -c_3 x_2 - c_4 x_3 + b u_q + f. \end{cases} \tag{3}$$

Setting

$$u_q = \frac{h + c_3 x_2 + c_4 x_3}{b}, \tag{4}$$

where h is the preset control amount.

Then formula (3) is further represented as follows:

$$\begin{cases} \dot{x}_1 = x_2, \\ \dot{x}_2 = -c_1 x_2 + c_2 x_3 - d, \\ \dot{x}_3 = h + f. \end{cases} \tag{5}$$

The system model (5) is a system with uncertain disturbance terms. Based on the Backstepping technology, this paper combines the ESO method to design a control method. It improves the anti-interference ability of the system and further ensures the stability and tracking performance of the system. The design method is described in the next section.

3. Compensation Control Design

According to the aforementioned model, the design steps of the control method are as follows.

Step 1. Define tracking error e_1 as follows:

$$e_1 = x_1 - x_{1r}, \tag{6}$$

where x_{1r} is the expected value, and the second order is derivable.

The Lyapunov function is defined as follows:

$$V_1 = \frac{1}{2} e_1^2. \tag{7}$$

Thus, it can be obtained as follows:

$$\dot{V}_1 = e_1 \dot{e}_1 = e_1 (x_2 - \dot{x}_{1r}). \tag{8}$$

Define the tracking error e_2 as follows:

$$e_2 = x_2 - \alpha_1, \tag{9}$$

where α_1 is the virtual controller.

From formulas (8) and (9), it can be obtained as follows:

$$\dot{V}_1 = e_1 (e_2 + \alpha_1 - \dot{x}_{1r}). \tag{10}$$

To ensure that $\dot{V}_1$ is negative, the virtual controller is designed as $\alpha_1 = -k_1 e_1 + \dot{x}_{1r}$, where $k_1 > 0$. Then, the following result can be obtained:

$$\dot{V}_1 = -k_1 e_1^2 + e_1 e_2. \tag{11}$$

In the above formula, the inequality $-k_1 e_1^2 \le 0$ is always established. The processing of the item $e_1 e_2$ is described in the next step.

Step 2. The Lyapunov function V_2 is chosen as:

$$V_2 = V_1 + \frac{1}{2} e_2^2. \tag{12}$$

Thus, it can be obtained that:

$$\dot{V}_2 = -k_1 e_1^2 + e_2 (e_1 - c_1 x_2 + c_2 x_3 - d - \dot{\alpha}_1). \tag{13}$$

Define tracking error e_3 as follows:

$$e_3 = x_3 - \alpha_2. \tag{14}$$

Thus, the system status is described as follows:

$$x_3 = e_3 + \alpha_2. \tag{15}$$

From formulas (13) and (15), it can be obtained as follows:

$$\dot{V}_2 = -k_1 e_1^2 + e_2 [e_1 - c_1 x_2 + c_2 (e_3 + \alpha_2) - d - \dot{\alpha}_1]. \tag{16}$$

In order to satisfy the inequality $\dot{V}_2 \le 0$, the virtual controller α_2 is designed as follows:

$$\alpha_2 = \frac{1}{c_2}\dot{\alpha}_1 + \frac{c_1}{c_2}x_2 + \frac{1}{c_2}d - \frac{1}{c_2}e_1 - \frac{k_2}{c_2}e_2. \tag{17}$$

Then, it can be obtained the following formula:

$$\dot{V}_2 = -k_1e_1^2 - k_2e_2^2 + c_2e_2e_3, \tag{18}$$

where $k_1 > 0$ and $k_2 > 0$. Therefore, $-k_1e_1^2 - k_2e_2^2 \le 0$ is established. Then, further design is needed to eliminate the impact of the error e_3 on system stability.

Formula (16) contains an externally bounded disturbance d. In order to ensure the stability of the system, the second-order ESO-1 is constructed to estimate the external uncertain, which is bounded interference. The construction method will be introduced in the subsection.

The ESO-1 is established as follows:

$$\begin{cases} e_{d1} = z_{d1} - x_2, \\ \dot{z}_{d1} = z_{d2} - \beta_{d1}e_{d1} - c_1x_2 + c_2x_3, \\ \dot{z}_{d2} = -\beta_{d2}fal(e_{d1}, \varepsilon_d, \delta_d). \end{cases} \tag{19}$$

The function $fal(e_{d1}, \varepsilon_d, \delta_d)$ is designed as follows:

$$fal(e_{d1}, \varepsilon_d, \delta_d) = \begin{cases} \dfrac{e_{d1}}{\delta_d^{\varepsilon_d - 1}}, & |e_{d1}| \le \delta_d, \\ |e_{d1}|^{\varepsilon_d} sign(e_{d1}), & |e_{d1}| < \delta_d, \end{cases} \tag{20}$$

where e_{d1} is the systematic error, ε_d is a constant in the interval $(0, 1)$. And δ_d is the length of the interval of the linear segment.

The stability of the second order ESO-1 of formula (19) is demonstrated as follows:

Setting

$$\begin{cases} e_{d1} = z_{d1} - x_2, \\ e_{d2} = z_{d2} - d. \end{cases} \tag{21}$$

Thus, it can be obtained as follows:

$$\begin{cases} \dot{e}_{d1} = e_{d2} - \beta_{d1}e_{d1}, \\ \dot{e}_{d2} = -\beta_{d2}fal(e_{d1}, \varepsilon_d, \delta_d) - \dot{d}. \end{cases} \tag{22}$$

Case 1. The error e_{d1} is satisfied with $|e_{d1}| > \varepsilon_d$, and then it can be obtained that $fal(e_{d1}, \varepsilon_d, \delta_d) = |e_{d1}|^{\varepsilon_d} sign(e_{d1})$.

$$\begin{cases} \dot{e}_{d1} = e_{d2} - \beta_{d1}e_{d1}, \\ \dot{e}_{d2} = \mp\beta_{d2}|e_{d1}|^{\varepsilon_d} - \dot{d}. \end{cases} \tag{23}$$

When the system is stable, it can be obtained that $\dot{e}_{d1} \to 0$ and $\dot{e}_{d2} \to 0$

$$\begin{cases} \dot{e}_{d1} = e_{d2} - \beta_{d1}e_{d1} = 0, \\ \dot{e}_{d2} = \mp\beta_{d2}|e_{d1}|^{\varepsilon_d} - \dot{d} = 0, \end{cases} \tag{24}$$

and

$$\begin{cases} e_{d1} = \mp\left|\dfrac{\dot{d}}{\beta_{d2}}\right|^{\varepsilon_d^{-1}}, \\ e_{d2} = \pm\beta_{d1}\left|\dfrac{\dot{d}}{\beta_{d2}}\right|^{\varepsilon_d^{-1}}. \end{cases} \tag{25}$$

Therefore, if the inequality $|\beta_{d2}| > |\dot{d}|$ was established with the true parameters, it could be obtained $z_{d1} \to x_2$, $z_{d2} \to d$.

Case 2. The error e_{d1} is satisfied by $|e_{d1}| \le \varepsilon_d$, it can be obtained $fal(e_{d1}, \varepsilon_d, \delta_d) = e_{d1}/\delta_d^{\varepsilon_d - 1}$.

Then,

$$\begin{cases} \dot{e}_{d1} = e_{d2} - \beta_{d1}e_{d1}, \\ \dot{e}_{d2} = -\beta_{d2}\dfrac{e_d}{\delta_d^{\varepsilon_d - 1}} - \dot{d}. \end{cases} \tag{26}$$

When the system is stable, it can be obtained that $\dot{e}_{d1} \to 0$ and $\dot{e}_{d2} \to 0$. Thus

$$\begin{cases} \dot{e}_{d1} = e_{d2} - \beta_{d1}e_{d1} = 0, \\ \dot{e}_{d2} = -\beta_{d2}\dfrac{e_d}{\delta_d^{\varepsilon_d - 1}} - \dot{d} = 0. \end{cases} \tag{27}$$

and

$$\begin{cases} e_{d1} = -\dfrac{\dot{d} \cdot \delta_d^{\varepsilon_d - 1}}{\beta_{d2}}, \\ e_{d2} = -\beta_{d1}\dfrac{\dot{d} \cdot \delta_d^{\varepsilon_d - 1}}{\beta_{d2}}. \end{cases} \tag{28}$$

Similarly, if the inequality $|\beta_{d2}| > |\dot{d} \cdot \delta_d^{\varepsilon_d - 1}|$ was established with the true parameters, it could be obtained $z_{d1} \to x_2$ and $z_{d2} \to d$.

From case 1 and case 2, the stability of the second-order ESO-1 can be ensured when the appropriate parameters are satisfied with $|\beta_{d2}| > |\dot{d}|$ and $|\beta_{d2}| > |\dot{d} \cdot \delta_d^{\varepsilon_d - 1}|$.

Step 3. The Lyapunov function V_3 is chosen as:

$$V_3 = V_2 + \frac{1}{2}e_3^2. \tag{29}$$

Thus, it can be obtained that:

$$\dot{V}_3 = -k_1e_1^2 - k_2e_2^2 + c_2e_2e_3 + e_3\dot{e}_3. \tag{30}$$

From formula (14), it can be obtained that $\dot{e}_3 = \dot{x}_3 - \dot{\alpha}_2$. Thus, $\dot{V}_3$ can be written as:

$$\dot{V}_3 = -k_1e_1^2 - k_2e_2^2 + c_2e_2e_3 + e_3(h + f - \dot{\alpha}_2). \tag{31}$$

In order to satisfy the inequality $\dot{V}_2 \le 0$, it can be designed as follows:

$$h = -f + \dot{\alpha}_2 - k_3e_3 - c_2e_2, \tag{32}$$

where $k_3 > 0$. Formula (30) contains an externally bounded disturbance f. Similarly, the second-order ESO-2 is designed to estimate the uncertainty disturbance.

Thus, the ESO-2 is established as follows:

$$\begin{cases} e_{f1} = z_{f1} - x_3, \\ \dot{z}_{f1} = z_{f2} - \beta_{f1}e_{f1} - c_3x_2 - c_4x_3 + bu_q, \\ \dot{z}_{f2} = -\beta_{f2}fal(e_{f1}, \varepsilon_f, \delta_f). \end{cases} \tag{33}$$

The function $fal(e_{f1}, \varepsilon_f, \delta_f)$ is designed as follows:

$$fal(e_{f1}, \varepsilon_f, \delta_f) = \begin{cases} \dfrac{e_{f1}}{\delta_f^{\varepsilon_f - 1}}, & |e_{f1}| \le \delta_f, \\ |e_{f1}|^{\varepsilon_f} sign(e_{f1}), & |e_{f1}| < \delta_f, \end{cases} \tag{34}$$

where e_{f1} is the systematic error, ε_f is a constant in the interval $(0, 1)$, and δ_f is the length of the interval of the linear segment.

Table 1: Parameters of synchronous generator.

Parameters	Ratings
Torque constant k_T	$0.14N \cdot m \cdot A^{-1}$
Number of pole pairs p	4
Stator phase resistance R	2Ω
Stator phase inductance L	$25mH$
Coefficient of friction B	$0.0001N \cdot m \cdot s \cdot rad^{-1}$
Moment of inertia J	$0.0086\ kg \cdot m^2$

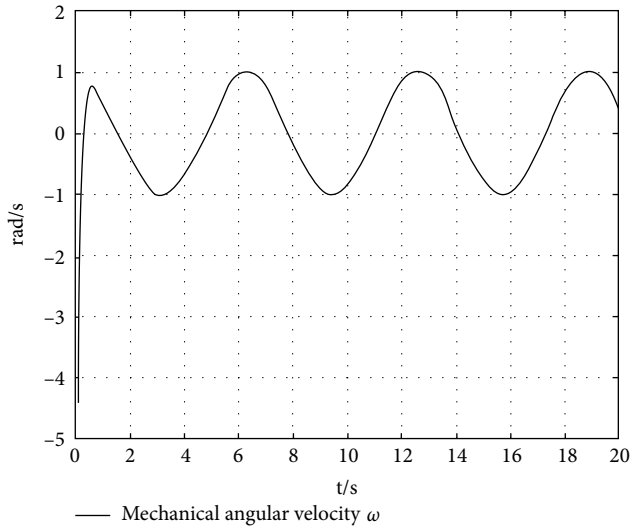

Figure 1: Mechanical angular velocity ω.

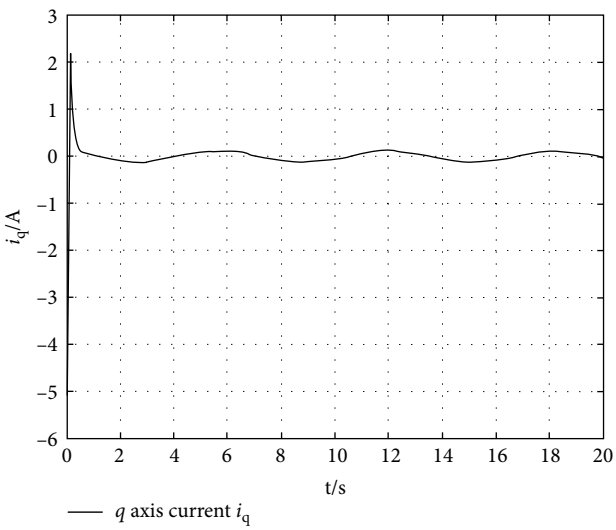

Figure 2: q axis current i_q.

Same as ESO-1 stability proof process, the stability of ESO-2 can be guaranteed when both $|\beta_{f2}| > |\dot{f}|$ and $|\beta_{f2}| > |\dot{f} \cdot \delta_f^{\varepsilon_f - 1}|$ are satisfied.

According to the aforementioned analysis, ESO-2 can accurately estimate the uncertainty disturbance f in real time. Therefore, formula (30) can be rewritten as:

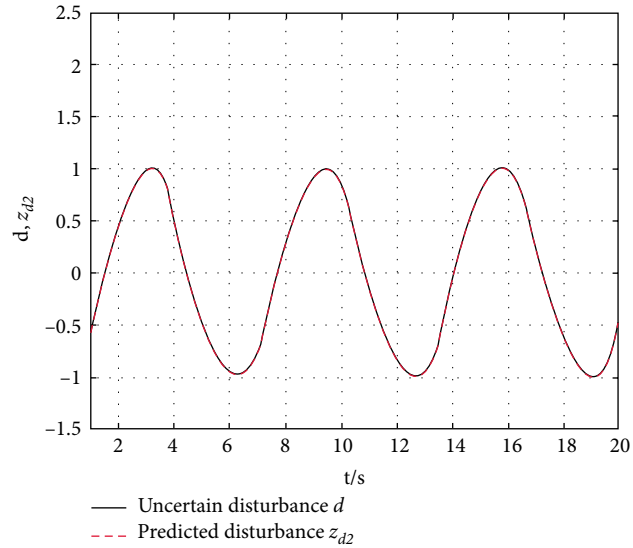

Figure 3: Uncertain disturbance d and predicted disturbance z_{d2}.

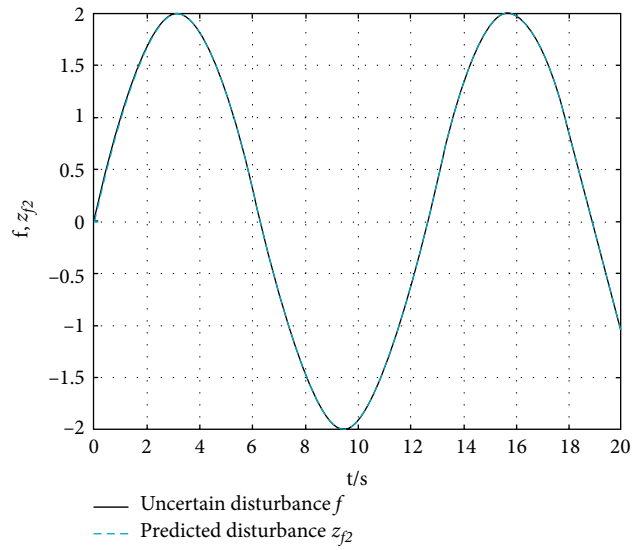

Figure 4: Uncertain disturbance f and predicted disturbance z_{f2}.

$$\dot{V}_3 = -k_1 e_1^2 - k_2 e_2^2 - k_3 e_3^2 \leq 0. \tag{35}$$

In summary, the system model (1) is stablity.

4. Simulation Results

In order to verify the feasibility of the above method, the following verification simulation is performed for the synchronous generator control system model. The parameters are shown in Table 1.

The parameters of the system model are derived from the data in Table 1. And choosing $c_1 = 0.5$, $c_2 = 16.28$, $c_3 = 26$, $c_4 = 80$, and $b = 40$. In the simulation, the initial value of the equation of state is set as $[\, x_1(0) \quad x_2(0) \quad x_3(0)\,] = [\,1 \quad 0 \quad 0\,]$. The parameters in the Backstepping technology are selected

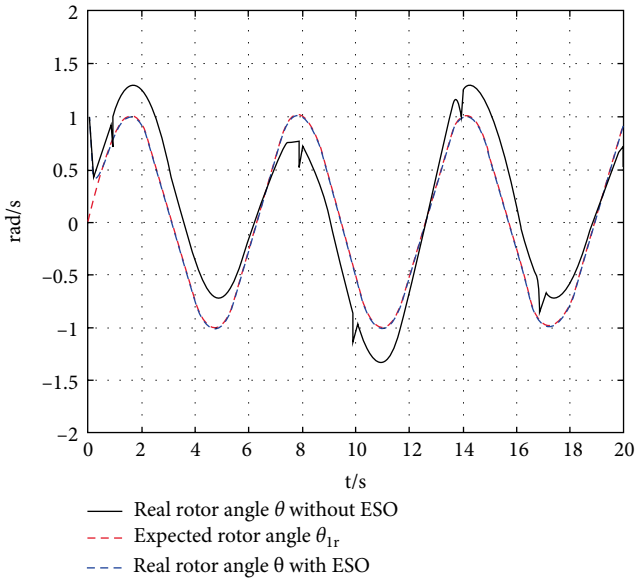

Figure 5: Rotor angle tracking curve.

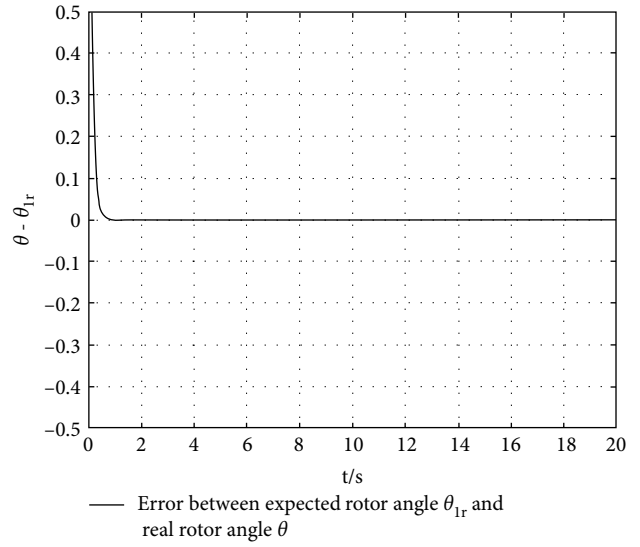

Figure 6: Error between expected rotor angle θ_{1r} and real rotor angle θ.

as: $k_1 = 30$, $k_2 = 40$, and $k_3 = 0.1$. The parameters in ESO are selected as: $\beta_{d1} = \beta_{f1} = 100$, $\beta_{f1} = \beta_{f2} = 100$, $\varepsilon_d = \varepsilon_f = 0.5$, and $\delta_d = \delta_f = 0.01$.

In order to track the rotor angle and verify the stability of the system, the expected value of the given rotor angle in the simulation example is $\theta_{1r} = x_{1r} = \sin(t) rad/s$. And assume that the system's uncertain disturbance terms are $d = \cos(t)$ and $f = 2 * \sin(t/2)$. The simulation results are shown in Figures 1–6.

It can be seen from Figures 1 and 2 that both the mechanical angular velocity and the q-axis current are bounded, which guarantees the stability of the system. It can be seen from Figures 3 and 4 that the established ESO can perform effective dynamic compensation for the uncertain interference term and good real-time tracking. Figure 5 is a comparison of the real rotor angle control with ESO and without ESO. The figure indicates that the system without ESO will more easily affect by the uncertain disturbances and generate the system jitter. This must not be allowed to exist in the practical engineering application. By using the proposed method, the system has stronger anti-interference ability and satisfies the practical engineering requirements. Figure 6 is the error between the two. The error curve is basically stable at 0, that is, the error is close to zero. It can be seen that the method proposed in this paper can improve the stability of the system and has great practical application value.

5. Conclusions

Based on the model of synchronous generator system, this paper proposes a new control method by combining Backstepping design method and ESO method. Firstly, a low-order ESO is constructed, which can estimate the uncertain disturbances in real-time. Secondly, the Lyapunov function of the synchronous generator system model is constructed effectively by using Backstepping method. On the premise of reducing the amount of calculation, a control method is designed to achieve effective tracking and strong antijamming performance of the system. The simulation results show that this method can improve the antijamming ability and tracking performance of the system, and has great application value.

Data Availability

The paper data used to support the findings of this study are included within the article.

Conflicts of Interest

The authors declare that there are no conflicts of interest regarding the publication of this paper.

Acknowledgments

This work has been supported by the National Natural Science Foundation of China Guangdong Joint Funds (Grant No. U1701262 and No. U1801263) and partly supported by the Guangdong Provincial Key Laboratory of Cyber-Physical System (Grant No. 2016B030301008) and the Guangdong applied science and technology R & D special funds (Grant No. 2015B090922013) and the Guangdong Province Science and Technology Project (Grant No. 2016B090918017) and the Guangdong NC First Generation Project (Grant No. 2013B011302007) and the Guangzhou Science and Technology Project (Grant No. 201604016107) and funding for Introduced Innovative R&D Team Program of Jiangmen (Grant No. 2018630100090019844) and Youth Scientific Research Fund Project of Wuyi University (2015ZK06).

References

[1] V. Natarajan and G. Weiss, "Almost global asymptotic stability of a grid-connected synchronous generator," *Mathematics of Control, Signals, and Systems*, vol. 30, no. 2, pp. 10, 2018.

[2] K. Sindhya, A. Manninen, K. Miettinen, and J. Pippuri, "Design of a permanent magnet synchronous generator using interactive multiobjective optimization," *IEEE Transactions on Industrial Electronics*, vol. 64, no. 12, pp. 9776–9783, 2017.

[3] X. Bai, L. Qu, and W. Qiao, "Robust AC optimal power flow for power networks with wind power generation," *IEEE Transactions on Power Systems*, vol. 31, no. 5, pp. 4163–4164, 2015.

[4] T. de Paula Machado Bazzo, J. F. Kolzer, R. Carlson, F. Wurtz, and L. Gerbaud, "Multiphysics design optimization of a permanent magnet synchronous generator," *IEEE Transactions on Industrial Electronics*, vol. 64, no. 12, pp. 9815–9823, 2018.

[5] T. Barisa, S. Iles, D. Sumina, and J. Matusko, "Model predictive direct current control of a permanent magnet synchronous generator based on flexible Lyapunov function considering converter dead time," *IEEE Transactions on Industry Applications*, vol. 54, no. 3, pp. 2899–2912, 2018.

[6] J. Wang, Z. Liu, Y. Zhang, C. L. P. Chen, and G. Lai, "Adaptive neural control of a class of stochastic nonlinear uncertain systems with guaranteed transient performance," *IEEE Transactions on Cybernetics*, pp. 1–11, 2019.

[7] X. Bai and W. Qiao, "Robust optimization for bidirectional dispatch coordination of large-scale V2G," *IEEE Transactions on Smart Gird*, vol. 6, no. 4, pp. 1944–1954, 2015.

[8] F. Mazenc and H. Ito, "Lyapunov technique and backstepping for nonlinear neutral systems," *IEEE Transactions on Automatic Control*, vol. 58, no. 2, pp. 512–517, 2013.

[9] X. Bai, W. Qiao, H. Wei, F. Huang, and Y. Chen, "Bidirectional coordinating dispatch of large-scale V2G in a future smart grid using complementarity optimization," *International Journal of Electrical Power & Energy Systems*, vol. 68, pp. 269–277, 2015.

[10] J. Wang, Z. Liu, Y. Zhang, and C. L. P. Chen, "Neural adaptive event-triggered control for nonlinear uncertain stochastic systems with unknown hysteresis," *IEEE Transactions on Neural Networks and Learning Systems*, pp. 1–13, 2019.

[11] G. Wen, S. S. Ge, and F. Tu, "Optimized backstepping for tracking control of strict-feedback systems," *IEEE Transactions on Neural Networks and Learning Systems*, vol. 29, no. 8, pp. 3850–3862, 2018.

[12] D. Sheng, Y. Wei, S. Cheng, and J. Shuai, "Adaptive backstepping control for fractional order systems with input saturation," *Journal of the Franklin Institute*, vol. 354, no. 5, pp. 2245–2268, 2017.

[13] C. Wei, M. Benosman, and T. Kim, "Online parameter identification for state of power prediction of lithium-ion batteries in electric vehicles using extremum seeking," *International Journal of Control, Automation and System*, 2019.

[14] K. Miroslav, K. Ioannis, and V. Petar, *Nonlinear and Adaptive Control Design*, Englewood Cliffs, NJ, 1994.

[15] J. Wang, H. Zhu, C. L. Zhang et al., "Adaptive hyperbolic tangent sliding-mode control for building structural vibration systems for uncertain earthquakes," *IEEE Access*, vol. 6, pp. 74728–74736, 2018.

[16] S. Wang, X. Ren, J. Na, and T. Zeng, "Extended-state-observer-based funnel control for nonlinear servomechanisms with prescribed tracking performance," *IEEE Transactions on Automation Science and Engineering*, vol. 14, no. 1, pp. 98–108, 2016.

[17] C. Wei, Z. Zhang, W. Qiao, and L. Qu, "An adaptive network-based reinforcement learning method for MPPT control of PMSG wind energy conversion systems," *IEEE Transactions on Power Electronics*, vol. 31, no. 11, pp. 7837–7848, 2016.

[18] X. Wang, C. Shi, and S. Wang, "Extended state observer-based motion synchronization control for hybrid actuation system of large civil aircraft," *International Journal of Systems Science*, vol. 48, no. 10, pp. 2212–2222, 2017.

[19] J. Wang, W. Chen, Z. Chen et al., "Neural terminal sliding-mode control for uncertain systems with building structure vibration," *Complexity*, vol. 2019, Article ID 1507051, 9 pages, 2019.

[20] C. Wei, Z. Zhang, W. Qiao, and L. Qu, "Reinforcement-learning-based intelligent maximum power point tracking control for wind energy conversion systems," *IEEE Transactions on Industrial Electronics*, vol. 62, no. 10, pp. 6360–6370, 2015.

Hindawi
Complexity
Volume 2019, Article ID 4824837, 15 pages
https://doi.org/10.1155/2019/4824837

Research Article

A Competitive Swarm Optimizer-Based Technoeconomic Optimization with Appliance Scheduling in Domestic PV-Battery Hybrid Systems

Bo Wang,[1] **Yanjing Li**,[1] **Fei Yang**,[2] **and Xiaohua Xia**[3]

[1]*Key Laboratory of Ministry of Education for Image Processing and Intelligent Control, Artificial Intelligence and Automation School, Huazhong University of Science and Technology, Wuhan 430074, China*
[2]*Department of Artificial Intelligence and Automation, School of Electrical Engineering and Automation, Wuhan University, Wuhan 430072, China*
[3]*Department of Electrical, Electronic and Computer Engineering, University of Pretoria, Pretoria 0028, South Africa*

Correspondence should be addressed to Bo Wang; wb8517@hust.edu.cn

Received 19 July 2019; Accepted 28 August 2019; Published 13 October 2019

Guest Editor: Chun Wei

A technoeconomic optimization problem for a domestic grid-connected PV-battery hybrid energy system is investigated. It incorporates the appliance time scheduling with appliance-specific power dispatch. The optimization is aimed at minimizing energy cost, maximizing renewable energy penetration, and increasing user satisfaction over a finite horizon. Nonlinear objective functions and constraints, as well as discrete and continuous decision variables, are involved. To solve the proposed mixed-integer nonlinear programming problem at a large scale, a competitive swarm optimizer-based numerical solver is designed and employed. The effectiveness of the proposed approach is verified by simulation results.

1. Introduction

Making best use of renewable energies has been a topic that receives continuous attention [1]. The photovoltaic (PV) energy is one of the most concerned renewable energy because of the ubiquity of solar irradiation and very low carbon emission [2]. The PV energy generation is therefore integrated into power grids in many countries [3]. However, because of PV energy's intermittent nature, it is difficult to use PV energy alone to support sustained power demands in the complicated context, such as domestic electrical loads. A popular paradigm to utilize the PV power source is to integrate the PV energy into hybrid energy systems, where multiple power sources are adopted and dispatched cooperatively [4]. There were an enormous number of studies on hybrid system optimization over the past twenty years. Advanced technologies have been applied to the economic power dispatch problem in hybrid energy systems [5–7]. Most of such studies focused on power flow control strategies where the demand side was rather considered constraints in the system. There were also studies that introduced demand-side management into hybrid energy system management [8, 9], whereas these studies hardly explored the potentials of controlling both power flows and load behaviors. In general, the potentials of incorporating the power dispatch with demand-side management remain to be explored at the current stage. Indeed, such a problem is difficult because of the complex correlations between power sources and loads and its large-scale nature.

In this paper, a technoeconomic optimization problem is extended and improved to investigate further energy efficiency and economic potentials in such a domestic grid-connected PV-battery hybrid energy system, based on a series of previous studies by Tazvinga et al. [10–15]. There are two parts of the interventions: the power dispatch that decides which power is to be supplied to which load and appliance time scheduling that decides when to activate a specific domestic appliance to fulfill the user requirements.

The optimization is implemented over a finite time horizon. There are three objectives involved in the optimization. Firstly, the overall energy cost over the horizon has to be minimized. The energy cost mainly comes from the consumed grid power, based on the time-of-use (TOU) tariff [16]. The battery wear cost is also integrated into the overall cost. Secondly, the usage of renewable energy has to be maximized. Given that the overall power demand from the loads is considered constant, this objective is transformed into the grid power consumption minimization. Thirdly, the user satisfaction has to be maximized. An inconvenience indicator has been proposed by Setlhaolo and Xia [12] so that the overall difference between the scheduled appliance operation and the baseline appliance operation is calculated. The objective is thus introduced by minimizing such an inconvenience indicator. A weighted sum approach is employed to simultaneously optimize the three objectives, subject to a series of system constraints.

The main contributions of this study are listed as follows: Firstly, the hybrid system design is improved. The major improvement from the design perspective is that separate power dispatch is introduced to each connected appliance, instead of considering the electrical load (consisting of a variety of appliances) as a whole. This is realized by introducing additional power lines between each pair of the appliances and power sources. The power dispatch is thus managed in a more flexible way. In the previous model, all appliances are compelled to choose the same power source at one time. In the improved system design, additional power lines and switches are deployed such that appliances can choose the power sources themselves. The supply that combines various power sources provides the system more flexible power dispatch choices. For example, at peak hours, the battery bank cannot support heavy loads independently because of its capacity limitation. According to the previous design, the battery bank can only work for a short time in the late evening; otherwise, the power demands cannot be matched. In the new design, the battery bank has a much longer possible working time by only supporting a part of the loads, which leaves more space for the load scheduling. Improved flexibility brings more energy efficiency potentials, and thus, more economic benefits can be achieved.

Secondly, the mathematical formulation of the technoeconomic optimization is improved, as the dimension of decision variables is minimized. The aforementioned flexibility improves at the cost of additional decision variables, i.e., the ON/OFF states of the additional switches. The number of decision variables grows largely as the problem scale grows spatially with the number of switches and longitudinally with the number of control intervals, in comparison with the previous system design. To reduce the resulting computational burden, the interplay among the switch behaviors is identified. Some switch behavior constraints are involved; for example, the battery can only charge or discharge at one time, and the appliance can only have one active power line connection. The correlated switches manifest finite states; as a result, a set of discrete state variables are introduced. The values of the discrete variables indicate the combination of ON/OFF states of the correlated switches. Given the constraints, the state variables choose values from a limited range. In this way, the number of variables to describe the complex and interacting switch behaviors is minimized. As the ON/OFF states of the switches are a major part of the decision variables, the dimension of the decision variables is largely reduced; therefore, the computational burden is smaller such that the problem is more promising to be solved within limited time.

Thirdly, an advanced numerical solver is designed for the proposed problem. A major difficulty to implement the technoeconomic optimization is the solver. The investigated problem involves nonlinear objective functions and constraints, as well as continuous and discrete decision variables. It is thus a mixed-integer nonlinear programming (MINLP) problem. Furthermore, as mentioned above, the decision variable can be a large number, e.g., over 700. A proper solver to such a complicated and large-scale optimization problem is thus required. An intelligent optimization algorithm, namely, the competitive swarm optimizer (CSO), is employed to design the numerical solver. Cheng and Jin firstly proposed the CSO algorithm to solve large-scale optimization problems [17]. The CSO algorithm is designed on the basis of the particle swarm optimization (PSO) algorithm with a very different searching mechanism. In the PSO algorithm, the term "particle" is employed to refer to the individual solutions. The particles are characterized with two vectors, namely, the position and velocity vectors. The position vector describes the value of a solution and the velocity vector the incremental of the value. The PSO updates the position vector with the velocity vector via interacting with the global best position in the swarm (the population of individuals) and the personal best position in history [18]. The CSO algorithm adopts the position and velocity vector modelling from PSO but employs a random pairwise competition mechanism such that the loser particle can learn from the winner particle to update its position and velocity. In this way, the CSO algorithm can reduce the opportunity of convergence to local optimum, thereby manifesting better and satisfying overall performances than large-scale PSO algorithms. The numerical solver is designed on the pairwise competition concept basis and modified to better match the investigated scenarios.

A case study is employed to test and verify the effectiveness of the proposed approach, where the power dispatch and appliance time scheduling on a daily basis are applied to a typical South African household hybrid system. To thoroughly investigate the effectiveness, results from three cases, where different objective functions are applied with the new flexible power dispatch and the previous dispatch method, are illustrated and analyzed. For all cases, the CSO-based numerical solver is employed, and thus, the power dispatch methods are focused and compared.

The remainder of this paper is structured as follows: Section 2 introduces the hybrid system component modelling. Section 3 takes advantage of the component modelling to formulate the technoeconomic optimization problem. Section 4 describes the CSO-based numerical solver. Section 5 shows the case study with simulation results and analysis. Section 6 draws the conclusion.

2. Domestic PV-Battery Hybrid System

A domestic grid-connected PV-battery hybrid system is hereby employed as the investigated hybrid system. The general layout of the PV-battery hybrid system is illustrated in Figure 1. The main purpose of such a system is to supply the daily activities of a number of domestic appliances, e.g., electrical water heater (EWH), stove, television set, and washing machine. The involved appliances are connected to both the power grid and the PV system. A battery bank is also introduced to facilitate the power dispatch. The battery bank is able to charge from the power sources, which in this case are the power grid and PV system, and discharge to supply the appliances. In order to make use of all possible power sources in the system, a power management unit (PMU) is thereby introduced to implement the energy conversion and the power dispatch. In this way, the PMU manages the operation of the system, including (1) the selection of energy flow to support the active appliances, (2) the time scheduling of the appliances, and (3) the energy conversion and voltage/current matching. It is clear that the PMU is the central piece of the hybrid system that manages from power quality to energy balance. An assumption is employed that the voltage/current matching is well maintained by the PMU. Our investigation focuses on the power scheduling.

The power management diagram is depicted in Figure 2. There are several components in the PMU. From the PV side, there are a solar charge controller and inverter. The charge controller integrates a DC/DC converter to tune the PV output to match the DC loads, including the battery. The inverter receives input from the charge controller and battery and converts the DC power inputs into the AC loads, which in this case refer to the appliances. From the grid side, there is an AC charger integrating an AC/DC converter that allows the battery be charged by the grid. There are also a number of controllable switches to implement switching control strategies. As Figure 2 depicts, there is one switch for each power line. The ON/OFF states of the switches control the power flows in the system, i.e., the pair of the appliance and its supplier. For each connected appliance, there are a set of switches that control whether the appliance is supplied by the PV, the battery, or the power grid. The arrows on each power line indicate the direction of the power flow. As mentioned above, the additional switches are deployed such that any connected appliance can choose among multiple power sources by adjusting the ON/OFF status of switches. Taking advantage of the developing smart grid and smart building technologies, appliances are equipped with open communication interfaces, which allow the PMU to schedule the activities of the appliances and switches simultaneously, in both wired and wireless manners. As a result, the system design in Figure 2 becomes feasible in practice.

Remark 1. There are more and more domestic loads that can be made DC in the modern daily life; for example, an AC light bulb can be replaced with a DC light-emitting diode (LED) bulb. In the future, it is possible to connect the DC loads directly to the DC power sources, e.g., the PV and battery bank. Such a system may reduce the operational cost of renewable energy resources. However, currently, most domestic appliances are made AC for the sake of standardization. Consequently, the system design mainly focuses on the AC loads at the current stage; therefore, all involved power sources are tuned to be AC suppliers. Direct connections between the DC suppliers and the DC loads can be involved in the future design.

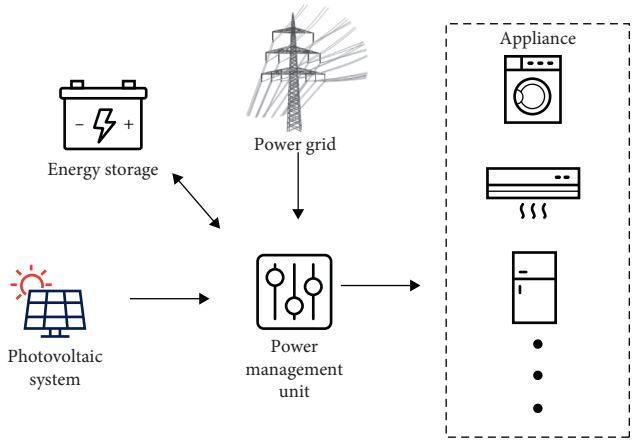

Figure 1: General layout of the hybrid system.

Assume that there are n appliances connected to the system. A set of binary variables are employed to denote the ON/OFF state of the switches. Let k denote the time instant during operation, $g_1(k)$ denotes the ON/OFF state of the switch between the PV charge controller and the battery, $g_2(k)$ the charge controller and the inverter, $g_3(k)$ the AC charger and the battery, and $g_4(k)$ the battery and the inverter. $g_{21}(k), g_{22}(k), \ldots, g_{2n}(k)$ denote the switches between the PV and the appliances, $g_{41}(k), g_{42}(k), \ldots, g_{4n}(k)$ the battery and the appliances, and $g_{51}(k), g_{52}(k), \ldots, g_{5n}(k)$ the grid and the appliances. t denotes the time instant over the operation. $P_1(k)$ and $P_4(k)$ denote the charging power from the PV and the grid, respectively. $P_2(k)$, $P_4(k)$, and $P_5(k)$ denote the power outputs of the respective power sources.

In this system, the operation of appliances is managed together with the power flows. In this study, the operation management is actually time scheduling, as the powers of appliances are considered known a priori and invariable. The time scheduling is implemented simultaneously with the power flow management such that the supply can match the demand and achieve higher energy efficiency potentials.

The mathematical formulations of the behavior for each component in the system are introduced as follows.

2.1. PV Systems. The PV consists of arrays of solar cells such that the solar energy is converted into electrical power. The converted power is proportional to the solar irradiation and the size of PV panels. As an alternative power source to the power grid, the power output is a major concern of the PV system. It is formulated as follows:

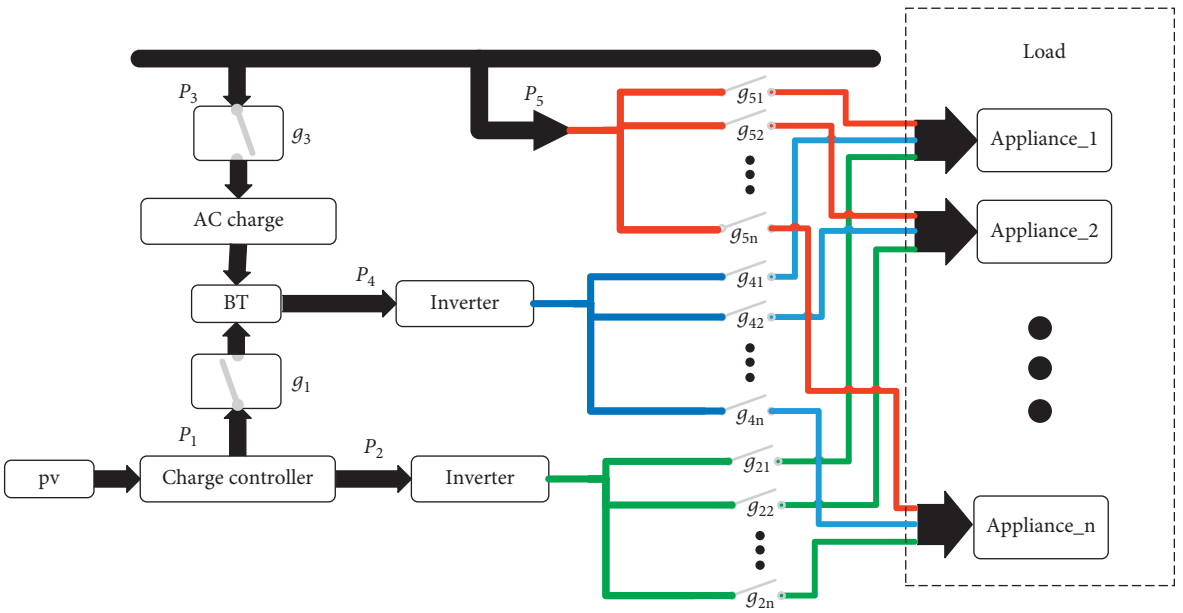

Figure 2: Schematic of the investigated power management system.

$$P_{pv} = \eta_{pv} I_{pv} A_c, \tag{1}$$

where P_{pv} denotes the hourly PV power output (kW), η_{pv} denotes the efficiency of the solar cells, I_{pv} denotes the hourly solar irradiation per unit area (kW/m^2), and A_c indicates the area of the PV panels that receive solar irradiation (m^2). There is an intermittent nature of the PV system; that is, I_{pv} can be absent at some sampling instants. An output profile of the PV system is therefore required. Usually, the PV outputs over succeeding 24 hours are predictable [19]. Q_{pv} denotes a time period where $P_{pv} > 0$. For $k \notin Q_{pv}$, P_{pv} is considered to be zero given a very small I_{pv}. A PV output profile is usually employed to indicate the hourly PV power outputs in a day . Q_{pv} can be identified via the PV output profile.

2.2. Battery Bank. The battery bank charges from other power sources and discharges to support electrical load activities. The battery bank behaviors are dynamic owing to the complicated scheduling of both power sources and appliances. The state of charge (SOC) is employed to characterize the battery bank status. The dynamics of the SOC can be formulated as follows:

$$\begin{aligned} \mathrm{Soc}(k+1) = \mathrm{Soc}(k) &+ \eta_B g_1(k) P_1(k) + \eta_B \eta_c g_3(k) P_3(k) \\ &- g_4(k) P_4(k), \end{aligned} \tag{2}$$

where $\mathrm{Soc}(k)$ denotes the SOC at sampling instant k; $g_1(k)$, $g_3(k)$, and $g_4(k)$ are binary variables that denote the ON/OFF state of the respective switches at instant k, as depicted in Figure 2; $P_1(k)$, $P_3(k)$, and $P_4(k)$ are the aforementioned power outputs; η_c denotes the energy conversion efficiencies of the AC charger; and η_B denotes the battery charging efficiency during operation. Given the current-stage battery system limitations, the simultaneous charging from two different sources or simultaneous charging and discharging are considered unpermitted. A constraint of the switches must be taken into account:

$$g_1(k) + g_3(k) + g_4(k) \le 1 \tag{3}$$

such that only one of the switches g_1, g_3, and g_4 can be turned on at the same time. Following (2), the SOC at a given time τ can be formulated as follows:

$$\begin{aligned} \mathrm{Soc}(\tau) = \mathrm{Soc}(0) &+ \eta_B \sum_{k=0}^{\tau} g_1(k) P_1(k) + \eta_B \eta_c \sum_{k=0}^{\tau} g_3(k) P_3(k) \\ &- \sum_{k=0}^{\tau} g_4(k) P_4(k), \end{aligned} \tag{4}$$

where $\mathrm{Soc}(0)$ denotes the initial state of the battery bank. $\mathrm{Soc}(k)$ is subject to the following constraint:

$$C^{\min} \le \mathrm{Soc}(k) \le C^{\max}, \tag{5}$$

where $C^{\min}$ and $C^{\max}$ denote the minimum and maximum available capacity (kWh), respectively.

The battery wear level is also evaluated. The wear cost is formulated as follows:

$$J_B(\tau) = \varphi_b C_D(\tau) \frac{B_C}{\mathrm{TH}}, \tag{6}$$

where $C_D(\tau) = \sum_{k=0}^{\tau} P_4(\tau)$ denotes the overall throughput of the battery bank until instant τ and B_C/TH denotes the battery wear cost per 1 kWh from throughput energy, in which B_C denotes the battery cost and TH denotes the overall throughput energy. The calculation of B_C/TH can be found from previous studies [15, 20, 21].

2.3. Power Grid. From the hybrid system viewpoint, the grid supplies infinite and stable electricity at an alternative

voltage level of 220 V. The grid power comes with a price, which results in the major operational costs. As mentioned above, a TOU tariff is introduced such that the demand response can be implemented. Let $\rho(k)$ denote the TOU electricity price at time k of a day. $\rho(k)$ changes according to which period the time k lies within. The overall operational cost at a given time τ can be formulated as follows:

$$\text{Cost}(\tau) = \sum_{k=0}^{\tau} \rho(k)\left[P_3(k) + P_5(k)\right]. \tag{7}$$

2.4. Appliances. The electrical loads consist of the load profiles of all appliances connected to the hybrid system. The boundary identification must be conducted before system design. Given the domestic scenario of the investigated system, several reasonable simplifications are made to characterize the demand-side activities. Firstly, all appliances within the system require standard AC power. Secondly, each appliance is subject to a respective constant operation duration. Control strategies can be involved to determine the operation of such appliances [22, 23].

According to previous studies [12–14], from the time-scheduling perspective, domestic appliances can be categorized into three types: the flexible loads, the shiftable loads, and the fixed loads. The flexible loads' working times can be scheduled freely, at any favorable working time. The shiftable loads' working times can be scheduled within a preferable but limited time period. The fixed loads' working times are fixed, unchangeable in any case. For an arbitrary appliance from any type, the operation duration is constant such that the time scheduling can be characterized as the selection of the starting instant.

In the investigated system, an appliance is connected to the PV, battery bank, and grid. An appliance i from the n appliances is given. As depicted in Figure 2, there is one switch for each power source connection. The ON/OFF states of the three switches at instant k are denoted by $g_{2i}(k)$, $g_{4i}(k)$, and $g_{5i}(k)$. The simultaneous supply from multiple power sources is unpermitted; therefore, a switch constraint is introduced as follows:

$$g_{2i}(k) + g_{4i}(k) + g_{5i}(k) \le 1, \quad i = 1, 2, \ldots, n. \tag{8}$$

Let St_i denote the starting instant of the appliance i and D_i the operation duration. The appliance continuously operates until the end instant, denoted by $En_i = St_i + D_i - 1$. A continuous operation constraint is introduced as Xia and Zhang proposed [24]:

$$\sum_{k=0}^{N-D_i+1} u_i(k)u_i(k+1)u_i(k+2)\ldots u_i\left(k+D_i-1\right) = 1, \quad i = 1, 2, \ldots, n, \tag{9}$$

where $u_i(k)$ is a binary variable that indicates whether the appliance i is active at time k, i.e., the time schedule, and N denotes the length of a finite scheduling period. In this case, $u_i(k) = 1$ if $St_i \le k \le En_i$, and $u_i(k) = 0$ if otherwise. It is notable that the continuous operation constraint is associated with the actual switch behavior in the following way:

$$\begin{cases} g_{2i}(k) + g_{4i}(k) + g_{5i}(k) = 1, & \text{if } u_i(k) = 1, \\ g_{2i}(k) + g_{4i}(k) + g_{5i}(k) = 0, & \text{if } u_i(k) = 0. \end{cases} \tag{10}$$

Let $\overline{p}_i(t)$ with $t = 0, 1, 2, \ldots, D_i - 1$ denote the load profile over the operation period $(0, D_i - 1)$ of the appliance i. Assuming that $\overline{p}_i(t)$ are known a priori, the power demand $p_i(k)$ can thus be determined: if $k = Si + t$, $p_i(k) = \overline{p}_i(t)$; otherwise, $p_i(k) = 0$.

2.5. System Constraints. A series of constraints must be introduced to the system such that the operation requirements are all satisfied and none of the physical laws is violated.

(a) The energy balance must be fulfilled anytime during operation, as indicated by the following equation:

$$\begin{bmatrix} \eta_{I2}P_2(k) \\ \eta_{I4}P_4(k) \\ P_5(k) \end{bmatrix} = \sum_{i=1}^{n} \begin{bmatrix} g_{2i}(k) \\ g_{4i}(k) \\ g_{5i}(k) \end{bmatrix} p_i(k), \tag{11}$$

where $P_2(k)$, $P_4(k)$, and $P_5(k)$ are the power flows from the PV output, battery bank discharge, and power grid supply and η_{I2} and η_{I4} denote the inverter efficiency of the PV and battery bank, respectively. For the convenience of calculation, a logical state variable $sw_i(k)$ is employed to describe the combination of $g_{2i}(k)$, $g_{4i}(k)$, and $g_{5i}(k)$. $sw_i(k)$ chooses a value from $\{0, 1, 2, 3\}$. $sw_i(k) = 0$ indicates the state that all switches are turned off and the switch states equal to 0. $sw_i(k) = 1$ indicates that only $g_{2i}(k) = 1$, $sw_i(k) = 2$ that only $g_{4i}(k) = 1$, and $sw_i(k) = 3$ that only $g_{5i}(k) = 1$.

(b) The capacity constraints must be followed such that the power flow is kept within the range of the component capacity. The power flows in the system are thus limited. The power flows $P_1(k)$ and $P_2(k)$ are subject to the following constraint:

$$0 \le P_1(k) + P_2(k) \le \eta_s P_{pv}(k), \tag{12}$$

where $P_{pv}(k)$, as mentioned above, is the PV output at time k and η_s denotes the charge controller efficiency. The power flows $P_2(k)$ and $P_4(k)$ as the supplier are subject to the following constraints:

$$\begin{cases} 0 \le \eta_{I2}P_2(k) \le P_{I2}(k), \\ 0 \le \eta_{I4}P_2(k) \le P_{I4}(k), \end{cases} \tag{13}$$

where $P_{I2}(k)$ and $P_{I4}(k)$ denote the inverter capacity of the PV and battery bank, respectively. The power flows $P_3(k)$ and $P_5(k)$ are subject to the following constraint:

$$0 \le g_3(k)P_3(k) + P_5(k) \le P_G^{\max}, \tag{14}$$

where $P_G^{\max}$ denotes the allocated grid maximum power for this grid-connected system. The power flows $P_2(k)$, $P_4(k)$, and $P_5(k)$ are obtained from the energy balance equation (11). $P_1(k)$ and $P_3(k)$ are decided by the scheduling algorithm, and they are part of the decision variables.

(c) The switch control strategies are also subject to constraints that prevent infeasible switch behaviors. These constraints are formulated in preceding sections along with the system component modelling, i.e., constraints (3) and (8)–(10). Some further associations of the switch behaviors are identified as follows:

$$\begin{cases} g_1(k) = 1, & \text{if } P_1(k) > 0, \\ g_1(k) = 0, & \text{if } P_1(k) = 0, \\ g_3(k) = 1, & \text{if } P_3(k) > 0, \\ g_3(k) = 0, & \text{if } P_3(k) > 0, \end{cases} \tag{15}$$

$$\begin{cases} g_2(k) = 1, & \text{if } \prod_{i=1}^{n} \left(\mathrm{sw}_i(k) - 1\right) = 0, \\ g_2(k) = 0, & \text{if otherwise}, \\ g_4(k) = 1, & \text{if } \prod_{i=1}^{n} \left(\mathrm{sw}_i(k) - 2\right) = 0, \\ g_4(k) = 0, & \text{if otherwise}. \end{cases} \tag{16}$$

In this way, the states of $g_1(k)$–$g_4(k)$ at time k can be identified from the values of $P_1(k)$, $P_3(k)$, and $\mathrm{sw}_i(k)$ with $i = 1, 2, \ldots, n$.

3. Problem Statement

The primary management objective of the investigated optimization problem is cost minimization. Secondly, the renewable energy penetration is involved; that is, the usage of grid power should be minimized as well. Owing to the TOU tariff, the two objectives manifest certain differences and must be equally considered in scheduling. Furthermore, the user satisfaction in time scheduling is taken into account. All these objectives are evaluated on a finite horizon basis. Let T denote the number of sampling instants. The optimization problem is formulated as follows.

3.1. Decision Variables. The involved decision variables consist of three parts: (1) the switch control strategy decision variables, (2) the charging power control variables, and (3) the appliance time-scheduling decision variables. It is given that $i = 1, 2, \ldots, n$ in the following discussion.

The switch control variables are $\mathrm{sw}_i(k)$, which can characterize the status of most switches in the system as constraints (15) and (16) imply. Given constraints (8)–(10), it is unnecessary to cover the whole finite horizon. For the appliance i, $\mathrm{sw}_i(k) > 0$ when $St_i \le k \le En_i$, and $\mathrm{sw}_i(k) = 0$ if k lies outside the working period. Therefore, the minimum required control variables are $\mathrm{sw}_i(k)$ with $k \in [St_i, En_i]$. The dimension of this part is $\sum_{i=1}^{n} D_i$.

The charging power control variables are $P_1(k)$ and $P_3(k)$. Given constraints (3) and (15), $P_1(k) * P_3(k) = 0$ at any given instant k; therefore, the dimension of this part is T.

As mentioned above, the appliance time scheduling is simplified with the known a priori and constant load profile $\overline{p}_i(t)$ and operation duration D_i. Taking advantage of the knowledge, the scheduling is implemented with decision variables St_i. The dimension of this part is n.

The dimension of the optimization is therefore $\sum_{i=1}^{n} D_i + T + n$. Comparing with the previous study [15], the problem is extended to a higher dimension but simplified by taking advantage of $\mathrm{sw}_i(k)$ and the constraints such that the dimension of the optimization grows slower than the problem scale.

3.2. Objectives. The cost minimization objective is formulated as follows:

$$J_c = \sum_{k=0}^{T} \rho(k)\left[P_3(k) + P_5(k)\right] + \varphi_b J_B(T), \tag{17}$$

where φ_b denotes a weight that indicates the preferable importance of the battery wearout to the decision-maker.

The renewable energy penetration objective is formulated as follows:

$$J_e = \sum_{k=0}^{T} \left[P_3(k) + P_5(k)\right]. \tag{18}$$

The user satisfaction is evaluated via an inconvenience indicator, which is adopted from the study of Setlhaolo and Xia [12]:

$$\beta = \sum_{i=1}^{n} \gamma_i \sum_{k=0}^{T} \left[u_i^{bl}(k) - u_i(k)\right]^2, \tag{19}$$

where γ_i denotes an importance factor of the appliance i and $u_i^{bl}(k)$ denotes the baseline time schedule of the appliance i. (19) quantifies the difference between the baseline time schedule and the adopted time schedule. Given the system modelling and constraints in this study, the user satisfaction evaluation is simplified as follows:

$$\beta = \sqrt{\sum_{i=1}^{n} \gamma_i \left[St_i^{bl} - St_i\right]^2}, \tag{20}$$

where St_i^{bl} denotes the baseline starting instant. Such a difference has to be minimized such that the user remains happy with the optimized appliance time schedule.

3.3. Technoeconomic Optimization. Taking advantage of the preceding objective functions and constraint formulations, the technoeconomic optimization problem is obtained by minimizing the following objective function:

$$J\left(\mathrm{sw}_i(k), P_1(k), P_3(k), St_i\right) = \lambda_c J_c + \lambda_e J_e + \lambda_b \beta, \quad (21)$$

subject to the battery dynamics (2) and constraints (3), (8)–(10), and (11)–(16).

According to the above formulations, there are nonlinear objective functions and constraints, as well as continuous and discrete decision variables in the problem. They result in a mixed-integer nonlinear programming (MINLP) problem, at a relatively large scale. The general theoretic approach of solving an MINLP problem remains an open question; as a result, numerical solvers are widely employed. In the previous study [15], an OTPI toolbox https://www.inverseproblem.co.nz/OPTI/index.php/DL/DownloadOPTI/ in MATLAB was adopted as the numerical solver. The former solver took quite a large amount of time for calculation. In this study, the implementation of intelligent optimization algorithms on such a problem is investigated. A newly proposed algorithm named the competitive swarm optimizer (CSO) is adopted as the numerical solver. The introduction to the CSO-based solver comes in the following section.

4. Numerical Solver Design

4.1. Competitive Swarm Optimizer. In the CSO algorithm, let x denote a particle and w and l the indices of the winner and loser particles in a pair. Assume that it is the G-th iteration, and there have been $k-1$ competitions. After the k-th competition, the next-generation winner particle $x_{w,k}(G+1)$ remains the same as $x_{w,k}(G)$. The loser particle $x_{l,k}(G+1)$, namely, the position vector, is thereby updated as follows:

$$x_{l,k}(G+1) = x_{l,k}(G) + V_{l,k}(G+1), \quad (22)$$

where $V_{l,k}(G+1)$ is the next-generation velocity vector, updated as follows:

$$V_{l,k}(G+1) = rn_1(k,G)V_{l,k}(G) + rn_2(k,G)\left[x_{w,k}(G) - x_{l,k}(G)\right] + \varphi rn_3\left[\overline{x}_k(G) - x_{l,k}(G)\right], \quad (23)$$

where rn_1, rn_2, and rn_3 are random vectors; $\overline{x}_k(G)$ is the center of neighborhood filed particles, i.e., a set of particles that are close enough to $x_{l,k}(G)$; and φ is the weighting coefficient of $\overline{x}_k(G)$. Such a neighborhood field is predefined. There is a special case that the neighborhood covers the whole swarm, where $\overline{x}_k(G)$ indicates the global mean position of the particles at iteration G. The velocity and position vectors are employed for the continuous cases. In a discrete case, e.g., the decision variables $\mathrm{sw}_i(k)$ in this study, other update mechanisms must be employed. A crossover mechanism is hereby employed as follows:

$$\begin{cases} x_{l,k}(rn, G+1) = x_{w,k}(rn, G), \\ x_{l,k}(\overline{rn}, G+1) = x_{l,k}(\overline{rn}, G), \end{cases} \quad (24)$$

where rn denotes randomly generated indices of the components in a particle x and $\overline{rn}$ the unselected indices. (24) suggests that the winner particle $x_{w,k}(G)$ selects and copies a part of its components into the next-generation loser particle $x_{l,k}(G+1)$. The unselected components of $x_{l,k}(G+1)$ remain the same as $x_{l,k}(G)$. In this way, the loser particle can learn from the winner particle.

For an MINLP problem, there are simultaneously continuous and discrete components in a particle. In this case, the continuous part and discrete part are separated, (23) and (22) are implemented on the continuous part, and (24) is implemented on the discrete part. After the learning process, the two updated parts are combined again to obtain the particle of next generation. The theoretical proof of the convergence of the CSO algorithm can be referred to [17].

The pseudocode of the CSO according to the preceding introduction is illustrated in Algorithm 1 [25].

Remark 2. The introduced CSO algorithm is mainly designed for continuous problems. For discrete decision variables, e.g., binary variables or integers, the discrete PSO algorithm [26, 27] can facilitate the algorithm design. The pairwise competition can be further introduced to other evolutionary algorithms, such as differential evolution (DE).

Remark 3. Given the investigated MINLP problem (21), the original CSO algorithm cannot be applied in a straightforward way. Modifications that match the decision variables are to be introduced such that satisfying performances can be achieved.

4.2. Modified CSO-Based Solver. In order to implement the CSO algorithm on a constrained problem, a penalty function is introduced to the original objective function (17). Given that there are N_C constraints to a problem, the penalty function is formulated as follows:

$$P_{\mathrm{en}} = \sum_{k=0}^{T} \sum_{i=0}^{N_C} \omega_{\mathrm{Pen},i} P_{\mathrm{en},i}(k), \quad (25)$$

where

$$P_{\mathrm{en},i}(k) = \begin{cases} 0, & \text{if constraint } i \text{ is obeyed,} \\ M, & \text{if constraint } i \text{ is violated,} \end{cases} \quad (26)$$

where M is a large positive number and $\omega_{\mathrm{Pen},i}$ is the weighting factor for constraint i. A fitness function is thereby formulated with (17), (25), and (26):

$$f(x) = J_c + P_{\mathrm{en}}. \quad (27)$$

In this way, for a minimization problem, a particle becomes much less competitive when any of the constraints

Definition:
x: the particle;
P: the swarm;
np: the swarm size, i.e., the number of particles;
G: number of iterations;
w and l: the indices of winner and loser particles;
$f(\cdot)$: the fitness function, assuming that this is a minimization problem;
Terminal condition: the maximum number of iteration Mg is reached;

Begin
Initialize population $P(1)$ with np particles;
while $G = 1$ to Mg **do**
  P$(G+1) = \varnothing$;
  while $P(G) \neq \varnothing$ **do**
    Generate two random indices r_1 and r_2 from np;
    if $f(x_{r_1}) \leq f(x_{r_2})$ **then**
      $w = r_1, l = r_2$;
    else
      $w = r_2, l = r_1$;
    end if
    put $x_w(G)$ into $P(G+1)$;
    If x is coded as continuous variables, update $x_l(G)$ with (23) and (22);
    If x is coded as discrete variables, update $x_l(G)$ with (24);
    If x contains both continuous and discrete parts, update the two parts separately;
    put the updated loser particle $x_l(G)$ into $P(G+1)$;
    remove particles x_{r_1} and x_{r_2} from $P(G)$;
  end while
  $G = G + 1$;
end while
choose x_{best} the particle with the best fitness $\widehat{f}(\cdot)$ from P_{Mg};
Return x_{best};
End

Algorithm 1: Pseudo code of the CSO algorithm.

is violated, given that a large positive will be added to the objective function.

After competition, the loser particle must learn from the winner particle. However, the MINLP search space and constraints in the investigated problem are quite complicated. The dynamics of the battery bank charging and discharging invoke further difficulty to search for the optimum. Consequently, the performance of Algorithm 1 is not satisfying. The following modifications are thereby employed to improve the performances on this specific problem.

Firstly, the learning strategies are modified to improve the searching efficiency. Let $\overline{f}(G)$ denote the mean fitness of the current swarm (at the G-th iteration). After competition, the fitness of both winner and loser particles is evaluated:

(i) If $f(x_{w,k}(G)) \geq \overline{f}(G)$, both winner and loser particles are considered inferior; therefore, the winner particle must learn from the global best particle $x_{\text{gbest}}(G)$, while the loser particle must learn from the winner.

(ii) If $f(x_{l,k}(G)) \leq \overline{f}(G)$, both winner and loser particles are considered superior; therefore, the winner particle is moved into $P(G+1)$, and the loser particle implements mutation subject to the genetic algorithm style.

(iii) If $f(x_{w,k}(G)) \leq \overline{f}(G) < f(x_{l,k}(G))$, the original CSO learning strategies are applied.

Secondly, constraints (3) and (15) are employed to generate battery bank charging and discharging states, namely, the "knowledge-guided solution filter". $\forall k$, $g_4(k)$ is firstly identified subject to (16). If $g_4(k) = 1$, then $P_1(k) = P_3(k) = 0$. If $g_4(k) = 0$, then $P_1(k)$ is randomly generated within $[0, P_{pv}(k) - P_2(k))$. If $g_4(k) = 0$ and $P_1(k) = 0$, then $P_3(k)$ is randomly generated. If the $\text{Soc}(k)$ reaches its upper bound at time k, then $P_1(k) = P_3(k) = 0$. In this way, the charging and discharging decision variables are guaranteed to be feasible. The knowledge-guided solution filter reduces cost of trial and error during optimization such that the algorithm can persist searching within a feasible space.

Remark 4. According to simulations, the modified solver constantly outperforms the original CSO algorithm on the investigated problem. There lacks a theoretical analysis on the performances, whereas a hypothesis is made that the superior performances are resulted from the knowledge-guided solution filter. Wang and Zheng [28] reported that exploitation of the algorithm is enhanced by knowledge-based local search. Further details and investigations are expected in future works.

Table 1: Typical usage profiles and baseline time schedules.

Appliances Index i	Power (kW)	Duration (min)	Baseline St_i	Baseline En_i	Preferable range of St_i
Shiftable					
(1) EWH	3.0	120	31	42	[19, 31]
		120	104	115	[91, 121]
(2) Stove	2.5	30	32	34	[25, 55]
		50	113	117	[97, 127]
(3) Washing machine	0.5	60	109	114	[43, 133]
(4) Electric dryer	2.0	30	116	118	[49, 139]
Fixed					
(5) Refrigerator	0.1	1440	1	144	N/A
(6) Television set	0.2	180	104	121	N/A
Flexible					
(7) Dishwasher	1.8	150	116	130	[1, 130]
(8) Bread maker	1.5	150	118	132	[1, 130]

5. Simulation Results and Analysis

5.1. Case Study. The case study investigates the operation of a household, grid-connected, PV-battery hybrid energy system. The data are retrieved from the South African domestic appliance operation studies [13–15]. There are eight appliances connected in the system. The usage profile of the appliances is shown in Table 1 on a daily basis, where there are 144 time slots, a.k.a., sampling instants. Each time slot lasts 10 minutes. The scheduling horizon is 24 hours, i.e., a whole day. The adopted usage profile and baseline time schedule are for the working day scheduling for a typical South African home. To emphasize, the power of the appliances is measured average power. The baseline time schedule reflects the preferable time according to the inhabitant's habits. For example, the inhabitant turns on the electrical water heater (EWH) twice a day for the hot water demand. In the morning, the EWH is turned on at 5 : 00 am (the 31-st time slot), operates for two hours, and is turned off at 7 : 00 am (the 42-nd time slot) such that the user can use heated water after breakfast. In the afternoon, the EWH is turned on again at 5 : 10 pm (the 104-th time slot) and turned off at 7 : 10 pm (the 115-th time slot) such that the hot water for the evening can be ready. This is the most convenient EWH operation plan for the user. Similarly, the stove must be turn on twice for the cooking demands. The other appliances have to be turned on and off only once daily.

There are several further constraints with the given scenario. Firstly, for the shiftable appliances, a preferable range of starting time slots are given in Table 1. The flexible appliance can start anytime in a day, and the only requirement is that the operation must be finished before the end of the horizon. The fixed appliance cannot be scheduled; therefore, the preferable range is not applicable (N/A). Secondly, the washing machine and electrical dryer work in a sequence; that is, the dryer must start after the washing machine job is finished. In this case, it results in an additional constraint to the preceding ones:

$$St_4 \geq St_3 + D_3. \tag{28}$$

Table 2: PV system and battery bank parameters.

PV capacity P_{pv}	3.5 kW$_p$
Battery bank maximum capacity $C^{\max}$	5.04 kWh
Battery bank minimum capacity $C^{\min}$	2.52 kWh
Battery bank cost (ZAR)	R5826
Initial state of the battery bank	60%$C^{\max}$
AC charger efficiency η_c	85%
PV charge controller efficiency η_s	90%
PV inverter efficiency η_{I2}	95%
Battery bank inverter efficiency η_{I4}	95%
Battery bank charging efficiency η_B	80%

Table 3: Hourly PV output.

Time slot k	[0, 39)	[39, 45)	[45, 51)	[51, 57)
$P_{pv}(k)$ (kWh)	0	0.15	0.85	1.65
[57, 63)	[63, 69)	[69, 75)	[75, 81)	[81, 87)
2.35	2.9	3	2.95	2.55
[87, 93)	[93, 99)	[99, 105)	[105, 111)	[111, 144)
2	1.45	0.75	0.1	0

The adopted PV system and battery bank have their own limitations, as shown in Table 2. The PV system integrates 14 solar panels with the rated power of 0.25 kW. Therefore, the overall capacity, i.e., the rated output, of the PV system is 3.5 kW. Actually, the PV system output at any given time slot depends on the solar irradiation profile. Such a profile is possible to forecast 24 hours ahead of the scheduling [19]. In the case study, the timely PV output is identified based on an hourly profile in [29], as shown in Table 3, where Q_{pv} is $k \in [39, 144)$. The battery bank consists of 4 lead-acid batteries, each with 12 V rated voltage and 105 Ah rated capacity; that is, the overall capacity is 5.04 kWh. The battery cost is calculated in South African rand (ZAR), which is R5826. The lifespan of the battery bank is 1000 cycles at 50% depth of discharge (http://www.trojanbattery.com/markets/renewable-energy-re/); therefore, the wear cost per 1 kWh throughput energy is $5826/(1000 * 0.5 * 5.04) = 2.312$ R/kWh. $\varphi_b = 0.1$

Table 4: TOU tariff.

Time periods	Electricity price	Hours
Peak hours	R2.2225/kWh	[08 : 00, 11 : 00) ∪ [19 : 00, 21 : 00)
Standard hours	R0.6773/kWh	[07 : 00, 08 : 00) ∪ [11 : 00, 19 : 00) ∪ [21 : 00, 23 : 00)
Off-peak hours	R0.3656/kWh	[00 : 00, 07 : 00) ∪ [23 : 00, 24 : 00)

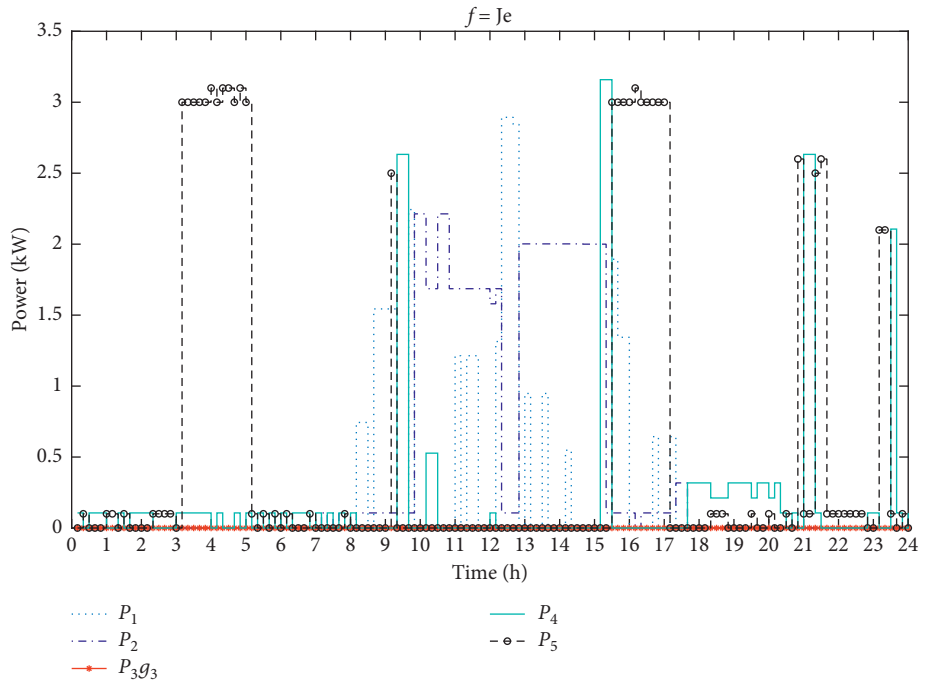

Figure 3: Power dispatch of the new design in case (i).

such that the usage of the battery is encouraged. The importance factors $\gamma_i = 1$ for each i, i.e., involved appliances, are considered equally important in this case. The efficiencies of the charge controller, AC charger, and inverters are given as well.

The power grid supply is described as follows: The maximum household current is 60 A, which is limited by the utility company. The charging power from the grid is considered constant in this case, which is 5 kW; that is, $P_3(k)$ can only be 0 or 5 kWh. Furthermore, the TOU tariff is adopted from the study in [13], as shown in Table 4.

5.2. Simulations. Simulations are programmed in C++ with the following running environment: the CPU is Inter Core i3-8100 CPU@3.60 GHz, the RAM is 16 GB, and the system is Windows 10 × 64. Three cases are adopted by adjusting the weighting factors in (21).

(i) $\lambda_e = 1$, $\lambda_c = 0$, and $\lambda_b = 0$ such that the optimization employs a single objective, i.e., the renewable energy penetration.

(ii) $\lambda_e = 0$, $\lambda_c = 1$, and $\lambda_b = 0$ such that only the cost minimization objective is optimized.

(iii) $\lambda_e = 1$, $\lambda_c = 1$, and $\lambda_b = 1$ such that the multi-objective optimization of (21) is implemented where J_c, J_e, and β are equally considered.

In each case, there are two demonstrated results. One result is from the proposed approach, and the other one is from the previous power dispatch model [15] as the comparative results. Both results are reported from the average of 20 runs, taking advantage of the proposed CSO-based optimizer. In the CSO algorithm, the swarm size is 1500 and the iteration number is 10000. The neighborhood field is defined to be the nearest superior particle and inferior particle. The details of such a neighborhood field can be referred to [30, 31].

5.3. Results and Analysis. The results are reported as follows:

(i) In the first case, the grid power supply is minimized to be 14 kWh, at the energy cost of R16.57 and inconvenience indicator of 14.25. The power dispatch is depicted in Figure 3. In the comparative result, the minimal grid power is 15.07 kWh, at the energy cost of R14.29 and inconvenience indicator of 14.59. The power dispatch is depicted in Figure 4. The improvement of the objective is 7.1%. The average running time is 18.43 minutes.

(ii) In the second case, the cost is minimized to be R7.06, while the overall power supply from the grid is 14.37 kWh. The inconvenience indicator is 13.89. The power dispatch is depicted in Figure 5. In the comparative result, the minimal cost is R7.72, with

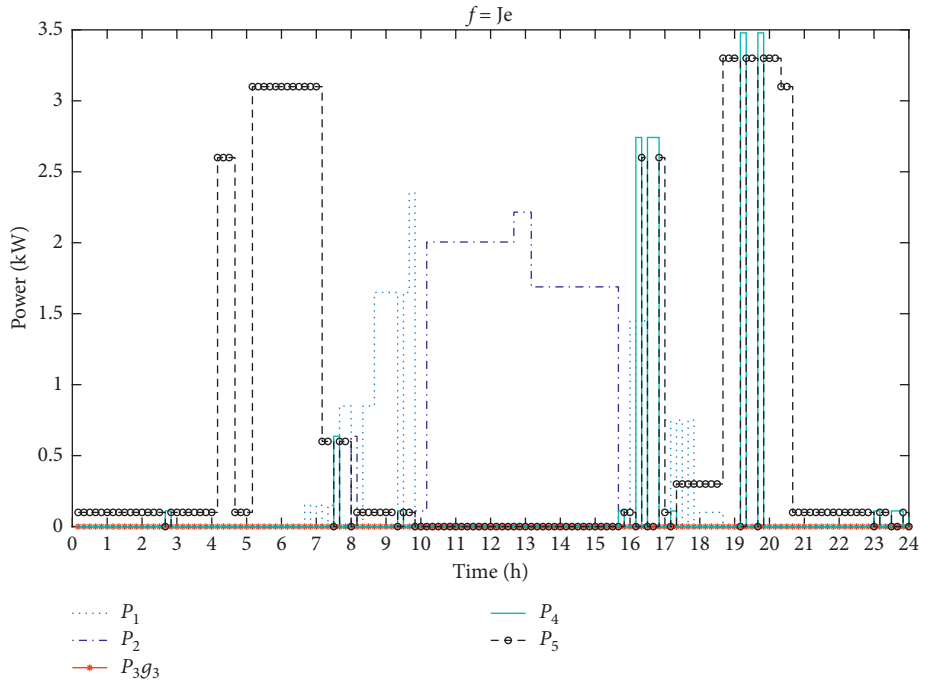

Figure 4: Power dispatch of the previous design in case (i).

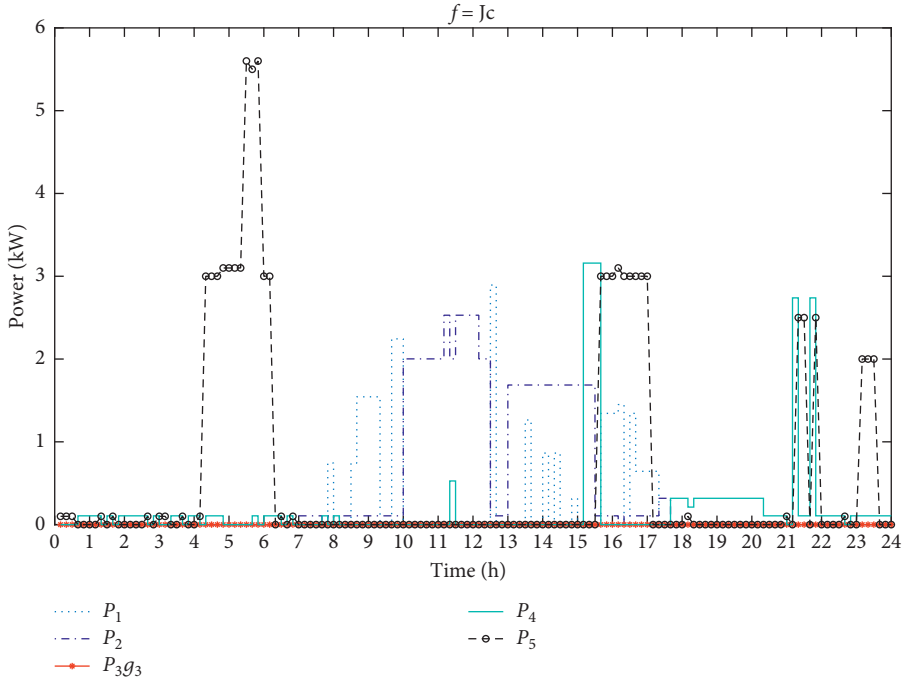

Figure 5: Power dispatch of the new design in case (ii).

the grid power supply of 15.57 kWh and inconvenience indicator of 15.03. The power dispatch is depicted in Figure 6. The improvement of the objective is 8.6%. The average running time is 18.36 minutes.

(iii) In the third case, the weighted sum of all objectives is minimized. The optimized objective function value is 34.64, when the energy cost is R8.29 and the grid power supply is 15.53 kWh, and the inconvenience indicator is 10.82. The power dispatch is depicted in Figure 7. In the comparative result, the objective function value is 39.97, where the energy cost is 9.53 and grid power is 18.78 kWh, with the inconvenience indicator of 11.66 as well. The power dispatch is depicted in Figure 8. The improvement of the objective is 13.3%. The average running time is 18.37 minutes.

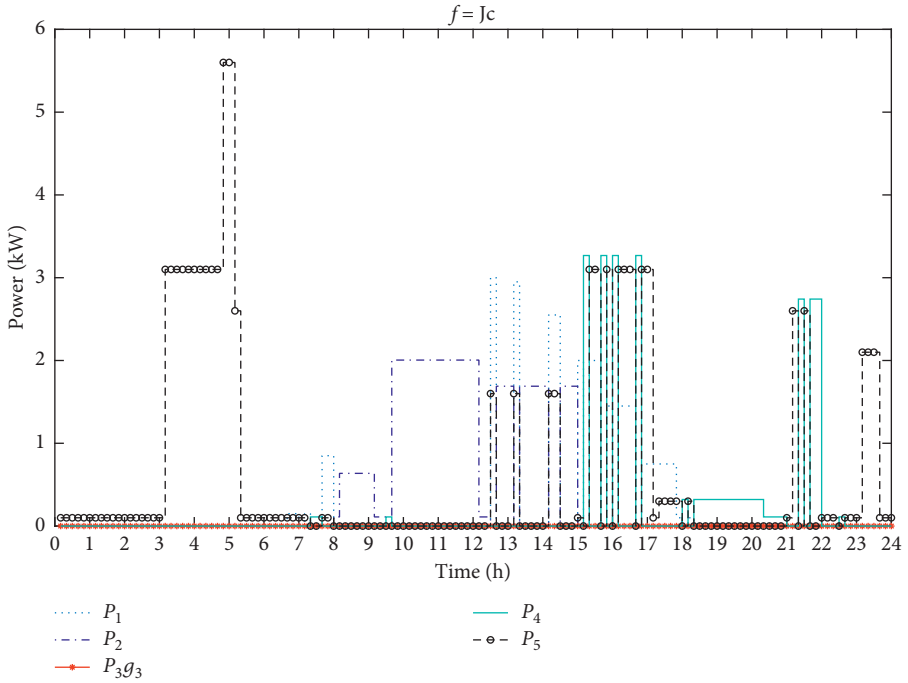

Figure 6: Power dispatch of the previous design in case (ii).

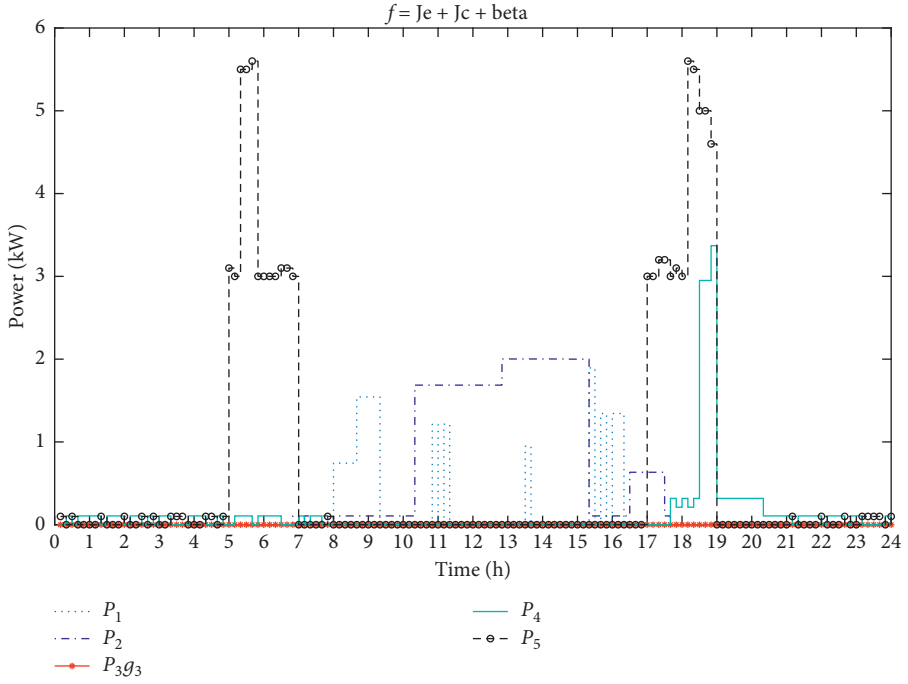

Figure 7: Power dispatch of the new design in case (iii).

From Figures 3, 5, and 7, overlaps between different power supplies can be observed especially during peak hours, while from Figures 4, 6, and 8, none of the time slots allows multiple power supplies. In these cases, the grid power outputs are smoothened under the dispatch with the proposed approach. From the comparative results, supplies become more intermittent because of the contradiction between the renewable penetration objective and the supply constraint. Allowing the combination of multiple power supplies reduces such an intermittent performance while, according to the energy and economy performances in case studies, making better use of the renewable energy sources.

As a conclusion, the proposed approach outperforms the previous model in all cases. When comparing the results of the new and previous designs, it appears that the flexible power dispatch allows more appliances to be scheduled to

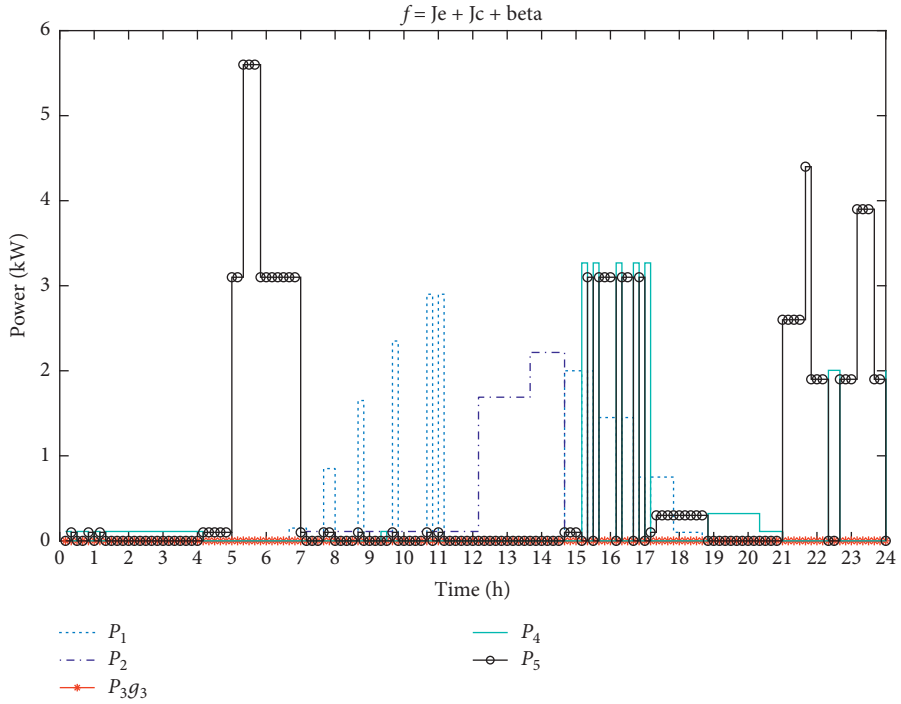

Figure 8: Power dispatch of the previous design in case (iii).

standard and off-peak hours, resulting in a lower energy cost. The objectives J_e and J_c manifest a certain level of trade-off. This is resulted from the employment of the TOU tariff, where some off-peak hours may be infeasible for the PV system because of its intermittent nature. When comparing the results among the three cases, it can be found that the first two cases can achieve lower energy cost and grid power consumption because of ignoring the inconvenience indicator β. It invokes an interesting topic for future studies that how to strike a balance between the conflicted interests of user satisfaction and energy efficiency in such a hybrid energy system management.

6. Conclusions

This paper investigates a technoeconomic optimization problem for a domestic grid-connected PV-battery hybrid energy system, via extending and improving a previously proposed system design. According to the previous design, the power dispatch is decided for the totality of the electrical loads. In the new model, appliances that comprise the electrical loads are supplied and managed, respectively, via additional power lines and switches from each power source. Furthermore, the appliance time scheduling is incorporated into such a flexible power dispatch. In this way, the system achieves better energy efficiency and economic performances via the technoeconomic optimization. The performances are evaluated by three optimization objectives: minimizing energy cost, maximizing renewable energy penetration, and increasing user satisfaction, over a finite horizon. There are nonlinear objective functions and constraints, as well as discrete and continuous decision variables, in such an optimization problem. As a result, the problem becomes an MINLP one at a large scale, which is difficult to solve. A competitive swarm optimizer-based numerical solver is thereby designed and employed.

In order to verify that the new design does improve the performances, a case study is investigated, where the power dispatch and appliance time scheduling on a daily basis are applied to a typical South African household hybrid system. There are three optimization cases, each with different objective functions, including only energy cost minimization, only renewable energy penetration maximization, and a weighted sum of the three objectives. Simulations are applied in these cases, where comparative results are also obtained via optimization of the previous system design. The same solver and system configurations are employed. In all cases, the results from the new design outperform results from the previous design. The improvement ranges from 7.1% to 13.3% and manifests that further energy efficiency and economic benefits can be achieved by the proposed approach. Furthermore, the solver generally takes around 18.4 minutes to obtain the solution. It verifies that the proposed approach has the potential for application in a real-time context.

There are several future works to investigate based on the current-stage results. Firstly, the performance evaluations, such as the battery wear cost and the renewable energy penetration, are simplified. More practical indicators can be introduced in the future. Secondly, uncertainties from the environment and user demands are inevitable in practice. The real-time feedback mechanism can be introduced to overcome such uncertainties. Thirdly, the game theory-based power dispatch and load scheduling considering conflicted interests call further study. Lastly, the CSO-based

numerical solver can be further investigated to improve the algorithm performance.

Data Availability

All relevant data used to support the findings of this study are included within the article.

Conflicts of Interest

The authors declare that there are no conflicts of interest regarding the publication of this paper.

Acknowledgments

This work was supported by the National Nature Science Foundation of China under Grant 61803162 and the Fundamental Research Funds for the Central Universities under Grant HUST: 2017KFYXJJ178.

References

[1] J. Soares, T. Pinto, F. Lezama, and H. Morais, "Survey on complex optimization and simulation for the new power systems paradigm," *Complexity*, vol. 2018, Article ID 2340628, 32 pages, 2018.

[2] B. Zhu, H. Tazvinga, and X. Xia, "Switched model predictive control for energy dispatching of a photovoltaic-diesel-battery hybrid power system," *IEEE Transactions on Control Systems Technology*, vol. 23, pp. 1229–1236, 2014.

[3] S. Shaahid and M. Elhadidy, "Economic analysis of hybrid photovoltaic–diesel–battery power systems for residential loads in hot regions—a step to clean future," *Renewable and Sustainable Energy Reviews*, vol. 12, pp. 488–503, 2008.

[4] P. Nema, R. Nema, and S. Rangnekar, "A current and future state of art development of hybrid energy system using wind and pv-solar: a review," *Renewable and Sustainable Energy Reviews*, vol. 13, pp. 2096–2103, 2009.

[5] X. Li, J. Lai, and R. Tang, "A hybrid constraints handling strategy for multiconstrained multiobjective optimization problem of microgrid economical/environmental dispatch," *Complexity*, vol. 2017, Article ID 6249432, 12 pages, 2017.

[6] T. Cheng, M. Chen, Y. Wang et al., "Adaptive robust method for dynamic economic emission dispatch incorporating renewable energy and energy storage," *Complexity*, vol. 2018, Article ID 2517987, 13 pages, 2018.

[7] X. Chen, B. Xu, and W. Du, "An improved particle swarm optimization with biogeography-based learning strategy for economic dispatch problems," *Complexity*, vol. 2018, Article ID 7289674, 15 pages, 2018.

[8] R. Kallel, G. Boukettaya, and L. Krichen, "Demand side management of household appliances in stand-alone hybrid photovoltaic system," *Renewable Energy*, vol. 81, pp. 123–135, 2015.

[9] S. Phiri and K. Kusakana, "Demand side management of a grid connected pv-wt-battery hybrid system," in *Proceedings of the 2016 International Conference on the Industrial and Commercial Use of Energy (ICUE)*, pp. 45–51, IEEE, Cape Town, South Africa, August 2016.

[10] H. Tazvinga, X. Xia, and J. Zhang, "Minimum cost solution of photovoltaic–diesel–battery hybrid power systems for remote consumers," *Solar Energy*, vol. 96, pp. 292–299, 2013.

[11] H. Tazvinga, B. Zhu, and X. Xia, "Energy dispatch strategy for a photovoltaic–wind–diesel–battery hybrid power system," *Solar Energy*, vol. 108, pp. 412–420, 2014.

[12] D. Setlhaolo and X. Xia, "Optimal scheduling of household appliances with a battery storage system and coordination," *Energy and Buildings*, vol. 94, pp. 61–70, 2015.

[13] S. M. Sichilalu and X. Xia, "Optimal energy control of grid tied pv–diesel–battery hybrid system powering heat pump water heater," *Solar Energy*, vol. 115, pp. 243–254, 2015.

[14] D. Setlhaolo and X. Xia, "Combined residential demand side management strategies with coordination and economic analysis," *International Journal of Electrical Power & Energy Systems*, vol. 79, pp. 150–160, 2016.

[15] F. Yang and X. Xia, "Techno-economic and environmental optimization of a household photovoltaic-battery hybrid power system within demand side management," *Renewable Energy*, vol. 108, pp. 132–143, 2017.

[16] C. Kagiri, E. M. Wanjiru, L. Zhang, and X. Xia, "Optimized response to electricity time-of-use tariff of a compressed natural gas fuelling station," *Applied Energy*, vol. 222, pp. 244–256, 2018.

[17] R. Cheng and Y. Jin, "A competitive swarm optimizer for large scale optimization," *IEEE Transactions on Cybernetics*, vol. 45, pp. 191–204, 2014.

[18] J. Kennedy, "Particle swarm optimization," in *Encyclopedia of machine learning*, C. Sammut and G. I. Webb, Eds., Springer, Boston, MA, USA, pp. 760–766, 2010.

[19] S. Leva, A. Dolara, F. Grimaccia, M. Mussetta, and E. Ogliari, "Analysis and validation of 24 hours ahead neural network forecasting of photovoltaic output power," *Mathematics and Computers in Simulation*, vol. 131, pp. 88–100, 2017.

[20] H. Bindner, T. Cronin, P. Lundsager, J. F. Manwell, U. Abdulwahid, and I. Baring-Gould, *Lifetime Modelling of Lead Acid Batteries*, Forskningscenter Risoe, Roskilde, Denmark, 2005.

[21] C. Wei, M. Benosman, and T. Kim, "Online parameter identification for state of power prediction of lithium-ion batteries in electric vehicles using extremum seeking," *International Journal of Control, Automation and Systems*, 2019, In press.

[22] C. Yin, X. Huang, S. Dadras et al., "Design of optimal lighting control strategy based on multi-variable fractional-order extremum seeking method," *Information Sciences*, vol. 465, pp. 38–60, 2018.

[23] F. Cheng, L. Qu, W. Qiao, C. Wei, and L. Hao, "Fault diagnosis of wind turbine gearboxes based on DFIG stator current envelope analysis," *IEEE Transactions on Sustainable Energy*, vol. 10, no. 3, pp. 1044–1053, 2018.

[24] X. Xia and J. Zhang, "Operation efficiency optimisation modelling and application of model predictive control," *IEEE/CAA Journal of Automatica Sinica*, vol. 2, pp. 166–172, 2015.

[25] R. Cheng, "Nature inspired optimization of large problems," Ph.D. thesis, University of Surrey, Guildford, UK, 2016.

[26] Q. Zhao and L.-y. Zhang, "Research on the effect of Dpso in team selection optimization under the background of big data," *Complexity*, vol. 2018, Article ID 1386407, 14 pages, 2018.

[27] J. Liu, H. Ma, X. Ren, T. Shi, P. Li, and X. Ma, "The continuous-discrete pso algorithm for shape formation problem of multiple agents in two and three dimensional space," *Applied Soft Computing*, vol. 67, pp. 409–433, 2018.

[28] L. Wang and X.-l. Zheng, "A knowledge-guided multi-objective fruit fly optimization algorithm for the multi-skill resource constrained project scheduling problem," *Swarm and Evolutionary Computation*, vol. 38, pp. 54–63, 2018.

[29] H. Tazvinga and T. Hove, *Photovoltaic/Diesel/Battery Hybrid Power Supply System*, VDM Publishers, Pretoria, South Africa, 2010.
[30] Z. Wu and T. W. Chow, "Neighborhood field for cooperative optimization," *Soft Computing*, vol. 17, pp. 819–834, 2013.
[31] N. Ao, M. Zhao, Q. Li, S. Qu, and Z. Wu, "Network characteristics for neighborhood field algorithms," *Neural Computing and Applications*, 2019.

Hindawi
Complexity
Volume 2019, Article ID 9361723, 12 pages
https://doi.org/10.1155/2019/9361723

Research Article

Performance Analysis of Reheat Steam Temperature Control System of Thermal Power Unit Based on Constrained Predictive Control

Xiaoli Li,[1,2,3] **Jian Liu**,[1] **Kang Wang**,[1] **Fuqiang Wang**,[4] **and Yang Li**[5]

[1] *Faculty of Information Technology, Beijing University of Technology, Beijing 100124, China*
[2] *Beijing Key Laboratory of Computational Intelligence and Intelligent System, Engineering Research Center of Digital Community, Ministry of Education, Beijing 100124, China*
[3] *Beijing Advanced Innovation Center for Future Internet Technology, Beijing University of Technology, Beijing 100124, China*
[4] *Technology Research Center, Shenhua Guohua Electric Power Research Institute Corporation, Beijing 100025, China*
[5] *School of International Studies, Communication University of China, Beijing 100024, China*

Correspondence should be addressed to Xiaoli Li; lixiaolibjut@bjut.edu.cn

Received 17 April 2019; Revised 28 June 2019; Accepted 8 July 2019; Published 5 August 2019

Guest Editor: Xiaoqing Bai

The reheat steam temperature control system of thermal power unit is a complex control object with time-varying parameters and large delay. In order to achieve precise control of reheat steam temperature, the performance of the reheat temperature control system is analyzed according to the data that are obtained based on the constrained predictive control algorithm. Firstly, the process and mathematical model of reheat steam temperature control system are introduced. Then the principle of constrained predictive control algorithm is analyzed. Finally, the steady-state values of control quantities of reheat steam temperature control system under different conditions are given by MATLAB simulation, and, by analyzing the steady-state values and steady-state time of the input and output of the system, the reference values and the regulating law of the control quantities and the specific constraint range of the control quantities of the system are given, which can provide reference data and theoretical basis for the field adjustment of the reheat steam temperature control system in power plant and improve the safety and effectiveness of the system.

1. Introduction

In recent years, China's electric power industry has developed rapidly. Ultra-supercritical thermal power unit, which has the characteristics of nonlinear, uncertain parameters and time-variation, has become the main unit in coal-fired power generation industry. Thus higher requirements for automatic control of coal-fired power plants are put forward. At the same time, China's clean energy industry has made great progress, and a variety of clean energy sources have entered the electricity market, which has a certain impact on the traditional coal-fired plants. In order to improve the market competitiveness of coal-fired plants, it is necessary to improve the efficiency of unit continuously. Increasing the pressure and temperature of steam is an effective means to improve competitiveness, but, due to the design requirement of the unit's infrastructure design and the limitation of metal material of boiler, the upgrading and transformation of operating parameters of unit require a large amount of investment of funds. Therefore, it is very important to improve the control effect of steam temperature on the existing basis.

In thermal power unit, reheat steam temperature is an important parameter that affects the economic value of unit. The reheat steam temperature control system is a complex object with the characteristics of large inertia and hysteresis, and the dynamic characteristics of the system are different during the load variation of generator unit, which make the control of reheat steam temperature extremely difficult. If the reheat steam temperature is too high, it may increase the corrosion of the metal material of pipeline and the heating surface of the boiler through which the steam flows, so

that the service life of unit may be reduced. If the steam temperature is too low, the humidity of steam will be very high, which not only makes the last turbine blades more vulnerable to damage, but also reduces the thermal efficiency of unit. The large variation of reheat steam temperature will also cause unit fatigue and reduce the service life of unit. Therefore, understanding the regulating law of the control quantities and the constraint range of the control quantities of the reheat steam temperature control system can not only ensure the safety of thermal equipment, but also have important significance to the stability of reheat steam temperature.

In order to improve the control effect of steam temperature, a large number of scholars have adopted a variety of advanced control strategies to study it. A new cascade feedback control system with load feed-forward of reheat steam temperature is proposed in [1]. Single-Neuron Self-adaptive PSD algorithm controller applied to outer loop and double-degree PID controller is applied to inner loop, which achieves good control effect. In [2], based on the characteristics of superheated steam temperature of a boiler, a new cascade control system is designed. The main regulator adopts multimodel observer control, and the secondary controller adopts weighted synthesizing proportional control. The system integrates the characteristics of the multimodel control with those of the state variable control with observer. The results show that the control system has strong robustness. In [3], an adaptive predictive control algorithm is designed for the reference model, and two compensators are introduced; one is two-order compensator for process; the other one is time delay compensator for the reference model. The algorithm has been applied in a 200MW peak regulating drum boiler for reheating temperature process, and high control accuracy is obtained. As the superheated steam temperature has large inertia, time-delay, and nonlinearity and its dynamic characteristics change with the operating conditions, a self-tuning PID controller based on fuzzy-RBF neural networks is presented for its control in [4], which has the advantages of traditional PID control, neutral networks control, and fuzzy control and optimizes online PID parameters. In [5], a new intelligent control algorithm of cloud models is proposed. The variant dimension cloud model intelligent controller, which contains a one-dimension cloud model controller to eliminate steady-state error, is designed, and it is used for superheated steam temperature control of a supercritical once-through 600MW boiler. In [6], a multimodel internal mode control strategy is proposed, and it has been successfully applied to a 1024 t/h supercritical pressure boiler. Performance studies show that the control strategy ensures that the superheated steam temperature stays within the desired range for both steady and varying loads. In [7], dynamic matrix control (DMC) is applied in controlling steam temperatures of a large-scale once-through boiler-turbine system. Online optimization is performed for the DMC using the step response model. The simulation results show satisfactory performance of the proposed DMC technique. Aiming at the characteristics of large inertia, large time delay, and nonlinearity of Reheater Temperature Control System, a hybrid optimization algorithm (MPSO-RBF) for radial basis function (RBF) neural network based on modified particle swarm optimization (MPSO) is presented in [8]. The results have proved that MPSO-RBF method has good performance index. In [9], a scheme combining neural network identification technology and adaptive inverse control technology is proposed for the control of boiler superheated steam temperature in fossil-fired power plant. The identified inverse model is preset as the controller and connected in series with the controlled object to form an adaptive inverse control system. In [10, 11], active disturbance rejection control (ADRC) is applied in the control of superheated steam temperature. Comparing with PID algorithm, the method achieved an excellent performance. In [12], a nonlinear control strategy for steam power plants is proposed. The strategy decomposes the overall plant into three separate subsystems and applies decoupling with dead time compensation for each one of them. The simulation results show that the method has good performance and robustness. When the superheated steam temperature is controlled by adjusting the cooling water, the nonlinear characteristics of the valve are caused by the flow rate. In [13], by collecting the valve input and output data and fitting the valve flow characteristic curve, a valve opening degree compensator based on the polynomial fitting method was designed. The simulation results show that the method can overcome the nonlinear problem caused by valve flow characteristics. In [14], a system of automatic control over the temperature of superheated steam for the boiler with three-tier steam cooling system is considered. A regulating algorithm rests on a cascade control method with the temperature error correction based on a force signal. The force signal is a speed of steam temperature change after the condensate injection. The simulation results show the effectiveness of the method. Besides, based on robust H∞ control method, the reheat steam temperature control system of boiler is studied in [15]. In [16], according to the characteristics of reheat steam temperature, a hybrid optimization method based on Biogeography-Based Optimization (BBO) algorithm is proposed to optimize the traditional PID controller. It turns out that the optimized PID controller has better tracking ability and better anti-internal and external interference performance in reheat steam control system.

Aiming at the difficulty of reheat steam temperature control, model predictive control is a useful control method. It can deal with multivariable, constrained, and time-delay problems effectively and has good dynamic control performance. Model predictive control (MPC) [17–20] was proposed in the 1980s. It has been improved and developed continuously in recent years and has been widely used in many industrial fields such as robots [21–24]. The control mechanism of MPC is that, at each sampling time, according to the current measurement information, an open-loop optimization problem in finite time domain is solved online, and the first element of the control sequence is acted on the controlled object. At the next sampling time, the above process is repeated; that is, the optimization problem is refreshed and resolved with new measurements. In addition, in the actual industrial control process, the physical quantity

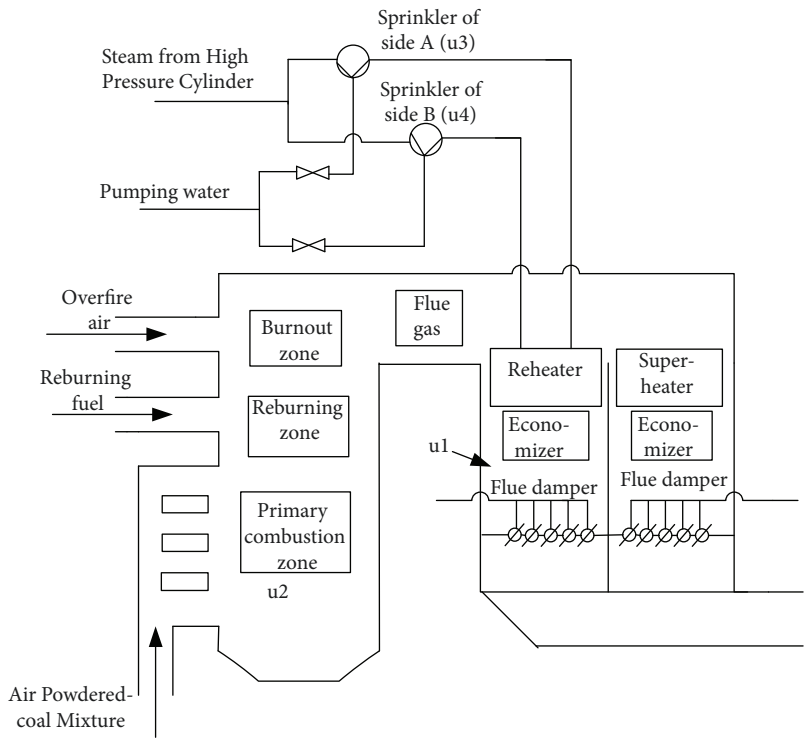

Figure 1: The process diagram of reheat steam temperature control system.

of the system can only be taken in a certain range, such that the opening range of the valve dampers in the unit of thermal power plant can only be taken from 0% to 100%. Executing agencies are not allowed to change too much to prevent damage to them. Therefore, in actual control process, the control input and output must be constrained according to the actual requirement, so that their values can be kept within a certain range. Considering the above factors, the reheat steam temperature control system of 660 MW Ultra-supercritical Once-through Boiler in a power plant is taken as the research object in this paper. And the control process of reheat steam temperature in coal-fired power plant is studied and analyzed by using constrained predictive control algorithm. Through the simulation results, the regulation law and the restriction range of system inputs during the reheat steam temperature system regulation are obtained, which provides theoretical and data support for field regulation. In this way, we can improve the safety and efficiency of reheat steam temperature control and the quality of reheat steam temperature control of ultra-supercritical coal-fired units.

The paper is organized as follows. In Section 2, the technological principle and mathematical model of reheat steam temperature control system are formulated. Then the principle of constrained predictive control algorithm is analyzed in Section 3. In Section 4, we apply constrained predictive control to reheat steam temperature control system and carry out MATLAB simulation. And, by analyzing the simulation results, the input regulation law and appropriate constraint range of system inputs are given. Finally, conclusions are given in Section 5.

2. The Technological Principle and Mathematical Model of Reheat Steam Temperature Control System

2.1. The Technological Principle of Reheat Steam Temperature Control System. At present, in order to improve the operation efficiency of large-scale thermal power unit, the steam which has finished the work in the high-pressure cylinder is reheated generally. The process of steam reheating involves three steps. At first, the steam discharged from high pressure cylinder is resent back to the boiler for heating. Then the reheat steam is heated to a certain temperature. Finally, the reheat steam is sent to the middle- and low-pressure cylinders for work.

There are many ways to regulate reheat steam temperature. The commonly used methods include adjusting flue gas damper opening, swinging burner swing angle, and spraying water to reduce temperature. The process diagram of reheat steam temperature control system is shown in Figure 1. In the control process of steam temperature, reheat steam pipe is generally divided into side A and side B. The burner and the flue gas baffle act on the reheat steam temperature of both sides at the same time. The sprinkler that is installed on the A side and the B side of the reheater can only control the reheat steam temperature of the A side and the B side, respectively. When reheat steam temperature is controlled by flue gas damper, the tail flue of the boiler is divided into two parallel flues. Low temperature reheater is arranged in the main flue, low temperature superheater is arranged in the bypass flue, and economizer is arranged behind them.

Temperature regulating damper is installed under economizer. By changing the opening of two flue dampers, the ratio of flue gas that flows through cryogenic reheater and cryogenic superheater is changed, so as to control the temperature of reheat steam. Specifically, when the opening of the flue gas damper increases, the reheat steam temperature increases; otherwise the reheat steam temperature decreases. The way of adjusting the swing angle of the burner is to change the up and down inclination angle of the swing burner nozzle, which will adjust the position of the high temperature flame center in the furnace, so as to change the flue gas temperature at the outlet of the furnace and control the reheat steam temperature. Similar to the flue gas damper, the reheat steam temperature increases with the increase of burner swing angle; otherwise the reheat steam temperature decreases. In case of emergency, sprinklers on both sides of reheater can spray water to cool down.

In general, adjusting flue gas damper opening and burner swing angle is the main control means in the control process of reheat steam temperature system. The performance of burner swing angle regulation and flue gas damper regulation is stable, and heat shock is small, so the two control methods have higher thermal economy. Although spray desuperheating has a rapid effect on reheat steam temperature control, it will reduce the thermal efficiency of the unit, so it is not the main method of regulation. Usually only in the process of unit start-up and shutdown, or in the case of accident, spray desuperheating is used as an auxiliary emergency means. Besides, in the normal operation of the unit, small amount of cooling water can be used intermittently, or it can be combined with other temperature regulation methods as a fine-tuning method of reheat steam.

2.2. The Mathematical Model of Reheat Steam Temperature Control System. From the above analysis, we can learn that the ideal control method for the reheat steam temperature should be to use the burner swing angle and the flue gas damper to adjust the reheat steam temperature roughly and use the method of water spraying to reduce the temperature to achieve fine adjustment. As an emergency safety measure, the sprinkler valve should be kept as small as possible. At the same time, the variance of burner swing angle and flue gas damper opening must be limited to a certain range.

According to the requirements of reheat temperature control process, the mathematical model [25] of reheat steam temperature control system for 660 MW ultra-supercritical once-through boiler in a power plant is established:

$$\begin{bmatrix} y_1 \\ y_2 \end{bmatrix} = \begin{bmatrix} G_{11} & G_{12} & G_{13} & 0 \\ G_{21} & G_{22} & 0 & G_{24} \end{bmatrix} \times \begin{bmatrix} u_1 \\ u_2 \\ u_3 \\ u_4 \end{bmatrix}. \tag{1}$$

where u_1, u_2, u_3, u_4 are the control quantities of the system and y_1, y_2 are the output of the system. It should be noted that the model is established based on the input variance and output variance of reheat steam temperature control system. For example, in model (1), y_1 is the variance of the reheat steam temperature on the A side of reheater, rather than the actual reheat steam temperature. If the initial temperature of reheat steam is 580°C and the expected temperature is 590°C, then y_1 is the change of the initial temperature, that is, 10°C. Similarly, y_2 is the variance of reheat steam temperature on the B side of reheater, u_1 is the variance of the flue gas damper opening, u_2 is the variance of the burner swing angle, u_3 is the variance of the sprinkler valve opening on the A side of reheater, and u_4 is the variance of the sprinkler valve opening on the B side of reheater.

The transfer functions of burner swing angle-reheat steam temperature, flue gas damper-reheat steam temperature, and spray desuperheating-reheat steam temperature can be described by the mode of first-order inertia plus pure delay. The expression of the transfer functions is as follows:

$$G(s) = \frac{K}{Ts + 1} \exp(-\tau s), \tag{2}$$

where K is the gain, T is the first-order inertia time, and τ is the delay time. The transfer function form of $G_{11}, G_{12}, G_{13}, G_{21}, G_{22}, G_{24}$ in model (1) is determined by (2).

3. Theoretical Analysis of Constrained Predictive Control [26]

The theoretical analysis of predictive control algorithm is usually based on the state space equation of the system model. Therefore, the transfer function model of the research object in this paper needs to be transformed into the state space model. The transformation method can be easily found in many data [27], so it is no longer detailed.

The state space incremental model of the linear discrete time system is considered as follows:

$$\Delta x(k+1) = A\Delta x + B_u \Delta u(k) + B_d \Delta d(k), \tag{3a}$$

$$y_c(k) = C_c \Delta x(k) + y_c(k-1), \tag{3b}$$

$$y_b(k) = C_b \Delta x(k) + y_b(k-1), \tag{3c}$$

where

$$\begin{aligned} \Delta x(k) &= x(k) - x(k-1), \\ \Delta u(k) &= u(k) - u(k-1), \\ \Delta d(k) &= d(k) - d(k-1). \end{aligned} \tag{4}$$

In the model ((3a), (3b), and (3c)), $\Delta x(k) \in \mathbb{R}^{n_x}$ is the state increment; $\Delta u(k) \in \mathbb{R}^{n_u}$ is the increment of control input; $\Delta d(k) \in \mathbb{R}^{n_d}$ is the increment of measurable external interference; $y_c(k) \in \mathbb{R}^{n_c}$ is the controlled output; $y_b(k) \in \mathbb{R}^{n_b}$ is the constrained output; A, B_u, B_d, C_c, C_b is the system matrix of the corresponding dimension.

The control objective is to make the controlled output y_c track the given reference input r. At the same time, the control

quantity, control increment, and output of the system satisfy the following control constraints and output constraints:

$$u_{\min}(k) \le u(k) \le u_{\max}(k), \quad \forall k \ge 0, \tag{5a}$$

$$\Delta u_{\min}(k) \le \Delta u(k) \le \Delta u_{\max}(k), \quad \forall k \ge 0, \tag{5b}$$

$$y_{\min}(k) \le y_b(k) \le y_{\max}(k). \quad \forall k \ge 0, \tag{5c}$$

At k time, the measured value of state is $x(k)$. According to the basic principle of predictive control, the optimization problem of constrained MPC is described as follows.

Question 1

$$\min_{\Delta U(k)} J(x(k), \Delta U(k)) \tag{6}$$

satisfies system dynamics ($i = 0, 1, \cdots, p$) and the following time-domain constraints ((8a), (8b), and (8c)):

$$\begin{aligned}\Delta x(k+i+1 \mid k) = {} & A\Delta x(k+i \mid k) + B_u \Delta u(k+i) \\ & + B_d \Delta d(k+i),\end{aligned} \tag{7a}$$

$$\Delta x(k \mid k) = \Delta x(k), \tag{7b}$$

$$\begin{aligned}y_c(k+i \mid k) = {} & C_c \Delta x(k+i \mid k) \\ & + y_c(k+i-1 \mid k), \quad i \ge 1,\end{aligned} \tag{7c}$$

$$y_c(k \mid k) = y_c(k), \tag{7d}$$

$$\begin{aligned}y_b(k+i \mid k) = {} & C_b \Delta x(k+i \mid k) \\ & + y_c(k+i-1 \mid k), \quad i \ge 1,\end{aligned} \tag{7e}$$

$$y_b(k \mid k) = y_b(k), \tag{7f}$$

$$\begin{aligned}u_{\min}(k+i) \le u(k+i) \le u_{\max}(k+i), \\ i = 0, 1, \cdots, m-1,\end{aligned} \tag{8a}$$

$$\begin{aligned}\Delta u_{\min}(k+i) \le \Delta u(k+i) \le \Delta u_{\max}(k+i), \\ i = 0, 1, \cdots, m-1,\end{aligned} \tag{8b}$$

$$\begin{aligned}y_{\min}(k+i) \le y_b(k+i) \le y_{\max}(k+i). \\ i = 0, 1, \cdots, p,\end{aligned} \tag{8c}$$

where

$$\begin{aligned}J(x(k), \Delta U(k)) = {} & \left\| \Gamma_y \left(Y_{p,c}(k+1 \mid k) - R(k+1) \right) \right\|^2 \\ & + \left\| \Gamma_u \Delta U(k) \right\|^2.\end{aligned} \tag{9}$$

In the above optimization problems, Γ_y and Γ_u are weighted matrices, and they are given as follows:

$$\begin{aligned}\Gamma_y &= \text{diag}\left\{ \Gamma_{y,1}, \Gamma_{y,2}, \cdots \Gamma_{y,p} \right\}_{p \times p}, \\ \Gamma_u &= \text{diag}\left\{ \Gamma_{u,1}, \Gamma_{u,2}, \cdots \Gamma_{u,m} \right\}_{m \times m},\end{aligned} \tag{10}$$

$R(k+1)$ is a reference sequence of control output, and it is given as

$$R(k+1) = \begin{bmatrix} r(k+1) \\ r(k+2) \\ \vdots \\ r(k+p) \end{bmatrix}_{p \times 1}, \tag{11}$$

$\Delta U(k)$ is a sequence of control quantity. As an independent variable for constrained optimization problems, it is defined as

$$\Delta U(k) \overset{def}{=} \begin{bmatrix} \Delta u(k) \\ \Delta u(k+1) \\ \vdots \\ \Delta u(k+m-1) \end{bmatrix}_{m \times 1}, \tag{12}$$

$Y_{p,c}(k+1 \mid k)$ is the p step control output based on model ((3a), (3b), and (3c)) prediction at k time, and it is defined as

$$Y_{p,c}(k+1 \mid k) \overset{def}{=} \begin{bmatrix} y_c(k+1 \mid k) \\ y_c(k+2 \mid k) \\ \vdots \\ y_c(k+p \mid k) \end{bmatrix}_{p \times 1}. \tag{13}$$

Specifically, the controlled output $y_c(k+i \mid k)$ and constrained output $y_b(k+i \mid k)$ of predictive control are calculated by equation ((7a), (7b), (7c), (7d), (7e), and (7f)), where (7b), (7d), and (7f) indicate that the measured states are the initial condition for predicting the future dynamics of the system. If the states are not all measurable, the estimated states are used as the initial conditions for predicting the future dynamics of the system.

$Y_{p,c}(k+1 \mid k)$ can be calculated by the equation

$$\begin{aligned}Y_{p,c}(k+1 \mid k) = {} & S_x \Delta x(k) + I y_c(k) + S_u \Delta U(k) \\ & + S_d \Delta d(k),\end{aligned} \tag{14}$$

where

$$S_x = \begin{bmatrix} C_c A \\ C_c A^2 + C_c A \\ \vdots \\ \sum_{i=1}^{p} C_c A^i \end{bmatrix}_{p \times 1},$$

$$I = \begin{bmatrix} I_{n_c \times n_c} \\ I_{n_c \times n_c} \\ \vdots \\ I_{n_c \times n_c} \end{bmatrix}_{p \times 1},$$

$$S_d = \begin{bmatrix} C_c B_d \\ C_c A B_d + C_c B_d \\ \vdots \\ \sum_{i=1}^{p} C_c A^{i-1} B_d \end{bmatrix}_{p\times 1},$$

$$S_u = \begin{bmatrix} C_c B_u & 0 & 0 & \cdots & 0 \\ \sum_{i=1}^{2} C_c A^{i-1} B_u & C_c B_u & 0 & \cdots & 0 \\ \vdots & \vdots & \vdots & & \vdots \\ \sum_{i=1}^{m} C_c A^{i-1} B_u & \sum_{i=1}^{m-1} C_c A^{i-1} B_u & \cdots & \cdots & C_c B_u \\ \vdots & \vdots & \vdots & & \vdots \\ \sum_{i=1}^{p} C_c A^{i-1} B_u & \sum_{i=1}^{p-1} C_c A^{i-1} B_u & \cdots & \cdots & \sum_{i=1}^{p-m+1} C_c A^{i-1} B_u \end{bmatrix}_{p\times m}. \quad (15)$$

The constrained optimization problem is a quadratic programming (QP) problem, so we transform it into a QP description. The specific transformation process is detailed in [15].

The constraint MPC optimization Question 1 is converted into the following QP problem description:

$$\min_{\Delta U(k)} \Delta U(k)^T H \Delta U(k) - G(k+1 \mid k)^T \Delta U(k) \quad (16a)$$

$$\text{satisfies } C_u \Delta U(k) \geq b(k+1 \mid k). \quad (16b)$$

The QP problem ((16a) and (16b)) has a solution to any weighting matrix $\Gamma_y \geq 0$, $\Gamma_u \geq 0$, which is denoted as $\Delta U^*(k)$. Obviously, $\Delta U^*(k)$ is a function that is related to the measured value $x(k)$, the control horizon m, and the prediction horizon p. According to the basic principle of predictive control, the first step of the obtained open-loop control sequence will be applied to the controlled system. At the next sampling time, the constrained optimization question 1, that is, QP problem ((16a) and (16b)), will be refreshed with the new measured value and solved again. Therefore, the closed-loop control law of constrained MPC is defined as

$$\Delta u(k) = \left[I_{n_u} \times I_{n_u} \quad 0 \quad \cdots \quad 0 \right] \Delta U^*(k). \quad (17)$$

4. Performance Analysis of Reheat Steam Temperature Control System with Variable Load

4.1. Simulation Results. The transfer functions [25] of spray desuperheating (valve opening), reheat steam temperature, burner swing angle, reheat steam temperature and flue gas damper, and reheat steam temperature of a 660MW ultra-supercritical once-through boiler under 400MW, 500MW, and 600MW load are shown in Tables 1, 2, and 3.

According to the mathematical model in Tables 1, 2 and 3, we simulate the control effect of reheat steam temperature system of boiler based on constraint predictive control algorithm when the loads of generator unit are 400MW, 500MW, and 600MW, respectively. The initial temperature of reheat steam is set to 580°C and the expected output temperature of reheat steam is set to 590°C; that is, the reference input is $r = 10$. The sampling period is 10 seconds. The prediction horizon is p=100, and the control horizon is m=3. The output error weighting matrix of quadratic performance index is ywt = [], and control quantity weighting matrix of quadratic performance index is uwt = [1 1 1 1].

Table 1: The model of flue gas damper-reheat steam temperature under 400 MW, 500 MW, and 600 MW.

Load	G_{11}	G_{21}
400MW	$\frac{0.34}{284.5s+1}e^{-251s}$	$\frac{0.31}{261.3s+1}e^{-250s}$
500MW	$\frac{0.69}{244.2s+1}e^{-170s}$	$\frac{0.67}{214.3s+1}e^{-152s}$
600MW	$\frac{0.85}{210.1s+1}e^{-121s}$	$\frac{0.81}{201.2s+1}e^{-121s}$

Table 2: The model of burner swing angle-reheat steam temperature under 400 MW, 500 MW, and 600 MW.

Load	G_{12}	G_{22}
400MW	$\frac{1}{345.6s+1}e^{-300s}$	$\frac{1.01}{324.1s+1}e^{-300s}$
500MW	$\frac{1.18}{375.1s+1}e^{-251s}$	$\frac{1.275}{384.2s+1}e^{-260s}$
600MW	$\frac{1.36}{397.3s+1}e^{-161s}$	$\frac{1.445}{289.5s+1}e^{-153s}$

In order to make comparison and analysis, the constraints of u_j are set to 0~8, 0~10, 0~12, and 0~15, respectively, where $j = 1, 2, 3, 4$. Note that if we want to rise the reheat steam temperature, u_1, u_2 should be greater than or equal to 0 and u_3, u_4 should be close to or equal to 0. Therefore, the constraints of u_j should start from 0. The unit of u_1, u_3, u_4 is %. The unit of u_2 is degree.

When the load of generator unit is 400MW, $u_j \in [0, 15]$, $\Delta u_j = 0.5$, the simulation results of reheat steam temperature control system are shown in Figures 2 and 3.

From Figures 2 and 3, we can see that the steady state values of u_1, u_2, u_3, u_4 are 13.94, 5.62, 0.26, and 0, respectively, and the time that is required for the input and output to reach the steady state is about 120 sampling periods, that is, 1200s. Similarly, we can obtain the steady state time of the u_j and $y_{1,2}$ and the steady state values of u_j under different loads and different input constraints, and they are shown in Tables 4, 5, 6, and 7. According to the data that is obtained from the simulation, we can analyze the control performance of the reheat steam temperature control system.

Since the dynamic characteristics of reheat steam temperature control system are different during the change of generators load, that is, the model parameters of reheat steam temperature control system are changing with the change of generator load, so the models of reheat steam temperature control system under one or several loads can only provide the system input under the one or several loads at the site,

Table 3: The model of spray desuperheating-reheat steam temperature under 400 MW, 500 MW, and 600 MW.

Load	G_{13}	G_{24}
400MW	$\frac{-1.4}{85s+1}e^{-40s}$	$\frac{-1.39}{82s+1}e^{-39s}$
500MW	$\frac{-1.11}{41s+1}e^{-35s}$	$\frac{-1.02}{40s+1}e^{-34s}$
600MW	$\frac{-0.81}{34s+1}e^{-26s}$	$\frac{-0.79}{31s+1}e^{-24s}$

Table 4: Steady-state values of u_j when $u_j \in [0, 15]$.

$u_j \in [0, 15]$	400MW				500MW				600MW			
Δu_j	0.5	1	1.5	2	0.5	1	1.5	2	0.5	1	1.5	2
Steady-state time of $y_{1,2}$	120	100	90	85	95	87	85	80	60	55	50	45
Steady-state time of u_j	120	100	90	85	95	87	85	80	60	55	50	45
Steady-state value of u_1	13.94	13.2	12.63	12.12	12.62	12.78	12.61	12.44	10.63	10.89	10.56	10.20
Steady-state value of u_2	5.62	5.84	6.02	6.18	1.21	1.13	1.22	1.34	0.96	0.82	1.00	1.20
Steady-state value of u_3	0.26	0.24	0.23	0.22	0.12	0.13	0.12	0.11	0.42	0.45	0.42	0.38
Steady-state value of u_4	0	0	0	0	0	0	0	0	0	0	0	0

Table 5: Steady-state values of u_j when $u_j \in [0, 12]$.

$u_j \in [0, 12]$	400MW				500MW				600MW			
Δu_j	0.5	1	1.5	2	0.5	1	1.5	2	0.5	1	1.5	2
Steady-state time of $y_{1,2}$	110	100	95	90	105	100	98	95	60	55	55	55
Steady-state time of u_j	110	100	95	90	105	100	98	95	60	55	55	55
Steady-state value of u_1	11.16	10.51	9.98	9.55	11.12	10.94	10.79	10.68	10.10	9.81	9.40	9.05
Steady-state value of u_2	6.48	6.67	6.84	6.97	2.00	2.09	2.17	2.23	1.26	1.42	1.65	1.85
Steady-state value of u_3	0.19	0.18	0.17	0.16	0.03	0.02	0.01	0	0.37	0.33	0.29	0.25
Steady-state value of u_4	0	0	0	0	0	0	0	0	0	0	0	0

Table 6: Steady-state values of u_j when $u_j \in [0, 10]$.

$u_j \in [0, 10]$	400MW				500MW				600MW			
Δu_j	0.5	1	1.5	2	0.5	1	1.5	2	0.5	1	1.5	2
Steady-state time of $y_{1,2}$	115	105	100	95	110	100	95	90	105	95	90	80
Steady-state time of u_j	115	105	100	95	110	100	95	90	105	95	90	80
Steady-state value of u_1	9.25	8.65	8.18	8.05	9.73	9.59	9.46	9.35	9.09	8.71	8.33	8.03
Steady-state value of u_2	7.06	7.25	7.39	7.43	2.78	2.87	2.92	3.01	1.82	2.04	2.25	2.42
Steady-state value of u_3	0.15	0.13	0.12	0.11	0	0	0	0	0.26	0.22	0.18	0.14
Steady-state value of u_4	0	0	0	0	0.07	0.08	0.01	0.01	0	0	0	0

Table 7: Steady-state values of u_j when $u_j \in [0, 8]$.

$u_j \in [0, 8]$	400MW				500MW				600MW			
Δu_j	0.5	1	1.5	2	0.5	1	1.5	2	0.5	1	1.5	2
Steady-state time of $y_{1,2}$	130	130	130	130	120	105	103	100	108	100	98	95
Steady-state time of u_j	130	130	130	130	120	105	103	100	108	100	98	95
Steady-state value of u_1	7.57	7.57	7.57	7.57	7.91	7.81	7.74	7.67	7.67	7.46	7.34	7.23
Steady-state value of u_2	7.58	7.58	7.58	7.58	3.85	3.90	3.95	3.99	2.62	2.74	2.81	2.87
Steady-state value of u_3	0.11	0.11	0.11	0.11	0	0	0	0	0.10	0.08	0.07	0.06
Steady-state value of u_4	0	0	0	0	0.20	0.21	0.22	0.22	0	0	0	0

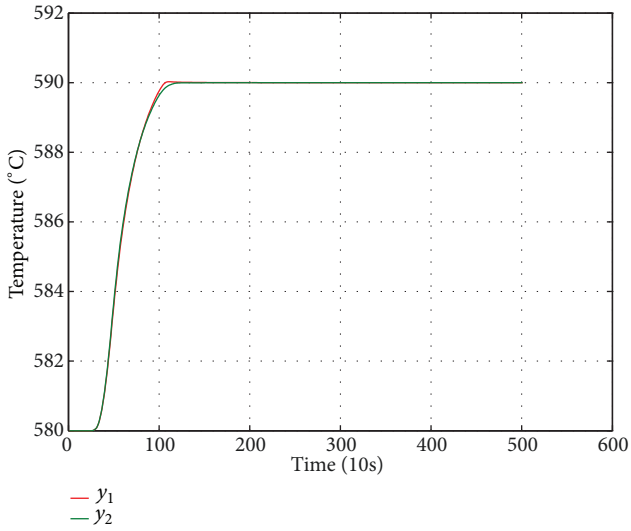

FIGURE 2: The variation curve of reheat steam temperature when the load of generator unit is 400MW, $u_j \in [0, 15]$, $\Delta u_j = 0.5$.

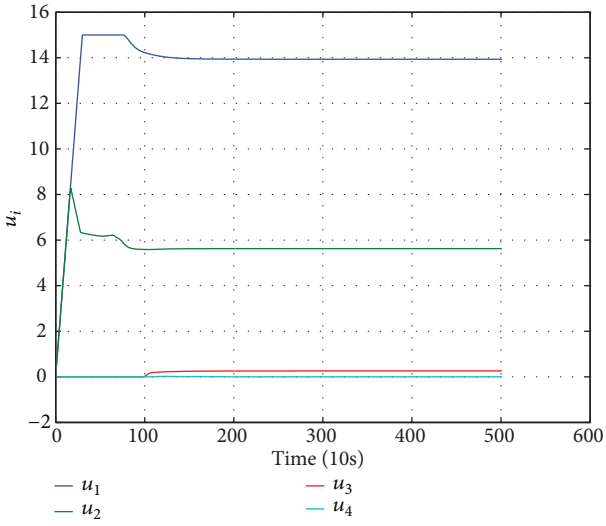

FIGURE 3: The variation curve of system input when the load of generator unit is 400MW, $u_j \in [0, 15]$, $\Delta u_j = 0.5$.

and they cannot provide the basis for the field adjustment of the control system under other loads. Therefore, we need to analyze the input and output of the system based on the existing models under the three loads and get the regulation law of the control quantities, which can provide a theoretical basis for the actual field adjustment.

4.2. Analysis of Control Quantities of Reheat Steam Temperature Control System. From the steady-state values of Tables 4, 5, 6, and 7, we can see that $u_1$and u_2 are relatively large, and they play major roles during the regulation of reheat steam temperature. u_3 and u_4 are close to 0, which means that the opening of the two sprinkler valves remains almost unchanged. It is consistent with the control requirement that spray desuperheating is not as the main regulating method during the regulation of reheat steam temperature.

Control quantities u_3 and u_4 do not play a major role during the control process of reheat steam temperature, so we mainly analyze u_1 and u_2. Firstly, the change of u_1 is analyzed. From the Tables 4–7, it can be seen that when Δu_j is equal and the constraint of control quantities is invariable, the three steady-state values of u_1 do not change much under the three loads. That is to say, when the reheat steam temperature rises from 580°C to 590°C and the load of generator unit is 400MW, the variance of flue gas damper opening is basically the same as that under 500MW and 600MW load. Besides, the smaller the constraint range of u_1 is, the closer the three steady-state values of u_1 are under the three loads. Thus, although the model parameters of reheat steam temperature control system change with the change of generator load, the adjustment of flue gas damper opening just has little change under different loads. Taking Table 7 as an example, when $u_j \in [0, 8]$ and $\Delta u_j = 0.5$, the three steady-state values of u_1, which are 7.57, 7.91, and 7.67, respectively, are the closest under the three loads. The variation range of u_1 is between 7.57 and 7.91, and the change is not obvious. Therefore, under any other load, the control quantity u_1 can take the value from 7.57 to 7.91.

Next, we analyze the change of u_2 according to the Tables 4–7. It can be seen that when the Δu_j is equal and the constraint of control quantities is invariable, u_2 changes greatly under the three loads. And the higher the generators' load is, the smaller the u_2 is. Taking Table 5 as an example, when $\Delta u_j = 0.5$, under 400MW, 500MW, and 600MW load, the steady-state values of u_2 are 6.48, 2.00, and 1.26, respectively, which means if the reheat steam temperature rises from 580°C to 590°C, the swing angle of the burner needs to be increased by 6.48 under 400 MW load, while the opening of burner swing angle needs to be increased by 2.00 and 1.26, respectively, under 500MW and 600MW loads. It shows that, in the process of regulating the reheat steam temperature control system, with the increase of the load of the generator unit, the adjusting range of burner swing angles should be gradually reduced. Therefore, in the actual field adjustment, the higher the generator load is, the smaller the adjustment range of the burner swing angles should be, so as to avoid damaging thermal equipment caused by excessive reheat steam temperature.

The correctness of the above analysis can also be verified by Simulink simulation. Taking Table 6 as an example, under different loads, we take the steady-state value of u_j, respectively, at $\Delta u_j = 0.5$, as the system input and set the increment of u_2 to 4 in the Simulink simulation. In this way, we can learn the effect of reheat steam temperature when the adjusting range of burner swing angles is too large. The simulation results are shown in Figures 4, 5, and 6.

From Figure 4, we can see that when the load of the generator unit is 400MW and the increment of u_2 is 4, that is, $u_2 = 7.06 + 4 = 11.06$, the reheat steam temperature rises by about 14°C. It is 4°C higher than the desired output, but it still meets the maximum deviation of system output, which is ±5°C. When the load of the generator unit is 500MW, we can see that the reheat steam temperature rises by about 14.8°C

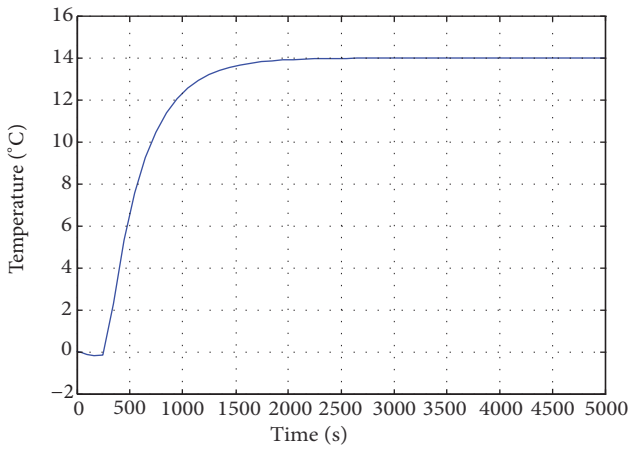

Figure 4: The variation curve of y_1 when the load of generator unit is 400MW, $u_j \in [0, 12]$, and the increment of u_2 is 4.

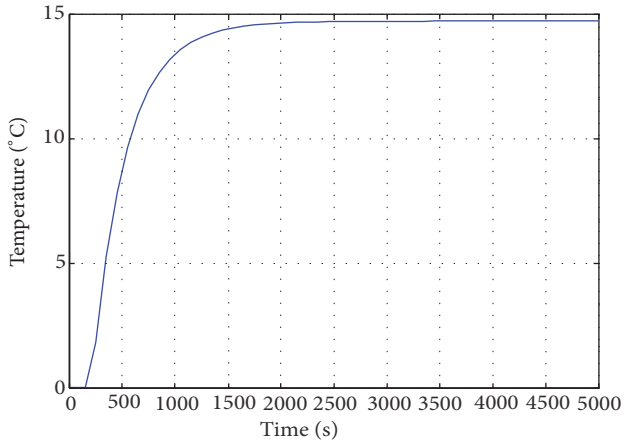

Figure 5: The variation curve of y_1 when the load of generator unit is 500MW, $u_j \in [0, 12]$, and the increment of u_2 is 4.

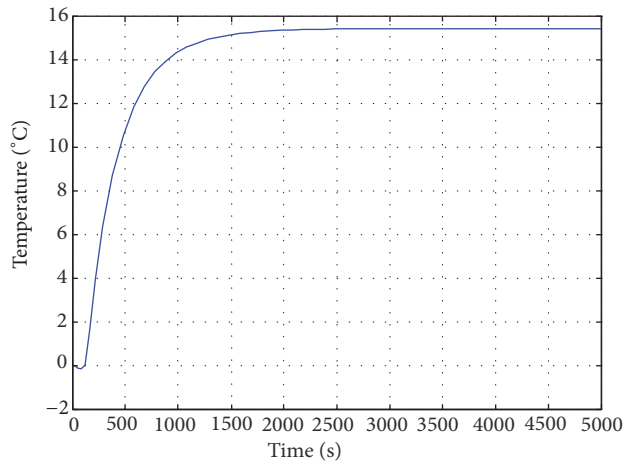

Figure 6: The variation curve of y_1 when the load of generator unit is 600MW, $u_j \in [0, 12]$, and the increment of u_2 is 4.

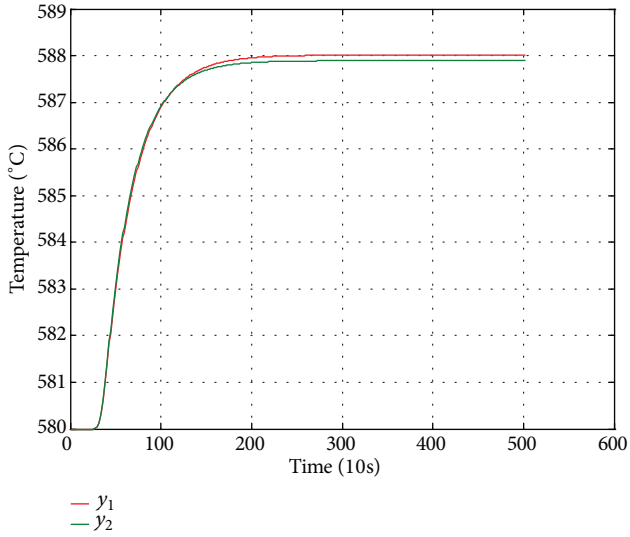

Figure 7: The variation curve of reheat steam temperature when the load of generator unit is 400MW, $u_j \in [0, 6]$, $\Delta u_j = 0.5$.

from Figure 5, and it is approaching the maximum deviation of output. From Figure 6, we can see that the reheat steam temperature rises by about 15.4°C under 600MW load, and it has exceeded the maximum deviation of system output. Thus, in order to ensure the safety of the thermal equipment, the higher the load of the generator unit is, the smaller the adjustment range of the burner swing angles should be.

4.3. Analysis of the Constraint Range of Control Quantities. In this paper, the control quantities u_j are the variance of system input. Taking the u_1 as an example, it is not the actual opening of the flue gas damper, but it is the opening variance of the flue gas damper. If the original opening of the flue gas damper is 50 and $u_1 = 10$, then the actual opening of the flue gas damper is 60. In the actual process, the opening of the control quantities has a maximum value, so it is necessary to restrict the range of control quantities of the system to ensure that the control quantities do not exceed their maximum value. Next, we analyze the constraints of the control quantities and give an appropriate constraint range for reference during field adjustment of reheat temperature control system.

Firstly, the constraint range of the control quantities should not be too small; otherwise the reheat steam temperature cannot reach the desired temperature. Figures 7 and 8 are the simulation results of input and output of the reheat steam temperature system when the generator load is 400MW, $u_j \in [0, 6]$, $\Delta u_j = 0.5$. The initial temperature of reheat steam is 580°C and the desired temperature is 590°C.

It can be easily seen from Figure 7 that when u_j is limited to 0~6, the steady state values of the reheat steam temperature are about 588.0 and 587.9, which do not reach the desired temperature. From Figure 8, we can be seen that the steady-state values of u_1, u_2 have reached the maximum value of input constraint range, which is 6, and the steady-state values of u_3, u_4 have almost reached the minimum value of input constraint range, which is 0. This shows that in the reheat

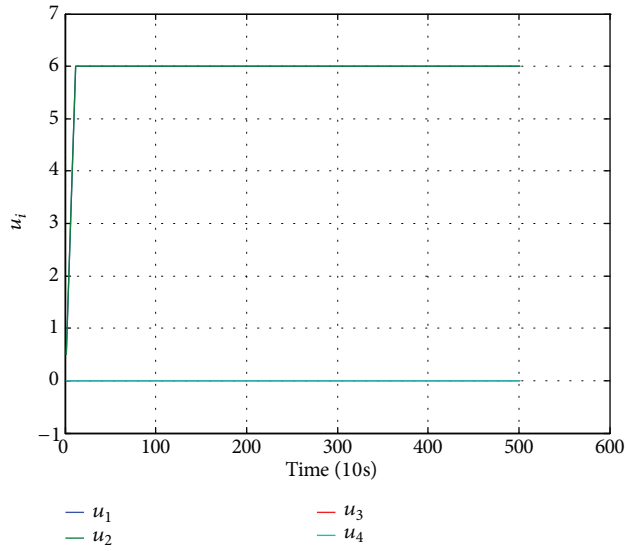

Figure 8: The variation curve of system input when the load of generator unit is 400MW, $u_j \in [0, 6]$, $\Delta u_j = 0.5$.

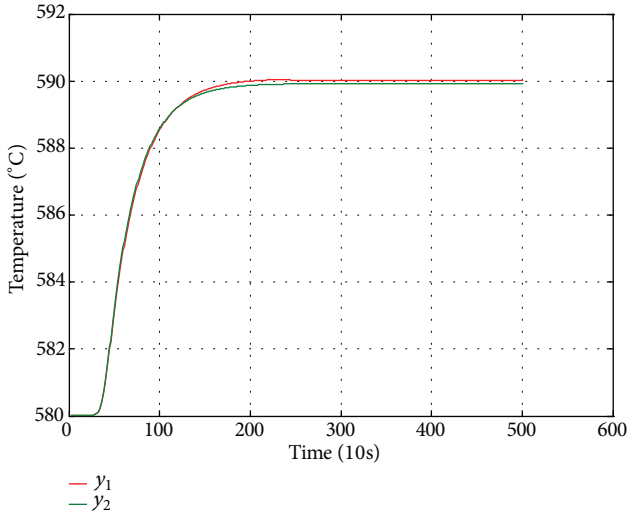

Figure 9: The variation curve of reheat steam temperature when the load of generator unit is 400MW and $u_j \in [0, 7.5]$.

steam temperature control system, if the constraint range of the control quantities is too small, even if u_1, u_2 reach the upper bound of the constraint range and the u_3, u_4 is close to lower bound, the final reheat steam temperature cannot reach the desired temperature. Therefore, there must be a minimum upper bound for the constraint range of the control quantities. Next, we try to find out the minimum upper bound of the constraint range of the control quantities under 400MW, 500MW, and 600MW loads, respectively, by simulation.

When the load of the generator unit is 400MW and $u_j \in [0, 7.5]$, the input and output of the system are shown in Figures 9 and 10. From Figure 10, we can see that the steady-state values of u_1, u_2 have reached the upper bound of input constraint range, which is 7.5, and the steady-state

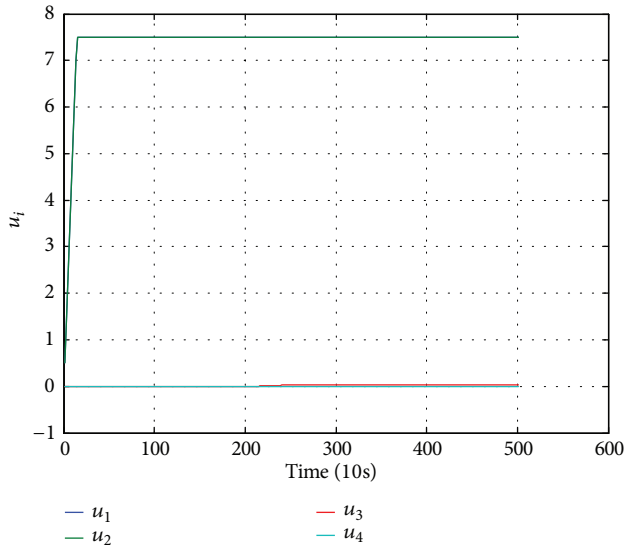

Figure 10: The variation curve of system input, when the load of generator unit is 400MW, $u_j \in [0, 7.5]$, $\Delta u_j = 0.5$.

values of u_3, u_4 are 0.03 and 0, respectively, which have almost reached the lower bound of input constraint range. As can be seen from Figure 9, the steady-state values of y_1, y_2 are 590 and 589.9, respectively, which reach the desired temperature basically. It can be considered that the minimum upper bound of input constraint is about 7.5 under 400MW load. Similarly, we can get the minimum upper bound of input constraint under 500MW and 600MW loads, which are about 5.3 and 4.5, respectively. From the minimum upper bound of the input constraint range under the three loads, we can see that the higher the generator load is, the smaller the minimum upper bound of the input constraint range is. This also shows that, in the actual operation process, with the increase of the generator load, the adjusting range of system inputs should be gradually reduced.

Next, we also make a simple analysis of the maximum upper limit of input constraint range. We can observe the change of system input by simulation when the constraint range of system inputs is too large. When the load of generator unit is 400MW, $u_j \in [0, 40]$, $\Delta u_j = 2$, the variation curve of input and output of the system is shown in Figures 11 and 12. From the two figures, we can see that although the system output can reach the desired value, the steady-state value of u_1 has reached 29.0, which means that if the initial opening of u_1 is greater than 71, the final value of u_1 has exceeded the maximum opening it can reach. This is obviously unreasonable. Therefore, the upper limit value of the control quantities constraint range should not be too large; otherwise it may exceed the maximum range of the control quantities opening. What is the maximum upper bound of the control quantities constraint range? If we want to get an exact value, we need a huge amount of data. Since our existing data is limited, we can only analyze it based on the existing data and get a rough analysis result. Compared with the steady-state value of u_1, u_2 in other constraint ranges, when the constraint range of system inputs is 0~15, the steady-state value of u_1, u_2 has

Table 8: Reference values of u_j and input constraint.

$u_j \in [0, 8]$, Δu_j=2	400MW	500MW	600MW
u_1	7.57	7.67	7.23
u_2	7.58	3.99	2.87
u_3	0.11	0	0.06
u_4	0	0.22	0

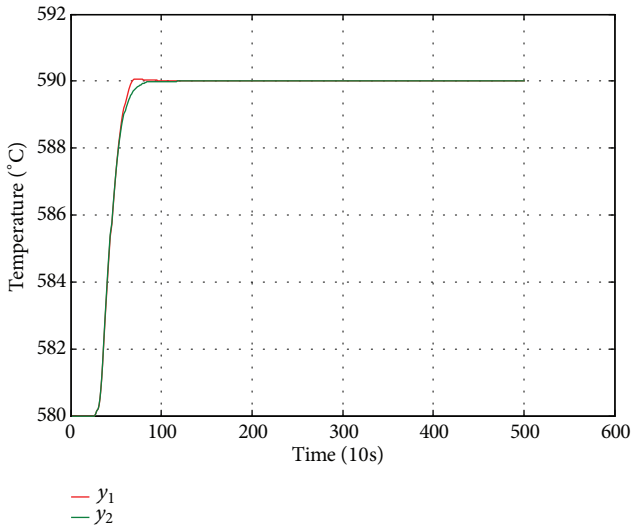

Figure 11: The variation curve of reheat steam temperature when the load of generator unit is 400MW, $u_j \in [0, 40]$, $\Delta u_j = 2$.

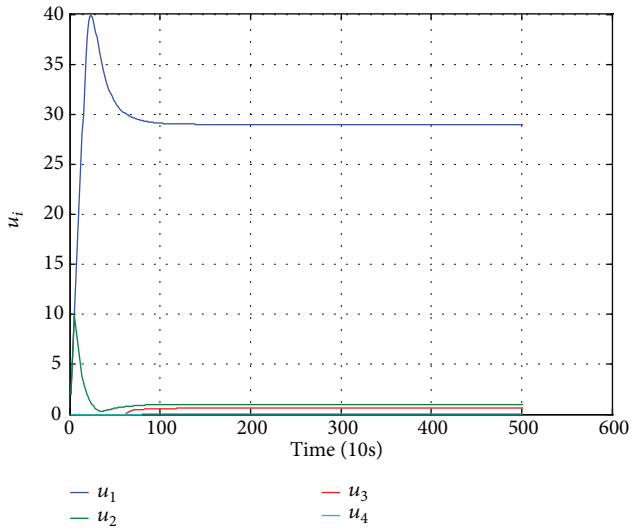

Figure 12: The variation curve of system input when the load of generator unit is 400MW, $u_j \in [0, 40]$,$\Delta u_j = 2$.

the largest fluctuation. Therefore, in the existing data, we can roughly consider that the maximum upper bound value of the constraint range of the control quantities is 15.

From the analysis of Section 4.3 of the control quantities of reheat steam temperature control system, we can learn that, with the increase of the load of the generator unit, the adjusting range of burner swing angles should be gradually reduced, and large adjustment of the control quantities may cause reheat steam temperature being too high and the equipment is damaged, which means that, under different loads, the smaller the fluctuation of u_j is, the better the stability and robustness of the system are. By observing and analyzing the data in Tables 4–7, we can see that when the constraint range of u_j is 0~ 8 and $\Delta u_j = 2$, the fluctuation of steady-state values of u_j is the smallest under different loads compared with that in other constraint ranges. In order to provide reference values of u_j and input constraint for adjustment of reheat steam temperature system in power plant, the most appropriate input values and input constraint in the existing data are given in Table 8.

5. Conclusions

Aiming at the problem of reheat steam temperature control, the reheat steam temperature control system of 660MW thermal power generator unit is studied based on the constrained predictive control algorithm in this paper. Under the condition of input constraint, steady state value of control quantities and the time that system reaches steady state in different constraint ranges are listed in tabular form. By analyzing the data in the tables, the reference values of system input and input constraint are given. These data and analysis provide reference for field adjustment of reheat steam temperature system in power plant.

Data Availability

The experimental data used to support the findings of this study are included within the article.

Conflicts of Interest

The authors declare that there are no conflicts of interest regarding the publication of this paper.

Acknowledgments

This work is supported in part by the National Natural Science Foundation of China under Grants 61873006, 61473034, and 61673053 and in part by the National Key Research and Development Projects 2018YFC1602704 and 2018YFB1702704 and Beijing Major Science and Technology Special Projects under Grant No. Z181100003118012.

References

[1] X. Zhao and Y. Jiao, "Single neuron self-adaptive PSD control and its application in reheat steam temperature control system," *Proceedings of the CSEE*, vol. 21, pp. 94–97, 2001.

[2] X. Luan, S. Li, and L. Li, "Adaptive control for the superheated steam temperature based on multi-model state observer," *IEEE*, pp. 978–982, 2004.

[3] H. Lu, J. Sun, and H. Deng, "Design and application of adaptive prediction controller in typical large time delay process in power plant," *Journal of Nanjing University of Aeronautics and Astronautics*, vol. 38, pp. 151–153, 2006.

[4] W.-Z. Wang, X.-T. Zhao, and Y.-P. Song, "Application of fuzzy-RBF-based PID controller in superheated steam temperature control system," *Electric Power Automation Equipment*, vol. 27, no. 11, pp. 48–50, 2007.

[5] E.-R. Zheng, L.-C. Hui, and X.-M. Wang, "Intelligent control algorithm of cloud models and simulation research of superheated steam temperature control," *Journal of System Simulation*, vol. 19, no. 1, pp. 98–100, 2007.

[6] Y. Ding, W. Zhao, L. Yuan, and Z. Wu, "Engineering applications of multi-model internal mode control for the superheated steam temperature," *Journal of Tsinghua University*, vol. 49, no. 11, pp. 1805–1808, 2009.

[7] W. Kim, U.-C. Moon, K. Y. Lee, W.-H. Jung, and S.-H. Kim, "Once-through boiler steam temperature control using dynamic matrix control technique," in *Proceedings of the IEEE PES General Meeting*, 2010.

[8] B. Xiao, J. Xiao, X. Dong, S. Li, and X. Wang, "Neural network adaptive control for superheated steam temperature based on MPSO-RBF hybrid optimization," *Journal of Basic Science and Engineering*, vol. 18, no. 4, pp. 705–713, 2010.

[9] W. Wang and J. Wang, "Adaptive inverse control of superheated steam temperature," *Electric Power Automation Equipment*, vol. 33, no. 9, pp. 54–57, 2013.

[10] G. Liang, W. Li, and Z. Li, "Control of superheated steam temperature in large-capacity generation units based on active disturbance rejection method and distributed control system," *Control Engineering Practice*, vol. 21, no. 3, pp. 268–285, 2013.

[11] H. Li, T. Pan, Z. Li, S. Ding, S. Guo, and M. K. Ahsan, "Reheated steam temperature control in thermal power plant using integral-linear active disturbance rejection control," in *Proceedings of the 2017 11th Asian Control Conference*, pp. 2636–2640, 2017.

[12] N. Alamoodi and P. Daoutidis, "Nonlinear control of coal-fired steam power plants," *Control Engineering Practice*, vol. 60, pp. 63–75, 2017.

[13] L. Wei and P. Xu, "Superheated steam temperature control based on valve nonlinear compensation," in *Proceedings of the 37th Chinese Control Conference*, pp. 631–635, 2018.

[14] O. V. Kolesnikova, A. D. Tsypkaikina, and R. A. Prosoedov, "Method of automation control of boiler steam temperature," in *Proceedings of the 2018 International Russian Automation Conference*, 2018.

[15] J. Liu, M. Wang, and Z. Hao, "Boiler reheat steam temperature control based on state variables approach via h∞technology," *Journal of Chinese Society of Power Engineering*, vol. 29, no. 12, pp. 105–110, 2009.

[16] H. Xue and P. Han, "Hybrid optimization control of reheat steam temperature based on BBO algorithm," in *Proceedings of the 7th International Conference on Intelligent Human-Machine Systems and Cybernetics, IHMSC 2015*, pp. 232–235, China, August 2015.

[17] D. Q. Mayne, J. B. Rawlings, C. V. Rao, and P. O. M. Scokaert, "Constrained model predictive control: stability and optimality," *Automatica*, vol. 36, no. 6, pp. 789–814, 2000.

[18] D. Q. Mayne, M. M. Seron, and S. V. Raković, "Robust model predictive control of constrained linear systems with bounded disturbances," *Automatica*, vol. 41, no. 2, pp. 219–224, 2005.

[19] S. Kouro, P. Cortés, R. Vargas, U. Ammann, and J. Rodríguez, "Model predictive control—a simple and powerful method to control power converters," *IEEE Transactions on Industrial Electronics*, vol. 56, no. 6, pp. 1826–1838, 2009.

[20] D. Q. Mayne, "Model predictive control: recent developments and future promise," *Automatica*, vol. 50, no. 12, pp. 2967–2986, 2014.

[21] H. Xiao, Z. Li, C. Yang et al., "Robust stabilization of a wheeled mobile robot using model predictive control based on neurodynamics optimization," *IEEE Transactions on Industrial Electronics*, vol. 64, no. 1, pp. 505–516, 2017.

[22] R. Luo, R. Bourdais, T. J. van den Boom, and B. De Schutter, "Multi-agent model predictive control based on resource allocation coordination for a class of hybrid systems with limited information sharing," *Engineering Applications of Artificial Intelligence*, vol. 58, pp. 123–133, 2017.

[23] H. Li, W. Yan, and Y. Shi, "Continuous-time model predictive control of under-actuated spacecraft with bounded control torques," *Automatica*, vol. 75, pp. 144–153, 2017.

[24] J. Ji, A. Khajepour, W. W. Melek, and Y. Huang, "Path planning and tracking for vehicle collision avoidance based on model predictive control with multiconstraints," *IEEE Transactions on Vehicular Technology*, vol. 66, no. 2, pp. 952–964, 2017.

[25] F. Wang, X. Li, Q. Zhang et al., "Fast calculation method of multivariable control for reheat steam temperature based on Smith control and predictive functional control," *Journal of Computer Applications*, vol. 35, no. 12, pp. 3597–3601, 2015.

[26] H. Chen, *Model Predictive Control*, Science Press, China, 2013.

[27] D. Zheng, *Linear System Theory*, Tsinghua University Press, China, 2002.

Hindawi
Complexity
Volume 2019, Article ID 8642027, 16 pages
https://doi.org/10.1155/2019/8642027

Research Article

A Repeatable Optimization for Kinematic Energy System with Its Mobile Manipulator Application

Ying Kong[1], **Ruiyang Zhang**[1], **Yunliang Jiang**[2] and **Xiaoyun Xia**[3]

[1]*Department of Information and Electronic Engineering, Zhejiang University of Science and Technology, China*
[2]*School of Information Engineering, Huzhou University, China*
[3]*College of Mathematics, Physics and Information Engineering, Jiaxing University, China*

Correspondence should be addressed to Yunliang Jiang; jyl@zjhu.edu.cn

Received 3 May 2019; Accepted 2 July 2019; Published 31 July 2019

Guest Editor: Chun Wei

For repeatable motion of redundant mobile manipulators, the flexible base platform and the redundant manipulator have to be returned to the desired initial position simultaneously after completing the given tasks. To remedy deviations between initial position and desired position of each kinematic joint angle, a special kind of repeatable optimization for kinematic energy minimization based on terminal-time Zhang neural network (TTZNN) with finite-time convergence is proposed for inverse kinematics of mobile manipulators. It takes the advantages that each joint of the manipulator is required to return to the desired initial position not considering the initial orientation of itself for realizing repeatable kinematics control. Unlike the existed training methods, such an optimization of kinematic energy scheme based on TTZNN can not only reduce the convergent position error of each joint to zero in finite time, but also improve the convergent precision. Theoretical analysis and verifications show that the proposed optimal kinematic energy scheme accelerates the convergent rate, which is tended to be applied in practical robot kinematics. Simulation results on the manipulator with three mobile wheels substantiate the timeliness and repetitiveness of the proposed optimization scheme.

1. Introduction

Robot tracking planning of redundant robotic manipulators is to achieve the motion actions to steer the end-effector along with the desired trajectories in the energy optimal system [1–3]. Tracking planning is an important part in engineering robotic applications, such as telecommunication [4], energetic optimization [5], and welding manufacturing [6]. Redundancy of the manipulators is defined as possessing more degrees of freedom (DOF) than the number that the given tasks are required to use. In other words, the end-effector of manipulators will not be able to fulfill a special task if it does not take enough DOF number. The structure of the robot manipulators is tended to be improved with more DOF for the reason of their ability to plan flexible motion trajectory and to optimize different types of kinematic schemes.

Redundant manipulators with fixed base have been investigated by many researchers [7–9]. For expanding the motion dimension of the manipulators and adding control flexibility of the manipulators, redundant mobile manipulators have been attracted more attention in engineering fields. Due to the unpredicted basements, as compared to the traditional redundant manipulators, the control solutions for trajectory planning give out many difficulties, for example, how to coordinate the relationship between the flexible basement driven by the given tasks and the motion trajectory steered by the integration of the redundant mobile manipulators. How to move to the desired path in time is a considerable problem for inverse kinematics of the mobile manipulators. It is generally known that pseudoinverse solution in joint-velocity formulation is the important method for inverse motion. However, the singularity of each joint angle is not able to be guaranteed when they are moving along the trajectory. Furthermore, each joint angle may not be in their desired initial position after completing the given tasks, which will not yield repetitive motion phenomenon of joint angles. The end-effector of the redundant manipulators may have

difficulties to do the same work when it is demanded for tracking a closed path in the workspace.

To solve these kinematic problems of redundant mobile manipulators, many perfect solving methods have been investigated in many literatures [10–12]. In [13], Tchon proposed a repetitive optimization for kinematic mobile manipulators in engineering fields using endogenous configuration algorithm. However, the joint limits of the manipulators were not considered when the broken phenomenon in mechanism may occur. Miah *et al.* [14] firstly proposed an online optimization algorithm for trajectory moving when the mechanism parameters and measurement error of the nonholonomic differential-drive mobile manipulators were unknown. Tao *et al.* [15] proposed a kind of adaptive neural network model for spacecraft given special tasks in a coordinated control with the consideration of arriving delays and operative uncertainties. In [16], a near-optimal trajectory planning scheme was proposed for receding-wheeled mobile manipulators. Xu [17] proposed a trajectory control method based on neural network for omnidirectional wheeled mobile redundant manipulators with unknown disturbances. In [18], a predictive control scheme with sum-of-squares approach for obstacle avoidance problems in an unknown environment with various polynomial systems was investigated. As the traditional forward kinematics problems concerned, it transformed the joint angles data into Cartesian space with pseudoinverse method for mobile manipulators. However, the solutions for inverse kinematics problems may have many multiple situations and appear deformity of each joint, which is more difficult to be solved directly [19, 20]. Actually, most of the given tasks with the end-effector are in Cartesian while the angular constraint works are in the joint space. How to coordinate the trajectory planning problem in two spaces is worth thinking about especially for inverse motion problem of redundant mobile manipulators.

With the development of neural technologies, a great number of neural networks have been sprung up for the ability of parallel processing, adaptability, memory capacitance, and convenient hardware implementation. Around adaptive neural networks, many research works have been proposed to discuss about. He *et al.* [21] put forward an adaptive neural network model for a health intelligent robot with unknown parameter dynamic system. Chen *et al.* [22] designed an effective adaptive neural network structure for controllers with uncertain information about input parameters and output slide constraints. In literature [23], a prescribed adaptive neural network model characterizing high computation and enough stability was introduced for a disturbed nonlinear system. Recently, with the deep learning of neural networks, a series of network structures are derived around adaptive dynamics. He [24] studied the adaptive fuzzy neural networks for trajectory designing of the mobile manipulators using impedance learning, which effectively integrate the robot arm and the surrounding environment and induce the robotic manipulators to arrive the destination freely. In [25], the adaptive neural network scheme with radial basis function (RBF) was developed to be applied to precision trajectory tracking of distributed movable manipulator device. After the widespread with Gradient recurrent neural network (GNN) [26], Chen *et al.* [27] proposed a Jacobian-matrix-adaption method based on Zhang neural network for path schematization of the manipulators only considering the input and output parameter information of the robotic models. Furthermore, another kind of recurrent neural network (RNN), which has the powerful energy for multirobot processing, is popularized in redundant mobile manipulators and learning systems [28]. Li *et al.* [29] considered the motion planning for multiple manipulators using distributed neural schemes while all the manipulators can reach the desired position as digital information received. Jin [30] introduced several RNN models from the perspective of control theorem to minimize dynamical error. A type of Zhang neural networks (ZNN) using RNN models is established for solving time-varying calculation problems. Recently, Zhang [31] proposed a varying-parameter Zhang neural network (VP-ZNN), which takes the exponential convergence in robotic engineering fields. In addition, convergence and robustness of VP-ZNN with different activation functions is presented in [32], which is deemed to be applied in repetitive kinematics of manipulators.

There are many solutions for the solving of mechanical kinematics with different types of redundant manipulators. Among these conventional kinematic problems, repetitive movements are often encountered in various engineering areas. Closed path when redundant manipulators have finished the given tasks is the basis of repetitive works especially in the operation process of redundant mobile manipulators. To achieve repetitive motion, a series of Zhang neural networks (ZNN) are proposed, which are formulated as quadratic problems subjected to equation and joint constraints [33–35]. As comparing to the traditional RNN neural methods, ZNN models have the ability of realize the repeatable motion for mobile manipulators as long as time is infinity. As a systematic methodology, zeroing neural dynamic models (ZND) [36–38] have been gradually formulated and situated in many applications, which can avoid the disturbance of internal noise produced by the dynamical systems. In order to shorten the convergent time with ZNN, Li *et al.* [39] firstly introduced a special kind of activation functions to accelerate the convergent speed of ZNN model in finite time, which greatly improved the convergent time. From then on, different ideals about Li's activation function have been studied in literatures and show the finiteness of ZNN combining with this novel nonlinear activated function [40–42]. Motivated by these research results, around the finite-time convergence of ZNN, we investigate a type of terminal-time Zhang neural network (TTZNN), which can reduce the convergent error of dynamic energy system to zero in appointed time. Based on this activation function, a repeatable optimization of kinematic energy system is constructed and systematic theory and finiteness analysis for motion planning of redundant mobile manipulators are provided. Experimental results and comparisons are illustrated the superiority and timeliness of the TTZNN for trajectory tracking of mobile manipulators.

The remainder of this paper is divided into five parts. In Section 2, a kinematic model of redundant mobile manipulator is presented. Section 3 gives out the theoretical

analysis and proof of TTZNN to guarantee the precision and timeliness of the proposed energy system. At the same time, a repeatable motion scheme is established. Stability and convergence of TTZNN are given out in Section 4. In Section 5, numerical simulations are visualized to validate the superiority of TTZNN. Section 6 concludes the paper with future prospects. Finally, the main contributions of this work are listed as follows.

(1) A novel repeatable optimization for kinematic energy system with finite-time convergence based on TTZNN for solving trajectory planning of redundant mobile manipulators is proposed. It is the first time to put forward such a finite-time kinematic criterion, which gives out a new inspiration in the area of robotic manipulator fields.

(2) A terminal-time Zhang neural network (TTZNN) is established for solving repeatable motion planning of mobile manipulators. It is the first time for providing such a neural activation function with finite-time convergence of ZNN as well as in the deep learning of mobile manipulators not considering the initial position of each joint.

(3) The model of the redundant mobile manipulator in this manuscript is the first time to be structured, which is composed of a three-wheel platform and a seven free joints redundant manipulator PA10. It makes a progress in the field for repetitive control of complex mobile manipulators.

(4) Numerical simulation experiments and comparisons with TTZNN optimization scheme of kinematic energy system verified the superiority and timelessness of the proposed trajectory planning optimization. Furthermore, different motion schemes and neural solutions for repeatable motion are compared in the end.

2. Kinematics Structure of Mobile Manipulators

In this section, a mobile manipulation which is composed of a mobile platform with three Swedish wheels and a seven-DOF manipulator PA10 is constructed to demonstrate the real-time of the repetitive motion scheme. The 3D model of the mobile manipulation is visualized in Figure 1. Three Swedish wheels of the mobile platform are all independent. For simplicity, only the end-effector position for given trajectories is considered. In the following paragraphs, the kinematics principle of the mobile platform is analyzed according to the content in literature [43]. Then, the kinematic equation of the PA10 manipulator with seven-DOF joints is given by [44]. Finally, the kinematics modeling of mobile system is obtained combining with the velocity kinematics equation.

2.1. Kinematic Formulation of The Mobile Platform. The geometrical rotation of the mobile base is visualized in Figure 2. Symbols described in Figure 2 are explained as below.

(1) C: center point of mobile base; the coordinates in base plane are (x_c, y_c, z_c). Besides, z_c is an invariable constant;

(2) L: distance between wheels and C;

(3) r: radius about each Swedish wheel;

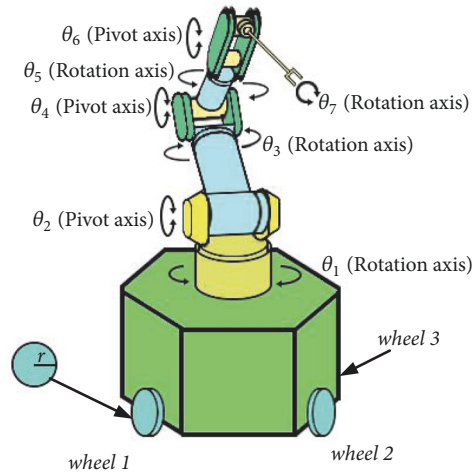

Figure 1: 3D integration model of mobile manipulator with three Swedish wheels.

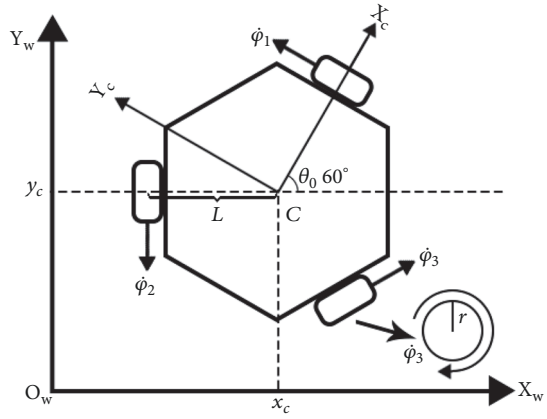

Figure 2: Geometrical modeling of the mobile platform.

(4) θ_0: heading angle of the kinematic base; angle derivative with time is the velocity $\dot{\theta}_0$;

(5) $\dot{\varphi}_1, \dot{\varphi}_2, \dot{\varphi}_3$: the rotational velocity of each Swedish wheel.

According to Figure 2, the kinematic formulation of mobile base can be easily got. For the derivative of heading angle with respect to time $\dot{\theta}_0$, we have

$$\dot{\theta}_0 = A\dot{\varphi} \tag{1}$$

where $A = [r/(3L), r/(3L), r/(3L)]$ and $\dot{\varphi} = [\dot{\varphi}_1, \dot{\varphi}_2, \dot{\varphi}_3]^{\mathrm{T}}$. And for the derivative of point C's coordinate values with respect to time $\dot{x}_c$ and $\dot{y}_C$, we have

$$\dot{P}_c = B\dot{\varphi} \tag{2}$$

where $\dot{P}_c = [\dot{x}_c, \dot{y}_c]^{\mathrm{T}}$ and B is a matrix related to the heading angle of mobile base θ_0.

$$B = \frac{2}{3}r\begin{bmatrix} -\sin(\theta_0) & -\sin\left(\frac{\pi}{3}-\theta_0\right) & \sin\left(\frac{\pi}{3}+\theta_0\right) \\ \cos(\theta_0) & -\cos\left(\frac{\pi}{3}-\theta_0\right) & -\cos\left(\frac{\pi}{3}+\theta_0\right) \end{bmatrix} \tag{3}$$

Table 1: D-H parameters of PA10.

Joint(rad)	Axis	a_i(m)	α_i(rad)	d_i(m)	θ_i(rad)
θ_1(Shoulder1)	Rotating	0	-π/2	0.317	θ_1
θ_2(Shoulder2)	Pivoting	0	π/2	0	θ_2
θ_3(Shoulder3)	Rotating	0	-π/2	0.45	θ_3
θ_4(Elbow1)	Pivoting	0	π/2	0	θ_4
θ_5(Elbow2)	Rotating	0	-π/2	0.48	θ_5
θ_6(Wrist1)	Pivoting	0	π/2	0	θ_6
θ_7(Wrist2)	Rotating	0	0	0.07	θ_7

Combining (1) and (2), the following equations can be obtained:

$$\begin{bmatrix} \dot{\theta}_0 \\ \dot{P}_C \end{bmatrix} = \begin{bmatrix} A \\ B \end{bmatrix} \times \dot{\varphi} \tag{4}$$

This article takes $r = 0.1$ m and $L = 0.3$ m.

2.2. Kinematics of PA10 Redundant Manipulator. The PA10 manipulator is a redundant robotic arm with seven-DOF joints. For any stationary manipulators, the end-effector matrix vector $r(t)$ is the kinematic path produced by the joint matrix vector $\theta(t)$. The forward equation of the kinematic manipulators is defined as

$$r(t) = f(\theta(t)) \tag{5}$$

In this manuscript, the end-effector vector of PA10 manipulator is written as $r_w(t) = [x_w, y_w, z_w]^T$ and the joint vector of PA10 manipulator is written as $\theta(t) = [\theta_1(t), \theta_2(t), \ldots, \theta_7(t)]^T$. The mechanical information about PA10 manipulator can be found in literature [44]. Due to the space limitation, details of each joint for PA10 manipulator are omitted here. The D-H parameters of the PA10 manipulator are listed in Table 1.

2.3. Integration Modeling of The Mobile Manipulator. After understanding the structure of the mobile base and the seven-joint manipulator, the model of the proposed mobile manipulator with three Swedish wheels is formulated by the kinematic integration of PA10 manipulator and the movable platform. In fact, the main difference between mobile manipulators and stationary manipulators is just the movable base. The movable platform may bring uncertainty prospect. Connecting the bottom coordinate system with global coordinate system by using the transformation matrix, an entirely new kinematical control equation based on global coordinate system can be described as follows

$$r_w = \begin{bmatrix} R(\theta_0) & P_C \\ 0 & \end{bmatrix} \begin{bmatrix} f(\theta) \\ 1 \end{bmatrix} = \begin{bmatrix} P_C \\ 0 \end{bmatrix} + R(\theta_0) f(\theta) \tag{6}$$

where $R(\theta_0)$ is the rotation matrix between PA10 manipulator and the mobile platform.

$$R(\theta_0) = \begin{bmatrix} \cos\theta_0 & -\sin\theta_0 & 0 \\ \sin\theta_0 & \cos\theta_0 & 0 \\ 0 & 0 & 1 \end{bmatrix} \tag{7}$$

By differentiating (6) with respect to time t, we have

$$\dot{r}_w = J(\theta_0, \theta) \begin{bmatrix} \dot{\theta}_0 \\ \dot{\theta} \end{bmatrix} + \begin{bmatrix} \dot{P}_C \\ 0 \end{bmatrix} \tag{8}$$

Jacobin matrix $J(\theta_0, \theta)$ is defined as $J(\theta_0, \theta) = \partial g(\theta_0, \theta)/\partial\omega$ with $\omega = [\theta_0; \theta]$. To simplify (8), substituting (4) into (8), (8) can be rewritten as

$$\dot{r}_w = J(\theta_0, \theta) \begin{bmatrix} A\dot{\varphi} \\ \dot{\theta} \end{bmatrix} + \begin{bmatrix} B\dot{\varphi} \\ 0 \end{bmatrix} \tag{9}$$

Set a vector $\Theta = [\varphi^T, \theta^T]^T$, and $\dot{\Theta} = [\dot{\varphi}^T, \dot{\theta}^T]^T$ is the time derivative of Θ. Equation (9) can be rewritten as follows:

$$\dot{r}_w = \left(J(\theta_0, \theta) \begin{bmatrix} A & 0 \\ 0 & I \end{bmatrix} + \begin{bmatrix} B & 0 \\ 0 & 0 \end{bmatrix} \right) \begin{bmatrix} \dot{\varphi} \\ \dot{\theta} \end{bmatrix} = K\dot{\Theta} \tag{10}$$

where I represents the identity matrix and parameter and K is a matrix and is defined as

$$K = J(\theta_0, \theta) \begin{bmatrix} A & 0 \\ 0 & I \end{bmatrix} + \begin{bmatrix} B & 0 \\ 0 & 0 \end{bmatrix} \tag{11}$$

The kinematical equation (10) of the proposed mobile manipulator system is finally derived on velocity-level solution.

3. Optimization of The Kinematic Energy System

As mentioned in Introduction part, a manipulator is redundant when its free joints are more than the minimum number of angles required to execute the special tasks with end-effector. An important issue in operating procedure carries out the inverse motion resolution problem, which is related to the kinematic designing of redundant manipulators. The traditional illustration of such a motion problem is that given the desired trajectory $r_d(t) \in R^m$ of the end-effector of the manipulators, the corresponding trajectory of each joint angle $\theta(t) \in R^n$ is required to be calculated online. In order to get the solution $\theta(t)$, consider the following mathematics:

$$f(\theta) \longrightarrow r_d \tag{12}$$

The kinematical function $f(\cdot)$ is a nonlinear unknown system. Mobile manipulators possess more free joints than the necessity to complete a specific task by the end-effector (in expression $m < n$). Therefore, the repetitive motion scheme for redundant manipulators in literature [7, 9] may not be taken effect for mobile manipulators. In addition, the initial position of each free joint angle has to be considered. For mobile manipulators, wheels of the stationary platform are rotatable and the manipulator upstairs is redundant, which is tended to cause kinematic uncertainty phenomenon. In literature [44], a repeatable motion scheme is proposed for mobile manipulators with two wheels as long as the convergent time is infinity. Motivated by the above research ideas,

we present a repeatable optimization for kinematic energy system with trajectory planning of mobile manipulators. Such an optimization criterion for kinematic control can not only minimize the distance between the initial joints state and the final joints state after executing time, but also reduce the convergent time of each joint angle to zero in limited time.

Let us consider the norm equation (13) for repeatable kinematic energy scheme

$$\begin{aligned} &\text{minimize} \quad \frac{1}{2}\left\|D\dot{\Theta}+g\right\|_2^2 \\ &\text{subject to} \quad K\dot{\Theta}=\dot{r}_{\text{wd}}+\kappa\left(r_{\text{wd}}-r_{\text{w}}\right) \end{aligned} \tag{13}$$

where $D = [C,0;0,I] \in R^{(n+m)\times(n+m)}$, $C = [A\cos(\theta_0);B]$. $g = [\beta_1\Psi(\sin(\theta_0)-\sin(\theta_0(0)));\beta_2\Psi(P_c-P_c(0));\beta_3\Psi(\theta-\theta(0))]$. $\theta_0(0)$, $P_c(0)$, and $\theta(0)$ represent the initial state of all free joints including the rotating platform. β_1, β_2, β_3, and κ are four adjustable parameters greater than 0. r_{wd} is the desired path of the end-effector; r_{w} is the trajectory of end-effector in action. The repetitive optimization of kinematic energy system for mobile manipulator (13) can be simplified as

$$\begin{aligned} &\text{minimize} \quad \frac{1}{2}\dot{\Theta}^{\text{T}}D^{\text{T}}D\dot{\Theta}+g^{\text{T}}\dot{\Theta} \\ &\text{subject to} \quad K\dot{\Theta}=\dot{r}_{\text{wd}}+\kappa\left(r_{\text{wd}}-r_{\text{w}}\right) \end{aligned} \tag{14}$$

3.1. Theoretical Analysis. To realize the repeatable kinematic control for mobile manipulators, there are three important factors in the designing mode, i.e., the each joint angle θ_i of the redundant manipulators located on mobile platform, the rotation direction θ_0 of the platform base, and the location point P_c of the redundant manipulator on the rotational platform. Obviously, three wheels of the mobile platform are likely to deviate from the desired initial position at first. At the same time, joints of the redundant manipulator with seven DOF are prompt to be fixed with incorrect state for the parameter deviation of the manipulator itself. Therefore, repeatable optimization for kinematic energy system with mobile manipulators is equivalent to get the repetitiveness of the three variable θ_i, θ_0, and P_c. By following the Zhang design rule in [9], we get the following realizing steps.

Firstly, the idea of terminal-time dynamic function $E(t)$ ($E(t) = e_i(t)$), i=1,2,...n, can be set up to face finite-time convergent solving problem. Secondly, we can choose a limited value activation function through the Zhang neural network designing rule so that the convergent time of the kinematic energy system is reduced to zero rapidly. We get the dynamic equation of TTZNN as below.

$$\dot{e}_i(t) = -\beta\sqrt{\frac{\left|e_i(t)\right|}{1/\delta+\left|e_i(t)\right|}}\,\text{sgn}\left(e_i(t)\right) = -\beta\Psi\left(e_i\right) \tag{15}$$

with $\beta_i > 0$, $0 < \delta < 1$. sgn(·) is sign function of the value −1, 0, 1. Finally, based on the terminal-time Zhang neural function (15), we expand the designing rule (15) for different error definition and we obtain the following three types of error functions:

$$E_1 = \sin\left(\theta_0\right) - \sin\left(\theta_0(0)\right) \tag{16}$$

$$E_2 = P_c - P_c(0) \tag{17}$$

$$E_3 = \theta - \theta(0) \tag{18}$$

where $\theta(0)$, $\theta_0(0)$, and $P_c(0)$ represent the initial position of θ, θ_0, and P_c. It is necessary to point out that the rotating platform is circulating at 360 degrees with time. The orientational angle θ_0 needs to be returned to the desired initial position. The position error $\theta_0 - \theta_0(0)$ is not possible for realizing repetitive kinematics of the mobile platform. Therefore, the sine function is activated and the disposal scheme of optimization energy system is easy to yield. By combining the design rule (15) of TTZNN, the following three time-varying dynamic equations can be obtained:

$$\dot{\theta}_0\cos\left(\theta_0\right) = -\beta_1\Psi\left(\sin\left(\theta_0\right) - \sin\left(\theta_0(0)\right)\right) \tag{19}$$

$$\dot{P}_c = -\beta_2\Psi\left(P_c - P_c(0)\right) \tag{20}$$

$$\dot{\theta} = -\beta_3\Psi\left(\theta - \theta(0)\right) \tag{21}$$

where $\beta_1 > 0$, $\beta_2 > 0$, and $\beta_3 > 0$ are the scalar parameters for convergent rate. Theoretical analysis in the next section has been proved the equation (19), (20), and (21) holds for $t > t_s$, where t_s shows a constant after e_{ij} converge to zero. Each joint angle of the mobile redundant manipulator system can move back to their desired initial place exponentially no matter the initial position of the mobile manipulator is wherever.

Actually, the important three variables in repeatable kinematic energy system of such mobile manipulator structure are θ_0, p_c and movable angles Θ. Equations (19)-(20) have to be evolved into matrix form. Let us recall the dynamic equations (1) and (2) in Section 2.1; the following matrix equation can be obtained

$$C\dot{\varphi} + \begin{bmatrix} \beta_1\Psi\left(\sin\left(\theta_0\right) - \sin\left(\theta_0(0)\right)\right) \\ \beta_2\Psi\left(P_c - P_c(0)\right) \end{bmatrix} = 0 \tag{22}$$

Then, the matrix-vector time-varying dynamical equation can be described as below:

$$D\dot{\Theta} + g = 0 \tag{23}$$

Combining with the definition of D and g, the corresponding parameters are $D = [C,0;0,I]$, $C = [A\cos(\theta_0);B]$, $g = [\beta_1\Psi(\sin(\theta_0) - \sin(\theta_0(0)));\beta_2\Psi(P_c - P_c(0));\beta_3\Psi(\theta - \theta(0))]$.

Remark 1. From the above derivation, we can get the conclusion that the solution for minimization of the kinematic energy system (14) is equal to solve the time-varying problem (23). The repetitive motion control of such mobile manipulator can be achieved while the convergent time is finite. It is necessary to mention that the kinematic scheme in (14) looks like a traditional optimization matrix equation, but the corresponding parameters of D and K in (14) result in different kinematics meaning. To avoid the occurrence of accidents

during the movement of each joint, it is better to compute the convergent error with $\|D\dot{\Theta} + g\|_2$. $\|\cdot\|_2$ represents a two-norm vector. Therefore, we get the optimization scheme for mobile manipulators for doing repetitive trajectory tasks in finite time not considering the initial position of each kinematic joint.

3.2. Designing for Kinematics Energy System. Analysis about the scheme for kinematics energy system (14) is stated. The optimal index of $\|D\dot{\Theta} + g\|_2^2$ is formulated as $(D\dot{\Theta} + g)^{\mathrm{T}}(D\dot{\Theta} + g)/2$. The optimal performance can be exploited as $X^{\mathrm{T}}D^{\mathrm{T}}DX/2 + g^{\mathrm{T}}DX + g^{\mathrm{T}}g/2$. Since the repetitive motion optimization scheme is based on velocity level and the variable $\dot{\Theta}$ is object to be optimized. The term $g^{\mathrm{T}}g/2$ is thought to be a constant matrix in the executing process. The repeatable optimization index of kinematics energy system can be defined as the following quadratic optimization problem:

$$\begin{aligned} &\text{minimize} \quad \frac{X^{\mathrm{T}}MX}{2} + P^{\mathrm{T}}X \\ &\text{subject to} \quad KX = \dot{r}_{\mathrm{wd}} + \kappa\left(r_{\mathrm{wd}} - r_{\mathrm{w}}\right) \end{aligned} \tag{24}$$

where $X = \dot{\Theta}$, $M = D^{\mathrm{T}}D \in R^{(n+3)\times(n+3)}$, and $P = D^{\mathrm{T}}g \in R^{n+3}$. Other parameters are defined as before. The performance index in (24) is for the repeatable motion planning of kinematics energy system and originated from the simplified formula of (13) and (14). The term of $KX = \dot{r}_{\mathrm{wd}} + \kappa(r_{\mathrm{wd}} - r_{\mathrm{w}})$ represents forward kinematics equation while the initial moving point is drifting from the desired path.

Remark 2. Let us look at the criterion (24); the kinematic scheme with equation limitation has not been considered joint limits of the redundant manipulator on mobile platform. Accidents may be happened while the unexpected trajectories are given and the redundant manipulators may be damaged, which leads to do nonrepeated motion. At the same time, we can not incorporate the physical limits of the redundant manipulators into the optimization scheme. Therefore, we set the maximum border of each angle joint in programming before simulation experiments are performed. The primary tasks will be completed accurately with this three-wheel manipulator system.

4. Terminal-Time ZNN Approach

In Section 3, a universal repeatable optimization of the kinematic energy system is presented and formulated for trajectory planning of mobile manipulators with three wheels. To solve the optimal scheme (24), we use the solution of terminal-time Zhang neural network (TTZNN) approach (15) to calculate the convergent time t. By deriving the variable $\dot{\Theta}$ with Lagrangian theory, we get the following time-varying equation:

$$W(t)\, y(t) - v(t) = 0 \tag{25}$$

with $W(t) = [M, K^{\mathrm{T}}(t); K(t), 0] \in R^{(n+m)\times(n+m)}$, $y(t) = [X(t); \lambda(t)] \in R^{n+m}$, and $v(t) = [-P; \dot{r}_{\mathrm{wd}} + \kappa(r_{\mathrm{wd}} - r_{\mathrm{w}})]$.

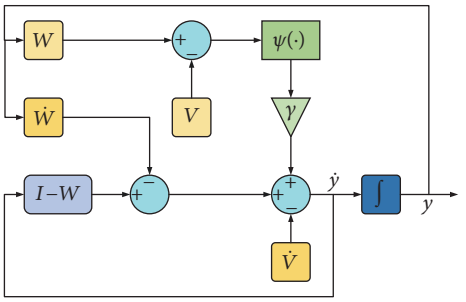

Figure 3: Diagram procedure of the TTZNN model (27).

The vector-valued convergent error function is given as

$$E(t) = W(t)\, y(t) - v(t) \tag{26}$$

To make the every vector $e_i(t)$ of convergent error to zero timely, following the TTZNN design formula (15), the repetitive kinematics modeling based on TTZNN can be depicted:

$$\dot{y} = (I - W)\,\dot{y} + \dot{v} - \dot{W}y - \beta\Psi\left(Wy - v\right) \tag{27}$$

The corresponding control diagram for TTZNN (27) is visualized in Figure 3.

Theorem 3. *Consider the repeatable kinematics scheme (24). Given any initial value of vector $y(0)$ in (27), the state value $y(t)$ of dynamic system (27) globally converges to the theoretical value $y^*(t)$ in finite time t_s:*

$$\begin{aligned} t_s \le \frac{1}{\beta\delta}\Bigg(&\frac{H^3\left(e_i(0)\right)}{\delta e_i(0)} - H\left(e_i(0)\right) \\ &- \frac{1}{2}\ln\left|\frac{H\left(e_i(0)\right) - 1}{H\left(e_i(0)\right) + 1}\right|\Bigg) \end{aligned} \tag{28}$$

where $H(e_i(0)) = \sqrt{1 + (\delta e_i(0))^{-1}}$.

Proof. The proof procedure is divided to two parts. Firstly, to prove the stability of the proposed TTZNN, we need to introduce the Lyapunov theorem candidate like $V(t) = e_i^2(t)/2$. The time derivative of $V(t)$ is expressed $\dot{V}(t) = e_i\dot{e}_i$. Therefore, we can get the equation

$$\dot{V}(t) = -\beta\sqrt{\frac{|e_i(t)|}{1/\delta + |e_i(t)|}}\,\mathrm{sgn}\left(e_i(t)\right)e_{ij}(t) \tag{29}$$

where $\beta > 0$, $\dot{V}(t) < 0$. $y(t)$ in TTZNN modeling (27) can converge to its theoretical value $y^*(t)$.

Secondly, let us consider the terminal-time dynamic system (15); if $e_i(t) \ge 0$, we get

$$\dot{e}_i(t) = -\beta\sqrt{\frac{e_i(t)}{\delta^{-1} + e_i(t)}} \tag{30}$$

In order to solve (30) with time t, we need to introduce symbol x, which satisfies $e_{ij} = (\delta x)^{-1}$. Then, we get

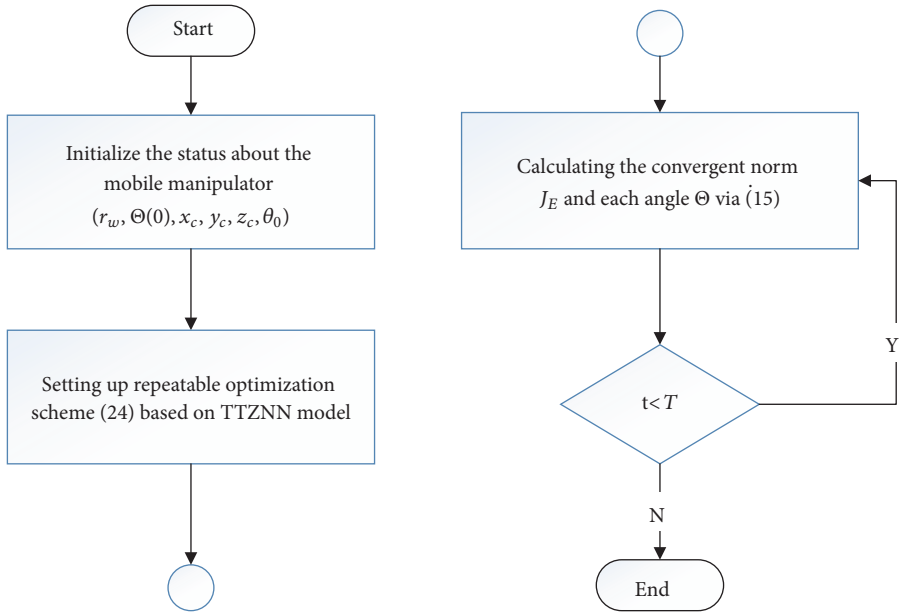

Figure 4: The flowchart of TTZNN model for kinematic planning of the mobile manipulator.

$dt = \sqrt{1+x}(\beta\delta x^2)^{-1}dx$. By means of integral methods, we obtain the solution of (30):

$$t = \frac{-1}{\beta\delta}\left[\frac{(1+x)^{3/2}}{x} - \frac{1}{2}\left(2\sqrt{1+x} + \ln\left|\frac{\sqrt{1+x}-1}{\sqrt{1+x}+1}\right|\right)\right]\Bigg|_{x(0)}^{x(t)} \tag{31}$$

Setting $x = (\delta e_i)^{-1}$, we have

$$t = \frac{-1}{\beta\delta}\left(\frac{H^3(e_i)}{(\delta e_i)^{-1}} - H(e_i) - \frac{1}{2}\ln\left|\frac{H(e_i)-1}{H(e_i)+1}\right|\right)\Bigg|_{x(0)}^{x(t)} \tag{32}$$

When $e_i(t) = 0$, the convergence time is calculated.

$$t_s \le \frac{1}{\beta\delta}\left(\frac{H^3(e_i(0))}{(\delta e_i(0))^{-1}} - H(e_i(0)) - \frac{1}{2}\ln\left|\frac{H(e_i(0))-1}{H(e_i(0))+1}\right|\right) \tag{33}$$

□

For better understanding, the solution steps for the entire executing process of kinematics energy optimization algorithm are visualized the in Figure 4.

5. Verification for Optimization of Kinematic Energy System

In this section, different trajectories with the three-wheel mobile manipulator visualized in Figure 1 are performed to illustrate the repetitiveness and finiteness of the proposed optimization scheme of the kinematics system based on TTZNN model (27). Comparisons among ZNN model, TTZNN model, and GNN model are analyzed from the perspective of convergence in form of $\|\cdot\|_2$. It is necessary to point out that the scalar parameters β, λ, κ, and δ are positive constant. In the executing procedure of mobile manipulators, the parameters β and λ are inappropriate to be set much larger as the hardware is not allowed. It will bring algebraic circles with simulation experiments and lead to termination of the mobile manipulator in motion.

5.1. Circular Path Tracking. To realize the repeatable kinematics of the proposed mobile manipulator model, the end-effector is required to complete a circular path with radius $r = 0.5$m. During the tracking procedure, the desired initial joints of the redundant manipulator PA10 are $\theta^*(0) = [0, -\pi/4, 0, \pi/2, 0, -\pi/4, 0]^T$. Joints of the three rotational wheels are $\varphi = [0, 0, 0]$. The actual initial joints are $\theta(0) = [0, -\pi/4, 0, \pi/2, 0, -\pi/4 + 2, 0]^T$. The deviation of the sixth angle with redundant manipulator is 2 rad. The executing recurrent time is $T = 10$s. The axes of X, Y, Z for the desired trajectory of the end-effector are given as

$$\begin{aligned} r_{wdx}(t) &= 0.2 \times \cos\left(2\pi\left(\sin\left(\frac{\pi t}{2T}\right)\right)^2\right) - 0.1646 \\ r_{wdy}(t) &= 0.15 \times \cos\left(\frac{\pi}{6}\right)\sin\left(2\pi\left(\sin\left(\frac{\pi t}{2T}\right)\right)^2\right) \\ r_{wdz}(t) &= 0.1 \times \cos\left(2\pi\left(\sin\left(\frac{\pi t}{2T}\right)\right)^2\right) + 0.5518 \end{aligned} \tag{34}$$

The corresponding simulation results are visualized in Figures 5, 6, and 7. Figure 5(a) shows the motion trajectory

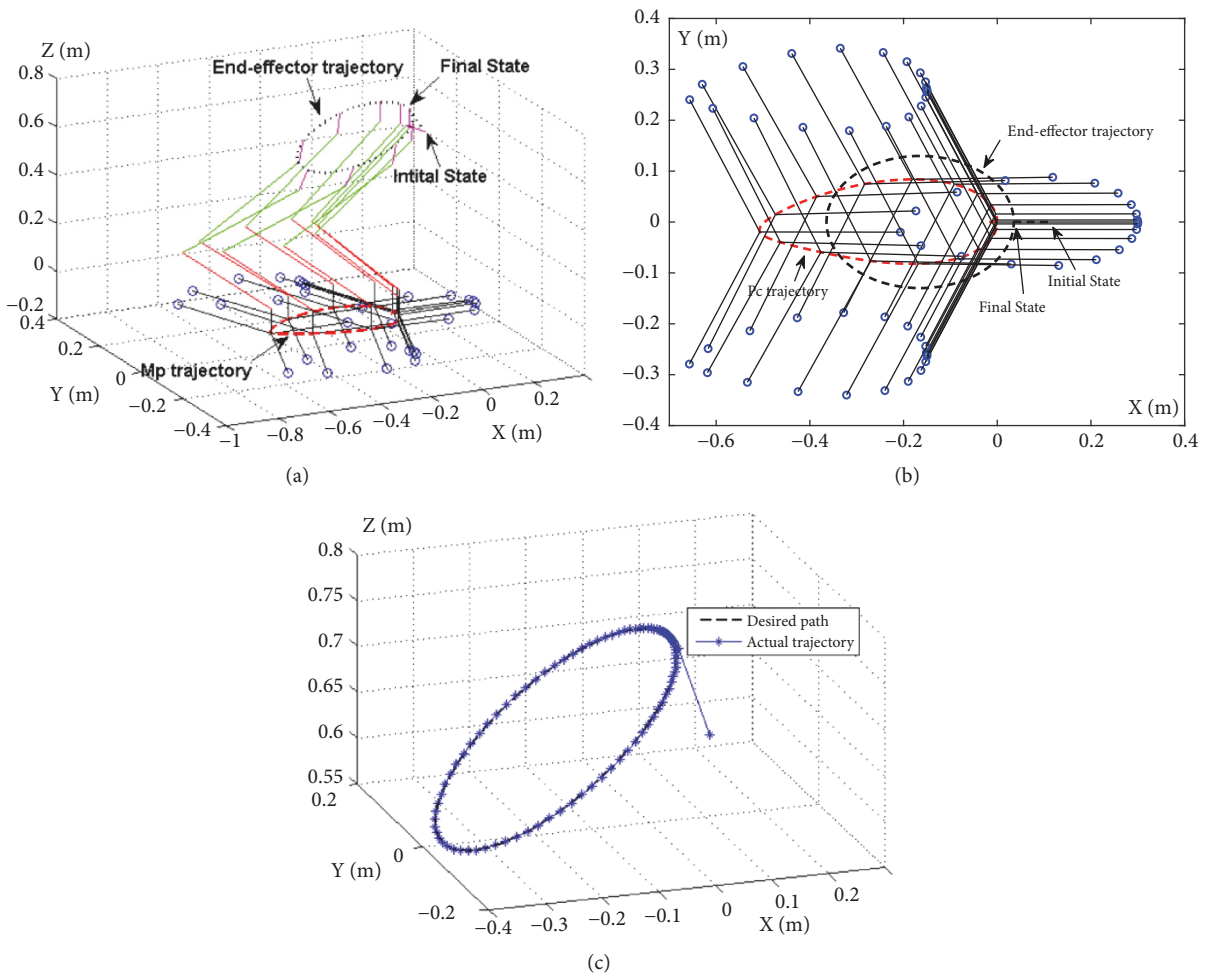

FIGURE 5: Simulation results about repeatable optimization of kinematic energy system with TTZNN solver when the end-effector is required to complete a circular path. (a) Motion trajectories with the entire mobile manipulator. (b) Vertical view for entire mobile manipulator. (c) Profiles of the desired trajectory and actual path of the end-effector.

of the entire mobile manipulator with ten free joints during the executing time. The actual path of the end-effector and the desired path of the end-effector are overlapped, which illustrates the kinematic repetitiveness. Figure 5(b) shows us the kinematic trajectories of the platform wheels, connection point C, and end-effector from vertical perspective. The motion direction of the end-effector of the redundant manipulator is visualized in Figure 5(c). The initial position of the end-effector is deviate from the desired trajectory at first. Then, it moves to the desired trajectory in few seconds. The corresponding convergent precision is specialized in Figures 6(b) and 6(a). The distance between the desired path and actual motion path is less than 10^{-4} in X, Y, Z three directions. The joints movements with the redundant manipulator depicted in Figure 7(a) are continuous and smooth, which illustrates the all the joints come back to the initial desired position.

For illustrating the movement of three wheels with mobile platform, Figures 6(c), 6(d), 7(b), and 7(c) are investigated to illustrate the finial position of the mobile wheels. At the beginning of the task, profiles of mobile platform ($x_c(0) = 0, y_c(0) = 0, z_c(0) = 0$) are specialized in Figure 7(b). Later, the mobile platform moves with the redundant manipulator quickly to complete the circular path. It is to say that the flexible platform takes larger kinematic space than fixed base manipulators. The change profile of the heading angle with the mobile platform θ_0 is shown in Figure 6(d), which coordinates with the rotation base. Figure 7(c) visualizes the trajectories of three wheels. At first, the three Swedish wheels are stationary. With increase of radius, the mobile base needs to help the redundant manipulator for tracking. Therefore, it moves away from the initial point $x_c(0), y_c(0), \theta_0(0)$ gradually but returns back to the desired space at last, which is synthesized with the profiles in Figures 6(c) and 6(d). The above experimental results substantiate the effectiveness of the proposed repeatable kinematic optimization (24) based on TTZNN neural solver.

5.2. Lissajous Path Tracking. To verify the finiteness and convergence of the proposed TTZNN method, we outline a

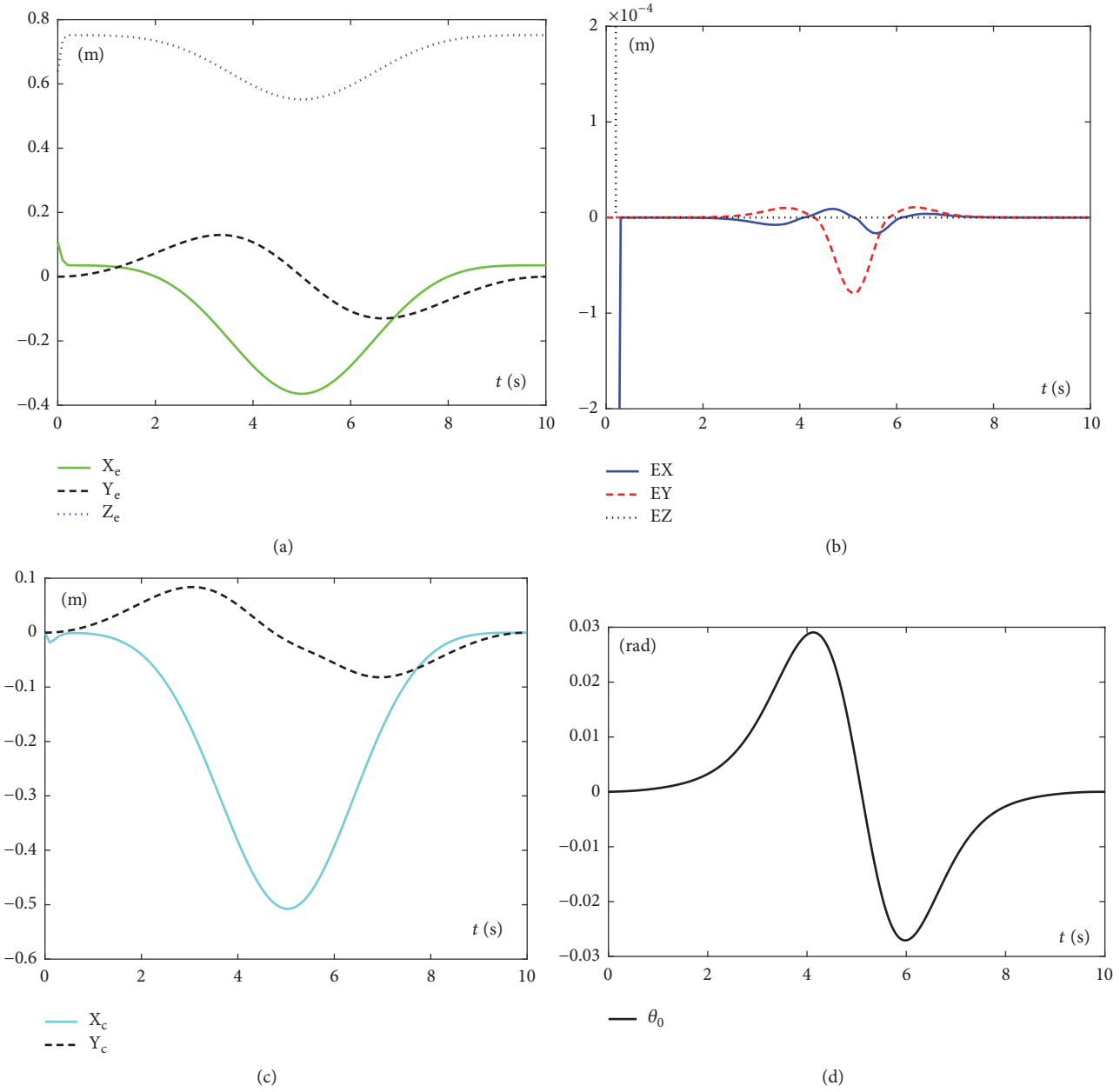

FIGURE 6: Circular planning profiles of the three-wheel mobile manipulator synthesized by TTZNN model (27). (a) Position files of the end-effector. (b) Position error of the end-effector in three dimensions. (c) Profiles of the mobile base for P_C. (d) Trajectory with heading angle θ_0.

desired Lissajous-shaped trajectory to be functioned by the end-effector of the mobile manipulator in three axis x, y, and z.

$$\begin{aligned} r_{\mathrm{wdx}}(t) &= 0.8\cos\left(4\pi\left(\sin\left(\frac{\pi t}{2T}\right)\right)^2 + \frac{\pi}{6}\right) - 0.7645 \\ r_{\mathrm{wdy}}(t) &= 0.8\sin\left(4\pi\left(\sin\left(\frac{\pi t}{2T}\right)\right)^2 + \frac{\pi}{6}\right) - 0.0073 \\ r_{\mathrm{wdz}}(t) &= 0.7518 \end{aligned} \tag{35}$$

The executing recurrent time is $T = 10$s. The designing parameters $\beta_1 = 10$, $\beta_2 = 10$ and $\beta_3 = 10$ are used in this manuscript. The initial desired position of the mobile base is set $x_c = 0, y_c = 0, z_c = 0$. The initial value of joint angles with redundant manipulator PA10 is given $\theta^*(0) = [0, -\pi/4, 0, \pi/2, 0, -\pi/4, 0]^{\mathrm{T}}$ rad. Deviation angle with the sixth joint of redundant manipulator PA10 is 2 rad.

The corresponding experimental results are shown in Figures 8–10 by the solution of TTZNN model (15) when the end-effector of the mobile manipulator is given to complete

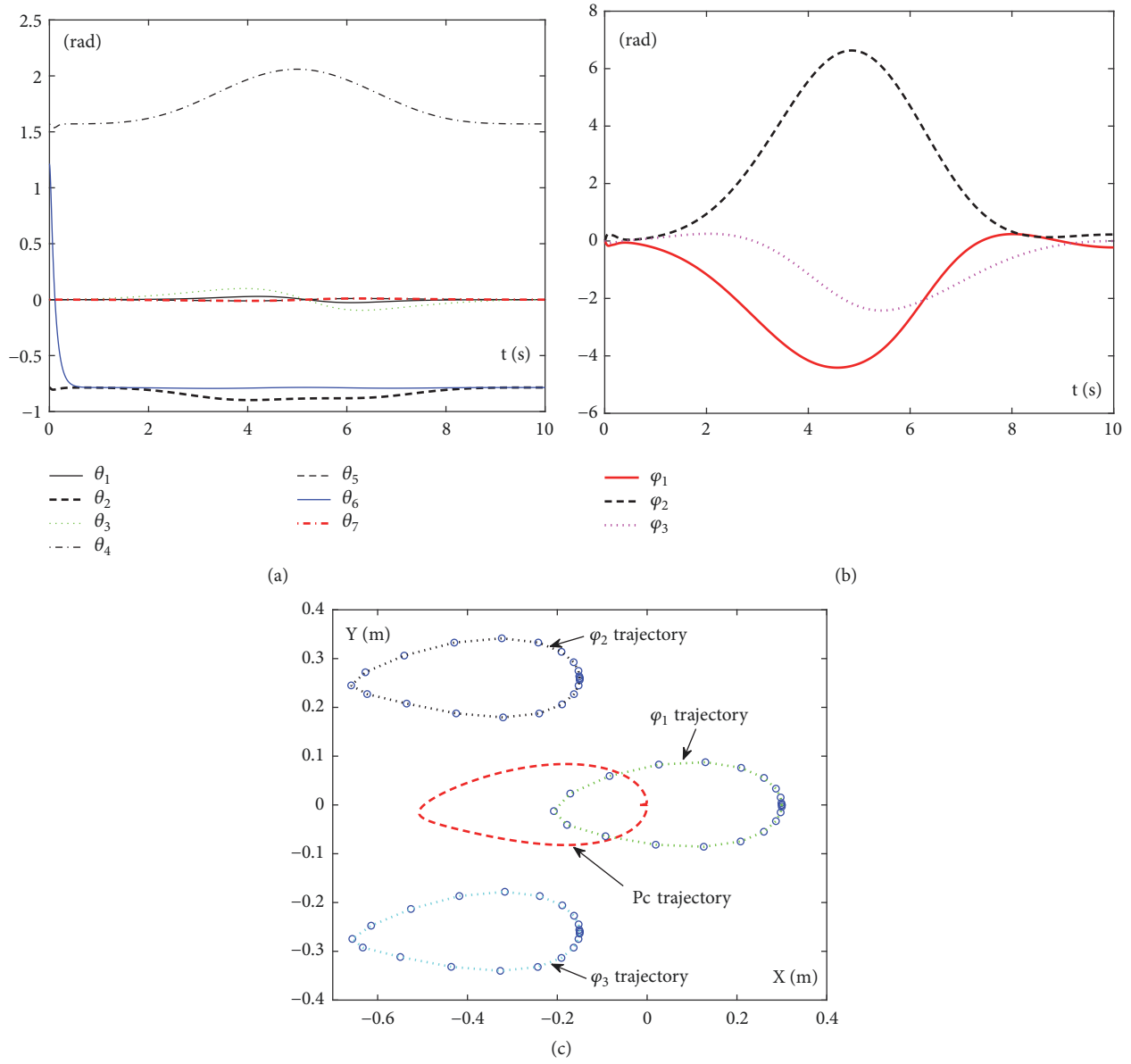

FIGURE 7: Profiles about the free joint angles of the mobile manipulator. (a) Motion trajectories of each joint angle of redundant manipulator PA10. (b) Rotating profiles for three wheels. (c) Motion trajectories with the mobile base.

the Lissajous-shaped path. Figure 8(a) shows that the desired trajectory and the actual motion path are coincide well with each other. From Figure 8(c), we can see the line with "+" symbol is not at the desired path at first and move near to the solid line in a few seconds. In Figure 8(b), two lines are overlapped in kinematic procedure. Figure 9(b) depicts the profiles of the position error E_x, E_y, E_z of the end-effector. The precision of position error in three dimensions is less than 10^{-4}, which is consistent with the theoretical analysis in Section 3.2. More simulation results about the kinematics of mobile manipulator are visualized in Figures 9(a) and 9(c). Obviously, each joint is smooth and regular. Furthermore, to verify the repetitive ness of the proposed kinematic optimization scheme (24) with the movable base, movements of the mobile platform with three wheels are illustrated in Figure 10. The details of the kinematic three wheels are shown in Figure 10(c). Pay attention to the statement of the three wheels. They are stationary during 1s. From $t = 1$s, three wheels begin to move away and reach 0.6m in five seconds. From $t = 5$s, three wheels move towards to the desired initial position, which can be seen in Figure 10(b). Because the Lissajous-shaped path can be reached by the redundant manipulator at the beginning, with the extension of kinematic path, the mobile base carrying the redundant manipulator moves together and returns to the desired initial position ($x_c(0) = 0, y_c(0) = 0$ and $\theta_0(0) = 0$) in the end, which is well displayed in Figures 10(a) and 10(d). All the free joints θ_i of the redundant manipulator PA10 return to their

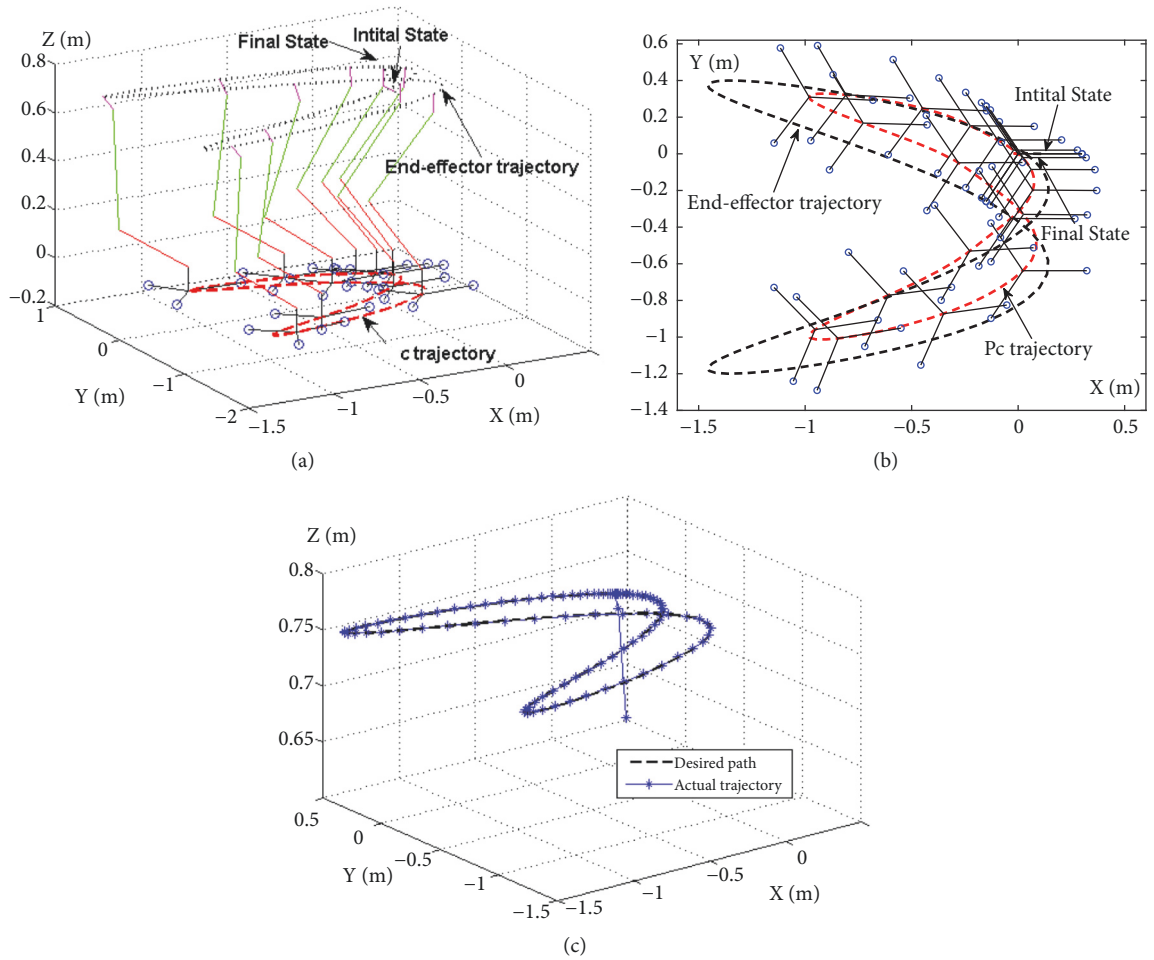

Figure 8: Lissajous path tracking profiles synthesized by TTZNN model (27). (a) Trajectories for the mobile manipulator. (b) Vertical view for the three-wheel mobile manipulator. (c) Lissajous tracking profiles of the end-effector.

desired state $\theta^*(0)$. The above simulation examples are fully verified the effectiveness of the repeatable motion planning by TTZNN model solution.

5.3. Comparisons with Existing Kinematic Energy Optimization. To witness the finiteness and precision of the proposed repeatable motion scheme with TTZNN model (15), the comparisons with the existed repetitive motion solutions (GNN, ZNN, and TTZNN) are simulated in the following part.

(1) Comparison with the Scheme of Gradient Neural Network (GNN) [26]. One kind of recurrent neural network models is Gradient neural network (GNN). It is an alternative for solving time-varying problems and is applied to kinematic planning of manipulators. The dynamic formula with GNN can be shown in (36):

$$\dot{y}(t) = -\gamma W^T(t)\left(W(t)\,y(t) - v(t)\right) \tag{36}$$

where $\gamma > 0$ is the adjustable parameter to scale the convergent speed. Linear activation function is considered. In the whole experimental process, $\gamma = 1$ is set. The repeatable motion plan is the same as (37). The simulation examples are shown in Figure 11(a) synthesized with GNN model when the end-effector of the mobile manipulator is assigned to execute a circle trajectory. Obviously, the motion trajectory of the end-effector is not coincided with the desired trajectory even after the execution time, which is visualized in Figure 11(a). Then convergent error of position XYZ axis with the end-effector takes larger value, which is a good explanation of the phenomenon in Figure 11(c). Comparing with the ZNN model for repetitive scheme in (24), GNN model does not possess the ability for time-varying inverse kinematics even the scalar parameters γ are set 10^4.

The above simulation profiles illustrate that GNN model is not effective for dealing time-varying problems. Simultaneous kinematics of the movable platform and the flexible manipulator makes the tracking tasks difficult within fixed time.

(2) Comparison with the Scheme of Zhang Neural Network (ZNN) [9]. Another kind of the recurrent neural network models is ZNN, which is designated to address time-varying problems. The convergent error of dynamic kinematic equation can rapidly reduce to zero as long as time is infinite. Motivated by the theorem of ZNN, a repetitive motion plan

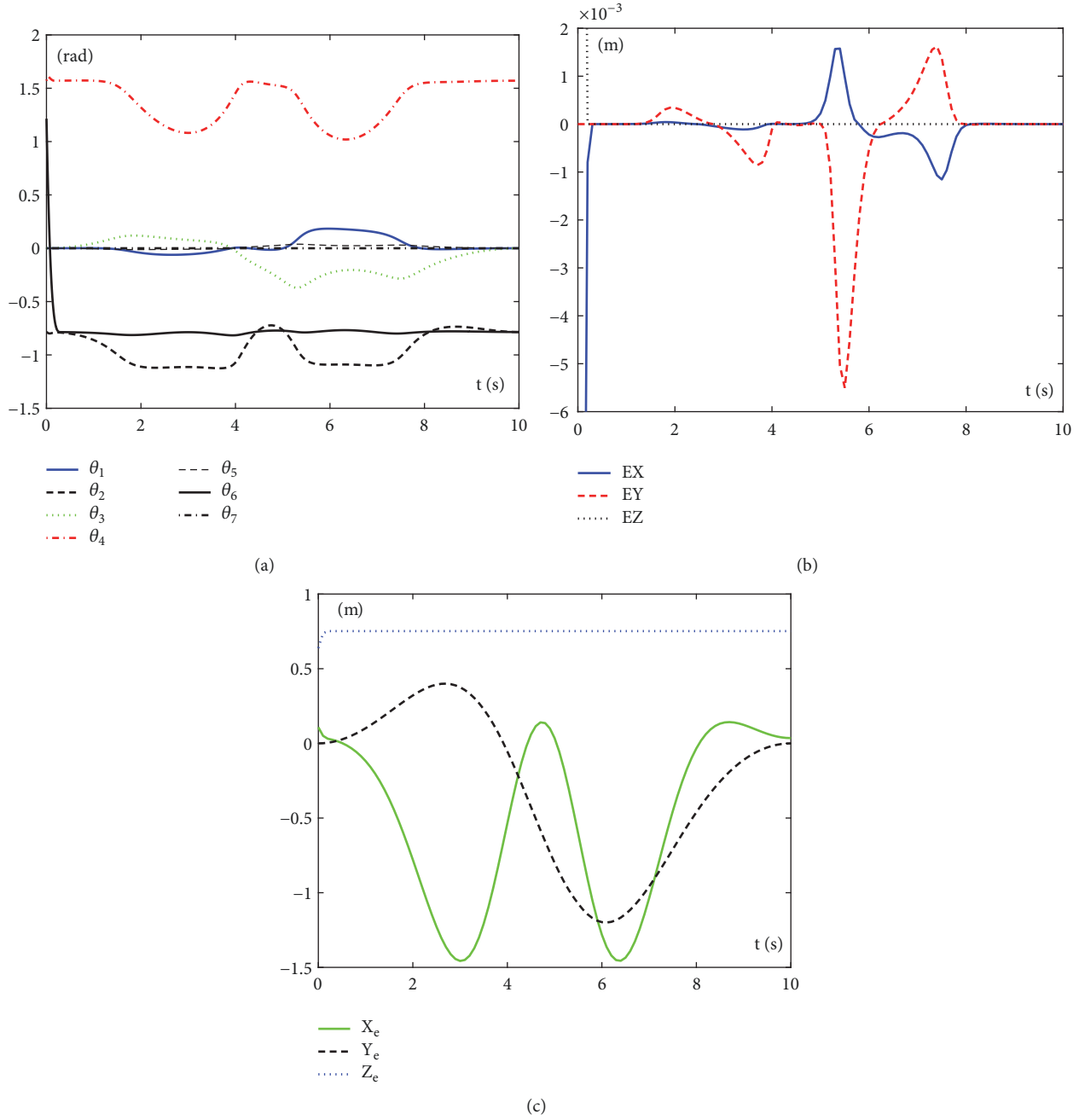

FIGURE 9: Simulated programs for the repeatable optimization of kinematic energy system (24) under the control of TTZNN. (a) Joints files. (b) Position error of the end-effector (c) Position changing profiles about the end-effector.

for redundant manipulators is set as: minimize $\dot{\theta}^{\mathrm{T}}\dot{\theta}/2 + u(\theta(t) - \theta(0))^{\mathrm{T}}\dot{\theta}$, subject to $J(\theta)\dot{\theta} = \dot{r} + \kappa(r - f(\theta))$. The ZNN model is defined as

$$\dot{y}(t) = -\dot{W}(t)\, y(t) + (I - W(t))\, \dot{y}(t) + \dot{v}(t) + \gamma\left[W(t)\, y(t) - v(t)\right] \tag{37}$$

where $\gamma > 0$ is used to scale the convergent rate. For comparisons, the scaling parameter $\gamma = 1$ is set. The corresponding profiles synthesized by ZNN (37) are visualized in Figures 11(b) and 11(d) when a circle tracking path is set. As seen from Figure 11(b), considering the deviation of the initial position, each joint of the mobile manipulator comes back to the desired place finally. The position error of E_x, E_y, E_z reaches 10^{-4} in Figure 11(d). After the motion task, the mobile manipulator has returned to the desired position as long as time goes infinity. To verify the convergence speed of three different neural network model (GNN, ZNN, and TTZNN), the residual error $J_E = \|W(t)y(t) - v(t)\|_2$ is supposed to show the different convergent rate when the end-effector is required to perform a circular path. In Figure 12, the blue trajectory (with TTZNN) sharply reduces to zero within

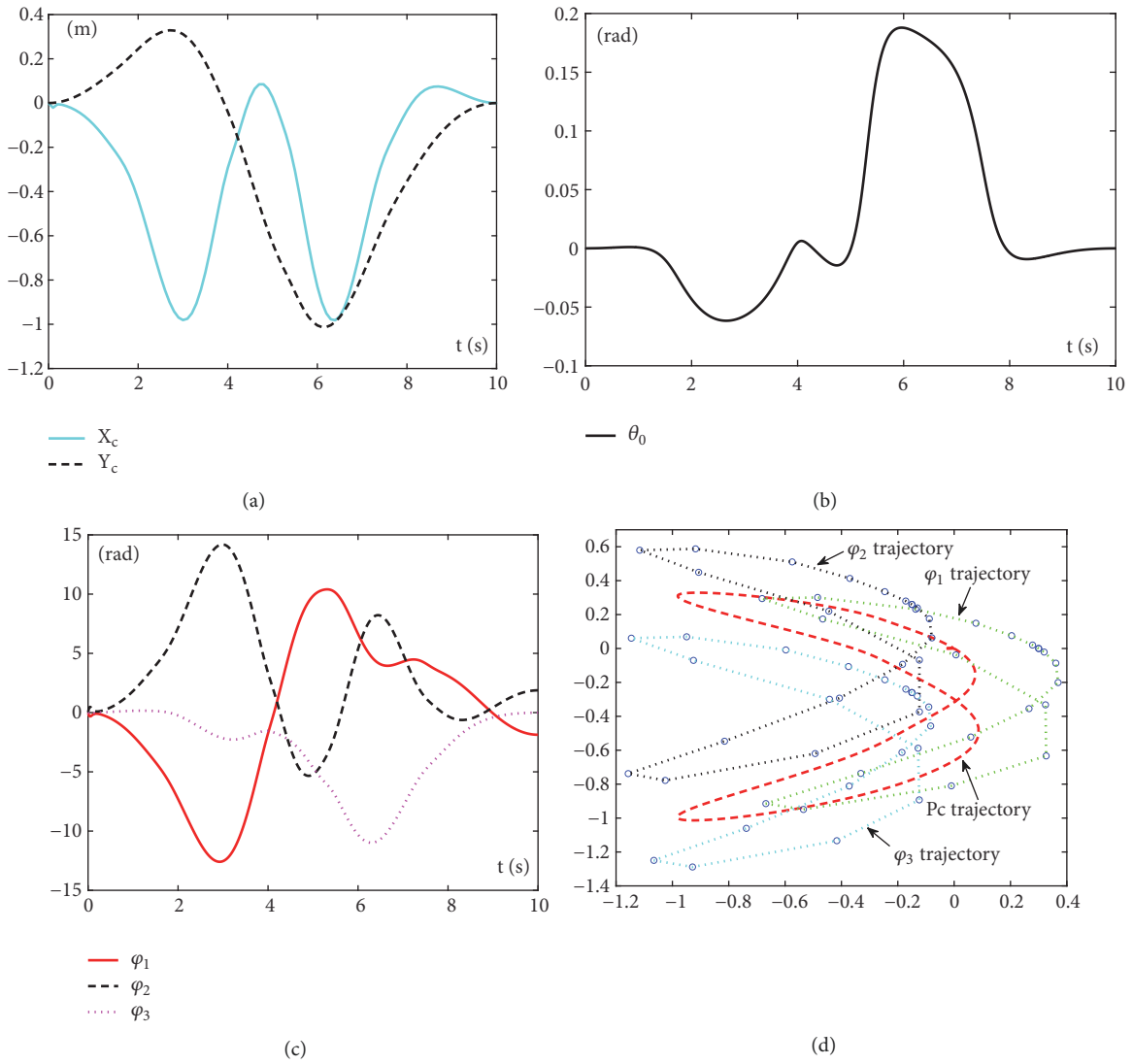

FIGURE 10: Simulated information about the mobile platform. (a) Position files of the mobile base. (b) Heading angle profiles. (c) Rotating profiles for three wheels. (d) Movable platform trajectories.

0.05s, while the red dotted line shows comparatively slower speed. The residual error with GNN in red color decreases very slow and even does not reach zero at $t = 10$s.

To show the different convergent precision withe the GNN, ZNN, and TTZNN, Table 3 lists the displacement of each joint with the proposed mobile manipulator model. From Table 3, under the repeatable optimization scheme in (24) with the solution of ZNN, the convergent precision displayed is less than 10^{-5} rad. The maximum joint distance with GNN is 0.1. When the repeatable optimization of kinematics system with TTZNN is operated, distance between desired position and initial position is around 10^{-8}, which can be seen in Table 3. Table 2 shows us the kinematic profiles of the mobile platform with three position parameters x_c, y_c, θ_0. From Table 2, under the repeatable motion planning (24) with GNN solver, x_c, y_c, θ_0 do not return to their initial position. On the contrary, with TTZNN and ZNN, the movable base has returned to the initial position in 10s. We can see the convergent precision has reached to 10^{-9}, while the corresponding position parameters x_c, y_c and θ_0 with

TABLE 2: Position profiles of the mobile base when its end-effector tracks a circle path using different neural models.

Variate	Scheme	$t = 0$	$t = 10$s	Position error
x_c(m)	GNN	0	0.081125	0.081125
	ZNN	0	-9.06238e-05	9.06238e-05
	TTZNN	0	-4.85327e-09	4.85327e-09
y_c(m)	GNN	0	-0.050597	0.050597
	ZNN	0	1.37810e-05	1.37810e-05
	TTZNN	0	7.45148e-09	7.45148e-09
θ_0(rad)	GNN	0	-0.169099	0.169099
	ZNN	0	-1.67426e-06	1.67426e-06
	TTZNN	0	4.97184e-09	4.97184e-09

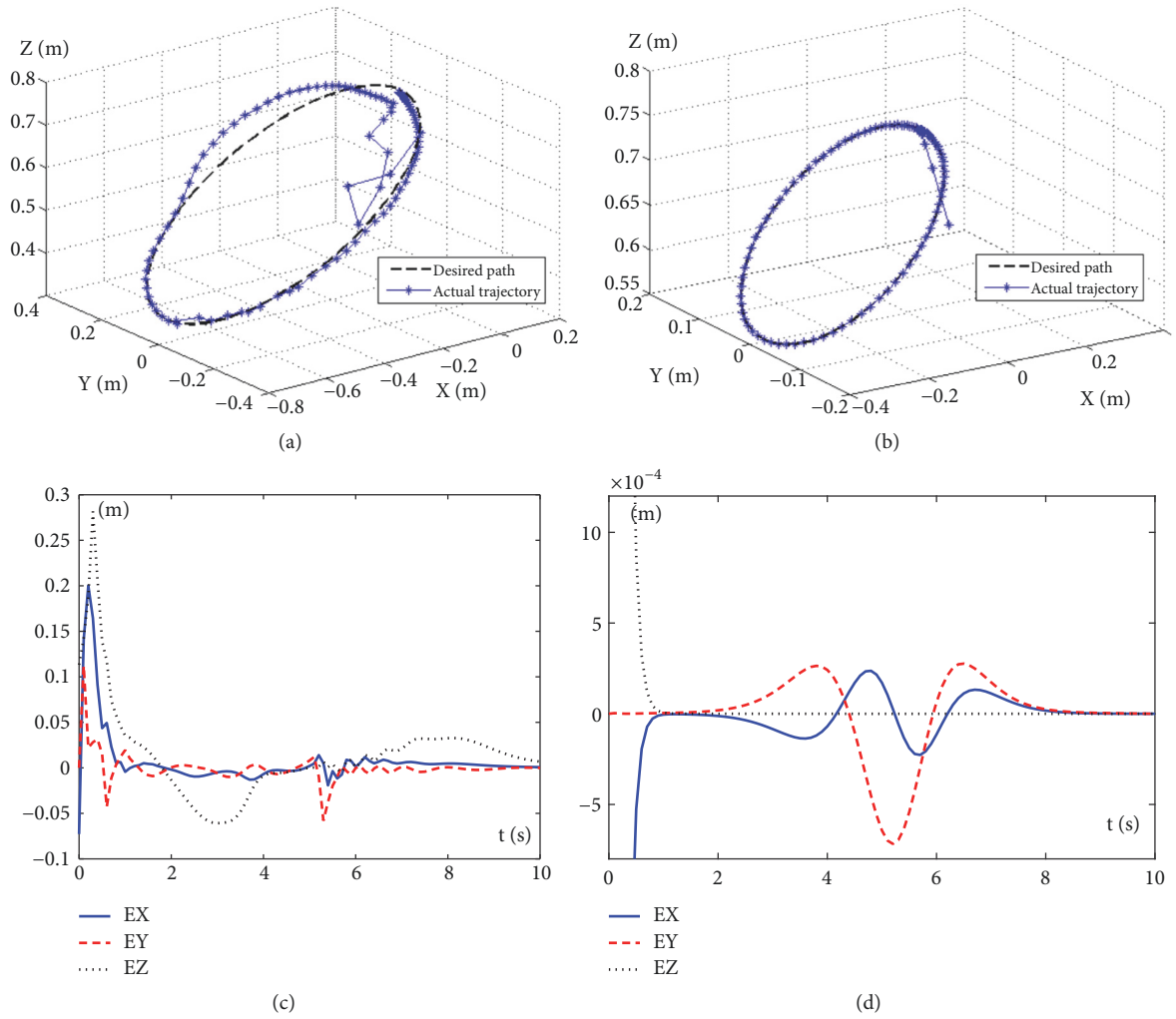

Figure 11: Comparison profiles using different neural optimization scheme. (a) Trajectories of the end-effector with GNN. (b) Trajectories of the end-effector with ZNN. (c) Position error of the end-effector with GNN. (d) Position error of the end-effector with ZNN.

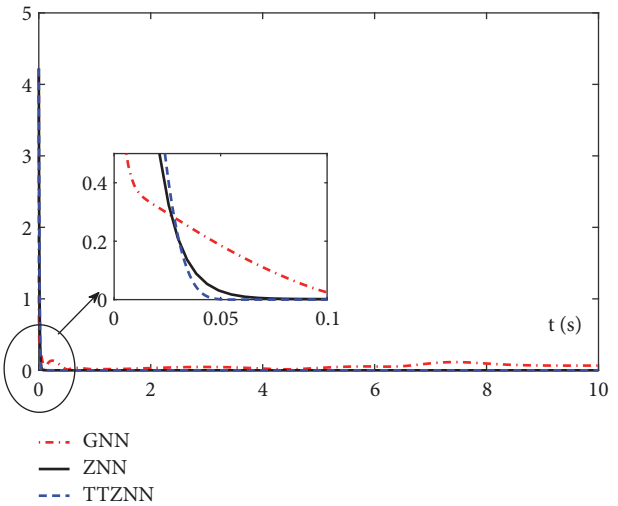

Figure 12: Residual error J_E with different neural networks under the kinematic repeatable scheme (24).

ZNN are less than 10^{-5}. It is necessary to state that the ZNN model can do better performance in trajectory planning of mobile manipulators when the adjusting parameter is more than $\gamma = 1000$. Though better experimental results can be obtained as the same results performed by TTZNN, the convergent time is infinite, which is not prompt to be applied in engineering fields.

6. Conclusion

To achieve the finite-time convergence for repetitive trajectory planning of mobile manipulators, an optimization scheme of kinematic energy system based on TTZNN is presented and analyzed. Theoretical finite time has been proved and the upper limitation of the convergent time has been calculated for the formulation of repeatable optimization scheme. A mobile platform of three wheels and a redundant manipulator of seven free joints are combined together to constitute a new mobile manipulator system.

Table 3: Free joints of the manipulator PA10 synthesized with scheme (24) with different neural solutions

Joint (rad)	Scheme	$\theta_i^*(0)$	$\theta_i(10)$	$\lvert\theta_i(10) - \theta_i^*(0)\rvert$
	GNN	0	-0.001243	0.001243
θ_1	ZNN	0	-4.98251e-05	4.98251e-05
	TTZNN	0	-5.21435e-09	5.21435e-09
	GNN	-0.785398	-0.886456	0.101058
θ_2	ZNN	-0.785398	-0.785275	1.23249e-04
	TTZNN	-0.785398	-0.785398	5.84480e-09
	GNN	0	0.087746	0.087746
θ_3	ZNN	0	-5.58358e-05	5.58358e-05
	TTZNN	0	-1.30718e-08	1.30718e-08
	GNN	1.57080	1.56293	0.007871
θ_4	ZNN	1.57080	1.57078	1.18503e-05
	TTZNN	1.57080	1.57080	5.74257e-10
	GNN	0	-0.009014	0.009014
θ_5	ZNN	0	6.14588e-06	6.14588e-06
	TTZNN	0	1.21890e-09	1.21890e-09
	GNN	1.21460	-0.796231	0.010832
θ_6	ZNN	1.21460	-0.785364	3.41855e-05
	TTZNN	1.21460	-0.785398	8.99498e-09
	GNN	0	0	0
θ_7	ZNN	0	0	0
	TTZNN	0	0	0

Numerical simulations via the proposed mobile manipulator fully substantiate the effectiveness of the optimization method for any initial joint position. Future work may focus on the realization for resisting disturbance of noise pollution when such a mobile manipulator is assigned to do repeatable work.

Data Availability

The source code and source data can be provided by contacting with the corresponding author.

Conflicts of Interest

The authors declare that there are no conflicts of interest regarding the publication of this paper.

Acknowledgments

This study was partly supported by National Natural Science Foundation of China (nos. 61771193, 61803338, and 61703183) and Public Projects of Zhejiang Province (LGG18F020011 and LGG19F030010).

References

[1] W. He, W. Ge, Y. Li, Y.-J. Liu, C. Yang, and C. Sun, "Model identification and control design for a humanoid robot," *IEEE Transactions on Systems, Man, and Cybernetics: Systems*, vol. 47, no. 1, pp. 45–57, 2017.

[2] Q. Chen, X. Ren, and J. Na, "Adaptive finite-time neural control of servo systems with non-linear dead-zone," *Neural Computing and Applications*, vol. 28, no. 2, pp. 3725–3736, 2017.

[3] J. Na, Z. Yang, S. Kamal, and L. Hu, "Bio-inspired learning and adaptation for optimization and control of complex systems," *Complexity*, vol. 2019, Article ID 9325364, 3 pages, 2019.

[4] Q. Chen, S. Xie, M. Sun, and X. He, "Adaptive non-singular fixed-time attitude stabilization of uncertain spacecraft," *IEEE Transactions on Aerospace and Electronic Systems*, vol. 54, no. 6, pp. 2937–2950, 2018.

[5] Y. Jiang, Y. Xu, and Y. Liu, "Performance evaluation of feature detection and matching in stereo visual odometry," *Neurocomputing*, vol. 120, pp. 380–390, 2013.

[6] F. Zhang, X. Liao, and G. Zhang, "Qualitative behavior of the Lorenz-like chaotic system describing the flow between two concentric rotating spheres," *Complexity*, vol. 21, no. S2, pp. 67–72, 2016.

[7] Z. Zhang and Y. Zhang, "Variable joint-velocity limits of redundant robot manipulators handled by quadratic programming," *IEEE/ASME Transactions on Mechatronics*, vol. 18, no. 2, pp. 674–686, 2013.

[8] L. Jin and Y. Zhang, "G2-Type SRMPC scheme for synchronous manipulation of two redundant robot arms," *IEEE Transactions on Cybernetics*, vol. 45, no. 2, pp. 153–164, 2015.

[9] Y. Zhang, Z. Tan, K. Chen, Z. Yang, and X. Lv, "Repetitive motion of redundant robots planned by three kinds of recurrent neural networks and illustrated with a four-link planar manipulator's straight-line example," *Robotics and Autonomous Systems*, vol. 57, no. 6-7, pp. 645–651, 2009.

[10] E. Maulana, M. A. Muslim, and A. Zainuri, "Inverse kinematics of a two-wheeled differential drive an autonomous mobile robot," in *Proceedings of the 2014 Electrical Power, Electronics, Communications, Controls and Informatics Seminar (EECCIS)*, pp. 93–98, Malang, Indonesia, August 2014.

[11] Q. Jiang and V. Kumar, "The inverse kinematics of cooperative transport with multiple aerial robots," *IEEE Transactions on Robotics*, vol. 29, no. 1, pp. 136–145, 2013.

[12] J. S. Kim, Y. H. Jeong, and J. H. Park, "A geometric approach for forward kinematics analysis of a 3-SPS/S redundant motion manipulator with an extra sensor using conformal geometric algebra," *Meccanica*, vol. 51, no. 10, pp. 2289–2304, 2016.

[13] K. Tchon, "Repeatability of inverse kinematics algorithms for mobile manipulators," *IEEE Transactions on Automatic Control*, vol. 47, no. 8, pp. 1376–1380, 2002.

[14] M. S. Miah and W. Gueaieb, "RFID-based mobile robot trajectory tracking and point stabilization through on-line neighboring optimal control," *Journal of Intelligent & Robotic Systems*, vol. 78, no. 3-4, pp. 377–399, 2015.

[15] M. Tao, Q. Chen, X. He, and M. Sun, "Adaptive fixed-time fault-tolerant control for rigid spacecraft using a double power reaching law," *International Journal of Robust and Nonlinear Control*, vol. 29, no. 12, pp. 4022–4040, 2019.

[16] C. Lian, X. Xu, H. Chen, and H. He, "Near-optimal tracking control of mobile robots via receding-horizon dual heuristic programming," *IEEE Transactions on Cybernetics*, vol. 46, no. 11, pp. 2484–2496, 2016.

[17] D. Xu, D. Zhao, J. Yi, and X. Tan, "Trajectory tracking control of omnidirectional wheeled mobile manipulators: robust neural network-based sliding mode approach," *IEEE Transactions on Systems, Man & Cybernetics, Part B: Cybernetics*, vol. 39, no. 3, pp. 788–799, 2009.

[18] G. Franzè and W. Lucia, "An obstacle avoidance model predictive control scheme for mobile robots subject to nonholonomic constraints: A sum-of-squares approach," *Journal of The Franklin Institute*, vol. 352, no. 6, pp. 2358–2380, 2015.

[19] M. Rolf and J. Steil, "Efficient exploratory learning of inverse kinematics on a bionic elephant trunk," *IEEE Transactions on Neural Networks and Learning Systems*, vol. 25, no. 6, pp. 1147–1160, 2014.

[20] L. Xiao and Y. Zhang, "Solving time-varying inverse kinematics problem of wheeled mobile manipulators using Zhang neural network with exponential convergence," *Nonlinear Dynamics*, vol. 76, no. 2, pp. 1543–1559, 2014.

[21] W. He, S. Ge, and Y. Li, "Neural network control of a rehabilitation robot by state and output feedback," *Journal of Intelligent and Robotic Systems*, vol. 80, no. 1, pp. 15–31, 2015.

[22] Q. Chen, L. Shi, J. Na, X. Ren, and Y. Nan, "Adaptive echo state network control for a class of pure-feedback systems with input and output constraints," *Neurocomputing*, vol. 275, pp. 1370–1382, 2018.

[23] J. Na, Q. Chen, X. Ren, and Y. Guo, "Adaptive prescribed performance motion control of servo mechanisms with friction compensation," *IEEE Transactions on Industrial Electronics*, vol. 61, no. 1, pp. 486–494, 2014.

[24] W. He and Y. Dong, "Adaptive fuzzy neural network control for a constrained robot using impedance learning," *IEEE Transactions on Neural Networks and Learning Systems*, vol. 29, no. 4, pp. 1174–1186, 2018.

[25] P. V. Cuong and W. Y. Nan, "Adaptive trajectory tracking neural network control with robust compensator for robot manipulators," *Neural Computing and Applications*, vol. 27, no. 2, pp. 525–536, 2016.

[26] B. Huang and C. Ma, "Gradient-based iterative algorithms for generalized coupled Sylvester-conjugate matrix equations," *Computers & Mathematics with Applications*, vol. 75, no. 7, pp. 169–179, 2018.

[27] D. Chen, Y. Zhang, and S. Li, "Tracking Control of Robot Manipulators with Unknown Models: A Jacobian-Matrix-Adaption Method," *IEEE Transactions on Industrial Informatics*, vol. 14, no. 7, pp. 3044–3053, 2018.

[28] Y. Wang, L. Cheng, Z.-G. Hou, J. Yu, and M. Tan, "Optimal formation of multirobot systems based on a recurrent neural network," *IEEE Transactions on Neural Networks and Learning Systems*, vol. 27, no. 2, pp. 322–333, 2016.

[29] S. Li, J. He, and Y. Li, "Distributed recurrent neural networks for cooperative control of manipulators: a game-theoretic perspective," *IEEE Transactions on Neural Networks and Learning Systems*, vol. 28, no. 2, pp. 415–426, 2017.

[30] L. Jin, S. Li, L. Xiao, R. Lu, and B. Liao, "Cooperative motion generation in a distributed network of redundant robot manipulators with noises," *IEEE Transactions on Systems, Man, and Cybernetics: Systems*, vol. 99, no. 1, pp. 217–227, 2017.

[31] Z. Zhang, Y. Lu, L. Zheng, S. Li, Z. Yu, and Y. Li, "A new varying-parameter convergent-differential neural-network for solving time-varying convex QP problem constrained by linear-equality," *IEEE Transactions on Automatic Control*, vol. 63, no. 12, pp. 4110–4125, 2018.

[32] Z. Zhang, L. Zheng, J. Weng, Y. Mao, W. Lu, and L. Xiao, "A new varying-parameter recurrent neural-network for online solution of time-varying sylvester equation," *IEEE Transactions on Cybernetics*, vol. 48, no. 11, pp. 3135–3148, 2018.

[33] Y. Zhang, Z. Xiao, D. Guo, and M. Miao, "Singularity-conquering tracking control of a class of chaotic systems using Zhang-gradient dynamics," *IET Control Theory & Applications*, vol. 9, no. 6, pp. 871–881, 2015.

[34] Y. Zhang, W. Li, and Z. Zhang, "Physical-limits-constrained minimum velocity norm coordinating scheme for wheeled mobile redundant manipulators," *Robotica*, vol. 33, no. 1, pp. 1325–1350, 2014.

[35] Y. Zhang, X. Yan, D. Chen, D. Guo, and W. Li, "QP-based refined manipulability-maximizing scheme for coordinated motion planning and control of physically constrained wheeled mobile redundant manipulators," *Nonlinear Dynamics*, vol. 85, no. 1, pp. 245–261, 2016.

[36] Y. Shen, P. Miao, Y. Huang, and Y. Shen, "Finite-time stability and its application for solving time-varying sylvester equation by recurrent neural network," *Neural Processing Letters*, vol. 42, no. 3, pp. 763–784, 2015.

[37] P. Miao, Y. Shen, and X. Xia, "Finite time dual neural networks with a tunable activation function for solving quadratic programming problems and its application," *Neurocomputing*, vol. 143, pp. 80–89, 2014.

[38] L. Xiao, B. Liao, S. Li, and K. Chen, "Nonlinear recurrent neural networks for finite-time solution of general time-varying linear matrix equations," *Neural Networks*, vol. 98, pp. 102–113, 2018.

[39] S. Li, S. Chen, and B. Liu, "Accelerating a recurrent neural network to finite-time convergence for solving time-varying sylvester equation by using a sign-Bi-power activation function," *Neural Processing Letters*, vol. 37, no. 2, pp. 189–205, 2013.

[40] L. Xiao, Z. Zhang, and S. Li, "Solving time-varying system of nonlinear equations by finite-time recurrent neural networks with application to motion tracking of robot manipulators," *IEEE Transactions on Systems, Man, and Cybernetics: Systems*, vol. 22, no. 8, pp. 1–11, 2018.

[41] Y. Kong, Y. Jiang, and J. Lou, "Terminal computing for Sylvester equations solving with application to intelligent control of redundant manipulators," *Neurocomputing*, vol. 335, pp. 119–130, 2019.

[42] L. Xiao and Y. Zhang, "From different zhang functions to various ZNN models accelerated to finite-time convergence for time-varying linear matrix equation," *Neural Processing Letters*, vol. 39, no. 3, pp. 309–326, 2014.

[43] G. Campion, G. Bastin, and B. Dandrea-Novel, "Structural properties and classification of kinematic and dynamic models of wheeled mobile robots," *IEEE Transactions on Robotics and Automation*, vol. 12, no. 1, pp. 47–62, 1996.

[44] Y. Zhang and Z. Zhang, *Repetitive Motion Planning and Control of Redundant Robot Manipulators*, Springer-verlag, London, UK, 2013.

Hindawi
Complexity
Volume 2019, Article ID 4358958, 13 pages
https://doi.org/10.1155/2019/4358958

WILEY | Hindawi

Research Article

Finite Control Set Model Predictive Control for Complex Energy System with Large-Scale Wind Power

Yang-Wu Shen,[1] **Jin-Rong Yuan**,[2] **Fei-Fan Shen**,[3] **Jia-Zhu Xu**,[4] **Chen-Kun Li**,[1] **and Ding Wang**[1]

[1] *State Grid Hunan Electric Power Company Limited Research Institute, Changsha, Hunan, China*
[2] *State Grid Changde Power Supply Company, China*
[3] *Technical University of Denmark, Lyngby, Denmark*
[4] *Hunan University, Changsha, Hunan, China*

Correspondence should be addressed to Yang-Wu Shen; shenyangwu@126.com

Received 9 April 2019; Accepted 23 June 2019; Published 28 July 2019

Guest Editor: Xiaoqing Bai

Complex energy systems can effectively integrate renewable energy sources such as wind and solar power into the information network and coordinate the operation of renewable energy sources to ensure its reliability. In the voltage source converter-based high voltage direct current system, the traditional vector control strategy faces some challenges, such as difficulty in PI parameters tuning and multiobjective optimizations. To overcome these issues, a finite control set model predictive control-based advanced control strategy is proposed. Based on the discrete mathematical model of the grid-side voltage source converter, the proposed strategy optimizes a value function with errors of current magnitudes to predict switching status of the grid-side converter. Moreover, the abilities of the system in resisting disturbances and fault recovery are enhanced by compensating delay and introducing weight coefficients. The complex energy system in which the wind power is delivered by the voltage source converter-based high voltage direct current system is modeled by Simulink and simulation results show that the proposed strategy is superior to the tradition PI control strategy under various situations, such as wind power fluctuation and fault occurrences.

1. Introduction

To deal with energy shortage and environment pollution issues, the development of complex energy systems, which can effectively coordinate the operation with various renewable energy sources such as wind and solar power to ensure its reliability, has drawn much attention from many countries. The focus is on the wind farm due to its high efficiency of wind power utilization and no occupation of land resources [1–4]. With the increasing capacity of the wind farm and innovations of power electronic technologies, many researchers focus on applications of the voltage source converter-based high voltage direct current (VSC-HVDC) technique and require better operational performance of the converter of the VSC-HVDC system.

The model predictive control (MPC) [5–9] has been extensively applied in the control of modular multilevel inverters [10], uninterruptible power systems [11], and neutral-point clamped converters [12] due to its advantages such as control flexibility and being free of modulators. The MPC strategies used for the control of the converter can be classified as the continuous control set MPC and the finite control set (FCS) MPC. For the continuous control set MPC, a modulator generates switching states based on the continuous output of the predictive controller. However, the FCS-MPC considers the limited number of switching states of the converter for solving optimization problems.

In [13], the MPC was applied to the low voltage ride-through (LVRT) of photovoltaic (PV) power plants to improve the transient stability of PV power plants. The proposed MPC based strategy is able to control the output current of the inverters quickly based on the reference current. After a fault in the grid, the proposed strategy can control the reactive power output of the PV power plant to

support the system voltage and improve the transient stability of the system. The simulation results show that the PV power plant is able to support the voltage with the proposed strategy in the low voltage situation.

In [14–17], the FCS MPC strategy was used to optimize the control of inverters. A mixed logical dynamical (MLD) model for inverters was proposed in [15]. By treating the MLD model as a predictive model, a FCS-MPC strategy for inverters was developed. The proposed strategy considers the discreteness of inverters and selects the switch state corresponding to the optimal objective value as the control signal for inverters to control the output voltage. The simulation and test results validate that the proposed FCS-MPC strategy can improve the output voltage quality of inverters. To improve the conventional FCS-MPC strategy, a multistep prediction FCS-MPC strategy for converters is proposed in [15], in which the optimal and suboptimal control actions are considered in one control cycle. The optimal control action is determined in a fashion that the control action is optimal in two control cycles. Simulation results show that the proposed multistep FCS-MPC scheme can improve the quality of the output voltage of the three-phase inverter and reduces the tracking error of the reference voltage as compared with the conventional FCS-MPC. In [16], the authors proposed a FCS-MPC strategy for a four-level converter to control output currents and voltages of flying capacitors. A discrete model of the converter is developed to obtain switching states. During each sampling period, the predicted variables are evaluated by an evaluation function and the optimal switching state with the minimum cost value is selected and applied to the converter. In [17], the authors proposed a simplified FCS-MPC with extended voltage vectors for two-level three-phase grid-connected converters. The proposed algorithm uses multiple voltage vectors for the prediction process to reduce the ripple in the grid current. Moreover, the proposed approach utilizes a preselection scheme along with a simplified MPC approach to reduce the number of voltage vectors used in the proposed strategy. Simulations show that the proposed strategy retains the effectiveness obtained in the case where all the voltage vectors are used, and at the same time the current ripple is not adversely affected and the control delay is effectively reduced.

Improved MPC strategies were proposed for the STATCOM and multilevel converters in [18, 19]. A novel control delay elimination for the MPC strategy was proposed in [18] for the control of the cascaded STATCOM. The MPC based optimization problem was proposed and simplified for the possible switching states. Based on the further recursion of the simplified MPC based model, the effect of control delay on the control performance is reduced. The simulation results show that the proposed delay elimination for the MPC strategy can improve current tracking control of the cascaded STATCOM and the system has strong robustness. In [19], the discrete mathematic model of the modular multilevel converter-based HVDC (MMC-HVDC) system is developed, and an improved MPC strategy is proposed for the five-level MMC. Moreover, the improved MPC strategy is combined with the voltage-sequencing algorithm to reduce computational burdens and realize the transmission power control in the MMC-HVDC system and circulating current elimination.

In [20–23], the MPC strategies were applied to the control of electric motors. In [20], the authors proposed a MPC strategy combined with a disturbance observer (DOB) for regulating the torque of a permanent magnet synchronous motor (PMSM) without the steady state error. In the proposed strategy, the online optimal solutions can be obtained without relying on a numeric algorithm based on the property of the input matrix of the PMSM. The results show that the proposed MPC strategy ensures satisfactory torque control performance. A quasideadbeat MPC strategy for induction motors was proposed in [21]. By building a rolling optimization problem, the optimal switching state corresponding to the optimal voltage vector was selected as the output of the inverter. The simulations and experimental results show that the proposed strategy can reduce computational time and ensure satisfactory static and dynamic performance for torque.

However, the above researches mainly focus on the steady state and have not studied operational performance of inverters under renewable energy integration and system disturbances. To deal with the above issues, a FCS-MPC based control strategy for the VSC-HVDC system is proposed. The control strategy generates the reference value through the outer loop and compares the reference value with the predicted value obtained under a given voltage vector. Then, the switching status corresponding to the value function with the smallest difference is obtained and used in the next sampling period, which can achieve the fast tracking of the reference value. Moreover, abilities of the system in resisting disturbances and fault recovery are enhanced by compensating delay and introducing weight coefficients. The VSC-HVDC connected OWF system is modeled in the MATLAB/Simulink and simulation results validate that the proposed FCS-MPC strategy is superior to the tradition PI control strategy under various situations, such as wind power fluctuation and fault occurrences.

The contributions of this paper are summarized as follows: (1) a FCS-MPC based control strategy for the complex energy system is proposed considering the renewable energy integration and system disturbances; (2) a MPC based delay compensation technique is proposed. Compared with the conventional PI control strategy, the proposed FCS-MPC has the following advantages: (1) it is easy to tune control parameters; (2) it can realize multiobjective optimization and incorporate constraints; (3) there is no need to implement the decoupling process; (4) no PMW modulators are required.

2. Control Strategies for Wind Farm-Side VSC and Direct Driven Permanent Magnet Synchronous Generator

Figure 1 shows the typical configuration of the OWF connected to an external AC grid through the complex energy system. The complex energy system consists of the wind farm-side VSC (WF-VSC), the grid-side VSC (GS-VSC), and the DC transmission system. To ensure utilization of the

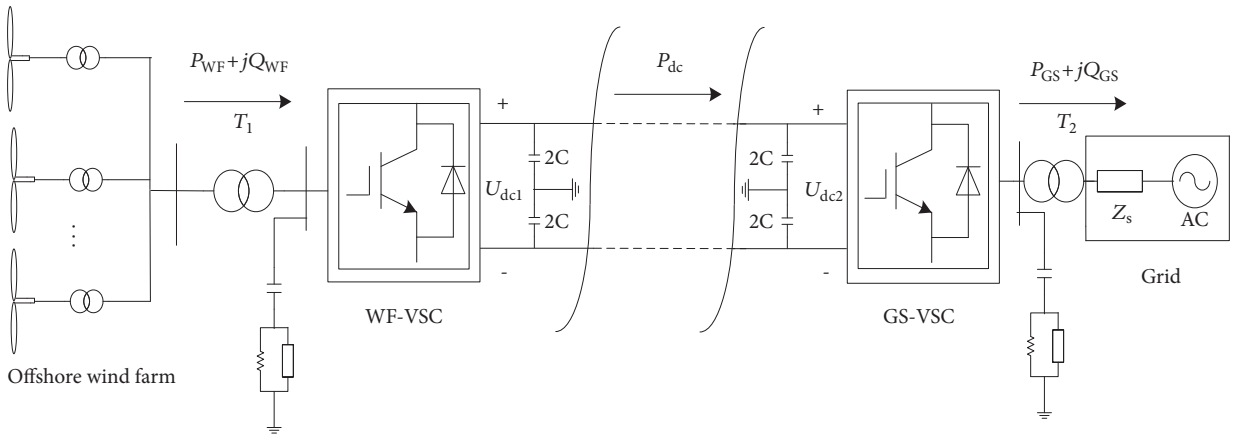

Figure 1: Typical configuration of the wind farm connected to an external AC grid though the complex energy system.

OWP and secure operation of the complex energy system, the GS-VSC should maintain the steady DC voltage of the DC transmission system.

2.1. Control Strategy for the WF-VSC. The mathematical model of the WF-VSC in the synchronized rotating d-q frame is formulated as below.

$$\begin{aligned} L\frac{\mathrm{d}i_{\mathrm{sd}}}{\mathrm{d}t} &= u_{\mathrm{sd}} - i_{\mathrm{sd}}R + \omega_s L i_{\mathrm{sq}} - v_{\mathrm{sd}} \\ L\frac{\mathrm{d}i_{\mathrm{sq}}}{\mathrm{d}t} &= u_{\mathrm{sq}} - i_{\mathrm{sq}}R - \omega_s L i_{\mathrm{sd}} - v_{\mathrm{sq}} \\ C\frac{\mathrm{d}u_{\mathrm{dc}}}{\mathrm{d}t} &= \frac{3}{2}\left(S_{\mathrm{sd}}i_{\mathrm{gd}} + S_{\mathrm{sq}}i_{\mathrm{sq}}\right) - i_{\mathrm{dc}} \end{aligned} \tag{1}$$

where u_{sd} and u_{sq} are the d-axis and q-axis components of the three-phase voltage, respectively; i_{sd} and i_{sq} are the d-axis and q-axis components of the three-phase current, respectively; v_{sd} and v_{sq} are the d-axis and q-axis components of the voltage at the converter side, respectively; S_{sd} and S_{sq} are the d-axis and q-axis components of the switching function, respectively; ω_s is synchronized angular velocity. The direct control strategy is applied to maintain the voltage magnitude and frequency at the WF side.

The control structure of the WF-VSC is shown in Figure 2. It can be seen that the voltage magnitude and phase at the WF side are controlled through commands in d-q axis and the synchronized angular velocity of the WF-VSC. To reduce control complexity, the initial voltage angle at the WS side is set as zero and voltage magnitude components in d-q-axis are used for feedback control. The differences between the reference values and real-time values of voltage magnitude are used to obtain the modulation ratio and generate the trigger pulse.

2.2. Control Strategy for Direct Driven Permanent Magnet Synchronous Generator. The typical configuration of the direct driven permanent magnet synchronous generator (PMSG) is shown in Figure 3. The direct driven PMSG system consists

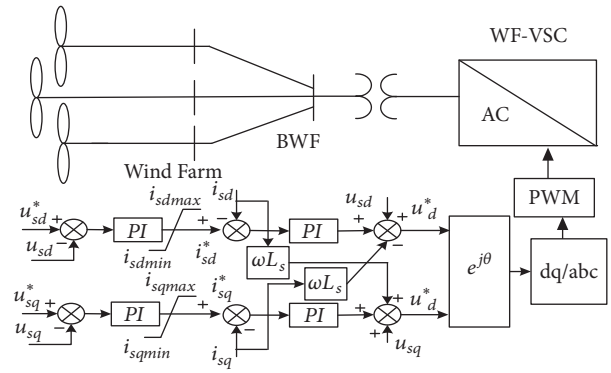

Figure 2: Control structure of the WF-VSC.

of the wind turbine, PMSG, generator-side converters, and grid-side converters.

The double closed loop control strategy, namely, the outer loop of angular velocity and inner loop of current, is applied to the generator-side converter to achieve the MPPT. The grid-side converter controls the DC voltage to ensure wind power integration. In this paper, the PMSG-based wind farm is represented by an equivalent single-machine model. Since the dynamic response speed of the grid-side converter is faster than the ones of the wind turbine and generator-side converters, the wind turbine, the PMSG, and generator-side converters are simplified as an equivalent voltage resource, as shown in Figure 3. Different levels of wind power output are simulated by controlling power output of the grid-side converter.

The control strategy for the grid-side converter is shown in Figure 4. In this paper, input wind power variation is simulated by controlling the grid-side converter of the PMSG because this study focuses on the verification of the abilities of the system with the proposed control strategy in resisting disturbances and fault recovery under different situations, such as wind speed variation and fault occurrence. As shown in Figure 4, the actual wind speed is simulated by the wind power generator, which generates the varying input wind power and obtains the d-axis component of the reference

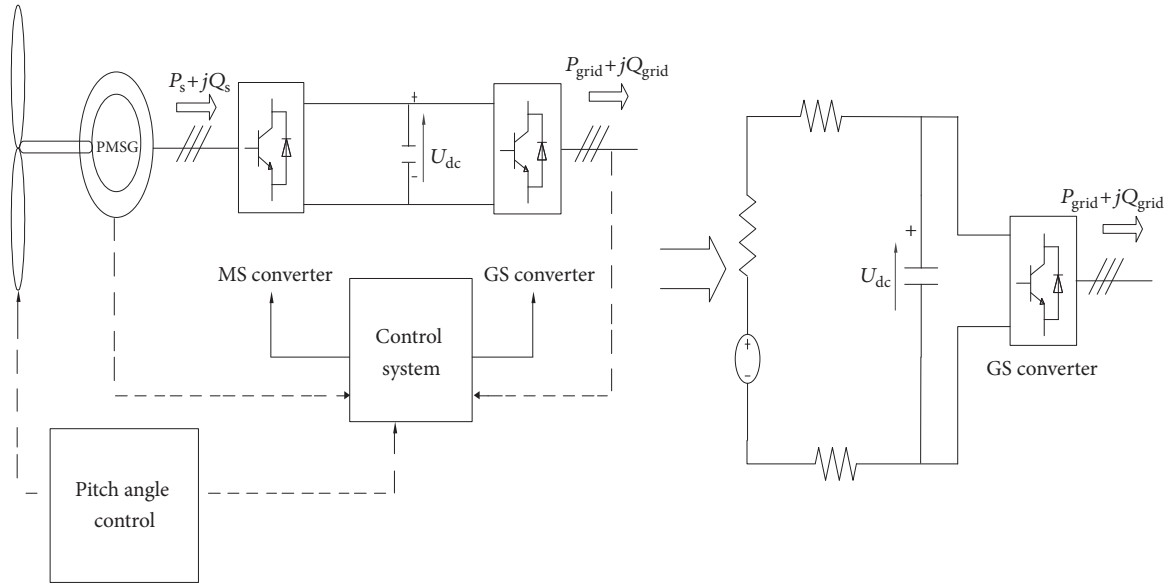

Figure 3: Typical configuration of the direct driven PMSG.

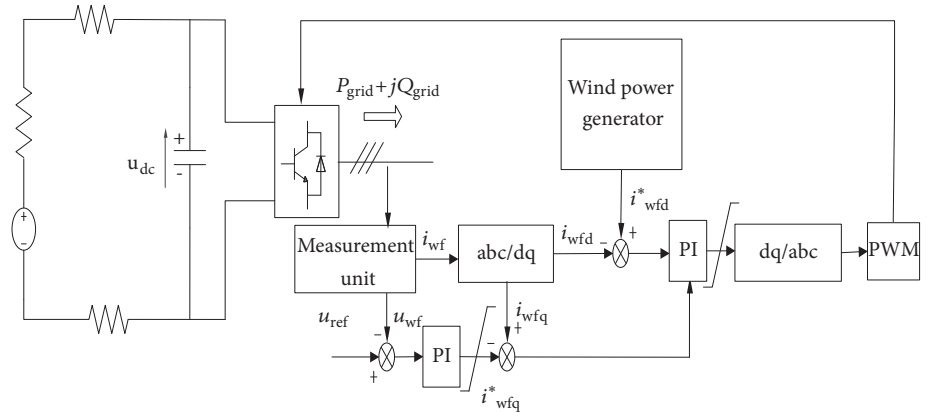

Figure 4: The PI control structure of grid-side controller of the PMSG.

value of the three-phase AC current. The reference value of the three-phase AC voltage is compared with the measure value to obtain the q-axis component of the reference value of the three-phase current through the PI unit. Then, the d-q axis components of the three-phase current are adjusted by PI units and transformed using Park inverse transformation to control the converter.

3. FCS-MPC Based Control Strategy for GS-VSC

The FCS-MPC based control strategy for the GS-VSC is shown in Figure 5. As shown in Figure 5, the proposed control strategy is applied to the DC voltage control of the GS-VSC. The DC voltage reference value u^*_{dc} is compared to the actual value u_{dc}, and the difference between them is used to generate the current reference value through the PI units. Then, the measurement unit collects three-phase grid voltage (e) and grid current (i), and these values are used to obtain the predicted values in the $\alpha\beta$ coordinate system by using the proposed predicted models. Finally, a value function is used to evaluate the difference between the predicted value and the reference value. The value function is optimized over a rolling horizon to obtain the optimal switching combination corresponding to the value function with the smallest value. Finally, the optimal switching combination is applied to control the GS-VSC.

As the most important blocks of the FCS-MPC based control strategy, the predicted model of the GS-VSC and the value function are described in detail in the following subsections. In addition, the method of delay compensation is also illustrated.

3.1. Discrete Predicted Model of the GS-VSC. The discrete predicted model of the GS-VSC is formulated and described in this subsection. The structure of the GS-VSC is shown in Figure 6. The GS-VSC consists of six IGBT and six antiparallel diodes. u_a, u_b, and u_c represent the three-phase output voltage

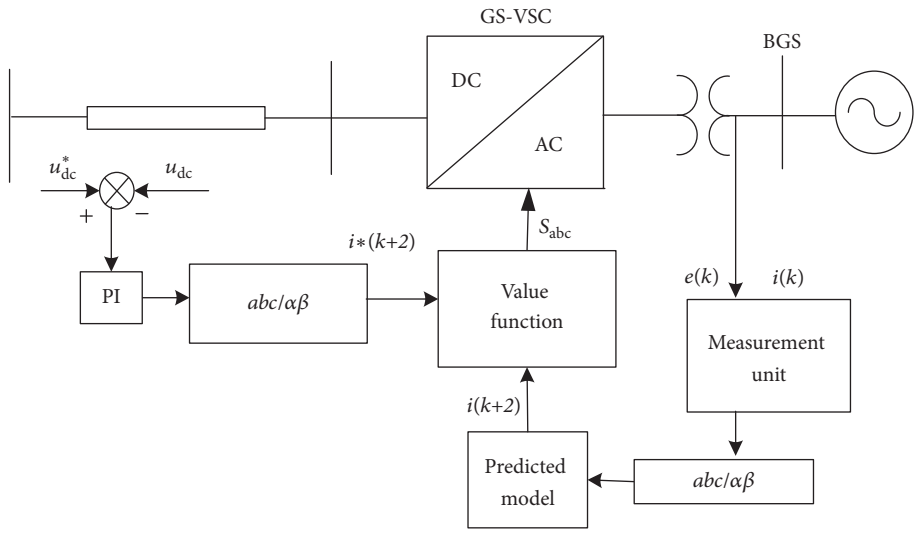

Figure 5: FCS-MPC based control strategy for the GS-VSC considering delay compensation.

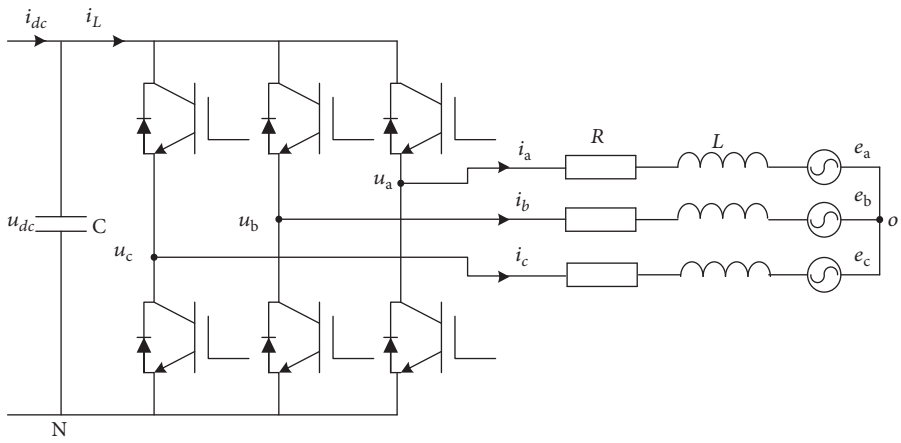

Figure 6: The structure of the GS-VSC.

of the converter; i_a, i_b, and i_c represent the three-phase grid current; e_a, e_b, and e_c represent the three-phase grid voltage; u_a, u_b, and u_c represent the three-phase output voltage of the converter. L is the reactance, R is the resistance, and C is the capacitance. u_{dc}, i_{dc}, and i_L are the DC voltage, DC input current, and DC output current, respectively. More details on the structure of the GS-VSC can be found in [24–27].

To derive the predicted model of the grid current, the GS-VSC should be modeled. The dynamic equation of the grid current in the three-phase stationary reference frame is as follows:

$$L\frac{\mathrm{d}\mathbf{i}}{\mathrm{d}t} = \mathbf{u} - \mathbf{e} - R\mathbf{i} \tag{2}$$

where $\mathbf{i}$ is the vector of current; $\mathbf{u}$ is the vector of output voltage of converter; $\mathbf{e}$ is the vector of the grid voltage. Vectors $\mathbf{i}$, $\mathbf{u}$, and $\mathbf{e}$ can be expressed as

$$\begin{bmatrix} \mathbf{i} \\ \mathbf{u} \\ \mathbf{e} \end{bmatrix} = \frac{2}{3} \begin{bmatrix} i_a & i_b & i_c \\ u_{aN} & u_{bN} & u_{cN} \\ e_a & e_b & e_c \end{bmatrix} \begin{bmatrix} 1 \\ a \\ a^2 \end{bmatrix} \tag{3}$$

where $a = e^{j2\pi/3}$; u_{aN}, u_{bN}, and u_{cN} represent the three-phase output voltage of the converter to the neutral point and can be obtained using the following equation:

$$u_{xN} = S_x u_{dc}, \quad (x = a, b, c) \tag{4}$$

where S_x is the switching function representing the switching status of each bridge arm of the converter; u_{dc} is the DC voltage. The S_x can be expressed as follows [28]:

$$S_x = \begin{cases} 0 & \textit{upper arm is open, lower arm is closed} \\ 1 & \textit{upper arm is closed, lower arm is open} \end{cases} \tag{5}$$

Suppose that the sampling period is T_s; the derivative of the grid current can be discretized using the forward Euler approximation method as below:

$$\frac{\mathrm{d}i}{\mathrm{d}t} \approx \frac{i(k+1) - i(k)}{T_s} \tag{6}$$

Table 1: Relation between the value function, switching status, and voltage vector.

Value function	Switching combinations (S_a, S_b, S_c)	Voltage vectors
g_0	000	$U_0 = 0$
g_1	100	$U_1 = 2/3u_{dc}$
g_2	110	$U_2 = 1/3u_{dc} + j\sqrt{3}/3u_{dc}$
g_3	010	$U_3 = -1/3u_{dc} + j\sqrt{3}/3u_{dc}$
g_4	011	$U_4 = -2/3u_{dc}$
g_5	001	$U_5 = -1/3u_{dc} - j\sqrt{3}/3u_{dc}$
g_6	101	$U_6 = 1/3u_{dc} - j\sqrt{3}/3u_{dc}$
g_7	111	$U_7 = 0$

where $i(k+1)$ and $i(k)$ are sampling current values in k+1th and k-th sampling periods, respectively. Substitute (6) into (2); the predicted current can be expressed as

$$i(k+1) = \frac{T_s}{L}(u(k) - e(k)) + \left(1 - \frac{RT_s}{L}\right) i(k) \tag{7}$$

The expression of (7) in the $\alpha\beta$ coordinate system can be obtained using Clarke transformation as below:

$$\begin{bmatrix} i_\alpha(k+1) \\ i_\beta(k+1) \end{bmatrix} = \frac{T_s}{L} \begin{bmatrix} u_\alpha(k) - e_\alpha(k) \\ u_\beta(k) - e_\beta(k) \end{bmatrix} + \left(1 - \frac{RT_s}{L}\right) \begin{bmatrix} i_\alpha(k) \\ i_\beta(k) \end{bmatrix} \tag{8}$$

where $i_\alpha(k+1)$ and $i_\beta(k+1)$ are α-axis and β-axis components of the current in k+1th period, respectively; $u_\alpha(k)$ and $u_\beta(k)$ are α-axis and β-axis components of the output voltage of converter in k-th period, respectively; $e_\alpha(k)$ and $e_\beta(k)$ are α-axis and β-axis components of the grid voltage in k-th period, respectively. As shown in (8), the current of the GS-VSC in k+1th period can be accurately predicted according to the current measurement of the GS-VSC in$k$-th period, which can achieve the fast tracking and control of the GS-VSC current and enhance the ability of the GS-VSC in resisting system disturbances.

3.2. Value Function. The main goal of the GS-VSC is to ensure power balance of the VSC-HVDC transmission system and achieve wind power integration. The control strategy of the GS-VSC is described as follows. According to the desired reference output and the current input of the GS-VSC, the output voltage vector (**U**) of the GS-VSC can be obtained by determining the switching function value, namely, switching status, of each bridge arm of the converter. Then, based on the output voltage vector (**U**), grid voltage vector (**E**), and equivalent reactance Z_s, the magnitude and angle controllable therephase current (i_a, i_b, i_c) can be obtained to control the input and output power of the GS-VSC. Therefore, it is important to determine the optimal output voltage vector (**U**) of the GS-VSC.

It can be seen from (4) and (5) that the output voltage vector (**U**) is determined by the switching functions of three bridge arms, namely, S_a, S_b, and S_c. In the study, it is assumed that the GS-VSC is a three-phase two-level converter. Considering there are three switching function values (S_a, S_b, and S_c), there are eight possible switching states and eight corresponding voltage vectors. Moreover, since $\mathbf{U}_0$=$\mathbf{U}_7$, seven possible voltage output vectors are shown in Table 1.

The traditional GS-VSC uses the double closed loop structure (outer loop of power and inner loop of current) to determine the switching functions (S_a, S_b, and S_c) to control the AC voltage output and current (power output) of the GS-VSC. However, parameters of the PI controller are sensitive to the system parameters and it is difficult to tune PI parameters. In addition, the feedforward compensator term affected by the circuit parameters is required to be decoupled in the traditional control strategy. To overcome these issues, a FCS-MPC based control strategy is proposed.

FCS-MPC is a model-based closed loop control method. Based on the eight possible switching combinations and eight corresponding voltage vectors (**U**), the predicted GS-VSC current value of the next period can be obtained using the discrete predicted model of the GS-VSC given by (8). Then, comparing the predicted value with the reference value using the value function defined in (9), the optimal switching combination corresponding to the smallest value of value function is obtained and used to generate trigger pulse, which can achieve the optimal control of the GS-VSC.

$$g = \left|i^*_{g\alpha}(k+1) - i_{g\alpha}(k+1)\right| + \left|i^*_{g\beta}(k+1) - i_{g\beta}(k+1)\right| \tag{9}$$

where $i_{g\alpha}(k+1)$ and $i_{g\beta}(k+1)$ are the real and imaginary parts of the predicted current vector in the k+1 period under a given voltage vector, respectively; $i^*_{g\alpha}(k+1)$ and $i^*_{g\beta}(k+1)$ are the real and imaginary parts of the predicted current vector in the k+1 period under a given voltage vector, respectively.

Repeat the above procedures in the following sampling periods and thus the output current of the GS-VSC is optimized and controlled over the rolling horizon. Based on the above analyses, compared with the traditional PI control-based double closed loop control strategy, the FCS-MPC strategy controls converters directly according to the limited switching combinations. As such, there is no need to implement the decoupling process and the complex PI tuning process. Moreover, no modulators are required and

multilevel constraints can be considered. In particular, there is the lowest calculation complexity when two-level converter is used.

3.3. Consideration of Delay Compensation in the Proposed Strategy. The difference between the current reference and current measurement is used to construct the objective function, namely, the value function in (9), which transforms the problem of finding the optimal modulation satisfying control targets into a problem of finding the optimal switching combination corresponding to the value function with the smallest value. However, the current reference in (9) is the value in the future period, which causes delay in the control of the GS-VSC and affects the control accuracy and response speed of the GS-VSC with the FCS-MPC strategy. To deal with this problem, this study proposes to modify the value function using the predicted current value in k+2th period. The predicted function of current in k+2th period is

$$i(k+2 \mid k) = \frac{T_s}{L}(u(k+1) - e(k+1)) + \left(1 - \frac{RT_s}{L}\right) i(k+1) \tag{10}$$

where $i(k+1)$ and $i(k+2 \mid k)$ are the predicted currents in the $(k+1)$-th and $(k+2)$-th periods using information collected in k-th period, respectively; $u(k+1)$ is the output voltage in the $(k+1)$-th period; $e(k+1)$ is the grid voltage in the k+1th period.

The value function considering the delay compensation is as follows:

$$\tilde{g} = \left|i^*_{g\alpha}(k+2 \mid k) - i_{g\alpha}(k+2 \mid k)\right| + \left|i^*_{g\beta}(k+2 \mid k) - i_{g\beta}(k+2 \mid k)\right| \tag{11}$$

To ensure the stability of the DC voltage under the fault occurrence and wind power fluctuation, the DC current error is introduced into the value function as below:

$$\hat{g} = \left|i^*_{g\alpha}(k+2 \mid k) - i_{g\alpha}(k+2 \mid k)\right| + \left|i^*_{g\beta}(k+2 \mid k) - i_{g\beta}(k+2 \mid k)\right| + \lambda \left|u^*_{dc} - u_{dc}\right| \tag{12}$$

where λ is the weight coefficient. The predicted value of the DC voltage is introduced to the value function to improve the stability of the DC voltage under steady state and fault occurrences.

3.4. The Algorithm of the FCS-MPC Based Control Strategy. The algorithm of the FCS-MPC based control strategy is illustrated in Figure 7 and has the following steps.

Step 1. Formulate the mathematical model of the GS-VSC based on the eight switching combinations and the relation between the switching combination and corresponding input/output voltage and current.

Step 2. Construct the discrete-time model in order to predict the values of control variables in future periods.

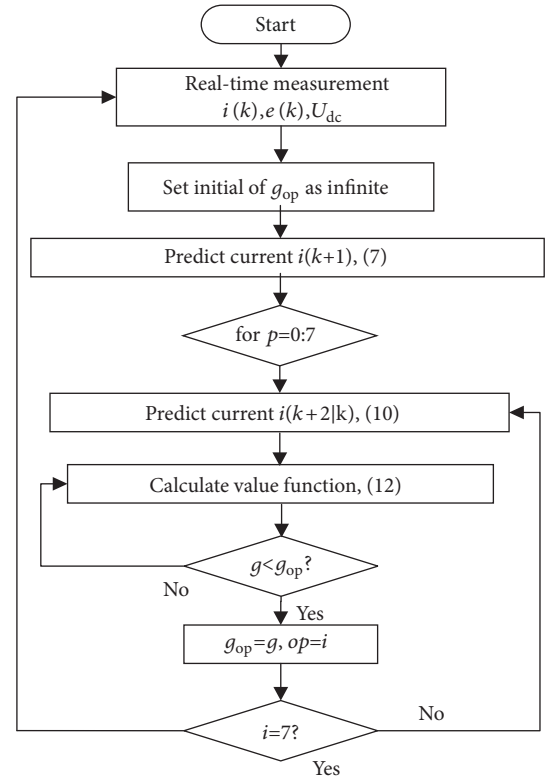

Figure 7: The flow chart of the FCS-MPC algorithm for GS-VSC.

Step 3. Based on the switching states currently applied, construct the discrete current model (8) in order to predict the current in k+1th period.

Step 4. Predict the current in k+2th period for each possible switching combination.

Step 5. Use the value function representing the expected performance of the system to evaluate all possible switching combinations.

Step 6. Choose the voltage vector corresponding to the value function with the smallest value and obtain the corresponding optimal switching combination.

Step 7. Update the status of switches based on the optimal switching combination and go back to step 2 for the next sampling period.

4. Case Studies

The VSC-HVDC connected offshore WF, as shown in Figure 1, is modeled in the MATLAB/Simulink to validate the efficiency of proposed FCS-MPC strategy. The simulation parameters are listed in Table 2.

4.1. Case 1: Wind Power Fluctuation. The comparisons between the proposed FCS-MPC strategy and traditional PI double closed loop control strategy under the wind power

Table 2: Simulation parameters.

Parameters	Values
Rated capacity of wind farms P/MW	4×300
DC voltageu_{dc}/kV	±320
Length of DC transmission line /km	300
DC capacitor C/μF	75
Reactance of line L/mH	200
Sampling periodT_s/μs	50
Number of time steps	60000

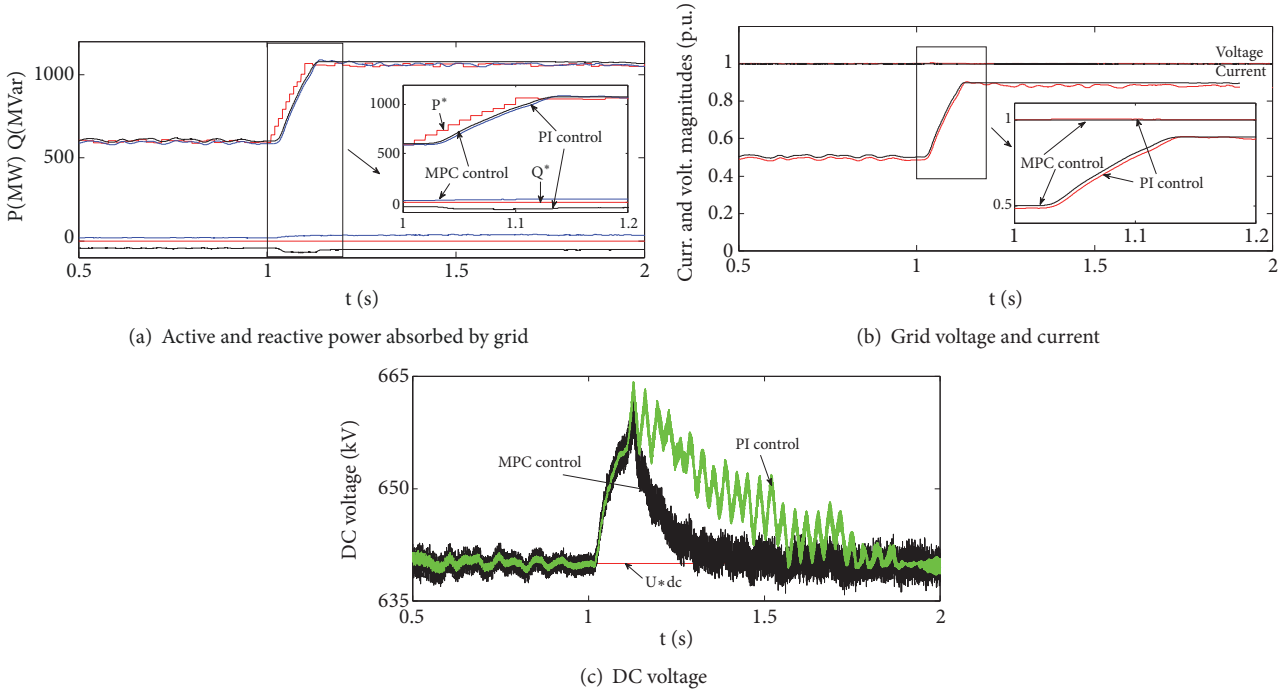

(a) Active and reactive power absorbed by grid

(b) Grid voltage and current

(c) DC voltage

Figure 8: Response characteristics with two strategies under wind power fluctuation.

fluctuation are carried out in this case. The wind power output is 600MW between 0s to 1s and increases to 1100MW at 1.1s and then remains unchanged. It is assumed that the wind farm operates with the unity power factor. The simulation results of the GS-VSC with two strategies are shown in Figures 8(a)–8(c).

As shown in Figures 8(a)–8(c), the GS-VSC with two strategies can quickly respond to the WF power output variation and achieve steady wind power integration. Compared with the traditional double closed PI control strategy, the FCS-MPC adopts the single loop (outer loop of voltage) control strategy, which enables the GS-VSC to have a faster response speed and higher response accuracy, as shown in Figures 9(a)–9(b). Moreover, as shown in Figure 9(c), the DC voltage of the VSC-HVDC system is restored to the reference value more rapidly when the FCS-MPC control strategy is used because the term involved in the DC predicted voltage is considered in the value function. Therefore, the GS-VSC with the proposed FCS-MPC strategy can ensure the steady operation of the VSC-HVDC system and has better performance under the steady state operation.

4.2. Case 2: AC Fault Occurrence at Grid Side. It is assumed that a three-phase short-circuit fault occurs at grid side at 2s and lasts for 10 ms. The response characteristic of the GS-VSC system is shown in Figures 9(a)–9(c).

As shown in Figure 9, when the traditional PI control strategy is applied to the GS-VSC, the fault occurrence has big impacts on the active/ reactive power outputs, voltage, and current outputs of GS-VSC and they are restored to the reference values slowly. In addition, due to the limited ability of the traditional PI control strategy in controlling the DC voltage, the DC voltage cannot be restored to reference value within 3s, as shown in Figure 9(c). However, when applying the proposed FCS-MPC strategy, the impacts of the fault occurrence on the outputs of GS-VSC are limited, and the active/reactive power outputs and voltage and current outputs of GS-VSC are restored to the reference values rapidly. Moreover, the DC voltage is restored to the reference value

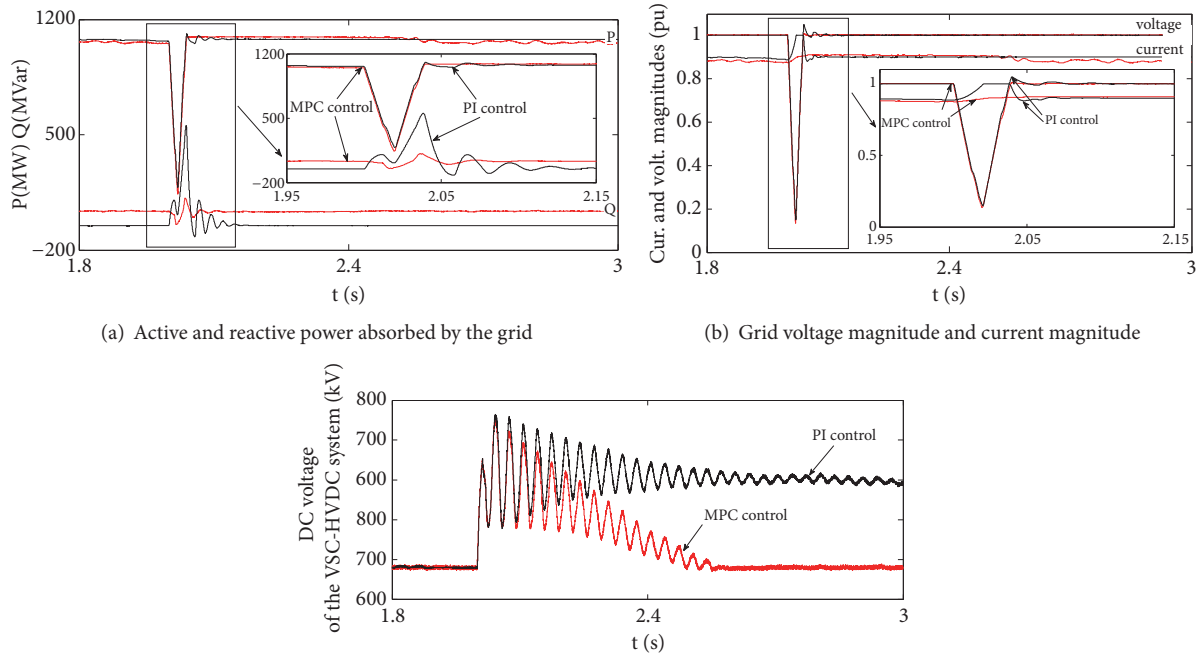

(a) Active and reactive power absorbed by the grid

(b) Grid voltage magnitude and current magnitude

(c) DC voltage of VSC-HVDC

FIGURE 9: Response characteristic VSC-HVDC with two strategies under AC fault occurrence at grid side.

within 2.5s because the predictive control for the DC voltage is considered in the proposed strategy, thus improving the ability of the GS-VSC in controlling the DC voltage under fault occurrences.

4.3. Case 3: DC Fault Occurrence. It is assumed that a DC line fault occurs at the left side of the DC transmission line at 2.0s and lasts for 100 ms. The response characteristics of the VSC-HVDC system with two control strategies are shown in Figures 10(a)–10(e).

As shown in Figure 10(a), the active and reactive power decrease to -2200MW and -2000MW, respectively, in the PI control strategy while both the active and reactive power decrease to -1000MW in the proposed FCS-MPC strategy. As shown in Figures 10(b) and 10(c), the AC voltage decreases to 0.75 p.u. and the maximum transient current reaches 5 p.u. that far exceeds the maximum tolerant level of the GS-VSC. When the FCS-MPC strategy is applied to the GS-VSC, as shown in Figures 10(d) and 10(e), the AC voltage decreases to 0.9 p.u and the maximum transient current is 2.4 p.u. It can been seen that the fluctuations of AC voltage, AC current, and active/reactive power are smaller in the proposed FCS-MPC strategy, which demonstrates the better performance of the FCS-MPC strategy.

4.4. Case 4: Grid Voltage Drops. To further validate the effectiveness of the proposed FCS-MPC strategy, the simulations are conducted when grid voltage drops. It is assumed that the grid voltage decreases from 1p.u. to 0.5 p.u. at 2.0s and the voltage remains 0.5 p.u. for 100 ms. The simulation results are shown in Figures 11(a)–11(e).

As shown in Figures 11(a)–11(e), when the proposed FCS-MPC strategy is applied, the active power decreases to 540MW and is restored to the normal level at 2.14s. The reactive power has a very small fluctuation. The AC voltage can be restored to 1.0 p.u. rapidly after the fault is cleared and there is a very small fluctuation in AC current. However, when the PI control strategy is used, the active power decreases to 550MW and is restored to the normal level at 2.25s. The reactive power increases to 500Mvar and is restored to the normal level slowly. Likewise, the AC voltage and AC current are restored to the normal level slowly. Therefore, the FCS-MPC strategy makes the system more resistant to system disturbances.

4.5. Case 5: Comparative Analysis of Harmonic Distortion Rates of Cases1-4. Perform the Fourier analyses under selected conditions, namely, the period (1.2s-1.4s) in Case 1 with the maximum wind power output and periods (2.3s-2.5s) in Case 2-Case 4. The distortion rates of the AC voltage and AC current under different operation conditions are shown in Table 1.

As shown in Table 3, Cases 1-4 represent the Fourier analysis results under the steady state conditions under the wind power fluctuation, under AC fault occurrence at the grid side, under DC fault occurrence, and under grid voltage drop, respectively. It can be seen from Table 1 that, in the proposed FCS-MPC strategy, the distortion rates of grid-connected voltage and current of GS-VSC are lower than 1%, which is far lower than the one in the traditional PI control strategy.

5. Conclusions

To overcome the issues in the operation of the complex energy system, this study proposes a FCS-MPC based novel

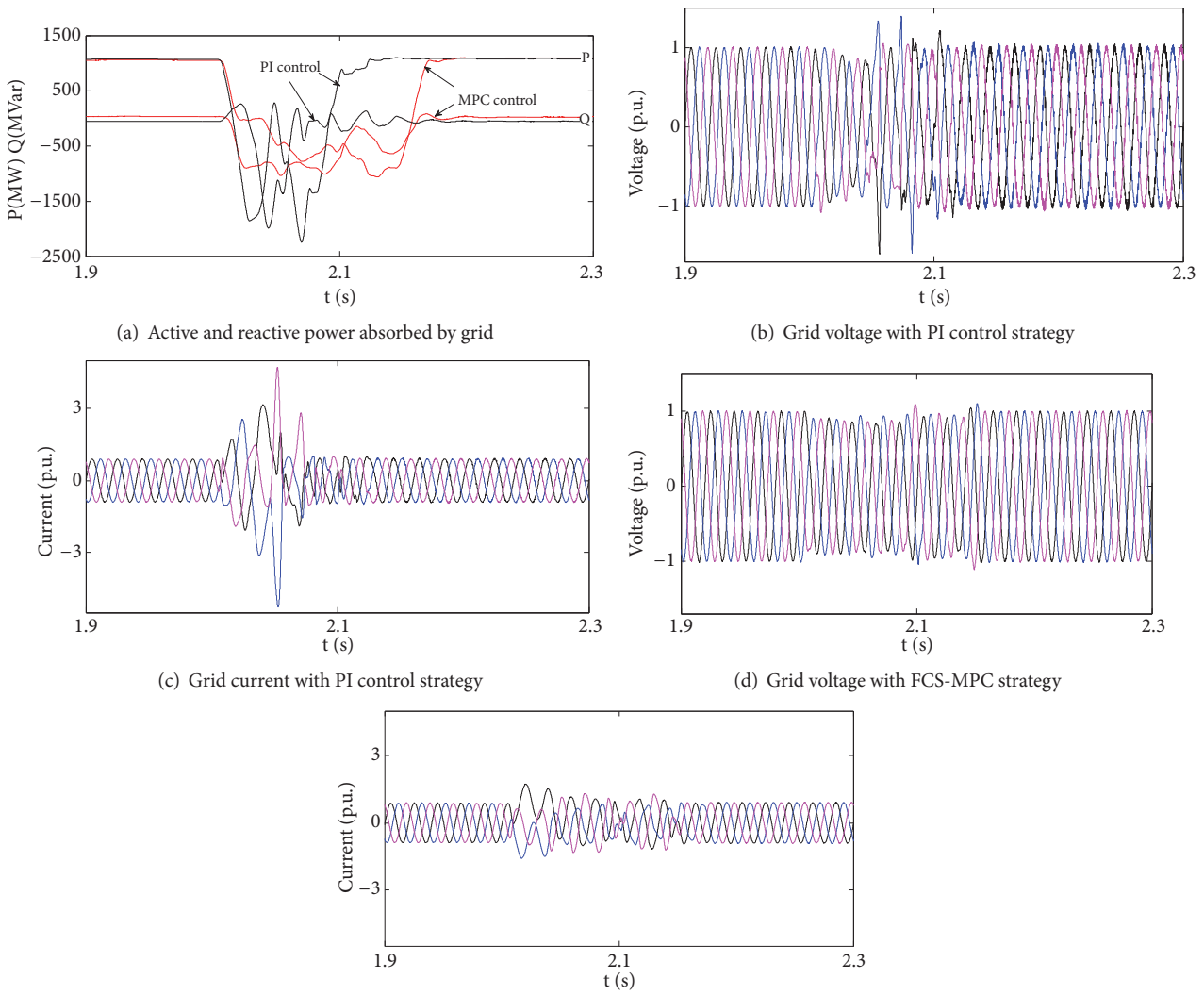

(a) Active and reactive power absorbed by grid

(b) Grid voltage with PI control strategy

(c) Grid current with PI control strategy

(d) Grid voltage with FCS-MPC strategy

(e) Grid current with FCS-MPC strategy

Figure 10: Response characteristic with two control strategies under DC fault.

Table 3: Harmonic distortion rates of Cases 1-4 with the FCS-MPC and PI strategy.

	Current		Voltage	
	FCS-MPC	PI	FCS-MPC	PI
case 1	0.98	1.55	0.53	2.25
case 2	0.62	2.05	0.48	2.94
case 3	0.37	4.22	0.42	5.20
case 4	0.48	3.59	0.75	6.94

control strategy. The proposed control strategy has a simple control structure, removes the inner loop of current and complex PI parameter tuning process, and achieves multiobjective optimization of the complex energy system. Moreover, the proposed control strategy considers the impact of delay and introduces the term of the DC voltage prediction in the value function to improve the stability of DC voltage control and enhances the abilities of the complex energy system in resisting disturbances and recovering after faults. The simulation results under the wind power fluctuation, three-phase short circuit fault, and grid voltage drop validate that the system with the FCS-MPC strategy has better dynamic characteristics and parameter robustness. Moreover, the proposed strategy improves the abilities of the VSC-HVDC in resisting disturbances and fault recovery and reduces distortion rates of the grid-connected voltage and current of the GS-VSC.

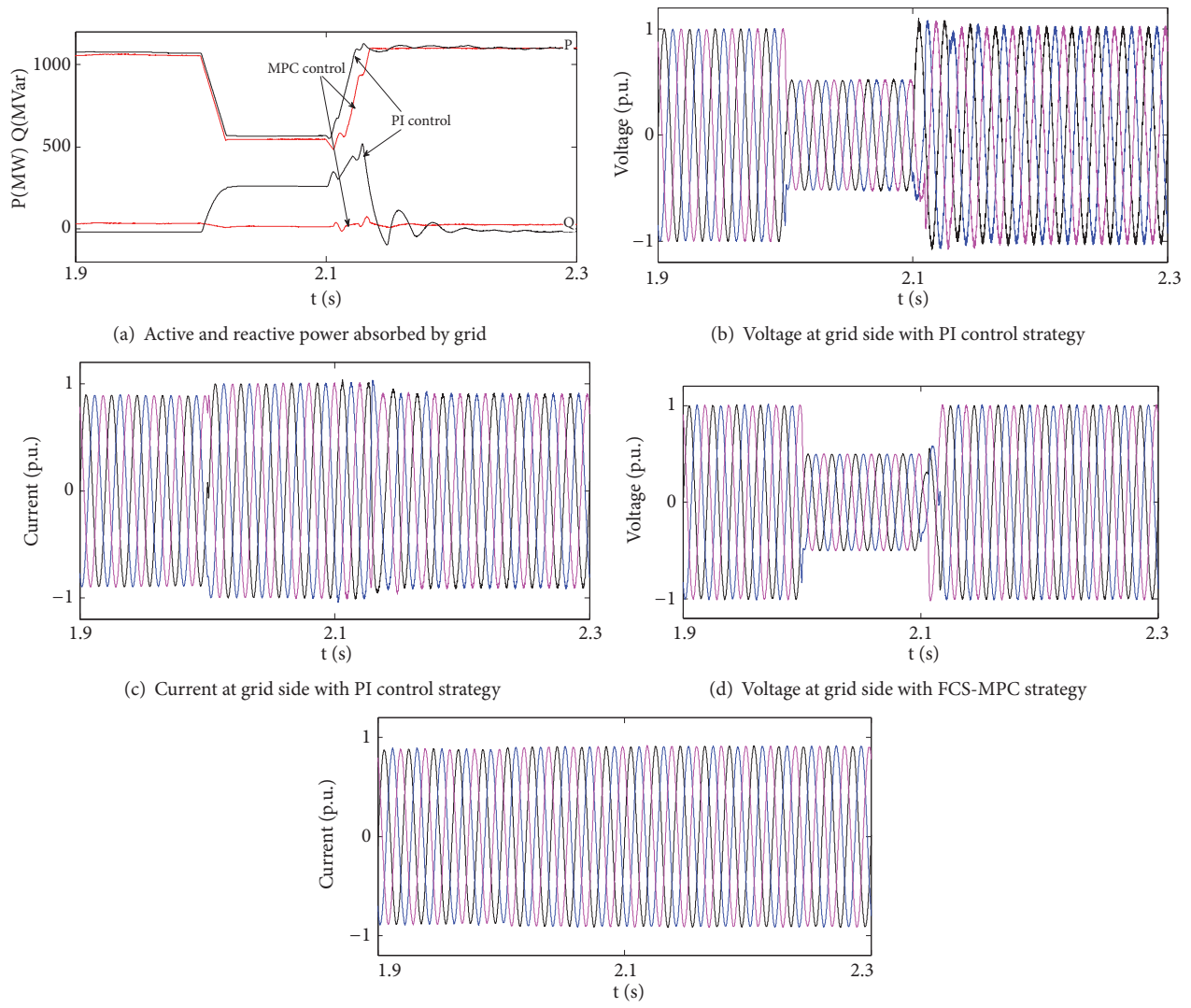

(a) Active and reactive power absorbed by grid

(b) Voltage at grid side with PI control strategy

(c) Current at grid side with PI control strategy

(d) Voltage at grid side with FCS-MPC strategy

(e) Current at grid side with FCS-MPC strategy

Figure 11: Response characteristic with two control strategies when grid voltage drops.

Nomenclature

u_{sd}, u_{sq}: d-axis and q-axis components of the three-phase voltage
i_{sd}, i_{sq}: d-axis and q-axis components of the three-phase current
v_{sd}, v_{sq}: d-axis and q-axis components of the voltage at the converter side
S_{sd}, S_{sq}: d-axis and q-axis components of the switching function
ω_s: Synchronized angular velocity
u_a, u_b, u_c: Three-phase output voltage of the converter
i_a, i_b, i_c: The three-phase grid current
e_a, e_b, e_c: The three-phase grid voltage
u_a, u_b, u_c: The three-phase output voltage of the converter
L: Reactance
R: Resistance
C: Capacitance
u_{dc}, i_{dc}, i_L: The DC voltage, DC input current, and DC output current
i, u, e: The vector of current, the vector of output voltage of converter, and the vector of the grid voltage
u_{xN}: x=a, b, c, the three-phase output voltage of the converter to the neutral point
S_x: x=a, b, c, the switching function representing the switching status of each bridge arm of the converter
u_{dc}: The DC voltage of the VSC-HVDC system
$i(k)$: The sampling current value in k-th sampling period
$i_\alpha(k+1)$: α-axis component of the current in (k+1)-th period
$i_\beta(k+1)$: β-axis component of the current in (k+1)-th period

$u_\alpha(k+1)$: α-axis component of the output voltage of the converter in (k+1)-th period
$u_\beta(k+1)$: β-axis component of the output voltage of the converter in (k+1)-th period
$e_\alpha(k+1)$: α-axis component of the grid voltage in (k+1)-th period
$e_\beta(k+1)$: β-axis component of the grid voltage in (k+1)-th period
$i_{g\alpha}(k+1)$: The real part of the predicted current in the (k+1)-th period under a given voltage vector
$i_{g\beta}(k+1)$: The imaginary part of the predicted current in the k+1th period under a given voltage vector
$i^*_{g\alpha}(k+1)$: The real part of the reference current in the (k+1)-th period under a given voltage vector
$i^*_{g\beta}(k+1)$: The imaginary parts of the reference current in the k+1th period under a given voltage vector
λ: The weight coefficient
$i(k+2 \mid k)$: The predicted current value in the (k+2)-th period using information collected from k-th period
g_{op}: The initial value of the value function.

Data Availability

The no secret-involvement data used to support the findings of this study are available from the corresponding author upon request.

Conflicts of Interest

The authors declare that they have no conflicts of interest.

Acknowledgments

This work has been funded by the State Grid Corporation Science and Technology Project titled "Research and Demonstration of the key technologies for application of group Electrochemical Energy Storage Power Stations in the UHV Hybrid AC/DC receiving-end power grid".

References

[1] O. Noureldeen and I. Hamdan, "Design of robust intelligent protection technique for large-scale grid-connected wind farm," *Protection and Control of Modern Power Systems*, vol. 3, no. 3, pp. 169–182, 2018.

[2] Y. W. Shen, D. P. Ke, Y. Z. Sun, D. S. Kirschen, W. Qiao, and X. Deng, "Advanced auxiliary control of an energy storage device for transient voltage support of a doubly fed induction generator," *IEEE Transactions on Sustainable Energy*, vol. 7, no. 1, pp. 63–76, 2016.

[3] D. Zheng, A. T. Eseye, J. Zhang, and H. Li, "Short-term wind power forecasting using a double-stage hierarchical ANFIS approach for energy management in microgrids," *Protection and Control of Modern Power Systems*, vol. 2, no. 2, pp. 136–145, 2017.

[4] Z. Ma, H. Chen, and Y. Chai, "Analysis of voltage stability uncertainty using stochastic response surface method related to wind farm correlation," *Protection and Control of Modern Power Systems*, vol. 2, no. 2, pp. 211–219, 2017.

[5] M. Soliman, O. P. Malik, and D. T. Westwick, "Multiple model predictive control for wind turbines with doubly fed induction generators," *IEEE Transactions on Sustainable Energy*, vol. 2, no. 3, pp. 215–225, 2011.

[6] M. D. Spencer, K. A. Stol, C. P. Unsworth, J. E. Cater, and S. E. Norris, "Model predictive control of a wind turbine using short-term wind field predictions," *Wind Energy*, vol. 16, no. 3, pp. 417–434, 2013.

[7] S. Kouro, P. Cortés, R. Vargas, U. Ammann, and J. Rodríguez, "Model predictive control—a simple and powerful method to control power converters," *IEEE Transactions on Industrial Electronics*, vol. 56, no. 6, pp. 1826–1838, 2009.

[8] A. Gosk, *Model Predictive Control of a Wind Turbine, [M.S. thesis]*, Technical University, Lyngby, Denmark, 2011.

[9] J. Rodriguez and P. Cortes, "Predictive control of power converters and electrical drives," *IEEE Transactions on Industrial Electronics*, vol. 63, no. 7, pp. 4472–4474, 2016.

[10] S. Rivera, S. Kouro, B. Wu et al., "Multilevel direct power control—a generalized approach for grid-tied multilevel converter applications," *IEEE Transactions on Power Electronics*, vol. 29, no. 10, pp. 5592–5604, 2014.

[11] G. Li and M. R. Belmont, "Model predictive control of sea wave energy converters – part i: a convex approach for the case of a single device," *Journal of Renewable Energy*, vol. 69, pp. 453–463, 2014.

[12] J. D. Barros, J. F. Silva, and E. G. Jesus, "Fast-predictive optimal control of npc multilevel converters," *IEEE Transactions on Industrial Electronics*, vol. 60, no. 2, pp. 619–627, 2013.

[13] G. Li, "Nonlinear model predictive control of a wave energy converter based on differential flatness parameterisation," *International Journal of Control*, vol. 90, no. 1, pp. 68–77, 2017.

[14] P. Cortés, G. Ortiz, J. I. Yuz et al., "Model predictive control of an inverter with output LC filter for UPS applications," *IEEE Transactions on Industrial Electronics*, vol. 56, no. 6, pp. 1875–1883, 2009.

[15] P. Cortes, A. Wilson, S. Kouro, J. Rodriguez, and H. Abu-Rub, "Model predictive control of multilevel cascaded H-bridge inverters," *IEEE Transactions on Industrial Electronics*, vol. 57, no. 8, pp. 2691–2699, 2010.

[16] M. Narimani, B. Wu, V. Yaramasu, C. Zhongyuan, and N. R. Zargari, "Finite control-set model predictive control (FCS-MPC) of nested neutral point-clamped (NNPC) converter," *IEEE Transactions on Power Electronics*, vol. 30, no. 12, pp. 7262–7269, 2015.

[17] K. S. Alam, D. Xiao, D. Zhang, and M. F. Rahman, "Simplified finite control set model predictive control (FCS-MPC) with extended voltage vectors for grid connected converters," in *Proceedings of the 2017 Australasian Universities Power Engineering Conference, AUPEC 2017*, pp. 1–6, Australia, November 2017.

[18] H. Jiefeng, Z. Jianguo, L. Gang, G. Platt, and D. G. Dorrell, "Multi-objective model-predictive control for high-power converters," *IEEE Transactions on Energy Conversion*, vol. 28, no. 3, pp. 652–663, 2013.

[19] L. Zhu, X. Fu, X. Hu et al., "Model predictive control of modular multilevel converter for HVDC system," *Power System Protection and Control*, vol. 42, no. 16, pp. 1–8, 2014.

[20] J. Holtz and S. Stadtfeld, "A predictive controller for the stator currentvector of AC machines fed from a switched voltage source," in *Proceedings of the International Power Electronics Conference*, pp. 1665–1675, 1983.

[21] J. Rodriguez and P. Cortes, *Predictive Control of Power Converters and Electrical Drives*, Wiley, Hoboken, NJ, USA, 2012.

[22] T. H. Mohaned, J. Morel, H. Bevrani, and T. Hiyama, "Model predictive based load frequency control design concerning wind turbines," *International Journal of Electrical Power & Energy Systems*, vol. 43, no. 1, pp. 859–867, 2012.

[23] A. Calle-Prado, S. Alepuz, J. Bordonau, J. Nicolas-Apruzzese, P. Cortes, and J. Rodriguez, "Model predictive current control of grid-connected neutral-point-clamped converters to meet low-voltage ride-through requirements," *IEEE Transactions on Industrial Electronics*, vol. 62, no. 3, pp. 1503–1514, 2015.

[24] R. Tao, F. Li, W. Chen, Y. Fan, C. Liang, and Y. Li, "Research on the protection coordination of permanent magnet synchronous generator based wind farms with low voltage ride through capability," *Protection and Control of Modern Power Systems*, vol. 2, no. 2, pp. 311–319, 2017.

[25] Y.-W. Shen, D.-P. Ke, W. Qiao, Y.-Z. Sun, D. S. Kirschen, and C. Wei, "Transient reconfiguration and coordinated control for power converters to enhance the LVRT of a DFIG wind turbine with an energy storage device," *IEEE Transactions on Energy Conversion*, vol. 30, no. 4, pp. 1679–1690, 2015.

[26] Y. W. Shen, L. Q. Liang, M. J. Cui, F. Shen, B. Zhang, and T. Cui, "Advanced control of DFIG to enhance the transient voltage support capability," *Journal of Energy Engineering*, vol. 144, no. 2, Article ID 04018009, 2018.

[27] T. S. L. V. Ayyarao, "Modified vector controlled DFIG wind energy system based on barrier function adaptive sliding mode control," *Protection and Control of Modern Power Systems*, vol. 4, no. 4, pp. 34–41, 2019.

[28] M. Alsumiri, L. Li, L. Jiang, and W. Tang, "Residue theorem based soft sliding mode control for wind power generation systems," *Protection and Control of Modern Power Systems*, vol. 3, no. 3, pp. 247–258, 2018.

Hindawi
Complexity
Volume 2019, Article ID 7890652, 14 pages
https://doi.org/10.1155/2019/7890652

Research Article

Power Grid Fault Diagnosis Method Using Intuitionistic Fuzzy Petri Nets Based on Time Series Matching

Mingyue Tan, Jiming Li, Xiangqian Chen, and Xuezhen Cheng

Department of the Electrical Engineering & Automation, Shandong University of Science and Technology, 579 Qianwangang Road, Huangdao District, Qingdao, Shandong Province 266590, China

Correspondence should be addressed to Xuezhen Cheng; zhenxc6411@163.com

Mingyue Tan and Jiming Li contributed equally to this work.

Received 25 March 2019; Revised 10 May 2019; Accepted 10 June 2019; Published 21 July 2019

Guest Editor: Chun Wei

To improve the reliability of power grid fault diagnosis by enhancing the processing ability of uncertain information and adequately utilizing the alarm information about power grids, a fault diagnosis method using intuitionistic fuzzy Petri Nets based on time series matching is proposed in this paper. First, the alarm hypothesis sequence and the real alarm sequence are constructed using the alarm information and the general grid protection configuration model, and the similarity of the two sequences is used to calculate the timing confidence. Then, an intuitionistic fuzzy Petri Nets fault diagnosis model, with an excellent ability to process uncertain information from intuitionistic fuzzy sets, is constructed, and the initial place value of the model is corrected by the timing confidence. Finally, an application of the fault diagnosis model for the actual grid is established to analyze and verify the diagnostic results of the new method. The results for some test cases show that the new method can improve the accuracy and fault tolerance of fault diagnosis, and, furthermore, the abnormal state of the component can be inferred.

1. Introduction

With the development of the power grid, an increasing number of new energy sources, such as solar energy, photovoltaics, and wind energy [1], have been integrated into power grids, which poses a potential threat to the safe operation of the grids [2]. It is becoming more and more urgent to form a fast and accurate power grid fault diagnosis method. At present, the mainly grid fault diagnosis method is that power grid dispatchers use the data which from Supervisory Control And Data Acquisition (SCADA) and their own experience to analyze the fault. However, the accuracy and speed of traditional fault diagnosis methods are difficult to meet the requirements of current power grids when complex faults [3] occur, so many automatic diagnosis methods are proposed as follows: Expert Systems [4], Artificial Neural Networks [5, 6], Bayesian Networks [7, 8], Rough Sets [9], and Petri Nets [10, 11]. In recent years, due to fuzzy Petri Nets' advantages of rapid concurrency and the ability to process uncertain information, the research adapting fuzzy Petri Nets to grid fault diagnosis has attracted increasing attention.

Wang L, Sun J [12, 13] proposed a fault diagnosis model based on fuzzy Petri Nets to solve the uncertainty of protection and circuit breaker action in grids. The matrix dimension reduction method has improved the calculation speed. Wang Y N and Cheng X Z [14, 15] used weighted fuzzy Petri Nets and the hierarchical transition method to analyze grid faults. In order to stratify the transition set and optimize the algorithm, the two-layer general model was established for each component. In [16], a fuzzy Petri Nets fault diagnosis method, considering protection and circuit breaker action timing, was proposed, which improved the ability of handling uncertain information and fault tolerance. Cheng X Z [17] proposed a fuzzy Petri Nets diagnosis method based on directional weighting. In this model, subnet models were established for each propagation direction, and different weights were assigned according to the degree of the influence of different components on the results. In [18], a weighted fuzzy Petri Nets

fault diagnosis method, based on multisource information fusion, was proposed, which introduced electrical quantity and took the time series attribute into consideration. In addition, fuzzy neural Petri Nets [19] were used in the field of fault diagnosis.

The fuzzy Petri Nets fault diagnosis models, mentioned above, take into account the uncertainty of protection and circuit breaker trip information, as well as the calculation and fault tolerance of the model. However, the impact of uncertain and incomplete information [21] on the fault diagnosis results is not fully considered in these models. In particular, timing data in the alarm information also needs to be further mined, and the use of big data to solve complex problems [22] in fault diagnosis has become a trend too.

Petri Nets are directed graph structures with timing constraints, and the temporal logic of the alert information is automatically considered when generating the Petri Nets model in an online application. However, the received alert information may have various conditions, such as rejection, misoperation, and timing disorder, which may reduce the accuracy of the diagnosis results. Against the background of the above research, the intuitionistic fuzzy Petri Nets fault diagnosis model, based on time series matching, is established to process time series information. The timing information is further mined using the method of timing matching, and the sequence difference and time difference at the time of the fault are calculated by the Edit Distance and the Dynamic Time Warping (DTW) Distance, respectively. At the same time, the description of information uncertainty is more precise by the intuitionistic fuzzy set considering the degree of membership and nonaffiliation of the information. This paper mainly does the following work.

(1) To study the timing properties of alert information, the time series confidence is calculated by analyzing the timing constraint relationship between the protection and the circuit breaker to verify and filter the alarm information and correct the confidence value of the initial position.

(2) To establish an intuitionistic fuzzy Petri Nets fault diagnosis model, the intuitionistic fuzzy algorithm is used to deal with the membership degree and nonmembership degree relationship of the alarm information, when the fault occurs, which can improve the model's ability to deal with uncertain and incomplete alarm information.

(3) To establish a two-layer fault diagnosis model, after the fault occurs, the nonmembership value of the terminal position is modified according to the number of remote backup protection actions of the component, and the membership value is optimized by the hierarchical transition technique and the Gaussian function.

The reasoning process based on matrix operation is given.

2. Intuitionistic Fuzzy Time Petri Nets

2.1. The Basic Theory of Intuitionistic Fuzzy Sets. The intuitionistic fuzzy set [25] has three aspects: membership degree, nonmembership degree, and hesitation degree. Therefore, the set is more accurate concerning the description of uncertain and incomplete information. Intuitionistic fuzzy sets can be defined according to the following [26].

Definition 1. Assuming that X is a given theoretical domain, the definition of the intuitionistic fuzzy sets of domain X is as follows:

$$A = \{\langle x, \mu_A(x), \gamma_A(x)\rangle \mid x \in X\} \tag{1}$$

(1) $0 \le \mu_A(x) + \gamma_A(x) \le 1$, where $\mu_A(x) : x \longrightarrow [0,1]$ and $\gamma_A(x) : x \longrightarrow [0,1]$ represent the membership function and the nonmembership function of set A, respectively, and for any element in set A, $x \in X$, $0 \le \mu_A(x) + \gamma_A(x) \le 1$.

(2) The function pair $(\mu_{A(x)}, \gamma_{A(x)})$ is defined as the intuitionistic fuzzy index in the X domain, which is composed of membership degree $\mu_{A(x)}$ and nonmembership degree $\gamma_{A(x)}$.

(3) $\pi_A(x) = 1 - \mu_A(x) - \gamma_A(x)$ is set as the degree of hesitation of x in the intuitionistic fuzzy set A in the domain of X, indicating that x belongs to the degree of uncertainty of set A. Additionally, for any $x \in X$, $0 \le \pi_A(x) \le 1$.

2.2. Time Series Model in the Power Grid. The time series model in the grid is defined on the basis of study [20].

$x = (v, t)$ is set as a single element in the timing collection, and the alert information v is defined as a triple: $v = (A, \Delta t, S)$

(1) A indicates component action or alarm information.

(2) Δt represents the length of the error of time, Δt and t constitute a time constraint, and the time when event A occurs is $[t - \Delta t/2, t + \Delta t/2]$.

(3) S denotes a fuzzy flag, $S = 0$: $x = (v, t)$ denotes a fuzzy term, and $S = 1$: $x = (v, t)$ denotes a certain term. The introduction of fuzzy items has a good distinction between uncertain and incomplete information caused by misoperation, refusal, and information loss in the power grid, which is beneficial for improving the accuracy of diagnosis. When A_i is indicated as an electrical equipment failure (Busbar, Line, Transformer) or circuit breaker and circuit breaker failure protection simultaneously trip, the time element $x_i = (v_i, t_i)$ is a fuzzy item.

2.3. Time Series Reasoning Process. The application of time series information in grid fault diagnosis, in [15, 17], is only used to filter alarm information. In this paper, time series similarity matching is used to calculate the Edit Distance and DTW Distance between the actual alarm time series and the alarm hypothesis time series, which is then converted to time confidence that can be used to correct the probability of the model.

The Edit Distance is a measure used to calculate the distance between two strings of sequences, which can be expressed as the minimum number of edit operations required to convert a string into another string (editing operations include insert, delete, and replace).

For example, string sequences $X = \{x_1, x_2, \ldots, x_n\}$, $Y = \{y_1, y_2, \ldots, y_n\}$, the Edit Distance $D_{n,k}$ can be calculated from $D_{0,0}$ by

$$D_{i,j} = \begin{cases} 0 & i = j = 0 \\ \min\left(D_{i-1,j-1} + L(x_i, y_i), D_{i-1,j} + 1, D_{i,j-1} + 1\right) & i > 0 \text{ or } j > 0 \end{cases} \tag{2}$$

In the formula, if $x_i = y_i$, then $L(x_i, y_i) = 0$; otherwise, $L(x_i, y_i) = 1$.

Editing Distance has been already a mature calculation method. However, due to the high uncertainty of information in the grid fault (the loss of, and erroneous, information, as well as timing chaos), it is difficult to make accurate judgments on sequences that are not synchronized. In this paper, the Editing Distance is combined with the Dynamic Time Warping Distance to form a time similarity matching calculation method to increase the processing ability of the asynchronous information. The specific discussion is as follows.

For time series X and time series Y,

$$\begin{aligned} X &= \{x_1 = (Vx_1, t_{x1}), x_2 = (Vx_2, t_{x2}), \ldots, x_n \\ &\quad = (Vx_n, t_{xn})\} \\ Y &= \{y_1 = (V_{y1}, t_{y1}), y_2 = (V_{y2}, t_{y2}), \ldots, y_n \\ &\quad = (V_{ym}, t_{ym})\} \end{aligned} \tag{3}$$

$$(n \le m)$$

If X and Y are not obscured, the distance [20] between them can be defined as

$$D(X, Y) = aD_{edit}(X, Y_s) + bD_{time}(X, Y_s) \tag{4}$$

$$D_{time}(X, Y_s) = \sum_{x_i \mid \in X, x_i \mid \notin Y_s} 1 \tag{5}$$

$$D_{time}(X, Y_s) = \sum_{x_i \mid = y_j', \beta \ge \gamma} \left(\frac{4}{\pi} \arctan\left(\frac{2\left| t_{xi} - t_{yj}' \right|}{\Delta t_{xi} + \Delta t_{yj}'} \right) - 1 \right) \tag{6}$$

(1) $\beta = |t_{xi} - t_{yj}'|, \gamma = |(\Delta t_{xi} + \Delta t_{yj}')/2|$ $i = 1, 2, \ldots, n$; $j = 1, 2, \ldots, p$.

(2) $Y_s = (y_1', y_1', \ldots y_p')$. For any $y_i' \mid \in Y_s$, there is $y_i' \mid \in X$, and y_i' is the element of time series Y, $(i = 1, 2, \ldots, p)$, and $D_{edit}(X, Y_s)$ denotes the Edit Distance of the time series X and Y_s for identifying information loss and timing disorder. Since Y_s is a time subsequence of the Y set, the simplified formula applies to the general case.

(3) $D_{time}(X, Y_s)$ represents the DTW Distance between time series X and Y_s; a is the weight of the Edit Distance, and b is the weight of the DTW Distance. Due to the special information, such as information error, information loss, or timing disorder, the alarm information, received by the system, may cause large deviations in timing matching. Based on this, the weight coefficients a and b are defined to quantify the deviation in order to adjust the proportion of the Edit Distance and the DTW Distance. The smaller the difference between the two time series, the more similar they are.

The confidence calculation method for timing matching is defined in [20], and the calculated distance between the actual alarm time series and the alarm hypothesis time series is mapped to the (0, 1) interval by (7). The smaller the distance between the two time series, the higher the confidence level obtained.

$$C_X = \begin{cases} 1 & \mathrm{D}(\mathrm{X}, \mathrm{Y}) \le 1 \\ \dfrac{1}{D(X, Y)} & 1 < \mathrm{D}(\mathrm{X}, \mathrm{Y}) \le 10 \\ 0.1 & \mathrm{D}(\mathrm{X}, \mathrm{Y}) > 10 \end{cases} \tag{7}$$

2.4. Intuitionistic Fuzzy Time Petri Nets (IFTPN). Intuitionistic Fuzzy Time Petri Nets (IFTPN) can be defined as a seven-tuple, $IFTPN = \{P, T_\lambda, F, T_t, I, O, M_{0,}\}$.

(1) $P = \{p_1, p_2, p_3, \ldots, p_n\}$ indicates a collection of finite places in IFIAPN.

(2) $T_\lambda = \{\lambda_1, \lambda_2, \lambda_3, \ldots, \lambda_n\}$ indicates a set of finite transitions in IFIAPN.

(3) $F = \{f_1, f_2, f_3, \ldots, f_n\}$ indicates a set of transition thresholds in IFIAPN, where $f_j = (\alpha_j, \beta_j)$, $j = 1, 2, 3, \ldots, m$ are intuitionistic fuzzy sets, and $\alpha_j \ge 0$, $\beta_j \ge 0$ represent the uncertainty and the uncertainty of transition λ_j, respectively.

(4) $T_t = \{t_1, t_2, t_3, \ldots, t_n\}$ indicates the time status information of the initial places.

(5) I represents the input matrix $I = (W_{Iij})_{n \times m}$, W_{Iij} represents the logic element, $W_{Iij} \in [0, 1]$, and $\sum_{0 \le i \le n} W_{Iij} = 1$. If there is a directed arc, from place p_i to transition t_i, then the value of W_{Iij} is the weight of the directed arc. If there is no directed arc from p_i to t_i, then $W_{Iij} = 0, i = 1, 2, 3, \ldots, n$; $j = 1, 2, 3, \ldots, m$

(6) O indicates the output matrix, $O = (W_{Oij})_{n \times m}$, W_{Oij} represents the logic element, and $W_{Oij} \in [0, 1]$. If there is a directed arc from transition t_j to place p_i, then the value of W_{Oij} is c_j of the confidence of the rule t_j, and $c_j = (\mu_c, \gamma_c)$ represents the weight parameter of the directed arc from transition t_j to place p_i. If there is no directed arc from t_j to p_i, then $W_{Oij} = 0, i = 1, 2, 3, \ldots, n$; $j = 1, 2, 3, \ldots, m$.

(7) M_0 is the initial state, $M_0 = [m_0(p_1), m_0(p_2), m_0(p_3), \ldots, m_0(p_i)]$, $m_0(p_i)$ is the initial state of the proposition p_i, $M_0(p_i) = (\mu_i, \gamma_i)$, where μ_i represents the degree of certainty of the place p_i, γ_i represents the uncertainty of the place p_i, and $M_0(p_i) \in [0, 1]$.

3. Grid Fault Diagnosis Based on Time Series Intuitionistic Fuzzy Petri Nets

In this paper, the IFTPN grid fault diagnosis model is constructed by the time series similarity matching method, including the intuitionistic fuzzy Petri Nets theory and the time series characteristics of grid component faults. The model focuses on the timing properties of protection\circuit breaker action, in grid faults, and adopts a layered transition model structure, which can be used to visually describe the logical relationship and timing characteristics of protection and circuit breakers.

3.1. IFTPN-Based Modeling Method. According to the relay protection setting rules, the components in the power grid are equipped with corresponding primary protection and backup protection, and different protections are provided for

different components. For example, the protection of the Busbar is composed of primary protection and remote backup protection. The protection of the line and the transformer provides corresponding primary protection, near backup protection, and far backup protection at the sending end and the receiving end.

The IFTPN model is built according to the above rules. When the grid fails, the protection and circuit breakers act in a sequence (main protection, main protection corresponding to the circuit breaker, near backup protection, near backup protection corresponding to the circuit breaker, far backup protection, and remote backup protection corresponding to the circuit breaker) to stop the action until the problem is resolved.

The time stamp of the first piece of alarm information received is used as a reference point. The alarm hypothesis time series is generated according to the component action delay: main protection (10 ms, 20 ms), near backup protection (485 ms, 545 ms), far backup protection (960 ms, 1070 ms), and circuit breaker trip delay (20 ms, 40 ms).

The IFTPN fault diagnosis model for Busbars, transformers, and lines is established, according to the actual grid model, shown in Figure 1. As shown in Appendix A, Figures 5 and 6 are fault diagnosis models for single Busbar A_1 and double Busbar B_2, respectively, and Figure 7 is the model for line L_2. The model structures of the transformer and line are the same; only the protection and circuit breaker components are different. This information is not included here.

To facilitate the description of the algorithm and simplify the reasoning process, the operator is defined as follows:

Suppose A, B, and C make up the $m \times n$ order matrix, D is the $m \times q$ matrix, and E is the $q \times n$ matrix.

(1) Direct multiplication operator $\bullet : C = D \bullet E$, that is, $c_{ij} = a_{ij}b_{ij}$.

(2) Comparison operator $\Theta : C = A\Theta B$; that is, $c_{ij} = (1, 0)$ when $a_{ij} \geq b_{ij}$; otherwise, $c_{ij} = (0, 1)$.

(3) Multiplication operator $\otimes : C = D \otimes E$; then $c_{ij} = \max_{1 \leq k \leq q} (d_{ik}e_{kj})$.

(4) Addition operator $\oplus : C = A \oplus B$; then $c_{ij} = \max(a_{ij}, b_{ij})$.

The components in the grid of this paper adopt the modeling method of hierarchical transition. For the Busbar, the first layer of the model is a submodel of the sending end and receiving end, including two layers of transitions, and the integrated model has one layer of transitions in the second layer. For the line, the first layer of the model includes two transitions in each direction, and the second layer of the model has one transition. When the topology changes, the architecture and operation matrix of the improved model are less adjusted, and the model is more versatile, because it does not need to make any modifications to the model but only update the values of the initial library in the first layer model.

3.2. Algorithm Improvement. The reasoning process of the algorithm described in [13] is complicated, and the number of iteration calculations is too many. Compared with study [13], the algorithm in [11] is optimized, but it is not applied in the process of matrix reasoning. The algorithm is improved in the following ways in this article.

(1) Algorithm Optimization for Certainty

$$\psi_{\mu}^{k} = f_{\psi}\left(O_{n\times 1}^{k} \otimes \psi_{\mu m\times 1}^{k-1}\right) \tag{8}$$

The deterministic value of the interlayer confidence is processed by the Gaussian function, which is applied to the matrix deduction process. $f_{\psi}(x)$ is the Gaussian function [13]:

$$f_{\psi}(x) = e^{-3(x-1)^2} \tag{9}$$

The application of this function can make the calculation results more in line with the characteristics of the fault diagnosis and make the probability of failure more of an ideal value within (0, 1). Assuming that Figure 2 is the Busbar B1 sending end model, place P_1 represents the line main protection, and place P_2 is the protection corresponding to the circuit breaker, if the uploaded protection and circuit breaker action information satisfy the time constraint, the deterministic value of place P_1 is set to 0.8564, and the deterministic value of place P_2 is set to 0.8333. The accumulative determinant value of transition input is 0.8564×0.5+0.8333×0.5=0.8448. After processing using the Gaussian function, the certainty value of place P_5 is $f_{\psi}(0.8448) = 0.93028$, which is significantly higher than the certain degree, before processing. This paper specifies that the transition is triggered by the deterministic value. The corresponding calculation is performed for each transition trigger, until the final vector of the model is obtained.

(2) Algorithm Optimization of Uncertainty

For a faulty component in the system, when the primary protection of the component and the corresponding circuit breaker are rejected, the backup protection of the component will act. The higher the number of protection and circuit breaker actions in the fault propagation direction, the greater the fault probability of the component, and the lower the uncertainty of the corresponding component actions. According to the above situation, the uncertainty value of the terminal place in the direction of the fault propagation is corrected by formula (11) in this paper.

$$\psi_{\gamma}^{k} = \gamma_{\psi}'\left(O_{n\times 1}^{k} \otimes \psi_{\gamma m\times 1}^{k-1}\right) \tag{10}$$

The uncertainty of the terminal place in the component failure propagation direction is set to γ, according to the actual spreading direction of the faulty component, after time series processing. The value of the uncertainty, after correction, is

$$\gamma' = \frac{\gamma}{Num} \tag{11}$$

The algorithm for the entire confidence is described as

$$\psi_{m\times 1}^{k} = \left(\psi_{\mu}^{k}, \psi_{\gamma}^{k}\right) \tag{12}$$

The improved algorithm includes the cumulative calculation of transition input values, threshold comparisons, and vector calculations for the terminal place. The specific confidence reasoning process is as follows.

(1) The initial state is set to $M^0_{n\times1}$. The input intuitionistic fuzzy value of the transition is calculated.

$$\eta^k_{m\times1} = I^T_{n\times m} \bullet M^k_{n\times1} \tag{13}$$

(2) The threshold of the transition is compared with the input intuitionistic fuzzy value of the transition, and then the transition set $\varphi^k_{m\times1}$, capable of triggering the transition, is obtained.

$$\varphi^k_{m\times1} = \eta^k_{m\times1} \Theta F_{m\times1} \tag{14}$$

(3) The input intuitionistic fuzzy value $\psi^k_{m\times1}$, which can trigger the transition based on the obtained set $\varphi^k_{m\times1}$ of the transitions that can be excited, is calculated.

$$\psi^k_{m\times1} = \eta^k_{m\times1} \bullet \varphi^k_{m\times1} \tag{15}$$

(4) The discriminant value $M^{k+1}_{n\times1}$ of the place, obtained by $k+1$ calculations, is calculated.

$$M^{k+1}_{n\times1} = O^k_{n\times1} \otimes \psi^k_{m\times1} \oplus M^k_{n\times1} \tag{16}$$

(5) If $M^{k+1}_{n\times1} = M^k_{n\times1}$, then the confidence matrix of the Petri Nets is stable; that is, the reasoning ends; otherwise, let $k = k+1$ and return to step (4).

3.3. Settings of Simulation Parameters

3.3.1. Identification Value Data. This paper uses the statistical probability data of long-term actual operation, provided by study [24]. The data are weighted by the timing confidence to assign values to the protection place and the circuit breaker place. The following settings are provided for the refusal, misoperation, and unoperated component place of the protection and circuit breakers in the grid.

Definition (μ_1, γ_1) is the identification value when the alarm information exists, and (μ_2, γ_2) is the identification value when the alarm information does not exist, or the protection and the circuit breaker are rejected or misplaced. The relationship is as follows:

$$\mu_2 = \omega \times \mu_1 \tag{17}$$

$$\gamma_2 = \frac{\gamma_1}{\omega} \tag{18}$$

The parameter ω is used to express great uncertainty in action fault events.

3.3.2. Setting the Model Network Parameters. (1) The initial value of the initial component place and virtual place is (0, 1).

(2) The input arc weight is $\omega = (1/N)$, where N is the number of inputs, from place to transition. If the place, connected through the output arc, is the component place, the output arc has an identification value of (0.95, 0.025); if the place, connected by the output arc, is a virtual place, the output arc has an identification value of (1, 0).

(3) Learning from study [24], it must be ensured that the model's fault-tolerant transition threshold is set to a value (0.2, 0.7).

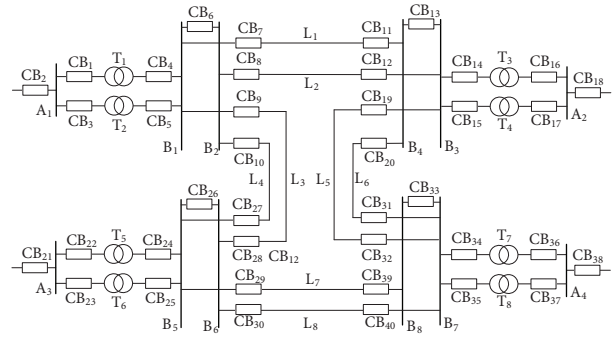

Figure 1: Actual grid model.

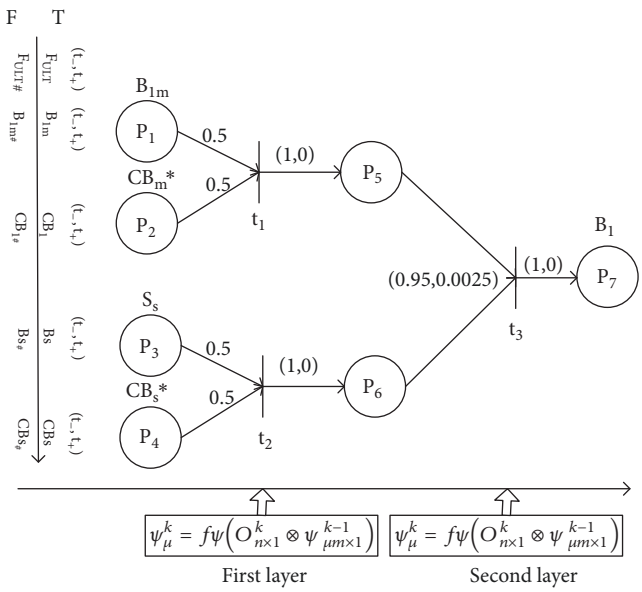

Figure 2: Basic structure diagram of IFTPN.

3.3.3. Fault Degree Parameter Threshold Setting. The metric function of the probability of failure of the device is

$$f(N) = \begin{cases} \dfrac{\mu - \gamma}{\mu}, & \mu > \gamma \\ 0, & \mu < \gamma \end{cases} \tag{19}$$

where N represents the faulty component and (μ, γ) represents the intuitionistic fuzzy identification value of the faulty component. When the metric value $f(N) > \theta$ of the faulty element, it is determined that the component N is faulty, where θ is the threshold for determining whether the component N has a fault. To ensure accurate operation, the degree of uncertainty of the fault should be much greater than the uncertainty, so the value of θ is set to 0.56.

4. IFTPN Troubleshooting Process

According to the fault alarm information, received by the power dispatching center, the fault area of the system is searched, the suspected fault component set is obtained, and

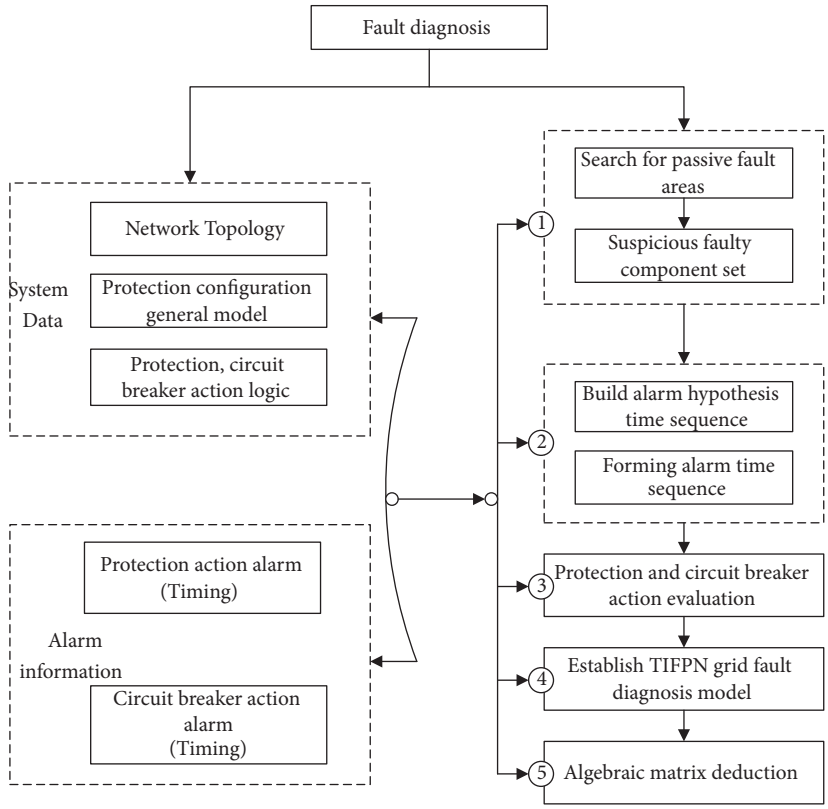

Figure 3: Fault diagnosis model frame structure.

Table 1: Comparison of the fault degree of the two methods in study [20].

Component	Transmission line L_8	Busbar B_7	Transmission line L_6
Weighted fuzzy Petri nets	0.76745	0.82152	0.51649
Time-series weighted fuzzy Petri nets	0.76745	0.79695	0.2
This article	0.96723	0.9975	0.1

Table 2: Comparison of the diagnostic results under the same conditions.

Number	Alarm information	Suspected Faulty device	Fault probability			
			The method of [13]	The method of [23]	The method of [24]	The method of this paper
1	L_{0407Rm}; L_{0407Sm}; CB_{0407}; CB_{0704} act	L_{0407}	0.99	0.8910	0.9968	0.9673
2	L_{0407Rm}; L_{0407Sm}; L_{0807Rs}; L_{0907Rs}; CB_{0407}; CB_{0807}; CB_{0907} act	L_{0407}	0.8798	0.8178	0.9601	0.9640
3	L_{0407Rm}; L_{0407Sm}; CB_{0704} act	L_{0407}	0.5705	0.7143	0.9506	0.9553
4	L_{0407Rm}; CB_{0407}; CB_{0704}; act	L_{0407}	0..6016	0.7125	0.9503	0.9550
5	L_{0407Rm}; L_{0407Sm}; L_{0807Rs}; L_{0907Rs}; CB_{0807}; CB_{0907} act	L_{0407}	0.5012	0.6411	0.9385	0.9412
6	L_{0407Sm} act	L_{0407}	0.4286	0.2688	0.1341	0

Table 3: Comparison of the proposed method and three existing methods for grid fault diagnosis.

Method	Processing of timing information	Consider uncertainty	Modeling form	Performance
Study [20]	Using time series matching method, making full use of time-scale information	No	Timing matching model	The calculation speed is fast but only considers the timing factor; too singular
Study [15]	Timing not considered	No	Fuzzy Petri nets model	High diagnostic efficiency; good fault tolerance; did not consider the impact of timing
Study [24]	Timing not considered	Yes	Intuitionistic Fuzzy Petri Nets Model	Full consideration of the impact of uncertain, incomplete information but does not take timing into account
The method of this paper	Using the time series matching method, making full use of time-scale information	Yes	Intuitionistic Fuzzy Petri Nets Model Based on Time Series Matching	Fully consider the timing information, and uncertain and incomplete information; better fault tolerance; precise fault diagnosis

Table 4: The code of alarm information.

Number	Fault type
a_1	L_2 sending end main protection action
a_2	L_2 receiving end main protection action
a_3	CB_8 trip
a_4	CB_{12} trip
a_5	Failure protection B_3 action
a_6	CB_{13} trip
a_7	T_3 far backup protection action
a_8	T_4 far backup protection action
a_9	L_5 far backup protection action
a_{10}	CB_{15} trip
a_{11}	CB_{14} trip
a_{12}	CB_{32} trip

the IFTPN fault diagnosis model is established. The fault diagnosis process is shown in Figure 3 and is divided into five parts: (1) the search and establishment of fault areas; (2) the similarity matching of the time series; (3) the evaluation of the action for the protection and the action of the circuit breaker; (4) the establishment of the fault diagnosis model; (5) the matrix deduction of fault cases.

The specific steps are as follows.

(1) After the grid fault occurs, according to the data information uploaded to the system, the fault area is first searched, then the suspected fault component is searched, and finally the suspicious fault component set is constructed.

(2) According to the principle of relay protection setting, a protection model is constructed for the protection device of the suspected faulty component to form a set of alarm hypothesis time series.

(3) The distance (Edit Distance and DTW Distance) between each time subsequence in the alarm hypothesis time series set and the alarm information sequence, received by the system center, are calculated by timing matching.

(4) The confidence level of the component protection action value is obtained by timing matching, and the state of the protection device that does not meet the time series matching is evaluated, including the action state of the protection and circuit breaker (rejection, misoperation, and information loss) and the time-scale accuracy of the alarm information (time-scale deviation and timing chaos).

(5) The IFTPN grid fault diagnosis model is established. The probability value of the initial library is corrected by the confidence of the protection and circuit breaker action. The inference algorithm is formed according to the intuitionistic fuzzy Petri Nets model, and the forward deduction is performed in the form of a matrix. Then, the fault probability value of the component is obtained.

5. Case Simulation

5.1. Case 1. In order to describe the entire reasoning process, the number of pieces of fault information is shown in Table 4, and the alarm information, with time stamps, is shown in Table 5. The sequence based on the case failure alert information is $X = \{x_1, x_2, x_3, \ldots, x_{11}\}$.

(1) Lines L_2, L_5, and Busbar B_3 search for the fault area according to the alarm information sequence to determine possible faulty elements.

(2) Since the information cannot be uploaded when the line, Busbar, and circuit breaker are faulty, the corresponding time-scale information is defined as a fuzzy item. According to the general model of the protection configuration, the time series inference rules and the time series of the alarm

Table 5: Actual alarm information.

Time series set	Alert message content	Time series number
(a_1, 0,1), 435)	L_2 sending end main protection action	x_1
(a_2, 0,1), 436)	L_2 receiving end main protection action	x_2
(a_3, 0,1), 460)	CB_8 trip	x_3
(a_5, 0,1), 740)	Failure protection B_3 action	x_4
(a_6, 0,1), 766)	CB_{13} trip	x_5
(a_7, 0,1), 936)	T_3 far backup protection action	x_6
(a_8, 0,1), 937)	T_4 far backup protection action	x_7
(a_9, 0,1), 938)	L_5 far backup protection action	x_8
(a_{10}, 0,1), 961)	CB_{15} trip	x_9
(a_{11}, 0,1), 963)	CB_{14} trip	x_{10}
(a_{12}, 0,1), 973)	CB_{32} trip	x_{11}

Table 6: Failure collection.

Transmission line L_2	{{a_1, a_3}, {a_2, a_4, a_5, a_6}, {a_2, a_4, a_5, a_8, a_{10}}, {a_2, a_4, a_5, a_7, a_{11}}, {a_2, a_4, a_5, a_9, a_{12}}}
Transmission line L_5	{a_{12}}
Busbar B_3	{a_5, a_6}

information, a time series hypothesis set for the failed component, and the values of a and b are both 5. The fault set of Busbar B_3 and lines L_2, L_5 is shown in Table 6.

(3) In the case of complex faults, the protection and circuit breaker only act in response to one faulty component. In this case, the fault set of line L_2 covers the fault set of line L_5 and Busbar B_3, and then the fault analysis of line L_2 is prioritized. The initial place reliability of the circuit breakers of the line L_5 protection configuration, of the protection of the Busbar B_3, and of the circuit breakers corresponding to the Busbar B_3 protection is corrected to (0.19666, 0.03147), (0.17128, 0.0579), and (0.16666, 0.04825), respectively.

(4) Taking line L_2 as an example, the time series confidence of the faulty component is calculated, as shown in Table 7, and it is used to correct the value of the initial place. Through the analysis of the time series, CB_{12} is refused. The maximum six propagation directions for the fault of line L_2 are (B_3, CB_{13}), (T_3, CB_{14}), (T_4, CB_{15}), (L_5, CB_{32}), (B_2, CB_6), and (L_4, CB_{27}).

According to the alarm information, four determined fault propagation directions are obtained and modeled separately. The intuitive fuzzy Petri Nets fault diagnosis model for line L_2 is shown in Figure 7. Taking the receiving end of line L_2 as an example in the direction of L_5 propagation, matrix reasoning is performed on the fault confidence of line L_2.

(1) Input Matrix I with Weights

$$I = \begin{bmatrix} 0.5 & 0.5 & 0 & 0 & 0 & 0 & 0 & 0 & 0 & 0 \\ 0 & 0 & 0.5 & 0.5 & 0 & 0 & 0 & 0 & 0 & 0 \\ 0 & 0 & 0 & 0 & 0.5 & 0.5 & 0 & 0 & 0 & 0 \\ 0 & 0 & 0 & 0 & 0 & 0 & 1 & 0 & 0 & 0 \\ 0 & 0 & 0 & 0 & 0 & 0 & 0 & 1 & 0 & 0 \\ 0 & 0 & 0 & 0 & 0 & 0 & 0 & 0 & 1 & 0 \end{bmatrix} \tag{20}$$

(2) Output Matrix O with Confidence

$$O = \begin{bmatrix} (0,1) & (0,1) & (0,1) & (0,1) & (0,1) & (0,1) & (1,0) & (0,1) & (0,1) & (0,1) \\ (0,1) & (0,1) & (0,1) & (0,1) & (0,1) & (0,1) & (0,1) & (1,0) & (0,1) & (0,1) \\ (0,1) & (0,1) & (0,1) & (0,1) & (0,1) & (0,1) & (0,1) & (0,1) & (1,0) & (0,1) \\ (0,1) & (0,1) & (0,1) & (0,1) & (0,1) & (0,1) & (0,1) & (0,1) & (0,1) & (0.95,0.025) \\ (0,1) & (0,1) & (0,1) & (0,1) & (0,1) & (0,1) & (0,1) & (0,1) & (0,1) & (0.95,0.025) \\ (0,1) & (0,1) & (0,1) & (0,1) & (0,1) & (0,1) & (0,1) & (0,1) & (0,1) & (0.95,0.025) \end{bmatrix} \tag{21}$$

(3) Transition Threshold Matrix

$$\Gamma = [(0.2,0.7),(0.2,0.7),(0.2,0.7),(0.2,0.7),(0.2,0.7),(0.2,0.7)] \tag{22}$$

(4) The Fuzzy Value Matrix of the Initial Place

$$M_0 = [(0.9913,0.006294),(0.19666,0.03094),(0.7930,0.007868),(0.16716,0.0364),$$

Table 7: The calculation of time series confidence.

Alarm hypothesis time series	ED	TD	TOD	TSC
$\{((a_1, 10, 1), 435), ((a_3, 10, 1), 460)\}$	0	0	0	1
$\{((a_2, 10, 1), 436), ((a_4, 10, 1), 461)\}$	1	0	5	0.2
$\{((a_2, 10, 1), 436), ((a_4, 10, 0), 461), ((a_5, 10, 1), 740), ((a_6, 0, 1), 765)\}$	0	0	0	1
$\{((a_2, 10, 1), 436), ((a_4, 10, 0), 461), ((a_5, 10, 1), 740), ((a_7, 0, 1), 936), ((a_{11}, 0, 1), 961)\}$	0	0	0	1
$\{((a_2, 10,1), 436), ((a_4, 10,0), 461), ((a_5, 10,1), 740), ((a_8, 10,1), 937), ((a_{10}, 0,1), 962)\}$	0	0	0	1
$\{((a_2, 10,1), 436), ((a_4, 10,0), 461), ((a_5, 10,1), 691), ((a_9, 10,1), 938), ((a_{12}, 10,1), 963)\}$	0	0	0	1

ED: Edit Distance; TD: DTW Distance; TOD: total distance;
TSC: time series confidence.

$$(0.6939, 0.008991), (0.7375, 0.008251), (0, 1), (0, 1), (0, 1), (0, 1)] \quad (23)$$

Derived by algorithm,

$$\begin{aligned} M_1 &= [(0.9913, 0.006294), (0.19666, 0.03094), (0.7930, 0.007868), (0.16716, 0.0364), \\ &\quad (0.6939, 0.008991)\ (0.7375, 0.008251), (0.59398, 0.018617), (0.48008, 0.022134), (0.7157, 0.008621), (0, 1)] \\ M_2 &= [(0.9913, 0.006294), (0.19666, 0.03094), (0.7930, 0.007868), (0.16716, 0.0364), (0.6939, 0.008991), \\ &\quad (0.7375, 0.008251), (0.59398, 0.018617), (0.48008, 0.022134), (0.7157, 0.008621), (0.7454, 0.008351)] \\ M_3 &= [(0.9913, 0.006294), (0.19666, 0.03094), (0.7930, 0.007868), (0.16716, 0.0364), (0.6939, 0.008991), \\ &\quad (0.7375, 0.008251), (0.59398, 0.018617), (0.48008, 0.022134), (0.7157, 0.008621), (0.7454, 0.008351)] \end{aligned} \quad (24)$$

When $M_3 = M_2$, the inference calculation ends. The value of the fuzzy confidence of line L_2 in the direction in which line L_5 propagates is (0.7454, 0.008351); that is, the degree of certainty of line L_2 in the direction in which line L_5 propagates is 0.7454, and the degree of uncertainty is 0.008351. According to the metric function formula, the fault probability of line L_2 is $F(L_{2t5}) = 0.9888$. Similarly, the probability of failure in other propagation directions is $F(L_{2t3}) = 0.9882$, $F(L_{2t4}) = 0.9882$, and $F(L_{2B3}) = 0.9869$.

A comparison curve, before and after data optimization, is shown in Figure 4.

Figure 4 shows a comparison of raw data values and optimized values between 0 and 1. If the certainty of the fault value is in (0.078135, 1), it will be optimized. Conversely, if it is in (0, 0.078135), no processing will be done. Taking the data point 0.561146 as the fault distinguishing point, it can be clearly seen from the Figure 4 that the fault discrimination degree of the data after optimization is significantly higher than the raw data. In Figure 4, the intersections of the four lines perpendicular to the x-axis and the two curves are a comparison of the raw data and the optimized data in Case 1. From the comparison results of each set of data in the figure, the method can improve the accuracy of the fault diagnosis results in line with expectations. In the direction of the sending end, the fault confidence of line L_2 is $F(L_{2CB_8}) = 0.96725$.

In summary, the final failure probability value of line L_2 is $F(L_2) = 0.9776$, and it is determined, by $F(L_2) > \theta$, that L_2 is the faulty item.

5.2. Case 2. In order to describe the entire reasoning process, the number of pieces of fault information is shown in Table 8, and the alarm information, with time stamps, is shown in Table 9. The sequence based on the case failure alert information is $X = \{x_1, x_2, x_3, \ldots, x_{10}\}$.

(1) Searching for the fault area, based on the alarm information received after the fault occurs, the suspect faulty component is determined as line L_8, Busbar B_7, and line L_6.

(2) According to the general protection configuration model and the timing matching rule, the alarm hypothesis time series is generated for the protection of each suspicious component and the corresponding circuit breaker. The

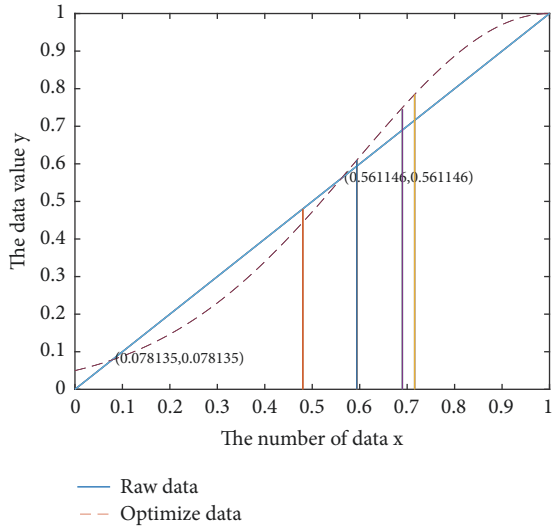

Figure 4: Data optimization comparison curve.

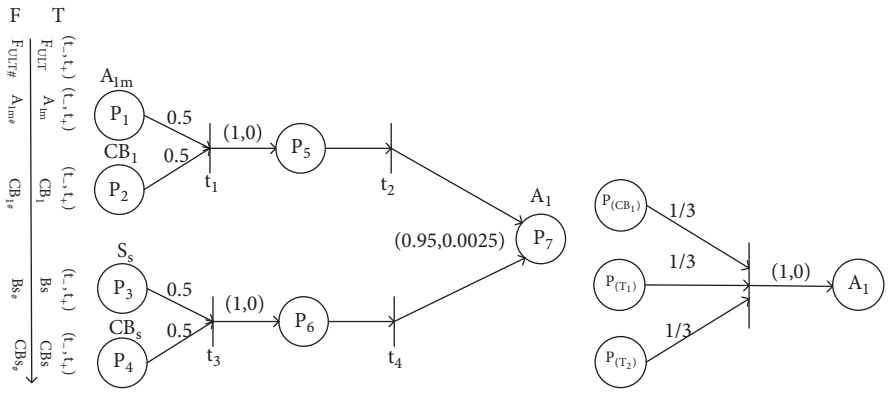

(a) Universal subnet diagnostic model

(b) Comprehensive diagnostic model

Figure 5: Single bus B_1 fault diagnosis model.

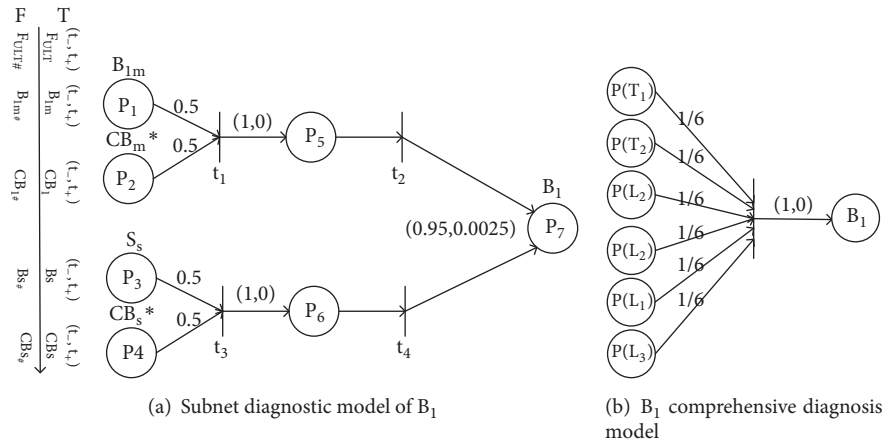

(a) Subnet diagnostic model of B_1

(b) B_1 comprehensive diagnosis model

Figure 6: Double bus B_1 fault diagnosis model.

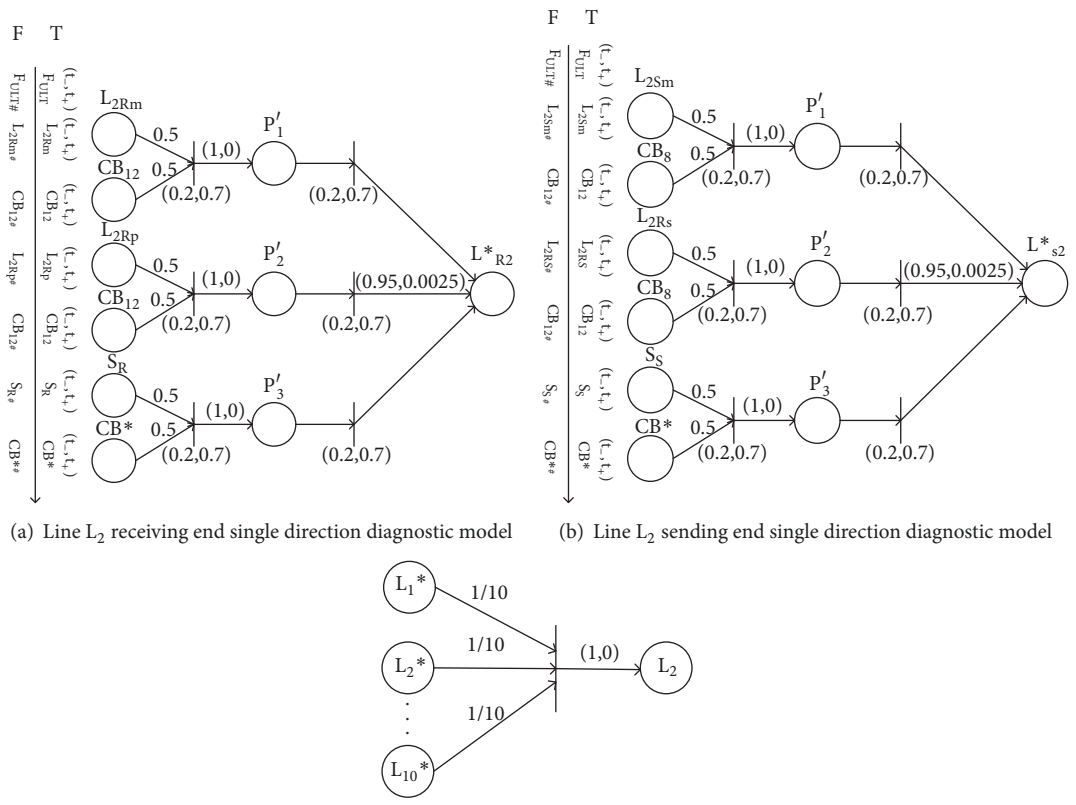

(a) Line L_2 receiving end single direction diagnostic model

(b) Line L_2 sending end single direction diagnostic model

(c) Second layer diagnostic model

Figure 7: Line L_2 fault comprehensive diagnosis model.

components related to line L_8 are L_8 sending end main protection, CB_{30} circuit breaker, and CB_{40} circuit breaker. The components related to Busbar B_7 are B_7 main protection, CB_{34} circuit breaker, CB_{35} circuit breaker, CB_{33} circuit breaker, L_6 transmission end remote backup protection, and CB_{20} circuit breaker. The components related to line L_6 are L_6 sending end remote backup protection and CB_{20} circuit breaker. The hypothetical time series of the corresponding suspicious elements can be constructed according to the fault set in Table 10.

(3) The distance between the hypothesis time and the actual alarm time series of all fault sets of line L_6, line L_8, and Busbar B_7 are calculated and then converted into timing confidence, wherein the default value of parameters a and b is 5. Table 11 is the total distance and the timing confidence after correction, and the reason for the correction is described in step (4).

(4) The time series confidence is calculated according to (4), as shown in Table 11. The probability values of the initial library are weighted using time series confidence. According to the timing matching, the main protection of the line L_8 transmitter is matched with the CB_{30} circuit breaker. The B_7 main protection is matched with the CB_{34} circuit breaker, CB_{35} circuit breaker, and CB_{33} circuit breaker and is matched with the line L_6 sending end backup protection and CB_{20} circuit breaker. The terminal primary protection information of line L_8 is missing, because the CB_{40} circuit breaker trip does not satisfy the time-scale matching of the fault set of Busbar B_7 but matches the time-scale of the line L_8 receiving end main protection. Therefore, it is determined that the information of the primary protection of the receiving end of L_8 is lost. The circuit breaker CB_{31} of the main protection of Busbar B_7 refuses to operate, and the far-end backup operation of line L_6 causes the CB_{20} circuit breaker to trip, which satisfies the timing matching of Busbar B_7 in the line L_6 fault propagation direction.

Table 8: The code of alarm information.

Number	Fault type
a_1	L_8 sending end main protection action
a_2	CB_{30} trip
a_3	CB_{40} trip
a_4	B_7 main protection action
a_5	CB_{34} trip
a_6	CB_{35} trip
a_7	CB_{33} trip
a_8	L_6 send end far backup action
a_9	CB_{20} trip
a_{10}	CB_{29} trip
a_{11}	L_8 receiving end main protection
a_{12}	CB_{31} trip

Table 9: Actual alarm information.

Time series set	Alert message content	Time series number
$((a_1, 0,1), 05: 315)$	L_8 sending end main protection action	x_1
$((a_2, 0,1), 05:344)$	CB_{30} trip	x_2
$((a_3, 0,1), 05:345)$	CB_{40} trip	x_3
$((a_4, 0,1), 06:315)$	B_7 main protection action	x_4
$((a_5, 0,1), 06:343)$	CB_{34} trip	x_5
$((a_6, 0,1), 05:327)$	CB_{35} trip	x_6
$((a_7, 0,1), 06:352)$	CB_{33} trip	x_7
$((a_8, 0,1), 06:824)$	L_6 send end far backup action	x_8
$((a_9, 0,1), 06:846)$	CB_{20} trip	x_9
$((a_{10}, 0,1), 08:100)$	CB_{29} trip	x_{10}

Table 10: Failure collection.

Transmission line L_8	$(\{\{((a_1, 10, 1), 05 : 315)\}, \{((a_2, 10, 1), 05 : 344)\}, \{((a_{11}, 10, 0), 05 : 315)\}, \{((a_3, 10, 1), 05 : 345)\}\})$
Busbar B_7	$(((a_4, 10, 1), 06 : 315), \{\{\{((a_5, 10, 1), 06 : 343)\}, \{((a_6, 10, 1), 05 : 327)\}, \{((a_7, 10, 1), 06 : 352)\}, \{((a_3, 0, 1), 05 : 345)\}\}, \{\{((a_{12}, 10, 0), 06 : 344)\}, \{((a_8, 10, 0), 06 : 824)\}, \{((a_9, 10, 0), 06 : 846)\}\}\})$
Transmission line L_6	$\{((a_8, 0, 1), 06 : 824)\}, \{((a_9, 0, 1), 06 : 846)\}$

Table 11: The calculation of time series confidence.

Alarm hypothesis time series		ED	TD	TOD	TSC
$\{((a_1, 10, 1), 05 : 315), ((a_2, 10, 1), 05 : 344)\}$	L_8	0	0	0	1
$\{((a_{11}, 10, 0), 05 : 315), ((a_3, 10, 1), 05 : 345)\}$		1	0	5	0.2
$\{((a_4, 10, 1), 06 : 315), ((a_5, 10, 1), 06 : 343)\}$	B_7	0	0	0	1
$\{((a_4, 10, 1), 06 : 315), ((a_6, 10, 1), 05 : 327)\}$		0	1	1	1
$\{((a_4, 10, 1), 06 : 315), ((a_7, 10, 1), 06 : 352)\}$		0	0	0	1
$\{((a_4, 10, 1), 06 : 315), ((a_3, 0, 1), 05 : 345)\}$		0	1	1	1
$\{((a_4, 10, 1), 06 : 315), ((a_{12}, 10, 0), 06 : 344)\}$		1	0	5	0.2
$\{((a_4, 10, 1), 06 : 315)\ ((a_8, 10, 0), 06 : 824)\}, \{((a_9, 10, 0), 06 : 846)\}$		0	0	0	1
$\{((a_8, 0, 1), 06 : 824)\}, \{((a_9, 0, 1), 06 : 846)\}$	L_6	1	1	10	0.1

ED: Edit Distance; TD: DTW Distance; TOD: total distance; TSC: time series confidence.

The circuit breaker CB_{29} has no relevant components to form a sequence with it, and the difference between the time stamps of other components is large, so CB_{29} is judged to be malfunctioning.

The CB_{40} circuit breaker exists in both the fault set of line L_8 and the fault set of Busbar B_7. Since CB_{40} satisfies the protection action time sequence of line L_8 and operates accurately, the CB_{40} circuit breaker should be within the fault set of line L_8. According to the fault sets of Busbar B_7, the CB_{35} circuit breaker should act on the fault of Busbar B_7, and the circuit breaker CB_{35} also does not satisfy the fault sets of other components. Thus, the error of the CB_{35} circuit breaker time mark in the Busbar B_7 fault sets can be judged. Therefore, the weights of the time distances of the CB_{40} circuit breaker and the CB_{35} circuit breaker in the Busbar B_7 fault sets should be corrected. In (4), the weights a and b are corrected to $a = 9$ and $b = 1$. The total distance of Busbar protection in this direction is 1. The initial probability values of the protection and circuit breakers are corrected using the time series confidence obtained.

Line L_6 does not satisfy the timing matching, and the failure probability can be directly considered as time series confidence P (L_6) =0.1.

(5) According to the IFTPN model inference algorithm, the confidence degree of the final line can be obtained. The fault of line L_8 is P (L_8) =0.96723, and the probability of the failure of Busbar B_7 is P (B_7) =0.9975.

The obtained data results are compared with study [24] in relation to the same faulty case. As shown in Table 1, the failure probability value of the component that should be faulted is significantly increased, and the failure probability value of the nonfaulty component is significantly reduced.

According to the reasoning process and the comparison in Table 1, the IFTPN grid fault diagnosis model, established in this paper, can accurately solve many complicated situations, such as timing chaos, protection, circuit breaker refusal, misoperation, and information loss. The results show that the probability of the failure of the same component is more accurate under the same fault condition (the failure probability of the faulty component is greater, and the probability of the failure of the nonfaulty component is smaller).

The fault diagnosis results, obtained by the method presented in this paper, through line L_{0407} in study [27], are shown in Table 2. Compared to the original method, the method proposed in this paper effectively improves the accuracy of fault diagnosis. A comparison of the grid fault diagnosis method, proposed in this paper, and the other three grid fault diagnosis methods is shown in Table 3. The proposed method has a better fault tolerance performance, higher accuracy of diagnosis results, and faster diagnosis speed.

6. Conclusion

(1) For uncertain and incomplete information in power grids, we propose the IFTPN fault diagnosis model in this paper. The influence of the combination of the intuitionistic fuzzy algorithm and Petri Nets on the fault diagnosis results is explored. The results show that the model can still make a rapid and effective diagnosis of power system faults, when the information is incomplete.

(2) In order to make full use of the alarm information, we introduce the concept of timing matching into the

intuitionistic fuzzy Petri Nets for grid fault diagnosis. The initial place data are corrected by timing confidence, and the case deduction shows that the diagnosis results are more accurate.

(3) In this paper, the degrees of certainty and uncertainty in the intuitionistic fuzzy algorithm are separately optimized in the calculation process. The optimization curve shows that the method improves the accuracy and reliability of fault diagnosis. In future work, we will research the electrical quantity itself and the effect of the time-constrained relationship between electrical quantity and component action on the diagnostic results.

Appendix

A.

(1) The IFTPN fault diagnosis model of the single Busbar A_1 is shown in Figure 5, and (a) is the subnet diagnostic model and (b) is the comprehensive diagnostic model. The sequence is $\{(A_{1m}, CB_1, Ss, CB_1); (A_{1m}, CB_2, T_{1s}, CB_2); (A_{1m}, CB_3, T_{2s}, CB_3)\}$.

(2) IFTPN fault diagnosis model of double Busbar B_1 is shown in Figure 6, and (a) is the subnet diagnosis model and (b) is the comprehensive diagnosis model. The sequence is $\{(B_{1m}, CB_4, T_{1s}, CB_4); (B_{1m}, CB_5, T_{2s}, CB_5); (B_{1m}, CB_6, L_{2Rs}, CB_{12}); (B_{1m}, CB_6, L_{4Rs}, CB_{27}); (B_{1m}, CB_7, L_{1Rs}, CB_{11}); (B_{1m}, CB_9, L_{3Rs}, CB_{28})$.

(3) The IFTPN fault diagnosis model of line L2 is shown in Figure 7, and (a) and (b) are the diagnostic model for the terminal network and (c) is the comprehensive diagnosis model. The sequence is $\{(\{\{L_{2Sm}, CB_8, L_{2Sr}, CB_8\}, \{T_{1s}, CB_4\}, \{T_{2s}, CB_5\}, \{L3_{Rs}, CB_{28}\}, \{L_{1Rs}, CB_{11}\}, \{L_{4Rs}, CB_{27}\}\}); (\{\{L_{2Rm}, CB_{12}, L2_{Rr}, CB_{12}\}, \{T_{3s}, CB_{14}\}, \{T_{4s}, CB_{15}\}, \{L_{5Rs}, CB32\}, \{L_{1Ss}, CB_7\}, \{L_{6Rs}, CB_{31}\}\})\}$.

B.

See Tables 4, 5, 6, 7, 8, 9, 10, and 11.

Data Availability

The data used to support the findings of this study are available from the corresponding author upon request.

Conflicts of Interest

The authors declare that there are no conflicts of interest.

Acknowledgments

The Project was supported by the National Natural Science Foundation of China Program (no. 61503224), Shandong Natural Science Foundation of China (no. ZR2017MF048), Major Research Development Program of Shandong province of China (no. 2016GSF117009), and Qingdao Minsheng Science and Technology Plan Project (no. 17-3-3-88-Nash).

References

[1] F. Cheng, L. Qu, W. Qiao, C. Wei, and L. Hao, "Fault diagnosis of wind turbine gearboxes based on DFIG stator current envelope analysis," *IEEE Transactions on Sustainable Energy*, pp. 1-1, 2018.

[2] X. Bai, L. Qu, and W. Qiao, "Robust AC optimal power flow for power networks with wind power generation," *IEEE Transactions on Power Systems*, vol. 31, no. 5, pp. 4163-4164, 2016.

[3] R. Jia, F. Ma, J. Dang, G. Liu, and H. Zhang, "Research on multidomain fault diagnosis of large wind turbines under complex environment," *Complexity*, 2018.

[4] D. Ma, Y. Liang, X. Zhao, R. Guan, and X. Shi, "Multi-BP expert system for fault diagnosis of powersystem," *Engineering Applications of Artificial Intelligence*, vol. 26, no. 3, pp. 937–944, 2013.

[5] S. Chen, J. Xie, G. Bi, J. Zhang, W. Zhang, and C. Gao, "A novel two terminal fault location method used ANN for UHVDC transmission line," *Transactions of China Electrotechnical Society*, vol. 30, no. 4, pp. 257–264, 2015.

[6] A. F. Novelo, E. Q. Cucarella, E. G. Moreno, and F. M. Anglada, "Fault diagnosis of electric transmission lines using modular neural networks," *IEEE Latin America Transactions*, vol. 14, no. 8, pp. 3663–3668, 2016.

[7] M. Eliassi, A. K. Dashtaki, H. Seifi, M.-R. Haghifam, and C. Singh, "Application of Bayesian networks in composite power system reliability assessment and reliability-based analysis," *IET Generation, Transmission & Distribution*, vol. 9, no. 13, pp. 1755–1764, 2015.

[8] X. Luo and X. Tong, "Structure-variable bayesian network for power system fault diagnosis considering credibility," *Power System Technology*, vol. 39, no. 9, pp. 2658–2664, 2015.

[9] R. Ghimire, C. Zhang, and K. R. Pattipati, "A Rough set-theory-based fault-diagnosis method for an electric power-steering system," *IEEE/ASME Transactions on Mechatronics*, vol. 23, no. 5, pp. 2042–2053, 2018.

[10] X. Cheng, C. Wang, Y. Yu, L. Yi, and Q. Chen, "An approach for three-phase asynchronous motor failure analysis based on fuzzy fault Petri nets," *Diangong Jishu Xuebao/Transactions of China Electrotechnical Society*, vol. 30, no. 17, pp. 132–139, 2015.

[11] X. Cheng, Q. Chen, Y. Yu, C. Wang, and J. Liu, "A fault diagnosis approach of power networks based on maximum likelihood decoding petri net models," *Diangong Jishu Xuebao/Transactions of China Electrotechnical Society*, vol. 30, no. 15, pp. 46–52, 2015.

[12] L. Wang, Q. Chen, Z. Gao et al., "Knowledge representation and general Petri net models for power grid fault diagnosis, in IET generation," *Transmission & Distribution*, vol. 9, no. 9, pp. 866–873, 2015 (Arabic).

[13] J. Sun, S.-Y. Qin, and Y.-H. Song, "Fault diagnosis of electric power systems based on fuzzy Petri nets," *IEEE Transactions on Power Systems*, vol. 19, no. 4, pp. 2053–2059, 2004.

[14] Y. N. Wang, J. F. Ye, G. J. Xu, Q. M. Chen, H. Y. Li, and X. R. Liu, "Novel hierarchical fault diagnosis approach for smart power grid with information fusion of multi-data resources based on fuzzy petri net," in *Proceedings of the 2014 IEEE International Conference on Fuzzy Systems (FUZZ-IEEE '14)*, pp. 1183–1189, July 2014.

[15] Q. Chen, X. Cheng, J. Liu et al., "Failure analysis of WFPN network based on hierarchical transition," *Transactions of China Electrotechnical Society*, vol. 31, no. 15, pp. 125–135, 2016.

[16] J. Yang and Z. He, "Power system fault diagnosis approach based on time sequence fuzzy Petri net," *Dianli Xitong*

Zidonghua/Automation of Electric Power Systems, vol. 35, no. 15, pp. 46–51, 2011.

[17] X. Cheng, X. Lin, C. Zhu, Q. Chen, and M. Cao, "A Method for fault diagnosis of fuzzy petri nets based on time series information," *Transactions of China Electrotechnical Society*, vol. 32, no. 14, pp. 229–237, 2017.

[18] W. Wu, F. Wen, Y. Xue et al., "A weighted fuzzy Petri nets based model with time-delay constraints for power system fault diagnosis employing Information from multiple sources," in *Automation of Electric Power Systems*, vol. 37, pp. 43–45, 2013.

[19] J. Li, X. Zhu, and X. Cheng, "Sensor fault diagnosis based on fuzzy neural petri net," *Complexity*, vol. 2018, Article ID 8261549, 11 pages, 2018.

[20] J. Zhong, Y. Zhang, F. Wen, and H. Zhu, "Transmission system fault diagnosis method based on time series similarity matching," in *Automation of Electric Power Systems*, vol. 39, pp. 60–67, 2015.

[21] J. Antucheviciene, M. Tavana, M. Nilashi, and R. Bausys, "Managing information uncertainty and complexity in decision-making," *Complexity*, Article ID 1268980, 3 pages, 2017.

[22] L. Zhihan, O. Kaoru, L. Jaime, X. Wei, and B. Paolo, "Complexity problems handled by big data technology," *Complexity*, Article ID 9090528, 7 pages, 2019.

[23] J. Yang, Z. He, and T. Zang, "Power system fault-diagnosis method based on directional weighted fuzzy petri nets," in *Proceedings of the CSEE*, vol. 30, pp. 42–49, 2010.

[24] X. Zhang, S. Yue, and X. Zha, "Method of power grid fault diagnosis using intuitionistic fuzzy Petri nets," *IET Generation, Transmission & Distribution*, vol. 12, no. 2, pp. 295–302, 2018.

[25] H.-C. Liu, J.-X. You, X.-Y. You, and Q. Su, "Fuzzy petri nets using intuitionistic fuzzy sets and ordered weighted averaging operators," *IEEE Transactions on Cybernetics*, vol. 46, no. 8, pp. 1839–1850, 2016.

[26] Z. Ai, Z. Xu, and Q. Lei, "Fundamental properties with respect to the completeness of intuitionistic fuzzy partially ordered set," *IEEE Transactions on Fuzzy Systems*, vol. 25, no. 6, pp. 1741–1751, 2017.

[27] J. Chen, *Research on Fault Diagnosis of Power System Uncertainty Based on Information Fusion*, Southwest Jiaotong University, Chengdu, Sichuan, China, 2014.

Hindawi
Complexity
Volume 2019, Article ID 4949265, 10 pages
https://doi.org/10.1155/2019/4949265

Research Article

Neural Network Identification and Sliding Mode Control for Hysteresis Nonlinear System with Backlash-Like Model

Ruiguo Liu and Xuehui Gao

Department of Mechanical and Electrical Engineering, Shandong University of Science and Technology, Tai'an 271019, China

Correspondence should be addressed to Xuehui Gao; xhgao@163.com

Received 14 March 2019; Revised 22 May 2019; Accepted 26 June 2019; Published 16 July 2019

Guest Editor: Jianwu Zeng

A new neural network sliding mode control (NNSMC) is proposed for backlash-like hysteresis nonlinear system in this paper. Firstly, only one neural network is designed to estimate the unknown system states and hysteresis section instead of multiscale neural network at former researches since that can save computation and simplify the controller design. Secondly, a new NNSMC is proposed for the hysteresis nonlinearity where it does not need tracking error transformation. Finally, the Lyapunov functions are adopted to guarantee the stabilities of the identification and control strategies semiglobally uniformly ultimately bounded (UUB). Two cases simulations are proved the effectiveness of the presented identification approach and the performance of the NNSMC.

1. Introduction

Many systems make hysteresis nonlinearities such as power systems, motor systems, and intelligent material systems. In some systems, the hysteresis can be applied to solve some problem. For example, some waveform generator systems utilized hysteresis to produce the designed waveform. But in most systems, the existence of the hysteresis nonlinearities will degrade the performance of the system and even lead to unstabilized in severe case. Therefore, the hysteresis investigations attract attention and also have many results for either system.

Due to the conflict of the fast development of economic and fossil energy lacking and pollution, it is inevitable to develop clean reproducible energy. Then, the new energy systems become more important and attract more attention than before. For example, the new energy vehicles will become the mainstream of the vehicle investigation and will occupy large scale market. But in most new energy systems, the existence of the hysteresis hinders the research progress and affects the improvement of the new energy application. Therefore, to investigate the hysteresis nonlinearity has important significance for new energy systems.

The hysteresis models have been investigated for many years. There are four familiar hysteresis models which are Preisach model, Prandtl-Ishlinskii (P-I) model, Bouc-Wen model, and backlash-like model. These hysteresis models are all mathematical models that have more extensive application compared with the physical models such as Jiles-Atherton's (J-A) model. The Preisach model is the premier mathematical hysteresis model to deal with the magnetic systems firstly, but now it has a broader application for most hysteresis systems. We [1] proposed a novel identification to estimate the discrete Preisach model, where the new approach utilized the lower triangular matrix calculating the Preisach density function. The proposed identification could save computation and deduce complexity contrasting with the classic identification. We also investigated the Bouc-Wen hysteresis model of motor systems in [2]. The hysteresis motor servo system with Bouc-Wen model firstly was transformed into a canonical state space form, then, a high-order neural network observer (HONN) was proposed and a filter for the tracking errors was adopted to simplify the controller design. Different from [2], we researched a backlash-like hysteresis system in [3]. A new Multiscale Chebyshev Neural Network (MCNN) was proposed to estimate the unknown system parameters and hysteresis section. Then the vector error was transformed into scalar error simplifying the controller and the stability of the closed system was guaranteed by Lyapunov function. In [3], two Chebyshev NN were applied to estimate the unknown

states and hysteresis sections, respectively, and the tracking error was transformed to simplify the adaptive controller design. Nevertheless, we continue to investigate the backlash-like hysteresis model in this paper since it is fewer parameters and has analytical solution, but we will propose new NN and no longer use adaptive controller designing the controller for hysteresis systems.

Neural network is an important intelligent approach for identification and control systems [4–8]. Different NN structure was proposed and applied for different systems. A high-order neural network (HONN) was utilized to identification and control nonlinear system in [9, 10]. A multitime-scale recurrent high-order neural networks (MSRHONN) was proposed in [10] for singularly perturbed systems by the optimal bounded ellipsoid algorithm. The new approach could achieve faster convergence and the controller structure was simplified. In [3], the Multiscale Chebyshev Neural Network (MCNN) was presented to identification the hysteresis nonlinear systems. As an important intelligent method, The NN will be attended broader.

Different from adaptive control [11, 12], sliding mode control (SMC) [13] draws more attention in recent years. In some circuit, the hysteresis was utilized by the overshoot of the output voltage response. Literature [13] took advantage of the inherently variable-structure of the DC-DC system to design a modified sliding mode control regulating the DC hysteresis circuit system. The fuzzy adaptive Proportional-Integral-Derivative (PID) SMC was proposed for hysteresis piezoactuated nanopositioning stage in [14]. Meanwhile, we also proposed SMC to control the hysteresis motor servo system with discrete Preisach model in [1]. A composite control consisting of discrete inverse model-based controller (DIMBC) and discrete adaptive sliding mode controller (DASMC) was presented for discrete hysteresis systems which could accelerate the reaching time and enhance the robustness of the controller. In this paper, we further utilize the SMC to deal with a continuous hysteresis system with Baclash-Like system. Since the existing of the chattering in SMC, the control performance will be degraded. If not handling it, when the chattering is serious, that will damage the equipment in real system. Several approaches can restrain the chattering. We have investigated the influence and the restrained method of the chattering in [1]. Then, in this paper, we adopt tanh(·) function replacing the sign(·) function; for the tanh(·) function is a continuous function, and it can well restrain the chattering of the SMC.

This research is a further investigation based on [3]. But it has three points different from [3]. First is one new NN designed to estimate the unknown states and hysteresis sections in this research which is different from two Multiscale Chebyshev Neural Networks (MSCNN) in [3] since the new design will simplify the controller and reduce the computation. We adopt one NN in this research because almost new energy systems only have one time scale, it does not need multiscale NN structure. But beyond that, the investigations of new energy system with NN controller are not common yet, one scale NN controller is researching, and multiscale NN will be investigate as well as other systems. Second is no tracking error transformation in this paper since the tracking error transformation in [3] could lead to the decline control performance. In this research, we transform the system into canonical form to avoid the complicated computation of controller design such as back-stepping. Since the system is converted, the tracking error transformation is not necessary to simplify the computation. After all, the tracking error transformation is exactly save the calculation but can degrade the control precision. Finally, in this paper, we design a sliding mode control (SMC) instead of the adaptive control in [3]. The SMC controller has more strong robustness which can preferably compensate the error and disturbance result from the NN and other external causes.

The rest of the paper is organised as follows: Section 2 states the problem formulation. The NN identification design is proposed in Section 3 and Section 4 shows SMC controller design. The simulations are given in Section 5. Section 6 concludes the papers. Data availability statement, conflicts of interest and acknowledgments are at the end of the paper.

2. Preliminaries

Considering a hysteresis nonlinear system is described as

$$\begin{aligned} \dot{x} &= f_1(x) + f_2(x)\, v \\ \dot{v} &= g(x,u)\, u \end{aligned} \tag{1}$$

with $f_i(0) = 0,\ i = 1, 2$ and $g(0,0) = 0$, where $x \in \mathbb{R}^n,\ v \in \mathbb{R}^m$ are the states and intermediate input, respectively, $u \in \mathbb{R}^l$ is the control input, $f_i, g, i = 1, 2$ denote unknown general nonlinear smooth functions, respectively, and v represents hysteresis nonlinearity. In this paper, we discuss the hysteresis nonlinearity v that is described by backlash-like model. The backlash-like hysteresis v can be expressed as follows [15]:

$$\dot{v} = g(x,u)\, u = \gamma\, |\dot{u}|\, (\alpha u - v) + \beta \dot{u}, \tag{2}$$

where $\gamma > 0, \alpha > 0$ are positive constants and $\alpha > \beta$.

The figure of backlash-like hysteresis is illustrated in Figure 1, where $\alpha = 2.3$, $\beta = 0.15$, $\gamma = 1.1$, and the input $u = K \sin(6t)$, $K_1 = 4$, $K_2 = 3$, and $K_3 = 2$.

To address the unknown system state function $f_1(x)$, $f_2(x)$, system (1) are rewritten as follows:

$$\begin{aligned} \dot{x} &= Ax + \overline{f}_1(x) + Bv + \overline{f}_2(x) \\ \dot{v} &= g(x,u)\, u, \end{aligned} \tag{3}$$

where $A \in \mathbb{R}^{n\times n}$ is Hurwitz matrix, $B \in \mathbb{R}^{n\times 1}$, A, B are controllable, and $\overline{f}_1(x) = f_1(x) - Ax$, $\overline{f}_2(x) = f_2(x) - B$.

Considering the Hurwitz state matrix A, given a positive definite matrix $P = P^T > 0$, there exists positive definite matrix $Q = Q^T > 0$ such that the inequality

$$A^T P + PA \le -Q \tag{4}$$

holds.

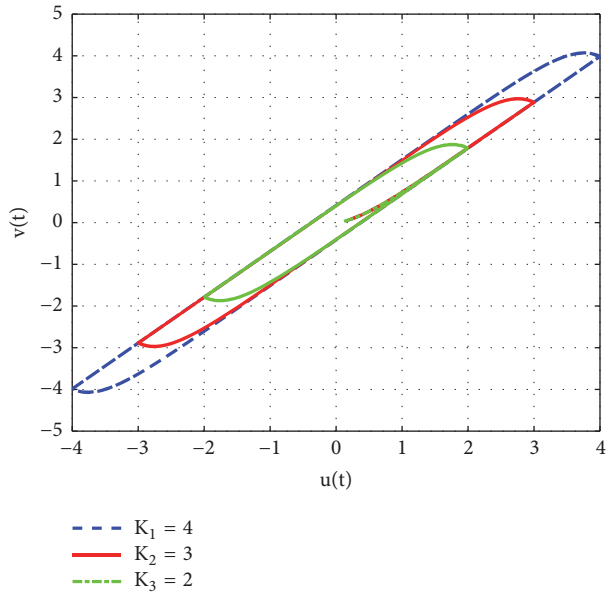

FIGURE 1: The curves of the backlash-like hysteresis models.

According to [3, 16], the equation $\dot{v} = g(x,u)u$ can be solved as

$$v = \alpha u + (v_0 - \alpha u_0)\, e^{-\gamma(u-u_0)\,\mathrm{sign}(\dot{u})} + e^{-\gamma u\,\mathrm{sign}(\dot{u})} \int_{u_0}^{u} (\beta - \alpha)\, e^{\gamma\xi\,\mathrm{sign}(\dot{u})} d\xi, \tag{5}$$

where v_0, u_0 are the initial values of v, u.

Then, substituting the backlash-like model (2) into system (3), we have

$$\dot{x} = Ax + \overline{f}_1(x) + B\alpha u + B(v_0 - \alpha u_0)\, e^{-\gamma(u-u_0)\,\mathrm{sign}(\dot{u})} + Be^{-\gamma u\,\mathrm{sign}(\dot{u})} \int_{u_0}^{u} (\beta - \alpha)\, e^{\gamma\xi\,\mathrm{sign}(\dot{u})} d\xi) + \overline{f}_2(x) \tag{6}$$

Define a smooth function as follows:

$$F(x) = \overline{f}_1(x) + \overline{f}_2(x), \tag{7}$$

then system (6) can be deduced as

$$\dot{x} = Ax + Bu + F(x) + B(v_0 - \alpha u_0)\, e^{-\gamma(u-u_0)\,\mathrm{sign}(\dot{u})} + Be^{-\gamma u\,\mathrm{sign}(\dot{u})} \int_{u_0}^{u} (\beta - \alpha)\, e^{\gamma\xi\,\mathrm{sign}(\dot{u})} d\xi). \tag{8}$$

3. NN Identification Design

Neural network (NN) can commendably approximate the nonlinearity systems. But different NN structure has different characteristics. In this paper, we adopt high-order neural network (HONN) to estimate the unknown general nonlinear smooth functions and hysteresis nonlinearity. The HONN is an excellent NN for nonlinear systems, where the big advantage is that only needs less neurons and computational costs. Thus the HONN developed high-order basis function connections so that it can easily approximate the high-order nonlinearities.

Considering system (8), the unknown function $F(x)$ and the hysteresis nonlinearity $B(v_0 - \alpha u_0)e^{-\gamma(u-u_0)\,\mathrm{sign}(\dot{u})} + Be^{-\gamma u\,\mathrm{sign}(\dot{u})} \int_{u_0}^{u} (\beta - \alpha)e^{\gamma\xi\,\mathrm{sign}(\dot{u})} d\xi)$ will be approximated by NN. Hence there exists unknown bounded NN weight matrix $W \in \mathbb{R}^{n\times p}$ and $\Psi(x) = [\Psi_1, \Psi_2, \ldots, \Psi_p]^T \in \mathbb{R}^p$ which can be identified by the following model:

$$\dot{\hat{x}} = A\hat{x} + Bu + W\Psi, \tag{9}$$

where the activation function $\Psi(x)$ is defined as

$$\Psi(x) = \left[\Psi_1, \Psi_2, \ldots, \Psi_p\right]^T \in \mathbb{R}^p$$
$$\Psi_k = \prod_{i\in L} \left[\psi(x)\right]^{d_i(k)}, \quad k = 1, 2, \ldots, p \tag{10}$$
$$\psi(x) = \frac{c}{1 + e^{-dx}} + h,$$

where L represent the collections of p node ordered subsets, c, d, h are designed parameters, and $d_i(k)$ is designed nonnegative integer.

Assuming an ideal NN can be approximated system (1) as

$$\dot{x} = Ax + Bu + W^*\Psi + \varepsilon, \tag{11}$$

where W^* means the ideal NN weight matrix, the NN $W^*\Psi$ completely substitutes the unknown function $F(x)$ and the hysteresis nonlinearity, ε is a bounded approximation error, *i.e.*, $\|\varepsilon\| \le \varepsilon_M$, and ε_M is a known positive constant vector.

Define the identification error e as

$$e = x - \hat{x}. \tag{12}$$

Then, the derivative of the error e can be deduced by (9) and (11):

$$\dot{e} = \dot{x} - \dot{\hat{x}} = Ae + \widetilde{W}\Psi + \varepsilon, \tag{13}$$

where $\widetilde{W} = W^* - W$.

The identification structure of HONN can be illustrated in Figure 2.

Considering references [9, 17], the following assumption is proposed.

Assumption 1. The error norm of NN weight matrix $\widetilde{W}$ is bounded by $\|\widetilde{W}\| \le W_M$, and the basis function of NN is bounded, *i.e.*, $\|\Psi\| \le \psi_M$.

Theorem 2. *Considering system (1) which is approximated by the NN of (11), if the identification error is defined as (12), based on the Assumption 1, the identification e is semiglobally uniformly ultimately bounded (UUB) and it converges to a small compact set around zero as* $\|e\| \le \sqrt{2(\eta_2/\eta_1)/\|P\|}$, *where* η_1, η_2 *are defined in (17).*

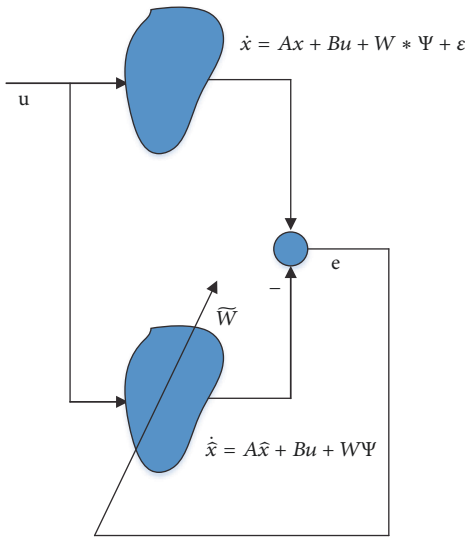

Figure 2: The structure of the NN identification.

Proof. Define the Lyapunov function as

$$V = \frac{1}{2}e^T Pe. \tag{14}$$

From (13), the derivative of V can be deduced as

$$\begin{aligned}
\dot{V} &= \frac{1}{2}\dot{e}^T Pe + \frac{1}{2}e^T P\dot{e} \\
&= \frac{1}{2}\left(Ae + \widetilde{W}\Psi + \varepsilon\right)^T Pe + \frac{1}{2}e^T P\left(Ae + \widetilde{W}\Psi + \varepsilon\right) \\
&= \frac{1}{2}e^T A^T Pe + \frac{1}{2}\Psi^T \widetilde{W}^T Pe + \frac{1}{2}\varepsilon^T Pe + \frac{1}{2}e^T PAe \\
&\quad + \frac{1}{2}e^T P\widetilde{W}\Psi + \frac{1}{2}e^T P\varepsilon \\
&\le -\frac{1}{2}e^T Qe + e^T P\left(\widetilde{W}\Psi + \varepsilon\right) \\
&\le -\frac{1}{2}e^T Qe + \left\|e^T\right\| \|P\| \left(\left\|\widetilde{W}\Psi\right\| + \|\varepsilon\|\right).
\end{aligned} \tag{15}$$

Invoking Young's inequality $ab \le (a^2 + b^2)/2$ on the term $\|e^T\|\|P\|(\|\widetilde{W}\Psi\| + \|\varepsilon\|)$, we have

$$\begin{aligned}
&\left\|e^T\right\| \|P\| \left(\left\|\widetilde{W}\Psi\right\| + \|\varepsilon\|\right) \\
&\quad \le \frac{\left\|e^T\right\|^2 \|P\|^2 + \left(\left\|\widetilde{W}\Psi\right\| + \|\varepsilon\|\right)^2}{2},
\end{aligned} \tag{16}$$

then considering Assumption 1 and (16), the derivative of V in (15) yields

$$\begin{aligned}
\dot{V} &\le -\frac{1}{2}e^T Qe + \frac{\left\|e^T\right\|^2 \|P\|^2 + \left(W_M\psi_M + \varepsilon_M\right)^2}{2} \\
&\le -\eta_1 V + \eta_2,
\end{aligned} \tag{17}$$

where $\eta_1 = ((1/2)e^T Qe + \|e^T\|^2\|P\|^2/2)/e^T Pe$; $\eta_2 = (W_M\psi_M + \varepsilon_M)^2/2$.

According to the Lyapunov theorem, V is UUB and the identification error e is bounded. Moreover, integrating both sides of (17) over the time $[0.t]$, the inequality can be solved as

$$V \le V_0 e^{-\eta_1 t} + \frac{\eta_2}{\eta_1}\left(1 - e^{-\eta_1 t}\right) \le \frac{\eta_2}{\eta_1} + V_0 e^{-\eta_1 t}. \tag{18}$$

Then, by applying (14), the bound of the identification error e can be solved as

$$\|e\| \le \sqrt{\frac{2\left(\eta_2/\eta_1 + V_0 e^{-\eta_1 t}\right)}{\|P\|}} \tag{19}$$

such that it has

$$\lim_{t\longrightarrow\infty}\|e\| \le \lim_{t\longrightarrow\infty}\sqrt{\frac{2\left(\eta_2/\eta_1 + V_0 e^{-\eta_1 t}\right)}{\|P\|}} = \sqrt{\frac{2\left(\eta_2/\eta_1\right)}{\|P\|}}. \tag{20}$$

That means the identification error e can be converged to a small compact set around zero.

The proof is completed. □

4. Controller Design

Considering system (1), if the system is a pure feedback system, in order to avoid the complicated computation of the back-stepping controller, new state variables are defined to transform the state variables into canonical form based on reference [9]. Therefore, the new alternative states can be defined as

$$\begin{aligned}
z_1 &= x_1 \\
z_2 &= \dot{z}_1 \\
z_i &= \dot{z}_{i-1}, \quad i = 2, 3, \ldots, n,
\end{aligned} \tag{21}$$

and the transformed canonical system is

$$\begin{aligned}
\dot{z}_1 &= z_2 \\
\dot{z}_i &= z_{i+1}, \quad i = 1, 2, \ldots, n-1 \\
\dot{z}_n &= \acute{a}_n\left(x_n\right) + \acute{b}_n u,
\end{aligned} \tag{22}$$

where the definition of $\acute{a}_n$, $\acute{b}_n$ can be obtained by the method of the reference [9].

For the existing of the hysteresis nonlinearity, we also can adopt the approach of reference [9] to avoid the complicated controller design. Considering A is Hurwitz matrix and A, B are controllable, without loss of generality, we can transform

the system (8) into a normalized form. Then, assume the matrixes A, B are

$$A = \begin{bmatrix} a_{11} & a_{12} & \cdots & a_{1n} \\ a_{21} & a_{22} & \cdots & a_{2n} \\ \vdots & \vdots & \ddots & \vdots \\ a_{n1} & a_{n2} & \cdots & a_{nn} \end{bmatrix},$$
$$B = \begin{bmatrix} b_1 \\ b_2 \\ \vdots \\ b_n \end{bmatrix}, \tag{23}$$

According to the fact that $z_2 = r_1(x) = \dot{z}_1 = a_{11}x_1 + a_{12}x_2 + \cdots + a_{1n}x_n + b_1u + \overline{f}_1(x(1)) + \overline{f}_2(x(1)) + b_1(v_0 - \alpha u_0)e^{-\gamma(u-u_0)\,\mathrm{sign}(\dot{u})} + b_1 e^{-\gamma u\,\mathrm{sign}(\dot{u})} \int_{u_0}^{u} (\beta - \alpha) e^{\gamma\xi\,\mathrm{sign}(\dot{u})} d\xi$, it has the following:

$$\begin{aligned} \dot{z}_2 = \ddot{z}_1 &= \frac{\partial r_1(x)}{\partial x_1}\dot{x}_1 + \frac{\partial r_1(x)}{\partial x_2}\dot{x}_2 \\ &= a_{11}\dot{x}_1 + a_{12}\dot{x}_2 + \frac{\partial \overline{f}_1(x_1)}{\partial x_1}\dot{x}_1 + \frac{\partial \overline{f}_2(x_1)}{\partial x_1}\dot{x}_1 \\ &\quad + \frac{\partial \overline{f}_1(x_1)}{\partial x_2}\dot{x}_2 + \frac{\partial \overline{f}_2(x_1)}{\partial x_2}\dot{x}_2. \end{aligned} \tag{24}$$

Then, we also can obtain

$$\begin{aligned} \dot{z}_3 &= \ddot{z}_2 \\ &= a_{12}\ddot{x}_2 + \frac{\partial\left(\partial \overline{f}_1(x_1)/\partial x_1\right)\dot{x}_1}{\partial x_2}\dot{x}_2 \\ &\quad + \frac{\partial\left(\partial \overline{f}_2(x_1)/\partial x_1\right)\dot{x}_1}{\partial x_2}\dot{x}_2 \\ &\quad + \frac{\partial\left(\partial \overline{f}_1(x_1)/\partial x_2\right)\dot{x}_2}{\partial x_2}\dot{x}_2 \\ &\quad + \frac{\partial\left(\partial \overline{f}_2(x_1)/\partial x_2\right)\dot{x}_2}{\partial x_2}\dot{x}_2 \\ &\quad + \frac{\partial\left(\partial \overline{f}_1(x_1)/\partial x_1\right)\dot{x}_1}{\partial x_3}\dot{x}_3 \\ &\quad + \frac{\partial\left(\partial \overline{f}_2(x_1)/\partial x_1\right)\dot{x}_1}{\partial x_3}\dot{x}_3 \\ &\quad + \frac{\partial\left(\partial \overline{f}_1(x_1)/\partial x_2\right)\dot{x}_2}{\partial x_3}\dot{x}_3 \\ &\quad + \frac{\partial\left(\partial \overline{f}_2(x_1)/\partial x_2\right)\dot{x}_2}{\partial x_3}\dot{x}_3. \end{aligned} \tag{25}$$

By parity of reasoning, we apply the method of reference [9], the canonical form of system (8) can be obtained as (22).

According to the preceding discuss, without loss of generality, the coefficient matrixes A, B can be adopted as

$$A = \begin{bmatrix} 0 & 1 & 0 & \cdots & 0 \\ 0 & 0 & 1 & \cdots & 0 \\ 0 & 0 & 0 & \cdots & 0 \\ \vdots & \vdots & \vdots & \ddots & \vdots \\ -a_1 & -a_2 & -a_3 & \cdots & -a_n \end{bmatrix},$$
$$B = \begin{bmatrix} 0 \\ 0 \\ 0 \\ \vdots \\ b \end{bmatrix}. \tag{26}$$

Then, the system is described by NN in (11) which can be rewritten as

$$\begin{aligned} \dot{x}_1 &= x_2 \\ \dot{x}_2 &= x_3 \\ &\vdots \\ \dot{x}_n &= -a_1x_1 - a_2x_2 - \cdots - a_nx_n + bu + CW^*\Psi + C\varepsilon, \end{aligned} \tag{27}$$

where $C \in \mathbb{R}^{1\times n}$ is a transformed vector parameters for the NN in (11).

Remark 3. For the existing of the hysteresis nonlinearity and the nonlinear smooth functions $\overline{f}_(x), \overline{f}_2(x)$, we cannot use the linear system method to transform the coefficient matrixes (23) into normalized form (26). But under some conditions, we also use the linear system method to transform the coefficient matrixes, that can be simplify the computation and is convenient for the controller design.

5. Define the Sliding Mode Manifold s as Follows

$$s = c_1e_1 + c_2\dot{e}_1 + \cdots + e_1^{(n)}, \tag{28}$$

where the error e_1 is defined as

$$e_1 = x_1 - x_d, \tag{29}$$

where x_d is the reference input signals.

Design the sliding mode controller input as follows:

$$u = \frac{1}{b}\left(-\varsigma\hat{s} - C\widehat{W}\Psi - \widehat{m} + \hat{z} + x_d^{(n+1)} - \text{sign}\left(\hat{s}\right)\right), \quad (30)$$

where $\varsigma > 0$, $\hat{z} = a_1\hat{x}_1 + a_2\hat{x}_2 + \cdots, a_n\hat{x}_n$, $\widehat{m} = c_1\dot{\hat{e}}_1 - c_2\ddot{\hat{e}}_1 - \cdots - c_{n-1}\hat{e}_1^{(n-1)}$, and $\hat{s} = c_1\hat{e}_1 + c_2\dot{\hat{e}}_1 + \cdots + \hat{e}_1^{(n)}$.

The NN update law is selected as

$$\dot{\widehat{W}} = -\rho s\Psi, \quad (31)$$

where ρ is designed parameter.

Define the errors as

$$\tilde{x}_i = x_i - \hat{x}_i, \quad i = 1, 2, \ldots, n. \quad (32)$$

Then, the following theorem holds.

Theorem 4. *Considering system (27), the sliding mode manifold is defined in (28), the controller is chosen as in (30), the NN update law is chosen as in (31), and then, the control system is semiglobally uniformly ultimately bounded (UUB).*

Proof. Define the Lyapunov function as

$$V_t = \frac{1}{2}s^2. \quad (33)$$

According to (28), (29), and (30), we have

$$\begin{aligned}
\dot{V}_t &= s\dot{s} = s\left(c_1\dot{e}_1 + c_2\ddot{e}_1 + \cdots + e_1^{(n+1)}\right) = s\left(c_1\dot{e}_1 + c_2\ddot{e}_1\right. \\
&+ \cdots - a_1x_1 - a_2x_2 - \cdots - a_nx_n + bu + CW^*\Psi \\
&\left. + C\varepsilon - x_d^{(n+1)}\right) = s\left(c_1\dot{e}_1 + c_2\ddot{e}_1 + \cdots - a_1x_1 - a_2x_2\right. \\
&- \cdots - a_nx_n + CW^*\Psi + C\varepsilon - \varsigma\hat{s} - \widehat{m} + \hat{z} \\
&\left. - \text{sign}\left(\hat{s}\right)\right) = s\left(-\varsigma\hat{s} - a_1\tilde{x}_1 + \left(c_1 - a_2\right)\tilde{x}_2 + \cdots\right. \\
&\left. + \left(c_{n-1} - a_n\right)\tilde{x}_n + C\widetilde{W}\Psi + C\varepsilon - \text{sign}\left(\hat{s}\right)\right) = -\varsigma s^2 \\
&+ s\left(-a_1\tilde{x}_1 + \left(c_1 - a_2\right)\tilde{x}_2 + \cdots + \left(c_{n-1} - a_n\right)\tilde{x}_n\right. \\
&\left. + C\widetilde{W}\Psi + C\varepsilon + \varsigma\tilde{s} - \text{sign}\left(\hat{s}\right)\right) = -\varsigma s^2 \\
&+ s\left(\left(c_1 - a_1\right)\tilde{x}_1 + \left(c_1 + c_2 - a_2\right)\tilde{x}_2 + \cdots\right. \\
&\left. + \left(c_{n-1} - a_n + 1\right)\tilde{x}_n + C\widetilde{W}\Psi + C\varepsilon - \text{sign}\left(\hat{s}\right)\right),
\end{aligned} \quad (34)$$

where $\tilde{s} = s - \hat{s} = c_1\tilde{x}_1 + c_2\tilde{x}_2 + \cdots + \tilde{x}_n$.

Define $\Delta_{max} \geq |(c_1 - a_1)\tilde{x}_1 + (c_1 + c_2 - a_2)\tilde{x}_2 + \cdots + (c_{n-1} - a_n + 1)\tilde{x}_n + C\widetilde{W}\Psi + C\varepsilon| - \text{sign}(\hat{s})$, according to Young's inequality, (34) can be deduced as

$$\dot{V}_t \leq -\varsigma s^2 + \frac{1}{2}\left(s^2 + \Delta_{max}^2\right) = -\left(2\varsigma - 1\right)V_t + \frac{1}{2}\Delta_{max}^2. \quad (35)$$

To solve inequality (35), we have

$$\begin{aligned}
V_t &\leq e^{-\varrho(t-t_0)}V\left(t_0\right) + \frac{1}{2}\Delta_{max}^2\int_{t_0}^{t} e^{-\varrho(t-\xi)}d\xi \\
&= e^{-\varrho(t-t_0)}V\left(t_0\right) - \frac{1}{2\varrho}\Delta_{max}^2\left(1 - e^{-\varrho(t-t_0)}\right),
\end{aligned} \quad (36)$$

where $\varrho = 2\varsigma - 1$.

Let the parameter $\varsigma > 1/2$, and one can obtain

$$\lim_{t\longrightarrow\infty} V_t \leq \frac{1}{2\varrho}\Delta_{max}^2. \quad (37)$$

Therefore, based on the Lyapunov theory, the controlled system is semiglobally uniformly ultimately bounded (UUB).

The proof is completed. □

Remark 5. Based on Theorem 4, all the closed loop signals are bounded. But on the structure of the NNSMC, we obviously known that the NN identification is a part of the closed loop and the update law of NN is deduced by the closed loop. Therefore, the identification connected with the control design, it is online estimating the nonlinear functions and online adjusting by the tracking errors.

6. Simulations

Considering a hysteresis system as follows:

$$\begin{aligned}
\dot{x}_1 &= x_2 \\
\dot{x}_2 &= \frac{1.3}{0.186}x_1 + \frac{\cos x_2}{0.186} \\
&\quad + \frac{2}{1 + \sin\left(-0.5\left(x_1 - x_2\right)\right) + 0.12\cos x_2}v \\
\dot{v} &= 0.08\left|\dot{u}\right|\left(2u - v\right) + 0.03\dot{u}.
\end{aligned} \quad (38)$$

6.1. Controller Design. In order to verify the effectiveness of the proposed NNSMC, A PID controller is designed to compare with the proposed NNSMC. The PID controller gains are chosen as $KP = 50, KI = 3, KD = 1.26$. Otherwise, for NNSMC, the sliding mode manifold is defined as in (28), the NNSMC controller is defined as in (30). The parameters are selected as $c = 6.28$, $d = 2$, $h = 1$, $c_1 = 5.95$, $a_1 = 6.99$, $a_2 = 5.38$, $b = 5.38$, $\rho = 0.05$, and $\varsigma = 2$.

We design two different control input signal to test the proposed approaches. Firstly, a square wave signal is selected for the hysteresis system, and then two amplitude sine signals are adopted with NNSMC which will compare with the PID controller.

The two different controllers will test the system (38) with reference input. The proposed NNSMC firstly estimates the unknown states and hysteresis part with NN and uses the sliding mode controller to control the hysteresis system online.

6.2. Control Results. Two different reference input signals are selected to test the proposed NNSMC. The NN identification is adopted estimating the unknown nonlinear functions and then the SMC is applied to control the closed loop. In order to verify the effectiveness of the NN identification and SMC, A square wave signal firstly utilizes tracking the system. Two amplitude sine signals are adopted with NNSMC and PID controller. The details are listed as follows.

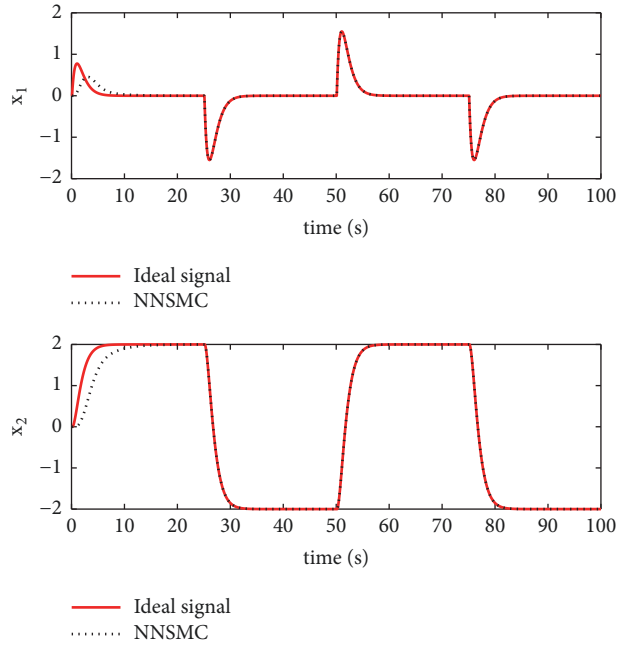

Figure 3: The control results of NNSMC versus PID control.

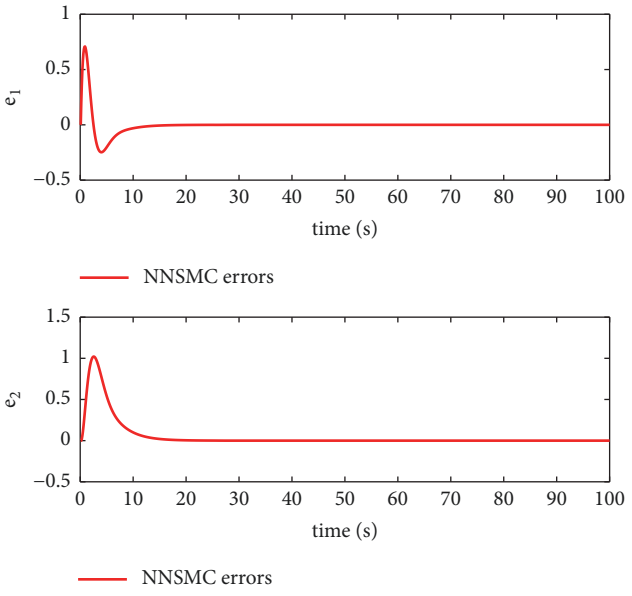

Figure 4: The control results of NNSMC versus PID control.

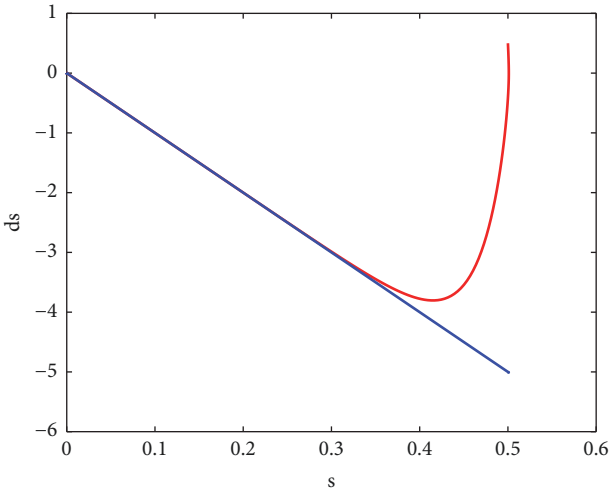

Figure 5: The control results of NNSMC versus PID control.

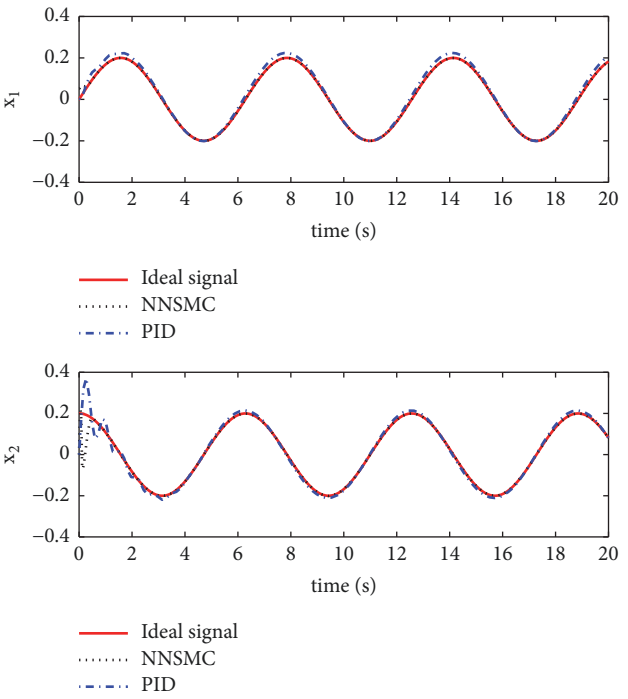

Figure 6: The control results of NNSMC versus PID control.

6.2.1. Case 1. We chose the reference square wave with amplitude which is $a = 2$, and the duty ratio is 50%. Then the tracking results are illustrated in Figure 3, the errors are shown in Figure 4, and the sliding mode reaching phase process is illustrated in Figure 5. From Figures 3 and 4, it is clear that the proposed NN identification and the NNSMC have a good tracking performance. The dynamic procedures are less than 10*s* and the errors are shown in the same phenomenon.

In order to restrain chattering of the SMC, we adopt tanh(·) function instead of the sign(·) function in the simulations. From Figure 5, we can see that the chattering is suppressed and the sliding mode quickly reaches the sliding mode manifold.

6.2.2. Case 2. The reference input is chosen as a sinusoidal signal $x_d = 0.2\sin(x)$. The controller results and errors are illustrated in Figures 6 and 7. It is shown that the proposed NNSMC can more precisely track the states than the PID controller with shorter dynamic adjustment time from Figure 6. The adjustment time of NNSMC for x_2 is less than 1*sec*, but the PID controller adjustment time is more than 3*sec*. The tracking errors also demonstrate the same conclusion from Figure 7. The mean absolute error

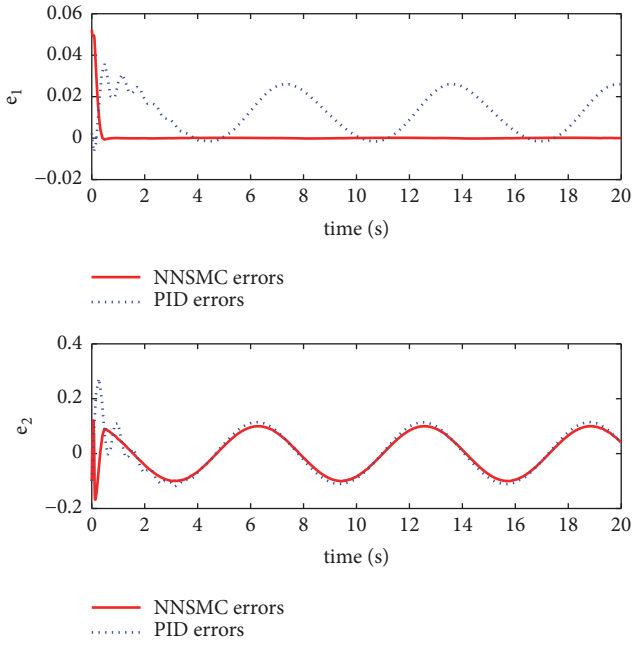

Figure 7: The tracking errors of NNSMC versus PID control.

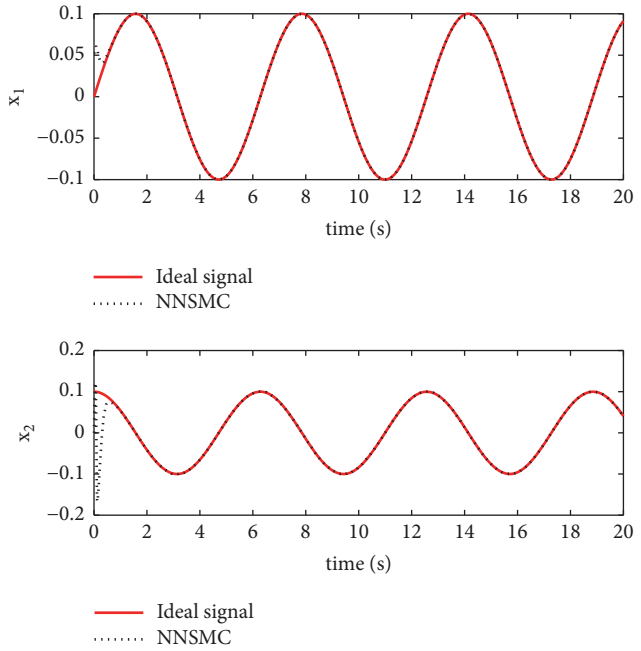

Figure 9: The control results of NNSMC with $x_d = 0.1\sin(x)$.

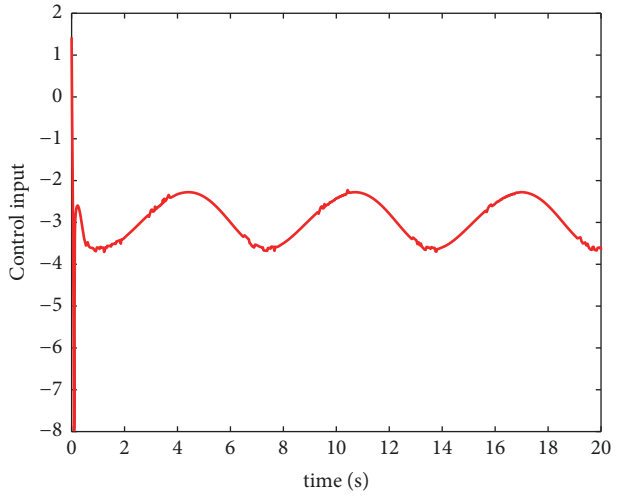

Figure 8: The control input of NNSMC.

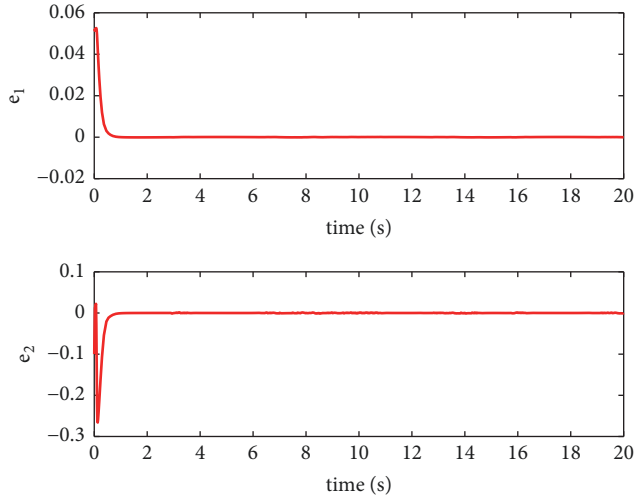

Figure 10: The tracking errors of NNSMC with $x_d = 0.1\sin(x)$.

(MAE) of NNSMC and PID controllers are listed in Table 1. According to the Table 1, the two approaches' MAE of MAE_1 are 0.0021, 0.0121 and the MAE of MAE_2 are 0.0066, 0.0078, respectively. It is obviously shown that the proposed NNSMC has better performance for the hysteresis nonlinear system. The NNSMC controller signal is illustrated in Figure 8. From the controller signal, one also finds that the dynamic adjustment time is less than 1*sec* in this simulation.

6.2.3. Case 3. In order to demonstrate the performance of the proposed NNSMC, the reference input is selected as $x_d = 0.1\sin(x)$ that has a smaller amplitude than Case 1 and the results are illustrated in Figures 9 and 10. The controller input

Table 1: The mean absolute errors of NNSMC and PID controller.

Controller	MAE_1	MAE_2
NNSMC	0.0021	0.0066
PID	0.0121	0.0078

is shown in Figure 11. It is clearly illustrated that the proposed NNSMC has excellent performance to track the hysteresis nonlinear system. The dynamic adjustment time only has about 0.5*sec*, then it keeps stable stage and the tracking error holds a neighbourhood of zero. From Figure 10, one can obviously find the same conclusion and the MAE of $MAE_1 = 0.0018$, $MAE_2 = 0.0056$, respectively. Compared with the

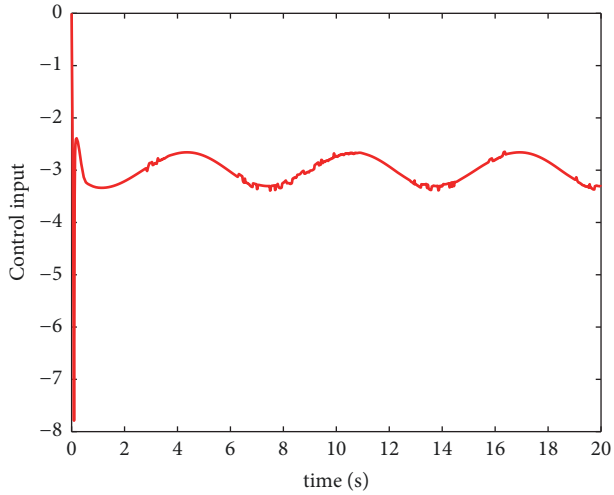

FIGURE 11: The control input of NNSMC with $x_d = 0.1\sin(x)$.

results of Case 1, the control precisions are higher on the small signals, that suit the real conditions. With the increase of the reference input signal, the control performance becomes degradation.

7. Conclusions

A new neural network identification approach and neural network sliding mode control were proposed for hysteresis nonlinear system with backlash-like model. Since classical adaptive control needs to deal with the tracking error (error transformation or back-stepping, *etc.*) on the controller design, in this paper a neural network sliding mode controller was designed where it did not need tracking error transformation. Moreover, the unknown system states and the unknown hysteresis section were estimated only by one neural network for saving the computation and simplifying the control design. The stability of the closed loop was guaranteed by Lyapunov theory and the simulation results verified the effectiveness of the presented approaches.

Data Availability

The data used to support the findings of this study are available from the corresponding author upon request.

Conflicts of Interest

The authors declare that there are no conflicts of interest.

Acknowledgments

This work is supported by Shandong Natural Science Foundation of China (ZR2017MF048), the National Natural Science Foundation of China (61803216), and Tai'an Science and Technology Development Program (2017GX0017).

References

[1] X. Gao, C. Zhang, C. Zhu, and X. Ren, "Identification and control for Hammerstein systems with hysteresis non-linearity," *IET Control Theory & Applications*, vol. 9, no. 13, pp. 1935–1947, 2015.

[2] X. Gao, "Adaptive neural control for hysteresis motor driving servo system with Bouc-wen model," *Complexity*, vol. 2018, Article ID 9765861, 9 pages, 2018.

[3] X. Gao and R. Liu, "Multiscale Chebyshev neural network identification and adaptive control for backlash-like hysteresis system," *Complexity*, vol. 2018, Article ID 1872493, 9 pages, 2018.

[4] Q. Chen, X. Ren, J. Na, and D. Zheng, "Adaptive robust finite-time neural control of uncertain PMSM servo system with nonlinear dead zone," *Neural Computing and Applications*, vol. 28, no. 12, pp. 3725–3736, 2017.

[5] Q. Chen, L. Shi, J. Na, X. Ren, and Y. Nan, "Adaptive echo state network control for a class of pure-feedback systems with input and output constraints," *Neurocomputing*, vol. 275, pp. 1370–1382, 2018.

[6] J. Na, A. S. Chen, G. Herrmann, R. Burke, and C. Brace, "Vehicle engine torque estimation via unknown input observer and adaptive parameter estimation," *IEEE Transactions on Vehicular Technology*, vol. 67, no. 1, pp. 409–422, 2018.

[7] S. Wang, J. Na, and X. Ren, "RISE-based asymptotic prescribed performance tracking control of nonlinear servo mechanisms," *IEEE Transactions on Systems, Man, and Cybernetics: Systems*, vol. 48, no. 12, pp. 2359–2370, 2018.

[8] S. Wang, H. Yu, J. Yu, J. Na, and X. Ren, "Neural-network-based adaptive funnel control for servo mechanisms with unknown dead-zone," *IEEE Transactions on Cybernetics*, pp. 1–12, 2018.

[9] J. Na, X. Ren, and D. Zheng, "Adaptive control for nonlinear pure-feedback systems with high-order sliding mode observer," *IEEE Transactions on Neural Networks and Learning Systems*, vol. 24, no. 3, pp. 370–382, 2013.

[10] D. Zheng, W. Xie, X. Ren, and J. Na, "Identification and control for singularly perturbed systems using multitime-scale neural networks," *IEEE Transactions on Neural Networks and Learning Systems*, vol. 28, no. 2, pp. 321–333, 2017.

[11] Q. Chen, S. Xie, M. Sun, and X. He, "Adaptive non-singular fixed-time attitude stabilization of uncertain spacecraft," *IEEE Transactions on Aerospace and Electronic Systems*, vol. 54, no. 6, pp. 2937–2950, 2018.

[12] M. Tao, Q. Chen, X. He, and M. Sun, "Adaptive fixed-time fault-tolerant control for rigid spacecraft using a double power reaching law," *International Journal of Robust and Nonlinear Control*, vol. 29, no. 12, pp. 4022–4040, 2019.

[13] S. H. Chincholkar, W. Jiang, and C. Chan, "A modified hysteresis-modulation-based sliding mode control for improved performance in hybrid DC–DC boost converter," *IEEE Transactions on Circuits and Systems II: Express Briefs*, vol. 65, no. 11, pp. 1683–1687, 2018.

[14] J. Fang, L. Zhang, Z. Long, and M. Y. Wang, "Fuzzy adaptive sliding mode control for the precision position of piezo-actuated nano positioning stage," *International Journal of Precision Engineering and Manufacturing*, vol. 19, no. 10, pp. 1447–1456, 2018.

[15] C.-Y. Su, Y. Stepanenko, J. Svoboda, and T. P. Leung, "Robust adaptive control of a class of nonlinear systems with unknown backlash-like hysteresis," *IEEE Transactions on Automatic Control*, vol. 45, no. 12, pp. 2427–2432, 2000.

[16] X. Gao, W. Zhao, S. Wang, M. Wang, and X. Ren, "A prescribed performance adaptive control for hysteresis hammerstein system," *Journal of Systems Science and Complexity*, pp. 1–14, 2018.

[17] J. Na, Q. Chen, X. Ren, and Y. Guo, "Adaptive prescribed performance motion control of servo mechanisms with friction compensation," *IEEE Transactions on Industrial Electronics*, vol. 61, no. 1, pp. 486–494, 2014.

Hindawi
Complexity
Volume 2019, Article ID 8525397, 12 pages
https://doi.org/10.1155/2019/8525397

Research Article

Frequency Regulation and Coordinated Control for Complex Wind Power Systems

Cheng Guo [1] **and Delin Wang** [2]

[1] *Yunnan Electrical Power Experiment Institute, Co., Kunming 650217, Yunnan, China*
[2] *School of Electric Engineering, Southwest Jiaotong University, Chengdu 610031, Sichuan, China*

Correspondence should be addressed to Cheng Guo; gc325@126.com

Received 25 February 2019; Accepted 17 April 2019; Published 16 May 2019

Guest Editor: Chun Wei

With the development of complex renewable energy systems, the frequency control and regulation of the power grid powered by such renewable energies (e.g., wind turbine) are more critical, since the adopted different power generators can lead to frequency variations. To address the frequency regulation of such power grids, we will present a variable coefficient coordinated primary frequency regulation scheme for synchronous generator (SG) and doubly fed induction generator (DFIG). The variable adjustment coefficient of DFIG is defined according to the current reserve capacity, which can be applied to adjust different operation conditions to regulate the frequency variation within a predefined allowable range. Since the DFIG can make full use of the reserve wind power in the system frequency regulation, the proposed method can address both the frequency regulation response and the economic performance. Simulation results indicate that the proposed coordinated control scheme can achieve satisfactory frequency regulation response and lead to reduced demand for frequency regulation of SG.

1. Introduction

The wind power industry in all countries of the world is developing at a relatively fast speed. By 2050, 100% renewable energy can be supplied to the world, of which wind power accounts for 40% [1, 2]. This indicates that wind energy will gradually become the main source of renewable energy in the future. Today, wind power technology is relatively mature; however, wind power has a highly uncertain nature because wind speed is greatly affected by environmental conditions such as temperature and airflow changes. The connection of more wind power to power grid not only has many problems in the operation of the wind farm itself but also brings difficulties to the operation and regulation of the power grid [3, 4]. The traditional doubly fed induction generator- (DFIG-) based wind turbine does not have frequency regulation capability because its rotor speed is completely decoupled from the system frequency. Thus, the inertial response and frequency regulation capability of the power grid are influenced in this configuration. Nowadays, some wind power industries in developed countries have required that wind farms should have a certain frequency regulation capability by proposing advanced strategies. However, it is recognized that the adjustable frequency range of DIFG-based wind turbines is seriously limited by the wind speed [5]. Moreover, the wind power is usually included in the frequency regulation, making it a complicated process during the coordination with the traditional synchronous generators [6].

To address the above issues, many efforts have been done to investigate the feasibility to incorporate wind power into power grid frequency regulation in recent years by developing advanced control strategies and frequency regulation schemes [7, 8]. In [9–11], the potential problems caused by the large-scale wind power integration were introduced, and the recent research progress of two essential related aspects, control strategy and frequency regulation capability, has been reviewed. In terms of DFIG control designs, the authors of [12–15] proposed using proportional, differential controller (PD controller) to construct a primary frequency regulation controller on the rotor side, where the corresponding converter was designed, so that DFIG can adapt quickly to the frequency changes induced in the system. Moreover,

after developing speed control schemes, the authors of [16–18] proposed several composite frequency control schemes for variable speed wind turbines by combining the variable pitch control approaches and virtual inertial control methods. In [19], the variable droop is introduced to enhance the primary frequency contribution of wind turbine generators (WTG), and the droop parameter of every WTG is regulated to optimize the power output according to the reserve power margin available. In [20], a reduced-order model-based integrated controller method was suggested, which can provide inertial response and primary frequency control for WTG. This controller allows for a coupled control of torque and pitch angle at all speed range of DFIGs. In [21], simulation results indicate that the inertial term can be omitted, and the synthetic inertia strategy reduces to a very fast droop control strategy. It is noted that all the above-mentioned methods have been proposed from either the perspective of the wind farms or the internal control synthesis of wind turbines to study the possibility and validity of using wind power in the frequency regulation of power grid. However, when the wind power with variable frequency is incorporated into the power grid as a new type of frequency regulation power supply, the economic performance of the DFIG-based wind turbines and the ability of system frequency regulation should be considered simultaneously. Therefore, in order to obtain better power grid response and frequency modulation ability, it is necessary to coordinate the frequency regulation outputs between the DFIGs and the synchronous generators, according to the adjustable frequency capacity of DFIG-based wind turbines under different wind speeds. In fact, this idea has been recognized as one of emerging research topics as it can improve the wind frequency regulation.

Inspired by the above discussion, this paper explores the feasibility of using DFIGs to implement frequency regulation from the point of view of the adjustment coefficient. We found that the adjustable frequency wind turbines can effectively undertake the frequency regulation responsibility of the power grid. We propose a coordinated primary frequency regulation strategy between the synchronous generators and the DFIG-based wind turbines by using the variable coefficients. The strategy considers the influence of wind speed variation upon DFIG's wind energy acquisition and improves the maximum power point tracking (MPPT) [22, 23] operation mode of traditional DFIG. In the MPPT region, DFIG achieves deloading operation by controlling the rotor speed to deviate from MPPT operating point; in the constant power region, DFIG operates in deloading operation by controlling the pitch angle so as to reserve active power for DFIG to participate in primary frequency regulation of power grid. This strategy takes into account the frequency regulation ability and economic performance. In the allowable range of frequency variations, the DFIG can make full use of spare capacity to participate in the system frequency regulation. It can not only reduce the frequency regulation pressure of the synchronous generators but also reduce the wind power curtailment indirectly. Finally, the simulation result demonstrates the effectiveness of the proposed strategy. The main contribution of this paper is to introduce a variable coefficient coordinated frequency regulation for SG and DFIG, which can adapt to different operation conditions to make full use of the reserve wind power, and address both the frequency regulation response and the economic performance.

The structure of this paper is described as follows: Section 2 provides the system modeling and problem formulation. Section 3 presents the coordinated control scheme for generators. The coordinated frequency regulation strategy is given in Section 4, and numerical simulations are shown in Section 5. Finally, some conclusions are given in Section 6.

2. System Formulation and Problem Statement

In this paper, the studied system includes the synchronous generator (SG) and DFIG-based wind turbine generator (WTG). The connection structure between SG and WTG is shown in Figure 1(a). The WTG system for primary frequency regulation consists of aerodynamics model, pitch angle control system as shown in Figure 1(b), DFIG with supplementary controller to realize inertial response, and lookup tables to compute maximum and deloading power.

In Figure 1(b), f is the current frequency, f_N is the rated frequency, ω^*_r is the expected angular velocity, ω_r is the current angular velocity, β_0 is the reserved pitch angle for load shedding, K_β is the proportional coefficient, T_β is the time constant of the controller, and $\beta_{\max}$ and $\beta_{\min}$ are the maximum and minimum limit of pitch angle. Compared with the traditional pitch angle control, the frequency response link of pitch angle is added, and the frequency deviation of power grid is used as input. By adjusting the pitch angle to respond to the frequency change, DFIG-based wind turbines can provide long-term power support for the power grid.

A simplified aerodynamic model is used when the electrical behavior of the wind turbine is the main interest of the study. The relationship between the wind speed and the aerodynamic torque can be described as

$$T_{\mathrm{W}} = \frac{1}{2}\rho\pi R^3 v^2 C_P(\theta, \lambda) \tag{1}$$

where T_{w} is the aerodynamic torque extracted from the wind, ρ is the air density, R is the wind turbine rotor radius, v is the equivalent wind speed, θ is the pitch angle of the rotor, λ is the tip speed ratio, and C_{p} is the aerodynamic efficiency of the rotor.

Numerical approximations have been developed to calculate C_{p} for given values of θ and λ. Here the following approximation is used as

$$C_P(\theta, \lambda) = 0.22\left(\frac{116}{\lambda_i} - 0.4\theta - 5.0\right)e^{-12.5/\lambda_i} \tag{2}$$

where

$$\lambda_i = \frac{1}{1/(\lambda + 0.08\theta) - 0.035/(\theta^3 + 1)} \tag{3}$$

Actually, the dynamic characteristics of DFIG and power grid are decoupled in conventional MPPT control method; the wind turbines cannot respond to the system frequency

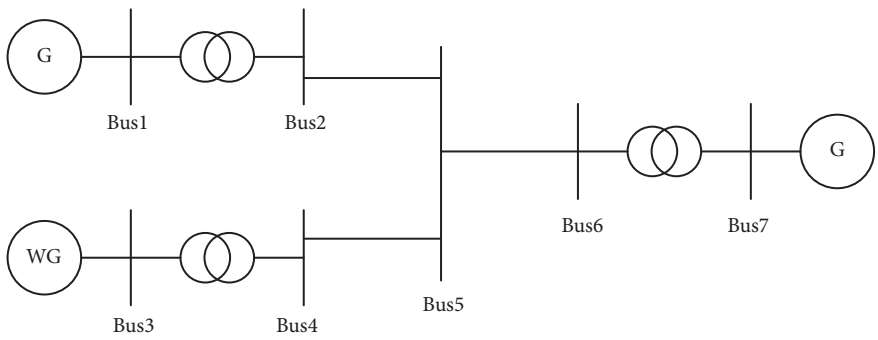

(a) Wiring diagram of WTG and SG

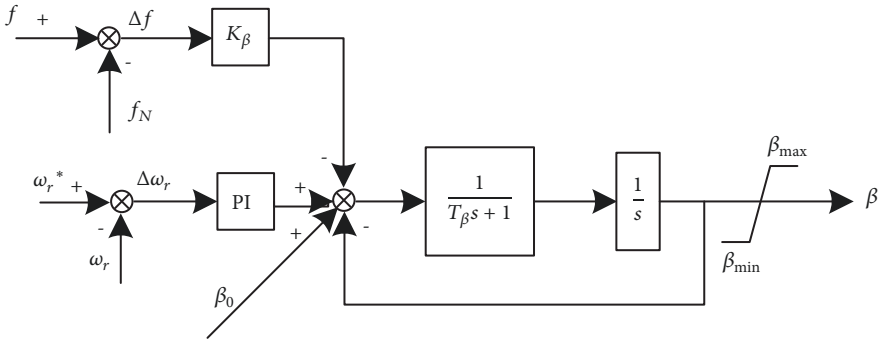

(b) Improved pitch angle control structure

Figure 1: Structure of power system including wind turbines and main controller.

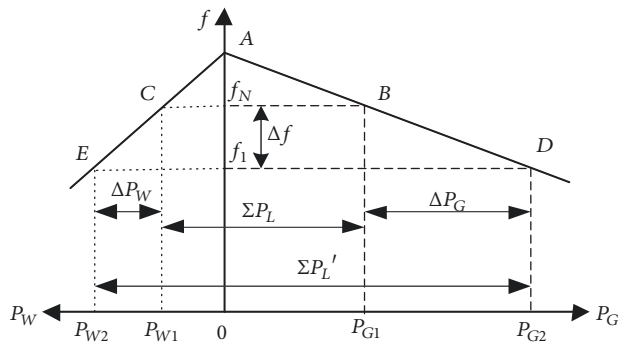

Figure 2: Frequency regulation characteristics of synchronous generator and DFIG-based wind turbine in parallel operation mode.

changes. However, the rotational inertia stored in WTG is remarkable; hence, there exists the waste of rotational inertia of DFIG rotor on the traditional operation mode. However, if there is an appropriate operation condition, it can be fully released and utilized through proper control strategy to support the system stability. The aim of this paper is to develop a new control strategy for WTG to participate in the primary frequency regulation, and the coordinated control strategy between SG and DFIG for primary frequency regulation is explored.

3. Coordinated Control of Synchronous Generators and DFIG-Based Wind Turbines

3.1. Frequency Regulation Characteristics. According to the primary frequency regulation principle of SG, the adjustment coefficient, namely, R_W, of the DFIG-based wind turbine is defined as

$$R_W = -\frac{\Delta f}{\Delta P_W} \tag{4}$$

where ΔP_W is the frequency regulation of DFIG and Δf is the frequency variation of system.

When a synchronous generator and a DFIG-based wind turbine are connected in parallel, the relationship between the frequency regulation characteristic and the active power allocation among generators can be illustrated in Figure 2. In the figure, $\overline{ABD}$ represents the adjusting characteristic curve of the synchronous generator. $\overline{ACE}$ represents that of the DFIG-based wind turbine. We suppose that the total load of the system is ΣP_L, which is corresponding to the line segment

$\overline{CB}$ in the figure. When the system frequency is f_N, the load carried by the synchronous generator is P_{G1}, and the load carried by the wind turbine is P_{W1}, such that

$$P_{G1} + P_{W1} = \sum P_L \tag{5}$$

After the system load increases ΔP_L and then is stable at f_1, the power output increase of the synchronous generator is ΔP_G and the total generated power output is P_{G2}; the power output increase of the wind turbine is ΔP_W and the total power output is P_{W2}. The sum of the increased power output of two generators is ΔP. According to Figure 1 and (4), we can obtain

$$\frac{\Delta P_{G*}}{\Delta P_{W*}} = \frac{R_{W*}}{R_{G*}} \tag{6}$$

where ΔP_{G*} and ΔP_{W*} represent the per unit values of power output of the synchronous generator and DFIG-based wind turbine, respectively; R_{G*} and R_{W*} are the per unit values of adjustment coefficients of the synchronous generator and DFIG-based wind turbine, respectively.

According to (6), when a synchronous generator and a DFIG are operated in parallel mode and the power increments of generators are retained at their respective per unit values, the power allocation between the SG and DFIG-based wind turbine is inversely proportional to the respective adjustment coefficients. That is, the generator with smaller adjustment coefficient has larger load increment, while the generator with larger adjustment coefficient has smaller load increment. Thus, the following can be concluded: (1) when a synchronous generator and a DFIG-based wind turbine run in parallel, the DFIG-based wind turbine participating in the frequency regulation can effectively reduce the frequency regulation pressure of the synchronous generator; (2) the frequency regulation output of the synchronous generator and DFIG-based wind turbine can be coordinated by adjusting the ratio of R_{G*} to R_{W*}.

3.2. Coordinated Control Strategy after DFIG-Based Wind Turbine Connected to the Power Grid. In the primary frequency regulation, the frequency regulation output of the synchronous generator is given by

$$\Delta P = -\frac{1}{R_*}\frac{\Delta f}{f_N}P_N \tag{7}$$

where Δf is the system frequency deviation, f_N is the system rated frequency, R_* is the per unit value of adjustment coefficient, and P_N is the rated capacity of the generator.

When a DFIG and n synchronous generators are operated in parallel, according to (7), the adjustment equations are given as follows:

$$\Delta P_{Gi} = -\frac{1}{R_{i*}}\frac{\Delta f}{f_N}P_{GiN} \quad (i = 1, 2, \ldots, n) \tag{8}$$

$$\Delta P_W = -\frac{1}{R_{W*}}\frac{\Delta f}{f_N}P_{WN} \tag{9}$$

where ΔP_{Gi} and ΔP_W are the frequency regulation outputs of synchronous generator i and DFIG-based wind turbine, respectively; P_{GiN} and P_{WN} are the rated capacity of synchronous generator i and DFIG-based wind turbine, respectively.

In the steady state, when the frequency variation of the whole system is Δf, the frequency regulation output of all generators in the system ΔP_Σ can be calculated as

$$\Delta P_\Sigma = \sum_{i=1}^{n}\Delta P_{Gi} + \Delta P_W \tag{10}$$

From (8)-(10), we can obtain

$$\Delta P_\Sigma = -\frac{\Delta f}{f_N}\left(\sum_{i=1}^{n}\frac{P_{GiN}}{R_{i*}} + \frac{P_{WN}}{R_{W*}}\right) \tag{11}$$

If all generators involved in the system are replaced by an equivalent generator, the frequency regulation output of the system is

$$\Delta P_\Sigma = -\frac{1}{R_{\Sigma*}}\frac{\Delta f}{f_N}P_{\Sigma N} \tag{12}$$

where $R_{\Sigma*}$ is the equivalent adjustment coefficient and $P_{\Sigma N}$ is the total capacity of the system. From (8) and (9), we can derive

$$-\Delta f_* = \frac{R_{i*}\Delta P_{Gi}}{P_{GiN}} = \frac{R_{W*}\Delta P_W}{P_{WN}} = \frac{R_{\Sigma*}\Delta P_\Sigma}{P_{\Sigma N}} \tag{13}$$

Based on (11) and (12), one can further obtain

$$R_{\Sigma*} = \frac{P_{\Sigma N}}{\sum_{i=1}^{n}\left(P_{GiN}/R_{i*}\right) + P_{WN}/R_{W*}} \tag{14}$$

Equations (12) and (15) illustrate that, from the point of view of the whole power network, when the capacity connected to the system is a constant, the smaller adjustment coefficient of each parallel operation generator is, the smaller equivalent adjustment coefficient $R_{\Sigma*}$ of the system will be, and the larger unit power regulation is, the better ability of primary frequency regulation will be; on the contrary, the larger adjustment coefficient of each parallel operation generator is, the larger equivalent adjustment coefficient $R_{\Sigma*}$ of the system will be, and the smaller unit power regulation is, the weaker ability of primary frequency regulation will be. From (13), when the system load changes, the power of each generator can be determined as

$$\Delta P_i = \frac{R_{\Sigma*}\Delta P_\Sigma}{P_{\Sigma N}} \times \frac{P_{GiN}}{R_{i*}} \tag{15}$$

When the wind turbines that have no frequency regulation ability are connected to the power grid, $P_{WN}/R_{W*} \approx 0$, and R_{W*} goes to infinity. Then the remaining synchronous generators use differential control schemes. If more wind turbines with no frequency regulation ability replace traditional synchronous generators, which are connected to the power grid, then we know that $P_{WN}/R_{W*} = 0$ and $R_{\Sigma*}$ of the system will become larger. Hence, connecting the large-scale wind turbines with no frequency regulation ability to the power network will obviously reduce the frequency regulation capability of the system.

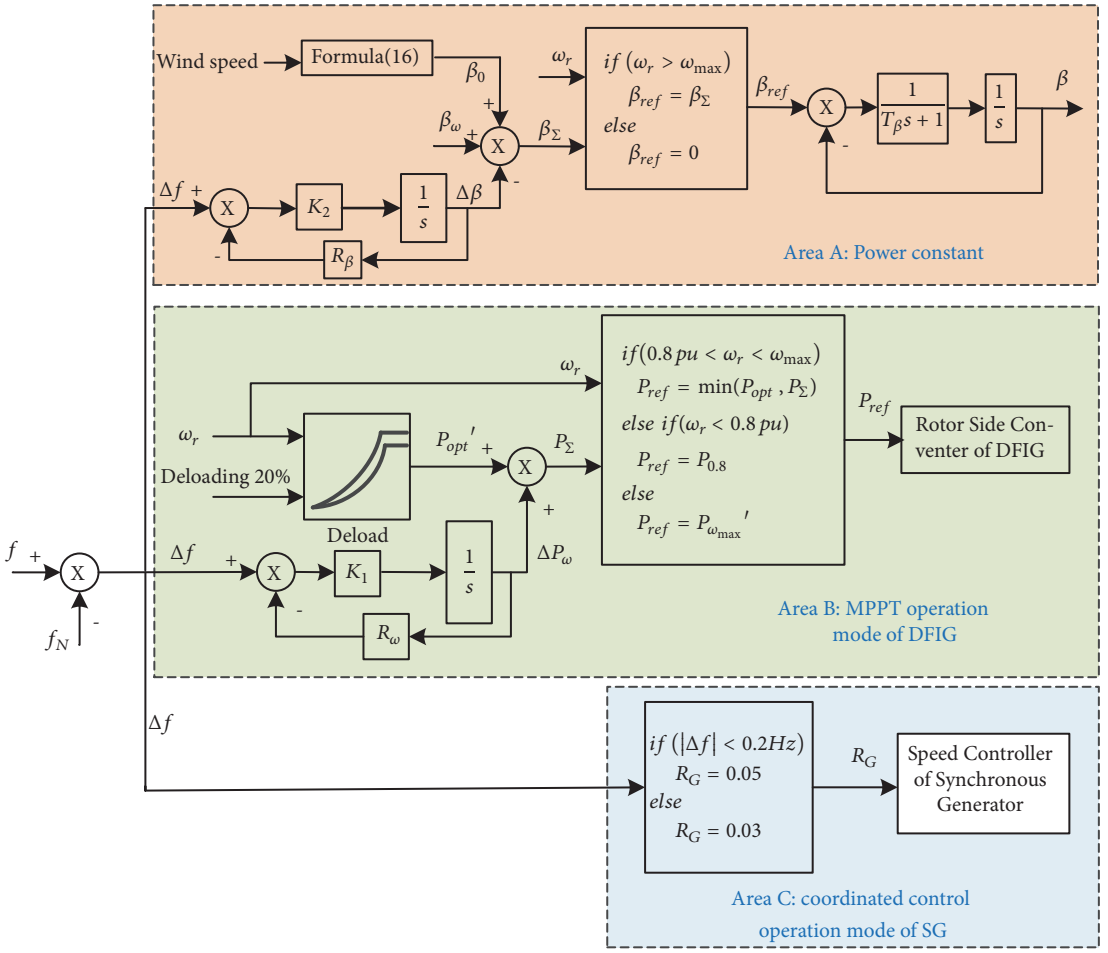

Figure 3: Primary coordinated frequency regulation structure of DFIG and synchronous generator.

4. Coordinated Strategy for Frequency Regulation

The primary frequency regulation control system coordinated by DFIGs and synchronous generators is shown in Figure 2. The overall system consists of three control modules: (1) area A: in this area, the power is constant; then through tuning the pitch angle action system, the active power output of DFIGs can be adjusted to adapt the change of the system frequency; (2) area B: this area is the maximum power point tracking module. It can realize the ability of power reservation by switching the running profile of the DFIG and adjusting the active power of the DFIG to participate in the frequency regulation according to the tuning variable adjustment coefficient; (3) area C: this area is the coordinated control module for the synchronous generator. According to the system frequency deviation, we choose the corresponding adjustment coefficient and coordinate the frequency regulation output between the synchronous generators and DFIGs.

4.1. Control Strategy of Primary Frequency Regulation with DFIG-Based Turbine. In this paper, the traditional operation mode of DFIG is modified and improved. In the maximum power point tracking area, the DFIG controls deloading operation through increasing or reducing the rotor speed. While in the constant power area, it can reserve the active power by adjusting the pitch angle, so that the DFIG has the frequency regulation capacity.

4.1.1. Maximum Power Point Tracking Control. Inspired by the principle of synchronous generator speed governor, a primary frequency regulation controller attached to the rotor side converter of a wind turbine is designed in this paper. We make the DFIG-based wind turbine whose load is reduced by 20% operate at the current wind speed, which is shown in area A in Figure 3. In this figure, ω_r is the corresponding rotor speed at the current wind speed, P_{opt}' is the suboptimal power when the wind turbine's load is reduced by 20%, R_ω is the adjustment coefficient of the DFIG maximum power point tracking module, f is the real-time frequency of the system, f_N is the rated frequency of the system, K_1 is the gain value, ΔP_ω is the frequency regulation power of DFIG-based wind turbine corresponding to the system frequency variation, and P_Σ is the sum of suboptimal power P_{opt}' and frequency regulation power ΔP_ω.

For the wind turbines, the frequency regulation power corresponding to the frequency variation is

$$\Delta P_\omega = -\frac{\Delta f}{R_\omega} = \frac{\Delta f}{\Delta f_0} P_0 \tag{16}$$

DFIG-based wind turbines can participate in the frequency regulation as the traditional synchronous generators if the variable adjustment coefficient is tuned at the maximum power point tracking area, and the adjustment coefficient can be adjusted automatically according to the current wind speed to determine the amount of frequency regulation power.

4.1.2. Control Strategy in Power Constant Area. In this paper, we introduce the regulation coefficient of the pitch angle. Through improving the traditional pitch angle control system, the DFIG can also realize the function of deloading reservation in the power constant area to respond to the system frequency variation. In the constant power area, deloading operation of DFIG can be achieved by presetting the pitch angle β_0, which is calculated by the following equation:

$$\begin{aligned}(1 - d\%)\, 0.44 \sin \frac{\pi(\lambda_c - 3)}{15} \\ = (0.44 - 0.0167\beta_0) \sin \frac{\pi(\lambda_c - 3)}{15 - 0.3\beta_0} \\ - 0.00184(\lambda_c - 3)\beta_0\end{aligned} \tag{17}$$

where the tip speed ratio of DFIG-based wind turbine is defined as $\lambda_c = R_{\omega\max}/v$.

According to the principle of synchronous generator governor, we design the controller of pitch angle for area B as shown in Figure 3. In the figure, β_ω is the pitch angle of the DFIG-based wind turbine when the power is constant. Δf is the difference between the system's current frequency f and the rated frequency f_N. R_β is the static adjustment coefficient of pitch angle. K_2 is the gain value. In the power constant area, the improved pitch angle control system enables DFIG to adapt to the current wind speed by adjusting the pitch angle according to its characteristic.

When the DFIG-based wind turbine is involved in the frequency regulation, the movement range of pitch angle is

$$\Delta\beta = -\frac{\Delta f}{R_\beta} = \frac{\Delta f}{\Delta f_0}\beta_0 \tag{18}$$

In the constant power area, the variable adjustment coefficient between the pitch angle and the frequency characteristic is introduced and tuned. DFIG-based wind turbines can respond to the system frequency variation through changing mechanical power captured by the DFIG according to the variation of system frequency. Thus, DFIG is able to participate in the frequency adjustment process.

4.2. Coordinated Strategy of Primary Frequency Regulation between DFIG and Synchronous Generator. For the system with multiple generators, the frequency adjustment can be coordinated and achieved by those generators which have frequency regulation ability. When DFIG-based wind turbines are connected to the system, it is necessary for the traditional generators to detect the inclusion of these new generators. When the system frequency changes, part of the frequency regulation power will be allocated to the wind turbines according to the wind speed [24, 25] and the induced frequency deviation. Therefore, it is necessary to divide the frequency regulation region of the system according to the magnitude of the system frequency deviation.

The control and coordination strategies of the synchronous generators are shown in area C in Figure 2. The basic methods are summarized as follows.

(1) When the system is in the normal operation region and the frequency deviation is within the allowable range (0.2 Hz), if DFIG-based wind turbines are used in the frequency regulation and deloading operation, it will lead to a wind power curtailment and reduction of the wind power's economic efficiency. In general, the adjustment coefficient of SG is between 0.03 and 0.05. In this case, in order to reduce the frequency regulation output of SGs, we set the regulation coefficient R_G to 0.05, so that the more reserved power of DFIG-based wind turbines will be used for the frequency regulation and the "abandoned air" will be reduced. In particular, in the power constant area, the reserved power of DIFG-based wind turbines is larger, and thus the adjustable frequency power output will be increased as well.

(2) The frequency deviation is large when the system is in the emergency regulatory area. In order to make the system run stably and accelerate the recovery of system frequency, the synchronous generators and DFIG-based wind turbines should be used in the system frequency regulation as much as possible. The adjustment coefficient of the synchronous generator is usually set to 0.03, so that the DFIGs participate in the system frequency regulation as much as possible according to the current wind speed.

The above-mentioned coordinate control strategies for the studied system with DFIGs and synchronous generator can be implemented by using the following steps:

(1) Measure the system frequency and calculate the frequency variations

(2) If the frequency variation is larger than 0.2 Hz, we set the adjustment coefficient of the SG as 0.03; otherwise, we set the adjustment coefficient of the SG as 0.05

(3) Measure the rotor's speed ω_r of the DIFG under the current wind speed

(4) If $\omega_r > \omega_{\max}$, we can calculate the pitch adjusting coefficient R_β in the constant area based on (17) and then apply the obtained R_β to the pitch operation system

(5) If $\omega_r \leq \omega_{\max}$, we can calculate the pitch adjusting coefficient R_ω in the maximum power tracking area based on (17) and then apply the obtained R_ω to the pitch operation system

(6) Calculate the primary frequency regulation of the synchronous generator, ΔP_G, based on the result of Step (2) and the primary frequency regulation of DFIG, ΔP_W, based on Step (4) or (5). Then we obtain the total frequency regulation of the system as $\Delta P_\Sigma = \Delta P_G + \Delta P_W$.

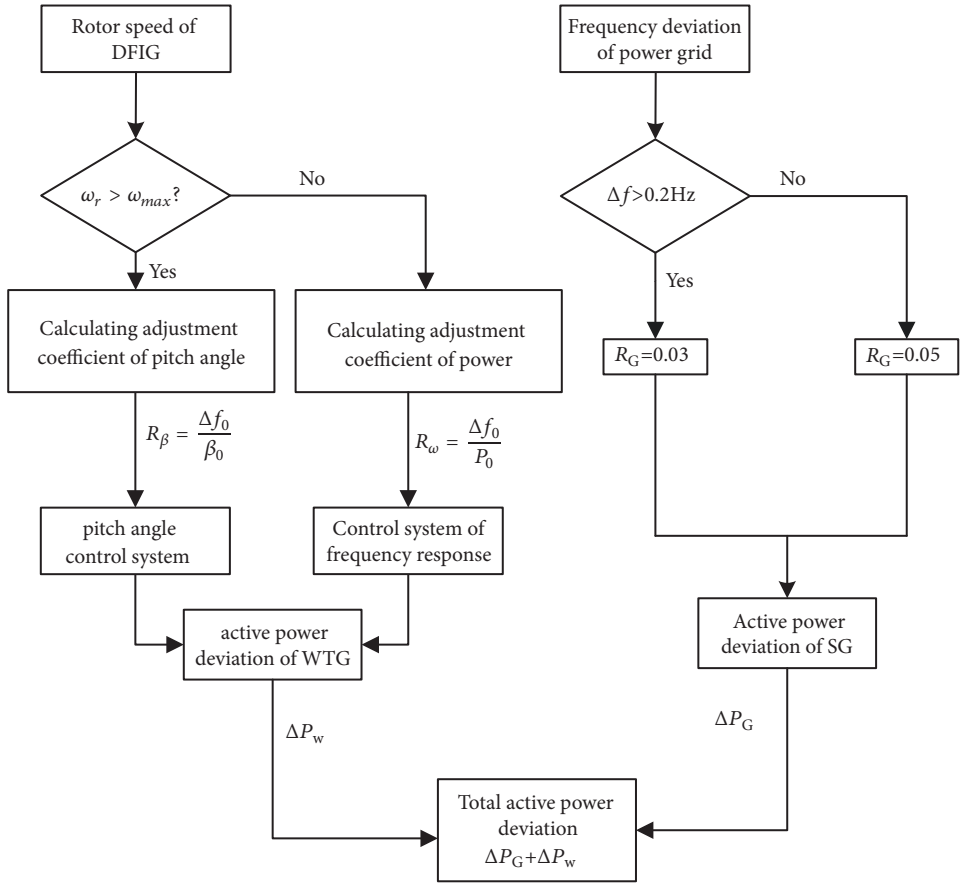

Figure 4: Flow chart of the proposed algorithm.

The practical implementation of the proposed algorithm can be found in Figure 4.

5. Simulations

In order to verify the effectiveness of the proposed frequency regulation strategy, we use Matlab/Simulink to carry out simulations, where the simulated model includes 4-generator and 2-area power grid [26]. The structure of this test system is shown in Figure 5. The power grid model consists of 3 traditional synchronous generators with a rated power of 700MW, and the inertial time constant is 6.5s. In addition, a DFIG-based wind turbine with equivalent capacity 800×15MW is connected to bus 2; the upper limit of active power per unit is 1, and the capacities of load L1 and L2 are 1200MW and 1800MW, respectively. The variable pitch time constant of the wind turbine is 3s and the rated wind speed is 12m/s. In the model, the DFIG-based wind turbine is operated in the condition of reducing 20% load, and there is a load jump on L1 at the time of 40s. In practical situations, wind farm participating in frequency regulation is generally selected in rich wind area. Moreover, when the scale of wind farm is very large, the gathering effect of wind energy is also significant as it can decrease the fluctuation of wind speed and output power. Accordingly, the wind speed becomes flatter. In this paper, the major focus is on the feasibility analysis of participation of wind turbine in frequency regulation; hence, we select a constant wind speed in the simulation. In this simulation, the output active power of DFIG and SG is per unite value based on S_B.

5.1. Load Variation in Maximum Power Point Tracking Area. Two cases are simulated in this study: (a) the frequency variation is less than 0.2 Hz and (b) the frequency variation is larger than 0.2 Hz.

In case (a), the wind speed is set to 9m/s. At the time of 40s, the applied load suddenly increases by 300MW, and then the frequency has a deviation less than 0.2Hz. The adjustment coefficients of the SG, R_G, are set to 0.03, 0.04, and 0.05, respectively. The corresponding simulation results are shown in Figure 6.

In Figure 6, we find that the frequency regulation output of the SG is gradually reduced as long as the adjustment coefficient increases (Figure 6(b)), while the frequency regulation output of the DFIG-based wind turbine is gradually increased (Figure 6(c)). From the point of view of the system frequency recovery, the frequency recovery response is the best when we set R_G=0.03 as shown in Figure 6(a). However, if the adjustment coefficient of the SG is small, the frequency regulation output of DFIG is limited as shown in Figure 6(c).

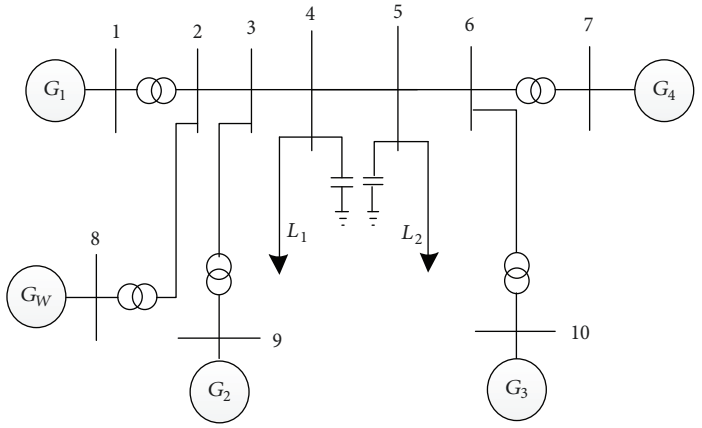

FIGURE 5: The structure of 2-area test system.

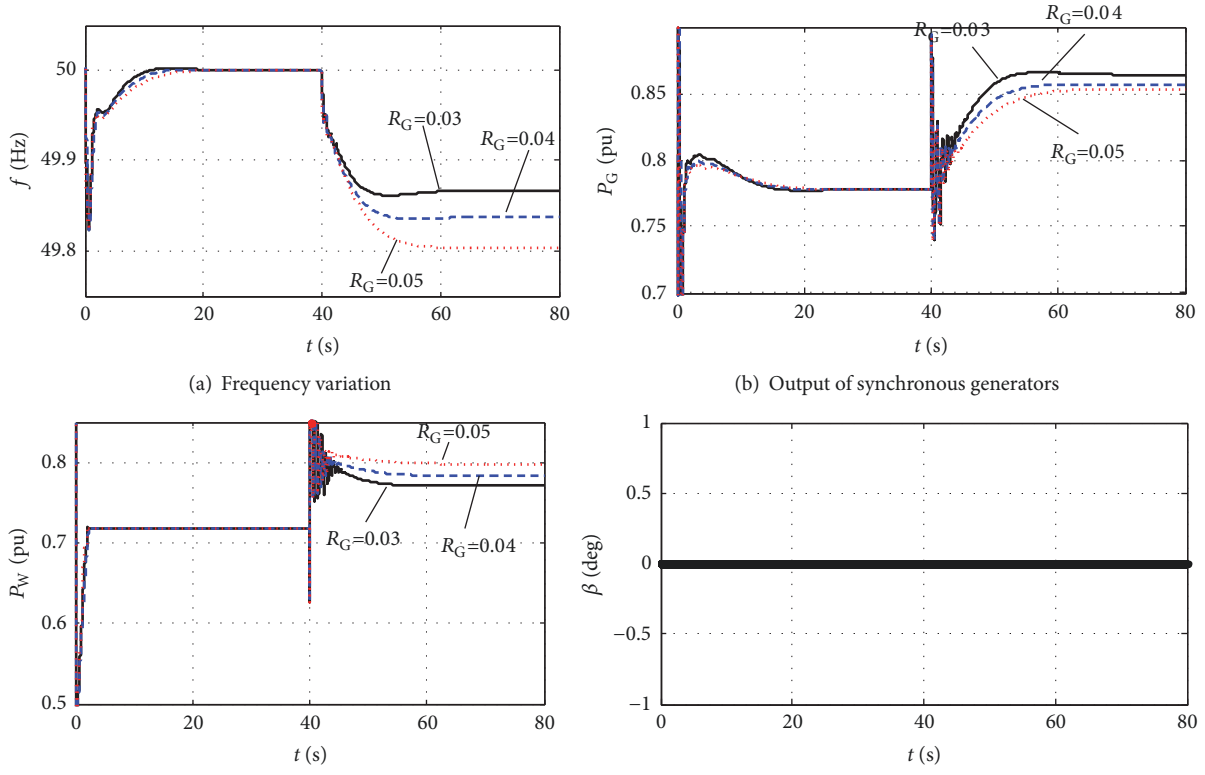

(a) Frequency variation

(b) Output of synchronous generators

(c) Output of DFIG-based wind turbine

(d) Pitch angle variation

FIGURE 6: Simulation results of the maximum power tracking area when frequency change is less than 0.2Hz.

When we set R_G=0.05, the frequency can also be retained within a bound around 0.2Hz, and the system frequency is relatively stable. Therefore, in order to increase the frequency regulation output of the DFIG-based wind turbines as much as possible and make full use of the restored power of the DFIG-based wind turbine for frequency regulation, we can take R_G=0.05. The pitch angle variation is also shown in Figure 6(d). The fluctuations shown in Figure 6 are due to the fact that the system is operated in the MTTP area and the frequency variation is larger than 0.2 Hz, so that it will take some transient periods to achieve a new steady state because of the limited control effect of Δf.

In case (b), the wind speed is also 9m/s. At the time of 40s, the applied load suddenly increases by 600MW; the frequency has a deviation larger than 0.2Hz. The adjustment coefficients of the synchronous generator are also the same as (a). The corresponding simulation results are shown in Figure 7. According to Figure 7(a), the frequency recovery response is the best when we set R_G=0.03. When the frequency change is greater than 0.2Hz, the system is in the

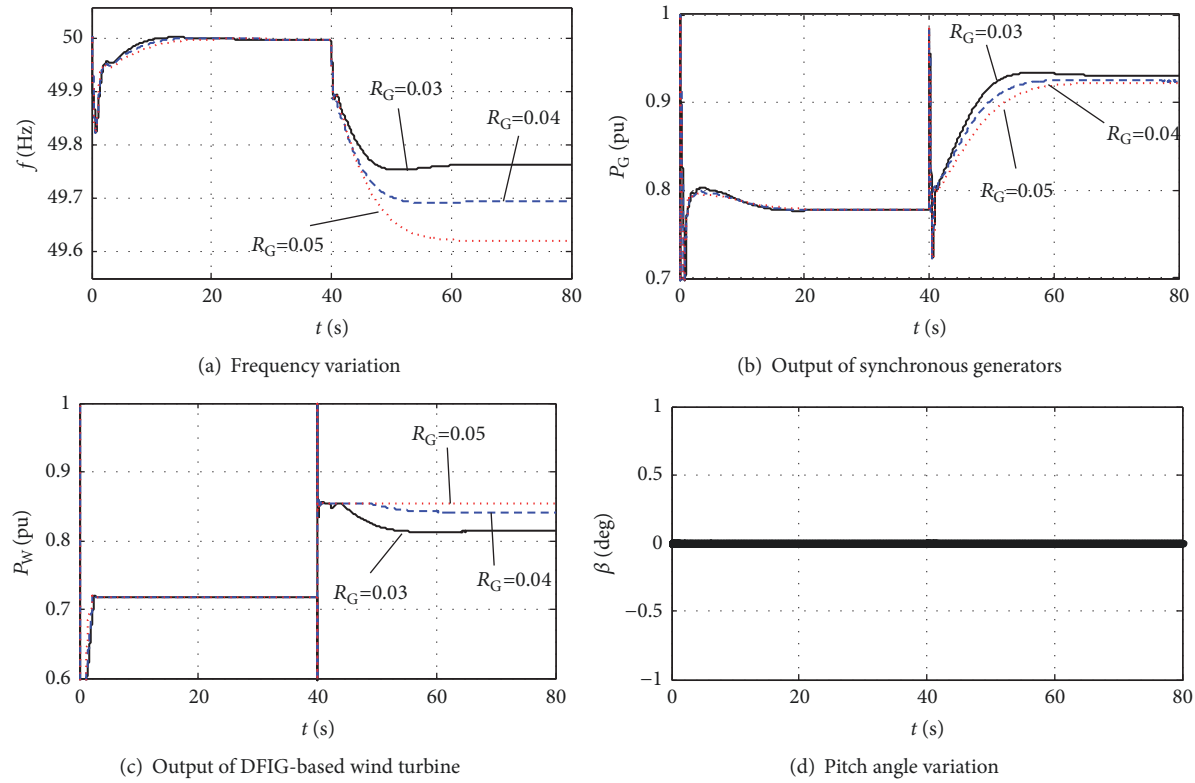

(a) Frequency variation

(b) Output of synchronous generators

(c) Output of DFIG-based wind turbine

(d) Pitch angle variation

FIGURE 7: Simulation curves of the maximum power tracking area when frequency change is greater than 0.2Hz.

emergency frequency modulation stage, and the ultimate goal is to improve the frequency recovery effect of the system. All synchronous generators and DFIGs should output power as much as possible, which are shown in Figures 7(b) and 7(c). According to the frequency recovery effect of Figure 7(a) and the pitch angle variation shown in Figure 7(d), the adjustment coefficient of the synchronous machine should be set as R_G=0.03.

5.2. Load Variation in Constant Power Area. Two cases at the constant power areas are simulated in this study: (a) the frequency variation is larger than 0.2 Hz, and (b) the frequency variation is less than 0.2Hz.

In case (a), in the constant power area, the wind energy captured by DFIG is mainly regulated by adjusting the pitch angle controlled by the pitch control mechanism. The wind speed is set as 15m/s. At the time of 40s, the load suddenly increases by 600MW; then the frequency has a deviation more than 0.2Hz. The adjustment coefficients of SG, R_G, are set as 0.03, 0.04, and 0.05 respectively. The simulation results are shown in Figure 8.

In Figure 8, when R_G is set as 0.03, the frequency recovery performance is the best among these three cases and the frequency deviation can be retained within a bound 0.02Hz as shown in Figure 8(a). Because the frequency deviation is more than 0.2Hz at one period during the process of frequency recovery, the magnitude of the frequency deviation is larger than the normal value. Thus, the system enters in the emergency control phase. In order to make the system frequency recover better, the DFIG-based wind turbine can make full use of the restored power for frequency regulation when the power is constant, the wind speed is fast, and the DFIG has much reserved power. From the frequency recovery result in Figure 8(a), when we take R_G=0.03, the DFIG-based wind turbine and synchronous generators can participate in the frequency regulation as much as possible (Figure 8(b)). Figure 8(c) also shows that the output of DFIG wind turbines has reached the upper limit of active power per unit. Thus, we can put 20% of the reserved power into the frequency regulation as a part of the frequency regulation power, such that the minimum value of the frequency drop and the steady-state deviation responses have been significantly improved. Figure 8(d) provides the corresponding pitch angle variation.

In case (b), the wind speed is set as 15m/s. At the time of 40s, the load suddenly increases by 300MW; the frequency has a deviation less than 0.2Hz. The adjustment coefficients of SG, R_G, are set to 0.03, 0.04, and 0.05, respectively. The simulation results are shown in Figure 9. When the system frequency is reduced within 0.2Hz, the frequency can be restored well when R_G = 0.03, 0.04, and 0.05 according to the frequency variation in Figure 9(a). Figure 9(d) shows that when R_G = 0.05, the action range of pitch angle is the largest, reaching 2.8°, and the reserve power of DFIG released amounts to 0.07 pu (Figure 9(b)), which reduces the steady-state frequency deviation of the system to 0.15 Hz. This shows that the DFIG effectively reduces the power change rate of

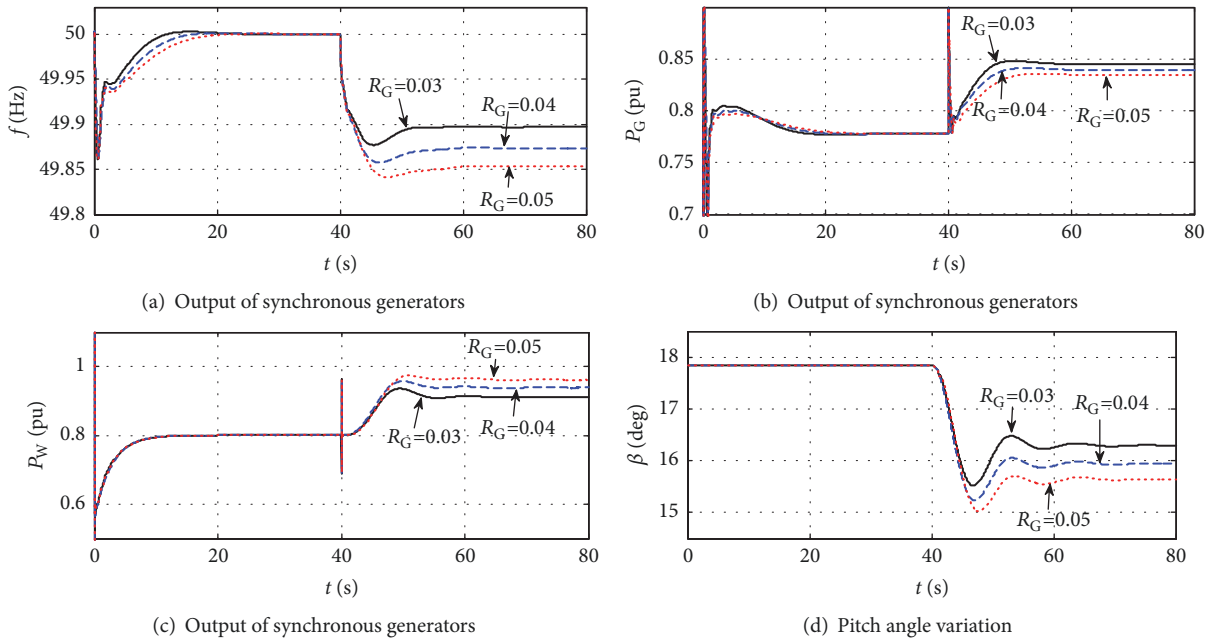

(a) Output of synchronous generators

(b) Output of synchronous generators

(c) Output of synchronous generators

(d) Pitch angle variation

FIGURE 8: Simulation diagram of the power constant area when frequency variation is greater than 0.2Hz.

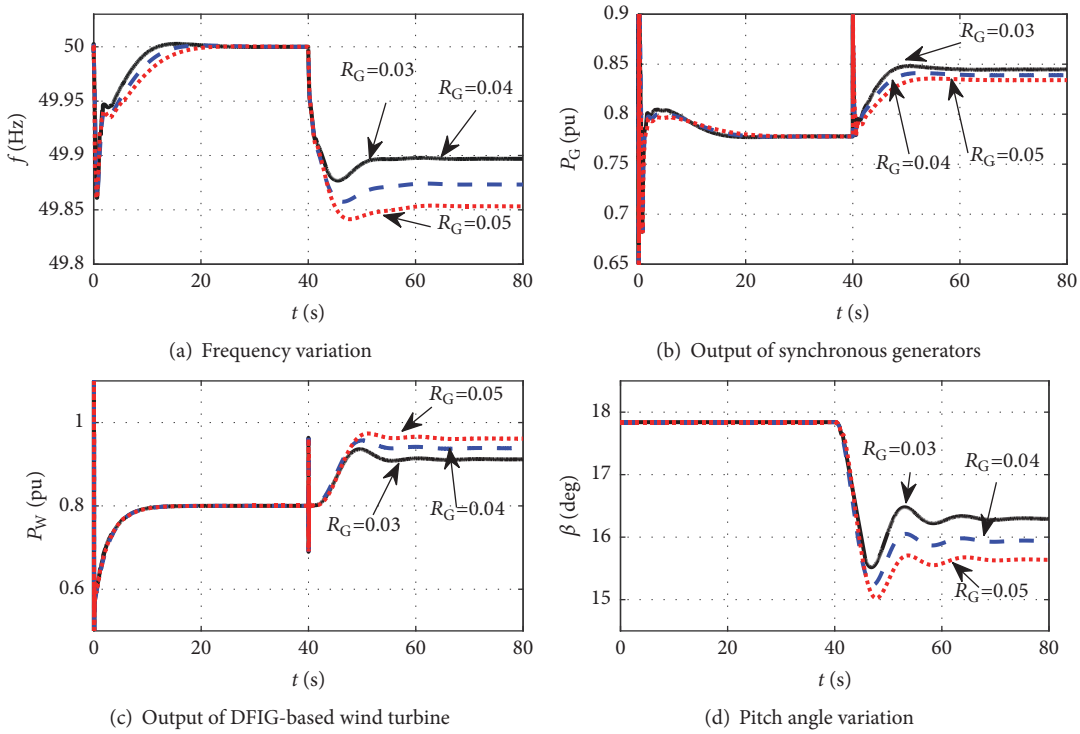

(a) Frequency variation

(b) Output of synchronous generators

(c) Output of DFIG-based wind turbine

(d) Pitch angle variation

FIGURE 9: Simulation diagram of the power constant area when frequency variation is less than 0.2Hz.

SG in the initial stage of frequency change (Figure 9(c)) and can continuously provide active power effective support for power grid.

In the process of frequency modulation, the reserve power of DFIG can be fully used for frequency regulation by increasing the power output of DFIG, thus indirectly reducing the wind abandonment. The simulation results of Figure 9 show that when the frequency varies within the allowable range, the larger the R_G value is, the smaller the static adjustment coefficient R_β of pitch angle will be. The range of pitch angle action will be larger, and the frequency regulation capability of DFIG will be enhanced, so that it can

undertake more power output and further reduce the steady-state frequency deviation of power grid.

6. Conclusions

In this paper, we presented a control strategy for system with the wind turbines being incorporated into the frequency regulation by further tailoring the primary frequency regulation principle of traditional synchronous generators. The DFIG can provide inertial power support to the power grid and participate in the frequency regulation together with the synchronous generators. Through theoretical analysis and simulation verifications, the following conclusions can be obtained:

(1) The wind turbines with adjustable frequency can effectively undertake the frequency regulation responsibility of the power grid, and the frequency regulation output between the synchronous generators and the DFIG-based wind turbines can be coordinated and allocated by adjusting R_{G*} and R_{W*}.

(2) The variable difference coefficient of DFIG in different wind speed sections is defined and calibrated. In corresponding to the wind speed changes in real time, the frequency regulation output can be determined considering the current reserved capacity.

(3) Through coordinating the frequency regulation output between the DFIG and the synchronous generators, the frequency deviation is retained within the allowable ranges, and the resorted power of the DFIG-based wind turbine can be used for the frequency regulation as much as possible. Those proposed methods can not only meet the demand of the power network frequency regulation but also minimize the "abandoned air" generated by the DIFG load reduction.

Future work will focus on validating the proposed coordinate and control strategies under more realistic wind speed and operation scenarios.

Data Availability

The data used to support the findings of this study are available from the corresponding author upon request.

Conflicts of Interest

The authors declare that there are no conflicts of interest regarding the publication of this paper.

Acknowledgments

This research was supported in part by the Yunnan Electrical Power Experiment Institute.

References

[1] J. Dong, G. Xue, M. Dong, and X. Xu, "Energy-saving power generation dispatching in China: Regulations, pilot projects and policy recommendations - A review," *Renewable & Sustainable Energy Reviews*, vol. 43, pp. 1285–1300, 2015.

[2] R. Saidur, N. A. Rahim, M. R. Islam, and K. H. Solangi, "Environmental impact of wind energy," *Renewable & Sustainable Energy Reviews*, vol. 15, no. 5, pp. 2423–2430, 2011.

[3] G. Lalor, A. Mullane, and M. O'Malley, "Frequency control and wind turbine technologies," *IEEE Transactions on Power Systems*, vol. 20, no. 4, pp. 1905–1913, 2005.

[4] J. Ekanayake and N. Jenkins, "Comparison of the response of doubly fed and fixed-speed induction generator wind turbines to changes in network frequency," *IEEE Transactions on Energy Conversion*, vol. 19, no. 4, pp. 800–802, 2004.

[5] H. Bevrani, A. Ghosh, and G. Ledwich, "Renewable energy sources and frequency regulation: Survey and new perspectives," *IET Renewable Power Generation*, vol. 4, no. 5, pp. 438–457, 2010.

[6] R. G. de Almeida and J. A. Peças Lopes, "Participation of doubly fed induction wind generators in system frequency regulation," *IEEE Transactions on Power Systems*, vol. 22, no. 3, pp. 944–950, 2007.

[7] J. E. Sierra and M. Santos, "Wind and payload disturbance rejection control based on adaptive neural estimators: application on quadrotors," *Complexity*, vol. 2019, Article ID 6460156, 20 pages, 2019.

[8] Q. Guo, Z. Sun, Y. Zhang, and W. Xu, "Time-delayed feedback control in the multiple attractors wind-induced vibration energy harvesting system," *Complexity*, vol. 2019, Article ID 7973823, 11 pages, 2019.

[9] N. Nguyen and J. Mitra, "An analysis of the effects and dependency of wind power penetration on system frequency regulation," *IEEE Transactions on Sustainable Energy*, vol. 7, no. 1, pp. 354–363, 2016.

[10] J. C. G. Arispe and H. J. Florero, "Wind farms integration in power system and frequency regulation effects," *IEEE Latin America Transactions*, vol. 15, no. 4, pp. 698–704, 2017.

[11] N. Nguyen and J. Mitra, "An analysis of the effects and dependency of wind power penetration on system frequency regulation," in *Proceedings of the 2016 IEEE Power and Energy Society General Meeting (PESGM)*, pp. 1-1, Boston, Mass, USA, July 2016.

[12] X. Tian, W. Wang, L. Yan et al., "Coordinative control strategy of virtual inertia and primary frequency of DFIGs based wind farms," in *Proceedings of the 2016 IEEE PES Asia Pacific Power and Energy Engineering Conference, APPEEC 2016*, pp. 2169–2174, Xi'an, China, October 2016.

[13] Z. Zhang, Y. Wang, H. Li, and X. Su, "Comparison of inertia control methods for DFIG-based wind turbines," in *Proceedings of the 2013 IEEE ECCE Asia Downunder - 5th IEEE Annual International Energy Conversion Congress and Exhibition, IEEE ECCE Asia 2013*, pp. 960–964, VIC, Melbourne, Australia, 2013.

[14] A. H. M. I. Ferdous, M. R. I. Sheikh, and M. A. Shobug, "Controlling of frequency fluctuation of wind turbine generator using wind speed controlled pitch controller," in *Proceedings of the 2nd International Conference on Electrical, Computer and Telecommunication Engineering, ICECTE 2016*, pp. 1–4, Rajshahi, Bangladesh, 2016.

[15] S. Hu and G. Zhu, "A vector control strategy of grid-connected brushless doubly fed induction generator based on the vector control of doubly fed induction generator," in *Proceedings of the 31st Annual IEEE Applied Power Electronics Conference and Exposition, APEC 2016*, pp. 3310–3316, Long Beach, Calif, USA, March 2016.

[16] J. Zhao, X. Lü, Y. Fu, and X. Hu, "Dynamic frequency control strategy of wind/photovoltaic/diesel microgrid based on DFIG

virtual inertia control and pitch angle control," *Proceedings of the Chinese Society of Electrical Engineering*, vol. 35, no. 15, pp. 3815–3822, 2015.

[17] J. Zhao, X. Lyu, Y. Fu, X. Hu, and F. Li, "Coordinated microgrid frequency regulation based on dfig variable coefficient using virtual inertia and primary frequency control," *IEEE Transactions on Energy Conversion*, vol. 31, no. 3, pp. 833–845, 2016.

[18] A. Žertek, G. Verbič, and M. Pantoš, "A novel strategy for variable-speed wind turbines' participation in primary frequency control," *IEEE Transactions on Sustainable Energy*, vol. 3, no. 4, pp. 791–799, 2012.

[19] K. V. Vidyanandan and N. Senroy, "Primary frequency regulation by deloaded wind turbines using variable droop," *IEEE Transactions on Power Systems*, vol. 28, no. 2, pp. 837–846, 2013.

[20] J. Van De Vyver, J. D. M. De Kooning, B. Meersman, L. Vandevelde, and T. L. Vandoorn, "Droop control as an alternative inertial response strategy for the synthetic inertia on wind turbines," *IEEE Transactions on Power Systems*, vol. 31, no. 2, pp. 1129–1138, 2016.

[21] S. Ghosh, S. Kamalasadan, N. Senroy, and J. Enslin, "Doubly fed induction generator (DFIG)-based wind farm control framework for primary frequency and inertial response application," *IEEE Transactions on Power Systems*, vol. 31, no. 6, pp. 1861–1871, 2016.

[22] C. Wei, Z. Zhang, W. Qiao, and L. Qu, "Reinforcement-learning-based intelligent maximum power point tracking control for wind energy conversion systems," *IEEE Transactions on Industrial Electronics*, vol. 62, no. 10, pp. 6360–6370, 2015.

[23] C. Wei, Z. Zhang, W. Qiao, and L. Qu, "An adaptive network-based reinforcement learning method for MPPT control of PMSG wind energy conversion systems," *IEEE Transactions on Power Electronics*, vol. 31, no. 11, pp. 7837–7848, 2016.

[24] I. Marović, I. Sušanj, and N. Ožanić, "Development of ANN model for wind speed prediction as a support for early warning system," *Complexity*, vol. 2017, Article ID 3418145, 10 pages, 2017.

[25] F. Cheng, L. Qu, W. Qiao, C. Wei, and L. Hao, "Fault diagnosis of wind turbine gearboxes based on DFIG stator current envelope analysis," *IEEE Transactions on Sustainable Energy*, Article ID 2859764, pp. 1–9, 2018.

[26] P. Kundur, N. J. Balu, and M. G. Lauby, *Power System Stability and Control*, McGraw-hill, New York, NY, USA, 1994.

Hindawi
Complexity
Volume 2019, Article ID 9053858, 11 pages
https://doi.org/10.1155/2019/9053858

Research Article

Homeomorphism Mapping Based Neural Networks for Finite Time Constraint Control of a Class of Nonaffine Pure-Feedback Nonlinear Systems

Jianhua Zhang[1,2] **Quanmin Zhu**[3] **Yang Li**[1,2] **and Xueli Wu**[1,2]

[1]*Hebei University of Science and Technology, Shijiazhuang, Hebei 050018, China*
[2]*Hebei Provincial Research Center for Technologies in Process Engineering Automation, Shijiazhuang, Hebei 050018, China*
[3]*Department of Engineering Design and Mathematics, University of the West of England, Coldharbour Lane, Bristol BS16 1QY, UK*

Correspondence should be addressed to Jianhua Zhang; jianhuazhang@aliyun.com

Received 15 February 2019; Revised 2 April 2019; Accepted 24 April 2019; Published 13 May 2019

Guest Editor: Chun Wei

This paper proposes a new scheme for solving finite time neural networks adaptive tracking control issue for the nonaffine pure-feedback nonlinear system. The procedure, based on homeomorphism mapping and backstepping, effectively deals with constraint control and design difficulty induced by pure-feedback structure. The most outstanding novelty is that finite time adaptive law is proposed for training weights of neural networks. Furthermore, by combining finite time adaptive law and Lyapunov-based arguments, a valid finite time adaptive neural networks controller design algorithm is presented to ensure that system is practical finite stable (PFS) rather than uniformly ultimately bounded (UUB). Because of using the finite time adaptive law to training weights of neural networks, the closed-loop error system signals are in assurance of bounded in finite time. Benchmark simulations have well demonstrated effectiveness and efficiency of the proposed approach.

1. Introduction

During the past decades, lots of studies have been done to solve neural networks (NNs) control and improve the adaptive law for training neural networks weights [1–3]. Among these works, the core is NNs which are used as online approximation functions for the unknown nonlinearities, due to their inherent approximation capabilities [4, 5]. Almost all the neural adaptive control designs and stability analyses are Lyapunov uniformly ultimately bounded (UUB) results [5]; based on the Krasovskii–LaSalle invariance principle, it is challenging to establish a generalized powerful framework for neural control [6–8], even though it has been used to get sufficient conditions for smooth stabilization for closed-loop systems [9–11].

Traditionally, Quadratic Lyapunov Functions are in common used to construct for analysis and control design of linear and nonlinear even time delay dynamic systems [12, 13]. There also exist some other formats of Lyapunov functions, such as integral Lyapunov function [14], barrier Lyapunov function [15, 16], and vector Lyapunov functions [17, 18]. Such attempts have enhanced Lyapunov function applications in control system design [19], for example, integral Lyapunov function for controller singularity problems and barrier Lyapunov function for output constraint problems. Nonlinear systems differ from linear system, because the complexity of the relation between states and input and therefore numerical techniques (open solutions) have played a significant role in controller design process [20–22]. Young's Inequality as an important lemma has been widespread used to realize UUB (uniformly ultimately bounded) in neural network based adaptive control [23].

In terms of complex of system structure such as pure-feedback and nonaffine, mean value theorem [24] is popular to use to eliminate. Due to its universal approximation capability for nonlinear systems, neural network has been extensively utilized to achieve modelling. Many elegant model structure design techniques, such as strict-feedback,

pure-feedback, affine form, and nonaffine systems [3, 25, 26], have been obtained based on backstepping procedure and Lyapunov synthesis.

Based on virtual control and iterative learning control [25], backstepping procedure provided an important methodology to control affine or nonaffine, strict-feedback, or pure-feedback form SISO nonlinear uncertain systems, which are split into several subsystems. In every subsystem, neural networks approximate the unknown nonlinear systems with adaptive law, based on Lyapunov stability theory, then the systems achieve the asymptotic stability or uniformly ultimately bounded stable. In order to better exploit the application of adaptive neural networks [27, 28], finite time stable results are more meaningful for uncertain system [29, 30], high order stochastic nonlinear system [31], and interconnected nonlinear system [32].

It should be noted that the research on finite time neural networks control is still in a very beginning stage. Although there exist a few of adaptive finite control algorithms which have been developed for some special systems and bench tested with simulations and applications [33–35], it is very hard to extend the research results to the general systems or algorithms. The key issue is how to systematically obtain finite time adaptive law of neural networks [9, 36] weight from finite time convergence of close loop systems [37]. In regard to neural network based such adaptive control to the authors' best knowledge, there are a few results about finite time adaptive neural networks control. That is because it is not easy to design the finite time neural networks adaptive controller and lack of relevant inequality skills to finish finite time stability analysis. There has been any reference to show finite time adaptive algorithm for weights of NNs having been expanded to solve the problems of finite control for pure-feedback nonaffine nonlinear systems.

Motivated by the above critical analyses, we investigated neural backstepping control via finite time adaptive algorithm. At the first stage, the homeomorphism mapping is proposed in place of barrier Lyapunov functions and commonly utilized in traditional constraints control. Then with finite adaptive algorithm, adaptive neural networks backstepping control procedure is designed for nonaffine pure-feedback nonlinear systems. Sufficient condition is given via Lyapunov finite time stability theory to make sure all the signals in the closed-loop system are global uniformly bounded in finite time and the tracking error is remained in a bounded compact set. The main contributions of this paper can be summarized as follows:

(1) This paper is the first study to propose the finite time adaptive law based on Young's inequality skill for adaptive neural networks control. The main advantages are that adaptive neural networks controls achieve finite time stabilization including weights of neural networks and closed-loop control system uniformly ultimately bounded stable in finite time.

(2) To keep full state constraints in a bounded compact set, the homeomorphism mapping is proposed in place of barrier Lyapunov functions and commonly utilized in traditional constraints control.

(3) New finite time adaptive neural networks techniques, including virtual control and finite adaptive law, are introduced for ensuring the successful design of the finite time adaptive neural networks backstepping control.

The rest of this paper is organized as follows. Section 2 gives problem formulation and preliminaries, including some definitions and necessary inequality with lemmas. Nonaffine pure-feedback nonlinear systems finite time adaptive neural networks control is considered in Section 3, and a new finite time adaptive law is developed for training neural networks. Lyapunov finite time stable theory is used to guarantee the closed-loop system signals with prescribed performance in finite time. Simulation study is presented in Section 4 to indicate efficiency and effectiveness of the procedure. The conclusion and future works are discussed in Section 5.

2. Problem Description and Preliminaries

In this section, problem description, the notation, basic definitions, and lemmas on the system stability are presented. Consider the following nonlinear system:

$$\begin{aligned} \dot{\xi}(t) &= \varphi(\xi(t), u(t), t), \quad t \geq 0 \\ \xi(t) &= \phi(t), \quad t = 0 \\ \zeta(t) &= \psi(\xi(t), u(t), t) \end{aligned} \tag{1}$$

where $\xi = (\xi_1 \ \xi_2 \ \cdots \ \xi_n)^T \in \mathfrak{R}^n$, $u \in \mathfrak{R}$, $\zeta \in \mathfrak{R}^m$, $\phi(t)$ are state variable, control input, output, and initial condition, respectively, and $\varphi(\cdot)$, $\psi(\cdot)$ are nonlinear smooth functions.

The ideal output is $\zeta_d(t)$; therefore, the objective is to design an adaptive state feedback to ensure the output $\zeta(t)$ tracking $\zeta_d(t)$ and controller in the form

$$\begin{aligned} u(t) &= \alpha\left(\xi(t), \widehat{\theta}(t)\right) \\ \dot{\widehat{\theta}}(t) &= \beta\left(\xi(t), \widehat{\theta}(t)\right) \end{aligned} \tag{2}$$

where $\widehat{\theta}$ indicate the estimated values of unknown parameters and the θ^* indicate the ideal values. For system (1) with the homeomorphism mapping,

$$H : (\underline{a}_1 \ \overline{a}_1) \times (\underline{a}_2 \ \overline{a}_2) \times \cdots \times (\underline{a}_n \ \overline{a}_n) \longrightarrow \mathfrak{R}^n \tag{3}$$

propose to transform the system to realize the constraints control, such as $x = H(\xi)$, and $\xi \in (\underline{a}_1 \ \overline{a}_1) \times (\underline{a}_2 \ \overline{a}_2) \times \cdots \times (\underline{a}_n \ \overline{a}_n)$, $x \in \mathfrak{R}^n$, and then system (1) changes into

$$\begin{aligned} \dot{x}(t) &= f(x(t), u(t), t), \quad t \geq 0 \\ x(t) &= \varsigma(t), \quad t = 0 \\ y(t) &= g(x(t), u(t), t) \end{aligned} \tag{4}$$

where $x = (x_1 \ x_2 \ \cdots \ x_n)^T \in \mathfrak{R}^n$, $u \in \mathfrak{R}$, $y \in \mathfrak{R}$, $\varsigma(t)$ indicate the state, control, output, and initial condition, respectively, and $f(\cdot)$, $g(\cdot)$ are nonlinear smooth functions.

For the homeomorphism mapping, both $x = H(\xi)$ and $\xi = H^{-1}(x)$ exist, and specially, $y - y_d = H(\xi - \xi_d)$ hold.

The adaptive controller in the form

$$\begin{aligned} u(t) &= \alpha\left(x(t), \widehat{\theta}(t)\right) \\ \dot{\widehat{\theta}}(t) &= \beta\left(x(t), \widehat{\theta}(t)\right) \end{aligned} \tag{5}$$

and the output of system (4) $y(t)$ track the $y_d(t)$.

If controller (5) is designed based on system (4), then put the controller into system (1); the states ξ are constraint where $\xi \in (\underline{a}_1 \ \overline{a}_1) \times (\underline{a}_2 \ \overline{a}_2) \times \cdots \times (\underline{a}_n \ \overline{a}_n)$, because the states ξ and x satisfy the of the homeomorphism mapping relation (3).

Remark 1. There are lots of researches about constraint control [15, 38, 39], which employ the barrier Lyapunov functions to realize constraints. The controller design is relatively complicated because of the complexity of derivation of barrier Lyapunov functions. The homeomorphism mapping skill is easy to achieve, as the mapping is used for transformation of states, which is independent for the controller design. After that, a new model emerged, then based on the new model, all control methods can be used, such as sliding model control [40], adaptive control [26, 41], and especially neural networks control which applied without model information. Such homeomorphism mapping is easy to choose as

$$\begin{aligned} \xi &= \frac{2a}{\pi}\arctan(x), \\ \xi &= b\tanh(x), \\ \xi &= \operatorname{sgn}(x)\, c\left(1 - e^{-x^2}\right)^{1/2} \end{aligned} \tag{6}$$

which satisfy $x \in \mathfrak{R}$ and $|\xi| < a, b, c$, respectively.

A continuous nonaffine pure-feedback nonlinear system can be described as follows:

$$\begin{aligned} \dot{\xi}_i &= \varphi_i\left(\overline{\xi}_{i+1}\right), \quad 1 \le i \le n-1 \\ \dot{\xi}_n &= \varphi_n\left(\overline{\xi}_n, u\right) \\ \zeta &= \xi_1 \end{aligned} \tag{7}$$

where $\xi = (\xi_1 \ \xi_2 \ \cdots \ \xi_n)^T \in \mathfrak{R}^n$, $u \in \mathfrak{R}$, $\zeta \in \mathfrak{R}$, $\varphi(t)$ indicate the state, control, output, and initial condition, respectively, and $\overline{\xi}_i = [\xi_1, \xi_2, \ldots, \xi_i]^T \in \mathfrak{R}^i$, $\varphi_i(\cdot)$ are smooth nonlinear functions.

Assumption 2. The nonlinear function φ in system (1) is as follows:

$$\begin{aligned} \frac{\partial \varphi_i}{\partial \xi_{i+1}} &\neq 0, \\ \frac{\partial \varphi_n}{\partial u} &\neq 0 \end{aligned} \tag{8}$$

when $1 \le i \le n-1$.

Based on homeomorphism mapping (7), nonlinear pure-feedback nonaffine system can be described as follows:

$$\begin{aligned} \dot{x}_i &= f_i\left(\overline{x}_{i+1}\right), \quad 1 \le i \le n-1 \\ \dot{x}_n &= f_n\left(\overline{x}_n, u\right) \\ y &= x_1 \end{aligned} \tag{9}$$

where $\overline{x}_i = [x_1, x_2, \ldots, x_i]^T \in \mathfrak{R}^i$, $x = (x_1 \ x_2 \ \cdots \ x_n)^T \in \mathfrak{R}^n$, $u \in \mathfrak{R}$, $y \in \mathfrak{R}$, and $\varphi(t)$ indicate the state, control, output, and initial condition, respectively, and $f_i(\cdot)$ are nonlinear smooth functions.

Assumption 3. Nonlinear function f_i in system (9) is as follows:

$$\begin{aligned} \frac{\partial f_i}{\partial x_{i+1}} &\neq 0, \\ \frac{\partial f_n}{\partial u} &\neq 0 \end{aligned} \tag{10}$$

when $1 \le i \le n-1$.

Notation. Throughout this paper, $W \in \mathfrak{R}^{m \times n}$ represents the matrix, $W = [w_{ij}]_{m \times n}$, rational number η, and matrix, matrix W^η denote element-by-element powers, $W^\eta = [w_{ij}^\eta]_{m \times n}$, $\widetilde{W}^{\eta^T}$ denote the transposition of matrix $\widetilde{W}^\eta$, such as $\widetilde{W}^{\eta^T} = (\widetilde{W}^\eta)^T$. W^*, $\widehat{W}$, $\widetilde{W}$ indicate ideal weight, estimated weight, and error between ideal and estimated weight.

In brief, the following radial basis function (RBF) NN is used to approximate the continuous function $F(x) : \mathfrak{R}^n \longrightarrow \mathfrak{R}$ over a compact set

$$F_{NN}(x, W) = W^T \Psi(x) \tag{11}$$

where input $x \in \Omega \subset \mathfrak{R}^n$, weight vector $W = [w_1 \ \cdots \ w_l]^T \in \mathfrak{R}^l$, and node vector $\Psi(x) = [\psi_1(x) \ \cdots \ \psi_l(x)]^T$, with the element $\psi_i(x)$ being chosen as the commonly used Gaussian function as below

$$\psi_i(x) = \exp\left[\frac{-(x - \mu_i)^T (x - \mu_i)}{\eta_i^2}\right], \quad i = 1, 2, \ldots, l. \tag{12}$$

where $\mu_i = [\mu_{i1} \ \cdots \ \mu_{in}]^T$, the center of the receptive field, and η_i is the width of the Gaussian function.

It has been proven that RBF NN can approximate any continuous function over a compact set $\Omega_x \subset \mathfrak{R}^n$ as

$$F(x) = W^{*T} \Psi(x) + \varepsilon(x) \tag{13}$$

where W^* is the ideal NN weight and $\varepsilon(x)$ is the NN approximation error.

$$W^* = \arg\min_{W \in \mathfrak{R}^l} \left\{\sup\left|F(x) - W^T \Psi(x)\right|\right\} \tag{14}$$

Definition 4. Consider system $\dot{x} = f(x, u)$, where x is a state vector and u is the input vector. The solution is practical finite stable (PFS) if for all $x(t_0) = x_0$, there exist $\varepsilon > 0$ and $T(\varepsilon, x_0) < \infty$, such that $\|x\| < \varepsilon$, for all $t \ge t_0 + T$.

Lemma 5. *Consider system $\dot{x} = f(x,u)$; suppose that there exist continuous function $V(x)$ and scalars $\lambda > 0$, $0 < \alpha < 1$, and $0 < \eta < \infty$ such that*

$$\dot{V}(x) \le -\lambda V^{\alpha}(x) + \eta \tag{15}$$

Then, the trajectory of system $\dot{x} = f(x,u)$ is PFS.

Proof. There exists a scalar $0 < \theta \le 1$ such that inequality (15) can be expressed as

$$\dot{V}(x) \le -\theta\lambda V^{\alpha}(x) - (1-\theta)\lambda V^{\alpha}(x) + \eta \tag{16}$$

Clearly, $\dot{V}(x) \le -\theta\lambda V^{\alpha}(x)$ if $V^{\alpha}(x) > \eta/\lambda(1-\theta)$. According to Lemma 5, the decrease of $V(x)$ in finite time drives the trajectories of the closed-loop system into $V^{\alpha}(x) \le \eta/\lambda(1-\theta)$. Therefore, the trajectories of the closed-loop system are bounded in finite time as

$$\lim_{\theta \longrightarrow \theta_0} x \in \left(V^{\alpha}(x) \le \frac{\eta}{\lambda(1-\theta)} \right) \tag{17}$$

where $0 < \theta_0 < 1$. And the time needed to reach (17) is bounded as

$$T \le \frac{V^{1-\alpha}(x_0)}{\lambda\theta_0(1-\alpha)} \tag{18}$$

where $V(x_0)$ is the initial value of $V(x)$. □

Lemma 6 ([42], Young's inequality). *For any constant $a, b \in \mathfrak{R}$, the following inequality holds:*

$$ab \le \frac{1}{p}a^{p} + \frac{1}{q}b^{q} \tag{19}$$

where $p > 1$, $q > 1$, and $1/p + 1/q = 1$.

Remark 7. Based on Young's inequality, then the following inequalities hold:

$$z\varepsilon \le \frac{3}{4}z^{4/3} + \frac{1}{4}\varepsilon^{4} \tag{20}$$

$$-\widetilde{W}^{T}\widehat{W}^{1/3} \le -\frac{1}{2}\widetilde{W}^{2/3^{T}}\widetilde{W}^{2/3} + W^{*2/3^{T}}W^{*2/3} \tag{21}$$

There are two key inequalities in adaptive neural networks finite time control.

3. Control Design and Stability Analysis

Consider system (9), using the coordinate transform as

$$\begin{aligned} z_1 &= x_1 - y_d \\ z_i &= x_i - \alpha_{i-1}, \quad i = 2, 3, \ldots, n \\ z_{n+1} &= u - \alpha_n \end{aligned} \tag{22}$$

where α_i is the virtual control and the ideal virtual control are

$$\begin{aligned} \alpha_1^{*} &= -k_1 z_1^{1/3} + x_2 - f_1 + \dot{y}_d \\ \alpha_i^{*} &= -z_{i-1} - k_i z_i^{1/3} + x_{i+1} - f_i + \dot{\alpha}_{i-1}^{*} \quad 2 \le i \le n-1 \\ \alpha_n^{*} &= -z_{n-1} - k_n z_n^{1/3} + u - f_n + \dot{\alpha}_{n-1}^{*} \end{aligned} \tag{23}$$

In the first step, consider system

$$z_1 = x_1 - y_d \tag{24}$$

Then it has

$$\dot{z}_1 = f_1(\overline{x}_2) - \dot{y}_d \tag{25}$$

Based on ideal virtual control law (23), choose the NN to approximate the nonlinear system f_1, $\overline{x}_2 \in \Omega_1 \subset \mathfrak{R}^2$, and Ω_1 is compact set

$$f_1(\overline{x}_2) - \dot{y}_d = W_1^{T*}\Psi_1(\overline{x}_2) + \varepsilon_1 \tag{26}$$

Therefore

$$\dot{z}_1 = W_1^{*T}\Psi_1(\overline{x}_2) + \varepsilon_1 \tag{27}$$

Choose the practical virtual control law

$$\alpha_1 = -k_1 z_1^{1/3} + x_2 - \widehat{W}_1^{T}\Psi_1(\overline{x}_2) \tag{28}$$

Choose the adaptive law

$$\dot{\widehat{W}}_1 = \Gamma_1\left[z_1\Psi_1(\overline{x}_2(t)) - \sigma_1\widehat{W}_1^{1/3} \right] \tag{29}$$

where $\Gamma_1 = \Gamma_1^{T} > 0$ and $\sigma_1 > 0$ is positive constant design parameters.

Then based on (27) and (28)

$$\begin{aligned} \dot{z}_1 = {} & W_1^{*T}\Psi_1(\overline{x}_2) + \varepsilon_1 - k_1 z_1^{1/3} + x_2 - \alpha_1 \\ & - \widehat{W}_1^{T}\Psi_1(\overline{x}_2) \end{aligned} \tag{30}$$

let

$$z_2 = x_2 - \alpha_1 \tag{31}$$

therefore

$$\dot{z}_1 = -\widetilde{W}_1^{T}\Psi_1(\overline{x}_2) - k_1 z_1^{1/3} + z_2 + \varepsilon_1 \tag{32}$$

where

$$\widetilde{W}_1 = \widehat{W}_1 - W_1^{*} \tag{33}$$

Choose Lyapunov candidate function

$$V_1 = \frac{1}{2}z_1^{2} + \frac{1}{2}\widetilde{W}_1^{\mathrm{T}}\Gamma_1^{-1}\widetilde{W}_1 \tag{34}$$

then

$$\begin{aligned} \dot{V}_1 &= z_1\dot{z}_1 + \widetilde{W}_1^{\mathrm{T}}\Gamma_1^{-1}\dot{\widetilde{W}}_1 \\ &= -k_1 z_1^{4/3} + z_1 z_2 + z_1\varepsilon_1 - \sigma_1\widetilde{W}_1^{\mathrm{T}}\widehat{W}_1^{1/3} \end{aligned} \tag{35}$$

Based on inequalities from Lemma 6 and Remark 7, the following hold:

$$z_1\varepsilon_1 \le \frac{3}{4}z_1^{4/3} + \frac{1}{4}\varepsilon_1^{4} \tag{36}$$

and

$$-\sigma_1 \widetilde{W}_1^T \widehat{W}_1^{1/3} \le -\frac{\sigma_1}{2} \widetilde{W}_1^{(2/3)\mathrm{T}} \widetilde{W}_1^{2/3} + \sigma_1 W_1^{*(2/3)\mathrm{T}} W_1^{*2/3} \tag{37}$$

Then based on (35), it gives

$$\begin{aligned} \dot{V}_1 = &-\left(k_1 - \frac{3}{4}\right) z_1^{4/3} + z_1 z_2 - \frac{\sigma_1}{2} \widetilde{W}_1^{(2/3)\mathrm{T}} \widetilde{W}_1^{2/3} + \frac{1}{4}\varepsilon_1^4 \\ &+ \sigma_1 W_1^{*(2/3)\mathrm{T}} W_1^{*2/3} \end{aligned} \tag{38}$$

then it has

$$\begin{aligned} \dot{V}_1 &\le z_1 z_2 - \eta_1 \left(\frac{1}{2} z_1^2\right)^{2/3} - \eta_1 \left(\frac{1}{2} \widetilde{W}_1^{\mathrm{T}} \Gamma_1^{-1} \widetilde{W}_1\right)^{2/3} \\ &\quad + \frac{1}{4}\varepsilon_1^4 + \sigma_1 W_1^{*(2/3)\mathrm{T}} W_1^{*2/3} \\ &\le z_1 z_2 - \eta_1 V_1^{2/3} + \delta_1 \end{aligned} \tag{39}$$

where

$$\begin{aligned} \eta_1 &= \min\left(4^{1/3}\left(k_1 - \frac{3}{4}\right), \frac{\sigma_1}{2^{1/3}\left(\lambda_{\max}\left(\Gamma_1\right)\right)^{2/3}}\right) \\ \delta_1 &= \frac{1}{4}\varepsilon_1^4 + \sigma_1 W_1^{*(2/3)\mathrm{T}} W_1^{*2/3} \end{aligned} \tag{40}$$

The ith step $2 \le i \le n-1$

$$z_i = x_i - \alpha_{i-1} \tag{41}$$

Choose the virtual control law (23), choose the NN to approximate the nonlinear system $f_i(\overline{x}_{i+1}) - \dot{\alpha}_{i-1}$, $\overline{x}_{i+1} \in \Omega_i \subset \mathfrak{R}^{i+1}$, and Ω_i is compact set

$$f_i\left(\overline{x}_{i+1}(t)\right) - \dot{\alpha}_{i-1} = W_i^{*T} \Psi_i\left(\overline{x}_{i+1}\right) + \varepsilon_i \tag{42}$$

where

$$\dot{\alpha}_{i-1} = \sum_{j=1}^{i} \frac{\partial \alpha_{i-1}}{\partial x_j} \dot{x}_j + \sum_{j=1}^{i-1} \frac{\partial \alpha_{i-1}}{\partial \widehat{W}_j^T} \dot{\widehat{W}}_j^T + y_d^{(i)} \tag{43}$$

Based on the system,

$$\dot{z}_i = W_i^{*T} \Psi_i\left(\overline{x}_{i+1}\right) + \varepsilon_i \tag{44}$$

Choose the practical virtual control law

$$\alpha_i = -z_{i-1} - k_i z_i^{1/3} + x_{i+1} - \widehat{W}_i^T \Psi_i\left(\overline{x}_{i+1}\right) \tag{45}$$

Choose the adaptive law

$$\dot{\widehat{W}}_i = \Gamma_i \left[z_i \Psi_i\left(\overline{x}_{i+1}\right) - \sigma_i \widehat{W}_i^{1/3}\right] \tag{46}$$

where $\Gamma_i = \Gamma_i^T > 0$ and $\sigma_i > 0$ is positive constant design parameters. Then

$$\dot{z}_i = -\widetilde{W}_i \Psi_i\left(\overline{x}_{i+1}\right) - z_{i-1} - k_i z_i^{1/3} + z_{i+1} + \varepsilon_i \tag{47}$$

where

$$\widetilde{W}_i = \widehat{W}_i - W_i^* \tag{48}$$

Choose Lyapunov candidate function

$$V_i = \frac{1}{2} z_i^2 + \frac{1}{2} \widetilde{W}_i^{\mathrm{T}} \Gamma_i^{-1} \widetilde{W}_i \tag{49}$$

then

$$\begin{aligned} \dot{V}_i &= z_i \dot{z}_i + \widetilde{W}_i \Gamma_i^{-1} \dot{\widetilde{W}}_i^{\mathrm{T}} \\ &= -z_{i-1} z_i - k_i z_i^{4/3} + z_i z_{i+1} + z_i \varepsilon_i - \sigma_i \widetilde{W}_i^{\mathrm{T}} \widehat{W}_i^{1/3} \end{aligned} \tag{50}$$

Based on Lemma 6 and Remark 7, the following inequalities hold:

$$z_i \varepsilon_i \le \frac{3}{4} z_i^{4/3} + \frac{1}{4}\varepsilon_i^4 \tag{51}$$

and

$$-\sigma_i \widetilde{W}_i^{\mathrm{T}} \widehat{W}_i^{1/3} \le -\frac{\sigma_i}{2} \widetilde{W}_i^{(2/3)\mathrm{T}} \widetilde{W}_i^{2/3} + \sigma_i W_i^{*(2/3)\mathrm{T}} W_i^{*2/3} \tag{52}$$

Then based on (49), it yields

$$\begin{aligned} \dot{V}_i &= z_i \dot{z}_i + \widetilde{W}_i^{\mathrm{T}} \Gamma_i^{-1} \dot{\widetilde{W}}_i \\ &= -z_{i-1} z_i - \left(k_i - \frac{3}{4}\right) z_i^{4/3} + z_i z_{i+1} \\ &\quad - \frac{\sigma_i}{2} \widetilde{W}_i^{(2/3)\mathrm{T}} \widetilde{W}_i^{2/3} + \frac{1}{4}\varepsilon_i^4 + \sigma_i W_i^{*(2/3)\mathrm{T}} W_i^{*2/3} \end{aligned} \tag{53}$$

And

$$\begin{aligned} \dot{V}_i &\le -z_{i-1} z_i + z_i z_{i+1} - \eta_i \left(\frac{1}{2} z_i^2\right)^{2/3} \\ &\quad - \eta_i \left(\frac{1}{2} \widetilde{W}_i^{\mathrm{T}} \Gamma_i^{-1} \widetilde{W}_i\right)^{2/3} + \frac{1}{4}\varepsilon_i^4 \\ &\quad + \sigma_i W_i^{*(2/3)\mathrm{T}} W_i^{*2/3} \\ &\le -z_{i-1} z_i + z_i z_{i+1} - \eta_i V_i^{2/3} + \delta_i \end{aligned} \tag{54}$$

where

$$\begin{aligned} \eta_i &= \min\left(4^{1/3}\left(k_i - \frac{3}{4}\right), \frac{\sigma_i}{2^{1/3}\left(\lambda_{\max}\left(\Gamma_i\right)\right)^{2/3}}\right) \\ \delta_i &= \frac{1}{4}\varepsilon_i^4 + \sigma_i W_i^{*(2/3)\mathrm{T}} W_i^{*2/3} \end{aligned} \tag{55}$$

The nth step is the most important step. Based on the system

$$z_n = x_n - \alpha_{n-1} \tag{56}$$

Choose the NN to approximate the nonlinear system $f_n(\overline{x}_n, u) - \dot{\alpha}_{n-1}$, $\overline{x}_{n+1}^T \triangleq \left[\overline{x}_n^T \;\; u\right] \in \Omega_n \subset \mathfrak{R}^{n+1}$, and Ω_n is compact set

$$f_n\left(\overline{x}_n, u\right) - \dot{\alpha}_{n-1} = W_n^{*T} \Psi_n\left(\overline{x}_{n+1}\right) + \varepsilon_n \tag{57}$$

where

$$\dot{\alpha}_{n-1} = \sum_{j=1}^{n} \frac{\partial \alpha_{n-1}}{\partial x_j} \dot{x}_j + \sum_{j=1}^{n-1} \frac{\partial \alpha_{n-1}}{\partial \widehat{W}_j^T} \dot{\widehat{W}}_j^T \tag{58}$$

Based on system

$$\dot{z}_n = W_n^{*T} \Psi_n \left(\overline{x}_{n+1}\right) + \varepsilon_n \tag{59}$$

Choose practical virtual control law

$$\alpha_n = -z_{n-1} - k_n z_n^{1/3} + u - \widehat{W}_n^T \Psi_n \left(\overline{x}_{n+1}\right) \tag{60}$$

Choose adaptive law

$$\dot{\widehat{W}}_n = \Gamma_n \left[z_n \Psi_n^T \left(\overline{x}_{n+1}\right) - \sigma_n \widehat{W}_n^{1/3} \right] \tag{61}$$

where $\Gamma_n = \Gamma_n^T > 0$ and $\sigma_n > 0$ are positive constant design parameters, then

$$\dot{z}_n = -\widetilde{W}_n^T \Psi_n \left(\overline{x}_n \left(t\right)\right) - z_{n-1} - k_n z_n^{1/3} + z_{n+1} + \varepsilon_n \tag{62}$$

where

$$\widetilde{W}_n = \widehat{W}_n - W_n^* \tag{63}$$

From the inequality

$$-\sigma_n \widetilde{W}_n^T \widehat{W}_n^{1/3} \leq -\frac{\sigma_n}{2} \widetilde{W}_n^{2/3^T} \widetilde{W}_n^{2/3} + \sigma_n W_n^{*2/3^T} W_n^{*2/3} \tag{64}$$

choose Lyapunov candidate function

$$V_n = \frac{1}{2} z_n^2 + \frac{1}{2} \widetilde{W}_n \Gamma_n^{-1} \widetilde{W}_n^{\mathrm{T}} \tag{65}$$

Then

$$\begin{aligned} \dot{V}_n &= z_n \dot{z}_n + \widetilde{W}_n \Gamma_n^{-1} \dot{\widetilde{W}}_n^{\mathrm{T}} \\ &= -z_{n-1} z_n - k_n z_n^{4/3} + z_n z_{n+1} + z_n \varepsilon_n - \sigma_n \widetilde{W}_n^{\mathrm{T}} \widehat{W}_n^{1/3} \end{aligned} \tag{66}$$

Based on the lemma, the following inequalities hold:

$$z_n \varepsilon_n \leq \frac{3}{4} z_n^{4/3} + \frac{1}{4} \varepsilon_n^4 \tag{67}$$

and

$$-\sigma_n \widetilde{W}_n^{\mathrm{T}} \widehat{W}_n^{1/3} \leq -\frac{\sigma_n}{2} \widetilde{W}_n^{(2/3)\mathrm{T}} \widetilde{W}_n^{2/3} + \sigma_n W_n^{*(2/3)\mathrm{T}} W_n^{*2/3} \tag{68}$$

Then, it gives

$$\begin{aligned} \dot{V}_n \leq & -z_{n-1} z_n - \left(k_n - \frac{3}{4}\right) z_n^{4/3} + z_n z_{n+1} \\ & - \frac{\sigma_n}{2} \widetilde{W}_n^{(2/3)\mathrm{T}} \widetilde{W}_n^{2/3} + \frac{1}{4} \varepsilon_n^4 + \sigma_n W_n^{*(2/3)\mathrm{T}} W_n^{*2/3} \end{aligned} \tag{69}$$

then

$$\begin{aligned} \dot{V}_n &\leq -z_{n-1} z_n + z_n z_{n+1} - \eta_n \left(\frac{1}{2} z_n^2\right)^{2/3} \\ &\quad - \eta_n \left(\frac{1}{2} \widetilde{W}_n^{\mathrm{T}} \Gamma_n^{-1} \widetilde{W}_n\right)^{2/3} + \delta_n \\ &\leq -z_{n-1} z_n + z_n z_{n+1} - \eta_n V_n^{2/3} + \delta_n \end{aligned} \tag{70}$$

where

$$\begin{aligned} \eta_n &= \min\left(4^{1/3}\left(k_n - \frac{3}{4}\right), \frac{\sigma_n}{2^{1/3}\left(\lambda_{\max}\left(\Gamma_n\right)\right)^{2/3}}\right) \\ \delta_n &= \frac{1}{4}\varepsilon_n^4 + \sigma_n W_n^{*(2/3)\mathrm{T}} W_n^{*2/3} \end{aligned} \tag{71}$$

The $n+1$th step is the most important step.

$$z_{n+1} = u - \alpha_n \tag{72}$$

Based on system

$$\dot{z}_{n+1} = v - \dot{\alpha}_n \tag{73}$$

Choose the NN to approximate the nonlinear system $-\dot{\alpha}_n(\overline{x}_{n+1})$, $\overline{x}_{n+1}^T = [\overline{x}_n^T \ u] \in \Omega_{n+1} \subset \mathfrak{R}^{n+1}$, and Ω_{n+1} is compact set

$$-\dot{\alpha}_n = W_{n+1}^{*T} \Psi_{n+1} \left(\overline{x}_{n+1}\right) + \varepsilon_{n+1} \tag{74}$$

where

$$\dot{\alpha}_n = \sum_{j=1}^{n} \frac{\partial \alpha_n}{\partial x_j} \dot{x}_j + \sum_{j=1}^{n} \frac{\partial \alpha_n}{\partial \widehat{W}_j^T} \dot{\widehat{W}}_j^T + y_d^{(n+1)} \tag{75}$$

Based on system

$$\dot{z}_{n+1} = v + W_{n+1}^{*T} \Psi_{n+1} \left(\overline{x}_{n+1}\left(t\right)\right) + \varepsilon_{n+1} \tag{76}$$

Choose adaptive law

$$\dot{\widehat{W}}_{n+1} = \Gamma_{n+1} \left[z_{n+1} \Psi_{n+1} \left(\overline{x}_{n+1}\right) - \sigma_{n+1} \widehat{W}_{n+1}^{1/3} \right] \tag{77}$$

where $\Gamma_{n+1} = \Gamma_{n+1}^T > 0$ and $\sigma_{n+1} > 0$ are positive constant design parameters.

$$v = -z_n - k_{n+1} z_{n+1}^{1/3} - \widehat{W}_{n+1}^T \Psi_{n+1} \left(\overline{x}_{n+1}\left(t\right)\right) \tag{78}$$

then

$$\dot{z}_{n+1} = -z_n - k_{n+1} z_{n+1}^{1/3} - \widetilde{W}_{n+1}^T \Psi_{n+1} \left(\overline{x}_{n+1}\right) + \varepsilon_{n+1} \tag{79}$$

where

$$\widetilde{W}_{n+1} = \widehat{W}_{n+1} - W_{n+1}^* \tag{80}$$

Choose Lyapunov candidate function

$$V_{n+1} = \frac{1}{2} z_{n+1}^2 + \frac{1}{2} \widetilde{W}_{n+1} \Gamma_{n+1}^{-1} \widetilde{W}_{n+1}^{\mathrm{T}} \tag{81}$$

then

$$\begin{aligned}\dot{V}_{n+1} &= z_{n+1}\dot{z}_{n+1} + \widetilde{W}_{n+1}\Gamma_{n+1}^{-1}\dot{\widetilde{W}}_{n+1}^{\mathrm{T}} \\ &= -z_n z_{n+1} - k_{n+1}z_{n+1}^{4/3} + z_{n+1}\varepsilon_{n+1} \\ &\quad - \sigma_{n+1}\widetilde{W}_{n+1}^{\mathrm{T}}\widehat{W}_{n+1}^{1/3}\end{aligned} \tag{82}$$

From the inequality

$$\begin{aligned}-\sigma_{n+1}\widetilde{W}_{n+1}^{T}\widehat{W}_{n+1}^{1/3} &\le -\frac{\sigma_{n+1}}{2}\widetilde{W}_{n+1}{}^{2/3^{T}}\widetilde{W}_{n+1}{}^{2/3} \\ &\quad + \sigma_{n+1}W_{n+1}^{*}{}^{2/3^{T}}W_{n+1}^{*}{}^{2/3}\end{aligned} \tag{83}$$

and

$$z_{n+1}\varepsilon_{n+1} \le \frac{3}{4}z_{n+1}^{4/3} + \frac{1}{4}\varepsilon_{n+1}^{4} \tag{84}$$

we have

$$\begin{aligned}\dot{V}_{n+1} &\le -z_n z_{n+1} - \left(k_{n+1} - \frac{3}{4}\right)z_{n+1}^{4/3} \\ &\quad - \frac{\sigma_{n+1}}{2}\widetilde{W}_{n+1}{}^{2/3^{T}}\widetilde{W}_{n+1}{}^{2/3} + \frac{1}{4}\varepsilon_{n+1}^{4} \\ &\quad + \sigma_{n+1}W_{n+1}^{*}{}^{2/3^{T}}W_{n+1}^{*}{}^{2/3}\end{aligned} \tag{85}$$

Then

$$\begin{aligned}\dot{V}_{n+1} &\le -z_n z_{n+1} - \eta_{n+1}\left(\frac{1}{2}z_{n+1}^{2}\right)^{2/3} \\ &\quad - \eta_{n+1}\left(\frac{1}{2}\widetilde{W}_{n+1}^{\mathrm{T}}\Gamma_{n+1}^{-1}\widetilde{W}_{n+1}\right)^{2/3} + \delta_{n+1} \\ &\le -z_n z_{n+1} - \eta_{n+1}V_{n+1}^{2/3} + \delta_{n+1}\end{aligned} \tag{86}$$

where

$$\begin{aligned}&\eta_{n+1} \\ &= \min\left(4^{1/3}\left(k_{n+1} - \frac{3}{4}\right), \frac{\sigma_{n+1}}{2^{1/3}\left(\lambda_{max}\left(\Gamma_{n+1}\right)\right)^{2/3}}\right) \\ &\delta_{n+1} = \frac{1}{4}\varepsilon_{n+1}^{4} + \sigma_{n+1}W_{n+1}^{*}{}^{(2/3)\mathrm{T}}W_{n+1}^{*}{}^{2/3}\end{aligned} \tag{87}$$

Choose Lyapunov candidate functions

$$V = \sum_{i=1}^{n+1} V_i \tag{88}$$

then based on (39), (54), (70), and (86), it has

$$\dot{V} \le -\eta V^{2/3} + \delta \tag{89}$$

where

$$\begin{aligned}&\eta = \min\left(\eta_i\right), \quad i = 1, 2, 3, \ldots, n+1 \\ &\delta = \sum_{i=1}^{n+1}\delta_i\end{aligned} \tag{90}$$

Theorem 8. *Under Assumptions 2 and 3 and Lemmas 5 and 6, consider nonlinear system (9) for which the model dynamics is approximated by neural networks (26), (42), (57), and (74), the control law (78) with the virtual control (28), (45), and (60), and adaptive laws (29), (46), (61), and (77), then the following statements hold:*

(1) *All the signals of the closed-loop system, including $x_i, \alpha_i, \widehat{W}_i$, remain bounded all the time.*

(2) *The closed-loop signal $z = [z_1 \;\; z_2 \;\; \cdots \;\; z_{n+1}]^T \in \mathfrak{R}^{n+1}$ converges to a compact set defined by*

$$\Omega_s = \left\{\mathrm{z} \mid \|\mathrm{z}\|^2 \le \frac{\delta}{\eta}\right\} \tag{91}$$

in finite time, where δ, η are constants related to the design parameters.

(3) *The finite time T is given by*

$$T \le \frac{3V^{1/3}\left(x_0\right)}{\eta\theta_0} \tag{92}$$

where η, θ_0 are constants related to the design parameters and $V(x_0)$ is constant related to Lyapunov candidate functional.

Proof. Considering Lyapunov function candidate (88) and (89), then V is bounded in finite time. Therefore, it can conclude that, for all $1 \le i \le n+1$, the error signals $z_i, \widetilde{W}_i$ are PFS. □

4. Simulation Examples

In this section, simulation examples show the validity and feasibility of the proposed NNs adaptive control design approach.

4.1. Mathematical Example. Consider the following dynamic system:

$$\begin{aligned}\dot{x}_1 &= 0.5\sin\left(x_1\right) - x_1 + \sin\left(x_2\right) + x_2 + 5\sin\left(t\right) \\ &\quad + 5\cos\left(t\right) \\ \dot{x}_2 &= -\sin\left(x_2\right) - 2x_2 + x_2 u + u + \sin\left(u\right) \\ y &= x_1\end{aligned} \tag{93}$$

where $x = \left[x_1 \;\; x_2\right]^T$, u, y, and $y_d = 5\sin(t)$ is state, control input, control output, and ideal output, respectively. The control objective of the proposed design method is to make the system output y follow the desired reference signal $y_d = 5\sin(t)$. Select the controller $\dot{u}$ and virtual control α_1, α_2 as follows:

$$\dot{u} = -z_2 - k_3 z_3^{1/3} - \widehat{W}_3^{T}\Psi_3\left(\overline{x}_2, u\right) \tag{94}$$

$$\alpha_1 = -k_1 z_1^{1/3} + x_2 - \widehat{W}_1^{T}\Psi_1\left(\overline{x}_2\right) \tag{95}$$

$$\alpha_2 = -z_1 - k_2 z_2^{1/3} + u - \widehat{W}_2^{T}\Psi_2\left(\overline{x}_2, u\right) \tag{96}$$

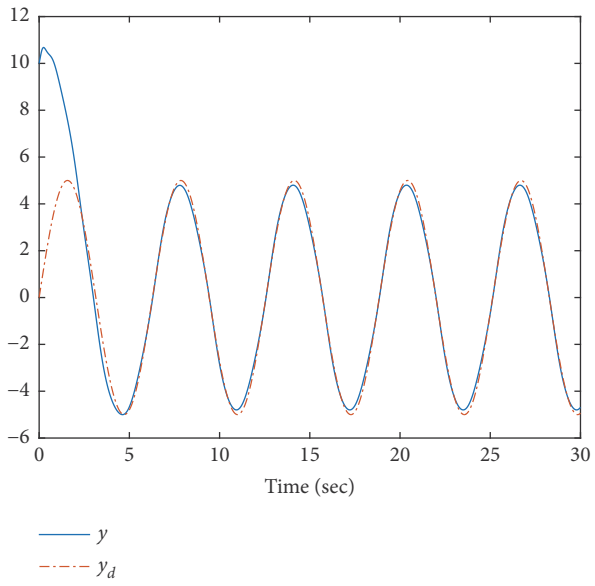

Figure 1: Trajectories of y, y_d.

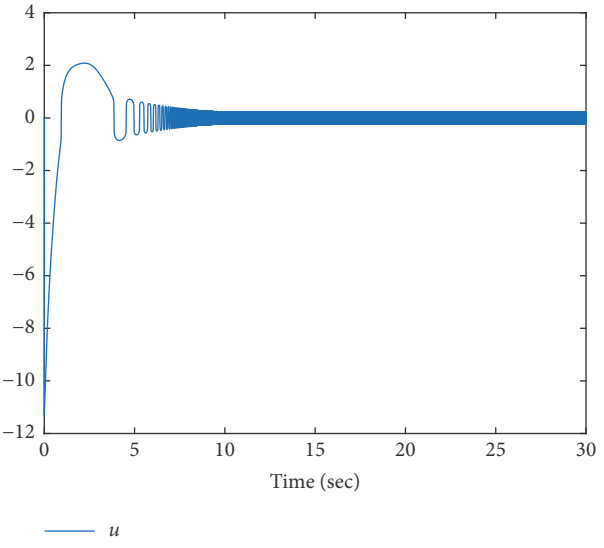

Figure 2: Trajectory of control input u.

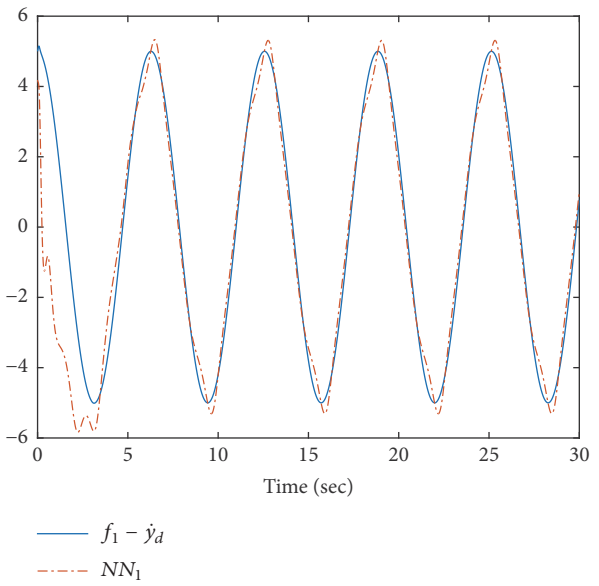

Figure 3: Trajectories of f_1, NN_1.

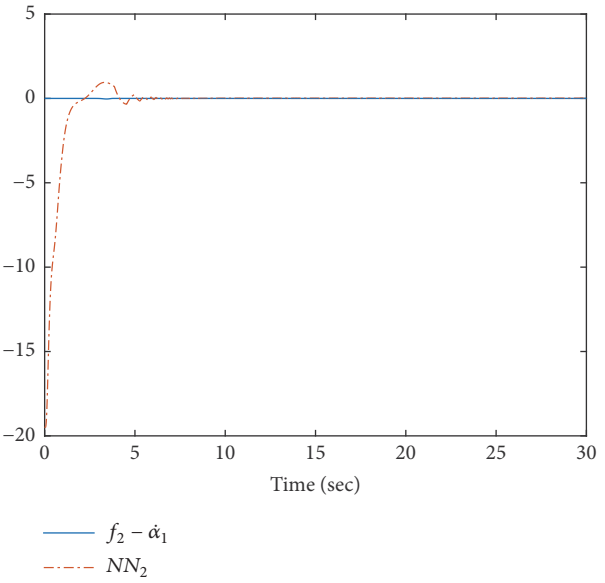

Figure 4: Trajectories of $f_2 - \dot{\alpha}_1$, NN_2.

The weight of NNs is updated by

$$\dot{\widehat{W}}_i = \Gamma_i \left[z_i \Psi_i \left(\overline{x}_{i+1} \right) - \sigma_i \widehat{W}_i^{1/3} \right], \quad i = 1, 2, 3 \tag{97}$$

with $z_1 = x_1 - y_d$, $z_2 = x_2 - \alpha_1$, and $z_3 = u - \alpha_2$; the initialization of the variables is selected by $x_1(0) = 4$, $x_2(0) = 4$, and $u(0) = 4$.

Applying finite time NNs control method, the simulation results are shown by Figures 1–5. Figure 1 shows the trajectory of output and desired reference trajectory. Figure 2 shows the trajectory of controller. Figures 3 and 4 show the trajectory of NNs and function which approximated by NNs. Compared with [3], the method in this paper is more generally used, and both output and weight of NNs are convergence in finite time.

4.2. Plate-Ball Example. Consider a Plate-Ball model [43] in form of

$$\begin{aligned} \left(m + \frac{I_b}{r_b^2} \right) \ddot{\xi}_x + m g u_x + f_x &= 0 \\ \left(m + \frac{I_b}{r_b^2} \right) \ddot{\xi}_y + m g u_y + f_y &= 0 \end{aligned} \tag{98}$$

where m is ball mass, I_b is ball moment of inertia, r_b is ball radius, u_x, u_y are plate inclination angle in the x or y direction, f_x, f_y are contain the centrifugal torque resulting from rotation and other modelling error, and y_{xd}, y_{yd} are ideal trajectory of ξ_x, ξ_y.

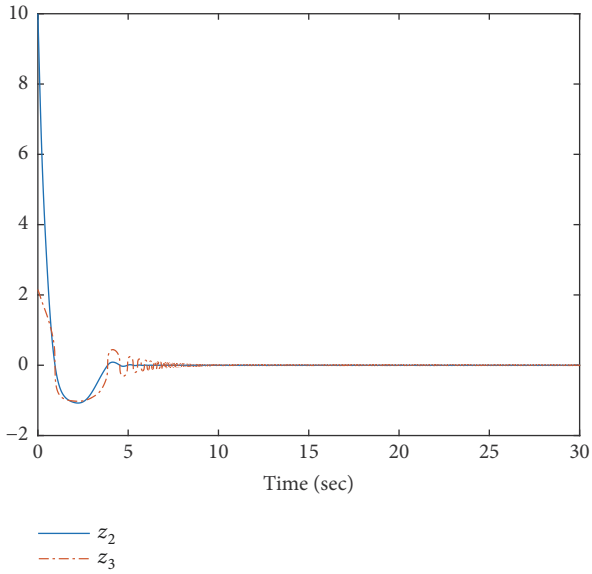

Figure 5: Trajectories of error system.

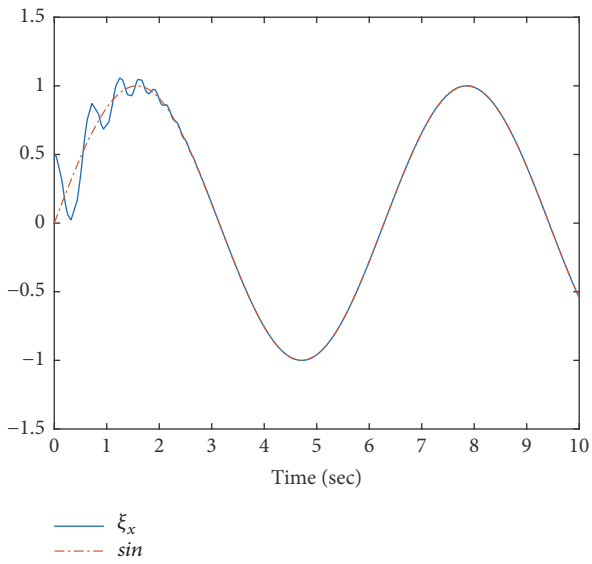

Figure 6: Trajectories of ξ_x and sinusoidal signal.

Based on homeomorphism mapping technique, choose

$$\xi_x - y_{xd} = r_x \tanh(x) \tag{99}$$

then x is new state variable, and therefore $|\xi_x - y_{xd}| \leq r_x$ all the time. About new state variable, we have

$$\dot{\xi}_x = \dot{y}_{xd} + r_x \left(1 - \tanh^2(x)\right) \dot{x} \tag{100}$$

and

$$\ddot{\xi}_x = \ddot{y}_{xd} - 2r_x \tanh(x)\, \dot{x}^2 + r_x \left(1 - \tanh^2(x)\right) \ddot{x} \tag{101}$$

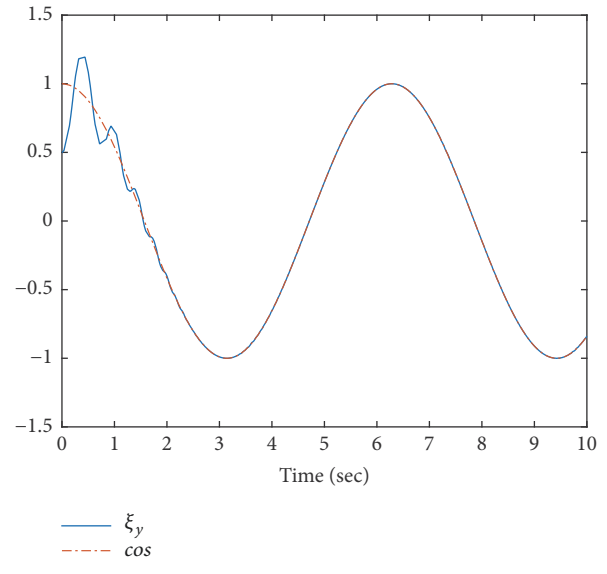

Figure 7: Trajectories of ξ_y and cosine signal.

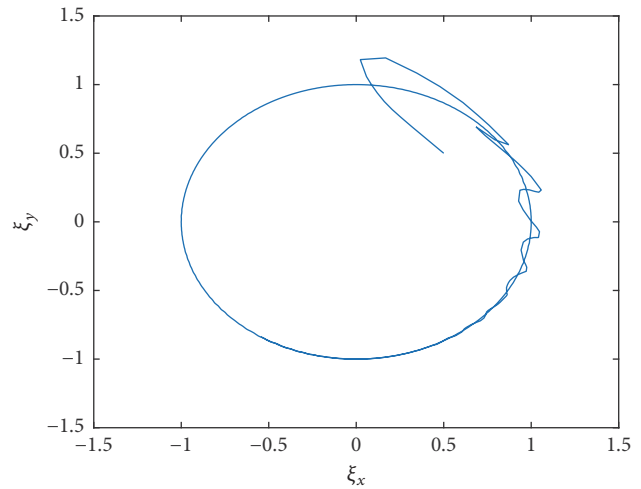

Figure 8: Trajectories of ball.

Let $x_1 = x$, $x_2 = \dot{x}$, then the above equations can be changed as

$$\begin{aligned} \dot{x}_1 &= x_2 \\ \dot{x}_2 &= \frac{f_x - \left(m + I_b/r_b^2\right) \ddot{y}_{xd} + 2r_x \left(m + I_b/r_b^2\right) \tanh(x_1)\, x_2^2 - mgu_x}{r_x \left(m + I_b/r_b^2\right) \left(1 - \tanh^2(x_1)\right)} \end{aligned} \tag{102}$$

then control u_x can be designed by regular control method based on Lyapunov theory, state variable x is not restricted, and ξ_x is restricted by reference signal y_{xd} and bound r_x.

Choose f_x as unknown function, reference signal as sinusoidal signal, and NNs control. The simulation result can be obtained by Figures 6 and 7 about ξ_y with cosine signal as reference signal. Figure 8 indicates trajectories of ball.

5. Conclusions

For technique completeness, the neural networks enhanced finite time constraint control framework for a class of uncertain nonaffine pure-feedback nonlinear systems has developed analysis/proof, design, algorithms, and computational experiments. For reference of neurocontrol, this study attempts to strengthen neural network function to deal with complex nonlinear uncertain system control with different design constraints, which confirms again that the universal approximation property of neural networks feasibly effectively integrated with control system specifications. In line with further expansion of the study, some issues have been identified on the research card, such as how to design better homeomorphism mapping to realize the constraint control, how to extend the general order in finite time adaptive neural networks control, and fast computation algorithms for online computation.

Data Availability

No data were used to support this study.

Conflicts of Interest

The funding did not lead to any conflicts of interest regarding the publication of this manuscript. There are not any other possible conflicts of interest in the manuscript.

Acknowledgments

This work is partially supported by the National Nature Science Foundation of China under Grants 61273188 and 61473312 and Taishan Scholar Construction Engineering Special Funding, Shandong, China. This work is supported by Hebei Province Nature Fund Grant F2015208128 and Project in Hebei Province Department of Education QN20140157 and BJ2016020.

References

[1] W. Chen, S. S. Ge, J. Wu, and M. Gong, "Globally stable adaptive backstepping neural network control for uncertain strict-feedback systems with tracking accuracy known a priori," *IEEE Transactions on Neural Networks and Learning Systems*, vol. 26, no. 9, pp. 1842–1854, 2015.

[2] R. Herzallah and D. Lowe, "Distribution modeling of nonlinear inverse controllers under a Bayesian framework," *IEEE Transactions on Neural Networks and Learning Systems*, vol. 18, no. 1, pp. 107–114, 2007.

[3] Q. Chen, X. Ren, J. Na, and D. Zheng, "Adaptive robust finite-time neural control of uncertain PMSM servo system with nonlinear dead zone," *Neural Computing and Applications*, vol. 28, no. 12, pp. 3725–3736, 2017.

[4] S. S. Ge, C. C. Hang, and T. Zhang, "Stable adaptive control for nonlinear multivariable systems with a triangular control structure," *Institute of Electrical and Electronics Engineers Transactions on Automatic Control*, vol. 45, no. 6, pp. 1221–1225, 2000.

[5] S. S. Ge and C. Wang, "Direct adaptive NN control of a class of nonlinear systems," *IEEE Transactions on Neural Networks and Learning Systems*, vol. 13, no. 1, pp. 214–221, 2002.

[6] C. Hua, T. Zhang, Y. Li, and X. Guan, "Robust output feedback control for fractional order nonlinear systems with time-varying delays," *IEEE/CAA Journal of Automatica Sinica*, vol. 3, no. 4, pp. 477–482, 2016.

[7] X. Yang, C. Hua, J. Yan, and X. Guan, "An exact stability condition for bilateral teleoperation with delayed communication channel," *IEEE Transactions on Systems, Man, and Cybernetics: Systems*, vol. 46, no. 3, pp. 434–439, 2016.

[8] L. Zhang, C. Hua, and X. Guan, "Distributed output feedback consensus tracking prescribed performance control for a class of non-linear multi-agent systems with unknown disturbances," *IET Control Theory & Applications*, vol. 10, no. 8, pp. 877–883, 2016.

[9] C. Hua, L. Zhang, and X. Guan, "Decentralized output feedback adaptive NN tracking control for time-delay stochastic nonlinear systems with prescribed performance," *IEEE Transactions on Neural Networks and Learning Systems*, vol. 26, no. 11, pp. 2749–2759, 2015.

[10] Y. Yang, C. Hua, and X. Guan, "Adaptive fuzzy finite-time coordination control for networked nonlinear bilateral teleoperation system," *IEEE Transactions on Fuzzy Systems*, vol. 22, no. 3, pp. 631–641, 2014.

[11] Q. Zhu, L. Liu, W. Zhang, and S. Li, "Control of complex nonlinear dynamic rational systems," *Complexity*, vol. 2018, Article ID 8953035, 12 pages, 2018.

[12] R. Herzallah and D. Lowe, "Robust control of nonlinear stochastic systems by modelling conditional distributions of control signals," *Neural Computing and Applications*, vol. 12, no. 2, pp. 98–108, 2003.

[13] J. Na, X. Ren, and D. Zheng, "Adaptive control for nonlinear pure-feedback systems with high-order sliding mode observer," *IEEE Transactions on Neural Networks and Learning Systems*, vol. 24, no. 3, pp. 370–382, 2013.

[14] S. S. Ge, F. Hong, and T. H. Lee, "Adaptive neural network control of nonlinear systems with unknown time delays," *IEEE Transactions on Automatic Control*, vol. 48, no. 11, pp. 2004–2010, 2003.

[15] K. P. Tee, S. S. Ge, and E. H. Tay, "Barrier Lyapunov functions for the control of output-constrained nonlinear systems," *Automatica*, vol. 45, no. 4, pp. 918–927, 2009.

[16] B. Ren, S. S. Ge, K. P. Tee, and T. H. Lee, "Adaptive neural control for output feedback nonlinear systems using a barrier lyapunov function," *IEEE Transactions on Neural Networks and Learning Systems*, vol. 21, no. 8, pp. 1339–1345, 2010.

[17] S. G. Nersesov and W. M. Haddad, "On the stability and control of nonlinear dynamical systems via vector Lyapunov functions," *Institute of Electrical and Electronics Engineers Transactions on Automatic Control*, vol. 51, no. 2, pp. 203–215, 2006.

[18] S. Wang, H. Yu, X. Gao, and W. Na, "Adaptive barrier control for nonlinear servomechanisms with friction compensation," *Complexity*, vol. 2018, Article ID 8925838, 10 pages, 2018.

[19] F. Cheng, L. Qu, W. Qiao, C. Wei, and L. Hao, "Fault diagnosis of wind turbine gearboxes based on DFIG stator current envelope analysis," *IEEE Transactions on Sustainable Energy*, pp. 1-1, 2018.

[20] J. H. Zhang, Q. M. Zhu, X. L. Wu, and Y. Li, "A generalized indirect adaptive neural networks backstepping control procedure for a class of non-affine nonlinear systems with pure-feedback prototype," *Neurocomputing*, vol. 121, no. 9, pp. 131–139, 2013.

[21] L. F. Zhang, Q. M. Zhu, and A. Longden, "A correlation-test-based validation procedure for identified neural networks," *IEEE Transactions on Neural Networks and Learning Systems*, vol. 20, no. 1, pp. 1–13, 2009.

[22] F. Ding, L. Xu, and Q. M. Zhu, "Performance analysis of the generalised projection identification for time-varying systems," *IET Control Theory & Applications*, vol. 10, no. 18, pp. 2506–2514, 2016.

[23] C. Hua, L. Zhang, and X. Guan, "Distributed adaptive neural network output tracking of leader-following high-order stochastic nonlinear multiagent systems with unknown deadzone input," *IEEE Transactions on Cybernetics*, vol. 47, no. 1, pp. 177–185, 2017.

[24] W. Rudin, *Principles of Mathematical Analysis*, McGraw-Hill, 3rd edition, 1976.

[25] Q. Chen, L. Shi, J. Na, X. Ren, and Y. Nan, "Adaptive echo state network control for a class of pure-feedback systems with input and output constraints," *Neurocomputing*, vol. 275, pp. 1370–1382, 2018.

[26] Q. Chen, S. Xie, M. Sun, and X. He, "Adaptive nonsingular fixed-time attitude stabilization of uncertain spacecraft," *IEEE Transactions on Aerospace and Electronic Systems*, vol. 54, no. 6, pp. 2937–2950, 2018.

[27] Y. Yang, C. Hua, and X. Guan, "Finite time control design for bilateral teleoperation system with position synchronization error constrained," *IEEE Transactions on Cybernetics*, vol. 46, no. 3, pp. 609–619, 2016.

[28] S.-M. Lu and D.-J. Li, "Adaptive neural network control for nonlinear hydraulic servo-system with time-varying state constraints," *Complexity*, vol. 2017, Article ID 6893521, 11 pages, 2017.

[29] X. Huang, W. Lin, and B. Yang, "Global finite-time stabilization of a class of uncertain nonlinear systems," *Automatica*, vol. 41, no. 5, pp. 881–888, 2005.

[30] Y. Hong, J. Wang, and D. Cheng, "Adaptive finite-time control of nonlinear systems with parametric uncertainty," *IEEE Transactions on Automatic Control*, vol. 51, no. 5, pp. 858–862, 2006.

[31] H. Wang and Q. Zhu, "Finite-time stabilization of high-order stochastic nonlinear systems in strict-feedback form," *Automatica*, vol. 54, pp. 284–291, 2015.

[32] C. Hua, Y. Li, H. Wang, and X. Guan, "Decentralised fault-tolerant finite-time control for a class of interconnected nonlinear systems," *IET Control Theory & Applications*, vol. 9, no. 16, pp. 2331–2339, 2015.

[33] D. Zhao, Q. Zhu, N. Li, and S. Li, "Synchronized control with neuro-agents for leader–follower based multiple robotic manipulators," *Neurocomputing*, vol. 124, pp. 149–161, 2014.

[34] D. Zhao, W. Ni, and Q. Zhu, "A framework of neural networks based consensus control for multiple robotic manipulators," *Neurocomputing*, vol. 140, pp. 8–18, 2014.

[35] K. Xing, P. Yang, J. Huang, Y. Wang, and Q. Zhu, "A real-time EMG pattern recognition method for virtual myoelectric hand control," *Neurocomputing*, vol. 136, pp. 345–355, 2014.

[36] C. Hua, C. Ge, and X. Guan, "Synchronization of chaotic lur'e systems with time delays using sampled-data control," *IEEE Transactions on Neural Networks and Learning Systems*, vol. 26, no. 6, pp. 1214–1221, 2015.

[37] J. Na, Y. Li, Y. Huang, G. Gao, and Q. Chen, "Output feedback control of uncertain hydraulic servo systems," *IEEE Transactions on Industrial Electronics*, pp. 1-1, 2019.

[38] Y.-J. Liu and S. Tong, "Barrier Lyapunov functions-based adaptive control for a class of nonlinear pure-feedback systems with full state constraints," *Automatica*, vol. 64, pp. 70–75, 2016.

[39] M. Z. Romdlony and B. Jayawardhana, "Stabilization with guaranteed safety using control Lyapunov–Barrier function," *Automatica*, vol. 66, pp. 39–47, 2016.

[40] Q. Chen, L. Tao, Y. Nan, and X. Ren, "Adaptive nonlinear sliding mode control of mechanical servo system with LuGre friction compensation," *Journal of Dynamic Systems, Measurement, and Control*, vol. 138, no. 2, pp. 021003–021003-9, 2016.

[41] J. Na, Q. Chen, X. Ren, and Y. Guo, "Adaptive prescribed performance motion control of servo mechanisms with friction compensation," *IEEE Transactions on Industrial Electronics*, vol. 61, no. 1, pp. 486–494, 2014.

[42] J. E. L. G. Hardy and G. Polya, *Inequalities*, Cambridge University Press, London, U.K, 2nd edition, 1989.

[43] D. Yuan and Z. Zhang, "Modelling and control scheme of the ball-plate trajectory-tracking pneumatic system with a touch screen and a rotary cylinder," *IET Control Theory & Applications*, vol. 4, no. 4, pp. 573–589, 2010.

Hindawi
Complexity
Volume 2019, Article ID 5376360, 12 pages
https://doi.org/10.1155/2019/5376360

Research Article

Steady-State Analysis and Output Voltage Minimization Based Control Strategy for Electric Springs in the Smart Grid with Multiple Renewable Energy Sources

Yun Zou,[1] **Michael Z. Q. Chen**,[1] **Yinlong Hu**,[2] **and Yun Zou**[1]

[1]*School of Automation, Nanjing University of Science and Technology, Nanjing 210094, China*
[2]*College of Energy and Electrical Engineering, Hohai University, Nanjing 210098, China*

Correspondence should be addressed to Michael Z. Q. Chen; mzqchen@outlook.com

Received 21 February 2019; Revised 1 April 2019; Accepted 8 April 2019; Published 9 May 2019

Guest Editor: Chun Wei

This paper presents a general steady-state analysis and proposes a minimal compensating voltage (MCV) control scheme for the second generation of electric springs (ES-2) in the power system with substantial penetration of intermittent renewable energy sources. For the steady-state analysis, the relationship among the fluctuating part of the supply voltage, the voltage at the point of common-coupling (PCC), and the compensating voltage provided by ES-2 is derived, which implies that the phase angle related to the PCC voltage can be used as a degree of freedom for the control design to obtain a minimal compensating voltage in a given system. Such a fact is utilized in the control design to obtain the reference of PCC voltage by tuning the above-mentioned phase angle. Once the phase angle of the PCC voltage is chosen, the maximal compensating voltage can be estimated based on the fluctuating part of the supply voltage which can be estimated *a priori*. Such a fact can be used to design suitable electric springs with appropriate compensating capacity to avoid overcapacity. Numerical simulations are conducted to verify the effectiveness of the steady-state analysis and the proposed control scheme for ES-2.

1. Introduction

In recent years, due to the energy crisis and the increasingly severe environmental issues, renewable energy sources are attracting more and more attention. Nowadays, wind [1–3] and solar energies are the two most widely used renewable energy sources for distributed generation [4–6]. However, due to the highly intermittent and unpredictable natures, renewable energy power generation brings a series of challenges to the power grid. Imbalance between the power supply and demand is one of the most prominent problems [7], which will cause the fluctuations of frequencies and voltages. Therefore, demand-side management has become a significant topic in the smart grid with intermittent renewable energy sources [8, 9].

Electric spring (ES) was first introduced in 2012 as a new generation of smart grid [10, 11] technology aiming to automatically balance the power generation and load demand without relying on the information and communication technology [12]. Generally speaking, ESs can be mainly divided into two categories. The first type called ES-1 works as a purely reactive power compensator to regulate the PCC voltage, while keeping the power consumption at the load side to be consistent with the power generation in real time. Examples of relevant research work on ES-1 are as follows. Dynamic modeling of ES and the influence of load ratios on compensation effects are described in [13]. Hardware and control implementation based on theoretical analysis are illustrated in [14]. Droop control and consensus control used to regulate the voltage by distributed ESs in the future smart grid are introduced in [15] and [16], respectively. However, just as a physical spring has limits for tension and compression, ES-1 also has its own compensation limits, exceeding which ES-1 will be invalidated. ES-2, which can provide six more operating modes in addition to the capacitive and inductive modes [17], can make up for these shortcomings. The difference in the topological structure between ES-1 and ES-2 is that the DC-link capacity in

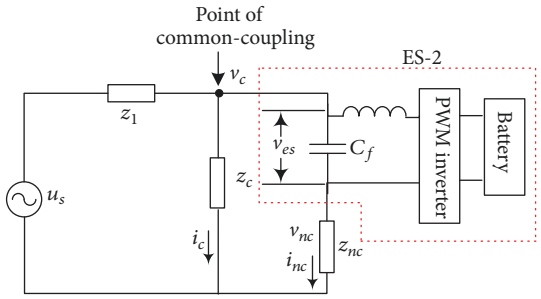

Figure 1: Simplified schematic of the power system with ES-2.

ES-1 is replaced by energy storage systems (such as batteries) on the DC side of the inverter in ES-2, thus the voltage phase angle of ES-2 is not restricted to be 90 degrees with respect to its current. At present, some research results of theoretical analysis and control schemes for ES-2 have been obtained. Regulating voltage and improving power quality (e.g., power factor correction and harmonics reduction) at the same time by ES-2 are introduced in [18], which are not possible with ES-1. In [19], a novel control strategy named δ control is proposed to obtain the instantaneous phase of PCC voltage to achieve specific power factor correction and constant power compensation. In [20], a radial-chordal decomposition (RCD) approach for ES-2 to regulate the PCC voltage is introduced, which can concurrently realize power factor correction by independent control of active and reactive powers.

However, these control strategies ignore the effect on ES-2 its own output value while focusing on the compensation functions. Note that it is meaningful to avoid overcapacity in terms of cost reduction in practice, and for ES-2, the relationship among the fluctuating part of the supply voltage, the PCC voltage, and the voltage provided by ES-2 is significant for determining the compensation capacity of electric springs. Therefore, in this paper, a general steady-state analysis for ES-2 is carried out to algebraically derive this relationship, which is depicted in a vector diagram. Based on the vector diagram, the detailed impact on compensating voltage caused by the fluctuating part of the supply voltage and a specific phase angle related to the PCC voltage is analyzed. Moreover, a control strategy to obtain the minimal compensating voltage (MCV) is proposed, the effectiveness of which is demonstrated by numerical simulations. These constitute the main contributions of this paper.

The rest of this paper is organized as follows. In Section 2, the operating principle of ES for the future smart grid is described. Sections 3 and 4 analyze the steady-state based on the vector diagram and propose a control scheme for ES-2, respectively. Numerical simulations are presented in Section 5 to verify the effectiveness of the analysis and the control scheme. Section 6 draws the conclusions.

2. Operation Principles of Electric Springs

Figure 1 shows a simplified schematic of the power system that is composed of an ES, noncritical loads, critical loads, a fluctuating AC voltage source, and transmission lines. One thing to note is that the noncritical loads can withstand a wide range of voltage fluctuation, while the critical loads are sensitive to voltage fluctuation. The ES shown in the red dashed box of Figure 1 mainly consists of an energy storage system (represented by batteries), a single-phase inverter [21–26], and an LC filter as a second-order low-pass filter to reduce the switching harmonics. The output of the ES is connected to the noncritical load z_{nc} to form a smart load. The critical load z_c and the smart load connect to the supply voltage source through the line impedance z_1. The voltages across the noncritical load and the filter capacitor C_f are represented as v_{nc} and v_{es}, respectively. i_{nc} denotes the current flowing through the noncritical load. The supply voltage source denoted by u_s in Figure 1 can be represented as follows:

$$u_s = u_f + \Delta u, \tag{1}$$

where u_f represents the voltage corresponding to the power generated by the power plant, which is stable and controllable, while Δu denotes the fluctuating part of the supply voltage caused by intermittent renewable energy sources, which is unstable and unpredictable. As the proportion of renewable energy connected to the power grid increases, Δu will increase correspondingly. Due to the requirements of being grid-connected, u_f and Δu will have the same frequency and phase angle.

Because of the randomness of renewable energy, the power delivered to the network is unstable. When exceeding the demand, the PCC voltage will be over the rated value, vice versa. For a change in Δu, ES will provide a corresponding compensating voltage v_{es} to keep the PCC voltage stable. In this way, the power generation and load demand can be balanced automatically, which is different from the existing control paradigm that the power generation should follow load demand.

Note that the ES-2 as shown in Figure 1 is equipped with batteries on the DC side of the inverter. The phase angle of the voltage provided by ES-2 is not limited to 90 degrees (lag or lead) with respect to the phase angle of i_{nc}. Therefore, active power can be provided in addition to reactive power. And for this reason, ES-2 has a larger compensation rang compared to ES-1. Consequently, new control strategies are required due to the structural change mentioned above, which will be described in detail in Section 4.

3. Steady-State Analysis of Electric Springs for Minimal Compensating Voltage

From Figure 1 and Kirchhoff's voltage and current laws, one obtains

$$v_c = v_{es} + v_{nc}, \tag{2}$$

$$v_{nc} = z_{nc} \cdot \left(\frac{u_s - v_c}{z_1} - \frac{v_c}{z_c} \right), \tag{3}$$

$$z_1 = R_1 + j\omega L_1, \tag{4}$$

where R_1 and L_1 are the equivalent resistance and inductance of the transmission lines, respectively.

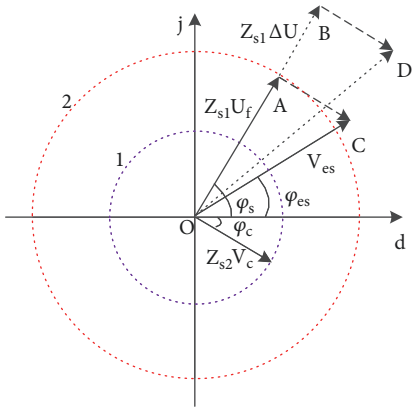

Figure 2: General vector diagram of a power system.

Solving (1)–(3), one obtains

$$v_{es} = z_{s1} \cdot u_f + z_{s1} \cdot \Delta u + z_{s2} \cdot v_c, \tag{5}$$

$$z_{s1} = -\frac{z_{nc}}{z_1}, \tag{6}$$

$$z_{s2} = 1 + \frac{z_{nc}}{z_1} + \frac{z_{nc}}{z_c}, \tag{7}$$

where z_{s1} and z_{s2} are determined by the parameters of the circuit elements which can be treated as constant values for a given system.

Equation (5) can be represented in the phasor form as

$$V_{es}\angle\varphi_{es} = Z_{s1}U_f\angle\varphi_s + Z_{s1}\Delta U\angle\varphi_s + Z_{s2}V_c\angle\varphi_c, \tag{8}$$

$$\varphi_s = \varphi_{s1} + \varphi_{s3}, \tag{9}$$

$$\varphi_c = \varphi_{s2} + \varphi_{c1}, \tag{10}$$

$$\Delta\varphi = \varphi_s - \varphi_c, \tag{11}$$

$$U_s = U_f + \Delta U, \tag{12}$$

$$V_{es} = \sqrt{\left(Z_{s2}V_c + Z_{s1}U_s\cos\Delta\varphi\right)^2 + \left(Z_{s1}U_s\sin\Delta\varphi\right)^2}, \tag{13}$$

where Z_{si} and φ_{si} are the magnitude and the displacement angle of z_{si} $(i = 1, 2)$, respectively. V_{es}, V_c, U_f, and ΔU are the root-mean-square (RMS) values of v_{es}, v_c, u_f, and Δu, respectively, and φ_{es}, φ_{c1}, and φ_{s3} are the phase angles of v_{es}, v_c, and u_s, respectively. $\Delta\varphi$ denotes the difference between φ_s and φ_c, which is related to φ_{s3} and φ_{c1} due to the fact that φ_{s1} and φ_{s2} are constants in a given system. The vector diagram among v_{es}, $z_{s1}u_f$, $z_{s1}\Delta u$, and $z_{s2}v_c$ is depicted in Figure 2. Since the PCC voltage (i.e., v_c) is maintained at its nominal reference level (e.g., 220 V), then $Z_{s2}V_c$ is a constant as the circle 1 showed in Figure 2. Similarly, $Z_{s1}U_f$ on the circle 2 represented by the solid line OA can be treated as a constant as well. The fluctuating part of the source voltage (ΔU) multiplied by Z_{s1} is represented by the dashed line AB. For a constant $\Delta\varphi$, if $Z_{s1}\Delta U$ changes from point A to point B, the compensating voltage v_{es} will change from line OC to line OD, correspondingly.

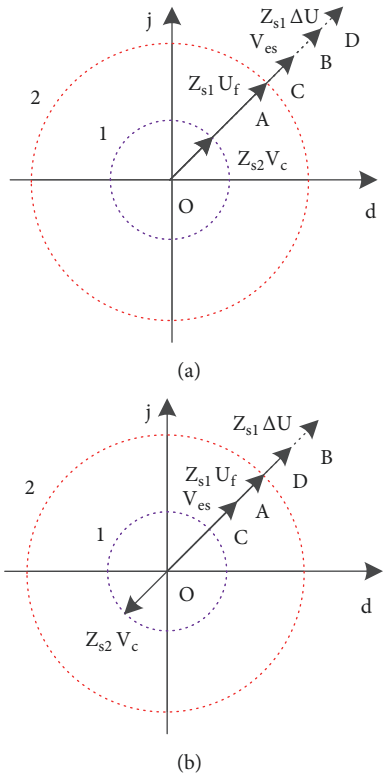

Figure 3: Vector diagram of the power system. (a) $\Delta\varphi = 0$; (b) $\Delta\varphi = \pi$.

Table 1: Simulated test system parameters.

Item	Value
line resistance R_1	0.1Ω
line inductance L_1	2.4mH
Critical load z_c	8Ω
Non-critical load z_{nc}	8Ω
Predefined reference value V_{c-ref}	220 V
Base voltage U_f	210 V

∗Parameters come from [27]

From Figure 2, one sees that ΔU, $\Delta\varphi$ are the two essential factors for v_{es}. Especially, if $\Delta\varphi = 0$, namely, $z_{s1}u_s$ and $z_{s2}v_c$ have the same phase angle, a maximal V_{es} will be obtained as shown in Figure 3(a). In contrast, a minimal V_{es} can be obtained with $\Delta\varphi = \pi$ as shown in Figure 3(b).

To quantitatively show the influence of ΔU and $\Delta\varphi$ on V_{es}, the parameters in Table 1 are employed. A three-dimensional representation among ΔU, $\Delta\varphi$, and V_{es} is given in Figure 4, where one sees that the minimal value of V_{es} is obtained at $\Delta\varphi = \pi$. Table 2 shows some representative values of ΔU, $\Delta\varphi$ and the corresponding V_{es} based on the parameters in Table 1. One sees that V_{es} is highly influenced by $\Delta\varphi$. For example, when $\Delta\varphi$ changes from π to 0, the variation percentages of V_{es} are up to 2177.64 for the cases ΔU=0. All the variation percentages shown in Table 2 are based on the values obtained at $\Delta\varphi = \pi$, where positive values indicate increment.

Table 2: Quantitative comparisons for different $\Delta\varphi$ and ΔU.

	$\Delta U = 0$	$\Delta U = 30$ V	$\Delta U = 50$ V
$\Delta\varphi$	V_{es} (V)	V_{es} (V)	V_{es} (V)
0	4620.42	4935.96	5146.32
	2177.64%	4280.51%	1493.10%
$\frac{1}{3}\pi$	4002.69	4275.04	4459.77
	1873.13%	3693.97%	1280.56%
$\frac{1}{2}\pi$	3270.28	3491.16	3646.16
	1512.09%	2998.30%	1028.70%
$\frac{2}{3}\pi$	2316.88	2469.91	2588.32
	1042.11%	2091.97%	701.24%
π	202.86	112.68	323.04

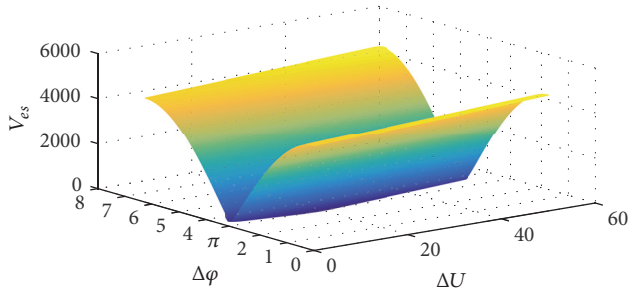

Figure 4: Three-dimensional relationships among ΔU, $\Delta\varphi$, and V_{es}.

In conclusion, $\Delta\varphi$ has a significant influence on V_{es}. In other words, V_{es} is so sensitive to the phase angle φ_{c1}, which implies that the phase angle of v_{c-ref} should be carefully selected when designing the proper control law for ES-2. If an appropriate phase angle has been chosen, then V_{es} is only determined by ΔU. Since the proportion of the intermittent renewable source injected to the power grid is limited, ΔU will fluctuate within a certain range. Once ΔU can be estimated in advance, the required voltage V_{es} can also be estimated. This provides guidelines for designing suitable ESs with appropriate compensating capabilities to avoid overcapacity.

4. Control Design for ES-2

The aim of control design is to minimize the error between the PCC voltage and its reference v_{c-ref} by a minimal ES voltage. In this paper, to show the effectiveness of the analysis in the Section 3, a minimal compensating voltage (MCV) based control strategy is proposed for ES-2 and a proportional resonant (PR) controller is employed because of the characteristic that PR control can track a sinusoidal signal with a zero steady-state error.

Figure 5 shows the system block diagram, where the red dotted box at the bottom of the figure shows how to obtain the reference signal v_{c-ref}. As can be seen from the steady-state analysis in Section 3, the magnitude of v_{es} is related to $\Delta\varphi$ and ΔU, so $\Delta\varphi$ can be treated as a degree of freedom for control design to obtain a minimal value of V_{es}. Since $\Delta\varphi$ is related to the phase angle of v_c (see (9)–(11)), the key point of the proposed control strategy is transformed to select an appropriate phase angle of v_{c-ref}. The supply voltage signal u_s is obtained by a sensor, and a single-phase lock loop (PLL) is used to acquire its phase angle φ_{s3}. Then φ_{c1} can be calculated through (9)–(11) based on the circuit parameters and φ_{s3}. One remark is that the value of arctan function belongs to the interval $(-\pi/2, \pi/2)$, which is corresponding to the argument of a complex number whose real part is positive. If the real part of the complex number is negative, then one need to add π when calculating the argument of a complex number, where care should be taken when calculating φ_{s1} and φ_{s2}. Thus, the complete reference signal can be obtained by combining the magnitude V_{c-ref} and the phase angle φ_{c1}. The expression of the PR controller used in this paper is as follows:

$$G(s) = K_p + \frac{K_R s}{s^2 + \omega^2}, \tag{14}$$

where ω is the angular frequency of the grid and K_p and K_R are the proportionality coefficient and resonance coefficient, respectively.

Equation (14) is an ideal PR controller, which has an infinite gain at angular frequency ω, but no phase transition and gain at other frequencies. Therefore, it can realize tracking a sinusoidal signal without any steady-state error. For this reason, a PR controller is introduced to regulate the PCC voltage (v_c) to its reference level by driving the difference between reference voltage v_{c-ref} and measured voltage v_c to zero. In addition to PR control, many other control methods, such as sliding-mode control [28, 29], robust control [30], model predictive control [31, 32], and event-triggered control [33] can also be considered in future studies based on the control strategy mentioned above.

5. Simulations and Discussions

To double verify the effectiveness of the aforementioned analysis and the MCV control strategy, simulations are conducted by using MATLAB/Simulink and LabVIEW/PXI based on the parameters shown in Table 1. Without loss of generality, the RMS of v_c is assumed to be 220 V.

5.1. The Simulations Conducted on MATLAB/Simulink

5.1.1. Voltage Support Mode with $\Delta U = 0$ V. In this case study, the effect of different $\Delta\varphi$ on V_{es} for voltage boosting is investigated. ΔU is set 0 to simulate insufficient output of power generation, so it can be seen that the RMS of the line voltage v_c is less than 220 V with the ES-2 deactivated from Figure 6. In order to restore V_c back to 220 V, ES-2 should play the role of voltage support. In the voltage support mode, different values of $\Delta\varphi$ are employed to verify the influence of $\Delta\varphi$ on V_{es}. The RMS of the compensating voltage v_{es} provided by ES-2 to regulate V_c at 220 V are considerably different as shown in Figure 7 for different $\Delta\varphi$, which are consistent with the algebraic calculations shown in Table 2. Taking the red line shown in Figure 7 as an example, the RMS is about 4600 V in the steady-state which is consistent with the value obtained from (13).

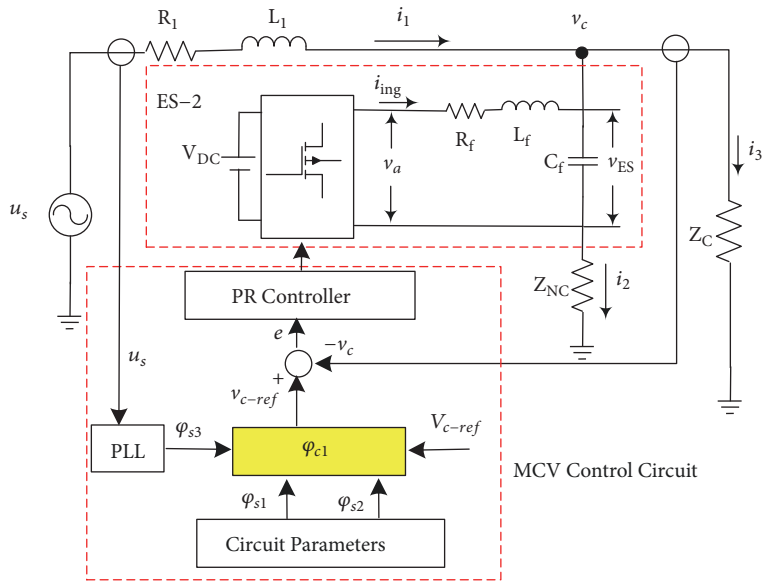

Figure 5: System block diagram of PR-controlled ES-2.

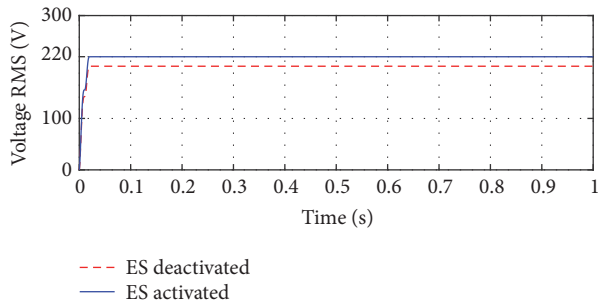

Figure 6: RMS of v_c with ES-2 deactivated and activated when ΔU = 0 V.

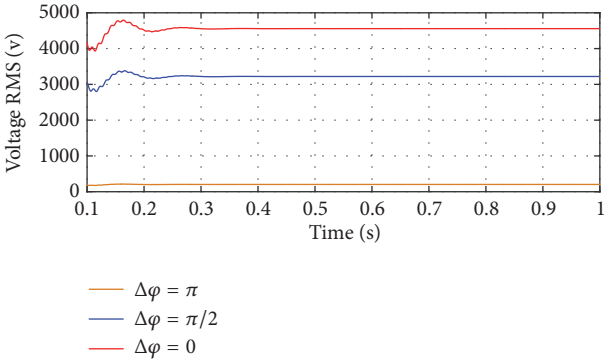

Figure 7: RMS of v_{es} of regulating v_c to the rated value under different $\Delta\varphi$.

5.1.2. Voltage Suppression Mode with ΔU = 30 V. In this case study, the effect of different $\Delta\varphi$ on V_{es} for voltage suppression is investigated. Figure 8 shows the RMS of the line voltage v_c with ES-2 activated and deactivated when ΔU = 30, which is used to simulate the overvoltage conditions. When ΔU = 30, the RMS of the line voltage v_c is about 230

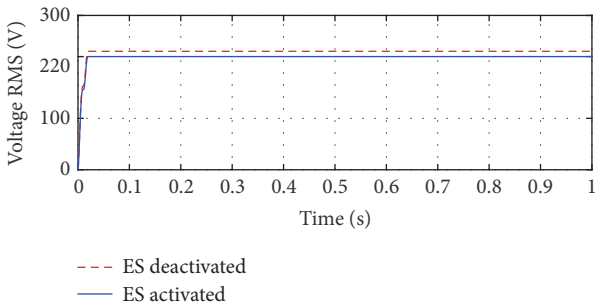

Figure 8: RMS of v_c with ES-2 deactivated and activated when ΔU = 30 V.

V with ES-2 deactivated. However, under the action of the ES-2, V_c is effectively controlled at 220 V. Similarly, for different $\Delta\varphi$, the compensating voltage injected to the power system is considerably different as shown in Figure 9. The simulation results correspond to the analyses mentioned in Section 3. As previously mentioned, for ES-1, the compensating capability is limited [19]. For example, by using the parameters in Table 1, it has been described in [27] that the variation range of U_s is 215.8 V to 236.7 V, which means that, if U_s is out of the range mentioned above, ES-1 cannot regulate V_c at 220 V. When ΔU = 0 V, that is to say U_s is 210 V, one can intuitively see that ES-1 can just adjust the voltage to 214 V as shown in Figure 10. Similarly, when ΔU = 30 V, which means that the supply voltage is higher than the upper compensation limit of ES-1, ES-1 can just adjust the voltage to 223 V in the best case. Such a fact indicates that ES-2 has a larger compensation range than ES-1. In some cases where the voltage fluctuation is large, ES-1 may fail to regulate the line voltage v_c, whereas ES-2 does.

5.1.3. ES-1 vs ES-2 within the Effective Regulation Range of ES-1. In this case study, ES voltage, compensation modes,

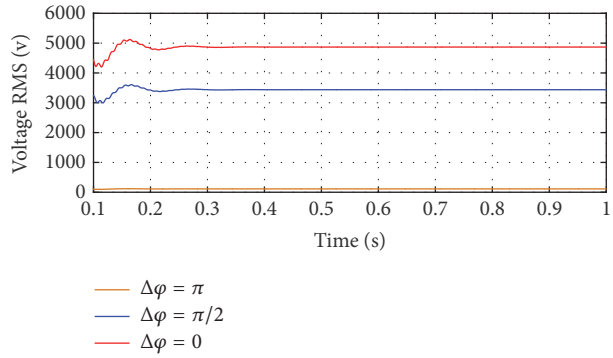

Figure 9: RMS of v_{es} of regulating v_c to the rated value under different $\Delta\varphi$.

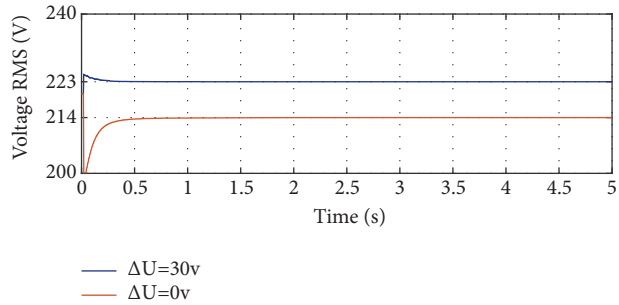

Figure 10: RMS of v_c with ES-1 activated when $\Delta U = 0$ V and $\Delta U = 30$ V.

and real and reactive powers are compared between ES-1 and ES-2 within the effective regulation range of ES-1. From Figure 11(a), one can see the ES voltages of ES-1 and ES-2 with the supply voltage $U_s = 216$ V, respectively, where the voltage of ES-2 (about 140 V) based on the MCV control strategy is less than the voltage of ES-1 (about 162 V) to regulate the line voltage v_c to 220 V. If one carefully observes the phase relationships in Figures 11(b) and 11(c), one will find that the ES-1 voltage lags its current about 90 degrees for capacitive compensation. Therefore, the real and reactive power of ES-1 are about 0 and -3000 Var as shown in Figures 11(d) and 11(e), respectively. For ES-2, its voltage lags its current by more than 90 degrees for negative resistive plus capacitive compensation. Therefore, ES-2 injects about 3600 Var reactive power, while injecting about 1200 W real power at the same time to regulate the line voltage to its rated value as shown in Figures 11(d) and 11(e).

Similarly, ES-1 and ES-2 are also compared in voltage suppression mode within the effective regulation range of ES-1. The ES voltages of ES-1 and ES-2 are about 97 V and 70 V with the supply voltage $U_s = 236$ V as shown in Figure 12(a). As can be seen from Figures 12(b) and 12(c), the ES-2 voltage leads its current by more than 90 degrees for negative resistive plus inductive compensation, while ES-1 is in inductive compensation mode to suppress voltage. Figures 12(d) and 12(e) show the corresponding real and reactive power injected into the power grid. One remark is that the ES currents in Figures 11(b), 11(c), 12(b), and 12(c) are enlarged for the ease of comparison while maintaining the phases.

The simulation results not only verify the effectiveness of the steady-state analysis and the MCV control scheme, but also show that ES-2 has a remarkable ability to regulate the PCC voltage. Theoretically, ES-2 has a wider range of compensation with respect to ES-1, in the sense that for any ΔU, there always exists a corresponding V_{es} to regulate V_c at its nominal level. In addition to this, the ES-2 voltage is less than the ES-1 voltage within the effective regulation range of ES-1 at the expense of some real power.

5.2. The Simulations Conducted on LabVIEW/PXI. To further verify the effectiveness of the steady-state analysis in Section 3 and the MCV control strategy in Section 4, hardware in the loop (HIL) simulations are conducted based on LabVIEW/PXIe-1071. For convenience, the ES currents shown in the following simulation results are actually the voltages across the noncritical roads. Since the current and the voltage of the resistive load are in the same phase, it does not affect the verification of the phase relationship.

5.2.1. The Influence of $\Delta\varphi$ on v_{es}. In this case study, the influence of $\Delta\varphi$ on v_{es} with $\Delta U = 0$ V and $\Delta U = 30$ V is further analyzed. From Figures 13(a), 13(c), and 13(e), we can see intuitively the sine waveforms of voltage v_{es}, whose RMS values are 4.587 V, 3.29 V, and 207.7 mV with $\Delta\varphi = 0$, $\Delta\varphi = (1/2)\pi$, and $\Delta\varphi = \pi$ when $\Delta U = 0$ V, respectively. It is worth noting that RMS values here are reduced by 1000 times due to the fact that HIL output constraint is ±10 V. Similarly, when $\Delta U = 30$, the corresponding RMS values are 4.901 V, 3.431 V, and 114.0 mV as shown in Figures 13(b), 13(d),

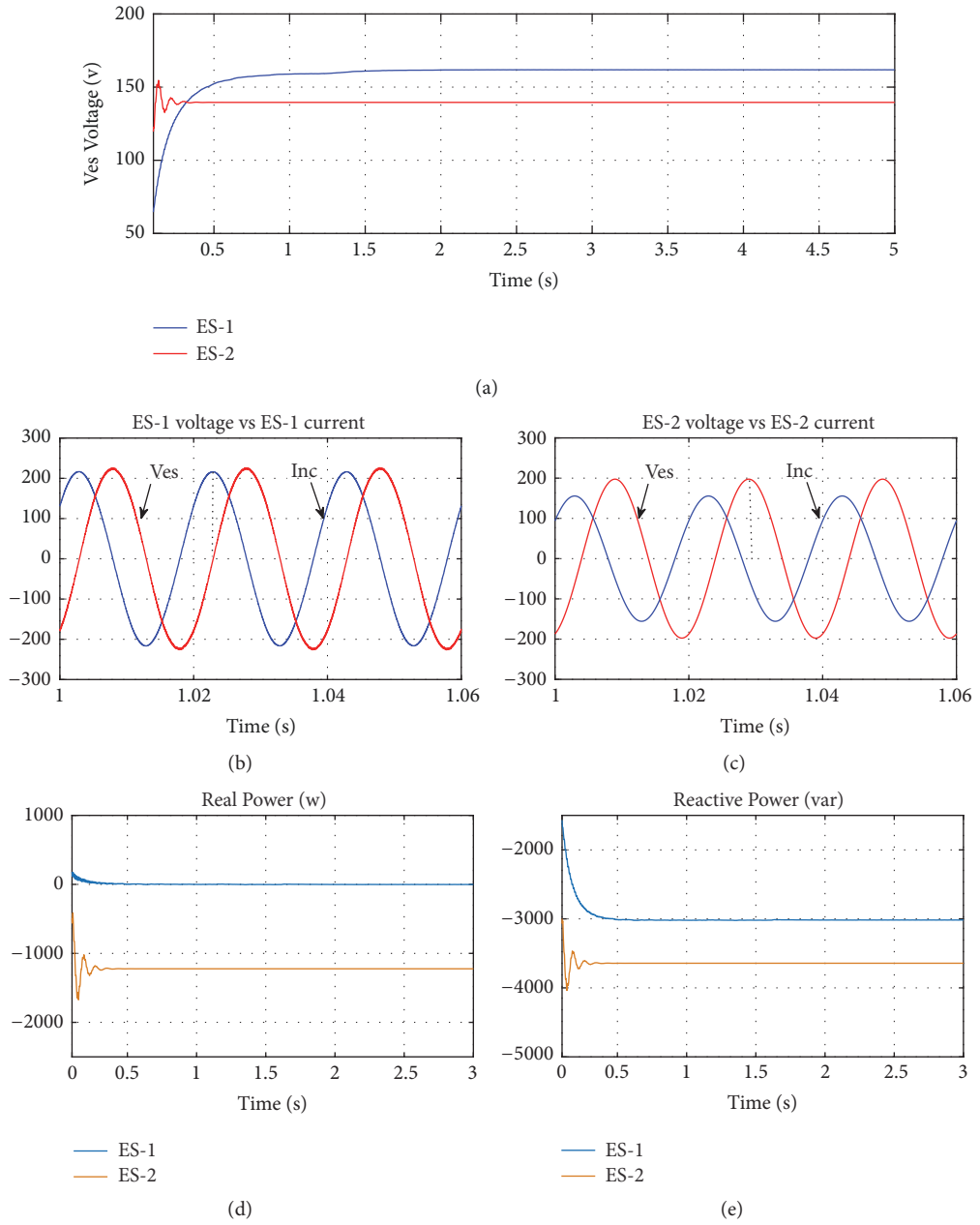

FIGURE 11: Comparing ES-1 with ES-2 when U_s = 216 V. (a) ES voltage; (b) ES-1 voltage vs ES-1 current; (c) ES-2 voltage vs ES-2 current; (d) real power; (e) reactive power. (All the current amplitudes are enlarged for the ease of comparison while maintaining the phases.)

and 13(f), respectively. The results of the HIL simulations and the Matlab simulations as well as the theoretical calculations are basically consistent, which means that v_{es} is extremely sensitive to $\Delta\varphi$. Moreover, it further indicates the necessity of MCV control strategy for ES-2 to regulate the line voltage due to the fact that DC side voltage of ES-2 is constrained.

5.2.2. Comparing ES-1 with ES-2 out of the Effective Regulation Range of ES-1. From the perspective of power electronics, ES-1 is a special reactive power compensator used to regulate the line voltage in the future smart grid with multiple renewable energy sources. However, due to the limitation of its compensation modes, only reactive power is exchanged with the power grid; thus ES-1 has compensation limits. In other words, once the supply voltage changes beyond a certain range, ES-1 will fail. With the introduction of real power for voltage regulation, ES-2 can well overcome this disadvantage. In this case study, the supply voltage is set at U_s = 240 V, which is out of the effective regulation range of ES-1. Figures 14(a) and 14(b) show the line voltage v_c with ES-1 and ES-2 activated, respectively. The RMS values, 4.47 V and 4.39 V, in Figures 14(a) and 14(b) are reduced by 50 times, which show that the ES-1 is unable to adjust v_c to its rated value. The phase relation in Figure 14(c) indicates ES-1

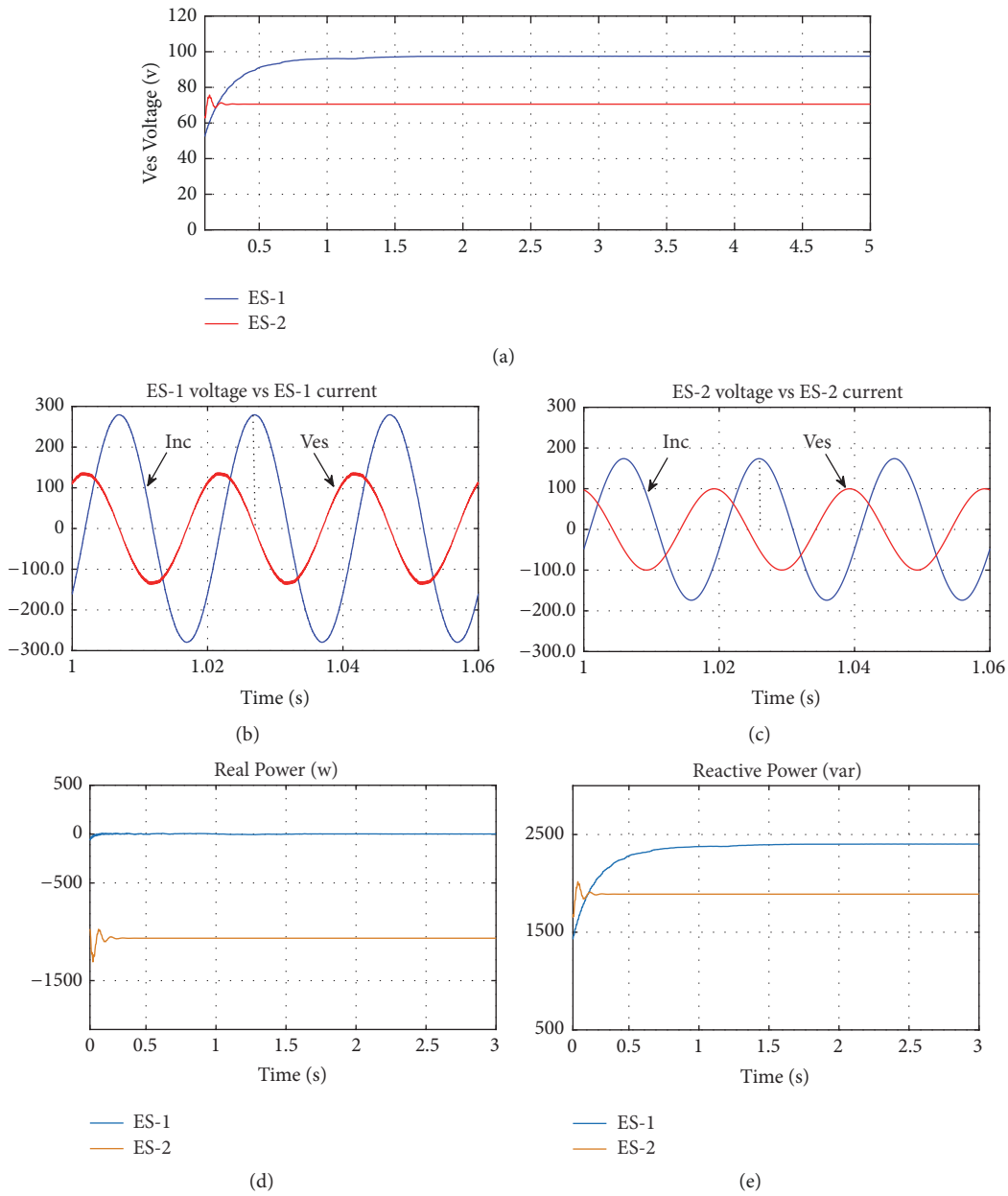

FIGURE 12: Comparing ES-1 with ES-2 when U_s = 236 V. (a) ES voltage; (b) ES-1 voltage vs ES-1 current; (c) ES-2 voltage vs ES-2 current; (d) real power; (e) reactive power. (All the current amplitudes are enlarged for the ease of comparison while maintaining the phases.)

is in inductive compensation mode, while ES-2 is in negative resistive plus inductive compensation mode as shown in Figure 14(d).

5.2.3. ES-1 and ES-2 for Voltage Boosting within the Effective Regulation Range of ES-1. ES-1 and ES-2 are compared for voltage boosting within the effective regulation range of ES-1 in this case study. The supply voltage is set at U_s = 216 V, which is within the effective regulation range of ES-1 and used to simulate undervoltage conditions. The phase relationships of ES-1 and ES-2 are shown in Figures 15(a) and 15(c), while the corresponding output voltages of ES-1 and ES-2 are shown in Figures 15(b) and 15(d), respectively. The simulation results show that the ES-2 based on the MCV control strategy has a smaller output voltage relative to ES-1 at the expense of injecting some real power to the power grid for voltage boosting.

5.2.4. ES-1 and ES-2 for Voltage Suppression within the Effective Regulation Range of ES-1. Similar to the voltage boosting mode, ES-1 and ES-2 are compared for voltage suppression within the effective regulation range of ES-1 in this case study. The supply voltage is set at U_s = 236 V, which is within the effective regulation range of ES-1 and used to simulate overvoltage conditions. As can be seen from Figure 16(a), the ES-1 voltage and ES-1 current are almost orthogonal and ES-1 voltage leads ES-1 current by almost 90 degrees for inductive compensation to suppress voltage, while the

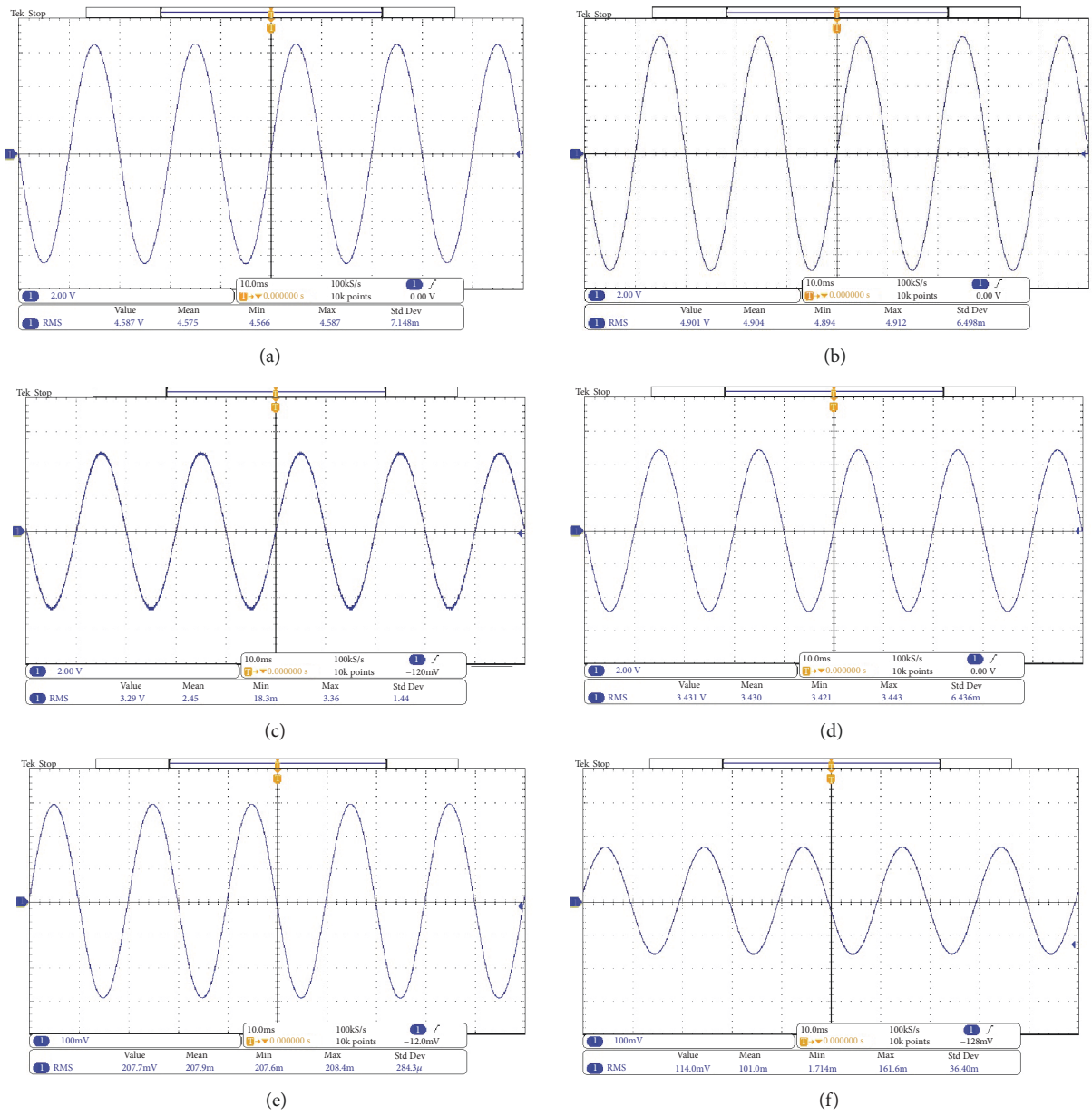

FIGURE 13: Sine waveforms of voltage v_{es} when $\Delta U = 0$ V and $\Delta U = 30$ V. (a) ES voltage when $\Delta\varphi = 0$ and $\Delta U = 0$ V; (b) ES voltage when $\Delta\varphi = 0$ and $\Delta U = 30$ V; (c) ES voltage when $\Delta\varphi = (1/2)\pi$ and $\Delta U = 0$ V; (d) ES voltage when $\Delta\varphi = (1/2)\pi$ and $\Delta U = 30$ V; (e) ES voltage when $\Delta\varphi = \pi$ and $\Delta U = 0$ V; (f) ES voltage when $\Delta\varphi = \pi$ and $\Delta U = 30$ V.

corresponding ES-1 voltage is shown in Figure 16(b). ES-2 works in negative resistive plus inductive compensation mode based on the MCV control strategy as shown in Figure 16(c), while its output voltage injected to the power grid is shown in Figure 16(d). In the same way, ES-2 based on the MCV control strategy has a smaller output voltage relative to ES-1.

6. Conclusion

ES-1 has compensation limits because of the constraints of its structure, while ES-2 can effectively remedy this defect at the expense of injecting real power. In this paper, ES-1 and ES-2 were compared in detail within and out of the effective regulation range. Moreover, for ES-2, the steady-state analysis was provided and a PR-based MCV control strategy was proposed to regulate the PCC voltage. For steady-state analysis, the relationship among the fluctuating part of the supply voltage, the PCC voltage, and the compensating voltage provided by ES-2 was derived, which implied that the phase angle of the PCC voltage could be used as a degree of freedom for control design to obtain a minimal compensating voltage in a given system. Once the phase angle of the PCC voltage was chosen, the maximal compensating voltage could be estimated based on the fluctuating part of the supply voltage which could be estimated *a priori*.

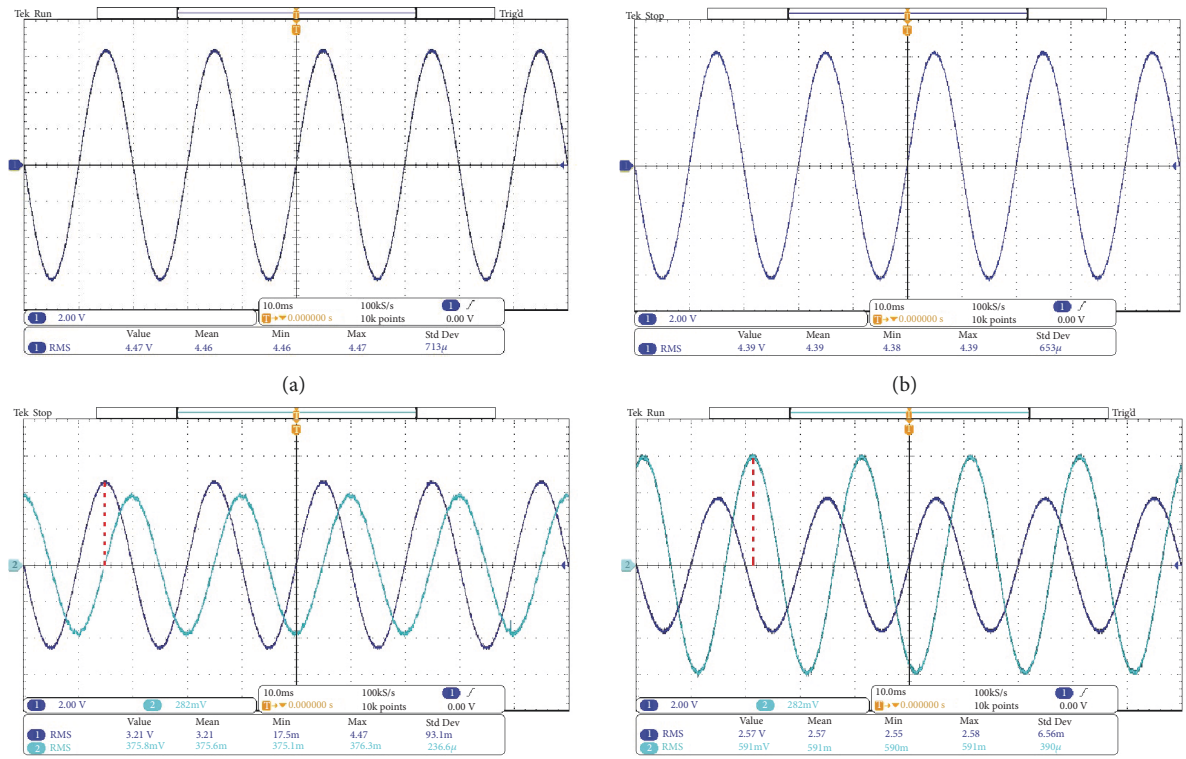

FIGURE 14: Comparing ES-1 with ES-2 when $U_s = 240$ V. (a) v_c with ES-1 activated; (b) v_c with ES-2 activated; (c) ES-1 voltage vs ES-1 current; (d) ES-2 voltage vs ES-2 current. (All the indicated ES currents are represented by the voltages of the resistive noncritical loads for the ease of comparison because of the same phase of the ES currents and the voltages of the resistive noncritical loads.)

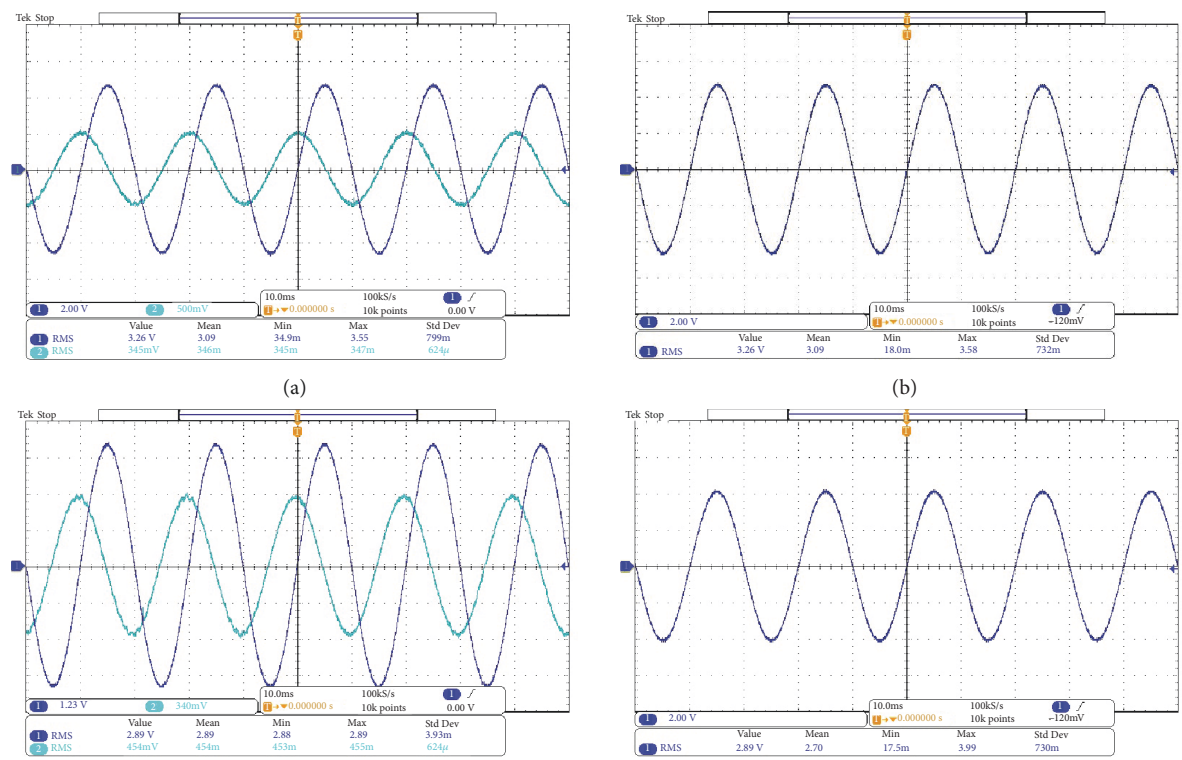

FIGURE 15: Comparing ES-1 with ES-2 when $U_s = 216$ V. (a) ES-1 voltage vs ES-1 current; (b) ES-1 voltage; (c) ES-2 voltage vs ES-2 current; (d) ES-2 voltage. (All the indicated ES currents are represented by the voltages of the resistive noncritical loads for the ease of comparison because of the same phase of the ES currents and the voltages of the resistive noncritical loads.)

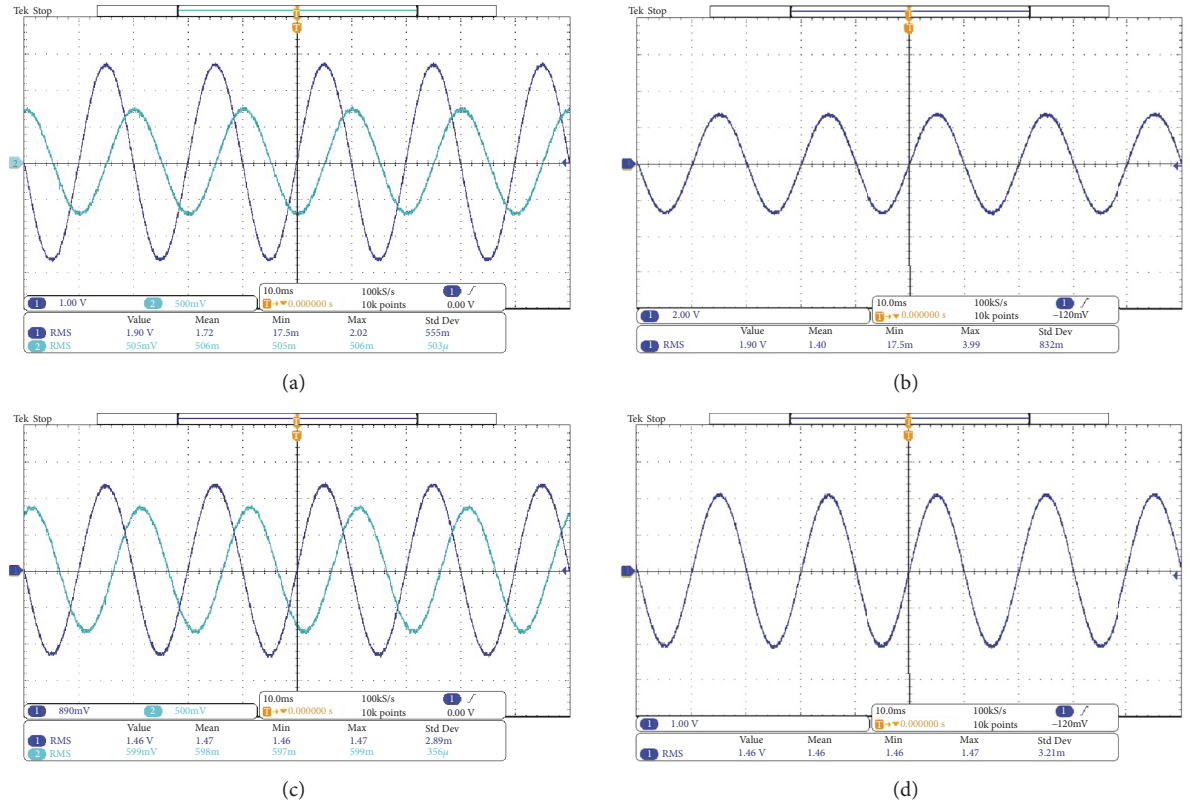

FIGURE 16: Comparing ES-1 with ES-2 when $U_s = 236$ V. (a) ES-1 voltage vs ES-1 current; (b) ES-1 voltage; (c) ES-2 voltage vs ES-2 current; (d) ES-2 voltage. (All the indicated ES currents are represented by the voltages of the resistive noncritical loads for the ease of comparison because of the same phase of the ES currents and the voltages of the resistive noncritical loads.)

Such a fact could be used for designing suitable electric springs with appropriate compensating capacity. Numerical simulations were conducted to demonstrate the effectiveness of the steady-state analysis and the control scheme.

Data Availability

All data can be accessed in the Simulation Studies section of this article.

Conflicts of Interest

The authors declare that there are no conflicts of interest regarding the publication of this article.

Acknowledgments

This research was supported by the National Natural Science Foundation of China [grant number 61873129].

References

[1] Y. Zhao, C. Wei, Z. Zhang, and W. Qiao, "A review on position/speed sensorless control for permanent-magnet synchronous machine-based wind energy conversion systems," *IEEE Journal of Emerging and Selected Topics in Power Electronics*, vol. 1, no. 4, pp. 203–216, 2013.

[2] Q. Guo, Z. Sun, Y. Zhang, and W. Xu, "Time-delayed feedback control in the multiple attractors wind-induced vibration energy harvesting system," *Complexity*, vol. 2019, Article ID 7973823, 11 pages, 2019.

[3] F. Cheng, L. Qu, W. Qiao, C. Wei, and L. Hao, "Fault diagnosis of wind turbine gearboxes based on dfig stator current envelope analysis," *IEEE Transactions on Sustainable Energy*, 2018.

[4] T. Kang, S. Kim, C. Hyoung, S. Kang, and K. Park, "An energy combiner for a multi-input energy-harvesting system," *IEEE Transactions on Circuits and Systems II: Express Briefs*, vol. 62, no. 9, pp. 911–915, 2015.

[5] K. T. Tan, X. Y. Peng, P. L. So, Y. C. Chu, and M. Z. Q. Chen, "Centralized control for parallel operation of distributed generation inverters in microgrids," *IEEE Transactions on Smart Grid*, vol. 3, no. 4, pp. 1977–1987, 2012.

[6] H. E. Espitia, I. Machón-González, H. López-García, and G. Díaz, "Proposal of an adaptive neurofuzzy system to control flow power in distributed generation systems," *Complexity*, vol. 2019, Article ID 1610898, 16 pages, 2019.

[7] Z. Yang, J. Xiang, and Y. Li, "Distributed consensus based supply-demand balance algorithm for economic dispatch problem in a smart grid with switching graph," *IEEE Transactions on Industrial Electronics*, vol. 64, no. 2, pp. 1600–1610, 2017.

[8] M. Pedrasa, T. Spooner, and I. MacGill, "Scheduling of demand side resources using binary particle swarm optimization," *IEEE Transactions on Power Systems*, vol. 24, no. 3, pp. 1173–1181, 2009.

[9] Z. Luo, J. Zhao, R. Yao, and Z. Shu, "Emergy-based sustainability assessment of different energy options for green buildings," *Energy Conversion and Management*, vol. 100, pp. 97–102, 2015.

[10] L. Xi, Y. Li, Y. Huang, L. Lu, and J. Chen, "A novel automatic generation control method based on the ecological population cooperative control for the islanded smart grid," *Complexity*, vol. 2018, Article ID 2456963, 17 pages, 2018.

[11] H. Zhong, D. Du, C. Li, and X. Li, "A novel sparse false data injection attack method in smart grids with incomplete power network information," *Complexity*, vol. 2018, Article ID 8503825, 16 pages, 2018.

[12] S. Y. Hui, C. K. Lee, and F. F. Wu, "Electric springs - a new smart grid technology," *IEEE Transactions on Smart Grid*, vol. 3, no. 3, pp. 1552–1561, 2012.

[13] N. R. Chaudhuri, C. K. Lee, B. Chaudhuri, and S. Y. R. Hui, "Dynamic modeling of electric springs," *IEEE Transactions on Smart Grid*, vol. 5, no. 5, pp. 2450–2458, 2014.

[14] C. K. Lee, B. Chaudhuri, and S. Y. Hui, "Hardware and control implementation of electric springs for stabilizing future smart grid with intermittent renewable energy sources," *IEEE Journal of Emerging and Selected Topics in Power Electronics*, vol. 1, no. 1, pp. 18–27, 2013.

[15] C. Kwan Lee, N. Ray Chaudhuri, B. Chaudhuri, and S. Y. R. Hui, "Droop control of distributed electric springs for stabilizing future power grid," *IEEE Transactions on Smart Grid*, vol. 4, no. 3, pp. 1558–1566, 2013.

[16] X. Chen, Y. Hou, and S. Y. Ron Hui, "Distributed control of multiple electric springs for voltage control in microgrid," *IEEE Transactions on Smart Grid*, vol. 8, no. 3, pp. 1350–1359, 2017.

[17] S.-C. Tan, C. K. Lee, and S. Y. Hui, "General steady-state analysis and control principle of electric springs with active and reactive power compensations," *IEEE Transactions on Power Electronics*, vol. 28, no. 8, pp. 3958–3969, 2013.

[18] S. Yan, S.-C. Tan, C.-K. Lee, B. Chaudhuri, and S. Y. R. Hui, "Use of smart loads for power quality improvement," *IEEE Journal of Emerging and Selected Topics in Power Electronics*, vol. 5, no. 1, pp. 504–512, 2017.

[19] Q. Wang, M. Cheng, Z. Chen, and Z. Wang, "Steady-state analysis of electric springs with a novel δ control," *IEEE Transactions on Power Electronics*, vol. 30, no. 12, pp. 7159–7169, 2015.

[20] K.-T. Mok, S.-C. Tan, and S. Y. R. Hui, "Decoupled power angle and voltage control of electric springs," *IEEE Transactions on Power Electronics*, vol. 31, no. 2, pp. 1216–1229, 2016.

[21] L. Diao, H. Du, Z. Shu, Y. Xue, M. Li, and S. M. Sharkh, "A comparative study between AI-HM and SPD-HM for railway auxiliary inverter with pulsating DC link," *IEEE Transactions on Industrial Electronics*, vol. 65, no. 7, pp. 5816–5825, 2018.

[22] X. Liu, A. M. Cramer, and F. Pan, "Generalized average method for time-invariant modeling of inverters," *IEEE Transactions on Circuits and Systems I: Regular Papers*, vol. 64, no. 3, pp. 740–751, 2017.

[23] X. Yan, Z. Shu, and S. M. Sharkh, "Hybrid modelling and control of single-phase grid-connected NPC inverters," in *Proceedings of the IEEE Applied Power Electronics Conference and Exposition (APEC)*, pp. 2223–2228, IEEE, Long Beach, CA, USA, 2016.

[24] J. Zeng, W. Qiao, C. Wei, and L. Qu, "A soft-switched three-port single-stage inverter for photovoltaic-battery systems," in *Proceedings of the IEEE Energy Conversion Congress and Exposition*, pp. 4568–4573, IEEE, Montreal, QC, Canada, 2015.

[25] X. Yan, Z. Shu, S. M. Sharkh, and T. Chen, "Output-feedback switching control of DC-DC cuk converters using multiple sampling," in *Proceedings of the International Automatic Control Conference (CACS)*, pp. 1–6, Yilan, Taiwan, 2015.

[26] J. Xiang, F. Ji, H. Nian, J. Zhang, and H. Deng, "Seamless transfer of single-phase utility interactive inverters with a synchronized output regulation strategy," *Journal of Power Electronics*, vol. 16, no. 5, pp. 1821–1832, 2016.

[27] X. Wei, Y. Liu, Z. Zhang, and J. Wang, "Steady-state analysis of electric spring for smart grid," in *Proceedings of the 12th World Congress on Intelligent Control and Automation (WCICA)*, pp. 905–909, Guilin, China, 2016.

[28] S. Wen, T. Huang, X. Yu, M. Z. Q. Chen, and Z. Zeng, "Sliding-mode control of memristive chuas systems via the event-based method," *IEEE Transactions on Circuits and Systems II: Express Briefs*, vol. 64, no. 1, pp. 911–915, 2017.

[29] C. Wei, W. Qiao, and Y. Zhao, "Sliding-mode observer-based sensorless direct power control of DFIGs for wind power applications," in *Proceedings of the IEEE Power and Energy Society General Meeting, (PESGM)*, IEEE, Denver, CO, USA, 2015.

[30] Y. Tang, H. Gao, and J. Kurths, "Distributed robust synchronization of dynamical networks with stochastic coupling," *IEEE Transactions on Circuits and Systems I: Regular Papers*, vol. 61, no. 5, pp. 1508–1519, 2014.

[31] Y. Xue, D. Meng, S. Yin et al., "Vector-based model predictive hysteresis current control for asynchronous motor," *IEEE Transactions on Industrial Electronics*, 2018.

[32] K. T. Tan, P. L. So, Y. C. Chu, and M. Z. Q. Chen, "Coordinated control and energy management of distributed generation inverters in a microgrid," *IEEE Transactions on Power Delivery*, vol. 28, no. 2, pp. 704–713, 2013.

[33] L. Zhang, M. Z. Chen, H. Su, and G. Chen, "Event-based asynchronous communication and sampled control for synchronization of multiagent networks with input saturation," *International Journal of Robust and Nonlinear Control*, vol. 28, no. 5, pp. 1871–1885, 2018.

Hindawi
Complexity
Volume 2019, Article ID 5897438, 15 pages
https://doi.org/10.1155/2019/5897438

Research Article

Complementary Configuration and Optimal Energy Flow of CCHP-ORC Systems Using a Matrix Modeling Approach

Wencong Huang,[1,2] Yufang Chang ,[2] and Youxin Yuan[1]

[1]*School of Automation, Wuhan University of Technology, 122 Luoshi Road, Wuhan 430070, China*
[2]*Hubei Key Laboratory for High-Efficiency Utilization of Solar Energy and Operation Control of Energy Storage System, Hubei University of Technology, 28 Nanli Road, Wuhan, Hubei 430068, China*

Correspondence should be addressed to Yufang Chang; changyf@hbut.edu.cn

Received 16 January 2019; Revised 13 March 2019; Accepted 28 March 2019; Published 18 April 2019

Guest Editor: Xiaoqing Bai

A mass of thermal energy from the combined cooling, heating, and power (CCHP) system will be wasted by the buildings with low ratio of heat to power demand. To further improve the using efficiency of the excess thermal energy, an active method, which adds the organic Rankine cycle (ORC) equipment in the CCHP system, is configured. A complementary configuration of this CCHP-ORC is also investigated. This paper presents a matrix modeling approach to establish a mathematical model of the CCHP-ORC system. The CCHP-ORC system can be viewed as a multiple input and multiple output (MIMO) model. Energy conversion of the system components is described as the efficiency matrices. Energy flow between the system components is described as dispatch matrices. Energy conversion and flow from the system input to output are modeled by a conversion matrix. The objective function and the constraints of the system are determined. The optimal operation strategies are obtained by solving the optimization problem of minimizing the evaluation criteria function. Comprehensive case studies are conducted based on a hypothetical CCHP-ORC system. The study results reveal that the effectiveness and economic efficiency of the proposed approaches outperform those obtained from conventional CCHP systems.

1. Introduction

According to the statistical data from the Energy Information Administration of the U.S. Department of Energy, in many countries, building energy consumption accounts for about 36% of the total energy consumption, and nearly 30% of greenhouse gas (GHG) emissions [1]. Particularly in China, the building energy consumption has an annual growth rate over 10% with the rapid development of economy [2, 3]. The increasing building energy consumption has led to serious building-related problems such as restricting economic development, exacerbating energy crisis, and environmental issues such as greenhouse effect and air pollution. To deal with these problems, combined cooling, heating and power (CCHP) systems which can improve energy utilization efficiency and reduce GHG emissions are developed.

A CCHP system is an integrated energy supply system, which can also be referred to as the trigeneration system [4]. It provides building users electricity, cooling energy, and heating energy by installing the power generation unit (PGU) [5, 6]. The CCHP system makes use of the rejected heat from the PGU to generate thermal energy for cooling and heating demands [7, 8]. As a result, the overall fuel energy utilization efficiency of CCHP systems can reach 70%-90%, which is significantly higher than that of separation production (SP) systems [9, 10]. As shown in the literature, CCHP systems have been broadly applied in office buildings, hotels, hospitals, commercial malls, and other building types.

Performance of the CCHP system depends on the system structure and the operation strategy. In [11], the authors propose a new CCHP system structure with both absorption and electric chillers to provide more flexibility in supplying energy. Four typical CCHP systems with existing technologies for various size ranges are illustrated in [12]. With the development of the renewable energy, solar-integrated CCHP systems [13–17], SOFC-trigeneration systems [18, 19], and biomass-trigeneration system [20] are studied.

Once the system structure is determined and implemented, the operation strategy is the crucial factor for the CCHP system design. There are two popular operation strategies [21–24]: following the electric load (FEL) and following the thermal load (FTL). However, as illustrated in the literature [11] both of the FEL and FTL strategies inherently waste a certain amount of energy. Therefore, designing an optimal operation strategy to improve the energy utilization efficiency by reducing the energy waste is urged.

Operation strategy design relies on the selection of evaluation criteria, which should be aligned with the stakeholders' objectives. Energy savings and environmental impacts are two popular aspects when constructing evaluation criteria. Fumo *et al.* proposed the evaluation criteria considering the primary energy consumption saving (PECS) and carbon dioxide emission reduction (CDER) [25, 26]. Li *et al.* established a mix-integer nonlinear programming (MINLP) model to evaluate economic efficiency and sensitivity of CCHP systems [27]. Wang *et al.* studied the energetic and environmental benefits of the CCHP system in comparison to SP systems based on a particle swarm optimization algorithm [28]. Jing *et al.* estimated the PEC and pollution emissions of the BCHP system in FEL and FTL operation strategies based on life cycle assessment (LCA) [29, 30].

For an existing CCHP system, when the electricity to thermal energy requirement ratio of building users is exactly equal to the output ratio of the PGU, the maximum efficiency of the CCHP system is achieved [31]. However, this ideal situation rarely happens due to the random variation of energy requirements. When the supply is insufficient, adding extra energy (fuel or electricity) is a direct treatment. However, when the supply exceeds the demand, the situation becomes complicated. In the case surplus electricity is generated, it can be sold back to power grid or converted to thermal energy. Similarly, the excess thermal energy can be stored in thermal storage units or converted to electricity by some special equipment, such as organic ranking cycle (ORC). In this paper, an active excess thermal energy treatment method which uses an ORC to convert the excess thermal to electricity is investigated.

In recent years, more attention has been put on the ORC system. A complementary structure of CCHP-ORC system is configured in [31, 32]. A biomass fuelled trigeneration system integrated with ORC is studied in [33]. Three trigeneration systems, combined SOFC with ORC, combined biomass combustor with ORC, and combined solar collectors with ORC, are analyzed in [34]. Liu *et al.* researched five kinds of building in Shanghai and evaluated the CCHP-ORC system [35]. The aforementioned literature shows that the ORC technology has advantages in using the thermal energy and its combination with trigeneration system has good application prospects. So we are going to adopt the CCHP-ORC structure which uses the gas turbine as PGU, an ORC as waste heat recycle equipment, and electric and absorption chillers as hybrid chillers. The advantages of our CCHP-ORC system are reflected by the higher energy utilization, and the adjustability of the electricity to thermal energy output ratio.

When the structure of the CCHP-ORC system is configured, the operation strategy should be designed. Firstly, the mathematical model of the CCHP-ORC system should be established. From the perspective of control theory, the CCHP-ORC system can be treated as the connection between the energy input and the building users' demand. We consider using transfer function in control theory to describe this input-output relation. Because the energy input includes fuel and electricity from the power grid, and the building users' demand includes cooling, heating, and power, the CCHP-ORC system is a multiple input and multiple output (MIMO) system. In [36], the concepts of dispatch factors and coupling matrix are used to describe the system, and the power flow and operation strategy are optimized using Karush-Kuhn-Tucker (KKT) conditions. In [37], the authors model the system by introducing the concepts of bifurcations, junctions, and the backtracking. However these modeling methods are too complicated.

The main contribution of this paper is that a more intuitive and comprehensive approach, a matrix transfer function modeling approach (referred to as matrix modeling approach), is proposed to model the CCHP-ORC system. Based on the matrix modeled system, sequential quadratic programming (SPQ) algorithm is adopted to optimize the linear objective function, which is subjected to the nonlinear equalities and inequalities. The result of the optimization problem is the optimal flow and operation strategy for the CCHP-ORC.

This paper is organized as follows. The configuration and matrix modeling of the CCHP-ORC system are described in Section 2. In Section 3, the performance criteria for the CCHP-ORC system are presented and the optimization problem is established. Finally, the effectiveness of the system configuration and operation strategy are verified through a case study of a hypothetical office building in Section 4. Section 5 concludes this paper.

2. System Configuration and Matrix Modeling

In this section, an optimal CCHP-ORC structure and an intuitive matrix modeling of the CCHP-ORC system will be introduced. In order to make full use of energy and improve the flexibility of energy supply, the configuration of the CCHP-ORC system is presented in Figure 1.

In addition to traditional equipment, a complementary ORC and an electric chiller are added as important components which can not only utilize the excess thermal energy but also dynamically adjust the electricity to thermal energy output ratio of the entire system. In Figure 1, when $Q_r + Q_b > Q_{hrc} + Q_{hrh}$, the excess thermal energy exists. The ORC is used to convert the excess thermal to electricity. The cooling load is provided by absorption and electric chillers. The electric chiller has a high coefficient of performance (COP) which leads to a high cooling efficiency. The output of the ORC and the electric chiller can be adjusted dynamically to keep the CCHP-ORC system running at the matched status according to the users' energy requirements.

2.1. Efficiency Matrices of System Components. The energy conversion of the components in the CCHP-ORC system

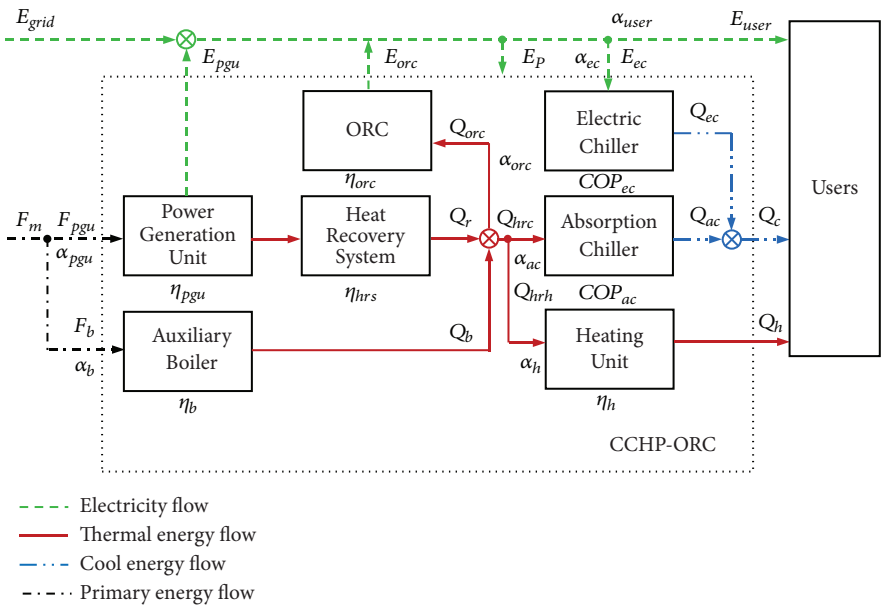

Figure 1: Structure diagram of a CCHP-ORC system.

can be described using efficiency matrices, namely, coupling matrices. In this paper, u is an equipment set and equipment $m \in u$, F, E, Q_c, and Q_h denote the fuel, electricity, cooling energy, and heating energy, respectively. The input and the output of the component m are defined as $V_i^m = [F_i^m \; E_i^m \; Q_{ci}^m \; Q_{hi}^m]^\top$ and $V_o^m = [F_o^m \; E_o^m \; Q_{co}^m \; Q_{ho}^m]^\top$, respectively. So the input-output relation of the component m can be described as

$$V_o^m = H^m V_i^m, \tag{1}$$

where H^m is the efficiency matrix of the component m.

Consequently, the input-output relation of the ORC can be represented in the following matrix form:

$$\begin{bmatrix} 0 \\ E_o^{orc} \\ 0 \\ 0 \end{bmatrix} = \begin{bmatrix} 0 & 0 & 0 & 0 \\ 0 & 0 & 0 & COP_{orc} \\ 0 & 0 & 0 & 0 \\ 0 & 0 & 0 & 0 \end{bmatrix} \begin{bmatrix} 0 \\ 0 \\ 0 \\ Q_{hi}^{orc} \end{bmatrix} = H^{orc} V_i^{orc}. \tag{2}$$

Following the same procedure, efficiency matrices for the PGU, auxiliary boiler, heat recovery system, heating unit, electric chiller, and absorption chiller can be obtained as

$$H^{pgu} = \begin{bmatrix} 0 & 0 & 0 & 0 \\ \eta_{pgu} & 0 & 0 & 0 \\ 0 & 0 & 0 & 0 \\ 1-\eta_{pgu} & 0 & 0 & 0 \end{bmatrix},$$

$$H^b = \begin{bmatrix} 0 & 0 & 0 & 0 \\ 0 & 0 & 0 & 0 \\ 0 & 0 & 0 & 0 \\ \eta_b & 0 & 0 & 0 \end{bmatrix},$$

$$H^{hrs} = \begin{bmatrix} 0 & 0 & 0 & 0 \\ 0 & 0 & 0 & 0 \\ 0 & 0 & 0 & 0 \\ 0 & 0 & 0 & \eta_{hrs} \end{bmatrix},$$

$$H^h = \begin{bmatrix} 0 & 0 & 0 & 0 \\ 0 & 0 & 0 & 0 \\ 0 & 0 & 0 & 0 \\ 0 & 0 & 0 & \eta_h \end{bmatrix},$$

$$H^{ec} = \begin{bmatrix} 0 & 0 & 0 & 0 \\ 0 & 0 & 0 & 0 \\ 0 & COP_{ec} & 0 & 0 \\ 0 & 0 & 0 & 0 \end{bmatrix},$$

$$H^{ac} = \begin{bmatrix} 0 & 0 & 0 & 0 \\ 0 & 0 & 0 & 0 \\ 0 & 0 & 0 & COP_{ac} \\ 0 & 0 & 0 & 0 \end{bmatrix}. \tag{3}$$

Each efficiency matrix represents the performance of the energy conversion of each component in the CCHP-ORC system.

2.2. Dispatch Matrices of System. The dispatch matrices indicate the energy flow between the components in the system. Usually, the dispatch factors exist at the bifurcations of the system. For example in Figure 1, the thermal energy produced by the heat recovery system and the auxiliary boiler will be

separated into three parts: one for the absorption chiller, one for the heating unit, and the last one for the ORC. Let α_{ac}, α_h, and α_{orc} denote the dispatch factors for the absorption chiller, the heating unit, and the ORC, respectively. Then we have

$$Q_{hrc} = \alpha_{ac}\left(Q_r + Q_b\right), \tag{4}$$

$$Q_{hrh} = \alpha_h\left(Q_r + Q_b\right), \tag{5}$$

$$Q_{orc} = \alpha_{orc}\left(Q_r + Q_b\right), \tag{6}$$

subject to

$$0 \le \alpha_{ac} + \alpha_h + \alpha_{orc} \le 1, \tag{7a}$$

$$0 \le \alpha_{ac} \le 1, \tag{7b}$$

$$0 \le \alpha_h \le 1, \tag{7c}$$

$$0 \le \alpha_{orc} \le 1. \tag{7d}$$

At the ORC side, we have

$$Q_{orc} = \left[\alpha_{pgu}\left(1-\eta_{pgu}\right)\eta_{hrs} + \alpha_b\eta_b\right]\alpha_{orc}F_m, \tag{8}$$

where α_{pgu} and α_b denote the dispatch factors for the PGU and the auxiliary boiler. To facilitate the later optimization-based operation strategy design, (8) can be rewritten in a matrix form as

$$\begin{aligned} V_i^{orc} &= \begin{bmatrix} 0 & 0 & 0 & 0 \\ 0 & 0 & 0 & 0 \\ 0 & 0 & 0 & 0 \\ \alpha_{orc}\left[\alpha_{pgu}\left(1-\eta_{pgu}\right)\eta_{hrs} + \alpha_b\eta_b\right] & 0 & 0 & 0 \end{bmatrix} \begin{bmatrix} F_m \\ E_{grid} \\ 0 \\ 0 \end{bmatrix} \\ &= T_{orc}V_i \end{aligned} \tag{9}$$

where T_{orc} is the dispatch matrix for the ORC and V_i is the system input.

By following the similar procedure, the dispatch matrices for the PGU, the auxiliary boiler, electric chiller, heat recovery system, heating unit, and absorption chiller can be defined as

$$T_{pgu} = \begin{bmatrix} \alpha_{pgu} & 0 & 0 & 0 \\ 0 & 0 & 0 & 0 \\ 0 & 0 & 0 & 0 \\ 0 & 0 & 0 & 0 \end{bmatrix},$$

$$T_b = \begin{bmatrix} \alpha_b & 0 & 0 & 0 \\ 0 & 0 & 0 & 0 \\ 0 & 0 & 0 & 0 \\ 0 & 0 & 0 & 0 \end{bmatrix},$$

$$T_{ec} = \begin{bmatrix} 0 & 0 & 0 & 0 \\ 0 & \alpha_{ec} & 0 & 0 \\ 0 & 0 & 0 & 0 \\ 0 & 0 & 0 & 0 \end{bmatrix},$$

$$T_{hrs} = \begin{bmatrix} 0 & 0 & 0 & 0 \\ 0 & 0 & 0 & 0 \\ 0 & 0 & 0 & 0 \\ \alpha_{pgu}\left(1-\eta_{pgu}\right) & 0 & 0 & 0 \end{bmatrix},$$

$$T_h = \begin{bmatrix} 0 & 0 & 0 & 0 \\ 0 & 0 & 0 & 0 \\ 0 & 0 & 0 & 0 \\ \alpha_h\left[\alpha_{pgu}\left(1-\eta_{pgu}\right)\eta_{hrs} + \alpha_b\eta_b\right] & 0 & 0 & 0 \end{bmatrix},$$

$$T_{ac} = \begin{bmatrix} 0 & 0 & 0 & 0 \\ 0 & 0 & 0 & 0 \\ 0 & 0 & 0 & 0 \\ \alpha_{ac}\left[\alpha_{pgu}\left(1-\eta_{pgu}\right)\eta_{hrs} + \alpha_b\eta_b\right] & 0 & 0 & 0 \end{bmatrix}. \tag{10}$$

Similarly, in addition to (7a), (7b), (7c), and (7d), we have

$$\alpha_{pgu} + \alpha_b = 1, \tag{11a}$$

$$\alpha_{user} + \alpha_{ec} = 1, \tag{11b}$$

$$\alpha_{ac} + \alpha_h + \alpha_{orc} = 1, \tag{11c}$$

$$0 \le \alpha_{pgu}, \alpha_b, \alpha_{user}, \alpha_{ec}, \alpha_{ac}, \alpha_h, \alpha_{orc} \le 1. \tag{11d}$$

2.3. Conversion Matrix of the CCHP-ORC System. The CCHP-ORC system modeled in a matrix form can be viewed as an input-out model. The conversion matrix of the CCHP-ORC system describes the relationship between the input and the output and represents the energy flow procedure of the system. From Figure 1, the system input and output are defined as

$$V_i = \left[F_m \;\; E_{grid} \;\; Q_{ci} \;\; Q_{hi}\right]^{\mathsf{T}} = \left[F_m \;\; E_{grid} \;\; 0 \;\; 0\right]^{\mathsf{T}}, \tag{12}$$

$$V_o = \left[F_o \;\; E_{user} \;\; Q_c \;\; Q_h\right]^{\mathsf{T}} = \left[0 \;\; E_{user} \;\; Q_c \;\; Q_h\right]^{\mathsf{T}}, \tag{13}$$

respectively.

Then the conversion matrix of the CCHP-ORC system, G, can be defined as

$$V_o = GV_i. \tag{14}$$

In order to obtain the conversion matrix G, the expression of the output elements, E_{user}, Q_c, and Q_h, should be written as functions of the system input. Without the loss of generality, the parasitic electricity E_p can be assumed to be a constant

and further assumed to be zero. The output element E_{user} can be represented as

$$\begin{aligned} E_{user} &= \alpha_{user}\left(E_{pgu} + E_{orc} + E_{grid}\right) = \left[\alpha_{user}\alpha_{pgu}\eta_{pgu}\right. \\ &+ \alpha_{pgu}\left(1-\eta_{pgu}\right)\eta_{hrs}\alpha_{orc}COP_{orc}\alpha_{user} \\ &\left.+ \alpha_b\eta_b\alpha_{orc}\eta_{orc}\alpha_{user}\right]F_m + \alpha_{user}E_{grid}. \end{aligned} \tag{15}$$

For the cooling part, we have

$$\begin{aligned} Q_c &= Q_{ec} + Q_{ac} = \alpha_{ec}COP_{ec}\left(E_{pgu} + E_{orc} + E_{grid}\right) \\ &+ \alpha_{ac}COP_{ac}F_m\left[\alpha_{pgu}\left(1-\eta_{pgu}\right)\eta_{hrs} + \alpha_b\eta_b\right] \\ &= \left[\alpha_{pgu}\eta_{pgu}\alpha_{ec}COP_{ec}\right. \\ &+ \left[\alpha_{pgu}\left(1-\eta_{pgu}\right)\eta_{hrs} + \alpha_b\eta_b\right] \\ &\cdot \alpha_{orc}COP_{orc}\alpha_{ec}COP_{ec} \\ &+ \left.\left[\alpha_{pgu}\left(1-\eta_{pgu}\right)\eta_{hrs} + \alpha_b\eta_b\right]\alpha_{ac}COP_{ac}\right]F_m \\ &+ \alpha_{ec}COP_{ec}E_{grid}. \end{aligned} \tag{16}$$

where the electric cooling to cool load ratio, which is inherently included in the modeling procedure and can be obtained through the optimization, is defined as $e = Q_{ec}/Q_c$.

The heating demand is solely provided by the heating unit. Thus, we have

$$\begin{aligned} Q_h &= \left(Q_r + Q_b\right)\alpha_h\eta_h \\ &= \left[\alpha_{pgu}\left(1-\eta_{pgu}\right)\eta_{hrs} + \alpha_b\eta_b\right]\alpha_h\eta_hF_m. \end{aligned} \tag{17}$$

The conversion matrix of the CCHP-ORC system can be obtained from (15)–(17) as

$$G = \begin{bmatrix} 0 & 0 & 0 & 0 \\ G_{21} & \alpha_{user} & 0 & 0 \\ G_{31} & \alpha_{ec}COP_{ec} & 0 & 0 \\ G_{41} & 0 & 0 & 0 \end{bmatrix}. \tag{18}$$

where

$$\begin{aligned} G_{21} &= \alpha_{user}\alpha_{pgu}\eta_{pgu} + \alpha_{pgu}\left(1-\eta_{pgu}\right) \\ &\cdot \eta_{hrs}\alpha_{orc}COP_{orc}\alpha_{user} + \alpha_b\eta_b\alpha_{orc}\eta_{orc}\alpha_{user}, \\ G_{31} &= \alpha_{pgu}\eta_{pgu}\alpha_{ec}COP_{ec} \\ &+ \left[\alpha_{pgu}\left(1-\eta_{pgu}\right)\eta_{hrs} + \alpha_b\eta_b\right] \\ &\cdot \alpha_{orc}COP_{orc}\alpha_{ec}COP_{ec} \\ &+ \left[\alpha_{pgu}\left(1-\eta_{pgu}\right)\eta_{hrs} + \alpha_b\eta_b\right]\alpha_{ac}COP_{ac}, \\ G_{41} &= \left[\alpha_{pgu}\left(1-\eta_{pgu}\right)\eta_{hrs} + \alpha_b\eta_b\right]\alpha_h\eta_h. \end{aligned} \tag{19}$$

The main objective of this paper is to determine the dispatch factors and the system input to optimize the performance criteria objective function.

3. Optimal Operation Strategy Design

Having the whole system modeled in a matrix form, we can formulate the operation strategy design as an optimization problem. The objective function and associated constraints will be illustrated in the rest of this section.

3.1. Performance Criteria for the CCHP-ORC System. As mentioned in Section 1. Evaluation of a CCHP system may contain many factors, including primary energy consumption, energy conversion efficiency, total cost of the system, environmental impact, life cycle assessment, and combination of multiple factors. In this paper, three popular criteria, i.e., primary energy consumption, the total cost of the system, and the environmental impact, are adopted to evaluate the performance of the CCHP-ORC system.

3.1.1. Primary Energy Consumption (PEC). PEC is a direct and common indicator to reflect the operating efficiency of a CCHP-ORC system. PEC is defined as

$$PEC \triangleq \frac{E_{user} + E_p}{\eta_e\eta_{grid}} + \frac{Q_c}{COP_{ec}\eta_e\eta_{grid}} + \frac{Q_h}{\eta_h\eta_b}, \tag{20}$$

where E_p is the parasitic electricity, η_e is the generation efficiency of the grid power plant, and η_{grid} is the transmission efficiency of grid.

3.1.2. Hourly Total Cost (HTC). In order to obtain the optimal energy flow and operation strategy for every hour, HTC is adopted as a key element in the operation strategy optimization. HTC of the CCHP-ORC system is defined as

$$\begin{aligned} HTC \triangleq\ & E_{grid}C_e + E_{grid}\mu_eC_{ca} + F_mC_f + F_m\mu_fC_{ca} \\ &+ \frac{\sum_{k=1}^{l}N_kC_k}{8760L}, \end{aligned} \tag{21}$$

where C_e and C_f are the unit prices of electricity and the fuel, respectively; μ_e and μ_f are the carbon conversion factors of the the electricity and fuel, respectively; C_{ca} is the carbon tax rate; N_k is the installed capacity of each equipment and C_k is the initial capital cost of each equipment; l is the number of equipment included in the CCHP-ORC system; and L is the life of each equipment, where we assume that all equipment have the same life time. 8760 (h) represents the hours number of the whole year.

3.1.3. Carbon Dioxide Emission (CDE). Greenhouse gas emission control is an emerging topic in the CCHP system design. In a CCHP-ORC system equipped with fossil-fuel combustion units, CDE serves as an indicator of environment impacts and can be calculated as

$$CDE \triangleq E_{grid}\mu_e + F_m\mu_f, \tag{22}$$

where μ_e and μ_f are the carbon conversion factors of the the electricity and fuel, respectively.

3.1.4. Performance Evaluation Criteria (EC) Function. To comprehensively evaluate the system performance, we define a performance evaluation criteria (EC) function as a weighted summation of the three above mentioned criteria. The most commonly used way to evaluate the performance of a CCHP-ORC system is to compare those factors with those of the SP system. Thus, the hourly EC function can be redefined as

$$EC_{hour} \triangleq \omega_1 \frac{PEC}{PEC^{SP}} + \omega_2 \frac{HTC}{HTC^{SP}} + \omega_3 \frac{CDE}{CDE^{SP}}, \tag{23}$$

where ω_1, ω_2, and ω_3 are the weights of PEC, HTC, and CDE, respectively. Three weights satisfy

$$\omega_1 + \omega_2 + \omega_3 = 1 \tag{24a}$$

$$0 \le \omega_1, \omega_2, \omega_3 \le 1. \tag{24b}$$

PEC^{SP}, HTC^{SP}, and CDE^{SP} are PEC, HTC, and CDE of the SP system and can be, respectively, calculated as (20), (21), and (22).

Consequently, the annual EC function can be written as

$$EC_{annual} \triangleq \sum_{i=1}^{365} \sum_{j=1}^{24} EC_{hourij} \tag{25}$$

where EC_{hourij} is the hourly EC function value on day i at hour j.

3.2. Optimization Problem Formulation. Formulating a complete optimization problem includes determining decision variables, designing objective function, and setting constraints. The whole procedure will be elaborated on this part.

3.2.1. Decision Variables. As mention in Section 2, dispatch factors and energy inputs are the variables that need to be adjusted to coordinate the energy flow of the system, meet the building demand, and minimize the objective function. Thus, the dispatch factors and system energy inputs can be selected as decision variables.

It can be readily observed from (7a), (7b), (7c), (7d) and (11a), (11b), (11c), (11d) that the dispatch factors α_{pgu}, α_b, α_{user}, α_{ec}, α_{ac}, α_{orc}, and α_h are dependent variables. Thus, the dispatch factors can be reduced to be α_{pgu}, α_{user}, α_{ac}, and α_{orc}, which are independent of each other.

The system energy inputs include F_m and E_{grid}. Thus, the optimizer consisting of all the above-mentioned decision variables can be defined as

$$x = \left[\alpha_{pgu} \;\; \alpha_{user} \;\; \alpha_{ac} \;\; \alpha_{orc} \;\; F_m \;\; E_{grid}\right]^{\mathsf{T}}. \tag{26}$$

3.2.2. Objective Function. By using the defined optimizer x, the EC_{hour} function in (23) can be written as a linear function of the optimizer x as

$$EC_{hour}(x) = \omega_1 \frac{Bx}{PEC^{SP}} + \omega_2 \frac{Cx + L}{HTC^{SP}} + \omega_3 \frac{Dx}{CDE^{SP}}. \tag{27}$$

where

$$B = \left[0 \;\; 0 \;\; 0 \;\; 0 \;\; 1 \;\; \frac{1}{\left(\eta_e^{SP}\eta_{grid}\right)}\right],$$

$$C = \left[0 \;\; 0 \;\; 0 \;\; 0 \;\; C_f + \mu_f C_{ca} \;\; C_e + \mu_e C_e\right],$$

$$D = \left[0 \;\; 0 \;\; 0 \;\; 0 \;\; \mu_f \;\; \mu_e\right],$$

$$L = \frac{\sum_{k=1}^{l} N_k C_k}{8760L}. \tag{28}$$

$EC_{hour}(x)$ will serve as the objective function of the optimization-based operation strategy design. ω_1, ω_2, and ω_3 can be set according to different evaluation requirements. For example, ω_3 would be set relatively higher if more emphases are put on the environmental aspect.

3.2.3. Equality Constraint. In the sense of balance, (14) will serve as the equality constraint of the optimization problem. Further, since some elements in G are represented by the decision variables, it is necessary to write G as a function of x. Thus we have

$$\begin{aligned} G = {} & \left(g_{211}W_{22} + g_{311}W_{33} + g_{313}W_{32} + g_{315}W_{34}\right. \\ & \left. - g_{411}W_{43}\right) xx^{\mathsf{T}}U_{11} + \left(g_{312}W_{33} + g_{314}W_{31}\right. \\ & \left. + g_{316}W_{34} + g_{411}W_{41} - g_{412}W_{43}\right) xQ_{11} + \left(g_{212}W_{22}\right. \\ & \left. - g_{316}W_{32} + g_{213}W_{22}\left(x^{\mathsf{T}}Q_1\right) - g_{315}W_{32}\left(x^{\mathsf{T}}Q_1\right)\right) \\ & \cdot xx^{\mathsf{T}}U_{41} + \left(g_{221}W_{22} - g_{321}W_{32}\right) xQ_{12} \\ & + \left(CON_{cop_{ec}} + CON_{\eta_h\eta_b}\right), \end{aligned} \tag{29}$$

where

$$W_{22} = \begin{bmatrix} 0 & 0 & 0 & 0 & 0 & 0 \\ 0 & 1 & 0 & 0 & 0 & 0 \\ 0 & 0 & 0 & 0 & 0 & 0 \\ 0 & 0 & 0 & 0 & 0 & 0 \end{bmatrix},$$

$$W_{31} = \begin{bmatrix} 0 & 0 & 0 & 0 & 0 & 0 \\ 0 & 0 & 0 & 0 & 0 & 0 \\ 1 & 0 & 0 & 0 & 0 & 0 \\ 0 & 0 & 0 & 0 & 0 & 0 \end{bmatrix},$$

$$W_{32} = \begin{bmatrix} 0 & 0 & 0 & 0 & 0 & 0 \\ 0 & 0 & 0 & 0 & 0 & 0 \\ 0 & 1 & 0 & 0 & 0 & 0 \\ 0 & 0 & 0 & 0 & 0 & 0 \end{bmatrix},$$

$$W_{33} = \begin{bmatrix} 0 & 0 & 0 & 0 & 0 & 0 \\ 0 & 0 & 0 & 0 & 0 & 0 \\ 0 & 0 & 1 & 0 & 0 & 0 \\ 0 & 0 & 0 & 0 & 0 & 0 \end{bmatrix},$$

$$W_{41} = \begin{bmatrix} 0 & 0 & 0 & 0 & 0 & 0 \\ 0 & 0 & 0 & 0 & 0 & 0 \\ 0 & 0 & 0 & 0 & 0 & 0 \\ 1 & 0 & 0 & 0 & 0 & 0 \end{bmatrix},$$

$$W_{43} = \begin{bmatrix} 0 & 0 & 0 & 0 & 0 & 0 \\ 0 & 0 & 0 & 0 & 0 & 0 \\ 0 & 0 & 0 & 0 & 0 & 0 \\ 0 & 0 & 1 & 0 & 0 & 0 \end{bmatrix},$$

$$Q_{11} = \begin{bmatrix} 1 & 0 & 0 & 0 \end{bmatrix},$$

$$Q_{12} = \begin{bmatrix} 0 & 1 & 0 & 0 \end{bmatrix},$$

$$Q_1 = \begin{bmatrix} 1 & 0 & 0 & 0 & 0 & 0 \end{bmatrix}^{\mathsf{T}},$$

$$U_{11} = \begin{bmatrix} 1 & 0 & 0 & 0 \\ 0 & 0 & 0 & 0 \\ 0 & 0 & 0 & 0 \\ 0 & 0 & 0 & 0 \\ 0 & 0 & 0 & 0 \\ 0 & 0 & 0 & 0 \end{bmatrix},$$

$$U_{41} = \begin{bmatrix} 0 & 0 & 0 & 0 \\ 0 & 0 & 0 & 0 \\ 0 & 0 & 0 & 0 \\ 1 & 0 & 0 & 0 \\ 0 & 0 & 0 & 0 \\ 0 & 0 & 0 & 0 \end{bmatrix},$$

$$CON_{COP_{ec}} = \begin{bmatrix} 1 & 0 & 0 & 0 \\ 0 & 0 & 0 & 0 \\ 0 & COP_{ec} & 0 & 0 \\ 0 & 0 & 0 & 0 \end{bmatrix},$$

$$CON_{\eta_h\eta_b} = \begin{bmatrix} 0 & 0 & 0 & 0 \\ 0 & 0 & 0 & 0 \\ 0 & 0 & 0 & 0 \\ \eta_h\eta_b & 0 & 0 & 0 \end{bmatrix}, \tag{30}$$

and

$$\begin{aligned} g_{211} &= \eta_{pgu}, \\ g_{221} &= 1, \\ g_{212} &= \eta_b COP_{orc}, \\ g_{213} &= \left(\left(1 - \eta_{pgu}\right)\eta_{hrs} - \eta_b\right) COP_{orc}, \\ g_{312} &= \eta_b COP_{ac}, \\ g_{313} &= -\eta_{pgu} COP_{ec}, \\ g_{321} &= -COP_{ec}, \\ g_{314} &= \eta_{pgu} COP_{ec}, \\ g_{412} &= \eta_h \eta_b, \\ g_{316} &= \eta_b COP_{orc} COP_{ec}, \\ g_{311} &= \left(\eta_{hrs} - \eta_{pgu}\eta_{hrs} - \eta_b\right) COP_{ac}, \\ g_{315} &= \left(\eta_{hrs} - \eta_{pgu}\eta_{hrs} - \eta_b\right) COP_{orc} COP_{ec}, \\ g_{411} &= \left(\eta_{hrs} - \eta_{pgu}\eta_{hrs} - \eta_b\right)\eta_h. \end{aligned} \tag{31}$$

Similarly, the system input V_i should also be represented by x as

$$V_i = Px, \tag{32}$$

where

$$P = \begin{bmatrix} 0 & 0 & 0 & 0 & 1 & 0 \\ 0 & 0 & 0 & 0 & 0 & 1 \\ 0 & 0 & 0 & 0 & 0 & 0 \\ 0 & 0 & 0 & 0 & 0 & 0 \end{bmatrix}. \tag{33}$$

Then the nonlinear equality constraint in (14) becomes

$$\begin{aligned} &\left(g_{211}W_{22} + g_{311}W_{33} + g_{313}W_{32} + g_{315}W_{34} - g_{411}W_{43}\right) \\ &\quad \cdot xx^{\mathsf{T}}U_{11}Px + \left(g_{312}W_{33} + g_{314}W_{31} + g_{316}W_{34}\right. \\ &\quad \left. + g_{411}W_{41} - g_{412}W_{43}\right) xQ_{11}Px + \left(g_{212}W_{22}\right. \\ &\quad \left. - g_{316}W_{32} + \left(g_{213}W_{22} - g_{315}W_{32}\right)\left(x^{\mathsf{T}}Q_1\right)\right) \\ &\quad \cdot xx^{\mathsf{T}}U_{41}Px + \left(g_{221}W_{22} + g_{321}W_{32}\right) xQ_{12}Px \\ &\quad + \left(CON_{cop_{ec}} + CON_{\eta_h\eta_b}\right) Px - V_o = 0. \end{aligned} \tag{34}$$

3.2.4. Inequality Constraints. The inequality constraints include the bound of the decision variables, various capacities of system components, and thresholds of the components output. The decision variables can be separated into two parts: one consists of dispatch factors, and the other consists of system input. To facilitate the later derivation, we define $\boldsymbol{\alpha}$ dispatch factor vector as

$$\boldsymbol{\alpha} = \begin{bmatrix} \alpha_{pgu} & \alpha_{user} & \alpha_{ac} & \alpha_{orc} \end{bmatrix}^{\mathsf{T}}. \tag{35}$$

According to (7a), (7b), (7c), (7d) and (11a), (11b), (11c), (11d), we have

$$-\boldsymbol{\alpha} \le \mathbf{0}, \tag{36a}$$

$$\boldsymbol{\alpha} - \mathbf{1} \le \mathbf{0}. \tag{36b}$$

In this paper, we assume that no electricity would be sold back; thus the constraints for fuel and electricity input can be represented by

$$\boldsymbol{\beta} = \left[F_m \quad E_{grid}\right]^{\mathsf{T}}. \tag{37}$$

$$-\boldsymbol{\beta} \le \mathbf{0}. \tag{38}$$

Inequalities in (36a), (36b), and (38) are linear inequality constraints seeing as the bounds of the decision variables.

Each component in the CCHP-ORC system has a specific capacity, which is the output upper bound. Denote F_{orcm} the capacity of ORC; then the upper bound of the ORC output can be represented as

$$\overline{V}_o^{orc} = \begin{bmatrix} 0 \\ \overline{E}_o^{orc} \\ 0 \\ 0 \end{bmatrix} = \begin{bmatrix} 0 \\ F_{orcm} COP_{orc} \\ 0 \\ 0 \end{bmatrix}. \tag{39}$$

The output upper bound of the PGU, heat recovery system, auxiliary boiler, electric chiller, absorption chiller, and heating unit can be denoted as $\overline{V}_o^{pgu}$, $\overline{V}_o^{hrs}$, $\overline{V}_o^{b}$, $\overline{V}_o^{ec}$, $\overline{V}_o^{ac}$, and $\overline{V}_o^{h}$ and defined in a similar way as in (39), respectively.

In addition, the lower bound of the ORC, PGU, heat recovery system, auxiliary boiler, electric chiller, absorption chiller, and heating unit can be denoted as V_o^{orc}, $\underline{V}_o^{pgu}$, $\underline{V}_o^{hrs}$, $\underline{V}_o^{b}$, $\underline{V}_o^{ec}$, $\underline{V}_o^{ac}$, and $\underline{V}_o^{h}$. The lower bound of a component implies that the output will be cut down when the expected output of the component is lower than this bound. In this paper, the lower bound can be set as 5 percent of the maximum capacity of each component.

Based on the above discussions, the bounding conditions for component output can be represented by

$$H^m V_i^m - \overline{V}_o^m \le 0, \tag{40a}$$

$$\underline{V}_o^m - H^m V_i^l \le 0. \tag{40b}$$

Then from (9) and (32), (40a), (40b) can be rewritten as

$$H^m T_m P x - \overline{V}_o^m \le 0, \tag{41a}$$

$$\underline{V}_o^m - H^m T_m P x \le 0, \tag{41b}$$

where T_m is the dispatch matrix for the component m in the CCHP-ORC system and can also be represented by the function of x by following the similar procedure of deriving (29) as

$$\begin{aligned} T_{pgu} &= W_{11} x Q_{11}, \\ T_b &= I_{11} - W_{11} x Q_{11}, \\ T_{hrs} &= \delta_1 W_{41} x Q_{11}, \\ T_{ec} &= I_{22} - W_{22} x Q_{12}, \\ T_{ac} &= \delta_2 W_{43} x x^T U_{11} + \delta_3 W_{43} x Q_{11}, \\ T_h &= -\delta_2 W_{43} x x^T U_{11} + \left(\delta_2 W_{41} - \delta_3 W_{43}\right) x Q_{11} \\ &\quad + CON_{\eta_b}, \\ T_{orc} &= \delta_2 W_{44} x x^T U_{11} + \delta_3 W_{44} x Q_{11}, \end{aligned} \tag{42}$$

where

$$W_{11} = \begin{bmatrix} 1 & 0 & 0 & 0 & 0 & 0 \\ 0 & 0 & 0 & 0 & 0 & 0 \\ 0 & 0 & 0 & 0 & 0 & 0 \\ 0 & 0 & 0 & 0 & 0 & 0 \end{bmatrix},$$

$$W_{44} = \begin{bmatrix} 0 & 0 & 0 & 0 & 0 & 0 \\ 0 & 0 & 0 & 0 & 0 & 0 \\ 0 & 0 & 0 & 0 & 0 & 0 \\ 0 & 0 & 0 & 1 & 0 & 0 \end{bmatrix},$$

$$I_{11} = \begin{bmatrix} 1 & 0 & 0 & 0 \\ 0 & 0 & 0 & 0 \\ 0 & 0 & 0 & 0 \\ 0 & 0 & 0 & 0 \end{bmatrix}, \tag{43}$$

$$I_{22} = \begin{bmatrix} 0 & 0 & 0 & 0 \\ 0 & 1 & 0 & 0 \\ 0 & 0 & 0 & 0 \\ 0 & 0 & 0 & 0 \end{bmatrix},$$

$$CON_{\eta_b} = \begin{bmatrix} 0 & 0 & 0 & 0 \\ 0 & 0 & 0 & 0 \\ 0 & 0 & 0 & 0 \\ \eta_b & 0 & 0 & 0 \end{bmatrix},$$

and $\delta_1 = 1 - \eta_{pgu}$, $\delta_2 = g_{411}/\eta_h$, and $\delta_3 = g_{412}/\eta_h$.

Therefore, (36a), (36b), and (38) are the linear inequality constraints, and (41a) and (41b) are the nonlinear inequality constraint of the optimization problem. The optimal solution can be obtained by solving

$$\begin{aligned} \min_x \quad & \omega_1 \frac{Bx}{PEC^{SP}} + \omega_2 \frac{Cx + L}{HTC^{SP}} + \omega_3 \frac{Dx}{CDE^{SP}} \\ \text{s.t.} \quad & (34), (36a), (36b), (38), (41a), \text{and } (41b). \end{aligned} \tag{44}$$

The objective function integrates three aspects, i.e., PEC, HTC, and CDE, into it, and it is comprehensive. Three weights ω_1, ω_2, and ω_3, can be selected according to different requirements. For example, if more priority is need to be given to environmental factors, the carbon dioxide emission (CDE) should be put on more emphasis, then ω_3 is raised, and ω_1 and ω_2 are accordingly decreased.

Table 1: Construction parameters of the office building.

Parameters	Values
Each floor area	1200 m^2 (30m × 40m)
Each floor height	3.2 m
Glass area	38% in each wall
Glazing heat transfer coefficient	4.128 W/(m^2K)
Exterior wall heat transfer coefficient	0.440 W/(m^2K)
Interior wall heat transfer coefficient	0.716 W/(m^2K)
Floor heat transfer coefficient	2.300 W/(m^2K)
Roof heat transfer coefficient	0.368 W/(m^2K)
Electric equipment, lights, and people densities	According to Wuhan's energy-saving design standard

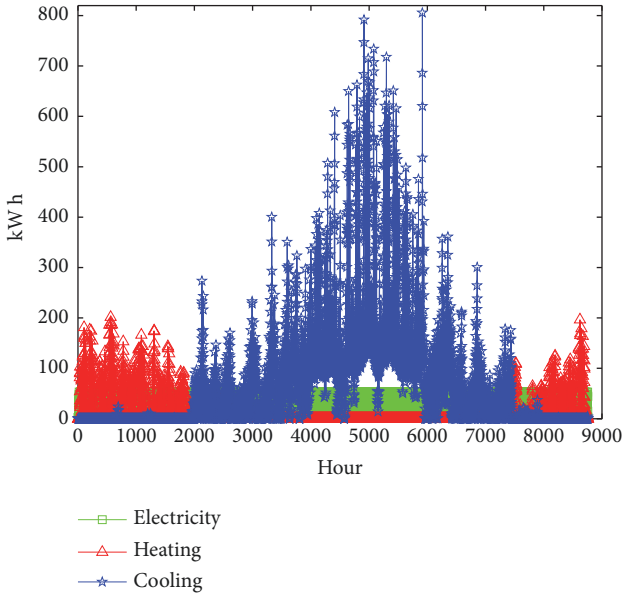

Figure 2: One-year energy consumption.

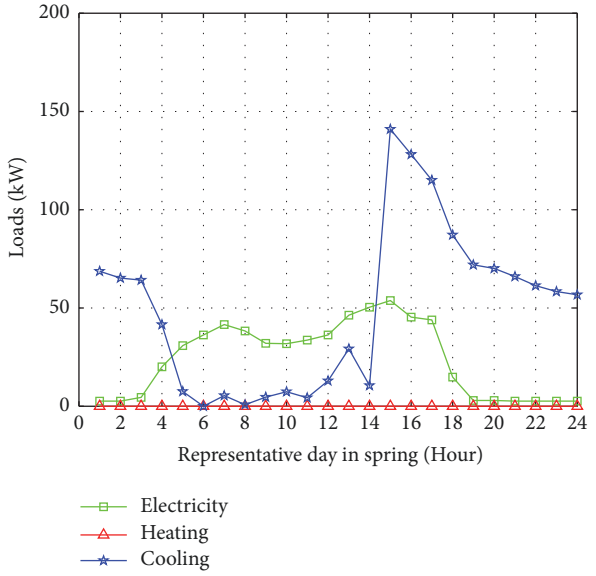

Figure 3: Hourly energy requirements in a spring day.

4. Case Study

4.1. Description of a Hypothetical Building. In this section, a CCHP-ORC system is installed for a hypothetical office building in Wuhan, Hubei, China, because the CCHP-ORC system is more suitable to the commercial building and the office building with low ratio of heat to power demand [35]. We chose EnergyPlus [38, 39] to analyze energy consumption of this building. This building is assumed to operate all year round and has five floors with a total construction area of 6000m^2. The first floor consists of 400m^2 exhibition halls and 800m^2 office rooms. The second to the fifth floors are office rooms. Some important construction parameters of the hypothetical office building are listed in Table 1.

The hourly cooling, heating, and power requirements in one year of the hypothetical office building are shown in Figure 2.

To ease the performance comparison, the hourly cooling, heating, and power requirements in representative days of spring, summer, autumn, and winter are shown in Figures 3–6, respectively.

From Figures 2–6, it can be noticed that the cooling requirements in summer are the most, the heating requirements in winter are more than those of other seasons, and the electricity requirements are substantially the same for each season.

4.2. Simulation Parameters. Table 2 shows a set of technical parameters of the installed CCHP-ORC system for the hypothetical building. In this paper, the fuel is the natural gas which is widely used in China. The gas turbine is chosen as PGU. For performance comparison, some parameters of a conventional CCHP system, coefficient of performance, and efficiency of the components in the CCHP-ORC system, conversion factors, and weight factors are included in Table 2. The weighting factors of the evaluation criteria can be chosen to satisfy different requirements. Some parameters listed in Table 2 fluctuate with the market, such as price of electricity, natural gas, and carbon tax. Most of the system parameters can be gotten from equipment manual and some references.

Table 2: System coefficients.

Symbol	Variable	Value
η_{pgu}	Efficiency of PGU in CCHP-ORC system	0.35
η_e^{SP}	Generation efficiency SP system	0.40
η_h	Efficiency of heating unit	0.78
η_b	Efficiency of auxiliary boiler	0.78
η_{hrs}	Efficiency of heat recovery system	0.81
COP_{orc}	Coefficient of performance of ORC	0.17
COP_{ac}	Coefficient of performance of absorption chiller	0.72
COP_{ec}	Coefficient of performance of electric chiller	2.98
η_{grid}	Transmission efficiency of local grid	0.92
μ_e	CO_2 emission conversion factor of electricity (g/kW h)	970
μ_f	CO_2 emission conversion factor of natural gas (g/kW h)	218
C_c	Carbon tax rates (yuan/kW h)	0.00002
C_e	Electricity rates (yuan/kW h)	0.642
C_f	Natural gas rates (yuan/kW h)	0.375
C_{pgu}	Unit price of PGU (yuan/kW h)	6800
C_b	Unit price of auxiliary boiler (yuan/kW h)	300
C_h	Unit price of heating unit (yuan/kW h)	200
C_{ac}	Unit price of absorption chiller (yuan/kW h)	1200
C_{ec}	Unit price of electric chiller (yuan/kW h)	970
C_{orc}	Unit price of ORC (yuan/kW)	12000
L	Facilities' lives (year)	20
ω_1	Coefficient of PEC	0.6
ω_2	Coefficient of HTC	0.3
ω_3	Coefficient of CDE	0.1

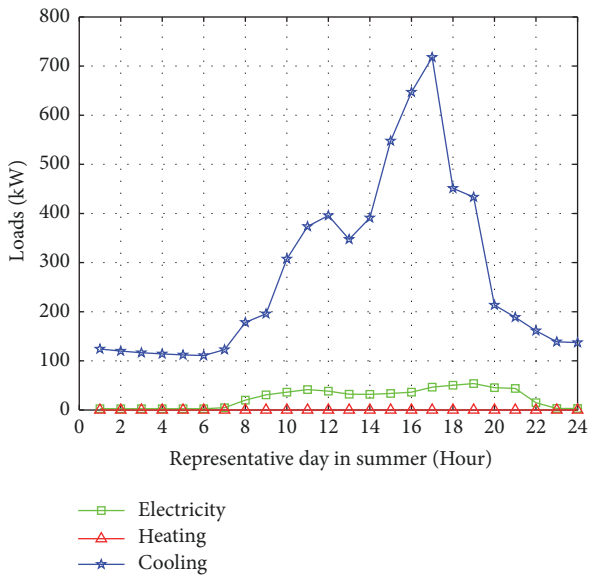

Figure 4: Hourly energy requirements in a summer day.

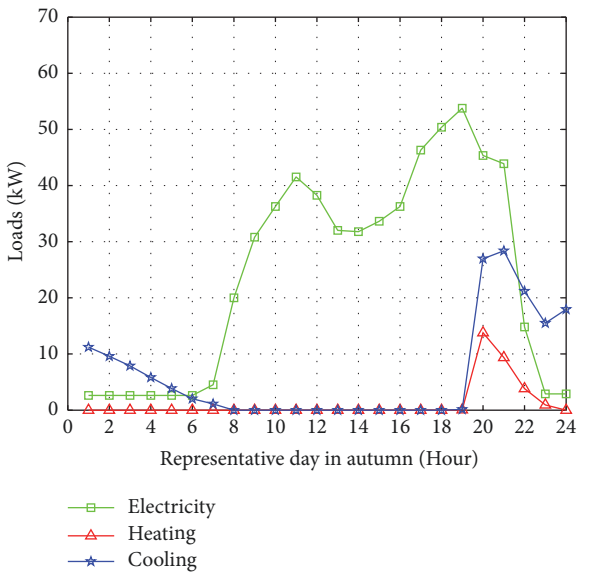

Figure 5: Hourly energy requirements in a autumn day.

4.3. Test Result. SQP algorithms have been proved highly effective for solving general constrained problems with smooth objective and constraint functions [40]. In this paper, we chose SQP algorithms to solve the optimization problem established in Section 3.2. In order to accelerate the convergence, some feasible initial points which are calculated from FEL and FTL strategies are manually designated. So the

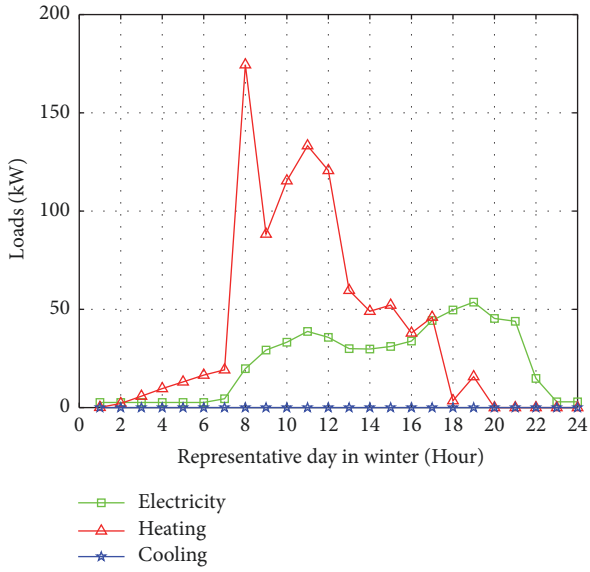

Figure 6: Hourly energy requirements in a winter day.

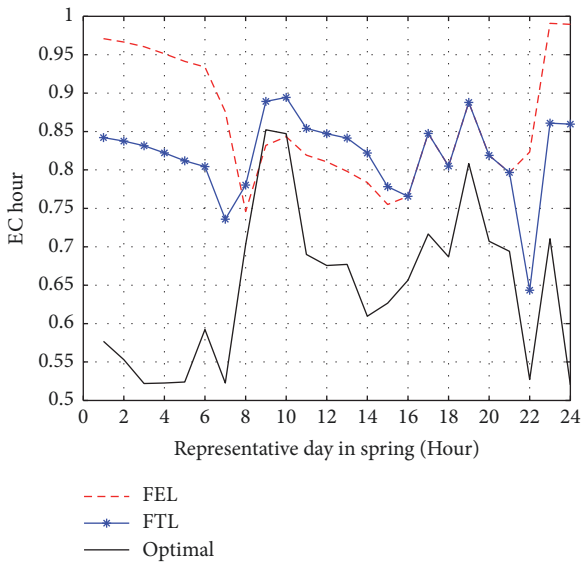

Figure 7: Comparison of three strategies in a spring day.

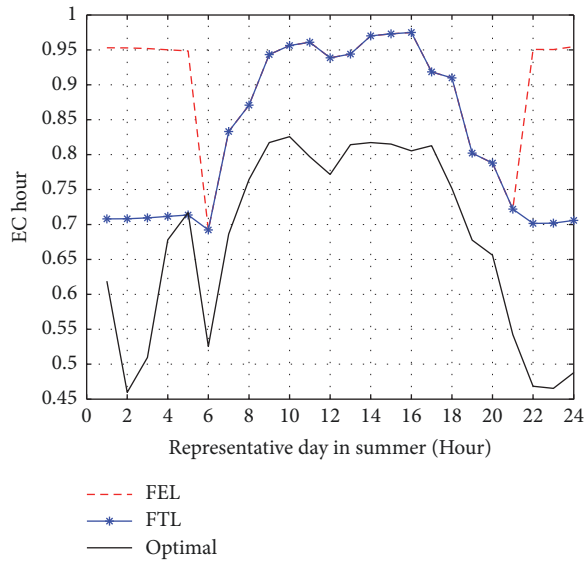

Figure 8: Comparison of three strategies in a summer day.

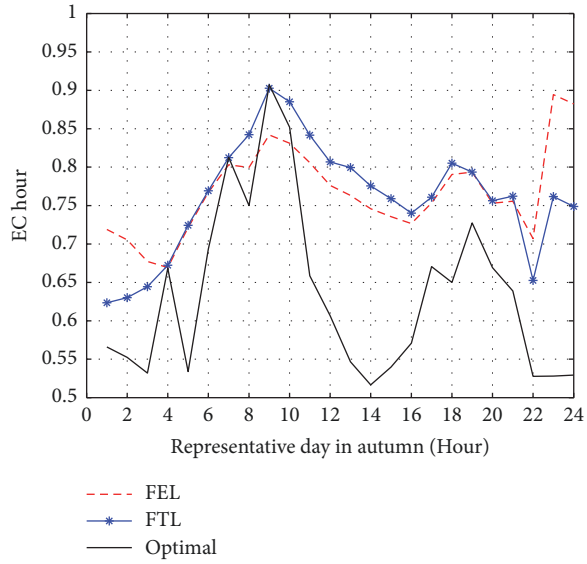

Figure 9: Comparison of three strategies in an autumn day.

local optimal solution can be avoided and the convergence time is significantly reduced.

The constructed optimization problem is solved in MATLAB by using fmincon.m. The computer used to solve this problem is configured with 2.6 GHz Intel Core i5-3230M processor and 4 GB 1067 MHz memory. Time elapsed for each step of optimization is about 0.25*s*. This time is much shorter than one hour; in other words, the optimal energy flow and operation strategy for the next hour can be quickly obtained at the beginning of this hour. Thus, we can say that the optimization method is appropriate for practical use.

The performance comparison of FEL, FTL, and the proposed optimal operation strategy is shown in Figures 7–10 which includes spring, summer, autumn, and winter, respectively. From Figures 8 and 10, all EC_{hour} values of the optimal operation strategy are obviously less than those of the FEL and FTL strategies. From Figures 7 and 9, most EC_{hour} values are also obviously less than those of FEL and FTL except 8:00-10:00. Because it is the beginning working time during 8:00-10:00, electricity requirements are very large, and there are almost no heating and cooling requirements. Taking into account the full day values, the performance of the optimal operation strategy is much better than that of FEL and FTL strategies. In spring, summer, and autumn, especially in the morning and in the evening, the optimal energy flow has excellent performance, while in the middle of a day, the advantage is not that evident. In winter, the performance in the middle of a day is much better than that in the morning and in the evening.

Table 3: Equipment's capacities.

Items	PGU	ORC	Auxiliary boiler	Electric chiller	Absorption chiller	Heating coil
CCHP (kW)	100	-	200	450	450	220
CCHP-ORC (kW)	80	20	100	450	450	220

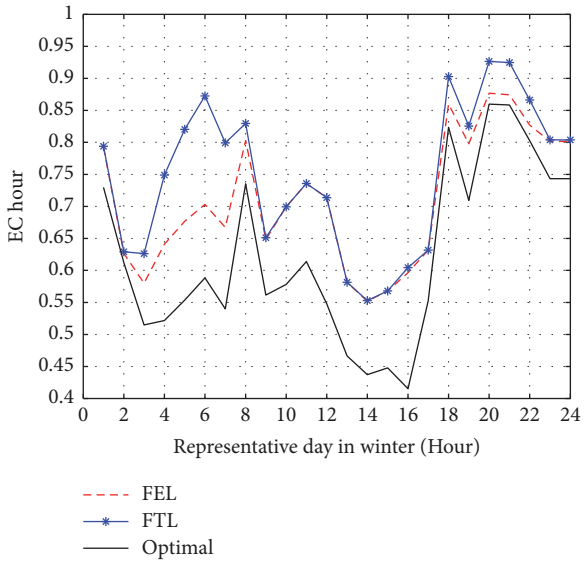

Figure 10: Comparison of three strategies in a winter day.

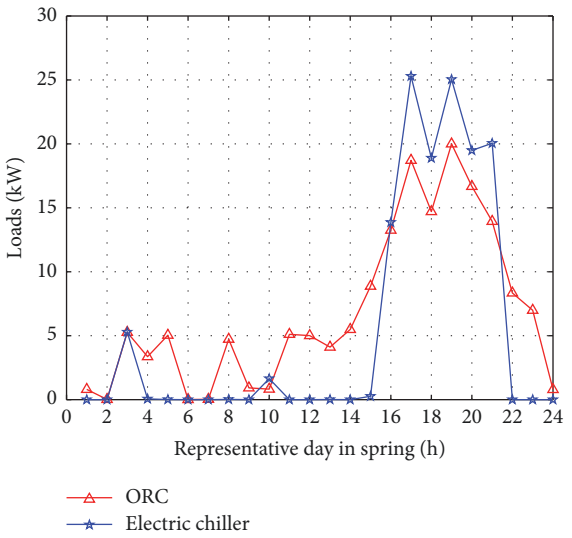

Figure 11: Hourly outputs of the EC and ORC in a spring day.

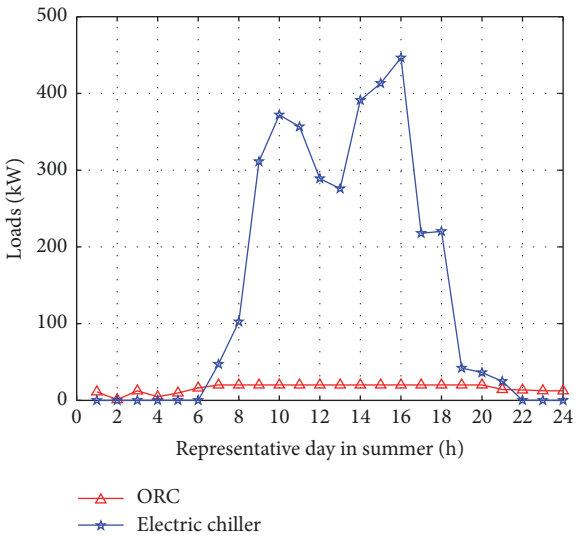

Figure 12: Hourly outputs of the EC and ORC in a summer day.

The reason for the proposed optimal operation strategy performing better than FEL and FTL strategies is that both FEL and FTL strategies are inevitably wasting energy. When operating at FEL mode, electricity for the building is firstly satisfied, and then if the thermal energy provided by PGU cannot meet the thermal demand, the auxiliary boiler will be activated; if the thermal supply exceeds the thermal demand, the excess thermal energy will be wasted. When operating at FTL mode, the thermal requirements are firstly satisfied, and then if the electricity provided by PGU cannot meet the electricity demand, additional electricity should be purchased from the power grid; if the electricity provided by PGU is sufficient, a certain amount of electricity will be wasted.

The CCHP-ORC system includes ORC component as a power generator to make full use of excess thermal energy, and its integration with CCHP system has good application prospects. According to the energy requirements in representative days shown in Figures 3–6, the hourly outputs of the electric chiller and the ORC in representative days can be calculated as Figures 11–14.

From Figures 11–14, we can find that the electric chiller has high utilization rate in summer because of the high temperature in Wuhan, and the ORC plays a significant role in other three seasons.

Substituting the primary energy consumptions, the daily total cost, and the carbon dioxide emission into (20)–(22), the daily performance criteria (i.e., PEC, DTC, CDE) for the CCHP-ORC and the CCHP system can be calculated. Capacities of all equipment in the CCHP-ORC and CCHP system are listed in Table 3.

In Table 3, the capacity of PGU in the CCHP system is 100 kW, which is searched in $[1, 500]$ with the whole year (8760h) data using enumeration algorithm. In the CCHP-ORC system, ORC is combined as power generator. In order to satisfy the power requirements, the sum capacity of PGU and ORC should be equal 100kW which is the optimal

Table 4: Performance comparisons of the CCHP-ORC system and the CCHP system.

Representative days	PEC(kWh)		DTC(Yuan)		CDE(g)	
	CCHP	CCHP-ORC	CCHP	CCHP-ORC	CCHP	CCHP-ORC
Spring day	3374.1	3230.9	1021.2	992.5	821740.0	790230.0
Summer day	11909.0	11455.0	3077.7	2986.7	2956700.0	2856900.0
Autumn day	2247.1	2214.3	762.5	758.3	548660.0	543260.0
Winter day	2626.3	2618.6	869.9	817.0	648430.0	607230.0

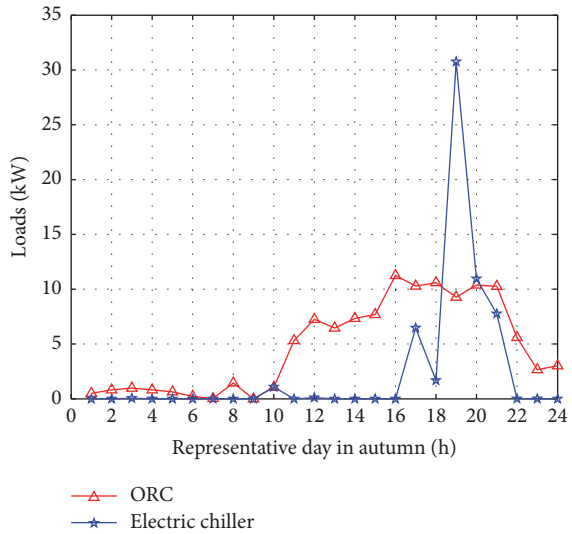

Figure 13: Hourly outputs of the EC and ORC in an autumn day.

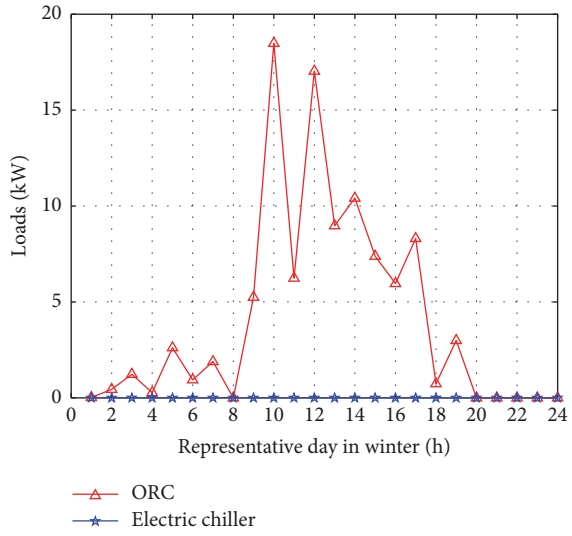

Figure 14: Hourly outputs of the EC and ORC in a winter day.

capacity in the CCHP system. In addition, efficiency of PGU is higher than that of the ORC. For the office building with low ratio of heat to power demand, power requirements are more than other requirements, so the capacity of PGU should be far larger than that of ORC. Through enumeration, the optimal capacity of PGU and ORC is 80kW and 20kW, respectively.

The performance comparisons of the CCHP-ORC system and the CCHP system are shown in Table 4. It is clear that all the performance values of the CCHP-ORC system are smaller than those of the CCHP system and the performances of the CCHP-ORC system are better than those of the CCHP system. The integration of ORC and PGU can improve the energy efficiency and reduce the capacity requirements of the auxiliary boiler and PGU. With the reduction of the ORC's price, the superiority of the CCHP-ORC system will be more and more outstanding.

If we assume that the price of ORC is about 100000 Yuan, from Table 4, we only consider the PEC and DTC, we can find the whole year's PEC saving is 58190.13 Yuan, the total consumption reduction is 16123.88 Yuan, and the sum of the whole year's PEC saving and the total consumption reduction is 74314 Yuan. So the CCHP-ORC system runs 1 year and 4 months, and the cost of ORC is recovered.

5. Conclusion

A complementary configuration of the CCHP-ORC system is investigated to further improve the utilization efficiency of the excess thermal energy from the CCHP system. A comprehensive and systematic matrix modeling approach is proposed to describe the CCHP-ORC system. The matrix model includes efficiency matrices of system components, system conversion matrix, and dispatch factors. The optimal operation strategy is obtained by solving the optimization problem. Both economic and environmental factors are considered in the objective function of the optimal operation strategy design. The weights of economic and environmental factors can be changed according to different requirements. At last, an illustrative case study is conducted to show that the effectiveness and economic efficiency of the proposed approaches outperform those obtained from conventional CCHP systems.

The main challenges of applying this method to real system are that some uncertainties in the CCHP-ORC system exist; for example, a likely source of uncertainty in the heat exchanger components of the CCHP-ORC system is fouling. The efficiencies of heat exchanger components are changed. In real system, we should consider these uncertainties by adding an error of less than 5% of the nominal value of the parameters.

The main problem of the CCHP-ORC system is high investment cost of the ORC. However the unit price of the ORC will continually decline because of the technology maturing in recent years. Therefore the CCHP-ORC system

will be more attractive and valuable. In addition, all calculation in this paper is based on an accurate load profile. While, in practical applications, accurate load profile does not exist, therefore, in future work, accurate load forecasting should be considered. In a further step, excess electricity sold back feature can be considered. In recent years, with the development of the renewable energy including solar energy, wind energy, and tide energy, more and more renewable energy should be incorporated into the CCHP system to make the trigeneration system more efficient.

Nomenclature

CCHP: Combined cooling, heating, and power
CDE: Carbon dioxide emission
COP: Coefficient of performance
DTC: Daily total cost
EC: Evaluation criteria
FEL: Following the electric load
FTL: Following the thermal load
HTC: Hourly total cost
ORC: Organic Rankine cycles
PEC: Primary energy consumption
PGU: Power generation unit
SP: Separation production.

Symbols

C: Cost
E: Electricity
F: Fuel
L: Facility life
N: Installed power
Q: Thermal energy
η: Efficiency
μ: Carbon conversion factor.

Subscripts

ac: Absorption chiller
annual: Annual value
b: Auxiliary boiler
c: Cooling
ca: Carbon
e: Electricity
ec: Electric chiller
f: Fuel
grid: Local power grid
h: Heating
hour: Hourly value
hrc: Recovered heat cooling
hrh: Recovered heat heating
m: Total consumption
orc: Organic Rankine cycles
p: Parasitic
pgu: Power generation unit
pgum: Capacity of PGU
r: Recovered.

Superscripts

SP: SP system.

Data Availability

All research data reported in this article are available. All of these data can be obtained free of charge. If you want to get these data, you can directly contact Yufang Chang; her email is changyf@hbut.edu.cn.

Conflicts of Interest

The authors declare that they have no conflicts of interest.

Acknowledgments

This work has been supported in part by the Green Industry Leading Program of Hubei University of Technology (CPYF2017003), the National Nature Science Fund of China (61601176) and the National Nature Science Fund of China (41601394).

References

[1] United State Environmental Protection Agency, *Epa green building strategy*, 2016, http://www.epa.gov/greenbuilding/pubs/about.htm.

[2] Chinese Electricity Council, *China Power Industry Annual Development Report 2011*, China Market Press, Beijing, China, 2011.

[3] W. Jiang-Jiang, Z. Chun-Fa, and J. You-Yin, "Multi-criteria analysis of combined cooling, heating and power systems in different climate zones in China," *Applied Energy*, vol. 87, no. 4, pp. 1247–1259, 2010.

[4] Y. Shi, M. Liu, and F. Fang, *Combined Cooling, Heating, and Power Systems: Modeling, Optimization, and Operation*, John Wiley & Sons, 2017.

[5] M. Liu, Y. Shi, and F. Fang, "Combined cooling, heating and power systems: a survey," *Renewable & Sustainable Energy Reviews*, vol. 35, pp. 1–22, 2014.

[6] S. Murugan and B. Horák, "Tri and polygeneration systems-a review," *Renewable & Sustainable Energy Reviews*, vol. 60, pp. 1032–1051, 2016.

[7] J.-J. Wang, Y.-Y. Jing, and C.-F. Zhang, "Optimization of capacity and operation for CCHP system by genetic algorithm," *Applied Energy*, vol. 87, no. 4, pp. 1325–1335, 2010.

[8] A. Mohamed, M. Hamdy, A. Hasan, and K. Sirén, "The performance of small scale multi-generation technologies in achieving cost-optimal and zero-energy office building solutions," *Applied Energy*, vol. 152, pp. 94–108, 2015.

[9] N. Fumo, P. J. Mago, and L. M. Chamra, "Analysis of cooling, heating, and power systems based on site energy consumption," *Applied Energy*, vol. 86, no. 6, pp. 928–932, 2009.

[10] F. Fang, Q. H. Wang, and Y. Shi, "A novel optimal operational strategy for the CCHP system based on two operating modes," *IEEE Transactions on Power Systems*, vol. 27, no. 2, pp. 1032–1041, 2012.

[11] M. Liu, Y. Shi, and F. Fang, "A new operation strategy for CCHP systems with hybrid chillers," *Applied Energy*, vol. 95, pp. 164–173, 2012.

[12] D. W. Wu and R. Z. Wang, "Combined cooling, heating and power: a review," *Progress in Energy and Combustion Science*, vol. 32, no. 5-6, pp. 459–495, 2006.

[13] E. A. Tora and M. M. El-Halwagi, "Integrated conceptual design of solar-assisted trigeneration systems," *Computers & Chemical Engineering*, vol. 35, no. 9, pp. 1807–1814, 2011.

[14] X. Meng, F. Yang, Z. Bao, J. Deng, N. N. Serge, and Z. Zhang, "Theoretical study of a novel solar trigeneration system based on metal hydrides," *Applied Energy*, vol. 87, no. 6, pp. 2050–2061, 2010.

[15] F. Calise, M. Dentice d'Accadia, A. Palombo, and L. Vanoli, "Dynamic simulation of a novel high-temperature solar trigeneration system based on concentrating photovoltaic/thermal collectors," *Energy*, vol. 61, pp. 72–86, 2013.

[16] A. Nosrat and J. M. Pearce, "Dispatch strategy and model for hybrid photovoltaic and trigeneration power systems," *Applied Energy*, vol. 88, no. 9, pp. 3270–3276, 2011.

[17] J. Wang, Y. Dai, L. Gao, and S. Ma, "A new combined cooling, heating and power system driven by solar energy," *Journal of Renewable Energy*, vol. 34, no. 12, pp. 2780–2788, 2009.

[18] A. Baghernejad, M. Yaghoubi, and K. Jafarpur, "Exergoeconomic comparison of three novel trigeneration systems using SOFC, biomass and solar energies," *Applied Thermal Engineering*, vol. 104, pp. 534–555, 2016.

[19] K. F. Fong and C. K. Lee, "Investigation on zero grid-electricity design strategies of solid oxide fuel cell trigeneration system for high-rise building in hot and humid climate," *Applied Energy*, vol. 114, pp. 426–433, 2014.

[20] M. Puig-Arnavat, J. C. Bruno, and A. Coronas, "Modeling of trigeneration configurations based on biomass gasification and comparison of performance," *Applied Energy*, vol. 114, pp. 845–856, 2014.

[21] P. J. Mago and L. M. Chamra, "Analysis and optimization of CCHP systems based on energy, economical, and environmental considerations," *Energy and Buildings*, vol. 41, no. 10, pp. 1099–1106, 2009.

[22] P. J. Mago, N. Fumo, and L. M. Chamra, "Performance analysis of CCHP and CHP systems operating following the thermal and electric load," *International Journal of Energy Research*, vol. 33, no. 9, pp. 852–864, 2009.

[23] S. Cao, A. Mohamed, A. Hasan, and K. Sirén, "Energy matching analysis of on-site micro-cogeneration for a single-family house with thermal and electrical tracking strategies," *Energy and Buildings*, vol. 68, pp. 351–363, 2014.

[24] J.-J. Wang, Y.-Y. Jing, C.-F. Zhang, and Z. J. Zhai, "Performance comparison of combined cooling heating and power system in different operation modes," *Applied Energy*, vol. 88, no. 12, pp. 4621–4631, 2011.

[25] N. Fumo and L. M. Chamra, "Analysis of combined cooling, heating, and power systems based on source primary energy consumption," *Applied Energy*, vol. 87, no. 6, pp. 2023–2030, 2010.

[26] P. J. Mago, L. M. Chamra, and J. Ramsay, "Micro-combined cooling, heating and power systems hybrid electric-thermal load following operation," *Applied Thermal Engineering*, vol. 30, no. 8-9, pp. 800–806, 2010.

[27] C. Z. Li, Y. M. Shi, and X. H. Huang, "Sensitivity analysis of energy demands on performance of CCHP system," *Energy Conversion and Management*, vol. 49, no. 12, pp. 3491–3497, 2008.

[28] J. Wang, Z. J. Zhai, Y. Jing, and C. Zhang, "Particle swarm optimization for redundant building cooling heating and power system," *Applied Energy*, vol. 87, no. 12, pp. 3668–3679, 2010.

[29] Y.-Y. Jing, H. Bai, J.-J. Wang, and L. Liu, "Life cycle assessment of a solar combined cooling heating and power system in different operation strategies," *Applied Energy*, vol. 92, pp. 843–853, 2012.

[30] Y.-Y. Jing, H. Bai, and J.-J. Wang, "Multi-objective optimization design and operation strategy analysis of BCHP system based on life cycle assessment," *Energy*, vol. 37, no. 1, pp. 405–416, 2012.

[31] F. Fang, L. Wei, J. Liu, J. Zhang, and G. Hou, "Complementary configuration and operation of a CCHP-ORC system," *Energy*, vol. 46, no. 1, pp. 211–220, 2012.

[32] Z. Li, W. Li, and B. Xu, "Optimization of mixed working fluids for a novel trigeneration system based on organic Rankine cycle installed with heat pumps," *Applied Thermal Engineering*, vol. 94, pp. 754–762, 2016.

[33] Y. Huang, Y. D. Wang, S. Rezvani et al., "A techno-economic assessment of biomass fuelled trigeneration system integrated with organic rankine cycle," *Applied Thermal Engineering*, vol. 53, no. 2, pp. 325–331, 2013.

[34] F. A. Al-Sulaiman, I. Dincer, and F. Hamdullahpur, "Thermoeconomic optimization of three trigeneration systems using organic rankine cycles: part i - formulations," *Energy Conversion and Management*, vol. 69, pp. 199–208, 2013.

[35] H. Liu, T. Zhu, and T. Zhang, "Evaluation and analysis of CCHP-ORC system for different buildings in Shanghai," *Zhongguo Dianji Gongcheng Xuebao/Proceedings of the Chinese Society of Electrical Engineering*, vol. 36, no. 12, pp. 3198–3205, 2016.

[36] M. Geidl and G. Andersson, "Optimal power flow of multiple energy carriers," *IEEE Transactions on Power Systems*, vol. 22, no. 1, pp. 145–155, 2007.

[37] G. Chicco and P. Mancarella, "Matrix modelling of small-scale trigeneration systems and application to operational optimization," *Energy*, vol. 34, no. 3, pp. 261–273, 2009.

[38] US Department of Energy, "Energy plus," https://energyplus.net/.

[39] N. Fumo, P. Mago, and R. Luck, "Methodology to estimate building energy consumption using energyplus benchmark models," *Energy and Buildings*, vol. 42, no. 12, pp. 2331–2337, 2010.

[40] A. Antoniou and W.-S. Lu, *Practical Optimization: Algorithms and Engineering Applications*, Springer, New York, NY, USA, 2007.